A large offshore oil platform with several cranes, situated in the ocean under a clear blue sky. The platform is a complex of steel structures with multiple levels and a central derrick.

# Essentials of Offshore Structures Framed and Gravity Platforms

D.V. Reddy and A.S.J. Swamidas



CRC Press  
Taylor & Francis Group



Essentials of  
Offshore Structures  
Framed and Gravity Platforms





# Essentials of Offshore Structures

---

## Framed and Gravity Platforms

D.V. Reddy  
A.S.J. Swamidas



**CRC Press**

Taylor & Francis Group

Boca Raton London New York

---

CRC Press is an imprint of the  
Taylor & Francis Group, an **informa** business

Cover photo courtesy of Hibernia Management and Development Company Ltd.

CRC Press  
Taylor & Francis Group  
6000 Broken Sound Parkway NW, Suite 300  
Boca Raton, FL 33487-2742

© 2014 by Taylor & Francis Group, LLC  
CRC Press is an imprint of Taylor & Francis Group, an Informa business

No claim to original U.S. Government works  
Version Date: 20130528

International Standard Book Number-13: 978-1-4822-2018-6 (eBook - PDF)

This book contains information obtained from authentic and highly regarded sources. Reasonable efforts have been made to publish reliable data and information, but the author and publisher cannot assume responsibility for the validity of all materials or the consequences of their use. The authors and publishers have attempted to trace the copyright holders of all material reproduced in this publication and apologize to copyright holders if permission to publish in this form has not been obtained. If any copyright material has not been acknowledged please write and let us know so we may rectify in any future reprint.

Except as permitted under U.S. Copyright Law, no part of this book may be reprinted, reproduced, transmitted, or utilized in any form by any electronic, mechanical, or other means, now known or hereafter invented, including photocopying, microfilming, and recording, or in any information storage or retrieval system, without written permission from the publishers.

For permission to photocopy or use material electronically from this work, please access [www.copyright.com](http://www.copyright.com) (<http://www.copyright.com/>) or contact the Copyright Clearance Center, Inc. (CCC), 222 Rosewood Drive, Danvers, MA 01923, 978-750-8400. CCC is a not-for-profit organization that provides licenses and registration for a variety of users. For organizations that have been granted a photocopy license by the CCC, a separate system of payment has been arranged.

**Trademark Notice:** Product or corporate names may be trademarks or registered trademarks, and are used only for identification and explanation without intent to infringe.

**Visit the Taylor & Francis Web site at**  
**<http://www.taylorandfrancis.com>**

**and the CRC Press Web site at**  
**<http://www.crcpress.com>**

*To the Almighty Creator of Planet Ocean, with its  
vast resources and mighty challenges.*



---

# Contents

Preface.....	xv
Authors.....	xvii
<b>Chapter 1</b> Offshore Operations and Structural Development.....	1
1.1 Introduction .....	1
1.2 Current State of the Industry .....	3
1.3 Commercial Projections for the Offshore Industry .....	6
1.4 Structural Concept Evaluation and Innovative Developments .....	15
1.5 Legal Jurisdiction .....	30
1.6 History of Offshore Structural Development .....	32
Exercise Problems .....	35
Appendix .....	39
References .....	43
<b>Chapter 2</b> Components of a Typical Offshore Structure.....	47
2.1 Introduction .....	47
2.2 Functional and Structural Requirements of an Offshore Platform .....	50
2.3 Components of a Fixed Jacket Steel Platform .....	51
2.3.1 Jacket Substructure.....	53
2.3.2 Pile Foundation .....	58
2.4 Components of a Steel Jack-Up Platform .....	60
2.5 Components of a Concrete Gravity Platform .....	63
2.6 Components of a Ship Structure.....	70
2.6.1 Modern Trends .....	75
2.7 Components of a Semi-Submersible.....	75
Exercise Problems .....	81
References .....	83
<b>Chapter 3</b> Ocean Environment: Wind, Wave, Current, Tides, Ice, and Seismic Effects.....	85
3.1 Introduction .....	85
3.2 Description of the Ocean Environment.....	85
3.2.1 Winds .....	85
3.2.2 Currents .....	88
3.2.3 Waves.....	89
3.2.4 Tides .....	90
3.2.5 Earthquakes.....	92
3.2.6 Sea Ice and Other Forms of Ice in the Ocean .....	95
3.2.6.1 Icebergs.....	97
3.3 Ocean Winds and Wind Statistics .....	100
3.3.1 Introduction to Wind .....	100
3.3.2 Theoretical Characterization of Wind Regime .....	102
3.3.2.1 Probabilistic Nature of Wind Regime .....	103
3.3.3 Wind Velocity Profile.....	107

3.4	Ocean Waves and Wave Statistics .....	110
3.4.1	Introduction to Waves.....	110
3.4.2	Airy's Two-Dimensional Small Amplitude Linear Wave Formulation .....	111
3.4.2.1	Wave Particle Velocity, Acceleration, and Orbit .....	115
3.4.2.2	Wave Pressure, Energy, and Flux (or Power).....	117
3.4.3	Nonlinear Wave Formulation.....	120
3.4.4	Wave Statistics and Spectral Characterization.....	124
3.4.4.1	Theoretical Prediction Based on Statistical Characterization of Waves.....	125
3.4.4.2	Wave Prediction from Wind Characteristics .....	132
3.5	Ocean Currents.....	135
3.5.1	Introduction to Ocean Currents.....	135
3.5.2	Current Velocity Profile .....	136
3.6	Solar and Lunar Ocean Tides .....	139
3.6.1	Introduction to Solar and Lunar Ocean Tides.....	139
3.6.2	Theory of Tidal Formation.....	140
3.6.3	Water Level Fluctuations Including Tides .....	142
3.7	Seismological Considerations, Earthquakes, and Seaquakes.....	147
3.7.1	Introduction to Seismological Considerations, Earthquakes, and Seaquakes .....	147
3.7.2	Characteristic Features of Earthquake Phenomena .....	147
3.7.3	Magnitude and Intensity of Earthquakes .....	150
3.8	Ice Environment and Properties .....	153
3.8.1	Introduction to Ice Environment and Properties.....	153
3.8.2	Ice Properties.....	154
3.8.3	Modes of Possible Ice–Structure Interaction .....	157
	Exercise Problems .....	160
	References .....	167
<b>Chapter 4</b>	<b>Seabed Mechanics.....</b>	<b>171</b>
4.1	Introduction .....	171
4.2	Ocean Floor Characteristics and Characterization .....	171
4.3	Offshore Site Investigation and Equipment Used.....	177
4.3.1	Introduction .....	177
4.3.2	High-Resolution Geophysical Surveys.....	178
4.3.3	Drill and Wire-Line Coring Techniques Using Surface Support Vessel.....	179
4.3.3.1	Drill and Wire-Line Coring Using Surface Support Vessel .....	179
4.3.3.2	Sea Bottom-Located Rotary Drills with Wire-Line Corers and Operated by Divers .....	180
4.3.3.3	Vibro-Coring or Flexo-Coring (with Equipment at Sea Bottom) from Surface Support Vessel.....	180
4.3.3.4	Using Remote-Controlled Rotary Corers .....	181
4.3.3.5	Use of Gravity or Stationary Piston Corers.....	181
4.3.4	Remote In Situ Measurements .....	184
4.3.4.1	Modular Seacalf Cone Penetrometers .....	184
4.3.4.2	Wire-Line Vane Shear Test Equipment.....	190

4.4	Ocean Bed Soil Mechanics .....	195
4.4.1	Introduction .....	195
4.4.2	Identification of Marine Soil Characteristics .....	196
4.4.3	Structure of Soil .....	196
4.4.4	Atterberg Limits .....	199
4.4.5	Permeability of Soils .....	201
4.4.6	Stresses in Ocean Soils and Effective Stress Principle .....	202
4.4.7	Shear Strength and Failure of Ocean Soils .....	205
4.4.7.1	Laboratory Tests to Measure Shear Strengths .....	206
4.4.7.2	Stress–Strain Curves and Shear Strength Computation .....	207
4.4.7.3	Simple Methods for Estimating Undrained Cohesion .....	210
4.4.8	Consolidation (or Compressibility) of Ocean Soils .....	212
4.4.9	Stiffness of Soils .....	217
4.5	Bearing Capacities of Offshore Platforms .....	220
4.5.1	General .....	220
4.5.1.1	Scour .....	220
4.5.1.2	Mudslides .....	220
4.5.1.3	Sand Waves, Dunes, Banks .....	221
4.5.1.4	Seabed Subsidence .....	221
4.5.2	Bottom-Fixed Jacket Platforms on Piles .....	221
4.5.2.1	Stability of Fixed Platforms in Piles .....	221
4.5.2.2	Bearing Capacity of Piles in Compression and Tension .....	224
4.5.3	Bottom-Supported Gravity Platforms .....	228
4.5.3.1	Geotechnical Issues Related to Installation of Platform Structure on Site .....	229
4.5.3.2	Stability of Gravity Platform Structure under Static Loads and under Cyclic Environmental Loads .....	229
4.5.3.3	Settlement of Soil beneath Gravity Platform Foundations .....	231
4.5.4	Stress Distribution beneath Gravity Platform Foundation .....	231
4.5.5	Computation of Stability of Gravity Platform Structure .....	232
4.5.5.1	Installation Requirements .....	233
4.5.5.2	Slip (or Sliding) of Foundation Structure .....	235
4.5.5.3	Vertical Bearing Capacity of Soil beneath Gravity Platform Structure .....	236
4.5.5.4	Stability of Gravity Platform Structure with Respect to Overturning .....	236
	Exercise Problems .....	242
	References .....	245
<b>Chapter 5</b>	<b>Materials and Their Behavior in the Ocean Environment .....</b>	<b>249</b>
5.1	Material Requirements for Offshore Structures .....	249
5.1.1	Introduction .....	249
5.1.2	Ocean Environment and Materials .....	252
5.1.2.1	Ocean Water Chemistry .....	253
5.1.2.2	Biological Considerations .....	254
5.1.2.3	Marine Atmosphere .....	254
5.1.3	Development of Materials for Ocean Structures .....	255
5.1.3.1	Material Issues Relating to Construction Phase .....	255
5.1.3.2	Material Issues Relating to Operation Phase .....	260

5.2	Mechanical Properties for Ocean Use.....	266
5.2.1	Introduction .....	266
5.2.2	Properties Related to Strength and Deformation .....	269
5.2.3	Properties Related to Failure, Fatigue, and Fracture.....	274
5.2.3.1	Failure Strength of Materials.....	275
5.2.3.2	Fracture Mechanics .....	277
5.2.3.3	Fatigue Failure and Crack Initiation.....	284
5.2.3.4	Fatigue Failure and Crack Propagation .....	286
5.2.4	Introduction to Properties of a Range of Materials Used in the Ocean .....	295
5.2.4.1	Alloys of Iron and Steel.....	296
5.2.4.2	Low-Carbon Steels .....	296
5.2.4.3	Medium-Strength Steels .....	296
5.2.4.4	High-Strength Steels.....	296
5.2.4.5	Aluminum Alloys .....	300
5.2.4.6	Titanium Alloys .....	300
5.2.4.7	Nonmetallic Materials .....	300
5.3	Range of Material Properties and Material Selection.....	306
5.3.1	Introduction .....	306
5.3.2	Range of Material Properties for Ocean Structures.....	307
5.3.3	Selection of Materials for Ocean Structures .....	307
5.4	Marine Corrosion and Biodegradation.....	311
5.4.1	Introduction .....	311
5.4.2	Basic Mechanisms in Corrosion.....	311
5.4.3	Corrosion and Microbial Effects of Ocean Environment .....	315
5.4.3.1	Ocean Atmosphere .....	315
5.4.3.2	Seawater.....	316
5.4.3.3	Mineral, Mud, and Hydrocarbon Products.....	317
5.4.3.4	Carbon Dioxide.....	318
5.4.3.5	Biological and Microbiological Environments.....	318
5.4.4	Forms of Corrosion .....	320
5.4.4.1	General Corrosion.....	320
5.4.4.2	Galvanic Corrosion.....	320
5.4.4.3	Crevice Corrosion .....	321
5.4.4.4	Pitting Corrosion.....	321
5.4.4.5	Intergranular Corrosion .....	322
5.4.4.6	Differential Environmental Influences .....	322
5.4.4.7	Fretting Corrosion.....	322
5.4.4.8	Corrosion–Erosion.....	322
5.4.4.9	Stress Corrosion Cracking .....	322
5.4.4.10	Corrosion Fatigue .....	323
5.4.5	Corrosion Protection .....	324
5.4.5.1	Protective Coatings.....	324
5.4.5.2	Cathodic Protection .....	325
5.4.5.3	Anodic Protection.....	326
5.4.5.4	Corrosion Inhibition and Electrolyte Modification .....	326
	Exercise Problems .....	327
	References .....	332



<b>Chapter 6</b>	Environmental Forces on Offshore Structures.....	337
6.1	Introduction .....	337
6.1.1	Permanent (or Dead) Loads.....	337
6.1.2	Operating (or Live) Loads .....	337
6.1.3	Environmental Loads (Forces).....	338
6.1.4	Construction and Installation Loads (Forces).....	338
6.1.4.1	Lifting Forces .....	339
6.1.4.2	Load-Out Forces.....	340
6.1.4.3	Transportation Forces .....	340
6.1.4.4	Launching and Upending Forces.....	342
6.1.5	Accidental Loads (Forces).....	344
6.2	Design Conditions for Loads (Forces) Acting on the Structure .....	345
6.2.1	Limit State, Probability, and Safety .....	345
6.2.2	Limit State Design.....	347
6.3	Environmental Forces.....	350
6.3.1	Introduction .....	350
6.3.2	Wind Forces .....	351
6.3.3	Wave Forces .....	362
6.3.3.1	Wave Statistics .....	363
6.3.4	Wave Forces on Offshore Structures.....	363
6.3.4.1	Wave Forces on Slender Vertical Cylindrical Members....	364
6.3.4.2	Linearization of Nonlinear Wave Drag Force .....	366
6.3.4.3	Wave Forces Obtained from Airy's Linear Wave Theory ....	368
6.3.4.4	Effects of Relative Motion of the Structure.....	370
6.3.4.5	Wave Forces on Arbitrarily Oriented Cylindrical Members...	373
6.3.4.6	Wave Forces on Large Diameter Structures.....	376
6.3.5	Current Forces.....	378
6.3.5.1	Current Velocity Profiles .....	378
6.3.5.2	Current Forces Exerted on the Structure.....	382
6.3.5.3	Forces Exerted on the Structure due to Current–Wave Interaction .....	382
6.3.6	Earthquake Forces.....	386
6.3.7	Ice Forces on Ocean Structures.....	388
6.3.7.1	Ice Loads on Vertical Cylindrical Structures .....	389
6.3.7.2	Ice Loads on Sloping Structures.....	392
6.3.7.3	Limit Loads due to Environmental Interaction .....	395
6.3.8	Tides .....	400
6.3.9	Marine Growth.....	400
	Exercise Problems .....	401
	References .....	415
<b>Chapter 7</b>	Fundamental Considerations for Framed Offshore Structural Analysis.....	419
7.1	Introduction .....	419
7.2	Site Characteristics and Modeling Procedures for Analyses .....	419
7.2.1	Structural Skeleton for Force Application and Analysis.....	419
7.3	Hydrostatic Pressure and Buoyancy .....	429
7.4	Preliminary Considerations for Static Analysis and Design.....	431
7.5	Finite Element Applications for Framed Offshore Structural Analyses .....	438
7.5.1	Introduction .....	438
7.5.2	Use of Truss Elements in Offshore Structural Modeling.....	439

7.5.3	Plane Trusses .....	439
7.5.4	Space Trusses .....	449
7.5.5	Use of Beam Elements in Offshore Structural Modeling .....	452
7.5.5.1	Plane Frames.....	453
7.5.5.2	Member Stiffness Matrix for Horizontal Beam Member.....	453
7.5.5.3	Member Stiffness Matrix for Arbitrarily Oriented Member.....	456
7.5.5.4	Relating Member Stiffness Matrix to System Axes .....	458
7.5.5.5	Space Frames.....	463
7.6	Formulation of Solid–Fluid Interaction Problems.....	471
7.7	Simplified Lumped Mass/Stiffness Considerations for Dynamic Analyses.....	474
7.7.1	Introduction .....	474
7.7.2	Characterization of Offshore Structure as an SDOF System.....	477
7.7.3	SDOF Models in Offshore Structures .....	480
7.7.4	MDOF Systems .....	485
7.7.4.1	Two-Degrees-of-Freedom System .....	485
7.7.4.2	Three-Degrees-of-Freedom System .....	486
7.7.4.3	Many-Degrees-of-Freedom System.....	487
7.7.4.4	Solution Procedures .....	488
	Exercise Problems .....	492
	References .....	503

## **Chapter 8** Analysis and Design Considerations for Framed Steel Offshore Platforms ..... 507

8.1	Introduction .....	507
8.1.1	Design Considerations.....	508
8.1.2	Design Codes and Provisions .....	510
8.2	Preliminary Design Considerations for Steel Jacket Offshore Structures ....	511
8.2.1	Typical Preliminary Design .....	511
8.2.2	Minimum Embedment Length of Piles (of Columns).....	513
8.2.2.1	Embedment Length .....	513
8.2.2.2	Equivalent Short Pile Length.....	515
8.2.2.3	Sufficiency of Selected Column Pile Section for Short Pile .....	516
8.2.3	Top Deck Analysis for Imposed Loads .....	516
8.2.3.1	Sufficiency of Vertical Column below Top Deck .....	517
8.2.3.2	Analysis and Design of Deck Framing Members.....	520
8.2.3.3	Truss Structures in the Top Deck .....	526
8.2.3.4	Reassessing Sufficiency of Vertical Column below the Top Deck.....	531
8.2.3.5	Tubular Members in Jacket Structure.....	532
8.2.3.6	Miscellaneous Considerations for Jacket Platform.....	535
8.3	Analysis of Pile Foundations for Offshore Structures.....	536
8.3.1	Introduction .....	536
8.3.2	Soil–Structure Interaction.....	536
8.3.2.1	Beam-on-Elastic (due to Hetenyi) Foundation .....	538
8.3.2.2	Beam-on-Winkler Foundation: $p$ – $y$ Curve Approach .....	540
8.3.2.3	Elastic Continuum Approach.....	541
8.3.2.4	Finite Element Approaches.....	541
8.4	$p$ – $y$ Curve Approach.....	541
8.5	Classical Derivations for Pile–Soil Interaction .....	546

8.6 Code-Based Foundation Design for Pile-Supported Offshore Structures .... 549

8.6.1 Axial Resistance of Piles..... 550

8.6.2 Soil Reaction for Laterally Loaded Piles ..... 555

8.6.2.1 Lateral Bearing Capacity for Piles in Soft Clay ..... 555

8.6.2.2 Load–Deflection Relationships for Piles in Soft Clay ..... 556

8.6.2.3 Lateral Bearing Resistance for Piles in Stiff Clay..... 557

8.6.2.4 Load–Deflection Relationship for Piles in Stiff Clay ..... 557

8.6.2.5 Lateral Bearing Capacity for Piles in Sand ..... 557

8.6.2.6 Load Deflection ( $p$ – $y$ ) Curves for Piles in Sand..... 558

8.6.3 Influence of Group of Piles ..... 558

8.6.4 Thickness of Pile Wall ..... 559

8.6.5 Length of Pile Sections ..... 560

Exercise Problems ..... 571

Appendix 8A ..... 579

Appendix 8B ..... 583

References ..... 586

**Chapter 9** Analysis and Design of Concrete Gravity Platforms ..... 591

9.1 Introduction and Design Environmental Conditions..... 591

9.1.1 Introduction ..... 591

9.1.2 Structural Components of Gravity Platform ..... 591

9.1.3 Typical Design Environmental Conditions ..... 593

9.1.4 Analysis and Design Aspects of Gravity Platform ..... 594

9.1.5 Salient Features to Be Considered in Analysis and Design ..... 597

9.2 Bearing Capacities of Gravity Platform Foundation..... 600

9.2.1 Requirements in Design ..... 600

9.2.2 Undrained Bearing Capacity of Foundation Soil..... 601

9.2.3 Drained Bearing Capacity of Foundation Soil..... 602

9.2.4 Sliding Resistance of Foundation Soil ..... 603

9.2.5 Ultimate Capacities of Shallow Foundations ..... 603

9.3 Static Deformation of Gravity Platform Foundation..... 609

9.3.1 Introduction ..... 609

9.3.2 Immediate or Short-Time Deformations ..... 609

9.3.2.1 API Code Provisions..... 610

9.3.3 Primary Consolidation ..... 610

9.3.3.1 Secondary Consolidation..... 611

9.3.3.2 API Code Provisions..... 611

9.3.4 Regional Subsidence..... 612

9.3.5 Other Considerations..... 612

9.4 Analysis and Design of Gravity Platform Subjected to Wind and Wave Loads ..... 612

9.4.1 Introduction ..... 612

9.4.2 Assumptions Made in Simplified Analysis ..... 614

9.4.3 Additional Considerations for Dynamic Behavior of Platform Components..... 616

Exercise Problems ..... 640

References ..... 649



# Preface

This textbook provides comprehensive coverage of the engineering concepts and design of offshore drilling platforms for exploration and production. The book is intended to provide the senior undergraduate or graduate student with a clear and adequate presentation of both the theory and application of the fundamental principles of structural, fluid, and geotechnical mechanics to offshore structures. Since the main focus is on the emphasis on pragmatic engineering applications for offshore structural design, research, and development, the text will also be very useful to those working in the design industry. In contradistinction to other books in the field, this text has numerous example and homework problems.

It is a pleasure to thank all the authors and publishers of the many books and articles, listed in the bibliography but too numerous to list here, who kindly permitted the reproduction of many figures and tables in the chapters. Thanks are due to Ms. Caroline Cynthia, who worked diligently for the processing of the figure and table permission requests and the typing of the manuscript. The publisher has been exceedingly cooperative in helping to meet the submission deadlines.

Finally, we must record our gratitude to our wives, Geetha and Melly, who stoically provided moral support to make this book possible.

## Suggested Method of Coverage for a 16-Week Course

Lectures	
Date	Topic
Week 1	Chapter 1 and Chapter 2, Reading Assignment, Assignment 1 Chapter 3: Sections 3.3, 3.4, 3.5, and 3.8 Chapter 3: Sections 3.3, 3.4, 3.5, and 3.8—continued
Week 2	Chapter 3: Sections 3.3, 3.4, 3.5, and 3.8—continued Chapter 3: Sections 3.3, 3.4, 3.5, and 3.8—continued Chapter 3: Sections 3.3, 3.4, 3.5, and 3.8—continued
Week 3	Chapter 3: Sections 3.3, 3.4, 3.5, and 3.8—continued Chapter 3: Sections 3.3, 3.4, 3.5, and 3.8—continued, Assignment 2 Chapter 4: Sections 4.2 and 4.5
Week 4	Chapter 4: Sections 4.2 and 4.5—continued Chapter 4: Sections 4.2 and 4.5—continued Chapter 4: Sections 4.2 and 4.5—continued
Week 5	Chapter 4: Sections 4.2 and 4.5—continued, Assignment 3 Chapter 5: Sections 5.1 and 5.3 Chapter 5: Sections 5.1 and 5.3—continued
Week 6	Chapter 5: Sections 5.1 and 5.3—continued Chapter 5: Sections 5.1 and 5.3—continued, Assignment 4 Chapter 6: Sections 6.3.1 to 6.3.5, and 6.3.8
Week 7	Chapter 6: Sections 6.3.1 to 6.3.5, and 6.3.8—continued Chapter 6: Sections 6.3.1 to 6.3.5, and 6.3.8—continued Chapter 6: Sections 6.3.1 to 6.3.5, and 6.3.8—continued
Week 8	Chapter 6: Sections 6.3.1 to 6.3.5, and 6.3.8—continued Chapter 6: Sections 6.3.1 to 6.3.5, and 6.3.8—continued Chapter 6: Sections 6.3.1 to 6.3.5, and 6.3.8—continued

Week 9	Chapter 6: Sections 6.3.1 to 6.3.5, and 6.3.8—continued, Assignment 5 Chapter 7: Sections 7.2 to 7.4 Chapter 7: Sections 7.2 to 7.4—continued
Week 10	Chapter 7: Sections 7.2 to 7.4—continued Chapter 7: Sections 7.2 to 7.4—continued Chapter 7: Sections 7.2 to 7.4—continued
Week 11	Chapter 7: Sections 7.2 to 7.4—continued Chapter 7: Sections 7.2 to 7.4—continued, Assignment 6 Chapter 8: Sections 8.2, 8.3.2.2, and 8.4
Week 12	Chapter 8: Sections 8.2, 8.3.2.2, and 8.4—continued Chapter 8: Sections 8.2, 8.3.2.2, and 8.4—continued Chapter 8: Sections 8.2, 8.3.2.2, and 8.4—continued
Week 13	Chapter 8: Sections 8.2, 8.3.2.2, and 8.4—continued Chapter 8: Sections 8.2, 8.3.2.2, and 8.4—continued Chapter 8: Sections 8.2, 8.3.2.2, and 8.4—continued, Assignment 7
Week 14	Chapter 9: Sections 9.2, 9.3, and 9.4 Chapter 9: Sections 9.2, 9.3, and 9.4—continued Chapter 9: Sections 9.2, 9.3, and 9.4—continued
Week 15	Chapter 9: Sections 9.2, 9.3, and 9.4—continued Chapter 9: Sections 9.2, 9.3, and 9.4—continued Chapter 9: Sections 9.2, 9.3, and 9.4—continued, Assignment 8
Week 16	Review Review

**Dr. D. V. Reddy**

*Florida Atlantic University*

*Boca Raton, FL*

*USA*

**Dr. A. S. J. Swamidas**

*Memorial University of Newfoundland*

*St. John's, Newfoundland and Labrador*

*Canada*

---

# Authors

**D. V. Reddy**, PhD (Liverpool), MS (Northwestern), DIC (Imperial College, London) BE (Madras), professor of civil, environmental, and geomatics engineering and director of the Center for Marine Structures and Geotechnique, Florida Atlantic University, is a registered professional engineer in Florida, Newfoundland and Labrador, and Alberta and a chartered engineer in the United Kingdom with a long and distinguished research, teaching, and administrative career on three continents. He has held professorships at the Indian Institute of Technology, Madras; Memorial University of Newfoundland, St. John's, Newfoundland; and the University of Florida, Gainesville, Florida, and visiting professorships at the University of Calgary, Alberta; South Dakota School of Mines and Technology, Rapid City, South Dakota; the Technical University of Hannover, Germany; and Chulalongkorn University (Fulbright scholar), Bangkok, Thailand. He has taught courses on offshore and coastal structures for over 30 years and worked in the industry (including consultancies) in India, the United Kingdom, and the United States. His research interests are in the areas of marine structures, materials, and geotechnical engineering, with particular focus on concrete technology and computational and analytical mechanics. He has authored over 370 papers, 3 books, and 3 conference volumes. He is a fellow of the American Concrete Institute and an active member of several of its technical committees. He was recognized as Distinguished Teacher of the Year 1988–1989 by Florida Atlantic University and Government Civil Engineer of the Year by the ASCE, South Florida Chapter in 1988. He is also the recipient of a number of outstanding research paper awards.

**A. S. J. Swamidas**, PhD (Indian Institute of Technology, Chennai), MSc (Madras University) and BEng (Hons) (Madras University) is an honorary research professor of engineering, Memorial University, St. John's, Newfoundland and Labrador, Canada. He has held professorships at the Indian Institute of Technology, Chennai, India, and at Memorial University, Newfoundland and Labrador (NL), Canada, with a distinguished academic, teaching, and research career. He has taught offshore structures to graduate and undergraduate students for more than 20 years and acted as a consultant to a number of companies. His research interests are in the area of dynamics of offshore and onshore structures with particular focus on computational mechanics and damage detection. He has authored over 210 papers/reports and two conference volumes. He was a registered professional engineer in Newfoundland and Labrador, Canada.





---

# 1 Offshore Operations and Structural Development

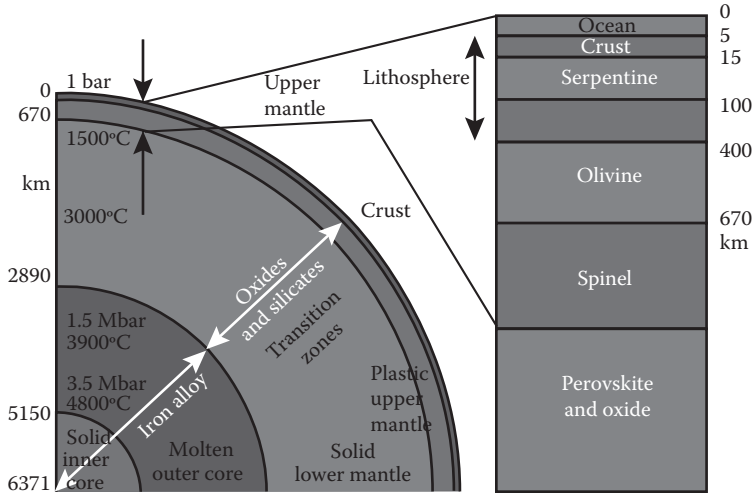
## 1.1 INTRODUCTION

The analysis of rounded well-worn pebbles, embedded in specimens of sedimentary rocks, reveals that the oceans have been in existence for at least 3 billion years. Over the intervening years, the topographical features of this planet, along with its oceans, have been changing continuously, although slowly relative to the human life span. Shorelines have distorted, continents have risen, fallen, and drifted apart, and the mean sea level has changed. The local and global weather systems, as well as the earth's ecology, have been greatly influenced and modified by the presence of the oceans.

Let us consider a simple, idealized model of the earth that assumes that it possesses geometric symmetry. As depicted in Figure 1.1 [1], this idealized earth would consist of three major concentric layers, viz., the inner core of variable (but generally large)-density solid material, the next layer of moderate-density liquid, and the outer layer of low-density gas. Gravitational attraction would hold these three regions together stratifying the substances into a central solid core of very heavy metal surrounded by successive smooth spherical balls of heavy rock, light rock, water, and finally gas layers. In reality, the land masses protrude through the surface of the hydrosphere, so that water covers only about 71% of the total surface area. Furthermore, the water to land ratio in the earth's southern hemisphere is considerably larger (4:1) than in the northern hemisphere (3:2).

Oceans constitute the most dominant feature on earth, and have an average depth of 4 km and a maximum depth, located at Challenger Deep in Marianas Trench, of about 11.0 km. Essentially, there is but one ocean and all continental land masses are islands. This continuous mass of water has acted both as a barrier and a corridor through which people and goods have moved with relative ease, spreading culture as they garnered earth's remote resources. Today, the ocean is valued for its ability to provide sources of renewable energy. It can stabilize its temperature helping to sustain life as we know it today. It is also a major supplier of water vapor that later falls as rain on the continental "islands." The great rivers of the earth drain this rain, providing fresh water for human beings, as well as the easiest and economical roadways into the interior of the continents. Man has built great cities around harbors into which the rivers empty. Ironically, the ocean, our valuable resource "silently" receives and quickly disperses, dilutes, and digests our "unwanted" waste, industrial and sewage effluents, the runoff of waste oil and nutrients from the farmlands of these cities. While man continues to understand the importance of oceans, generations have come to respect this goliath of nature. Large waves, produced by its inhospitable temperament, have destroyed even the largest oceangoing vessels. Even today, men's attempts to protect their coastlines have been overwhelmed by the ocean's fierceness.

During the latter half of the twentieth century, as mankind increased its population and its activities in an exponential manner, technological exploitation of the oceans had become inevitable. A number of structures, installed in the ocean, exploit it for the benefit of humans, as shown in Figure 1.2 [2]. Ship types and modes seen in the field of ocean transport include containerization, catamarans, hovercraft, and very large crude oil carriers, along with large numbers of boats and barges that ply the inland rivers. With the development of transport has come increased capability to exploit more of the oceans resources. Ocean thermal energy conversion (OTEC) programs examine thermal



**FIGURE 1.1** View of earth’s interior. (From H.W. Green II, Solving the paradox of deep earthquakes, *Scientific American*, Volume 9, pp. 64–71, 1994. Available at [www.seafriends.org.nz/oceano/oceans.html](http://www.seafriends.org.nz/oceano/oceans.html). With permission.)

attributes of the ocean for producing energy. Ocean sediments are recognized as a major source of mineral wealth, both hard minerals and petroleum. Offshore oil and gas now supply almost one third of the world’s energy needs. While manganese nodules have been recovered from the deep ocean floors of the tropical and subtropical areas, coastal sediments have also been exploited since they are rich in “industrial minerals” of gold, tin, chromium, platinum, and even sand and gravel.

Offshore hydrocarbons, a much sought after energy resource, are associated primarily with the continental margins of the world, as shown in Figure 1.3 [3]. These margins surround the continents and constitute 25% of the total ocean area. Extending from shore to the deep ocean floor, the continental margin consists of three units—shelf, slope, and rise. Typically, an ocean may be about a thousand times as wide as it is deep, and a cross section might be similar to that shown in Figure 1.4 [4]. As seen in Figure 1.4, the main regimes, in relation to distance from the land, are the (onshore) coastal plain, the continental shelf, the continental slope, the continental rise, and the deep ocean floor. The continental shelf extends out generally to a water depth of 200 m, with an average gentle slope of 1 in 500. The steeper continental slope extends from 200 m to a depth of 2500 m, sometimes with a steep slope of 1 in 20. The continental rise extends from a depth of 2500 m to a depth

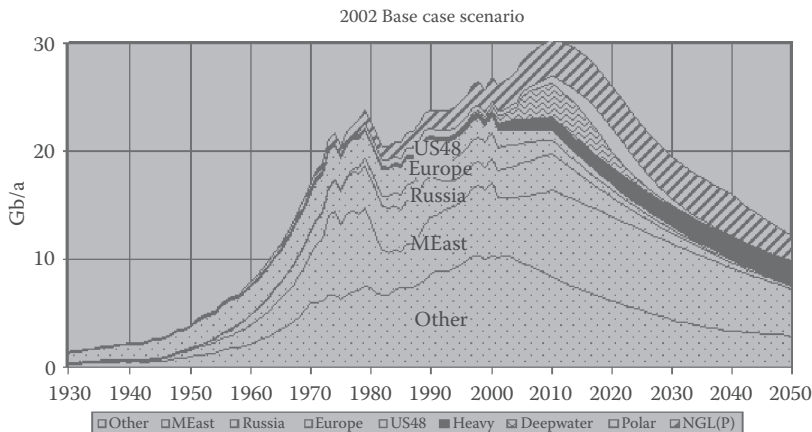


**FIGURE 1.2** Number of opportunities for developing marine structures. (From T. Moan, *Marine Structures for the Future—A Sea of Opportunities*, The Inaugural Keppel Lecture, National University of Singapore, July 18, 2003. With permission.)

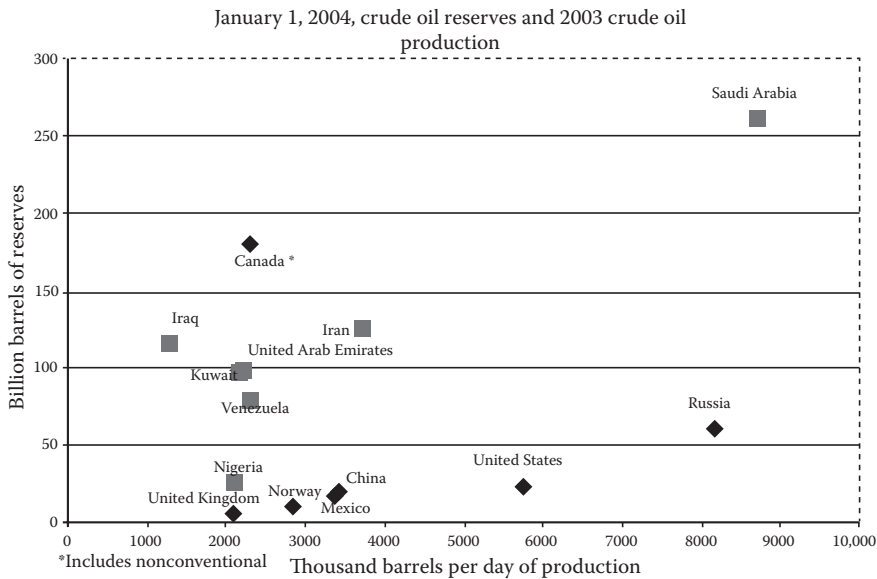


by 1970, 155 billion barrels by 1980, 400 billion barrels (discovered), and a yet to be discovered 350 (probable mean) billion barrels by 1996 [6]; this has swelled to 849 billion barrels by 2007 [7–9]. This is in contrast to the onshore oil reserves that were estimated at 555.78 billion barrels by 1970, 658.557 billion barrels by 1980, 1.0075 trillion barrels by 1996, 1.266 trillion barrels by 2004 (probable mean), and a yet to be discovered 724.228 billion of barrels [7, 8]. The identified gas reserves were 6094.4 trillion ft.<sup>3</sup> and a yet to be discovered 5374.6 trillion ft.<sup>3</sup> (probable mean) by 1991 [7]. Assessment of the total future resource is hampered by our sketchy knowledge of the oceans over large areas, while in some other contexts the available information is proprietary. In addition to the above, some specific geological problems must be overcome for a precise assessment in the future, viz., (i) better methods for gas hydrates prediction and (ii) direct rather than indirect methods to locate gas traps and hydrocarbon reserves. The overall picture of oil and gas hydrates depletion around the world is shown in Figure 1.5 [10]. It is plotted in terms of the amount of reserves depleted per year, starting from the year 1930 to the projected year 2050. The deepwater discoveries, heavy oil, and natural gas liquids are projected to supplement the heavy depletion of petroleum by industrialized countries. The production rate of oil and natural gas hydrates is expected to start dropping from 2015. The oil reserve to production ratio (in years) for the enormous Saudi Arabian oil reserves, for instance, was projected to be 84.3 years by 2003 [11]. Alternately, as per the oil reserve data available in 2001, the world oil reserve was 1.032 trillion of barrels, the annual production was 28.180 billion barrels per year, and the consumption rate was 28.460 billion barrels per year [12]. Projecting from these data, the oil reserves will last only for another 36 years, at the present rate of consumption. As a consequence, continued exploration and exploitation of oil and gas reserves is inevitable to meet the market demands and ensure that sufficient oil and gas reserves are discovered during the coming years [6].

According to a recent oil and gas report on crude oil reserves and production, shown in Figure 1.6, Canada ranks behind Saudi Arabia in the proven oil reserves [13], leaving others, such as Iraq, Iran, Kuwait, and Venezuela, behind; it must be mentioned here that the Canadian oil reserves include the oil and gas produced from nonconventional tar sands. The world's oil supply comes from a wide variety of sources. While the Middle East was the largest producing region in 2003, with 29% of total world production, North America accounted for 20%, with the remaining 51% dispersed fairly evenly throughout the globe. The Organization of the Petroleum Exporting Countries (OPEC), consisting of 13 member countries, accounted for about 38% of world total oil production in 2003 [14].



**FIGURE 1.5** General scenario of depletion rate of world oil and gas reserves. (From Association for the Study of Peak Oil (ASPO), *ASPO News*, Newsletter No. 21, September 2002, 9 pp. Available at <http://www.asponews.org/ASPO.newsletter.021.php/>, 2001. With permission.)



**FIGURE 1.6** Crude oil reserves and production. (From US EIA, Office of Oil and Gas, 2004. Courtesy of eia.doe.gov.)

The largest oil producing companies in the world are Saudi Aramco (3100 million barrels per day), Exxon Mobil, USA (2542), Royal Dutch Shell, UK/Netherlands (2220), Chevron Texaco (1959), British Petroleum Amoco, UK (1931), Yukos, Russia (1507), Total Fina Elf, France (1454), Lukoil, Russia (1200), Conoco Phillips, USA (1019), and Surgutneftegas, Russia (884). In contrast, the largest oil reserves owning companies are Saudi Aramco (259,100 million of barrels), Lukoil, Russia (17,360), Yukos, Russia (17,281), Gazprom, Russia (14,902), Exxon Mobil, USA (12,312), Royal Dutch Shell, UK/Netherlands (9469), Chevron Texaco, USA (8710), British Petroleum Amoco, UK (8376), Tyumen, Russia (7300), and Total Fina Elf, France (6961) [12, 14–16].

In terms of largest oil production, the top ten countries are the former Soviet Union (8.60 to 9.04 million of barrels per day), United States (5.17 to 8.1), Saudi Arabia (7.7 to 9.55), Iran (3.7 to 4.14), Mexico (3.33 to 3.6), Norway (2.7 to 3.4), China (3.3 to 3.61), Venezuela (1.98 to 2.8), Canada (1.28 to 2.8), and United Kingdom (1.65 to 2.6) [14]. The largest ten oil fields in the world are Gawar, Saudi Arabia (75–83 billion barrels), Burgan, Kuwait (66–72), composite Bolivar Coastal, Venezuela (30–32), Safaniya-Khafji, Saudi Arabia (30), Rumaila, Iraq (20), Tengiz, Kazakhstan (15–26), Ahwaz, Iran (17), Kirkuk, Iraq (16), Marun (16), and Gachsaran, Iran (15). In comparison, the reserves of two of the largest oilfields discovered in the western subcontinent are Marlim, Campos Basin, Brazil (10–14 billion barrels), and Prudhoe Bay, Alaska, USA (9.9). Of the proven gas reserves of 4980 trillion ft.<sup>3</sup> of gas, Russia has the largest reserves of natural gas (1748 trillion ft.<sup>3</sup> of gas), and is followed by the United States (1475), Iran (742), Qatar (245), Abu Dhabi (188), and Saudi Arabia (185). Of the top ten largest natural gas fields of the world, eight are located in Russia, the largest of them being Urengoy in West Siberia, Russia (>275 trillion ft.<sup>3</sup> of gas) [14].

According to recent statistics, offshore oil exploration and exploitation has been carried out in 7105 fields spread over 120 countries. Drilling and producing operations use 14,531 offshore platforms (fixed, gravity, and floating) and 8218 subsea units throughout the world. There are 29,319 offshore pipelines that transport offshore oil and gas to onshore facilities [17]. A recent survey carried out during 2001 states that there are more than 105 gravity-based offshore structures all over the world [18]. A number of floating platforms [over 217 during 1995–2004], containing storage and offloading provisions, were recently installed for deepwater exploitation. Another 184 deepwater

and 27 ultra-deepwater fields (water depths ranging from 1000 to 5000 ft.) have been slated for development during 2004–2008, which will also use similar floating systems [19]. There are 1040 single point moorings, located all over the world in offshore locations, which assist in the offloading of oil and gas to oil carriers. Besides these offshore facilities, there are 559 onshore oil terminals servicing the offshore industry [17]. As is evident from this survey, the offshore industry is continuously called upon to innovate and develop structural systems that will meet the ever-changing needs and demands of the offshore fields.

Following the installation, during 1988, of the world's tallest conventional fixed platform Bullwinkle at a water depth of 1350 ft. (411 m), Shell Exploration and Production Company (SEPCo) has proved itself to be a world leader in moving into deep water [20]. In 1993, they installed, Auger, a tension leg platform (TLP) in the Garden Banks block 426, at a water depth of 2860 ft. (872 m). They followed this with the Ursa TLP in Mississippi Canyon Block 809 at a water depth of 3800 ft. (1158 m). In another innovative development, SEPCo tied its deepwater subsea developments at Mensa field, at a water depth of 5300 ft. (1615 m), to a shallow water steel platform, West Delta 143, located in a water depth of 370 ft. (113 m), using a 68-mi.-long (95 km) tieback with 12" (0.305-m diameter) flow lines. During 2004, it installed the sixth subsea completion to produce natural gas from its Coulomb field development, in the Mississippi Canyon 474, at a record water depth of 7570 ft. (2307 m). This subsea completion was part of a development containing six fields (Kepler, Ariel, East Anstey, Herschel, Fourier, and Coulomb) at Na Kika oil and gas fields. This subsea completion was also tied to a floating production storage and offloading (FPSO) system located at a water depth of 6300 ft. (1920 m). In contrast, the deepest FPSO installation in the Campos Basin, Brazil, is that of South Marlim 3B, located at a water depth of 5607 ft. (1709 m). In 2004, Gulf Terra Energy partners announced that they had installed the Marco Polo Tension Leg Platform in the Gulf of Mexico (in Green Canyon block 608) at a water depth of 4300 ft. (1463 m).

During 1996, Kerr-McGee Oil and Gas Corporation had installed the world's first production spar, Neptune, in the Mississippi Canyon block 826 at a water depth of 1851 ft. (564 m). BP later installed an innovative truss spar design, named Horn Mountain, at Mississippi Canyon Block 127, at a water depth of 5400 ft. (1646 m). Recently, during 2003, another truss Spar, named Devil's Tower, was installed in the Mississippi Canyon block 773 at a still deeper water depth of 5610 ft. (1710 m). According to recent projections, these truss Spar designs are suitable even to a water depth of 10,000 ft. (3048 m) [21]. The world's deepest drilling and production platform using a deep draft caisson vessel, a variant Spar design, was installed during 2000 by Exxon-Mobil and BP team, at the Hoover and Diana fields, at a water depth of 4800 ft. (1463 m). The first compliant guyed tower platform, Exxon's Lena, supported by 20 guy wires, was installed at a water depth of 1018 ft. (310 m). This was followed by the third generation compliant tower platform Baldpate, located at Garden Bank's Block 260 in the Gulf of Mexico, at a water depth of 1650 ft. (503 m), and, BP's Petronius at a water depth of 1754 ft. (535 m). By 2003, Marathon and Total Fina Elf had set the record for the deepest production well at a water depth of 7210 ft. (2198 m) and linked it by pipeline to a natural gas field development at Canyon Express. Recently, the deepest oil well was spudded in 10,011 ft. of water (3052 m) at Alaminos Canyon Block 951, by Transocean drill ship Discover Deep Seas.

### 1.3 COMMERCIAL PROJECTIONS FOR THE OFFSHORE INDUSTRY

According to current commercial projections, the exploration and exploitation of the large offshore/onshore reserves of oil and gas will be influenced by a number of factors. Some of these factors for oil/gas developing companies are (i) the potential for undiscovered significant oil reserves that will support, for many years, their downstream operations such as transporting, refining, and marketing of petroleum and its derivatives; and (ii) the financial exposure and risk as they encounter the political uncertainty of countries where oil reserves are being discovered. In general, the development of offshore hydrocarbon reserves is spurred by the anticipated demand for energy around the world. As the world population grows, the search and exploitation of energy is complicated by the wide



variation that exists between national economies in terms of wealth, technological capability, political goals, and economic philosophies [22]. The expected costs of exploration and field development need to be known, with the amount of investment required and the targeted rate of return, so that sound financial decisions can be made by the developing company. In order to assess these, detailed information on factors such as the terms and length of contract to be made with the country owning the reserve, size of the reserves, depth of water, and operating environment need to be known beforehand. Tables 1.1 and 1.2 specify costs to consider for onshore and offshore energy development around the world [22–24]. Figure 1.7 gives a flowchart overview of the economic factors that need to be taken into account when developing an offshore field [25]. The overall economic analysis requires the knowledge of resources from the discovered field, price of oil, recovery of invested capital, field development requirements, available technology for field development, selection of platform concept to be used, capital requirement, and the evaluation of the viability of financial investment.

The financing of hydrocarbon development may fall into either the public or the private sector. The public sector will involve domestic funds supplied by government allocation from the national budget or foreign funds supplied as aid or loan funds to develop natural resources. The motivation

---

**TABLE 1.1**  
**Some Representative Offshore Cost Figures (Modified)**

1. Exploration	a. Seismic	\$300 to \$500
	per km (processed) per day (Arctic)	\$20,000
2. Production	b. Drilling	i. Jack-up rigs: \$30 to 40 million (or \$33,000 per day)
		ii. Semi-submersible drilling rig: \$60 to 80 million (or \$55,000 per day)
		iii. Well drilling: \$100,000 per well in shallow waters <ul style="list-style-type: none"> <li>• \$20 million for 4000 m deep well in 1500 m water depth</li> <li>• \$40 million per well in Beaufort Sea</li> </ul>
		iv. Ice platform: \$500,000 per one unit
		v. Drilling fleet in Beaufort Sea: \$240 million
2. Production	a. Platforms	i. Few thousand dollars for a tripod
		ii. \$1.0 billion in North Sea waters
		iii. \$4 to 8 million in Gulf of Mexico
		iv. \$110 to 200 million in Bering Sea (Gravity Platform)
2. Production	b. Per BOPD of new production	i. \$2000 to 3000 in shallow Louisiana waters
		ii. \$20,000+ in deep Louisiana waters
		iii. \$6000 to 14,000 in North Sea
		iv. \$40,000 to 50,000 for synthetic fuels, oil shale
2. Production	c. Automation	For example: \$21.0 million for Zakum Field, with centralized production control (300 wells, 90 platforms, 4 separator platforms, power generation, etc.)
3. Transportation	Pipelines (only indicative)	i. \$600,000 per km of 30" pipeline in North Sea
		ii. \$150,000 to 300,000 per km in Gulf of Mexico

*Sources:* M. Forrer, The future of offshore petroleum development, in: *The Future of Offshore Petroleum*, McGraw-Hill (in cooperation with the United Nations), New York, pp. 3–26, 1981. Measuring Worth: Purchasing Power of Money in the United States from 1774 to 2007, From Current Value of Old Money. Available at [www.projects.ex.ac.uk/RDavies/arian/current/howmuch.html](http://www.projects.ex.ac.uk/RDavies/arian/current/howmuch.html).

*Note:* Prices given in 1980 dollars (US\$1.00 in 1980 ≈ US\$2.51 in 2007).

---

**TABLE 1.2**  
**Cost of Energy Development (Modified)**

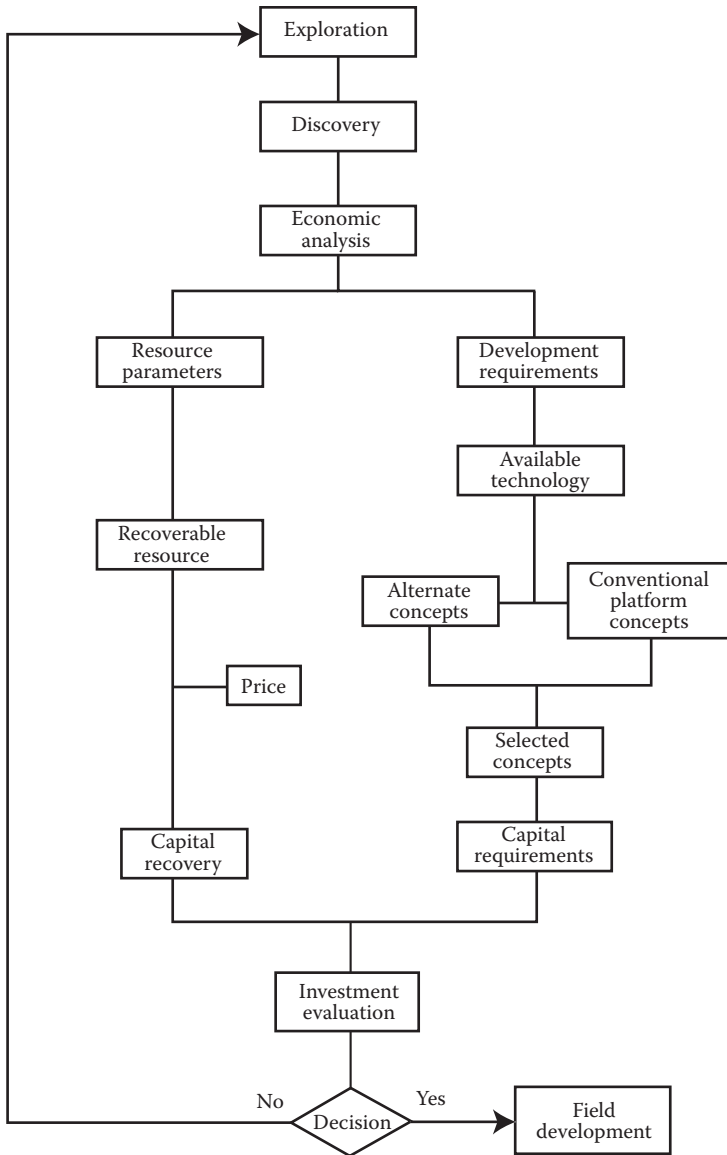
1. Exploration	a. Onshore	Representative costs (good conditions)	Representative costs (bad conditions)
	Geological and geophysical surveys	2–3 units	6–10 units
	3 wells to 3000 m	4–5 units	10–15 units
	Overhead, miscellaneous, and contingencies	1.5–2 units	4.5–6 units
		Total = 7.5–10 units	Total = 20.5–31 units
	*(1.0 unit ~ \$1.5 to 2.0 million)		
	b. Offshore	Representative costs (good conditions)	Representative costs (bad conditions)
	Geophysical surveys	1–2 units	2–3 units
	3 wells to 3000 m	9–12 units	20–30 units
	Overhead, miscellaneous, and contingencies	3–5 units	5–10 units
		Total = 13–19 units	Total = 27–43 units
	*(1.0 unit ~ \$1.5 to 2.0 million)		
2. Development (outside OPEC)	Onshore	\$8000 to 10,000 per daily barrel of production	- do.-
	Offshore	\$15,000 to 20,000 per daily barrel of production	- do.-
	Heavy oil	\$15,000 to 25,000 per daily barrel of production	- do.-
3. Related infrastructures: refineries	a. Distillation capacity: million tons per year (barrels per day)	Typical DC refinery 1 (20,000)	World-scale refinery 6 (120,000)
	b. Investment cost per daily barrel	\$4450	\$2100
	c. Unit investment cost per ton per year of distillation capacity	\$89	\$42
	d. Operating costs per barrel of throughput	\$4.5	\$2.1
4. Enhanced recovery	–	\$15,000 per daily barrel	–
5. Oil shale–tar sands	–	\$30,000 per daily barrel	–

*Sources:* W.E. Pelley, 1981, Economic and financial issues of offshore petroleum development, in: *The Future of Offshore Petroleum*, McGraw-Hill (in cooperation with the United Nations), New York, pp. 179–198. Measuring Worth: Purchasing Power of Money in the United States from 1774 to 2007, From Current Value of Old Money. Available at [www.projects.ex.ac.uk/RDavies/arian/current/howmuch.html](http://www.projects.ex.ac.uk/RDavies/arian/current/howmuch.html).

*Note:* Prices given in 1980 dollars (US\$1.00 in 1980 ≈ US\$2.51 in 2007).

for this type of financing is usually political or diplomatic, and the profits to be derived may not be intended to be purely economic. Frequently, domestic and foreign funds are joined at the government level in a joint venture effort, basing it on the contribution of technology from one side, geologic prospects from the other, mutual agreement concerning profit sharing, and a preferential market for the foreign investor. In any case, the financial risks assumed rest on the host country's credit rating. Private sector financing is normally associated with the activities of privately owned companies, such as the major oil corporations or government-owned oil companies mandated to function as private companies. In any of the above three situations, the amount of money required for exploration is provided by one or both the parties, as an equity risk. Only after the commercial production of oil is proven will the banking industry join the effort. After determining the political





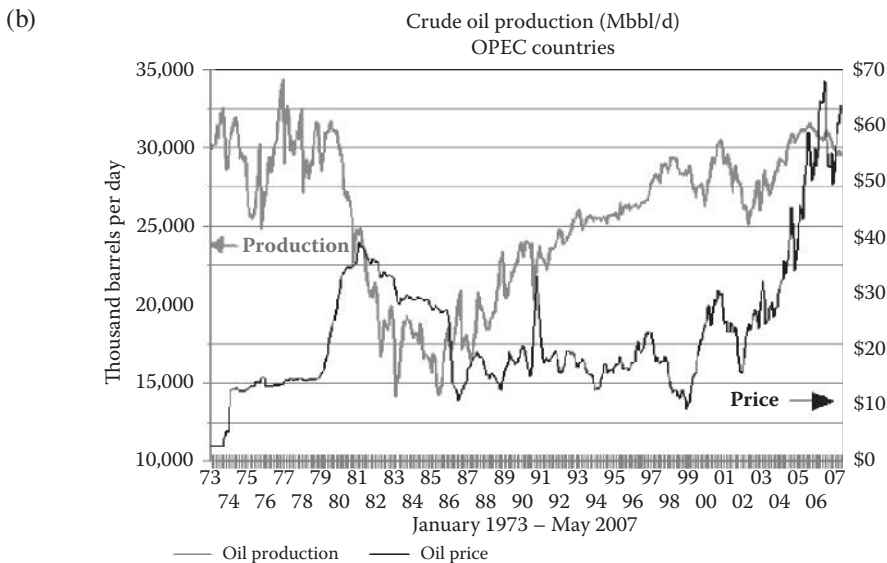
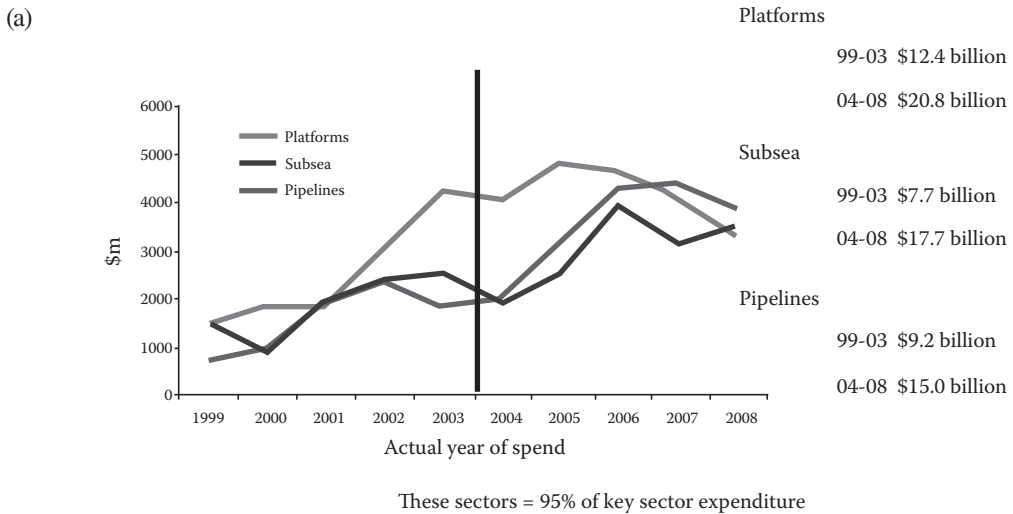
**FIGURE 1.7** Flowchart of the economic factors for offshore field development. (From Short Course on Design of Fixed Offshore Structures. Courtesy of University of Texas, Austin, 1979. With permission.)

risk involved in the financing effort, and the sanctity of contract executed between the borrower and the host government and its long-term viability, the banking industry will determine whether investment in the project is economically attractive or not. The banks must also be satisfied with the managerial ability of the operator in the field and that enough of the operator’s money is invested as equity to assure his continued interest in handling the project efficiently. Generally, banks would like to see 20% to 50% of the total cost carried by the equity investors.

If the banks find the political risk and the management expertise of the operator acceptable, then they will evaluate the reserves and its economic potential. The economic potential of the reserves depends on the timing of development, the rate at which reserves will be produced, assurances of timely completion of the project, and the review of the market to which the product will be supplied. The production rate needs to be modified based on the cash flow available for debt servicing. The

basic judgment, of the bank, on the loan request from the operator is decided based on the present worth of future incomes; it is usually no less than twice the size of the loan request and may be greater in some cases [22].

According to the recent projections of Rowley [17] shown in Figure 1.8a, the total investment in the world on offshore structures (consisting of platforms, subsea completions and pipelines) will grow steadily from \$29.3 billion dollars during 1999–2003 to \$52.7 billion during 2004–2008. In Figure 1.8a, Rowley [17] also predicts the growth and development in different types of offshore platforms from 1984 to 2014. He states that there will be a reduction in the amount invested on offshore structures from 2005 (as shown in Figure 1.8a) onward due to (i) more subsea completions



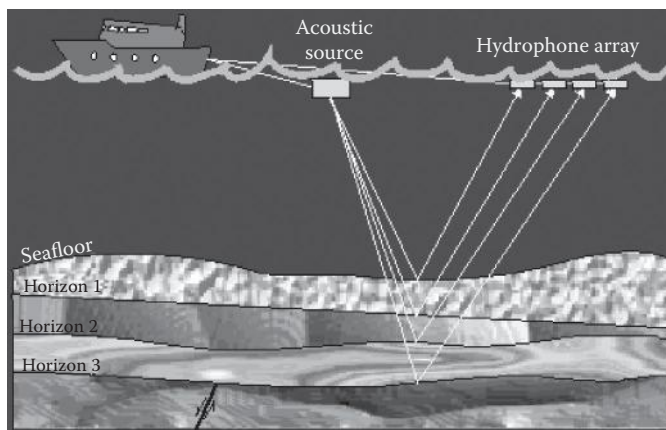
**FIGURE 1.8** (a) Possible offshore structures investment. (From W. Rowley, 2004, “Deepwater, Key Sectors,” Paper presented at the Deepwater International Conference, London, February, 12 pp, <http://www.infield.com>.) (b) Pictorial view of the world oil price fluctuations, 1970–2007. (From James L. Williams. Courtesy of WTRG Economics Newsletter. London, AR, 2007. With permission.)

with tiebacks to earlier-installed structures; (ii) lower unit costs through generic design and construction; and (iii) more conversions of existing structures for newer installations. Figure 1.8b [26] gives a pictorial view of the world oil price fluctuations, starting from the year 1970 to the year 2003.

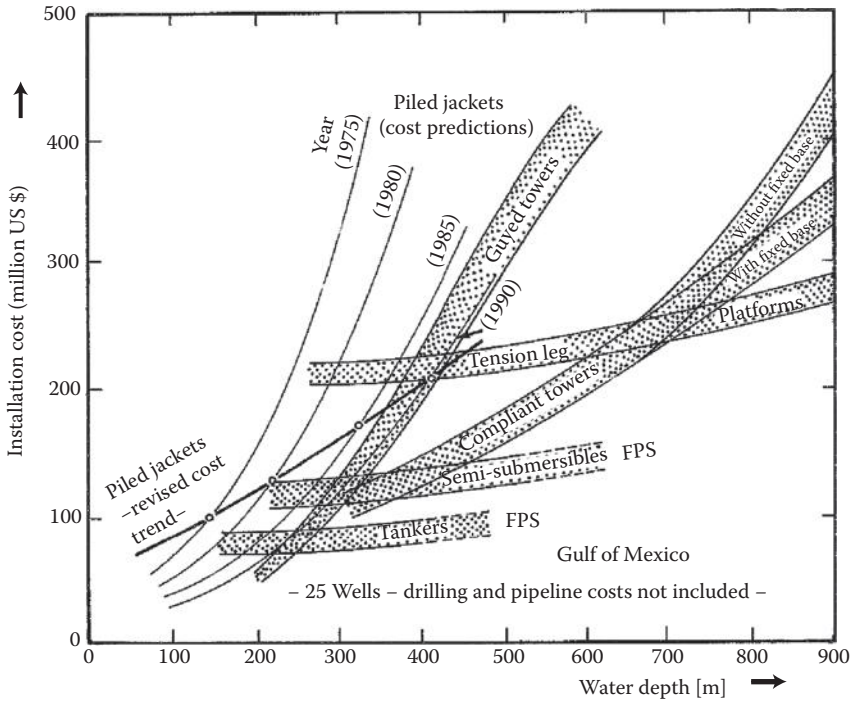
Table 1.2 shows that the exploration technology costs are relatively minor compared with the exploitation costs. As per 1980 prices, a 3000-km seismic line survey costs around \$1.5 million, depending on the drilling water depth. In seismic surveys, detailed geophysical examination of the seafloor is done using the seismic reflection method (with air gun, sparker, boomer or chirp systems) and survey ships, as shown in Figure 1.9 [27]. Seismic surveying is accomplished by towing or mounting, to the exploration vessel, a sound source that emits acoustic energy at timed intervals. The acoustic energy transmitted through the water is reflected from the seabed soil layer boundaries with different acoustic impedances. The reflected acoustic signal is received by a hydrophone (or an array of hydrophones) located in the floating vessel or by a tuned transducer array that is towed behind the exploration vessel. The receiver converts the reflected signal to an analog signal that is digitized and logged with a high-speed computer.

An exploration well costs from half a million dollars in shallow waters to \$20 million for a 4000-m-deep drilling in 1500-m-deep water. Costs increase when production is predicted, depending on the number of development wells required, equipment incorporated (such as separators, tanks, living quarters, etc.) and whether it is in deep waters or not. Sometimes the platform cost alone can reach \$1.0 billion or more. Pipeline costs are site-specific, costing from \$150,000 to \$300,000 (per 1-km-long, 16-in.-diameter pipeline) in the Gulf of Mexico to around \$1.0 million or higher in the North Sea. Over 56% of the costs are associated with the production of the offshore oil and gas, while 44% of the costs are spent on infrastructures needed for transport [23]. Costs triple when going from 30 to 300 m deep and drilling costs can go up 3 to 10 times between wells on land and offshore. Much of the drilling cost is in the riser, which for a well in 1500-m-deep water can cost from \$7 to 10 million.

Other costs associated with drilling are the costs associated with the type of drilling rig used in the 1500 m water depths; a deep water floating rig can cost more than \$100,000 per day to operate and the well may easily take more than 100 days to drill. Other special costs associated with deep water and hostile climates are (i) construction of artificial islands for drilling in ice-infested waters of the Arctic; (ii) ice-strengthened drill ships for drilling in Arctic waters; (iii) artificially strengthened natural ice covers for drilling in the Arctic north; (iv) special floating disconnecting systems for structures in iceberg alley, off the coasts of Newfoundland and Labrador; and (v) other items



**FIGURE 1.9** Offshore seismic reflection method for conducting geophysical surveys. (From Woods Hole Science Center Seismic Profiling Systems, [franklinccd.org/WelcometotheUSGS-U.S. Geological Survey.html](http://franklinccd.org/WelcometotheUSGS-U.S.GeologicalSurvey.html), 2007. With permission.)



**FIGURE 1.10** Relative costs associated with the various offshore structural concepts. (With kind permission from Springer Science+Business Media: *Conceptual Design and Hydromechanics*, Offshore structures, Vol. I, 1992, p. 135, G. Clauss, E. Lehmann, and C. Östergaard.)

mentioned earlier. Availability, costs, and development of new technologies to go in deep water and hostile offshore areas will greatly influence the future policies for offshore petroleum development.

The weight of a fixed steel/gravity platform increases exponentially as water depth increases, and this results in increased costs associated with offshore production. Hence, the costs associated with the structure selected for field exploitation need to be minimized. The relative costs associated with the various offshore concepts have been compared in Figure 1.10 [28]. It is seen that TLPs, compliant structures, semi-submersibles, FPSOs, etc., are more economical than fixed steel or gravity concrete platforms.

Two problems have been worked out below to illustrate the computation of preliminary costs and turnovers associated with the installation of any offshore platform at a specified site. Tables 1.1 and 1.2, developed during the 1980s, have been utilized for computing the preliminary costs of the specified offshore structure. Since the costs given in the tables are based on the pricing available in the 1980s, a multiplying constant has been evaluated regarding the worth of 1980 dollars during 2008; this computation is based on the best engineering judgment that could be exercised by the authors from the available published research papers. Hence, the computations given are only approximate values and should not be taken as the correct prices and turnovers.

**Example 1.1**

A low-production shallow-water oilfield has been recently discovered in the North Sea at a depth of 2000.0 m below the mean sea level; the depth of water at site was 100.0 m. The total recoverable reserves of crude oil were estimated to be 75.0 million barrels, and the average maximum output from the field was determined as 9000.0 barrels per day. (a) Outline the possible scenarios

for the exploitation of oil from the field. Also, estimate the life of the field. The distance of the field from the onshore tanker terminal (point of delivery) is 300.0 km. (b) Determine the required preliminary capital outlay for the field development. (c) Assuming the cost of one barrel of oil at the point of delivery to be US\$40.0, compute the total turnover from the field.

(a) Possible scenarios:

(i) Fixed platform with tanker transport and (ii) fixed platform with pipeline transport.

$$\text{Life of the field} = (75,000,000)/[(9000)*(365)] = 22.83 \sim 23.0 \text{ years.}$$

(b) Required capital outlay

Assume bad weather conditions to prevail during the exploration period. Using Table 1.2,

(i) Fixed platform with tanker transport:

Exploration costs (maximum) =  $(43.0)(2.0) = \text{US\$}86.0$  million.

Development costs (at \$20,000.0 per day) =  $(9000.0)(20,000.0)/(1,000,000) = \text{\$}180.0$  million.

Transportation costs: From Table 1.1, take the charges per day, for the use of a 50,000 metric ton tanker to be \$50,000.0; also take 1.0 metric ton of crude oil to be equivalent to 7.33 barrels.

Volume of oil in one tanker =  $(50,000)(7.33)/(1,000,000) = 0.3665$  million barrels

Number of passages of the tanker =  $(75.0)/(0.3665) = 204.63$  trips  $\sim 205.0$  trips

Time of travel from the field to the point of delivery (at 15.0 knots) =  $(300.0)/[(15.0)*(1.852)] = 10.8$  hours

(1.0 knots = 1.825 kmph)

Assuming 10 days for each trip back and forth, the total number of working days for the ship =  $(205)(10) = 2050.0$  days

Tanker charges =  $(2050.0)(50,000)/(1,000,000) = \text{\$}102.5$  million

Total capital required in 1980 =  $86.0 + 180.0 + 102.5 = \text{US\$}368.5$  million

Total capital required in 2007 =  $(368.5)(2.51) = \text{US\$}924.94$  million

(US\$1.00 in 1980 = US\$2.51 in 2007; see Table 1.1)

(The above amount does not include the charges for borrowing money from banks.)

(ii) Fixed platform with pipelines transport:

Exploration costs remain the same as before = US\$86.0 million.

Development costs remain the same as before = \$180.00 million.

Using Table 1.1, transportation cost for 300.0 km is =  $(300.0)(0.6) = \text{\$}180.0$  million.

Total capital required in 1980 =  $86.0 + 180.0 + 180.5 = \text{US\$}446.0$  million.

Total capital required in 2007 =  $(446.0)(2.51) = \text{US\$}1119.46$  million.

(c) Total turnover from the field:

At \$40.00 per barrel, total turnover from the field =  $(40.0)(75,000,000.0)/(1,000,000) = \text{\$}3000.0$  million

### Example 1.2

A shallow-water high-production oilfield was discovered in the North Sea at a depth of 3000.0 m below the mean sea level; the water depth at the site was 100.0 m. The total recoverable reserves at the site were estimated to be 900.0 million barrels of crude oil. The average maximum output from the field is expected to be 150,000 barrels of oil per day. (a) Outline the possible scenarios for the possible exploitation for the field. Also estimate the life of the field. The distance of the onshore tanker terminal (point of delivery) is 300.0 km from the field. (b) Determine the capital outlay required for each of the proposed scenarios. (c) Assuming the cost of one barrel of oil at the point of delivery to be US\$40.0, compute the total turnover from the field. (d) Assuming the same requirements as in cases (a), (b), and (c), determine the capital outlay and the total turnover from the field if the field is located in the Arctic zone, viz., Beaufort Sea.

(a) Possible scenarios:

- (i) Fixed platform with tanker transport; (ii) fixed platform with pipeline transport; (iii) gravity platform with tanker transport; and (iv) gravity platform with pipeline transport.

$$\text{Life of the field} = (900,000,000)/[(150,000)(365)] = 16.44 \text{ years} \sim 16.5 \text{ years}$$

(b) Required capital outlay:

Assume bad weather conditions to prevail during the exploration period. Using Table 1.2,

- (i) Fixed platform with tanker transport:

Exploration costs are the same as before = US\$86.0 million.

Development (or production) costs =  $(20,000.0)(150,000)/(1,000,000) = \$3000.00$  million.

Transportation costs: from Table 1.1, take the charges per day, for the use of a 50,000 metric ton tanker, to be \$50,000.0.

Number of passages for the tanker =  $(900,000,000)/[(50,000)(7.33)] = 3001.4 \sim 3000$  trips

Since the tanker point of delivery is the same (10 days per to and fro trip), number of Tanker days required for depleting the whole field =  $(3000)(10) = 30,000$  days

Tanker charges =  $(30,000)(50,000.0)/1,000,000.0 = \$1500.0$  million

Total capital required in 1980 =  $86.0 + 3000.0 + 1500.0 = \text{US\$}4586.0$  million

Total capital required in 2007 =  $(4.586.0)(2.51) = \text{US\$}11,510.86$  million

(The above amount does not include the charges for borrowing money from the banks)

- (ii) Fixed platform with pipeline transport:

Exploration costs are the same as before = \$86.0 million

Development costs are the same, being = \$3000.0 million

Transportation costs: Using Table 1.2, charges are US\$600,000.0 for 30-in.-diameter pipes. Considering the same diameter pipes,

Flow in one pipe per day at a flow velocity of 0.20 m/s =  $[(\pi/4)(30/39.37)^2](0.20)(60)(60)(24) = 7880.35 \text{ m}^3 = (7880.35)(6.29) = 49,567.38$  barrels per day.

(1 m<sup>3</sup> of oil = 6.29 barrels)

Use four parallel pipelines to carry the average maximum flow of 150,000 barrels per day output.

Cost of the pipelines =  $(4)(300.0)(600,000.0)/(1,000,000) = \$720.0$  million.

(No maintenance or replacement costs are included).

Total capital required in 1980 =  $86.0 + 3000.0 + 720.0 = \text{US\$}3806.0$  million

Total capital required in 2007 =  $(3806.0)(2.51) = \text{US\$}9553.06$  million

- (iii) Gravity platform with tanker transport:

Exploration costs are the same = US\$86.0 million.

Using Table 1.1, development cost will include platform costs and development costs.

Platform costs = US\$1000.00 million.

BOPD costs =  $(14,000.0)(150,000)/1,000,000 = \$2100.00$  million

Transportation costs will remain the same as in section (i) = \$1500.00 million

Total capital required in 1980 =  $86.0 + 1000.0 + 2100.0 + 1500.00 = \text{US\$}4686.0$  million

Total capital required in 2007 =  $(4686.0)(2.51) = \text{US\$}11,761.86$  million

- (iv) Gravity platform with pipeline transport:

Exploration, platform, and BOPD costs will remain the same as in section (iii).

Pipeline costs will be the same as section (ii) = \$720.0 million

Total capital required in 1980 =  $86.0 + 1000.00 + 2100.00 + 720.0 = \text{US\$}3906.0$  million

Total capital required in 2007 =  $(3906.0)(2.51) = \text{US\$}9804.00$  million



- (c) Total turnover from the field:

At \$40.00 per barrel, total turnover from the field =  $(40.0)(900,000,000)/(1,000,000) =$   
US\$36,000.00 million

- (d) Fixed platform with pipeline transport in Beaufort Sea:

Using Table 1.1, exploration costs will include seismic survey costs and drilling fleet costs.

Exploration costs for four months =  $(120)(20,000.0)/(1,000,000) =$  US\$2.4 million

Drilling fleet costs = US\$240.0 million

Development (or Production) costs include the platform costs, BOPD, and automation costs.

Platform costs = \$200.0 million

BOPD costs (using Louisiana costs) =  $(20,000.0 + 5000.0)(150,000)/(1,000,000) =$   
\$3750.00 million

Automation costs = \$21.0 million

Transportation costs will be the same as in section (ii) = \$720.0 million

Total capital required in 1980 =  $2.4 + 240.0 + 200.0 + 3750.0 + 21.0 + 720.0 =$   
US\$4933.4 million

Total capital required in 2007 =  $(4933.4)(2.51) =$  US\$12,382.83 million

## 1.4 STRUCTURAL CONCEPT EVALUATION AND INNOVATIVE DEVELOPMENTS

The overriding need for technology is pervasive in all oil and gas developments, especially offshore. Technology underlies every aspect of offshore operations, from the geological assessment through exploration, drilling, production, transportation, and even to environmental aspects. The availability of requisite technology deeply affects the economics as well as many policy issues of offshore oil and gas development.

The water depths at which exploration drilling has been carried out is an indicator of future requirements for oil production. Production platforms should be capable of carrying large amounts of development drilling and oil processing equipment. The process equipment has to separate water, gas, and sand from crude oil and keep the crude oil ready for transportation by providing storage space and a transportation pumping station. At the same time, the hydrocarbon depletion procedures may require gas lift (which involves the use of gas to assist in raising the oil if the reservoir pressure is insufficient) and water injection procedures to increase the reservoir pressure and the extraction of greater amounts of oil. Also, directional drilling may be required to deplete a larger plan area of the oil and gas reservoir. The world's longest horizontal drilling record was set by BP during 2000, when it spudded a horizontal well at a total depth of 7836 m, made up of a true vertical depth of 3003 m (9854 ft.) a directional offset of 6722 m (22,056 ft.). Seafloor penetration by drill string, for scientific research, has been achieved (during 1989) in water depths over 10,000 m and for oil and gas exploration at 7620 m below the sea surface. The deepest producing natural gas well was drilled to a depth of 6668 m in 1991, in the Gulf of Mexico. Recently (2003), oil wells have been spudded in water depths of more than 3051 m [16, 29] and the earlier prediction of 4000 m water depths for drilling may become feasible in the near future [23].

Production in shallow and intermediate depths of water (<300 m) offshore used the same methods as onshore, viz., the drilled wells flowed naturally, or were pumped/gas-lifted using the same methods and hardware used onshore, using pressure maintenance and secondary recovery. For deeper waters, the economics of using the same procedures has become limited and doubtful. Tiebacks, hubs, automation of the entire production process (control, accounting, testing, shut-down, etc.) including blow-out preventers, early warning provisions, production valves, firefighting equipment, etc., and subsea storage are required to facilitate deep sea operations. Gas and oil offshore pipelines of large diameters (up to and larger than 36 in. in diameter and 450 km long) have been laid down. Production is either transported onshore through pipelines or loaded onto tankers offshore, through a variety of single-point mooring and loading buoys. Progress has been made in environmental

technology from the design of safety features on drilling and production platforms to the development of repair or remedial technology and control of blowouts or pipeline breaks.

Pipelines carry 50% of all oil and 100% of all gas produced offshore, and, as mentioned earlier, they are quite expensive. Deep water pipeline laying faces formidable obstacles for design, materials, laying, and operations. Large reserves are needed to pay for long and large diameter lines. It is stated that 55 billion m<sup>3</sup> of oil will be needed make pipeline laying economical and feasible, along the Eastern Coast of Canada; for economical gas transport, through pipelines, it has been stated that 550–825 billion m<sup>3</sup> of gas reserves are required. Besides the pipelines, ships (tankers) carry a large amount of petroleum and petroleum products. Very large tankers of 550,000 deadweight tonnage or DWT (includes weight of cargo and fuel and excluding the self-weight of ship) carry oil, in conjunction with liquefied natural gas carriers, and transport oil and gas from offshore fields. Offshore facilities known as single point moorings are used for loading and unloading of oil and gas offshore. The buoys are anchored or fixed to the seafloor, and the tanker receives or discharges its cargo moored to the buoy; the buoys are supplied with oil and gas by pipelines (called flow lines) from the subsea oil and gas fields.

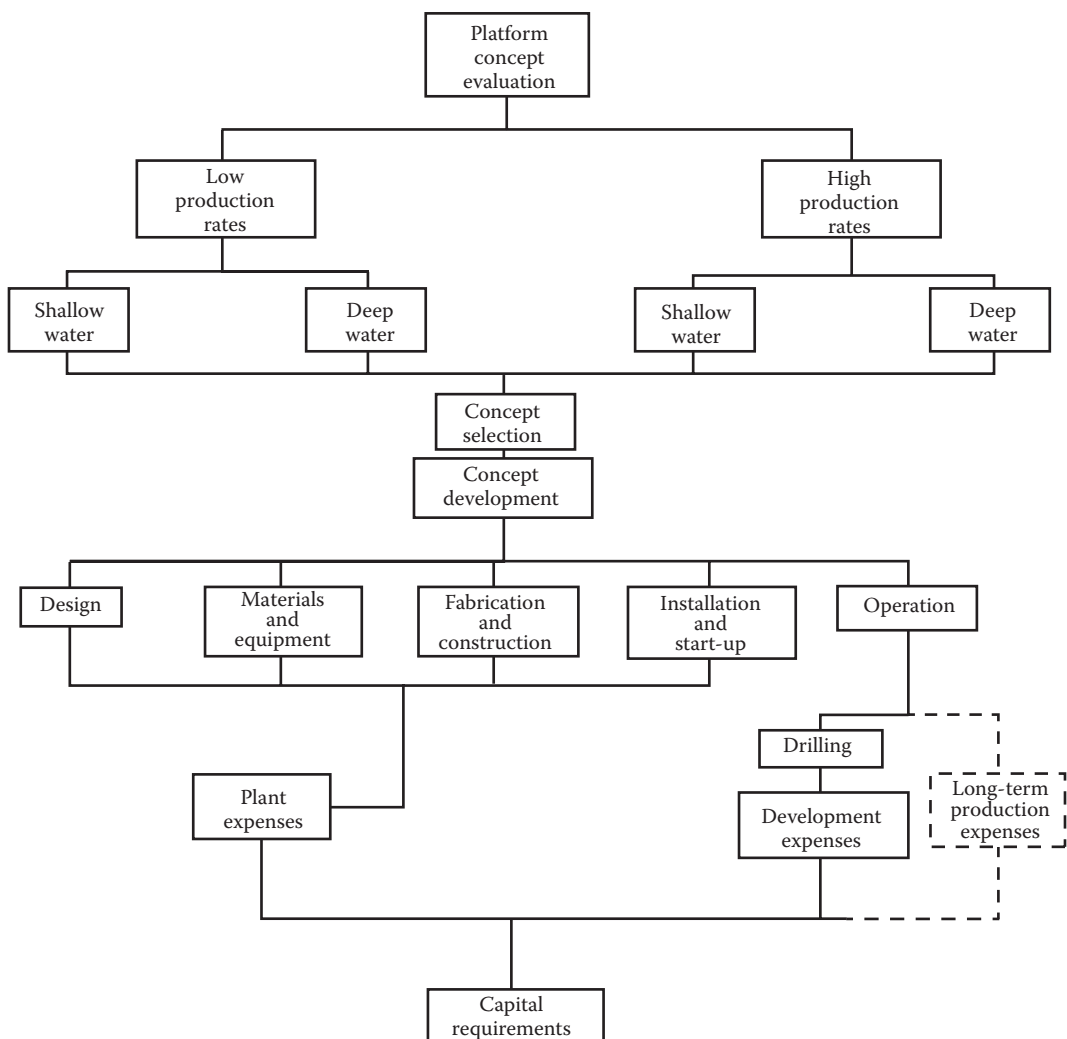
Extraction of oil/gas from a virgin field is undertaken in typically four stages: exploration and appraisal; development; production; and abandonment. This is an oversimplification since within each phase there are a number of technical, commercial, and operational considerations. These are

- (i) Exploration and Appraisal: Using the seismic data gathered, a subsurface picture of the reservoir is obtained. Based on earlier geological knowledge and experience, a more detailed depiction of the reservoir is generated. Since seismic data cannot give any specific details about the nature of the fluids present in the reservoir, exploratory wells need to be drilled to determine the nature, size, and type of the oil/gas field. Questions concerning the nature of additional seismic data required [3D or 4D (including time) seismic data], ability of such studies to remove uncertainties concerning the field characteristics, sharing of risk between partners based on the inherent uncertainty of the field, and how many exploration wells are required to remove the uncertainties present in the earlier seismic data need to be finalized to make the proper financial decisions.
- (ii) Development: Once sufficient data have been obtained (from seismic or exploratory wells) to make an educated judgment on the size of the field, one enters into the development phase. Here one has to decide upon the most commercially viable way for exploiting the resource by engineering the number (and type) of producing wells, process facilities, and transportation. One must also establish whether any pressure supports from below is needed to produce the wells. Valid development options include (a) number and order of wells to be drilled, type of wells (deviated or horizontal or vertical), (b) number of platforms and drilling rigs required, number of wells in which future work-over is required, (c) number of well injectors and their location, (d) size of the processing facility on top of the platform, (e) sharing of processing methodology with adjacent fields (waiting to be developed), (f) pipeline or other mode of transporting the resources, and the like.
- (iii) Production: Depending on the size of the reserve (and how prolific the wells are) the engineer must manage this resource as carefully as any other valuable asset. Reservoir management has become increasingly important over the past decade. Older, less technically advanced, production methods were inefficient, often leaving 75% or more of the oil in the ground. Increasing the efficiency of the production from the reservoirs has become crucial to any engineering effort. The required production options include “unswept” areas and additional wells required, “farming-out” of assets to other companies for economical operations, required additional seismic data, converting the existing production wells into injection wells to improve the overall field performance, possibility of extending the life of the field, reentering, and performing operations to improve the well performance and the like.



- (iv) Decommissioning (or Abandonment): Once reserves have been depleted, the infrastructure can either be left to decay or, increasingly, it must be dismantled in an environmentally and economically efficient manner. The following options need to be considered: cost of ultimate abandonment, need to include or phase out this cost during the initial project phase or otherwise, contingency plan for changing legislation, threshold of abandoning the field, and the like.

Adequate planning and concept evaluation should be carried out before the actual design is started in order to obtain a workable and economical offshore platform that will perform the specified functions. The initial planning and evaluation should include all the criteria and factors that will influence the design, construction, installation, and maintenance of the platform to obtain a workable and economical offshore platform, fulfilling all its required function. Figure 1.11 [25] gives a flowchart for the offshore platform development.



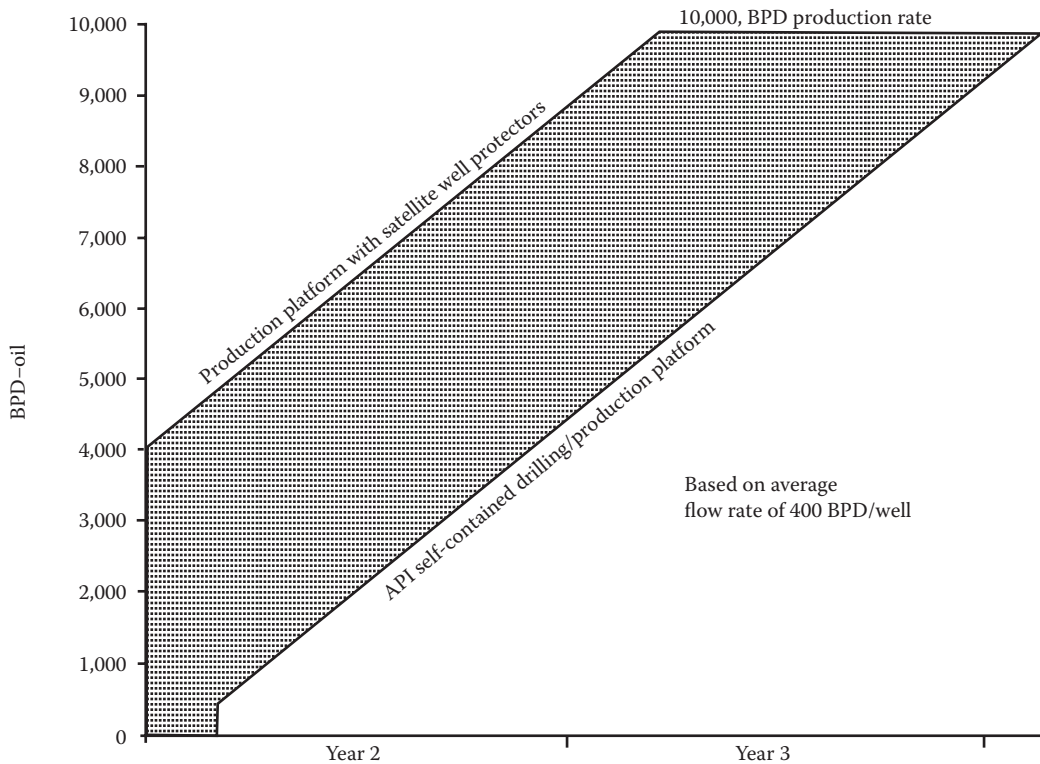
**FIGURE 1.11** Platform concept evaluation flowchart for offshore field development. (From Course Notes on General Design of Fixed Offshore Structures, University of Texas, Austin, TX, p. 3.1. Also Course Notes EOC 6431, 2001, *Offshore Structures: Framed Platforms*, Florida Atlantic University, Florida, 100 pp., 1979. With permission.)

The evaluation should take into consideration the following factors for an efficient and economical project and capital requirements, viz., (i) low or high production rate of oil/gas from the field, in shallow or deep waters; (ii) selection of platform types; (iii) operational and environmental considerations; (iv) design features, material, equipment, fabrication and construction, installation and start-up, operation (drilling, development, long-term production, and maintenance), and (v) platform reuse/dismantling costs. These are illustrated for a fixed platform in Figures 1.12 to 1.15 [25].

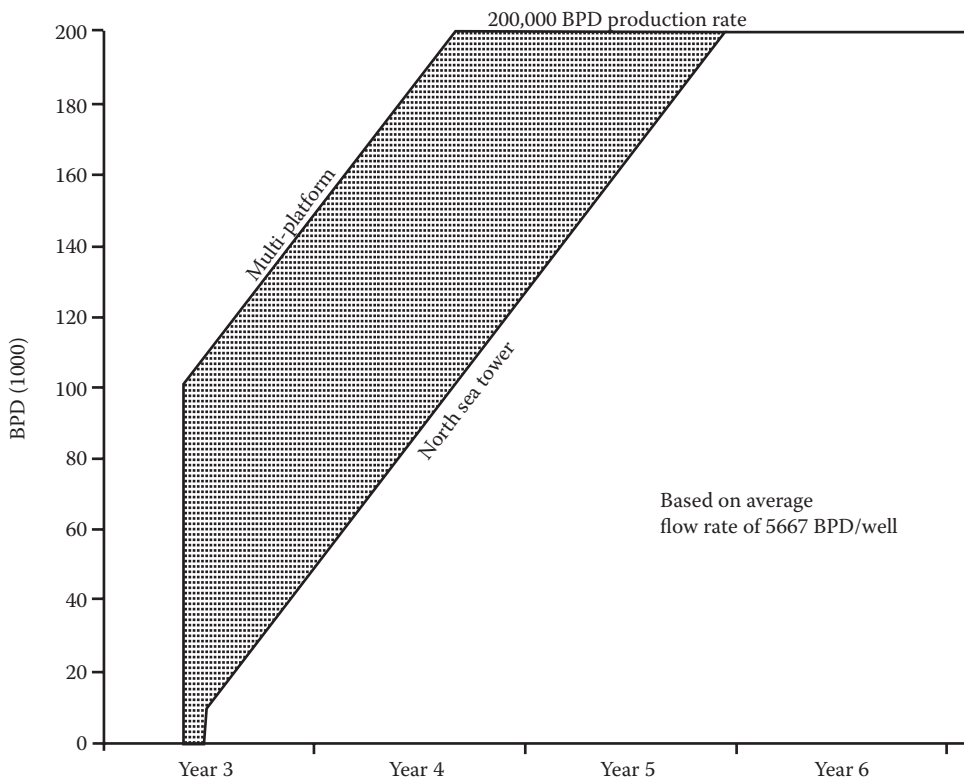
Much of the offshore technology was originally developed for on land operations. When oil and gas developments went offshore, additional technology was created. This technology was needed for sonar/seismic measurements (oil/gas reserves identification/estimation and for water depth measurements), underwater cameras and robots (for remote operation/control), sea bottom samplers, accurate navigation systems including inertial guidance, vertical/inclined/horizontal drilling technology, dual gradient drilling, extended reach drilling from shore for low volume coastal fields, extended use of subsea satellites, hub installations, minimization of topside facilities, reduction of offshore manning, extended use of temporary/mobile drilling rigs, and the like.

Since seismic surveys cannot produce results that will lead to the production phase, exploration drilling is needed. This requires offshore structures to assess and delineate the extent and quantity of oil and gas reserves in the field. These structures include submersible platforms, jack-ups, and floating moored or dynamically positioned drill ships, as shown in Figure 1.16 [30].

Drilling from a floating vessel is unique since the blow-out preventers (BOPs) are placed on the seafloor and operated remotely by a hydraulic control system. The drill riser is a pipe that extends from the BOP stack to the vessel. It serves to guide the drill bit into the well and to conduct the drilling fluid from the well back to the vessel. The riser system also includes connectors, flexible joints, and a telescoping section to accommodate the heaving motions of the vessel. Specially designed



**FIGURE 1.12** Production rate comparison for a low water low production oil field. (From Short Course on Design of Fixed Offshore Structures. Courtesy of University of Texas, Austin, 1979. With permission.)

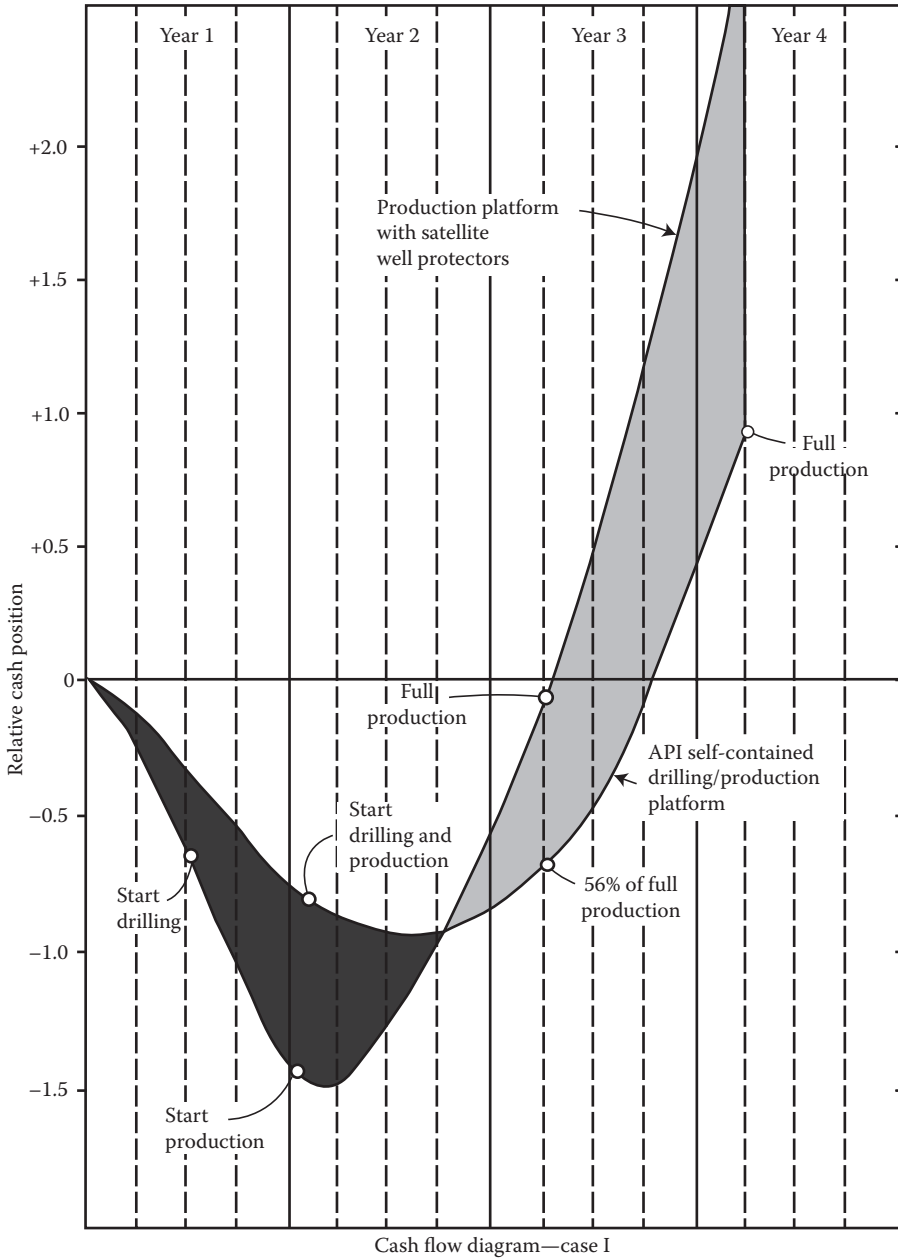


**FIGURE 1.13** Production rate comparison for a deepwater, high production oil field. (From Short Course on Design of Fixed Offshore Structures. Courtesy of University of Texas, Austin, 1979. With permission.)

tensioners are mounted on the vessel to support the top of the riser and prevent its collapse. For drilling in water depths beyond 600 m, the offshore industry has developed dynamically positioned vessels, similar to that shown in Figure 1.17 [31]. These vessels do not employ mooring lines but maintain their position in the ocean relative to a fixed acoustic beacon on the seafloor [5, 31].

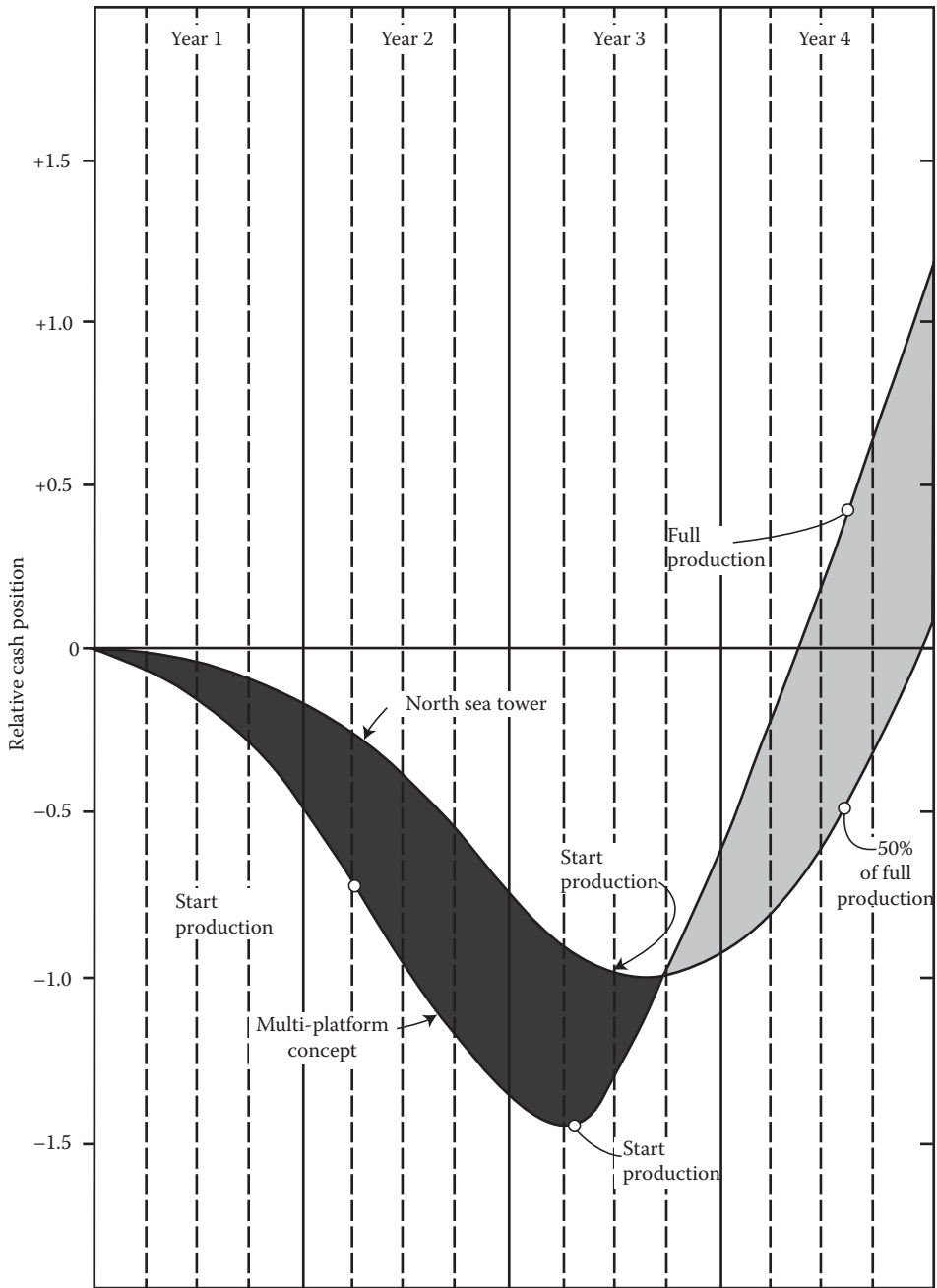
Once a commercially attractive hydrocarbon field has been discovered and delineated, it becomes essential to fabricate and install the required offshore structure and the necessary equipment. This process will require equipment to drill and complete the producing wells, process the oil and gas onboard, and transport the processed product to markets. On the continental shelves, the most widely used platform structure is the pile-founded steel template shown in Figure 1.18 [32]. Table 1.3 gives the number of fixed platforms installed and removed in the federally controlled continental shelves of the United States from 1942 to 1999 [33].

The technology associated with the design and installation of these structures has been refined over the past 60 years, with better methods for predicting the environmental loads and structure's resistance. The jacket structure is fabricated in a coastal fabrication yard as a single or multiple-connected structure, loaded onto barges, towed to the site of installation, launched into water and upended onto the exact location by using controlled flooding. Simultaneously, the deck and deck facilities are fabricated onshore, along with the drilling rig, processing equipment, utilities, and modular living quarters. The decks and modules are transported by barges to the platform location, lifted by a crane barge onto the platform and placed on the platform. The modules are then interconnected with the main template structure and the deck to provide an integrated platform from which the wells are drilled, completed, and produced. For efficient hydrocarbon production, the producing wells must penetrate the reservoir at regularly spaced intervals over its horizontal extent. This is done offshore by deviated drill wells, as shown in Figure 1.19 [34]. Drilling deviated wells are quite costly, and the costs increase with the angle of deviation from



**FIGURE 1.14** Yearly cash flow position for a shallow water, low production oil field. (From Short Course on Design of Fixed Offshore Structures. Courtesy of University of Texas, Austin, 1979. With permission.)

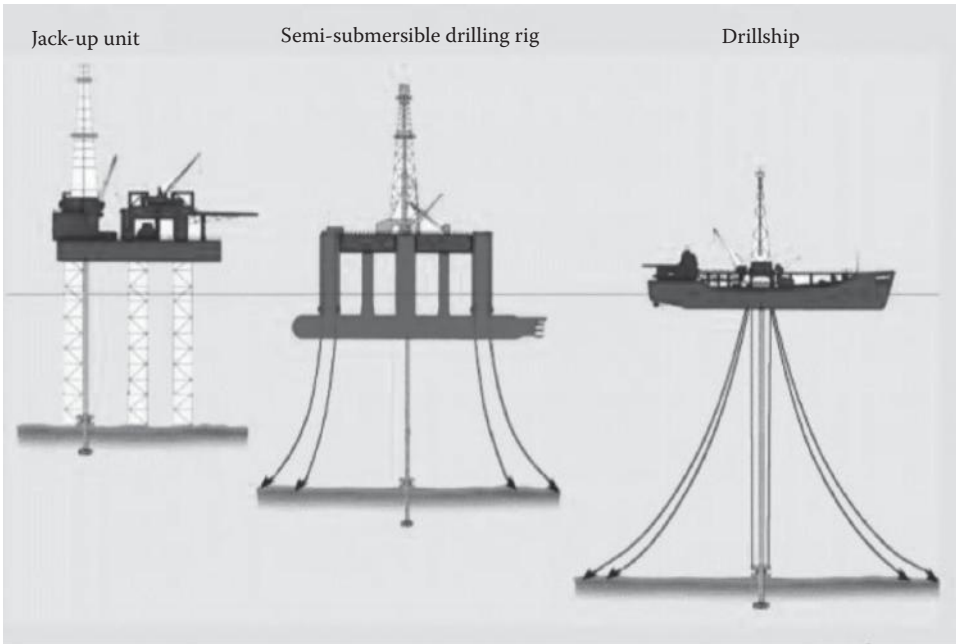
vertical. Typical costs of drilling and completing 18 wells in the Gulf of Mexico, to a vertical depth of 2100 m, is about US\$50 million [23]. When distribution avenues exist near the platform location, the most common method of transportation is the subsea pipeline. The pipelines are laid on the seafloor by specially designed barges called lay barges. When no such nearby distribution avenues are available, oil can be loaded directly on to the tanker by using an offshore loading terminal, shown in Figure 1.20 [5]. In this case, a short pipeline, called flow line, connects the platform to the loading terminal; the loading terminal also serves as a mooring for the tanker.



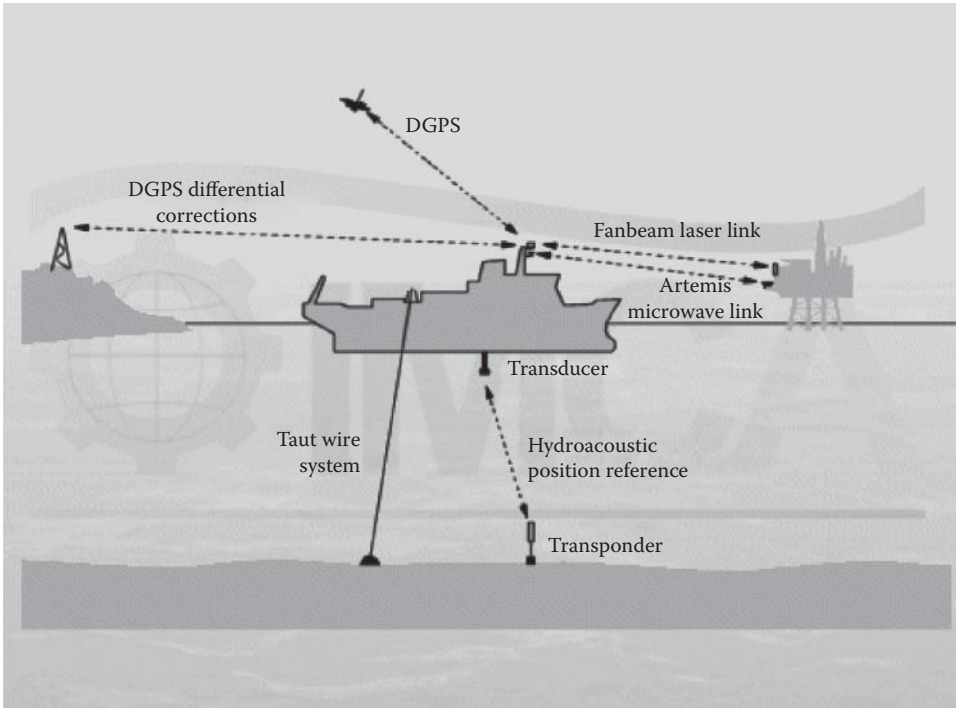
Cash flow diagram—case II

**FIGURE 1.15** Yearly cash flow position for a deepwater, high production oil field. (From Short Course on Design of Fixed Offshore Structures. Courtesy of University of Texas, Austin, 1979. With permission.)

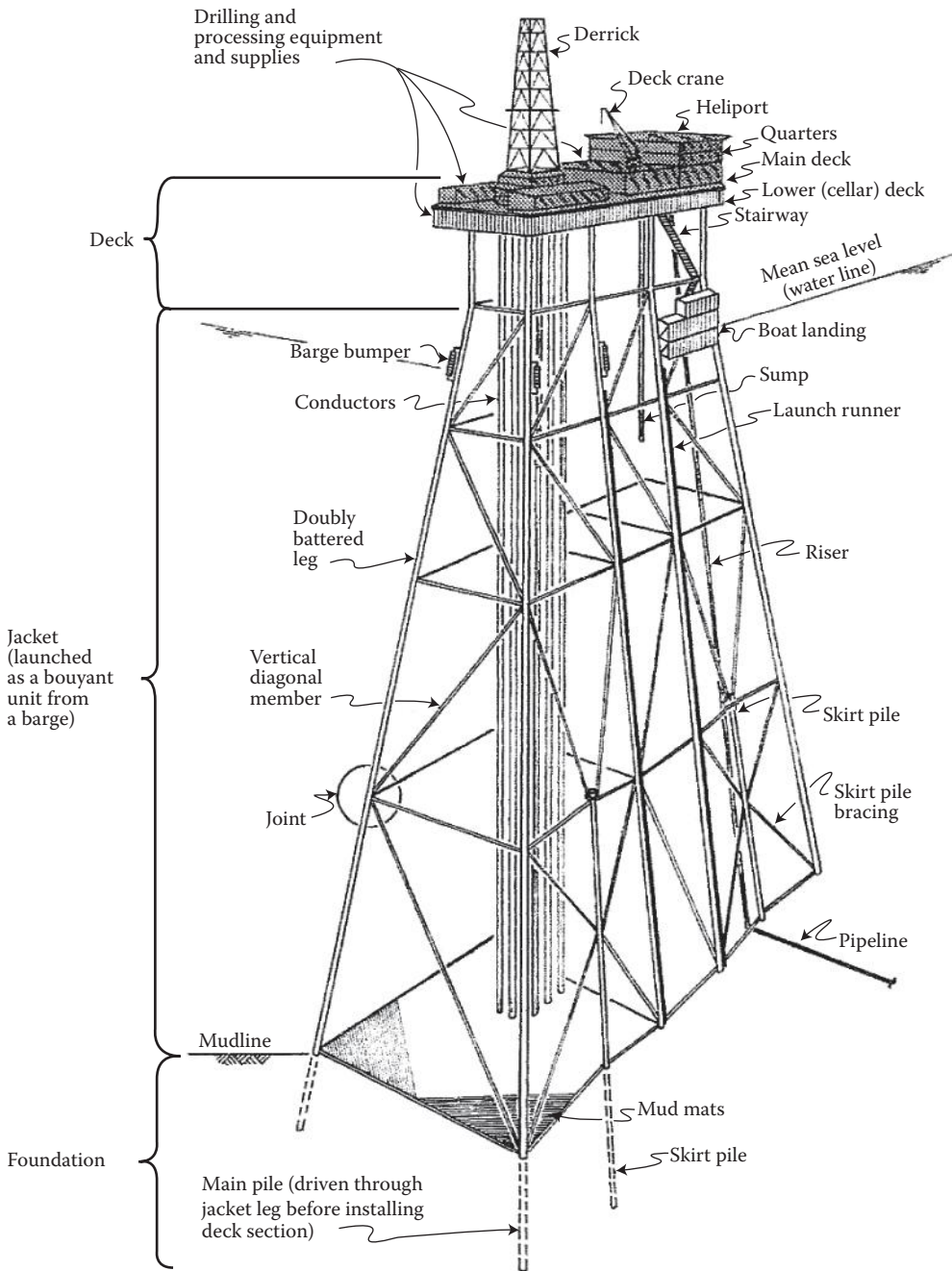
The gravity structure, shown in Figure 1.21 [35], is constructed of concrete, and is fabricated complete with decks and topside facilities. The completed structure is towed to the installation site, ballasted with seawater and set on the exact location marked on the seafloor. Instead of piling, it is held in place by its own weight, which can range from 200,000 to 500,000 t. This compares with a weight of 19,000 t for a steel template platform in the North Sea.



**FIGURE 1.16** Types of mobile drilling platforms used for offshore exploration. (From The United Kingdom Offshore Oil and Gas Industry Association, *Facts, Figures and Explanation: Drilling for Oil*. Available at [www.oilandgas.org.uk/education/students/drilling.cfm](http://www.oilandgas.org.uk/education/students/drilling.cfm), 2008. With permission.)



**FIGURE 1.17** Deepwater dynamic positioning system. (From International Marine Contractors Association (IMCA), *Introduction to Dynamic Positioning*. Available at [en.wikipedia.org/wiki/Dynamic\\_Positioning](http://en.wikipedia.org/wiki/Dynamic_Positioning). 2003. Courtesy of IMCA, [imca-int.com](http://imca-int.com). With permission.)



**FIGURE 1.18** Typical pile-founded steel jacket type offshore platform. (From J.B. Weidler and D.I. Karsan, Analytical models and three-dimensional analysis, in: *Planning and Design of Fixed Offshore Platforms*, edited by B. McClelland and M.D. Reifel, Van Nostrand Reinhold Company, New York, p. 548, 1986. With permission.)

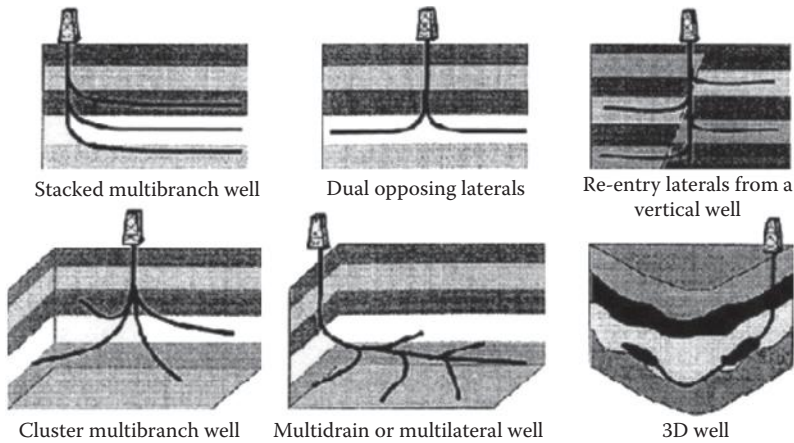
For water depths beyond 300 m, several new concepts have been developed [5]. They are compliant guyed towers, tension leg platforms (TLP), compliant towers and spars. Figure 1.22 [36] shows the Exxon Lena compliant guyed tower, installed at a water depth of 310.0 m. It is similar to the pile-founded steel template platform as it uses a conventional tubular steel frame and has the wellheads on the platform, above the sea level. Unlike the steel template platform, it retains a constant cross

**TABLE 1.3**  
**Installation and Removal of Production Platforms on the**  
**Federal Outer Continental Shelf**

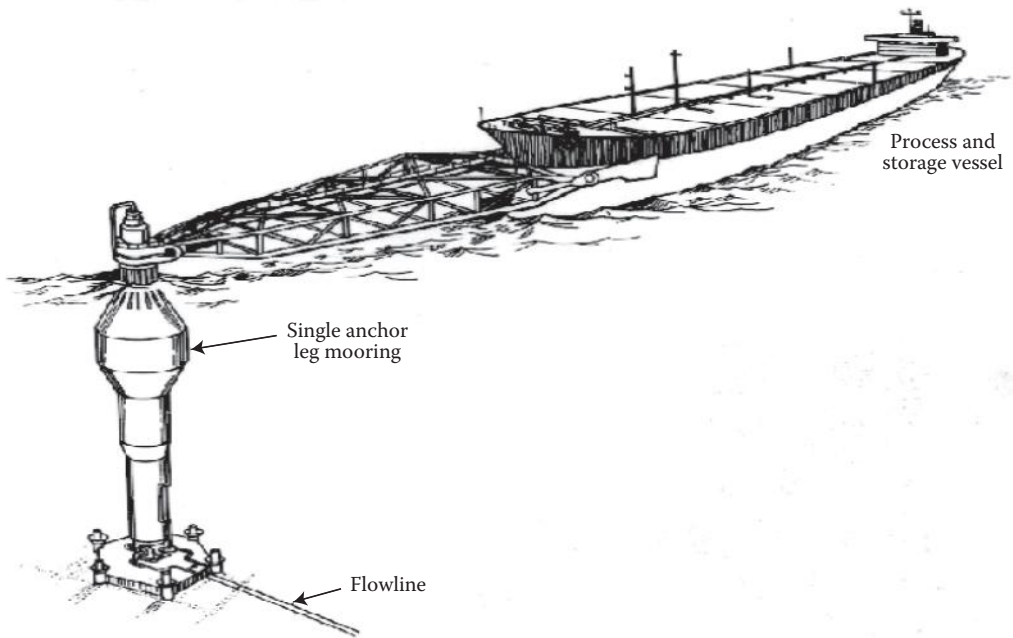
Year	Gulf of Mexico		Pacific	
	Installed	Removed	Installed	Removed
1942–1960	459	0	0	0
1961	108	0	0	0
1962	123	0	0	0
1963	89	0	0	0
1964	127	0	0	0
1965	129	0	0	0
1966	118	0	0	0
1967	133	0	1	0
1968	109	0	3	0
1969	112	0	1	0
1970	117	0	0	0
1971	102	0	0	0
1972	132	0	0	0
1973	95	1	0	0
1974	56	5	0	0
1975	102	36	0	0
1976	115	30	1	0
1977	114	17	1	0
1978	166	26	0	0
1979	162	35	2	0
1980	175	36	3	0
1981	168	24	3	0
1982	195	15	0	0
1983	179	38	1	0
1984	226	53	1	0
1985	212	55	3	0
1986	115	34	1	0
1987	116	23	1	0
1988	169	99	0	0
1989	197	94	2	0
1990	177	108	0	0
1991	156	117	0	0
1992	92	105	0	0
1993	126	171	0	0
1994	179	124	0	1
1995	138	117	0	0
1996	159	121	0	0
1997	155	176	0	0
1998	142	75	0	0
1999	–	–	0	0
Totals	5744	1735	24	1

Source: OCS Pacific Region Study MMS 2001–2006. Courtesy of USDIA, MMS.



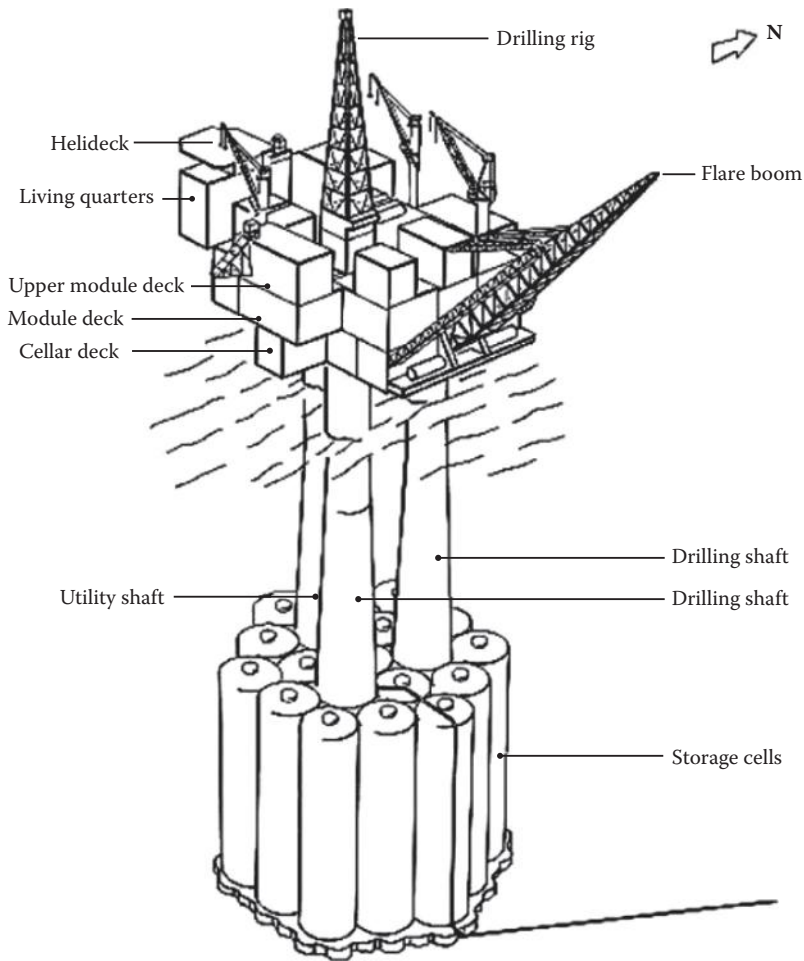


**FIGURE 1.19** Deviated wells drilled from an offshore platform. (G. Renard and E. Delamaide, *Complex Well Architecture IOR and Heavy Oils*, Vol. Production, Proc. of the 15th World Petroleum Congress. 1998. Copyright Wiley-VCH Verlag GmbH & Co. KGaA. Reproduced with permission.)



**FIGURE 1.20** Single anchor leg mooring offshore loading terminal. (From G.A. Lock, Technological factors in offshore hydrocarbon exploration, in *The Future of Offshore Petroleum*, McGraw-Hill (in cooperation with the United Nations), New York, pp. 87–146, 1981. With permission.)

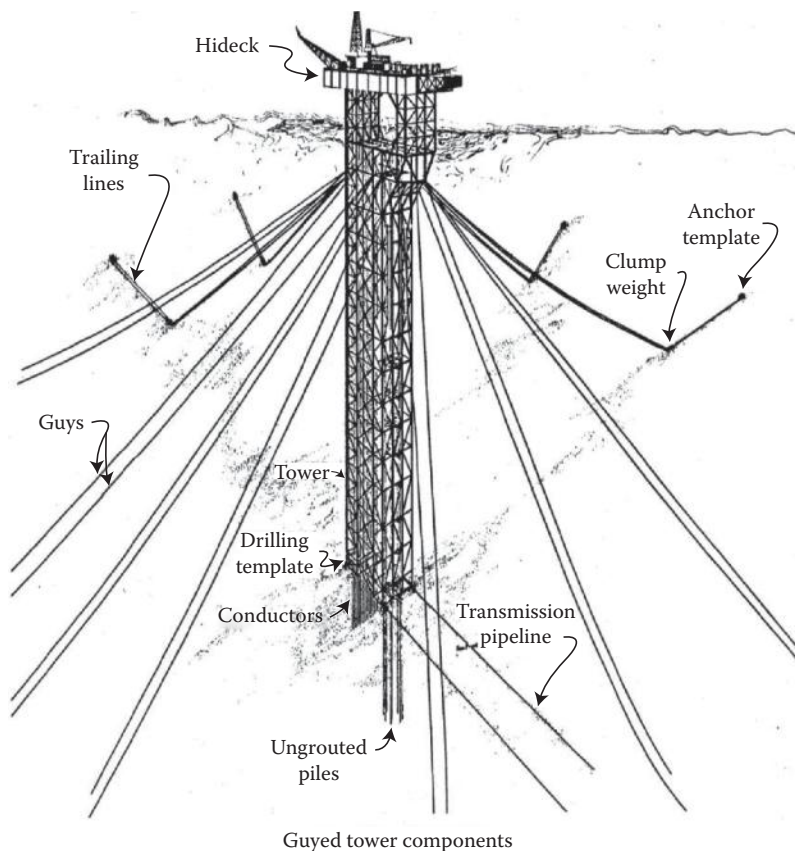
section with depth, thus greatly reducing the amount of steel required for the structure. Transverse loads on the structure, exerted by normal winds, waves, and currents are resisted by an array of guy lines extending to anchor piles driven into the seafloor. Clump weights, shown in Figure 1.22, are attached to these guy lines to permit the tower to sway lightly or “comply” with extreme waves. This compliance greatly reduces the peak tensions exerted on the guy lines.



**FIGURE 1.21** Condeep concrete gravity structure. (From S. Tanaka, Y. Okada, and Y. Ichikawa, *Offshore Drilling and Production Equipment, Encyclopedia of Life Support Systems (EOLSS)*, EOLSS Publishers, Oxford, UK (Fig. 15), 2005. With permission.)

The tension leg platform (TLP) Brutus, shown in Figure 1.23 [37], was installed by Shell at a water depth of 910.0 m, and consists of a large, buoyant, semi-submersible-type platform held in place by vertical mooring tethers. The platform is submerged deeper than its floating draft, thereby maintaining the tension on the vertical tethers. It is designed so that even in the troughs of extreme waves, these tethers or “legs” will remain in tension. The TLP is compliant and moves with the waves. The mooring tethers are equipped with special flexible joints at top and bottom to accommodate this movement.

Other recent developments, such as compliant piled towers and spars, for deepwater are shown in Figures 1.24 [38] and 1.25 [39]. Figure 1.24 shows the tallest Compliant Tower Platform Petronius, located at Viosca Knoll, block 786, approximately 208.0 km southeast of New Orleans. It is installed at a water depth of 535.0 and is 640.0 m high (from mud-line to tip of flare boom). The compliant tower is a statically stable structure, with a greater degree of lateral deformation (up to 2.5%) compared with land-based structures (usually 0.5% or less). Actually, the Petronius tower is able to operate within a 25-ft. sway envelope at the surface (1.4%), which is facilitated by the 12 deep piles (3 at each corner) extending over 450 ft. into the seabed. Figure 1.25 shows two typical designs used in the fabrication of spar platform structures. The figure on the left is similar to the Chevron-Texaco’s

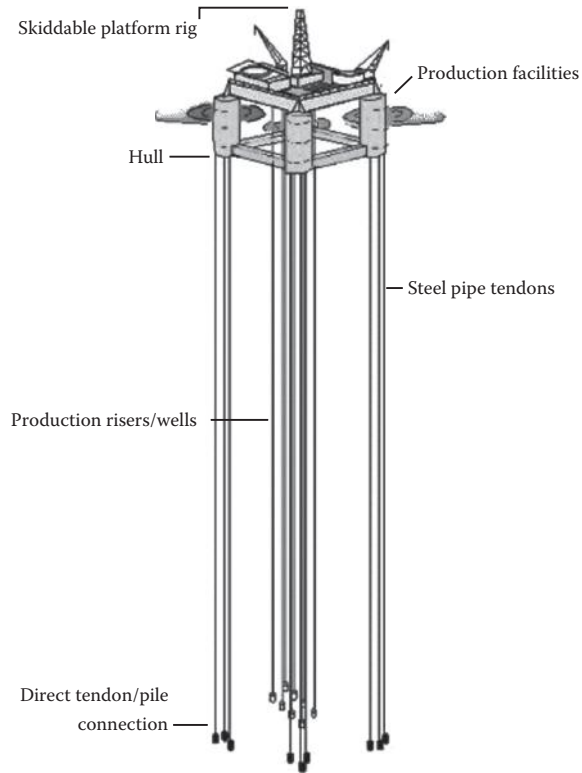


**FIGURE 1.22** The Exxon Lena compliant guyed tower concept. (From Report by Brown and Root Development, Inc., *State-of-the-Art Report on Guyed Towers Platforms*, NBS GCR 83-443, National Bureau of Standards, Gaithersburg, MD, September 1983. Available at [www.mms.gov/tarprojects/052.htm](http://www.mms.gov/tarprojects/052.htm).)

Genesis Spar platform structure, located 210.0 km south of New Orleans, across the three Green Canyon blocks 160, 161, and 205, where the water depth varies from 760.0 to 900.0 m. The Genesis production facility is moored in 793.0 m of water. The figure on the right is similar to the Dominion's Devil's Tower located at a water depth of 1710.0 m. Recently, Spar platform structures have been proposed for water depths varying from 500.0 to 2500.0 m.

In waters deeper than 600 m, the costs and technical difficulties associated with above water wellheads grow in magnitude. For these deeper waters, a subsea production system may prove more economical. In the subsea system, the wellheads and associated equipment are mounted on a seafloor template or frame instead of on a platform. Wells are drilled and completed through this template, using a floating drilling vessel. Subsea systems can be placed in one or two categories, viz., wet and dry. In a dry system, all the basic components are enclosed in a dry, one-atmosphere chamber; manned intervention is envisaged for maintenance and some installation requirements. In the more commonly used wet subsea system, shown in Figure 1.26 [5], all the basic components are open to the influences of the ocean environment. For this type of system, higher-reliability components are used to minimize component malfunctions. The seafloor equipment is modularized so that maintenance is reduced for the most part to replacement of components. Producing operations can be controlled remotely from a nearby surface facility. Submerged production system technology has advanced nicely with several deepwater system configurations.

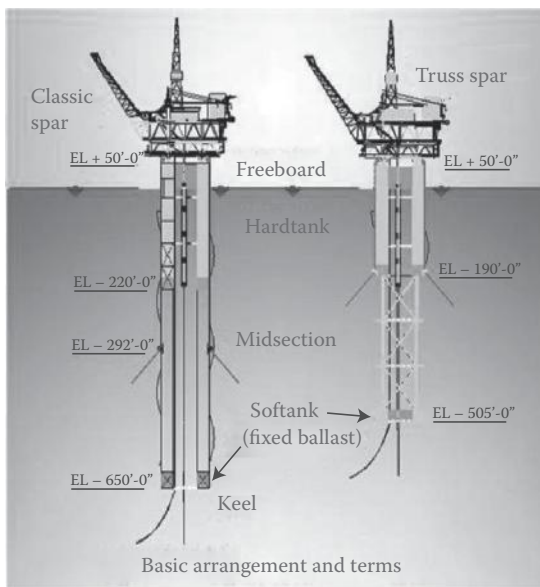
The subsea production system shown in Figure 1.27, located in the BP's King Field in the Gulf of Mexico (90.0 km offshore) [40], consists of a subsea template system to produce the reservoir, flow



**FIGURE 1.23** Tension leg platform BRUTUS. (From Brutus, *Gulf of Mexico*. Available at [www.offshore-technology.com/projects/brutus/](http://www.offshore-technology.com/projects/brutus/), 2004. With permission.)

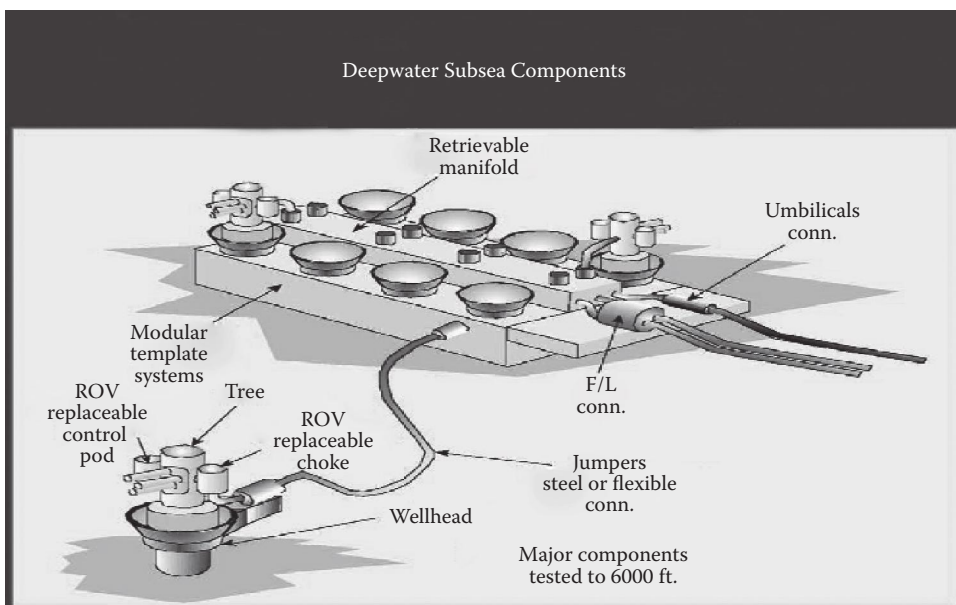


**FIGURE 1.24** Petronius compliant piled tower platform. (From Petronius Compliant Tower. Courtesy of [offshore-technology.com](http://offshore-technology.com). With permission.)

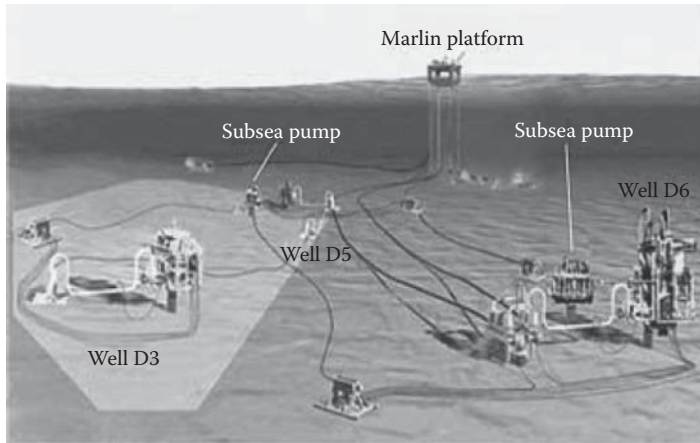


**FIGURE 1.25** Typical compliant spar platforms. (From Global Security.Org, *Military: Spar Platform*. Available at <http://www.globalsecurity.org/military/systems/ship/platform-spar.html>, 2006. With permission.)

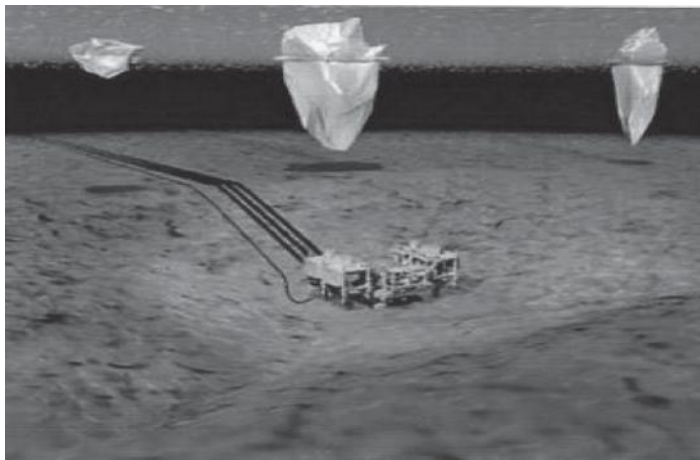
lines, a deepwater offshore terminal (to offload oil and gas), and a floating processing and storage vessel. It represents a breakthrough in the world of multiphase subsea pumping, where “the pumps and associated equipment” are pumping the wellhead fluids to the host platform, which is 27 km away. The subsea wells tagged as D3, D5, and D6, located in water depths 1525–1655 m, carry well fluids through flow lines to the Marlin platform located 27.0 km away where oil, gas, and water from



**FIGURE 1.26** Wet subsea production system, with wellhead components exposed to water. (From Dinamica de Plataformas de Agua Profunda, 2001. Courtesy of ingen.unam.mx. With permission.)



**FIGURE 1.27** BP’s Marlin platform located in the King Subsea Field in the Gulf of Mexico. (From T. Knott, *Subsea king*, *Frontiers*, April 2008, pp. 34–38. Available at [www.bp.com/sectiongenericarticle.do?categoryId=9023215&contentId=7043112](http://www.bp.com/sectiongenericarticle.do?categoryId=9023215&contentId=7043112), 2008. With permission.)



**FIGURE 1.28** Subsea wellhead system located below the seabed in “Glory Holes” to prevent gouging of the equipment by the keel of free-drifting icebergs in Grand Banks. (From Project Update, *Boskalis covers itself in glory in Terra Nova Field*, *Dredging News Online*, 3 pp. Available at [www.sandandgravel.com/news/article.asp?v1=8050](http://www.sandandgravel.com/news/article.asp?v1=8050), 1999. With permission.)

King, and other fields are separated and processed before export [41]. Another interesting development is found in the shallow-water FPSO system used in the ice-floe and iceberg-infested Terra Nova Field (at 90.0–100.0 m water depth), located 350.0 km away from the coasts of Newfoundland and Labrador in Canada. The subsea production wellhead is buried in an 11.5-m-deep pit (termed as “glory holes”) located on the seabed, as shown in Figure 1.28 [42]. This prevents the keel of icebergs from gouging the seabed and subsequently damaging the subsea production equipment.

## 1.5 LEGAL JURISDICTION

Questions regarding (i) the extent of the coastal and offshore areas that can be used for exploration by oil companies; (ii) the possibility of a country or state not permitting a ship carrying



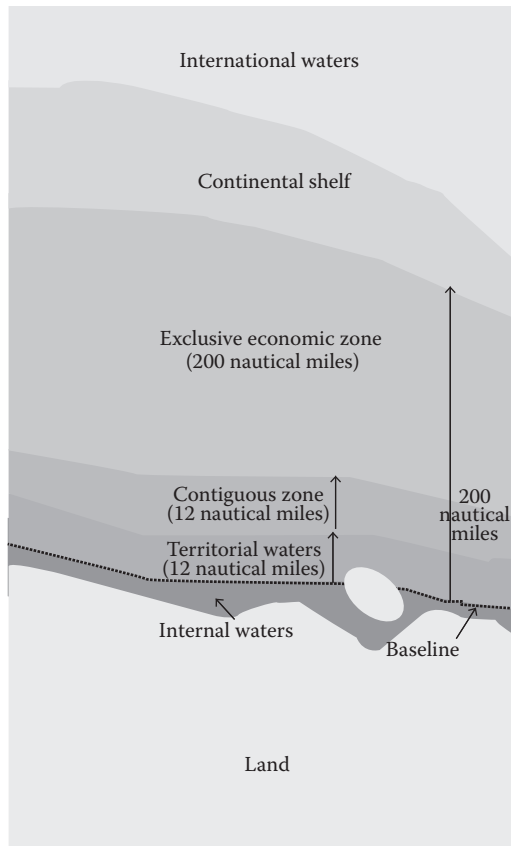
dangerous cargo, such as toxic waste or radioactive matter, within certain distance from its coasts; (iii) superpowers deploying submarine listening devices near the shores of the other superpowers; and (iv) conducting genuine scientific research along the coasts of another country, have been dealt with under the international law of the sea [43, 44]. Offshore activities are regulated by a combination of the international law of the sea and the national law. The international law of the sea sets a general framework, leaving the matters of detail to be regulated by the national laws. This process creates rules and regulations that can widely vary from one country/state to the other. In relation to oil and gas exploitation, the international law of the sea prescribes the area within which any country/state can regulate such activities and authorizes it to permit drilling platforms to be placed. Such structures should not cause excessive interference with other users of the sea. However, national laws govern matters of detail, such as safety standards for the platform operation, tax levied on the oil companies, etc.

Although there is no centralized legislature in international law, a number of international organizations play a vital part in law making. Of the United Nation's specialized agencies, the International Maritime Organization (IMO) plays a vital role in formulating conventions and regulations of navigation for shipping lanes and pollution from ships. It also plays a quasi-legislative role in applying these conventions and legislations to situations encountered in the high seas. The other UN bodies, which are particularly involved in marine affairs, are the Food and Agriculture Organization (FAO) and the United Nations Educational Scientific and Cultural Organization (UNESCO). FAO reviews the state of the world's fisheries and when necessary establishes regional fisheries bodies to advice on fisheries management. It also provides assistance to many under developed countries to develop their own fishing industries. UNESCO promotes and coordinates marine scientific research.

Legally, the sea is divided up into various zones: territorial, contiguous, exclusive economic zones, and high seas zones. The nearer a zone is to land, the greater the rights of the adjacent country/state to exploit the resources of the zone and regulate activities in the zone. Other countries/states have fewer rights in this zone. Correspondingly, the farther from land the zone is located, the fewer the rights of the coastal country/state and greater are the rights of other countries/states. Beyond these zones, which are subject to the varying jurisdictions of the coastal country/state, are the high seas, which are in principle open to equal use by all the countries/states of the world. Figure 1.29 [45] shows the various zones limited by the international law of the sea.

The widths of the different maritime zones are given in terms of nautical miles, measured from the baseline. Normally, the baseline is the low-water line along the stretch of coast; but there are many exceptions to this rule. Some of them are (i) coasts dotted with island chains, where a state may draw straight baselines, connecting the outermost points of the coast and/or islands; and (ii) mouth of bays, when less than 24 nautical miles, can be connected by straight lines. Terms such as internal waters, territorial sea, archipelagic waters, contiguous zone, continental shelf, exclusive economic zone, high seas, and international seabed area have particular meanings in the context of the international law of the sea and need to be properly understood for proper use of the lands adjacent to the country/state. Figure 1.29 also shows, in nautical miles, the region of applicability of various zonal limits. In the case of international seabed area, wherever applicable, if the continental shelf extends beyond 200 nautical miles, the area is under the control of the national laws.

Lying on the deep seabed, mainly beyond the geological continental shelf, are large quantities of manganese nodules, consisting of manganese, iron, nickel, copper, and cobalt. As per the authorization of the International Seabed Authority (ISA), formed under the auspices of the UN Conference on Law of the Sea, mining could take place only under the authorization of the ISA. Oil companies that would like to exploit these nodules and other ocean ores should be authorized by the ISA and comply with its rules. Similarly, there are rules for shipping (nationality, safety, and traffic management), pollution, fishing, and military uses in the high seas.



**FIGURE 1.29** Maritime zones. (From Wikipedia, The Free Encyclopedia. *Exclusive Economic Zone*, Available at [en.wikipedia.org/wiki/Exclusive\\_Economic\\_Zone](http://en.wikipedia.org/wiki/Exclusive_Economic_Zone), 2008.)

## 1.6 HISTORY OF OFFSHORE STRUCTURAL DEVELOPMENT

The origin of oil is legendary. Ancient Greeks and Chinese writers record the use of petroleum products for light. At least 5000 years ago, Sumerians, Assyrians, and Babylonians wrote about using a sticky petroleum product in paints, as mortar for setting stones, as cement in mosaic tile work, as waterproofing for baskets, mats, and boats, and in road building [46]. Legend says that Alexander the Great gathered oil from seeps near the south end of the Caspian Sea in 4th century BC. Oil wells were drilled in China by 347 AD, up to a depth of 800 ft., using bits attached to bamboo poles. Marco Polo described seeing the mining of large seeps of oil near Baku, Azerbaijan, in the thirteenth century. Oil seeps were collected in the Carpathian Mountains of Poland during the 1500s and used to light street lamps [47, 48]. According to a recent state-of-the-art review of the oil and gas industry in the United States, the sighting of oil on land was recorded in Texas during 1543 by Luis de Marcoso, a survivor of the Desoto expedition [49]. Subsequently, during 1667, a land oil strike was reported at Lagan, Lancashire, UK, from naturally seeping oil. Oil sands were mined and the oil extracted at Alsace, France, during 1735.

The first recorded oil well on land, using the present mode of drilling, was drilled by a Russian engineer in Azerbaijan in 1848, 11 years before Colonel Drake's well in Northwestern Pennsylvania (1859). The first oil well in North America was drilled in Ontario, Canada, in 1858. In 1859 the Rathbone Brothers Company produced 200 barrels of oil per day in West Virginia. This oil well produced a peak amount of 16 million barrels of oil in 1900 [50]. The discovery and production of

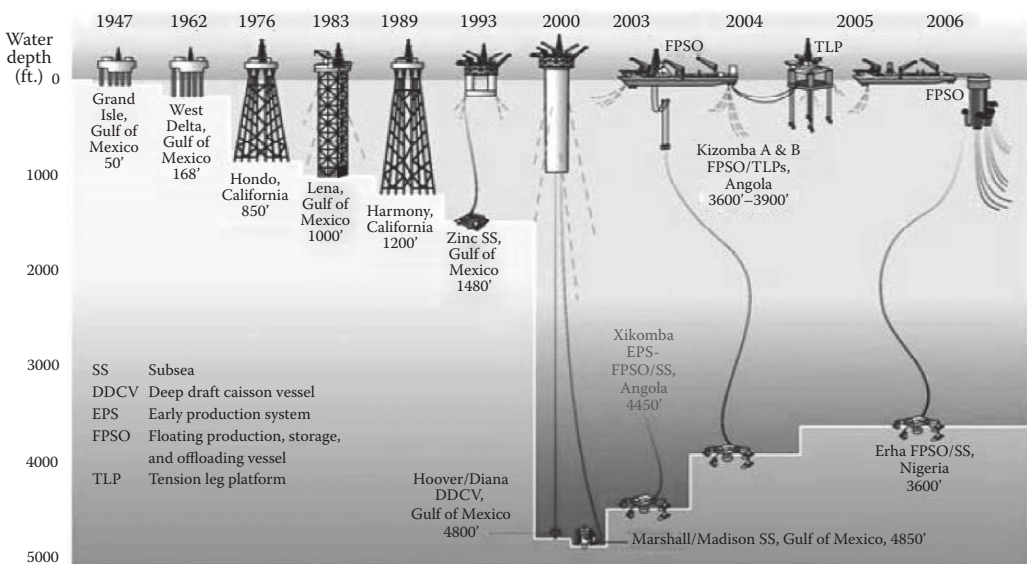


oil in the United States occurred sporadically during the second half of the nineteenth century. The first economically significant discovery of oil in Texas was made in 1894 in Navarro County near Corsicana. The field produced a peak amount of 839,000 barrels of oil during 1900.

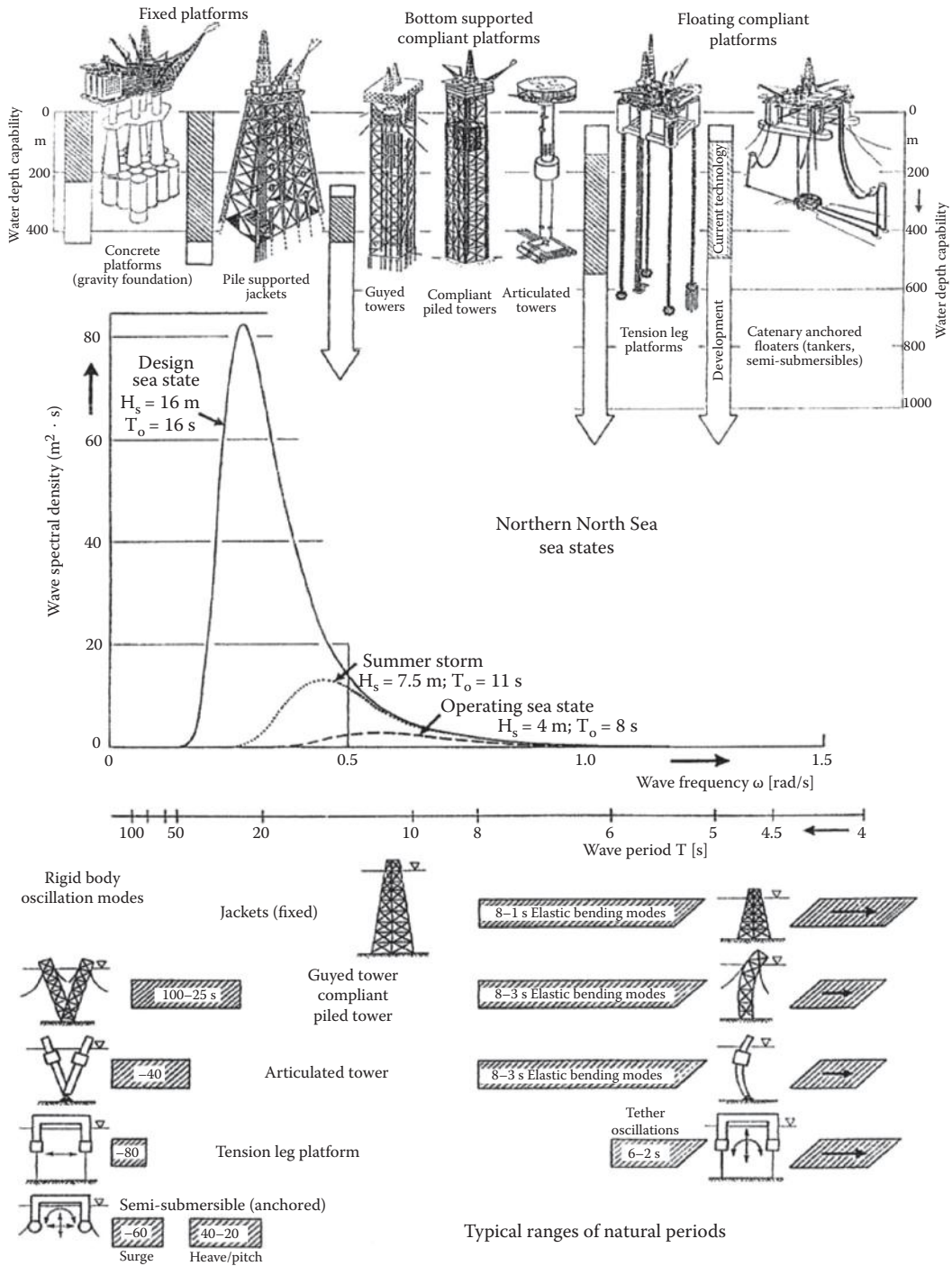
Exploration for offshore oil started in 1887 from a wooden wharf, in a few feet of water, off the coast of California. The first offshore oil well was drilled at Summerland field in Santa Barbara, California, in 1896. The oil wells were drilled from piers extending from shore, sometimes stretching nearly 1230 ft. into the ocean. A series of additional oil discoveries offshore resulted in the installation of offshore piers at Rincon, Ellwood, and Capitan, in Santa Barbara, California, by 1920. The year 1932 saw the erection of the first offshore steel oil platform in the world at Santa Barbara Channel, Southern California. The platform was located at a depth of 38 ft. The platform was in during 1940 by large waves that battered the platform during a storm [51, 52]. Much earlier, in 1910, an offshore oil well was drilled at Ferry Lake, Louisiana. This was followed by the development of the offshore Creole Field in the Gulf of Mexico in 1930, off the coast of Louisiana, at a water depth of 4.7 m. Offshore wells were also drilled in Lake Maraca Ibo, Venezuela, in 1929.

The first on-the ocean offshore platform was constructed by Humble Oil Company in 1947 in the Gulf of Mexico, at a water depth of 60 ft. (18 m). In 1956 Shell Oil Company installed a shallow water platform at a water depth of 100 ft. (30.5 m) off Grand Isle, Louisiana. The Persian Gulf and North Sea experienced oil finds and subsequent platform developments during the 1960s. Explosive offshore developments took place during 1970s, and a large number of offshore platforms were installed in greater water depths.

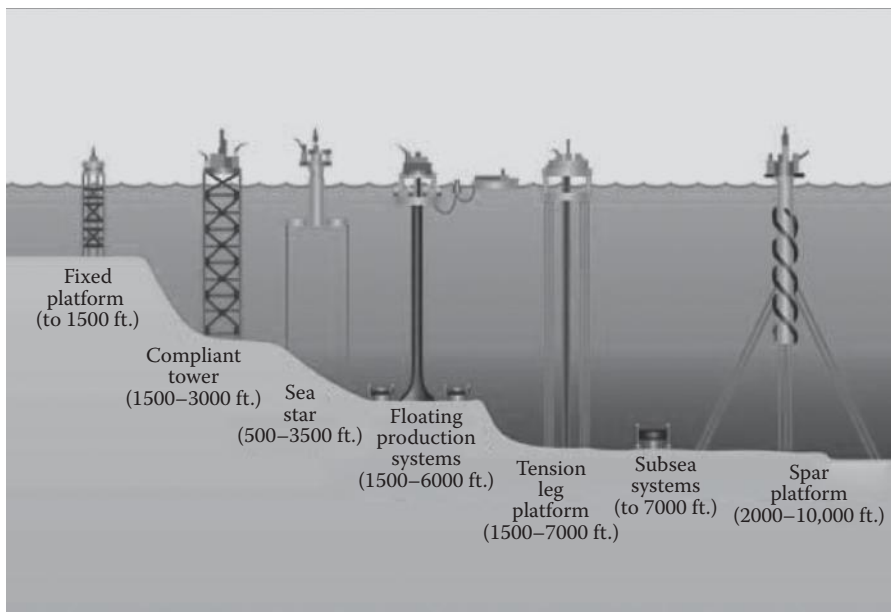
Figure 1.30 [53] gives a pictorial history of offshore structural developments that have occurred during recent times. Exxon installed the Hondo platform in 1978 at a water depth of 850 ft. (259.1 m) near Santa Barbara, off the California coast. Shell Oil Company placed their Cognac platform at a water depth of 1025 ft. (312.5 m) in the Gulf of Mexico [28]. Other significant developments that have taken place subsequently have already been outlined earlier in Section 1.2. Since the structures shown in Figure 1.30 vary in their dynamic characteristics, they respond to the wave excitation differently as shown in Figure 1.31 [28]. The massive and stiffer fixed or ground supported platforms have their fundamental periods of vibration in the range of 0.0 to 3.0 s and the free-floating,



**FIGURE 1.30** Historical development of deepwater production platforms. (From D. O’Neill, *Deepwater Development—ExxonMobil, NNPC-NAPIMS Workshop, Nigeria, September 28, 3 pp., 2006. With permission.*)



**FIGURE 1.31** Environmental conditions and structural characteristics for Northern North Sea. (With kind permission from Springer Science+Business Media: *Conceptual Design and Hydromechanics*, Offshore structures, Vol. I, 1992, p. 135, G. Clauss, E. Lehmann, and C. Östergaard.)



**FIGURE 1.32** Optimum water depth limitations for the various offshore concepts. (From Shell Co., *What Is a Spar?* Available at [www.shell.com/home/content/usa/aboutshell/strategy/major\\_projects/perdido/about\\_spar.html](http://www.shell.com/home/content/usa/aboutshell/strategy/major_projects/perdido/about_spar.html), 2008. With permission.)

compliant, and flexible platforms have theirs in the range of 20.0 to 100.0 s. The dominant wave excitation periods range between 3.0 and 20.0 s. Hence the dominant response will be dynamical for the massive and fixed platforms, while it will be quasi-static for the free-floating, compliant, and flexible platforms. In addition to the dynamic characteristics, the choice of specific platform is also governed by the depth of the location in which the offshore field is located, as shown in Figure 1.32 [54].

## EXERCISE PROBLEMS

1. (a) Describe the distribution of water and land on the earth. (b) The area of the ocean varies depending on its depth below the mean sea level. At which 1000-m depth interval would the greatest change in ocean area occur?
2. (a) Assuming that you are traveling in a submersible from New York to Spain, draw a simple ocean bottom profile showing each bathymetric feature you would encounter as you move across the bottom of the ocean; name each of those features. (b) Compare the above features with those between the coast of Chile and the east coast of Australia.
3. (a) How much oil and gas are there in the world today? (b) State the top ten producing and consuming countries of the world, and the amount consumed by each of them.
4. (a) How much oil does the world consume each day? Each year? (b) Give a brief discussion on the future of oil production in the following countries: (i) Saudi Arabia; (ii) Canada; (iii) United States; (iv) Russia; (v) Venezuela; (vi) Iraq; (vii) India; and (viii) China.
5. (a) List the countries that have the world's larger proven offshore crude reserves, and the amount they have. (b) What are the smallest and largest world offshore oil discovery estimates; how can that be optimized?

6. (a) Using the text and recent literature on the subject, write a summary report comparing the field characteristics, structural characteristics, field development/production costs, and design features of the following offshore oil production fields: (i) Safaniah (Saudi Arabia); (ii) Ninian (North Sea, UK); (iii) Hutton (North Sea, UK); (iv) Gulfaks (North Sea - Norway); (v) Cognac (Gulf of Mexico); and (vi) Hibernia (Newfoundland, Canada). (b) Compare and list the advantages and merits of each type of platform for the environmental conditions of the field.
7. (a) Describe the continental shelf and the continental margin, as well as the type of sediments you would expect to find in these two regions. (b) Discuss the implications for the marine environment as exploitation of ocean resources continue, especially through drilling for oil and gas and for mining; consider separately the influences on continental shelves, in Arctic and Antarctic waters, and in the open ocean.
8. You have been asked to head a group that is in charge of recommending a concept for detailed design consideration and cost estimation. The structure is to be installed for an ice-infested region (with no icebergs and multiyear ice intrusion) subjected to extreme winds and waves. List the factors you would take into consideration while assessing these three possible concepts: (i) gravity platform; (ii) floating platform; and (iii) fixed jacket structure.
9. (a) Using the text and recent literature on the subject, write a summary report comparing the field characteristics, platform structural features, field development/production costs, design details, subsequent modifications required to utilize the structure optimally, etc., for the following offshore oil production fields: (i) Safaniyah (Saudi Arabia); (ii) Statfjord (Norway, UK); (iii) Manatee (Gulf of Mexico, USA); (iv) Cantarell–Abkatun Complex (Mexico); (v) Hibernia (Newfoundland, Canada); (vi) Campos Basin (Brazil); and (vii) Bolivar Coastal field (Venezuela). (b) Compare and list the advantages and merits of each type of platform used for the existing environmental conditions at the field.
10. Worldwide offshore developments have centered predominantly around certain offshore areas such as: (i) Persian Gulf; (ii) North Sea Sector; (iii) Gulf of Mexico; (iv) Campos Basin and Bolivar field; (v) Prudhoe and Mackenzie Bays; (vi) South China Sea; and (vii) Eastern Seaboard of Canada. (a) Give a brief review of the various fields developed focusing on quantity of oil/gas involved, types of platforms used, soil and foundation conditions at the site, platform structure used, and amount of money spent on these developments in each area. (b) Compare and contrast the various structural innovations developed as the offshore industry sought to exploit the oil and gas reserves in the deep ocean.
11. The range and type of offshore structures used in the ocean environment are quite large and diverse. Briefly describe the various types of structural systems used for offshore drilling and production. Give their relative advantages/limitations, compare them with respect to their production capacities, water depths, costs, and fabrication/transportation facilities required.
12. An offshore structural concept is to be chosen for the Gulf of Mexico based on (i) dynamic characteristics; (ii) wind and wave environment; and (iii) currents. (a) Using Figure 1.31 and Table P1.1, select the best concept. Give reasons for your choice. (b) If the economy is also to be considered according to Figure 1.10 and Table P1.2, which would be the best choice? Give reasons for your choice.
13. An offshore structural concept is to be chosen for the Northern North Sea (with water depths of more than 350 m) where the maximum possible output per day is around  $20,000.0 \text{ m}^3$  ( $1.0 \text{ m}^3 \sim 680.0 \text{ kgf}$ ). The field is quite large with proven reserves of 1.1 billion barrels ( $1 \text{ t} \sim 7.333 \text{ barrels}$ ). (a) Using Figure 1.31 and Table P1.1, select the best possible concept. Give reasons for your choice. (b) If economy is also to be considered according to Figure 1.10 and Table A.1 (in Appendix), which would be the best choice? Give reasons for your choice.

**TABLE P1.1**  
**Comparison of Extreme Environmental Criteria**

	Northern North Sea	Gulf of Mexico	Campos Basin, Brazil
100-Year extreme design wave			
Max. wave height	31 m	22 m	8.4 m
Related period	14 to 18 s	12 to 15 s	11 s
1-Year summer storm			
Max. wave height	14 m	Longer periods of small waves; less severe than North Sea conditions	
Related period	9 to 11 s		
Extreme current			
Surface	1.5 m/s	0.26 m/s steady current; strong currents in the Mississippi Delta (mudslide area)	2.5 m/s
Bottom	0.75 m/s		1.0 m/s
Extreme wind	41 m/s; 10 min duration 10 m above sea level	Sustained wind velocity 45 m/s	46 m/s

*Source:* With kind permission from Springer Science+Business Media: *Conceptual Design and Hydromechanics*, Offshore structures, Vol. I, 1992, p. 135, G. Clauss, E. Lehmann, and C. Östergaard.

14. (a) Describe the role of oil and natural gas in the economy of: (i) advanced countries; (ii) developing countries; and (iii) underdeveloped countries. Cite three cases in each category. (b) Will oil remain the most important source of energy for years to come?
15. Describe the roles played by each of the following: (i) legal jurisdiction of different countries (on resource exploitation); (ii) countries that own the resources to be exploited; (iii) petroleum company operator; and (iv) other engineering contractors and construction firms in the development of offshore petroleum resources around the world (including the Arctic and the Antarctic regions), and bringing it to the market.
16. (a) Draw schematic flowcharts and describe the various stages involved in the economic analysis and concept evaluation of any offshore oil/gas field development. (b) A marginally viable (economically) field is located in the continental shelf of the Grand Banks (off the southeastern coast of Newfoundland and Labrador, Canada) and is subjected to the prevailing environmental extremes. Discuss the various options you would consider and the option you would select as the most feasible one (use the data given in Figure 1.10 and Table P1.2).
17. Which U.S. states and Canadian provinces have the longest coastlines and offshore oil/gas fields? Name the prominent oil and gas fields in these states/provinces.
18. Since seismic data cannot tell the type and quantity of oil and gas present in a hydrocarbon bearing strata, the subsequent decisions are made based on the data from the exploratory wells. Hence, an engineer has to make decisions concerning the 3-D or 4-D seismic data necessary for reservoir assessment and delineation. Will the exploratory drilling reduce the uncertainty concerning the nature and size of the reservoir to pay off the investment? Why or why not?

**TABLE P1.2**  
**Extreme Environmental Criteria**

Particulars	Grand Banks Region
100-Year extreme design wave	
Max. wave height	31.0 m
Related period	14.0 to 19.0 s
1-Year winter storm	
Max. wave height	15.0 m
Related period	9.0 to 15.0 s
Extreme current	
Surface	1.2 m/s
Bottom	0.5 m/s
Extreme wind	40 m/s at 10.0 above msl (return period: 100 years)
Averaging period	1.0 h
Extreme ice conditions	
Thickness of ice	1.0 m thick ice floes
Iceberg conditions	
Mass of extreme iceberg	15.0 million t
Velocity of motion	0.9 m/s
One impact possible every 10 years (smaller size)	—
Geotechnical conditions	Top 50 m is characterized by horizontal layers of sand with various amounts of fines content

19. Write a brief note on some of the most important factors that need to be considered in the planning and designing of facilities and utilities for offshore platforms. List some of the early decisions that must be made which would have a major impact on facilities' layout and design. Which factors have the largest influence on the overall dimensions and layout of the facilities and utilities on the offshore platforms?
20. (a) Discuss how the drilling operation (from a platform) affects the platform design. (b) In order to properly develop the oil and gas reservoirs, many of the wells have to be directional. Outline some of the problems encountered in the process.
21. Name the comparative advantages and disadvantages of: (i) jackups; (ii) semi-submersibles; (iii) drill ships; and (iv) drill barges.
22. Name the comparative advantages and disadvantages of: (i) a conventional mooring system and (ii) a dynamic positioning system.
23. (a) Explain the need for: (i) geophysical and (ii) geotechnical site investigations in developing an offshore field. (b) Explain how the geophysical/geotechnical site investigations would vary for: (i) piled steel platform; (ii) gravity platform; and (iii) tension leg platform.
24. (a) Describe the primary factors that limit the water depth application of conventional steel platforms. (b) What are the major design parameters that affect the weight of a steel platform?



25. (a) Outline the various factors that influence the use of gravity platforms in the North Sea. (b) What natural geographic features made Norway an attractive construction location for typical North Sea-type gravity structures? How?
26. What nonstructural factors might favor the use of a concrete structure over a steel jacket structure in certain areas?
27. Identify and briefly describe at least four major elements of: (i) steel jacket platform; (ii) concrete gravity structure; (iii) tension leg platform; (iv) compliant guy structure; and (v) truss spar.
28. (a) Describe the need for offshore terminals in developing offshore oil fields. (b) Discuss, in detail, the facilities and utilities needed in developing offshore terminals.
29. (a) Outline, briefly, the need for, and the relevance of, the use of subsea systems for offshore oil and gas development. (b) Describe five different types of subsea systems used in different areas of the world.
30. Explain why equipment reliability is more important for a subsea system than for a jacket platform.
31. (a) Describe the various components of a floating production system. (b) Why do we consider a floating production system during project planning? (c) Give examples of three different types of floating production systems.
32. The owner of an offshore oilfield has to decide between two options in order to exploit the marginal oilfield that the company has discovered recently, at a water depth of 100.0 m. The field is located at a distance of 200.0 km from the land (point of delivery), and the nominal oil price at the point of delivery is to be US\$40.00 per barrel. The oil is to be transported to land by tankers. The total recoverable reserves, in the field, are 80 million barrels with a maximum output of 10,000 barrels per day. The company has to decide between a production platform with satellite well protectors and a self-contained drilling and production platform. Find the (i) probable life of the field; (ii) amount of investment needed to bring the field to its full potential in 2007; and (iii) probable financial return from the field at the end of its life (use 2007 costs).
33. A high-production oilfield was discovered in the Gulf of Mexico at a depth of 2500.0 m below the mean sea level. The water depth is 400.0 m at the discovery site. The total recoverable reserves were estimated to be 1.4 billion barrels, and the maximum output from the field could be as high as 200,000 barrels per day. The distance of the field from the tanker terminal (point of delivery) is 300.0 km. (a) Mention the possible scenarios that could be used for the exploitation of oil from the field, and compute the life of the field. Take the oil price to be US\$40.00 per barrel. (b) Find the required capital outlay for the field development (for each of the scenario given) and the probable financial return from the field for each of these scenarios.

## APPENDIX

See Table A.1.

**TABLE A.1**  
**North Sea Oil and Gas Field**

Field	Platforms		UWC	SBM	Pipeline Connection (Ø mm)		Water Depth (m)	Development Cost (million US\$)	Recoverable Reserves		Peak Flow Capacity		Design Capacity		
	Steel	Concrete			Compliant or FPS	Oil			Gas	Oil (10 <sup>6</sup> m <sup>3</sup> )	Gas (10 <sup>6</sup> m <sup>3</sup> )	Oil (10 <sup>9</sup> m <sup>3</sup> )	Gas (10 <sup>3</sup> m <sup>3</sup> /d)	Oil (10 <sup>6</sup> m <sup>3</sup> /d)	Gas (10 <sup>3</sup> m <sup>3</sup> /d)
<b>United Kingdom</b>															
Magnus	1		7		609		186	2755	106	3.5	23.4	1.7	19.1	1.7	
Thistle	1		7	SALM	400		161	1580	74	60	25.4		41.3		
Murchison	1		3		400		156	1150	60.4	4	19.1		26.2		
Dunlin		1			610		151	924	49.3		18.3		23.9	1.1	
Tern	1				400		168	1300	27.8		8.7				
Cormorant		1	10		910		150	1700	30.4		8.7	0.5	9.5	0.8	
N-Cormorant	1				508	254	161	1600	63.3		28.6		28.6	0.8	
Brent	1	3		SPAR	910		140-2	7700	349	4.5	77.9	14	87.5	34.6	
NW-Hutton			32				148	1800	30.2	2.7	17.5		23.9		
Hutton	1				508		150	1250	32.6	9	15.9	1	17.2		
Heather	1				400		143	710	14.8		5.1		11.9		
Ninian	2	1			910		141-3	4000	175	3.4	50		87.5		
N-Alwyn	2				305	610	130	2640	31.8		14.3	8	15.7	10	
Beryl	1	1	9	ALT			120-2	2600	133		18.3		47.7	14.2	
N-Brae	1				457		100	1500	31.8	27	11.9	11	11.9	11	
S-Brae	1				762		112	1800	44.5		20.8	4	17.5		
Piper	1				760		144	1260	151	19	44.5	2	52.5		
Claymore/Scapa	1		11		760		111	1160	91.4		15.5		26.2		
Tartan/Highlander	1		23				140	765	21.5	0.7	5.4	0.34	14.2	12	
Balmoral			19	ALT	250		140	720	10.7		5.6		6.4		
Maureen	1 <sup>a</sup>						97	1400	23.9		13.4		12.7		
Buchan			2				120	500	12.9		11.1		11.4		





**TABLE A.1 (Continued)**  
**North Sea Oil and Gas Field**

Field	Platforms			Compliant or FPS	UWC	SBM	Pipeline Connection (Ø mm)		Water Depth (m)	Development Cost (million US\$)	Recoverable Reserves		Peak Flow Capacity		Design Capacity		
	Fixed		Oil				Gas	Oil (10 <sup>6</sup> m <sup>3</sup> )			Gas (10 <sup>6</sup> m <sup>3</sup> )	Oil (10 <sup>9</sup> m <sup>3</sup> /d)	Gas (10 <sup>3</sup> m <sup>3</sup> /d)	Oil (10 <sup>6</sup> m <sup>3</sup> /d)	Gas (10 <sup>3</sup> m <sup>3</sup> /d)		
	Steel	Concrete															
Eldfisk	3								70		48	31	39.8	15.3			
Edda	1								70		3	2	6.4	2.9			
Valhall	3			1		508	508	508	69	1200	39.3	21	9.5	5.7	26.7	9.9	
<b>Denmark</b>																	
Rolf	1					200			37		1.7				10		
Tyra	9						760		37			70			11		
Gorm	5								40		11.1		8				
Skjold	1					152			39		22.3		5.6				
Dan	8								40		12.7		4.3		11.1		
<b>The Netherlands</b>																	
K-7; K-8; K-11	6														10		
L-7; L-4	9						400		30			32			10		
L-10; L-11; L-13	9						90		27			42			10		
K-13; K-10	9						910		25			112			17.2		
K-14	2								27			50			14		
K-15	2								27			12			7.4		
K-18	2					300			27			29			10		
Helm, Helder, etc.	6					510			25-7	372	4		4				
										304	9.9		4.8				
<b>Germany</b>																	
Mittelplate	1 <sup>c</sup>											1					
Schwedeneck	2								20-5	150		20			10	2.4	

*Source:* With kind permission from Springer Science+Business Media: Conceptual Design and Hydromechanics, Offshore Structures, Vol. 1, 1992, p. 135, G. Clauss, E. Lehmann, and C. Östergaard.

*Note:* Abbreviations: ALT, articulated loading tower; AT, articulated tower; EL SBM, exposed location single buoy mooring; FPS, floating production system; SBM, single anchor leg mooring; SBM, single buoy mooring; SPAR, single leg storage buoy; SS, semi-submersible; TLP, tension-leg platform; UWC, underwater completion.

<sup>a</sup> Gravity; <sup>b</sup>Petrojarl 1; <sup>c</sup>Manmade island.

## REFERENCES

1. H.W. Green II, 1994. Solving the paradox of deep earthquakes, *Scientific American*, Volume 9, pp. 64–71. Available at [www.seafriends.org.nz/oceano/oceans.html](http://www.seafriends.org.nz/oceano/oceans.html) (Accessed July 15, 2008).
2. T. Moan, 2003. *Marine Structures for the Future—A Sea of Opportunities*, The Inaugural Keppel Lecture, National University of Singapore, July 18, 2003.
3. K. Albaugh and T. Nutter, 2005. *Deepwater Solutions & Records for Concept Selection, Going Deeper with Production Technology*, prepared by E. Kurt Albaugh [BHP Billiton Petroleum (Americas) Inc.] and Tillie Nutter (Mustang Engineering).
4. J.F. Anthoni, 2000. *Oceanography: Oceans Continental Drift and the Origins of Oceans*. Available at [www.seafriends.org.nz/oceano/oceans.html](http://www.seafriends.org.nz/oceano/oceans.html) (Accessed July 20, 2008).
5. G.A. Lock, 1981. Technological factors in offshore hydrocarbon exploration, in *The Future of Offshore Petroleum*, McGraw-Hill (in cooperation with the United Nations), New York, pp. 87–146.
6. Green Peace, 1999. *A Guide to Oil Reserves and Resources, Protect the Arctic, Stop Global Warming*, 12 pp. Available at <http://www.greenpeace.org/climate/arctic99/reports/oilreserve.html> (Accessed July 25, 2008).
7. Energy Information Administration, Office of Oil and Gas, 1993. *International Oil and Gas Exploration and Development 1991*, U.S. Department of Energy, Washington, DC, 97 pp.
8. USGS Digital Data Series—DDS-60 (Region 7), 1996. *World Assessment Summaries*, USGS World Energy Assessment Team, 6 pp. Available at <http://pubs.usgs.gov/dds-060/sum1.html> (Accessed July 28, 2008).
9. I. Sandra and R. Sandra, 2007. Exploration trends show continued promise in world's offshore basins. Growth expected in global offshore crude oil supplies, *Oil and Gas Journal*, March 5 and 12, 2007, 17 pp.
10. Association for the Study of Peak Oil (ASPO), 2001. *ASPO News*, Newsletter No. 21, September 2002, 9 pp. Available at <http://www.asponews.org/ASPO.newsletter.021.php/> (Accessed August 5, 2008).
11. PennWell, 2004. *Worldwide Reserves Grow; Oil production Climbs in 2003*, 6 pp. Available at [http://os.pennwellnet.com/Articles/Article\\_Display.cfm?](http://os.pennwellnet.com/Articles/Article_Display.cfm?) (Accessed August 5, 2008).
12. World Oil Production, 2003. *Oil Reserves, Production and Consumption in 2001*. Available at [www.scaruffi.com/politics/oil.html](http://www.scaruffi.com/politics/oil.html) (Accessed August 10, 2008).
13. U.S. Energy Information Administration, Office of Oil and Gas, 2004. *OPEC Revenues Fact Sheet*, June, 5 pp. Available at <http://www.eia.doe.gov/emeu/cabs/opecrev.html> (Accessed August 12, 2008).
14. Energy Information Administration, Office of Oil and Gas, 2004. *Non-OPEC Fact Sheet*, June, 6 pp. Available at <http://www.eia.doe.gov/emeu/cabs/nonopec.html>. Also available in Energy Information Administration's International Energy Outlook Report, 2007. Chapter 3 on *Petroleum and Other Liquid Fuels*, pp. 29–38 (Accessed August 14, 2008).
15. Gibson Consulting, 2004. Some interesting oil industry statistics, *Oil Industry*, 13 pp. Available at <http://www.gravmag.com/oil.html> (Accessed August 14, 2008).
16. Oil and gas sector analysis, 2001. *Oil and Gas Report*, 13 pp. Available at <http://www.us-saudi-business.org/oireports00> (Accessed August 17, 2008).
17. W. Rowley, 2004. *Deepwater, Key Sectors*, paper presented at the Deepwater International Conference, London, February, 12 pp. Available at <http://www.infield.com> (Accessed August 20, 2008).
18. Arup Energy, 2001. 2001 Survey of gravity-based offshore structures, *Offshore*, February, 2 pp. Available at <http://www.offshore-mag.com> (Accessed August 22, 2008).
19. J. Greenberg, 2001. Deepwater exploration and production initiatives, *Oil and Gas Online*, 4/11/2001, 6 pp. Available at <http://www.oilandgasonline.com/content/news/article.asp?> (Accessed August 24, 2008).
20. Shell Exploration and Production Company, 2004. *Shell in the Gulf of Mexico*, 2 pp. Available at <http://www.shellus.com/sepcowhere/offshore> (Accessed August 25, 2008).
21. ABS Offshore News, 2002. *Truss spars Proliferate in Gulf of Mexico*, May, pp. 7–9.
22. W.E. Pelley, 1981. Economic and financial issues of offshore petroleum development, in: *The Future of Offshore Petroleum*, McGraw-Hill (in cooperation with the United Nations), New York, pp. 175–198.
23. M. Forrer, 1981. The future of offshore petroleum development, in: *The Future of Offshore Petroleum*, McGraw-Hill (in cooperation with the United Nations), New York, pp. 3–26.
24. Measuring Worth: Purchasing Power of Money in the United States from 1774 to 2007, From Current Value of Old Money. Available at [www.projects.ex.ac.uk/RDavies/arian/current/howmuch.html](http://www.projects.ex.ac.uk/RDavies/arian/current/howmuch.html) (Accessed September 5, 2008).

25. Course Notes on General Design of Fixed Offshore Structures, 1979. University of Texas, Austin, TX, p. 3.1. Also Course Notes EOC 6431, 2001. *Offshore Structures: Framed Platforms*, Florida Atlantic University, Florida, 100 pp.
26. J.L. Williams, 2007. *Oil Price History and Analysis (Updating)*, *Energy Economics Newsletter of WTRG Economics*, Arkansas, 12 pp.
27. Woods Hole Science Center Seismic Profiling Systems, 2007. [franklinccd.org/Welcome to the USGS-U.S. Geological Survey.html](http://franklinccd.org/Welcome%20to%20the%20USGS-U.S.%20Geological%20Survey.html).
28. G. Clauss, E. Lehmann, and C. Östergaard, 1992. Offshore structures, in: *Conceptual Design and Hydromechanics*, Vol. I, Springer-Verlag, p. 135.
29. U.S. Energy Information Administration, 2004. *World Oil Market and Oil Price Chronologies: 1970–2003*, March, 55 pp. Available at [www.eia.doe.gov/emeu/cabs/chron.html](http://www.eia.doe.gov/emeu/cabs/chron.html) (Accessed September 20, 2008).
30. The United Kingdom Offshore Oil and Gas Industry Association, 2008. *Facts, Figures and Explanation: Drilling for Oil*. Available at [www.oilandgas.org.uk/education/students/drilling.cfm](http://www.oilandgas.org.uk/education/students/drilling.cfm) (Accessed September 30, 2008).
31. International Marine Contractors Association (IMCA), 2003. *Introduction to Dynamic Positioning*, Available at [en.wikipedia.org/wiki/Dynamic Positioning](http://en.wikipedia.org/wiki/Dynamic_Positioning) (Accessed October 10, 2008).
32. J.B. Weidler and D.I. Karsan, 1986. Analytical models and three-dimensional analysis, in: *Planning and Design of Fixed Offshore Platforms*, edited by B. McClelland and M.D. Reifel, Van Nostrand Reinhold Company, New York, p. 548.
33. U.S. Department of the Interior, Minerals Management Service, 2001. The Politics, Economics, and Ecology of Decommissioning Offshore Oil and Gas Structures, *Final Study Report and Technical Summary*, OCS Pacific Region Study MMS 2001-006, 99 pp.
34. G. Renard and E. Delamaide, 1998. *Complex well architecture IOR and heavy oils*, Vol. Production, Proc. of the 15th World Petroleum Congress, John Wiley & Sons.
35. S. Tanaka, Y. Okada, and Y. Ichikawa, 2005. *Offshore Drilling and Production Equipment, Encyclopedia of Life Support Systems (EOLSS)*, EOLSS Publishers, Oxford, UK (Fig. 15).
36. Report by Brown and Root Development, Inc., 1983. *State-of-the-Art Report on Guyed Towers Platforms*, NBS GCR 83-443, National Bureau of Standards, Gaithersburg, MD, September. Available at [www.mms.gov/tarprojects/052.htm](http://www.mms.gov/tarprojects/052.htm) (Accessed October 20, 2008).
37. Brutus, 2004. *Gulf of Mexico*, Available at [www.offshore-technology.com/projects/brutus/](http://www.offshore-technology.com/projects/brutus/) (Accessed October 22, 2008).
38. S.A. Will, 1999. Compliant Towers: the Next Generation, *Offshore*, 3 pp. (Accessed October 27, 2008).
39. Global Security.Org, 2006. *Military: Spar Platform*, Available at <http://www.globalsecurity.org/military/systems/ship/platform-spar.html> (Accessed October 30, 2008).
40. 2001. PowerPoint Presentations on *Dinamica de Plataformas de Agua Profunda*. Available at [www.iingen.unam.mx/Recursos/20Energicos/07/Dinamica/de/Plataformas.p./](http://www.iingen.unam.mx/Recursos/20Energicos/07/Dinamica/de/Plataformas.p/) (Accessed November 5, 2008).
41. T. Knott, 2008. Subsea king, *Frontiers*, April 2008, pp. 34–38. Available at [www.bp.com/sectiongenericarticle.do?categoryId=9023215&contentId=7043112](http://www.bp.com/sectiongenericarticle.do?categoryId=9023215&contentId=7043112) (Accessed November 5, 2008).
42. Project Update, 1999. *Boskalis covers itself in glory in Terra Nova Field*, Dredging News Online, 3 pp. Available at [www.sandandgravel.com/news/article.asp?v1=8050](http://www.sandandgravel.com/news/article.asp?v1=8050) (Accessed November 20, 2008).
43. R. Churchill, 1990. Maritime law, in: *Marine Technology Reference Book*, edited by Nina Morgan, Butterworths, London, 27 pp.
44. B.C. Gerwick, 2000. Introduction, in: *Construction of Marine and Offshore Structures*, CRC Press, Boca Raton, FL, pp. 1–13.
45. Wikipedia, The Free Encyclopedia, 2008. *Exclusive Economic Zone*, Available at [en.wikipedia.org/wiki/Exclusive\\_Economic\\_Zone](http://en.wikipedia.org/wiki/Exclusive_Economic_Zone).
46. Lincoln Petroleum Group, Inc., 2000. History of the oil, *History of Oil*, 2 pp. Available at <http://www.lincolngroup.com/site/> (Accessed November 25, 2008).
47. R. Cunningham, 2000. *Exxon Mobil focuses on six regions in search of Tomorrow's Oil and Gas*, The Lamp (corporate publications), Spring, 8 pp. Available at [http://www.exxonmobil.com/Corporate/Newsroom/Publications/c...lamp/c\\_page1.html](http://www.exxonmobil.com/Corporate/Newsroom/Publications/c...lamp/c_page1.html).
48. San Joaquin Geological Society, 2002. *The History of Oil Industry*, 16 pp. Available at <http://www.sjgs.com/history.com/>.
49. 2002. *Handbook of Texas Online; Oil and Gas Industry*, Texas State Historical Association (produced in partnership with the University of Texas Library, University of Texas at Austin).
50. West Virginia Geological and Economic Society, 2004. *History of WV Mineral Industries—Oil and Gas*, 2 pp. Available at <http://www.wvgs.wvnet.edu/www/geology/geoldvog.html>.
51. U.S. Department of the Interior, Minerals Management Service, 2003. *U.S. Offshore Milestones*, November, 6 pp. Available at <http://www.mms.gov/stats/PDFs/milestones.pdf>.

52. Minerals Management Service, California, 2003. The ecological role of oil and gas production platforms and natural outcrops on fishes in Southern and Central California: A synthesis of information, OCS Study Report MMS 2003-032.
53. D. O'Neill, 2006. *Deepwater Development—ExxonMobil*, NNPC-NAPIMS Workshop, Nigeria, September 28, 3 pp.
54. Shell Co., 2008. *What Is a Spar?* Available at [www.shell.com/home/content/usa/aboutshell/strategy/major\\_projects/perdido/about/spar.html](http://www.shell.com/home/content/usa/aboutshell/strategy/major_projects/perdido/about/spar.html) (Accessed December 1, 2008).



---

# 2 Components of a Typical Offshore Structure

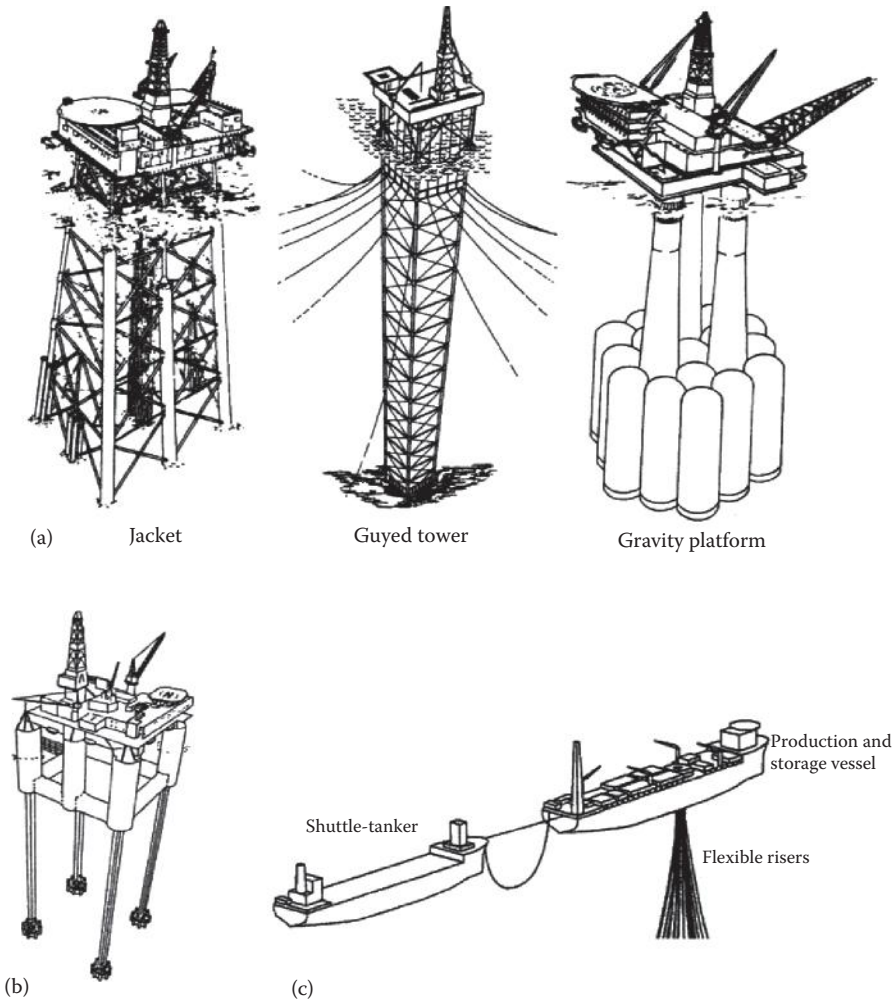
## 2.1 INTRODUCTION

One third of the estimated global reserves of oil and gas, viz., 1.3 trillion barrels of oil and 6.2 quadrillion cubic feet of gas, occur in continental margin sediments, which cover about 28% of the oceanic area [1, 2]. In developing these natural resources for human benefit, a variety of offshore structures have been developed and utilized to meet the need. These structures are used to facilitate the process of geophysical reconnaissance, exploratory drilling, production, and transportation of offshore oil to the essential infrastructures located on land.

Exploratory structures are used for the purpose of reconnaissance and detailed geophysical surveys that are required to find out the quantity, nature, and the exact location of oil and gas deposits in the vast expanse of the ocean; this is a high-risk venture since it has been estimated earlier (by Lewis G. Weeks, the chief geologist at Exxon during the 1960s) that only 3% of the area covered under exploratory reconnaissance surveys will contain commercial amounts of oil and gas [3]. While drill ships are invariably used for reconnaissance surveys that establish the availability of economically recoverable oil and gas reserves at a location, structures such as jack-ups, drill ships, semi-submersibles, and submersibles (Figures 2.1 [4] and 2.2 [5]) are used for the exploratory drilling that will exactly delineate the vertical and horizontal extents of the reservoir. Drill ships and semi-submersibles are highly mobile and can be used in small or large water depths, submersibles can be used only near the coastal areas. Jack-ups are stationary structures that can be moved to and used in any shallow water locations (Figure 2.2) to carry out detailed exploratory drilling activities. While jack-ups and drill ships can be used only under moderate weather conditions, semi-submersibles can be used under severe weather conditions.

Once the commercial viability of the discovered offshore oil and gas field has been established, then it becomes essential to design, fabricate, and install the requisite structure and equipment that will facilitate the drilling and completion of producing wells; in addition the produced oil and gas need to be processed and transported to the markets. The most widely used structure in the continental shelf region and beyond (up to a depth of 500.0 m) is the pile-founded steel template platform, which is fabricated into a three-dimensional frame by welding together steel tubular members and is held in place by tubular steel piles driven into the seafloor. This steel template platform resists the transverse and vertical loads imposed on it by the wind, wave, current, ice and seismic environments, and the weight of the platform and the equipment on the platform.

The severe and the shallow-water environment of the North Sea spurred the development of another type of offshore structure known as the concrete gravity platform (Figure 2.1). The components of these structures, such as the concrete oil storage cells, concrete vertical columns, module support frame, living quarters, drilling and processing equipment, helipad, flare stack, and others are fabricated on near-shore dry-dock-type fabrication yards and assembled on the supporting base of storage cells and vertical columns in the nearby sheltered ocean sites. The assembled structure is transported to the installation site and set on the seafloor. These concrete structures are really massive and can range from 200,000 to 500,000 t. The environmental forces exerted on the platform, along with its massive weight, will require various considerations regarding its stability at

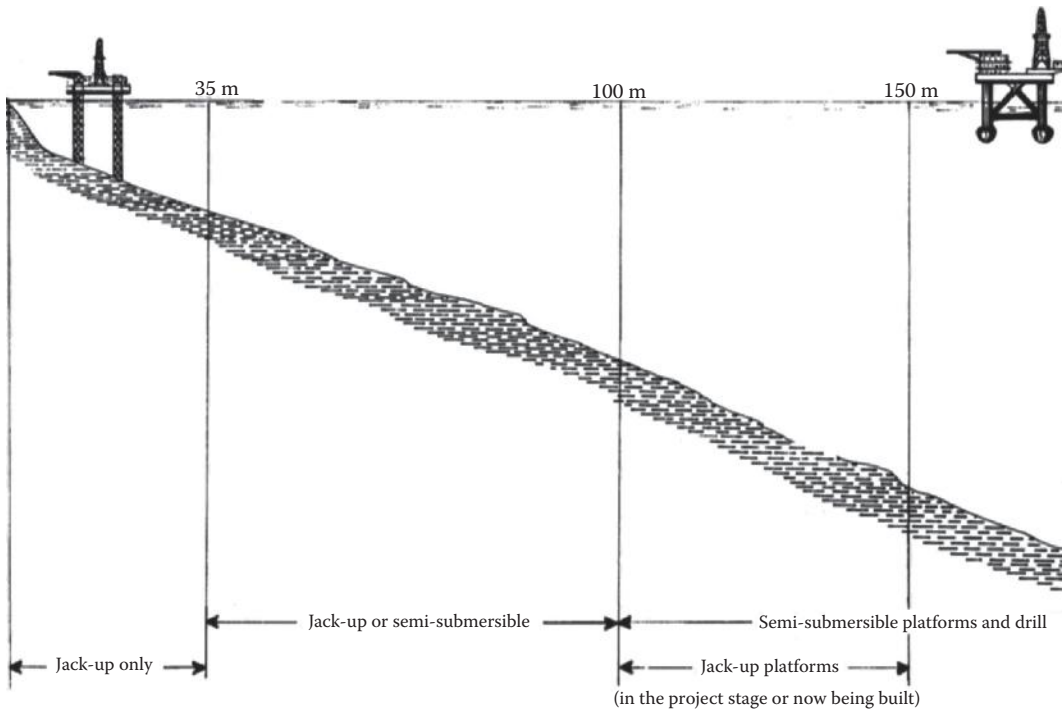


**FIGURE 2.1** Types of offshore structures encountered in the ocean environment. (From T. Moan, *Offshore structures* (Chapter 7), in: *Modeling Complex Engineering Systems*, edited by R.E. Melchers and R. Hough, ASCE Press, Reston, VA, pp. 173 and 175, 2007. With permission.)

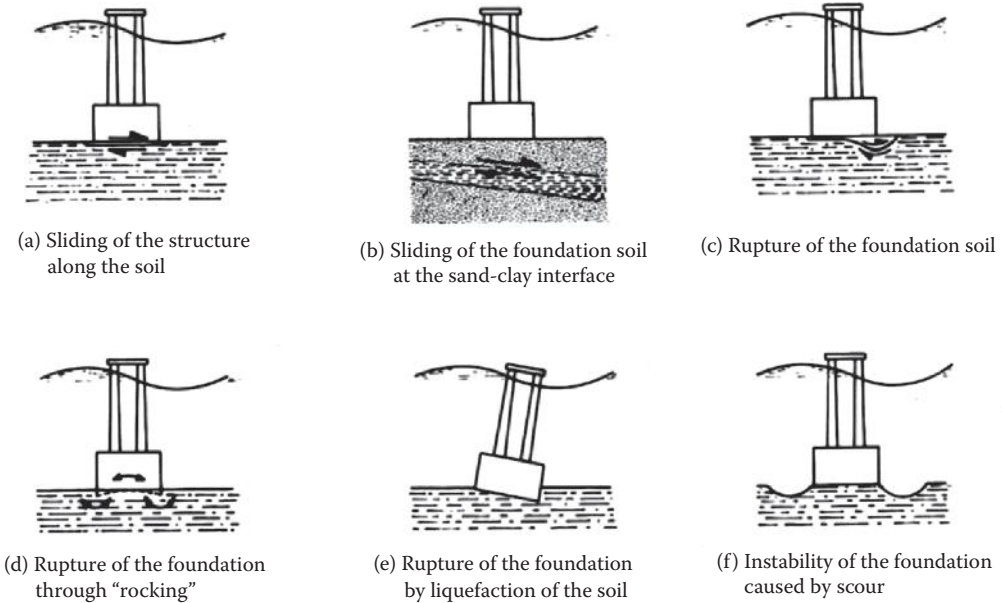
the installed location. These considerations are pictorially illustrated in Figure 2.3 [6]. The bearing strength and the transverse sliding resistance of the structure will be primary considerations in the siting of the structure. Even though the gravity platforms eliminate the operations of open-sea piling and installation of deck structure required for the steel template structures, the installation costs associated with gravity platforms are often enormous.

Compliant guyed platforms (see Figure 2.1) have been found to be economical for seawater depths varying from 300.0 to 900.0 m (continental slope regions). Compliant guyed platforms are similar to the pile-founded jacket structures, but are more flexible (due to its almost constant cross section); they are connected to the seabed through drilled piles and through cables carrying clump weights. They resist the transverse loads in a compliant manner. The regular transverse loads on the structure are mainly resisted by an array of inclined guy lines extending from the platform to the anchor piles at the seafloor through clump weights that could be lifted off the floor (by a large transverse load acting on the platform due to extreme wind and wave conditions) to provide greater compliance to the load.





**FIGURE 2.2** Common depths of water for jack-up platforms used in offshore exploration. (From P. Le Tirant, *Seabed Reconnaissance and Offshore Soil Mechanics*, Editions Technip 27, Paris, France, p. 400, 1979. With permission.)



**FIGURE 2.3** Various considerations made in the location of a gravity platform. (From P. Le Tirant, *Seabed Reconnaissance and Offshore Soil Mechanics*, Editions Technip 27, Paris, France, p. 347, 1979. With permission.)

The tension leg platform (TLP) shown in Figure 2.1 consists of a large, buoyant semi-submersible-type platform tautly moored at the location by vertical tethers, located below the vertical columns of the semi-submersible structure. The tethers are stranded wire ropes of composite materials that will sustain very large tensile loads. In order to maintain the tensile loads in the tethers, the semi-submersible-type platform is held submerged much deeper than its free-floating draft. The tension in the tethers is computed such that even during the extreme storms the tethers will not become slack and lose their tensile forces. The wellheads and all the production facilities are located on the platform, above the water; the TLP may also have a submerged production system where the wellheads, and the production systems are located at the seabed. The water depths at which they can economically operate are between 450.0 and 2100.0 m.

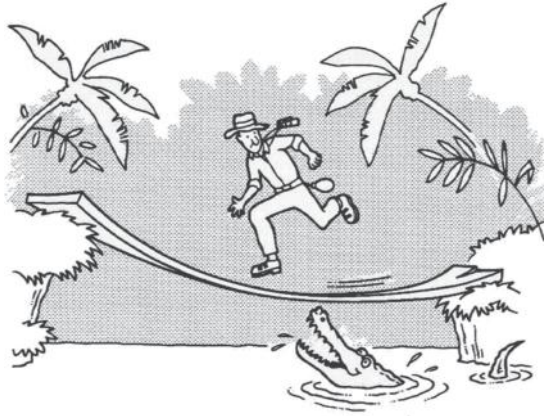
The floating production and storage systems (FPSOs), shown in Figure 2.1, consist of large barge-shaped ship structures moored to the seabed through turret-moored systems. The turret enables the FPSO to weather-wane during extreme weather conditions and to minimize the forces the structure resists during such conditions. Also, the risers used in FPSOs are quite flexible and are able to sustain the large motions of the floating FPSO.

Besides the above-mentioned offshore structures, there are many other structures such as SPARs or deep draft caisson vessels, offshore loading terminals, articulated towers, subsea systems, man-made gravel, and ice islands for ice-infested regions, wind power platforms, and many others. Only a selected few of the structures, mentioned above, will be discussed in detail in this chapter.

## 2.2 FUNCTIONAL AND STRUCTURAL REQUIREMENTS OF AN OFFSHORE PLATFORM

Offshore platforms consist of two broad components, viz., (i) the facilities known as topsides, for drilling and production of oil and gas and (ii) the supporting structure and its foundations, known as substructures. The topsides define the functions to be carried out by the structure, and the substructures define the type of platform as fixed template, gravity, jack-up, compliant, or TLP structure. The substructure components must secure the topside facilities against the environmental forces acting on them, providing a safe and protected area for equipment and the personnel at work. Although the purpose of the installation of offshore structures all over the world is similar in intent, viz., to extract oil and gas from the ocean depths and transport them to the processing facilities located onshore, the actual development plans will vary significantly depending upon (i) the size, shape, reservoir/water depth, and reservoir productivity; (ii) logistical considerations in moving the oil and gas to market; and (iii) lead time required to acquire, design, and fabricate the platforms, drilling rigs, production facilities, pipelines, and other required downstream facilities. The topside components, which primarily define the function of the platform, into drilling or drilling and production, include drilling rigs and associated components, oil and/or gas processing equipment, oil and gas pumping facilities and compressors, living quarters, helideck, and other requisite utilities.

Structures are always built with a purpose in mind, and this separates a real functioning structure from a sculpture, which stands for itself alone. An offshore structure and all its component parts are expected to fulfill certain functional requirements and be in a state of static and dynamic equilibrium during their lifetime [7]. This also implies that the structure or any of its component parts will not move or deform excessively under the applied environmental loads; the permissible displacements will be usually very small compared with its dimensions (see Figure 2.4 [8]). In Figure 2.4, only a beam-type bridge is visualized, but an offshore structure is more complex, and the analyst has to consider not only the structure and its components but also the influence of the soil foundation that supports the structure. As a corollary to the equilibrium of the whole structure, the structure must also be stable in its location. A case in point is illustrated in Figure 2.3, which shows the various states of stability conditions expected from a gravity platform structure. In addition to its vertical bearing strength, the platform must also possess transverse resistance against sea-bottom or subsea-bottom sliding of the structure and its foundations for the transverse forces exerted on it.



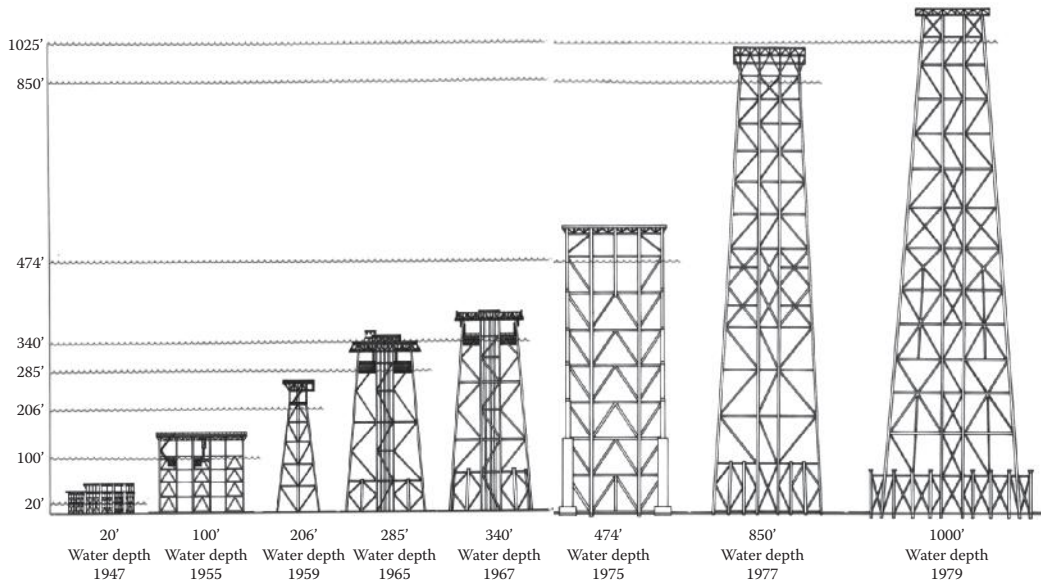
**FIGURE 2.4** Structural requisites: structure with adequate strength but excessive flexibility. (From A.J. McDonald, *Structure and Architecture*, Architectural Press, London, p. 20, 2001. With permission.)

As indicated in Figure 2.3, the foundation of a gravity structure must also be stable against unexpected rupture or uneven excessive settlement (due to liquefaction of subsurface soil) of the seabed. The type of soil existing below the foundation of the offshore structure will determine the possibility of liquefaction and rupture in soil under seismic or wave loading. Since strength is required for the on-site integrity of the structure and its foundation, the limit loads and moments of the structure and its foundations need to be much higher than the gravity and environmental loads acting on the structure to account for unexpected uncertainties in loading conditions and material properties. This becomes very important when new materials and innovative structural developments are used in the offshore context. Numerical results, obtained from detailed and complex structural analyses, need to be correlated by small-scale experimental studies and sometimes through tests on full-scale structures to ensure the on-site integrity of the structure against all expected and unexpected forces exerted on the structure.

Five different types of platforms are described below to give an overview to the readers regarding the complexity of the structure and the conceptual understanding required by the structural engineer as he/she considers the analysis and design of a structure for the offshore context. The structures described consist of (i) a fixed jacket steel platform; (ii) a steel jack-up platform; (iii) a concrete gravity platform; (iv) a semi-submersible platform; and (v) a ship structure. While the jacket and the gravity platforms are utilized for drilling and production purposes, the jack-up and semi-submersible platforms are primarily used for exploratory drilling purposes; some production semi-submersibles are also available and are used as a component for floating production storage and off-loading (FPSO) system; the tension-leg platforms, which are a variant of the semi-submersible-type platforms, are used nowadays for production in deep seas. The ship-type structures are primarily used for transportation of oil and gas, goods, and personnel; a variant of the ship-type structure, known as drill ship, is used for reconnaissance and exploratory drilling purposes.

### 2.3 COMPONENTS OF A FIXED JACKET STEEL PLATFORM

The first offshore steel fixed jacket steel platform was installed in 1947 in the Gulf of Mexico at a water depth of 20.0 ft. As indicated in Figure 2.5 [9], over the past 60 years, the water depths for such platforms have progressively increased to 100.0 ft. (30.0 m) in 1955, 285.0 ft. (85.5 m) in 1965, 474.0 ft. (142.0 m) in 1975, 1025.0 ft. (312.0 m) in 1979 (Cognac platform), and 1350.0 ft. (412.0 m) in 1989 (Bullwinkle platform). The 1500.0-ft. (450.0-m) water depth seems to be the upper limit for an economically feasible fixed jacket steel platform. The weight of the platform has grown from less



**FIGURE 2.5** Evolution of jacket structures from their humble beginnings. (From Technical Brochure of McDermott Inc., *The Story of Oil and Gas*, p. 21, 1981. With permission.)

than 1000 tons in 1947 to 46,000 tons in 1989 (the maximum operating weight was 77,000 tons). The typical weight estimates for a North Sea drilling rig platform (producing around 50,000 barrels of oil per day) are given in Table 2.1 [10], and additional weights, required for a typical production platform, are given in Table 2.2 [10]. The topside weights will be influenced by a number of factors such as gas/oil ratio, reservoir pressure, pressure-maintenance equipment, environmental loads exerted, and optimized design of the topsides. The dry weight of any offshore platform can be

**TABLE 2.1**  
**Weight Estimates for a Drilling Rig, with a Production Rate of 50,000 BOPD**

Item	Dry Weight Short Tons	Operating Weight Short Tons
Power package (4 × 1 MW) <sup>a</sup>	335	380
Substructure subbase	115	115
Substructure	285	285
Derrick	200	205
Bulk storage package	205	850
Sack storage package	220	725
Mud pump package	220	560
Pipe rack load <sup>b</sup>	0	850
Shaker package	100	190
Hook load <sup>b</sup>	0	380
Setback <sup>b</sup>	0	275
Drill line, blowout preventor, riser, tools	110	110
Total estimated rig loads	1790	4925

Source: S.L. Landes, Operational loadings, in: *Planning and Design of Fixed Offshore Platforms*, edited by B. McClelland and M.D. Reifel, Van Nostrand Reinhold Company, New York, USA, pp. 27–45, 1986. Courtesy of Van Nostrand Reinhold.

<sup>a</sup> Includes transformers and switchgears.

<sup>b</sup> May or may not occur simultaneously.

**TABLE 2.2**  
**Typical Production Platform Equipment Weights**

Equipment	Dry Weight Range, Tons
Production manifold	10–100
Well control panel	2–3
Oil–gas separators	5–100
Oil coolers	5–30
Crude oil pumps	5–20
Crude metering skid	10–60
Crude booster pumps	3–5
Produced water separator	6–20
Gas compression package(s), scrubbers, and intercoolers	10–200
Fuel-gas scrubber	1–5
Fuel-gas reheat exchanger	2–5
Fuel-gas chiller	2–5
Gas reinjection package	40–200
High-pressure relief vessel	4–10
Low-pressure relief vessel	4–10
Atmospheric vent vessel	2–4
Gas dehydrator(s)	10–100
Condensate treatment	5–10
Oil–water treatment	5–50
Water-injection manifold <sup>a</sup>	10–40
Water-injection well control panel <sup>a</sup>	1–3
Seawater deaerator, each <sup>a</sup>	10–20
Water filters, each <sup>a</sup>	10–40
Water injection pump, each <sup>a</sup>	10–40
Chlorine generator	1–2
Circulation pump, each	1–4

Source: S.L. Landes, Operational loadings, in: *Planning and Design of Fixed Offshore Platforms*, edited by B. McClelland and M.D. Reifel, Van Nostrand Reinhold Company, New York, pp. 27–45, 1986.

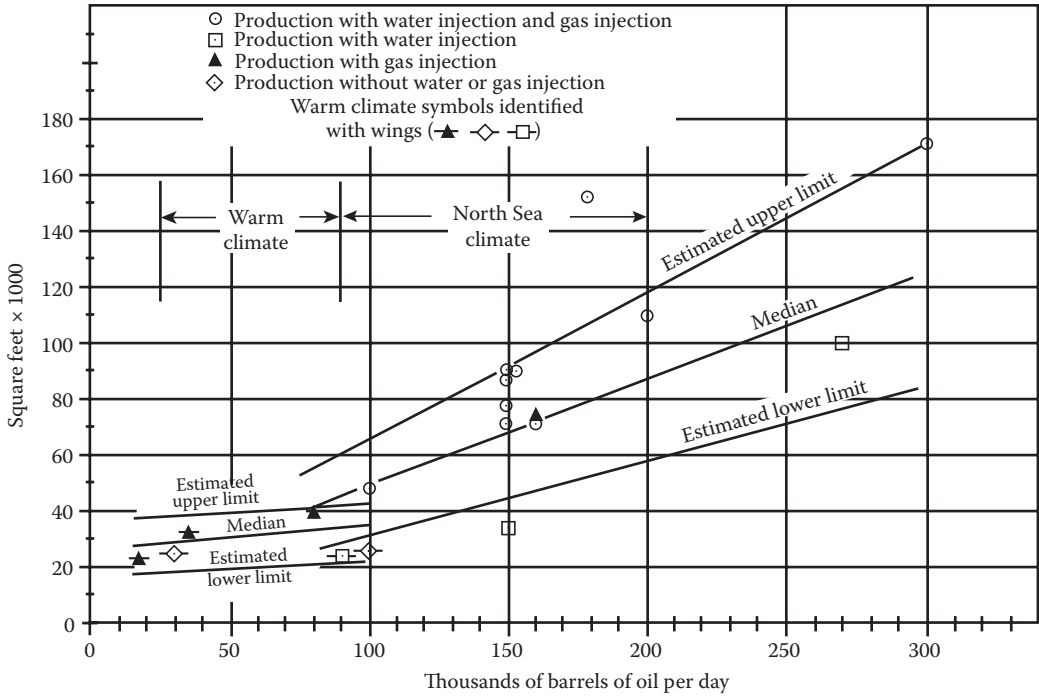
<sup>a</sup> Items required for water-injection system.

approximately estimated using Figures 2.6 and 2.7 [10], which give the topside dry weight and the topside platform area as a function of the oil production rate. Using these two tables, if the barrel output per day of the field is known, then the approximate platform weight and platform topsides area can be computed.

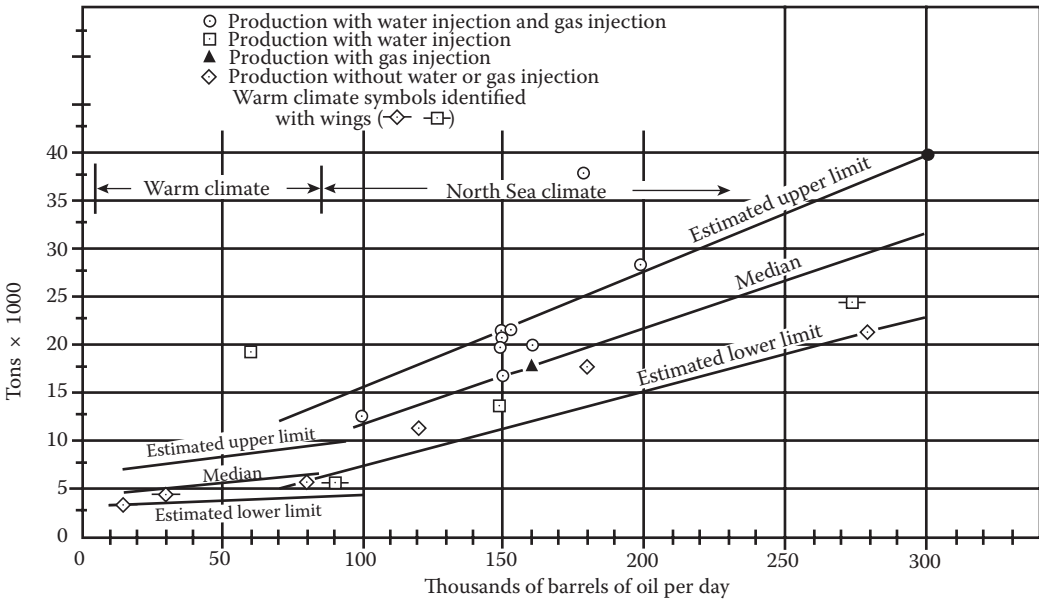
A brief description of the various components of a fixed jacket steel platform is given below. The various components of a fixed jacket platform can be observed to be (from the details given in Figure 2.8 [11]): (i) jacket substructure; (ii) module support frame; (iii) pile foundation; (iv) drilling derrick; (v) production modules and associated equipment; (vi) living quarters module; (vii) heli-deck; (viii) flare stack; (ix) drilling conductors; (x) pipeline risers; and (xi) pipelines.

### 2.3.1 JACKET SUBSTRUCTURE

The jacket substructure, which is a braced tubular tower structure, and its piles foundation (i) provide a supporting deck for the topside facilities; (ii) provide resistance against transverse environmental forces and a safe and rigid base for all the topside operations; and (iii) protect the well conductors and pipeline risers. The supporting deck of the offshore platform provides

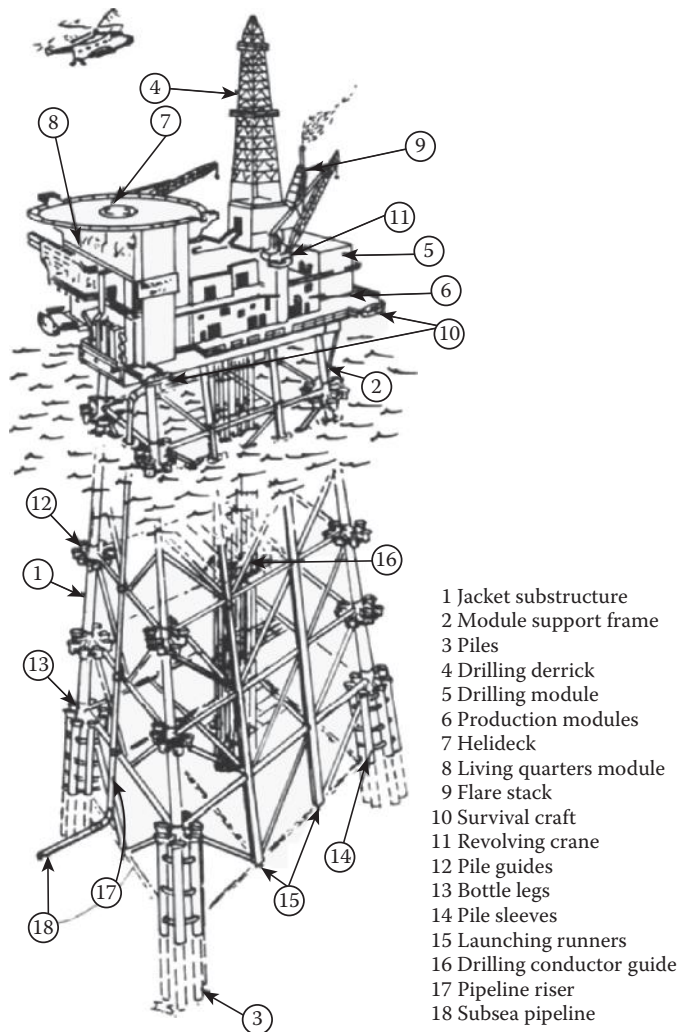


**FIGURE 2.6** Platform topside area as a function of oil production rate. (From S.L. Landes, Operational loadings, in: *Planning and Design of Fixed Offshore Platforms*, edited by B. McClelland and M.D. Reifel, Van Nostrand Reinhold Company, New York, pp. 27–45, 1986. With permission.)



**FIGURE 2.7** Platform dry weight as a function of oil production rate. (From S.L. Landes, Operational loadings, in: *Planning and Design of Fixed Offshore Platforms*, edited by B. McClelland and M.D. Reifel, Van Nostrand Reinhold Company, New York, pp. 27–45, 1986. With permission.)





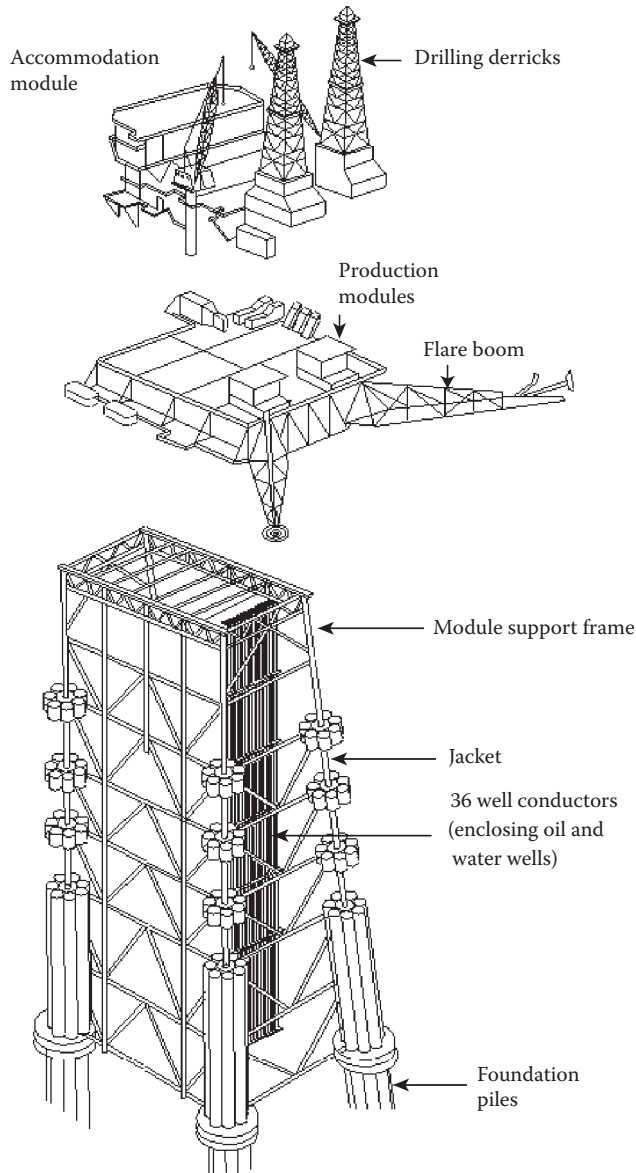
**FIGURE 2.8** Components of a steel-piled self-contained drilling and production platform. (From J.G. Timar, *Lectures on Offshore Engineering*, Institute of Building Technology and Structural Engineering, Aalborg University Centre, Aalborg, Denmark, 1978. With permission.)

primarily support for well work-over and control equipment, production modules (consisting of separators, pumps/compressors, power generators etc., required for transporting the product onshore), accommodation module for operating and maintenance staff. A number of jacket framing plans have been utilized over the years in fabricating the jacket structure, as shown in Figure 2.9 [12]. Jacket bracing patterns have typically consisted of single-diagonal, K-braced panels, and/or X-braces. The use of X-braces would require careful modeling and detailing to avoid undesirable load conditions on the platform. Jacket leg spacing is dependent on platform rig requirements, number of piles required to carry the loads acting on the structure, well spacing and location, and launch runner spacing. For jackets located in water depths below 600 to 750 ft. (180 to 250 m), the optimum spacing of legs may vary between 30 × 30 ft. (9.0 m × 9.0 m) and 45 × 45 ft. (13.5 m × 13.5 m). For deeper water structures, the leg spacing may be increased appropriately. The maximum range of leg batter is between 1:8 and 1:16 (or 20), leading to a maximum true corner batter of 1:5.7 along the diagonal.



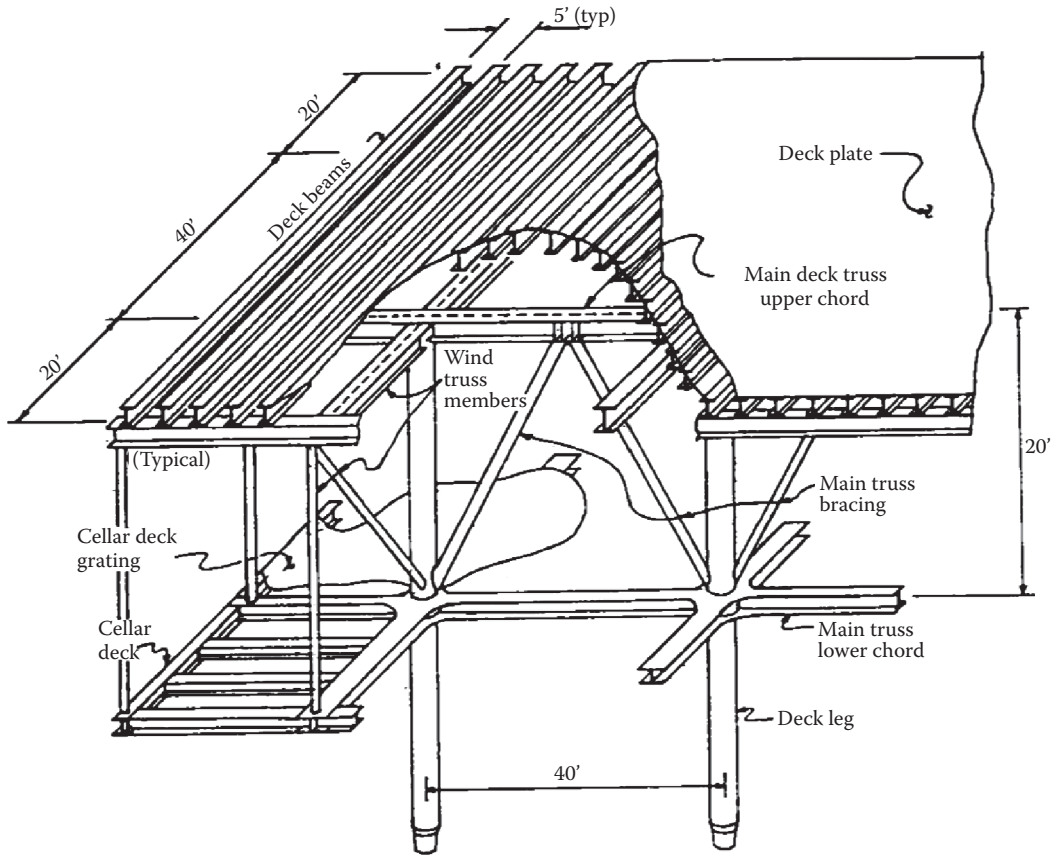


Basically, two types of topside facilities have been utilized in the offshore context, viz., integrated and modularized topsides, which could be positioned either on a jacket or on a concrete gravity sub-structure, as shown in Figure 2.10 [13]. The single integrated deck concept can be utilized up to a total platform weight of 10,000 tons (10,200.0 t); when the platform weight exceeds this load, the modularized topsides consisting of a module support frame carrying a series of requisite modules are used, as shown in Figure 2.11 [14]. In the integrated jacket, the facilities to be located on the top



Note the launching girders in the jacket and the conventional pile guides

**FIGURE 2.11** Modular assembly of jacket platform components with launch girders. (From ESDEP [The European Steel Design Education Program] Lecture Series, *Offshore Structures*, Lecture 15A.1. Available at <http://www.esdep.org/members/master/wg15a/10100.htm>, 1993. With permission.)



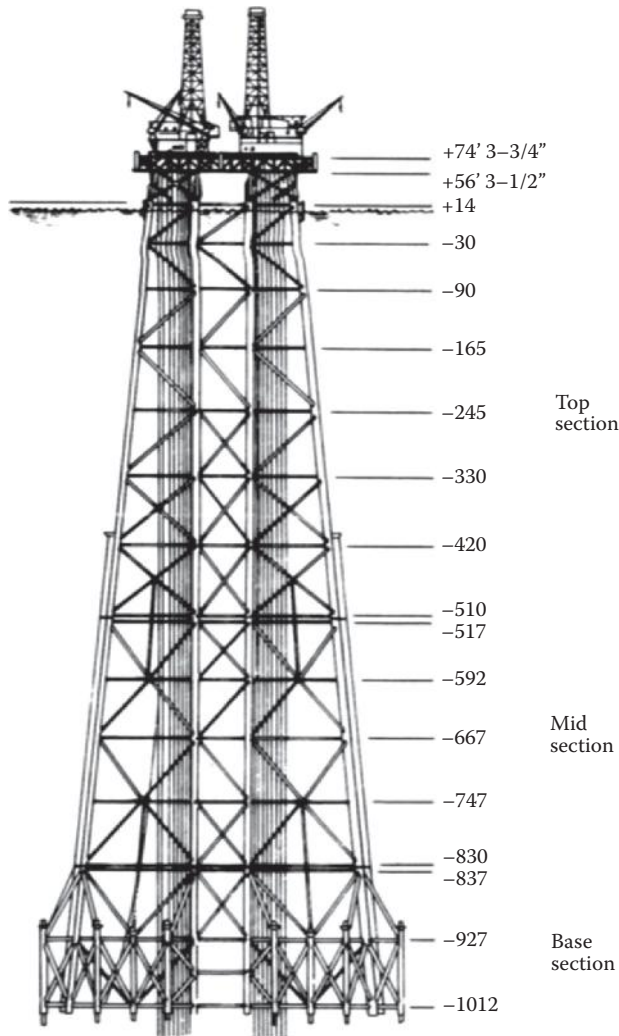
**FIGURE 2.12** Cutaway view of the deck structure. (From W.J. Graff, *Introduction to Offshore Structures: Design Fabrication and Installation*, Gulf Publishing Company, Houston, TX, p. 219, 1981. With permission.)

deck are assembled in the onshore fabrication yard, and then transported to the offshore site of the already upended jacket structure, lifted from the transportation barge and installed over the jacket. In the integrated deck concept, the supporting deck structure consists of trusses or portal frames without diagonals, as shown in Figure 2.12 [15]. A modularized topside structure can weigh from 20,000 to 40,000 tons (20,400 to 40,800 t). For the modularized jacket structure the modular support frame (MSF), located on the top of the jacket substructure, is a heavy tubular structure (Figure 2.12), with lateral bracings down to the top of the bottom jacket substructure. It will be shown later that the MSF configuration will be different for other types of offshore structures.

In the case of jacket platforms located in waters of depth above 200.0 m, for instance, in the case of Cognac platform (Figure 2.13 [16]), located in Mississippi Canyon Block, the jacket substructure was fabricated as three separate components, and then mated together by controlled flooding at the offshore location of the field. The individual components of the jacket substructure are shown in Figure 2.14 [17].

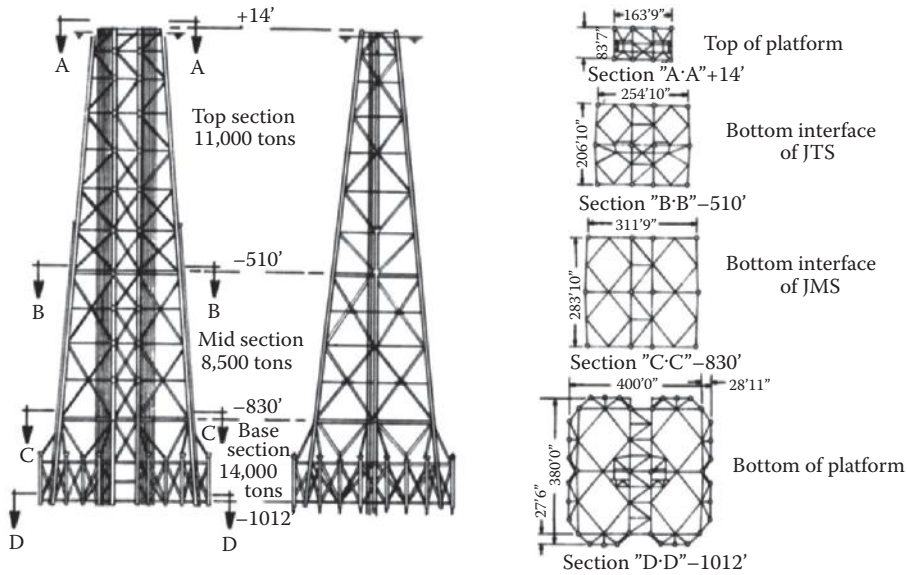
### 2.3.2 PILE FOUNDATION

The foundation for a steel jacket platform is provided by open-ended tubular steel piles, with diameters up to 2 m. The piles are driven approximately to a depth of 40–80 m below the seabed, and in some cases, the piles penetrate to a depth of 120 m below the seabed. Three types of pile/jacket

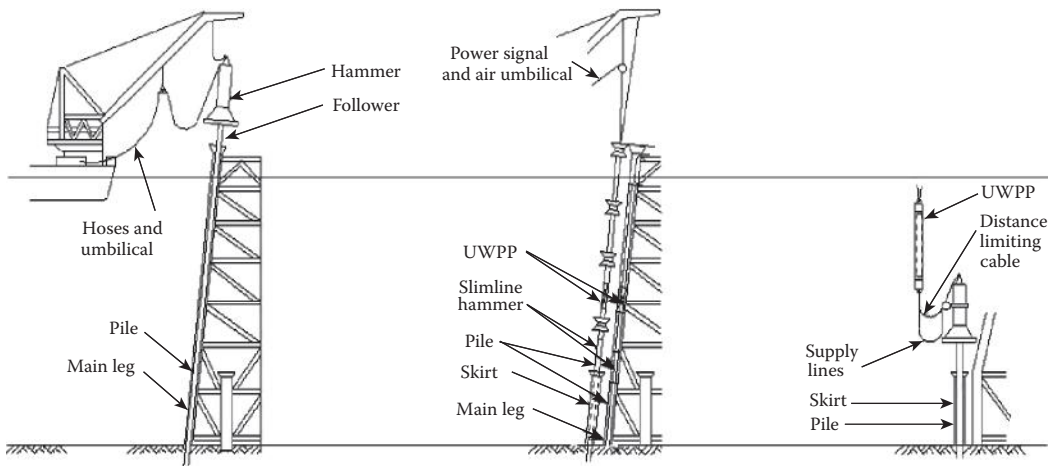


**FIGURE 2.13** Assembled components of the Cognac platform located in the Mississippi Canyon, Gulf of Mexico, at a water depth of 1026.0 ft. (From W.J. Graff, *Introduction to Offshore Structures*, Gulf Publishing Company, Houston, TX, p. 49, 1981. With permission.)

arrangement are used to fix the jacket substructure to the seabed, as shown in Figure 2.15 [17], viz., (i) pile-through-the-leg concept, where the piles are driven through the corner legs of the jacket substructure; (ii) skirt-piles-through-the-pile-sleeves concept, where the piles are driven through the guides attached to the jacket legs on the outside. The skirt piles are grouped around the base of each jacket leg (see also Figures 2.8 and 2.11). (iii) Vertical piles are driven directly through the pile sleeves located at the jacket base. The vertical piles provide reduced pile stiffness to the structure than the inclined piles used in case (ii). Additional piles, called “skirt piling” or “outrigger piling,” may be added to the structure through sleeves framed into the bottom of the jacket below the level of high wave force.



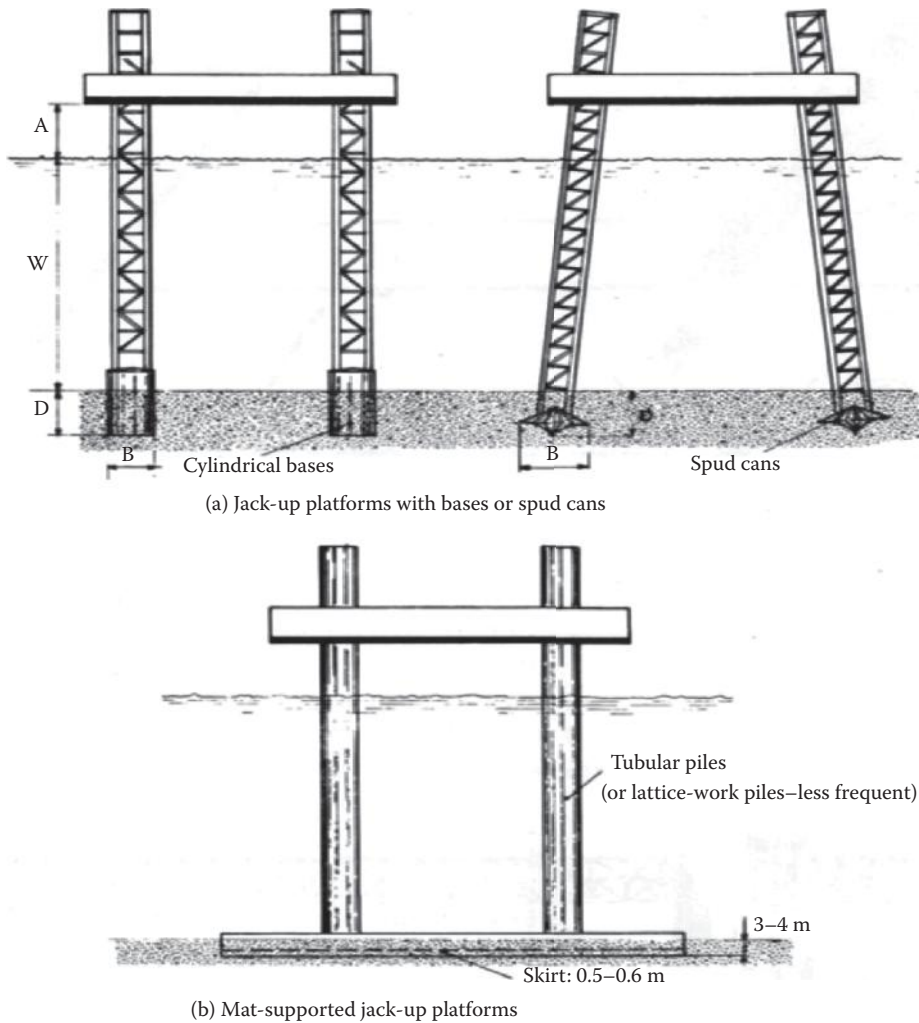
**FIGURE 2.14** Constituent Subcomponents of the Jacket Structure. (From W.J. Graff, *Introduction to Offshore Structures*, Gulf Publishing Company, Houston, TX, p. 56, 1983. With permission.)



**FIGURE 2.15** Conventional and New Pile Driving Technologies Utilized in Offshore Jacket Structures. (From ESDEP [The European Steel Design Education Program], Lecture Series, *Offshore Structures*, Lecture 15A.1. Available at <http://www.esdep.org/members/master/wg15a/10100.htm>, 1993. With permission.)

### 2.4 COMPONENTS OF A STEEL JACK-UP PLATFORM

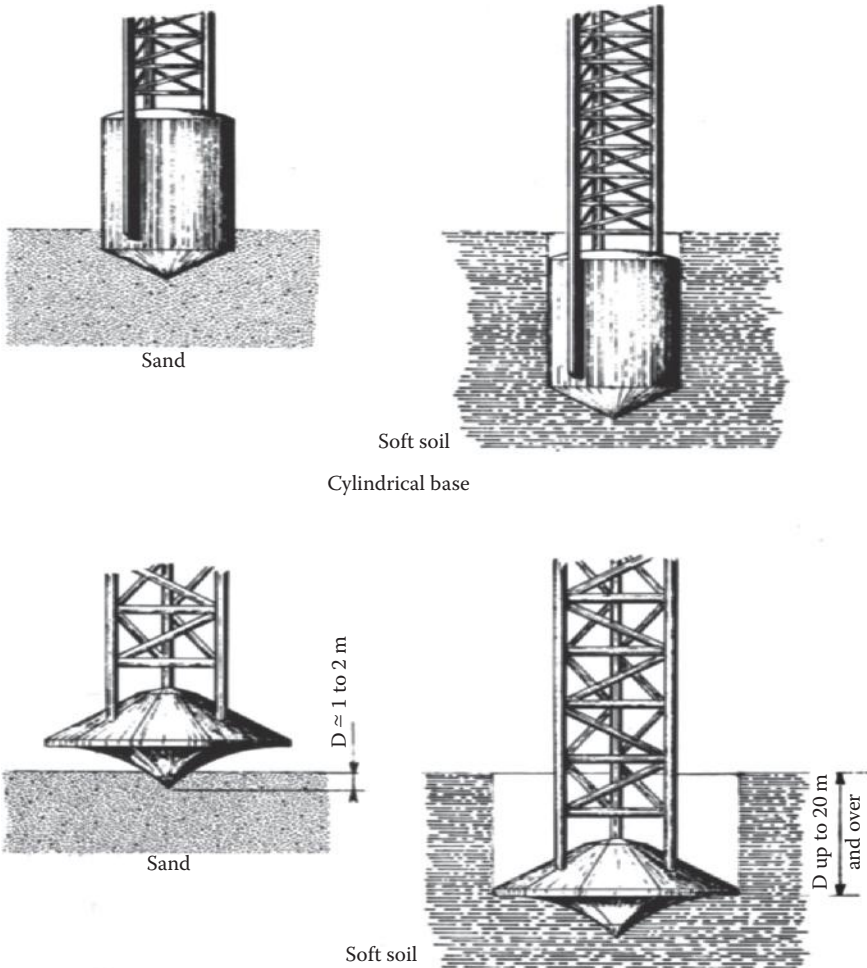
In water depths less than 500.0 ft. (150 m), as indicated in Figure 2.3, exploration platforms are used to carry out reconnaissance and detailed geophysical surveys of the oil and gas field using acoustic procedures and drill exploratory wells; sometimes, these platforms are also used to drill development wells. Two main types of jack-up platforms are used in the offshore context, namely, (i) Truss column-supported platforms with spud can bases and (ii) Mat-supported platforms with hollow tubular columns, as shown in Figure 2.16. As shown in Figure 2.16 [18], the legs of the truss column-supported jack-up platforms may be vertical or inclined (with a slope of 0° to a maximum of 15°) to increase the stability under lateral loads. For the truss column-supported jack-up platforms, a large



**FIGURE 2.16** Types of jack-up platforms used in offshore exploration. (From P. Le Tirant, *Seabed Reconnaissance and Offshore Soil Mechanics*, Editions Technip 27, Paris, France, p. 401, 1979. With permission.)

variety of configurations have been developed, with the number of vertical (or inclined) columns varying from 3 to 14; the most common types have three or four truss columns. The diameter of the spud cans at the bottom varies from 5.0 to 15.0 m. A number of geometries were investigated for the spud can configuration in sandy and clayey soils, but only two types, namely, (i) a spud can with a cylindrical base and (ii) spud cans with conical polyhedral bottoms, are currently in usage, as indicated in Figure 2.17 [19]. The height to diameter ratio of the spud can is around 1.0 for the spud can with cylindrical base, whereas for the conical spud can with polyhedral bottom, the ratio is around 0.5. The mat-supported jack-up platforms were designed for the offshore locations where soils with low bearing capacities were encountered. The geometry of the mat foundation varied from a single rectangular A-shaped mat with central opening to one (or two) hydrodynamic-shaped mat. The mat is connected to the top platform by hollow tubular columns (sometimes lattice-work columns were also used). The overall dimensions of the rectangular mat foundation varied from 170.0 to 200.0 ft. (50 to 60 m), with a base area of 11,000 to 28,000 ft.<sup>2</sup> (1000.0 to 2500 m<sup>2</sup>).

The platform contains everything that is required for the exploratory or development drilling operation that is to be carried out from the jack-up platform. The drilling derrick is located at one

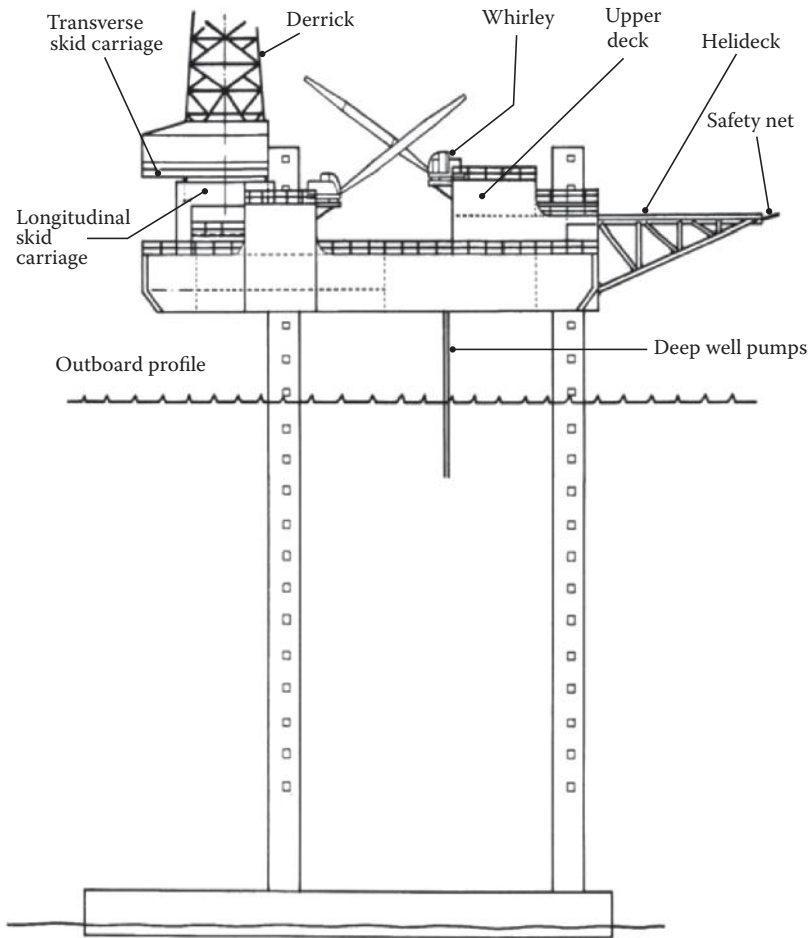


**FIGURE 2.17** Types of bases used in jack-up platforms for seabed penetration. (From P. Le Tirant, *Seabed Reconnaissance and Offshore Soil Mechanics*, Editions Technip 27, Paris, France, p. 437, 1979. With permission.)

end of the top deck of the jack-up platform, and the heliport is located at the opposite end of same deck of the platform, as shown in Figures 2.18 [20] and 2.19a [21]. Within the interior of the platform are the tanks for liquid mud, dry bulk mud, cement storage, drilling water, potable water, and fuel oil located in the lower deck (Figure 2.19c). The space for the living quarters, pipe rack, and machinery space are located in the main deck, as shown in Figure 2.19a and b.

Year-round air-conditioned living quarters contain berthing facilities, gallery, cafeteria-type dining accommodations, recreation space, and offices. The mat foundation is a large steel barge-type structure, in the shape of a squared “A,” and is supported by the ocean floor. The major portion of the mat is flooded and open to the sea, during normal operations. The mat foundation is designed to resist overturning forces generated on the structure by the winds and waves of hurricane level force. The three cylindrical legs are integral to the mat and are connected to the platform through hydraulic jacking units. The lengths of the vertical columnar legs and the bottom mat area are determined by the operating depth of the structure and the environmental forces acting on it.





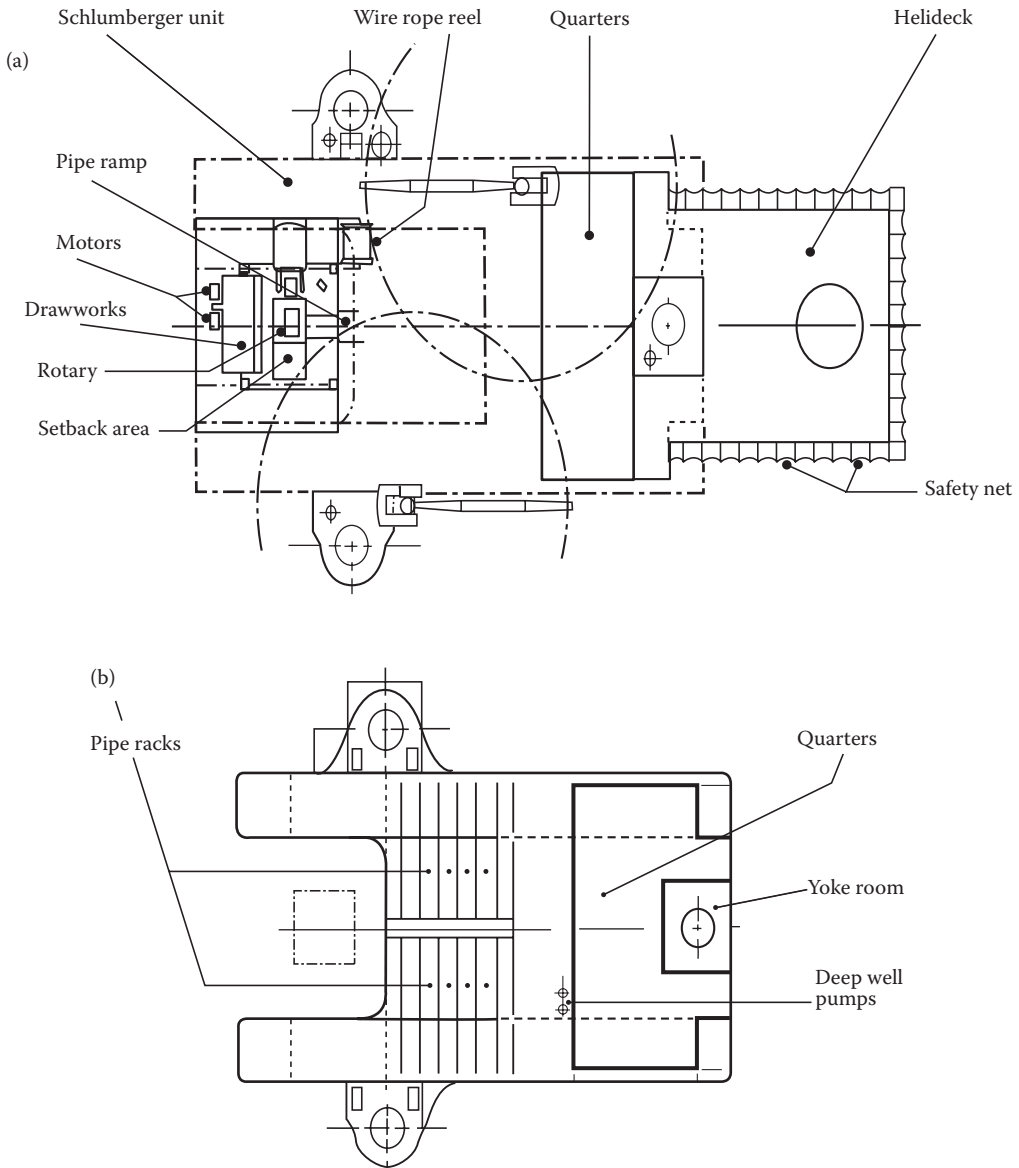
**FIGURE 2.18** Elevation of a mat-supported jack-up platform. (From Bethlehem Steel Corporation, Jack-up designs for drilling, production and storage, *Technical Brochure*, p. 5, 1975. With permission.)

## 2.5 COMPONENTS OF A CONCRETE GRAVITY PLATFORM

Another major type of offshore structure is the gravity-based concrete structure, shown in Figure 2.20 [14, 22], which has been dominantly used in the North Sea around the Norwegian and British sectors; some have also been used in the offshore areas around Brazil, Australia, Russia, and the Philippines. They have been used in the oil and gas industry for drilling, extraction, and storage of crude oil or natural gas.

In general, they have proved to be a more economical solution than jackets or floating systems in water depths up to about 300 m, especially when one or more of the following conditions apply: (i) the field is far from shore and there are no existing pipeline export systems; (ii) on-site storage of oil or condensate becomes essential; (iii) the platform is required to support heavy topsides; and (iv) the ground conditions are soft or unsuitable for piling. The offshore concrete structures have been gravity-based structures, supported on top of a prepared surface of the sea bottom.

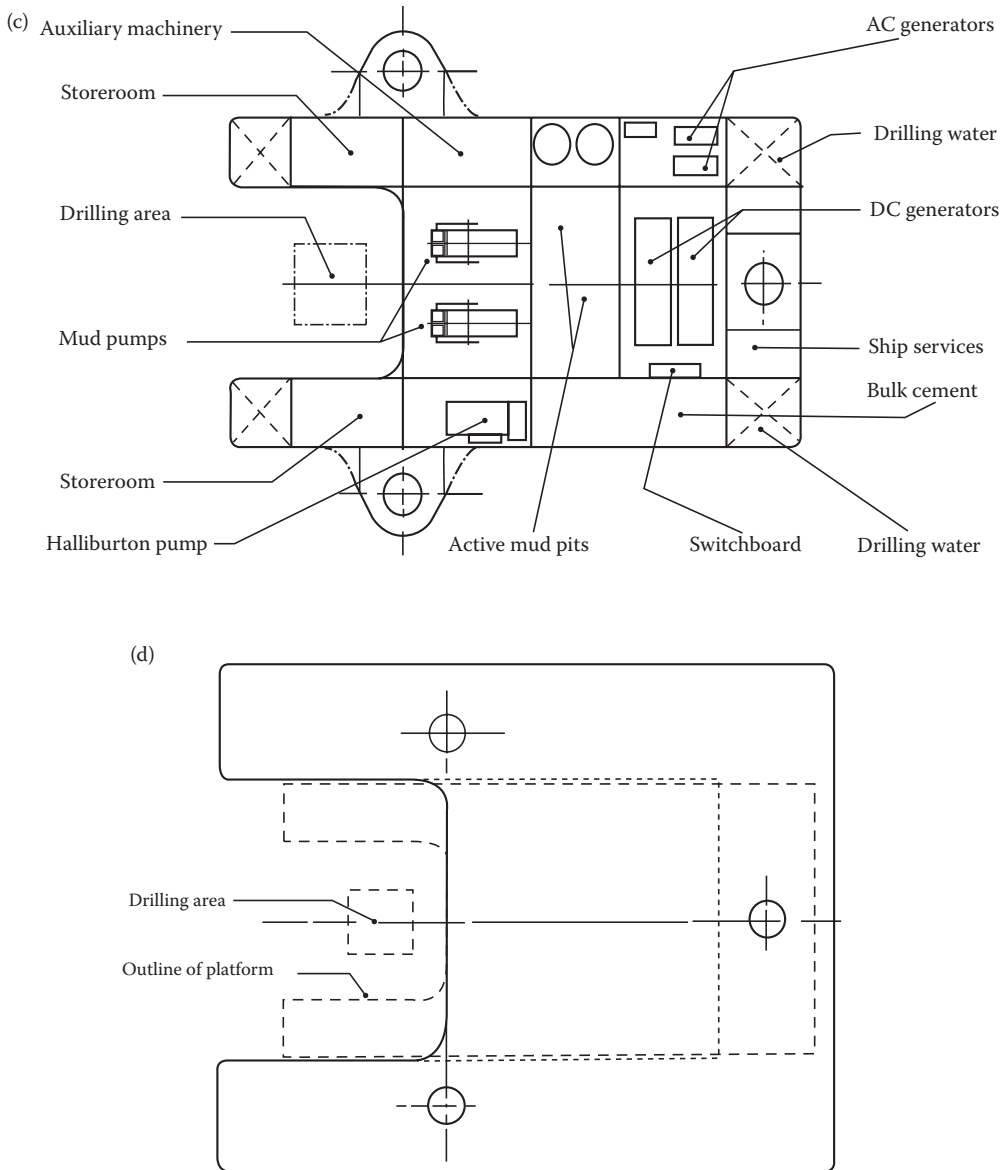
Gravity platforms are built as concrete gravity-based structures (GBS or CGS), in which concrete caissons (or columns) have been used to transmit the heavy platform loads down through the bottom storage cells (used as storage cells for oil and other condensates) to the uppermost soil layers as bearing pressures. The caissons and the bottom storage cells provide buoyancy during construction



**FIGURE 2.19** Structural details of a jack-up platform (a) skid unit and upper deck; (b) main deck; (c) lower deck; and (d) mat and drilling platform. (From Bethlehem Steel Corporation, Jack-up designs for drilling, production and storage, *Technical Brochure*, pp. 4 and 5, 1975. With permission.)

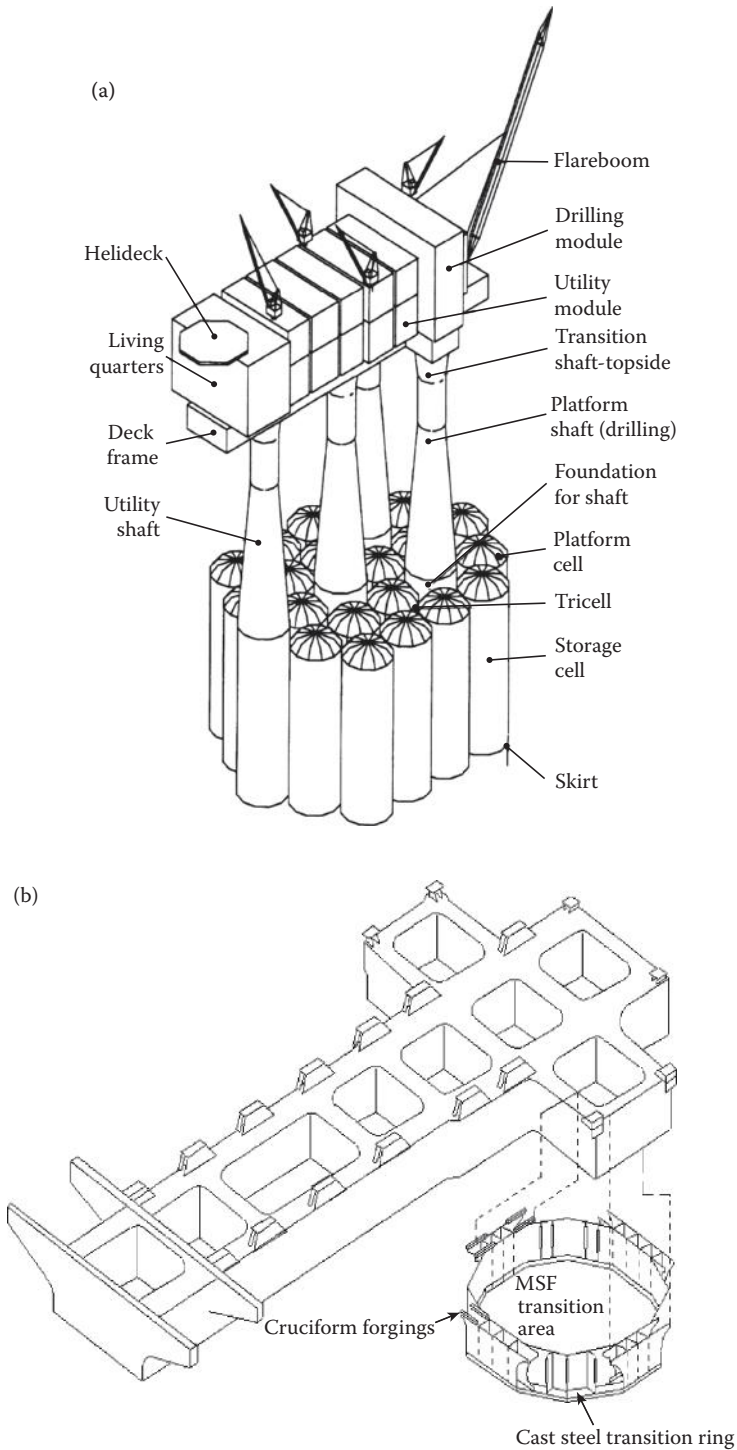
and towing. Concrete offshore structures have shown excellent durability and have been free of corrosion degradation, experienced by the steel jacket structures; they also do not need regular and sustained maintenance as the steel structures. They are highly suitable for the harsh environment of the North Sea and the ice-bound regions of the Arctic. Since the 1970s, several concrete platforms (more than 40) have been installed, as shown in Table 2.3 [23]. Most of these structures, as shown in Figure 2.20a [22], have a large number of cylindrical storage cells (usually more than 15 to 20) at the bottom, and three to four caissons (or columns) penetrating the water surface to carry the top-side structure. The topside structure is connected to the columns through a module support frame,





**FIGURE 2.19** (Continued) Structural details of a jack-up platform (a) skid unit and upper deck; (b) main deck; (c) lower deck; and (d) mat and drilling platform. (From Bethlehem Steel Corporation, *Jack-up designs for drilling, production and storage*, *Technical Brochure*, pp. 4 and 5, 1975. With permission.)

similar to the one shown in Figure 2.20b [14]. Utility systems for offloading, drilling, draw down, and ballast are located in these vertical caissons, as shown in Figure 2.21 [24]. The earliest gravity-based platform in the North Sea was the Ekofisk Tank type, with Jarlan walls to minimize the wave forces acting on the platform. This tank form was developed to provide enough storage for the oil extracted from the Ekofisk reservoir and is installed at the offshore site where the sea-bottom soils consisted of very dense sands. The foundation of the tank-type structure had an area of nearly 5000 m<sup>2</sup>; it also had short “skirts” (see Figures 2.21 and 2.22 [25]) that penetrated a few meters into the seabed soils around the platform and prevented the scour of soil below the tank bottom.



**FIGURE 2.20** (a) Components of a typical condeep gravity platform. (From T. Holland et al., *Design of Offshore Concrete Structures*, Spon Press, London, p. 18, 2000. With permission.) (b) Module support (or deck) frame (MSF) for a gravity platform. (From ESDEP [The European Steel Design Education Program] Lecture Series, *Offshore Structures*, Lecture 15A.1. Available at <http://www.esdep.org/members/master/wg15a/10100.htm>, 1993. With permission.)

Gravity-based concrete platform was subsequently modified for very soft clay locations, using long concrete skirts that penetrated deep into the subsea soil foundation and transferred the load from the structure into stronger soils at deeper depths (see Figure 2.22). For instance, the skirts of the Gullfaks C GBS penetrated into the foundation, up to a depth of 25 m below the seabed. Four different types of concrete designs have been used for concrete gravity structures, viz., (i) condeep type (with one, two, three, or four columns); (ii) ANDOC type (with four columns); (iii) Sea Tank type (with two or four columns); (iv) Ekofisk type with Jarlan walls. Table 2.3 summarizes some of the major existing offshore concrete structures.

The topsides to be supported by a gravity-based substructure, shown in Figure 2.20, weigh from 20,400 to 51,000 tons. The supporting base for the topsides of the gravity platform structure, known as module support structure (MSG) is a system of heavy box-girders with a height of approximately 35.0 ft. (~10 m) and a width of approximately 40.0 to 50.0 ft. (12 to 15 m) given in Figure 2.22. The MSG of the deck is rigidly connected to the concrete column and acts as a beam supporting the deck modules. One problem due to the rigid connection between the MSG and the concrete columns is the introduction of wave-generated fatigue in the deck structure. Consequently, in the new designs of the topsides, a flexible connection has been provided between the deck and the concrete column to eliminate fatigue cracking in the deck.

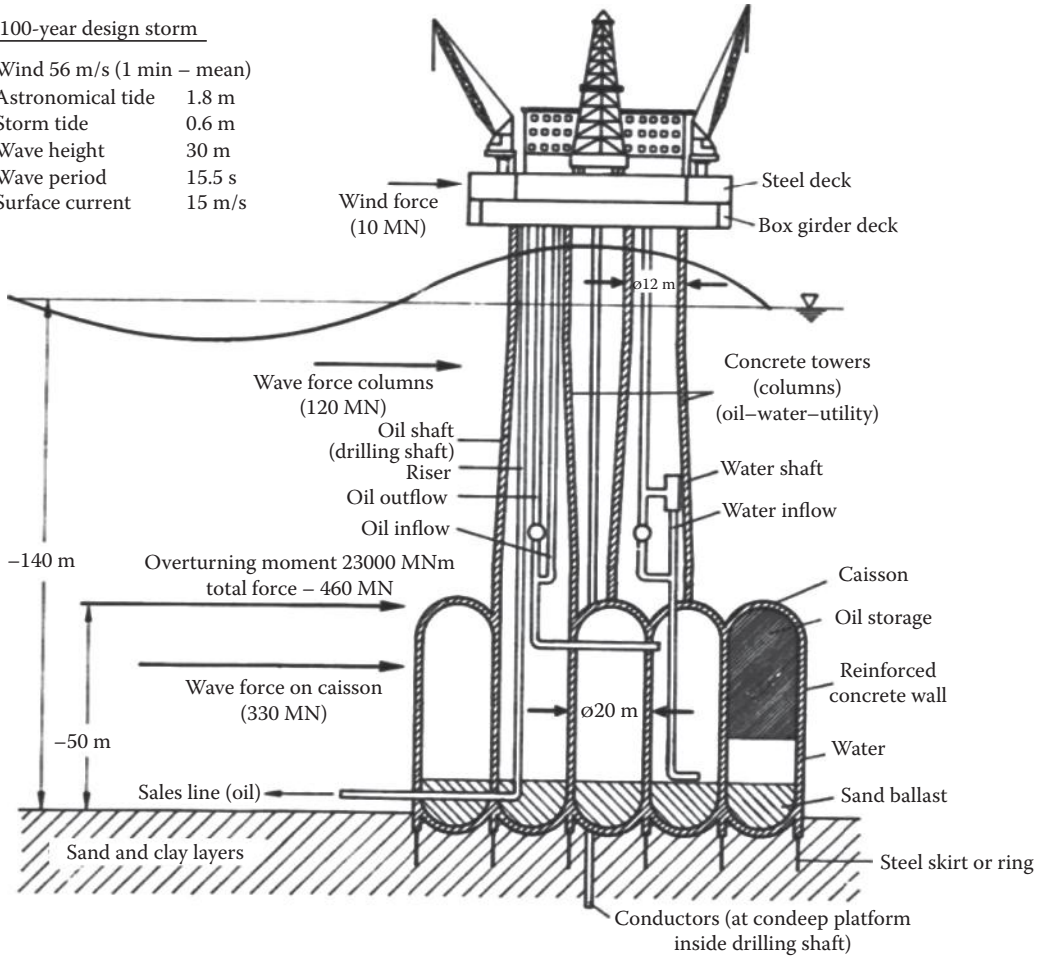
**TABLE 2.3**  
**Some of the Major Gravity-Based Structures**

No.	Year Installed	Operator	Field/Unit	Structure Type	Depth	Location	Design by
1	1973	Phillips	Ekofisk Tank	GBS, Jarlan Wall	71 m	North Sea (N)	DORIS
2	1975	Mobil	Beryl A	Condeep, 3 columns	118 m	North Sea (UK)	NC/Olav Olsen
3	1975	Shell	Brent B	Condeep, 3 columns	140 m	North Sea (UK)	NC/Olav Olsen
4	1976	Elf	Frigg TP1	GBS, 2 columns	104 m	North Sea (UK)	Sea Tank
5	1976	Elf	Frigg MCP-01	GBS, Jarlan wall	94 m	North Sea (N)	DORIS
6	1977	Shell	Dunlin A	GBS, 4 columns	153 m	North Sea (UK)	ANDOC
7	1978	Shell	Cormorant A	GBS, 4 columns	149 m	North Sea (UK)	Sea Tank
8	1978	Chevron	Ninian Central	GBS, Jarlan wall	136 m	North Sea (UK)	DORIS
9	1984	Mobil	Statfjord C	Condeep, 4 columns	145 m	North Sea (N)	NC/Olav Olsen
10	1987	Statoil	Gullfaks B	Condeep, 3 columns	141 m	North Sea (N)	NC/Olav Olsen
11	1988	Norsk Hydro	Oseberg A	Condeep, 4 columns	109 m	North Sea (N)	NC/Olav Olsen
12	1989	Statoil	Gullfaks C	Condeep, 4 columns	216 m	North Sea (N)	NC/Olav Olsen
13	1989	Phillips	Ekofisk P.B	GBS Protection Ring	75 m	North Sea (N)	DORIS
14	1993	Shell	Draugen	Condeep Mono-tower	251 m	North Sea (N)	NC/Olav Olsen
15	1995	Shell	Troll A	Condeep, 4 columns	303 m	North Sea (N)	NC/Olav Olsen
16	1996	Esso	West Tuna	GBS, 3 columns	61 m	Australia	Kinhill/DORIS
17	1997	Mobil	Hibernia	CGS, 4 columns	80 m	Canada	DORIS
18	2000	Shell	Malampaya	GBS, 4 columns	43 m	Philippines	Ove Arup
19	2005	SEIC	Lunskoye A	GBS, 4 columns	48 m	Sakhalin (R)	AK/GMAO
20	2005	SEIC	Sakhalin PA-B	GBS, 4 columns	30 m	Sakhalin (R)	AK/GMAO

*Source:* T.O. Olsen, 2002, Recycling of Offshore Concrete Structures: State-of-the-Art Report, International Federation of Structural Concrete (fib), Federal Institute of Technology, Lausanne-EPFL, Departement Genie Civil, ISSN 1562-3610, pp. 1–2. Table was modified and made up-to-date.

100-year design storm

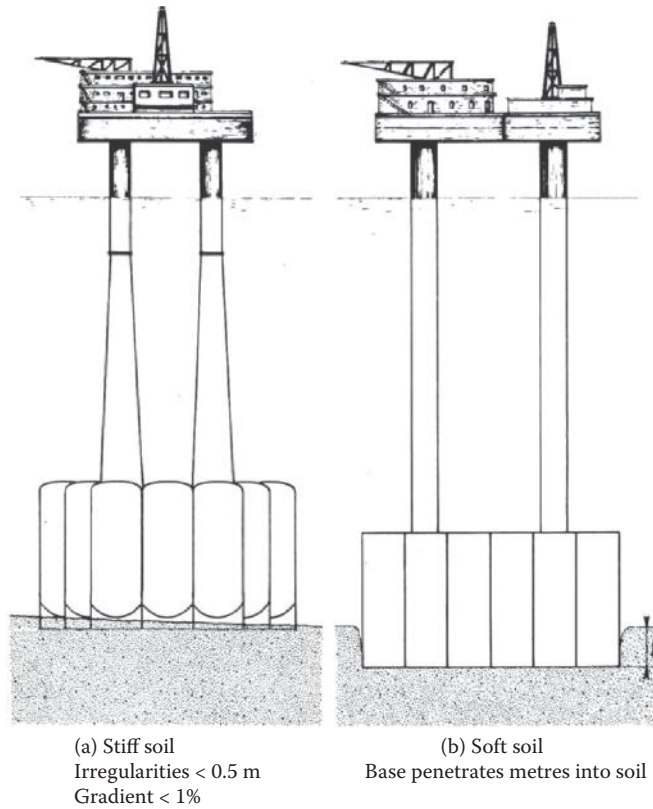
Wind	56 m/s (1 min – mean)
Astronomical tide	1.8 m
Storm tide	0.6 m
Wave height	30 m
Wave period	15.5 s
Surface current	15 m/s



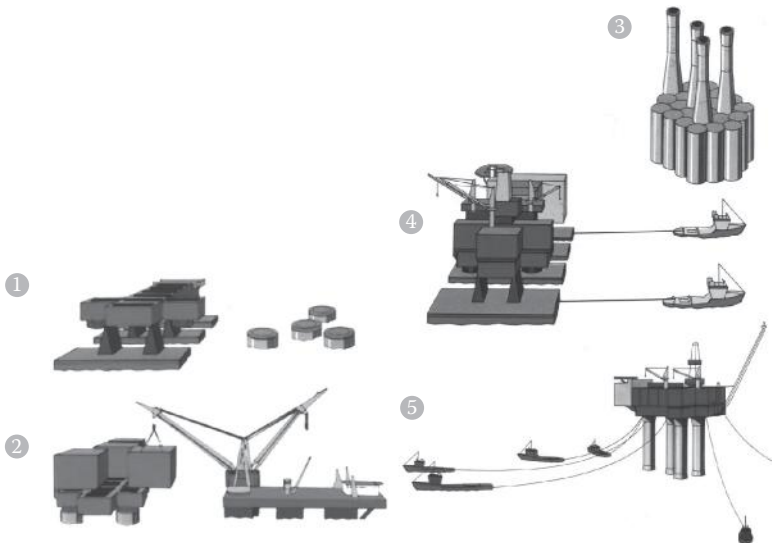
**FIGURE 2.21** Cross section of the gravity platform Brent B and D. (With kind permission from Springer Science+Business Media: *Offshore Structures: Conceptual Design and Hydromechanics*, Volume I, 1992, p. 66. G. Clauss, E. Lehmann, and C. Ostergaard.)

Since the concrete GBS is a very heavy structure, and it has to be moved over large distances to install it on site, economizing operational procedures have been built into the design and installation of such structures. As shown in Figure 2.23 [26], which shows the construction and installation procedures for the Gullfaks A gravity platform, the topsides are of modular construction, with each module built self-contained in the onshore fabrication yard. The modular support frame (MSG) of the topsides is moved to the transportation barge, and properly connected to it; thereafter, the respective modules are loaded on to the barge and properly fixed on the MSG. Meanwhile, the cellular concrete base of the GBS is built in a dry dock and then floated to an adjacent and almost calm deepwater site; the top caissons are built on the floating concrete base. The loaded transportation barge is then brought over to this deepwater site and assembled over the lowered caissons by ballasting the cellular caissons with water. Finally, the assembled gravity platform structure is towed to the final location and installed on site.

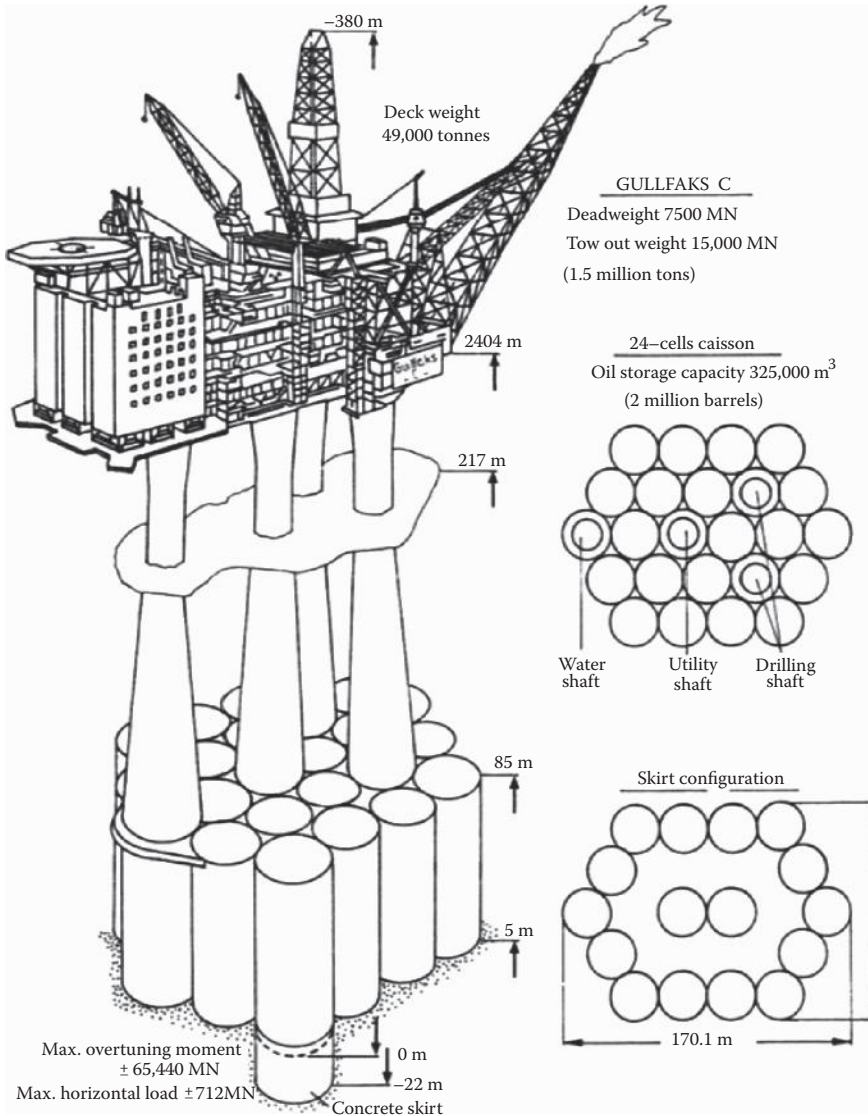
The North Sea Concrete Gravity Base Structure (GBS) Gullfaks C with a total height of 380 m, a dead weight of 750,000 tons, and a crude oil storage capacity of 2 million barrels (320,000 m<sup>3</sup>) is shown in Figure 2.24 [27]. It had a weight of 1.5 million tons during tow-out, which was almost equivalent to one third of the mass of the Great Pyramid of Khufu (or Cheops), in Egypt. Thus,



**FIGURE 2.22** Penetration of the skirt into soil (stiff and soft) in a gravity platform. (From P. Le Tirant, *Seabed Reconnaissance and Offshore Soil Mechanics*, Editions Technip 27, Paris, France, p. 437, 1979. With permission.)



**FIGURE 2.23** Components of an offshore gravity platform: (1) modular support frame ; (2) modules loaded and fixed on support frame; (3) floating gravity-based structure; (4) transportation barge towed to the deepwater site; (5) assembled gravity platform structure is towed to the final location for installation. (From Technical Brochure of Statoil, Aker and Norwegian Contractors, *Gullfaks A Gravity Platform*, pp. 3–4, 1986. With permission.)



**FIGURE 2.24** Assembled structural components on the gravity platform: Gullfaks C. (With kind permission from Springer Science+Business Media: *Offshore Structures: Conceptual Design and Hydromechanics*, Volume I, 1992, p. 67. G. Clauss, E. Lehmann, and C. Ostergaard.)

Gullfaks C platform became one of the heaviest objects, ever moved by man. The platform was installed in a water depth of 217.0 m, and the concrete skirts at the foundation had a penetrating depth of 22 m. Another structure of note is the Troll GBS, towering 472 m above the sea bottom; it required concrete skirts that penetrated even deeper than the Gullfaks C platform, into the sea floor, to a depth of 36 m. It was installed in a water depth of 305-m waters and produces 80 million m<sup>3</sup> of natural gas per day, which tallies to about 1.3 trillion m<sup>3</sup> during its 50-years operation off Norway.

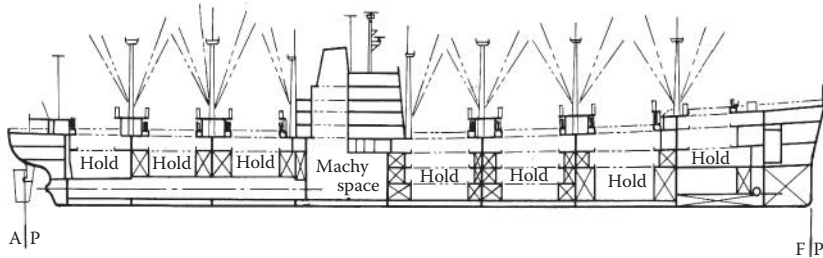
## 2.6 COMPONENTS OF A SHIP STRUCTURE

Ships, and its forerunner the rafts, have been in use on the earth, over many thousands of years. The expertise of the raft craftsmen was passed down the generations of Greeks, Romans, and the



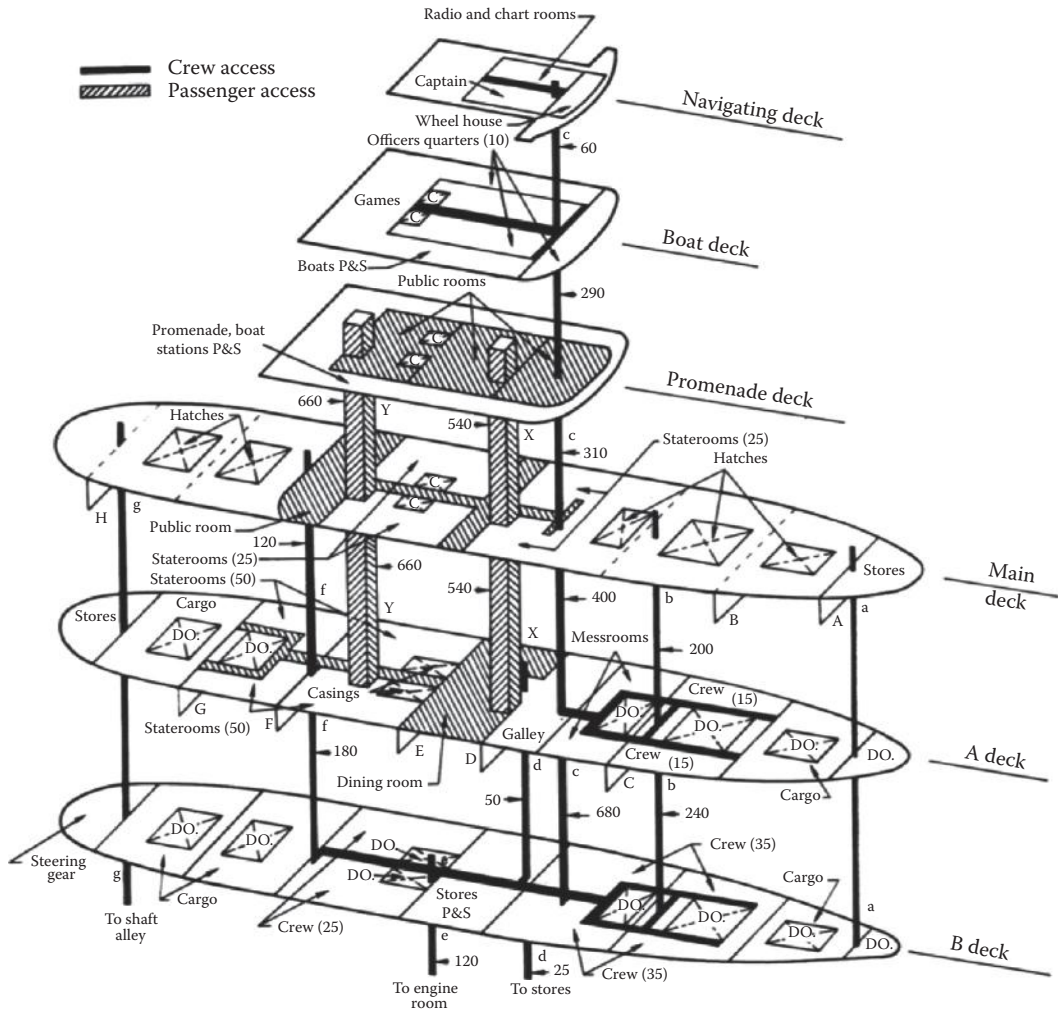
Vikings. Although ships have been in existence for more than 4 millennia, the scientific approach to the design of ships is rather very recent. Even now, the design of ships is rather a combination of art and science due to the requirements of (i) balancing ship safety, performance, and geometry; (ii) matching of size, tonnage, deadweight, endurance, speed, life, resistance, propulsion, maneuverability, and others for optimizing performance; (iii) many thousands of room spaces in passenger and aircraft carriers; (iv) more than 50 different piping and ducting systems; (v) comfort and facilities to enable the crew to function efficiently; (vi) loading and unloading in ports with speed; (vii) economy and construction arrangements; and (viii) aesthetics of ship geometry to serve the functional needs of merchant ships, warships, etc. [28]. As a consequence, ships are designed to meet the conflicting requirements of owners such as merchants who carry cargo and persons from place to place or the requirements of war needing speed, maneuverability, firepower, and formidability.

The size and geometry of a large cargo ship prepared for the use of the owner, shown in Figure 2.25 [29], depends on a number of factors such as amount of cargo (requiring refrigeration or not), fuel, fresh water, stores, passenger/crew accommodation, machinery, and containerization. The beam to transverse length ratio is around 1:7. At full load, the displacement of the ship is equal to 32,000 t. The total deadweight of the ship is given as 22,200.0 t, and the molded draft at full load is given as 10.7 m. The speed of the ship is equal to 20.5 knots, and the maximum rated shaft horsepower of the ship is equal to 24,000.0. Figure 2.26 [30] gives the three-dimensional arrangement of the various components of the ship, categorizing the ship decks into navigating, boat, promenade, main, A, and B decks. Also, the various decks have been classified into crew and passenger access decks.



Length overall . . . . .	184.4 m (605.0 ft.)
Length between perpendiculars . . . . .	177.5 m (582.5 ft.)
Beam, molded . . . . .	25.0 m (82.0 ft.)
Depth to main deck at side, molded . . . . .	14.0 m (46.0 ft.)
Draft, full load (scantling), molded . . . . .	10.7 m (35.0 ft.)
Light ship . . . . .	9,787 t
Passengers, crew effects and stores . . . . .	60 t
Fuel oil . . . . .	3,596 t
Fresh water . . . . .	608 t
Refrigerated cargo . . . . .	218 t
Liquid cargo . . . . .	2,377 t
General cargo . . . . .	15,349 t
Total deadweight . . . . .	22,208 t
Displacement, full load (scantling) draft . . . . .	31,995 t
Cargo volume, bale . . . . .	
Refrigerated volume, net . . . . .	30,645 m <sup>3</sup> (1,082,207 ft. <sup>3</sup> )
Containers in hold . . . . .	618 m <sup>3</sup> (21,839 ft. <sup>3</sup> )
Containers on deck . . . . .	325
Passenger accommodation . . . . .	84
Crew accommodation . . . . .	12
Shaft horsepower, ABS . . . . .	41
Speed, knots . . . . .	24,000
Propeller 4 blades, diam . . . . .	20.8
Propelling machinery, cross compound, double reduction geared turbine . . . . .	6.7 (22.0 ft.)

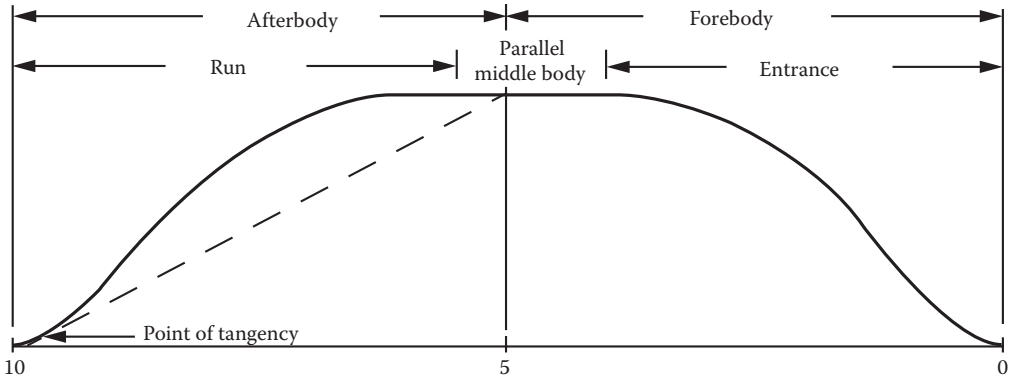
**FIGURE 2.25** Typical general arrangement in a large cargo ship. (From R.E. Taggart, *Ship Design and Construction*, SNAME, New York, pp. 137–138, 1980. With permission.)



**FIGURE 2.26** Details of decks in a general cargo ship. (From R.E. Taggart, *Ship Design and Construction*, SNAME, New York, p. 131, 1980. With permission.)

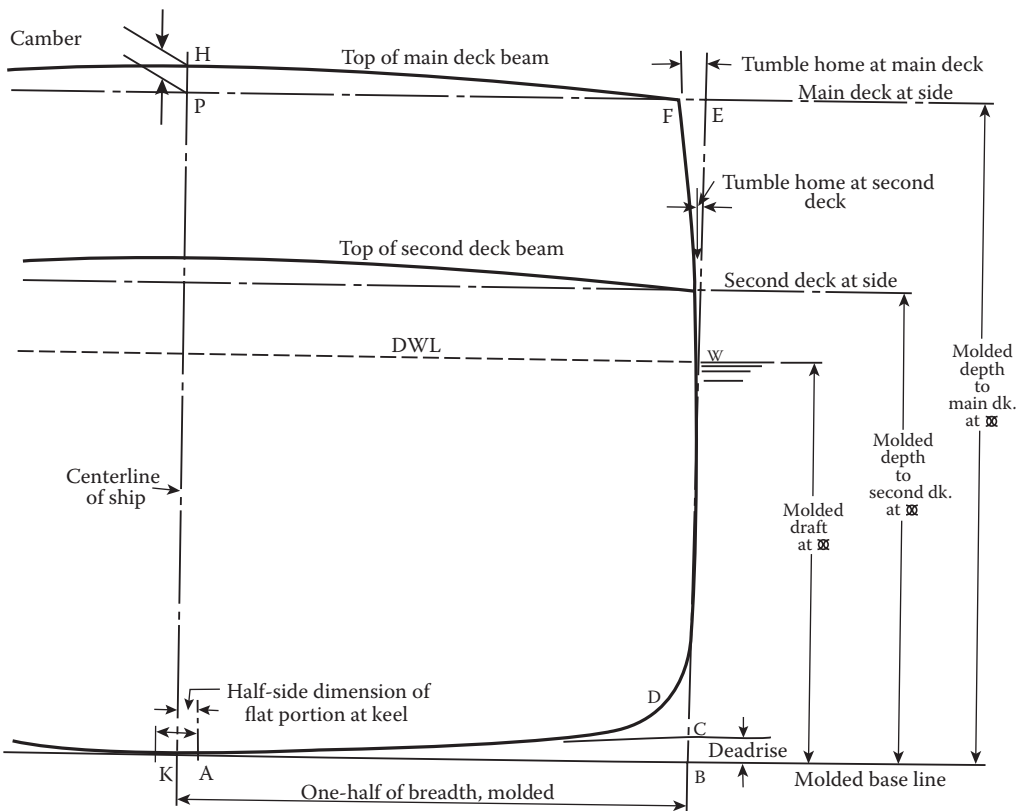
The longitudinal vertical cross-sectional curve of the ship, at midbeam, is shown in Figure 2.27 [31]. It represents the longitudinal distribution of area below the design waterline (DWL); Figure 2.27 also shows the customary division of the underwater portion of the ship structure into forebody and afterbody, forward of and abaft midships, respectively. The area under curve represents the volume of water displaced by the vessel, per unit width, up to the DWL. The figure also shows the entrance and run, which represent the ends of the vessel forward of and abaft the middle body. The molded depth and the cross section of a typical ship form, at its midship section, are given in Figure 2.28 [32]. The distance from K to B is one half the molded beam or molded breadth of the vessel. The distance AC is known as the floor line, and BC, the dead rise, which represents the rise of the bottom (floor). The horizontal distance EF is known as the tumble home. The distance PH is called the camber of beam and is used to drain the rain water and the seawater splashed onto the ship. Standard practice is to provide 2% of the beam as camber in the midship region and to use the same curve for other fore and aft locations of the ship.



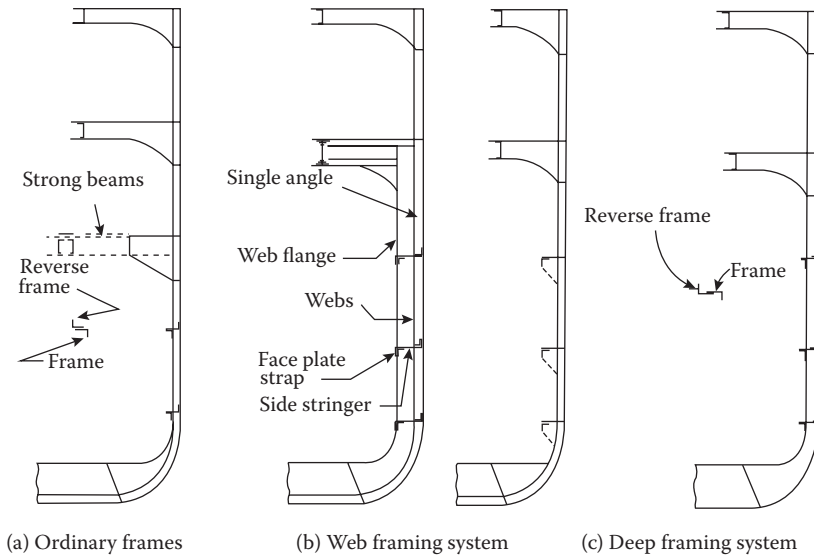


**FIGURE 2.27** Geometry of longitudinal vertical section area curve. (From E.V. Lewis, *Principles of Naval Architecture*, SNAME, New York, p. 4, 1989. With permission.)

A series of closely spaced ribs, known as transverse frames, strengthen the ship along the length of the ship, as shown in Figure 2.29 [33]. These comprise of floors (bottom), webs, web flanges, and beams. The transverse frames stiffen the shell and deck plating of the ship, which contribute to the primary longitudinal strength of the ship. In addition, they also keep the ship the ship-shape and in addition resist the hydrostatic and cargo loadings.



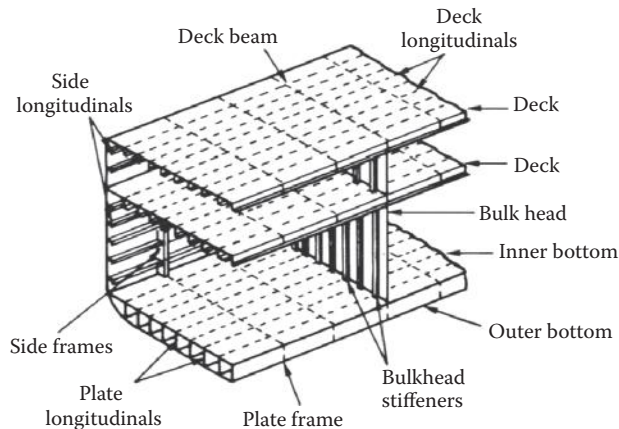
**FIGURE 2.28** Molded form of a mid-ship section in a typical ship structure. (From E.V. Lewis, *Principles of Naval Architecture*, SNAME, New York, p. 5, 1989. With permission.)



**FIGURE 2.29** Different types of ship frames. (From R.E. Taggart, *Ship Design and Construction*, SNAME, New York, p. 212, 1980. With permission.)

Three types of web frames are given in Figure 2.29, namely, (i) ordinary frames; (ii) web frames; and (iii) deep frames. Web frames are continuous with the horizontal girders of the ship. Later, these web frames were replaced by deep frames because the web frames interfered with the cargo stowage. The single bottom floors have been improved by replacing it with the double bottoms to facilitate larger amounts of cargo handling.

An idealized three-dimensional view of a double-bottomed ship is given in Figure 2.30 [34]. Besides the earlier divisions of ship into decks and bulkheads, the web plating is stiffened longitudinally by (deck, side, and floor plate) longitudinal and transversely by bulkheads, side frames, and deck beams. These components supply the ship with local strength and stiffness. An unstiffened ship would require far less welding and save on the fabrication costs but would need impractical thick plates.



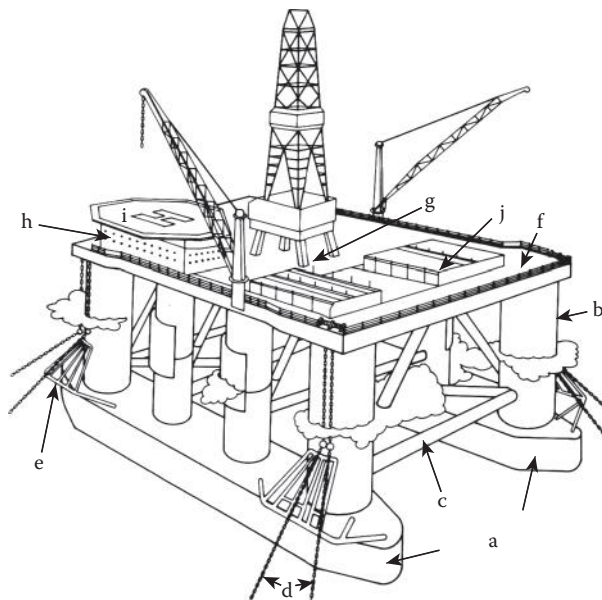
**FIGURE 2.30** Cut-away section of one side of a typical ship structure with double bottom. (From N. Morgan, Marine technology reference book, in: *Ships and Advanced Marine Vehicles*, Butterworths, London, p. 3.43, 1990. With permission.)

### 2.6.1 MODERN TRENDS

Modern ships have become highly complex and specialized, and many are of enormous size since more than 70% of world trade and 95% of the international transport are utilizing ships, to move fuels, raw materials, food, and manufactured goods, across the oceans. Increase in size is needed to improve transportation efficiency. Currently, the designs of massive bulk carriers, 450 m long and carrying a cargo of 600,000 tons, are being pursued. Container ships of 15,000 TEU (20-ft. equivalent unit), with a speed of 25–30 knots, are also being explored. LNG vessels with a capacity of 300,000 m<sup>3</sup> are being assessed for economy in operations. Large passenger ships of 150,000 GT are being constructed for cruising vessels. The largest tanker in operation today is around 300,000 DWT. Due to new environmental regulations resulting from the Exxon Valdez accident in 1989 and Erika in 1999, more than 2000 single-hull oil tankers (with a DWT of more than 175,000) are being phased out and replaced by double-hull vessels [4].

### 2.7 COMPONENTS OF A SEMI-SUBMERSIBLE

The semi-submersible, shown in Figure 2.31 [34], is an offshore drilling platform with two horizontal pontoons, eight vertical columns, and a top deck with a drilling derrick, accommodation quarters, helideck, anchor chains, and mooring cables. The structure floats buoyant and submerged to a predetermined draft (~30.0 m) in the ocean, when the pontoons and columns are ballasted with seawater. The number of pontoons and columns are governed by the size and weight of the work platform and its payload being supported by the platform. Even though the platform undergoes relatively large motions under the prevalent wave action, it remains highly stable, in rough and deep seas, with a large part of its structure under water. The structure is held in location by eight chain-link spread-mooring arrangement with huge mooring anchors, each weighing more than 10 t metric tons. In deeper waters, they can be held in position by dynamic positioning using thrusters,



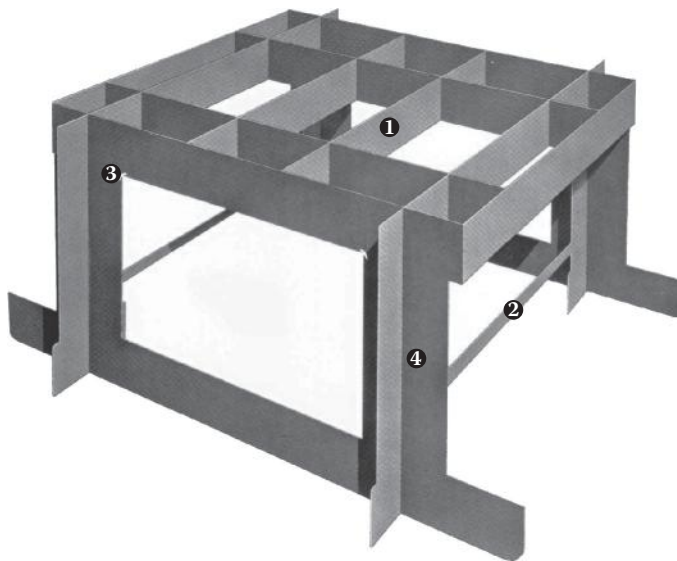
**FIGURE 2.31** Components of a semi-submersible structure: (a) submerged pontoon; (b) surface piercing columns; (c) bracing members; (d) mooring line; (e) anchor rack; (f) deck; (g) moonpool; (h) accommodation; (i) helicopter pad; and (j) drill pipe. (From N. Morgan, Marine technology reference book, in: *Ships and Advanced Marine Vehicles*, Butterworths, London, 1990.)

controlled by an onboard computer. Since the platform has to operate for months, away from shore, over 100 people would be on board to carry out the drilling and production operations. Currently available semi-submersibles have the capacity to drill in water depths of 180 to 10,600 m [35, 36].

The platform uses catenary-shaped risers to connect the subsea BOP (blowout preventer) stack to the floating semi-submersible platform, so that the drill mud can be taken to the surface. The risers are either flexible or rigid and extend from the seafloor to the work platform, with the heavy well-head equipment installed on the seafloor. The catenary shape of the riser is to absorb the large heave and horizontal motions of the conventional semi-submersible platform. Due to their large motions, conventional semi-submersible platforms cannot support high-pressure, top-tensioned risers.

The horizontal pontoon (or hull) and the column of the semi-submersible platform are divided into several closed compartments having a buoyancy, that can be suitably changed for the purpose of flotation and trim. It contains a pumping system for pumping ballast water into and out of the compartments. The compartments are typically stiffened by horizontal and/or vertical bulkheads in the pontoons and columns. Normally, the compartments of the horizontal pontoon and the lower compartments of the columns are filled with water ballast when the platform is in its operational configuration, and the upper compartments of the columns provide buoyancy for the platform. The deck and the topsides are installed on the hull at the dry dock of the shipyard, over the columns, and then transported to the offshore site, using a heavy lift vessel.

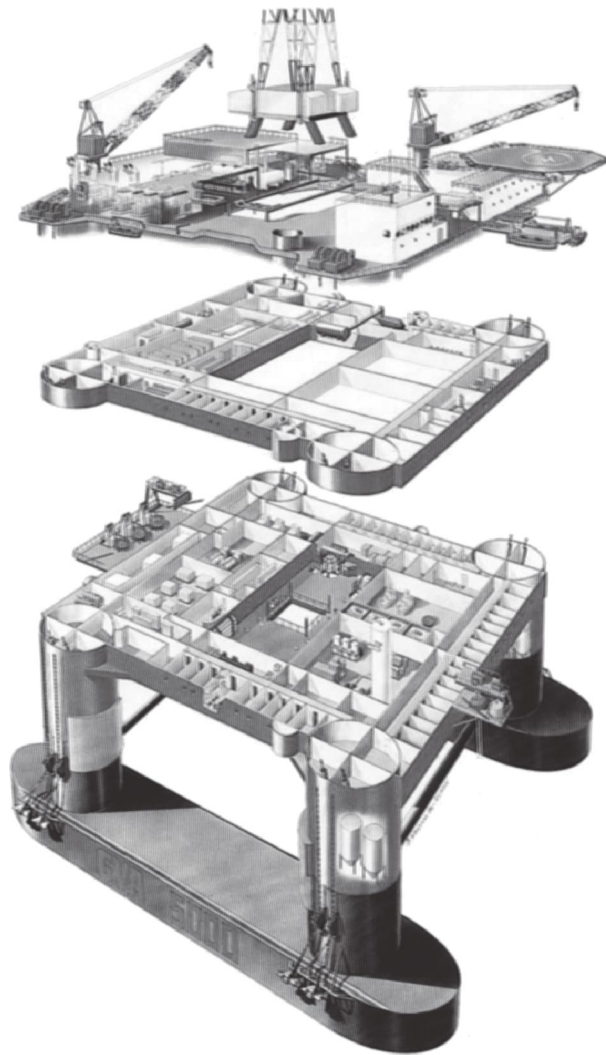
Various types of semi-submersible platforms are envisaged for fulfilling different functions in the oil and gas industry. Some platforms are required for exploratory drilling to identify hydrocarbons during reconnaissance and location surveys. The main functional requirements of such platforms are payload capacity and area for drilling equipment with limited motions and good mobility. Other types of semi-submersible platforms are needed for producing hydrocarbons. Production platforms carry chemical plants, which consist of separators, pumps, etc. Mobility is normally not needed for production platforms when the production period corresponds to the platform service life. The layout and size of production platforms vary, depending upon water depth, production rate, etc. Floating production semi-submersible platforms and their variants include TLP, floating production, storage, and offloading (FPSO) types of structures, and the commonly used semi-submersibles.



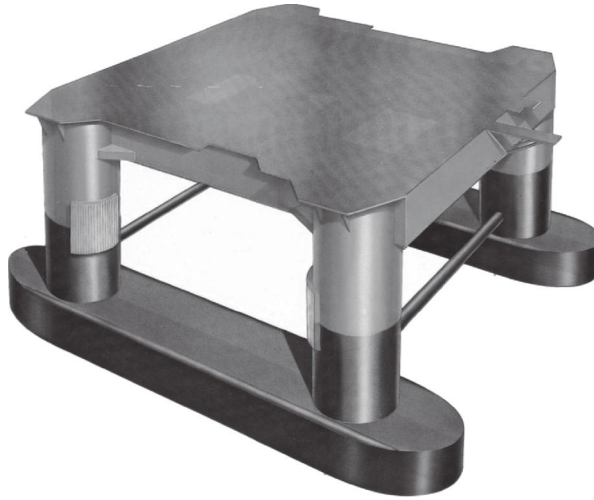
**FIGURE 2.32** The skeleton of a production semi-submersible: (1) rigid box structure of the continuous bulkhead; (2) bracing; (3) stress-reducing joint; (4) column bulkheads. (From Technical Brochure of Gotaverken Arendal, Sweden, *Balmoral*, GVA 5000 Floating Production Unit, p. 3, 1988. With permission.)

The components of a typical twin pontoon and four-column semi-submersible can be considered to be made up of (i) the skeleton of the structure, which provides the backbone to the semi-submersible (Figure 2.32 [37]); (ii) the main deck, columns, and the horizontal pontoons (Figure 2.33 [37] and 2.34 [38]); (iii) the processing and diving units of the semi-submersible (Figure 2.35 [38]); (iv) the drilling units (Figure 2.36 [38]); and (v) the final assembled form of the semi-submersible (Figure 2.37 [38]).

Since the semi-submersible unit experiences large wave and wind forces in its offshore location, it needs to be properly designed so that it will be able to withstand the forces exerted on it. This is provided by the stiff and rigid box structure of the continuous bulkhead shown in Figure 2.32. The bracing that connects the two forward columns of the two pontoons keeps the semi-submersible from splitting apart as it rides the heaving and rolling sea. The stress-relieving joint, provided on top of the columns, minimizes the fatigue damage inflicted on the column by the incessantly rolling seas. The column bulkheads keep the columnar shape of vertical columns. Figure 2.33 shows the top, intermediate, and bottom decks of the semi-submersible, and illustrates clearly how the



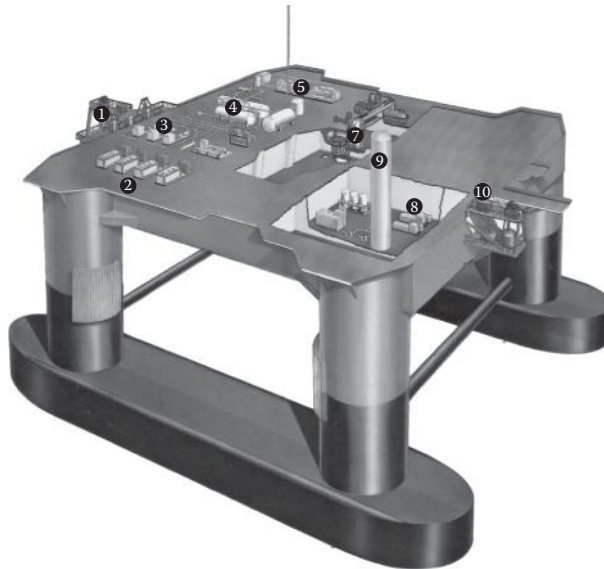
**FIGURE 2.33** Component decks of a (GVA 5000) semi-submersible unit. (From Technical Brochure of Gotaverken Arendal, Sweden, *Balmoral*, GVA 5000 Floating Production Unit, p. 3, 1988. With permission.)



**FIGURE 2.34** The production semi-submersible platform: main deck and steel shell. (From Technical Brochure of Gotaverken Arendal, Sweden, *GVA Are Leaders on Floaters*, 22 pp., 1986. With permission.)

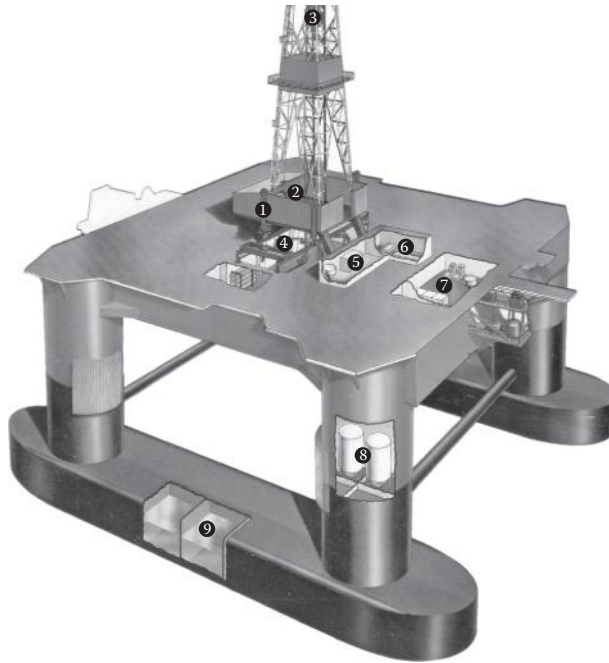
pontoons, columns, and the deck are suitably wrapped around the central skeleton, providing the backbone of the semi-submersible with steel plates. Figure 2.34 shows the fully covered pontoons, columns, and deck of the semi-submersible.

The processing and diving units of the semi-submersible, shown in Figure 2.35, consist of: (i) risers for oil and gas; (ii) gas turbines for power generation; (iii) crude oil export pumps; (iv) separators; (v) gas treatment and compression area; (vi) flare; (vii) saturation diving system; (viii) water injection room; (ix) de-aerator; and (x) risers for water injection. The risers are pipes that carry hydrocarbons from the subsea reservoirs to the platforms and can rightly be called the umbilical

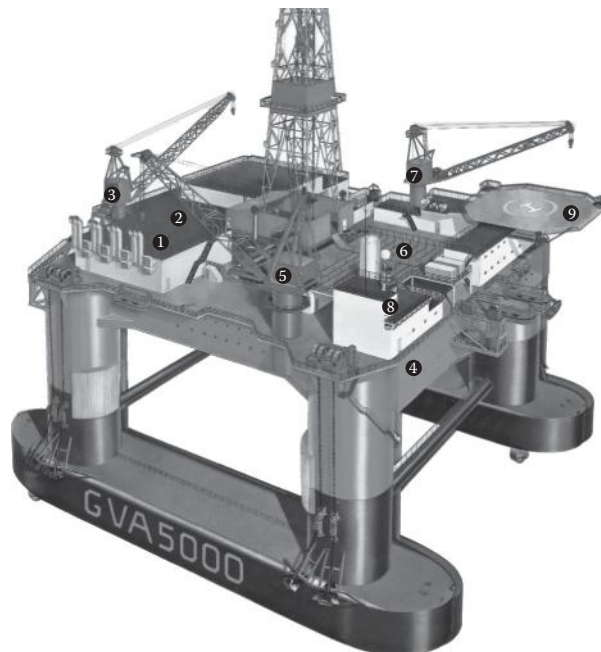


**FIGURE 2.35** Processing and diving units in the semi-submersible: (1) risers for oil and gas; (2) gas turbines for power generation; (3) crude oil export pumps; (4) separators; (5) gas treatment and compression plants; (6) flare (omitted due to size limitation); (7) saturation diving system; (8); water injection room; (9) de-aerator; and (10) risers for water injection. (From Technical Brochure of Gotaverken Arendal, Sweden, *GVA Are Leaders on Floaters*, 22 pp., 1986. With permission.)





**FIGURE 2.36** Drilling units of the production semi-submersible: (1) four riser tensioners; (2) drill floor; (3) heave compensators; (4) BOP and LMR package handling area; (5) cement unit room; (6) shale shaker room; (7) mud pump room; (8) bulk tanks; (9) drill water tanks. (From Technical Brochure of Gotaverken Arendal, Sweden, *GVA Are Leaders on Floaters*, 22 pp., 1986. With permission.)



**FIGURE 2.37** The exterior of the production semi-submersible: (1) gas turbine house; (2) process plant; (3) 10-ton crane; (4) accommodation module; (5) 75-ton crane; (6) pipe rack deck; (7) 25-ton crane; (8) communication tower; (9) helideck. (From Technical Brochure of Gotaverken Arendal, Sweden, *GVA Are Leaders on Floaters*, 22 pp., 1986. With permission.)

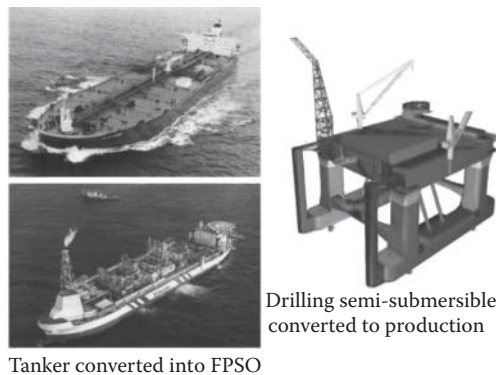
cords of the platforms. The risers for oil and gas mud transport the drilled mud to the gas treatment and compression plants; finally, it is processed into oil and gas in the chemical process plant, located on top of the platform. Water injection is made to the subsea-bottom reservoir to keep the reservoir pressure the same and to prevent the collapse of the seafloor.

Figure 2.36 shows the platform components associated with the task of drilling of oil and gas in the production semi-submersible. The drilling components consist of (i) four riser tensioners; (ii) drill floor; (iii) heave compensators; (iv) BOP and LMR package handling area; (v) cement unit room; (vi) shale shaker room; (vii) mud pump room; (viii) bulk tanks; and (ix) drill water tanks. Additional components assembled on the top of the production semi-submersible are shown in Figure 2.37. They are (i) gas turbine house; (ii) process plant; (iii) 10-ton crane; (iv) accommodation module; (v) 75-ton crane; (vi) pipe rack deck; (vii) 25-ton crane; (viii) communication tower; and (ix) helideck.

In some offshore oil and gas fields, conversion of existing structures is a good alternative to constructing new structures. Usually, tankers are converted into floating production, storage, and offloading (FPSO) units, but drilling rigs, such as exploratory semi-submersibles, are modified to production semi-submersible units. Figure 2.38 shows the mode of increasing the buoyancy for a semi-submersible by adding extra parts, indicated by red, to increase its payload capacity when it is converted to a production platform. Simultaneously the platform also has to be strengthened to carry more the increased payload and to resist the larger wave loads.

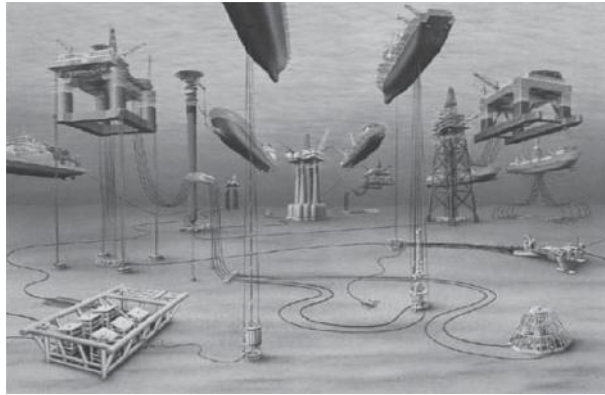
Even though platform topsides provide a dry environment for the production facilities, various kinds of underwater structures and equipment are required for the proper functioning of an offshore platform. When the water depth is large, it is considered to be an advantage to place the production equipment on the seafloor. Moreover, the subsea equipment needs to be remotely operated, various kinds of disciplines, such as marine technology, mechanical engineering, and computer science have to be combined to deal with such systems. Some of the offshore platforms and the associated subsea structures and equipment associated with them are shown in Figure 2.39.

Design of different types of production platforms for the offshore environment is a challenging and an exciting task. Generally, in connection with any new field development in the oceans, the oil company has to compare a number of scenarios and alternate production platforms on the basis of minimizing costs, improving flexibility with respect to future extended use and the associated risk (see Figure 2.40). The actual choice of field development technology would depend upon a number of factors such as production rate and volume, distance to shore, environmental conditions etc. Moreover, field developments in deeper water introduce new aspects in the choice between production plants on the platforms or on the seafloor.

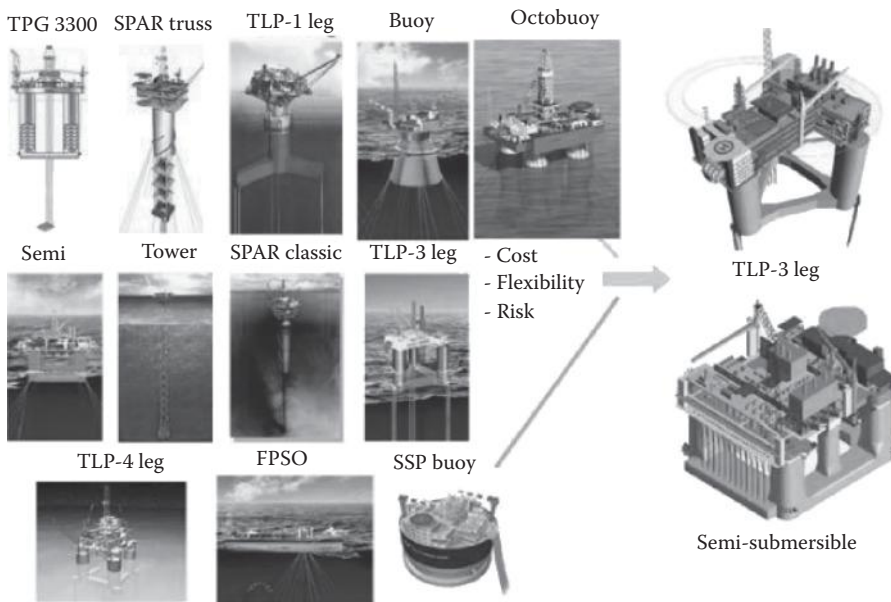


**FIGURE 2.38** Conversion of platforms from drilling to production units. (From T. Moan, *Offshore structures* (Chapter 7), in: *Modeling Complex Engineering Systems*, edited by R.E. Melchers and R. Hough, ASCE Press, Reston, VA, pp. 173 and 175, 2007. With permission.)





**FIGURE 2.39** Sub-sea structures and equipment associated with offshore structures. (From T. Moan, Offshore structures (Chapter 7), in: *Modeling Complex Engineering Systems*, edited by R.E. Melchers and R. Hough, ASCE Press, Reston, VA, pp. 173 and 175, 2007. With permission.)



**FIGURE 2.40** Sub-sea structures and equipment associated with offshore structures. (From T. Moan, Offshore structures (Chapter 7), in: *Modeling Complex Engineering Systems*, edited by R.E. Melchers and R. Hough, ASCE Press, Reston, VA, pp. 173 and 175, 2007. With permission.)

**EXERCISE PROBLEMS**

1. Produce a figure of a fixed jacket platform structure and name all the components of the structure. Describe the functions of the various components of the platform.
2. Describe, with neat sketches, the various framing plans used for a jacket structure, and explain how they are brought together to form an integral jacket structure.
3. A steel jacket is to be designed for a water depth of (i) 100.0 m and (ii) 500.0 m. Will you follow the same plan of designing and fabricating the jacket structure for both the water

- depth conditions or something different? If not, outline the difference in the design and fabrication procedures. Also, state the reasons for the change.
4. Assuming that the jacket structure is to be fabricated from tubular steel structural members, explain, with sketches, how the members are connected together to form a complete jacket structure.
  5. (a) Describe the various components that form the superstructure of a fixed jacket structure, using a neat figure (or sketches). Describe in detail how the assembled components on the cellar deck and the top deck of the jacket platform structure are configured. (b) Briefly describe the modular construction in a fixed jacket platform, using a building block representation.
  6. A jacket platform is to be installed at an offshore site (150.0 m water depth) where the top layer of the soil is silty and clayey, up to a depth of 100.0 m, with a layer of hard and stiff soil below it. Illustrate with neat figures or sketches how the jacket structures will be fixed to the seabed.
  7. Explain the functional difference between a fixed jacket platform and a jack-up steel platform. Give a neat sketch of a jack-up steel structure, describing the function of its various components for (i) jack-up platform with spud cans and (ii) a jack-up platform with mat-type foundation.
  8. A mat-type jack-up platform structure is to be used for offshore exploration in Bombay High, where the soil is very soft, with a surface bearing strength of 50.0 kPa. The mat-type platform has to resist a maximum vertical load of 10,000.0 kips; in addition, it has to resist an overturning moment of 2000.0 kip ft. State how you would design the mat so that no tension is developed in the soil.
  9. Differentiate between the deck structural components of a fixed jacket production structure and an exploratory jack-up type structure with mat-type foundation; use neat sketches.
  10. Describe, in detail, the functions of various structural components of a gravity platform structure giving the roles played by each.
  11. Give a cross-sectional view of a storage tank and the column of a condeep-type gravity platform, and name the salient structural components.
  12. Briefly describe, with neat sketches, the structural configuration of a gravity platform deck.
  13. Give simplified transverse and longitudinal cross-sectional views of a light typical ship. Describe the major structural and auxiliary components of a typical ship.
  14. Describe the load-resistant skeletal structure of a semi-submersible platform, giving neat sketches. Also give the outer structure of this skeleton that actually bears the load coming on the semi-submersible and safely transmits it to the underlying skeletal structure.
  15. Explain, with a neat sketch, the oil and gas processing and other auxiliary facilities provided on the cellar deck of a semi-submersible.
  16. With a neat sketch describe the drilling facilities provided on the deck of a semi-submersible (and in the other parts of the semi-submersible).
  17. The production semi-submersible houses a number of modular structures on the deck. Describe with neat sketches, the deck modules required in the production platform.
  18. With a suitable figure, describe the salient features of a spar oil and gas production system, giving an overview of the various components that contribute to its location-maintenance and the resistance to applied forces in the ocean.
  19. Give neat sketches of the internal components of (i) the main columnar portion of the classic spar and (ii) the submerged portion of the truss spar.
  20. With suitable figures (or neat sketches) describe the important components of a subsea production system.

## REFERENCES

1. P.J. Cook and C. Carleton, 2000. *Continental Shelf Limits: The Scientific and Legal Interface*, Oxford University Press Inc.
2. PennWell Corporation, 2007. *Oil & Gas Journal*, Volume 105.48. Available at <http://www.eia.doe.gov/emeu/international/reserves.html> (Accessed on November 27, 2008).
3. G.A. Lock, 1981. Technological factors in offshore hydrocarbon production, in: *The Future of Offshore Petroleum*, produced by United Nations' Department of Technical Cooperation for Development, McGraw-Hill, Inc., New York, CCCN 81-83943, ISBN 07-606783-1, p. 95.
4. T. Moan, 2007. Offshore structures (Chapter 7), in: *Modeling Complex Engineering Systems*, edited by R.E. Melchers and R. Hough, ASCE Press, Reston, VA, pp. 173 and 175.
5. P. Le Tirant, 1979. *Seabed Reconnaissance and Offshore Soil Mechanics*, Editions Technip 27, Paris, France, p. 400.
6. P. Le Tirant, 1979. *Seabed Reconnaissance and Offshore Soil Mechanics*, Editions Technip 27, Paris, France, p. 347.
7. M.G. Salvadori and R. Heller, 1975. Structural requirements, in: *Structure in Architecture: The Buildings of Buildings*, Prentice Hall, Inc., Englewood Cliffs, NJ, pp. 57–78.
8. A.J. McDonald, 2001. *Structure and Architecture*, Architectural Press, London, p. 20.
9. Technical Brochure of McDermott Inc., 1981. *The Story of Oil and Gas*, p. 21.
10. S.L. Landes, 1986. Operational loadings, in: *Planning and Design of Fixed Offshore Platforms* edited by B. McClelland and M.D. Reifel, Van Nostrand Reinhold Company, New York, pp. 27–45.
11. J.G. Timar, 1978. *Lectures on Offshore Engineering*, Institute of Building Technology and Structural Engineering, Aalborg University Centre, Aalborg, Denmark.
12. W.J. Graff, 1981. *Introduction to Offshore Structures*, Gulf Publishing Company, Houston, p. 111.
13. J.W. Bunce, 1984. The integrity of platform superstructures—Background to new API RP2A recommendations, in: *Platform Superstructures—Design and Construction*, edited by L.F. Boswell, Granada, London, UK, p. 69.
14. ESDEP (The European Steel Design Education Program), 1993. Lecture Series. *Offshore Structures*, Lecture 15A.1. Available at <http://www.esdep.org/members/master/wg15a/10100.htm> (Accessed on December 2, 2008).
15. W.J. Graff, 1981. *Introduction to Offshore Structures: Design Fabrication and Installation*, Gulf Publishing Company, Houston, TX, p. 219.
16. W.J. Graff, 1981. *Introduction to Offshore Structures*, Gulf Publishing Company, Houston, TX, p. 49.
17. W.J. Graff, 1983. *Introduction to Offshore Structures*, Gulf Publishing Company, Houston, TX, p. 56.
18. P. Le Tirant, 1979. *Seabed Reconnaissance and Offshore Soil Mechanics*, Editions Technip 27, Paris, France, p. 401.
19. P. Le Tirant, 1979. *Seabed Reconnaissance and Offshore Soil Mechanics*, Editions Technip 27, Paris, France, p. 437.
20. Bethlehem Steel Corporation, 1975. Jack-up designs for drilling, production and storage, *Technical Brochure*, p. 5.
21. Bethlehem Steel Corporation, 1975. Jack-up designs for drilling, production and storage, *Technical Brochure*, pp. 4 and 5.
22. T. Holland, O.T. Gudmestad and E. Jersin, 2000. *Design of Offshore Concrete Structures*, Spon Press, London, p. 18.
23. T.O. Olsen, 2002. Recycling of Offshore Concrete Structures: State-of-the-Art Report, International Federation of Structural Concrete (fib), Federal Institute of Technology, Lausanne-EPFL, Departement Genie Civil, ISSN 1562-3610, p. 1–2. Table was modified and made up-to-date.
24. G. Clauss, E. Lehmann and C. Ostergaard, 1992. *Offshore Structures: Conceptual Design and Hydromechanics*, Volume I, Springer Verlag, Berlin, Germany, p. 66.
25. P. Le Tirant, 1979. *Seabed Reconnaissance and Offshore Soil Mechanics*, Editions Technip 27, Paris, France, p. 437.
26. Technical Brochure of Statoil, Aker and Norwegian Contractors, 1986. *Gullfaks A Gravity Platform*, pp. 3–4.
27. G. Clauss, E. Lehmann and C. Ostergaard, 1992. *Offshore Structures: Conceptual Design and Hydromechanics*, Volume I, Springer Verlag, Berlin, Germany, p. 67.
28. K.J. Rawson and E.C. Tupper, 1983. *Basic Ship Theory: Volume I*, Longman Group Ltd., London, pp. 2–3.
29. R.E. Taggart, 1980. *Ship Design and Construction*, SNAME, New York, pp. 137–138.

30. R.E. Taggart, 1980. *Ship Design and Construction*, SNAME, New York, p. 131.
31. E.V. Lewis, 1989. *Principles of Naval Architecture*, SNAME, New York, p. 4.
32. E.V. Lewis, 1989. *Principles of Naval Architecture*, SNAME, New York, p. 5.
33. R.E. Taggart, 1980. *Ship Design and Construction*, SNAME, New York, p. 212.
34. N. Morgan, 1990. Marine technology reference book, in: *Ships and Advanced Marine Vehicles*, Butterworths, London, p. 3.43.
35. Wikipedia, The Free Encyclopedia, 2008. *Semi-Submersible Platform*. Available at [http://en.wikipedia.org/wiki/semi-submersible\\_platform](http://en.wikipedia.org/wiki/semi-submersible_platform).
36. N. Morgan, 1990. Marine technology reference book, in: *Offshore Structures* edited by M. Patel, Butterworths, London, p. 2.5.
37. Technical Brochure of Gotaverken Arendal, Sweden, 1988. *Balmoral*, GVA 5000 Floating Production Unit, p. 3.
38. Technical Brochure of Gotaverken Arendal, Sweden, 1986. *GVA Are Leaders on Floaters*, 22 pp.

---

# 3 Ocean Environment

## *Wind, Wave, Current, Tides, Ice, and Seismic Effects*

### 3.1 INTRODUCTION

In order to understand the nature and the characteristics of the ocean environment, one must start from the heat budget of the incoming solar energy and examine how it is balanced by the changes it effects on the earth and its environs and by the amount it gets reflected and re-radiated back into the space from where the energy was received in the beginning. In order to prevent the progressive heating or cooling of the earth, the earth must lose the same amount of heat energy it receives from the outer space; on an average, it must re-radiate back into space as much heat as it receives. The changes of the ocean environment are caused primarily by 47.5 parts of the energy absorbed by the solid and fluid parts of earth. The environmental changes caused by the local heat budget vary with respect to time and space, showing daily/seasonal and spatial variations; more heat is gained than lost at the equatorial regions, and more heat is lost than gained at the higher-latitude regions [1].

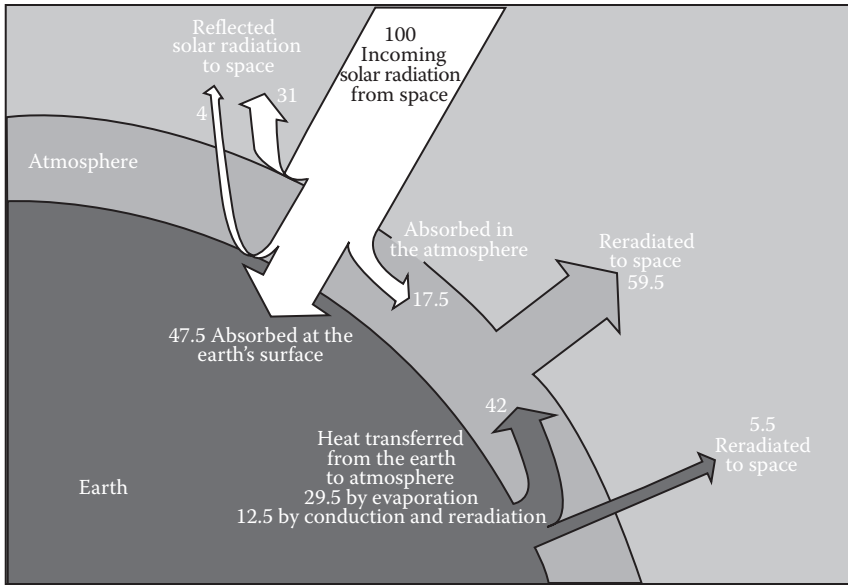
### 3.2 DESCRIPTION OF THE OCEAN ENVIRONMENT

The earth is surrounded by two fluid envelopes, viz., the atmosphere and the oceans, which are essential to the integrity of the whole earth. The ocean contains 97.2% of the water of the earth, while the rest is contained in freshwater [constituting frozen ice and glaciers (2.1%); rivers, lakes, and groundwater (0.7%); atmospheric water vapor (0.001%); and living organisms (0.00004%)]. The atmosphere and the oceans are in constant motion, and the motions are generated by earth's rotation, earth's gravity, and the density changes that occur in both of them due to the impinging radiated solar energy absorbed by each of them (Figure 3.1 [1]).

The changes that occur in earth due to the impinging radiated solar heat energy, through the hydrological changes, are pictorially illustrated in Figure 3.2 [2]. Within the hydrological cycle, the total amount of water removed from the oceans and the amount of water returned to it remain about the same; otherwise, the oceans' volumes would fluctuate considerably and consequently mean sea levels (MSLs) would change. However, climatic changes and changing of MSLs do occur over thousands of years [2].

#### 3.2.1 WINDS

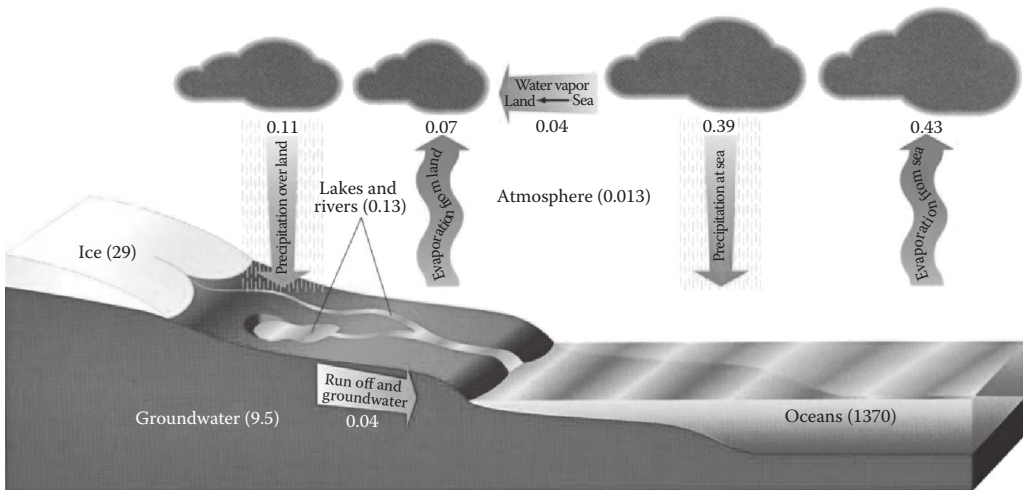
The winds are responsible for the generation of the major surface currents and waves of the world's oceans. Consequently, one needs to know about the generation of winds and its motion in the atmosphere that forms an envelope around the earth. The atmosphere, which surrounds the earth as a thin multilayered envelope, extends to about 700.0 km above the earth's surface. The two layers of interest in the atmosphere, for wind generation and motion, are the troposphere, which exists near the earth's surface (to a height of 10.0 to 16.0 km), and the stratosphere, which is above it extending



**FIGURE 3.1** Heat budget of the earth. (From A.C. Duxbury and A.B. Duxbury, *Introduction to the World's Oceans*, Wm. C. Brown Publishers, Dubuque, IA, p. 163, 1991. With permission.)

up to 50.0 km. In the troposphere, the major up and down (as well as horizontal) motion of the warmed (by the solar heat) air takes place, while in the stratosphere, a horizontal (or parallel to the surface of earth) motion of air occurs, with fast moving air streams. Moreover, the top layer of stratosphere is abundant with ozone, which traps much of the potentially harmful ultraviolet solar radiations from reaching the earth.

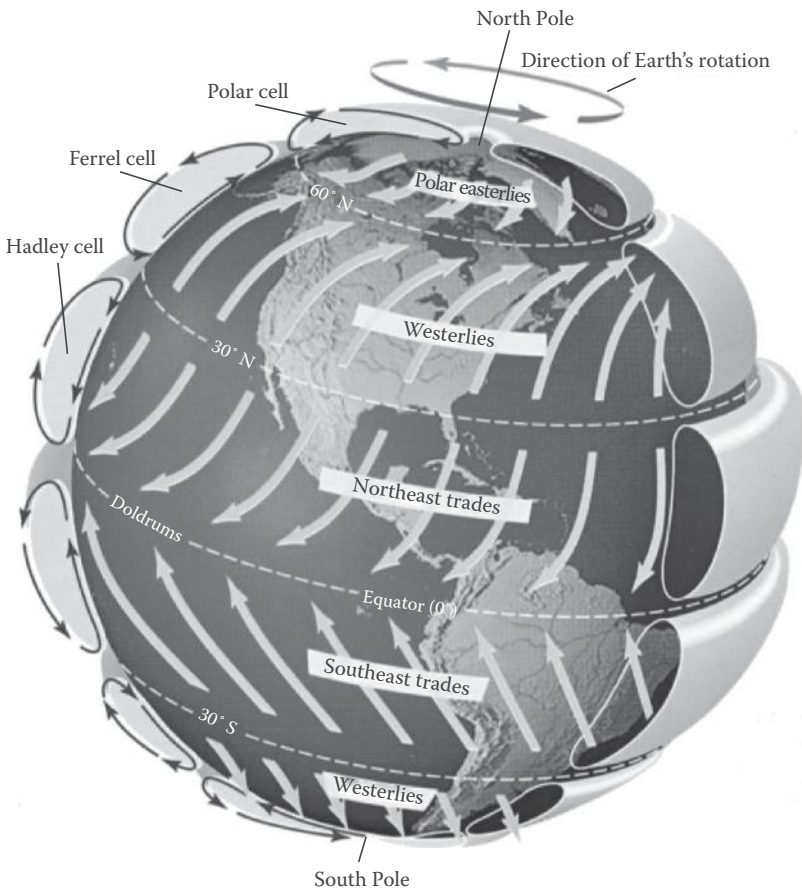
The unequal heating of the earth's surface by the sun generates the circulation of the air (wind) in the atmosphere (in the troposphere and stratosphere). Higher intensity solar radiation is received at the equator and the Tropics (during the summer), whereas the poles receive lower amounts of



**FIGURE 3.2** The hydrological cycle (numbers in million units). (From T. Day, *Oceans*, Facts on File Inc., Hong Kong, p. 28, 1999. With permission.)



solar radiation; this solar radiation received in various parts of the earth also varies according to the seasons. The tropical air gets heated up, becomes less dense, and rises up creating a low-pressure zone beneath. Cooler and denser air, from the higher latitudes, move horizontally toward the tropics to replace the warm air that has risen up. The rising warm air travels up the troposphere into the stratosphere and starts moving horizontally toward the poles with higher speeds; as it moves toward the poles, it cools, becomes dense, and sinks down gradually. This region is shown by the Hadley cell in Figure 3.3. When equatorial heating takes place due to normal incidence of solar rays, this sinking of air takes place at 30° north and south latitudes, generating a high-pressure region in the region of descent. Even though there is a continual transfer of heat energy between the tropics and the poles, the wind does not move in a direct north–south direction; this deviation occurs due to the rotation of the earth in its own axis. The wind is deflected by the earth’s rotation. At the equator, the speed of rotation of the earth is around 1600.0 kmph, but this decreases to zero at the poles. As indicated in Figure 3.3 [3], the earth rotates counterclockwise when observed from the North Pole. Considering a northward-moving wind, earth’s rotation deflects the wind eastward (generating a westerly wind), and a southward-moving wind will get deflected to west (generating an easterly wind), in the northern hemisphere. This can be conceived in a different manner; winds in the Northern Hemisphere always get deflected to the right of their movement. In the Southern



**FIGURE 3.3** Global wind system with dominant equatorial Hadley cell. (From T. Day, *Oceans*, Facts on File Inc., Hong Kong, p. 63, 1999. With permission.)



Hemisphere, the wind gets deflected to the left of its movement. This deflection of wind (or air stream) due to the rotation of the earth is called the Coriolis effect, which is clearly illustrated in Figure 3.3.

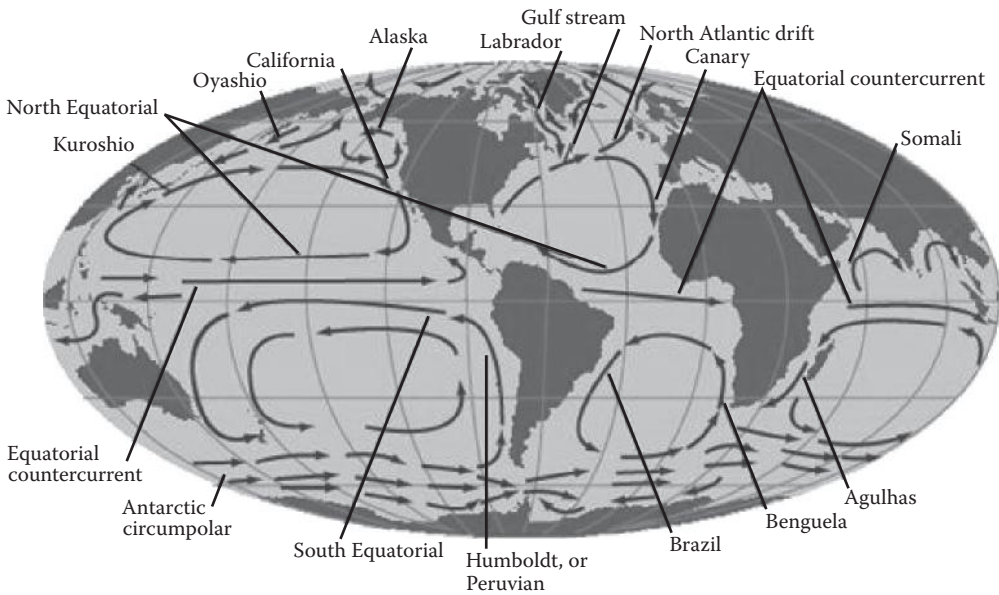
Moreover, not all the air that descends down at  $30^\circ$  north travels toward the equator; part of the descending air also travels northward toward the north pole until it meets the cold polar air around  $60^\circ$  north. Thereafter, the warmer poleward-moving air rises up to the stratosphere at  $60^\circ$  north and becomes colder and denser; part of this air travels toward  $30^\circ$  north, to the Tropics; this second type of circulation is called the Ferrel cell, as shown in Figure 3.3. This rising air also generates a low-pressure region around its region of ascent. A portion of the ascending air also travels toward the North Pole, setting up another smaller cell, called polar cell (similar to a Hadley cell—see Figure 3.3), and descends at the pole; thereafter, the cold (north) polar wind travels southward toward the equator. Once again, the Coriolis effect deflects the southward-moving polar wind toward the right of its direction of motion, forming the characteristic polar easterlies. A similar action occurs when the wind moves from the equator towards the South Pole, in the southern hemisphere. The above explanation does not consider the effects of seasonal changes (due to the tilting of the earth's axis) or the relative differences in the rate of heating between the land and the oceans; if these were also considered, then Figure 3.3 will be modified further.

It is not only the wind system that is affected by the rotation of the earth; the major ocean water currents also are affected in a similar manner. In the case of winds, the rotational motion takes place in an upward–downward plane, whereas in the case of currents, the Coriolis effect sets up clockwise currents in the Northern Hemisphere (called gyres) and anti-clockwise currents in the Southern Hemisphere, in the horizontal (or parallel-to-the-surface of earth) plane; at the same time, there is also a vertical mixing of current in the ocean due to the thermal and saline variations in the body of the oceans.

### 3.2.2 CURRENTS

As a consequence of the winds blowing across the ocean surface, pressure and (dynamic) friction forces are generated on the ocean water; these forces disturb the equilibrium of the ocean water surface and generate surface currents and waves. These forces transfer kinetic and potential energies from the air to the water, over large ocean surface areas for varying lengths of time, forming currents and waves. Considering the current alone, the surface layer of the ocean is pushed and dragged along the prevailing wind direction by the blowing wind. The wind is deflected to its right by the Coriolis effect in the Northern Hemisphere; consequently, the ocean currents also get influenced by this effect. Furthermore, the ocean currents are also constrained and modified by the land masses and continental shelves. In the open ocean, there are more than 40 ocean currents, and some of these major surface currents are shown in Figure 3.4 [4]. The combined effects of wind on the surface of ocean and its deflection to right (in the Northern Hemisphere) due to Coriolis effect generate the characteristic gyral pattern observed in the wind-driven currents of the ocean.

From Figure 3.4, it can be seen that the major Pacific Ocean currents are the clockwise North Pacific (and also Equatorial) and Kuroshio currents forming a clockwise gyre; in the southern hemisphere of the Pacific Ocean, a similar but counterclockwise gyral motion is set up by the South Australian, Peru, and South Equatorial currents. In the northern Atlantic Ocean, the Gulf Stream, North Atlantic, Canary, and North Equatorial currents form a clockwise gyre, while the Brazil, South Equatorial, and Benguela currents form a counterclockwise gyre in the southern Atlantic Ocean. In the Indian Ocean, the South Equatorial, West Australian, Agulhas, and Subtropical Convergence currents form a counterclockwise gyre. The West Wind Drift or the Antarctic circumpolar current forms the major current system of the Antarctic Ocean, and the Labrador Current forms the major current in the Arctic Ocean. Along the equatorial regions of the world's oceans, the Equatorial Counter current forms the transition between the North and South Equatorial current



**FIGURE 3.4** World’s major surface ocean currents. (From Capital Region District, Environmental Services, Victoria, Vancouver, 2008. [www.crd.bc.ca/watersheds/protection/geology-processes/globaloceancurrents.htm](http://www.crd.bc.ca/watersheds/protection/geology-processes/globaloceancurrents.htm).)

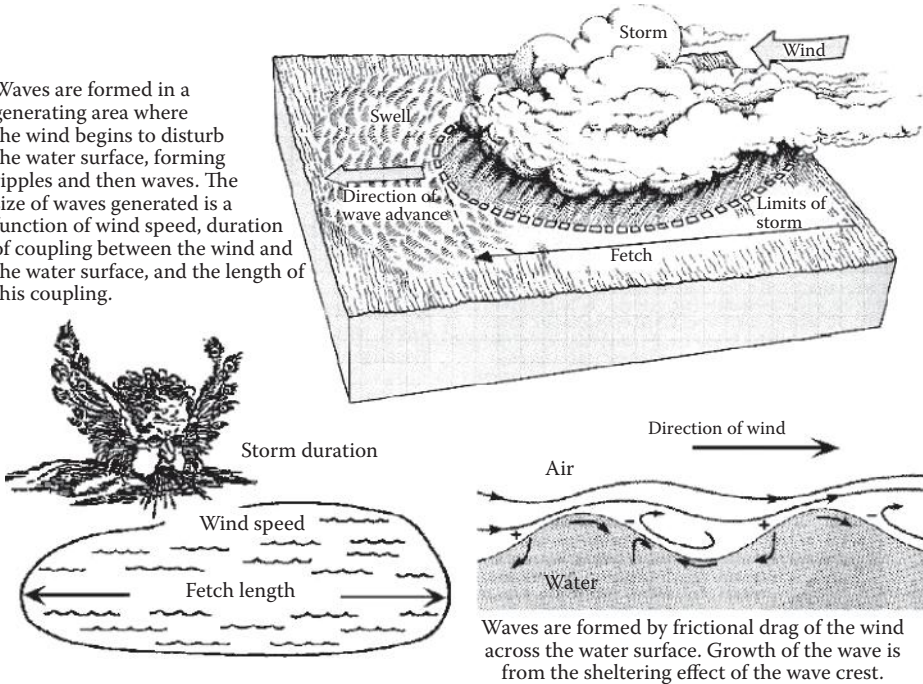
systems. Gulf Stream current is one of the largest and fastest current systems of the world, carrying nearly 90 million m<sup>3</sup> of water (per second) past Chesapeake Bay (US); it travels northward with a current speed varying between 0.5 and 2.0 m/s.

### 3.2.3 WAVES

In addition to the ocean currents, the winds are also responsible for the generation of waves in the ocean. When wind blows, energy is transferred to the ocean water over large areas and at different energy intensities. Waves form in the ocean, first as capillary waves (or ripples or cat’s paws) and thereafter grow to small amplitude irregular waves, and finally to regular ocean wave swells; the wave surface becomes increasingly rough as it increases in length and amplitude. Due to the increased frictional drag generated by the rough surface, the wind imparts additional energy to ocean surface. The added energy increases the amplitude and period of the wave. Consequently, it must be realized that the wave is the result of a generating force such as wind and the restoring force that may be the surface tension and gravity. Since ocean waves are the consequence of energy transfer between winds and waves, it must be borne in mind that its propagation from place to place is also due to the energy transfer from one location to another. It is different from the current motion where the transfer of mass from one point to another point takes place. Waves possess potential and kinetic energies; kinetic energy of the wave is due to the orbital motion of wave particles, and potential energy is due to the displacement of the wave particle above or below the sea surface.

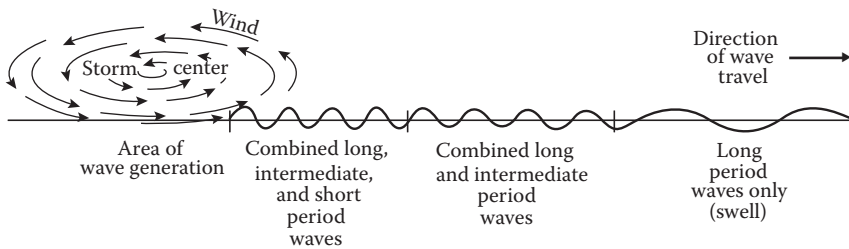
A pictorial illustration of wave formation in wind is given in Figure 3.5 [5]. The resultant wave heights,  $H_i$ , and the wave period,  $T_i$ , are related to factors that influence the energy transfer between wind and the ocean, such as the extent of the region over which the wind blows (fetch  $F_i$ ), the average wind velocity  $U_i$ , and the duration  $t_i$ , during which the wind blows over the ocean surface. When

Waves are formed in a generating area where the wind begins to disturb the water surface, forming ripples and then waves. The size of waves generated is a function of wind speed, duration of coupling between the wind and the water surface, and the length of this coupling.



Waves are formed by frictional drag of the wind across the water surface. Growth of the wave is from the sheltering effect of the wave crest.

**FIGURE 3.5** Pictorial illustration of energy transfer between the blowing wind and the ocean resultant surface. (From Geology Department, College of Arts and Sciences, University of Puerto Rico, Mayaguez Campus, Puerto Rico, <http://geology.uprm.edu/Morelock/waves.htm>. With permission.)



**FIGURE 3.6** Wave generation and propagation. (From A.C. Duxbury and A.B. Duxbury, *An Introduction to the World's Oceans*, Wm. C. Brown Publishers, Dubuque, IA, p. 219, 1991. With permission.)

the formed irregular waves move away from the generating region (with long, intermediate, and short period waves), the waves settle down to become regular monochromatic waves, called swells, as shown in Figure 3.6 [6]. The wave formation has been described by mariners in a simplified manner, using the Beaufort scale, as shown in Table 3.1 [7]; the Beaufort scale relates the wind velocity to the state of the ocean and indirectly to the wave heights (or amplitudes).

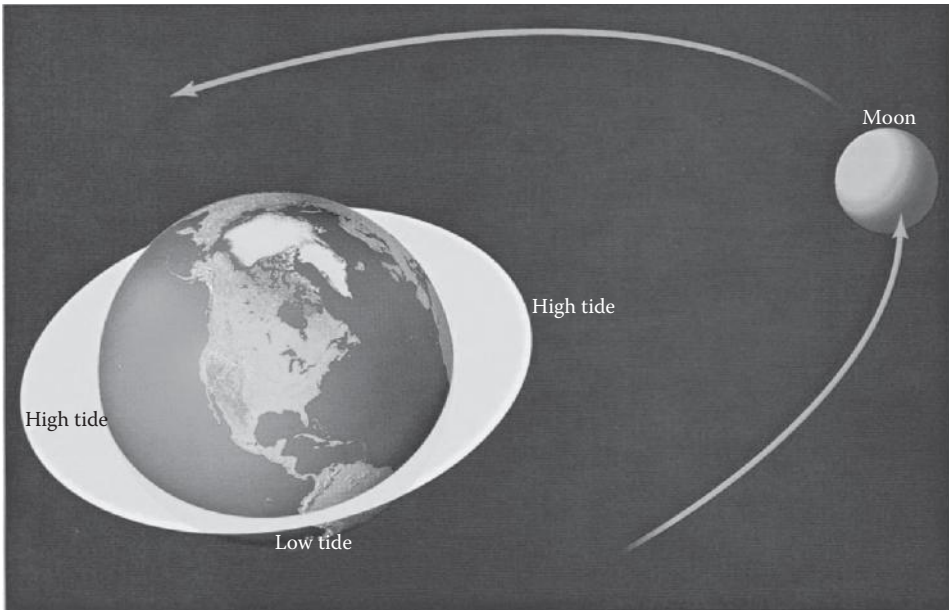
### 3.2.4 TIDES

In addition to the generation of waves, another mega-scale disturbance occurs, on the oceans, due to the gravitational attraction caused by the presence of large massive bodies, within the gravitational influence of the earth; this is called the tidal motion of the oceans. The major influences on the

**TABLE 3.1**  
**Beaufort Wind Scales and Resultant Sea Description**

Sea		Wind			Beaufort Scale	State of the Surface for Fully Developed Sea, Wave Heights
Description	Force	Mariners' Description	Velocity (m/s)	Knots		
Smooth	0	Calm	0–0.2	<1	0	Mirrorlike, glassy
Rippled	1	Light air	0.3–1.5	1–3	1	Small ripples; no foam crests
Gentle	2	Light breeze	1.6–3.3	4–6	2	Small wavelets, crests show glassy appearance and do not break (0–0.3 m)
Gentle	2	Gentle breeze	3.4–5.4	7–10	3	Crest begin to break; foam has glassy appearance; occasional whitecaps (0.3–0.61 m)
Light	3	Moderate breeze	5.5–7.9	11–16	4	Waves small, becoming longer; fairly frequent whitecaps
Moderate	4	Fresh breeze	8.0–10.7	17–21	5	Moderate waves, taking more pronounced long form; mainly whitecaps some spray (61–1.21 m)
Heavy	5	Strong breeze	10.8–13.8	22–27	6	Large waves begin to form; crests break forming large areas of white foam; some spray (1.21–2.44 m)
Very heavy	6	Near gale	13.9–17.1	28–33	7	Sea heaps up, white foam from breaking waves begins to be blown in streaks along the direction of the wind (2.44–4 m)
–	–	Gale	17.2–20.7	34–40	8	Moderately high waves with crests of considerable length; edges of crests break into spindrift; foam is blown in well-marked streaks in wind direction (4–6 m)
High	7	Strong gale	20.8–24.4	41–47	9	High waves; dense streaks of foam in direction of wind; crests of waves begin to roll; spray may reduce visibility
Very high	8	Storm whole gale	24.5–28.4	48–55	10	Very high waves with long overhanging crests; foam causes sea surface to appear and shocklike; visibility reduced (6–9.2 m)
Exceptionally high sea	9	Violent storm	28.5–32.6	56–63	11	Exceptionally high wave; edges of wave crests are blown into froth; spray reduces visibility (9.2–13.7 m)
Exceptionally high sea	9	Hurricane	32.7–36.9	>64	12	Air filled with foam and spray; sea completely white; visibility seriously reduced (over 13.7 m)

*Source:* Courtesy of U.S. Coast Guard. D.E. Ingmanson and W.J. Wallace, *The Waves*, Wadsworth Publications Inc., CA, p. 189, 1989. With permission.



**FIGURE 3.7** Generation of tides due to the motion of moon around the earth in 29.5 days and the earth's rotation around its own axis in 24 h. (From T. Day, *Oceans*, Facts on File, Inc., p. 70, 1999. With permission.)

earth's oceans are caused by the presence of moon and sun, around the vicinity of earth. The moon, being much closer to the earth than the sun, exerts a larger gravitational force on the surface of the earth; this pulls the ocean surface waters (as well as the solid earth) toward the moon so that waters near the moon's surface (as well as on the opposite side of the earth) form a bulge in that region, as shown in Figure 3.7 [8]; this results in a tidal period of 12 h.

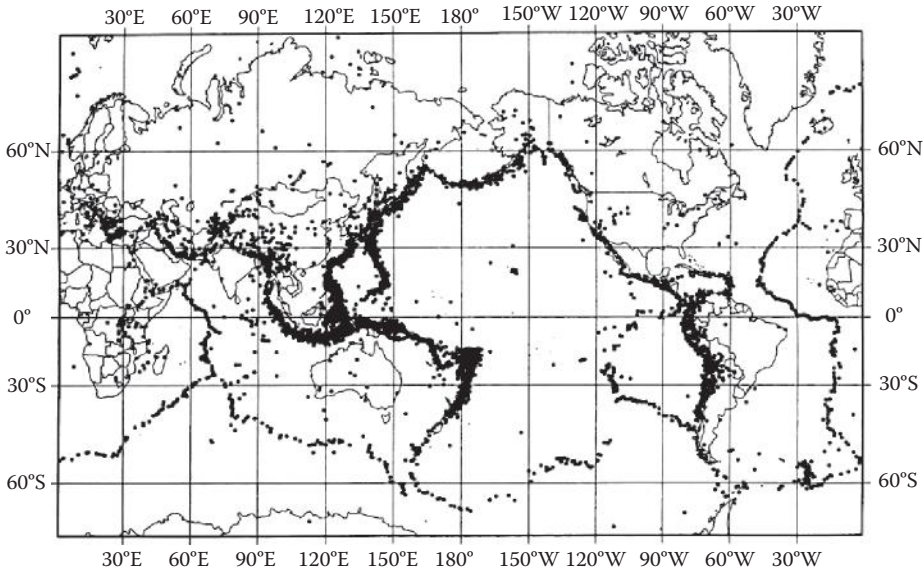
Two types of tide occur in the earth due to the gravitational pull of the moon on earth: one that occurs when the location under consideration is at its nearest distance to the moon (high tide) and one that is at its farthest distance from the moon (low tide). This tidal motion is complicated further by the gravitational attraction exerted on earth by the sun. When the gravitational attractions of the sun and moon are in alignment, the gravitational influence of the moon on earth is enhanced by that of the sun, and this produces the largest tide in earth, called the spring tide. About 1 week later, when the sun and moon are oriented at  $90^\circ$  to one another, their gravitational attractions have opposing effects on the tidal bulge produced on earth resulting in a lower tide, called neap tide.

### 3.2.5 EARTHQUAKES

One of the most frightening and destructive phenomena of nature is a severe earthquake and its terrible aftereffects, which can occur anywhere in earth, either onshore or offshore. An earthquake is a sudden movement of the earth, caused by an abrupt release of strains that have accumulated over a long time, in between the huge plates that form the earth's surface, as these plates slowly move over, under, and past each other. Sometimes this movement is gradual, and at other times, the plates are locked together, unable to release the accumulating energy. When the accumulated energy in between these locked plates grows strong enough, the plates break free; this breaking free of the plates causes the earthquakes.

Figure 3.8 [9] shows the distribution of earthquakes, of Richter magnitudes greater than 5.0, that have occurred over a period of 25 years (from 1963 to 1988), at depths 70.0 km below the solid

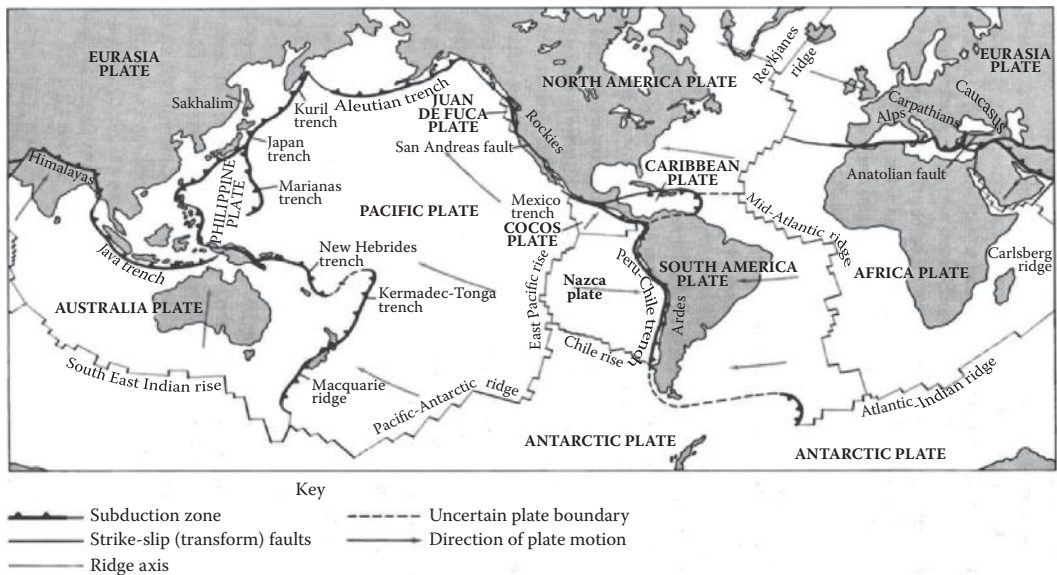




**FIGURE 3.8** Map of global seismicity, of intensity greater than Richter 5.0, occurring at depths of less than 70 km below the earth’s surface. (From B.A. Bolt, *Earthquakes*, W.H. Freeman and Co., New York, p. 35, 2004. With permission.)

surface of the earth. Figure 3.9 [10] shows the locations of major tectonic plates, mid-oceanic ridges, trenches, and transform faults in the world map. When a comparison is made between Figures 3.8 and 3.9, it can be seen that the earthquakes occur along the regions where these tectonic plates join or butt against one another.

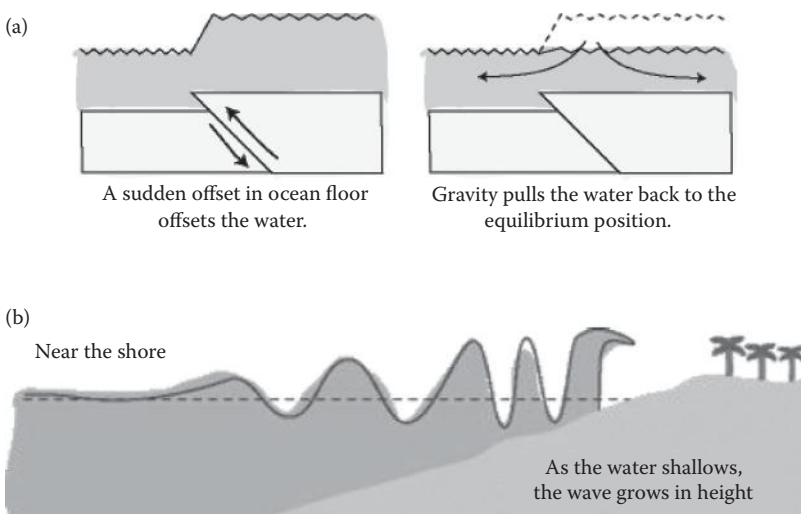
Three types of plate boundaries are observed from Figure 3.9, viz., spreading zones, transform faults, and subduction zones. At the spreading zones, the molten rock rises, pushing the two



**FIGURE 3.9** Major tectonic plates, mid-oceanic ridges, trenches, and transform faults. (From B.A. Bolt, *Earthquakes*, W.H. Freeman and Co., New York, p. 149, 2004. With permission.)

plates apart and adding new material at their edges. Most spreading zones are found in oceans, for example, the North American and Eurasian plates that are spreading apart along the mid-Atlantic ridge. Spreading zones usually have earthquakes at shallow depths (within 30 km of the surface). Transform faults are found where plates slide past one another. An example of a transform-fault plate boundary is the San Andreas Fault, along the coast of California and northwestern Mexico. Earthquakes at transform faults tend to occur at shallow depths and form fairly straight linear patterns. Subduction zones are found where one plate overrides, or subducts another, pushing it downward into the mantle where it melts. An example of a subduction-zone plate boundary is found along the northwest coast of the United States, Western Canada, and Southern Alaska and the Aleutian Islands. Subduction zones are characterized by deep-ocean trenches, shallow to deep earthquakes, and mountain ranges containing active volcanoes.

Earthquakes beneath the ocean floor sometimes generate very large sea waves or tsunamis. These waves travel across the ocean at speeds as great as 960 kmph (597 mph) and may be 15 m (49 ft.) high or higher by the time they reach the shore [11]. The 2004 Indian Ocean earthquake was one of the largest undersea earthquakes that occurred on December 26, 2004, with an epicenter off the west coast of Sumatra, Indonesia. The earthquake was caused by the subduction of the tectonic plates joining at Java Trench, which triggered a series of devastating tsunamis along the coasts of most landmasses bordering the Indian Ocean, killing more than 225,000 people in eleven countries and inundating coastal communities with waves of height 30 m (100 ft.). It was one of the deadliest natural disasters in history with a seismic magnitude of between 9.1 and 9.3. It proved to be the second largest earthquake ever recorded on a seismograph. This earthquake had the longest duration of faulting ever observed, between 8.3 and 10 min; a sudden offset of the seabed changed the elevation of the ocean differentially and initiated a water wave that travelled outward from the region of sea-floor disruption, as shown in Figure 3.10 [12]. In deepwater, the tsunami waves are not large and do not pose any danger. They have very large wavelengths of hundreds of kilometers and surface wave heights are much smaller, being around 1 m. As the tsunami waves approach the shore, where the water depth is much smaller, wave speed decreases, the wave height increases dramatically, and then the wave surges onto the land [12].



**FIGURE 3.10** Effect of subsea earthquake: (a) sudden offset and (b) waves amplify near shore. (From C.J. Ammon. Available at [http://eqseis.geosc.psu.edu/~cammon/HTML/Classes/IntroQuakes/Notes/earthquake\\_effects.html](http://eqseis.geosc.psu.edu/~cammon/HTML/Classes/IntroQuakes/Notes/earthquake_effects.html), 2001.)



### 3.2.6 SEA ICE AND OTHER FORMS OF ICE IN THE OCEAN

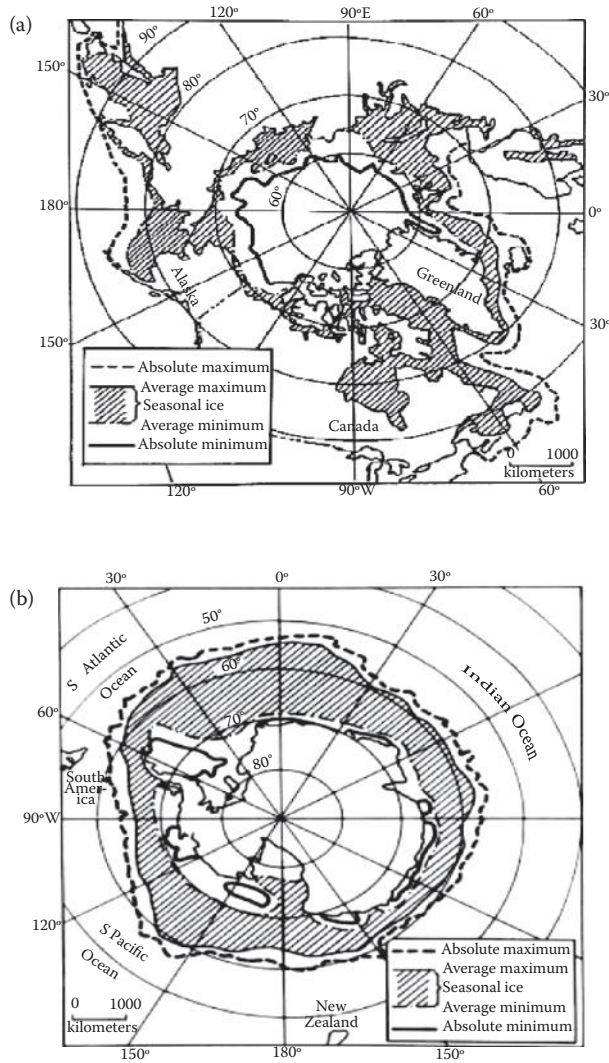
Sea ice is the frozen ocean water that is generated in the ocean as it cools during the winter months. As freshwater cools, it contracts until the maximum density is reached at 4°C. Also due to the presence of salinity in seawater, the temperatures of maximum density and freezing are lowered; it is observed that the temperature of maximum density and the freezing temperature coincide at -1.3°C when the salinity of seawater is 24.7 parts per thousand. Further cooling of seawater results in expansion and formation of ice. At a salinity of 35 parts per thousand, which is the approximate average salinity for the oceans, the freezing point is -1.88°C. The vertical salinity distribution in the polar region is such that the surface waters are underlain at shallow depth by waters of higher salinity, and consequently, only the water at top freezes while the underlying water remains unfrozen. During the winter season, ice thickness and ice coverage of the ocean increase progressively; around 15% of the world's oceans are covered by sea ice during this part of the year. As the spring season approaches, sea ice (first-year ice) decays (or melts) in the ocean; but some sea ice remains all year in certain northern/southern ocean regions (forming multiyear ice). Figure 3.11a and b [13] shows the extent of Arctic and Antarctic ice in the Polar Regions.

When sea ice (of thickness up to 10.0 cm) forms on ocean surface, it develops initially as small individual, needle-like crystals of ice, called frazil ice (or spicules), suspended in the top few centimeters of seawater, and giving the sea surface an oily appearance. Thereafter, frazil ice coagulates to form a greasy layer on the surface, giving the sea a matte appearance; on further freezing, and depending upon wind exposure, sea states, and salinity, the greasy ice develops into an elastic crust called nilas (up to 10 cm in thickness).

As ice ages, it becomes hard and brittle; and forces generated by the frictional drag of currents, waves, tides, and winds and by the temperature variations in ice act on sea ice and deform it. When the newly formed ice is plastic, it deforms readily and conforms virtually to any shape required by the forces acting on it; as it becomes older, thicker, and more brittle and gets exposed to the influence of wind and wave action, it generally separates into circular pieces (called pancake ice) of diameters up to 3.0 m and of thickness up to 10.0 cm, with raised edges. When larger pieces of relatively flat sea ice, of size less than 20 m across, are formed, they are called ice cakes; depending on wind or wave action, these individual ice cakes and pancake ice either freeze together to form a continuous sheet or unite into pieces of ice 20 m or more across. These larger pieces are called ice floes, which may further freeze and join together to form ice-covered areas of ocean, greater than 10 km across; these are called ice fields. Sea ice has been observed to grow to a thickness of almost 3 m during its first year [13, 14].

Greater thicknesses in both first and multiyear ice have been attained through the deformation of the ice floes and ice fields due to the action of winds, currents, waves, and temperature variations; these processes transform the relatively flat sheets of ice into pressure ice fields, which have rough surfaces, as shown in Figure 3.12a [14]. Bending and rafting of ice take place as one sheet of ice overrides another; when this pile-up action occurs in a haphazard manner over a long line forming a wall or line of broken ice (called a ridge), the resulting profile is called as an ice pressure ridge. When the pressure ice forms a topography consisting of numerous mounds or hillocks, then it is called as hummocked ice, each mound being a hummock.

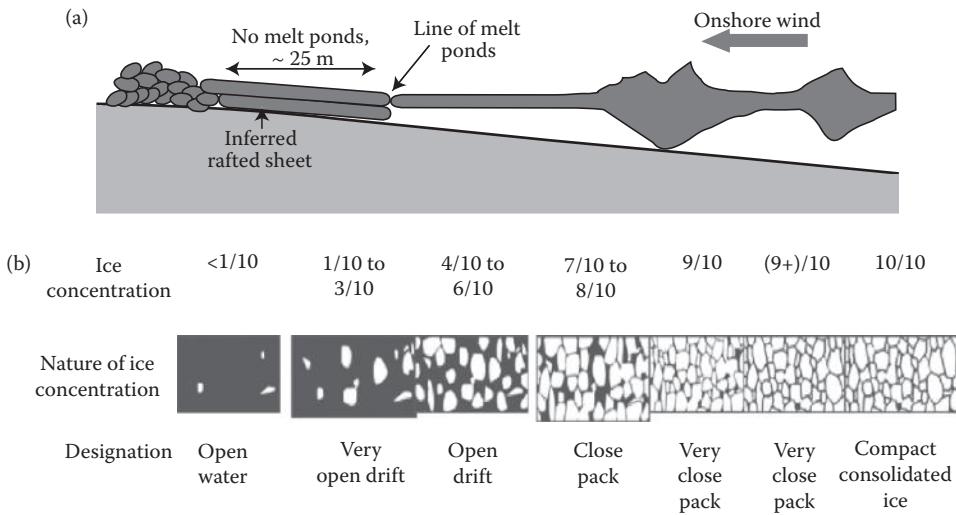
In the Arctic region, the near-shore regions are characterized by the seasonal occurrence of shore-fast ice, which sometimes reaches a height of 2.0 m or more during winter. Until this ice begins to break during the late spring, it remains stationary being attached to the shore. The seaward extent of this shore-fast ice is called the pack ice. This pack ice is not usually attached to the shore and is in continual motion; during winter, the near-shore ice keeps the pack ice offshore, roughly along water depths of 18.0 m. The transition from fast ice to pack ice often occurs between water depths of 12.0 to 30.0 m, consists of a variety of irregular and grounded ice features, and varies in width from a few hundreds of meters to tens of kilometers. The mobile pack ice also contains multiyear ice that has been in existence for more than 2 years besides the first-year ice. Sometimes



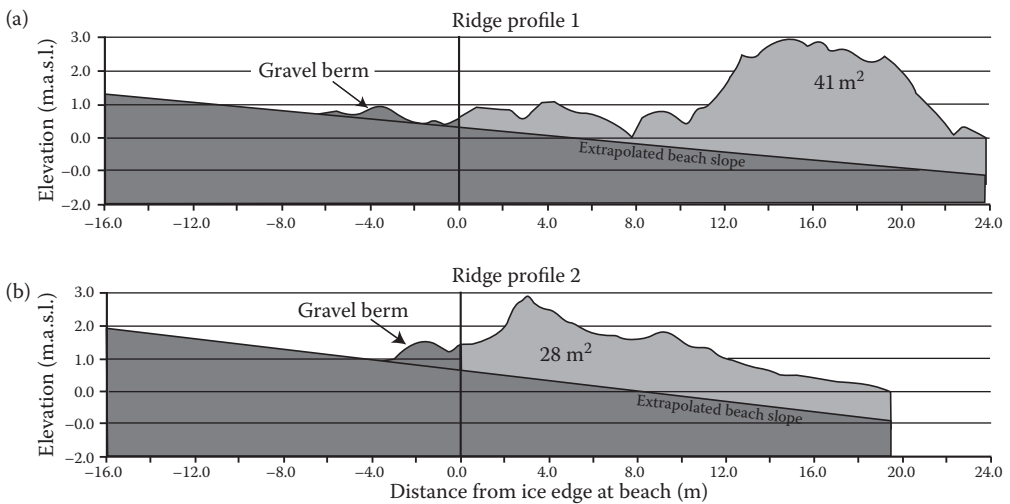
**FIGURE 3.11** Average maximum and minimum extent of (a) Arctic and (b) Antarctic coverage of sea ice. (From N. Bowditch, 1995, *Ice in the Sea* (Chapter 34), National Imaging and Mapping Agency, available at <http://www.irbs.com/bowditch/pdf/chapt34.pdf>.)

the pack ice has velocities similar to the local ocean current and may move more than 0.3 kmph; in sheltered areas, the pack ice may move more slowly with speeds of 30.0 or more meters/hour. Pack ice is classified according to ice concentration observed in the moving ice pack; it expresses the mean aerial density of ice floes (or ice mass) for a given pack ice area. It is classified as open water, open pack, close pack, and very close pack, as shown in Figure 3.12b [15].

Ice shoves or push-ups of land-fast ice against the coastal area occur throughout the ice cover, as shown in Figure 3.13 [14]. The onshore motion of the land-fast ice during a shove event produces two modes of deformation, termed as “ride-up” and “pile-up.” During the ride-up process, ice advances up the beach, sometimes several hundred meters over land. The pile-up involves the building of a ridge of broken blocks of ice at the beach with little encroachment onto land. Ice shoves occur in land-fast ice when an onshore force is applied such that the land-fast ice moves and deforms. Force is required to overcome the gravitational forces associated with the weight or buoyancy of the ice



**FIGURE 3.12** (a) Schematic of ridge building and rafting in a shore-fast ice. (From H. Mahoney et al., *Journal of Glaciology*, 50, 169, pp. 195–207, 2004. With permission.) (b) Pack ice coverage. (From Environment Canada, ~2002. Fact Sheet on Icebergs, Environment Canada, Ice Service, 2009. <http://ice-glaces.ec.gc.ca/App/WsvPageDsp.cfm>.)



**FIGURE 3.13** Ice shoves in coasts showing (a) rubble pile-up and (b) stacked rafts. (From H. Mahoney et al., *Journal of Glaciology*, 50, 169, pp. 195–207, 2004. With permission.)

when moving it up a beach or building a ridge. Additional forces are required to overcome dissipative forces, which include friction at sliding interfaces and those involved in bending, buckling, and breaking the ice.

### 3.2.6.1 Icebergs

In contrast to the above ice forms, icebergs, glaciers, and ice shelves originate on land. Glaciers are considered land ice, and icebergs are chunks of ice that break off of glaciers and fall into the

ocean. Ice of land origin is formed on land by the freezing of freshwater or the compacting of layers upon layers of snow. Under great pressure due to the overlying snow layers, ice becomes slightly plastic and is forced downward along an inclined surface. When a large area is relatively flat, as in the Antarctic plateau, or if the outward flow of snow is obstructed, as in Greenland, an ice cap forms and remains on the land throughout the year. The thickness of these ice caps ranges from nearly 1 km in Greenland to as much as 4.5 km in the Antarctic. Wherever ravines or mountain passes permit flow of the moving ice, a glacier is formed; this mass of snow and ice continuously flows to lower levels until it reaches a comparatively level area, where it spreads out. If a glacier flows into the sea, the buoyant force of the water breaks off pieces from time to time, and these float away as icebergs. Figure 3.14 [15] shows an iceberg, which was calved from the glaciers of Western Greenland, and is embedded in sea ice.

Icebergs extend to a considerable distance below the ocean surface and have relatively small “sail areas” compared to their subsurface mass; soon after a berg is calved, while remaining in the far northern waters, 60–80% of its bulk is submerged. Therefore, the near-surface current is thought to be primarily responsible for drift; however, observations have shown that wind also can be a dominant force that governs iceberg drift at a particular location or time. Generally, it can be stated that currents tend to have a greater effect on deep-draft icebergs, while winds tend to have a greater effect on shallow-draft icebergs.

The empirical height-to-draft ratios obtained for various types of icebergs are shown in Table 3.2 [13]. The drift of iceberg will be to the right in the Northern Hemisphere, while it will be to the left in the Southern Hemisphere. A number of factors such as wind-generated current, Coriolis force, uniform or varying wind speed, and the gradient current will influence the motion of icebergs. When a strong current and wind speeds are in the same direction, the drift of iceberg occurs to the right of both the wind and the current; when wind and a strong current are in opposite directions, drift occurs to the left of the current. The drift speed and the drift angles, as a ratio of wind speed, for various sizes of icebergs, are given in Table 3.3 [13].



**FIGURE 3.14** Iceberg embedded in sea ice. (From Environment Canada, ~2002. Fact Sheet on Icebergs, <http://ice-glaces.ec.gc.ca>. Environment Canada, Ice Service, 2009. <http://ice-glaces.ec.gc.ca/App/WsvPageDsp.cfm>.)

**TABLE 3.2**  
**Height-to-Draft Ratios for Various Types of Icebergs**

Iceberg Type	Height/Draft Ratio
Blocky or tabular	1:5
Rounded or domed	1:4
Picturesque or Greenland (sloping)	1:3
Pinnacled or ridged	1:2
Horned, winged, valley, or spired (weathered)	1:1

Source: N. Bowditch, National Imaging and Mapping Agency, 1995; irbs.com.

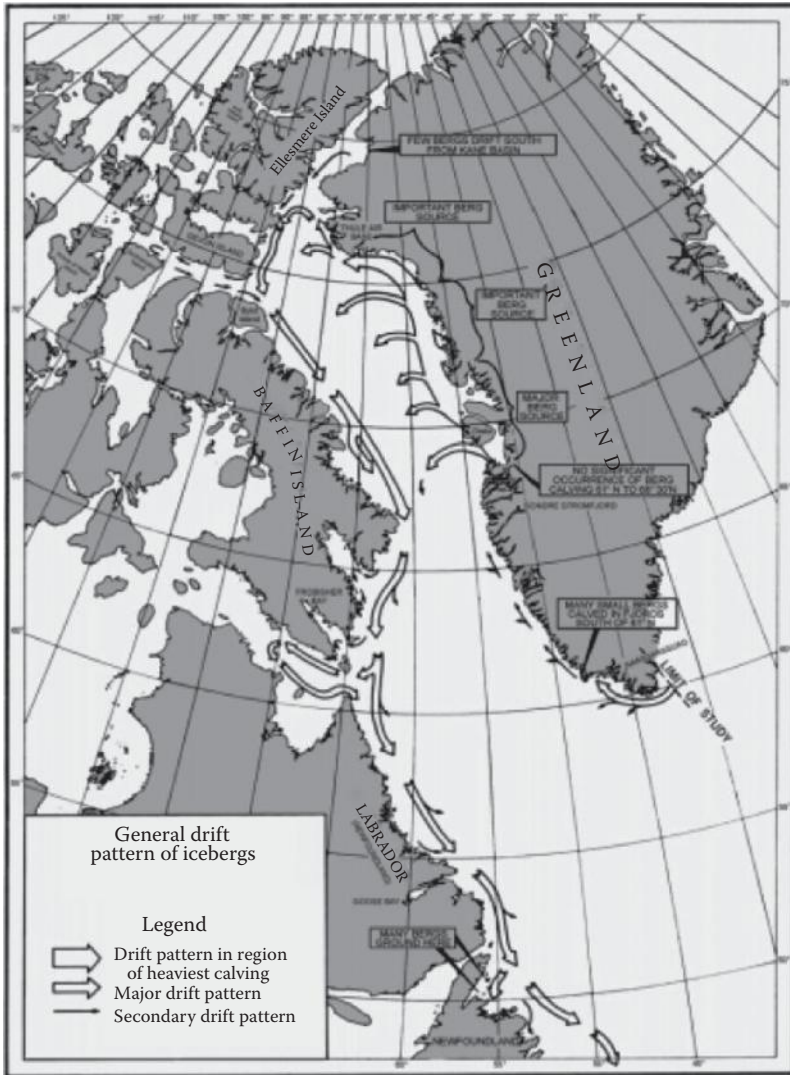
**TABLE 3.3**  
**Drift Speed of Iceberg as Percentage of Wind Speed**

Wind Speed (knots)	(Ice Speed)/(Wind Speed) (%)		Drift Angle (°)	
	Small Berg	Medium Berg	Small Berg	Medium Berg
10	3.6	2.2	12	69
20	3.8	3.1	14	55
30	4.1	3.4	17	36
40	4.4	3.5	19	33
50	4.5	3.6	23	32
60	4.9	3.7	24	31

Source: N. Bowditch, National Imaging and Mapping Agency, 1995; irbs.com.

A floating iceberg also melts nonuniformly due to nonhomogeneity in ice, thermal differences above and below the waterline portions, exposure of one side to the sun, strains, cracks, mechanical erosion, etc. As a result, changes in equilibrium take place, which may cause the berg to periodically tilt or capsize. Parts of it may break off or calve, forming separate smaller bergs called bergy-bits and growlers. Also as icebergs change their shape due to melting, erosion, and calving, their height-to-draft ratios tend to approach 1:1 during their last stage of decay, when their shapes tend to become valley-, wing-, horn-, or spire-shaped.

The main source of the icebergs, encountered in the North Atlantic, is the west coast of Greenland between 67°N and 76°N, where approximately 10,000–15,000 icebergs are calved each year. The West Greenland Current carries icebergs from this area northward and then westward until they encounter the south flowing Labrador Current; they are transported farther southward by the Labrador Current. The general drift patterns of icebergs are shown in Figure 3.15 [13]. Observations over a 79-year period show that an average of 427 icebergs per year reach latitudes south of 48°N, with approximately 10% of this total carried south of the Grand Banks (43°N) before they melt. Icebergs may be encountered during any part of the year, but in the Grand Banks area, they are most numerous during spring. The maximum monthly average of iceberg sightings below 48°N occurs during April, May, and June, with May having the highest average of 129 [13].



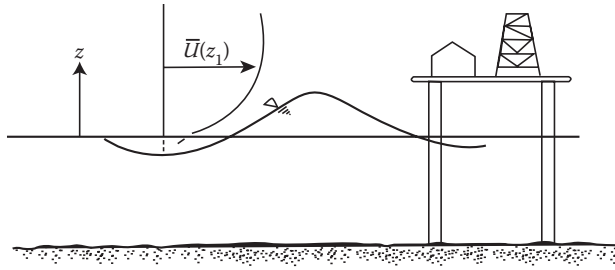
**FIGURE 3.15** General drift pattern of icebergs in the Northern Atlantic Ocean. (From N. Bowditch, National Imaging and Mapping Agency, 1995; irbs.com.)

### 3.3 OCEAN WINDS AND WIND STATISTICS

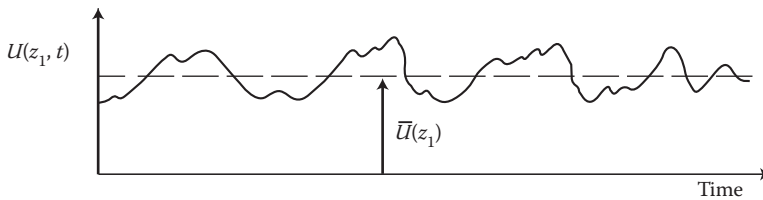
#### 3.3.1 INTRODUCTION TO WIND

Even though the currently accepted design methods consider the wind loads acting on an offshore structure to be made up of only static loads, the actual wind loads exerted on the offshore structures are more complex than this simplified assumption; actual wind velocity is made up of a mean component  $\bar{U}(z_1)$  (contributing to the static load exerted on the structure) and a time-varying component [called wind gust =  $U(z_1,t) - \bar{U}(z_1)$ ] that contributes to the dynamic component of the wind load exerted on the structure, as shown in Figures 3.16 and 3.17 [16, 17]. The static load design indirectly incorporates the dynamic component of the load into the structural design by computing the actual wind loads acting on the structure by multiplying the computed static loads by a gust factor, and





**FIGURE 3.16** Spatial variation of mean wind velocity. (From B. McClelland and M.D. Reifel, *Planning and Design of Fixed Offshore Platforms*, Van Nostrand Reinhold Co., New York, p. 319 (modified), 1986. With permission.)



**FIGURE 3.17** Wind speed variation at a fixed elevation  $z_1$ . (From B. McClelland and M.D. Reifel, *Planning and Design of Fixed Offshore Platforms*, Van Nostrand Reinhold Co., New York, p. 319 (modified), 1986. With permission.)

designs the structure to resist these loads; this gives a rather reasonable method for computing the effects of actual wind loads exerted on the structure. But it neglects the degradation of fatigue resistance that takes place in the structure. In actuality, the dynamic component should also be incorporated into the design since it contributes to the fatigue resistance of offshore structures.

The turbulent gusts that are present in wind are dependent on the surface roughness of the area over which the wind blows, as well as the mean wind velocity and the height above ground, at which it is measured. As observed in Section 3.2, the differential heating of the earth by the sun causes large-scale pressure variations over the area under consideration and generates the mean wind speed at the location, causing it to flow from a high-pressure region to a low-pressure region. The direction of wind flow is dependent on the atmospheric pressure difference (or gradient) mentioned above and the Coriolis force acting on the wind. This wind velocity is a constant value (depending on the pressure difference) at the upper reaches of the atmosphere (usually varying from 500 to 3000 m) and is approximately parallel to the isobars (lines of equal pressure); this constant velocity of wind at the upper reaches of the atmosphere is called the gradient wind speed ( $\bar{U}_G$ ) and is directly related to the external pressure gradient at that location. In the lower region of the atmosphere, the surface roughness (which varies generally from point to point) generates eddies (which are rather random in nature) in the blowing wind, and these eddies are carried along the wind at its mean speed. Consequently, the wind gusts vary randomly with respect to time and space and consequently influence the wind loads acting on the structure in a similar manner.

Moreover, the wind is highly influenced by its stability conditions. When the wind time history can be characterized by its stationarity (in statistical terms), then the wind is considered to be stable; and if the wind time history is nonstationary, then the wind is characterized as unstable. The description given below is applicable only to winds that exist under stable conditions. Stable wind conditions are assumed to exist when the wind speed, at a height of 10.0 m above the ocean surface, is above 20.0 m/s, and the fetch length of wind is greater than 30.0 km.



### 3.3.2 THEORETICAL CHARACTERIZATION OF WIND REGIME

The wind velocity at any point can be represented by

$$U(x, y, z, t) = \bar{U}(x, y, z) + U_x(t) + U_y(t) + U_z(t) \tag{3.1}$$

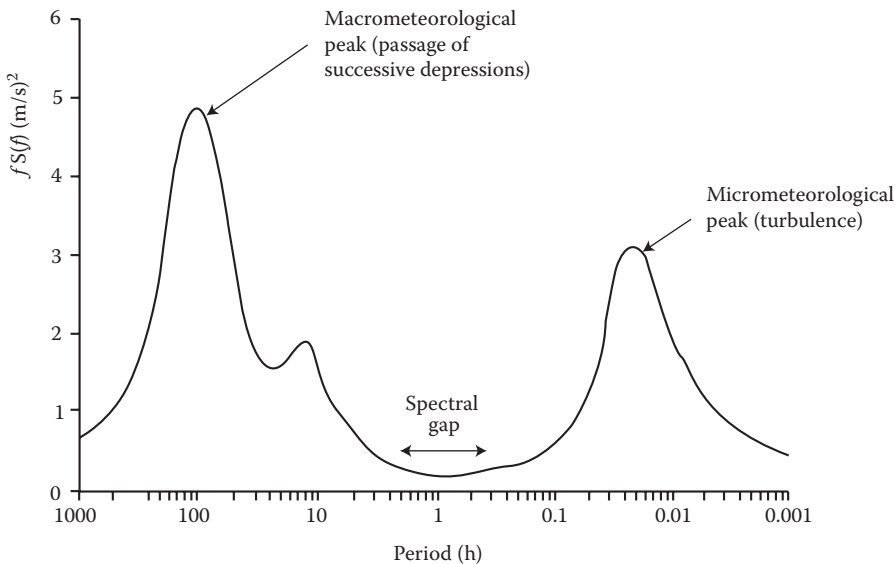
where  $U(x, y, z, t)$  is the wind velocity at a location designated by the coordinates  $(x, y, z)$ ,  $\bar{U}(x, y, z) \equiv \bar{U}(z_1)$  is the mean wind velocity at that location in the direction of its flow (Figure 3.16), and  $U_x(t)$ ,  $U_y(t)$ , and  $U_z(t)$  are, respectively, the  $x$ ,  $y$ , and  $z$  components of the wind gust at that location. The variation of mean wind velocity  $\bar{U}(z_1)$  is independent of the coordinates  $x$  and  $y$ , since wind velocity is specified in the direction of the flow of wind.

Figure 3.17 [16] shows the variation of  $\bar{U}(z_1)$  as a function of time  $t$ . Visualizing Figure 3.17, in a three-dimensional space, the mean wind field velocity given as  $\bar{U}(z_1)$  at any height  $z_1$  should be the same as  $\bar{U}(x, y, z)$  in Equation 3.1; consequently,  $\bar{U}(x, y, z)$  can be represented by

$$U(z_1) = U(x, y, z, t) = \bar{U}(z_1) + U_x(t) + U_y(t) + U_z(t) \tag{3.2}$$

where the wind velocity is measured at a reference height  $z_1$  as shown in Figure 3.16. The assumption made here is that the mean wind flow at any location is always parallel to the earth's surface and is dependent only upon the height  $z_1$ . The variation of wind gust velocity [ $U_x(t)$ ,  $U_y(t)$ , and  $U_z(t)$ ] in the  $x$ ,  $y$  and  $z$  directions are produced only by the dynamic components of gust at the height  $z_1$  and are independent of the spatial coordinates  $(x, y)$ .

As explained above, for analytical considerations, the wind is separated into mean and dynamic components; and since the wind velocity varies continuously with respect to time, the mean wind and the associated dynamic components of wind need to be calculated over a suitable averaging period. When a spectral analysis of the wind velocity time history is carried out over a long period (a number of days), one obtains the energy spectrum of the wind as shown in Figure 3.18 [18]. Figure 3.18 shows that the wind spectrum is made of two major components, namely, (1) a short-period



**FIGURE 3.18** Energy spectrum of wind speed. (From Van Der Hoven, I., *Journal of Meteorology*, 14, pp. 160–164, 1957. With permission.)

variation caused by the wind gusts ranging in period from 3.6 to 360.0 s and (2) a long-period variation caused by the passage of successive pressure systems, ranging in period from 1.6 to 1000 h. The peak of the short-period variation, termed the *micrometeorological peak*, occurs at about 25.0 to 30.0 s, and the peak of the long-period variation, termed the *macrometeorological peak*, occurs at about 8.0 to 12.0 days. Another secondary peak also occurs in the long-period variation at about 12.0 h, being the contribution from the daily thermal cycling of the atmosphere. In between the two major peaks, there is a low energy region called the spectral gap, resulting from the lack of contribution from any physical causes; it occurs in the period ranges between 360.0 s and 1.6 h. If the wind averaging period is placed in this spectral gap, then the two effects can be neatly separated, with the passage of large pressure systems appearing as slowly varying changes in the mean and the gust (or turbulence) effects appearing as rapid changes about the mean. Consequently, an averaging period of 1 h is chosen for wind.

**3.3.2.1 Probabilistic Nature of Wind Regime**

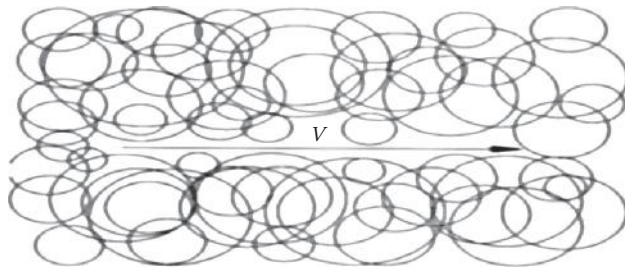
The fluctuating wind is a random mixture of gusts (or eddies) of various sizes and periods, as shown in Figure 3.19 [19]. They are also distributed randomly in time and space, and the wind gusting also varies randomly in time and space. Consequently, the three components of the wind gust velocity [ $U_x(t)$ ,  $U_y(t)$ , and  $U_z(t)$ ] vary randomly in time and space and could be characterized in statistical terms such as variance, auto- or cross-covariance, and auto- or cross-spectral density functions.

As mentioned earlier, in addition to static analysis, two more analyses need to be carried out to account for the effects of wind gusts on an offshore structure, viz., (1) fatigue analysis (for fatigue life) and (2) extreme response analysis (for peak stresses). Figure 3.20 [20] represents a typical wind speed and direction data at a North Sea site, required for carrying out the fatigue analysis; it shows how the wind speed changes its magnitude and direction as a function of its occurrence. Fatigue analysis would require the occurrence data of mean wind speed and direction, which would give the probability of occurrence of the omnidirectional mean value  $\bar{U}(z_1)$  over a succession of 1-h periods. It has been observed that the omnidirectional wind speed, given in Figure 3.21 [21], will conform closely to a Rayleigh distribution given by

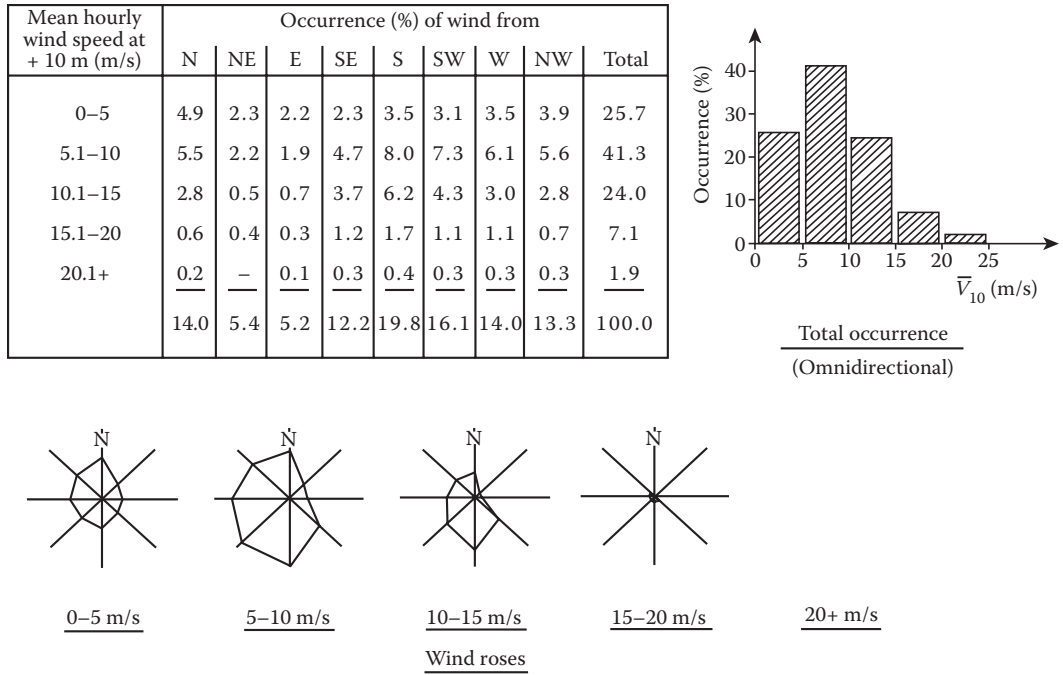
$$P(\bar{U}) = 1.0 - \exp\left[-\{4 - \pi\}/4(\bar{U}/\sigma_{\bar{U}})^2\right] \tag{3.3a}$$

where  $P(\bar{U})$  is the probability of value  $\leq \bar{U}$ , and  $\sigma_{\bar{U}}$  is the standard deviation of  $\bar{U}$ .

It has been observed that a Weibull distribution with a  $k$  value between 1.7 and 2.5 would give a better fit for on-site wind average speed variation than a Rayleigh distribution, as shown



**FIGURE 3.19** Visualization of turbulence in wind of velocity  $V$ . (From N.D.P. Barltrop and A.J. Adams, *Dynamics of Fixed Marine Structures*, Butterworth-Heinemann Ltd., Oxford, UK, p. 405, 1991. With permission.)



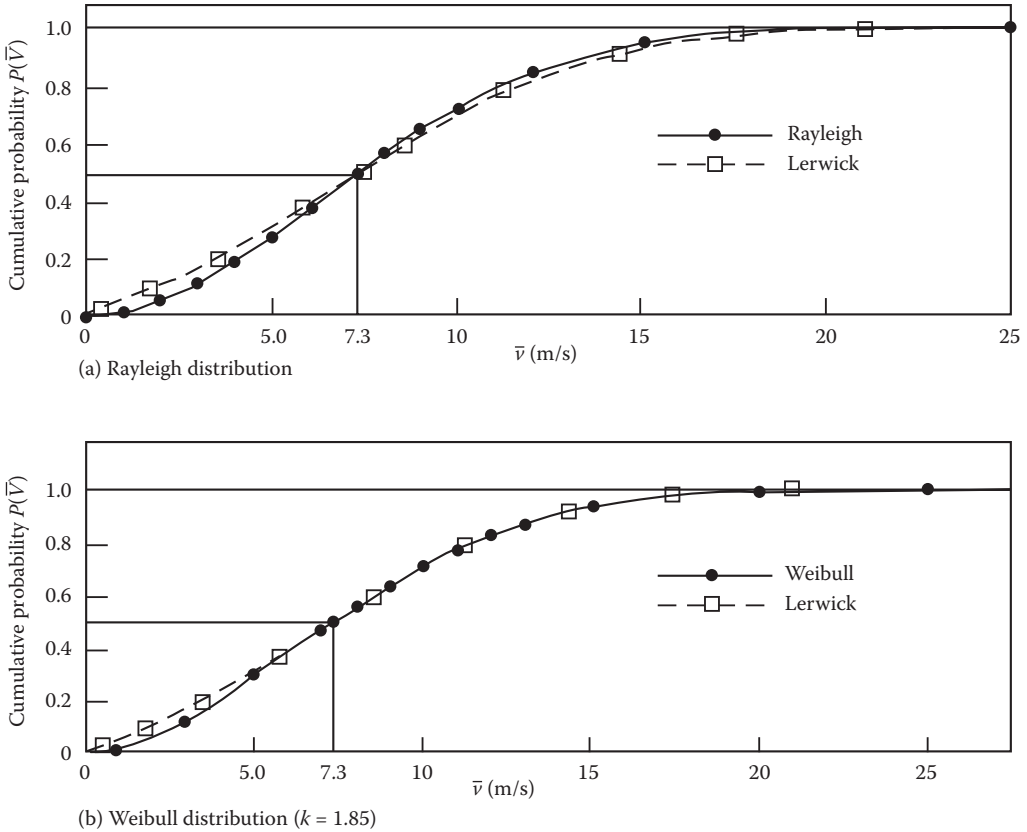
**FIGURE 3.20** Wind speed occurrence data for a typical North Sea site. (From N.D.P. Barltrop and A.J. Adams, *Dynamics of Fixed Marine Structures*, Butterworth-Heinemann Ltd., Oxford, UK, p. 405, 1991. With permission.)

in Figure 3.21. The best-fit Weibull distribution for the Lerwick site data (in UK), shown in Figure 3.21(b), is given by

$$P(\bar{U}) = 1.0 - e^{\{-\bar{U}/(2.005\sigma\bar{U})\}^{1.85}} = 1.0 - e^{\{-\bar{U}/(2\sigma\bar{U})\}^{1.85}} \tag{3.3b}$$

where  $P(\bar{U})$  is the probability of value  $\leq \bar{U}$ ; the Weibull distribution shows good agreement with the site data.

The probability distribution given in Figure 3.21 gives the results from one observation: the parent distribution. This would be sufficient to carry out the fatigue response of the structure during the period of observation for which the above data were available; but in order to carry out the extreme value analysis for the wind data, one needs to have the extreme value data for the site over a large number of years, or one needs to have the probability density of these extreme events. For instance, if we have 8760 annual mean hourly speed data, then the maximum of these mean hourly data is only one, being the highest of the recorded 8760 values. Consequently, the parent value distribution cannot give any accurate information concerning the extreme events. This can be obtained from a different family of distributions, called Fisher–Tippet type distributions, as shown in Table 3.4 [21]. Figure 3.22 [22] shows the relationship between the parent and extreme value distributions for mean hourly wind speeds at a particular location, viz., Lerwick in UK. Since the extreme response analysis requires extreme value data from a large number of years (which will be always a limited set of data), one can only say that a given speed has a certain probability of being exceeded at that time.



**FIGURE 3.21** Probability distribution of mean hourly wind speeds. (From N.D.P. Barltrop and A.J. Adams, *Dynamics of Fixed Marine Structures*, Butterworth-Heinemann Ltd., Oxford, UK, pp. 395–491, 1991. With permission.)

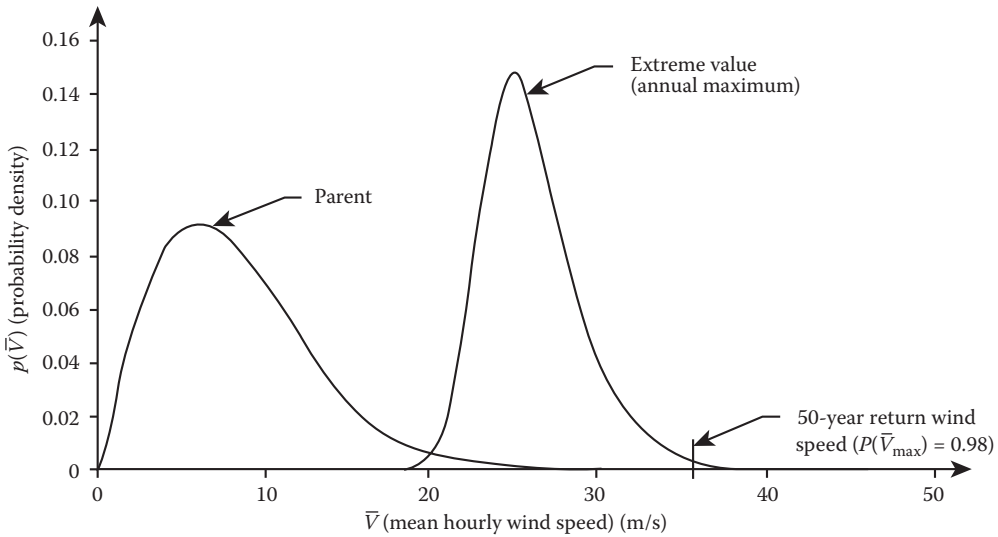
The design wind speeds are usually specified in terms of their return periods; the return period of an extreme event, defined as the period  $R$  of a random event of magnitude  $\bar{U}$ , is the average length of time in which the event of magnitude  $\bar{U}$  is exceeded only once.  $R$  is represented by

$$R = 1/(1 - P(\bar{U})) \tag{3.4}$$

**TABLE 3.4**  
**Parent and Extreme Value Distributions for Mean Hourly Wind Speeds**

#	Details	Parent Distribution	Extreme Value Distribution
1	Population	All the 1-h mean hourly wind speeds	Maximum of the 1-h mean wind speed in each year, over a number of years
2	Sampling period	1 h	1 year
3	Probability distributions	Rayleigh distribution Weibull distribution	Fisher–Tippett Type I distribution
4	Cumulative probability $P(\bar{U})$	Probability of value $\leq \bar{U}$ in one observation	Probability of value $\leq \bar{U}$ in one year (out of 8760 observations)

Source: Modified from N.D.P. Barltrop and A.J. Adams, *Dynamics of Fixed Marine Structures*, Butterworth-Heinemann Ltd., Oxford, UK, p. 421, 1991. With permission.

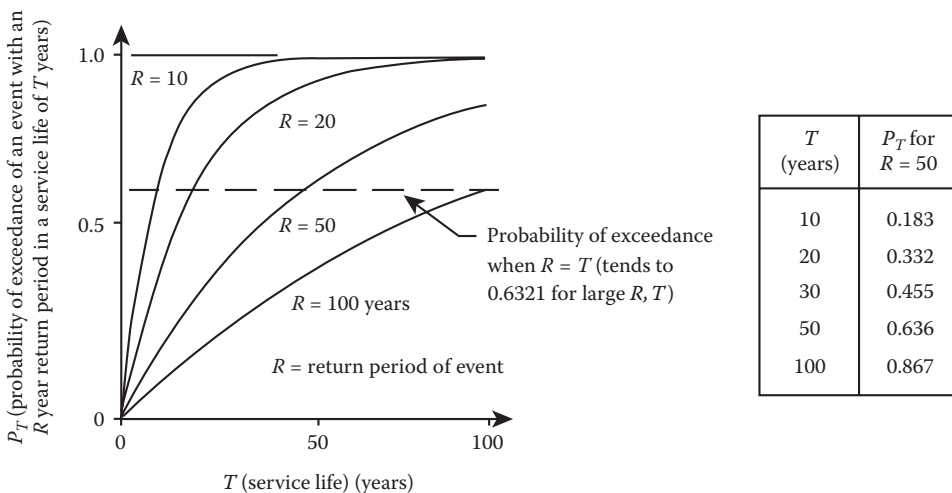


**FIGURE 3.22** Parent and extreme value distributions. (Modified from N.D.P. Barltrop and A.J. Adams, *Dynamics of Fixed Marine Structures*, Butterworth-Heinemann Ltd., Oxford, UK, p. 422, 1991. With permission).

This does not always mean that  $\bar{U}$  is always exceeded only once, since the mean wind speed  $\bar{U}$  is a random value that can be exceeded more than once in a year. The probability of exceedance ( $P_T$ ) of the event of magnitude  $\bar{U}$  over a (structural) service life of  $T$  years is given by

$$P_T = 1 - \{1 - (1/R)\}^T = 1 - \{P(\bar{U})\}^T \tag{3.5}$$

The plot of  $P_T$  as a function of the (structural) service life  $T$  is given in Figure 3.23 for a number of return periods ( $R$ ) of the event  $\bar{U}$ . As shown in Figure 3.23 (right) [23], for a 50-year service life ( $T$ ) of an offshore structure, the probability of exceedance ( $P_{50}$ ) is 0.636 with a return period of the event (maximum wind speed) of 50 years.



**FIGURE 3.23** Probability of exceedance plots as a function of  $T$  and  $R$ . (From N.D.P. Barltrop and A.J. Adams, *Dynamics of Fixed Marine Structures*, Butterworth-Heinemann Ltd., Oxford, UK, p. 423, 1991. With permission.)

### 3.3.3 WIND VELOCITY PROFILE

Once the appropriate value of the basic design wind speed (in m/s)  $\bar{U}_{10}$  (at a height of 10.0 m above the MSL) is obtained from the above calculations, then the distribution of wind speed  $\bar{U}_z$  over the structure, at any height  $z$ , can be obtained by following the analytical derivations given by Harris and Deaves [24]. They obtained the logarithmic equation given by

$$\begin{aligned} \bar{U}_z &= 2.5u_* \left\{ \ln(z/z_0) + 5.75(z/h) - 1.875(z/h)^2 - 1.333(z/h)^3 + 0.25(z/h)^4 \right\} \\ &\simeq 2.5u_* \left\{ \ln(z/z_0) + 5.75(z/h) \right\} \end{aligned} \tag{3.6}$$

The shortened form given in Equation 3.6 can be used when  $z$  is  $\leq 200.0$  m. In the above equation, the frictional velocity  $u_*$  is given by

$$u_* = \bar{U}_{10} / \{2.5 \ln(10/z_0)\} \text{ (in m/s)} \tag{3.7}$$

and  $z_0$ , the surface roughness parameter, is to be computed in an iterative manner from Charnock's law [25] given as

$$u_*^2 / (z_0 g) = c = 60 \tag{3.8}$$

Since  $u_*$  and  $z_0$  are unknown parameters, Equation 3.8 is solved in an iterative manner by assuming a suitable value for  $Z_0$  from the values given in Table 3.5 [26];  $g$  is the gravitational constant in appropriate units. Introducing this value of  $Z_0$  in Equation 3.7, the value of  $U_*$  is calculated. Then a new value of  $Z_0$  is obtained from Equation 3.8; this process is repeated until a converged value of  $Z_0$  is obtained. The value of the boundary layer height,  $h$ , in Equation 3.6 is given by

$$h = u_* / (6f_c) \text{ (in m)} \tag{3.9}$$

where  $f_c$ , the Coriolis parameter, is given by

$$f_c = 2\Omega \sin(\theta) \tag{3.10}$$

with  $\Omega$  being the angular velocity of the earth ( $= 72.9 \times 10^{-6}$  rad/s) and  $\theta$  being the latitude (in degrees) of the location at which the velocity  $\bar{U}$  is being computed.

**TABLE 3.5**  
**Typical Values of Terrain Parameter  $Z_0$**

#	Terrain Conditions	Surface Roughness Parameter, $Z_0$ (m)
1	Open level country with few trees and hedges and isolated buildings; typical farmland	0.03
2	Fairly level grass plains, with isolated trees	0.01
3	Flat areas with short grass and no obstructions (runways in airports)	0.003
4	Snow-covered farmland or flat desert or arid areas	0.001

Source: Modified from N.D.P. Barltrop and A.J. Adams, *Dynamics of Fixed Marine Structures*, Butterworth-Heinemann Ltd., Oxford, UK, p. 426, 1991. With permission.

**TABLE 3.6**  
**Gust Factors for Various Durations of Measurement**

Measured Fastest Mile of Wind or Basic Design Wind Speed $\bar{U}_{10}$ (mph)	Average Duration Used in Computing Gusts (s)					
	> 60	30	20	10	5	0.25
60.0	1.0	1.08	1.12	1.18	1.24	1.37
120.0	1.0	1.0	1.04	1.10	1.12	1.29

Source: T.H. Dawson, *Offshore Structural Engineering*, Prentice Hall, Inc., Englewood Cliffs, NJ, pp. 90–93, 1983. With permission.

Other formulae have also been used in the computation of wind velocity profiles. The logarithmic equation for wind speed (in ft./s) given by Wu [27] is

$$\bar{U}_z = \bar{U}_{10} \ln\{(z + z_0)/z_0\} / \ln\{(z_R + z_0)/z_0\} \text{ (ft.)}, \quad (3.11)$$

with  $z_0 = 2.91 \times 10^{-5} (\bar{U}_{10}^2 / g)$

with  $z_R$  being the reference wind measurement height of 33.0 ft. Another simpler equation, used by Dawson [28], is obtained from the assumption of a power law distribution for wind velocity and is given as

$$\bar{U}_z = \bar{U}_{10} (z/10)^{1/7} \text{ (ms)} \quad (3.12)$$

While designing structures, the above-mentioned basic design wind speed  $\bar{U}_{10}$  has to consider the effect of wind fluctuation (or the effect of wind gusts). These fluctuations are accounted for in the design by multiplying the basic design winds, given by Equations 3.6, 3.11, and 3.12, by a gust factor. The gust factor is dependent on the averaging time used in computing the gusts, as well as on the basic wind speed  $\bar{U}_{10}$ . These gust factors will influence the various components of an offshore structure in different ways, and as such, the averaging duration for gusts will be specified by the governing code. The values of the gust factors, used in offshore structural design, are given in Table 3.6 [28]. Recently, these gust factors have been accounted for by modifying the power law coefficient 1/7 to vary from 1/13 to 1/8 (see Addendum in [28]), depending on the sea state, the distance from land, and the averaging time interval. It is approximately equal to 1/13 for gusts and 1/8 for sustained winds in the open ocean; also  $\bar{U}_{10}$  is taken as the measured wind speed at the reference height of 10.0 m at the location site.

### Example 3.1

The following components of an offshore gravity platform deck are to be analyzed for wind loads on structures, viz., deck house, drilling derrick, and the two loading cranes; the wind averaging periods for the three components are 10.0 min, 15.0 s, and 3.0 s. The center of the deck house is located at a height of 40.0 m above the MSL; the base of the drilling derrick, which is 30.0 m high, is located at 35.0 m above MSL, and the bases of the loading cranes (each 20 m high) are located at 40.0 m above the MSL. Find the design wind velocities for the three structural components using the three wind velocity equations given above, viz., Equations 3.6, 3.11, and 3.12. The gust factors are to be taken from the values given in Table 3.6. Take the 1-h mean wind speed at a height of 10.0 m above the MSL to be 45.0 m/s. Take the latitude of the location as 45°.



(1) Using Equation 3.6:  $\bar{U}_z = 2.5u_*\{\ln(z/z_0) + 5.75(z/h)\}$

The value of  $z_0$  is obtained by iteratively solving the equations  $u_*^2/(z_0g) = c = 60$ ; and  $u_* = \bar{U}_{10}/\{2.5 \ln(10/z_0)\}$  (in m/s).

Solving the above equations iteratively, one obtains  $z_0 = 0.01225$ ;  $h = u_*/(6f_c)$  and  $fc = 2\Omega \sin(\theta)$ ;  $h = (4.34)(10^3)$  m.

$$\begin{aligned} \text{(a)} \quad \bar{U}_{z(\text{deckhouse})} &= [(2.5)(\bar{U}_{10})/(16.762)] [\ln(z/z_0) + 5.75(z/h)], \text{ (with } z = 40.0\text{m)} \\ &= (2.5)(45)/16.762 [8.0911 + 0.054] \\ &= 54.663\text{m/s} \end{aligned}$$

Gust factor for 10.0 min = 1.0.

Design wind speed for the deck house = (1.0)(54.663) = 54.663 m/s.

$$\begin{aligned} \text{(b)} \quad \bar{U}_{z(\text{drilling derrick})} &= [(2.5)(u_*)] [\ln(z/z_0) + 5.75(z/h)], \text{ (with } z = 50.0\text{m)} \\ &= [(2.5)(45)/(16.762)] [\ln(50/0.01225) + 5.75\{50/\{(4.3)(10^3)\}\}] = 56.353 \text{ m/s.} \end{aligned}$$

Gust factor for 15.0 s = 1.15.

Design wind speed for drilling derrick = (56.353)(1.15) = 64.691 m/s.

$$\begin{aligned} \text{(c)} \quad \bar{U}_{z(\text{loading crane})} &= [(2.5)(u_*)] [\ln(z/z_0) + 5.75(z/h)], \text{ (with } z = 50\text{m)} \\ &= [(2.5)(45)/(16.762)] [\ln(50/0.01225) + 5.75\{(50)/(4.3)(10^3)\}] = 56.253 \text{ m/s} \end{aligned}$$

Gust factor for 3.0 s = 1.295.

Design wind speed for the loading crane = (56.253)(1.295) = 72.848 m/s.

(2) Using Equation 3.11

(a) For the deck house:

$$\begin{aligned} \bar{U}_{z(\text{deckhouse})} &= \bar{U}_{10} \ln\{(z + z_0)/z_0\} / \ln\{(z_R + z_0)/z_0\} \text{ (ft.), with } z_0 = 2.91 \times 10^{-5} (\bar{U}_{10}^2/g) \\ \bar{U}_z &= (45.0) [\ln\{(40 + 0.006)/(0.006)\} / \ln\{(10 + 0.006)/(0.006)\}] = 53.405 \text{ m/s.} \end{aligned}$$

Gust factor for 10.0 min = 1.00.

Design wind speed for deck house = (53.405)(1.00) = 53.405 m/s.

(b) In a similar manner, for the drilling derrick,  $\bar{U}_z = 54.759$  m/s.

Gust factor for 15.0 s = 1.15.

Design wind speed for the drilling derrick = (54.759)(1.15) = 62.973 m/s.

(c) In a similar manner, for the loading crane,

$$\bar{U}_z = 54.759 \text{ ms.}$$

Gust factor for 3.0 s = 1.295.

Design wind speed for the loading crane = (54.759)(1.295) = 70.913 ms.

(3) Using Equation 3.12

(a) For the deck house,  $\bar{U}_z = \bar{U}_{10} (z/10)^{1/7}$ ,

$$\bar{U}_z = (45.0)[(40.0)/10.0]^{(1/7)} = 54.856 \text{ m/s.}$$

Gust factor 10 min = 1.00

Design wind speed for the deckhouse = (54.856)(1.0) = 54.856 m/s.

(b) In a similar manner, for the drilling derrick with  $z (= 50.0 \text{ m})$ ,  $\bar{U}_z = 56.632$  m/s.

Gust factor = 1.15.

Design wind speed for the drilling derrick = (56.632)(1.15) = 65.127 m/s.

(c) In a similar manner, for the loading crane, with  $z (= 50.0 \text{ m})$ ,  $\bar{U}_z = 56.632$  m/s.

Gust factor is = 1.295.

Design wind speed for the loading crane = (56.632)(1.295) = 73.338 m/s.

All three equations give values that are very close to one another.

### Example 3.2

Using the omnidirectional plot for the wind data given in Figure 3.20, determine the basic design wind speed, if the design wind speed is taken as the average of the highest 5% of the available wind speed data. Use a Rayleigh plot to fit the data given in Figure 3.20.

From the given percentage distribution of omnidirectional wind, the standard deviation of the wind speed can be determined:

$$\begin{aligned}\sigma_{\bar{U}} &= \sqrt{[(0.257)(2.5^2 + (0.413)(7.5)^2 + (0.240)(12.5)^2 + (0.071)(17.5)^2 + (0.019)(22.5)^2)]} \\ &= 9.68 \text{ m/s}\end{aligned}$$

Using Equation 3.3a,  $P(\bar{U}) = 1.0 - \exp[-\{(4 - \pi)/4\}(\bar{U}/\sigma_{\bar{U}})^2]$

The probability of the average of the highest 5.0% of wave exceeding the design wind speed is given by  $(1.0 - 0.05/2) = 0.975 = 1.0 - \exp[-\{(4 - \pi)/4\}(\bar{U}/\sigma_{\bar{U}})^2]$ .

Solving the above equation,  $\bar{U} = 40.1 \text{ m/s}$ .

### Example 3.3

The extreme value wind plot, similar to that shown in Figure 3.22, is obtained from the wind speed data available for the site from the meteorological data available. One hundred years of hourly mean wind speed data are available for the location at which the offshore structure is to be installed. If the service life of the structure is 50 years, determine the probability of exceedance of the computed maximum mean wind speed for the location. Using the plot given in Figure 3.22 as a sample value (for 100-year data), what would be the approximate design value of wind  $\bar{U}$  for a 50-year service period?

Return period = 100.00 years

$1.0 - P(\bar{U}) = 1/100$ . Therefore,  $P(\bar{U}) = 0.99$ .

The probability of exceedance of the computed maximum mean wind speed of 40.1 m/s is given by

$$P_T = 1.0 - (1.0 - 1/100)^{50} = 0.395$$

If  $P(\bar{U}) = 0.99$ , then the Weibull distribution equation 3.3b will give the value for a 50-year design period:

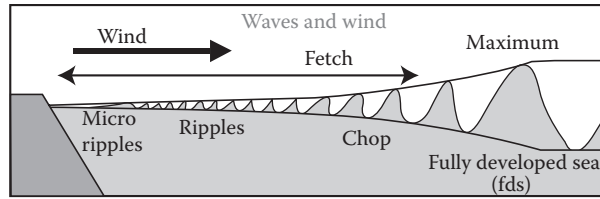
$$P\bar{U} = 1 - e^{\{-\bar{U}/(2.008\sigma_{\bar{U}})\}^{1.85}} = 1 - e^{\{-\bar{U}/(2\sigma_{\bar{U}})\}^{1.85}}$$

Solving the above equation,  $\bar{U} = 44.2 \text{ m/s}$ .

## 3.4 OCEAN WAVES AND WAVE STATISTICS

### 3.4.1 INTRODUCTION TO WAVES

To an observer, standing on the ocean shore, the waves often appear on the ocean surface as a randomly changing train of crests and troughs, especially when they are under the influence of onshore or offshore winds. Under the influence of an offshore wind, the ocean surface will



**FIGURE 3.24** Formation of ocean waves due to the passage of steady wind. (From J.F. Anthoni, Oceanography of waves. [www.seafriends.org.nz/oceano/waves.htm](http://www.seafriends.org.nz/oceano/waves.htm), 2000. With permission.)

change its shape as shown in Figure 3.24 [29]. When wind blows over the ocean surface, the energy transferred to the ocean water causes waves to form first as capillary waves (having a minimum wave speed of 0.23 m), and then the formed capillary waves grow to small amplitude irregular waves called wavelets, having different amplitudes and periods. During the initial stage of capillary wave formation, they travel at angles of 70–80° to the wind direction, and later on change to 30° from the wind direction, as the wave amplitude and period change. If the wind is a nonfluctuating steady wind, with a constant wind speed and fetch length blowing over the area for a number of hours, then the generated irregular wave may finally grow to a fully developed sea having regular ocean waves. Under a steady-state condition, the wave amplitude and period become constant, since the exciting wind force becomes equal to the restoring gravity force. The surface wave form becomes harmonic, executing a sinusoidal motion. In the case of single-frequency (or period) linear plane waves in deepwater, particles move in circular paths, making the ocean surface waves a combination of longitudinal (back and forth) and transverse (up and down) wave motions. If the winds tend to transfer more energy to the undulating and rough wave surface, the amplitudes and periods of the surface waves tend to keep on increasing. When the wave amplitude (height) and period increase, the particle paths do not anymore form closed orbits; rather, after the passage of each crest, particles tend to get displaced a little forward (in the forward direction of wind) from their previous positions, generating a phenomenon known as Stokes drift [30].

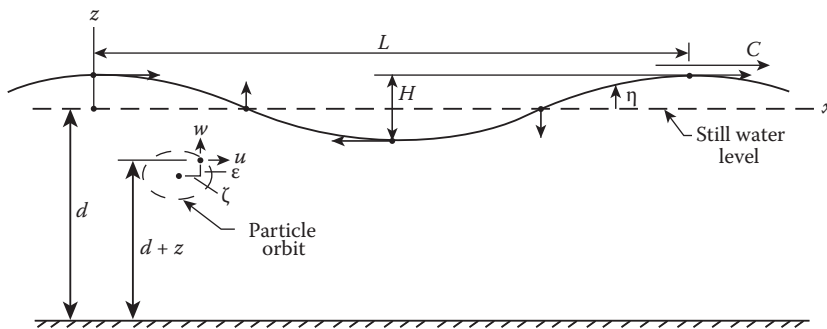
As seen from Figure 3.24, the actual wave formation mechanism is quite complex and not easy to describe due to the random manner in which waves are formed, significance of contribution from the nonlinearities present in wave formation process, and three-dimensional behavior during wave formation. Hence, for the purpose of modeling the ocean surface through simplified mathematical formulations, two descriptions given by Airy [31] and Stokes [32] will be presented in this section. These two wave descriptions are sufficient to visualize and predict the characteristics of waves present in intermediate and deepwater depth oceans; but for shallow water depth oceans, other formulations have to be used. Airy’s wave formulation can be considered as the first approximation to a complex set of mathematical formulations that can be used in the description of waves; Stokes wave formulations can be visualized as a summation of a number of successive approximations to wave forms, where each of the additional terms can be regarded as a correction to the preceding term.

### 3.4.2 AIRY’S TWO-DIMENSIONAL SMALL AMPLITUDE LINEAR WAVE FORMULATION

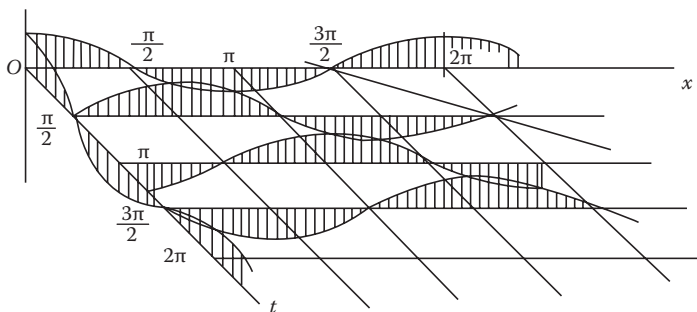
Figure 3.25 [33] gives a number of parameters that will be used in the characterization of a wave. The coordinate system to be used is the  $x, z$  coordinate system, with  $x$ -axis being placed along the still-water surface and the origin of the  $z$ -axis (positive upward) being placed such that the crest of the wave is located at the origin. The sea bottom is located at a depth of  $d$  ( $z = -d$ ) below the still-water level (SWL). The surface wave amplitude at any location is specified by  $\eta$  (given by the value of  $z$  at the wave surface), with  $\eta$  being a function of  $x$  and  $t$ , the time coordinate. The length of the

single frequency wave is  $L$ , and it moves in the forward direction (as indicated in figure) with a wave speed of  $C$ ; hence, the period of the wave is given by  $T (= L/C)$ . The wave height is taken as  $H$ , with the maximum wave amplitude being  $H/2$ . The arrows shown on the wave profile show the direction of water (wave) particle motion at salient points along the direction of wave propagation. The figure also shows that the orbital path of the water (wave) particle is oscillatory in nature; the coordinates of the orbital motion of the water particle are given by  $(\zeta, \epsilon)$ , with  $\zeta$  being the  $x$ -coordinate of the orbital motion and  $\epsilon$  being the  $y$ -coordinate of the orbital motion. Also the following two terms ( $k, \sigma$ ) will be used to designate the wave number  $k (= 2\pi/L)$  and angular wave frequency  $\sigma$  ( $\omega = 2\pi/T$ ). Also one can see from these two parameters that wave speed  $C = \sigma/k$ . Another term that is often used in describing a wave is the wave steepness, which is defined by the term  $(H/L)$ . In order to have a clear comprehension of the variation of  $z$  as a function of  $(x, t)$ , a space–time representation of the wave is also shown in Figure 3.26 [34].

The small amplitude wave theory is based on the assumption of irrotational flow of water particles in the ocean space under consideration, and this implies that there is no shear stress at the air–water interface; hence, the wave theories will be valid throughout the ocean space except the thin water surface at the top, in contact with the shearing wind action. Instead of considering the waves as generated due to wind–wave interaction, the waves can also be considered as regular monochromatic waves, termed as *swells*, generated by a storm acting on an ocean surface located far away



**FIGURE 3.25** Definition of wave parameters. (R.M. Sorensen: *Basic Wave Mechanics: For Coastal and Ocean Engineers*, p. 8. 1993. Modified. Copyright Wiley-VCH Verlag GmbH & Co. KGaA. Reproduced with permission.)



**FIGURE 3.26** Space–time representation of a progressive wave. (J.F. Wilson: *Dynamics of Offshore Structures*, p. 81. 1984. Modified. Copyright Wiley-VCH Verlag GmbH & Co. KGaA. Reproduced with permission.)

from the ocean region under consideration. In addition to the absence of wind shear on the ocean wave surface, the pressure on the free surface of the wave is also considered to be a uniform value of  $p_\eta = \text{constant}$  (or equal to zero).

Assumption of the existence of irrotational motion throughout the ocean space under consideration leads to the existence of a velocity potential, which should satisfy the continuity equation given by

$$\nabla \cdot \mathbf{V} = \nabla \cdot \nabla \phi = \nabla \cdot (\partial \phi / \partial x i + \partial \phi / \partial z k) = \nabla^2 \phi = \partial^2 \phi / \partial x^2 + \partial^2 \phi / \partial z^2 = 0 \tag{3.13}$$

In the above Laplace equation,  $V$  is the flow velocity given by the two components,  $V_x (= \partial \phi / \partial x = u)$ , and  $V_z (= \partial \phi / \partial z = w)$ , with  $\phi$  as the velocity potential. The solution to Equation 3.13 should be a function of  $d, H, L, T$ , and the coordinates  $(x, y, t)$ . In addition, the solution should also satisfy the following conditions, viz.,

(1) No flow occurs normal to the bottom at  $z = -d$ , which leads to

$$w = \partial \phi / \partial z = 0 \tag{3.14}$$

(2) Also, according to the kinematical surface boundary condition at the wave surface, the vertical component of the wave particle velocity  $w$  is given by

$$w = \partial \eta / \partial t + u \partial \eta / \partial x, \quad z = \eta \tag{3.15}$$

(3) The pressure  $p$ , at the ocean wave surface, is zero, which leads to the dynamic surface boundary condition given by the reduced form of the Bernoulli equation:

$$(1/2)(u^2 + w^2) + g\eta + \partial \phi / \partial t = 0, \quad \text{at } z = \eta \tag{3.16}$$

For small amplitude waves, Equation 3.15 reduces to

$$w = \partial \eta / \partial t, \quad z = 0 \tag{3.17}$$

and Equation 3.16 reduces to

$$g\eta + \partial \phi / \partial t = 0, \quad \text{at } z = \eta \tag{3.18}$$

Consider the wave surface elevation,  $\eta$ , for a progressive wave, to be represented by a harmonic form given by

$$\eta = (H/2) \cos(kx - \sigma t) = (H/2) \cos(2\pi x/L - 2\pi t/T) = (H/2) \cos\{2\pi(x/L - t/T)\} \tag{3.19}$$

As can be observed from Figure 3.25, the wave surface is defined in a cosine form and is also represented by the form given by Equation 3.19; this assumption is reasonable for small amplitude waves, but for larger amplitude waves, additional corrective terms need to be incorporated into the above equation. The solution of Equation 3.13, subject to the above assumption given in Equation 3.19, and satisfying the conditions given by Equations 3.14, 3.17, and 3.18, leads to

$$\phi = (gH/2\sigma) [\cosh k(d + z)/\cosh kd] \cos(2\pi)(x/L - t/T) \tag{3.20}$$

Differentiating Equation 3.18 with respect to  $t$ , substituting the value of  $\phi$ , and using  $w = (\partial\eta/\partial t = (\partial\phi/\partial z)_{z=0})$ , the following relationship is obtained:

$$C^2 = (g/k) \tanh(kd) = (gL/2\pi) \tanh(2\pi d/L) \quad (3.21)$$

Since wave speed  $C = L/T$ , Equation 3.21 could also be expressed as

$$C = (gT/2\pi) \tanh(kd) \quad (3.22)$$

The wavelength  $L (= CT)$  can also be expressed as

$$L = (gT^2/2\pi) \tanh(kd) \quad (3.23)$$

If wave period  $T$  and water depth  $d$  are known, then the wavelength and wave speed (or celerity) can be computed from Equations 3.22 and 3.23 in an iterative manner; otherwise, standard tables available in Shore Protection Manual [35] can be used to determine these values. In Equation 3.23, if  $(d/L) = 1/2$ , the equation reduces to

$$\begin{aligned} L_0 &= gT^2/2\pi = 5.12T^2 \quad (\text{in FPS system of units}) \\ &= 1.561T^2 \quad (\text{in metric system of units}) \end{aligned} \quad (3.24a)$$

The wavelength  $L_0$  is called the deepwater wavelength since it is independent of the water depth, and the wave is called the deepwater wave [ $(d/L)_{\text{for deepwater}} = d/L_0 \geq 1/2$ ]; hence, the deepwater water depth is  $d_{\text{deepwater}} = L_0/2$ , beyond which the ocean depth is designated as very deep. It can also be stated that for deepwater,

$$(d/L)_{\text{deepwater}} = d/(gT^2/2\pi) \geq 1/2; \text{ this leads to } (d/gT^2)_{\text{deepwater}} \geq 1/4\pi \geq 0.08 \quad (3.24b)$$

Moreover, it is also seen that

$$C/C_0 = L/L_0 \tanh(2\pi d/L) \quad (3.25)$$

where  $C_0 = [gT/2\pi = 5.125T$  (in FPS system)  $= 1.561T$  (in metric system)] is the deepwater wave speed. Another interesting set of relationships is obtained when the relative depth ratio  $(d/L)$  is smaller than 0.05; this relative water depth is called the shallow water depth. For a shallow water ratio of  $d/L \leq 0.05$  (for this ratio,  $d/gT^2 \leq 0.0025$ ), the value

$$\tanh(kd) \simeq kd \quad (3.26)$$

Hence, Equation 3.21 becomes

$$C_{\text{shallow}} = \sqrt{gd} \quad (3.27)$$

and the shallow water wavelength  $L_{\text{shallow}}$  is given as

$$L_{\text{shallow}} = T\sqrt{gd} \quad (3.28)$$

**TABLE 3.7**  
**Error in Shallow Water and Deepwater Wavelength and Wave Speed Approximations**

Details		Actual Value	Approximate Value	Error in Calculation
Deepwater wave	$d/L = 0.5$	$\tanh(\pi) = 0.9963$	1.00	-0.37%
Shallow water wave	$d/L = 1/20$	$\tanh\{(2\pi)(1/20)\} = 0.3042$	$(kd) = (2\pi)(1/20) = 0.3142$	-3.29%
	$d/L = 1/30$	$\tanh\{(2\pi)(1/30)\} = 0.2064$	$(kd) = (2\pi)(1/30) = 0.20944$	-1.47%
	$d/L = 1/40$	$\tanh\{(2\pi)(1/40)\} = 0.1558$	$(kd) = (2\pi)(1/40) = 0.1571$	-0.83%

The range of water depth ratio between  $d/L \leq 1/2$  and  $d/L \geq 0.05$  is termed the intermediate (or transitional) water depth. The error involved in these deepwater and shallow water approximations are given in Table 3.7. It is seen from Table 3.7 that the error in the deepwater approximation is -0.37%, and the error in the shallow-water approximation limit is -3.29%.

**3.4.2.1 Wave Particle Velocity, Acceleration, and Orbit**

The water particle velocity and acceleration components in a monochromatic wave can be obtained from the velocity potential equation given in Equation 3.20. The horizontal and vertical velocities of the water particle (in a wave) are obtained as follows:

$$\begin{aligned}
 u &= \partial\phi/\partial x = \partial\left[\left(gH/2\sigma\right)\left(\cosh(d+z)/\sinh kd\right)\sin(kx - \sigma t)\right]/\partial x \\
 &= (\pi H/T)\left(\cosh k(d+z)/\sinh kd\right)\cos(kx - \sigma t)
 \end{aligned}
 \tag{3.29}$$

$$\begin{aligned}
 w &= \partial\left[\left(\pi H/T\right)\cosh(k(d+z)/\sinh kd)\sin(kx - \sigma t)\right]/\partial z \\
 &= (\pi H/T)\left[\sinh k(d+z)/\sinh kd\right]\sin(kx - \sigma t)
 \end{aligned}
 \tag{3.30}$$

The horizontal particle velocity of the wave is obtained from

$$\begin{aligned}
 a_x &= du(x, z, t)/dx = \left\{(\partial u/\partial x)(\partial x/\partial t) + (\partial u/\partial z)(\partial z/\partial t)\right\} + (\partial u/\partial t) \\
 &= u\partial u/\partial x + w\partial u/\partial z + \partial u/\partial t
 \end{aligned}
 \tag{3.31}$$

where the first two terms are the convective contribution to the acceleration and the last one is the local acceleration term. Since the magnitudes of the convective acceleration terms are much smaller (due to the multiplication of two small terms) than the local acceleration, they are neglected in the calculation of the acceleration magnitude.

Hence, the horizontal particle acceleration of the wave is given as

$$a_x \simeq \partial u/\partial t = (2\pi^2 H/T^2) \left\{\cosh k(d+z)/\sinh(kd)\right\}\sin(kx - \sigma t)
 \tag{3.32}$$

In a similar manner, the vertical acceleration of the water particle velocity in the wave is given by



$$\begin{aligned}
 a_z &= dw/dt = u\partial w/\partial x + w\partial w/\partial z + \partial w/\partial t \simeq \partial w/\partial t \\
 &= (2\pi^2 H/T^2)(\sinh k(d+z)/\sinh kd) \cos(kx - \sigma t)
 \end{aligned}
 \tag{3.33}$$

It is seen from Equations 3.32 and 3.33 that there is a phase difference of 90° between the velocity and acceleration terms of the x- and z-directions. Since the velocities *u* and *w* are particle velocities in the wave, the particle motions in the wave can also be determined from them by integrating these velocity terms. Hence, the particle motions ( $\zeta$ ,  $\epsilon$ ) are obtained as

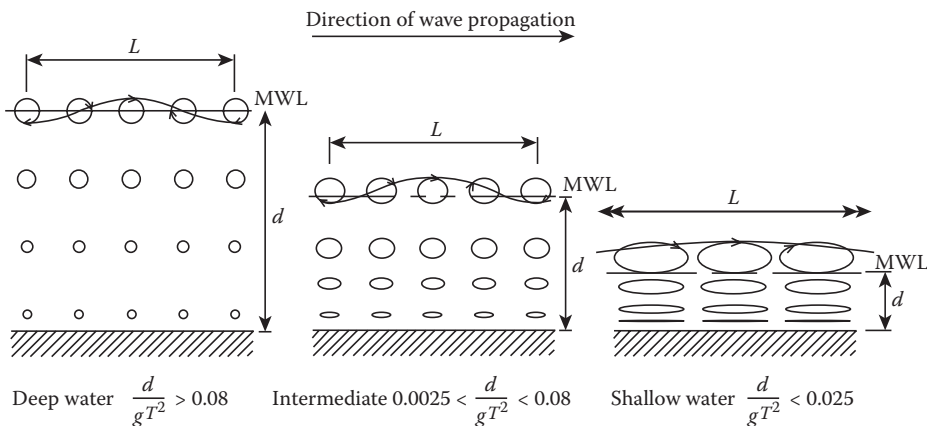
$$\begin{aligned}
 \zeta &= \int u dt = \int [(\pi H/T)\{\cosh k(d+z)/\cosh kd\} \cos(kx - \sigma t)] dt \\
 &= -(H/2)\{\cosh k(d+z)/\sinh kd\} \sin(kx - \sigma t)
 \end{aligned}
 \tag{3.34}$$

$$\begin{aligned}
 \epsilon &= \int w dt = \int [(\pi H/T)\{\sinh k(d+z)/\sinh kd\} \sin(kx - \sigma t)] dt \\
 &= (H/2)\{\sinh k(d+z)/\sinh kd\} \cos(kx - \sigma t)
 \end{aligned}
 \tag{3.35}$$

The plot of the particle motions for deep, intermediate, and shallow water waves are shown in Figure 3.27. It is seen that the particle orbits are circular for deepwater waves, whereas they are elliptical for intermediate and shallow waters. In deepwater, the orbits of the particle motions are circular, with a diameter equal to the wave height at the wave surface; the particle orbit decreases exponentially and is equal to 4.0% of the wave height when the depth (below ocean surface) is equal to half the wavelength [36]. At the ocean bottom, the particle orbit in deepwater is zero, since it cannot have a vertical velocity. As shown in Figure 3.27 [37], in intermediate and shallow waters, the particle orbits are elliptical and become flatter and flatter as the point of interest moves toward the bottom.

The equations for  $\phi$ , *u*, *w*, *a<sub>x</sub>*, *a<sub>z</sub>*,  $\zeta$  and  $\epsilon$  can be reduced further for deepwater and shallow water conditions as shown in Table 3.8. The reduction is due to the following conditions that can be achieved in the relevant equations for the specified water depths. For deepwater conditions,

$$\cosh k(d+z)/\sinh kd = \{e^{k(d+z)} + e^{-k(d+z)}\}/(e^{kd} - e^{-kd}) \simeq e^{k(d+z)}/e^{kd} = e^{kz}
 \tag{3.36}$$



**FIGURE 3.27** Particle orbits in deep, intermediate, and shallow water waves. (From N.D.P. Barltrop and A.J. Adams, *Dynamics of Fixed Marine Structures*, Butterworth-Heinemann Ltd., Oxford, UK, p. 253, 1991. With permission.)

**TABLE 3.8**  
**Reduced Form of Equations in Wave Formulation**

Particulars	Shallow Water Wave ( $d/L \leq 1/20$ )	Deepwater Wave ( $d/L \geq 1/2$ )
Horizontal particle velocity	$u = (H/2)\left(\sqrt{g/d}\right)\cos(kx - \sigma t)$	$u = (\pi H/T)e^{kz}\cos(kx - \sigma t)$
Vertical particle velocity	$w = (\pi H/T)(1 + z/d)\sin(kx - \sigma t)$	$w = (\pi H/T)e^{kz}\sin(kx - \sigma t)$
Horizontal particle acceleration	$a_x = (\pi H/T)\sqrt{(g/d)}\sin(kx - \sigma t)$	$a_x = (2\pi^2 H/T^2)e^{kz}\sin(kx - \sigma t)$
Vertical particle acceleration	$a_z = -(2\pi^2 H/T^2)(1 + z/d)\cos(kx - \sigma t)$	$a_z = -(2\pi^2 H/T^2)e^{kz}\cos(kx - \sigma t)$
Horizontal particle displacement	$\zeta = -(HT/4\pi\sqrt{g/d})\sin(kx - \sigma t)$	$\zeta = -(H/2)e^{kz}\sin(kx - \sigma t)$
Vertical particle displacement	$\epsilon = (H/2)(1 + z/d)\cos(kx - \sigma t)$	$\epsilon = (H/2)e^{kz}\cos(kx - \sigma t)$
Subsurface water pressure	$p = \rho g(\eta - z)$	$p = \rho g\eta e^{kz} - \rho g z$

In a similar manner,

$$\cosh k(d + z)/\cosh kd = \{e^{k(d+z)} + e^{-k(d+z)}\}/(e^{kd} + e^{-kd}) \simeq e^{kz} \tag{3.37}$$

For shallow water wave conditions,

$$\cosh k(d + z)/\sinh kd \simeq 1/kd \tag{3.38}$$

$$\sinh k(d + z)/\sinh kd \simeq k(d + z)/kd = 1 + z/d \tag{3.39}$$

The above reductions make the equations given in Table 3.8 self-evident.

### 3.4.2.2 Wave Pressure, Energy, and Flux (or Power)

The water wave pressure at any point within the ocean space can be obtained by using the Bernoulli equation given in Equation 3.16 as

$$(1/2)(u^2 + w^2) + gz + \partial\phi/\partial t = 0 \tag{3.40}$$

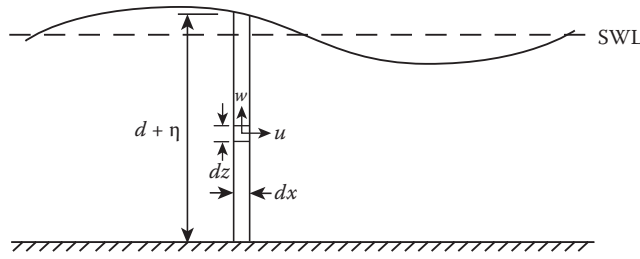
For small amplitude waves, the nonlinear term ( $u^2 + w^2$ ) can be taken as negligible, and Equation 3.40 can be rewritten as

$$p = -\rho g z - \rho \partial\phi/\partial t = -\rho g z + (\rho g H/2) [\cosh k(d + z)/\cosh(kd)] \cos(kx - \sigma t) \tag{3.41}$$

The first term on the right-hand side of Equation 3.41 is the regular hydrostatic pressure term, and the second term on the right is the hydrodynamic pressure term, generated due to wave particle acceleration. It should also be noted that due to the application of surface condition at  $z = 0$ , Equation 3.41 is valid below the ocean surface. A pressure transducer placed below the ocean surface (at  $z \leq L/2$ ) will be able to sense the constant hydrostatic pressure and the varying dynamic pressure; consequently, the pressure transducer can be used as a device to measure wave surface elevations, wave heights, as well as wave periods.

It is also possible to estimate the wave energy present in the waves. Since the waves possess kinetic and potential energies, the total energy present in the waves can be obtained by adding the two together. Using Figure 3.28 [38], the kinetic energy,  $E_k$ , present in the wave, per unit width, is obtained by integrating the contributions from the dynamic wave velocity components ( $u, w$ ) over a wavelength:

$$E_k = \int_0^L \int_{-d}^0 (1/2)\{\rho g(u^2 + w^2)\} dx dz = \rho g H^2 L/16 \tag{3.42}$$



**FIGURE 3.28** Parameters required for wave energy formulation. (R.M. Sorensen, *Basic Wave Mechanics for Coastal and Ocean Engineers*, p. 19. 1993. Copyright Wiley-VCH Verlag GmbH & Co. KGaA. Reproduced with permission.)

The potential energy of the wave, per unit width, is computed as

$$E_p = \int \rho g (d + \eta) \left\{ (d + \eta) / 2 \right\} dz - \rho g d L (d / 2) = \rho g H^2 L / 16 \quad (3.43)$$

In Equation 3.43, the second term is the potential energy present in still seawater. Hence, the total energy present in the wave, per unit width, is obtained by adding Equations 3.42 and 3.43 and is given as

$$E = \rho g H^2 L / 8 \quad (3.44)$$

The rate at which the wave energy is transmitted from one point to another point is termed the energy flux or power of a wave. It is given by the product of the dynamic wave force (represented by the second term of Equation 3.41) acting on a vertical plane (normal to the direction for wave propagation) and the particle velocity (given by Equation 3.29) across this plane. This leads to

$$\begin{aligned} P &= (1/T) \int_0^T \int_{-d}^0 (p_{\text{dynamic}}) u \, dz \, dt = (1/T) \int_0^T \int_{-d}^0 \left\{ (\rho g H / 2) (\cosh k(d+z) / \cosh kd) \cos(kx - \sigma t) \right\} \\ &\times \left\{ (\pi H / T) \cosh k(d+z) / \cosh kd \right\} \cos(kx - \sigma t) \, dz \, dt \\ &= (\rho g H^2 L / 16 T) \left\{ 1 + (2kd / \sinh 2kd) \right\} = (En / T), \\ &\text{with } n = (1/2) \left[ 1 + (2kd / \sinh 2kd) \right] \end{aligned} \quad (3.45)$$

with  $n$  being equal to 0.5 for deepwater and 1.0 for shallow water. Equation 3.45 can be rewritten as

$$P = nE/T = n\bar{E}C, \quad (3.46)$$

where wave celerity  $C = L/T$ ,  $\bar{E}$  = energy density of a wave =  $E/(1)(L) = \rho g H^2 / 8$ , and  $nC$  is termed as the group wave celerity.

### Example 3.4

A typical Airy's deepwater wave has a period of 10.0 s and a shallow water depth of 2.0 m. Determine the length and celerity of wave in (a) deepwater; (b) shallow water; and (c) intermediate water depths. Also determine the limit of deepwater depth.

In deepwater:

$$\begin{aligned} \text{Wavelength} &= (gT^2/2\pi) = (9.81/2\pi)(10^2) = 156.13 \text{ m.} \\ \text{Wave celerity} &= (gT/2\pi) = (2.81/2\pi)(10) = 15.613 \text{ m/s.} \\ \text{Limit of deepwater depth} &= L/2 = 156.13/2 = 78.06 \text{ m.} \end{aligned}$$

In shallow water:

$$\begin{aligned} \text{Wavelength} &= T\sqrt{gd} = (10)\left[\sqrt{(9.81)(2.0)}\right] = 44.3 \text{ m.} \\ \text{Wave celerity} &= \sqrt{gd} = \sqrt{(9.81)(2.0)} = 4.43 \text{ m/s.} \end{aligned}$$

In intermediate depth water:

$$\begin{aligned} \text{Wavelength: } &44.3 \text{ m} \leq L \leq 156.13 \text{ m.} \\ \text{Wave celerity: } &4.43 \text{ m/s} \leq C \leq 15.613 \text{ m/s.} \end{aligned}$$

### Example 3.5

A wave tank at the US Army Coastal Engineering Research Center is 193.0 m long, 4.57 m wide, and 6.1 m deep. The tank is filled with freshwater to a depth of 5.0 m, and a 1.0-m-high and 4.0-s-period wave is generated. Find (a) the wave celerity and length; (b) the water-particle velocities and wave pressure at a point located at 4.0 m ahead of the wave crest and 2.0 m below the SWL (assume  $t = 0.0$  s for all numerical computations); and (c) the horizontal and vertical dimensions of the water particle's orbit at this point.

(a) Wave celerity and length:

$$\text{Deepwater wavelength} = L_0 = (gT^2/2\pi) = (9.81)(4.0^2)/(2\pi) = 24.98 \text{ m.}$$

$d/L_0 = 0.2002 < 0.5$ ; hence, the water depth is intermediate water depth; the equation to be used is  $L = (gT^2/2\pi)[\tanh(2\pi d/L)]$ ; the equation is nonlinear, and as a result, the length  $L$  has to be obtained by solving the equation in an iterative manner or by using relevant tables available in the US Army Corps of Engineers Coastal Engineering Research Center, 1984 (Shore Protection Manual, Volume II). Using the tables,  $L = 22.195$  m. Also  $C = L/T = 22.195/4 = 5.549$  m/s.

(b) Wave particle velocities and pressure:

$$u = (\pi H/T) (\cosh k(d+z)/\sinh kd) \cos(kx - \sigma t) = (\pi H/T) (\cosh k(d+z)/\sinh kd) \cos(kx)$$

when  $t = 0.0$  s. Substituting the values of the variables in the above equation,  $u = 0.2379$  m/s.

Also  $w = (\pi H/T) [\sinh k(d+z)/\sin kd] \sin(kx - \sigma t) = (\pi H/T) [\sinh k(d+z)/\sin kd] \sin(kx)$ , when  $t = 0.0$  s. Substituting the values of the variables in the above equation,  $w = 0.305$  m/s.

$$\text{Wave pressure } p = -\rho gz + (\rho gH/2)[\cosh k(d+z)/\cosh(kd)], \text{ (when } x \text{ and } t = 0.0 \text{ s.}$$

Substituting the values of the variables in the above equation,

$$p = -(1025)(9.81)(-2.0) + 1351.8 = 21,462.30 \text{ N/m}^2.$$

(c) Wave particle displacements:

$$\zeta = -(H/2) \{ \cosh k(d+z)/\sinh(kd) \} \sin(kx), \text{ when } t = 0.0 \text{ s} = -0.323 \text{ m.}$$

$$\varepsilon = -(H/2) \{ \sinh k(d+z)/\sinh(kd) \} \cos(kx), \text{ when } t = 0.0 \text{ s} = \pm 0.1046 \text{ m.}$$

### Example 3.6

A pressure gauge, placed on top of a 1.0-m-diameter pipeline, located in 10.0-m depth of water, measures an average maximum pressure of 10.0 N/cm<sup>2</sup>, when a wave of period 10.0 s passes over it. Find the wavelength, wave height, and wave pressure, exerted at the bottom of the pipeline (per unit length).

Maximum wave pressure =  $-\rho gz + (\rho gH/2)[\cosh k(d+z)/\cosh(kd)]$ , when  $x$  and  $t$  are equal to 0.0 =  $-(1026.0)(9.81)(-9.0) + [(1026)(9.81)(H/2)] \cosh[(2\pi)(10.0+z)/L]/\cosh[(2\pi)(10.0)/L]$ .

The wavelength is an unknown nonlinear function and has to be obtained by iteration or by using the available tables, as mentioned in the earlier problem:

$$L = (gT^2/2\pi) \tanh(2\pi d/L) = (9.81)(10^2)/(2\pi) \tanh[(2\pi)(10.0)/L] = 156.13 \tanh(62.832/L)$$

For  $d/L_0 = 10.0/156.13 = 0.0645$ ,  $d/L$  (from the tables) = 0.1082.

Hence,  $L = 10/0.1082 = 92.42$  m.

$$p = 90,585.6 + (5032.5H)(0.8105) \text{ N/m}^2 = (10.0 \text{ N/cm}^2)(10^2)^2. H = 2.32 \text{ m.}$$

Wave pressure at the bottom of the pipeline =  $-(1026.0)(9.81)(-10.0) + (5032.5)(2.32)(0.8105) = 110,139.69 \text{ N/m}^2 = 11.014 \text{ N/cm}^2$ .

### Example 3.7

Determine the surface profile and the pressure variation at an elevation of 30.0 ft., above the seabed, for a linear wave that has a period of 6.0 sand a height of 8.0 ft. and is propagating in a constant water depth of 50.0 ft.

$$L_0 = gT^2/2\pi = (32.2)(6^2)/(2\pi) = 184.493 \text{ ft.}$$

$d/L_0 = 50/184.493 = 0.271$ ; for this value,  $d/L$  (from the given tables) = 0.2865.

$$L = 50/0.2865 = 174.53 \text{ ft.}$$

$$\begin{aligned} \text{Wave profile} = \eta &= (H/2) \cos(kx - \omega t) = (8/2) (\cos[(2\pi x/174.53) - (2\pi t/6.0)]) \\ &= 4.0 \cos(0.036x - 1.047t) \text{ ft.} \end{aligned}$$

$$\begin{aligned} \text{Wave pressure} &= -\rho gz + (\rho gH/2)[\cosh k(d+z)/\cosh(kd)]\cos(kx - \omega t) \\ &= -(64.0)(-20) + (64.0)(8.0/2)[\cosh\{(0.036)(50.0 - 20.0)\}/\cosh\{0.036(50)\}] \\ &\quad [\cos(0.036x - 1.047t)] = 1280 \pm 135.28 \cos(0.036x - 1.047t) \text{ lbf/ft.}^2 \end{aligned}$$

Note that, later on, this wave will be shown to be nonlinear, and the nonlinear computations will be performed.

### 3.4.3 NONLINEAR WAVE FORMULATION

The linear formulation for wave propagation, given in Section 3.4.2, is applicable to only small amplitude waves; this linearity would require that the ratios  $H/d$  and  $H/L$  be small compared to unity. In addition, the free surface boundary conditions were also linearized and applied at the SWL. As a result, the small amplitude wave formulation was meaningfully applied over the complete range of relative water depths ( $d/L$ ), provided that the amplitude of wave was sufficiently small. At present,

there is no single wave formulation that would apply for the whole range of water depths ( $d$ ), wave heights ( $H$ ), and wave periods ( $T$ ). A number of nonlinear wave theories have been developed by relaxing the requirements of  $H/d$  or  $H/L$  being small that would be applicable for a specific range of relative water depths ( $d/L$ ). Two types of nonlinear wave theories have been developed till date, viz., (1) wave theories based on the use of power series and (2) wave theories based on numerical procedures. In the use of power series for the nonlinear wave formulation, the velocity potential and wave amplitudes are defined by power series, with the successive term of the series becoming a corrective term for the preceding ones. By suitably truncating the power series with the inclusion of sufficient corrective terms, the complexities in the solution are avoided. Detailed information for nonlinear wave formulations could be obtained from the books of Ippen [39] and Sarpkaya and Isaacson [40].

Stokes wave formulation uses the power series procedure for characterizing the wave parameters such as  $\phi$ ,  $\eta$ ,  $u$ ,  $w$ ,  $a_x$ , and  $a_z$ . The direction of nonlinear wave propagation occurs in the forward ( $x$ ) direction, and no variation of wave parameters is assumed to occur in the  $y$  direction. Following the wave formulations given by Myers et al. [41] and Dean and Dalrymple [42], the wave potential,  $\phi$ , and wave amplitude,  $\eta$ , are represented using the perturbation approach by

$$\begin{aligned} \phi &= \xi\phi_1 + \xi^2\phi_2 + \xi^3\phi_3 + \dots \\ \eta &= \xi\eta_1 + \xi^2\eta_2 + \xi^3\eta_3 + \dots \end{aligned} \tag{3.47}$$

where  $(\phi_1, \eta_1)$  represents the linear solutions to the potential and amplitude functions,  $(\phi_2, \eta_2)$ ,  $(\phi_3, \eta_3)$  represent the corrective terms to the linear solutions of the potential function and wave amplitude, the assumed small quantity,  $\xi (= kH/2)$ , and so on.

Following the above approximating procedure, a number of higher order solutions have been obtained for the Stokes procedure, viz., second-order Stokes equation, third-order Stokes equation, etc. In this section, only the second-order perturbation solution will be presented and discussed. The Stokes second-order velocity potential function is given by

$$\begin{aligned} \phi &= (gH/2\sigma)(\cosh k(d+z)/\cosh kd)\sin(kx - \sigma t) + (3\pi CH/16)(H/L) \\ &\times (\cosh 2k(d+z)/\sinh^4(kd))\sin 2(kx - \sigma t) \end{aligned} \tag{3.48}$$

As mentioned earlier, the first term in the above equation is the wave potential function obtained for the linear case, and the second term is the corrective term that is dependent on the wave steepness term ( $H/L$ ) with its excitation frequency being twice that of the linear case. The wave surface profile is given by

$$\eta = (H/2)\cos(kx - \sigma t) + \{(\pi H/8)(H/L)\} \cdot \{\cosh kd(2 + \cosh 2kd)/\sinh^3 kd\} \cos 2(kx - \sigma t) \tag{3.49}$$

In Equation 3.49, the second term has twice the frequency of the first term and increases the surface amplitude of the wave at the crest and decreases it at the trough. When the wave is a deepwater wave (with  $d/L \geq 1/2$ ), Equation 3.49 reduces to

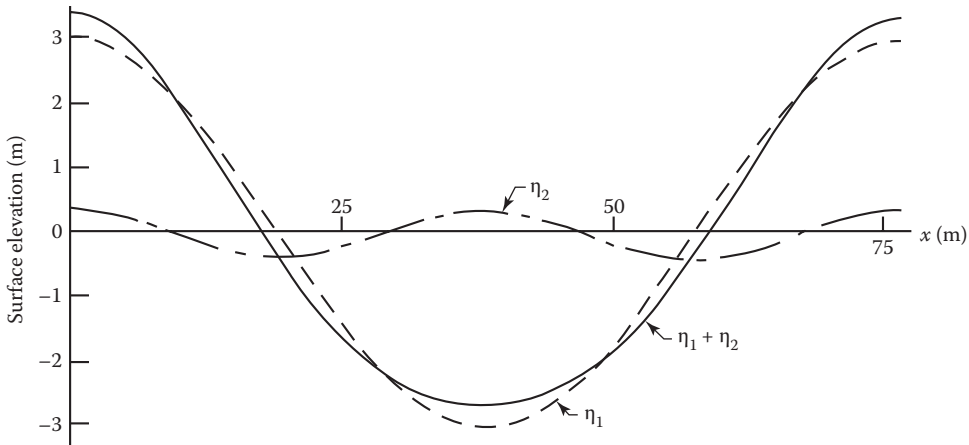
$$\eta = (H/2) \cos(kx - \sigma t) + (\pi H/4)(H/L)\cos 2(kx - \sigma t) \tag{3.50}$$

A plot of Equation 3.50 is given in Figure 3.29 [43] for a deepwater wave height of 6.0 m and a period of 7.0 sec. Using Equation 3.50, the wave amplitude ratios at the crest and trough can be obtained as

$$(a_c/H), (a_t/H) = (1/2) \pm (\pi/4)(H/L) \tag{3.51}$$

This can be easily observed from Figure 3.29.

For a limiting deepwater wave steepness ratio of  $[(H_0/L_0) \simeq 0.14]$ , it can be easily shown that Equation 3.51 reduces to  $a_c = 0.611 H$  and  $a_t = 0.389 H$ . The wave particle velocities, accelerations,



**FIGURE 3.29** Stokes second-order wave profile;  $H = 6.0$  m,  $T = 7.0$  s. (R.M. Sorensen, *Basic Wave Mechanics for Coastal and Ocean Engineers*. 1993. Copyright Wiley-VCH Verlag GmbH & Co. KGaA. Reproduced with permission.)

and displacements are given in Table 3.9. In this table, the parameters  $((u)_*, (w)_*, (a_x)_*, (a_z)_*, (\zeta)_*, (\epsilon)_*, (p)_*)$  are those obtained as  $(u, w, a_x, a_z, \zeta, \epsilon, p)$  for the linear wave formulation. The second-order terms in the particle velocities and accelerations, given in Table 3.9, would lead to kinematic asymmetries. As a consequence, the horizontal velocity component of the wave particle orbit is not closed. It is to be remembered that the last term in the function for the  $x$ -displacement  $\zeta$  has a linearly varying time component, which indicates the drifting of the particle from the initial position due to a constant drifting speed in the  $x$ -direction. This drifting speed is given as

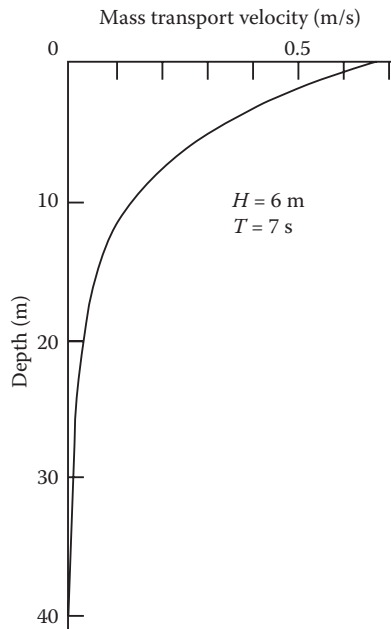
$$\bar{u} = (\pi^2 H^2 / 2TL) (\cosh 2k(d+z) / \sinh^2 kd) \tag{3.52}$$

Figure 3.30 [44] gives a plot of this drifting speed for a 6.0-m-high and 7.0-s wave. It is seen from the figure that the drifting speed of this particle at the wave surface is around 0.63 m/s; in comparison, the wave speed (or celerity) for this wave is 10.91 m/s. This mass transport velocity is a maximum at the water surface and decreases drastically below the ocean surface [44].

**TABLE 3.9**  
**Wave Particle Velocities, Accelerations, Displacements, and Pressure for Second-Order Stokes Wave**

#	Wave Parameter	Characteristic Equations for the Wave Parameter Given in Column 2
1	$u$	$(u_*) + (3(\pi H)^2 / 4TL) (\cosh 2k(d+z) / \sinh^4 kd) \cos 2(kx - \sigma t)$
2	$w$	$(w_*) + (3(\pi H)^2 / 4TL) (\sinh 2k(d+z) / \sinh^4 kd) \cos 2(kx - \sigma t)$
3	$a_x$	$(a_x)_* + (3\pi^3 / T^3) (H^2 / L) (\cosh 2k(d+z) / \sinh^4 kd) \sin 2(kx - \sigma t)$
4	$a_z$	$(a_z)_* + (3\pi^3 H^2 / T^2 L) (\sinh 2k(d+z) / \sinh^4 kd) \cos 2(kx - \sigma t)$
5	$\zeta$	$(\zeta)_* + (\pi H^2 / 8L \sinh^2 kd) (1 - 3 \cosh 2k(d+z) / 2 \sinh^2 kd) \sin 2(kx - \sigma t) + (\pi H^2 / 4L) / (\cosh 2k(d+z) / \sinh^2 kd) (\sigma t)$
6	$\epsilon$	$(\epsilon)_* + (3\pi H^2 / 16L) (\sinh 2k(d+z) / \sinh^4 kd) \cos 2(kx - \sigma t)$
7	$p$	$(p)_* + (3\pi \rho g H^2 / 4L \sinh 2kd) (\cosh 2k(d+z) / \sinh^2 kd - (1/3)) \times \cos 2(kx - \sigma t) - (\pi \rho g H^2 / 4L \sinh 2kd) (\cosh 2k(d+z) - 1)$





**FIGURE 3.30** Mass transport speed in Stokes second-order formulation;  $H = 6.0$  m,  $T = 7.0$  s. (R.M. Sorensen: *Basic Wave Mechanics for Coastal and Ocean Engineers*, p. 60. 1993. Copyright Wiley-VCH Verlag GmbH & Co. KGaA. Reproduced with permission.)

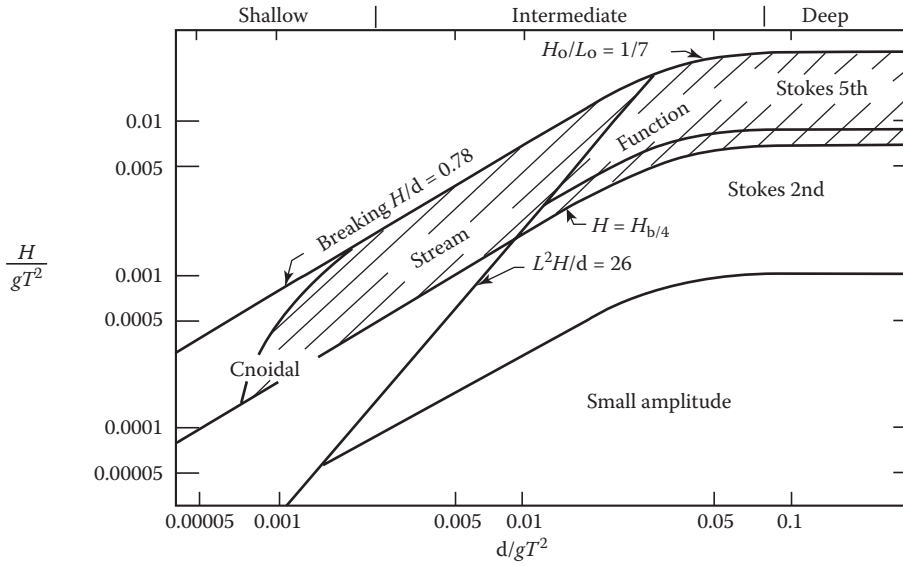
A number of other theories have been developed to characterize the wave behavior in the various regimes of transitional and shallow waters. Besides the higher order Stokes waves (fifth and sixth order), Cnoidal wave theory [45] for finite height waves in shallow waters, solitary wave theory for translatory shallow water waves developed by Russell [46] and Rayleigh [47], and numerical (stream function) wave theory developed by Dean [48] are some of the notable ones.

The ranges of applicability of different wave theories, developed over the years, have been compared in Figure 3.31 [49] as a function of  $H/gT^2$  and  $d/gT^2$ . It is always not possible to specify the precise ranges in which the different waves mentioned earlier are valid. It can be said that the small amplitude wave theories are valid for deepwater and transitional (intermediate depth) waves if the wave is not very steep. From Figure 3.31, it can be observed that when the value of  $H/gT^2$  is larger than 0.001, the Stokes waves should be employed. The higher order Stokes waves are good for very steep waves in deepwater, and for transitional waves, when the wave is not very steep. For steeper waves in shallow water and in parts of transitional water depths, the Cnoidal wave theory gives very good results. For steep waves in any water depth, numerical wave theory always gives very good results. Figure 3.31 also gives the range of wave heights beyond which the waves will break.

**Example 3.8**

Consider Example 3.4 and show that it is a nonlinear wave. Compute the nonlinear wave profile and wave pressure at the specified point in Problem 3.4. Using Figure 3.31, the suitable wave can be determined:

$$d/gT^2 = 50.0/[(32.2)(6^2)] = 0.431; \text{ also } H/gT^2 = 8/[(32.2)(6^2)] = 0.0069.$$



**FIGURE 3.31** Recommended ranges for selected wave theories. (R.M. Sorensen: *Basic Wave Mechanics for Coastal and Ocean Engineers*, p. 60. 1993. Copyright Wiley-VCH Verlag GmbH & Co. KGaA. Reproduced with permission.)

Using these values, it can be determined from Figure 3.31 that we should use Stokes second-order wave theory:

$$\eta = (H/2)\cos(kx - \sigma t) + \{(\pi H/8)(H/L)\} \cdot \{\cosh kd(2 + \cosh 2kd)/\sinh^3 kd\} \cos 2(kx - \sigma t)$$

From earlier calculations, the first term in the above equation becomes

$$\eta_1 = 4.0 \cos (0.036x - 1.047t)$$

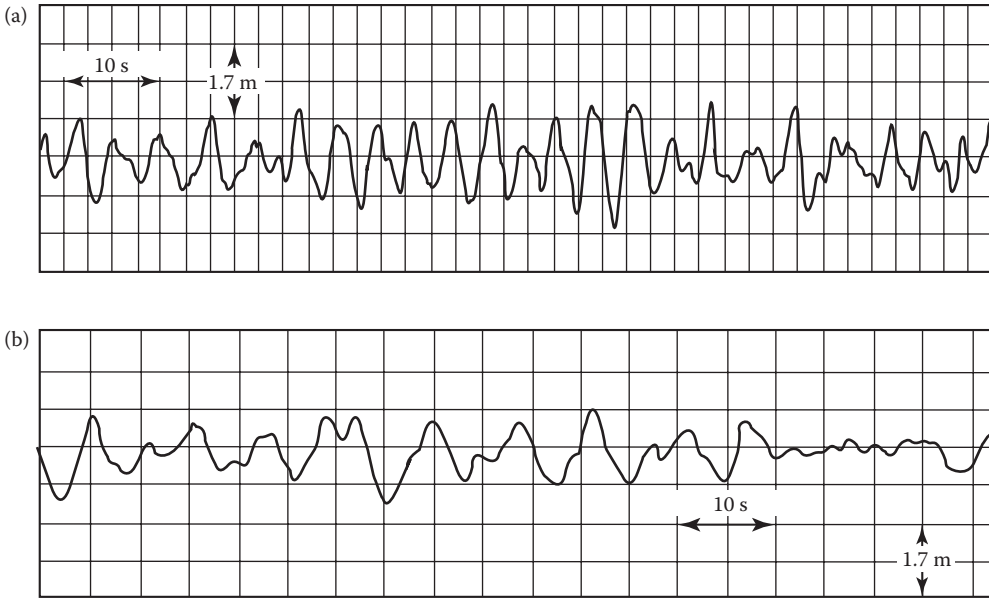
The second term becomes  $\eta_2 = \{(\pi(8)/8)\}(8/174.53) \cosh \{(2\pi)(50/174.53)\}[2.0 + \cosh \{(2\pi)(50/174.53)\}/\sinh^3 \{(2\pi)(50/174.53)\}] \cos 2(0.036x - 1.047t) = (0.144)(3.1076)\{(2.0 + 3.1076)/2.942^3\} \cos 2(0.036x - 1.047t) = 0.089 \cos 2(0.036x - 1.047t)$

$$\eta = \eta_1 + \eta_2 = 4.0 \cos (0.036x - 1.047t) + 0.090 \cos 2(0.036x - 1.047t) - \text{wave profile}$$

Since the wave height is not large, the corrections are also very small. In a similar manner, the wave pressure can also be computed using the values given in Table 3.9.

### 3.4.4 WAVE STATISTICS AND SPECTRAL CHARACTERIZATION

In the earlier descriptions given in Sections 3.3.1 to 3.3.3, the wave was characterized as regular monochromatic waves (or its multiples) that can be considered in a deterministic sense. Surface waves were considered from the standpoint of a mathematical description of the ocean surface; moreover, the still-water (or mean sea) level was assumed to be known in the analysis.



**FIGURE 3.32** Wave amplitude versus time history: (a)  $H_s = 1.7$  m;  $T_s = 4.0$  s; and (b)  $H_s = 1.7$  m and  $T_s = 8.0$  s. (From US Army Corps of Engineers, Coastal Engineering Research Center, 1984. Courtesy of Coastal and Hydraulics Laboratory.)

In this section, wave characterization is derived from the observation of ocean waves from nature. Wind-generated ocean waves generally contain waves of many amplitudes (or heights) and many periods. Typical wave records obtained from on-site measurements indicate that the wave heights (or amplitudes), periods, and even directions keep on changing. For instance, Figure 3.32 shows two time histories of waves of the same significant wave height of 1.70 m, but of two different significant wave periods of 4.0 and 8.0 s, respectively. In the figure, the ocean wave surface fluctuates in a random (or irregular) manner, and one needs to identify certain essential wave parameters that can characterize the wave surface. Some of these parameters, which are used to characterize the irregular ocean behavior, are obtained from the data analysis of ocean wave surface profiles; the important ones among these statistical parameters are significant wave height, significant wave period, and wave spectra.

**3.4.4.1 Theoretical Prediction Based on Statistical Characterization of Waves**

The significant wave height ( $H_{1/3}$  or  $H_s$ ) is the average wave height of the one-third highest of all the waves and was observed from measurements in the field to be equal to average height of waves estimated by an experienced observer. In a similar manner, the significant wave period ( $T_s$ ) is defined as the average period of the highest one-third of the wave periods measured at site, whose crests are above and troughs are below the MSL (zero up-crossing method). As shown in Equation 3.46, the energy density of a wave is given by  $(\rho g H^2/8)$ ; consequently, the wave energy spectrum is defined as the summation of the squared heights of all the wave frequency components (multiplied by  $\rho g/8$ ) present in the wave history obtained at the site. Generally, the wave height spectrum is used instead of the wave energy spectrum to designate the characteristic of an irregular sea; in this formulation, the term  $\rho g$  is removed from the wave energy spectrum, and the wave height spectrum is defined as the one-eighth the summation of the squared heights of all the frequency components in the wave history at the site.

Since the wave amplitude (= height/2) versus time history, seen in Figure 3.32a and b [50], contains many waves, each having its own amplitude (or height) and frequencies, it can be represented in a series form as

$$\eta(t) = \sum_{m=1}^M (H_m/2) \cos(\sigma_m t - \delta_m) \tag{3.53}$$

where  $H_m$  is the height of each wave component,  $\sigma_m$  is the frequency of each wave, and  $\delta_m$  is the phase difference present in each wave component. Let us say that a wave field record contains 100 or more frequency components of wave heights, and these heights are arranged in an increasing order of the heights. It has been observed from the analyses of wave data from a number of sources that these would typically yield a distribution of the type shown in Figure 3.33. This distribution of the number of occurrences (or the probability) versus the height of the individual wave component is observed to fit closely to the statistical distribution given by Rayleigh [51], as shown in Figure 3.33 [52]; hence, it is represented by a Rayleigh distribution, given by

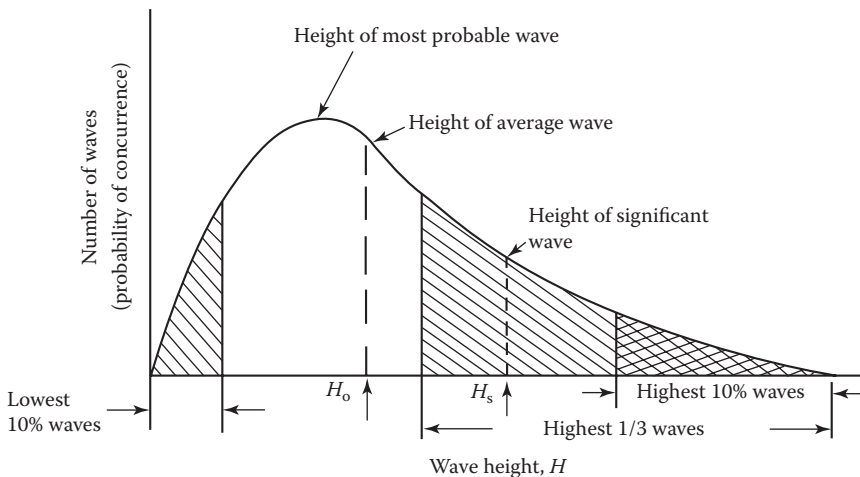
$$p(H) = (2H/(H_{rms})^2) e^{-(H/H_{rms})^2} \tag{3.54}$$

The cumulative probability distribution  $P(H)$ , that is, the percentage of waves having a height equal to or less than  $H$ , is given by

$$P(H) = \int_0^H p(H) dH = 1 - e^{-(H/H_{rms})^2} \tag{3.55}$$

The percentage of waves having a height greater than a specified wave height is given by

$$1 - P(H) = e^{-(H/H_{rms})^2} \tag{3.56}$$



**FIGURE 3.33** Wave height versus number of occurrences, represented by Rayleigh distribution. (J.F. Wilson: *Dynamics of Offshore Structures*, p. 159. 1984. Copyright Wiley-VCH Verlag GmbH & Co. KGaA. Reproduced with permission.)

This distribution is used to predict theoretically (or forecast) the wave height and period properties. On the basis of the above distribution, the wave field from which the data were obtained could be characterized as given below:

$$\begin{aligned}
 \text{Root-mean-squared value, } H_{\text{rms}} &= \sqrt{(1/M) \sum_{m=1}^M H_m^2} \\
 \text{Average wave height, } H_0 \text{ (or } \bar{H}) &= 0.886 H_{\text{rms}} = 0.625 H_s \\
 \text{Significant wave height, } H_s &= 1.416 H_{\text{rms}} \\
 \text{Average of the highest 10\% of all waves, } H_{1/10} &= 1.27 H_s = 1.80 H_{\text{rms}} \\
 \text{Average of the highest 1\% of all waves, } H_{1/100} &= 1.67 H_s = 2.37 H_{\text{rms}} \\
 H_{\text{max}} &= 0.707 H_s \sqrt{\ln(N)}, \text{ or } 2.0 H_s, \text{ with } N = \text{number of waves in the record}
 \end{aligned}
 \tag{3.57}$$

**Example 3.9**

Based on the analysis of wave records at a near-shore location, the significant wave height  $H_s$  was estimated to be 5.0 m. Determine (1) the average of the highest 10.0% of all waves that are likely to occur at the site and (2) the average of the highest 1.0% of all the waves that are likely to occur at the site.

$$\begin{aligned}
 H_{1/10} &= 1.27 H_s = (1.27)(5.0) = 6.35 \text{ m.} \\
 H_{1/100} &= 1.67 H_s = (1.67)(5.0) = 8.35 \text{ m.}
 \end{aligned}$$

The same results can be obtained by using the results given in Figure 3.34.

In Figure 3.34, the x-axis is given as  $\hat{U}/H_{\text{rms}}$ , and the y-axis is given as the cumulative probability. Consequently, for a probability of 0.10, curve *b* gives  $(H_{1/10})/H_{\text{rms}} = 1.80$ .

$$\text{Significant wave height} = H_s = 1.416 H_{\text{rms}}, \quad H_{\text{rms}} = 0.706 H_s$$

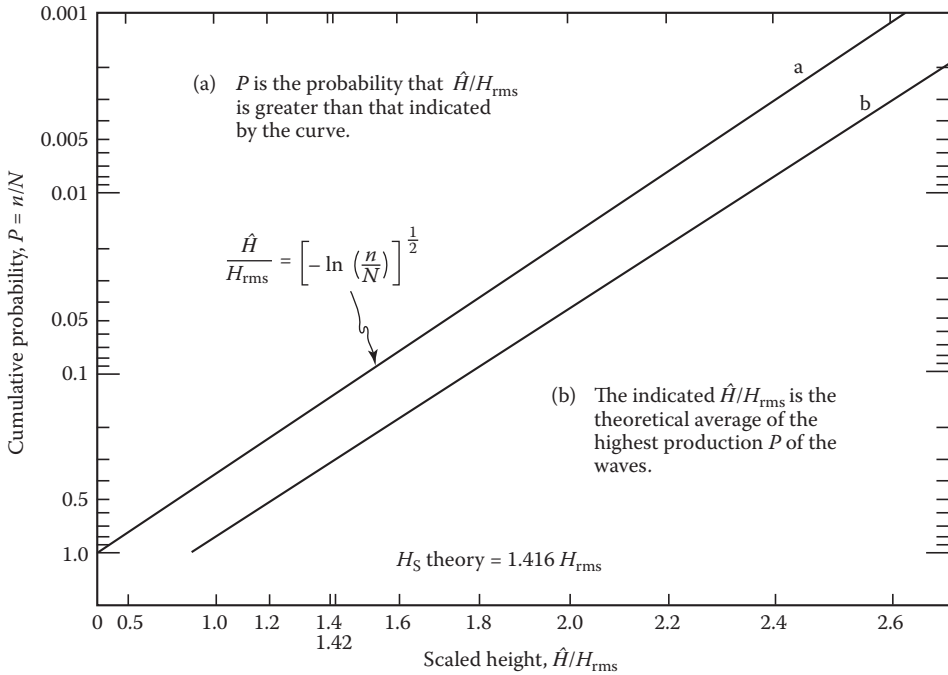
This leads to  $(H_{1/10})/H_s = (1.80)(0.706) = 1.27$ , which will lead to the same results as given earlier. In a similar manner, it can be shown that  $(H_{1/100})/H_{\text{rms}} = 2.36$ , from curve *b* of Figure 3.34; this once again will lead to the result  $(H_{1/100})/H_s = (2.36)(0.706) = 1.67$ , which will lead to the same results as before.

**Example 3.10**

A statistical wave height versus number of waves obtained from a wave time history data are given below in tabular format. Using the data, determine the heights of average wave, significant wave,  $H_{1/10}$ , and  $H_{1/100}$ .

Wave Height (ft.)	2.0	4.0	6.0	8.0	10.0
Number of waves	45	35	25	5	2
Total number of waves = 112					

Number of waves constituting the significant waves = 1/3 of the highest waves =  $112/3 \sim 37$  waves.  
 Number of waves constituting the highest 1/10 waves =  $112/10 = 11$  waves.  
 Number of waves constituting the highest 1/100 waves =  $112/100 \sim 1$  wave.



**FIGURE 3.34** Theoretical wave height distribution due to Rayleigh: (a) probability  $n$  of the waves higher than the magnitude of the highest fraction of waves considered and (b) theoretical average of the highest fraction of waves. (From Shore Protection Manual, Vol. II, 1984. Courtesy of the US Army Corps of Engineers, Washington, DC.)

Average wave height =  $(1/(\text{number of waves})) \sum (\text{number of waves})(\text{wave height})$   
 $= (1/112)\{(45)(2.0) + (35)(4.0) + (25)(6.0) + (5)(8.0) + (2)(10.0)\} = 3.93 \text{ ft.}$   
 Average of highest 1/3 waves =  $(1/37)\{(2)(10.0) + (5)(8.0) + (25)(6.0) + (5)(4.0)\} = 6.22 \text{ ft.}$   
 Average of highest 1/10 waves =  $(1/11)\{(2)(10) + (5)(8.0) + (4)(6.0)\} = 7.64 \text{ ft.}$   
 Average of the highest 1/100 waves =  $(1/1)\{(1)(10.0)\} = 10.0 \text{ ft.}$   
 Comparing with the last sub-equation given in Equation 3.57,  $H_{\text{max}} = 0.707H_s[\ln(N)]^{(1/2)}$   
 $= 9.55 \text{ m (slightly less than } 10.0 \text{ m).}$

*Alternate procedure:* The above values can also be computed in another manner. Using the first sub-equation given in Equation 3.57, viz.,

$$H_{\text{rms}} = \sqrt{(1/M) \sum_{m=1}^M H_m^2}$$

$$H_{\text{rms}} = [(1/112)\{(45)(2^2) + (35)(4^2) + (25)(6^2) + (5)(8^2) + (2)(10^2)\}] = 4.392 \text{ ft.}$$

$$H_s = 1.416 H_{\text{rms}} = 6.22 \text{ ft.}$$

$$H_{1/10} = 1.80 H_{\text{rms}} = 7.91 \text{ ft.}$$

$$H_{1/100} = 2.37 H_{\text{rms}} = 10.41 \text{ ft.}$$

Note that since the number of waves is very small, the  $H_{1/10}$  and  $H_{1/100}$  waves are a little higher than the previous values; if larger number wave data, with finer intervals of wave heights, were available, the computed values will be much closer than these values.

Figure 3.34 [53] gives the relationship between the Rayleigh probability distribution and the theoretical wave heights predicted from the assumption of the validity of Rayleigh’s distribution to waves. The upper curve (a) shows the probability  $P$  (given by Equation 3.56) that any wave height ( $\hat{H}/H_{rms}$ ) is greater than the magnitude of the highest fraction of waves considered in curve b. For instance, it can be seen that for a value of  $H_s/H_{rms}$  equal to 1.416, the upper figure indicates a value of 0.135, showing that 13.5% of the waves are greater than the significant wave height. The lower curve (b) shows that for the value of  $H_s/H_{rms}$  equal to 1.416, the probability  $n$  of the highest percentage of waves is 0.333 (or 33.33%).

The mean zero-crossing period ( $\bar{T}$ ) is obtained from the mean time between up-crossings of the mean water level. It is usually estimated after the extreme wave height has been determined on the basis of steepness of the higher waves in the area. Using spectral analysis, the  $n$ th spectral moment can be represented by

$$m_n = \int_0^\infty S_\eta(f) f^n df \tag{3.58}$$

Using the derivation given in Equation 3.58, the average zero-up-crossing period,  $T_z$ , can be obtained:

$$\bar{T} = \sqrt{(m_0/m_2)} \tag{3.59}$$

Usually a range of periods should be considered with the extreme wave height. According to the UK Department of Energy Guidance Notes [54], the range of mean zero-crossing periods should be

$$3.2\sqrt{H_{s50}} < \bar{T} < 3.6\sqrt{H_{s50}} \tag{3.60}$$

and the individual wave periods would range between

$$1.05 \bar{T} < T < 1.40 \bar{T} \tag{3.61}$$

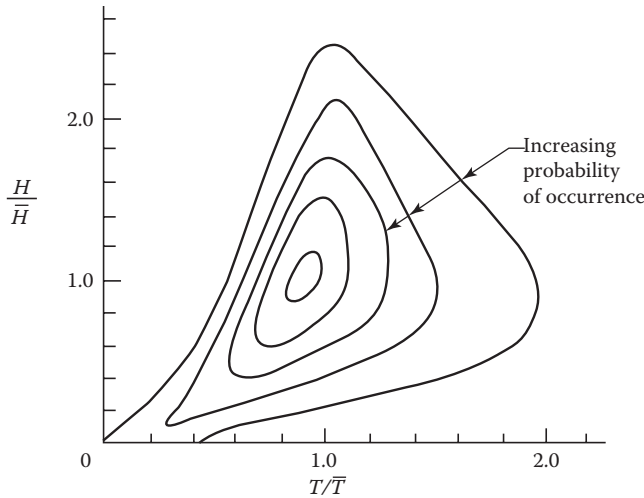
If regular wave measurements (e.g., 20-min measurements of wave amplitude–time history made every 3 h for determining  $H_s$ ) are made over a large period, then it is reasonable to assume that available statistical methods could be used to estimate the extreme values of wave heights and periods. The wave amplitude (or height)–time history can be visualized to be composed of a large number of regular sinusoidal waves (or wavelets), each superimposed over the other with or without a phase lag, to obtain the actual wave amplitude–time history.

As one can observe from Equation 3.60, the wave periods and the wave heights are related and as such have a joint probability distribution relationship. Figure 3.35 [55] shows the joint probability distribution of wave heights and wave periods. The distribution is a bell-shaped curve with its peak at the average period ( $T/\bar{T} \simeq 1.0$ ), indicating that most of the up-crossing periods are clustered around the average wave period. Also it is seen that for smaller wave heights, the distribution of wave periods is rather wide in comparison with the higher wave heights. It has also been observed that the average wave period is less stationary than the significant period,  $T_s$  (equal to the average of the highest one-third of wave periods), or the spectral peak period,  $T_p$ . It is recommended from empirical studies that  $T_s = 0.95T_p$ .

Generally, the energy in the ocean waves is direction-dependent; the energy is dependent on wave amplitudes, periods, phases, and directions of wave motion. For the sake of ease in description, only one-directional waves are considered in the following sections. Using Equation 3.53 to represent the wave amplitude (or height) versus time history record, the mean total energy in the wave, per unit surface area, as given by Equation 3.46, can be written as

$$E = (\rho g/8)(H_1^2 + H_2^2 + H_3^2 + H_4^2 + \dots H_n^2 + \dots) \tag{3.62}$$



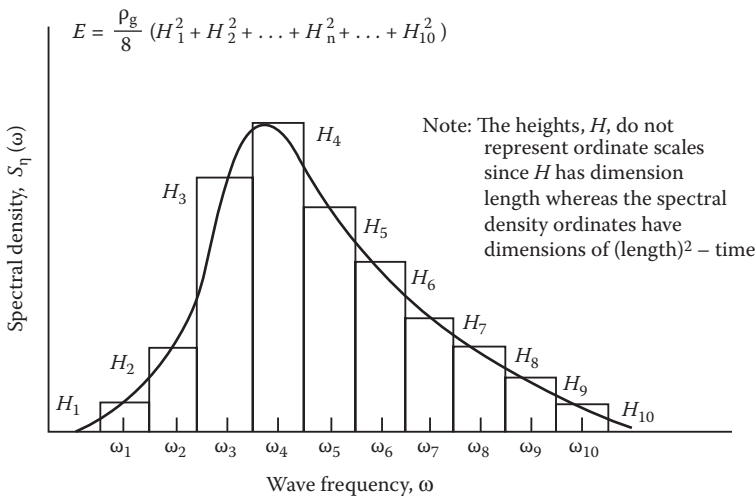


**FIGURE 3.35** Joint wave height versus period probability distribution. (R.M. Sorensen: *Basic Wave Mechanics for Coastal and Ocean Engineers*, p. 129. 1993. Copyright Wiley-VCH Verlag GmbH & Co. KGaA. Reproduced with permission.)

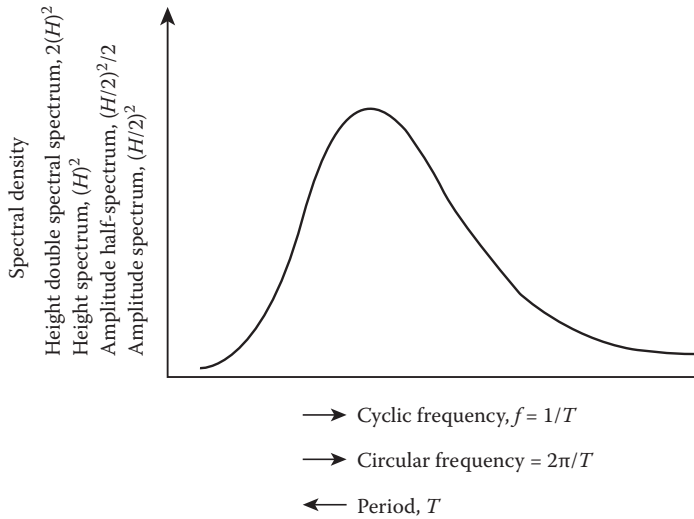
where  $(H_1, H_2, H_3, H_4, \dots, H_n, \dots)$  are the wave heights associated with the given discrete circular frequencies  $(\omega_1, \omega_2, \omega_3, \omega_4, \dots, \omega_n, \dots)$  or periods  $(T_1, T_2, T_3, T_4, \dots, T_n, \dots)$ . If Equation 3.62 is plotted in a graphical format, then it will appear as shown in Figure 3.36 [56].

Instead of using harmonic analysis for the determination of wave heights (or amplitudes) and periods, the available time history record can be digitized, and discrete Fourier transform procedures can be utilized to get the wave energy or wave height (or amplitude) spectrum.

The wave height (or amplitude) spectrum is shown in Figure 3.37 [57], where the plot uses three measures of  $\omega$  (circular frequency =  $2\pi/T$ , in radians per second),  $f$  (cyclic frequency =  $1/T$ , in hertz), and period ( $T$ , in seconds) to characterize the amplitude (or height) spectrum. In the figure, the term  $\rho g$  has been removed in the spectral descriptions given. Figure 3.37 also shows different types of representations used to characterize the amplitude of the spectral density function; the relationships



**FIGURE 3.36** Simplified representation of wave energy spectrum. (J.F. Wilson: *Dynamics of Offshore Structures*, p. 162. 1984. Copyright Wiley-VCH Verlag GmbH & Co. KGaA. Reproduced with permission.)



**FIGURE 3.37** Wave height (or amplitude) spectrum. (J.F. Wilson: *Dynamics of Offshore Structures*, p. 163. 1984. Copyright Wiley-VCH Verlag GmbH & Co. KGaA. Reproduced with permission.)

**TABLE 3.10**  
**Relationship between Various Spectral Density Descriptions**

#	Type of Spectral Density Curve	Characteristic Properties
1	Amplitude spectrum: the formulations are due to Pierson and Pierson, Neumann, and James	$H_s = 2.83\sqrt{\text{area under the amplitude spectrum curve}}$
2	Amplitude half-spectrum	$H_s = 4\sqrt{\text{area under the amplitude half-spectrum curve}}$
3	Height spectrum	$H_s = 1.416\sqrt{\text{area under the height spectrum curve}}$
4	Height double spectrum	$H_s = \sqrt{\text{area under the height double spectrum curve}}$

between these various descriptive measures, such as amplitude, amplitude half, height, and height double spectrum are given in Table 3.10.

A number of different semiempirical wave spectral density formulations have been derived using the available wave data. Although there are some differences in the formulations given by various researchers for the wave spectra they proposed, the generic form has been

$$S_{\eta}(\omega) = A_0 \omega^{-m} e^{-B\omega^{-n}} \tag{3.63}$$

with  $m = 5$  and  $n = 4$ . The commonly used wave spectra include spectral density formulations for fetch-unlimited and fetch-limited deepwater ones. The differences between these spectral formulations have been based on the parameter used to describe these spectral formulations. Some use the wind speed, whereas others use wave height and period, fetch length, and some other parameters. Some of the commonly used spectral descriptions are given in Table 3.11. It must be stated that the spectral density descriptions given in Table 3.11 are for amplitude half-spectrum, and as such, the significant wave height is equal to four times the area under the spectral density curve, as shown in Table 3.10. For greater details concerning the different spectral descriptions given in Table 3.11 and their characterization, the Shore Protection Manual [58] and the book by Sorensen [59] should be consulted.

**TABLE 3.11**  
**Available Spectral Density Formulations for Deepwater and Finite-Depth Waters**

#	Particulars	Form of Equation
1	Bretschneider spectrum	$S_{\eta}(T) = \left( \alpha g^2 / (2\pi)^4 \right) T^3 e^{-(0.675(gT/2\pi U F_2)^4)}$ <p>with <math>\alpha = 3.437 \left( F_1^2 / F_2^2 \right)</math>, <math>F_1 = g\bar{H}/U^2</math>, <math>F_2 = (g\bar{T}/2\pi U)</math>,  <math>U</math> = wind speed, <math>\bar{H}</math> = average wave height, <math>\bar{T}</math> = average wave period</p>
2	Ochi's spectrum	$S_{\eta}(\omega) = (1.25/4) \left( \omega_m^4 / \omega^5 \right) H_s^2 e^{-1.25 (\omega_m/\omega)^4}$ <p>with <math>\omega_m = (2\pi/T_m)</math></p>
3	Pierson–Moskowitz wind speed spectrum	$S_{\eta}(f) = \left( \alpha g^2 / (2\pi)^4 f^5 \right) e^{-0.74(g/2\pi U f)^4}$ , with $\alpha = (8.1)(10^{-3})$ , and wind speed measured at a height of 19.5 m, above mean sea level
4	Pierson–Moskowitz wave height-period spectrum	$S_{\eta} = (8.1)(10^{-3}) g^2 / \omega^5 e^{-(B/\omega^4)}$ , where $B = 0.74(g/U)^4 = 3.11/H_s^2$
5	ITTC formula	$S_{\eta}(\omega) = (A'/\omega^2) e^{-(B/\omega^2)}$ , with $A' = 488H_s^2/T_m^4$ , $B = 1948/T_m^4$
6	Fetch-limited JONSWAP spectrum (Joint North Sea Wave Project)	$S_{\eta}(f) = \left( \alpha g^2 / \{ (2\pi)^4 f^5 \} \right) e^{-1.25 (f_p/f)^4} \cdot \gamma^a$ , with $a = e^{-[(f-f_p)^2/2\sigma^2 f_p^2]}$ , $\sigma = 0.07$ when $f < f_p$ ; $\sigma = 0.09$ when $f \geq f_p$ ; $\alpha = 0.076(gF/U^2)^{-0.22}$ , $f_p = (3.5g/U)(gF/U^2)^{-0.33}$ , with $\gamma$ as the spectral shape factor, $1.6 \leq \gamma \leq 6.0$ , with $\gamma_{\text{recommended}} = 3.3$
7	TMA spectrum-modified JONSWAP spectrum for finite water depths	$S_{\eta}(f)_{\text{TMA}} = S_{\eta}(f)_{\text{JONSWAP}} \cdot \Phi(f, d)$ where $\Phi(f, d) = (2\pi f^2 d)/g$ for $f < (2\pi d/g)^{-0.5}$ and $\Phi(f, d) = 1 - 0.5[2 - (2\pi f)(d/g)^{0.5}]^2$ for $f > (2\pi d/g)^{-0.5}$

#### 3.4.4.2 Wave Prediction from Wind Characteristics

For simpler wave prediction models, one needs to know the average values of wind speed, fetch length, and the duration of the wind. The wind data should be obtained from the wind speed/direction records supplied for the location of interest by the local or national meteorological office; this would imply that the measurements were made over the water for a sufficient length of time to do a proper analysis. The wind speeds can also be obtained from the upper level atmospheric pressure contours by experienced forecasters. Some corrections should be made in these data before they are used for making wave predictions, viz., correction of the obtained wind speeds to the standard 10.0 m above the ground level and corrections for the averaging time for the wind measurements used in the study.

In the wind speed corrections for the proper height, Equation 3.6, 3.11, or 3.12 could be utilized. The wind speeds also need to be corrected for the averaging time used in the study to arrive at the specified wind speed. As per the Shore Protection Manual [35], the adjustments are made as per the following equations, viz.,

$$\begin{aligned} (U_t/U_{3600}) &= 1.277 + 0.296 \tanh[0.9 \log_{10}(45/t)], \text{ for } 1.0 \text{ s} < t < 3600 \text{ s or} \\ (U_t/U_{3600}) &= 1.533 - 0.15 \log_{10}(t), \text{ for } 3600 \text{ s} < t < 36,000 \text{ s} \end{aligned} \quad (3.64)$$

where  $t$  is the averaging time in seconds,  $U_t$  is the wind speed at the averaging time of  $t$  seconds, and  $U_{3600}$  is the average wind speed measured over 1 h.

During the earlier part of the twentieth century, the prediction model proposed by Sverdrup, Munk, and Bretschneider (the SMB method)—see Table 3.11—was used to predict the wave heights and wave periods from the measured wind data. The method is based on the dimensional analysis of deepwater wave generation relation given by

$$(H_s, T_s) = \text{function of } (U, F, t_d, g) \tag{3.65}$$

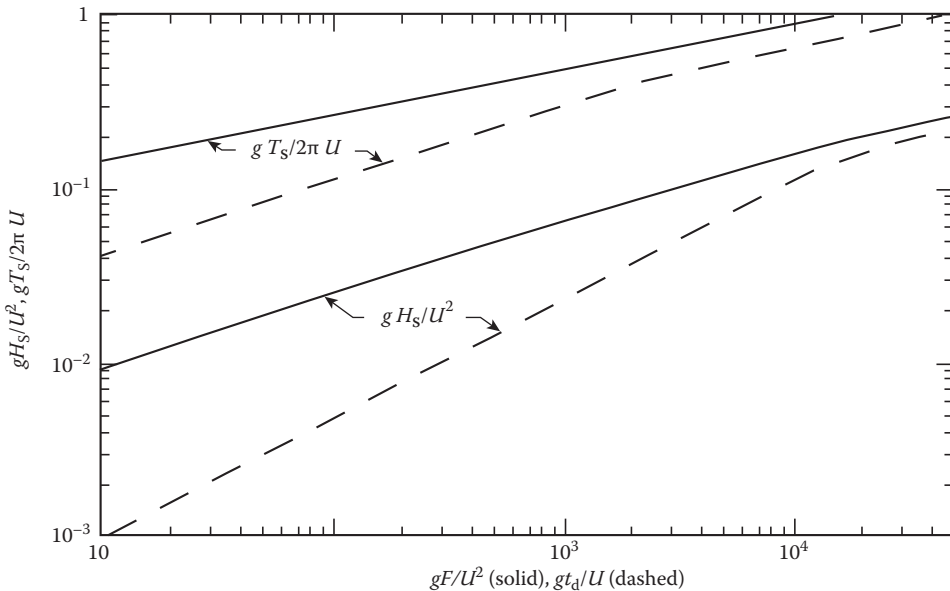
where  $U$  is the measured average wind velocity at a height of 10.0 m above the mean water surface,  $F$  is the length of fetch over which a constant velocity of wind  $U$  blows, and  $t_d$  is the time duration during which this constant speed wind blows over the location. The dimensional analysis yields the following two equations for predicting the significant wave height and significant wave period:

$$\left. \begin{aligned} (gH_s/U^2) \\ (gT_s/2\pi U) \end{aligned} \right\} = \text{function of } (gF/U^2, gt_d/U) \tag{3.66}$$

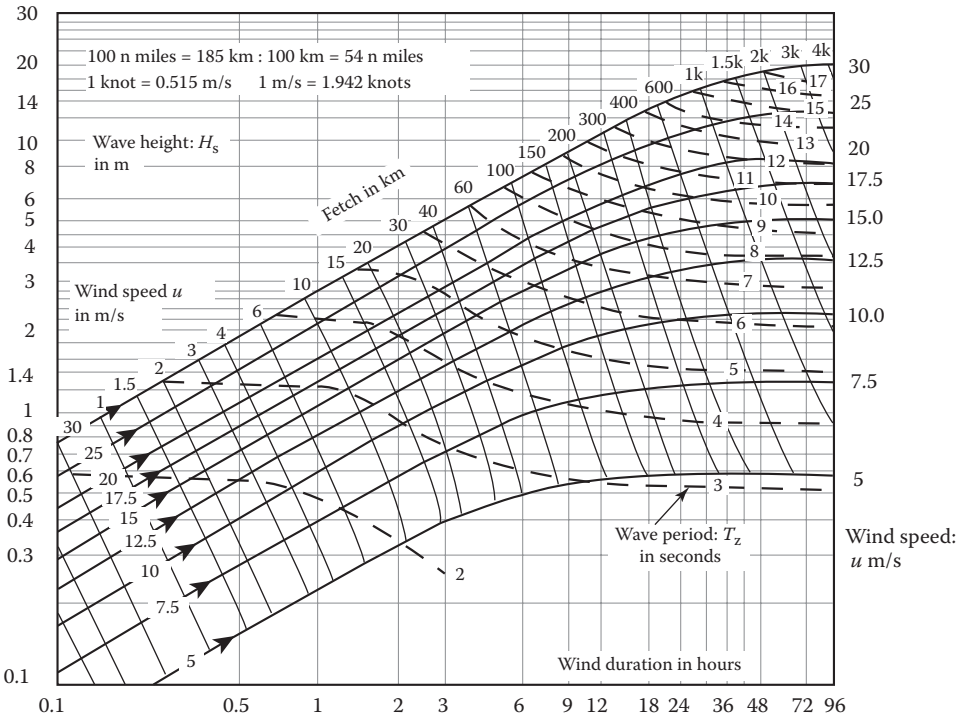
The relationship defined by Equation 3.66 is given in a graphical form by Figure 3.38.

Once the values of  $gF/U^2$  and  $gt_d/U$  are known, then the values of  $gH_s/U^2$  can be determined from the corresponding curves of Figure 3.38 [60]. Thereafter, the values of  $H_s$  and  $T_s$  can be computed.

An alternate procedure has been developed by the World Meteorological Organization (WMO) to predict the significant wave height  $H_s$  and the mean zero-crossing wave period  $\bar{T} \equiv T_z$ , depending on the measured parameters such as fetch length ( $F$ ), average wind speed ( $U$ ), and wind duration ( $t_d$ ). Figure 3.39 [61] gives the plot developed by WMO. By traversing along the corresponding average wind speed and wind duration direction, the intersecting point along the fetch can be obtained. The location of the intersecting point will give the corresponding values of  $H_s$  and  $\bar{T}$ .



**FIGURE 3.38** Growth of wave spectra along a fetch. (R.M. Sorensen: *Basic Wave Mechanics for Coastal and Ocean Engineers*, p. 149. 1993. Copyright Wiley-VCH Verlag GmbH & Co. KGaA. Reproduced with permission.)



**FIGURE 3.39** Manual wave-forecasting diagram. (From N.D.P. Barltrop and A.J. Adams, *Dynamics of Fixed Marine Structures*, Butterworth-Heinemann Ltd., Oxford, UK, p. 270, 1991. With permission.)

**Example 3.11**

The wave climate at a particular offshore location is represented by the Pierson–Moskowitz wind speed spectrum, with a wind speed of 30.9 m/s. Determine the significant wave height generated by this spectral representation.

The Pierson–Moskowitz wind speed spectrum is taken from Table 3.11:

$$S_{\eta}(f) = (\alpha g^2 / (2\pi)^4 f^5) e^{-0.74(g/2\pi U f)^4}, \text{ with } \alpha = (8.1)(10^{-3}),$$

and wind speed measured at a height of 19.5 m, above mean sea level.

Solving the above equation using numerical integration, and using the values given for significant wave height in Table 3.10, the magnitude of the significant wave height for the Pierson–Moskowitz spectrum can be determined.

The RMSS (root mean of sum of squares or root mean square) value for the Pierson–Moskowitz spectrum is ~6.17 m.

Significant wave height (from Table 3.10) = (2.83)(6.17) = 17.461 m.

**Example 3.12**

A wind with a sustained speed of 60.0 knots blows over a 400.0 nautical mile long fetch for 18.0 h. Determine the significant wave height and period at the end of the fetch (at  $t = 18.0$  h). Compare the above values against the WMO forecasting diagram (1 knot = 1 nautical mile per hour = 1.152 mi./h = 1.854 kmph).

$$U = (60)(1854) / \{60(60)\} = 30.9 \text{ m/s}$$

Using Equation 3.66,

$$gF/U^2 = (9.81)(400)(1854)/(30.9)^2 = (7.619)(10^3)$$

$$gt_d/U = (9.81)(18)(60)(60)/30.9 = 20,572$$

From Figure 3.38, for the above value of  $gF/U^2$ ,

$$gH/U^2 = 0.141 \text{ and } gT/(2\pi U) = 0.86$$

Also from Figure 3.38, for the above value of  $gt_d/U$ ,

$$gH/U^2 = 0.135 \text{ and } gT/(2\pi U) = 0.835$$

Hence, the second condition, namely, the duration-limited condition, controls the wave development conditions.

$$H (= H_s) = (0.135)(30.9)^2/9.81 = 13.14 \text{ m}$$

$$T (= T_s) = (0.835)(2\pi)(30.9)/9.81 = 16.53 \text{ s}$$

Using the WMO prediction diagram (Figure 3.39),

for a value of  $F = (400)(1854/1000) = 741.6 \text{ km}$  and  $U = 30.9 \text{ m/s}$ ;  $H_s \sim 14.5 \text{ m}$  and  $T_s \sim 15.2 \text{ s}$

for a value of  $t_d = 18.0 \text{ h}$ ,  $H_s \sim 13.0 \text{ m}$ ;  $T_s \sim 13.2 \text{ s}$

Hence, this value controls.

Note that the WMO prediction gives a much lower value for the significant wave period, whereas the significant wave height is almost the same.

### 3.5 OCEAN CURRENTS

#### 3.5.1 INTRODUCTION TO OCEAN CURRENTS

Currents are generated due to the horizontal movement of water, resulting from a number of different sources such as (1) tidal motion (tidal currents); (2) wind drag forces exerted on top of the ocean surface (wind currents); (3) global circulation caused by temperature differences between various ocean thermal regimes and Coriolis effects (e.g., Gulf Stream); (4) river discharge (river or hydraulic currents); (5) internal waves (generated by density gradients caused by salinity or thermal differences); (6) eddies generated in the horizontal velocity gradients transverse to the global circulation; and (7) shelf edge currents (caused by thermal differences causing density gradients and water surface equilibrium caused by density differences between the equator and poles). In terms of their influence on ocean structures, the first four impose the major drag forces on them and as such need to be considered in any analysis. Currents impose drag forces on fixed or moored or floating ocean structures and modify their motions. Ocean currents also transport ocean ice and debris from one location to another, produce scouring or deposition of ocean bottom material, and also affect the corrosion rates in the materials of the ocean structures.

Tidal current velocities vary periodically, being similar to the sinusoidal nature of the tidal ocean water motions with very long periods. Moreover, offshore tidal currents are rotational in nature and change their directions throughout the tidal cycles. Near the shores, bays, and estuaries, the tidal currents are more typically reversing in nature, flowing in the same or opposing directions,

dependent on the flooding or ebbing nature of the tidal waters; it should be borne in mind that the tidal ranges around the world vary widely, from a foot (0.30 m) or less to 40.0 ft. (12.0 m) or more, inside certain constricted bays or basins. The maximum value of the current generally occurs near the mid-tide; but sometimes the maximum current may lag or precede the maximum water level fluctuation. The magnitude and direction of the tidal currents, at the water surface, are estimated from local field measurements.

Wind drag currents, which are noticed only during extreme wind conditions, are primarily surface currents and for design purposes may be approximated to vary linearly from a maximum of 1.0% to 3.0% of the sustained wind speed, at the surface, to zero at the sea bottom. Wind stress currents may exceed 1 knot (0.5144 m/s) under certain conditions and should be added vectorially to the prevailing tidal currents. The effect of peak river discharge rates due to a storm runoff or spring thaws should be considered at river sites and estuaries, where the ebb currents are likely to be stronger than the flood currents. If a current of 0.15 m/s occurs at the bottom (measured at 0.305 m, above the sea bottom), then it is likely to erode the bottom, if the bottom material is fine or medium sands; for silts and gravels, it is much higher.

### 3.5.2 CURRENT VELOCITY PROFILE

Current velocity profiles vary vertically with the highest values near the surface, although this need not be true always, as shown below. In some stratified estuaries (or even deepwater oceans) where different types of density waters (freshwater from the river and seawater from the ocean) mix, a current shear may exist resulting in the bottom current to be opposite to the surface current. Figure 3.40 [62] shows some typical current profiles. For engineering purposes, it is usually assumed that the depth variation of tidal currents follows the one-seventh power law (see Equation 3.12) and that for the wind-generated current speed, the variation follows the linear relationship, being a maximum at the water surface and zero at the sea bottom.

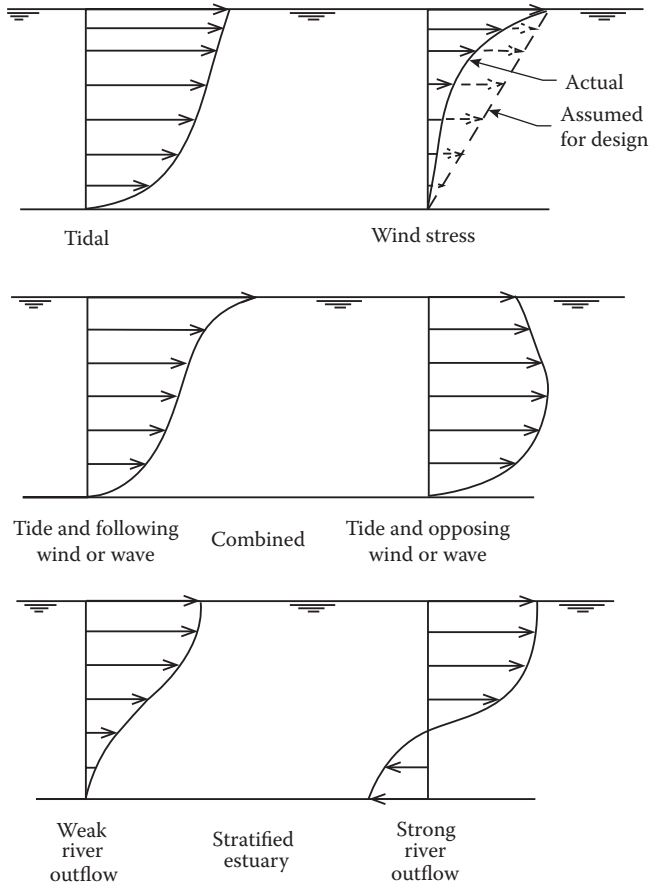
During extreme wind or storm conditions, wind-generated currents will also exist simultaneously with the motion of surface water waves; in addition, the direction of wind-current velocities and wave particle velocities will not be along the same or opposite directions, but inclined at an angle. However, for the sake of conservative design of structures, the wind-generated current may always be assumed to act in the same direction as that of wave particle velocities (holds true for deepwater depths); the wind-generated current profile, for the Gulf of Mexico [63], given in Figure 3.41 [64], can be used as a typical current velocity profile for deepwater depths. According to API codes, for shallow and intermediate water depths, the current velocities must be added vectorially to the wave particle velocities (based on wave-current joint probability) before using these velocities for force computation. For instance, the design of offshore structures in the Gulf of Mexico is generally governed by the hurricane-related wind and wave conditions; the wave-current interactions must be taken into account by accounting for the interaction angle between the design wave direction, the modification factor, and the direction of wind-generated current. Details are to be obtained by consulting the code provisions.

In cases where detailed provisions are not available for wind-generated current velocity profiles, the following equation given by Reid [65] may be used:

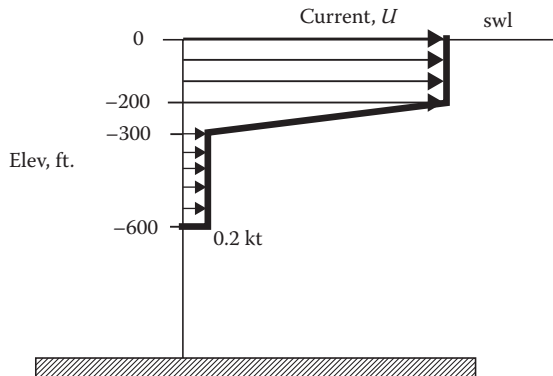
$$u_c = \left( u_{* \text{ current}} / \kappa (1 + z_{0 \text{ bottom}} / h + z_{0 \text{ surface}} / h) \right) \cdot \left[ \ln [(z_{0 \text{ bottom}} + z) / z_{0 \text{ bottom}}] - \ln [(h + z_{0 \text{ surface}} - z) / (h + z_{0 \text{ surface}})] \right] \quad (3.67)$$

In Equation 3.67,  $z_{0 \text{ bottom}}$  ( $\simeq 0.2$ ) and  $z_{0 \text{ surface}} = (3.3) \times (10^{-4})h$  represent the characteristic roughness lengths of the ocean bottom and surface, respectively, where  $h$  is the depth of water at the site,





**FIGURE 3.40** Current velocity profiles. (From J.W. Gaythwaite, *Design of Marine Facilities—for the Berthing, Mooring and Repair of Vessels*, Van Nostrand Reinhold, New York, p. 80, 1990. With permission.)



**FIGURE 3.41** API design deepwater current profile for Gulf of Mexico, north of 27°N and west of 86°W. (From API RP 2A–LRFD, *Recommended Practice for Planning, Designing and Constructing Fixed Offshore Platforms—Load and Resistance Factor Design*, American Petroleum Institute, Washington, DC, p. 41, 1993. With permission.)

$z$  is the depth of the point under consideration,  $u_{*current}$  is the shear speed of current expressed as a function of reference wind speed  $= (1.82) \times (10^{-3})U_R$ , and  $\kappa$  is the von Karman's constant ( $= 0.4$ ).

The use of Equation 3.67 gives a current velocity profile similar to the tidal current velocity profile given in Figure 3.40 for tidal current velocity; this may be applicable to the Gulf of Mexico region where the water circulation is caused by temperature differences between various ocean thermal regimes, boundary currents, and Coriolis effects on wind, producing the Gulf Stream. For a general wind-shear situation on the ocean surface, the linear current velocity profile given in Figure 3.40 would be more relevant than that given by Equation 3.67.

**Example 3.13**

Assuming the surface current speed, at a particular location, to be given by Equation 3.67, determine the current speed profile for the location and compare it against Figure 3.41. The maximum sustained wind speed at the location is given as 70.0 mi./h. Assume that the depth of water at the location is 600.0 ft. State which of the current speed profiles given in Figure 3.40 will be closer to the calculated wave profile.

$$z_{0_{bottom}} = 0.2 \text{ ft.}; z_{0_{surface}} = (3.3)(600.0)/(1000.0) = 0.198 \text{ ft.}$$

$$u_{*current} = (1.82)[(70)(5280)/(3600)]/1000.0 = 0.1869 \text{ ft./s}$$

$$\kappa[1.0 + (z_{0_{bottom}})/h + z_{0_{bottom}}] = (0.4)[1.0 + (0.2)/600 + (3.3)(600)/1000] = 1.1982$$

$$u_{*current} / \kappa[1.0 + (z_{0_{bottom}})/h + z_{0_{surface}}] = 0.1869/(1.1982) = 0.156 \text{ ft./s}$$

current speed profile

$$\begin{aligned} &= (0.156)\{\ln [(z_{0_{bottom}} + z)/z_{0_{bottom}}] - \ln [(h + z_{0_{surface}} - z)/(h + z_{0_{surface}})]\} \\ &= (0.156)\{\ln [(0.2 + z)/(0.2)] - \ln [(600.0 + 0.198 - z)/(600.0 + 0.198)]\} \\ &= (0.156)\{\ln [5(0.2 + z)] - \ln [(0.001666)(600.198 - z)]\} \end{aligned}$$

Z (ft.)	0.0	50	100	150	200	250	300	400	450	500	550	580	590	598	599
$U_c$ (ft./s)	0.0	0.88	1.00	1.08	1.14	1.20	1.25	1.36	1.42	1.50	1.62	1.77	1.89	2.12	2.22

$u_c$  (at  $z = 600.0$  ft.) = 2.50 ft./s; seems to be OK.

Check: As an approximate check, the surface current speed is around 2.0% of surface wind speed (see addendum in [64]).

$$= (.02)(70.0)(5280)/3600 = 2.05 \text{ ft./s.}$$

Comparing with Figure 3.40, the current profile seems to be closer to the (tide + follower) wave or wind profile. For comparing with Figure 3.41, take the surface current speed as  $0.02U_R$ .

Area of curve (approximate) given by Equation 3.67 =  $[(0.0 + 0.88)(50)/2 + (0.88 + 1.00)(50)/2 + (1.00 + 1.08)(50)/2 + (1.08 + 1.14)(50)/2 + (1.14 + 1.20)(50)/2 + (1.20 + 1.25)(50)/2 + (1.25 + 1.36)(100)/2 + (1.36 + 1.42)(50)/2 + (1.42 + 1.50)(50)/2 + (1.50 + 1.62)(50)/2 + (1.62 + 1.77)(30)/2 + (1.77 + 1.89)(10)/2 + (1.89 + 2.12)(8)/2 + (2.12 + 2.22)(1.0)/2 + (2.22 + 2.50)(1.0)/2 = [22.0 + 47.0$

$$+ 52.0 + 55.50 + 58.5 + 61.25 + 130.50 + 69.50 + 72.50 + 78.0 + 50.85 + 18.3 + 16.04 + 2.17 + 2.36] = 736.47$$

$$\text{Moment of the area of the curve about the base} \sim [(22.0)(50)(2/3) + (47.0)(50 + 25) + (52.0)(100.0 + 25.0) + (55.50)(150.0 + 25.) + (58.50)(200 + 25.0) + (61.25)(250 + 25.0) + (130.50)(300 + 50) + (69.50)((400 + 25.0) + (72.50)(450.0 + 25.0) + (78.0)(500 + 25) + (50.85)(550 + 15.0) + (18.3)(580.0 + 5.0) + (16.04)(590 + 4.0) + (2.17)(598 + 0.5) + (2.36)(599 + 0.5)] = [733.7 + 3525 + 6500 + 9712.5 + 13,162.5 + 16,843.75 + 45,675 + 29,537.5 + 34,437.5 + 40,950.0 + 28,730.25 + 10,705.5 + 9527.76 + 1298.75 + 1414.82] = 229,817.7$$

Considering Figure 3.41, with  $u_c = 2.05$  ft./s, and bottom current speed =  $(0.2)(0.515)(1.00/0.3048) = 0.338$  ft./s.

$$\text{Area} = (2.05)(200.0) + (2.05 + 0.338)(200.0)/2 + (0.338)(200) = 410.0 + 238.8 + 67.6 = 716.4$$

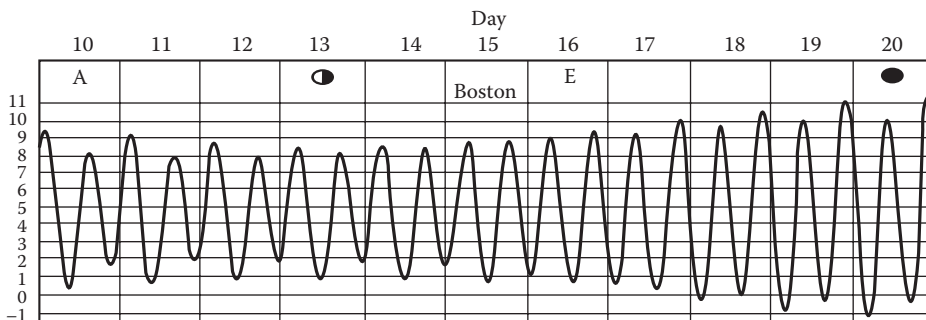
$$\text{Moment of the area of the curve about the base} = [(410.0)(400.0 + 100.0) + [(0.338)(200)(300.0) + (2.05 - 0.338)(200)\{200.0 + (2/3)(200)\}/2 + (67.6)(100.0)] = [205,000 + 20,280.0 + 114,132.19 + 6760.0] = 346,172.19.$$

Use of Figure 3.41 for current effect computation will lead to a much higher current influence on the structure (giving a larger bending effect about the base of the structure).

### 3.6 SOLAR AND LUNAR OCEAN TIDES

#### 3.6.1 INTRODUCTION TO SOLAR AND LUNAR OCEAN TIDES

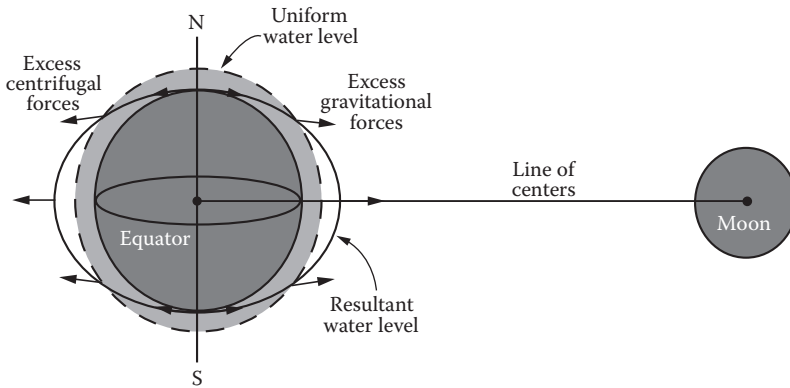
The tide is the regular rising and falling of the ocean’s surface caused primarily by the moon’s grav-ity (and, to a lesser degree, the sun’s); despite the fact that the sun is much bigger than the moon, it exerts only 0.46 times of the moon’s tidal force since it is much farther away from the earth. The high tide and low tide are the crest and trough of a wave with a length of hundreds of kilometers. The tidal wave height is not very large in the open deepwater ocean, being around 0.50 m; however, the wave heights increase to 10.0 m or more (at some locations), as the tidal wave approaches the coast. Tidal fluctuations follow the motion of the moon much more closely than that of the sun. There are usually two high (one higher than the other) and two low waters in a tidal or lunar day, as shown in the tidal curve for Boston in Figure 3.42 [66]; since the lunar day is 50.0 min longer than the solar day, tides occur 50 min later each day. It can also be seen from the figure that the tidal highs and lows vary over the 10-day period; this is due to the synchronization of the lunar and solar tidal effects on earth as the moon rotates around the earth on 28 days, with the maximum (spring) and minimum (neap) tides occurring when the sun and moon are in the same line or at 90° out of phase.



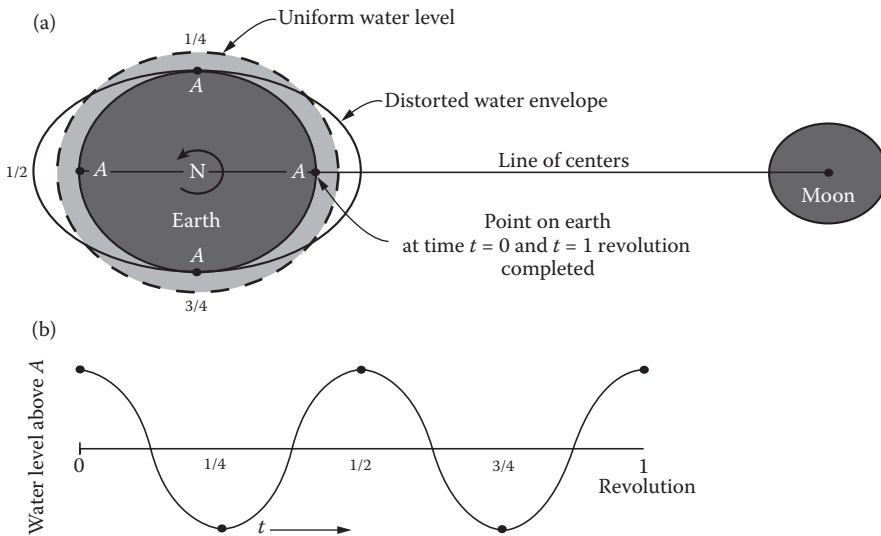
**FIGURE 3.42** Typical tidal fluctuations at Boston over a 10-day period. (From US Army Corps of Engineers Coastal Engineering Research Center, Shore Protection Manual, Volume I, Chapter 3 on Wave and Water Level Predictions, pp. 3–90, 1984. With permission.)

### 3.6.2 THEORY OF TIDAL FORMATION

Considering only the gravitational pull between the moon and earth, the gravitational and centrifugal forces are exact and opposite to one another so that the planets remain at a constant distance apart; in the process, each particle of the earth experiences both the centrifugal and moon's attraction forces. As can be seen from Figure 3.43 [67], a parcel of water directly in line with the centers of the earth and moon (and also nearer to the moon's surface) experiences a slightly greater attraction toward the moon than the centrifugal force exerts in the opposite direction. A particle, exactly on the opposite side of the earth will also experience the same force since the centrifugal force on that side will be slightly greater than the gravitational attraction of the moon. Thus, two identical bulges, one on the side of earth under the moon and the other exactly on the opposite side of the earth, are produced as shown in Figure 3.43. Figure 3.44a [67] shows the change of water level (or the tidal wave amplitude) at the points shown as A, during one rotation of the earth; the difference



**FIGURE 3.43** Distribution of tide-raising forces on earth. (From A.C. Duxbury and A.B. Duxbury, *An Introduction to the World's Oceans*, Wm. C. Brown Publishers, Dubuque, IA, p. 244, 1991. With permission.)

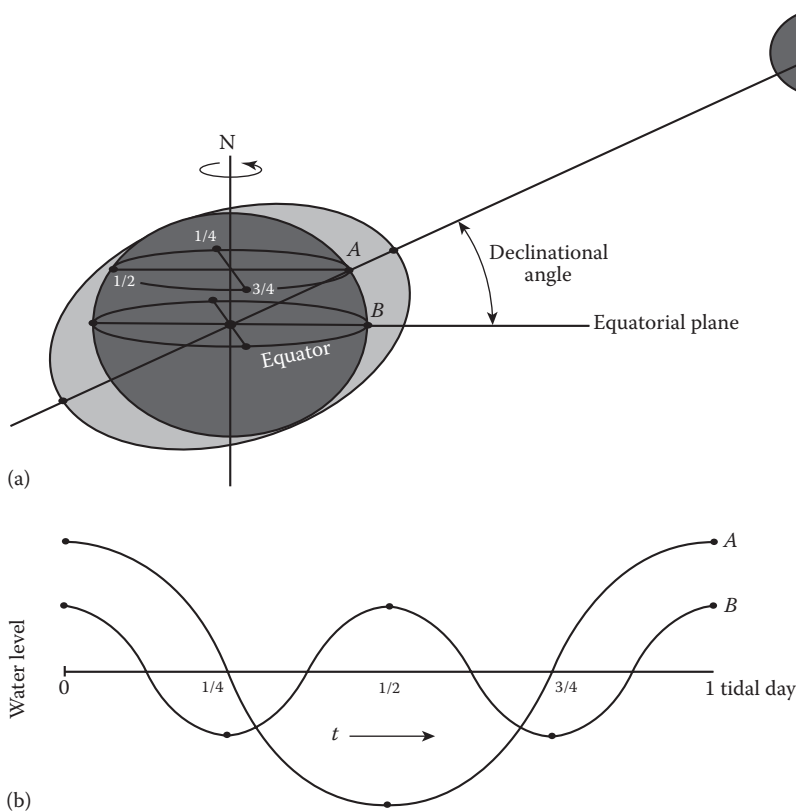


**FIGURE 3.44** (a) Uniform and distorted water envelope around the earth surface, before and after the tidal force acts on the water envelope; and (b) the change in water level at point A during one full rotation of the earth, after the action of tidal force on the uniform water envelope. (From A.C. Duxbury and A.B. Duxbury, *An Introduction to the World's Oceans*, Wm. C. Brown Publishers, Dubuque, IA, p. 244, 1991. With permission.)

between the four points will be that the tidal amplitudes will be the identical positive values at zero and 1/2 points and be identical negative values at 1/4 and 3/4 points. The period of the sinusoidal variation of the water level shown in Figure 3.44b is equal to 12.0 h.

Besides the dominant influence of the sun's gravitational attraction on earth's surface-occupying material, two more factors will modify the tidal characteristics, viz., (1) alignment of the earth, moon, and sun during the motion of the moon around the earth and (2) declination of the axis of moon's rotational plane with respect to the earth's rotational plane. As the moon travels around the earth in 709 h (29.5 days), viz., the time between successive new moon days, the tidal fluctuations will vary depending on the strength of lunar gravitational attraction on the earth and the consequent earth's centrifugal force at the location. Measuring time from the beginning of a new moon, the maximum tidal fluctuation will be observed when the moon occupies the new and full moon positions; the resultant tide will be the highest (spring) tide. When the moon occupies the first quarter (1/4 position in a clock) and the last quarter positions, the tidal fluctuations will be the minimum (neap) tide. Figure 3.45 [68] illustrates the situation.

Declinational tides occur due to the angular difference between the earth-sun orbit and moon-sun orbit; the declination of earth's orbit with respect to earth-sun orbit is 23.5°N (summer solstice) and 23.5°S (at winter solstice), and the corresponding declination of moon's orbit to earth-sun orbit is 5°N and 5°S. Therefore, the moon's declination with respect to sun-earth orbit varies between



**FIGURE 3.45** (a) Uniform and distorted water envelope around the earth's surface, before and after the action of tidal force on the water envelope, when there is a declination between the equatorial plane of the earth and the plane connecting the centers of earth and moon; and (b) the change in water level, produced by a diurnal tide at latitude A, and a semidiurnal tide at latitude B, during one full rotation of the earth. (From A.C. Duxbury and A.B. Duxbury, *An Introduction to the World's Oceans*, Wm. C. Brown Publishers, Dubuque, IA, p. 247, 1991. With permission.)

28.5°N and 28.5°S; as a consequence, the gravitational force of attraction and the centrifugal force due to rotation act differently at different points. This results in the tidal variations between various points of the earth as illustrated between points A and B in Figure 3.45.

In verifying the nature of tidal variations at specific locations, Newton's law of gravitation is invariably used. As per the Newton's above-stated law, the attractive force exerted on each other by two dissimilar spherical bodies ("m" stands for moon and "e" stands for earth) of radii  $r_e$  and  $r_m$ , and of masses  $M_e$  and  $M_m$ , separated by a radial distance  $R_{m-e}$ , is given by

$$F = GM_e M_m / R_{m-e} \quad (3.68)$$

Considering two points, C (nearer to the moon) and D (farther away from the moon) on opposite sides of the earth along the radius connecting the two spheres, the relative acceleration due to attraction of moon on a unit mass located at point A and the center of the earth is given as

$$= GM_m / (R_{m-e} - r_e)^2 - GM_m / R_{m-e} \quad (3.69a)$$

Reduction of the above equation leads to the relative acceleration between point A and the center of the earth as

$$= \left( GM_m / R_{m-e}^2 \right) \cdot \left( -(2r_e / R_{m-e}) + (r_e / R_{m-e})^2 \right) / \left( 1 - (r_e / R_{m-e}) \right)^2 \quad (3.69b)$$

In a similar manner, the relative acceleration between point B and the earth's center is given by

$$\begin{aligned} &= GM_m / (R_{m-e} + r_e)^2 - GM_m / R_{m-e} \\ &= \left( GM_m / R_{m-e}^2 \right) \cdot \left( (2r_e / R_{m-e}) + (r_e / R_{m-e})^2 \right) / \left( 1 + (r_e / R_{m-e}) \right)^2 \end{aligned} \quad (3.69c)$$

From Equations 3.69b and 3.69c, if one considers the ratio  $r_e / R_{m-e}$  to be negligible, then

$$\text{relative acceleration at A} = + \left( 2GM_m r_e / R_{m-e}^3 \right) \quad (3.70a)$$

This shows that the acceleration at A is outward. Similarly, at B,

$$\text{relative acceleration at B} = - \left( 2GM_m r_e / R_{m-e}^3 \right) \quad (3.70b)$$

The acceleration at B is also outward. Thus, the forces exerted at A and B are outward resulting in equal bulges in the ocean water surface level. The astronomical tides are obtained by hindcasting from measured tidal fluctuations at various locations using the procedure developed by Bowditch [69] and refined by Nos Tidal Datums Publ. [70].

### 3.6.3 WATER LEVEL FLUCTUATIONS INCLUDING TIDES

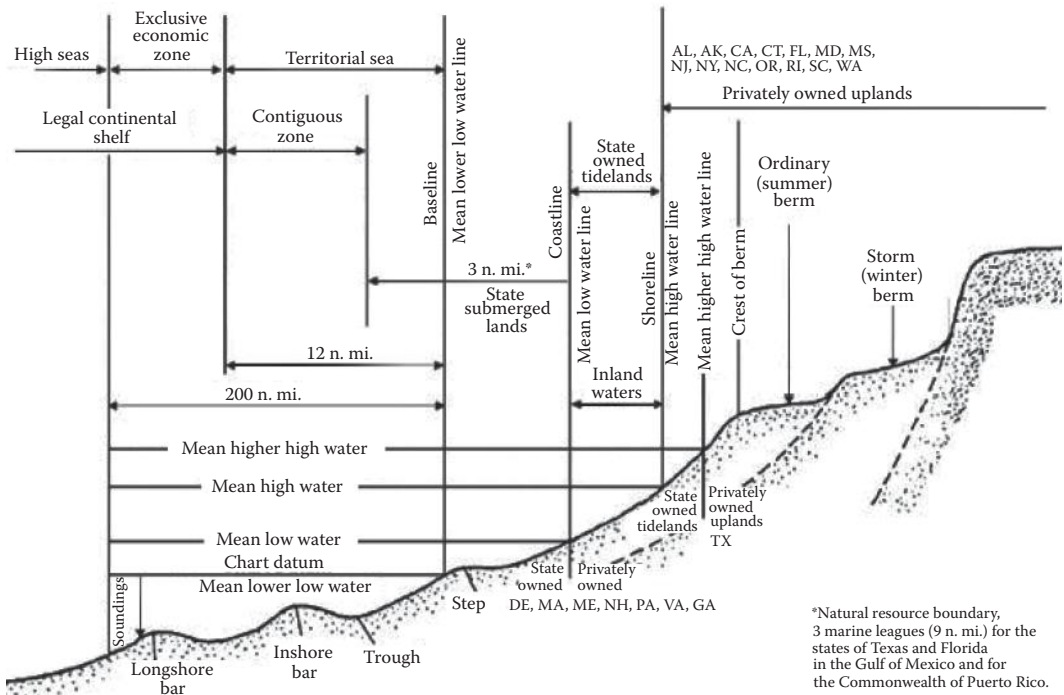
Establishment of a fixed reference plane, for the design and installation of near-shore and offshore structures, is of great importance since many factors contribute toward it. Obviously, one would like to use the term SWL or MSL for defining the rise (or fall) in the water level due to the presence of

waves, as if it is a fixed reference in the ocean that can be determined easily at any time; but this is not true since many factors contribute to the water level fluctuations in the ocean. These are as follows: (1) astronomical tidal variations; (2) tsunami effects; (3) seiches (or standing waves); (4) wave setup (the elevation of water level caused by incoming waves); (5) storm surges; and (6) climatological and secular variations. In order to establish a datum (or fixed reference) for designation and use, all the above effects must be included [58]. The first five fluctuation categories have periods that range from a few minutes to a few days, whereas the two causes given in the sixth category have periods ranging from semiannual to many years.

In order to obtain the tidal fluctuations, the corresponding tidal tables and charts developed by the corresponding agencies and sold by private dealers should be consulted. In Canada, the charts are developed by the Canadian Hydrographic Service (with active cooperation from Fisheries and Oceans Canada) in conjunction with private dealers, whereas in the United States, the charts are developed by the Center for Operational Oceanographic Products and Services (with active cooperation from the National Oceanic and Atmospheric Administration, Washington, DC) in conjunction with private dealers.

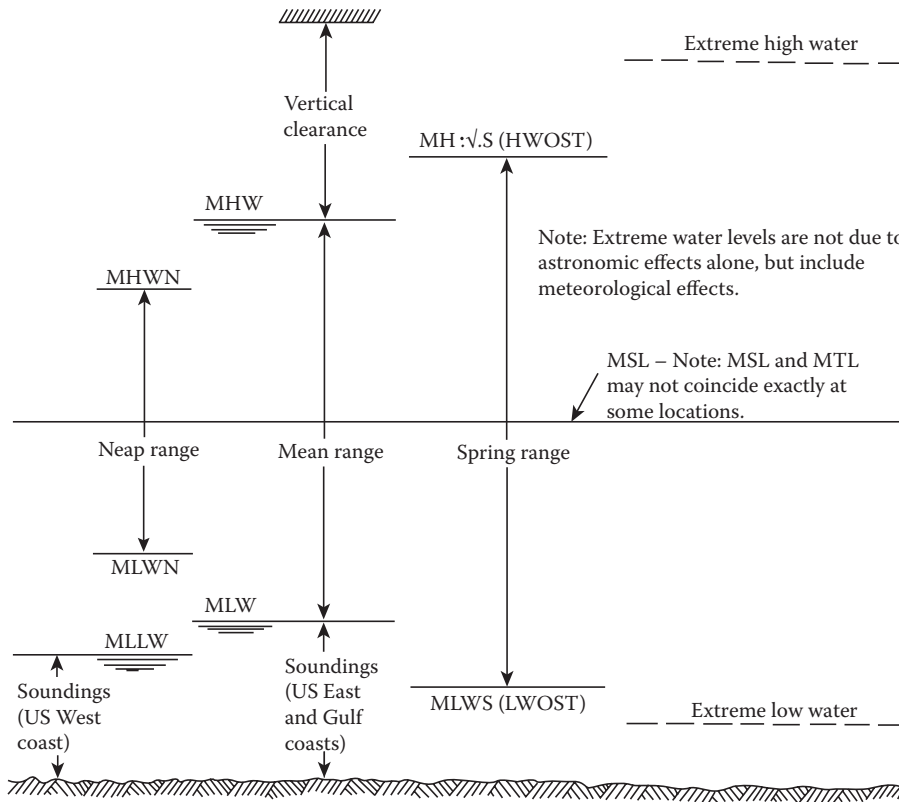
The fixed reference (or datum) for measuring water levels for the installation of structures in the ocean varies from country to country. In the United States and Canada, the mean lower low water (MLLW) is taken as the fixed reference, and the MSL (or SWL) should be fixed with reference to that datum; other countries use mean low water (MLW), low water (LW), lowest astronomical tide (LAT), or MLW spring (MLWS) as the datum. An offshore structural designer and the constructor need to be aware of these changes as they work in a global market place. Figures 3.46 [70] and 3.47 [72] outline the various water level fluctuations associated with an offshore structure.

As per the API code, the structures located in the Gulf of Mexico should have the bottom of the deck located according to the specifications given in Figure 3.48 [71]. The API code also states that a minimum air gap of 1.5 m (or 5.0 ft.) must be present below the bottom of an offshore platform.



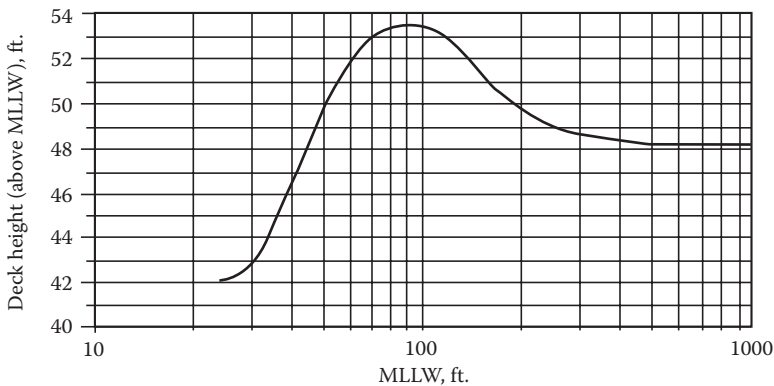
**FIGURE 3.46** Establishment of a datum for ocean measurements and water level fluctuations. (From N. Bowditch. In Chapter 9 on *Tides and Tidal Currents*, *The American Practical Navigator: An Epitome of Navigation* Publication Office, p. 137, 1977. With permission.)





**FIGURE 3.47** Tidal data. (From J.W. Gaythwaite, *Marine Environment and Structural Design*, Van Nostrand Reinhold Co., New York, p. 209 & 210, 1981. With permission.)

This would considerably influence the design and installation of near-shore and offshore structures located in shallow and intermediate depth waters. From Figure 3.48, it can also be seen that the mean tidal level (MTL) is often taken as the MSL (or still water level); it also points out that the MTL and MSL may not coincide always. The tide ranges for selected locations in the North American continent are given in Table 3.12 [72].



**FIGURE 3.48** Design deck (bottom) height above MLLW level. (From API RP 2A–LRFD, Recommended Practice for Planning, Designing and Constructing Fixed Offshore Platforms—Load and Resistance Factor Design, American Petroleum Institute, Washington, DC, 1993. With permission.)

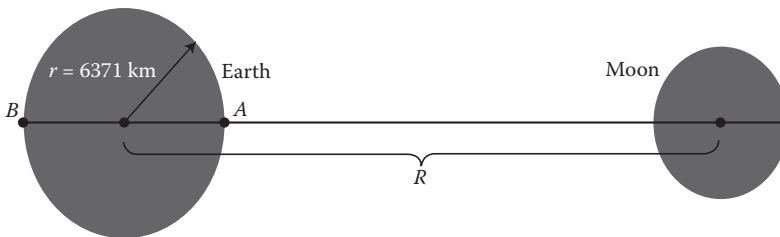
**TABLE 3.12**  
**Tide Ranges for Selected North American Locations**

Location	Mean Range (ft.)	Spring Range (ft.)	Type of Tide	Chart Datum
Quebec, P.Q.	13.7	15.5	Mixed	LNLW
St. John, N.F.	2.6	3.5	Semi-diurnal	
Halifax, N.S.	4.4	5.3		
St. John, N.B.	20.2	23.6		
Portland, Maine	8.9	10.2		MLW
Boston, Mass.	9.5	11.0		
New York, N.Y.	4.4	5.3		
Philadelphia, Pa.	5.9	6.2		
Baltimore, Md.	1.1	1.3		
Norfolk, Va.	2.8	3.4		
Charleston, S.C.	5.1	6.0		
Jacksonville, Fla.	2.0	2.3		
Miami, Fla.	2.5	3.0		
Galveston, Tex.	1.0	1.4	Mixed	
San Diego, Calif.	4.2	5.8		MLLW
San Francisco, Calif.	4.0	5.7		
Columbia River, Oreg.	1.8	2.4		
Seattle, Wash.	7.6	11.3		
Juneau, Alaska	14.0	16.6		
Anchorage, Alaska	26.7	29.6		

Source: J.W. Gaythwaite, *Marine Environment and Structural Design*, Van Nostrand Reinhold Co., New York, p. 210, 1981. With permission.

**Example 3.14**

Show that the vertical component of the tide-generating force acting along the line of earth–moon centers on the side of the earth facing the moon is slightly larger than the force on the side of the earth facing away from the moon.  $R_{m-e} = (384.4)(10^5)$  km;  $r_e = 6371.0$  km.



Using Equations 3.70a and 3.70b  
Relative acceleration at A

$$\begin{aligned}
 &= \left( GM_m / R_{m-e}^2 \right) \cdot \left( (2r_e / R_{m-e}) + (r_e / R_{m-e})^2 \right) / \left( 1 - (r_e / R_{m-e}) \right)^2 \\
 &= - (GM_m) / (R_{m-e})^2 \left[ - (2.0) \{ (6371.0) / (384.4)(10^5) \} + \{ (6371.0) / (384.4)(10^5) \}^2 \right] / \\
 &\quad \left[ 1.0 - \{ (6371.0) / (384.4)(10^5) \} \right]^2
 \end{aligned}$$

$$= - (GM_m)/(R_{m-e})^2 [- 0.0003315 + 0.000000028]/0.9996690 = - (GM_m)/(R_{m-e})^2 [- 0.00033158]$$

Relative acceleration at B

$$= (GM_m/R_{m-e}^2) \cdot ((2r_e/R_{m-e}) + (r_e/R_{m-e})^2) / (1 + (r_e/R_{m-e})^2)$$

$$= - (GM_m)/(R_{m-e})^2 [+ 0.0003315 + 0.000000028]/1.0003315 = - (GM_m)/(R_{m-e})^2 [+ 0.00033142].$$

Hence, the relative acceleration at point A (earth's surface nearer to the moon) is slightly greater than the relative acceleration at B (earth's surface farther away from the moon).

### Example 3.15

Calculate the approximate length and celerity of tides in three ocean basins using the simple progressive water-wave theory, if the average water depths are 4.0 km, 2.0 km, and 100.0 m, respectively.

Considering the wave to be a shallow one, with a wave period of 12 h and 25.0 min,

$$(1) d = 4.0 \text{ km}; L = T\sqrt{gd} = [(12)(3600) + (25.0)(60)] \sqrt{\{(9.81)(4000)\}/(1000.0)} = 8854.66 \text{ km}$$

$$C = L/T = (8854.66)(1000.0)/[(12)(3600) + (25)(60.0)] = 198.06 \text{ m/s.}$$

$$(2) d = 2.0 \text{ km}; L = T\sqrt{gd} = [(12.0)(3600) + (25.0)(60)]\sqrt{\{(9.81)(2000)\}/(1000.0)} = 6261.19 \text{ km}$$

$$C = L/T = 140.17 \text{ m/s}$$

$$(3) d = 100.0 \text{ m}; L = [(12.0)(3600.0) + (25.0)(60.0)] \sqrt{\{(9.81)(100.0)\}/(1000.0)} = 1400.05 \text{ km}$$

$$C = L/T = [(1400.05)(1000.0)]/[(12.0)(3600.0) + (25.0)(60.0)] = 31.321 \text{ m/s}$$

### Example 3.16

A single column gravity platform structure is to be installed in a water depth (MSL) of 80.0 m, near Anchorage, AK. The maximum storm surge, at that location, is 0.70 m; the maximum wave height that is likely to occur at that site is computed to be 23.0 m, with a wave period of 18.0 s. Minimum air gap needed for the platform is 1.5 m. Determine the elevation of the bottom of the deck, above the MSL, and compare your results with those given in Figure 3.48.

$$\text{Height of bottom of the deck from above MSL} = \text{storm surge} + (\text{wave height})/2$$

$$+ \text{deck clearance} + \text{nominal tidal height} = 0.70 + (23.0)/2 + 1.5 + 0.5 = 14.2 \text{ m}$$

In order to use Figure 3.48, one needs to know the MLLW for the site under consideration. Using the data in Table 3.12, MLLW = water depth at the site – (neap tidal height)/2

$$= 80.0 - (29.6)(0.3048)/2 = 75.49 \text{ m (247.67 ft.)}$$

From Figure 3.48, minimum deck height (above MLLW) ~ 14.87 m (48.8 ft.).

Height above the MSL = 75.49 + 14.87 – 80.0 = 10.36 m (minimum)

Hence, the computed height of 14.2 m is OK.

### 3.7 SEISMOLOGICAL CONSIDERATIONS, EARTHQUAKES, AND SEAQUAKES

#### 3.7.1 INTRODUCTION TO SEISMOLOGICAL CONSIDERATIONS, EARTHQUAKES, AND SEAQUAKES

Usually, in the design of an offshore structure, the major forces exerted on the platform will result from the winds, waves, and currents that occur at the site, which are generated by the associated storm conditions. These forces and the consequent motions are dependent on the wave height, wave period, wind speed, and the fetch over which the wind blows. However, in a seismically active offshore area, usually the earthquake generates forces and motions that contribute significantly to the forces acting on the structure and the consequent motions; wave and wind forces do not seem to contribute significantly to the total forces acting on the structure. These seismic forces are mainly dependent on the magnitude of earthquake shaking and the associated stiffness, mass distribution, energy dissipation, and the strength characteristics of the superstructure-foundation-cum-soil at the offshore location. Hence, a dual-level approach is used in the analysis and design of structures located in seismically active regions of the offshore locations. The first one is a lower-level design requirement that would apply a lower level of strong ground shaking to the structure wherein the structure does not suffer any significant damage; the lower level of strong ground shaking is chosen such that it has a reasonable likelihood of occurring once during the life of the structure. The second one is a higher (or stronger) level of ground shaking for which the structure is to resist it without any catastrophic failure or loss of life. This higher level of shaking will represent an earthquake excitation that has a low probability of being exceeded during the lifetime of the structure. In the second level of analysis, some sort of nonlinear analysis will be required to show that the structure can safely resist this extreme load condition.

The above two level conditions are included in the API RP 2A [71], and they provide a requisite set of guidelines for providing good design and construction practice. The API guidelines, through the two-level design considerations, would satisfy the two distinct requirements of strength and ductility. In the first requirement, the platform is configured and sized so that it has sufficient stiffness and strength to resist the applied loads (through the first-level seismic shaking) without any significant damage. The second requirement is that the platform should have requisite ductility so that it will maintain its structural integrity and stability during any subsequent occurrence of a rare intense earthquake.

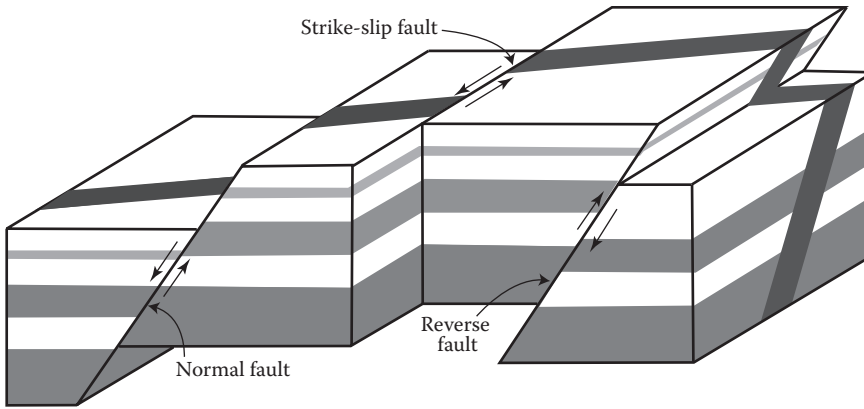
For platforms built in seismically active areas, the first step in the seismic design process is to specify the seismicity of the site under consideration; this would require a quantitative description of both the severity and the likelihood of occurrence of possible subsequent ground motions at the proposed platform site. As per API RP 2A provisions for earthquake design, this would require the designation of the intensity and frequency contents of the appropriate earthquake ground motion. These are specified in terms of appropriate seismic zoning map available for the specific coastal/offshore waters and the proper design amplification spectra.

#### 3.7.2 CHARACTERISTIC FEATURES OF EARTHQUAKE PHENOMENA

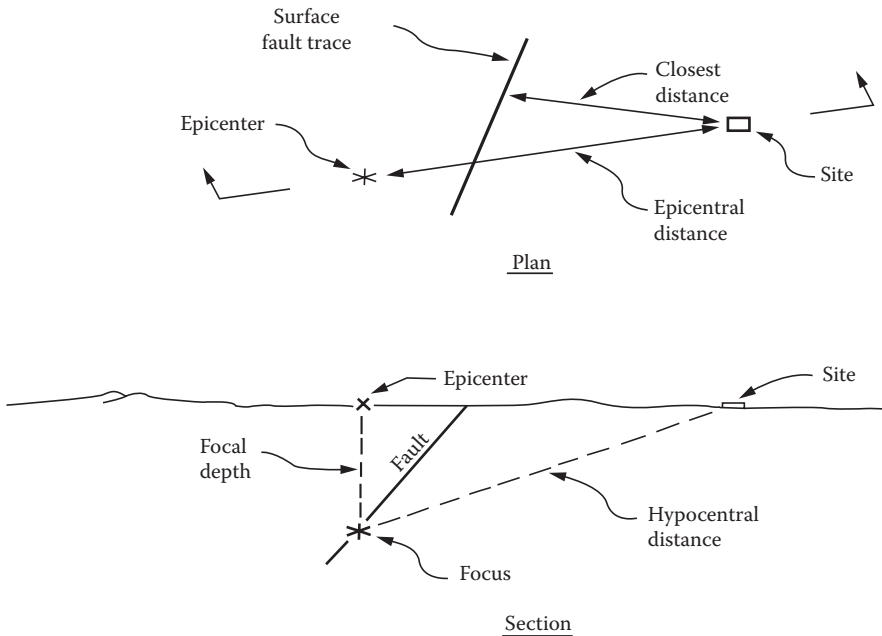
Earthquakes occur due to the sudden release of strain energy accumulated in the solidified crust of the earth, which generally occur as a result of slippages along preexisting faults. These fault displacements can be classified into three types, whether they occur in the land or in the ocean. The strike of the fault is the angle between the north and the line along which the plane of the fault intersects the horizontal plane on the surface of the earth. Generally, the fault plane is not vertical but dips at an angle down into earth, varying between  $0^\circ$  and  $90^\circ$ . The three types of fault are as follows: (1) Normal fault occurs when the rock on the side of the fault hanging over the fracture slips downward. (2) Reverse fault occurs when the rock on the side of the fault hanging over the fracture moves upward. (3) While the above two faults are called “dip-slip faults,” the third one is called a

strike-slip fault, where a horizontal movement occurs in the fault slip plane. Figure 3.49 [73] illustrates these three types of faults occurring in the crust of the earth.

The simplified model of the cross-section and plan of the fault slippage, occurring in a fault zone, is shown in Figure 3.50 [74]. It shows the analytically determined focus (or hypocenter) of an earthquake, from where the earthquake is initiated, in the earth's crust. It also shows the epicenter of the focus, which is the point on the surface of the earth that is vertically above the focus of the earthquake. Generally, when the earthquake is initiated at the focus, the slippage of the earth's surface can propagate along the fault at speeds of the order of 1.6 to 3.2 km/s. The areal extent of the fault



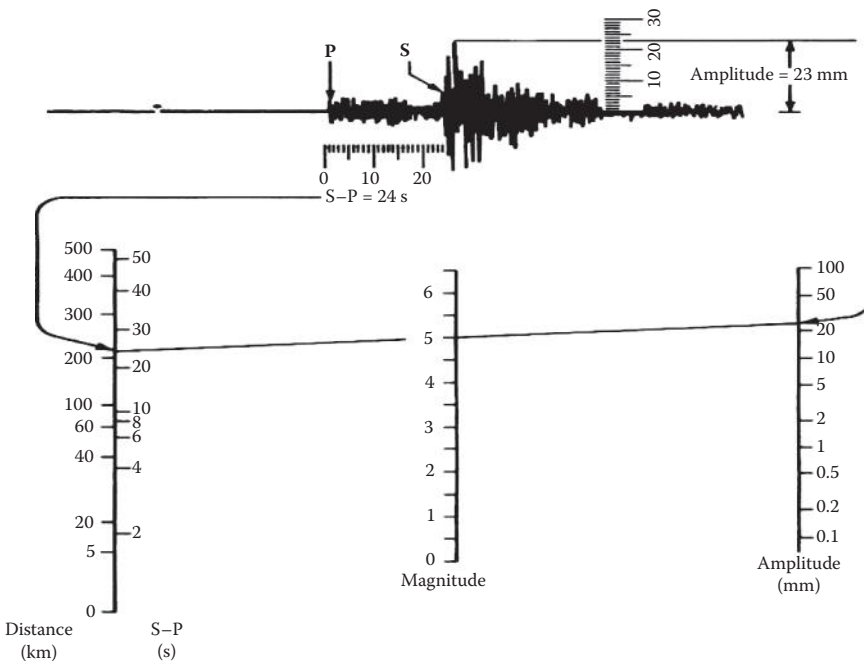
**FIGURE 3.49** Three main types of fault motion during an earthquake. (Modified from B.A. Bolt, *Earthquakes*, W.H. Freeman and Co., New York, p. 57, 2004. With permission.)



**FIGURE 3.50** Earthquake source and details. (Modified from B. McClelland and M.D. Reifel, *Planning and Design of Fixed Offshore Platforms*, Van Nostrand Reinhold Co., New York, p. 393, 1986. With permission.)

slippage can range from a few square kilometers to a few thousand square kilometers; accordingly, the amount of slip or dislocation between the two sides of the fault might also range from a small 0.1 m to several tens of meters.

At the fault slippage surface, compression (P) and shear (S) waves are generated, and they propagate away from the earthquake source in all directions. The P and S waves have different physical forms and have different particle motions. While the P waves produce small motions in the seismogram, the S waves will produce large motions in the seismogram. The ratio of P wave to S wave propagation velocities is usually in the range of 4:3. Shear wave propagation velocities vary from a few thousand meters to a few hundred meters per second (in soft soil deposits). Since P and S waves are propagated in all directions from the source of the fault, they get reflected and refracted at the geologic interfaces and discontinuities that are present in the earth's crust. Due to the occurrence of wave mode conversion from one type to another, waves such as Rayleigh and Love waves are generated on the earth's surface. As a consequence of the different arrival times of the energy (in the form of wave motions) generated by the earthquake, the measured ground motions obtained from the seismograph appear often varying in a chaotic manner, as shown in Figure 3.51 [75].



Procedure for calculating the local magnitude,  $M_L$

1. Measure the distance of the focus using the time interval between the S and the P waves ( $S-P = 24$  s).
2. Measure the height of the maximum wave motion on the seismogram (23 mm).
3. Place a straightedge between appropriate points on the distance (left) and amplitude (right) scales to obtain magnitude  $M_L = 5.0$ .

**FIGURE 3.51** Calculation of magnitude of earthquake using Richter's seismic magnitude scale. (From B.A. Bolt, *Earthquakes*, W.H. Freeman and Co., New York, p. 165, 2004. With permission.)

### 3.7.3 MAGNITUDE AND INTENSITY OF EARTHQUAKES

As shown in Figure 3.51, the primary compression (or dilation) P wave is generated in the beginning of seismic excitation, and the secondary shear S wave (producing larger motions) is generated later. The time delay between the P and S waves can be computed from the seismic time trace, as shown in Figure 3.51; in addition, the height of the maximum wave motion, shown on the seismogram, can also be measured, as shown in the figure.

Then using the nomogram procedure developed by Richter [76], shown in Figure 3.51, the Richter's magnitude of the earthquake event can be computed by noting the intersection point of the straight line between the amplitude and differential time (between P and S waves) on the earthquake magnitude scale. Richter magnitude is defined as the logarithm to base 10 of the maximum seismic-wave amplitude (in thousandths of a millimeter) recorded on a standard seismograph at an epicentral distance of 100.0 km.

The commonly used unit to specify the earthquake effects at a location is the modified Mercalli intensity scale, which relates the earthquake intensity to the degree of structural damage, amount of visible ground surface disturbance, and the human/animal reaction to earthquakes. It can also be noted from the left-hand scale given in Figure 3.51 [75] that an approximate relationship given as  $(S-P \simeq d/8)$  can be obtained for shorter epicentral distances. Table 3.13 [76] gives the relationships that exist between the Richter's (magnitude) and modified Mercalli (intensity) scales.

Strong earthquake shaking near the surface of the earth is of great importance to structural designers. The most complete description of strong ground motion is that provided by the measurement of acceleration versus time on three mutually perpendicular (two horizontal and one vertical) axes; each of these time records is designated as an accelerogram. United States Geological Survey (USGS) and many others maintain earthquake measurement stations in seismically active regions of the world. The measured accelerograms are corrected and digitized in series of reports; in addition, the (numerically) integrated velocity and displacement data are also included in these reports. One such set of data is shown in Figure 3.52 [77].

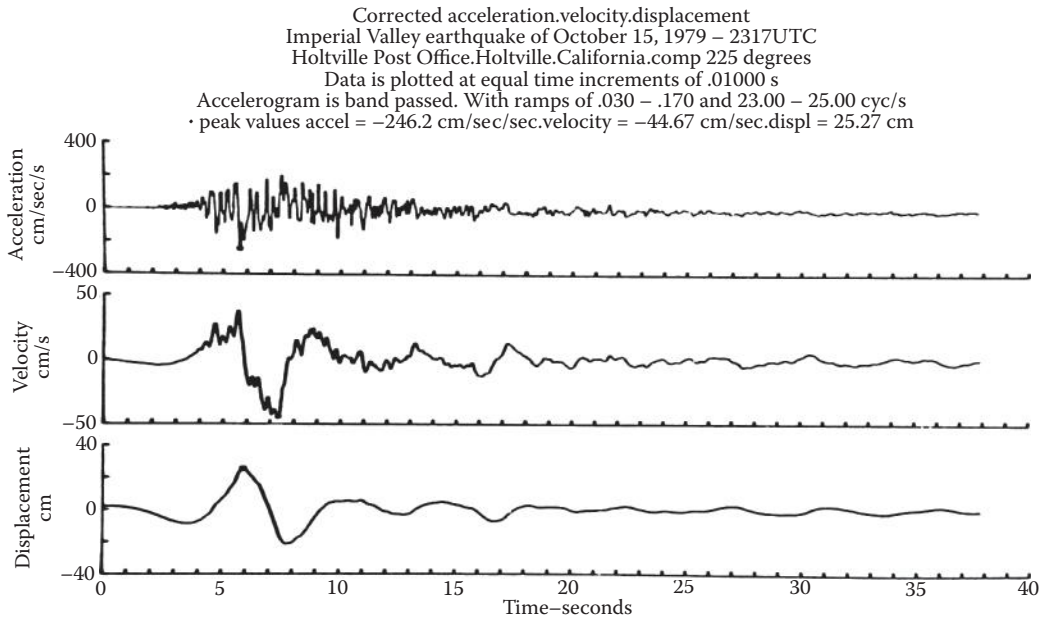
An approximate method of estimating the response of linear structures to earthquake excitation is called the response spectrum method. In this approach, the (maximum) response envelope of a single-degree-of-freedom structure (with a certain amount of energy dissipation in terms of damping), having different natural frequencies, to the specified base excitation is determined, smoothed, and plotted, as shown in Figure 3.53 [78]. This procedure is used as a method to characterize the earthquake motion at a point. If it can be assumed that the critical damping of the structure is less

**TABLE 3.13**  
**Approximate Relationship between Earthquake Magnitude, Intensity, Worldwide Occurrence, and Distance over Which Earthquake Is Felt**

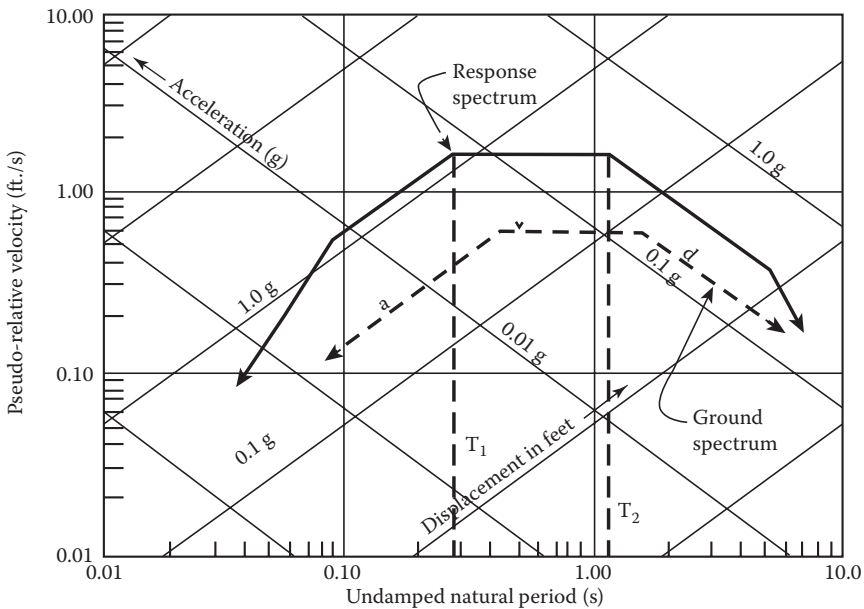
General Description	Richter Magnitude	Modified Mercalli Intensity	Expected Annual Incidence	Distance Felt (miles)
Microearthquake	below 2.0	—	600,000	—
Perceptible	2.0–2.9	I–II	300,000	—
Felt generally	3.0–3.9	II–III	49,000	15
Minor	4.0–4.9	IV–V	6000	30
Moderate	5.0–5.9	VI–VII	1000	70
Large (Strong)	6.0–6.9	VII–VIII	120	125
Major (Severe)	7.0–7.9	IX–X	18	250
Great	8.0–8.9	XI–XII	1.1	450

Source: C.F. Richter, *Elementary Seismology*, W.H. Freeman and Company, San Francisco, CA, 1976. With permission.

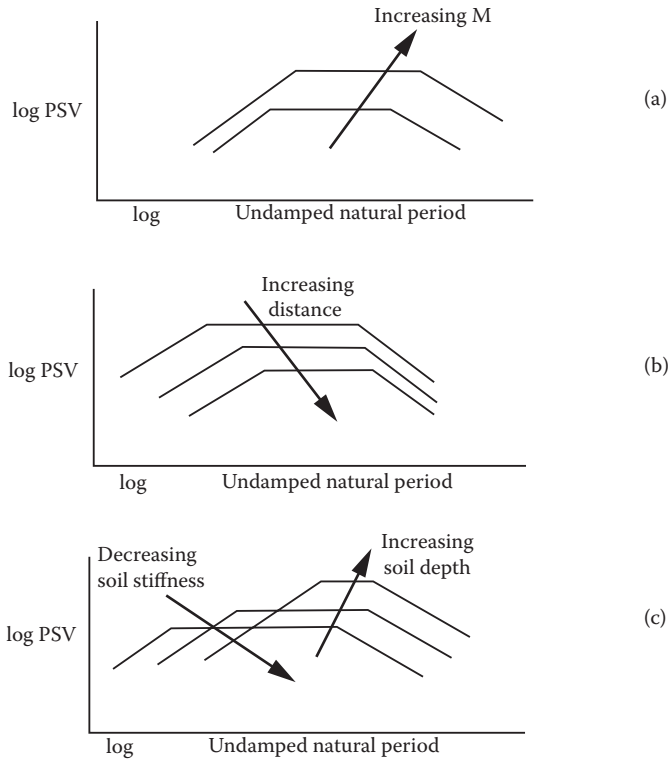




**FIGURE 3.52** Acceleration, velocity, and displacement record of an Imperial Valley Earthquake. (From J.P. Reger, Earthquakes in Maryland, Maryland Geological Survey, A Division of Maryland Department of Natural Resources, MD. <http://mgs.dnr.md.gov/esic/brochures/earthquake.html>, 2005. With permission.)



**FIGURE 3.53** Smoothed response spectra. (Modified from B. McClelland and M.D. Reifel, *Planning and Design of Fixed Offshore Platforms*, Van Nostrand Reinhold Co., New York, p. 403, 1986. With permission.)



**FIGURE 3.54** Factors affecting response spectral shape. (From B. McClelland and M.D. Reifel, *Planning and Design of Fixed Offshore Platforms*, Van Nostrand Reinhold Co., New York, p. 405, 1986. With permission.)

than 10% of the critical damping of the structure, then an approximate relationship between the acceleration, velocity, and displacement (pseudo) spectral plots can be given as

$$PSA = \omega PSV = \omega^2 PSD \tag{3.71}$$

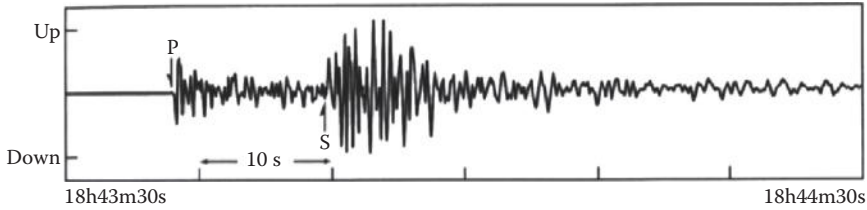
where PSA, PSV, and PSD represent the pseudo spectral acceleration, velocity, and displacement magnitudes of the response spectral plots, respectively.

Since the three components PSA, PSV, and PSD are related through Equation 3.71, it is convenient to represent this as a tripartite plot as shown in Figure 3.53 [78]. The term *pseudo* is used since the displacement or velocity or acceleration plots are only smoothed relative displacement (with respect to ground motions) plots and also are approximately valid only for low-damped structures. The response spectral values (or plots) are dependent on the variations of earthquake magnitudes (or intensities), source-to-site distances, and local site (soil) conditions; this dependence is illustrated in Figure 3.54 [79]. As seen in Figure 3.54a through c, the PSV increases as the magnitude of the earthquake increases, decreases as the distance to the earthquake source increases, increases as the depth of the soil layer below the structure increases, and decreases as the stiffness of soil, at site, decreases.

**Example 3.17**

The figure below shows a seismogram measured at a certain location and shows a true-to-scale seismic (displacement) wave motion (up and down) at the measured location. (a) Measuring the

amplitude of the displacement (in millimeters), with a scale, and knowing that the seismograph amplified the ground motion by approximately 3000 times, calculate the greatest amplitude of actual ground motion. Could you feel such a small motion? (b) Also using the time scale given to find the time difference between P and S waves, determine the epicentral distance of the earthquake. (Hint: Use Figure 3.51.)



- (a) As per the given scale, the time difference between the P–S waves is  $= (22/19)(10) = 11.6$  s. Maximum measured displacement from the above plot  $\sim 19.0$  mm. Hence, the actual maximum ground displacement  $\sim (19.0)/(3000) \sim 0.00633$  mm. This very small displacement will not be felt by anyone.
- (b) Using Figure 3.51, the epicentral distance  $\sim 100.0$  km.

**Example 3.18**

An earthquake, epicenter 100.0 km from the University of California, Berkeley, had a Richter magnitude of 5.0 measured on a Wood–Anderson seismograph there. What was the approximate maximum ground displacement at Berkeley if the seismograph’s magnification is 3000? Would you expect resulting damage to the old buildings on the campus?

Use of the plots given in Figure 3.51 shows that the maximum amplitude of ground displacement  $\sim 100.0$  mm.

Also the maximum ground displacement  $\sim (100.0)/(3000) \sim (1/30)$  mm.

Assuming a ground frequency of 3.0 Hz, the peak acceleration is  $\sim -(\omega^2)(\text{displacement}) \sim (2\pi f)^2(\text{displacement}) \sim [(2\pi)(3.0)]^2 (1/30) \sim 11.844$  mm/s<sup>2</sup> = 0.00121g which is less than Richter magnitude 1.0.

Hence, the earthquake will not be injurious to the buildings on the Berkeley campus.

**Example 3.19**

In an earthquake, a fault ruptures through your property. Would you gain or lose land in strike-slip faulting? Normal faulting? Thrust faulting? Discuss the legal implications for such a property in a built-up area.

- (1) Through strike-slip faulting, I will neither gain nor lose land.
- (2) Through normal faulting, I will gain since adjacent land will come within our boundaries.
- (3) Through thrust faulting, I will lose land depending on the angle of dip of the fault.

**3.8 ICE ENVIRONMENT AND PROPERTIES**

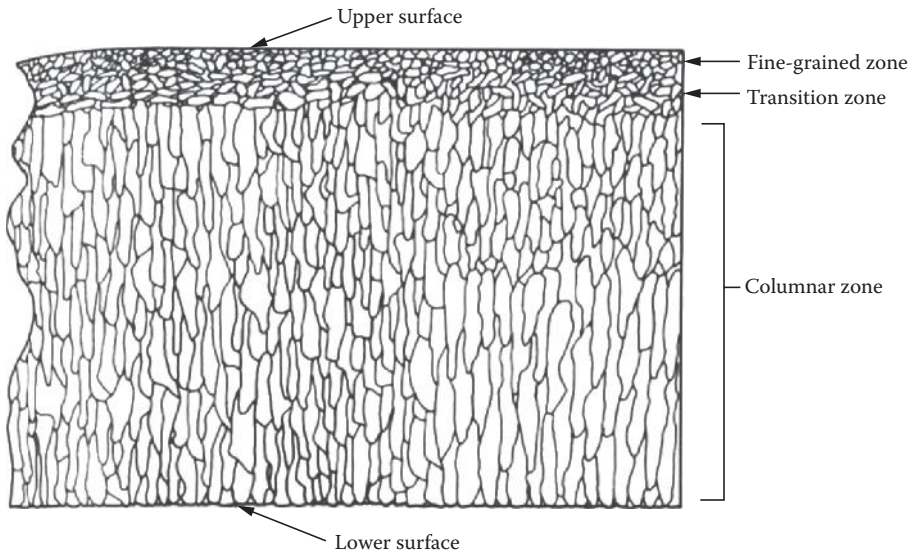
**3.8.1 INTRODUCTION TO ICE ENVIRONMENT AND PROPERTIES**

Ocean structures designed for many offshore areas of the world, such as the Arctic, Antarctic, and even some temperate zones, have to be designed to withstand the effects of ice. The nature and magnitude of forces exerted by ice depend on the nature of ice (such as thickness, concentration,

mass, mechanical properties, ice velocity, etc.) and the probable location of the offshore structure. The design of a fixed or floating offshore structure in the ice-infested region will likely be governed by ice loads exerted by ice floes, pack ice, and ice masses (such as icebergs, growlers, etc.), whereas the near-shore structures in a temperate zone may be exposed to damaging ice effects less frequently; consequently, the designer has to weigh the design against the economics of potential damage. The nature and magnitude of ice forces exerted on the structure will vary greatly depending on the structure type and the existing ice conditions (such as driving of the pack ice against the structure), impact of the moving mass of ice, vertical uplift and “jacking” forces of frozen ice (due to water level fluctuations) at the bottom of coastal structures such as jetties, piles of marinas, etc. Hence, the ice forces, exerted on the offshore or near-shore structures, are dependent on the local site and climatic conditions, type and properties of ice encountered, type and configuration of the structure, etc. While designing an offshore structure, the designer should always compile statistical ice data that are specific for the location under consideration and should include information on the concentration, distribution and type of ice, thickness of ice floes, mass of drifting ice mass, drift speed and direction, physical and mechanical properties of ice, air temperature range, tide range, probability distribution of ice thickness and speed, and probability of encounter of icebergs.

### 3.8.2 ICE PROPERTIES

The process of formation of ice and its structure in the ocean will be helpful to the understanding of the mechanical properties of ice. When the ice forms in the ocean during the fall and winter seasons, the initial surface layer has a more or less random structure, as shown in Figure 3.55 [80]; but as the ice grows in its thickness in the downward direction, a predominant polycrystalline structure develops, as seen in Figure 3.55. The ice sheet primarily consists of an array of more or less parallel, vertical, columnar crystals; the length of the crystal may extend over the whole thickness of the ice sheet. The horizontal dimensions of the crystal are only a small fraction of its length. Associated



**FIGURE 3.55** Columnar structure of ice. (From B. McClelland and M.D. Reifel, *Ice Forces*, Chapter 13, *Planning and Design of Fixed Offshore Platforms*, Van Nostrand Reinhold Co., New York, p. 369, 1986. With permission.)

with each of these crystals is a reference crystallographic axis, known as the *c*-axis of the crystal; the *c*-axis for the various crystals in the ice sheet tends to be horizontal. The *c*-axis of these crystals will be distributed at random through all directions in the horizontal plane; as a result, the mechanical property of ice tends to be isotropic in the horizontal plane. It tends to be different in the vertical direction and as such leads to the anisotropic characterization of the ice properties.

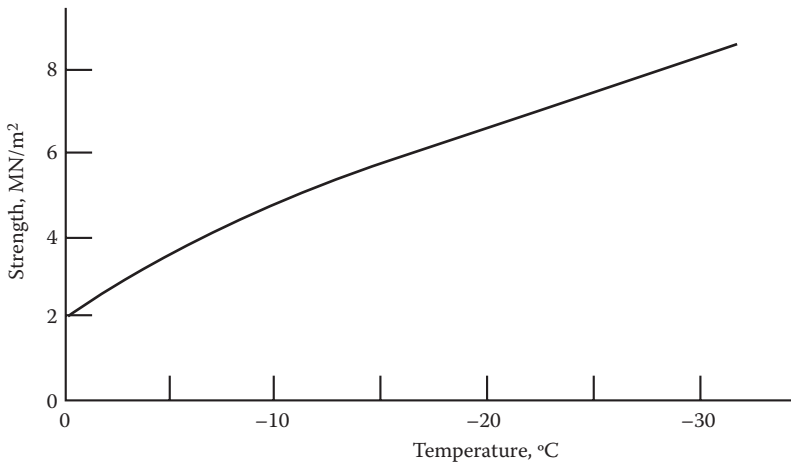
When ice sheet is formed in the presence of a prevailing current direction, the horizontal *c*-axis gets oriented in a particular direction and, as such, leads to a total anisotropic property in ice. Ice crystals tend to incorporate the brine solution (salinity) in between the columnar crystals as they grow; the presence of brine solution within the interstices of the columnar crystals of the ice sheet reduces the strength and the stiffness properties of ice. Over time, the brine solution within the interstices of the columnar ice sheet tends to migrate downward and drain out of the ice sheet. The ice strength is dependent on the salinity and the temperature of ice sheet.

According to Timco and Frederking [81], the sea ice strength  $\sigma$  (in megapascals), perpendicular and parallel to the columnar axis (at  $-10^\circ\text{C}$ ), can be written as

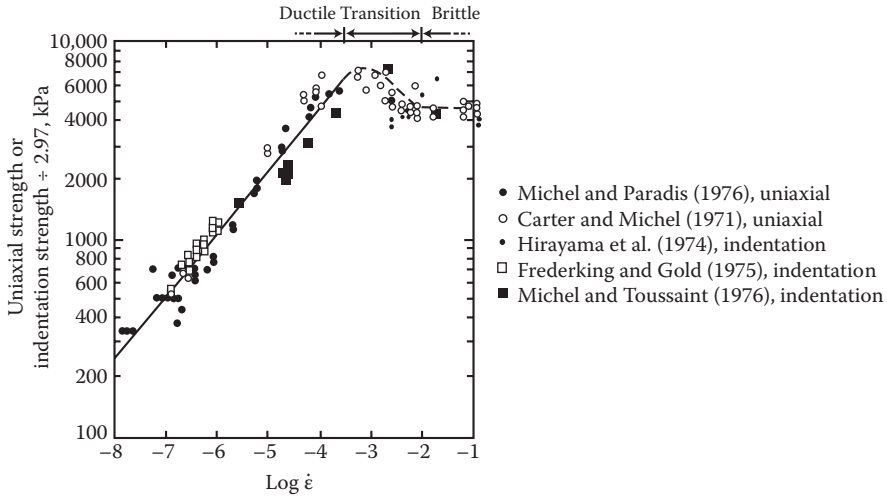
$$\begin{aligned} \sigma_{\perp} &= (39.0) (\dot{\epsilon}_n)^{0.26} \left(1.0 - \sqrt{(v_t/320)}\right) \\ \sigma_{\parallel} &= (150.0) (\dot{\epsilon}_n)^{0.22} \left(1.0 - \sqrt{(v_t/280)}\right) \end{aligned} \tag{3.72}$$

In Equation 3.72,  $\dot{\epsilon}_n$  is the nominal strain rate used in ice strength testing ( $10^{-5} \geq \dot{\epsilon}_n \geq 10^{-3}$ ), and  $v_t$  is the total porosity ( $\approx$  salinity) of ice. The temperature-dependent compressive strength of sea ice is shown in Figure 3.56 [82]. The loading history affects the ice forces in two ways, viz., (1) ice failure strength depends on loading rate, and (2) creep effects decrease the final ice failure strength. Ice failure strength increases first with the loading rate (or strain rate) where the ice behavior is ductile; the maximum strength is obtained before the ice becomes brittle. In the brittle region, the ice strength decreases by about 30% to 60%, as shown in Figure 3.57 [83].

Loading rate and stress (or strain) rate are directly proportional to ice velocity. Once the stress (or strain) field in the vicinity of the indentation of ice, as it impinges on the structure, is known,



**FIGURE 3.56** Temperature versus strength curve. (From B. McClelland and M.D. Reifel, *Ice Forces*, Chapter 13, *Planning and Design of Fixed Offshore Platforms*, Van Nostrand Reinhold Co., New York, p. 372, 1986. With permission.)



**FIGURE 3.57** Dependence of ice strength on strain rate [with strain rate =  $V/(4D)$ ,  $V$  = speed and  $D$  = diameter of indenter). (From M. Maattanen, Ice Forces, Chapter 4, *Offshore Structures*, Ed. D.V. Reddy and M. Arockiasamy, Krieger Publishing Company, Malabar, FL, p. 151, 1991. With permission.)

the stress (or strain) rate can be computed. According to Blenkarn [84], the stress rate of ice sheet, moving with a velocity of  $V$  against a circular pile of radius  $R$ , is given by

$$\dot{\sigma} = ((4\sigma_c V)/(\pi R)) \tag{3.73}$$

In order to solve for stress rate  $\dot{\sigma}$ , the equation has to be solved in an iterative manner, since the strength  $\sigma_c$  itself is dependent on stress rate; hence, the dependence is nonlinear. Once the stress rate

**TABLE 3.14**  
**Typical Properties of Sea Ice Suggested for Engineering Use**

Specific gravity	0.86 to 0.92 (average values)
Compressive strength	400 to 600 psi (up to 3000 psi for pure freshwater ice)
Tensile strength	100 to 200 psi
Shear strength	Few test results
Modulus of elasticity	$1.4 \times 10^6$ psi
Modulus of rupture	200 psi
Poisson's ratio	0.35
Coefficient of thermal expansion	0.000028 (average between $-20^\circ\text{F}$ and $32^\circ\text{F}$ )
Coefficient of friction	0.15 metal to sea ice 0.10 metal to freshwater ice 0.01 "wet" ice
Adhesion	30 to 100 psi
Volumetric expansion	9% (on freezing) maximum pressure exerted: 30,000 psi

Source: J.G. Gaythwaite, *The Marine Environment and Structural Design*, Van Nostrand Reinhold Company, New York, p. 244, 1981. With permission.

\* Above values to be used in lieu of observations or experimental data. Note well that the properties of sea ice are highly variable with respect to temperature, salinity, and the rate of freezing. Ice is an *anisotropic* material!

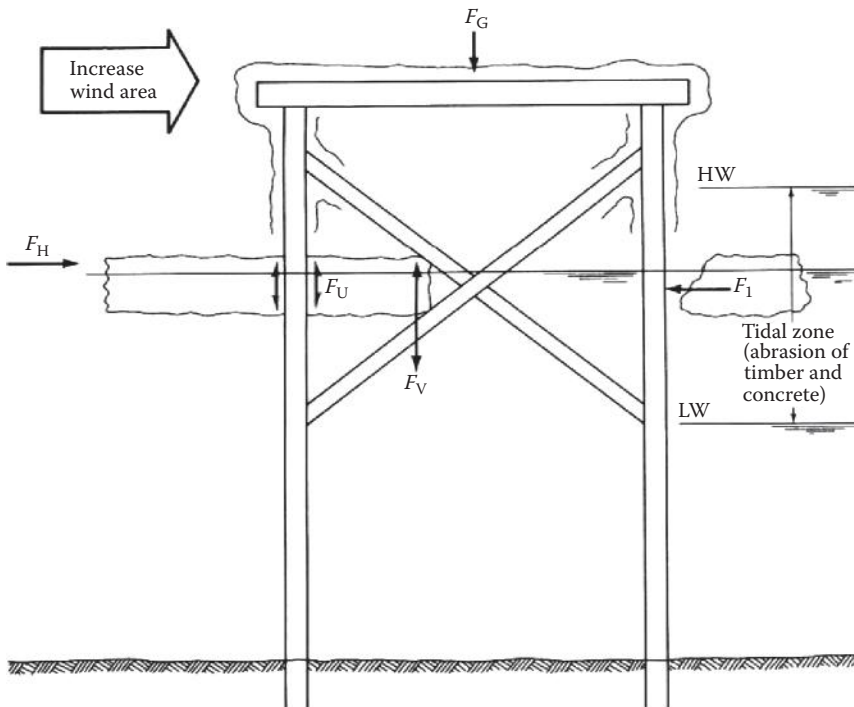
is calculated, then the strain rate can be obtained by dividing it by the Young’s modulus. Table 3.14 [85] gives some of the typical ice properties that can be used in the initial design process.

### 3.8.3 MODES OF POSSIBLE ICE–STRUCTURE INTERACTION

Some of the most important methods by which ice force can be exerted on an offshore structure are shown in Figure 3.58. Ice loads can be exerted in both the horizontal and vertical directions during this interaction process. The magnitude of the ice forces exerted on the structure depends on a number of factors, viz., (1) mode of interaction; (2) relative speed of ice movement with respect to structural movement; (3) flexibility of the structure; (4) configuration of the ice–structure interface; (5) characteristics of the ice cover or mass impinging on the structure; and (6) mechanical properties of ice.

Water trapped in crevices or pockets will expand by around 9.0% during the freezing process. Also it has been observed that above a temperature of  $-23^{\circ}\text{C}$ , a pressure of 207.0 MPa [86] would cause melting of ice. Consequently, this pressure can be taken as the upper limit for the pressure exerted on the structure. Ice accretion due to rain and freezing spray will increase the area exposed to wind action. It has been observed that ice accretion due to freezing spray alone can be of the order of 0.30 to 0.60 m or more in thickness. The vertical load  $F_G$  (due to gravity) exerted due to the ice accumulation on structure can be computed by assuming the unit weight of  $8830\text{ N/m}^3$  for the frozen ice (see Figure 3.58 [86]).

As indicated in Figure 3.58, ice exerts horizontal loads due to the pressure of an ice floe (or sheet) that is pushed against the structure by the action of wind, current, and/or thermal expansion. The



**FIGURE 3.58** Types of ice–structure interaction ( $F_I$  = ice impact loads,  $F_V$  = vertical load due to self-weight of ice,  $F_H$  = horizontal ice force,  $F_U$  = uplift ice forces, and  $F_G$  = gravitational ice load). (From J.G. Gaythwaite, *The Marine Environment and Structural Design*, Van Nostrand Reinhold Co., New York, p. 247, 1981. With permission.)



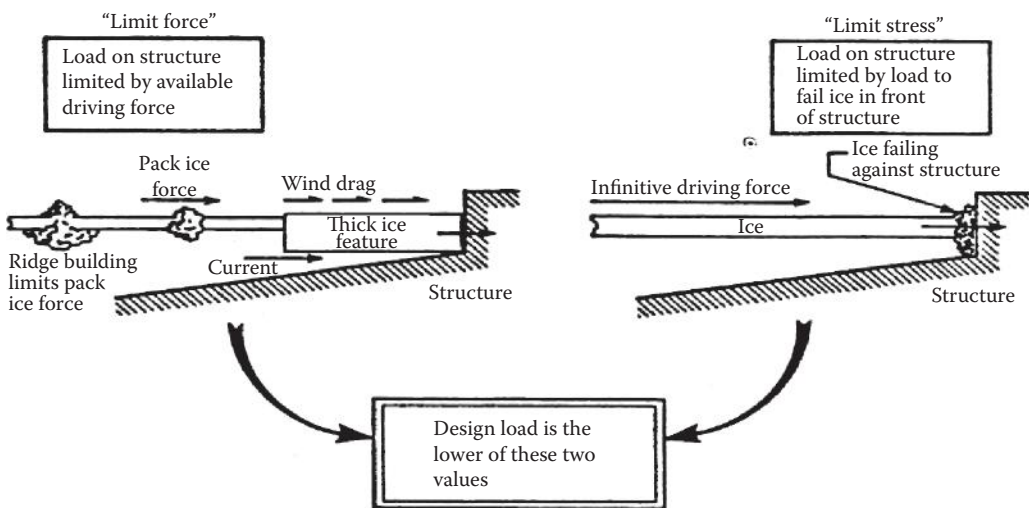
force  $F_H$  (see Figure 3.58) acting on the structure due to the wind/current/thermal action may be such as to cause a continuous failure of the ice floe (or sheet) on the ice–structure interface. When this continuous failure of ice floe occurs on structures, the resulting pressure gradients within the ice sheet may generate transient vibrations on the structure.

Ice masses (or bergs and growlers) driven by wind or currents may also impact a structure and generate large impact forces  $F_I$ . In addition to the above forces, ice frozen onto piles and cross bracings may also exert uplift forces  $F_U$  (see Figure 3.58) due to water level fluctuations, generated by tides, winds, waves, etc.

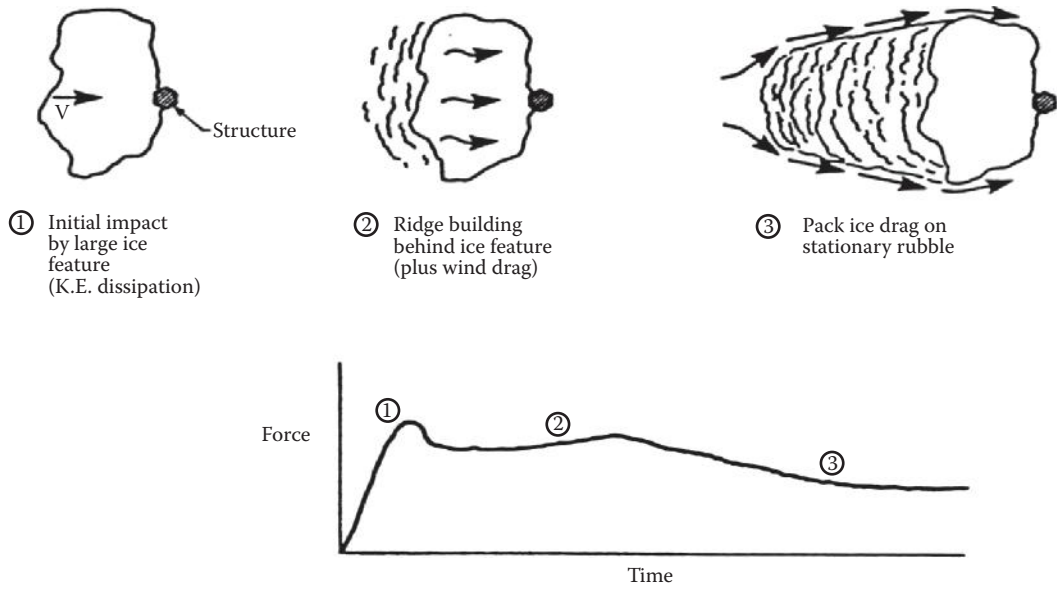
As explained earlier, the horizontal ice forces,  $F_H$ , transmitted to the structure are generated by natural environmental influences such as wind, wave, current, and thermal expansion. Due to these actions, the large ice sheet (or floe) may fail at the ice–structure interface when the failure strength of the ice sheet is less than the environmental forces exerted on the structure. This failure is termed as the “limit stress” failure, as shown in Figure 3.59 [87]. This failure may be generated by the crushing of the ice on the ice–structure interface or the bucking of ice plate in the near zone.

Instead, if the ice strength is such that no failure occurs on the ice–structure interface, the failure tends to occur in the ice field in the far zone, away from the ice–structure interface. The structure restrains the ice field from moving, and this causes the environmental forces acting on the structure to increase. When these forces increase to a certain value, failure may occur in the resisting ice field resulting in the formation of ice ridges in the pack ice. This failure is termed the “limit force” failure since the force exerted on the offshore structure is limited by the failure that has occurred in the ice field. The ridge-building may continue to occur around the stationary ice field. Thereafter, the failure occurs around the built ice ridge and the stationary ice field and the multiyear ice may continue to move around this blocked region, as shown in subfigure 3 of Figure 3.60 [87]. The possible ice force exerted on the structure, during this ice–structure interaction scenario, is shown in Figure 3.60, where the maximum force is stated to occur during the initial impact of the ice field with the structure. The ice forces continue to decrease as ridge-building occurs and may decrease further when ice flows around the blocked ice field, as shown in the figure.

Ice forces are very much influenced by the stress versus deformation characteristics of ice; we see quite a different load behavior at different strain rates and geometries. Figure 3.61 [88, 89] shows a load deformation map for failure in ice floes (or sheets), proposed by Ponter et al., in which the

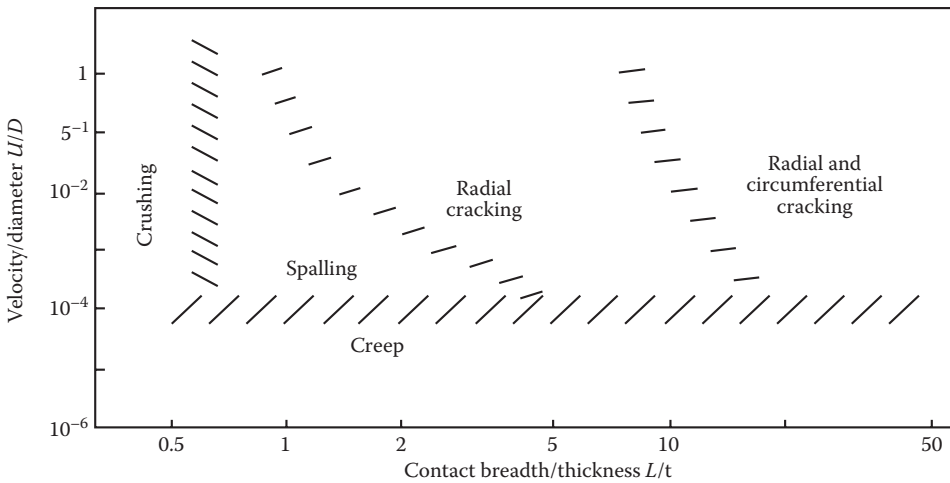


**FIGURE 3.59** Logic for design ice load. (From K.R. Croasdale, Symposium in Ice Engineering and Cold Ocean Engineering, Calgary, Ice Engineering II, Section 2.0, 1984. With permission.)



**FIGURE 3.60** Stages in ice–structure interaction. (From K.R. Croasdale, Symposium in Ice Engineering and Cold Ocean Engineering, Calgary, Ice Engineering II, Section 2.0, 1984. With permission.)

failure modes occur according to the strain rates and geometry of the ice–structure interface. It is seen that when both the ice strain rate ( $U/D$  ratio) and the (ice thickness)/(leg diameter) ratio are small, the failure in ice occurs due to creep alone. When the strain rate is large and the (ice thickness)/(leg diameter) is small, the failure occurs by crushing alone. When these ratios vary, the failure may change from creep or crushing to spalling or radial cracking of radial and circumferential cracking. Hence, the use of a single ice force equation for the whole ice–structure scenario is not possible; each situation has to be considered separately and the forces determined from the proper assessment of the failure mode and failure scenario.



**FIGURE 3.61** Ice deformation map. (From A.R.S. Ponter, A.C. Palmer, D.J. Goodman, M.F. Ashby, A.G. Evans and J.W. Hutchinson, *Cold Regions Science and Technology*, 8 (2), pp. 109–118, 1983. With permission.)

**Example 3.20**

Determine the strength of first-year sea ice at a total porosity of 10 parts per thousand and at strain rates of testing of (i)  $(2)(10^{-4})$  and (ii)  $(1.0)(10^{-5})$ . The temperature of testing is given as  $-10^\circ\text{C}$ , and the ice is loaded perpendicular to its columnar axis.

$$\text{The ice strength } \sigma_{\perp} = (39.0) (\dot{\epsilon}_n)^{0.26} \left(1.0 - \sqrt{(v_t/320)}\right)$$

$$\text{(i) } \sigma_{\perp} = (39.0)[(2.0)(10^{-4})]^{0.26}[1.0 - \sqrt{(10/320)}] = (39.0)(0.1092)(1.0 - 0.1768) \\ = 3.506 \text{ MPa.}$$

Check: Using Figure 3.57,  $\sigma_{\perp} \sim 3.9$  MPa. Hence, the stress value seems to be OK.

$$\text{(ii) } \sigma_{\perp} = (39.0)[(1.0)(10^{-5})]^{0.26}[1.0 - \sqrt{(10/320)}] = (39.0)(0.05012)(1.0 - 0.1768) \\ = 1.609 \text{ MPa.}$$

Check: Using Figure 3.57,  $\sigma_{\perp} \sim 2.25$  MPa. The stress seems to be a little lower.

**Example 3.21**

An ice floe is moving against the 0.30-m diameter, vertical steel column of an offshore structure with a speed of 1.0 m/s; the ice floe is cut through by the steel column, and the ice floe moves through the structure with almost the same speed as before. Determine the strain rate of failure in ice using Blenkarn's equation given earlier. Take  $E_{\text{ice}} = 9.5$  GPa.

The stress rate is given by  $\dot{\sigma} = (4\sigma_c V)/(\pi R)$ ; using the value of  $E$ , the stress and strain can be converted to strain rate, using  $\dot{\epsilon} = (\dot{\sigma})/E$  and stress  $\sigma_c = \sigma_{c_0} (\dot{\epsilon}/\dot{\epsilon}_0)^{1/n}$  [89], with  $n = 3.0$ . Hence, the equation to be solved is

$$\dot{\sigma} = (4\sigma_c V)/(\pi R); \text{ that is, } (\dot{\sigma}) = E\dot{\epsilon} = (4\sigma_{c_0} (\dot{\epsilon}/\dot{\epsilon}_0)^{1/n} V)/(\pi R)$$

The equation has to be solved in an iterative manner. From Figure 3.57,  $\sigma_{c_0} = 8.5$  MPa at  $\dot{\epsilon}_0 = 10^{-3}$ . From the given problem,  $R = 0.30$  m;  $E = (9.5)(10^3)$  MPa; and  $V = 1.0$  m/s. Solving the problem iteratively,

$$\dot{\epsilon} = (7.9)(10^{-3}) \text{ m/m/s}$$

**Example 3.22**

A very large ice floe, of nominal thickness 0.50 m, moves against: (a) a vertical steel column of diameter 0.60 m and of wall thickness 0.05 m and (b) an offshore island, protected with inclined (at an angle of  $\sim 15^\circ$ ) concrete slabs and of diameter 100.0 m. Discuss the type of failure that takes place in ice.

- Since the ice sheet thickness is not large, and the column diameter is also small, the failure will be "limit stress" failure.
- Even though the ice thickness is not large, the width of the island is quite large, and as such a "limit force" failure will govern the failure around the island.

**EXERCISE PROBLEMS**

- Using the extreme environmental conditions provided for the Grand Bank region (Newfoundland, Canada), given in Table P1.2, outline, in detail, the other environmental parameters and site characteristics that need to be gathered for the design and installation of a gravity production platform. Explain how you would use the collected data in the design.

2. A fixed steel platform is to be installed in an ocean environment with winds, waves, and currents, which are stochastic in nature. The water depth at the site is 100.0 m. Explain the various environmental data you would require to install the structure. The weather window required for installation is five full days over a prepared base. The maximum wave height allowed during installation is 1.5 m, and the maximum wind speed allowed is 20 kmph.
3. Wind data for hourly mean wind speeds are available for the last 50 years from the meteorological office. Explain how you would use the above data for computing (1) the design wind speed for a 50-year return period and (2) data for carrying out fatigue analysis of tower masts using wind roses and the associated omnidirectional wind speed distribution.
4. You are the lead structural engineer in an “Offshore Platform Design” group. A framed steel platform is to be designed for the Gulf of Mexico for a water depth of 200.0 ft. Outline the various design scenarios and the loads/forces you would consider as you plan to design the platform. Take into account the various seasonal environmental conditions, transportation of the platform to the site, and the final placement of the platform on the site.
5. As the lead engineer in a marine construction firm, you have been placed in charge of installing the underwater concrete storage tanks of a hybrid fixed platform. The storage tanks are built over a thick concrete slab having thick and stiff steel skirts all around the periphery and on the inside of the bottom surface. The structure is to be installed at a water depth of 100.0 m; the wind and wave conditions, at the site of installation, are influenced by severe winter storms. Explain the various environmental and site parameters you would require, and the data you would generate, as you consider the installation of the concrete storage tanks. The whole installation operation was expected to take four full days, and the maximum wave height and period, to which the structure can be exposed to during the installation, is 1.0 m and 6.0 s, respectively. Also, outline other precautions you would take to ensure the operation is a safe one.
6. Explain clearly, with neat sketches, each of the following: (1) wind speed variation as a function of the height parameters ( $z/h$ ), where  $z$  is the point at which wind velocity is required and  $h$  is the reference height ( $h = 10.0$  m), giving its variation over the ocean, a rough coastal area, an obstructed area over land, and an unobstructed area over land; (2) ocean currents that have significant effects on ocean operations and their speed variation with respect to the depth of the ocean; (3) techniques that will inhibit the shedding of vortices around structural surfaces subjected to wind flow; (4) factors that influence the trajectory of an iceberg; and (5) stability of a towed concrete structure.
7. Wind velocity is dependent on the mean wind flow and the time-varying gust components caused by eddies in the wind flow; the gust speeds vary randomly in both time and space. Similarly, the wind forces on the structures also vary in a random manner. How would you characterize this wind velocity so that it can be used in the estimation of wind forces on structures? Discuss this as (i) physical characterization problem and (2) code-based design criteria. [Use the Canadian (CSA), American (API), or European code.]
8. “Real wind is not of constant speed, but consists of a mean flow containing gusts of random strength, size, and direction.” Explain the dynamic wind characteristics clearly and describe how you would characterize this wind velocity vectorially, and use the wind spectrum, wind-averaging period, and gust factors to compute the design wind speeds on various components of an offshore platform.
9. Using the wind occurrence and directional data given in Table P3.1, draw the following: (1) wind speed–direction plots (that show the variation of wind speed and direction, within certain velocity ranges); (2) percentage wind occurrence versus speed (range) plot; and (3) wind–rose plot, which shows the average wind speed variation as a function of direction for the whole year. In the wind–rose plot, also draw the average wind-speed contours.

**TABLE P3.1**  
**Wind Speed Occurrence for Typical North Sea Site**

Hourly Average Wind Speed (for 1 year) at $z_0$ , Height of 10.0 m (m/s)	Occurrence (%) of Wind from								
	N	NE	E	SE	S	SW	W	NW	Total
0.0–5.0	5.0	2.4	2.1	2.1	3.7	3.0	3.1	4.1	25.5
5.0–10.0	5.7	2.0	1.6	5.0	8.3	7.0	5.9	5.8	41.3
10.0–15.0	2.9	0.7	0.5	3.6	6.5	4.5	3.0	2.6	24.3
15.0–20.0	0.8	0.5	0.4	1.1	1.9	1.2	1.0	0.5	7.4
20.0 +	0.1	0.0	0.0	0.2	0.5	0.2	0.3	0.2	1.5
Total	14.5	5.6	4.6	12.0	20.9	15.9	13.3	13.2	100.0

10. Plot the variation of wind velocity with respect to height, at an offshore site, having a wind speed of 40.0 m/s at a height of 10.0 m above MSL; the latitude of the site is  $45^\circ\text{W}$ . Use Table P3.1 as a guideline and use the following wind velocity profile equation:

$$v_z = 2.5u_* \left[ \ln\left(\frac{z}{z_0}\right) + 5.75\left(\frac{z}{h}\right) \right],$$

where  $v_z$  = wind velocity at a height  $z$  above the zero-plane;  $u_*$  = friction velocity;  $z_0$  = surface roughness parameter;  $z$  = height above the zero-plane; and  $h$  = height of boundary layer.

- Write short notes on (1) wind roses; (2) parent and extreme value distributions of mean hourly wind speeds; and (3) mean wind speed, gusts, and gust factor.
- The extreme value distributions of the annual maximum wind speeds taken over a number of years of wind data is given in Figure 3.22. Compute (1) return period and (2) probability of exceedance for a mean hourly wind speed of 33 m/s.
- Explain the concept of the wind energy spectrum (using sketches) and the averaging period for wind.
- (a) Briefly describe the various mechanisms by which waves are generated from their initiation to the fully developed sea. (b) Discuss several ways in which breaking of smaller waves will add energy to the longer wave. (c) Characterize the storm and swell waves and give reasons for their existence. (d) Discuss how tropical and extratropical storms differ with respect to generation of waves.
- (a) Give the regions of the world's oceans where you expect the greatest storm energy and give reasons for it; also give the coasts of the world that experience the greatest swell energies. (b) What is the general nature of the wave conditions that exist around the minimum swell coasts?
- Explain the various types of waves encountered in the ocean, categorizing them by (i) wave frequency (or period); (2) primary disturbing force; and (3) primary restoring force.
- Give pertinent answers for the following: (a) Bernoulli's equation for fluid pressure is given by

$$\frac{\partial \Phi}{\partial t} + gy + \frac{1}{2}(u^2 + v^2) + \frac{p}{\rho} = f(t).$$

Linearize the above equation for fluid pressure on the free surface ( $y = h$ ), for incompressible flow, and clearly state when this linearized dynamic free surface condition is not valid.

(b) The linearized surface wave velocities are given by

$$u = \frac{\partial \Phi}{\partial x}, \text{ and } w = \frac{\partial \Phi}{\partial y}$$

with

$$\Phi = \left( \frac{ag}{\omega} \right) \left[ \frac{\cosh k(y+h)}{\cosh kh} \right] [\sin(kx - \omega t)]$$

$$c^2 = \left( \frac{g}{k} \right) \tanh kh$$

$$L = cT = \left( \frac{gT^2}{2\pi} \right) \tanh \left( \frac{2\pi h}{L} \right)$$

$$k = \frac{2\pi}{L}$$

$$a = \frac{H}{2} \text{ (amplitude of wave)}$$

Reduce the above equation for (i) deepwater and (2) shallow water and find the velocities; also state the errors involved in the above reduction.

18. A wave tank is 200.0 m long, 12.00 m wide, and 7.0 m deep. The tank is filled with fresh-water to a depth of 5.5 m, and a wave of 1.0-m height and 4.0-s period is generated. Find (1) wave celerity and length; (2) the water particle velocities and wave pressure at a point located at 5.0 m, ahead of the wave crest, and at a depth of 1.5 m below the SWL (assume  $t = 0.0$  s for all numerical computations); and (3) the horizontal and vertical dimensions of the orbit of the water particle at this location.
19. A fixed platform is to be installed at  $91^\circ\text{W}$  and  $29^\circ\text{N}$  in the Gulf of Mexico. Determine (1) omnidirectional wave height; (2) principal direction of the wave; (3) wave direction factors; (4) currents associated with the wave height; (5) wave period; (6) storm tide; (7) wind speed; (8) wave kinematics factor; and (9) thickness of marine growth. (Use the provisions in the API code.)
20. An Airy's wave of length 600.0 ft. is generated in waters of depth 90.0 ft. Determine (1) the maximum horizontal and vertical particle velocities and accelerations at a depth of 2.0 ft. below the MSL; (2) the wave speed  $C$ ; and (3) the values of  $n$  and  $L/L_0$  (with  $n$  being the fraction of the mechanical energy that is being transmitted forward for each wave period and  $L_0$  being the deepwater wavelength), and plot them as a function of  $h/L$ , with  $h/L$  varying from 0.50 to 0.05.
21. (a) A steel tower is installed in a water depth of 90.0 ft. to gather site-specific oceanographic data. A dynamic pressure gauge located 60.0 ft. above the bottom senses an average maximum dynamic pressure of 160.0 lb./ft.<sup>2</sup> at a period of 11 s. Find the height and length corresponding to this wave. Is this the maximum wave height that is present at the site? (b) We know that surface tension forces become very important as the wavelengths decrease. In particular, as wavelengths approach 1.00 in., the surface tension forces become important, relative to the gravity forces. We wish to make a model study of a semisubmersible platform (200 ft.  $\times$  200 ft.) as it is excited by waves with periods ranging from 4 to 15 s. What is the minimum scale ratio that is acceptable? What factors other than surface tension effects should be considered in the determination of the scale ratio?

22. A pressure sensor mounted at the ocean bottom indicates a wave pressure varying between 56 and 41 kN/m<sup>2</sup>, when a train of waves, of period 5.6 s, passes over it moving toward the shore. Determine (1) the depth of the pressure sensor below the sea level; (2) the wave height, wave speed, group wave speed, energy, and power, as the waves pass over the sensor; (3) wave particle velocity at a height of 2.0 m above the seabed, as the wave crest passes over the sensor; and (4) the deepwater wave speed, length, group speed, energy, and power, assuming that no wave refraction occurs as the wave moves from deepwater toward the shore.
23. The wave celerity,  $C$ , is defined by

$$C^2 = \left( \frac{gL}{2\pi} \right) \tanh \left( \frac{2\pi d}{L} \right)$$

where  $d$  = the water depth to MSL and  $L$  = the regular wavelength. Using the above equation, find the relationship that governs the wavelength and the period of the wave. How does the above equation get modified for shallow water and deep wave conditions?

24. A deepwater wave having a length of 1000.0 ft. and a height of 10.0 ft. travels toward the shore. (a) What are the values of the length and celerity at the position where the water depth is (1) 50 ft. and (2) 5 ft.? (b) What are the values of the total wave energy and the energy flux (per unit width) of the wave in deepwater (assume salt water with  $\rho = 2.00$  slugs/ft.<sup>3</sup>)?
25. A wave of length 150.0 ft., height 6.0 ft., and period 6.0 s is traveling toward the coast from deepwater, with the wave crests parallel to the coast. Determine (1) wave speed as it approaches the coast; (2) the depth at which the wave would begin to change form due to bottom friction; (3) wavelength, period, and height at a water depth of 5.0 ft.; (4) the total energy of the wave in ft./lbf per foot of wave width; and (5) the horsepower that the above wave (of width 1.0 ft.) would generate if the conversion took place without any energy loss.
26. For small amplitude waves (Airy's waves), the water depth at a location is 150.0 ft., the wave period is 12.0 s, and the wave height is 22.0 ft. (a) Determine the length of the wave at that location. (b) If a finite amplitude, Stokes' second-order wave is assumed to be present at the location, determine the profile and length of the wave.
27. A wave, having a height of 8.0 m and period of 9.0 s, is moving toward the shore at a water depth of 25.0 m. (a) Calculate the water surface profiles over one wavelength and plot them (in a single figure) for (1) linear Airy's wave and (2) Stokes' second-order wave. (b) Repeat the above for the water particle speeds at a depth of 1.5 m below the surface of the SWL. (c) Plot the mass transport speed as a function of its position (along a vertical line) above the seabed level.
28. A wave with period 10.0 s moving normal to the shore undergoes shoaling as it feels the bottom while moving from the deep to shallow water. Determine the wavelength in water depths of (1) 400.0 ft.; (2) 300.0 ft.; (3) 150.0 ft.; (4) 75.0 ft.; (5) 30.0 ft.; (6) 15.0 ft.; and (7) 6.0 ft.
29. A deepwater wave having a height of 2.8 m and period of 9.0 s is moving perpendicular toward the shore. A water particle velocity of 0.28 m/s, at the bottom of the sea, is required to cause a movement of the sand particles at the bottom. Compute the water depth at which the sand particles will start to move as the wave shoals.
30. The section of a shore has a bottom surface layer of coarse stones, of average diameter 80.0 mm, and the depth of water at that location is 2.0 m. If the required speed to start the motion of these coarse stones is 1.6 m/s, will a wave with a height of 1.6 m start the coarse stones to move?



31. (a) Make a sketch of an ideal linear and progressive wave, and list its various components. (b) Distinguish between (1) sea and swell; (2) wave height and wave steepness; (3) plunger and spiller wave; and (4) node and antinode. (c) A surfer surfing along the sea slides downward on the face of a wave. The steepness of the wave face is governed by the decrease in wavelength ( $L$ ) and the increase in wave height ( $H$ ), as the wave slows in shallow water. Explain how the surfer must adjust the board to stay on the face of the wave as the wave approaches the coast.
32. An offshore drilling platform is to contain a deck structure whose bottom must be at least 2.0 m above the reach of the highest 1/10 wave at the site. The worst storm conditions at the site can be assumed to be that due to a fully developed sea due to a 45.0-knot wind at a height of 19.5 m. If the platform is located at a water depth of 150.0 ft., compute the height required for the underside of the platform, above the highest tide and surge level.
33. The particle velocity ( $u$ ) of a progressive wave, at a point ( $x, y, t$ ) within the body of the moving liquid, is represented by  $u(x, y, t)$ . Derive the equation for the horizontal component of local and convective particle accelerations within the wave.
34. A storm wave has a significant wave height of 4.25 m. (a) Plot the Rayleigh distribution for this storm and indicate  $H_{1/100}$ ,  $H_{rms}$ , and  $H_s$  on the figure. (b) Determine the percentages of waves that will exceed the average wave height, the rms height, and  $H_{1/10}$ .
35. The analysis of a wave height versus time record, at a location, gives the following data:

Wave height (m)	0.6	1.2	1.6	2.4	2.0
Number of waves	52	42	30	6	2

From the above data, compute (1)  $H_{1/3}$ , (2)  $H_{1/10}$ , (3)  $H_{1/100}$ , and (4)  $H_{av}$ .

36. The following results were obtained from the analysis of a very long wave height–time history record:

Wave height range (m)	0.00 to 0.60	0.60 to 1.20	1.20 to 1.80	1.80 to 2.40	2.40 to 3.00
Number of waves	4500	5400	3800	2200	500

Plot the wave histogram using the above data and compare it with the Rayleigh’s distribution.

37. Wave data are measured (through a pressure gauge) at an identified installation site (for an offshore structure) over a period of 1 year. The pressure gauge is monitored daily for a period of 30.0 min, and the highest significant wave height computed for each week (using the measured time history). Due to the gauge malfunction, data were obtained only for 47 weeks. The computed data of the significant wave height are given below (wave heights in meters):  
 1.10, 1.87, 3.75, 2.06, 2.50, 1.51, 3.52, 0.98, 2.56, 1.34, 1.16, 3.08, 1.85, 1.70, 2.07, 2.04, 2.30, 1.44, 3.36, 2.54, 0.84, 1.88, 2.09, 3.10, 1.63, 3.05, 3.00, 2.95, 1.44, 3.15, 1.38, 1.54, 2.40, 1.18, 2.52, 2.84, 4.58, 3.35, 1.63, 1.48, 2.36, 2.24, 4.50, 1.31, 2.55, 1.39, 3.33  
 (a) Plot the above data on a Gumbel plot and estimate the 10- and 50-year return period significant wave heights (smaller amount of data used than the actual amount of data for Gumbel’s prediction). (b) Determine the possibility of this wave height occurring in any 5-year period.
38. Draw the wave scatter diagram from the following data (with contours at every increment of 15 wave data), given in Table P3.2.
39. Fully developed sea conditions exist at a location under the following conditions: steady wind speed  $V = 105.0$  ft./s (at a height of 64.0 ft., above sea level);

**TABLE P3.2**  
**Wave Scatter Data**

Significant Wave Height Data $H_2$ (m)	Number of Wave Height Data								
	Zero Crossing Wave Period, $T_2$ (s)								
	4–5	5–6	6–7	7–8	8–9	9–10	10–11	11–12	12–13
0.0–0.5	1	1	2	0	0	0	0	0	0
0.5–1.0	2	18	19	14	10	5	1	1	0
1.0–1.5	5	30	42	25	18	14	5	2	1
1.5–2.0	2	21	50	42	24	14	8	1	1
2.0–2.5	0	11	52	54	25	8	4	1	0
2.5–3.0	0	2	33	40	25	7	2	1	0
3.0–3.5	0	1	17	35	23	10	5	1	0
3.5–4.0	0	0	5	27	21	9	3	1	1
4.0–4.5	0	0	2	21	20	12	3	2	1
4.5–5.0	0	0	0	9	20	11	3	0	1
5.0–5.5	0	0	0	3	11	10	3	1	1
5.5–6.0	0	0	0	2	6	10	4	1	0
6.0–6.5	0	0	0	0	4	10	5	1	0
6.5–7.0	0	0	0	0	2	5	3	1	0
7.0–7.5	0	0	0	0	0	3	2	0	0
7.5–8.0	0	0	0	0	0	1	3	1	0
8.0–8.5	0	0	0	0	0	0	2	0	0
8.5–9.0	0	0	0	0	0	0	1	0	0

$$gH_s/V^2 = 0.283$$

$$gT_s/2\pi = 1.2$$

and

$$T_s = 0.946/f_0.$$

- (a) Plot the following spectra (as a function of frequency) for the above data: (1) Neumann spectrum; (2) Pierson–Moskowitz spectrum; (3) Bretschneider spectrum; and (4) JONSWAP spectrum. (b) Determine the error involved in computing  $H_{1/3}$  by the Pierson–Moskowitz method, when the wind speeds accepted at a height of 64.0 ft. (above sea level) are actually those recorded from a height of 25.0 ft.
40. Discuss, clearly, how limit stress or limit force will govern the loads experienced by (1) a narrow vertical cylinder and (2) a wide dredged artificial island (with a hard perimeter), when a mobile ice pack, with embedded multiyear ice floes, moves against them.
41. (a) Describe, with neat sketches, the failure scenario and the limit loads experienced by an Arctic ice pack as it moves against a gravelly and sandy offshore island (well protected on its sides by heavy and thick concrete slabs). (b) Explain, clearly, the concept of rubble formation, mixed mode of failure, and ridge building.

42. Distinguish between any two of the following: (1) limit stress and limit force ice loads on offshore structures; (2) ice failure scenario around a vertical and a conical structure in the sub-Arctic regions; and (3) ice deformation map and universal ice pressure map.
43. (a) A seismogram is shown in Figure 3.51, which shows the arrival of P-waves and S-waves. Use the values of 8.0 km/s for the velocity of P-waves (compressive) and 4.4 km/s for that of the S-waves (shear); check the distance between the seismograph station and the focus of the earthquake. (Hint: Measure the time interval between the phases of the P- and S-waves marked with P and S in the figure.) (b) In addition, measure with the ruler the largest wave amplitude given in the figure, and if the seismograph amplifies the actual displacement approximately by 3000 times, and that the figure has been reproduced at the original scale, compute the greatest amplitude (as a fraction of 1 mm) of the actual ground motion. Could a human being feel such a small motion?
44. (a) Taking the mean speed of compressive P-waves through the earth to be 10 km/s, find the approximate time taken by the P-wave to travel from one side of the earth to the other side. (b) Could a seismograph on a ship detect an earthquake? (c) At the present rate of slip along the San Andreas Fault (~30.0 mm per year), find the time it would take before Los Angeles becomes a suburb of San Francisco. (d) Explain why fish are stunned, or killed, by strong earthquakes originating below the sea.
45. (a) Assuming that six damaging earthquakes have occurred in your area during the last 120 years, and during that time, 600 small earthquakes have been recorded by the local seismograph station, determine the simple chance that the next earthquake will be a damaging one. (b) During a major earthquake, often, the largest number of collapses occurs in 10- to 12- story concrete-frame apartment houses. Discuss why such tall buildings collapse rather than shorter buildings. (c) Consider a square wood column of side  $b$  and height  $h$  that stands on the floor; the column is constrained such that the block can only overturn but not slide. Show that, if a constant acceleration  $a$  is applied at the ground, perpendicular to one edge, the block will overturn if  $a > g \left( \frac{b}{h} \right)$ , where  $g$  is the acceleration due to gravity.

## REFERENCES

1. A.C. Duxbury and A.B. Duxbury, 1991. *Introduction to the World's Oceans*, Wm. C. Brown Publishers, Dubuque, IA, p. 163.
2. T. Day, 1999. *Oceans*, Facts on File Inc., Hong Kong, p. 28.
3. T. Day, 1999. *Oceans*, Facts on File Inc., Hong Kong, p. 63.
4. Capital Region District, Environmental Services, 2008. Victoria, Vancouver, Available at [www.crd.bc.ca/watersheds/protection/geology-processes/globaloceancurrents.htm](http://www.crd.bc.ca/watersheds/protection/geology-processes/globaloceancurrents.htm).
5. Available at <http://geology.uprm.edu/Morelock/waves.htm>.
6. A.C. Duxbury and A.B. Duxbury, 1991. *An Introduction to the World's Oceans*, Wm. C. Brown Publishers, Dubuque, IA, p. 219.
7. D.E. Ingmanson and W.J. Wallace, 1989. Oceanography, An introduction, Chapter 3 on *The Waves*, Fourth Edition, Wadsworth Publications Inc., Belmont, CA, p. 189.
8. T. Day, 1999. *Oceans*, Facts on File, Inc., Hongkong, p. 70.
9. B.A. Bolt, 2004. *Earthquakes*, W.H. Freeman and Co., New York, p. 35.
10. B.A. Bolt, 2004. *Earthquakes*, W.H. Freeman and Co., New York, p. 149.
11. K.M. Shedlock and L.C. Pakiser, 1997. Available at <http://pubs.usgs.gov/gip/earthq1/>.
12. C.J. Ammon, 2001. Available at [http://eqseis.geosc.psu.edu/~cammon/HTML/Classes/IntroQuakes/Notes/earthquake\\_effects.html](http://eqseis.geosc.psu.edu/~cammon/HTML/Classes/IntroQuakes/Notes/earthquake_effects.html).
13. N. Bowditch, 2002. *Ice in the Sea*, Available at <http://www.irbs.com/bowditch/pdf/chapt34.pdf>.
14. Mahoney, H. Eicken, L. Shapiro and T.C. Grenfell, 2004. Ice motion and driving forces in spring on the Alaskan chukchi coast, *Journal of Glaciology*, Volume 50, Issue 169, pp. 195–207.
15. Environment Canada, 2002. *Fact Sheet on Icebergs*, Available at <http://ice-glaces.ec.gc.ca>. Environment Canada, Ice Service, 2009. Available at <http://ice-glaces.ec.gc.ca/App/WsvPageDsp.cfm>.
16. B. McClelland and M.D. Reifel, 1986. *Planning and Design of Fixed Offshore Platforms*, Van Nostrand Reinhold Co., New York, p. 319 (modified).

17. N.D.P. Barltrop and A.J. Adams, 1991. *Dynamics of Fixed Marine Structures*, Butterworth-Heinemann Ltd., Oxford, UK, p. 395–491.
18. I. Van Der Hoven, 1957. Power spectrum of horizontal wind speed in the frequency range from 0.007 to 900 cycles per hour, *Journal of Meteorology*, Volume 14, pp. 160–164.
19. N.D.P. Barltrop and A.J. Adams, 1991. *Dynamics of Fixed Marine Structures*, Butterworth-Heinemann Ltd., Oxford, UK, p. 405.
20. N.D.P. Barltrop and A.J. Adams, 1991. *Dynamics of Fixed Marine Structures*, Butterworth-Heinemann Ltd., Oxford, UK, p. 420.
21. N.D.P. Barltrop and A.J. Adams, 1991. *Dynamics of Fixed Marine Structures*, Butterworth-Heinemann Ltd., Oxford, UK, p. 421 (modified from).
22. N.D.P. Barltrop and A.J. Adams, 1991. *Dynamics of Fixed Marine Structures*, Butterworth-Heinemann Ltd., Oxford, UK, p. 422 (modified from).
23. N.D.P. Barltrop and A.J. Adams, 1991. *Dynamics of Fixed Marine Structures*, Butterworth-Heinemann Ltd., Oxford, UK, p. 423.
24. R.I. Harris and D.M. Deaves, 1981. *The Structure of Strong Winds*, Proceedings of CIRIA Conference “Wind Engineering in the Eighties,” November 1980, Paper 4, London.
25. H. Charnock, 1955. Wind stress on a water surface, *Quarterly Journal of royal Meteorological Society*, Volume 81, pp. 639–640.
26. N.D.P. Barltrop and A.J. Adams, 1991. *Modified from Dynamics of Fixed Marine Structures*, Butterworth-Heinemann Ltd., Oxford, UK, p. 426.
27. J. Wu, 1969. Wind stress and surface roughness at air-sea interface, *Journal of Geophysical Research*, Volume 74, Issue 2, pp. 444–455.
28. T.H. Dawson, 1983. *Offshore Structural Engineering*, Prentice Hall, Inc., Englewood Cliffs, NJ, pp. 90–93. (a) API-RP2A, 1989. *Recommended Practice for Planning, Designing and Constructing Fixed Offshore Platforms*, American Petroleum Institute, Washington, DC, 18th ed.
29. J.F. Anthoni, 2000. *Oceanography of Waves*. Available at [www.seafriends.org.nz/oceano/waves.html](http://www.seafriends.org.nz/oceano/waves.html).
30. Yahoo Answers, 2008. [answers.yahoo.com/question/index?qid=20080420183028AA0n2ly](http://answers.yahoo.com/question/index?qid=20080420183028AA0n2ly).
31. G.B. Airy, 1845. *On Tides and Waves*, Encyclopedia Metropolitana, Italy.
32. G.G. Stokes, 1947. On the theory of oscillatory waves, *Transactions of the Cambridge Philosophical Society*, Volume 8, pp. 441–455.
33. R.M. Sorensen, 1993. *Basic Wave Mechanics: For Coastal and Ocean Engineers*, John Wiley & Sons, Inc., New York, pp. 8 (modified).
34. J.F. Wilson, 1984. *Dynamics of Offshore Structures*, John Wiley & Sons, New York, p. 81 (modified).
35. US Army Corps of Engineers, 1984. *Shore Protection Manual*, Vol. II, Coastal Engineering Research Center, Waterways Experiment Station, (two volumes); also pp. 3.28–3.29.
36. R.M. Sorensen, 1993. *Basic Wave Mechanics for Coastal and Ocean Engineers*, John Wiley & Sons, New York, p. 16.
37. N.D.P. Barltrop and A.J. Adams, 1991. *Dynamics of Fixed Marine Structures*, Butterworth-Heinemann Ltd., Oxford, UK, p. 253.
38. R.M. Sorensen, 1993. *Basic Wave Mechanics for Coastal and Ocean Engineers*, John Wiley & Sons, New York, p. 19.
39. A.T. Ippen, 1966. *Estuary and Coastline Hydrodynamics*, McGraw-Hill Book Co., New York.
40. T. Sarpkaya and M. Isaacson, 1981. *Mechanics of Wave Forces on Offshore Structures*, Van Nostrand Reinhold, New York.
41. J.J. Myers, C.H. Holm and R.F. McAllister, 1969. *Handbook of Ocean and Underwater Engineering*, McGraw-Hill Book Co., New York, pp. 12.26–12.29.
42. R.G. Dean and R.A. Dalrymple, 1984. *Water Wave Mechanics for Engineers and Scientists*, Prentice Hall, Inc., Englewood Cliffs, NJ, pp. 296–305.
43. R.M. Sorensen, 1993. *Basic Wave Mechanics for Coastal and Ocean Engineers*, John Wiley & Sons, New York, p. 57.
44. R.M. Sorensen, 1993. *Basic Wave Mechanics for Coastal and Ocean Engineers*, John Wiley & Sons, New York, p. 60.
45. D.J. Kortweg and G. deVries, 1895. On the change of form of long waves advancing in a rectangular canal and on a new type of long stationary waves, *Philosophical Magazine*, Volume 39, pp. 422–443. Available at [http://en.wikipedia.org/wiki/Diederik\\_Korteweg](http://en.wikipedia.org/wiki/Diederik_Korteweg) Accessed on October 30, 2008.
46. J.S. Russell, 1844. *Report on Waves*, Fourteenth Meeting of the British Association for the Advancement of Science, Published in York, UK, September, p. 311–390.

47. L. Rayleigh, 1876. On waves, *Philosophical Magazine and Journal of Science*, Volume 1, Issue 4, 1876, pp. 257–279.
48. R.G. Dean, 1965. Stream function representation of nonlinear ocean waves, *Journal of Geophysical Research*, Volume 70, pp. 4561–4572.
49. R.M. Sorensen, 1993. *Basic Wave Mechanics for Coastal and Ocean Engineers*, John Wiley & Sons, New York, p. 60.
50. US Army Corps of Engineers Coastal Engineering Research Center, 1984. Shore protection manual, volume I, in: *Wave and Water Level Predictions*, p. 3.3.
51. L. Rayleigh, 1880. On the resultant of a large number of vibrations of the same pitch and of arbitrary phase, *Philosophical Magazine*, Volume 10.
52. J.F. Wilson, 1984. *Dynamics of Offshore Structures*, John Wiley & Sons, New York, p. 159.
53. US Army Corps of Engineers Coastal Engineering Research Center, 1984. Shore protection manual, volume I, in: *Wave and Water Level Predictions*, p. 3.9.
54. Department of Energy, 1990. Metocean Parameters—Wave Parameters—Supporting Document to Offshore Installations: Guidance on Design, Construction and Certification – Environmental Considerations. OTH 89 299.
55. R.M. Sorensen, 1993. *Basic Wave Mechanics for Coastal and Ocean Engineers*, John Wiley & Sons, New York, p. 129.
56. J.F. Wilson, 1984. *Dynamics of Offshore Structures*, John Wiley & Sons, New York, p. 162.
57. J.F. Wilson, 1984. *Dynamics of Offshore Structures*, John Wiley & Sons, New York, p. 163.
58. US Army Corps of Engineers Coastal Engineering Research Center, 1984. Shore protection manual, volume I, in: *Wave and Water Level Predictions*, pp. 3.1–3.143.
59. R.M. Sorensen, 1993. *Basic Wave Mechanics for Coastal and Ocean Engineers*, John Wiley & Sons, New York, p. 115–168.
60. R.M. Sorensen, 1993. *Basic Wave Mechanics for Coastal and Ocean Engineers*, John Wiley & Sons, New York, p. 149.
61. N.D.P. Barltrop and A.J. Adams, 1991. *Dynamics of Fixed Marine Structures*, Butterworth-Heinemann Ltd., Oxford, UK, p. 270.
62. J.W. Gaythwaite, 1990. *Design of Marine Facilities – for the Berthing, Mooring and Repair of Vessels*, Van Nostrand Reinhold, New York, p. 80.
63. API RP 2A–LRFD, 1993. *Recommended Practice for Planning, Designing and Constructing Fixed Offshore Platforms – Load and Resistance Factor Design*, American Petroleum Institute, Washington, DC, pp. 34–42.
64. API RP 2A–LRFD, 1993. *Recommended Practice for Planning, Designing and Constructing Fixed Offshore Platforms – Load and Resistance Factor Design*, American Petroleum Institute, Washington, DC, p. 41.
65. R.O. Reid, 1957. *Modification of the Quadratic Bottom-Stress Law for Turbulent Channel Flow in the Presence of Surface Wind Stress*, TM # 93, Beach Erosion Board, Washington, DC.
66. US Army Corps of Engineers Coastal Engineering Research Center, 1984. Shore protection manual, volume I, in: *Wave and Water Level Predictions*, pp. 3–90.
67. A.C. Duxbury and A.B. Duxbury, 1991. *An Introduction to the World's Oceans*, Wm. C. Brown Publishers, Dubuque, IA, p. 244.
68. A.C. Duxbury and A.B. Duxbury, 1991. *An Introduction to the World's Oceans*, Wm. C. Brown Publishers, Dubuque, IA, p. 247.
69. N. Bowditch, 1977. In Chapter 9 on *Tides and Tidal Currents*, *The American Practical Navigator: An Epitome of Navigation*, Publication #9, USA National Mapping and Imaginary Agency. US Government Printing Office, p. 137.
70. NOS Tidal Datums Publ. (in Naval Postgraduate School). Available as a Public Domain image in [http://www.oc.nps.navy.mil/nom/day1/partc.html#figure:ahhttp://www.oc.nps.navy.mil/nom/day1/tidal\\_datums\\_fig17.gif](http://www.oc.nps.navy.mil/nom/day1/partc.html#figure:ahhttp://www.oc.nps.navy.mil/nom/day1/tidal_datums_fig17.gif), Accessed on August 20, 2010.
71. API RP 2A–LRFD, 1993. *Recommended Practice for Planning, Designing and Constructing Fixed Offshore Platforms – Load and Resistance Factor Design*, American Petroleum Institute, Washington, DC, p. 43.
72. J.W. Gaythwaite, 1981. *Marine Environment and Structural Design*, Van Nostrand Reinhold Co., New York, p. 209 & 210.
73. B.A. Bolt, 2004. *Earthquakes*, W.H. Freeman and Co., New York, p. 57.
74. B. McClelland and M.D. Reifel, 1986. *Planning and Design of Fixed Offshore Platforms*, Van Nostrand Reinhold Co., New York, p. 393.

75. B.A. Bolt, 2004. *Earthquakes*, W.H. Freeman and Co., New York, p. 165.
76. C.F. Richter, 1976. *Elementary Seismology*, W.H. Freeman and Company, San Francisco, CA.
77. J.P. Reger, 2005. *Earthquakes in Maryland, Maryland Geological Survey*, A Division of Maryland Department of Natural Resources, Baltimore, MD. Available at <http://mgs.dnr.md.gov/esic/brochures/earthquake.html>.
78. B. McClelland and M.D. Reifel, 1986. *Planning and Design of Fixed Offshore Platforms*, Van Nostrand Reinhold Co., New York, p. 403.
79. B. McClelland and M.D. Reifel, 1986. *Planning and Design of Fixed Offshore Platforms*, Van Nostrand Reinhold Co., New York, p. 405.
80. B. McClelland and M.D. Reifel, 1986. Planning and design of fixed offshore platforms, in: *Ice Forces*, Van Nostrand Reinhold Co., New York, p. 369.
81. G.W. Timco and R.M.W. Frederking, 1986. Confined compression tests: Outlining the failure envelope of columnar sea ice, *Journal of Cold Regions Science and Technology*, Volume 12, pp. 13–28.
82. B. McClelland and M.D. Reifel, 1986. Planning and design of fixed offshore platforms, in: *Ice Forces*, Van Nostrand Reinhold Co., New York, p. 372.
83. M. Maattanen, 1991. Ice forces, in: *Offshore Structures*, edited by D.V. Reddy and M. Arockiasamy, Krieger Publishing Company, Malabar, FL, p. 151.
84. K.A. Blenkarn, 1970. *Measurement and analysis of ice forces on cook inlet structures*, Offshore Technology Conference, Dallas, TX, Volume II, pp. 365–378.
85. J.G. Gaythwaite, 1981. *The Marine Environment and Structural Design*, Van Nostrand Reinhold Company, New York, p. 244.
86. J.G. Gaythwaite, 1981. *The Marine Environment and Structural Design*, Van Nostrand Reinhold Company, New York, p. 247.
87. K.R. Croasdale, 1984. Symposium in Ice Engineering and Cold Ocean Engineering, Calgary, Ice Engineering II, Section 2.0.
88. A.R.S. Ponter, A.C. Palmer, D.J. Goodman, M.F. Ashby, A.G. Evans and J.W. Hutchinson, 1983. The force exerted by a moving ice sheet on an offshore structure: I: the creep mode, *Cold Regions Science and Technology*, Volume 8, Issue 2, pp. 109–118.
89. A.B. Cammaert and D.B. Mugeridge, 1988. *Ice Interaction With Offshore Structures*, Van Nostrand Reinhold, New York, p. 80.



---

# 4 Seabed Mechanics

## 4.1 INTRODUCTION

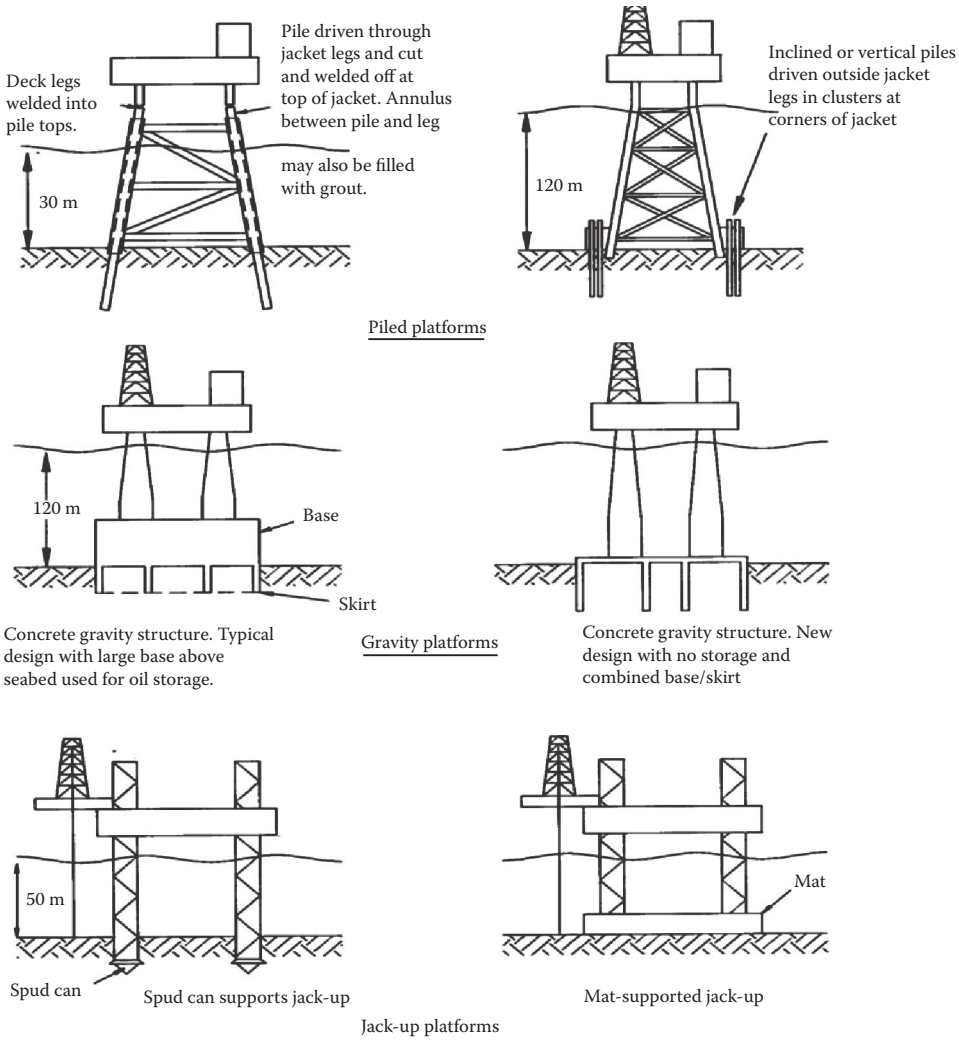
Offshore platforms are free-floating, anchored, and bottom fixed by means of piled foundations or supported on massive or thick foundation slabs (or mats or spud cans). Some of these platforms are shown in Figure 4.1 [1]. Interaction and load transfer occur between the structural foundations and the seabed soil since the structures are supported over the soil through the foundations, and the static/dynamic forces applied/generated on the structure are transferred to the soil below through this interaction process. If the structure is supported over a stiff soil, the interaction effects between the soil and structure are much less, and the structure almost acts as if it is supported over a rigid bottom; whereas if the soil below is flexible, the interaction effects are much higher. Moreover, the structure supported over a flexible soil decreases its natural frequency, which, in turn, increases the dynamic response of the structure.

Consequently, the study of the mechanics of seabed sedimentary soils grew as a practical outcome of the need to understand the behavior of seabed, when subjected to the various engineering operations carried out in the ocean such as exploration, surveying, drilling, mining, or installation of structures. The proper estimation of seabed sediment properties will allow the structural designer to predict more reliably the behavior of offshore structures. In addition, the seabed sediments behave in a nonlinear manner when subjected to loads; this nonlinear interaction completely changes the stiffness, strength, and other characteristic properties of soil, depending on the dynamic nature of the applied loads. The pore water pressures in soil are also considerably influenced by the repeated load cycles applied on the soil, depending on the nature of soil (such as sands, clays, silts, low relative density, overconsolidated or normally consolidated, etc.). Hence, it becomes essential that a detailed study of seabed mechanics is made before a designer proceeds to carry out the analysis and design of offshore structures.

## 4.2 OCEAN FLOOR CHARACTERISTICS AND CHARACTERIZATION

The continental shelf and the abyssal plains of the ocean receive a steady stream of deposits, called sediments, from sources such as land, atmosphere, dead marine organisms, and others. Figure 4.2 [2] shows the distribution of the principal ocean sediment types at the bottom of the world's oceans. Thick deposits of sediments are mainly found along the continental regions, while a thinner layer of sediments gets accumulated over the deep sea floor. These sediments are classified according to their source as (1) lithogenous sediments, when they are derived from rocks broken down by natural processes such as wind, water, and temperature (freezing and thawing) and transported by water, wind, gravity, and ice; (2) biogenous sediments, derived from living organisms, which may include shells, coral fragments, and hard skeletal parts of single-celled plants and animals that live in ocean waters (forming calcareous/siliceous oozes); (3) hydrogenous sediments, such as carbonates (that form limestone-type deposits), phosphorites (in nodular and crustal forms), and nodular manganese, which are formed (in deep water or in areas of rapid bottom currents) as a result of chemical processes that occur in the water received by the ocean; (4) iron-rich cosmogenous sediments that are deposited on the ocean surface from cosmic bombardments, which, in turn, are found on ocean bottom scattered over the surface of other sediments; and (5) a red (or brown) clay or brown mud,



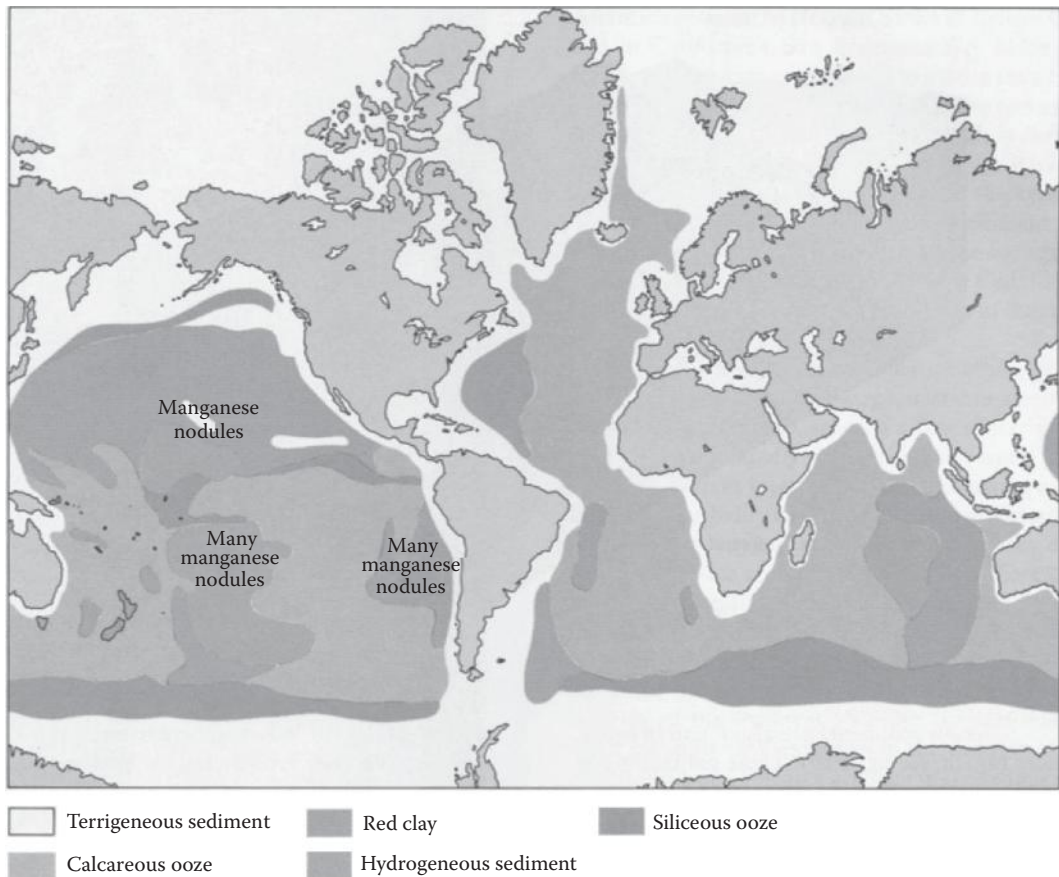


**FIGURE 4.1** Typical foundations for offshore structures. (From N.D.P. Barltrop and A.J. Adams, Dynamics of fixed marine structures, in: *Foundations*, Butterworth Heinemann Ltd., Oxford, UK, p. 172, 1991. With permission.)

found deposited in deep ocean floor, derived from the soil blown out to sea (by wind), or dumped by rain into the ocean from the suspended particles held in air [2].

In an alternate manner, ocean sediment deposit patterns enable the scientists to classify them according to the area over which they are deposited, as shown in Figure 4.3 [3]. Terrigenous sediments are deposited close to their land source (viz., gravel, sand, silt, wood chips, and sewage sludge) in the continental shelf. Neritic (or coastal) sediments (or deposits) are found under the shallow waters of the continental shelf. The deep ocean pelagic sediments are found in ocean areas (abyssal plains), far away from the direct influence of land. They consist of siliceous/calcareous oozes and red clays; the term *ooze* is used to specify its source (or origin), which is mostly biogenic. More specifically, when the sediment consists of more than 30% of skeletal debris, it is classified as ooze. Whatever their provenance, all pelagic sediments accumulate very slowly at no more than a few centimeters per millennium.

Nearly 75% of the ocean sediments are observed to be terrigenous, and most of them are found to be lithogenous, which are supplied by rivers and wave erosion along the coasts. While the coarser

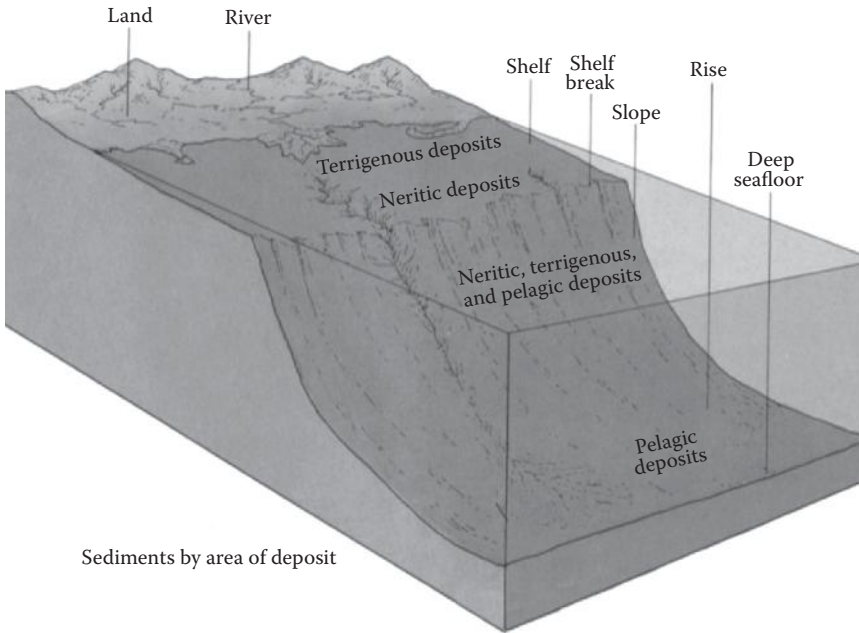


**FIGURE 4.2** Distribution of principal sediment types. (From A.C. Duxbury and A.B. Duxbury, *An Introduction to the World's Oceans*, William C. Brown Publishers, Dubuque, IA, pp. 67–68, 1991. With permission.)

sediments are found deposited near the coasts, finer particles are held in suspension and carried far away from the coasts. Due to the rapid accumulation of sediments on the continental shelf, large unstable and steep-sided deposits are formed, which generally slump and move (or flow) rapidly down the continental slopes, in turbidity currents. The varying amounts of deposits of sediments found near the coast, due to the seasonal water flow into the oceans, are deposited in layers; in addition to the coastal deposits, the deep oceanic sediments are also deposited in layers. The layers are recognized by the changes in color, particle size, and kinds of particles. The biological changes that occur over long periods of geologic time, due to climatic changes, could also be recognized from the detailed analysis of these sediment layers.

The sediment classification by particle size, used by engineers and scientists, is given in Table 4.1 [4]. The coarser particles of gravel, such as granules to boulders, range from a size of 2.0 to 264 mm. The sand particles, containing fine to coarse materials, vary from a size of 0.0625 to 2.0 mm. The mud particles, consisting of clay and silt, vary from a very small size (0.0039 mm) to 0.0625 mm. Moreover, the rates at which the sediments accumulate in the ocean bed vary enormously due to the variability of the deposition processes. For the deep oceans, the accumulation rate varies (on an average) from 5.0 to 10.0 mm/(1000 years). The deposition rate near the river estuaries may be, sometimes, more than 8.0 m/year, whereas that in a quiet bay may be around 5 mm/year. On the continental shelves and slopes, the deposition rate may vary from 0.1 to 0.4 mm per year.

The continental shelves of the world cover an area of approximately 18% of the earth's total land area. Most of the earlier offshore structures were located in the continental regions. The ocean



**FIGURE 4.3** Classification of sediments by location of deposit. (From A.C. Duxbury and A.B. Duxbury, *An Introduction to the World’s Oceans*, William C. Brown Publishers, Dubuque, IA, p. 58, 1991. With permission.)

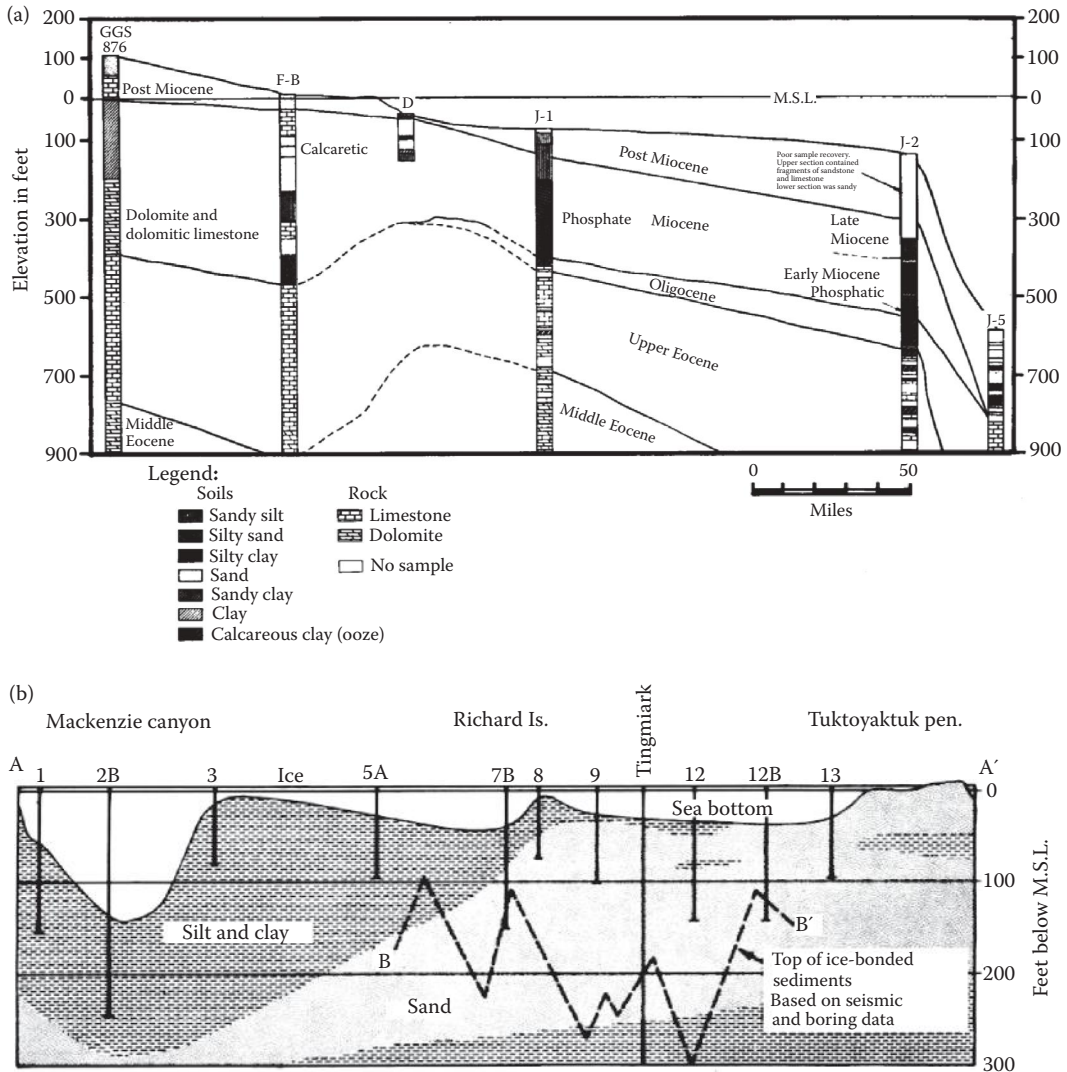
engineers had to determine the geotechnical characteristics of these soils before installing the offshore structures on site. This need led to the geotechnical exploration and the subsequent analysis of data, gathered through thousands of borings made on the continental shelf region. Even though most of these data were site-specific, consistent generalizations could be made from the study of these data. The majority of continental shelf regions consist of sedimentary and rocky strata (such as limestone and dolomite), overlain by a layer of variable thickness soils.

**TABLE 4.1**  
**Particle Classification by Size—Wentworth Scale**

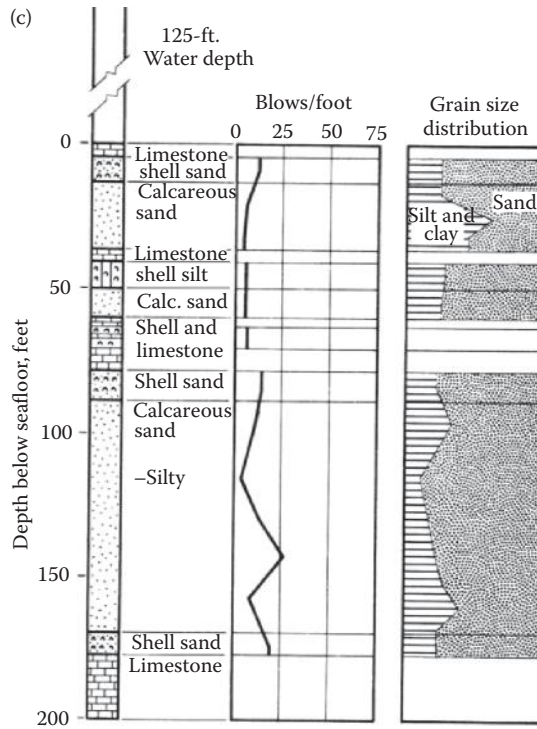
	Generic Name	Diameter in	Wentworth Scale	Diameter, mm
		Powers of 2, mm	Size Range ( $\phi$ )	
Gravel	Boulder	$>2^8$	$>8$	$>256.0$
	Cobble	$2^6-2^8$	6–8	65.0–256.0
	Pebble	$2^2-2^6$	2–6	4.0–64.0
	Granule	$2^1-2^2$	1–2	2.0–4.0
Sands	Very coarse	$2^0-2^1$	0–1	1.0–2.0
	Coarse	$2^{-1}-2^0$	–1–0	0.50–1.0
	Medium	$2^{-2}-2^{-1}$	–2––1	0.25–0.50
	Fine	$2^{-3}-2^{-2}$	–3––2	0.125–0.25
	Very fine	$2^{-4}-2^{-3}$	–4––3	0.0625–0.125
Mud	Silt	$2^{-8}-2^{-4}$	–8––4	0.0039–0.0625
	Clay	$<2^{-8}$	$<-8$	$<0.0039$

Source: A.C. Duxbury, *The Earth and Its Oceans*, Addison-Wesley Publishing Company, Reading, Boston, MA, p. 99, 1971. With permission.

Figure 4.4a [5] shows the geologic cross section from North Jacksonville, Florida, extending from the coastal area [200.0 ft. above the mean sea level (msl)] to a depth of 900.0 ft. below the msl. Generally, the existence of sedimentary rocks indicates the potential for containing a significant amount of hydrocarbon deposits. In Figure 4.4a, the borings, at section J-1, encountered layers of silty sands and clays, even to a depth of 300.0 ft. below the seabed. The geologic characterizations (such as post-Miocene nearly 3.6 million years ago; Miocene nearly 3.6 to 14.0 million years ago; Oligocene nearly 18 to 30 million years ago; upper-Eocene nearly 30.0 million years ago; and



**FIGURE 4.4** (a) Geologic section from North Jacksonville, Florida, to continental slope. (From B. McClelland and M.D. Reifel, *Planning and Design of Fixed Offshore Platforms*, Van Nostrand Reinhold Company, New York, p. 163, 1986. With permission.) (b) East-west geological section, in the American Beaufort Sea. (From B. McClelland and M.D. Reifel, *Planning and Design of Fixed Offshore Platforms*, Van Nostrand Reinhold Company, New York, p. 167, 1986. With permission.) (c) Typical soil profile on carbonate shelf in Persian Gulf. (From B. McClelland and M.D. Reifel, *Planning and Design of Fixed Offshore Platforms*, Van Nostrand Reinhold Company, New York, p. 172, 1986. With permission.) (d) Typical soil profile on carbonate shelves, in Bombay High. (From B. McClelland and M.D. Reifel, *Planning and Design of Fixed Offshore Platforms*, Van Nostrand Reinhold Company, New York, p. 171, 1986. With permission.)



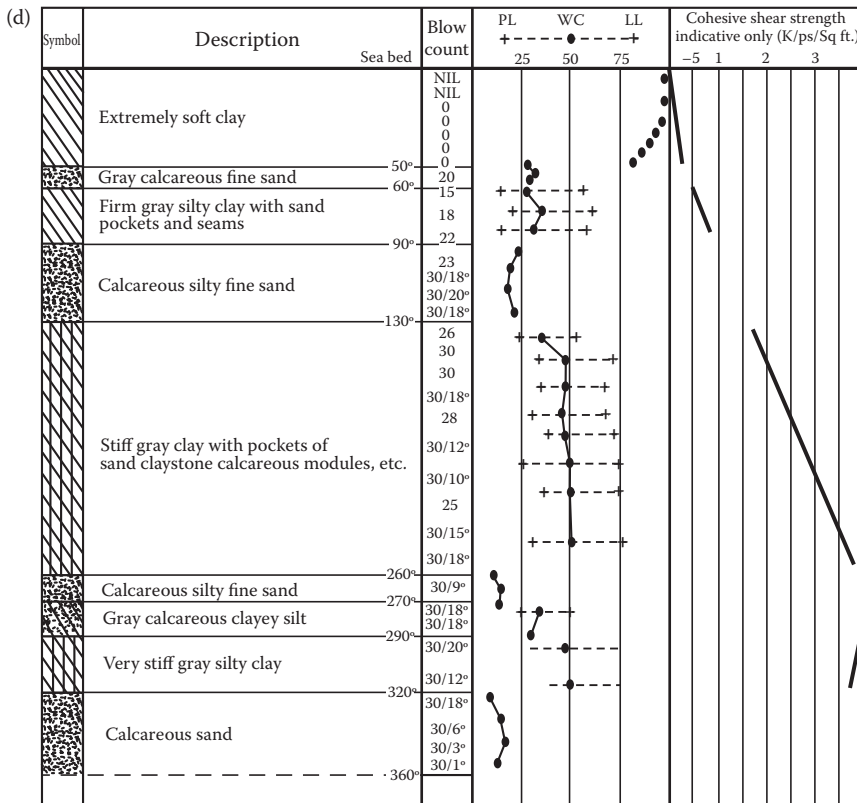
**FIGURE 4.4** (Continued) (a) Geologic section from North Jacksonville, Florida, to continental slope. (From B. McClelland and M.D. Reifel, *Planning and Design of Fixed Offshore Platforms*, Van Nostrand Reinhold Company, New York, p. 163, 1986. With permission.) (b) East-west geological section, in the American Beaufort Sea. (From B. McClelland and M.D. Reifel, *Planning and Design of Fixed Offshore Platforms*, Van Nostrand Reinhold Company, New York, p. 167, 1986. With permission.) (c) Typical soil profile on carbonate shelf in Persian Gulf. (From B. McClelland and M.D. Reifel, *Planning and Design of Fixed Offshore Platforms*, Van Nostrand Reinhold Company, New York, p. 172, 1986. With permission.) (d) Typical soil profile on carbonate shelves, in Bombay High. (From B. McClelland and M.D. Reifel, *Planning and Design of Fixed Offshore Platforms*, Van Nostrand Reinhold Company, New York, p. 171, 1986. With permission.)

middle-Eocene nearly 45.0 million years ago) of the ocean bed, shown in Figure 4.4a, will give the approximate age for the formation of the layer beneath the seabed.

Figure 4.4b [6] shows the geotechnical characterization of the seabed through soil borings and seismic explorations made in the frozen continental shelf of the Beaufort Sea, along the mouth of the McKenzie river delta. Deltaic silts and clays, probably of Holocene age (during recent times, around 5000 to 10,000 years ago) or late Pleistocene period (10,000 to 1.6 million years ago), form a deep wedge of sediments; sands, probably of Pleistocene age, underlie these silts and clays. These, in turn, are underlain by another silt and clay unit, encountered in the 300-ft. deep Tingmiark boring. It can also be noted that the top of the ice-bonded sediments that occur below the seabed are marked with broken straight lines.

The geotechnical characterizations of the carbonate continental shelves, existing in the Persian Gulf and the west coast of India, in the Bombay High region, are shown in Figure 4.4c and d [7, 8]. The carbonate deposits range from clay-sized particles to huge mollusks and coral heads, many feet across. Holocene deposition, made up of soft clay, calcareous sand, limestone shell sand, and stiff clay on carbonate shelves, varies from a few inches to around 100.0 ft. Below these Holocene deposits, one can sometimes see Pleistocene carbonate deposits, varying from 400 to 500 ft. in thickness. The ocean designer needs to know the detailed geotechnical characteristics of the ocean beds since





**FIGURE 4.4** (Continued) (a) Geologic section from North Jacksonville, Florida, to continental slope. (From B. McClelland and M.D. Reifel, *Planning and Design of Fixed Offshore Platforms*, Van Nostrand Reinhold Company, New York, p. 163, 1986. With permission.) (b) East–west geological section, in the American Beaufort Sea. (From B. McClelland and M.D. Reifel, *Planning and Design of Fixed Offshore Platforms*, Van Nostrand Reinhold Company, New York, p. 167, 1986. With permission.) (c) Typical soil profile on carbonate shelf in Persian Gulf. (From B. McClelland and M.D. Reifel, *Planning and Design of Fixed Offshore Platforms*, Van Nostrand Reinhold Company, New York, p. 172, 1986. With permission.) (d) Typical soil profile on carbonate shelves, in Bombay High. (From B. McClelland and M.D. Reifel, *Planning and Design of Fixed Offshore Platforms*, Van Nostrand Reinhold Company, New York, p. 171, 1986. With permission.)

soil resistance varies from one type of soil to another; for instance, the piles driven in carbonate sands have a much inferior resistance to those driven in silica sands.

### 4.3 OFFSHORE SITE INVESTIGATION AND EQUIPMENT USED

#### 4.3.1 INTRODUCTION

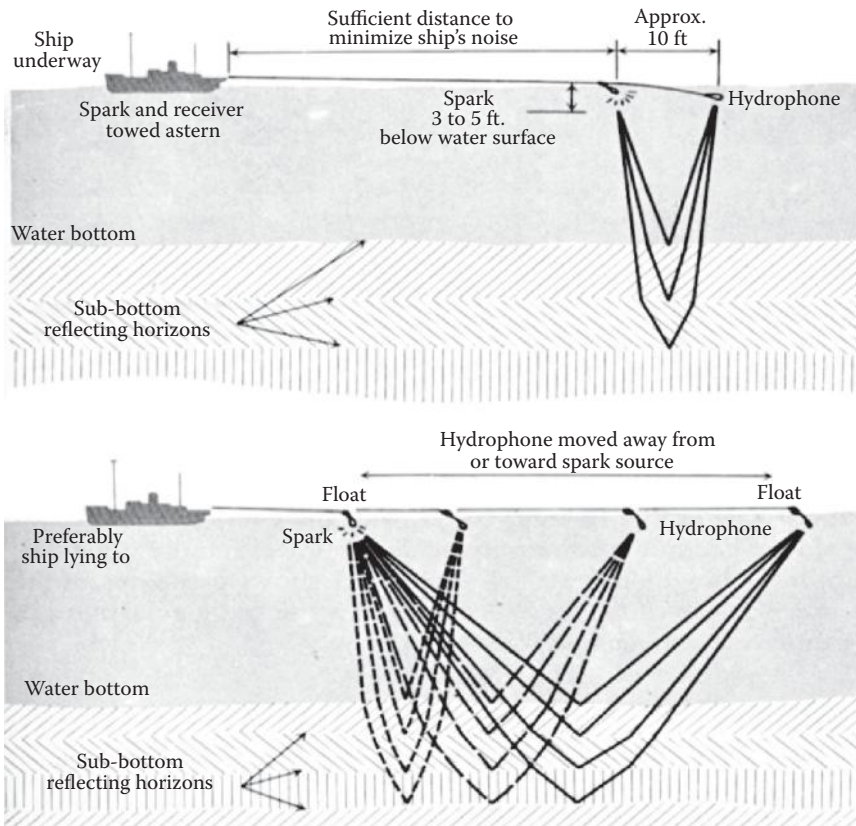
Offshore site investigation has been carried out by (1) high-resolution geophysical surveys; (2) drill with wire-line coring techniques using a surface support vessel; and (3) remote in situ measurements. High-resolution geophysical surveys have been widely used for studying the top 100 m of soil beneath the sea floor. This enables the detection and mapping of geologic features such as landslides, mudflows, faults, sand waves, irregular and rocky seafloor, shallow gas regions, etc. However, these procedures do not help in the determination of the nature of subsurface soils or in the assessment of their physical and mechanical properties, while some properties may be obtained from the geophysical (or seismic) data (such as the state of consolidation), yet they should be verified by testing the extracted core samples or by in situ geotechnical measurements. For deeper water depths, the

geotechnical properties of the seabed sediments have been determined from a remote surface support vessel using in situ measurements. These procedures are outlined in the sections given below.

### 4.3.2 HIGH-RESOLUTION GEOPHYSICAL SURVEYS

All geophysical methods used currently for the seismic exploration of soils use the continuous reflection method, shown in Figure 4.5 [9]. An alternate method called the refraction method is used when the reflection method becomes difficult to handle or when the obtained results do not give the required accuracy. Seismic surveys can be classified as (1) reconnaissance surveys carried out over an area, ranging from hundreds to several thousand square miles; and (2) site-specific surveys, done over much smaller areas, principally to detect potential hazards to drilling equipment and to provide detailed information on soil properties that will assist in the location of the platform structure. While the grid-line spacing for reconnaissance surveys will vary from 0.5 to 1.5 mi., it will vary from 500 (or 1000 ft.) by 1000 (or 3000) ft. for site-specific surveys. In some areas, the grid spacing may still be reduced to account for a rapid variation in the topography of the seabed.

Several types of devices are used in the high-resolution seismic surveying of the ocean bed, viz., (1) sediment sounders (or penetrators); (2) boomers consisting of an induction coil, with a spring-loaded aluminum plate, and a bank of capacitors (connected to a sparking circuit) producing electrical discharges through a coil, at regular intervals; and (3) sparkers in which the seismic shock is emitted by the spark, generated by discharge from a battery of capacitors.



**FIGURE 4.5** Typical procedures for continuous seismic profiling: (top) normal incidence reflection and (bottom) oblique reflection. (From A.C. Duxbury, *The Earth and Its Oceans*, Addison-Wesley Publishing Company, Reading, Boston, MA, p. 105, 1971. With permission.)



Sediment sounders are also known as pinger probes and use the principles of the echo sounders for surveying the seabed surface (few tens of meters deep). It is a low-frequency echo sounder (from 1 to 7 kHz) that sends an acoustic pulse toward the ocean bottom. The pulse, after reflection from the sea-bottom soil, and from the soil layer beneath, is received and recorded. This sound wave may penetrate the sea bottom soil surface to a depth of a few to 40 m, with a minimum resolution depth of 0.30 m. The sediment sounder is used by attaching it to the hull of a support vessel (floating on the sea surface) or by mounting it in a fish (ocean monitoring instrument), towed behind the vessel submerged a few feet, below the water surface. The efficiency of the sediment sounders reduces as the depth of water increases. The limiting condition used in its operation is as follows: speed of support vessel should be below 6.0 knots, with a maximum sea state of 4 to 5 (with possible waves of 1.20 m, maximum height). Actually, a lower vessel speed may be used to get good data.

The boomer is an electromechanical source that induces eddy currents in an aluminum plate (supported by springs) due to the discharged electric field (from the capacitors), causing the plate to move away violently; this triggers the acoustic pulse. The sound spectrum of the discharged acoustic pulse ranges from 100.0 to 2000.0 Hz, with a pulse duration of 5.0 ms. Another type of a boomer is called uniboom, which emits a pulse of duration 0.2 s; the spectral frequencies, emitted by this boomer, range from 500.0 to 10,000 Hz. The boomers have an ocean bed penetrating power around 75.0 m, with a minimum resolution depth of 0.40 m.

In the sparker, the seismic shock signal is emitted by the spark produced in the sparker, and it evaporates the surrounding water and creates an energy-charged bubble of gas; as this gas bubble expands, it releases the seismic shock signal. The disadvantage produced by the expansion of the large air bubble (lower signal-to-noise ratio), produced by the sparker, can be minimized by having multiple mini-electrode sparkers (up to 900 electrodes) that will produce small bubbles. The depth of penetration of the seabed by the sparker signals varies from 50.0 to 150.0 m, with a minimum resolution depth of 1.5 to 6.0 m [10].

### **4.3.3 DRILL AND WIRE-LINE CORING TECHNIQUES USING SURFACE SUPPORT VESSEL**

A considerable number of drill and wire-line coring techniques, using different drilling and coring units, have been developed over the decades for the assessment of the properties of marine soils. The penetration depths of soil, using these coring techniques for the assessment of geotechnical properties, vary from a few meters to over 100.0 m. The quality of soil cores extracted depends on the technique and equipment used and the nature of soil from which the cores are obtained. The geotechnical properties assessed from these cores include (1) identification of soils, which includes the determination of water content, voids, densities, particle distribution, Atterberg limits, permeability, and the like; (2) shear strength of soils (drained or undrained and with/without consolidation); and (3) compressibility of soils, including settlement and phases of consolidation.

The various drill and wire-line coring techniques used for the geotechnical exploration of soils consist of the following: (1) drill and wire-line corers; (2) rotary drilling units, located at the sea bottom and operated by divers; (3) vibro- or flexo-coring (with equipment at sea bottom) from a surface support vessel; (4) use of remote-controlled rotary corers; and (5) use of gravity or stationary piston corers.

#### **4.3.3.1 Drill and Wire-Line Coring Using Surface Support Vessel**

The assessment of the soils in the seabed is done either by drilling down to the preselected level identified for taking the soil core sample or by wire-line coring through the guide tubes, installed during the drilling process. The core sampling barrel is made to penetrate the soil seabed by percussion or push. The drilling down method (to a preselected level) consists of a drill rig (of an approximate weight of 8.0 t and a height of 8.20 m, located on the seabed) that uses hydraulic pressure and drill strings to drill to the required depth; then the soil sample corer is pushed into the ground by a drive motor. In this push method, greater lengths of soil cores can be extracted with the least amount of soil disturbance. In the percussion type of penetration, the soil sampling corer (of outside diameter 57 to

76 mm and of length 0.60 to 0.90 m) is driven into the soil by the load exerted on the top of the soil corer by repeated impacts of a falling weight. The falling weight (of nearly 80.0 kg, falling from a height of 1 to 3.0 m) is dropped onto the core sampler using a wire-line actuating device (the number of repetitions depends on the cohesive strength of clayey soils or the relative density of sandy soils).

This method is quite effective up to a maximum water depth of 100.0 to 200.0 m; and the depth of penetration into the soil can be a maximum of 150.0 to 200.0 m. When supply boats (of lengths less than 50 to 55 m) are used as surface support vessels, a maximum wave height of 3.0 m is acceptable, whereas when the vessel is a large ship (of length 75 to 80 m), then a wave height of 4.0 to 5.0 m is permitted during its operation. Wind speeds cannot be allowed to exceed 50.0 km/h, and a maximum current speed of 2.0 m/s is also permitted.

The integrity of the sampled soil cores, obtained by the wire-line methods, is influenced in the following manner: (1) In soft muds or clays, highly disturbed cores are obtained; nevertheless, they can be used for determining the shear strength of soils. (2) In consolidated or highly consolidated clays, moderately disturbed cores are obtained; these cores give fairly representative values for the soil's mechanical properties. (3) In loose sands, samples obtained are highly disturbed and can be used only for lithological identifications. (1) In the percussion or push methods, the length of the core is almost that of the core barrel in soft clays with a cohesive strength smaller than 50.0 kPa. (2) In soils of average consolidation (cohesive strength varying between 100.0 and 200.0 kPa), the wire-line coring method gives satisfactory samples with very limited sample soil disturbance. (3) In highly overconsolidated clays (of North Sea type), the length of the soil core obtained rarely exceeds 20.0 to 30.0 cm, and the soil strength should be less than 500.0 kPa. Also the soil disturbance may be quite considerable. (4) In loose sands, the soil may contain drilling mud used in the operation and give a much higher density than that at site.

#### **4.3.3.2 Sea Bottom-Located Rotary Drills with Wire-Line Corers and Operated by Divers**

Application of this method using submerged rotary drilling machines, operated by divers at the sea bottom, is limited to a water depth of 40.0 m (due to compression–decompression sickness in divers); the time on the bottom of the sea, for each diver, is about 35 to 40 min. The rotary drill used for this operation is of the Wirth (for hard or consolidated soils) or Mazier (for sandy terrains) type, driven by two hydraulic motors of 50.0 hp capacity (located on the surface support vessel), and using wire-line coring or in situ measurements. The drill unit consists of a reinforced outer barrel, with rotating core bit at its bottom, and an inner core barrel inside the rotary string. The penetration of the drill string below the seabed may vary from 20.0 m to a maximum of 100.0 m, depending on the rotary drilling machine used. The length of the corer barrel is 1.5 m and has a diameter ranging between 68 and 105 mm. After the core barrel has penetrated to the requisite depth into the soil (during its rotary drilling process), it is lifted to the surface by the wire line (consisting of a grapple that fits onto the head of the corer barrel). The drilling fluids for the drill bits consist of (1) seawater in consolidated soils and (2) mud, with a density of 1.10, for drilling in loose sediments. The controlling wave height for ocean operation is 3.0 to 4.0 m, with a current speed of 1.0 to 1.5 m.

#### **4.3.3.3 Vibro-Coring or Flexo-Coring (with Equipment at Sea Bottom) from Surface Support Vessel**

Vibro-corers are submerged devices, driven by an electric motor and operated by vibration or vibro-percussion. They are used for coring in loose formations and for driving of piles or conductor pipes. The system consists of three main components: (1) a vibration generator consisting of two (or four) out-of-balance weights, rotating in opposite directions and driven by a hydraulic motor of 600 to 1500 rpm capacity, with a flow rate of 300 to 400 L/min; (2) a device for converting the vibrations into percussions (hammer and anvils) by means of cylinders and springs; and (3) a system for clamping onto drilling strings through hydraulic jacks. The bottom-to-surface link consists of flexible tubes capable of resisting an internal pressure of 20.0 to 25.0 MPa. The coring operation takes place continuously in a single run until the corer refuses to penetrate or until the whole length of the corer penetrates the

soil. The length of the corer tube varies from 3 to 9.0 m and its diameter from 100 to 300 mm. The maximum water depth in which the vibro-corers can operate is around 100 to 200 m, with a maximum wave height of 2.0 to 3.0 m and a current speed of 1.0 to 1.5 m/s; moreover, for the submerged bottom frame to be stable, the current speed cannot exceed 1.0 m/s. Vibro-corers can be used in soft soils, and the vibro-percussion units can be used for soils of average consolidation, sands, or gravels. Soil sample cores produced by vibration methods are good for soils with cohesive strengths of less than 50.0 to 100.0 kPa; the percussion core samples are found to be good for large diameter cores (more than 150 to 200 mm) and for high cohesive strength soil formations (shear strengths greater than 100.0 kPa).

Flexo-coring method is similar to the above method except that the surface support vessel is a specialized drilling vessel, able to operate in waters of depth varying from 200.0 to 300.0 m. The ocean electro-corer is a submerged and remote-controlled device used for drilling and coring.

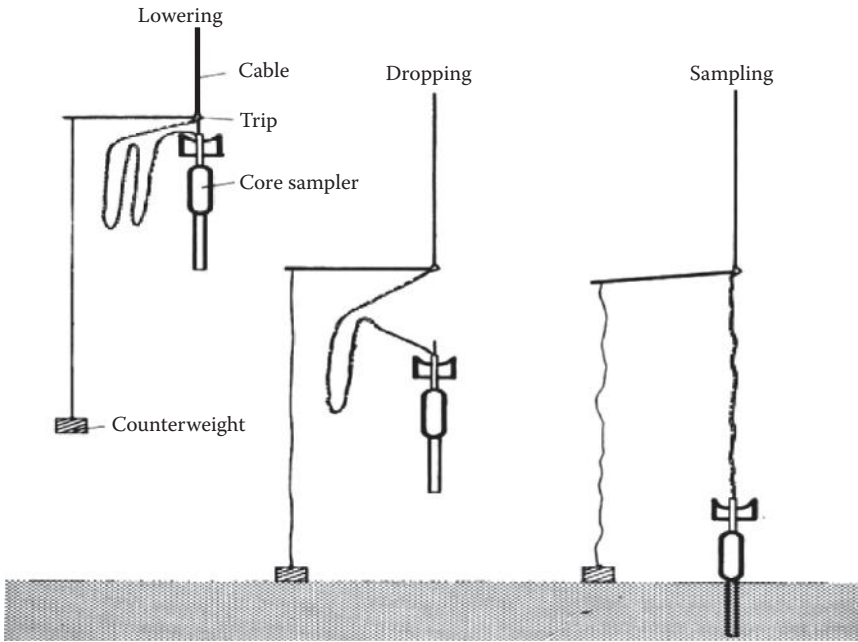
#### 4.3.3.4 Using Remote-Controlled Rotary Corers

Several subset remote-controlled rotary coring devices are available in the market, which have been used for geological or geotechnical surveys of marine soils in water depths, varying from 200.0 to 1800.0 m. Systems such as Maricor (by Atlas Copco), NCEL sampler (by Ocean Science Engineering), TSO seabed sampler (Taylor Woodrow group), and others have been developed and tested in deep sea waters. Maricor operates in water depths up to 200.0 m (with a coring soil depth up to 60.0 m), NCEL sampler operates in water depths up to 1800.0 m (with a coring soil depth of 15.0 m), and TSO sampler operates up to 900.0 m (with a coring soil depth of 90.0 m). The submerged corer is controlled from a console on the surface support vessel; the console controls the setting of the equipment at the sea bottom, implementation of the various monitoring and measuring systems, powering of the equipment, and all the other parameters required for proper data acquisition. The cores obtained from the seabed vary from a length of 2.20 m (Maricor), 1.50 m (NCEL), and 3.00 to 6.00 m (TSO). The diameter of the soil cores vary from 57.0 mm (Maricor), 76.0 mm (NCEL), to 44.0–102.0 mm (TSO).

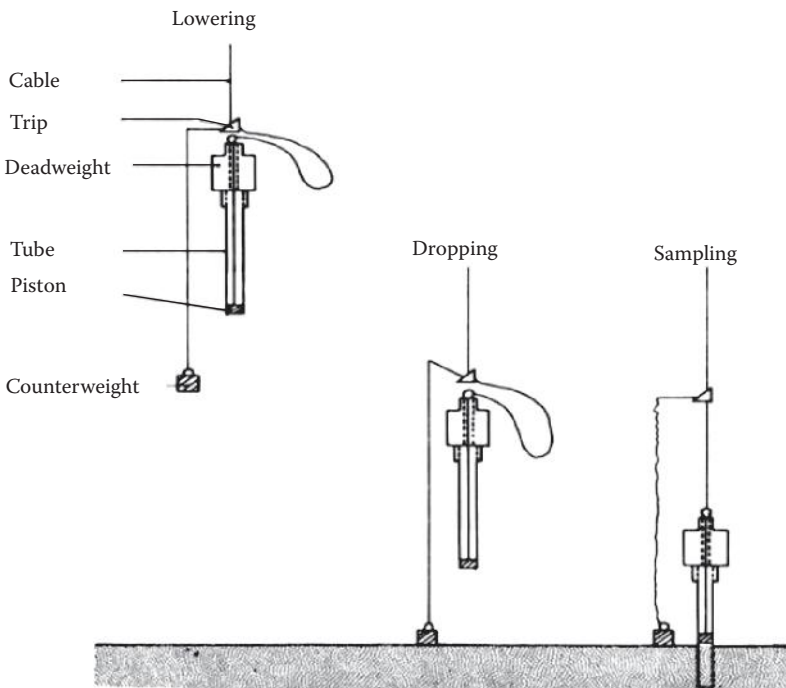
#### 4.3.3.5 Use of Gravity or Stationary Piston Corers

A great variety of free-fall corers using gravity, stationary piston, and other means are available to carry out seabed surface soil survey. Two types of gravity corers, viz., (1) free-fall gravity corer (Figure 4.6 [11]) and (2) stationary piston-type corer (Figure 4.7 [12]), are described below to get some intuitive understanding of the principles involved in the operation of the device. The stationary piston corer is an improvement of the free-fall gravity corer. The gravity corer is dropped from a limited height and penetrates into the soil merely under gravity. The stationary piston corer is also a gravity corer, which also drops in free fall from a limited height but has a lower end enclosed by a piston; the lower end remains closed until the corer starts penetrating into the soil. The presence of the piston generates a negative pressure in the coring tube, as it penetrates into the soil; thus, the frictional forces of the soil core (on the internal walls of the coring tube) are reduced to give a larger length of penetration. The piston is connected to the main cable by a wire, which becomes taut when the coring tube comes into contact with the bottom. The mass of the unit can vary from 300.0 to 1500.0 kg. The diameter of the core barrel varies from 0.40 to 1.20 m, and the height of the core barrel depends on the soil encountered at the site, being a few meters in sands and 10 to 20 m in muds and very soft clays.

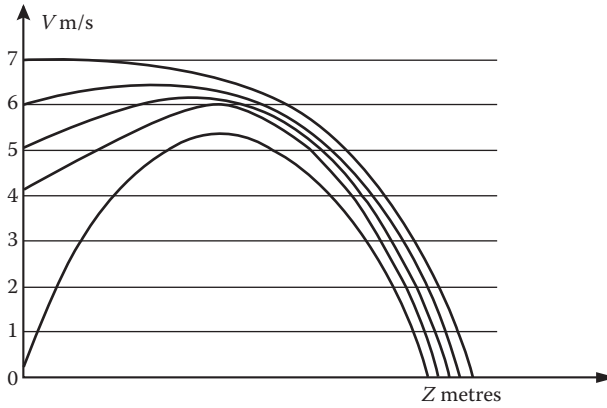
The penetration of the core barrel into soil is essentially a function of the kinetic energy of impact, which is dependent on the impact velocity and weight of the corer, and the resistance of the soil formations. The impact velocity of the corer is dependent on the falling velocity of the corer in water, which is dependent on the mass and the mean density of the corer, the water drag forces exerted on the corer (approximately equal to  $0.12V^2$  dynes/cm<sup>2</sup>), and the distance between the point of release and the position of the corer at any time. The initial velocity of release of the corer does not influence much the penetration depth of the corer into soil, as seen in Figure 4.8 [13], which gives the penetration depth ( $z$ ) for various initial velocities; the difference in penetration seems to be very slightly influenced by the initial velocity of drop of the corer. Figure 4.9 [14] shows the free-fall speeds of the corer (of different weights) as a function of distance  $x$  traveled by the corer in water (initial velocity of the corer is  $\approx 1.0$  m).



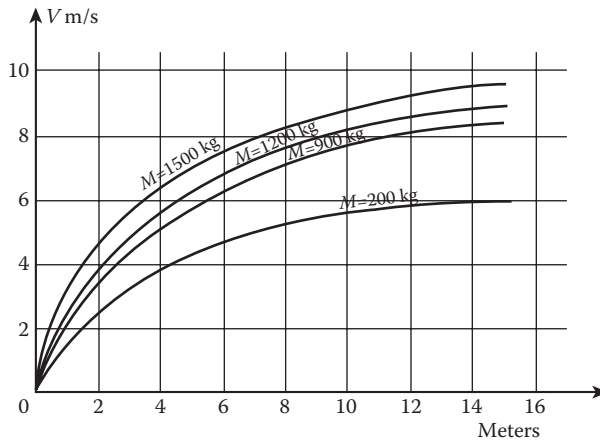
**FIGURE 4.6** Operating principle of a gravity core sampler—Kullenberg type. (From P. Le Tirant, *Seabed Reconnaissance and Offshore Soil Mechanics*, Editions Technip 27, Paris, France, p. 206, 1979. With permission.)



**FIGURE 4.7** Operating principle of the stationary piston core sampler. (From P. Le Tirant, *Seabed Reconnaissance and Offshore Soil Mechanics*, Editions Technip 27, Paris, France, p. 207, 1979. With permission.)



**FIGURE 4.8** Penetration velocity of corer into the soil in terms of initial velocity  $V_0$  and the depth of penetration (mass = 1200 kg; inside diameter = 80 mm; frictional resistance per meter = 100.0 kgf). (From P. Le Tirant, *Seabed Reconnaissance and Offshore Soil Mechanics*, Editions Technip 27, Paris, France, p. 213, 1979. With permission.)



**FIGURE 4.9** Free-fall speed of a corer in water, as a function of its dropped height ( $x$  meters) and mass ( $M$  kilograms) (initial velocity of drop  $\approx 1.0$  m). (From P. Le Tirant, *Seabed Reconnaissance and Offshore Soil Mechanics*, Editions Technip 27, Paris, France, p. 208, 1979. With permission.)

It can be seen from Figure 4.9 that as the height of drop of the corer becomes greater than 12.0–14.0 m (for a corer of mass 200.0 kg), the free-fall speed tends to become a constant, called the terminal velocity of the free-falling body; it is observed from Figure 4.9 that the terminal height is much higher for larger masses of corers. Basically, the terminal velocity of an object through a liquid is given by

$$(1/2)C_D A_p \rho_f V^2 = \text{volume}(\gamma_o - \gamma_f) \tag{4.1}$$

where  $C_D$  is the drag coefficient,  $A_p$  is the projected area of the object in the direction of motion,  $V$  is the velocity of the object,  $\rho_f$  is the fluid density,  $V$  is the velocity of motion of the object,  $\gamma_o$  is the density of the object, and  $\gamma_f$  is the fluid density. The resistance of the sediment to penetration is given by

$$(1/2)MV^2 = Q_{ult} \cdot x_{max} \tag{4.2}$$

where  $M$  is the mass of the falling object,  $V$  is the initial velocity of penetration into the soil,  $Q_{ult}$  is the ultimate bearing capacity of the object, obtained for the soil, and  $x_{max}$  is the maximum penetration into seabed.

The pullout effort required for extracting the core barrel from the soil depends on penetration and the nature of soil formation, viz., (1) for penetrations of 1.0 to 3.0 m (3.0 to 4.0 m long coring barrel) in sands, the pullout force is relatively low; and (2) for penetrations of 8.0 to 10.0 m (10.0 m long coring barrel) in relatively consolidated soils, the surface support vessel must be equipped with sufficient hoisting facilities, with a clearance length of at least 4.0 to 5.0 m. The theoretical rate of taking seabed cores (each of length 2.0 to 3.0 m), at water depths of 200.0 m, can reach a maximum of 2 to 3 cores per hour. Actual sampling rates could reach (1) 15 to 25 cores (2.0 to 3.5 m length) per day, at 150.0 m water depth; and (2) 20 to 25 cores (5.0 to 10.0 m length) per day, at water depths of 60.0 to 70.0 m. Due to the sudden release of tension in the operational cable, when the corer impacts the seabed soil, sudden shock waves are generated in the cable and the soil sample gets disturbed beneath the coring piston. Due to this disturbance, the cores taken are generally not very representative of the geotechnical properties of the soil formation. Measurements of shear strength and settlement made through this method are only approximate indications of the actual strength and settlement. Also, in a gravity corer, the depths of penetration are generally confined to the top 10.0 to 15.0 m, and they are not sufficient for selecting a site for an offshore structure, which would require data from a much larger depth. These data would be more profitable if the above data are only used for planning a route for underwater pipelines.

### Example 4.1

A solid and spherical mass of weight 16,000.0 N and of diameter 1.0 m is dropped into the ocean from a surface support vessel. The coefficient of drag, for the sphere (with a Reynolds number  $\geq 80,000$ ), is taken to be 0.55. The ultimate bearing strength of the spherical ball, in soil, is estimated to be 60,000 N/m<sup>2</sup>. Compute the penetration depth of the ball into the seabed.

$$\text{Volume of the sphere} = (4/3)(\pi)(0.5)^3 = 0.524 \text{ m}^3.$$

Taking the unit weight of seawater to be 1030.0 kgf/m<sup>3</sup> (= 10,100 N/m<sup>3</sup>), the weight of displaced water = (0.524)(10100) = 5292.4 N.

$$\text{Buoyant weight of the solid sphere is} = [16,000 - 5292.4] \text{ N} = 10,707.6 \text{ N}.$$

Using Equation 4.1,  $V^2 = [(2)(10,707.6)]/[(0.55)(\pi)(0.5^2)(10,100/9.81)] = 48.152 \text{ (m/s)}^2$ .

Hence,  $V = 6.939 \text{ m/s}$ .

Reynolds number =  $VD/\mu = (6.939)(1.0)/[(1.05)(10^{-5})] = (6.61)(10^5) > 80,000$  and hence OK.

Using Equation 4.2, maximum penetration into soil =  $[(1/2)(16,000/9.81)(48.152)]/(60,000) = 0.655 \text{ m}$ .

## 4.3.4 REMOTE IN SITU MEASUREMENTS

The difficulties experienced in obtaining undisturbed soil core samples in the ocean have led to the development of remote in situ measurements of soil strengths below the seabed. Even though good soil strengths can be obtained by remote in situ testing procedures, the results must be compared with those obtained from testing of soil cores in the laboratory and reconciled. The in situ measurement techniques used in the ocean use measurement procedures and devices (penetrometers, pressuremeters, vanes, drilling logs, etc.) similar to those used on land. It is proposed to examine only two types of in situ measurement devices in this chapter, viz., (1) Modular Seacalf cone penetrometer, developed by Fugro Inc., and (2) wire-line vane shear test equipment, developed by McClelland Engineers Inc.

### 4.3.4.1 Modular Seacalf Cone Penetrometers

Seacalf cone penetrometer is a frame-mounted penetrometer lowered to the seabed by means of bearing cables and controlled remotely from the surface support vessel; the frame weighs from 10.0 to 30.0 t, has a square base, and is of length 2.5 to 3.0 m. The ocean operation, with the Seacalf cone penetrometer, is similar to that of the standard cone penetrometer shown in Figure 4.10 [15]. The

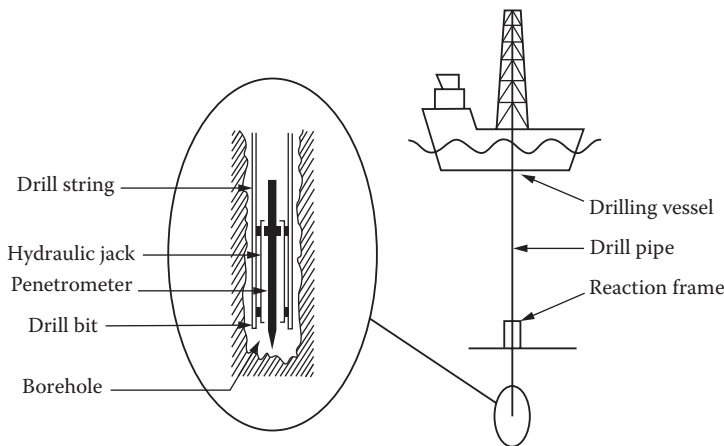


penetrometer cone is inserted into the soil in successive sequences by means of a hydraulic cylinder; the reactive force necessary for the successive insertion into the soil is resisted by the self-weight of the frame. The penetrometer cone carries two strain gauges that provide a continuous indication of (1) tip resistance load intensity,  $R_p$  (in  $t/m^2$ ), and (2) the lateral frictional resistance (in  $t/m^2$ , acting on the outside sleeve of the penetrometer); the readings are provided on a recorder located in the support vessel.

The penetrometer system, with a subsea unit, consists of (1) the ballasted frame; (2) a hydraulic cylinder with a piston, controlled from the surface support vessel, to push in the drill string in successive sequences of about 0.60 m—the piston returns under pressure from a hydraulic accumulator; (3) a string of drill pipes, 36 mm in diameter, and about 30.0 m in length, and carrying the 36-mm diameter penetrometer cone (Figure 4.11 [16]); (4) an inclinometer to monitor the deviation of the drilling string; (5) operating winches to raise/lower the subsea unit and for extracting the drill string from the seabed; (6) a central hydraulic power plant to operate the hydraulic cylinder; and (7) a recording instrument to record the  $R_p$  and  $f$  data (Figure 4.12 [17]). The system is found to be suitable for 100.0- to 150.0-m water depths in the North Sea; for deeper water depths, a submerged central hydraulic power plant would be required. The surface support vessel can safely operate in an ocean environment with wave heights around 3.0 to 4.0 m.

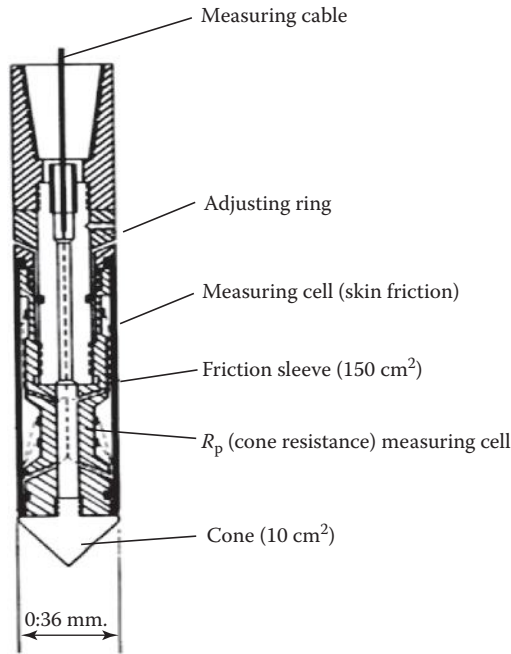
The penetrometer cone details are as follows: (1) a cone summit angle of  $60^\circ$ , cone diameter of 36 mm, cross-sectional area of  $1000\text{ mm}^2$ , and a lateral surface area (for friction measuring sleeve) of  $15,000\text{ mm}^2$ ; (2) maximum reactions for penetration of the cone are about 8.0 t for 10.0-t frame, and 20.0 t for 25.0-t frame; (3) cone penetration, in one insertion, of 0.60 m; (4) rate of penetration of 1.0 m/min; (5) measuring cells of a cone penetrometer, designed to carry a maximum load of (a)  $R_p$  equal to 5000 to 6000  $t/m^2$  in sands and overconsolidated clays and 750.0  $t/m^2$  in clays and muds and (b) frictional resistance  $f$  equal to 50.0  $t/m^2$ ; and (6) penetration depth of the cone varying from a few meters in dense sands to a maximum depth of 25.0 to 30.0 m in slightly overconsolidated soils.

The modular penetrometer is the best device available for measuring the mechanical characteristics of (loose or dense) sands and consolidated clays; also this penetrometer has the least disturbance of the ocean soil strata. However, in sands of medium density ( $\gamma_d \approx 1.50$  to  $1.60\text{ t/m}^3$ ), the continuous operation of the penetrometer compacts the soil below the cone and gives higher values for the cone resistance. The cone penetrometer cannot be used (1) when the cohesion of the surface sediment is below 2.0 to 3.0  $t/m^2$  ( $\sim 30.0\text{ kPa}$ ) and (2) when the seabed soil contains banks of pebbles and indurated or highly dense sand zones, where  $R_p > 5000.0\text{ t/m}^2$  (50.0 MPa).



**FIGURE 4.10** In situ soil sampling using standard cone penetrometer. (From N.D.P. Barltrop and A.J. Adams, Dynamics of fixed marine structures, in: *Foundations*, Butterworth Heinemann Ltd., Oxford, UK, p. 188, 1991. With permission.)





**FIGURE 4.11** Seacalf electric cone penetrometer. (From P. Le Tirant, *Seabed Reconnaissance and Offshore Soil Mechanics*, Editions Technip 27, Paris, France, p. 227, 1979. With permission.)

In sands, the tip resistance  $R_p$  increases very rapidly with the dry density  $\gamma_d$  (or the relative density  $D_r$ ). Figure 4.13 [18] shows the relationships between the magnitude of  $R_p$  (mean values) and those of dry density ( $\gamma_d$ ) and relative density ( $D_r$ ) for sandy soils. For sands with relative densities  $D_r$  approaching 90% to 100%, the tip resistance lies between 700 (~ 7.0 MPa) and 5000 t/m<sup>2</sup> (~ 50.0 MPa). In clays, the undrained cohesion  $c_u$  lies between  $R_p/10$  and  $R_p/20$ , depending on the consolidation of clays.

In Scandinavian clayey soils, the undrained shear strength  $s_u$  is related to the cone resistance  $R_p$  of a penetrometer by the following relationship (see Figure 4.14 [19]):

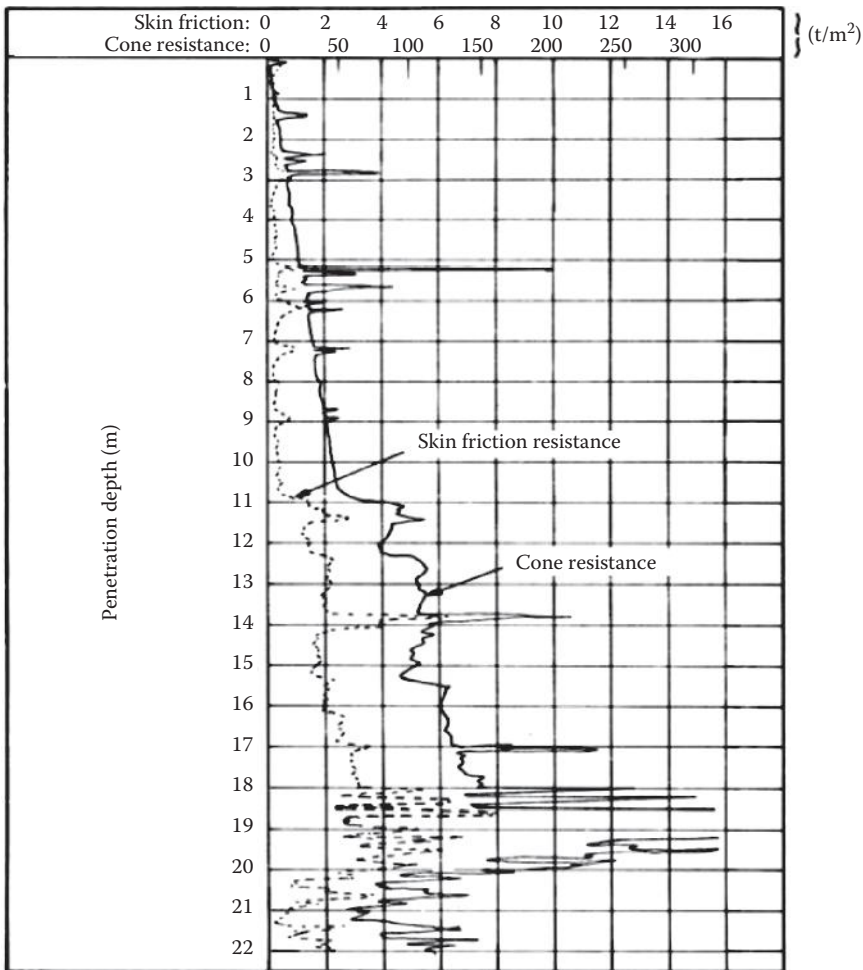
$$s_u = (R_p - \gamma'z)/N_c \quad (4.3)$$

where  $R_p$  is the penetrometer cone resistance,  $\gamma'$  is the buoyant density of soil,  $z$  is the depth of the layer below the seabed, and  $N_c$  is a dimensionless parameter varying from 5.0 to 20.0.  $N_c$  ranges from 8 to 12 for stiff clays (with  $s_u$  varying between 5.0 and 30.0 t/m<sup>2</sup>) and from 12 to 20 for soft clays. If the tip resistance in soil ( $R_p$ ) is greater than 300.0 t/m<sup>2</sup> (~ 3.0 MPa), then the lateral friction resistance can be related to tip resistance, as shown in Table 4.2 [19]. The value of  $N_c$  depends on the undrained shear strength or cohesion  $c_u$ , the rate of penetration, the permeability and compressibility of clays, and the sensitivity of the clay medium.

The correlation between  $N_{SPT}$  values [being the number of blows per 0.30 m (penetration) of hammer weighing for a hammer of 65.0 kgf (~ 636.0 N) falling 0.75 m] is related to the undrained shear strength of different ocean clays in Table 4.3 [20]. The standard penetrometer corrections and other relevant equations are given in Table 4.4 [21].

### Example 4.2

A cone penetrometer test has been conducted and has measured a cone resistance (corrected for field procedures) of 85.0 kgf/cm<sup>2</sup> at a depth of 10.0 m. The vertical effective stress at this depth is



**FIGURE 4.12** Soil resistance curves obtained from a cone penetrometer. (From P. Le Tirant, *Seabed Reconnaissance and Offshore Soil Mechanics*, Editions Technip 27, Paris, France, p. 229, 1979. With permission.)

150.0 kPa, and the OCR is 2. The soils at this depth are quartz sands. Compute the relative density and classify the soils according to Table 4.4.

Assume the sands to be moderately compressible.

$$D_r = (\sqrt{A(B)})(100.0\%);$$

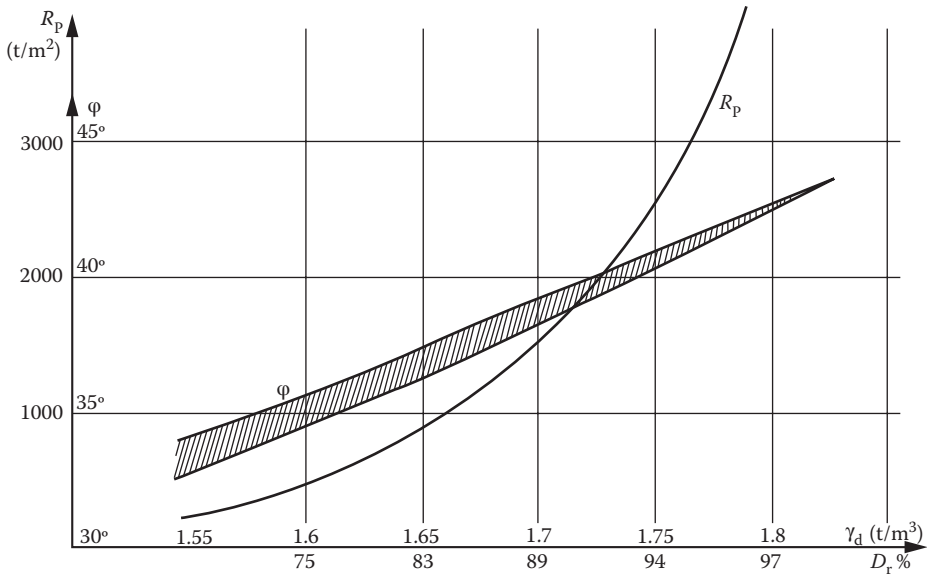
$$A = q_c / \{(315 Q_c (OCR)^{0.18})\}; \text{ and } B = \sqrt{\{(100.0 \text{ kPa}) / \sigma'_c\}}$$

$$A = (85.0) / \{(315)(1.00)(2.0)^{0.18}\} = 0.238.$$

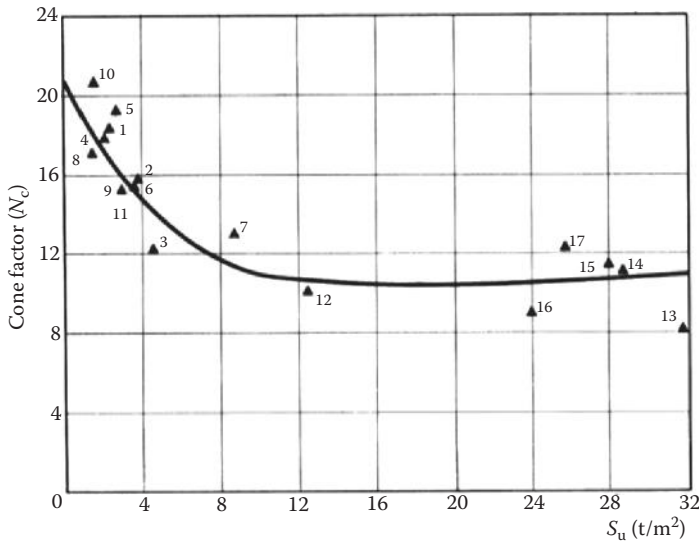
$$B = \sqrt{[(100.0) / (150.0)]} = 0.816.$$

$$D_r = (100.0) / \{(0.238)(0.816)\}^{0.5} \% = 44.1\%.$$

The sand is medium dense sand.



**FIGURE 4.13** Angle of friction and tip resistance in terms of dry density ( $\gamma_d$ ) and relative density ( $D_r$ ). (From P. Le Tirant, *Seabed Reconnaissance and Offshore Soil Mechanics*, Editions Technip 27, Paris, France, p. 240, 1979. With permission.)



**FIGURE 4.14** Correlation between the undrained shear strengths of soils measured on a vane shear and cone penetrometer equipment, in terms of  $N_c$ , for Scandinavian soils. (From P. Le Tirant, *Seabed Reconnaissance and Offshore Soil Mechanics*, Editions Technip 27, Paris, France, p. 241, 1979. With permission.)

**TABLE 4.2**  
**Soil Classification Based on Values of Tip Resistance  $R_p$  and Lateral Friction Resistance  $f$**

#	Ratio of $f/R_p$	Nature of Soils
1	Between 0.6% and 2%	Sands and gravels
2	Between 2.0% and 4.0%	Mixtures of sands and silts
3	Between 4.0% and 8.0%	Clays

Source: P. Le Tirant, *Seabed Reconnaissance and Offshore Soil Mechanics*, Editions Technip 27, Paris, France, p. 241, 1979. With permission.

**TABLE 4.3**  
**Relationships between  $N_{SPT}$  and Undrained Shear Strengths for Clays**

Soil Consistency	Very Soft to Soft	Soft to Medium Stiff	Medium Stiff to Stiff	Stiff to Very Stiff	Hard
$N_{SPT}$ [blows per foot (0.3 m) of penetration]	0–2	2–4	4–8	8–16	16–32
Typical Depth <sup>a</sup> (m)	0.03–3.0	4.5–7.5	7.5–12.0	12.0–24.0	24.0–30.0
Shear Strength <sup>b</sup> (kPa)	12.0	25.0	50.0	100.0	200.0

Source: B.C. Gerwick, Jr., *Construction of Marine and Offshore Structures*, CRC Press, Boca Raton, FL, p. 49, 1999. With permission.

<sup>a</sup> Depth of normally consolidated clay associated with the shear strength shown.

<sup>b</sup> Results from vane shear tests in field.

### Example 4.3

- (a) The results shown in Figure 4.12 were obtained in a cone penetration test on (1) soft clay stratum and (2) stiff clay stratum. The buoyant weight of soil is  $0.7 \text{ t/m}^2$ . Determine the undrained shear strength of the seabed layer at depths of 10.0 and 15.0 m below the top of the seabed. (b) If the relative density of the seabed soil is 89% and the angle of internal friction of wet soil is  $38.5^\circ$ , determine the possible ranges of the undrained shear strength of sand given that the data should conform to the ranges given in Table 4.2.

### Solution for Example 4.3

- (a)
- (i) *Soft clay stratum:* From Figure 4.12, at a depth of 10.0 m below the seabed,  $R_p = 50.0 \text{ t/m}^2$  and  $f = 10.0 \text{ t/m}^2$ .  
 As per Equation 4.3,  $s_u = (R_p - \gamma'z)/N_c$ .  
 Also as per the discussions given in Section 4.3.3.1, take  $N_c = 16$  for soft clayey soil.  
 Using Equation 4.3,  $s_u = (R_p - \gamma'z)/N_c = [50.0 - (0.7)(10.0)]/16 = 2.69 \text{ t/m}^2$ , at a depth of 10.0 m below the seabed.  
 For a depth of 15.0 m (see Figure 4.12, below the seabed,  $s_u = [100.0 - (0.7)(15.0)]/16 = 5.59 \text{ t/m}^2$ , at a depth of 15.0 m below the seabed.

**TABLE 4.4**  
**Equations Relevant for Cone Penetration Test Computations**

Parameter	Equation	Details
Relative density ( $D_r$ ) ( $D_r$ from 0% to 15% is very loose sand; from 15% to 35% is loose sand; from 35% to 65% is medium dense; from 65% to 85% is dense; and from 85% to 100% is very dense)	$D_r = \left( \frac{\sqrt{(A)(B)}}{100.0} \right) (100.0\%),$ where $A = q_c / \{ (315 Q_c (\text{OCR})^{0.18}) \}$ $B = \sqrt{ \{ (100.0 \text{ kPa}) / \sigma'_c \} }$	$q_c$ = cone resistance in $\text{kgf/cm}^2$ . $Q_c$ = compressibility factor; = 0.91 for highly compressible sands; = 1.00 for moderately compressible sands; and = 1.09 for slightly compressible sands. OCR = Overconsolidation ratio. $\sigma'_c$ = vertical effective stress (kPa). $N^{60}$ = SPT $N$ -value corrected for field procedures
SPT $N$ -value ( $N_1$ ) corrected for field procedure and overburden stress	$(N_1)_{60} = N_{60} \sqrt{ (100.0 \text{ kPa}) / \sigma'_c }$	$N^{60}$ = SPT $N$ -value corrected for field procedures
SPT $N$ -value obtained in the field ( $N$ )	$N_{60} = [(E_m C_B C_S C_R N) / (0.60)]$	$E_m$ = hammer efficiencies (0.45 for donut type and 0.55–0.60 for safety type). $C_B$ = borehole diameter factor (1.00 for 65 to 115 mm; 1.05 for 150 mm; and 1.15 for 200 mm). $C_S$ = sampling method factor (1.00 for standard sampler and 1.20 for sampler without liner). $C_R$ = rod length factor (0.75 for 33 to 4 m; 0.85 for 4 to 6 m; 0.95 for 6 to 10.0 m; and 1.00 for greater than 10 m).

Source: D.P. Coduto, *Geotechnical Engineering: Principles and Practices*, Prentice Hall, Upper Saddle River, NJ, p. 104, 1999. With permission.

Note that the variation in undrained shear strength of soil is much steeper in soft clay.

- (ii) *Stiff clay stratum*: From the discussions given following Equation 4.3,  $N_c$  ranges between 8.0 (say, at 10.0 m) and 12.0 (say, at 15.0 m). Hence, take  $N_c = 10.0$ .

For a depth of 10.0 m, below the seabed,  $s_u = [50.0 - (0.7)(10.0)]/8.0 = 5.38 \text{ t/m}^2$ .

For a depth of 15.0 m, below the seabed,  $s_u = [100.0 - (0.7)(15.0)]/12.0 = 7.46 \text{ t/m}^2$ .

Note that the variation in undrained shear strength of soil is less steep in stiff clay.

- (b) *Sandy stratum*

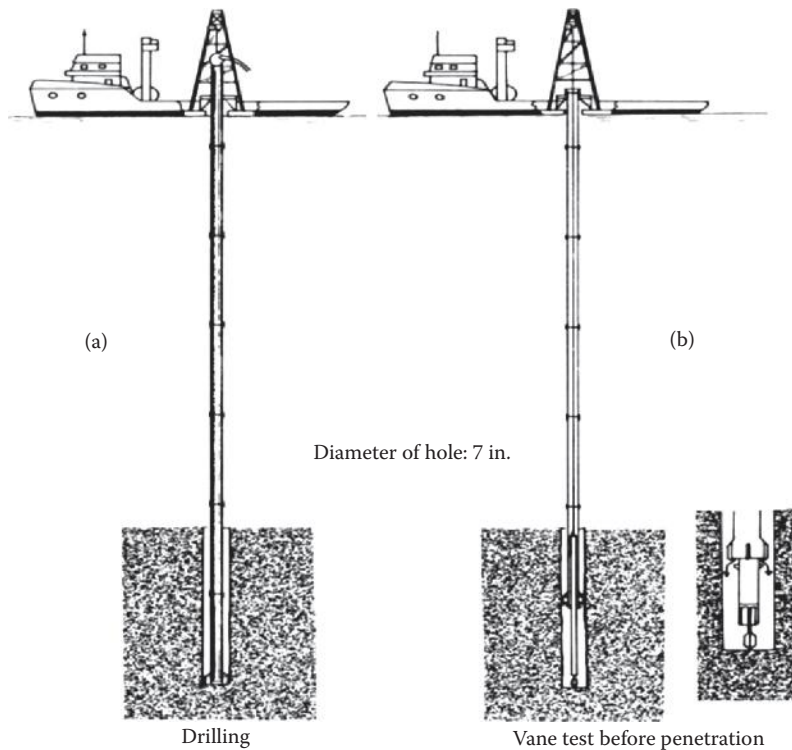
Using the data given in Figure 4.13, for the given values of the relative density of the seabed soil (89%) and the angle of internal friction of wet soil ( $38.5^\circ$ ), the value of  $R_p \sim 1,750.0 \text{ t/m}^2$ . Hence, using the ranges of values given in Table 4.2, for soil consisting of sands of silts, ( $f/R_p$ ) ranges between 2% and 4%.

The unconfined frictional shear strength of sand ranges between  $[(2)(1750)/(100.0)] \equiv f = 35.0 \text{ t/m}^2$  and  $[(4)(1750)/100] = 70.0 \text{ t/m}^2$ .

Hence, the unconfined frictional shear strength of a sandy–silty stratum seems to vary between 35.0 and 70.0  $\text{t/m}^2$ .

#### 4.3.4.2 Wire-Line Vane Shear Test Equipment

The wire-line vane is operated through the drill string (in a one-stage operation) or in alternation with the wire-line corer, from surface support vessels, fitted for the purpose (in a two-stage operation) as shown in Figure 4.15 [22]. The vane shear test is used to evaluate the undrained shear strength in soft to stiff clays and silts. In this procedure, the borehole is first sunk to a depth about 0.60 m above the elevation selected for determining the shear strength (to minimize the soil disturbance at the selected location, by the coring process). During this process, a maximum load of 4.0 t

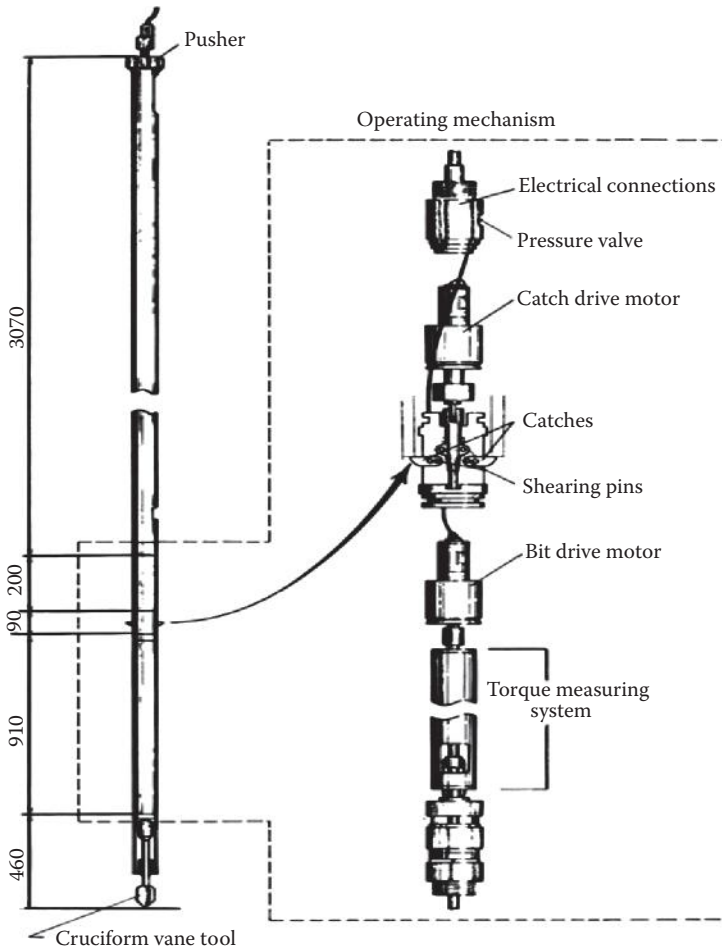


**FIGURE 4.15** Remote soil sampling of seabed using vane shear probe: (a) drilling into the seabed, before lowering the vane; and (b) the lowered vane is pushed into the soil to the desired depth by remote-controlled procedure. (From P. Le Tirant, *Seabed Reconnaissance and Offshore Soil Mechanics*, Editions Technip 27, Paris, France, p. 264, 1979. With permission.)

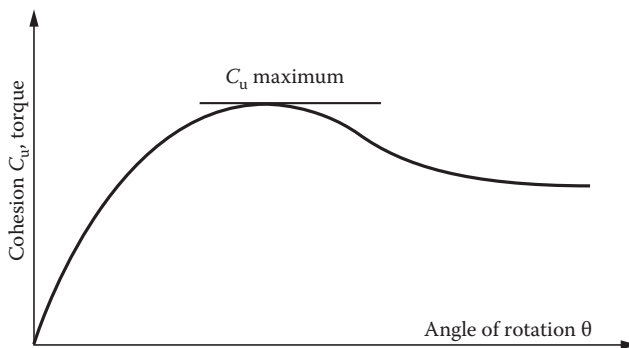
is applied on the drill bit through the hydraulic jack, as it drills through the soil strata with a rotating speed of 70.0 to 120.0 rpm (see Figure 4.15). The drill fluid consists of a mixture of sea water and natural clay (with or without bentonite). Then the drill bit is raised by 2.0 m, and the vane tool is lowered by wire line through the drill string (Figure 4.16 [23]).

The vane tool (made up of three different tools), consisting of two rectangular plates (of radius 1.5 to 2.5 cm and height equal to 2.0 to 3.0 times the radius) arranged in a cruciform manner (see Figures 4.15 and 4.16), is rapidly pushed into the seabed soil (to the required depth) by remote control from the surface support vessel. The soil is broken up by the rotation of the tool, and the (torsional) shear strength is deduced from the torsional moment measured. The maximum torque that can be applied through the vane tool is 1.15 m.kg, and the rotating speed of the tool can range from 0.14°/s to 0.89°/s. Then the procedure is repeated until the required depth for soil strength determination is reached. The vane shear test determines the undrained shear strength of the soil, since the speed of test does not allow any dissipation of the interstitial pore pressure in soil. The tool can measure only up to a maximum undrained cohesive strength of 10.0 t/m<sup>2</sup> (100.0 kPa); consequently, the maximum depth for soil strength reconnaissance can rarely exceed more than 100.0 m below the seabed.

The torque recorded in terms of the angle of rotation  $\theta$  of the vane at a constant angular speed goes through a maximum, corresponding to the value of undrained cohesive strength,  $c_u$ , of the soil, as shown in Figure 4.17 [24]. It is assumed that the angle of internal friction of the sheared soil is zero or negligible. Then the undrained cohesive strength of the soil is given by



**FIGURE 4.16** McClelland's vane shear apparatus (scissometer). (From P. Le Tirant, *Seabed Reconnaissance and Offshore Soil Mechanics*, Editions Technip 27, Paris, France, p. 265, 1979. With permission.)



**FIGURE 4.17** Relationship between the torque measured and the angle of rotation for vane shear tests. (From P. Le Tirant, *Seabed Reconnaissance and Offshore Soil Mechanics*, Editions Technip 27, Paris, France, p. 268, 1979.)



$$c_u = M/[2\pi R^2\{h + (2R/3)\}] \tag{4.4}$$

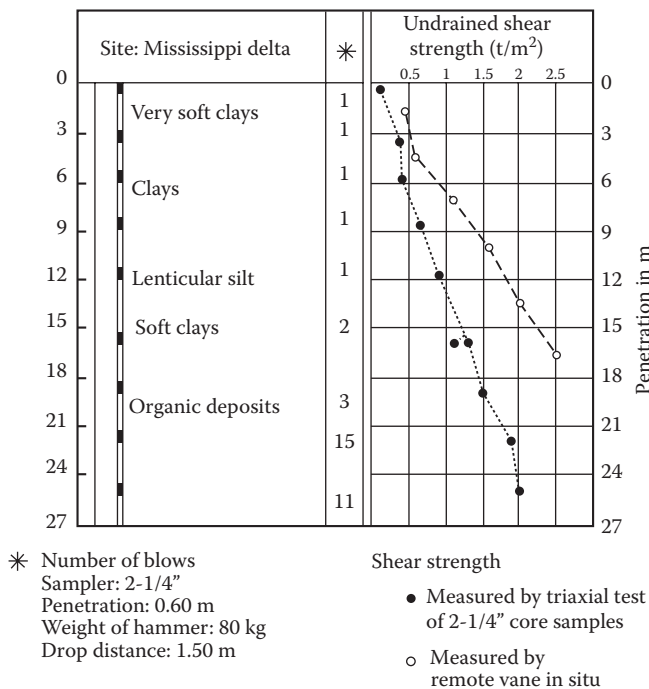
where  $M$  is the maximum torque measured during the test,  $R$  is the radius of the plate, and  $h$  is the height of the blades. The maximum shear strength that can be measured, with the three types of vane shear tools, is shown in Table 4.5 [25].

It has also been observed that the undrained shear strength of the soil is slightly dependent on the rotating speed of the tool and the dimension of the vane blades. The vane shear test measures the shear strength in the horizontal direction; owing to the anisotropy of the soil, the shear strength in the vertical direction is normally above this shear strength in the horizontal direction, as observed from results for soil cores. Also it is found that the shear strengths observed from in situ vane shear tests are generally greater than the strength observed from soil cores, due to the fact that the coring process disturbs the soil fabric (see Figure 4.18 [26]).

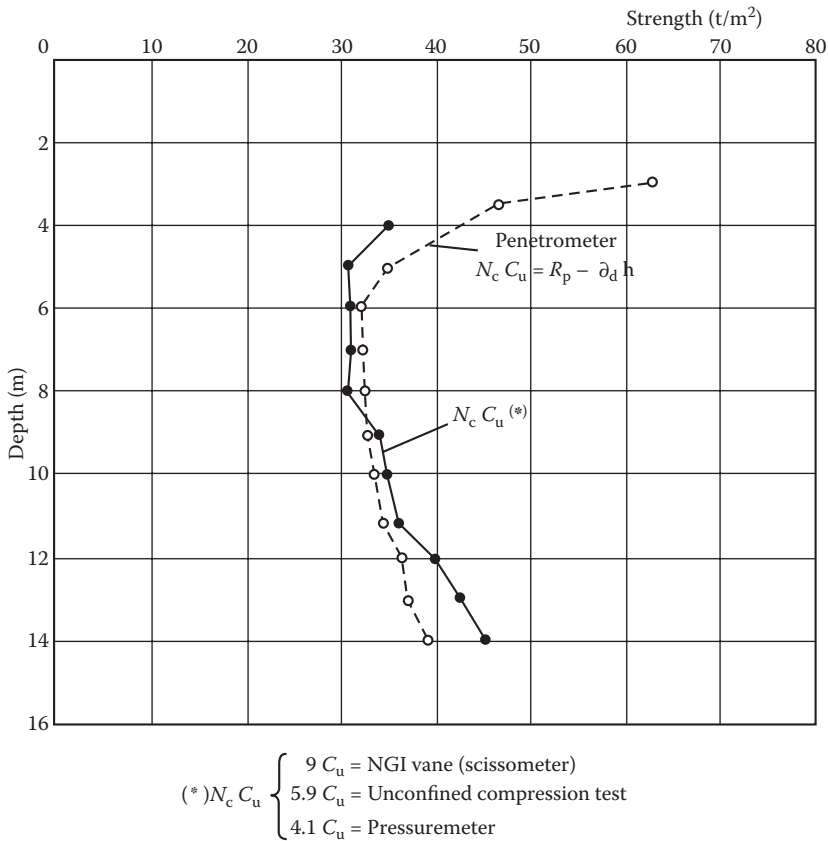
**TABLE 4.5**  
**Relationship between Maximum Cohesive Strength of Soil and Its Classification**

Approximate Radius of Blades (mm)	Maximum Cohesive Strength (t/m <sup>2</sup> )	Classification of Clay
15.0	10.0	Stiff
20.0	3.0	Medium
25.0	1.2	Soft to very soft

Source: P. Le Tirant, *Seabed Reconnaissance and Offshore Soil Mechanics*, Editions Technip 27, Paris, France, p. 269, 1979.



**FIGURE 4.18** Comparison of shear strengths obtained from core samples and from vane shear tests. (From P. Le Tirant, *Seabed Reconnaissance and Offshore Soil Mechanics*, Editions Technip 27, Paris, France, p. 270, 1979.)



**FIGURE 4.19** Comparison of shear strengths obtained from different instruments. (From P. Le Tirant, *Seabed Reconnaissance and Offshore Soil Mechanics*, Editions Technip 27, Paris, France, p. 272, 1979.)

The undrained cohesive strength,  $c_u$ , of low consolidation obtained from the penetrometer tests, depends on the value of  $N_c$  assumed. If one assumes that  $N_c$  is equal to 9.0, then

$$(c_{u \text{ penetrometer}})/(c_{u \text{ vane}}) \approx 1.5 \text{ to } 2.0 \tag{4.5}$$

For instance, Figure 4.19 [27] shows the variation of  $N_c c_u$  as a function of the depth at which the strength was obtained, in clays of medium consolidation. In fact, the value of  $N_c$  depends on the method of measuring the undrained cohesive strength,  $c_u$ . Moreover, in sands, the formation of a rigid zone near the cone of the penetrometer will result in a higher angle of friction.

**Example 4.4**

The test results given in Figure 4.18 show that the undrained shear strength, recorded in the selected soil strata, increases gradually as the depth increases. The recorded torsional moments at the depths of 6.0 and 18.0 m (below the seabed) are, respectively, 0.135 and 0.378 m kgf. Determine the cohesive strength of clay, at these depths, and compare them with the results given in Figure 4.18.

Equation 4.4 relates the torsional moment registered in the vane shear device to the undrained shear strength of clay soil, viz.,  $c_u = M/[2\pi R^2\{h + (2R/3)\}]$ . Choosing the soil to be medium stiff clay,

the radius  $R$  of the vane shear test equipment is given by Table 4.5 as 20 mm; also  $h$  = the height of the blades that are taken as equal to  $(3R) = 60$  mm.

(i) At a depth of 6.0 m below the seabed:

$$c_u = (0.135)/\{[(2\pi)(0.02)^2]\{(3)(0.02) + (2/3)(0.02)\}\} = (0.135)/\{(0.00251)(0.055)\} = 977.9 \text{ kgf/m}^2 \\ = 0.978 \text{ t/m}.$$

From Figure 4.18, the undrained cohesive (shear) strength = 0.95 t/m<sup>2</sup>.

Both are the same.

(ii) At a depth of 18.0 m below the seabed:

$$c_u = (0.378)/\{[(2\pi)(0.02)^2]\{(3)(0.02) + (2/3)(0.02)\}\} = (0.378)/\{(0.00251)(0.055)\} = 2738.1 \text{ kgf/m}^2 \\ = 2.74 \text{ t/m}^2.$$

From Figure 4.18, the undrained shear strength is 2.66 t/m<sup>2</sup>.

Both are the same.

## 4.4 OCEAN BED SOIL MECHANICS

### 4.4.1 INTRODUCTION

Since seabed soil is made up of granular materials, it is discontinuous in a microscopic scale; but from an engineering viewpoint, the soil is considered to be continuous. The volume between these granular materials is filled with water and gas. Hence, the deformation of the soil skeleton is dependent on the variation of pressure in the water and gas, and the movement of water particles (and gas, if present) within the volumetric space available in between these grains. The differences between marine and terrestrial soils are dependent on (i) the chemical, physical, and textural character (termed the *diagenesis*) of ocean soil; (ii) the proportion of various elements constituting the ocean soil [such as calcareous sands, high clay-to-sand ratio (especially at large depths)]; (iii) the total/partial saturation of ocean soils (sometimes decompression of the water takes place due to large amount of dissolved gases); and (iv) erosion of soils by water that changes the surface properties of ocean soils. It must be borne in mind that even though the characterization of ocean soil properties is similar to that used for terrestrial soils, yet due to the difficult terrain and environmental conditions in which the marine soils are situated, the assessment of marine soil properties is as follows: (i) They are less comprehensive and less adequate. (ii) They are uncertain and as such lead to the design of heavier or larger structure due to their approximate physical/mechanical properties and the larger safety factors used in the design. (iii) They are very important since the installed ocean structures are very large and massive (gravity platform foundations are of more than 100.0 m in diameter, and pile penetration can also be more than 100 m in depth) and laid more or less on irregular seabeds. (iv) The lateral forces exerted on these structures are much larger than those exerted on land structures.

The laboratory testing of soil cores leads to the determination of the following properties of ocean soils, viz., (i) identification of soils, which would require the determination of mineralogy, particle size, water content, porosity, void ratio, densities (dry, wet, buoyant, and relative), Atterberg limits of liquid limit, and plasticity index and permeability; (ii) shear strength properties of ocean sediments such as sands/silts/clays using direct-shear/triaxial tests to determine the unconsolidated/consolidated strength with/without water drainage; and (iii) the compressibility of soils considering phases of consolidation, settlement, and state of consolidation. It must be kept in mind that the results of tests on marine soils are open to criticism, since the core samples of ocean soils will be disturbed as they are acquired from the ocean bed and are also poorly conserved, and

liable to handling disturbances. In order to avoid these problems, the ocean properties are determined aboard the surface support vessel as the cores are acquired, or they are determined on site in a remote manner.

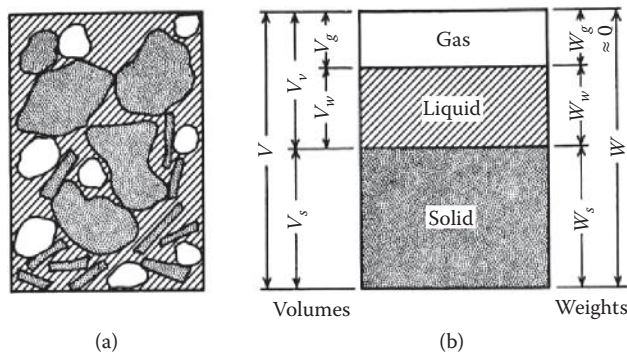
#### 4.4.2 IDENTIFICATION OF MARINE SOIL CHARACTERISTICS

Identification of soils consists of characterizing the soils sufficiently so that they can be compared to other soils in a distinct manner. Since soil is a particulate system, it can be represented by the multiphase system consisting of solid (mineral) particles, gas, and liquid (usually water), shown in Figure 4.20 [28]. Figure 4.20a represents the natural state of the soil system, and Figure 4.20b shows the separated phases of the soil system, in terms of the volumes (on the left-hand side of Figure 4.20) and in terms of its weight (on the right-hand side). There are three important relationships that are based on volume, viz., porosity, void ratio, and degree of saturation, and one relationship based on weight, viz., water content. Secondary sets of relationships based on the volume and weight of the soil system are termed the unit weights and specific gravities of the given soil system; all these terms are given in Table 4.6 [29, 30]. Some typical physical properties of ocean soils are given in Table 4.7 [29–32].

#### 4.4.3 STRUCTURE OF SOIL

A sample of soil consists of an assemblage of many individual soil particles, with air and/or liquid filling the void spaces in between the particles. Some of the minerals constituting the particulate nature of the soil system are silica (or quartz), feldspars (K-, or Na–Ca-), calcite, dolomite, muscovite, biotite, chlorite, pyrophyllite, serpentine, kaolinite, halloysite, illite, montmorillonite, olivine, rutile, and others [33, 34]. All these constitute the various particles that aggregate to form the different types of sand, silt, and clay mixtures present in natural soils. Soil particles vary in size from  $(1.0)(10^{-6})$  mm to a large rock, several meters in thickness. The particle sizes and their designation in terms of boulder, cobble, gravel, sand, silt, and clay have already been given in Table 4.1. Particle shapes for marine sands and silts can be termed as almost cubic (or rectangular prismatic) or spherical and to be almost well rounded; but the same cannot be said of particles in the clay range, which are more plate-, rod-, disc-, and lath-shaped. The structures of typical marine soils are shown in Figure 4.21 [35].

Moreover, every particle of soil carries an electrical charge; although theoretically a soil particle may carry either a negative or positive charge, only negative charges have been measured. The net electrical charge may arise from any one or a combination of the following factors:



**FIGURE 4.20** Relationship among soil phases. (T.W. Lambe and R.V. Whitman, *Soil Mechanics*, p. 30. 1979. Copyright Wiley-VCH Verlag GmbH & Co. KGaA. Reproduced with permission.)

**TABLE 4.6**  
**Definition of Specific Properties of Marine Soils**

#	Property Based on	Properties	Definition	Comments
1	Volume	Porosity	$n = V_v/V = e/(1+e)$ $= 1 - (\gamma_d/G)$	—
1		Void ratio	$e = V_v/V_s$	—
1		Degree of saturation	$S = V_w/V_v$	—
2	Weight	Water content	$w = W_w/W_s = 1/\gamma_d - 1/G$	—
3	Weight and volume	Total unit weight (or wet density)	$\gamma_t = W/V$ $= [(G + Se)/(1+e)]\gamma_w$ $= [(1+w)/(1+e)]G\gamma_w$	$G =$ Specific gravity of solids; for most common soils, $G = 2.7$
3		Unit weight of solids	$\gamma_s = W_s/V_s = G$	—
3		Unit weight of water	$\gamma_w = W_w/V_w$	—
3		Dry unit weight	$\gamma_d = W_s/V = [G/(1+e)]\gamma_w$ $= G\gamma_w/(1+wG/S)$ $= \gamma_t/(1+w)$	—
3		Submerged buoyant unit weight	$\gamma_b = \gamma_t - \gamma_w$ $= [(G - 1 - e(1-S))/(1+e)]\gamma_w$ $= [(G-1)/(1+e)]\gamma_w$	—
3		Relative density (%)	$D_r = (e_{\min} - e)/(e_{\min} - e_{\max})$ $= [(\gamma_d - \gamma_{d\min})/(\gamma_{d\max} - \gamma_{d\min})]$ $\times (\gamma_{d\max}/\gamma_d) \times (100)$	$\gamma_{d\max}$ and $\gamma_{d\min}$ represent dry density at maximum and minimum compacting
4	Unit weights	Specific gravity of soil	$G_m = \gamma_w/\gamma_0$	$\gamma_0 =$ unit weight of water at $4^\circ\text{C} \approx \gamma_w$ . Also note that $G_w = Se$ .
4		Specific gravity of water	$G_w = \gamma_w/\gamma_0$	—
4		Specific gravity of solids in soil	$G(= G_s) = \gamma_s/\gamma_0$	—
5		Sensitivity of soils	Ratio of undisturbed to remolded strength at natural water content	—

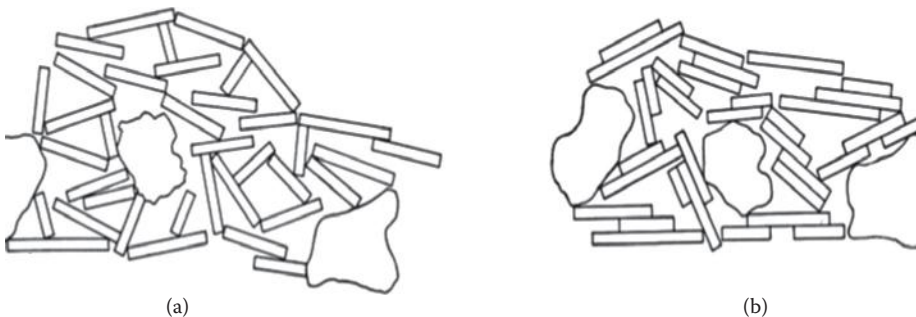
(i) isomorphous substitution (of one kind of atom—of similar form—for another), which is the most important cause for the electrical charges in the soil particles; (ii) surface disassociation of hydroxyl ions; (iii) absence of cations in the crystal lattice; (iv) adsorption of anions; and (v) presence of organic matter. The electrical charge carried by the soil particle is related to the particulate surface area; the influence of this charge on the behavior of the particle (relative to the influence of mass forces or weight of the particles) is dependent on the surface area per unit mass of the particle (termed as *specific surface*). Since clay particle has a large surface area, its behavior is controlled by surface-derived forces than mass-derived forces; hence, clay is colloidal

**TABLE 4.7**  
**Typical Properties of Ocean Soils**

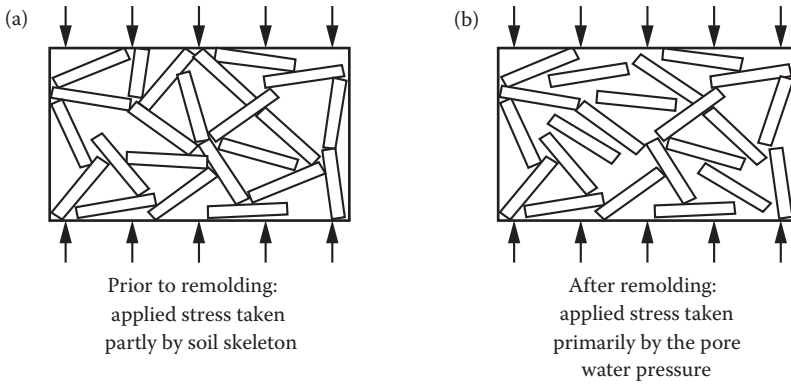
Property of Soils	Sand Range (Average)	Sandy Silt or Silty Sand Range (Average)	Silt Range (Average)	Clay Ranges (Average)	Calculated Ooze Range (Average)
Porosity (%)	35–50 (45)	45–70 (55)	50–85 (73)	50–85 (77)	45–85 (60)
Water content (%)	15–35	—	—	30–60 (n.c) 20–25 (o.c) 10–15 (s.c)	—
Void ratio	0.20–1.10 0.80–1.10 (loose) 0.20–0.50 (dense)	0.30–0.90	0.40–1.10	—	—
Saturated density ( $\gamma_s$ ) (t/m <sup>3</sup> )	1.80–2.10 (1.90)	1.50–1.90 (1.75)	1.25–1.85 (1.45)	1.18–1.80 (1.40)	1.25–1.95 (1.70)
Dry density (t/m <sup>3</sup> )	1.60–1.70	—	—	1.30–1.70	—
Relative density (%)	30–100	—	—	—	—
Sensitivity	—	3–8 (5)	2–9 (5)	2–9 (5)	2–24 (7)
Permeability (cm/s)	10.0 to 10 <sup>-4</sup> (dense sand has $K = 10^{-3}$ )	—	10 <sup>-4</sup> –10 <sup>-7</sup>	10 <sup>-7</sup> –10 <sup>-10</sup>	—

in nature. Particles of silt size and above have smaller specific surface values and have very little colloidal behavior.

Due to its colloidal nature, clay in its natural state forms a particulate structure, as shown in Figure 4.22a [36]. When the soil is disturbed and remolded, other interparticulate actions such as flocculation and dispersion are brought into play due to the attractive and repulsive forces generated in the clay medium (as a result of ionization and exchangeability of surface minerals) resulting in the flocculated structure shown in Figure 4.22b. Any load, applied to the remolded soil, is primarily carried by pore water pressure than by the soil skeleton; the soil becomes weaker in the process [37]. Sensitivities of clays vary greatly from one type of clay to another. It has been found that normally consolidated clays have sensitivities ranging from 4 to 8, whereas the sensitivity of extrasensitive or quick clays can exceed 100.



**FIGURE 4.21** Structure of natural soil. (a) Undisturbed salt water deposit and (b) undisturbed freshwater deposit. (From W. Lambe and R.V. Whitman, *Soil Mechanics*, p. 73. 1979. Copyright Wiley-VCH Verlag GmbH & Co. KGaA. Reproduced with permission.)



**FIGURE 4.22** Effect of remolding on sensitive clays. (From N.D.P. Barltrop and A.J. Adams, Dynamics of fixed marine structures, in: *Foundations*, Butterworth Heinemann Ltd., Oxford, UK, p. 183, 1991. With permission.)

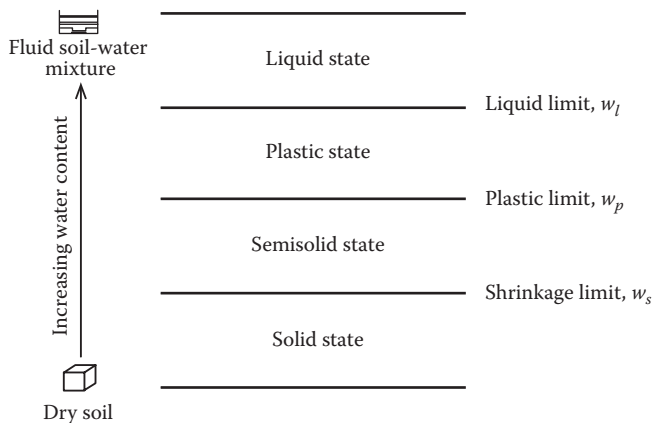
**4.4.4 ATTERBERG LIMITS**

Atterberg limits are used to classify the states of the soil and are based on the concept that a fine-grained soil can exist in any of the four states, viz., solid, semisolid, plastic, and liquid states, depending on the water content retained by the soil; they are determined on the fraction of soils whose grain size is less than 0.4 mm. This soil will pass successively through solid, semisolid, plastic, and liquid states when water content is progressively increased. The water contents at the boundaries between the adjacent states are termed as shrinkage limit, plastic limit, and liquid limit, as shown in Figure 4.23 [38]. The plasticity index, indicating the difference between the liquid and plastic limits, is given as

$$\text{Plasticity index} = I_p = W_L - W_p \tag{4.6}$$

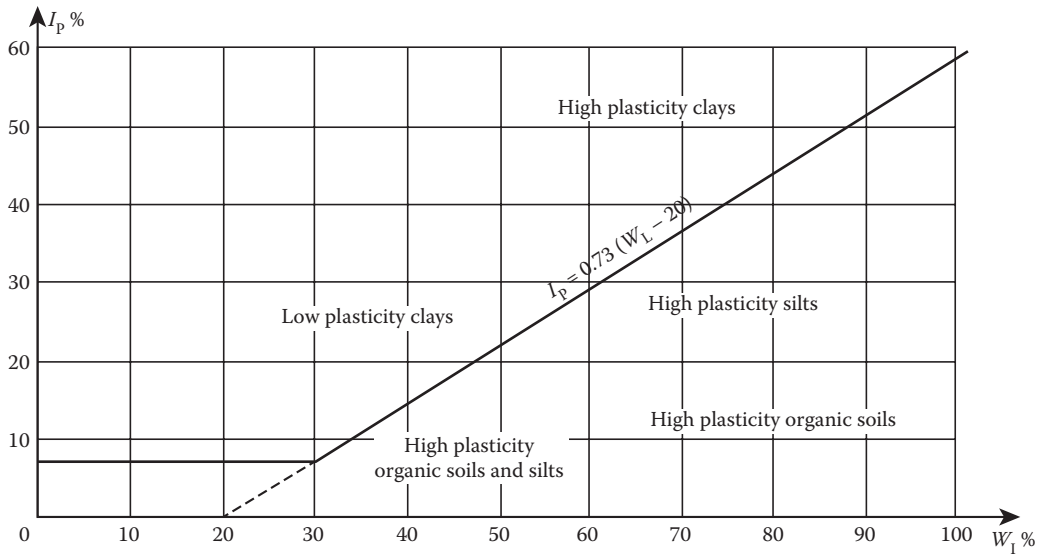
A highly useful classification of soil based on the soil states was given by Casagrande [39], shown in Figure 4.24 [40], which relates the plasticity index,  $I_p$ , and liquid limit,  $W_L$ , as shown below:

$$I_p = 0.73(W_L - 20) \tag{4.7}$$



**FIGURE 4.23** Atterberg limits and related indices. (W. Lambe and R.V. Whitman: *Soil Mechanics*, p. 33, 1979. Copyright Wiley-VCH Verlag GmbH & Co. KGaA. Reproduced with permission.)





**FIGURE 4.24** Relationship between liquid and plasticity limits (Atterberg limits) of a soil. (From P. Le Tirant, *Seabed Reconnaissance and Offshore Soil Mechanics*, Editions Technip 27, Paris, France, p. 11, 1979. With permission.)

Casagrande's soil classification system separates the soils into low/high plasticity clays, low/high plasticity silts, and high plasticity organic soils. Also it is observed that if  $I_p \approx 10.0\%$ , the soil is only slightly clayey, and if  $I_p > 30.0\%$ , the soil is highly clayey. Also overconsolidated clays encountered in many of the North Sea sites have an index of plasticity  $I_p \approx 20.0\%$  to  $30.0\%$ , and a water content of  $20.0\%$  to  $25.0\%$ . It must be remembered that these limits do not give any indication of the particle fabric or residual bonds between particles, which may have been developed in the natural soil and have been destroyed in the preparation of the specimen for tests.

#### Example 4.5

A certain soil has the following properties, viz.,  $G = 2.70$ ;  $n = 43.0\%$ ;  $w = 24.0\%$ . Find the degree of saturation,  $S_r$  and the unit weight of soil,  $\gamma_t$ .

Using Figure 4.20 and considering  $1.0 \text{ m}^3$  as the total volume of the soil–water–air mixture:

$$n = (V_v/V) = 0.430; \text{ hence, } V_v = (0.430)(1.0) = 0.430 \text{ m}^3.$$

$$\text{Volume of solids} = V_s = V - V_v = 1.0 - 0.430 = 0.570 \text{ m}^3.$$

$$G = (W_s)/(V_s \gamma_w) = 2.70; \text{ hence, } W_s = (GV_s)(\gamma_w) = (2.70)(0.570 \text{ m}^3)(9.81 \text{ kN/m}^3) = 15.10 \text{ kN}.$$

$$\text{Also, } w = (W_w/W_s)(100.0\%) = 24.0\%; \text{ hence, } W_w = (24.0)(15.10)/(100.0) = 3.624 \text{ kN}.$$

$$\text{Total weight} = W = 15.10 + 3.624 = 18.724 \text{ kN}.$$

$$\text{Also, } \gamma_w = W_w/V_w; \text{ hence, } V_w = (3.624 \text{ kN})/(9.81 \text{ kN/m}^3) = 0.369 \text{ m}^3.$$

$$\text{Consequently, volume of air} = V_a = 1.00 - 0.570 - 0.369 = 0.0610 \text{ m}^3.$$

$$\text{Saturation} = S = [(V_w)/(V_v)](100.0\%) = [(0.369)/(0.430)](100.0\%) = 85.81\%.$$

$$\text{Also, } \gamma_t = W/V = [(15.10 + 3.624) \text{ kN}]/(1.0 \text{ m}^3) = 18.724 \text{ kN/m}^3.$$

**Example 4.6**

A 300-m<sup>3</sup> mass of saturated clay had a void ratio of 0.95 and a specific gravity of solids of 2.71. A fill was placed over this clay, causing it to compress. During this process, some of the water was squeezed out of the voids. However, the volume of solids remained unchanged. After the consolidation was complete, the void ratio had become 0.75. Compute (i) the initial and final moisture contents of the clay; (ii) the new volume of the clay; and (iii) the volume of water squeezed out of the clay.

- (a) Initially the porosity is related to the void ratio by the equation  $n = V_v/V = e/(1 + e) = 1 - (\gamma_d/G)$ ; hence,  $n = (0.95)/(1 + 0.95) = 0.4872$ .

$$V_v = (0.4872)(300) = 146.16 \text{ m}^3$$

$$V_s = 300.0 - 146.1 = 153.84 \text{ m}^3$$

$$G = W_s/V_s; \text{ hence, } W_s = (153.84)(2.71)(1000.0) = 416,906.1 \text{ kgf.}$$

Assuming that the saturated clay does not contain any air,  $W_w = (146.16)(1000.0) = 146,160.0 \text{ kgf.}$

$$\gamma_d = 416,906.1/[(300)(1000.0)] = 1.39.$$

Also  $n = 1.0 - \gamma_d/G$ ; that is,  $\gamma_d = G(1.0 - n) = 2.71(1.0 - 0.487) = 1.39$ . Hence OK.

$$\text{Moreover, } \gamma_d = W_s/V = [G/(1 + e)]\gamma_w = G\gamma_w/(1 + wG/S) = \gamma_t/(1 + w).$$

Total weight of clay =  $W_w + W_s = 146,160.0 + 416,906.1 = 563,066.1 \text{ kgf.}$

$$\gamma_t = W/V = 563,066/300/1000 = 1.877.$$

Also,  $\gamma_d = \gamma_t/(1 + w)$ ; hence,  $w = \gamma_t/\gamma_d - 1.0 = 1.877/1.39 - 1.0 = 0.351$ .

Moreover,  $w = W_w/W_s$ ;  $w = 146,160/416,906 = 0.351$ ; hence, the initial water content of  $w (= 0.351)$  is OK.

- (b) Similarly, for the fully consolidated case:

$$n_{\text{final}} = 0.429; V_{v \text{ final}} = 128.7 \text{ m}^3$$

Volume of water squeezed out of clay =  $146.16 - 128.7 = 17.46 \text{ m}^3$

Final water content =  $w_{\text{final}} = (128.7)(1000.0)/(416,906) = 0.309$ .

$$\gamma_{t \text{ final}} = \gamma_d (1 + w) = (1.39)(1 + 0.309) = 1.82.$$

$$\text{Since } \gamma_{t \text{ final}} = W_{\text{final}}/V_{\text{final}} = (416,906 + 128,700)/V_{\text{final}}.$$

$$\text{New volume of clay} = V_{\text{final}} = 545,606/1.82 = 299.84 \text{ m}^3$$

**4.4.5 PERMEABILITY OF SOILS**

Water can generally flow easily through the void spaces in between soil particles, especially in sand. As the soil particles reduce in size, the wetted area of the solid particles, in a unit volume of

soil, increases; this increases the viscous forces exerted by the fluid-coated soil particles (adsorbed water) against the free flow of water through the soil mass, resulting in a smaller permeability. The flow of water in soil is given by Darcy's law, which states that

$$V = K i \quad (4.8)$$

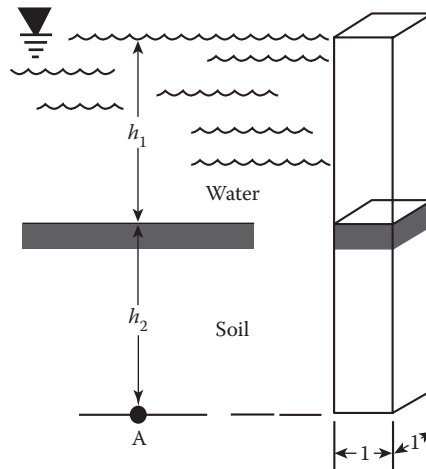
where  $V$  is the percolation velocity of water in soil,  $K$  is the coefficient of permeability (in m/s), and  $i$  is the hydraulic gradient. For sands, an approximate relationship can be obtained by Hazen's formula, given as

$$K = 100D_{10}^2 \quad (4.9)$$

with  $D_{10}$  representing the diameter of the grain for which 10.0% of the elements in soil are smaller in size. Permeability of soil varies considerably with the nature of the soil, even within the same type of soil and soil taken from the same location. Typical values of permeability of soil for different soil types are already given in Table 4.7. Clays are nearly impermeable, as seen from the low values of permeability given in the table; furthermore, clays that are structured so that the soil (particle) plates are laid almost parallel to one another have lower permeabilities than those with a more random orientation. The significant difference observed in the permeability values given for sands and clays, in Table 4.7, influences the behavior and analyses of structures founded on such soils.

#### 4.4.6 STRESSES IN OCEAN SOILS AND EFFECTIVE STRESS PRINCIPLE

Saturated ocean soils may be considered to be composed of a relatively incompressible fluid and a compressible mineral skeleton. Stresses within the soil are caused by external loads applied to the soil, water pressure at the point of interest, and the self-weight of the soil column above the point of interest. Of the stresses that are applied to these components of soil (soil skeleton and water), the mechanical properties of the ocean soil are primarily controlled by the stresses that are carried out by the soil skeletons. Consider a soil column element, shown in Figure 4.25 [41] and located at a



**FIGURE 4.25** Water-sediment column of unit dimensions. (From H. Schenck, Jr., *Introduction to Ocean Engineering*, McGraw-Hill Book Company, New York, p. 52, 1975. With permission.)

depth of  $h_2$  below the seabed in a water depth of  $h_1$  below the ocean surface. The total stresses ( $\sigma_T$ ) acting on this element are given by

$$\sigma_T = \bar{\sigma} + (1 - a)u \quad (4.10)$$

where  $\bar{\sigma}$  is the average effective stress in the soil skeleton,  $u$  is the hydrostatic or pore water pressure, and  $a$  is the effective contact area between soil particles; from earlier observations, the value of  $a$  has been found to be close to zero [42, 43]. Hence, Equation 4.10 reduces to

$$\sigma_T = \bar{\sigma} + u \quad (4.11)$$

The relationship represented by Equation 4.11 seems to be more accurate for granular soils than for clays, since intergranular attractive and repulsive forces that exist between clay particles seem to have some influence on it; it represents one of the most important concepts in soil mechanics.

Consider the case of a saturated column element of soil in a static ocean environment, shown in Figure 4.25. At point  $A$  in the sediment,

$$\begin{aligned} \sigma_T &= [[h_1(1.0)(1.0)\gamma_w + h_2(1.0)(1.0)\gamma_t]/[(1.0)(1.0)]] \\ &= (h_1\gamma_w + h_2\gamma_t) \\ u &= (h_1 + h_2)\gamma_w \\ \bar{\sigma} &= \sigma_T - u = (h_1\gamma_w + h_2\gamma_t) - (h_1 + h_2)\gamma_w \\ &= h_2\gamma_b = \text{submerged (or buoyant weight of the soil column)} \end{aligned} \quad (4.12)$$

Taking a saturated sediment volume  $V$  and assuming that it is subjected to an increase in total stress  $\Delta\sigma_T$ , the decrease in soil skeleton volume is given by

$$\Delta V = (C_c)(V)(\Delta\bar{\sigma}) \quad (4.13a)$$

where  $C_c$  is the coefficient of compressibility of the soil skeleton. The decrease in the volume of pore water is given by

$$\Delta V = (C_w)(n)(V)(\Delta u) \quad (4.13b)$$

where  $C_w$  is the coefficient of compressibility of pore water, and  $n$  is the porosity of water. If no drainage is permitted in the sediment volume, then these changes must be equal and opposite. Hence,

$$\begin{aligned} (C_c)(V)(\Delta\bar{\sigma}) &= (C_c)(V)(\Delta\sigma_T - \Delta u) \\ &= (C_w)(n)(V)(\Delta u) \end{aligned} \quad (4.14)$$

Hence, Equation 4.14 can be rewritten as

$$\begin{aligned} \Delta u &= [1.0/[1.0 + (nC_w/C_c)]]\Delta\sigma_T \\ &= B\Delta\sigma_T \end{aligned} \quad (4.15)$$

$$\text{where } B = 1.0/[1.0 + (nC_w/C_c)]$$

In Equation 4.15, since the coefficient of compressibility of water  $C_w$  is very small, it can be neglected and the value of  $B$  tends to unity for most of the sediments; the change of stress is equal to the change of pore pressure, signifying that in an undrained situation, the change in stress is accommodated by the change in pore water pressure. Also Equation 4.15 shows that the effective stress in saturated sediments is independent of the ambient stress in the sediment.

Considering the three-dimensional undrained soil element, shown in Figure 4.26 [44], the effective stresses are changed to  $(\Delta\sigma - \Delta u)$  in direction 1 and to  $\Delta u$  in directions 2 and 3. The volume change in direction 1 is equal to  $C_c V(\Delta\sigma - \Delta u)$ , and the volume increase due to pore pressure increases in directions 2 and 3 is given by  $(2C_s V \Delta u)$ , where  $C_s$  is analogous to the Poisson ratio in solid mechanics. Hence, in the undrained state,

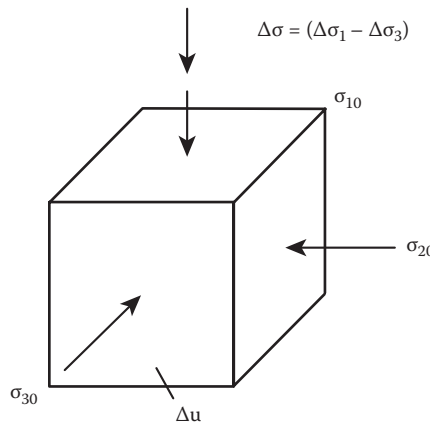
$$C_c(\Delta\sigma - \Delta u) = 2C_s \Delta u$$

$$\therefore \Delta u = \Delta\sigma / [1.0 + 2(C_s/C_c)] = A_f \Delta\sigma \tag{4.16}$$

Combining Equations 4.15 and 4.16 and using the notations given in Figure 4.26, one obtains

$$\Delta u = B \Delta\sigma_3 + A_f(\Delta\sigma_1 - \Delta\sigma_3) \tag{4.17}$$

The coefficients  $A_f$  and  $B$  are stress-dependent but are considered to be constants at the level of the shear strength of soil. Some experimentally measured values of  $A_f$  are given in Table 4.8 [45].



**FIGURE 4.26** Undrained three-dimensional soil element, submerged at a depth of  $h_2$  below the seabed. (From H. Schenck, Jr., *Introduction to Ocean Engineering*, McGraw-Hill Book Company, New York, p. 53, 1975. With permission.)

**TABLE 4.8**  
**Values of Constant  $A_f$**

#	Material	$A_f$
1	Very loose and fine sand	2.0–3.0
2	Sensitive clay	1.50–2.50
3	Normally consolidated clay	0.70–1.30
4	Lightly overconsolidated clay	0.30–0.70
5	Heavily overconsolidated clay	–0.50–0.00

Source: H. Schenck, Jr., *Introduction to Ocean Engineering*, McGraw-Hill Book Company, New York, p. 54, 1975. Reproduced with permission.

### 4.4.7 SHEAR STRENGTH AND FAILURE OF OCEAN SOILS

Shear strength of saturated soils is not a unique value, being dependent upon the failure criteria, method of testing, rate of strain, consolidation pressure, and sample integrity. The strength of saturated sediment is uniquely related to the effective stress at failure. When Mohr–Coulomb theory of failure is taken as the governing theory of failure for soils, then failure in soil will occur when the shear stress on any plane (in the soil) equals the shear strength of the soil material. As shown in Figure 4.27 [46], for a general soil, the stress failure condition can be expressed as

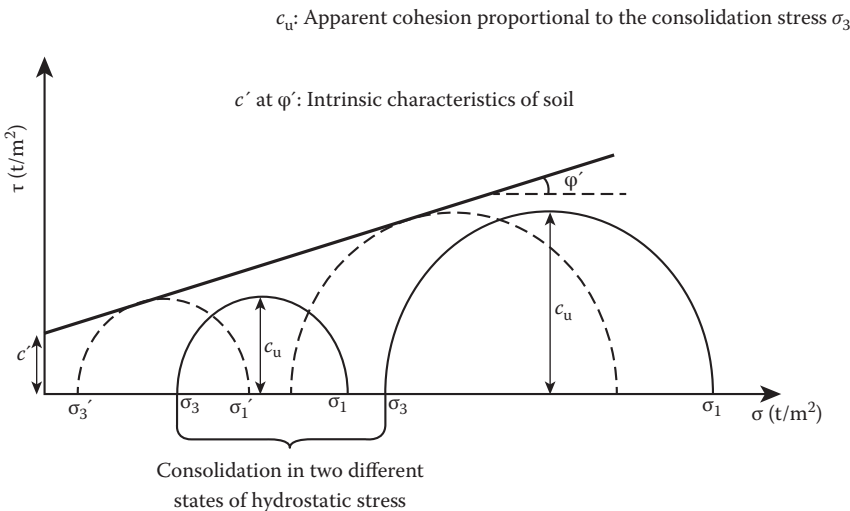
$$\tau = (\bar{c}) + (\bar{\sigma})_{\text{eff}} \tan(\bar{\phi}) \tag{4.18}$$

where  $\tau$  is the shear stress (at failure) on the failure plane,  $(\bar{\sigma})_{\text{eff}}$  is the effective normal stress on the failure plane, and  $\bar{c}$  and  $\bar{\phi}$  are, respectively, the cohesion and friction angle (saturated soil). For sands, Equation 4.18 becomes

$$\tau = (\bar{\sigma})_{\text{eff}} \tan(\bar{\phi}) \tag{4.19}$$

As indicated in Figure 4.27, the Mohr–Coulomb plot is for a general unconsolidated soil. When the soil is consolidated in stages (it takes many days for full consolidation to occur), there is a corresponding value of shear strength known as apparent or undrained cohesion ( $c_u$ ), as shown in Figure 4.27. For clays, it is seen from the figure that the apparent cohesion ( $c_u$ ) varies linearly with the consolidation stress, namely, the stress imposed by the soil skeleton overburden. It must also be borne in one’s mind that in a normally consolidated clay soil, which has not been subjected to any previous compressive loads than in its existing location, the soil may have a negligible cohesion, whereas in an overconsolidated clay soil, which has been subjected to increased compression in the past (caused by past erosion of higher soil layers), the soil will typically have a higher cohesion.

Effective stress is the appropriate stress to be used in designating the soil behavior under different conditions. When a sandy soil is under static loading conditions, drainage of soil prevents excess pore water pressure buildup. The static water pressure is readily computed as  $\rho_w g h$ , and the effective



**FIGURE 4.27** Triaxial test on unconsolidated, undrained soil;  $c' = (\bar{c})$ ,  $\phi' = (\bar{\phi})$ , and  $\sigma' = (\bar{\sigma})_{\text{eff}}$ . (From P. Le Tirant, *Seabed Reconnaissance and Offshore Soil Mechanics*, Editions Technip 27, Paris, France, p. 17, 1979. With permission.)

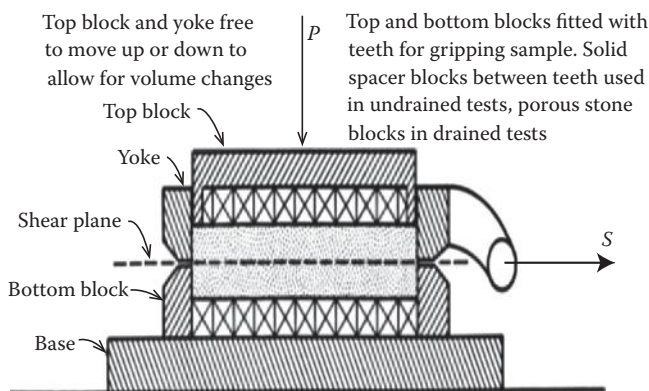
stress at any location can be easily determined thereafter. When waves exert their dynamic loads on any offshore gravity structure, a significant part of the dynamic loading on the soil is taken up by the changing of pore water pressure, since the water in the soil does not have sufficient time (during one wave load cycle) to flow out of the intergranular soil spaces. This leads to the existence of undrained or partially drained dynamic conditions in soil. Under repeated dynamic loading, some portion of sand, below the foundation, will suffer a reduction in effective stress, and more stress will be carried by the pore water pressure. The sand particles get compacted and the water takes more of the effect of the repeated loading. As a result of this increase in pore water pressure, the effective stresses in between the soil particles tend to get reduced and become almost zero. At this juncture, the whole load of the structure is carried by water pressure alone, and the soil skeleton particles tend to flow out as if they were fluid. This phenomenon is called liquefaction of soil; when this liquefaction occurs, the whole structure becomes unstable and tends to sink into the soil. Care must be taken to avoid this condition.

#### 4.4.7.1 Laboratory Tests to Measure Shear Strengths

Direct shear test, shown in Figure 4.28 [47], was the first practical test to measure the soil shear strengths. Recently, the test has fallen into disfavor due to (i) high stress gradients set up in the soil; (ii) difficulties in controlling the drainage in soil; and (iii) rotations of principal stress directions, along the shearing interface, during the test.

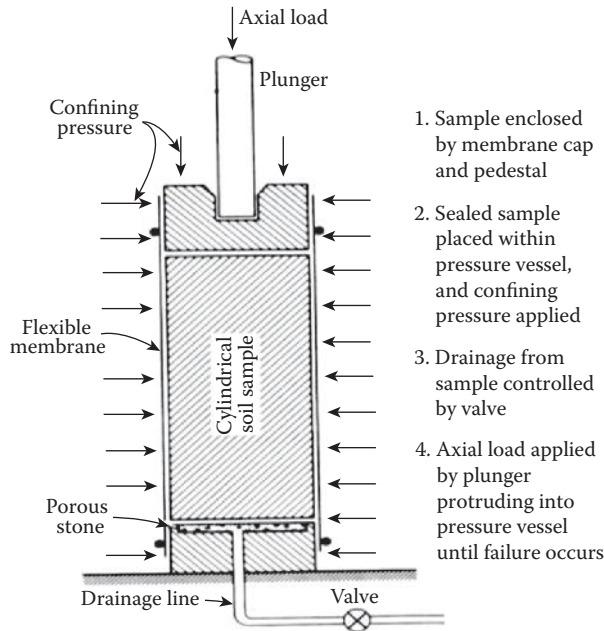
The triaxial compression test, shown in Figure 4.29 [48], is the most widely used test for determining the shear strength of soils. The major principal stress  $\sigma_1$  acts along the vertical direction, while the intermediate principal stress  $\sigma_2$  is equal to the minor principal stress  $\sigma_3$ , both acting in two mutually perpendicular, horizontal directions. The test equipment is designed to carry out controlled rates of strain and also can control the drainage during consolidation and shear. Three different cases can be simulated in the triaxial shear test equipment, viz., (i) UU tests—unconsolidated undrained tests; (ii) CD tests—consolidated, drained tests; and (iii) CU tests—consolidated undrained tests.

In the UU tests, the cylindrical specimen is placed in between the end platens of the test equipment, and the ambient pressures are applied until the soil core fails in shear as shown in Figure 4.30 [49]. In the CD test, the sample is placed on a porous disk, which is connected to a burette; this allows consolidation to take place under ambient pressure. Once the consolidation is complete, the sample is sheared slowly, allowing further drainage. The CU test is similar to the CD test, except that during shear test, no drainage is allowed.

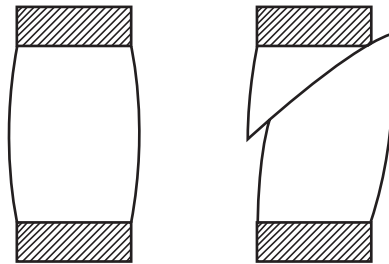


**FIGURE 4.28** Direct shear test apparatus. (W. Lambe and R.V. Whitman, *Soil Mechanics*, p. 120. 1979. Copyright Wiley-VCH Verlag GmbH & Co. KGaA. Reproduced with permission.)





**FIGURE 4.29** Essential features of a triaxial cell for testing soil. (W. Lambe and R.V. Whitman, *Soil Mechanics*, p. 118. 1979. Copyright Wiley-VCH Verlag GmbH & Co. KGaA. Reproduced with permission.)

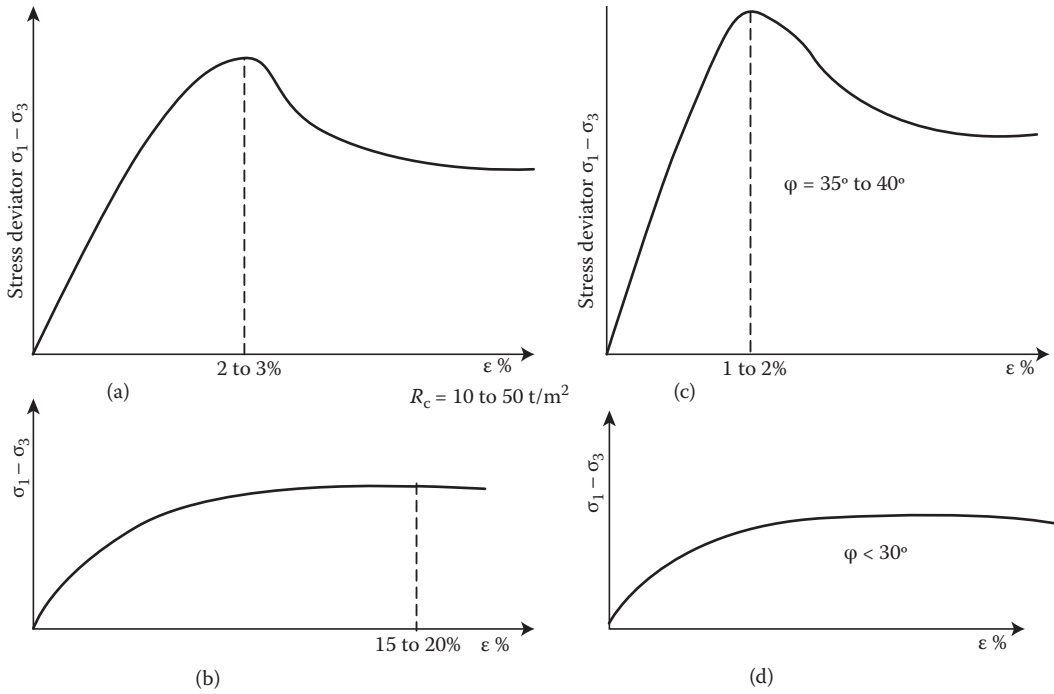


**FIGURE 4.30** Typical failure shapes of triaxial soil specimens tested between rigid end caps. (W. Lambe and R.V. Whitman, *Soil Mechanics*, p. 119. 1979. Copyright Wiley-VCH Verlag GmbH & Co. KGaA. Reproduced with permission.)

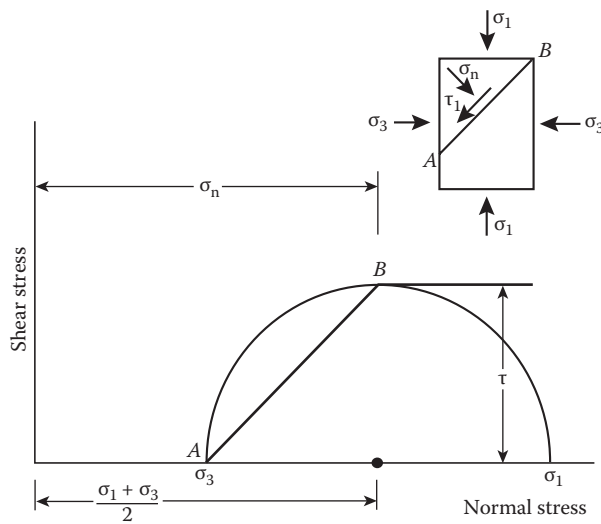
**4.4.7.2 Stress–Strain Curves and Shear Strength Computation**

From the triaxial shear strength tests, stress–strain curves typical for the different soil materials tested (sand- or clay-soils) are given in Figure 4.31 [50]; the strains are plotted along the  $x$ -axis, and the deviatoric stresses  $(\sigma_1 - \sigma_3)_{failure}$  are plotted along the  $y$ -axis. It has been observed from earlier tests that failure is reached for (i) soft or loose sands at 15% to 25% strains; (ii) dense sands at around 5%; and (iii) normally consolidated clays at 3% to 5% strain. It should be noted that at large strains, both loose, soft, and dense sands have the same strength and density.

Mohr’s method of stress computation is used to compute the normal and shear stresses from the triaxial shear strength test results. The notations used for drawing the Mohr’s stress diagram are shown in Figure 4.32 [51]. Once the stresses  $\sigma_1$ ,  $\sigma_2$ , and  $\sigma_3$  are known, the shear stress in the soil is obtained as  $(\sigma_1 - \sigma_3)/2$ . Also the stresses on any plane, viz.,  $(\sigma_n, \tau_1)$ , shown in Figure 4.32, can be computed from Mohr’s stress diagram.



**FIGURE 4.31** Stress–strain curves for various ( $R_c < 10 + / m^2$ ) types of soil: (a) overconsolidated stiff clay; (b) soft sand; (c) dense sand; and (d) loose sand; in the figures,  $R_c$  is the unconfined compressive strength of soil. (From P. Le Tirant, *Seabed Reconnaissance and Offshore Soil Mechanics*, Editions Technip 27, Paris, France, p. 15, 1979. With permission.)



**FIGURE 4.32** Notations used for Mohr's stress diagram. (From H. Schenck, Jr., *Introduction to Ocean Engineering*, McGraw-Hill Book Company, New York, p. 62, 1975. With permission.)

Consider a triaxial test on a sample of clay, consolidated in a triaxial apparatus, which is subjected to a constant radial stress  $[(\sigma_3 = \sigma_2)$ , and with no drainage] and an axial stress equal to  $\sigma_1$ , which is increased until failure of the specimen occurs. The total principal stress at failure is given by

$$\begin{aligned}\sigma_{1f} &= \sigma_3 + (\sigma_1 - \sigma_3)_f \\ \sigma_{3f} &= \sigma_3\end{aligned}\quad (4.20)$$

It is also observed that the deviatoric stress also induces a pore pressure  $(\Delta u_f)$  according to Equation 4.17. Hence at failure,

$$\begin{aligned}\Delta u_f &= \Delta \sigma_3 + A_r(\Delta \sigma_1 - \Delta \sigma_3) \\ \text{and the effective stresses at failure} \\ \sigma_{1f} &= \sigma_1 + (1.0 - A_r)(\Delta \sigma_1 - \Delta \sigma_3) \\ \sigma_{3f} &= \sigma_3 + A_r(\Delta \sigma_1 - \Delta \sigma_3)\end{aligned}\quad (4.21)$$

The undrained shear strength  $c_u$  is obtained as  $(\sigma_1 - \sigma_3)_f/2$ . It is also equal to

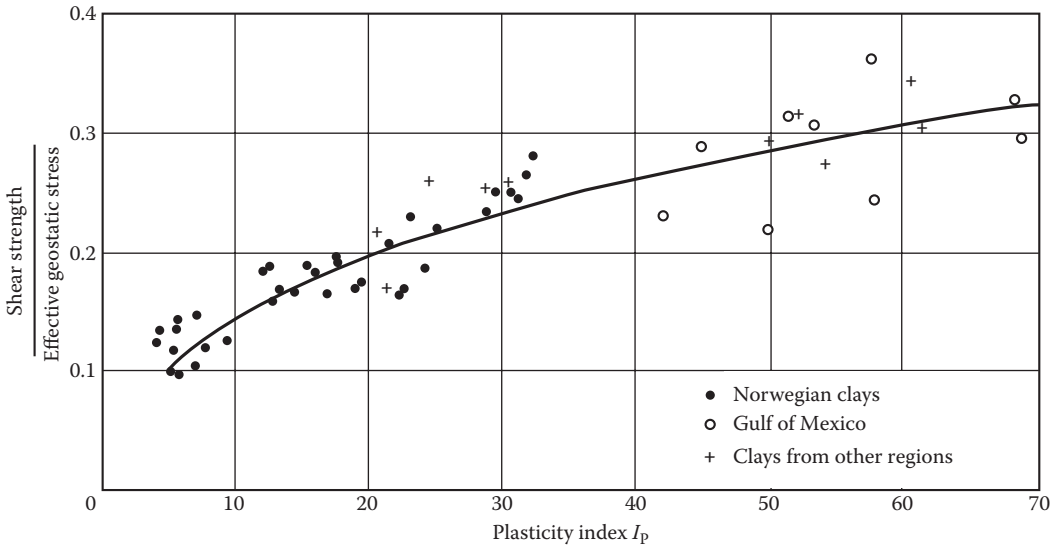
$$c_u = \left[ (\bar{\sigma})_c \sin(\bar{\phi}) \right] / \left[ 1.0 + (2A_r - 1.0) \sin(\bar{\phi}) \right] \quad (4.22)$$

The consolidation pressure,  $\bar{\sigma}_c$ , at a particular depth  $h$ , below the sea bottom, is obtained by multiplying the sediment submerged weight  $\gamma_b$  with  $h$ . Hence, the value of  $(\bar{\phi})$ , under undrained conditions, can be computed from Equation 4.22. In problems involving a mass of sediment of substantial thickness, an average consolidation pressure is usually considered and is illustrated in the solved examples given at the end.

In the case of sands, the loading rate is generally not important as with clayey soils. However, if the sand is subjected to fast loading, for instance, under the effect of water waves (period of wave between 5.0 and 15.0 s), drainage does not occur under each loading cycle, and the excess interstitial pore water pressures do not dissipate. The friction angle of sand under undrained conditions (fast test) corresponding to the maximum of the stress–strain curve is less than the friction angle under drained conditions (slow test). In the undrained test, the friction of soil is only partially mobilized to resist the applied load, and as such, the strain is very low. In the drained test, the friction is mobilized completely in resisting the applied load, and hence, the strain is much higher (2% to 3%). As an example, it has been observed that for North Sea soils with 100.0% relative density, the frictions angles are given as

$$\begin{aligned}(\bar{\phi})_{\text{drained}} &\approx 43^\circ \\ (\bar{\phi})_{\text{drained}} &\approx 34^\circ\end{aligned}\quad (4.23)$$

The aim of the soil core sample testing in the laboratory is to establish the in situ properties of soils at site. Ideally the test results obtained from the laboratory, and those from in situ remote testing, should be the same. It has been observed that in spite of making every effort to obtain undisturbed soil core samples from the seabed, in situ strength of soil is found to be significantly different (generally higher) from that obtained in laboratory testing. This is due to the fact that disturbance of the soil core sample is created in the acquiring process and in the subsequent transportation,



**FIGURE 4.33** Variation of the soil shear with respect to plasticity index. (From P. Le Tirant, *Seabed Reconnaissance and Offshore Soil Mechanics*, Editions Technip 27, Paris, France, p. 18, 1979. With permission.)

storage, and trimming procedures. Hence, the emphasis in testing soil core samples in laboratories must be made in minimizing the effects of transportation, storage, and trimming of samples.

**4.4.7.3 Simple Methods for Estimating Undrained Cohesion**

Many empirical relationships have been proposed to estimate the shear strength of clayey soils on the basis of density and Atterberg limits. Skempton’s equation [52] gives the relationship as

$$(s_u)/p = 0.11 + 0.0037 I_p \tag{4.24}$$

where  $p$  is the submerged geostatic stress [ $p = (\gamma_b)h$ ], and  $I_p$  is the plasticity index. Also the experimental results, given in Figure 4.33 [53], can be used to compute the shear strength of clayey soils.

**Example 4.7**

A submerged stratum of clay has a thickness of 30.0 ft., the average water content is 54%, and the specific gravity of the solid minerals is 2.76. What is the vertical effective stress at the base of the stratum?

$$\text{Water content} = (W_w/W_s) = [1/\gamma_d - 1/G]$$

$$0.54 = (1/\gamma_d) - (1/2.76) = 1/\gamma_d - 0.362$$

$$1/\gamma_d = 0.902; \text{ hence, } \gamma_d = 1/0.902 = 1.109$$

$$\gamma_d = \gamma_t/(1 + w); \text{ hence, } \gamma_t = \gamma_d (1 + w) = (1.109)(1 + 0.54) = 1.708$$

$$\begin{aligned} \text{Effective vertical stress at the bottom of soil} &= (30)(1.708)(62.4) - (30)(62.4) \\ &= 1325.4 \text{ psi (9.142 MPa).} \end{aligned}$$

**Example 4.8**

A consolidated undrained triaxial test on a silty soil gave the following data:

Test 1:  $\sigma_1 = 22.8$  psi;  $\sigma_3 = 12.0$  psi;  $u = 8.4$  psi

Test 2:  $\sigma_1 = 43.8$  psi;  $\sigma_3 = 23.4$  psi;  $u = 16.4$  psi

Plot the graphs representing the stress circles based on total and effective stresses. Determine the strength parameters  $\bar{\phi}$ ,  $\bar{c}$ , and  $A_f$ .

Effective stress values—test 1:  $\sigma_1 = 22.8 - 8.4 = 14.4$  psi;  $\sigma_3 = 12.0 - 8.4 = 3.6$  psi

test 2:  $\sigma_1 = 43.8 - 16.4 = 27.4$  psi;  $\sigma_3 = 23.4 - 16.4 = 7.0$  psi

Figures A and B are based on total stresses; figures C and D are based on effective stresses.

Based on total stresses,  $\phi_u = 26.5^\circ$  and  $c_u = 0.5$  psi.

Based on effective stresses,  $\phi' = 35.0^\circ$  and  $c' = 0.2$  psi.

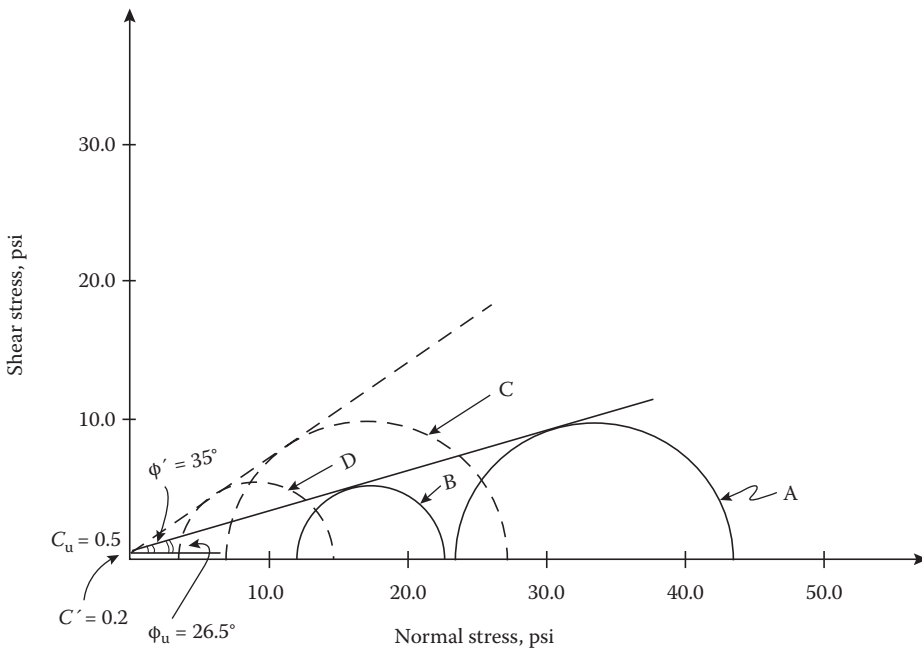
Hence,  $(\bar{c}, \bar{\phi})$  are given as  $\bar{c} = 0.5$  psi and  $\bar{\phi} = 26.5^\circ$ .

The undrained shear strength is given as  $c_u = (\sigma_{1f} - \sigma_{3f})/2 = (22.8 - 12.0)/2 = (10.8)/2 = 5.4$ . Hence,

$$c_u = \left[ (\bar{\sigma})_c \sin(\bar{\phi}) \right] / \left[ 1.0 + (2A_f - 1.0)\sin(\bar{\phi}) \right]$$

$$5.4 = 22.8 \sin(26.5) / [1.0 + (2A_f - 1.0)\sin(26.5)]$$

$$A_f = 1.487$$



**Example 4.9**

The results given below were obtained from tests on a saturated clayey soil.

(a) Results from undrained triaxial tests:

Cell pressure ( $\sigma_3$ , kPa)	104.00	172.0	241.0
Principal stress difference at failure ( $\sigma_1 - \sigma_3$ , kPa)	139.00	146.00	132.00

The inclination of the plane of rupture was  $52^\circ$  to the plane of the cross section.

(b) Results from shear box tests:

Normal stress (kPa)	61.40	123.50	184.90
Shear stress (kPa)	72.40	98.60	128.25

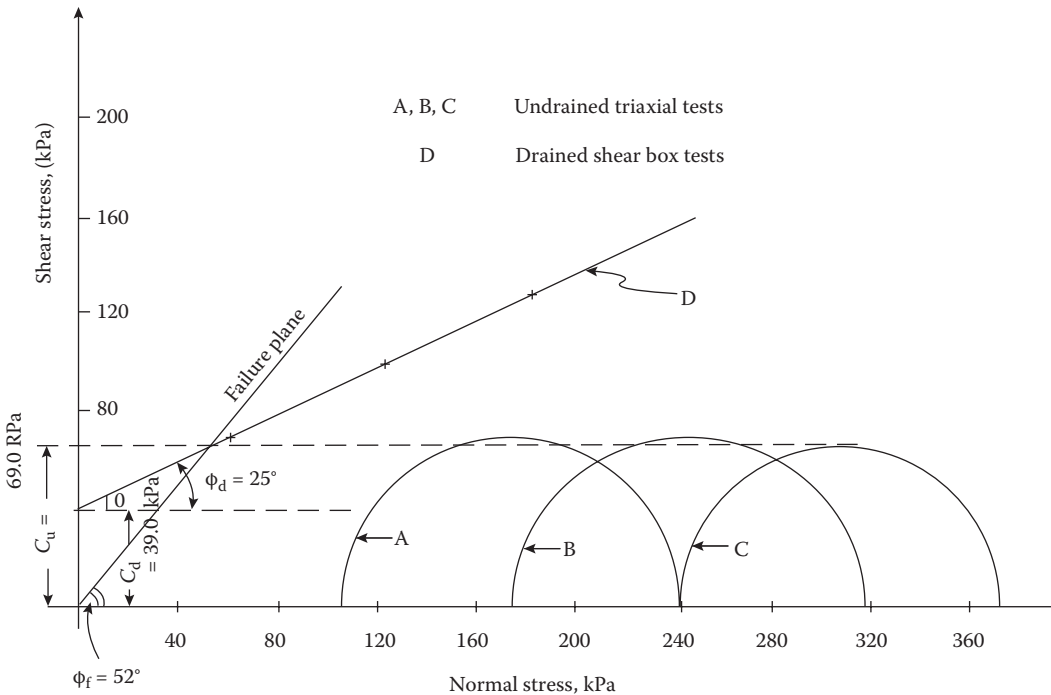
From the above results determine the shear strength properties of drained and undrained saturated clayey soil.

From undrained triaxial tests given in (a):

$$c_u = 69.0 \text{ kPa}; \text{ also } 45^\circ + (\phi_f/2) = 52^\circ. \text{ Hence, } \phi_f = 14.0^\circ.$$

From drained shear box tests given in (b):

$$C_d = 39.0 \text{ kPa}; \phi_d = 25.0^\circ.$$



#### 4.4.8 CONSOLIDATION (OR COMPRESSIBILITY) OF OCEAN SOILS

When the seabed is subjected to loads from the structures built on it, it undergoes deformation due to (i) deformation of the soil skeleton; (ii) expulsion of water, within the seabed foundation soil, which corresponds to the dissipation of excess pore water pressure in the interstices of soil; and (iii) creep of soil skeleton under sustained structural loads; this additional settlement is negligible in the case of normally consolidated or overconsolidated clays and considerable in the case of muds and soft clays. When the seabed soil is primarily of sand, the settlement is rather small and of short

duration; hence, it does not call for long duration tests to determine the settlement properties of the foundation soils. If the seabed is primarily made up of clayey soils, the settlement takes place over a long time and would call for protracted tests.

This is illustrated in Figure 4.34 [54], which shows the measured settlement histories over a long period of time (in terms of years and months) for North Sea platforms located over clayey soils; the excess pore water developed in the interstices of clay particles is dissipated and water particles squeezed out very slowly. The consolidation settlement can be classified into (i) instantaneous settlement of soil, due to the undrained deformation of soil; (ii) primary settlement, which corresponds to the dissipation of excess interstitial pore water pressures; and (iii) secondary settlement, which is the consequence of creep of soil material.

The consolidation settlement of soils is obtained in the laboratory using: (i) conventional Terzaghi oedometer tests or (ii) triaxial long duration drained tests. The oedometer diagram is shown in Figure 4.35 [55], which gives a plot of void ratio as a function of consolidation pressure,  $p_c (= \sigma_1)$ , in a semilogarithmic plot.

From Figure 4.35, one can obtain the following parameters required for interpreting the oedometer test results, from the linear part of the oedometer diagram:

$$(i) \epsilon_1 = \Delta h/h = \Delta e/(1.0 + e) = -(2.3/C) \log(1.0 + \Delta\sigma_1/\sigma_1),$$

where  $C$  = compressibility constant;

$$(ii) \Delta e = -C_c \log(1.0 + \Delta\sigma_1/\sigma_1),$$

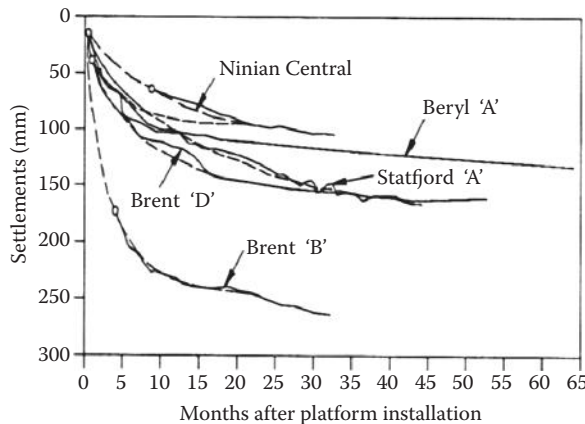
(4.25)

where  $C_c$  is the compressibility index; and

$$(iii) E_0 = 2.3[\sigma_1(1.0 + e)/C_c],$$

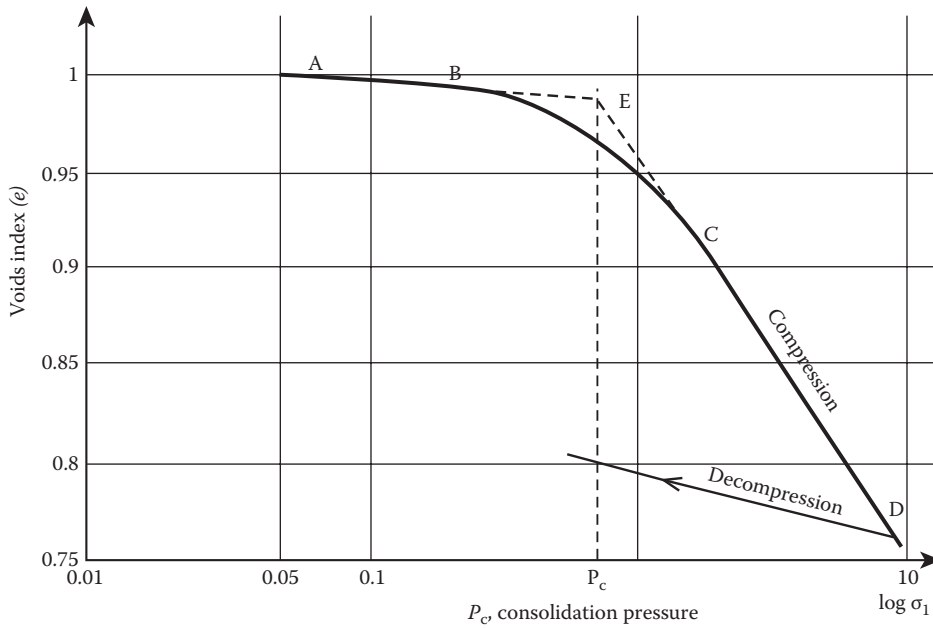
where  $E_0$  is the oedometric modulus.

In the above relationships,  $\Delta h$  is the change in thickness of soil in oedometer,  $h$  is the thickness of soil layer in the oedometer,  $e$  is the void ratio of soil used, and  $\Delta e$  is the reduction in the voids ratio due to an increase in  $\Delta\sigma_1$ , in the vertical consolidation stress  $\sigma_1$ , applied in the oedometer test. Table 4.9 [56] indicates a set of typical values, obtained for compressibility index,  $C_c$ , and oedometric modulus,  $E_0$ .



**FIGURE 4.34** Consolidation settlements for five North Sea platforms located on clayey strata. (From N.D.P. Barltrop and A.J. Adams, Dynamics of fixed marine structures, in: *Foundations*, Butterworth Heinemann Ltd., Oxford, UK, p. 182, 1991. With permission.)





**FIGURE 4.35** Sample oedometric curve for normally consolidated clay. (From P. Le Tirant, *Seabed Reconnaissance and Offshore Soil Mechanics for the Installation of Petroleum Structures*, Editions Technip 27, Paris, France, p. 23, 1979. With permission.)

From the  $e$  versus  $\log(\sigma_1)$  oedometric diagram, the geotechnical significance of the state of consolidation could be defined. In principle, the oedometer diagram is defined by the two branches AB and CD, intersecting at the point E, which gives the consolidation pressure  $p_c$  of the soil. The past history of loading on the soils will have significant effects on the state of the soil and its properties. The OCR gives information about the stress history of the soil under consideration. OCR is defined as the ratio of the maximum past pressure to the existing effective overburden pressure. The soil states can be defined as follows: (i) If  $p_c = \gamma_b h$ , the clay is normally consolidated—this means that the soil has never been subjected to a load greater than the existing overburden pressure. (ii) If  $p_c > \gamma_b h$ , then the soil is overconsolidated—this means that the soils have been subjected to loads exceeding the present overburden pressures (perhaps due to past glaciation overburden as in the case of the near surface North Sea clays, which are heavily overconsolidated; these clays are only lightly overconsolidated away from the surface). (iii) If  $p_c < \gamma_b h$ , then the soil is underconsolidated—this means that the existing effective vertical stress is less than the existing overburden pressure, which happens when a soil stratum is subjected to an excess hydrostatic pressure that does not allow the soil to consolidate under the overburden pressure, as in the case of clays found in the Gulf of Mexico.

**TABLE 4.9**  
**Typical Values for Compressibility Index and Oedometer Modulus**

#	Parameter from Oedometer Tests	Sands	Stiff or Fairly Stiff Clays ( $c_u > 5.0 \text{ t/m}^2$ )	Soft Clays
1	Compressibility index, $C_c$	0.02–0.01	0.10–0.25	$\geq 2.0$
2	Oedometer modulus, $E_0$ ( $\text{t/m}^2$ )	Several hundred	2000 to 500	200 to 50

Source: P. Le Tirant, *Seabed Reconnaissance and Offshore Soil Mechanics*, Editions Technip 27, Paris, France, p. 24, 1979. Used with permission.

The validity of laboratory test results obtained for estimating settlement in clays is highly variable depending on the nature of soils. (i) In the case of homogeneous clays, normally consolidated with little sensitivity, the laboratory results are highly reliable, with an error of less than 10%; (ii) in the case of thin heterogeneous layers, many tests may be required to determine reliably the compressibility index and its mean value; in these cases, the errors in results obtained may exceed 50% to 100% in highly overconsolidated or sensitive soils. The major difficulty seems to be in the estimation of the consolidation duration.

Based on one-dimensional consolidation theory [57], very simple equations have been given for the consolidation of soil sediments under sustained loads. The given equations are as follows:

$$(e_0 - e)/(1 + e_0) = \Delta h/h_0 \dots\dots(a)$$

$$e = e_0 - C_{ci} \log(\bar{\sigma}/\bar{\sigma}_0), \dots\dots(b), \text{ and}$$

$$\Delta h = [h_0/(1 + e_0)](C_{ci}) \log[(\bar{\sigma}_0 + \Delta\bar{\sigma}_0)/\bar{\sigma}_0] \dots\dots(c)$$

where  $e_0$  = initial void ratio,  $e$  = void ratio under any pressure; (4.26)

$\Delta h$  = compression settlement in soil,  $h_0$  is the initial soil thickness;

$C_{ci}$  = Compression index of soil under consideration;  $\bar{\sigma}_0$  = initial soil stress;

$\Delta\bar{\sigma}_0$  = stress increase under the applied load

Also, using the theory of one-dimensional consolidation mentioned earlier, the degree of consolidation,  $U$ , and the dimensionless time,  $T$ , are related as

$$U = f(c_v t/H^2) = f(T),$$

where (nondimensional)  $T = (c_v t/H^2)$ , and the coefficient of consolidation  $c_v$  is given by

$$c_v = [K/(\gamma_w m_v)] \text{ (m}^2/\text{day)} \tag{4.27}$$

with  $m_v$  being a coefficient of volume change (m<sup>2</sup>/MN) given by  $m_v = \Delta\varepsilon_v/\Delta\sigma_v$ .

where  $H$  is the maximum drainage path of water in the soil layer considered for consolidation,  $t$  is the time in seconds (since the application of the load),  $K$  is the permeability of the soil, and  $\gamma_w$  is the unit weight of water. The relationship between  $U$  and  $T$  is given in Table 4.10 [58]. If only one face

---

**TABLE 4.10**  
**Relationship Governing Consolidation (%) and Nondimensional Time  $T$**

#	$U$ (%)	$T$	#	$U$ (%)	$T$
1	10	0.008	6	60	0.287
2	20	0.031	7	70	0.403
3	30	0.071	8	80	0.567
4	40	0.126	9	90	0.848
5	50	0.197	—	—	—

Source: H. Schenck, Jr., *Introduction to Ocean Engineering*, McGraw-Hill Book Company, New York, p. 56, 1975. Used with permission.

---

is drained in the experiment, then  $H = h_0$ , the thickness of the consolidated layer; if drainage takes place from both faces of the consolidated soil, then  $H = (h_0/2)$ .

If  $0.0 < U < 0.5$ , then the relationship between  $U$  and  $T$  can be simplified to give the equation given below:

$$U = (2.0)(T/\pi)^{0.5} \quad (4.28)$$

The difference between the observed and computed consolidation settlements can be attributed to (i) use of one-dimensional consolidation equation solutions instead of three-dimensional consolidation equations; (ii) use of elastic settlement equations for estimating deformations of the medium; and (iii) presence of secondary or creep deformation.

### Example 4.10

A 10.0-m-thick, soft clay layer is underlain by a stiff clay stratum. According to laboratory test data, the coefficient of consolidation  $c_v = 0.0025 \text{ m}^2/\text{day}$ . Compute the percentage of consolidation after a period of 1000 days.

Since the soft clay layer is underlain by a stiff clay, the maximum drainage path of the layer = 10.0 m.

As per Equation 4.28,  $U = (2.0)(T/\pi)^{0.5}$ .

Also, as per Equation 4.28,  $T = (c_v t/H^2) = (0.0025)(1000)/10^2 = 0.025$ .

$$U = (2.0)(0.025/\pi)^{(0.5)} = 0.1784.$$

The percentage of consolidation = 17.84%.

### Example 4.11

Data from a consolidation test on clay include the following: (i)  $e_1 = 1.204$  with  $p_1 = 1.50 \text{ kgf/cm}^2$ ; and (ii)  $e_2 = 1.054$  with  $p_2 = 3.00 \text{ kgf/cm}^2$ . The tested sample was 3.0 cm thick, and the time required to reach 50.0% consolidation was found to be 16.0 min. Considering a soil stratum of the same material 40.0 m in thickness, determine the time required to reach the same degree of consolidation if (a) drained from both top and bottom and (b) drained from top only.

For one-dimensional consolidation (from Equation 4.26),  $e = e_0 - C_{ci} \log(\bar{\sigma}/\bar{\sigma}_0)$ .

$$1.054 = 1.204 - C_{ci} \log(3.0/1.5); C_{ci} = (1.204 - 1.054)/\log(2.0) = 0.15/(0.301) = 0.498.$$

Hence, the soil is a fairly stiff clay, as per Table 4.9.

From Equation 4.28,  $U = (2.0)(T/\pi)^{0.5}$ , that is,  $0.50 = (2.0)(T/\pi)^{0.5}$ .

Therefore,  $T = 0.1964$ .

Also, as per Equation 4.27,  $T = (c_v t/H^2)$ ; for this test,  $t = 16.0 \text{ min}$  and  $H = 3.0 \text{ cm}$ .

Hence,  $c_v = (0.1964)(0.03)^2/[(16)(60)] = 1.84125 \times 10^{-7} \text{ m}^2/\text{s} = 0.01591 \text{ m}^2/\text{day}$ .

(a) Drained from both top and bottom:  $h = 20.0 \text{ m}$ .

Hence, for  $U = 0.50$ ,  $T = 0.1964$ , and  $t = (0.50)(20)^2/(0.01591) = 12,572.0 \text{ days} = 34.42 \text{ years}$ .

(b) Drained from top only:

$$t = (0.50)(40)^2/(0.01591) = 50,283.0 \text{ days} = 137.67 \text{ years}.$$

### 4.4.9 STIFFNESS OF SOILS

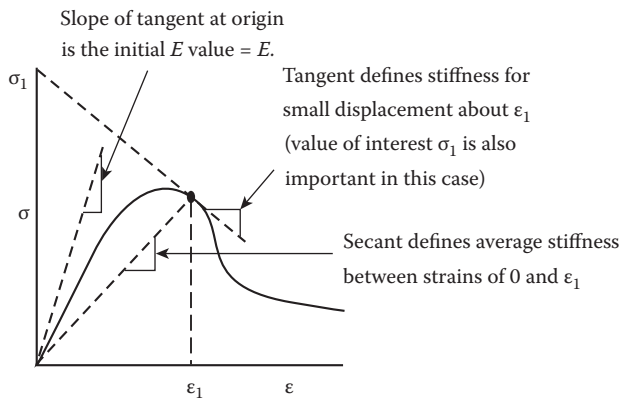
Soil stiffness can be determined using different types of tests. The usual stiffness properties are the Young’s modulus ( $E$ ), shear modulus ( $G$ ), bulk modulus ( $B$ ), and Poisson’s ratio ( $\nu$ ); for an isotropic soil, these properties are also interrelated as  $[E = 2(1 + \nu)G] = 3B(1 - 2\nu)$ . Since soils are nonlinear in their stress–strain ( $\sigma$  vs.  $\epsilon$ ) behavior, as shown in Figure 4.36 [59], the values of these parameters vary with the amount of loading imposed and the amount of deformation experienced by the soil; the nonlinearity is caused by the relative movement of the soil particles under the applied loads and also due to the drainage occurring during the test.

In carrying out dynamic analyses for small strains on soils,  $G$  and  $\nu$  are taken to be independent of the drainage conditions. The procedure for estimating the appropriate value of  $G$  starts with the estimation of the initial tangent shear stiffness  $G_0$  (or  $E_0$  from Figure 4.36) and then to adjust the value of  $G$  for the actual dynamic amplitude.  $G_0$  should be preferably computed from remote shear wave propagation velocity measurements made on the actual clayey soils under consideration; but usually it is taken from an empirical correlation between shear modulus ( $G_0$ ) and the undrained shear strength ( $s_u$ ) given for clay as  $G_0 = (1000 \text{ to } 3000)s_u$  [60]. For sands, the relationship is given in terms of confining effective compressive stress,  $\sigma'_c$ , and the void ratio  $e$  by the equation given below [61]:

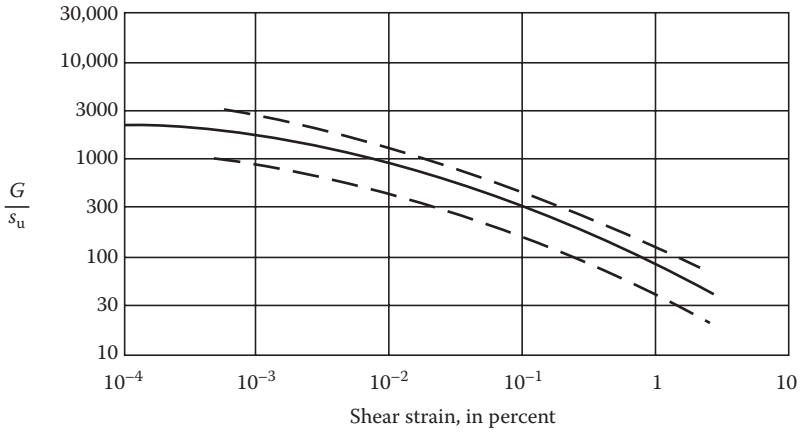
$$G_0 = (691.0)[(2.17 - e)^2 / (1.0 + e)]\sqrt{(\sigma_r \sigma'_c)} \tag{4.29}$$

where  $e$  is the void ratio,  $\sigma_r$  is a dimension-correcting stress (equivalent to 100.0 kPa), and  $\sigma'_c = [(\sigma'_1 + \sigma'_2 + \sigma'_3)/3]$  is the effective confining stress. If no specific values of  $s_u$ ,  $e$ , and  $\sigma'_c$  are available for the site, then these values can be obtained from Figures 4.37 and 4.38 [61].

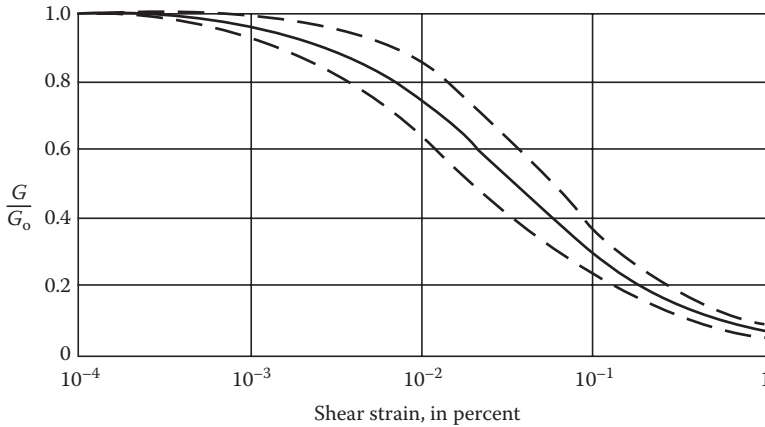
The energy dissipation mechanism, which reduces the dynamic response in soils, is made up of two components, viz., internal and radiation damping. Internal damping is material damping and is mainly caused by viscous and frictional effects within the soil; it is essentially due to the nonlinear stress–strain behavior in soils. The radiation damping is an elastic property associated with the propagation of stress waves away from the generation location; if the hard nearby soil layers or the far-away boundary reflects the stress waves back toward the structures, it will reduce the damping effect of this radiated waves. Seed and Idriss [60] have given the values of damping for both sands and clays. Figure 4.39 [62] gives the material damping present in sandy soils.



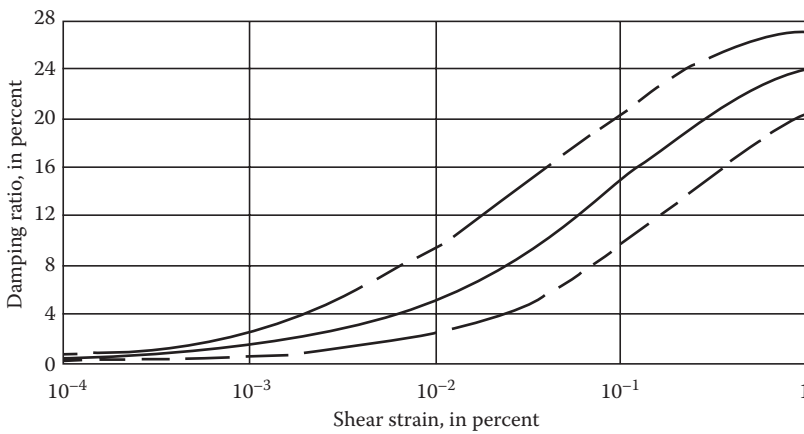
**FIGURE 4.36** Nonlinear soil stiffness of soil, showing the concepts of tangent and secant moduli. (From N.D.P. Barltrop and A.J. Adams, Dynamics of fixed marine structures, in: *Foundations*, Butterworth Heinemann Ltd., Oxford, UK, p. 184, 1991. With permission.)



**FIGURE 4.37** In situ shear moduli for saturated clays. Upper and lower bounds of the relationships are given in dashed lines. (From N.D.P. Barltrop and A.J. Adams, Dynamics of fixed marine structures, in: *Foundations*, Butterworth Heinemann Ltd., Oxford, UK, p. 185, 1991. With permission.)



**FIGURE 4.38** Normalized soil moduli for sands. (From N.D.P. Barltrop and A.J. Adams, Dynamics of fixed marine structures, in: *Foundations*, Butterworth Heinemann Ltd., Oxford, UK, p. 185, 1991. With permission.)



**FIGURE 4.39** Damping ratios for sands. (From N.D.P. Barltrop and A.J. Adams, Dynamics of fixed marine structures, in: *Foundations*, Butterworth Heinemann Ltd., Oxford, UK, p. 187, 1991. With permission.)

**TABLE 4.11**  
**Typical Physical and Mechanical Properties of Ocean Soils**

Type of Soil	Effective Cohesion (kPa)	Friction Angle $\varphi'$ (°)	Undrained Shear Strength (t/m <sup>2</sup> )	Tangent Shear Modulus $G_0$ (MPa)	Secant Shear Modulus $G_1$ (MPa)	Undrained Poisson's Ratio	Drained Poisson's Ratio
Soft to firm clay	5.0–10.0	19.0–24.0	10.0–50.0	15.0–75.0	4.0–20.0	0.5	0.4
Stiff clay	10.0–20.0	22.0–29.0	50.0–100.0	75.0–150.0	20.0–40.0	0.5	0.4
Very stiff to hard clay	20.0–50.0	27.0–31.0	100.0–400.0	150.0–600.0	40.0–160.0	0.5	0.4
Silt	0.0	27.0–35.0	10.0–50.0	$400\chi$ – $1800\chi$	—	0.5	0.30–0.35
Loose sand	0.0	29.0–30.0	—	$350\chi$ – $600\chi$	$45\chi$	0.5	0.2–0.35
Med. dense sand	0.0	30.0–40.0	—	$600\chi$ – $1300\chi$	$130\chi$	0.5	0.35–0.40
Dense sand	0.0	35.0–45.0	—	$1300\chi$ – $2400\chi$	$215\chi$	0.5	0.30–0.40
Gravel	0.0	35.0–55.0	—	$350\chi$ – $2800\chi$	$45\chi$ – $350\chi$	0.5	0.20–0.40

Source: N.D.P. Barltrop and A.J. Adams, Dynamics of fixed marine structures, in: *Foundations*, Butterworth Heinemann Ltd., Oxford, UK, p. 189, 1991. Used with permission.

Note:  $\langle \chi = \sqrt{(\sigma_r \sigma'_c)} \rangle$ , with  $\sigma_r$  being a dimension correcting reference stress (in MPa or other equivalent units), and  $\sigma'_c$  is the confining effective stress =  $(\sigma'_1 + \sigma'_2 + \sigma'_3)/3$  (in MPa or other equivalent units).

The typical ranges of some physical and mechanical properties that may be present in soils are given in Table 4.11 [63]. These may be used in the preliminary design, but actual site-specific investigations must be carried out before a detailed design is undertaken.

### Example 4.12

Estimate the shear modulus for the following in situ soil conditions:  $e = 0.83$ ;  $\varphi' = 32.0^\circ$ ; the soil is silty sand (fairly dense);  $\gamma_w = 16.9$  kN/m<sup>3</sup>. Also the effective depth for modulus estimation is 4.0 m.

$$G_0 = (691.0)[(2.17 - e)^2 / (1.0 + e)] \sqrt{(\sigma_r \sigma'_c)}$$

$$K_0 = \text{coefficient of rest} = 1 - \sin(\varphi') = 1.0 - \sin(32.0^\circ) = 1.0 - (0.53) = 0.47$$

$$\sigma_1 = (16.9)(4.0) = 67.6 \text{ kPa}$$

$$\sigma_2 = K_0 \sigma_1 = (0.47)(67.6) = 31.8 \text{ kPa}$$

$$\sigma_3 = \sigma_2 = 31.8 \text{ kPa}$$

$$\sigma_r = (\sigma_1 + \sigma_2 + \sigma_3) / 3 = (67.6 + 31.8 + 31.8) / 3 = 43.73 \text{ kPa}$$

$$G_0 = (691.0)[(2.13 - 0.83)^2 / (1.0 + 0.83)] \sqrt{[(43.73)(100.0)]} = 42,199.0 \text{ kPa} = 42.2 \text{ MPa}$$

As per Table 4.11, for silt,  $G_0$  ranges from  $400\chi$  to  $1800\chi$ .

$$400\chi = 400 \sqrt{(\sigma_r \sigma'_c)} = 400[(43.73)(100)]^{0.5} = (400)(66.12) = 26.45 \text{ MPa}$$

$$1800\chi = 1800 \sqrt{(\sigma_r \sigma'_c)} = (1800)(66.12) = 119.03 \text{ MPa}$$

For the given silt, the computed  $G_0$  (of 42.2 MPa) is in between 26.45 and 119.03 MPa; hence, the result is OK.

## 4.5 BEARING CAPACITIES OF OFFSHORE PLATFORMS

### 4.5.1 GENERAL

A variety of changes occur around the base of an offshore structure located in the ocean, viz., (i) soil scour around the base; (ii) mudslides; (iii) sand waves, dunes, banks, etc.; and (iv) subsidence of seabed.

#### 4.5.1.1 Scour

Any structure located on the seabed, whether it is a single columnar structure or a wider footing-type structure, changes the wave and current regimes around its location. This change results in the seabed soils around the structure, being disturbed and perhaps scoured away. Generally, if the sea floor is of gravel or of highly cohesive clayey soil, then the disturbance may not be extensive; but if the soil is sandy, then there is a possibility that the soil around the platform base may be scoured away by any changes occurring in the wave and current regimes. This may result in either a local scour or a global scour (an area of typically twice that covered by the platform).

For scour to occur at the base, the water particle velocities must be sufficiently high to lift the seabed sediment particles, hold them in suspension, and carry them away from the area. The fluid turbulence generated at the location (especially on the downstream side of the structure), due to the presence of the structure, assists this process of scouring by loosening the soil and breaking up the consolidated sediments. The vertical components of the water particle velocities produce uplift forces on the particles, lift the soil particles, and cause them to move away from their locations. Substantial scour of the sea floor affects the strength and stability of the offshore platform. Scouring around the piles lowers the point of fixity, leaving shorter lengths of embedded piles to support the piled platform structure; in addition, it also reduces the shear strength of the foundation soil by the reduction of overburden pressure. For gravity structures, scour increases the settlements of its foundation.

In the design of a jacket structure, it is a common practice to allow about 1.5 times the leg diameter for the occurrence of local scour and 1.0 m for the occurrence of global scour. Scour must be monitored throughout the life of the platform structure, and if an increased scour occurs around the structure, then the cause should be diagnosed and preventive measures taken to reduce the scour. Only moderate scour (a maximum of 2.0 m) has been observed around most of the concrete structures located in the deep waters of the North Sea. There is a possibility of the destabilization of a jack-up platform due to scour around its base.

Several methods of scour prevention have been used around offshore platform structures: (i) Gravel grout bags and sand bags have been effectively used to fill the scoured area. (ii) Ballasted (used) car tires have been tied together to suit the geometry of local scour holes, dropped to the seabed and positioned by divers. (iii) Plastic seaweed is used to minimize the scour velocities around the structure. (iv) There is a provision of deep foundation skirts for gravity platform foundations.

#### 4.5.1.2 Mudslides

Passage of large waves induces large pore pressure changes on the sea floor, causing a remolding of soil and reduction of its shear strength. This in turn may lead to a shear failure in soft unconsolidated marine sediments on sloping ground, resulting in submarine mudslides; such soils are found in deltaic deposits deposited over a short period of time. Thick layers of normally consolidated clays/silts are also prone to such sliding. If the site is susceptible to mudslides, then the designer must consider this and design the structure such that it occurs above the lowest (plan) bracing level.



#### 4.5.1.3 Sand Waves, Dunes, Banks

Current-generated bed forms can, in extreme cases, reach a height of 15.0 m [64]. It is normally caused by moderate currents in sediments coarser than 0.1 to 0.2 mm; other bed forms found in sandy ocean bottoms include current ripples, ridges, dunes, and banks. These bed forms can also migrate to nearby locations. If the underlying features below these sandy deposits are stable, then the migration of these bed forms is minimized. It is similar to the scouring of seabed, and the measures suggested to minimize the scour of seabeds can also be used in these situations.

#### 4.5.1.4 Seabed Subsidence

Subsidence of offshore seabeds is caused by the consolidation of soil and rock formations, below the structural foundation, as the oil and gas fluids are extracted from the ocean depths. Subsidence results from (i) weak reservoir rock (such as loose sands and compressible calcareous soils); (ii) shallow depth oil and gas reservoirs (< 2000.0 m); (iii) thick reservoir depletion; and (iv) significant gas pressure reductions in reservoirs. The largest reported subsidence occurred at the base of the Ekofisk platform, in the North Sea (a bowl-shaped depression, with a subsidence depth of 4.0 m at the center), resulting in reduced air gap for the bottom of platform deck on top. Measures such as reinjection of gas and fluids back into the depleted reservoir locations must be taken to minimize these effects.

### 4.5.2 BOTTOM-FIXED JACKET PLATFORMS ON PILES

Over the past 60 years, a large number of bottom fixed platforms on piles have been installed at increasing water depths all over the world. The steel jacket platforms are secured to the ocean bottom by means of either driven or drilled piles, to depths greater than 150.0 (Cognac platform) to 200.0 m [65], below the seabed. The geotechnical problems associated with the pile-supported steel platforms are (i) stability of platforms under the effect of vertical and transverse loads acting on them and (ii) siting of piles by driving and/or drilling.

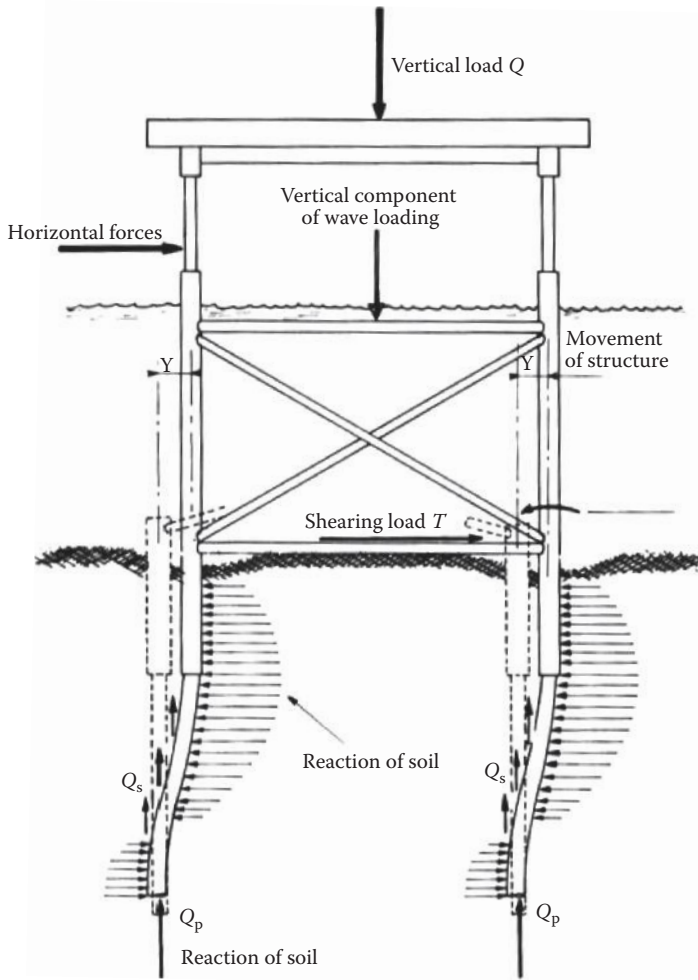
#### 4.5.2.1 Stability of Fixed Platforms in Piles

The stability considerations for pile founded structures should consider the following: (i) compressive (or bearing) capacity or pullout strengths of pile foundations; (ii) behavior of piles under the effect of lateral loads; (iii) possibility of liquefaction of soils during driving or during seismic excitations; and (iv) risk of scour near the piles. These effects are shown in Figure 4.40 [66].

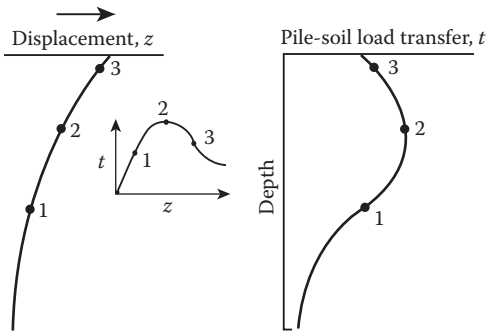
The bearing capacity of a pile is dependent on its diameter, depth of insertion, and the shear strength of the soil. The shear strength can be defined by the undrained or drained shear strength. It can also be defined in terms of its tip resistance and the lateral friction measured in the soil. The pullout force is much lower than the bearing (compressive) resistance of piles; its existence must be checked when there is a large overturning force exerted on the platform due to the environmental forces acting on the platform.

The reaction of the soil to lateral movement of a pile subjected to a horizontal load, as shown in Figure 4.41 [67], is dependent on the load resistance ( $p$ ) per unit length versus deformation ( $y$ ) characteristics of the soil. In clays, the soil tends to move around the pile, as shown in Figure 4.42a [68] (at greater depths), and shears in wedge-shaped manner near the surface, as shown in Figure 4.42b [68]. In sands, it tends to fail in a planar (wedge) manner, as shown in Figure 4.43a (at greater depths), and similar to Figure 4.43b [69] near the surface.

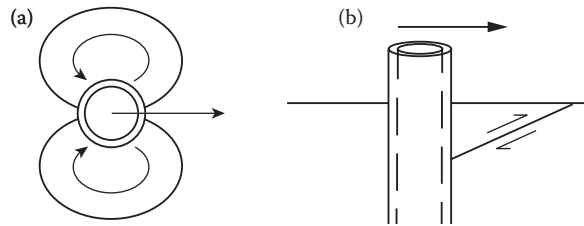
Steel piles for any steel jacket offshore structure are either driven into soft (or low-consolidation) soils or first the main pile (of the jacket leg) is driven into the hard soil to refusal, and then a pilot hole is drilled through the main pile for inserting a smaller diameter cylindrical tube called “insert pile” and cemented into the soil and to the main pile using cement grouting (see Figure 4.44 [70]).



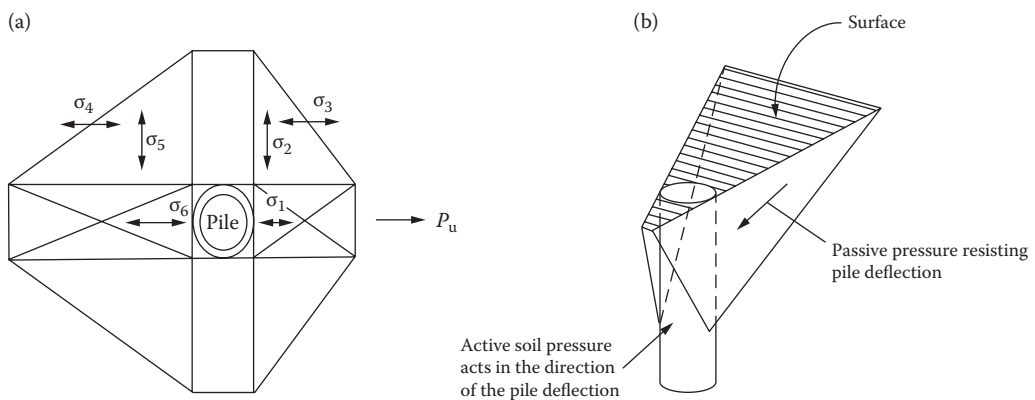
**FIGURE 4.40** Platform resistance and deformation under applied loads. (From P. Le Tirant, *Seabed Reconnaissance and Offshore Soil Mechanics for the Installation of Petroleum Structures*, Editions Technip 27, Paris, France, p. 291, 1979. With permission.)



**FIGURE 4.41** Transfer of load to soil due to transverse deformation along a long pile. (From B. McClelland and M.D. Reifel, *Planning and Design of Fixed Offshore Platforms*, Van Nostrand Reinhold company, New York, p. 765, 1986. With permission.)



**FIGURE 4.42** (a) Flow of clay around the pile, for transverse movement, at deeper depths. (b) Flow of clay near the surface. (From N.D.P. Barltrop and A.J. Adams, *Dynamics of fixed marine structures*, in: *Foundations*, Butterworth Heinemann Ltd., Oxford, UK, p. 212, 1991. With permission.)

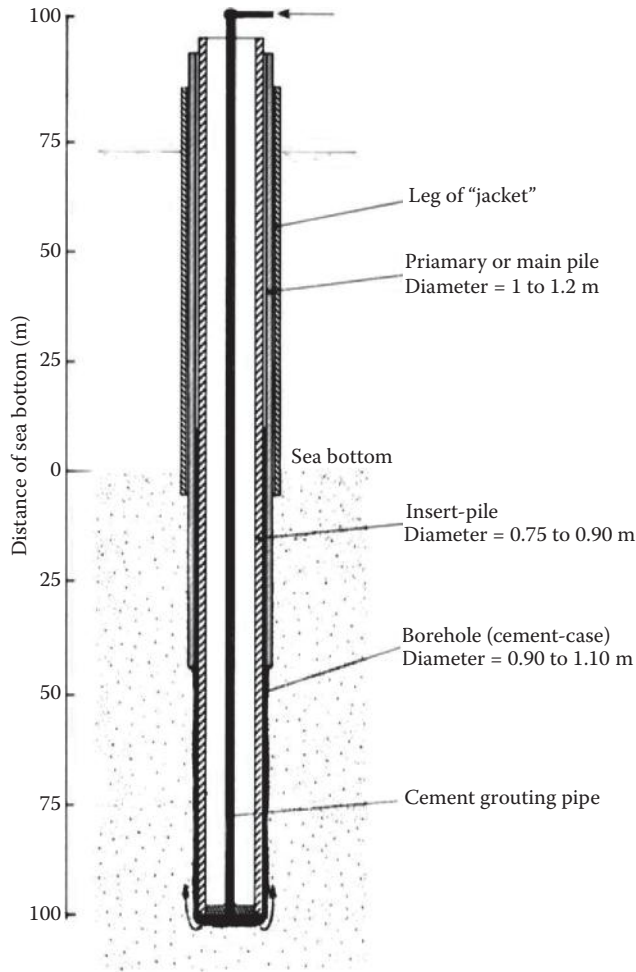


**FIGURE 4.43** (a) Failure of sand encasing the pile, for transverse movement, at deeper depths. (b) Failure of sand near the surface. (From N.D.P. Barltrop and A.J. Adams, *Dynamics of fixed marine structures*, in: *Foundations*, Butterworth Heinemann Ltd., Oxford, UK, p. 213, 1991. With permission.)

A large number of empirical pile driving equations are available in literature, which can be used to compute the driving length of piles into soil [71].

For smaller steel jacket type of platforms, built in the Gulf of Mexico, soils were of relatively low consolidation and the average oceanographic conditions with a 100-year wave amplitude was less than 15.0 m. In the case of larger dimension jacket structures, carrying heavier loads, the foundations would consist of (i) four to eight main piles of diameter 1.0 to 1.20 m, penetrating the ocean soil to a depth of 80.0 to 100.0 m; and (ii) a number of secondary “skirt piles” that penetrate the seabed soil to a lesser depth, with a height of 10.0 to 15.0 m above the seabed and properly tied to the jacket structure. The purpose of the skirt piles was to ensure a better distribution of the horizontal and vertical loads acting on the jacket structure.

These types of piled jacket structures are used generally in soils whose undrained shear strength is around 50.0 to 100.0 kPa. The piles consist of individual lengths of 30.0 m each and welded together to produce longer lengths, as driving of piles proceeds. The acceptable vertical load for each pile, penetrating to a depth of 90.0 to 100.0 m, is around 2000.0 t (or 20.0 MN). The main piles are generally separated by a distance of 12.0 to 20.0 m, and the skirt piles are separated by a distance of 8.0 to 10.0 m from the main piles. A factor of safety of at least 1.5 is used in designing the piles against the repeated wave loads. Under the hostile extreme environment of the North Sea, a different design is utilized, wherein the foundation has four main legs, each consisting of a



**FIGURE 4.44** Principles used in the process of “pile insertion.” (From P. Le Tirant, *Seabed Reconnaissance and Offshore Soil Mechanics for the Installation of Petroleum Structures*, Editions Technip 27, Paris, France, p. 298, 1979. With permission.)

group of 4 to 12 secondary piles of diameter 1.0 to 1.40 m; the overall diameter of each pile group is around 10.0 to 12.0 m. In some cases, intermediate piles, spaced at 15.0 to 20.0 m from the main piles, are also used in the North Sea structures to distribute the platform loads more evenly to the seabed.

**4.5.2.2 Bearing Capacity of Piles in Compression and Tension**

The static (vertical) bearing capacity of a pile driven into the soil to a depth  $h$  is given by the sum of two components, viz., frictional resistance and the end bearing resistance:

$$Q = Q_s + Q_p = \sum_{i=1}^n f_i A_{si} + q A_p \tag{4.30}$$

with  $n$  = the number of diametral variations present in the pile

where  $Q_s$  is the lateral frictional resistance mobilized on the pile surface,  $Q_p$  is the end bearing resistance of the pile,  $A_s$  is the frictional surface area of the pile,  $A_p$  is the cross-sectional area of the pile end,  $f$  is the lateral frictional stress on the pile, and  $q$  is the bearing stress exerted at the end of the pile. The values of  $f$  and  $q$  depend on the nature and consolidation of the soils, the type and dimension of the pile, and the method of inserting the pile into the ground. The values of  $f$  and  $q$  for different types of soils and their conditions are given in Table 4.12 [72, 73].

The high overturning moment applied to an offshore structure can result in tension forces in some of the piles. While calculating the ultimate tensile capacity, the end bearing component is neglected; however, the weight of the pile and the soil plug inside the pile may be included. Some of the earlier researchers [73] have stated that the skin friction is much lower than the values obtained for compression, viz.,

$$f' = kf, \text{ with } (0.5 < k < 1.0) \quad (4.31)$$

However, recent research has concluded that the residual stresses induced in the pile during driving could have contributed to the lower value in the skin friction during the pullout. Consequently, it is not necessary to differentiate between the skin friction values during compression or tension.

**TABLE 4.12**  
**Relationships Developed for  $f$  and  $q$**

Type of Soil	Value of $f$ (kPa)	Value of $q$ (kPa)
Sand	$f = K_0(\sigma_{v0}') \tan \delta$ , with $\sigma_{v0}' =$ effective vertical stress in the soil $= \gamma_b h$ , $K_0 = 0.3$ to $0.7$ for driven piles, $0.1$ to $1.4$ for drilled piles, and $0.5$ for tension; $\delta =$ effective friction angle; and $h =$ depth of penetration of pile.	$q = (\sigma_{v0}')N_q$ , with $q$ being the limiting effective pressure and $N_q$ the dimensionless bearing capacity factor for sand.
Underconsolidated or normally consolidated clays	$f = s_u$ , where $s_u$ is the undrained shear strength. For soft clays, $c_u < 48.0$ kPa. For stiff clays, $f < c_u$ ; use Figure 4.45 [74].	$q = s_u N_c$ , with $N_c$ being the dimensionless bearing capacity factor for clay; here $N_c = 9.0$ ( $s_u \equiv c_u$ ).
Overconsolidated clays	(i) The larger of $s_{u(nc)}$ or $48.0$ kPa, with $s_{u(nc)}$ being the shear strength expected from the same clay in a normally consolidated condition; or (ii) $f = 0.3c_u$ (Le Tirant [67]); or (iii) $f = 0.4c_u$ (API [75]).	$Q = s_u N_c$ , with $N_c$ being the dimensionless bearing capacity factor for clay; here $N_c = 9.0$ ( $s_u \equiv c_u$ ).
Overconsolidated clays	(i) $f = \alpha s_u$ , with (a) $\alpha = (0.5)(\psi)^{-0.5}$ for $\psi > 1.0$ and (b) $\alpha = (0.5)(\psi)^{-0.25}$ for $\psi \leq 1.0$ and $\alpha < 1.0$ . Also, $\psi = s_u/\sigma_{v0}'$ ; Uses a knock-down factor to the present overburden strength; or (ii) $f = 0.3c_u$ (Le Tirant); or (iii) $f = 0.4c_u$ (API).	$q = s_u N_c$ , with $N_c$ being the end bearing coefficient for clay; here $N_c = 9.0$ .
Other stiff clays	$F = \alpha s_u$ , with $\alpha = 1.0$ for $s_u < 24.0$ kPa. Also for $s_u > 72.0$ kPa, $\alpha = 0.5$ . For $24.0 < s_u < 72.0$ , the value of $\alpha$ is linearly interpolated.	$q = s_u N_c$ , with $N_c$ being the end bearing coefficient for clay; here $N_c = 9.0$ .
Calcareous soils	Lower than the skin friction in fine- or coarse-grained particles of carbonates, due to crushing, depending on the degree of cementation of these particles.	—

Sources: N.D.P. Barltrop and A.J. Adams, Dynamics of fixed marine structures, in: *Foundations*, Butterworth Heinemann Ltd., Oxford, UK, pp. 217–221, 1991. P. Le Tirant, *Seabed Reconnaissance and Offshore Soil Mechanics for the Installation of Petroleum Structures*, Editions Technip 27, Paris, France, pp. 312–326, 1979. Used with permission.

For fixed platforms, the embedded length of pile may be replaced by a short pile of length  $h_1$  equal to [76]

$$\begin{aligned} h_1 &= 1.8 \sqrt[3]{(EI/n_h)} \text{ for piles in granular soils} \\ &= 1.4 \sqrt[4]{(EI/k_s)} \text{ for piles in preloaded clays} \end{aligned}$$

where  $n_h$  is the coefficient modulus,  $0.27 \text{ MN/m}^3 < n_h < 8.1 \text{ MN/m}^3$ ;

$k_s$  is the subgrade modulus for clay  $\approx 67.0 c_u$ ;

$c_u$  is the undrained shear strength of clayey soil

Also  $(3D) < h_1 < (8.5D)$ , where  $D$  is the outer diameter of the pile.

### Example 4.13

A 1.00-m-diameter pile is driven into a subset soil, consisting of normally consolidated soil, and has to support a load of 2500 t. (i) Determine the penetration depth required for the pile and (ii) determine the penetration depth if the soil is dense sand.

Using Equation 4.30 and Table 4.12 (see also Figure 4.45), for a normally consolidated clay,

$$Q = Q_s + Q_p = fA_s + qA_p$$

- (i) For normally consolidated clay soil

From Table 4.12,  $f = s_u$ , with  $s_u =$  undrained shear strength of soil. Take  $s_u = 48.0 \text{ kPa}$ ; hence,  $f = 48.0 \text{ kPa}$ .

Also  $q = 9s_u = (9.0)(48.0) = 432.0 \text{ kPa}$ . Taking  $h$  to be the penetration depth of the pile,

$$(2500)(9.81) = (48.0)\{\pi(1.0)\}h + (\pi)\{(1)^2/4\}(432.0) = 150.8 h + 339.3$$

Hence,  $h = 160.0 \text{ m}$  (in normally consolidated clay).

- (ii) For dense sand:

From Table 4.12,  $f = K_0(\sigma_{v0'}) \tan \delta$  and  $q = (\sigma_{v0'})N_q$ .

As per Table 4.12, the angle of internal friction in ocean soil is given as  $\phi$  ranging from  $35^\circ$  to  $40^\circ$ . Also as per Table 4.7, the saturated density  $\gamma_t$  ranges between  $1.80$  and  $2.10 \text{ t/m}^3$ .

Take  $\phi = 37^\circ$  and  $\gamma_t = 1.90 \text{ t/m}^3$ . Hence,  $\gamma_b = 1.90 - 1.025 = 0.875 \text{ t/m}^3$ .

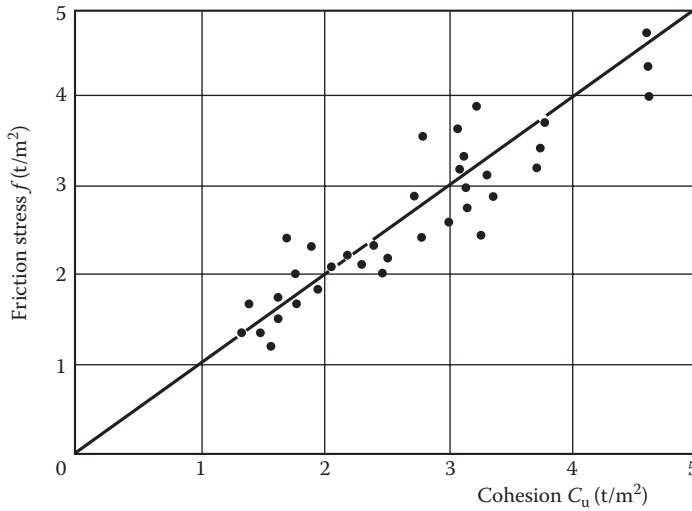
Also  $\sigma_{v0'} = \gamma_b h$ . Take  $K_0 = 0.60$ .  $N_q \sim 52.0$  (Figure 4.52)

$$\begin{aligned} (2500)(9.81) &= \int (0.6)(0.875)(9.81)(h)\{\tan(37^\circ)\}\{\pi(1.0)dh + \{(\sigma_{v0'})N_q\}\{\pi(1)^2/4\} \\ &= 12.12(h^2/2.0) + (0.875)(h)(9.81)(52.0)(0.785) = 6.06h^2 + 350.4h. \end{aligned}$$

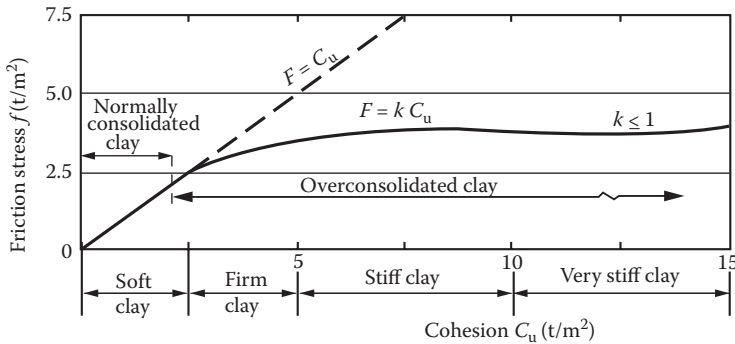
Solving the quadratic equation,  $h = 40.97 \text{ m}$  (in sand).

### Example 4.14

In the above problem, instead of a normally consolidated clay, if the soil at site was an overconsolidated clay, then find the penetration depth  $h$  of the pile into the seabed.



(a) Soft to firm clays (according to McClelland)



(b) Firm to stiff clays (according to McClelland)

**FIGURE 4.45** Relationship between cohesion and skin friction of piles in soils. (From P. Le Tirant, *Seabed Reconnaissance and Offshore Soil Mechanics for the Installation of Petroleum Structures*, Editions Technip 27, Paris, France, p. 314, 1979. With permission.)

As per Table 4.12, the pile design is based on the following three conditions:

- (i)  $f = \alpha s_u$ , with (a)  $\alpha = (0.5)(\psi)^{-0.5}$  for  $\psi > 1.0$ , (b)  $\alpha = (0.5)(\psi)^{-0.25}$  for  $\psi \leq 1.0$ , and  $\alpha < 1.0$ . Also,  $\psi = s_u/\sigma_{v0'}$  (uses a knock-down factor to the present overburden strength)
- (ii)  $f = 0.3c_u$
- (iii)  $f = 0.4c_u$ .

$\psi = s_u/\sigma_{v0'} = (48.0)/\{(0.875h)(9.81)\} = 1.0$ ; hence, for  $h \leq 5.60$  m,  $\psi \geq 1.0$ . For  $h \geq 5.60$ ,  $\psi \leq 1.0$ . When  $h \leq 5.60$  m,  $\alpha = (0.5)[(48.0)/\{(0.875)(5.60/2)(9.81)\}]^{-0.5} = 0.354$ .

When  $h \geq 5.60$ ,  $\alpha = (0.5)(\psi)^{-0.25} = 0.5 [(48.0)/\{(0.875)(100.0/2)(9.81)\}]^{-0.25} = 1.729$  ( $h$  is taken to be approximately 100.0 m).

Also,  $q = s_u N_q$

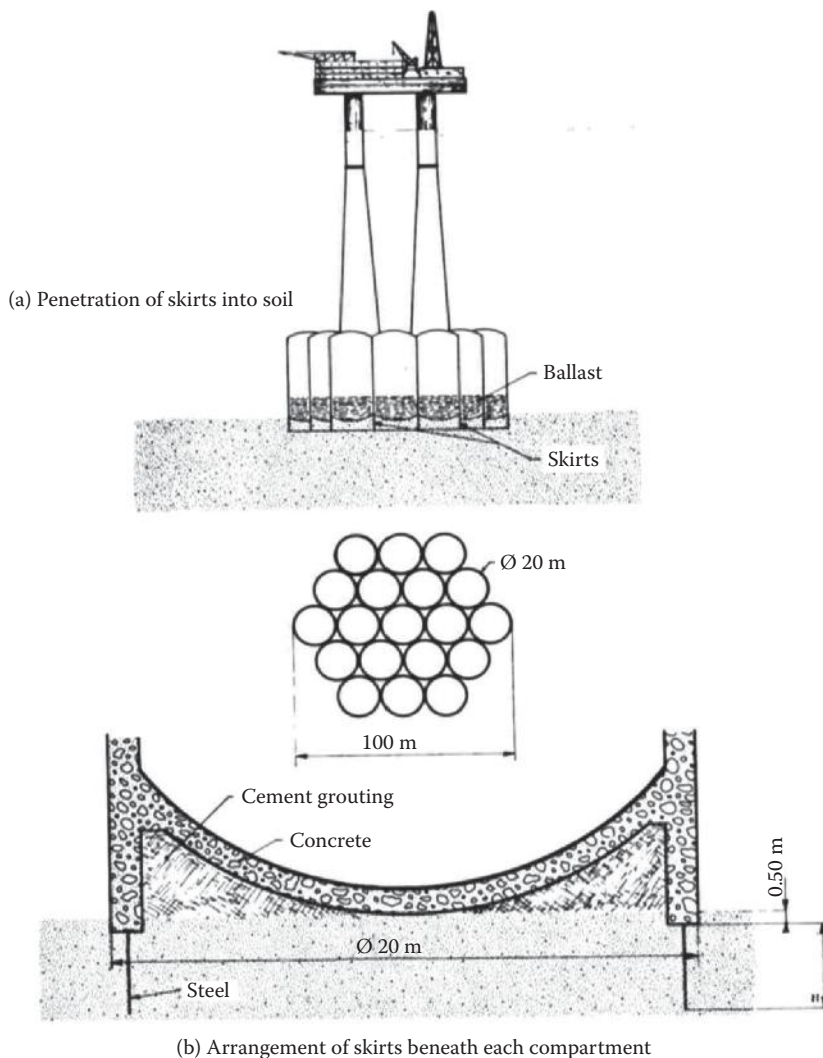
$$(2500)(9.81) = \{(0.354)(48.0)(\pi)(1.0)(5.60) + (1.729)(48.0)(\pi)(1.0)(h - 5.60)\} + (9)(48.0)(\pi)(1^2/4) = 298.94 + 260.73h - 1460.07 + 339.29.$$

Hence,  $h = 97.21$  m (in overconsolidated clay) and therefore OK.



### 4.5.3 BOTTOM-SUPPORTED GRAVITY PLATFORMS

Bottom-supported gravity platform structures are generally fabricated or reinforced or prestressed concrete (even though hybrid types of steel-concrete gravity platform have also been used). These structures are built in a deep water coastal site, towed to the installation site, and ballasted to place it on the bottom location. The structures are designed in such a way as to be stable under their own weight and ballast, as well as by their transverse dimensions; generally, these types of structures would not require any anchoring in soil, even though vertical skirts are required at the platform foundation bottom to make it more stable under the horizontal wind and wave loads. Several types of gravity platforms, differing considerably in their geometries and dimensions of their base, have been designed, viz., Doris' concrete Ekofisk Tank, Condeep type concrete platform structures (having hexagonal, rectangular, square, and tripod foundations), and hybrid/all-steel gravity platforms. A typical structure is shown in Figure 4.46 [77], which shows the general arrangement



**FIGURE 4.46** Details at the base of a gravity platform structure facilitating load transfer. (From P. Le Tirant, *Seabed Reconnaissance and Offshore Soil Mechanics for the Installation of Petroleum Structures*, Editions Technip 27, Paris, France, p. 345 1979. With permission.)

of octagonal-shaped cluster of subset storage tanks, concrete columns, top platform, and the steel skirts below the foundation.

A number of geotechnical problems associated with the installation of a gravity structure in marine soils need to be considered while designing structures for various offshore locations, viz., (i) installation of offshore gravity structures, with the skirts, on the seabed; (ii) stability of the gravity platform structure, under its self-weight and other vertical loads, as well as under the cyclic environmental loads; (iii) vertical and horizontal movements of the structure; (iv) settlement of the soil beneath the structure; and (v) soil scour around the foundation of the structure.

#### 4.5.3.1 Geotechnical Issues Related to Installation of Platform Structure on Site

The gravity platform foundation may or may not be fitted with steel/concrete skirts on its underside, depending on the type of soil encountered and the slidability (horizontal)/erodability of the seabed terrain. In addition, the nature of soil encountered below the gravity platform presents two more problems for the foundation designer, viz., (i) the amount of penetration of skirts into soil and (ii) the type of contact and contact stresses between the soil and platform foundations due to the irregularities at the seabed surface.

Skirt depths can vary from 0.30 (or 0.40 m) to a few meters, depending on the type of soil encountered at the ocean bottom. It is very important to note that for the horizontal sliding stability of the platform structure, the entire design height of the skirt must penetrate into the ocean bottom (see Figure 4.46). Penetration depth of the skirts should be computed based on the maximum shear strength of the soil at site. The penetration of the skirts is dependent on the weight of the structures, ballasted with water (and if necessary, with sand); it is also slightly influenced by the reduction of water pressure inside the skirts and below the foundation base, especially in low permeability clays. In the case of irregular or sloping seabed, the free void spaces inside the skirt and the bottom of the foundations must be filled with cement grout. Also if boulders or rough surfaces are present below the platform foundation slab, they must be removed or made level.

The contact stresses between the soil and the bottom foundation slab depend on the topography of the site and the characteristics of the soils. In the case of very dense sands or very stiff clays, one should have detailed information about the topography of seabed soil in order to carry out a proper design. Generally, for North Sea structures, a soil depth variation of a few decimeters and a slope of  $1.0^\circ$  can be considered to be inconsequential. For soft or low consolidation soils, the irregularities of the surface are of no consequence, since the installation of the gravity platform structure will result in the consolidation of the soil, due to lateral creep, until equilibrium is reached between the weight of the structure and the bearing capacity of the soil. Usually, gravity platform structures need a dense sandy or very stiff clay soil, at the seabed, for a safe installation of the structure.

#### 4.5.3.2 Stability of Gravity Platform Structure under Static Loads and under Cyclic Environmental Loads

The design of a gravity platform must take into account the stability and deformation of the platform base. Stability of the platform structure is governed by the static or dynamic loading conditions, and the deformation of the foundation is governed by the total or differential settlement of the foundations. Figure 2.3 outlines the various scenarios that should be taken into account as one considers that stability of the gravity platform structure to instability in the vertical and horizontal directions, viz., (i) sliding of the structure along the soil due to the applied horizontal environmental loads; (ii) sliding of the structure due to instability at the sand–clay interface; (iii) rupture of the soil due to excessive shear stress in soil, leading to heavy stress concentration and plastic rupture on the leeward side, due to applied loads; (iv) rupture of soil due to cyclic rocking and consequent softening of soil due to applied environmental loads; (v) uneven settlement and instability of foundation structure due to liquefaction caused in seabed soil; and (vi) instability of foundation caused by scour around the foundation base.

Slip between the base of the structure and the surface of soil occurs when the surface shear strength of soil–structure interface is less than the applied horizontal stress at the interface. The

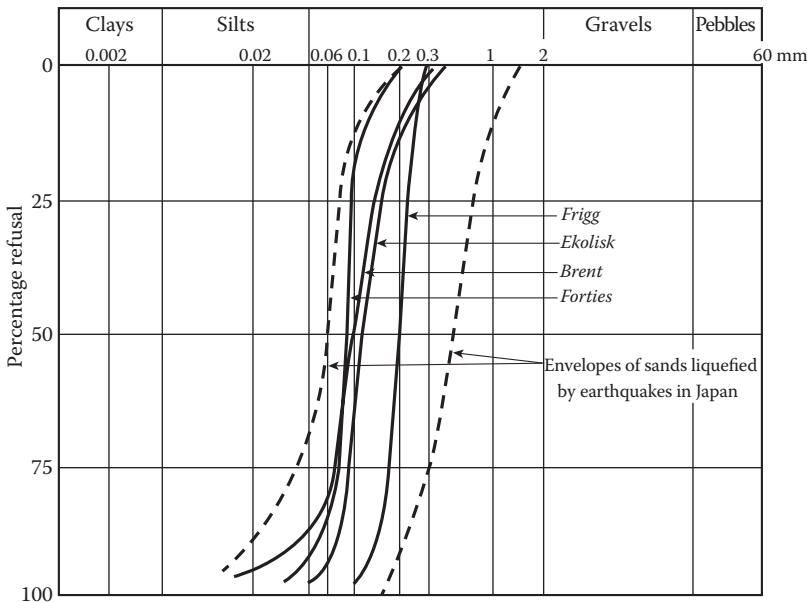
probability of slip of the structure is reduced by the fitting of skirts (penetrating several meters into the soil); it should be borne in mind that horizontal slip of the structure can occur even at this penetration of the skirt, if the soil is weaker. Slip of the platform in the horizontal direction can occur due to the sliding of the subsea bottom clay layer, overlain by a sandy layer, when the applied stress is much higher than the interfacial shear strength of the clay layer or when the angle of inclination of the sand–clay interface exceeds 10°. The risk of slip at the clay–sand interface is increased by the development of negative pore pressures in layers of clay of low permeability.

When slight structural movements (vertical or rocking) occur at the soil–structure interface, under the wave/wind loads, the shear stress in the soil is increased due to the reduction of the effective bearing area of the structure. Moreover, the decrease in the effective shear strength of soil, due to pore pressure buildup in clayey soil, increases the risk of rupture in clayey soil. In sands, the possibilities of rupture under repeated environmental loads depend on the undrained shear strength of soil, and this should be checked in the design.

Due to the repeated environmental loads acting on the platform, high shear stresses are set up along the edges of the foundation footing; this generates a large amount of distortions in soils present along the periphery of the footing. This concentration of stresses in soil leads to a softening of the soil around the periphery of the foundation; in addition to softening of soil at the edges, an apparent hardening of soils also occurs at the central section of the foundation base.

Depending on the nature of the soils at the bottom of the gravity platform structure, liquefaction and subsequent instability of the platform structure could occur under (i) repeated cyclic loading on the structure, due to severe stormy conditions, and (ii) seismic excitation of the seabed foundation below the structure. In sands, during dynamic excitation, the pore pressure in between the sand grains tends to build up and reduce the effective shear stresses; as a result, under certain dynamic loadings, the soil may lose its effective strength totally and behave like a fluid. This condition leads to structural failure under the repeated environmental wave loads.

Figure 4.47 [78] illustrates the various ranges of ocean soils present under the gravity platform structures installed in the North Sea, as well as the envelope of soil grain sizes under which



**FIGURE 4.47** Size distributions of surface sands in the North Sea, along with the envelope of sands liquefied in Japan, under seismic excitation. (From P. Le Tirant, *Seabed Reconnaissance and Offshore Soil Mechanics for the Installation of Petroleum Structures*, Editions Technip 27, Paris, France, p. 349, 1979. With permission.)

liquefaction under laboratory conditions. The figure indicates that liquefaction failure is possible for all the platforms located in the North Sea under optimum excitation conditions.

Scour at the ocean bottom occurs depending on the speed of ocean bottom currents and the grain size distribution in seabed sediments. Scour around the foundation may undermine the foundation and lead to failure by horizontal sliding or in the loss of the bearing strength of seabed soil.

#### 4.5.3.3 Settlement of Soil beneath Gravity Platform Foundations

In the North Sea, where most of the gravity platform structures are located, the soils are invariably highly consolidated. Hence, the major problem for these structures will be stability rather than settlement of foundations due to soil deformations. Since the stability and deformation criteria are interrelated for soils of lower consolidation, the settlement conditions should also be considered in this section.

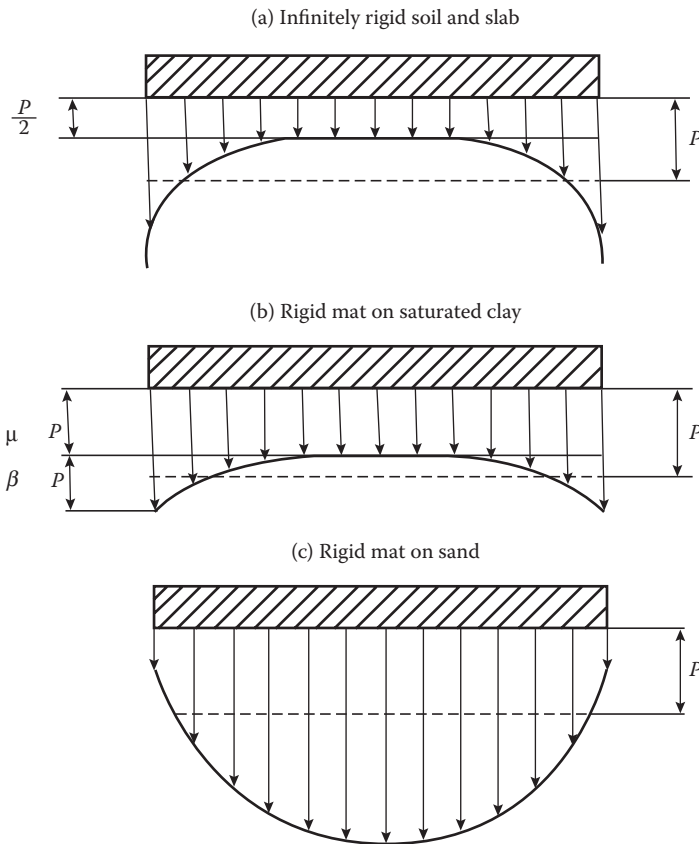
Under static loads, viz., self-weight and other platform loads, settlement in foundation occurs due to volumetric compression and shear distortion under the submerged weight of the structure. In the case of dense sands and consolidated clays, settlement comprises instantaneous deformation and primary consolidation (of very short duration); the probable settlement under the usual platform loads for a gravity platform foundation will be around a few tens of centimeters. In the case of soft soils (on the surface or at low depths below the seabed), the settlement consists of the instantaneous deformation, the (short-term) primary consolidation, and the secondary consolidation lasting several years or even decades. These can be estimated by the use of available empirical formulae.

Under cyclic loading, the vertical loads resulting from the ocean waves keep on varying (due to the random nature of wave heights), and this variation leads to a discontinuous settlement of the foundation; this will be difficult to determine. For dense sands and highly consolidated clays, the settlement can be computed by extrapolating from small-scale laboratory experiments. Also the settlements will occur very quickly. For the case of soft soils and loose sands, settlements will occur over a long period.

#### 4.5.4 STRESS DISTRIBUTION BENEATH GRAVITY PLATFORM FOUNDATION

From earlier theoretical analysis carried out by Boussinesq [79, 80] for a rigid circular footing on the top of an elastic soil foundation, the vertical stresses beneath the foundation are shown in Figure 4.48 [81]. It has been found that (i) a contact stress equal to half the mean stress ( $p/2$ ) exists at the center of the footing and (ii) a theoretical infinite stress exists at the edge. In actuality, due to the rupture of soil at the edge of the footing (caused by the high local shear stress), a new plastic state of equilibrium exists; this leads to the adaptation of the maximum stress at the edge of the footing, as shown in Figure 4.48a. In the case of a saturated homogeneous isotropic and elastic clay (where the foundation is partly buried), the vertical stress distribution is parabolic in nature (see Figure 4.48b), with the minimum pressure ( $\alpha p$ ) at the center and an edge pressure of  $(\alpha p + \beta p)$  at the edges, with the condition  $[(\alpha p + \beta p/2) = p]$ . Consequently, for elastic clayey soil, the values of  $\alpha$  and  $\beta$  tend to be equal to 0.70 and 0.60, respectively. For the case of homogeneous and elastic sand, with a linearly increasing modulus of elasticity based on depth, the pressure would be a maximum at the center of the footing and a minimum at the edges, as shown in Figure 4.48c. However, when the size of the footing becomes considerable, the distribution of the contact pressure tends to become a uniform value across the width of the foundation. This assumption is accepted as valid for a rigid foundation on sand.

In the case of a rigid circular footing resting on a homogeneous and isotropic saturated clayey soil, assuming the parabolic shape shown in Figure 4.48b, the relative vertical  $\alpha p$  and horizontal  $\Delta\sigma_3/p$  stresses induced in the soil at the center of the foundation are given in Figure 4.49 [82]. It is also observed that  $\Delta\sigma_1/p$  is independent of the Poisson ratio effect. Figure 4.49 also shows the values of  $\Delta\sigma_1/p$  and  $\Delta\sigma_3/p$  for two different values of  $\nu$  (0.25 and 0.5) and for two different types of footing



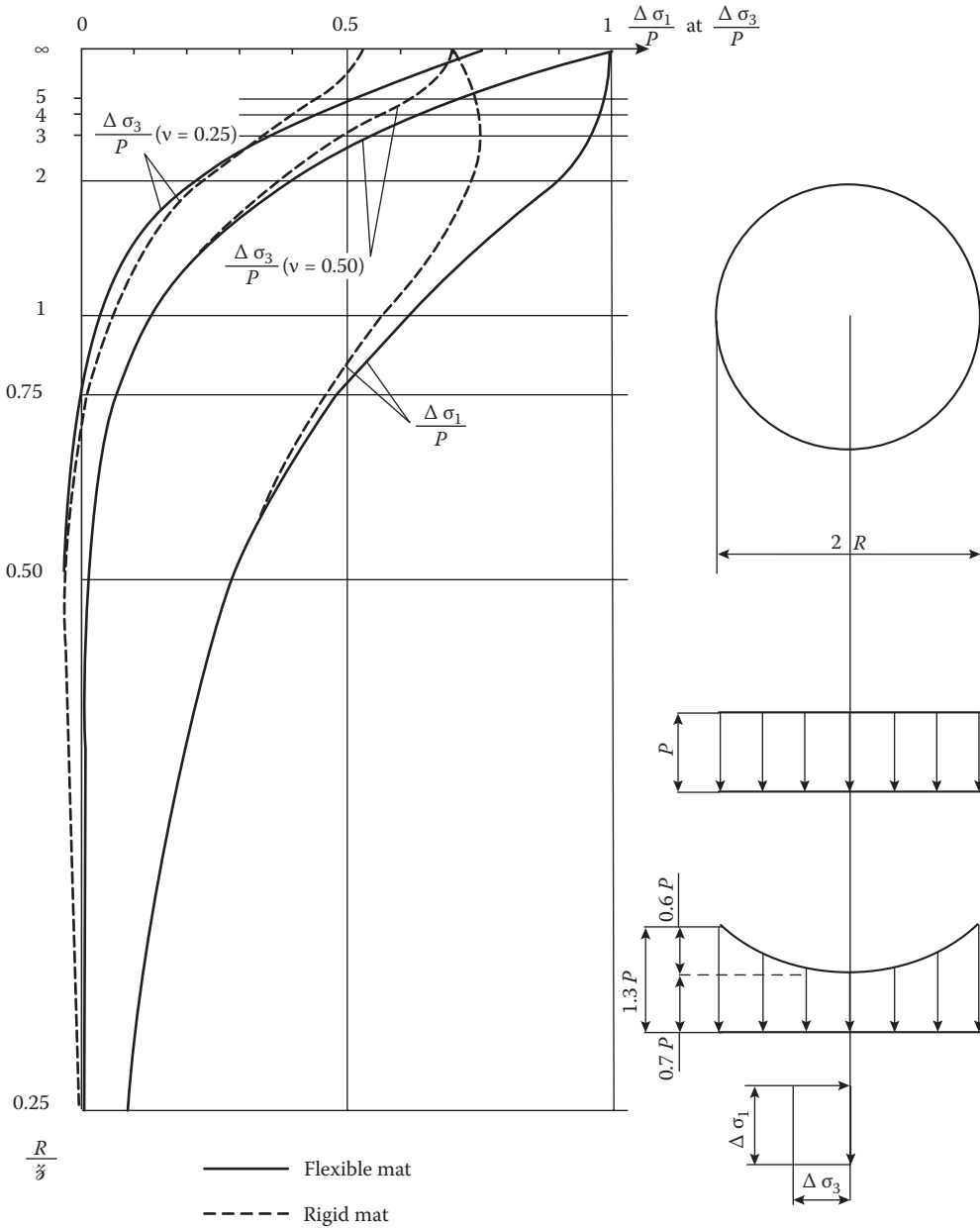
**FIGURE 4.48** Stress distributions beneath a rigid circular raft foundation. (From P. Le Tirant, *Seabed Reconnaissance and Offshore Soil Mechanics for the Installation of Petroleum Structures*, Editions Technip 27, Paris, France, p. 355, 1979. With permission.)

(rigid and flexible). It is found that the Poisson ratio effect is dominant only up to a depth of 0.2 times the radius of the foundation.

The vertical stress bulb induced beneath a square foundation with a side  $B$  is shown for (i) a homogeneous, elastic, and isotropic soil medium (as per Boussinesq's solution) in Figure 4.50a [83] and (ii) a homogeneous, elastic, and stratified terrain (as per Westergaard's solution) in Figure 4.50b [83]. In actual foundations, consisting of layered soils (of different kinds and mechanical characteristics, such as sands and clays of varying consolidation), the distributions of stresses do not conform to the theoretical patterns shown in Figures 4.49 and 4.50. The vertical stresses are much less in a realistic layered soil foundation, as shown in Table 4.13 [84].

#### 4.5.5 COMPUTATION OF STABILITY OF GRAVITY PLATFORM STRUCTURE

A number of factors need to be verified for ascertaining the stability of the platform at the site, viz., (i) installation requirements; (ii) stability of the platform with respect to horizontal sliding; (iii) stability of the foundation with respect to overturning; and (iv) settlement of the soil beneath the foundations.

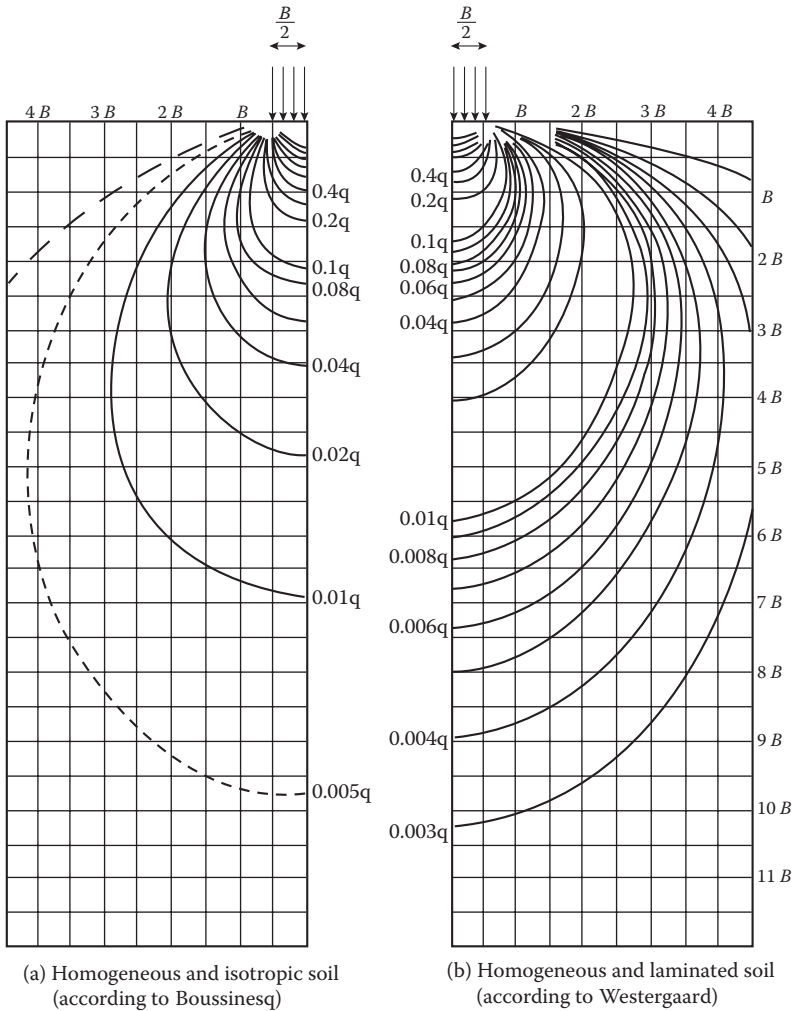


**FIGURE 4.49** Stress distributions beneath a rigid and flexible circular raft foundation, with  $R$  as the radius of the foundation slab. (From P. Le Tirant, *Seabed Reconnaissance and Offshore Soil Mechanics for the Installation of Petroleum Structures*, Editions Technip 27, Paris, France, p. 356, 1979. With permission.)

**4.5.5.1 Installation Requirements**

From the geotechnical standpoint, the installation requirements consist of (i) penetration of skirts into the soil and (ii) contact stresses between the structure and the soil.

Skirts are required for gravity platform foundations, since it (i) reduces the effect of scour on the platform foundation laid on a sandy seabed soil and (ii) reduces the possibility of slipping of the



**FIGURE 4.50** Stress distributions beneath a rectangular raft foundation ( $\sigma_v = \alpha p$ , where  $p$  is the consolidation pressure,  $\alpha$  is the coefficient given in the figure, and  $\sigma_v$  is the vertical pressure at the location). (From P. Le Tirant, *Seabed Reconnaissance and Offshore Soil Mechanics for the Installation of Petroleum Structures*, Editions Technip 27, Paris, France, p. 358, 1979. With permission.)

**TABLE 4.13**  
**Vertical Stress Distributions in Isotropic and Layered Soil Strata for Rectangular Load Distribution**

#	Depth Ratio ( $z/B$ )	Vertical Stress Distribution ( $\Delta\sigma_v/p$ ) beneath the Center Line of Foundation	
		Isotropic Soil (Boussinesq's Solution)	Layered Soil (Westergaard's Solution)
1	0.5	0.7	0.5
2	1.0	0.4	0.2
3	1.5	0.2	0.13
4	2.0	0.12	0.08

Source: P. Le Tirant, *Seabed Reconnaissance and Offshore Soil Mechanics for the Installation of Petroleum Structures*, Editions Technip 27, Paris, France, p. 357, 1979. With permission.



platform laid on clayey soils. Considering the penetration of skirts into soil, it is observed that the total force resisting the penetration of skirt into soil is given by

$$F = \pi deR_{p_{\max}} + 2\pi dhf_{\max}$$

where  $F$  = force opposing the penetration of skirt in a single tank

$R_{p_{\max}}$  = maximum cone resistance of surface soil

$f_{\max}$  = transverse frictional strength measured with a penetrometer (4.33)

$d$  = diameter of skirt

$e$  = thickness of the skirt

$h$  = penetration of skirt into soil

The force  $F$  will be the average statical force (including self-weight) that is applied over each cylindrical storage tank, as the gravity platform is placed in position.

If the seabed is perfectly flat, then the stress distribution on the soil depends on the flexibility of the seabed and the mechanical characteristics of the seabed soil. For the sake of simplicity, if the floor is assumed to be a perfectly rigid floor, the preliminary design of the foundation structure should be designed as per (i) a stress at the edge (of foundation raft) twice that at the center of a raft, if the cone resistance  $R_p < 2.0$  MPa (or 200.0 t/m<sup>2</sup>), viz., the soil will undergo considerable deformation; and (ii) a uniform stress distribution beneath the raft, if  $R_p > 6.0$  MPa (or 600.0 t/m<sup>2</sup>), in which case the seabed soil is only slightly deformable. Also the presence of “hard points” or local bumps on the surface of soil will introduce large stress concentrations beneath the structure in contact with the soil; in order to compute this stress, the average nominal stress on the hump should be multiplied by the stress concentration factor. Stress concentrations will lead to settlement of the soil around the hump and to a gradual reduction of the average contact stress; also routing of cement soon after the structure is installed on location will allow the soil surface to be made more uniform, thus reducing the stress concentration in soil.

#### 4.5.5.2 Slip (or Sliding) of Foundation Structure

Slip (or sliding) of the structure under horizontal loads can occur as a result of (i) slip of the structure on the surface of soil and (ii) slip in between the soil layers below the seabed. If the soil below the gravity platform raft is on sand, then the maximum (horizontal) frictional force  $F_{\text{hor max}}$  that maintains the stability of the platform structure under the most unfavorable conditions is given by

$$F_{\text{hor max}} = F_{\text{vert min}} \tan(\lambda) \quad (4.34)$$

where  $F_{\text{vert min}}$  is the minimum vertical force acting on the structure,  $F_{\text{hor max}}$  is the minimum horizontal force acting on the structure, and  $\lambda$  = mobilized frictional angle at the sand–structure interface or at the sand–clay interface; also  $\tan(\lambda) < \tan(\phi)$ , with  $\phi$  as the minimum internal friction at the sand–structure interface or at the sand–clay interface.

The factor of safety (FS), with respect to slip of the structure, is given by

$$\text{FS} = \{\tan(\phi)/\tan(\lambda)\} \quad (4.35)$$

As per the recommendations of Det Norske Veritas [85], the FS should be at least 1.2; or a multiplying factor of 1.3 should be used on the computed value of  $F_{\text{hor max}}$ , while using Equation 4.34 with  $\lambda \equiv \phi$ .

If the soil below the platform base is clay, then the factor of safety of the platform against horizontal sliding is given by

$$FS = (A \tau_f) / F_{\text{hor max}} \quad (4.36)$$

where  $A$  = area of the base structure, and  $\tau_f$  = shear strength of clay.

As per the recommendations of Det Norske Veritas [85], the shear strength of clay at the interface is taken as  $(c_u/1.4)$ , where  $c_u$  is the undrained cohesive strength of clay below the base of the platform structure; otherwise, a multiplicand of 1.3 should be used to increase the maximum horizontal load acting on the structure, with  $\tau_f = c_u$ . The minimum factor of safety is around unity when the undrained cohesive strength of clay is equal to 100.0 kPa; it is expected to be more than 100.0 kPa.

#### 4.5.5.3 Vertical Bearing Capacity of Soil beneath Gravity Platform Structure

For a rectangular footing, the drained bearing capacity of the surface (or embedded at shallow depths) foundation is given by the formula by Hansen and Meyerhof [86, 87]:

$$Q = [(\eta\gamma'BN_\gamma + c_uN_c + \gamma'D_fN_q)](BL) \quad (4.37)$$

where  $Q$  = vertical bearing capacity of foundation soil,  $B$ ,  $L$  = width and length of foundation, respectively (or  $BL$  = area of the foundation slab),  $\eta$  is a factor for shape of the foundation (circular or square or rectangular),  $D_f$  = embedment depth of foundation in soil,  $\gamma'$  = submerged density of soil,  $c_u$  = undrained cohesive strength of soil, and  $N_\gamma$ ,  $N_c$ ,  $N_q$  are dimensionless factors for foundation soil.

The factor  $\eta$  is sometimes taken as equal to 0.4 for a rectangular shape and 0.3 for a circular shape [21]; generally, it is taken as equal to 0.5. For the case of dense sands or stiff clays, the depth  $D_f$  to which the platform foundation is buried will be very small; hence, the contribution from that component (viz., the third term in Equation 4.37) will be neglected. The dimensionless factors  $N_\gamma$ ,  $N_c$ ,  $N_q$  are dependent on the wet angle of friction of soil; the bearing capacity factors are given in Figure 4.51 [88]. Also if the platform foundation rests on top of sandy soil, then  $c_u = 0.0$ ; consequently, the second term can also be neglected. Also the sand is assumed to be drained for this computation. Under the vertical loads acting on the gravity platform structure, the failure pattern in the soil foundation is given in Figure 4.52 [89]; the failure occurs along the slip surface and the passive wedges that participate in the failure.

If the structure rests on a stiff clay foundation soil (with the angle of internal friction = 0.0), then Equation 4.37 gets reduced to

$$Q = (c_uN_c)(\text{area}) \quad (4.38)$$

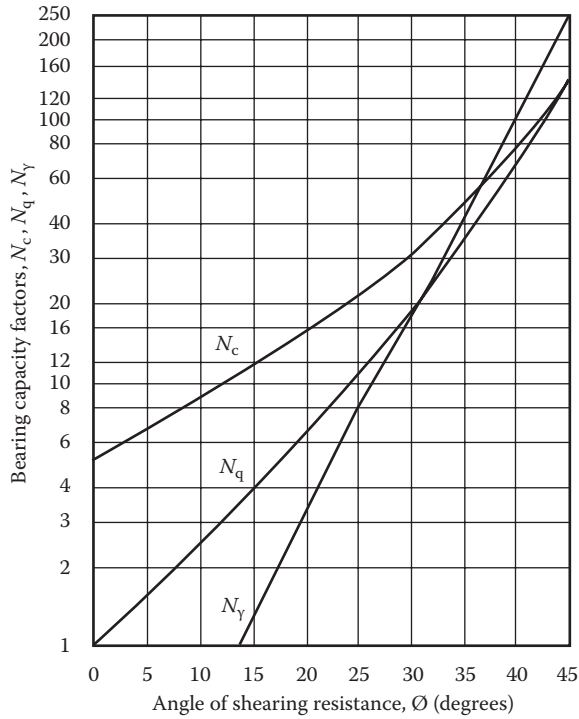
#### 4.5.5.4 Stability of Gravity Platform Structure with Respect to Overturning

If it is assumed that the platform soil is dense sand (which is drained), then the bearing strength of the foundation soil can be given as

$$Q = F_{\text{vert}} = [\eta\gamma'BN_\gamma](BL) \quad (4.39)$$

When the environmental load is acting horizontally, the effective load on the platform foundation (bottom) will act in an inclined manner, at an eccentricity of  $e$  ( $= E/B$ ) from the center of the foundation slab (or base), as shown in Figure 4.53 [90]; this will reduce the effective width of the foundation base to be  $B' < B$ . The effective width then becomes

$$B' = B(1 - 2e) = B - 2E \quad (4.40)$$



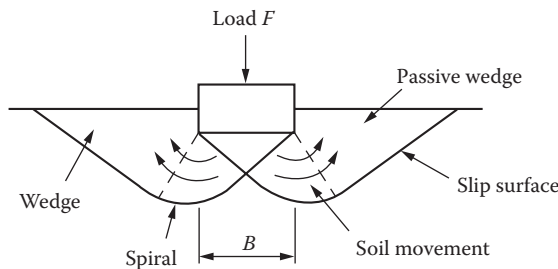
**FIGURE 4.51** Bearing capacity factors  $N_c$ ,  $N_q$ , and  $N_\gamma$  as a function of the angle of internal friction. (From P. Le Tirant, *Seabed Reconnaissance and Offshore Soil Mechanics for the Installation of Petroleum Structures*, Editions Technip 27, Paris, France, p. 377, 1979. With permission.)

where  $E$  is the distance from the center of the slab to the point of intersection of the inclined at the bottom of the foundation slab.  $E = (M/F_{\text{vert min}})$ , where  $M$  = moment of overturning forces about the bottom of the foundation slab.

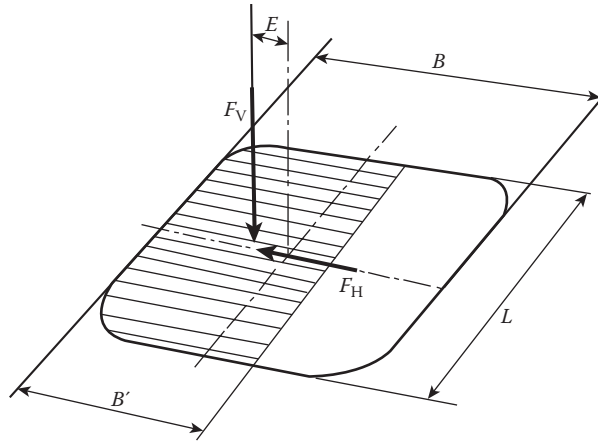
Other factors used in the computation of the bearing capacity of the foundation soil is given as

$$s_\gamma = [1 - (0.4)(B'/L)i_\gamma] \tag{4.41}$$

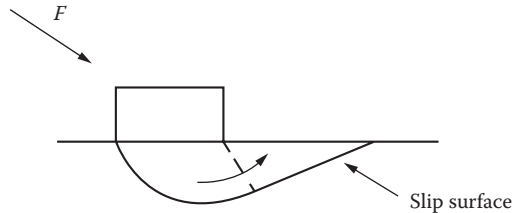
where  $s_\gamma$  = correction factor for the shape of the structure;  $i_\gamma = [1 - (0.7)(F_{\text{hor}}/F_{\text{vert min}})]$ , where  $i_\gamma$  is the correction factor for the inclination of force, acting on the structure.



**FIGURE 4.52** Failure surfaces assumed for foundation bearing capacity calculations, under vertical compressive loads. (From N.D.P. Barltrop and A.J. Adams, *Dynamics of fixed marine structures*, in: *Foundations*, Butterworth Heinemann Ltd., Oxford, UK, p. 206, 1991. With permission.)



**FIGURE 4.53** Bearing force on a surface foundation resting on sand ( $E =$  eccentricity of load  $= e$ ). (From P. Le Tirant, *Seabed Reconnaissance and Offshore Soil Mechanics for the Installation of Petroleum Structures*, Editions Technip 27, Paris, France, p. 379, 1979. With permission.)



**FIGURE 4.54** Failure of foundations under an inclined load. (From N.D.P. Barltrop and A.J. Adams, Dynamics of fixed marine structures, in: *Foundations*, Butterworth Heinemann Ltd., Oxford, UK, p. 207, 1991. With permission.)

The vertical bearing resistance of the platform foundation becomes

$$F_{\text{vert}} = [\eta\gamma'BN_{\gamma}(1 - 2e)^2s_{\gamma}i_{\gamma}](\text{effective area}) \tag{4.42}$$

The value of  $N_{\gamma}$  is given in Figure 4.51 and depends on the angle of internal friction  $\phi$ . The failure of the foundation soil under an inclined load is shown in Figure 4.54 [91].

For a structure resting on a stiff clay (with  $\phi = 0.0$ ), the bearing capacity of the platform foundation is given by

$$F_{\text{vert}} = [c_uN_c(1 - 2e)s_c i_c](\text{effective area}) \tag{4.43}$$

in which the terms  $s_c$  and  $i_c$  are given by

$$s_c = 1 + 0.2(B'/L) \text{ and } i_c = (1 - \alpha/90)^2, \text{ with } \alpha = \arctg(F_{\text{hor}}/F_{\text{vert min}}) \tag{4.44}$$

The value of  $N_c = \pi + 2 \sim 5$ .

**Example 4.15**

A 60.0-ft. cylindrical underwater habitat is placed on the top of the seabed in the ocean. The contact pressure between the habitat and the seabed has been measured as 450.0 lb./ft.<sup>2</sup>. Determine

the ultimate settlement and the settlement after 6 years under the center line of the structure, given the following soil properties. Use the Boussinesq's data given in Figure 4.51. The unit weight of soil at site is 110.0 lb./ft.<sup>3</sup>;  $e = 1.10$ ;  $c_v = 0.0290$  ft.<sup>2</sup>/day; and  $C_{ci} = 0.80$ .

From Figure 4.50, it can be seen that the settlement occurs due to deformations that occur within the top soil layer, whose depth is approximately equal to  $(2.0)R = (2.0)(30.0) = 60.0$  ft. Also it can be seen that the equivalent vertical stress  $p_1$  under which consolidation can be taken to occur is equal to  $0.70q$  at a depth of  $R (= 30.0$  ft.) below the surface ( $q =$  applied surface pressure at the soil surface);  $q = 450.0$  lb./ft.<sup>2</sup>.

Using the results shown in Figure 4.50, the increase in stress at the same point due to the placement of the habitat  $= (0.70)p = (0.70)(450) = 315.0$  psi.

Also, along the center line, the initial consolidation pressure = weight of soil above that location  $= (30.0)(110.0 - 64.0) = 1380.0$  lb./ft.<sup>2</sup>.

- (i) The ultimate settlement of the foundation (Equation 4.26)

$$\begin{aligned} \Delta h &= \{h_0 / (1 + e_0)\} (C_{ci}) \log\{(\bar{\sigma}_0 + \Delta\bar{\sigma}) / (\bar{\sigma}_0)\} \\ &= \{(60.0) / (1 + 1.10)\} (0.80) \log\{(1380.0 + 315.0) / (1380.0)\} = 2.034 \text{ ft.} \end{aligned}$$

After 6 years,  $T$ , the nondimensional time factor, is given (Equation 4.27) as

$$= c_v t / H^2 = (0.0290)(6)(365.25) / (60^2) = 0.1765.$$

Using Table 4.10, the consolidation ratio  $\sim 40\% + [(0.1765 - 0.126) / (0.197 - 0.126)](10\%) = 40\% + 7.12\% = 47.12\%$ .

- (ii) Settlement after 6 years  $= (47.12/100)(2.034) = 0.960$  ft. = 11.52 in.

### Example 4.16

- (1) Consider a condeep platform structure consisting of 19 vertical cylindrical storage cells [arranged in a 110.0-m (overall) hexagonal shape, with each cell being of 20.0-m diameter]. The buoyant weight of the platform is 250,000 t. Additional details provided for the platform are as follows: area of soil in contact with the platform base  $\sim 9500$  m<sup>2</sup>; maximum and minimum static platform loads are  $F_{v \max} = 250,000$  t,  $F_{v \min} = 180,000$  t,  $M = (2.7)(10^6)$  t m; forces generated on the platform due to a 100-year wave (of height 32.0 m and 16.0-s period) are vertical force  $\Delta F_v = \pm 12,000$  t, horizontal force  $F_h = 57,000$  t, overturning moment  $= (2.35)(10^6)$  t m. Assume that the platform rests on top of the soil foundation, without any skirt. Determine the stability of the platform with respect to (i) horizontal sliding; (ii) bearing capacity of the foundation soil; and (iii) overturning. Assume that the platform is founded on (a) sand and (b) stiff clay. (2) Consider each of the 19 cylindrical tanks to be equipped with a steel skirt of height  $h_1$ . Take each skirt to penetrate into the soil under a load of 13,000 t. Determine the required height of the skirt for horizontal sliding resistance.

1. Stability of the platform structure:

- (i) Sliding resistance of the structure:

- (a) On sand:

From Table 4.11, angle of internal friction for sand varies from 30.0° to 40.0°.

Use Equations 4.34 and 4.35.

From the given data, angle of sliding  $= \delta = \tan^{-1}\{(F_h) / (F_{v \min})\}$

$$= \tan^{-1}(57,000) / (180,000 - 12,000) = \tan^{-1}(0.339) \text{ radians}$$

$$= 0.3271 \text{ radians} = 18.74^\circ.$$

Available minimum factor of safety =  $\tan(\varphi')/\tan(\delta) = \tan(30^\circ)/\tan(18.74^\circ)$   
 $= (0.5773)/(0.3393) = 1.702 > 1.2$  (recommended by DNV) and hence safe.

(b) On stiff clay:

From the given data in Table 4.11, transverse undrained shear strength of clay =  $50.0 - 100.0 \text{ t/m}^2$ .

Use Equation 4.36.

Minimum shear strength of clay at the interface =  $50.0/(1.4) = 35.71 \text{ t/m}^2$ .

Available factor of safety =  $(9500)(35.71)/(57,000) = 5.95 > 1.0$  and hence OK.

(ii) Bearing capacity of the platform structure:

(a) On sand:

As per Equation 4.37, the bearing capacity of the foundation is given by

$$Q = [(\eta\gamma'BN_\gamma + c_uN_c + \gamma'D_fN_q)] (\text{area})$$

For sand,  $N_c = 0.0$ , and the third term also becomes zero due to zero embedment.

For sand,  $\gamma' = (1.8 \text{ to } 2.1) \text{ t/m}^2$  (from Table 4.7);  $\varphi' = 30^\circ - 40^\circ$ . From Figure 4.52,  $N_\gamma = 18.0$ .

Consequently,  $Q = [\eta\gamma'BN_\gamma] (\text{area}) = (0.3)(1.80 - 1.0)(110.0)(18.0)(9500)$

$= 4,514,400.0 \text{ t} \gg 250,000 \text{ t}$ , the given load, and hence safe.

(b) On clay:

As per Equation 4.38, the bearing capacity of a foundation is given by  $Q = (c_uN_c)(\text{area}) = (35.71)(5.00)(9500) = 1,696,225.0 \text{ t/m}^2 > 250,000 \text{ t}$  and hence safe.

(iii) Resistance to overturning:

(a) On sand:

Since relationships are not given for a circular foundation, an approximate procedure is followed by converting the circular foundation to an equivalent square foundation.

$$\text{Side of the square} = \sqrt{(9500)} = 97.5 \text{ m.}$$

Use Equation 4.42.  $F_{\text{vert}} = [\eta\gamma'BN_\gamma(1 - 2e)^2s_\gamma i_\gamma](\text{effective area})$ , where  $\text{area} = B'L$ .

$E = \text{eccentricity of load} = (M/F_{\text{v min}}) = (2.7)(1,000,000.0)/(180,000 - 12,000) = 16.07 \text{ m.}$

$$e = (16.07)/(97.5) = 0.1648$$

From Equation 4.41,

$$s_\gamma = [1 - (0.4)(B'/L)i_\gamma]$$

where  $s_\gamma = \text{correction factor for the shape of the structure;}$

$i_\gamma = [1 - (0.7)(F_{\text{hor}}/F_{\text{vert min}})]$ , where  $i_\gamma$  is the correction factor for the inclination of force, acting on the structure.

$$B' = B - 2E = 97.5 - (2.0)(16.07) = 65.36 \text{ m.}$$

$$i_\gamma = \{1.0 - (0.7)(57,000)/(168,000)\} = 0.7625.$$

$$s_\gamma = [1.0 - (0.4)(65.36)(0.7625)/(97.5)] = 0.7955.$$

$$F_{\text{vert}} = [(0.4)(0.800)(97.5)(18.0)\{1.0 - (2.0)(0.1648)\}^2(65.36)(97.5)]$$

$$= (561.6)(0.449)(6372.6) = 1,606,905 \text{ t} \gg 250,000 \text{ t, the applied vertical load on the structure.}$$

Hence, the structure is safe against overturning in sand.

(b) On stiff clay:

Use Equations 4.43 and 4.44.

Equation 4.44 is given by

$$s_c = 1 + 0.2(B'/L) \text{ and } i_c = (1 - \alpha/90)^2, \text{ with } \alpha = \arctg(F_{\text{hor}}/F_{\text{vertmin}})$$

$$s_c = 1.0 + (0.2)(65.36/97.5) = 1.0 + 0.1341 = 1.1341.$$

$$\alpha = \text{Arctg}(57,000/168,000) = 19.44^\circ.$$

Equation 4.43 gives the vertical resistance of the soil

$$= F_{\text{vert}} = [c_u N_c (1 - 2e) s_c i_c] (\text{effective area})$$

$$= (35.71)(5.00)\{1 - (2.0)(0.1648)\}(1.1341)\{(1.0 - (19.44/90))\}$$

$$= (178.55)(0.6704)(1.1341)(0.784)\{(65.36)(97.5)\}$$

$$= 678,231.5 \text{ t} > 250,000.0 \text{ t, the applied vertical load on the structure.}$$

Hence the platform is safe against overturning in stiff clay.

2. Depth of the skirt at the bottom of the foundation:

(i) For sand at the seabed:

The soil pressure at the bottom of the foundation is neglected.

The soil resistance, as the skirt foundation penetrates the soil, is given by Equation 4.33 as

$$F = \pi d e R_{p \max} + 2 \pi d h f_{\max}$$

where  $F$  = force opposing the penetration of  $m$  skirts in a single tank,  $R_{p \max}$  = maximum cone resistance of surface soil,  $f_{\max}$  = transverse frictional strength measured with a penetrometer,  $d$  = diameter of skirt,  $e$  = thickness of the skirt, and  $h$  = penetration of skirt into soil.

Assuming the height of skirt to be  $h_1$  meters,  $R_{p \max} = 400.0 \text{ t}$  for  $\phi' = 30^\circ$  (see Figure 4.13).

Also as per Table 4.2,  $f_{\max}/R_{p \max} = 4.0\%$  (for silts and sands).

Hence,  $f_{\max} = 16.0 \text{ t}$ .

Assume the thickness of skirt to be 3.0 cm (= 0.03 m). For a single tank, the vertical load carried is 13,000 t.

Using Equation 4.33,  $F = (\pi)(20.0)(0.03)(400.0) + (2)(\pi)(20.0)(h_1)(16.0) = 754.0 + 2010.6h_1 = 13,000.0$

$h_1 = 6.09 \text{ m}$ . This height can be reduced considerably if the bottom soil resistance is taken into account in the computations.

(ii) For stiff clay at the seabed:

From Table 4.11, undrained shear strength for clay =  $s_u = 50.0$  to  $100.0 \text{ t/m}^2$ . Take  $s_u = 50.0 \text{ t/m}^2$ . Also, as per Figure 4.14, for this clay,  $N_c = 12.0$  to  $14.0$ ; take  $N_c = 13.0$ .

Also as per Equation 4.3,  $R_p = N_c s_u + \gamma' z$ .



Consider the penetration of skirt to be  $h_1$  and thickness of skirt to be 0.03 m (as before). Also as per Table 4.2,  $f/R_p$  varies between 4% and 8%. Take the ratio to be 6.0%. As per Table 4.7,  $\gamma' = 1.40 \text{ t/m}^3$  (average). Hence,  $R_p = (13.0)(50.0) + (1.40)h_1 \sim 650.0 \text{ t/m}^2$ . Also  $f = (0.06)(650.0 + 1.40h_1) \sim 39.0 \text{ t/m}^2$ .

Therefore

$$\begin{aligned} F &= \pi d e R_{p_{\max}} + 2\pi d h f_{\max} = (\pi)(20.0)(0.03)(650.0) + (2.0)(\pi)(20.0)(h_1)(39.0) \\ &= 1,225.2 + 4900.9h_1 = 13,000.0 \text{ t.} \\ h_1 &= 2.403 \text{ m.} \end{aligned}$$

## EXERCISE PROBLEMS

- List five events that caught national/international attention and which were influenced by effects on marine soil.
- (a) Explain how two types of clays having the same chemical composition would have very different physical properties. (b) State which method you would choose to stabilize an expansive clayey soil: (i) drilling holes and filling them with quicklime; (ii) drilling holes and filling them with hydrated lime; or (iii) drilling holes and mixing hydrated lime with the soil, referred to as "hydrated lime."
- An undisturbed soil sample, whose weight is 55.0 N, is coated with paraffin and weighed in water by suspending it by a string to give a submerged weight of 26.0 N. If the sample contains 15% moisture and has a specific gravity of 2.65, compute the following soil properties: (i) wet density; (ii) dry density; (iii) void ratio; (iv) porosity; (v) degree of saturation; (vi) voids ratio; and (vii) percentage of solids.
- Discuss each of the following in detail: (a) moisture content in soil exceeding 100%; (b) the constituents of soil, which cause the moisture contents in soil to exceed 100%; and (c) the advantages of defining moisture content in soil in terms of dry weight rather than total weight.
- A plastic container filled with dry sand weighs more than a plastic container (of the same volume and weight) with wet sand. Give reasons for this.
- Direct shear tests was conducted on three samples of clay giving the results shown in Table P4.1. Draw the (direct) shear strength versus normal stress diagram, and determine the cohesion and the angle of internal friction. Determine the intrinsic stress in the soil.
- Triaxial compression tests were carried out on three identical cylindrical soil specimens, and the results are given in Table P4.2. (a) Draw the Mohr's circle diagram and determine (i) cohesion and (ii) angle of internal friction for the soil. (b) Compute for each specimen (i) failure angle; (ii) normal stress; (iii) shearing stress; and (iv) resultant stress on the failure plane.

---

**TABLE P4.1**  
**Stress at Failure for Direct Shear Tests**

Specimen #	Normal Stress at Failure (kPa)	Shearing Stress at Failure (kPa)
1	15.0	30.21
2	29.9	37.2
3	52.4	47.4

---

**TABLE P4.2**  
**Triaxial Compression Test Results**

Specimen #	Lateral Stress (kPa)	Axial Stress (kPa)
1	45.0	216.1
2	90.0	342.0
3	135.3	440.6

8. A vertical, cylindrical water tower standing in equilibrium on sand for nearly 40 years suddenly develops a severe rotation (or tilt) and is in danger of collapse. Prepare for a class discussion by developing at least three working hypotheses to explain the sudden tilt of the tower, and indicate what evidence should be gathered to test and verify each hypothesis. Which would you say is most plausible?
9. An expert witness for the other side in a lawsuit states that ocean soils are hard because they have been compacted by the weight of the water of the ocean standing above the soil level. Can you refute the statement in a form such that it can be understood by an ordinary layperson?
10. Porosity of saturated sea sand is 0.35 and the specific gravity of sand is 2.66. Determine (i) the void ratio ( $e$ ); (ii) the unit weight of sea sand ( $\gamma_T$ ); (iii) the submerged unit weight of sea sand ( $\gamma_b$ ); and (iv) the water content ( $w$ ).
11. A saturated sample of soil taken from the seabed has a volume of 1.0 ft.<sup>3</sup> and a weight of 128 lb. The specific gravity of soil particles is 2.75. (a) Assuming that the pores in the soil are filled with pure water, determine the water content ( $w$ ) and the void ratio ( $e$ ). (b) Assume that the pores in the saturated soil sample are filled with salt water of specific gravity 1.028. Determine the void ratio ( $e$ ) and the following ratios: (i)  $w_w/w_s$ ; (ii)  $(w_w + w_d)/w_s$ ; and (iii)  $w_w/(w_s + w_d)$ .
12. The following data were obtained for an undisturbed core sample of sandy soil (obtained above the water table level). The net weight of the sample was 450.0 g before drying and 395.0 g after drying. The core sample is 50.0 mm in diameter and has a height of 110.0 mm. If the specific gravity of solid grains in the core sample is equal to 2.68, compute (i) water content; (ii) porosity; (iii) void ratio; (iv) saturation percentage; and (v) bulk density.
13. The topsoil stratum at the seabed consists of clay to a depth of 20.0 ft. The average water content over this strata is 0.56, and the specific gravity of solid particles is 2.76. What is the vertical effective stress due to the clay stratum at its base?
14. A soil has the following vertical soil profile: (i) 0.0 to 3.0 m;  $\gamma_T = 17.28 \text{ kN/m}^3$ ; (ii) 3.01 to 7.50 m;  $\gamma_T = 14.93 \text{ kN/m}^3$ ; and (iii) 7.51 to 15.0 m;  $\gamma_T = 17.75 \text{ kN/m}^3$ . Taking the stress conditions to be geostatic, what is the vertical stress at a depth of 12.0 m?
15. A sample of dense dry sand is subjected to a triaxial test. The angle of internal friction is 35° and the confining pressure is 2.2 kPa. Determine the compressive stress at which the sample is likely to fail.
16. The time for a marine clay layer to achieve 99% consolidation was 12 years. What time would be required to achieve the same consolidation if the clay layer was (i) twice as thick? (ii) Four times more permeable? (iii) Two times more compressible?
17. Consolidation tests carried out on 25-mm-thick clay medium showed that the void ratio  $e_1$  at a consolidation pressure of 152.0 kPa was 1.22 and  $e_2$  at a consolidation pressure of 305.0 kPa was 1.056. The time required to obtain 50% consolidation was observed to be 12.0 min. At a certain location, the clay strata of the same material were found to be 10.0 m thick. Determine the time required for consolidation if water was drained from (i) top and bottom; and (ii) the top only.

18. Consolidated, undrained triaxial tests were conducted on two specimens of a silty soil, and the results obtained from the study are given in the following: test I— $\sigma_{1f} = 20.00$  psi,  $\sigma_{3f} = 10.50$  psi, and  $u_f = 7.40$  psi; and test II— $\sigma_{1f} = 38.00$  psi,  $\sigma_{3f} = 20.30$  psi, and  $u_f = 14.10$  psi. After plotting the stress circles based on total stresses and effective stresses, compute the strength parameters of (i) effective cohesive strength and (ii) effective friction angle.
19. Triaxial compressive tests were performed on two samples of a clayey soil, and the results are given as follows: test I— $\sigma_{1f} = 12.00$  psi,  $\sigma_{3f} = 7.60$  psi, and  $u_f = 5.20$  psi; and test II— $\sigma_{1f} = 18.20$  psi,  $\sigma_{3f} = 28.0$  psi, and  $u_f = 11.80$  psi. Compute the (i) effective cohesive strength and (ii) effective friction angle.
20. (a) During a standard penetration test on a sandy soil, the blow count was 20 blows/320 mm at a depth of 6.0 m. Compute the friction angle of the soil. (b) Suppose the blow count at a 12.0-m depth was exactly the same. Is the sand at 12.0 m looser or denser than the sand at 6.0 m? Give reasons for your answer. (c) If at a 6.0-m depth, the sand at two locations A and B had the same compactive effort (viz., the penetration was the same for the same blow counts) and that the sand at A had rounded particles and that at B had well-graded angular particles, determine which sand will have the larger (i) void ratio and (ii) friction angle.
21. The sand at the site of a tank structure has an average standard penetrometer blow count of 20 blows/305 mm. Design a footing to carry a load of 2000 kN with a maximum settlement of 60 mm and a minimum safety factor of 3 against shear failure.
22. Describe several seabed soil characteristics and structural characteristics that would influence (i) pile foundations and (ii) spread footing or raft foundations.
23. A circular area on the surface of an elastic mass of great extent carries a uniformly distributed load of 2800 lb./ft.<sup>2</sup>. The radius of the area over the load applied is 22.5 ft. Using Boussinesq's solution for a loaded elastic half-space (given in Figure 4.51), determine horizontal and vertical stresses at a point: (i) 12.0 ft. beneath the center of the loaded circle and (ii) located at the same depth but below the edge of the circular loaded area.
24. A rectangular footing, 6.0 ft. long and 4.5 ft. wide, with a depth of 3.0 ft. is embedded 2.0 ft. into the marine sediment. The total unit weight of the sediment is given as 106 lb./ft.<sup>3</sup>, effective cohesion as zero, effective friction angle = 23°, and  $A_f = 0.83$ . Determine (i) the ultimate bearing capacity of the footing at the end of the installation in the ocean site and (ii) the ultimate bearing capacity after the full consolidation has occurred. (Take the relevant bearing capacity coefficients from given tables in the textbook.)
25. A 1.0-m-diameter concrete spherical mass weighing 1300.0 kgf is dropped overboard into the ocean in deep water. Taking  $C_D$ , the coefficient of drag, to be equal to 0.5 (for Reynolds number values above 80,000), and the ultimate bearing resistance of the ocean sediment at the site to be 65.0 kN/m<sup>2</sup> (during the process of penetration of the sphere into the marine sediment at the site), estimate the penetration depth of the spherical mass. (Hint: Assume all the kinetic energy of the impacting sphere is absorbed by the penetration resistance of the soil.)
26. A concrete cylindrical structure with a diameter 20.0 m and height 40.0 m is placed in a bay at a water depth of 30.0 m. The contact pressure exerted by the cylinder is determined to be equal to 30.0 kPa. The soil at the site is a clayey soil of unit weight 19.0 kN/m<sup>3</sup>, with a clay layer depth = 20.0 m, coefficient of consolidation = 1.95 m<sup>2</sup>/year, initial void ratio = 1.15, and compression index = 0.82. Use the data given in Figure 4.51.
27. A cylindrical loaded area, produced by the footprint of the base of a cylindrical structure, is located at the seabed, located 20.0 ft. below the msl. There is a layer of 30.0-ft-thick clay strata lying below the footprint of the habitat, and this layer of clay is underlain by a sandy strata. (a) Assuming that the base of the structure is flexible, and that the distributed load on the footprint is 200 lb./ft.<sup>2</sup>, determine the final settlement at the center and edge of the habitat. (b) If the clayey layer is 60.0 ft. thick, determine the consolidation settlement of the habitat, at its center and at its edge.

28. A saturated sample of soil on the sea bottom is carefully scooped into an 18-in.<sup>3</sup> box by a diver. The undrained sample weighs 1.25 lbs. It is then oven-dried and the weight reduces to 0.91 lb. (a) Find  $\gamma_T$ ,  $\gamma_b$ ,  $G$ ,  $n$ , and  $e$ . (b) What is the stress on an object that is under 7.0 ft. of this soil with the objects' bottom at 12.0 ft. below this soil?
29. Illustrate (with sketches) and explain the following: (i) bearing capacity of a foundation soil; (ii) gross and net bearing capacities; (iii) differential settlement; and (iv) factors of safety with respect to bearing failure.
30. Distinguish between each of the following: (i) a caisson, a pier, and a pile; (ii) friction, end-bearing, and compaction piles (with sketches); (iii) materials used for deep foundation piles; and (iv) bored-and-belled piles.

## REFERENCES

1. N.D.P. Barltrop and A.J. Adams, 1991. Dynamics of fixed marine structures, in: *Foundations*, Butterworth Heinemann Ltd., Oxford, UK, p. 172.
2. A.C. Duxbury and A.B. Duxbury, 1991. *An Introduction to the World's Oceans*, William C. Brown Publishers, Dubuque, IA, pp. 67–68.
3. A.C. Duxbury and A.B. Duxbury, 1991. *An Introduction to the World's Oceans*, William C. Brown Publishers, Dubuque, IA, p. 58.
4. A.C. Duxbury, 1971. *The Earth and Its Oceans*, Addison-Wesley Publishing Company, Reading, Boston, MA, p. 99.
5. B. McClelland and M.D. Reifel, 1986. *Planning and Design of Fixed Offshore Platforms*, Van Nostrand Reinhold Company, New York, p. 163.
6. B. McClelland and M.D. Reifel, 1986. *Planning and Design of Fixed Offshore Platforms*, Van Nostrand Reinhold Company, New York, p. 167.
7. B. McClelland and M.D. Reifel, 1986. *Planning and Design of Fixed Offshore Platforms*, Van Nostrand Reinhold Company, New York, p. 172.
8. B. McClelland and M.D. Reifel, 1986. *Planning and Design of Fixed Offshore Platforms*, Van Nostrand Reinhold Company, New York, p. 171.
9. A.C. Duxbury, 1971. *The Earth its Oceans*, Addison-Wesley Publishing Company, Reading, Boston, MA, p. 105.
10. P. Le Tirant, 1979. *Seabed Reconnaissance and Offshore Soil Mechanics*, Editions Technip 27, Paris, France, pp. 110–119.
11. P. Le Tirant, 1979. *Seabed Reconnaissance and Offshore Soil Mechanics*, Editions Technip 27, Paris, France, p. 206.
12. P. Le Tirant, 1979. *Seabed Reconnaissance and Offshore Soil Mechanics*, Editions Technip 27, Paris, France, p. 207.
13. P. Le Tirant, 1979. *Seabed Reconnaissance and Offshore Soil Mechanics*, Editions Technip 27, Paris, France, p. 213.
14. P. Le Tirant, 1979. *Seabed Reconnaissance and Offshore Soil Mechanics*, Editions Technip 27, Paris, France, p. 208.
15. N.D.P. Barltrop and A.J. Adams, 1991. Dynamics of fixed marine structures, in: *Foundations*, Butterworth Heinemann Ltd., Oxford, UK, p. 188.
16. P. Le Tirant, 1979. *Seabed Reconnaissance and Offshore Soil Mechanics*, Editions Technip 27, Paris, France, p. 227.
17. P. Le Tirant, 1979. *Seabed Reconnaissance and Offshore Soil Mechanics*, Editions Technip 27, Paris, France, p. 229.
18. P. Le Tirant, 1979. *Seabed Reconnaissance and Offshore Soil Mechanics*, Editions Technip 27, Paris, France, p. 240.
19. P. Le Tirant, 1979. *Seabed Reconnaissance and Offshore Soil Mechanics*, Editions Technip 27, Paris, France, p. 241.
20. B.C. Gerwick, Jr., 1999. *Construction of Marine and Offshore Structures*, CRC Press, Boca Raton, FL, p. 49.
21. D.P. Coduto, 1999. *Geotechnical Engineering: Principles and Practices*, Prentice Hall, Upper Saddle River, NJ, p. 104.

22. P. Le Tirant, 1979. *Seabed Reconnaissance and Offshore Soil Mechanics*, Editions Technip 27, Paris, France, p. 264.
23. P. Le Tirant, 1979. *Seabed Reconnaissance and Offshore Soil Mechanics*, Editions Technip 27, Paris, France, p. 265.
24. P. Le Tirant, 1979. *Seabed Reconnaissance and Offshore Soil Mechanics*, Editions Technip 27, Paris, France, p. 268.
25. P. Le Tirant, 1979. *Seabed Reconnaissance and Offshore Soil Mechanics*, Editions Technip 27, Paris, France, p. 269.
26. P. Le Tirant, 1979. *Seabed Reconnaissance and Offshore Soil Mechanics*, Editions Technip 27, Paris, France, p. 270.
27. P. Le Tirant, 1979. *Seabed Reconnaissance and Offshore Soil Mechanics*, Editions Technip 27, Paris, France, p. 272.
28. T.W. Lambe and R.V. Whitman, 1979. *Soil Mechanics*, John Wiley & Sons, New York, p. 30.
29. P. Le Tirant, 1979. *Seabed Reconnaissance and Offshore Soil Mechanics*, Editions Technip 27, Paris, France, pp. 7–9.
30. W. Lambe and R.V. Whitman, 1979. *Soil Mechanics*, John Wiley & Sons, New York, pp. 29–32.
31. N.D.P. Barltrop and A.J. Adams, 1991. Dynamics of fixed marine structures, in: *Foundations*, Butterworth Heinemann Ltd., Oxford, UK, p. 182–190.
32. H. Schenck, Jr., 1975. *Introduction to Ocean Engineering*, McGraw-Hill Book Company, New York, pp. 48–51.
33. W. Lambe and R.V. Whitman, 1979. *Soil Mechanics*, John Wiley & Sons, New York, p. 30.
34. K. McSweeney and S. Grunwald, 1999. Primary components of (marine) soils, *Web-Based Notes*, p. 325. Available at <http://www.soils.wisc.edu/courses/SS325/soilscience325.html>.
35. W. Lambe and R.V. Whitman, 1979. *Soil Mechanics*, John Wiley & Sons, New York, p. 73.
36. N.D.P. Barltrop and A.J. Adams, 1991. Dynamics of fixed marine structures, in: *Foundations*, Butterworth Heinemann Ltd., Oxford, UK, p. 183.
37. W. Lambe and R.V. Whitman, 1979. *Soil Mechanics*, John Wiley & Sons, New York, pp. 52–56.
38. W. Lambe and R.V. Whitman, 1979. *Soil Mechanics*, John Wiley & Sons, New York, p. 33.
39. A. Casagrande, 1948. Classification of soils, *Transactions ASCE*, Volume 113, pp. 901–992.
40. P. Le Tirant, 1979. *Seabed Reconnaissance and Offshore Soil Mechanics*, Editions Technip 27, Paris, France, p. 11.
41. H. Schenck, Jr., 1975. *Introduction to Ocean Engineering*, McGraw-Hill Book Company, New York, p. 52.
42. K. Terzaghi, 1936. *Stability of slopes in natural clay*, Proceedings of first International Conference on Soil Mechanics, Cambridge, MA, pp. 161–165.
43. A.W. Bishop and A.K. Eldin, 1950. Undrained triaxial test on ...shear strength, *Geotechnique*, Volume 2, pp. 13–32.
44. H. Schenck, Jr., 1975. *Introduction to Ocean Engineering*, McGraw-Hill Book Company, New York, p. 53.
45. H. Schenck, Jr., 1975. *Introduction to Ocean Engineering*, McGraw-Hill Book Company, New York, p. 54.
46. P. Le Tirant, 1979. *Seabed Reconnaissance and Offshore Soil Mechanics*, Editions Technip 27, Paris, France, p. 17.
47. W. Lambe and R.V. Whitman, 1979. *Soil Mechanics*, John Wiley & Sons, New York, p. 120.
48. W. Lambe and R.V. Whitman, 1979. *Soil Mechanics*, John Wiley & Sons, New York, p. 118.
49. W. Lambe and R.V. Whitman, 1979. *Soil Mechanics*, John Wiley & Sons, New York, p. 119.
50. P. Le Tirant, 1979. *Seabed Reconnaissance and Offshore Soil Mechanics*, Editions Technip 27, Paris, France, p. 15.
51. H. Schenck, Jr., 1975. *Introduction to Ocean Engineering*, McGraw-Hill Book Company, New York, p. 62.
52. A.W. Skempton and L. Bjerrum, 1957. A contribution to the settlement analysis of foundations on clay, *Geotechnique*, Volume 7, pp. 168.
53. P. Le Tirant, 1979. *Seabed Reconnaissance and Offshore Soil Mechanics*, Editions Technip 27, Paris, France, p. 18.
54. N.D.P. Barltrop and A.J. Adams, 1991. Dynamics of fixed marine structures, in: *Foundations*, Butterworth Heinemann Ltd., Oxford, UK, p. 182.
55. P. Le Tirant, 1979. *Seabed Reconnaissance and Offshore Soil Mechanics for the Installation of Petroleum Structures*, Editions Technip 27, Paris, France, p. 23.



56. P. Le Tirant, 1979. *Seabed Reconnaissance and Offshore Soil Mechanics*, Editions Technip 27, Paris, France, p. 24.
57. H. Schenck, Jr., 1975. *Introduction to Ocean Engineering*, McGraw Hill Book Company, New York, p. 54–57.
58. H. Schenck, Jr., 1975. *Introduction to Ocean Engineering*, McGraw Hill Book Company, New York, p. 56.
59. N.D.P. Barltrop and A.J. Adams, 1991. Dynamics of fixed marine structures, in: *Foundations*, Butterworth Heinemann Ltd., Oxford, UK, p. 184.
60. H.B. Seed and I.M. Idriss, 1970. Soil moduli and damping factors, Report # EERC 70-10, Earthquake Engineering Research Center, University of California, Berkeley, CA.
61. N.D.P. Barltrop and A.J. Adams, 1991. Dynamics of fixed marine structures, in: *Foundations*, Butterworth Heinemann Ltd., Oxford, UK, p. 185.
62. N.D.P. Barltrop and A.J. Adams, 1991. Dynamics of fixed marine structures, in: *Foundations*, Butterworth Heinemann Ltd., Oxford, UK, p. 187.
63. N.D.P. Barltrop and A.J. Adams, 1991. Dynamics of fixed marine structures, in: *Foundations*, Butterworth Heinemann Ltd., Oxford, UK, p. 189.
64. N.D.P. Barltrop and A.J. Adams, 1991. Dynamics of fixed marine structures, in: *Foundations*, Butterworth Heinemann Ltd., Oxford, UK, p. 196.
65. H. Kuhn, 1988. Tests extend range for underwater pile driving, *Ocean Industry*, pp. 42–47.
66. P. Le Tirant, 1979. *Seabed Reconnaissance and Offshore Soil Mechanics for the Installation of Petroleum Structures*, Editions Technip 27, Paris, France, p. 291.
67. B. McClelland and M.D. Reifel, 1986. *Planning and Design of Fixed Offshore Platforms*, Van Nostrand Reinhold company, New York, p. 765.
68. N.D.P. Barltrop and A.J. Adams, 1991. Dynamics of fixed marine structures, in: *Foundations*, Butterworth Heinemann Ltd., Oxford, UK, p. 212.
69. N.D.P. Barltrop and A.J. Adams, 1991. Dynamics of fixed marine structures, in: *Foundations*, Butterworth Heinemann Ltd., Oxford, UK, p. 213.
70. P. Le Tirant, 1979. *Seabed Reconnaissance and Offshore Soil Mechanics for the Installation of Petroleum Structures*, Editions Technip 27, Paris, France, p. 298.
71. J.M. Girard, 1975. Battage des piles, Forages, Bulletin # 68, July–September.
72. N.D.P. Barltrop and A.J. Adams, 1991. Dynamics of fixed marine structures, in: *Foundations*, Butterworth Heinemann Ltd., Oxford, UK, p. 217–221.
73. P. Le Tirant, 1979. *Seabed Reconnaissance and Offshore Soil Mechanics for the Installation of Petroleum Structures*, Editions Technip 27, Paris, France, p. 312–326.
74. P. Le Tirant, 1979. *Seabed Reconnaissance and Offshore Soil Mechanics for the Installation of Petroleum Structures*, Editions Technip 27, Paris, France, p. 314.
75. API – RP2A, 1974. *Recommended Practice for Planning, Designing and Construction of Fixed Offshore Platforms*, Fifth Edition, January. (Also see API – RP2A – LRFD), 1993, p. 67.
76. J.N. Gaythwaite, 1990. *Design of Marine Facilities for the Berthing, Mooring, and Repair of Vessels*, Van Nostrand Reinhold, New York, pp. 247–248.
77. P. Le Tirant, 1979. *Seabed Reconnaissance and Offshore Soil Mechanics for the Installation of Petroleum Structures*, Editions Technip 27, Paris, France, p. 345.
78. P. Le Tirant, 1979. *Seabed Reconnaissance and Offshore Soil Mechanics for the Installation of Petroleum Structures*, Editions Technip 27, Paris, France, p. 349.
79. J. Boussinesq, 1885. *Application des Potentials a L'Etude de L'Equilibre et du Mouvement des Solides Elastiques*, Gauthier-Villars, Paris.
80. Rocscience Inc., 2007–2009. *Settle3D – Three dimensional Settlement for Foundations, Stress Analysis Verif. Manual*. Available at [http://www.rocscience.com/downloads/settle3d/webhelp/pdf\\_files/verification/Settle3D\\_Stress\\_Verification.pdf](http://www.rocscience.com/downloads/settle3d/webhelp/pdf_files/verification/Settle3D_Stress_Verification.pdf).
81. P. Le Tirant, 1979. *Seabed Reconnaissance and Offshore Soil Mechanics for the Installation of Petroleum Structures*, Editions Technip 27, Paris, France, p. 355.
82. P. Le Tirant, 1979. *Seabed Reconnaissance and Offshore Soil Mechanics for the Installation of Petroleum Structures*, Editions Technip 27, Paris, France, p. 356.
83. P. Le Tirant, 1979. *Seabed Reconnaissance and Offshore Soil Mechanics for the Installation of Petroleum Structures*, Editions Technip 27, Paris, France, p. 358.
84. P. Le Tirant, 1979. *Seabed Reconnaissance and Offshore Soil Mechanics for the Installation of Petroleum Structures*, Editions Technip 27, Paris, France, p. 357.
85. Det Norske Veritas, 1974. *Rules for the Design, Construction and Inspection of Fixed Offshore Structures*.

86. J.B. Hansen, 1973. A general formulae for bearing capacity, *Geotechnical Bulletin*, Volume 5, Issue 11.
87. N.D.P. Barltrop and A.J. Adams, 1991. Dynamics of fixed marine structures, in: *Foundations*, Butterworth Heinemann Ltd., Oxford, UK, p. 207.
88. P. Le Tirant, 1979. *Seabed Reconnaissance and Offshore Soil Mechanics for the Installation of Petroleum Structures*, Editions Technip 27, Paris, France, p. 377.
89. N.D.P. Barltrop and A.J. Adams, 1991. Dynamics of fixed marine structures, in: *Foundations*, Butterworth Heinemann Ltd., Oxford, UK, p. 206.
90. P. Le Tirant, 1979. *Seabed Reconnaissance and Offshore Soil Mechanics for the Installation of Petroleum Structures*, Editions Technip 27, Paris, France, p. 379.
91. N.D.P. Barltrop and A.J. Adams, 1991. Dynamics of fixed marine structures, in: *Foundations*, Butterworth Heinemann Ltd., Oxford, UK, p. 207.



---

# 5 Materials and Their Behavior in the Ocean Environment

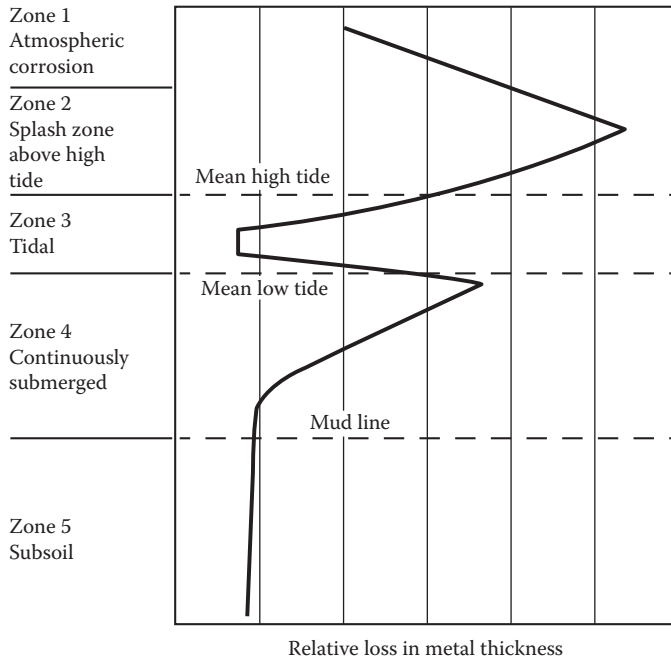
## 5.1 MATERIAL REQUIREMENTS FOR OFFSHORE STRUCTURES

### 5.1.1 INTRODUCTION

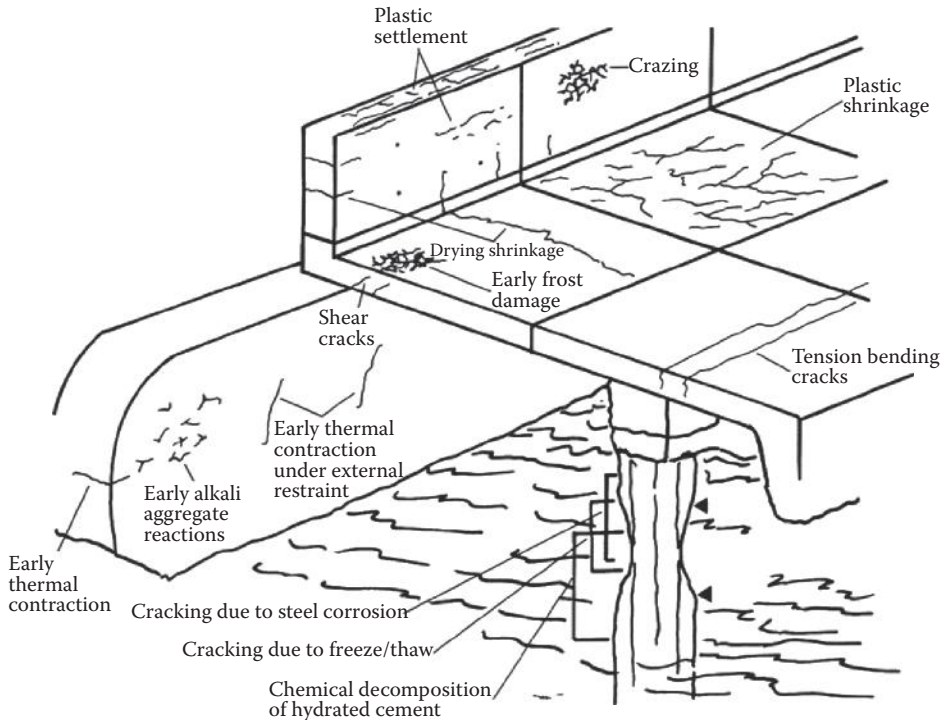
Modern offshore structures, including ships, require high-strength structural girders/plates/tubulars/shells and other lightweight structural components, over large portions of the structural envelope for weight reduction, better stability, increased payload, increased mobility, and survivability. During their service lives, offshore structures are subject to a complex spectrum of loads and degenerative environments, and the structural and the joining materials used in the structural/hull fabrication must possess high durability and fracture toughness under these extreme conditions. The expected dynamic/other loads in service include wave loading, sea slap, slamming, water current load, structural vibration, thermal variation effects (in both tropical and Arctic seas), structural/cargo buoyancy, aircraft/helicopter landing impacts, and accidental/incidental fire hazard and impacts/explosions. The integrity of these structures must be assured for continuous ocean operation under these adverse and severe corrosive environments, as well as in their response to the effects of accidental/incidental fire/collisions/explosions.

Ocean structures are subjected to a number of deteriorating influences throughout their lifetime; the extent of deterioration depends on the properties of seawater and its seasonal variation, tidal/wave-height ranges, and type of materials used in the construction. Figure 5.1 [1] shows the effects of relative immersion of the steel ocean structures in seawater with regard to its vertical height. Marine atmosphere over the ocean contains some small amount of salt, which tends to corrode the steel ocean structures exposed to it. The splash zone, consisting of the region from the mean high water (MHW) level and the upper level attained by spray, is subjected to alternate wetting and drying, and consequently experiences the highest amount of corrosion degradation. The corrosion degradation is the least in the tidal variation level. Below the tidal level, the corrosion is from moderate to light, depending on the aeration of seawater and the biological growth on the structure. At the seabed level of the ocean structure, sometimes the corrosion may be higher due to the presence of sulfate-reducing bacterial (SRB) action on the oil sludge that may be deposited at its bottom.

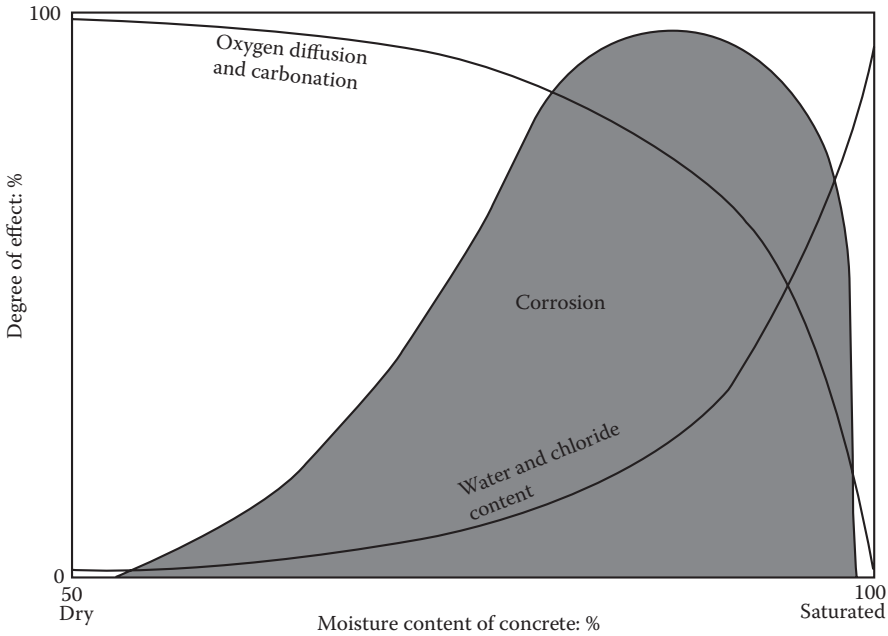
Figure 5.2 [2] gives more details regarding various deterioration mechanisms that function in the breakdown of marine concrete structures. The types of degradation experienced by concrete structures are those due to alternate wetting and drying resulting in corrosion of reinforcement (due to chloride intrusion and carbonation), freeze–thaw in cold oceans, salt scaling resulting from deicing salts or ocean spray, and chemical/biological action on structural concrete surface exposed to alternate wetting/drying and aeration. The amount of corrosion degradation, occurring in concrete structures due to concrete–steel interaction, is clearly illustrated in Figure 5.3 [3]. Another degradation that occurs in steel offshore structures is the cracking due to material fatigue experienced by steel offshore structures as a consequence of the randomly cycling wave loads exerted on the structural members; usually, the cracking in structures occurs at locations of the highest stress concentration, as shown in Figure 5.4 [4]. This cracking of material is enhanced by the corrosive action of the structure in seawater.



**FIGURE 5.1** Five zones of corrosion on steel in seawater. (From R. Reuben, 1990, Corrosion and defect evaluation, Chapter 10, in *Marine Technology Reference Book*, ed. N. Morgan, Butterworths, London.)



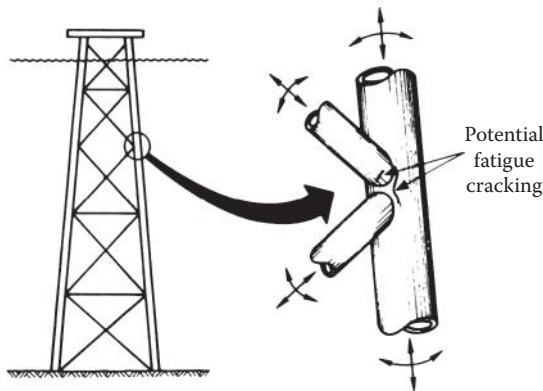
**FIGURE 5.2** Types of deterioration in marine concrete. (With kind permission from Springer Science+Business Media: *Materials in Marine Technology*, Marine corrosion and bio-deterioration [Chapter 3], 1994, p. 60, R. Reuben.)



**FIGURE 5.3** Influence of moisture on corrosion of reinforcement bars in concrete. (From M.B. Leeming, Durability of Concrete in and near the Sea [Chapter 3], in *Concrete in Coastal Structures* [Ed. R.T.L. Allen], Thomas Telford, London, p. 79, 1998. With permission.)

The integrity, durability, and fracture safety of offshore structures are addressed through the use of suitable structural and joining materials for hull fabrication that demonstrate high durability, fracture toughness, corrosion resistance, and flaw tolerance for these extreme service conditions [5, 6]. In addition, the key requirements for offshore structural steels and other materials are also driven by economics, in order to keep an affordable structural acquisition cost. These factors can be easily visualized in the case of a naval warship, subjected to an explosive shock and possible fire events, as shown in Figure 5.5 [6].

In a perfect world, material engineers and corrosion/other specialists would always assist designers with material selection tasks to ensure that components and systems are designed with longevity in mind. However, in the real world, this is not found to be always true. Designers typically select the materials of construction themselves, with these decisions based on meeting critical performance



**FIGURE 5.4** Hot spots in offshore structures susceptible to fatigue damage. (J.F. Wilson: Dynamics of Offshore Structures, p. 450, 1984. Copyright Wiley-VCH Verlag GmbH & Co. KGaA. Reproduced with permission.)



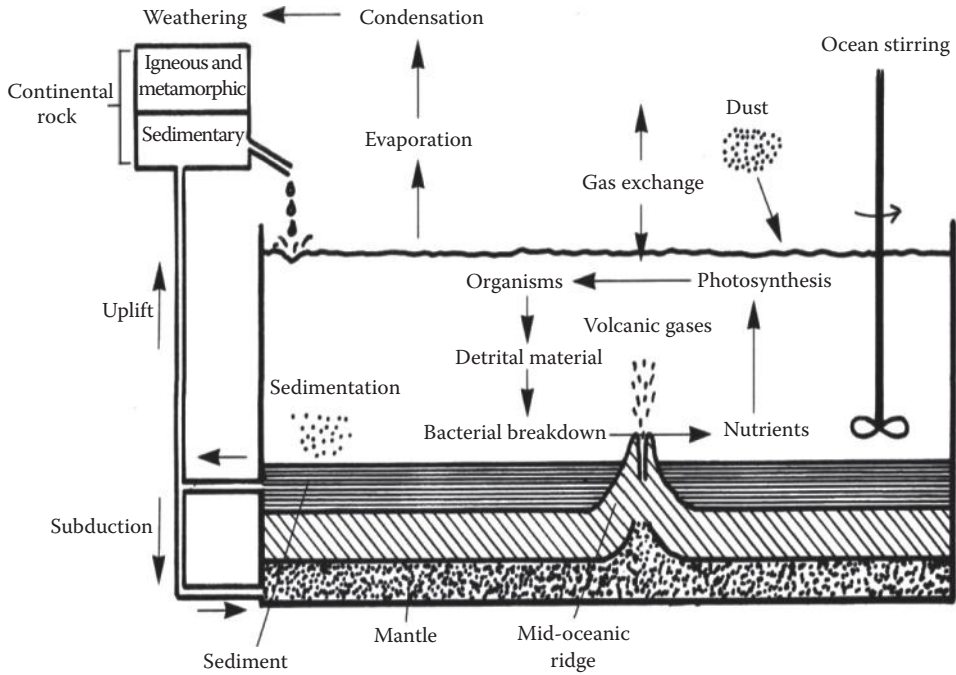
**FIGURE 5.5** Naval shipbuilding materials require strength, weldability, fire resistance, and fracture toughness under sudden explosive shock loads. (From E.J. Czyryca et al., 2003, Meeting the challenge of higher and lighter warships, *Advanced Materials and Processes Technology Information Analysis Center [AMPTIAC] Quarterly*, Vol. 7, # 3, pp. 63–70.)

requirements. Other factors such as corrosion/fire prevention and control are often given minimal consideration.

For instance, a material's inherent corrosion resistance is largely determined by its elemental composition; in addition, it is also influenced by its processing history, surface morphology, geometry, and, in some cases, its size. As a consequence, two very similar materials may have quite different resistances to corrosion; to minimize this effect, a large number of factors would have to be considered, and there will be no single path to making the most efficient selection. Ultimately, designers are left to their best "engineering judgment" to select the optimum material, considering corrosion resistance in addition to other performance requirements, and other tangible factors, which would include cost, availability, and maintainability. It is important to realize that one will seldom find the "perfect" choice, since most affordable commercial materials will corrode under the right set of conditions. As a result, designers would be forced to choose the best material and associated corrosion prevention/control practices that would meet the project's budgetary constraints, while also ensuring acceptable corrosion resistance over the structure's life cycle. Reasonable (and budgeted) life cycle costs and high readiness rates (due to reduced maintenance requirements) are two of the most important contributions to lower operating costs, while ensuring long service life of the structure and its safety. Regular maintenance will reduce the possibility of a material failure due to extreme operating environments. For instance, the durability of a material that is susceptible to corrosion in a marine environment (both steel and concrete) could be enhanced if the deposited salt is periodically washed off. Generally, it is good to develop a maintenance plan before the system is put into service.

### 5.1.2 OCEAN ENVIRONMENT AND MATERIALS

A structural designer should become aware that the ocean environment is quite different from that of the land in its chemical, biological, and physical nature. The chemical composition of ocean water can vary substantially according to the season as well as its geographic location; these variations are due to the modifying influences of rock weathering, riverine transport and sedimentation, water precipitation and evaporation, photosynthesis, seismic upheaval, and biological activities, which work relentlessly to modify the large body of water called ocean. These effects are illustrated in Figure 5.6 [7], which shows the effects of river discharge into the oceans and the consequent sedimentation of suspended particles, biological activity in the ocean, and seismic uplift/subduction effects of the ocean bed.



**FIGURE 5.6** Schematic description. (With kind permission from Springer Science+Business Media: *Materials in Marine Technology*, Marine structures and the role of materials technology [Chapter 1], 1994, p. 2, R. Reuben.)

**5.1.2.1 Ocean Water Chemistry**

Table 5.1 [5–10] shows the chemical composition of ocean water in different parts of the world, with the seawater from the Middle East showing higher chloride, sulfate, and sodium ion concentrations. The amounts of some salts vary sizably from one location to the other, depending primarily on the composition of the weathering rocks.

**TABLE 5.1**  
**Chemical Composition of Ocean Water (mg/L)**

Constituent	In Typical Seawater	In Seawater at Eastern Mediterranean	In Seawater at Arabian Gulf at Kuwait	In Seawater at Red Sea at Jeddah
Hydrogen	110.00	110.00	110.00	110.00
Oxygen	883.00	883.00	883.00	883.00
Chloride	18.98	21.20	23.00	22.22
Sodium	10.56	11.80	15.85	14.26
Magnesium	1.26	1.40	1.77	0.74
Calcium	0.40	0.42	0.50	0.23
Potassium	0.38	0.46	0.46	0.21
Strontium	0.01	—	—	—
Bromide	0.07	0.16	0.08	0.07
Sulfate	2.65	2.95	3.20	3.08
Bicarbonate	0.14	—	0.14	0.15
Borate	0.03	0.07	—	—
Total dissolved solids (salinity)	34.48	38.60	45.00	41.00

From the engineering point of view, the most important chemical properties of the ocean are its salinity, pH, dissolved oxygen content, and temperature; these properties also affect the biological activity and its intensity in the ocean. Salinity of seawater is the total amount of dissolved solids in parts per thousand (‰ or ppt) by weight in a water sample. Salinity (average) of the ocean is around 35 ppt; usually, it varies from a minimum of 31 to 36 ppt, but at some relatively enclosed sea locations, it may be as high as 45 ppt, as indicated in Table 5.1. Salinity has a major effect on the corrosion of steel specimens in seawater; it also affects the speed of propagation of sound, seawater density, and the buoyant forces exerted on ocean structures. Salinity affects the corrosivity of seawater by increasing its conductivity, thus exposing large areas of ocean structures to electrolytic contact. Another important factor affecting the corrosivity of seawater is the oxygen content of saltwater, which substantially increases the corrosion rates of carbon steels; even other metals such as stainless steels do not perform well in poorly aerated waters (due to oxygen depletion and less noble potential, explained later under galvanic series). Studies carried out in the USA have indicated that nearly 3.14% of GDP is spent annually in remedying the effects of corrosion on structures. In order to reduce these costs, advanced composites have been recently used in offshore structures owing to their higher stiffness-to-weight ratio, greater endurance under cyclic loading, and resistance to chemical attack, resulting in better corrosion resistance. A significant concern in the use of composite materials in offshore structures is the decreased fire resistance of composite materials.

#### 5.1.2.2 Biological Considerations

Biological activity in the vicinity of ocean structures, in terms of fouling, is of importance to their durability. Fouling can be defined as the accumulation of marine fauna and flora on the accessible, immersed, and partially exposed surfaces of ocean structures. Fouling can occur due to a variety of organisms comprising the families of Algae, Coelenterates (Hydrozoas and Anthozoas), Annelidae, Arthropoda, and Mollusca. The type and degree of fouling vary with the season (depending on the temperature), water depth, changes in seawater properties, species abundance, and so on. In the Tropics, typically hard mussel fouling may be 0.30 m or thicker, and the apparent mass and the projected area may be as much as double that of the original one. It has been observed that a 0.05-m increase in thickness of fouling resulted in a 5.0% increase in the overall loads, exerted on a typical offshore platform. Bio-fouling can have few or significant effects on the durability of ocean structures. The effects of fouling are (i) increased structural loading depending on the size of biological growth on the structure (caused by increased drag and inertial wave loads and gravity loads), (ii) increased corrosion rates due to destruction of protective coatings and the increased oxygen concentration half-cell effects at the point of attachment of marine organisms such as barnacles, (iii) abrasion and possible severance of cable lines, (iv) general bio-deterioration due to the direct deteriorating effects of organisms such as *Enteromorpha* (an algae), *Tubularia* species (one type of hydroid colony), *Anomidae* and *Hiatella Arctica* (mollusks), *Proteobacteria* and *Thermodesulfobacteria* (which are SRB) and the like, and (v) deposition of hard-to-remove calcium on the outside structural surface due to prolific growths of corals and tubeworms [11, 12]. Clogging of water filters (at the micro level) and water intakes (at the macro level) would also cause problems to offshore structures. While the presence of offshore structures has been found to have a beneficial effect on the local ecology (increased fish catches near such structures), they can also be harmful to the ecology of the site.

#### 5.1.2.3 Marine Atmosphere

The constituents of the marine atmosphere will impact mainly the corrosion aspects of the above-sea-level exposed surfaces of ocean structures. The principal constituents of the marine atmosphere that will contribute to corrosion are the temperature, amount of moisture in wind that will tend to condense, and the salt content of windborne spray; the amount of airborne pollutants such as carbon dioxide and sulfur dioxide could also contribute negatively to the corrosion of ocean structures. The wind velocity would also contribute to the increase of loads exerted on ocean structures;



according to Reuben [13], wind forces account for 15.0% of the total fluid loading on ocean structures, and the overturning moments on floating structures may be much higher on floating ocean structures.

### 5.1.3 DEVELOPMENT OF MATERIALS FOR OCEAN STRUCTURES

As outlined in Chapter 1, a number of structures have been utilized in the ocean, both to exploit its oil and mineral resources and to transport different goods from the area of production/dispatch to the area of delivery. Starting from fixed steel/concrete ocean structures to the floating semi-submersibles/ships, and to the ocean-bottom-laid pipelines, a variety of materials have been used in their fabrication. Selection of materials plays an important role in the design, construction, and operation of these ocean structures. Even though steel and concrete are the most common and economical materials used in structural fabrications, aluminum, titanium, stainless steels, and composites have also been used in ocean structures. Recently, ocean structural designers have developed new structural forms and automated construction procedures that optimize the fabrication/delivery times required for such structures. High yield strength steels of 400 to 700 MPa have been used in the fabrication of such ocean structures; they also require more lightweight metals and structural composites. These high-strength steels and other materials used in the structural design should meet significant toughness and formability (such as rolling, welding, and other joining) requirements, especially at cold temperatures.

Basic strength, weldability, fracture toughness, and forming characteristics for metals are to be satisfied in the construction phase of ocean structures. Then there are additional parameters that dictate the structure's eventual performance, such as weight, shock loads, vibration, fracture toughness in environmental extremes, and fire performance during their operation phase. Since these two aspects of a structure's life are governed by different needs in terms of material performance, they are treated separately, knowing that neither operation of the structure nor its construction can be examined independently. Most of the ocean structures are constructed of steel or concrete, except for a few special-purpose ships that have structures above the waterline fabricated of aluminum and more recently of glass reinforced polymer (GRP) composites.

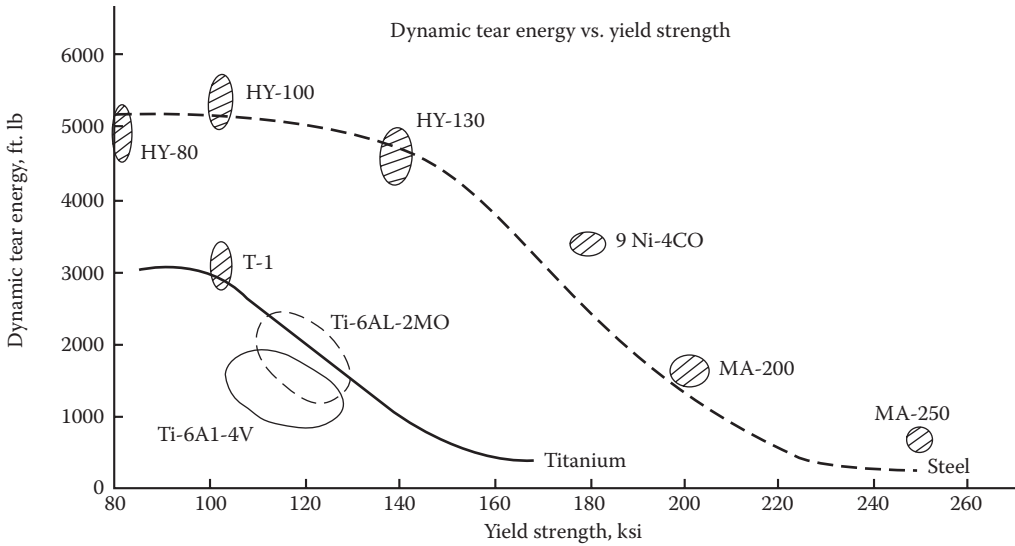
#### 5.1.3.1 Material Issues Relating to Construction Phase

It should be borne in the mind of the designer that all the material parameters considered during the construction phase will also impact the operational characteristics downstream. For instance, the time and procedures required to weld or join the various structural components together can lead to major cost overruns during the construction of an ocean structure. Hence, there will be a significant effort made to reduce these cost overruns by considering alternate scenarios; therefore, the weldability (or joinability) of the various structural components to form the requisite structure can become very critical. Moreover, if welds/joints are not done carefully while minimizing the costs, they can become potential sites for initiation and growth of flaws/cracks and will thus critically impact the service performance of the vessel in operation.

##### 5.1.3.1.1 Strength

The overall size of any structure is often a function of the strength of its component materials. In the case of ships, high-strength steels with yield stresses ranging from 350 to 900 MPa (50 to 130 ksi) are typically used, as shown in Figure 5.7 [14]; the plot shows the drop test (DT) tear energy as a function of material strength for steel and titanium alloys. Figure 5.8 [15] shows an additional facet of the DT tear energy as a function of strength and temperature. It is observed from these two figures that as the strength of steel increases, the tear energy of the material is reduced considerably; in addition, as the temperature of the material is reduced, the ductility of the metal also reduces along with a corresponding decrease in the tear energy of the material, as well as its fracture resistance (as indicated in Figure 5.8). Generally, a major portion of a ship's structure will be made from 350

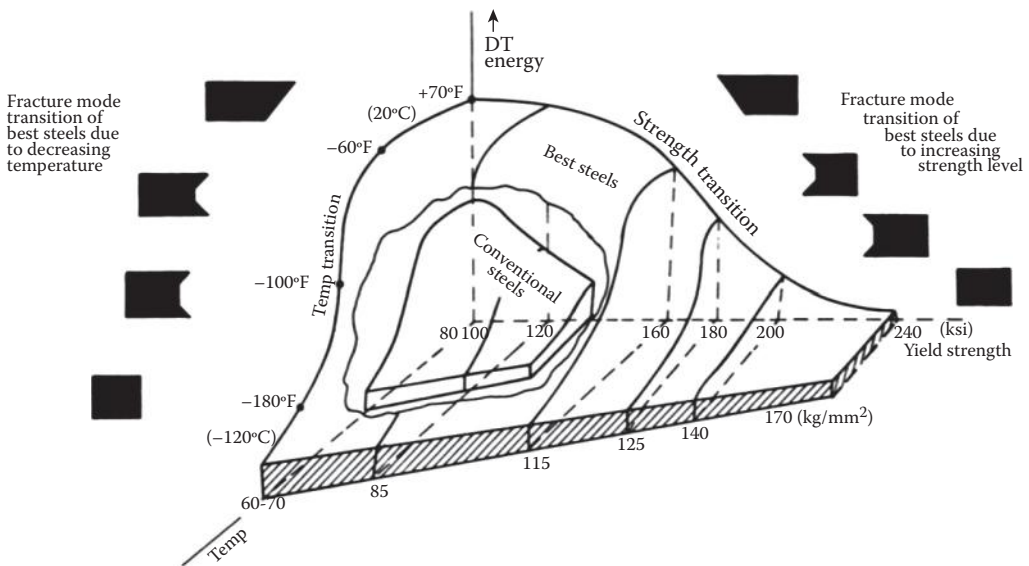




**FIGURE 5.7** Approximate correlation between tear energy and yield strength for steel and titanium alloys. (From H. Sheets, 1975, Selection of materials for ocean application, Chapter 6, *Introduction to Ocean Engineering*, ed. H. Schenck, Jr., McGraw-Hill Book Company, New York.)

to 560 MPa (50 or 80 ksi) yield stress steel, with critical areas making use of stronger grades of steel as needed. Lighter alloys of aluminum could be used for topside structures; recently, structural composites are also finding their use in ships (mostly for topside structures—less commonly for hulls). The current ultimate load-carrying abilities (tensile and compressive) of reasonably cost effective GRP all-composite hull lengths are limited to 60.0 m (200 ft.).

A more important facet of the overall strength consideration is the ability of a structure to fulfill its intended job. For instance, when a designer calls for a 0.5-inch-thick plate with a yield stress of



**FIGURE 5.8** Three-dimensional drop-weight tear (DT) test energy surface (as a function of temperature and strength). (From K. Masubuchi, 1979, *Materials for Ocean Engineering*, MIT Press, Cambridge, MA.)

350 MPa (50 ksi), it might seem appropriate to substitute a thinner, 560-MPa (80 ksi) plate. Design of ship structures (and most of the other large ocean structures, for that matter) is never that simple. Generally, ship plate steel is welded into contiguous monolithic structures with interconnecting “I” and “T” cross-section beams. Hull or deck plating is then welded into place creating a “grillage” structure. Thinner plate (even with a higher yield stress) will behave differently, often buckling much sooner than a thicker plate. For this reason, careful attention needs to be paid to buckling modes of overall structures, and a thicker plate is often required even when its specific strength is well overmatched to the task.

In a similar manner, the overall length of a ship or any other floating ocean structure determines its loading characteristics. In a shorter ship (up to ~45.0 m or 150 ft.), its constituent structural components will perform well in bending (stiffness characteristics) and be stiff. For a ship hull longer than 60.0 m (200 ft.), the ultimate tensile and compressive strength of its components will take over. While composites can be made with extremely high strength capabilities, the cost of their component materials and fabrication grows rapidly (especially as more complex components are chosen). Generally, a steel structure can be fabricated more economically to handle the requisites of both loading scenarios (stiffness and ultimate strength, based on length) [16].

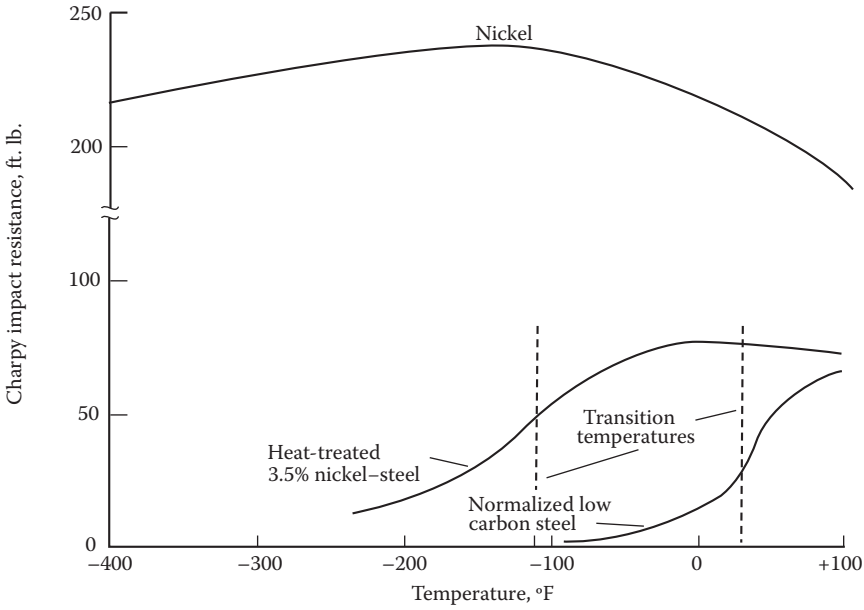
#### 5.1.3.1.2 Toughness

In addition to strength, toughness is one of the most important characteristics of metallic structures. Toughness is defined as the ability of a structural component to absorb energy before fracture occurs in the component under consideration; the toughness of the component is obtained by impact testing of the component using Charpy’s impact test on a standard bar with a V-notch or drop weight tear test on precracked test specimens. In ocean structures, especially in ships, fracture toughness is a critical requirement for the overall structure and its component materials (both plates and weld metals), as they must be able to deform plastically to some extent, as well as tolerate cracks and flaws while maintaining the overall structural integrity. This is complicated by the fact that these structures should be capable of operating in every ocean environment, from the frozen Arctic to the stormy and hot tropics.

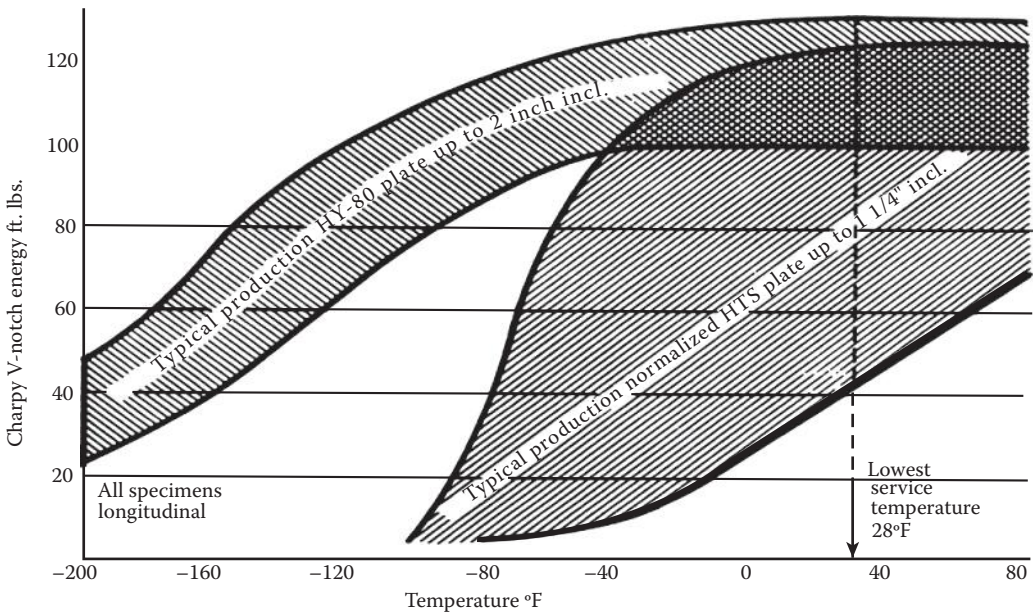
Low-carbon steels, however, have a sudden ductile-to-brittle transition in toughness as temperature decreases, as shown in Figure 5.9 [17]. In Figure 5.9, fracture toughness of two types of steel alloys and a pure metal (nickel) have been compared using Charpy’s impact strength; it is found that the nil ductility temperature of low-carbon steel is found to be  $-2^{\circ}\text{C}$  (or  $28^{\circ}\text{F}$ , see Figure 5.10 [18]), whereas the nil ductility temperature of 3.75% Ni steel is found to be  $-85^{\circ}\text{C}$  ( $-120^{\circ}\text{F}$ ) carbon; below this temperature, the material tends to become brittle and reduce its fracture toughness. Figure 5.10 gives the fracture toughness of thicker and thinner high-strength plates, as a function of temperature. Fracture toughness (as well as the nil ductility temperature of a metal) is a function of temperature, loading rate, and microstructure of the steel. Below a temperature specific to each steel grade (nil ductility or transition temperature), the material will have little resistance to catastrophic crack growth. In the transition regime, the combination of dynamic loading and cracks or defects in areas of stress concentration may result in unimpeded, rapid crack propagation through the material. For steels used in shipbuilding (or ocean structures, operating in cold ocean environments), it is imperative to select grades with a low fracture toughness transition temperature (below the expected operational temperature range). For the higher-strength steels used in ships, alloying and processing methods are used to produce grades with very low fracture toughness transition temperatures, but again, this will increase cost and reduce availability of the grade [16].

#### 5.1.3.1.3 Weldability/Joinability and Formability

A very large amount of welding is required to build a steel ocean structure. Thousands of pieces of various components need to be cut and assembled, requiring miles of welds at the joints. Many of these joints would require multiple passes of welding to fabricate the component. By far, welding (or joining, in case of composites) is the most labor-intensive portion of constructing an ocean structure. Welds (or joining procedures) of an ocean structure may also be very critical to its overall strength, durability, and toughness. Even small defects in weldments (joints) can create the



**FIGURE 5.9** Effect of low temperature on the impact resistance of two types of metals (face-centered cubic nickel and body-centered nickel-steel alloy). (From H. Sheets, 1975, Selection of materials for ocean application, Chapter 6, *Introduction to Ocean Engineering*, ed. H. Schenck, Jr., McGraw-Hill Book Company, New York.)



**FIGURE 5.10** Charpy energy bands for high tensile steel (HTS) and HY-80. (From K. Masubuchi, 1979, *Materials for Ocean Engineering*, MIT Press, Cambridge, MA.)

initiation points for the subsequent larger cracks and eventual failures. Because of the large amount of welding (joining) required and its importance to the structural integrity of the structure, careful welding (or joining) processes should be stringently adhered to. For instance, while high-strength low-alloyed (HSLA) steels require diligent attention to detail and procedures during welding, the HY-series steels require even more weld preparation and postweld treatments. One of the reasons for the push to replace HY-series steels with HSLA grades in the 1990s for ship steels was the reduction in labor required during welding. In general, any steel grade meeting the strength, toughness, and other requirements, but which is simpler to weld with a lower predisposition to weld flaws, is desirable. The cost of alloying steels to increase weldability must be balanced against the added cost of welding labor associated with a less weldable grade.

Ocean structural shapes and component frame/grillage structures require steel or composite materials to be formed into a variety of complex shapes. The considerable amount of welding (or joining) required to fabricate component steel (or structural composites) structures also would embed a significant amount of residual stresses, as well as often unwanted deformations/distortions in the finished structures; this deformation may require postforming straightening procedures. The initial forming requirements combined with postassembly straightening of deformed plates (or other components) may require that the steels chosen for ship construction be amenable to a wide range of forming procedures. The labor associated with these forming procedures must be balanced with the cost of alloying or preprocessing of steel plate to increase formability. In addition, transferring of structural loads and accommodating of thermal expansion mismatch between various structural components are not trivial endeavors, especially in large structures; in fact, materials joining technology (including composite-to-composite and composite-to-steel) is one of the most limiting (and potentially the most promising) areas of development in material technology. All of these factors must be balanced carefully in the material selection process.

#### 5.1.3.1.4 *Corrosion Degradation*

Structures located/operating in the ocean environment are intended for use in one of the most corrosive environments on the planet, and as such, corrosion is considered carefully in the design phase of any ocean structure. There are various materials options, design strategies, coating methodologies, and cathodic protection technologies available to the designer and the builder. Painting the ocean structures is a coating methodology that is used to protect the vessel from the sea's corrosive effects; from the simple act of scraping, sanding, or grinding a small area, to the significant removal, surface preparation, and reapplication of painting on a large area, coating maintenance is a never-ending process that eats up significant labor resources and time. These paints have many different formulations, each specifically engineered to perform critical tasks around the ship. Some paints require very rigorous surface preparation and curing processes, which would place additional drains on manpower requirements and financial resources. Various structural components must allow for periodic inspection for corrosion and recoating, and some components must allow for replacement if they are particularly susceptible to corrosion.

Efforts have been made to replace corrosion-prone steels with other metals like aluminum or titanium. These alternative metals offer a lower density (which can reduce the structural weight) and some corrosion resistance, but they present their own unique problems, such as suitability for larger span. In short, marine-grade aluminum (5000 series) is the only nonferrous, corrosion-resistant metal that has seen widespread use in ocean structures such as ships, on their topside structures, over the past 35 years. This is mainly due to its availability at relatively low costs, as well as due to its well-understood fabrication and welding processes.

#### 5.1.3.1.5 *Considerations of Economy, Including Availability*

For the foreseeable future, one of the most pressing factors in materials selection for ocean structures is their affordability. Generally, labor costs are continually rising and often outpace the costs of raw materials. Hence, proper material selection methodology must be to carefully accommodate and anticipate how these decisions would impact construction material costs and labor expenses. Along

with the above short-term costs, long-term costs of maintenance and structure readiness must also be included in the overall costs. Choice of the cheapest material in the construction phase alone cannot be considered a success if the choice requires a significant increase in construction labor and creates significant maintenance problems, during the 30- to 50-year expected lifetime of the platform.

Traditional steels and newer composite materials each offer specific advantages. Compared to composite materials, steels are less expensive to purchase, relatively less expensive to fabricate, and potentially more expensive to maintain. When considering the cost of building a ship from steel, one must always factor in the long-term costs of repeated painting and corrosion mitigation. Structural composites cost more to fabricate but offer the promise of lowered maintenance cost through their corrosion resistance, but other problems such as long-term maintenance and rehabilitation costs, and environmental attack causing delamination of material layers introduce uncertainties in estimating their lifetime costs.

Moreover, more than 40–50% of the steel used by the US defense department is consumed in naval ship fabrication. The HY-series steels were specific to naval applications, forcing the manufacturers to divert production from common grades and increasing the lead time required for production. When this production delay is combined with the unique alloying requirements of the HY series, these factors make HY steels considerably more expensive than more common industrial grades. Recent efforts to utilize industrial-standard HSLA steel grades have helped to increase the effective amount of steel available for naval construction, as well as to lower the costs of procurement.

### 5.1.3.2 Material Issues Relating to Operation Phase

Once the ocean structure has been placed on site, many of the materials selection decisions made earlier during the design and construction phases still continue to influence its day-to-day operation.

#### 5.1.3.2.1 Weight

Weight reduction, in ocean structures such as ships, is very important, though not quite critical as air and spacecrafts. Weight reduction in ships results in increased payload, speed, and range, as well as a reduction in fuel requirements. There are additional benefits to reducing the topside weight of a ship structure, such as increasing the sea-keeping ability of the ship via improved stability of the platform in a seaway. This is due the fact that the reduced mass higher up on the structure lowers the center of gravity and reduces roll moments. Many ship structures currently in use have lighter aluminum topsides; they employ modern high-strength aluminum alloys, in the design and fabrication of conventional welded grillage decks and stiffened side walls. Composites have also been used very recently for some limited topside structures, such as mast enclosures and compartments. Most recent research efforts to reduce weight have focused on using higher yield stress steel thin plate and other structural members to replace those with lower yield stresses, thus reducing the weight. However, proper design considerations have to be exercised since buckling of component members becomes an ever-increasing concern. Other developments such as the advanced double-hull (ADH) construction seek to replace conventional construction methods with new techniques that reduce the overall number of metal piece parts needed for construction. Composites have been used on hulls shorter than 200 ft. long with great success. The raw material and labor costs to build composite material hulls are still too high for applications without specific requirements (such as reduced vessel signature) [16].

#### 5.1.3.2.2 Fracture Toughness

As discussed earlier, fracture toughness is a critical property required in the steels and weld metals of ocean structures, since they have to withstand the day-to-day rigors associated with thermal extremes, impacts from piers and other docking boats, and impulsive sea conditions. It is defined as a property of the material that describes the ability of the material containing a crack to resist fracture. For naval vessels, another important operating condition is the shock loading from hostile weapon effects, such as air and underwater explosive devices requiring protective measures against shock, blast, and penetration. Consequently, steels/composites and the welding/joining procedures used in naval vessels should have



a greater ability to withstand fracture and a greater flaw tolerance under shock loading conditions than more common structural grades. This allows them to remain ductile and sustain damage without rupture or fracture. The acceptance tests for such steels (plate, forgings, castings, weld metals, etc.) would require fracture toughness testing from small impact tests to large-scale, full-thickness explosion tests.

5.1.3.2.3 Ocean Corrosion

Ocean structures are expected to do their job in one of the most corrosive naturally occurring environments. Salt water and sea spray cover every surface of an ocean structure and constantly attack the material out of which the structure is made. In addition to general corrosion, which is more uniform on the structural surface, differential galvanic corrosion (produced by the differences in electronic potential between component metals aboard the structure, which are electrically connected via the structure to the ionically conductive seawater) is also a critical concern, as shown in Figure 5.11 [19]. In addition to the above two corrosion modes, the figure also shows pitting


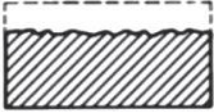
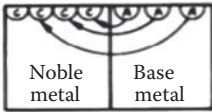
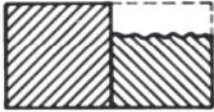


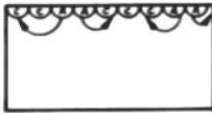

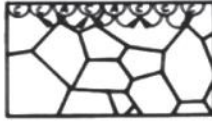

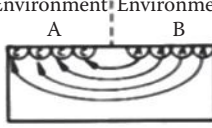
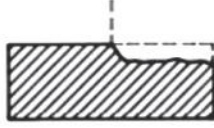
Mechanism	Schematic distribution of anodes and cathodes	Overall macroscopic effect
General corrosion		
Galvanic corrosion	 Noble metal   Base metal	
Crevice corrosion		
Pitting		
Intergranular corrosion		
Differential environment effects	 Environment A   Environment B	

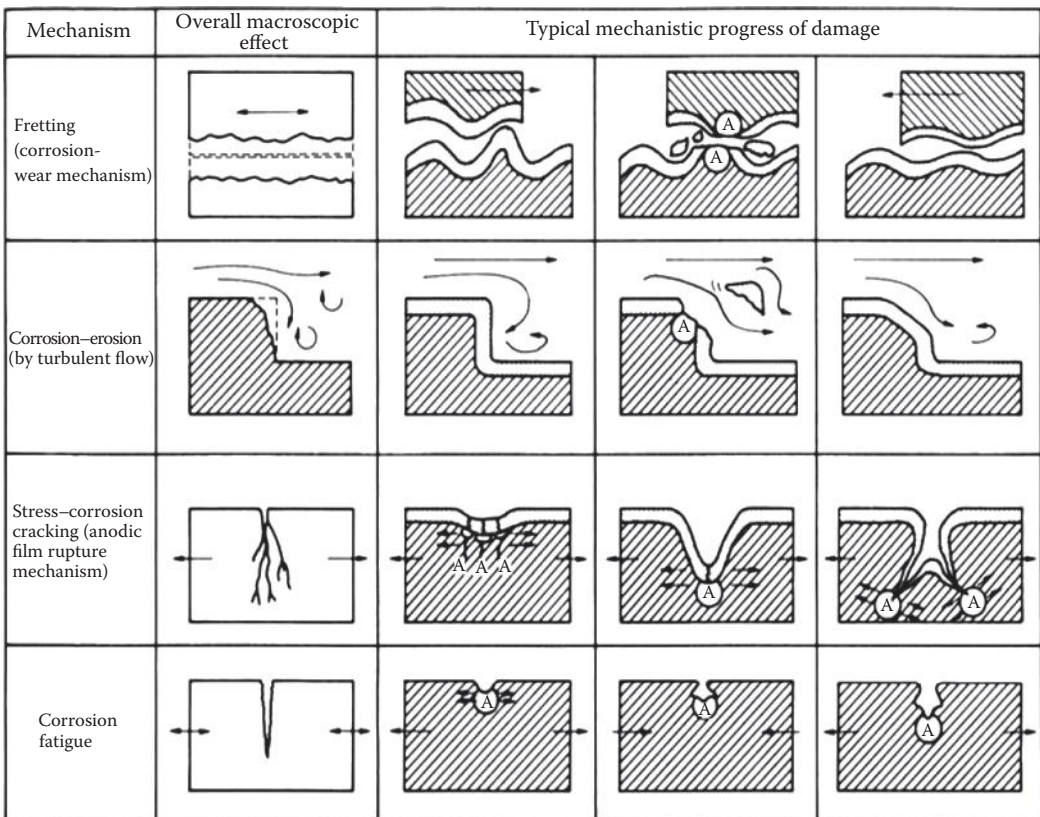
FIGURE 5.11 Electrochemical corrosion mechanisms. (From R. Reuben, 1990, Corrosion and defect evaluation, Chapter 10, in *Marine Technology Reference Book*, ed. N. Morgan, Butterworths, London.)

corrosion caused by nonhomogeneity in the material composition, crevice-corrosion damage, intergranular corrosion due to dissimilarities at grain boundaries, and differential environmental corrosion effects on the exposed portions of structures above the waterline.

Figure 5.12 [20] outlines other sources of corrosion damage produced due to mechanical actions of interfacial wear and tear, erosion, stress corrosion, and high-cycle fatigue.

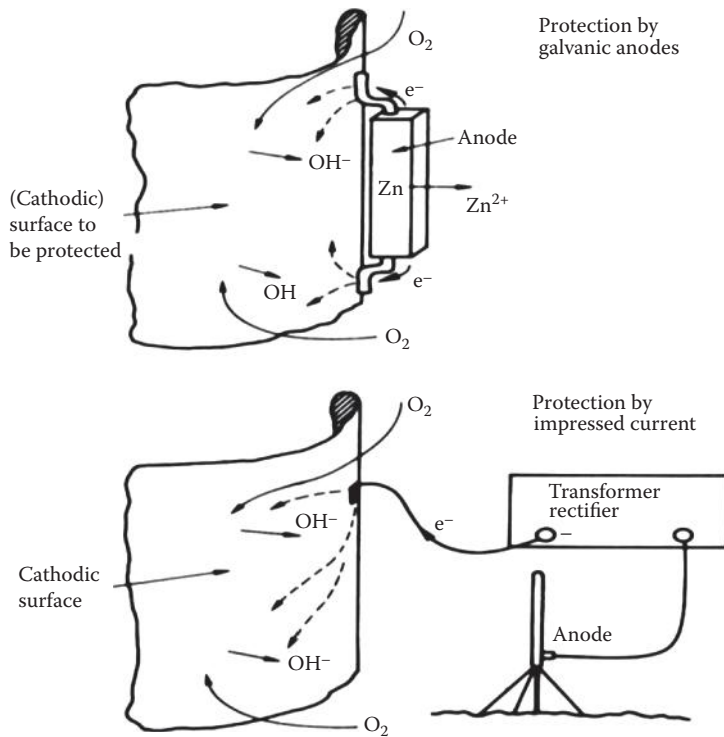
Moreover, the structure itself generates combustion products (through combustion engine-powered systems) that are high in corrosive compounds of sulfur and some acids. Topsides of the ocean structures are subject to these airborne pollutants. As mentioned in the first section, there are various materials options, design strategies, cathodic protection, and coating technologies available to the designer and shipbuilder. Once the vessel is in service, combating corrosion becomes a major maintenance requirement.

As stated earlier, coatings are used to protect the steel structural components from attack by salt water and other water- and airborne corrosive compounds. Also, if there is a discontinuity (or degradation) in the coating, corrosive attack is mitigated by cathodic protection, either by sacrificial anodes or by impressed current systems. The sacrificial anodes are typically blocks of zinc alloy, electrically coupled with the steel hull and which preferentially corrode, protecting the exposed steel, as shown in Figure 5.13 [21]. The anodes are positioned about the hull of the ship and replaced periodically as they deteriorate. Impressed current systems use permanent anodes on the hull and generate a potential field to counteract the corrosion potential of exposed steel (see Figure 5.13).



**FIGURE 5.12** Combined electrochemical-mechanical corrosion mechanisms; areas marked as “A” show sites of anodic corrosion, and shaded areas show the films or corrosion product layers. (From R. Reuben, 1990, Corrosion and defect evaluation, Chapter 10, in *Marine Technology Reference Book*, ed. N. Morgan, Butterworths, London.)





**FIGURE 5.13** Sacrificial anodes and impressed current systems used for cathodic protection in ocean structures. (From R. Reuben, 1990, Corrosion and defect evaluation, Chapter 10, in *Marine Technology Reference Book*, ed. N. Morgan, Butterworths, London.)

#### 5.1.3.2.4 Biological Attack

In addition to corrosion protection, the structural coating (or painting) below the waterline should also possess antifouling properties to maintain the exposed (to possible bio-fouling) surface free of any extraneous coating. In ship structures, fouling should be prevented as much as possible to maintain its hydrodynamic performance and fuel efficiency. The most commonly used ocean structural coatings prevent or slow down the attachment of bio-fouling organisms by containing compounds toxic to the animals, thus preventing them from attaching in the first place. Another method is to apply a kind of paint whose chemistry or surface morphology prevents the creatures' attachment, thus allowing them to be removed by water flow.

#### 5.1.3.2.5 Fire

Fire is probably one of the most dangerous events that can threaten the safety of an ocean structure and its crew. Onboard fires must be fought with firefighting systems available on the structure or vessel. The crew must fight and defeat the fire if the vessel is to survive; hence, crew training in firefighting and damage control are critical to the structure's survival. All structural steels are vulnerable to softening with exposure to fire-generated heat, thus allowing the component structures to collapse. Presence of composites on the body of the structure can be a fuel source for fires, thus exacerbating the already-existing serious situation. Active and passive fire insulation systems are used to keep structural members protected from heat and flame for a certain period of time—presumably long enough to get the fire under control. For composites, great care should be taken to select component materials with higher levels of fire resistance.

An additional fire hazard is the production of smoke and toxic fumes from burning materials. Ocean structures contain many flammable and nonflammable compounds (liquids like fuel, oil,

greases, paint, etc.; solids like furnishings, electronics, composite structures, metals, etc.), which, when exposed to either heat or flame, can burn, volatilize, or smolder. The smoke and fumes generated are of great concern since they (i) hinder the ability of the crew to get near a fire's source to extinguish it and (ii) pose a significant threat to large portions of the structure, even if the fire itself is small and easily controllable. Ocean structures, and especially naval vessels, should be designed with materials and structures that meet the highest standards of fire resistance and control. Moreover, active fire suppression systems should also be incorporated into the structure even though its affordability may become exorbitant.

#### 5.1.3.2.6 *Signature*

This aspect is of importance to naval ships. Since ships are very difficult to hide on the open water, its main defense against detection is to reduce the amount of electromagnetic, acoustic, or thermal radiation it emits or reflects. In order to do this, a number of technologies are available to absorb and deflect enemy radar, reduce thermal and acoustic emission, and in general increase the stealth characteristics of warships. By providing a composite (material) shrouding around the very reflective metal masts on current ships, the electromagnetic signature of a ship can be dramatically reduced. Future warships will use predominantly composite topside structures to further reduce electromagnetic signatures. Composite hull forms and new steel double-hull technologies offer the promise of reduced thermal and acoustic signatures. Composites can insulate the internal components from the water, while double-hull designs allow for flooded compartments, which can act as thermal and acoustic barriers.

#### 5.1.3.2.7 *Cyclic Wave Loading and Consequent Fatigue Damage*

The structural envelopes of ocean-operating structures or vessels are subjected to the action of randomly varying low-frequency wave pressures and loads that tend to cause fatigue damage in the material of these structures. Even though the stresses caused by these wave loads may not be very high over major portions of the structure, the structure tends to accumulate fatigue damage in the regions of the structure that are subjected to large stress concentrations. Due to the large number of repeated actions of these stress reversals in the highly stressed regions of the structure, the material of the structure tends to exceed its endurance limit and develop cracking around these critical regions; this damage is also shown in Figure 5.12. Figure 5.12 also shows that these fatigue cracks tend to get degraded more in the presence of corrosion damage in these regions. As the ocean structures, including ships, encounter a continuous succession of random wave loads, they deform elastically generating repetitive and varying wave bending moments on various portions of the structure. If not checked, these small fatigue cracks tend to grow, coalesce, and propagate (due to the repeated action of wave loads and moments) until they become dangerous to the safety or life of the structure. Moreover, the fatigue strength of a welded steel structure does not increase relative to the strength of the steel. Therefore, the use of higher-strength steels in offshore structures, and especially ships, requires detailed design against fatigue cracking over the life of the ship. Fatigue testing of structural joints and computational techniques are employed in modern offshore structural design to characterize the fatigue life of the structure.

#### 5.1.3.2.8 *Vibration*

Vibration is a constant phenomenon experienced in any ocean operating structure or vessel since it is subjected to a constant barrage of varying wave loads. In addition, there are hundreds of pieces of equipment aboard a vessel chugging away at their own individual tasks, each one imparting its own characteristic vibration behavior into the vessel's structure. While most large equipment is built on vibration-isolating spring mounts, none of these systems is perfect and always some vibratory load is transferred to the substructure. Even when large equipment is well isolated, its acoustic noise induces vibrational loading into the surrounding structure/medium. Vibration can induce fatigue, fretting, and other forms of degradation into structural materials. It also produces detectable noise transmitted through the water and which interferes with the ships' own sonar system effectiveness. Constant small movements cause surfaces to wear, and tiny amounts of elastic deformation may

induce fatigue-like failures over time. Since vibration cannot be eliminated, material and structure decisions must take these degradation mechanisms into account.

#### 5.1.3.2.9 *Structural Survivability*

Ocean structures, especially ships, are always susceptible to structural rupture from collision with floating/fixed objects (floating barges, debris, rocks, piers, sea walls, etc.) or due to extreme seismic loads. Naval ships also face the possibility of having explosives detonated close by (leading to hull whipping and blast loading) or being impacted by projectiles and fragments. Unlike merchant vessels, naval ships are expected to maintain a high level of performance even when damaged. Consequently, structural/hull survivability is part of the structural design of ocean structures. In a warship, the grillage is analyzed and built such as to limit the amount of damage caused by perceived threats. New designs such as double hulls (and some composite structures) have additional, built-in resistance to hull rupture. Materials with high fracture toughness are obviously prime choices to limit damage propagation. Specific materials are often used in critical areas of the hull. The hull structure must be fracture resistant under high-intensity loading at temperatures as low as  $-40^{\circ}\text{F}$ .

#### 5.1.3.2.10 *Degradation in Concrete*

Concrete, made of aggregate sand and cement, is often treated as a homogeneous material, but in reality it has an inhomogeneous and complex structure. The concrete has a porous structure (with voids of different sizes) and a series of interconnected capillary-sized microcracks, but it is free of macrodefects. These microcracks are formed due to shrinkage and differential temperatures generated during the process of setting. Concrete has significant variation in properties (such as strength, porosity and permeability) with respect to depth into the cover zone [22]. Strength is high near the surface (due to better curing process) and becomes the normal value in the body of concrete. Porosity and permeability is also higher near the surface of concrete. All these factors have a strong influence on the durability of concrete in the ocean environment. Temperature of the ocean structure and the surrounding ocean affects many of the chemical processes that occur in concrete (and in reinforced concrete). Ocean temperature varies from  $-2^{\circ}\text{C}$  (near the sub-Arctic regions) to  $36^{\circ}\text{C}$  (in the Arabian Gulf and the Red Sea). The ocean environment above the ocean varies from  $-40^{\circ}\text{C}$  (in the sub-Arctic regions) to  $\sim +40^{\circ}\text{C}$  (equatorial regions). Hence the ocean structures experience the changes which these temperatures effect on the ocean environment these structures. As indicated earlier in Figure 5.1, the degradation in concrete is expected to occur in three different zones, viz., the atmospheric, the splash (tidal zone included) and the submerged zones. In the atmospheric zone, the concrete is exposed to attack by the humid and salt-laden atmosphere. In the submerged zone, the surfaces of concrete structures are saturated with the seawater, with limited access to oxygen or air. In the splash (including the tidal) zone, the concrete is subjected to alternate wetting and drying, with varying degree of access to atmospheric oxygen or air; this zone is the most vulnerable zone for deterioration, especially the corrosion of the steel reinforcement. The deterioration occurring in concrete are (i) chemical/physical deterioration of concrete itself, (ii) physical damage to concrete, and (iii) corrosion of reinforcement.

#### 5.1.3.2.11 *Chemical/Physical Deterioration in Concrete*

A number of deterioration mechanisms are present in the chemical and physical degradations that occur in the concrete, some of which are sulfate attack, alkali silica reaction, and high-alumina cement conversion. Ocean waters high in sulfate content react with the aluminates in concrete to form ettringite and gypsum, which are expansive; this leads to cracking damage in concrete. This is controlled by using sulfate-resistant concrete or fly-ash containing high-strength concrete in these structures. Alkali silicate reaction results from the use of certain reactive aggregates with cements having high alkali metal content; when this reaction is present, concrete swells (in the presence of moisture) and cracks. The use of high-alumina cement (HAC) leads to its conversion into a weaker crystalline form in the presence of moisture and higher ocean temperatures; recent compositions of HAC are found to be more resistant of this reaction [23].

### 5.1.3.2.12 *Physical Damage in Concrete*

The types of physical damage suffered by ocean concrete are given as freeze–thaw damage, salt (in seawater) crystallization, salt scaling, marine growth, and fire. Freezing of water, within the pores of concrete, leads to cracking when the water temperature cycles from freezing to thawing. Use of air entrained concrete, hydraulically pressed concrete, or dense well-compacted concrete minimizes this damage considerably. In the salt crystallization process, water from the salt-bearing seawater drawn by capillary action and permeability of concrete (into the concrete) gets evaporated from a drying concrete region, leaving behind salt crystals in the pores of concrete. This damage is found to occur in the hotter climates of the ocean. A dense and well-compacted concrete resists this damage considerably. Salt scaling is a process similar to the above occurring on exposed horizontal surfaces of ocean structures. The salts, deposited on the surface of horizontal concrete surfaces, gain entry into the concrete and tend to weaken the concrete by scaling. Once again, the use of dense and well-compacted concrete prevents this type of damage. In some marine fouling situations, concrete-eating sea organisms of the Mollusca family tend to damage concrete surfaces on which they get deposited. The limestone content of the concrete should be reduced in such contexts.

### 5.1.3.2.13 *Corrosion of Reinforcement in Concrete*

As explained earlier for Figure 5.3, the presence of moisture within concrete can lead to a complex state of interaction within the concrete. Generally, concrete provides an alkaline environment in which stable and strongly adherent films of corrosion products form on the surface of steel reinforcement (in the presence of moisture) and prevents further corrosion of reinforcement surfaces (within concrete). Other forms of corrosion damage can be present in ocean structures due to (i) chloride ingress, (ii) carbonation, (iii) gas diffusion, (iv) intense local corrosion, and (v) stray current corrosion. The presence of chloride ions in concrete, due to chloride in concrete-mixing water or due to the ingress of chloride-bearing seawater into concrete (based on Fick's law of diffusion), leads to a breakdown of the corrosion-resistant film of corrosion products on the surface of steel reinforcement; this degrades the steel reinforcement within the concrete. Diffusion of carbon dioxide from air into concrete (called carbonation) reduces the alkalinity of concrete; when the pH value of concrete falls below 9, the passivity of steel surfaces breaks down and leads to corrosion of the steel reinforcement. When the concrete is saturated with water or is completely wet, the diffusion of carbon dioxide or oxygen into the interior of the concrete is restricted. When the relative humidity of concrete becomes more than 50% or when alternate wetting and drying lead to a large diffusion of oxygen and carbon dioxide into the concrete structure, this can provide adequate electrolyte to set up a corrosion cell that will lead to corrosion of the reinforcement. Localized corrosion pitting in reinforcement steel can occur when a small area of steel in the submerged concrete is linked electrically to an efficient cathode above water. This can occur when open static cracks are present in concrete or when dynamic “opening and closing” fatigue cracks expose the steel surfaces to water/gas intrusion. A properly implemented crack control strategy in concrete can minimize this form of local corrosion. Also it has been observed that severe steel reinforcement corrosion can occur when strong electrical fields (perhaps due the presence of cathodic protection systems in the vicinity) occur in the vicinity of reinforced concrete. This can be eliminated by making the reinforcement system electrically continuous [23].

## 5.2 MECHANICAL PROPERTIES FOR OCEAN USE

### 5.2.1 INTRODUCTION

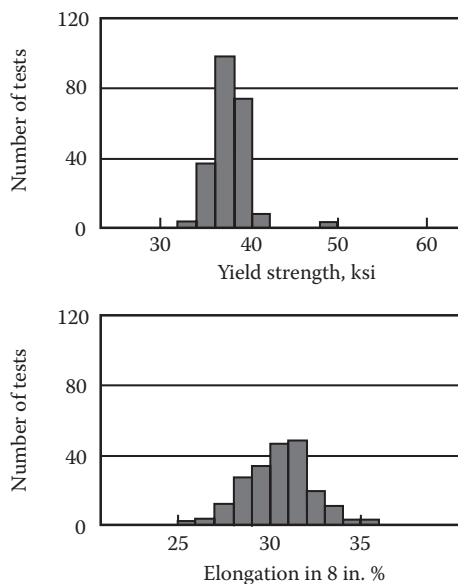
Materials used in the ocean environment should not be prone to catastrophic failures such as running brittle fracture, sudden plastic/buckling collapse under extreme projectile/impact loads, and hazardous fire conditions; in addition, the design should also take into account the overturning and capsizing under extreme wind/wave conditions. Of the various material characteristics, those relating to (i) deformation and strength, (ii) fatigue and fracture, and (iii) corrosion are of substantial interest. Corrosion, which requires special treatment, is dealt with separately in Section 5.4. Since

speed of loading and temperature also affect the response of the materials in the ocean environment, they are also considered under deformation and strength of materials.

Structural configuration and the ocean loading scenarios control the behavior of structural members used in the fabrication of ocean structures. Most of the ocean structures (including ships) are made up of a combination of beams (rolled steel sections, tubulars, built-up sections, etc.), plates, shells, and reinforced/stiffened members; many of the framed ocean structures are made up of interconnected beam members to obtain the desired optimum configuration. In most of the ocean structures, steel is still the most commonly used material and, as such, are joined together by welding, which locks in a considerable amount of residual stresses at various locations of the structures. Special welding procedures (shot peening, sandblasting, etc.) or annealing of joints after welding need to be carried out to minimize or eliminate large residual stresses at critical joints. In some cases, high-strength steels, high-grade aluminum alloys, and structural composites are used to strengthen and reduce the topside (deckhouses, superstructures, and other appurtenances) weight of these structures, which lowers the center of gravity of ocean vessels.

Special design considerations must be taken to estimate the compressive, bending, and buckling strengths of the various structural components of ocean structures. In many cases, especially in ocean structures and ships operating under Arctic or sub-Arctic conditions, thermal stresses are set up due to the substantial temperature differences that exist between the atmospheric and ocean waters. In small ocean structures (such as a buoy or a boat), these thermal stresses do not play any significant part, but in large ocean structures, the effect of large temperature differences between the various structural components must be carefully analyzed and action must be taken to minimize their effects.

Conventional isotropic properties of materials such as yield and ultimate strengths, Young's modulus of elasticity, and Poisson's ratio need to be known properly to characterize the material response. This characterization will become more complex as the modern composites and concrete materials are taken into account, since more material constants need to be determined. It must be remembered that these material properties are determined using standard tests specified for them, and they exhibit statistical variations as shown in Figure 5.14 [24]. Figure 5.14 gives the statistical behavior of carbon steel strength (tensile) and deformation for grade C steels (produced from open



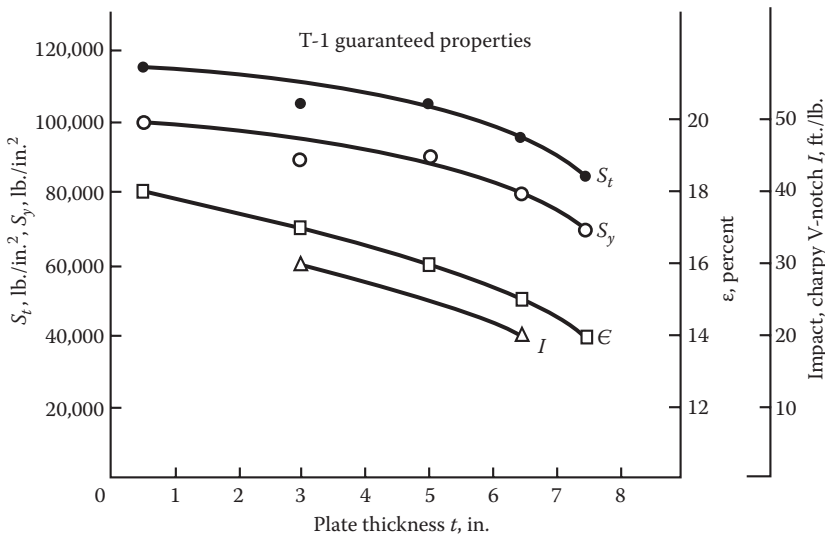
**FIGURE 5.14** Distribution of tensile strength and deformation properties of carbon steel plate (Grade C). (From J.F. Young et al., 1998, *The Science and Technology of Civil Engineering Materials*, Prentice Hall, Upper Saddle River, NJ.)

hearth, electrical arc, or basic oxygen furnaces); the mean values are given as standard properties. It is seen from Figure 5.14 that these properties vary, and for a proper characterization, they need to be specified as mean with a standard deviation of their specific properties.

Along with this statistical variation, the designer must also bear in mind the reduction in strength, deformation, and toughness characteristics of thicker plates, due to the presence of microdefects and property variations present in the larger volumes of thicker plates; this is shown in Figure 5.15 [25], where the yield and ultimate strengths (tensile), total deformation, and the toughness (Charpy impact value) of T1 steel plates of various thicknesses are shown. It is observed that as the thickness of the plate increases, the strength, deformation, and toughness values are decreased.

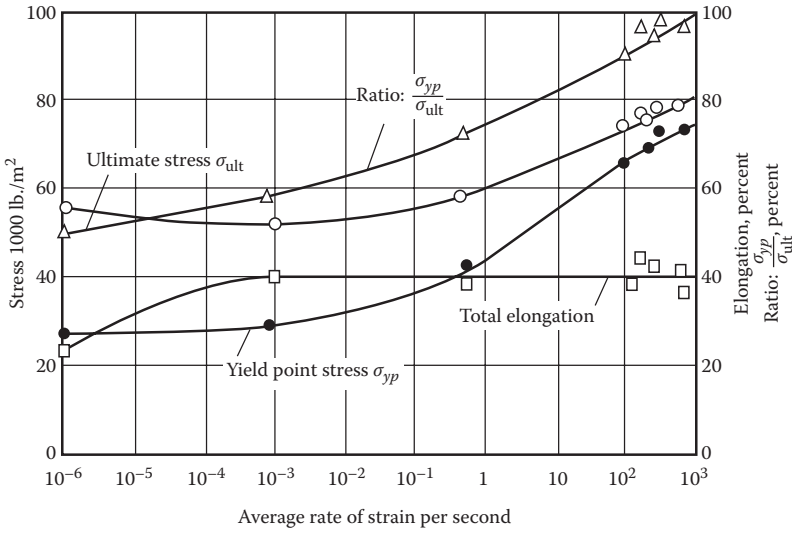
The strain rate also influences the strength and deformation of different materials; Figure 5.16 [26] shows the strain rate dependence of mild (low-carbon) steel on its yield and ultimate strengths and total deformation. It also shows that the ratio of  $(\sigma_{yield})/(\sigma_{ultimate})$  almost tends to 1.00 as the strain rate becomes larger and larger, indicating that at very large strain rates, the material tends to fail in brittle fracture. Also it is seen from Figure 5.16, that at very low strain rates, viz., between  $10^{-6}/s$  and  $10^{-3}/s$ , the yield strength almost remains a constant. The difference between brittle and ductile strengths of materials can be observed from Figure 5.17 [27], where the low-temperature strength of steel is shown in terms of ductile yield strength and brittle strength (in terms of its ultimate tensile strength). When the nil ductility temperature strength is reached, the ductile yield strength becomes the brittle strength of carbon steels. It is seen from Figure 5.17 that the brittle strength of carbon steels changes very little with temperature, whereas the (ductile) yield strength increases substantially with the reduction in temperature. Generally, if the brittle strength of the material is reached during a loading procedure, separation of surfaces occurs, whereas during yielding of the material, only sliding of grain boundaries occurs, resulting in material flow. Above the nil ductility temperature  $T_c$  (see Figure 5.17), the resistance to sliding is decreased than that to separate, and the specimen will yield plastically. In a similar manner, if the temperatures are lower than the nil ductility temperature  $T_c$ , then the brittle strength is smaller than the yield strength and the material will fail by separation (brittle fracture) without any plastic deformation.

Figure 5.18 [28] shows the values of yield strength, tensile strength (ultimate), and Young's modulus as a function of temperature. It is seen that the strength and modulus decrease significantly as the temperature of steel increases beyond  $400^{\circ}C$ .

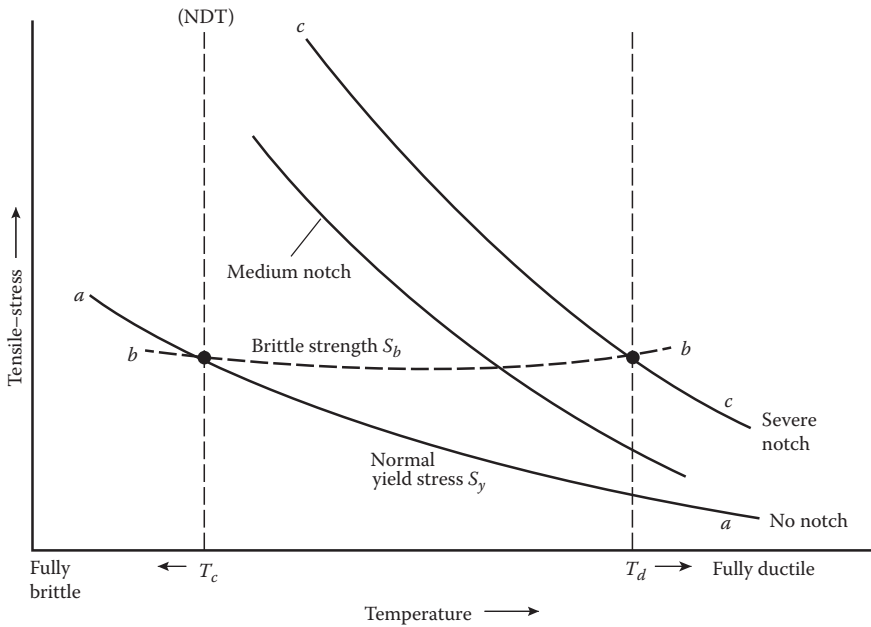


**FIGURE 5.15** Effect of plate thickness on T-1 steel properties. (From H. Sheets, 1975, Selection of materials for ocean application, Chapter 6, *Introduction to Ocean Engineering*, ed. H. Schenck, Jr., McGraw-Hill Book Company, New York.)





**FIGURE 5.16** Effect of strain rate on mild steel tensile properties. (From H. Sheets, 1975, Selection of materials for ocean application, Chapter 6, *Introduction to Ocean Engineering*, ed. H. Schenck, Jr., McGraw-Hill Book Company, New York.)

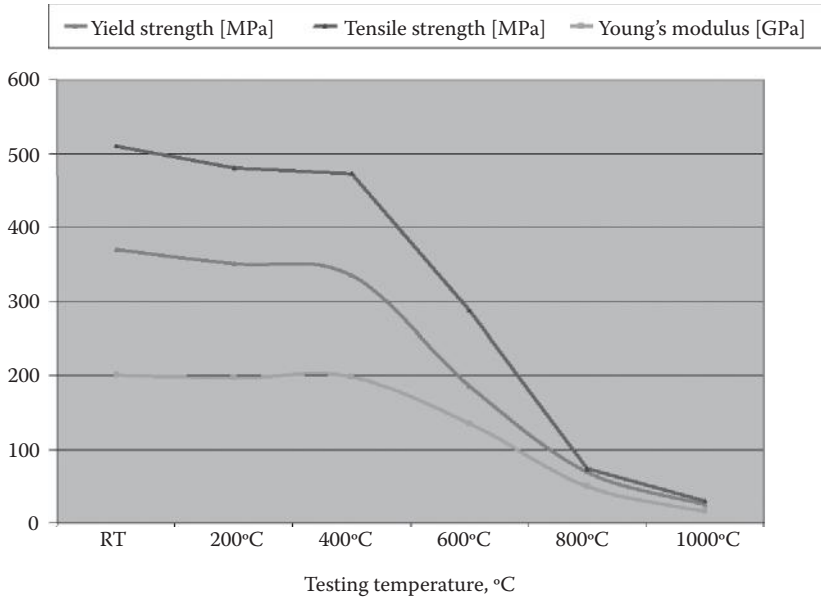


**FIGURE 5.17** Temperature vs. strength, showing the ductile and brittle zones for steel. (From H. Sheets, 1975, Selection of materials for ocean application, Chapter 6, *Introduction to Ocean Engineering*, ed. H. Schenck, Jr., McGraw-Hill Book Company, New York.)

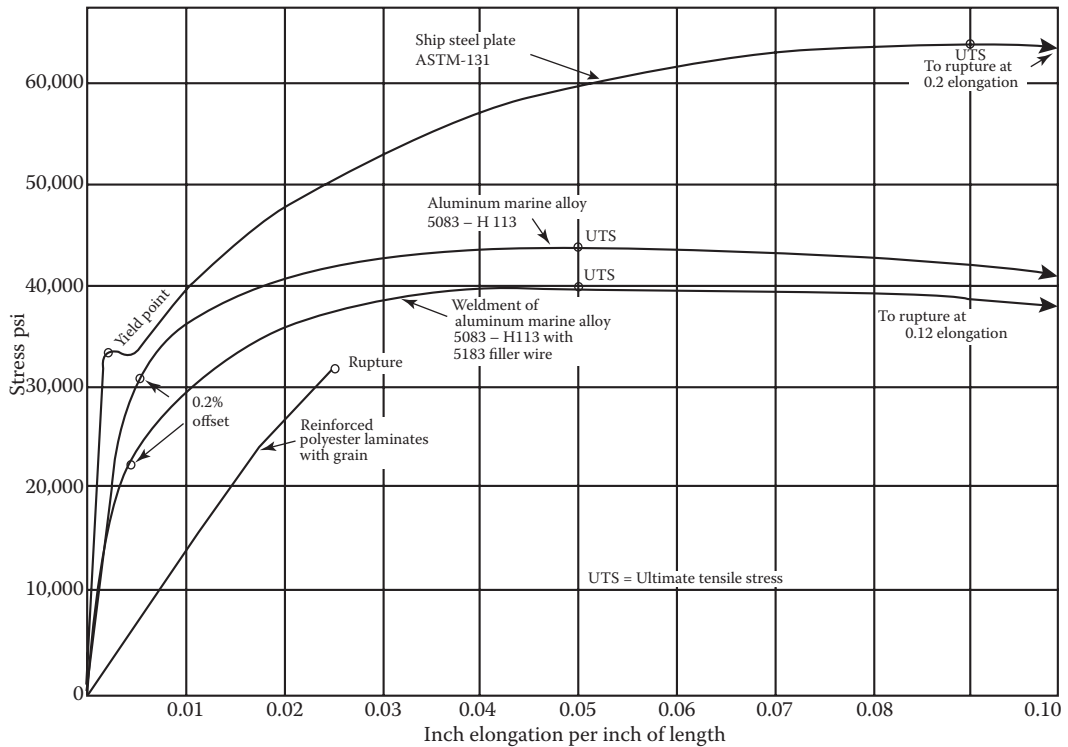
**5.2.2 PROPERTIES RELATED TO STRENGTH AND DEFORMATION**

The properties related to strength and deformation can be obtained from the well-known load-extension or nominal stress–strain tests on standard samples of the material. Figure 5.19 [29] shows the typical (nominal) stress–strain relationship obtained for some materials such as low-carbon steel (ASTM-131), aluminum alloy (5083-H113), weldment of 5083-H113 with 5183 filler wire and





**FIGURE 5.18** High temperature strength and Young’s modulus of high-strength steel. (From Material Data Sheet, 2006, Air hardening steels, in hot and cold rolled state, Salzgitter Flachstahl, Ein Unternehmen der Salzgitter Gruppe, Germany, 10 pp. Available at <http://www.salzgitter-flachstahl.de/en/>)



**FIGURE 5.19** Typical stress–strain diagrams for various ocean applications. (From K. Masubuchi, 1979, *Materials for Ocean Engineering*, MIT Press, Cambridge, MA.)

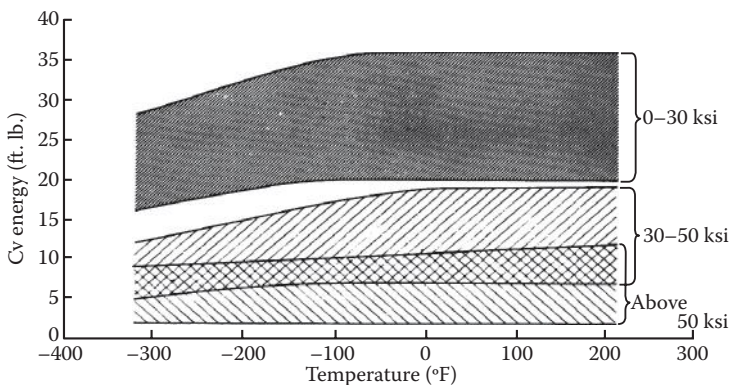
reinforced polyester laminate with grain, used in the ocean environment. It is also seen that the yield stress (or proof stress) is noted at a given level of plastic strain, viz., at 0.2%. Another quantity defined as “flow stress” is also determined, which is the mean of the yield and ultimate tensile stresses.

It is observed from Figure 5.19 that the maximum tensile strength and yield strengths of aluminum are comparable to those of low-carbon steels. It has been found that most of the aluminum alloys used in the ocean environment have tensile strengths in the range of 220 to 440 MPa (31,000 to 63,000 psi), while the steels have tensile strengths in the range of 400 to 500 MPa (58,000 to 71,000 psi) [30]. However, on the strength-to-weight ratio basis, aluminum is stronger than the steels used in the ocean environment; aluminum weighs about half as much as steel with the same strength and deflection. Figure 5.20 [31] gives the Charpy V-notch impact energy levels of aluminum alloys, as a function of strength levels. It is observed from the figure that the impact energy levels do not change abruptly with temperature as observed for steels. It is also observed from Figures 5.9, 5.10, and 5.20 that the impact energy levels of aluminum alloys are considerably lower than steel alloys. It is also observed from Figure 5.20 that the impact energy level generally decreases with an increase in the strength of aluminum alloys.

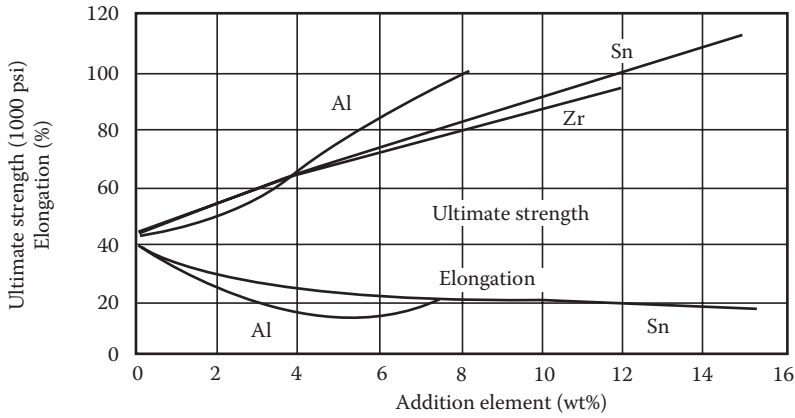
Figures 5.21 [32] and 5.22 [33] show that the strength and deformation characteristics of alpha titanium alloys are dependent on the percentage of alloying elements used, and the temperature of the specimen under test. In Figure 5.21, it is seen that the increase in the percentage of alloying elements, viz., aluminum, tin, and zinc, increase the ultimate tensile strengths of the alpha titanium alloys; it is also observed that the increase in the alloying element stiffens the titanium alloy and decreases the deformation of the specimen. Figure 5.22 shows the Charpy impact strength data of titanium alloys with different levels of yield strength. As the level of strength increases, the Charpy’s V-notch toughness decreases. Moreover, it is also seen that the titanium alloys do not show a sharp transition in Charpy’s fracture toughness with temperature, as shown by steel alloys in Figures 5.9 and 5.10.

In polycrystalline metals, such as those mentioned above, directionality of mechanical properties is not considered. One exception to this is the rolled steel plates, wherein the plate experiences through-the-thickness stresses. The precipitation of spherical inclusions of manganese sulfides leads to pancake forms during the rolling process; this reduces the through-the-thickness homogeneity as well as the strength of steel plates and leads to lamellar tearing.

In general structural design, the yield stress (or the proof stress) is used as the absolute design maximum, and many load (or safety) factors are normally used to ensure that the stresses remain well below the yield. For more complex states of stress, a yield criterion (von Mises’ or Tresca’s) is used to determine whether yielding is likely to occur at any point in the structures under investigation.

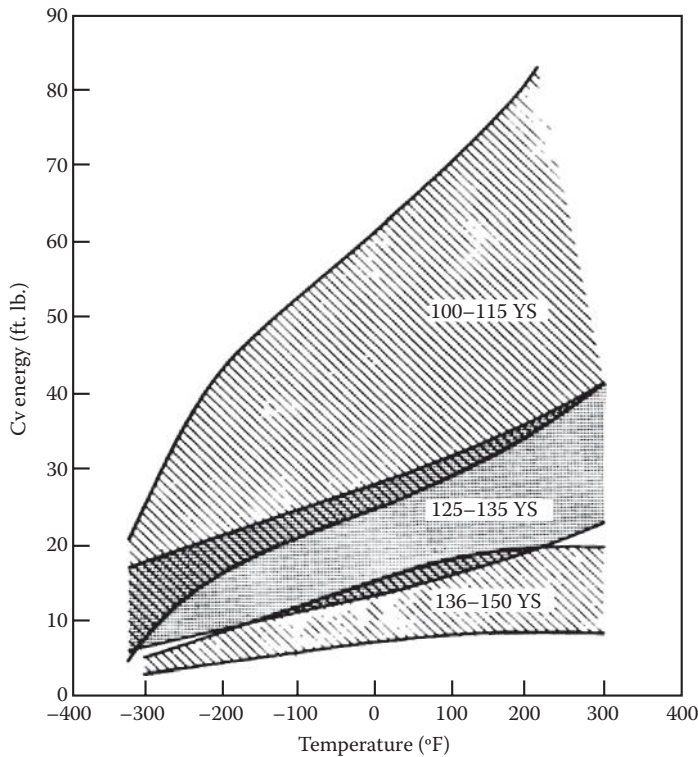


**FIGURE 5.20** Summary of Charpy V-notch impact energies of aluminum alloys as a function of strength. (From K. Masubuchi, 1979, *Materials for Ocean Engineering*, MIT Press, Cambridge, MA.)



**FIGURE 5.21** Effect of alloy addition on mechanical properties of alpha titanium alloys. (From K. Masubuchi, 1979, *Materials for Ocean Engineering*, MIT Press, Cambridge, MA.)

Recent design guides also specify plastic (or ultimate strength) analysis of structures, with or without the presence of defects. When the deformation of structures becomes a function of time as evidenced for metallic structures under high temperatures or polymeric or composite materials, the viscoelastic and viscoplastic behavior (referred to as creep) of materials should be considered. Usually, ocean structural materials do not show any creep behavior, but it should be considered for turbines, flare boom tips, and internal parts of engines where higher temperatures are expected to occur.

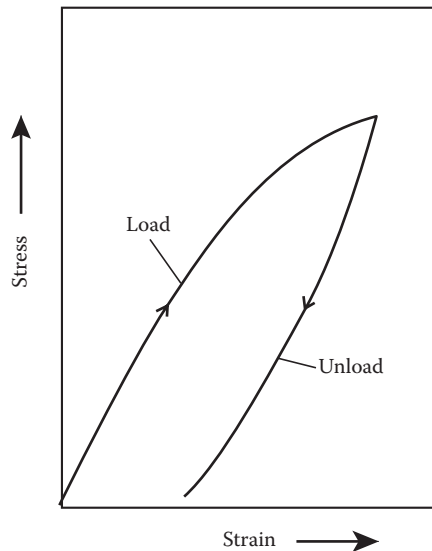


**FIGURE 5.22** Summary of relationships between Charpy V-notch curves for titanium alloys and different levels of yield strength. (From K. Masubuchi, 1979, *Materials for Ocean Engineering*, MIT Press, Cambridge, MA.)

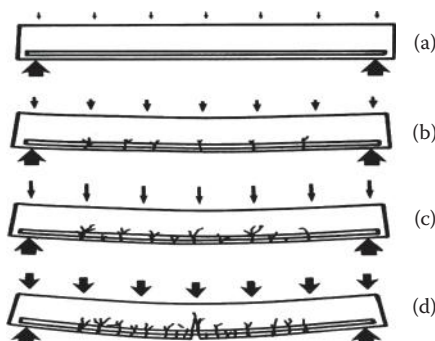
When polymeric materials (such as vulcanized rubber, thermoplastics, and thermosetting plastics, etc.) are used in the ocean context, the stress–strain characteristics will be different under loading and unloading conditions. For these materials, a viscoplastic analysis should be carried out.

Concrete is used in many of the recent gravity ocean structures as well as in hybrid concrete–steel gravity ocean structures; concrete has been used not only for gravity structures but also for floating semi-submersible ocean platforms. Concrete is brittle, and its stress–strain characteristic is shown in Figure 5.23 [34], where the loading–unloading paths are different. Most of the structural concrete is either reinforced or prestressed and also shows a composite material behavior; addition of reinforcing steel (or GFRP bars, recently) increases the load-carrying capacity of concrete structures, introducing the stronger tensile characteristics of steel bars in the weaker tensile regions of concrete.

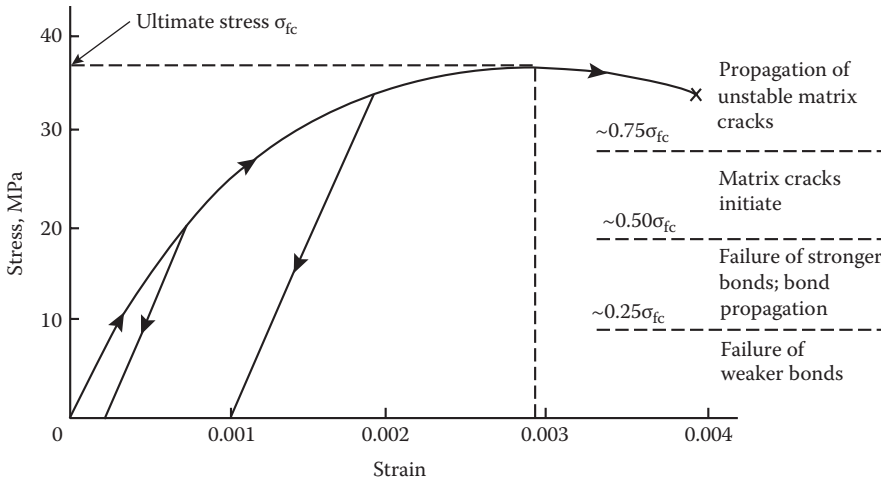
The load-carrying behavior of reinforced concrete structures is illustrated through the load–deformation behavior of a concrete beam, shown in Figure 5.24 [34]. When the steel beam is loaded,



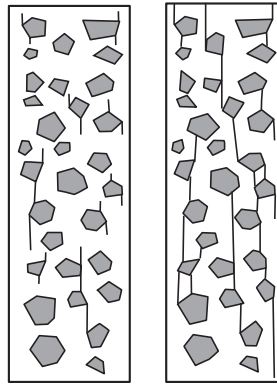
**FIGURE 5.23** Typical loading and unloading stress–strain curves for concrete. (With kind permission from Springer Science+Business Media: *Materials in Marine Technology*, Mechanical properties and design for marine use [Chapter 2], 1994, p. 23, R. Reuben.)



**FIGURE 5.24** Behavior of a concrete beam as load is increased until failure: (a) light loading with concrete intact, (b) increased loading with cracking on concrete on tension side, (c) load at which reinforcement yields, and (d) concrete fails in compression side. (With kind permission from Springer Science+Business Media: *Materials in Marine Technology*, Mechanical properties and design for marine use [Chapter 2], 1994, p. 23, R. Reuben.)



(a)



(b)

**FIGURE 5.25** Behavior of concrete under compression: (a) stress–strain curve and (b) modeling of failure in concrete matrix under low (left) and higher (right) loads. (From J.F. Young et al., 1998, *The Science and Technology of Civil Engineering Materials*, Prentice Hall, Upper Saddle River, NJ.)

the beam deforms, taking additional loads; at a certain load, the beam section slowly develops cracks on the tension side of the loaded beam, as shown in Figure 5.24b; the bending stiffness of the concrete beam is reduced as the cracks continue to grow. Thereafter, as the load on the concrete beam is increased, the cracking tends to grow as shown in Figure 5.24c and d; this occurs until the concrete on the compression side of the dominantly cracking section of the beam fails in compressive crushing. This load gives the ultimate (strength) load of the beam; thereafter, the load will reduce as the beam continues to deform. The state of cracking and the stress–strain characteristics of concrete are better illustrated in Figure 5.25 [35].

### 5.2.3 PROPERTIES RELATED TO FAILURE, FATIGUE, AND FRACTURE

When a material is unable to fulfill the purpose for which it was originally made, it is assumed to have failed. Conditions such as the environment and operating loads are often observed to be the main causes leading to a material's failure. Examples of harsh environments that induce failure of materials include corrosive, high-temperature, and high-energy (waves, cyclones, and ice impacts)

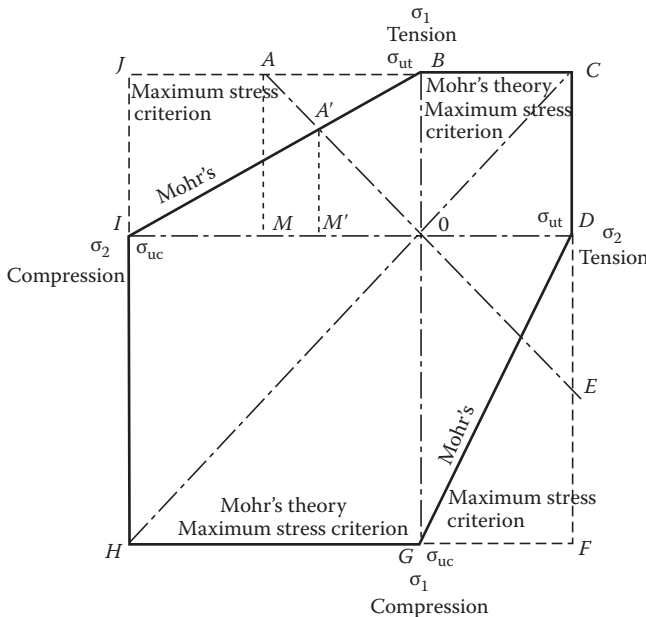
environments. Operational loading conditions such as cyclic stresses, impacts, and frictional loading frequently cause material failures. A critical combination of harsh environments and operating mechanical loads often leads to a more rapid wear-out and failure of materials.

**5.2.3.1 Failure Strength of Materials**

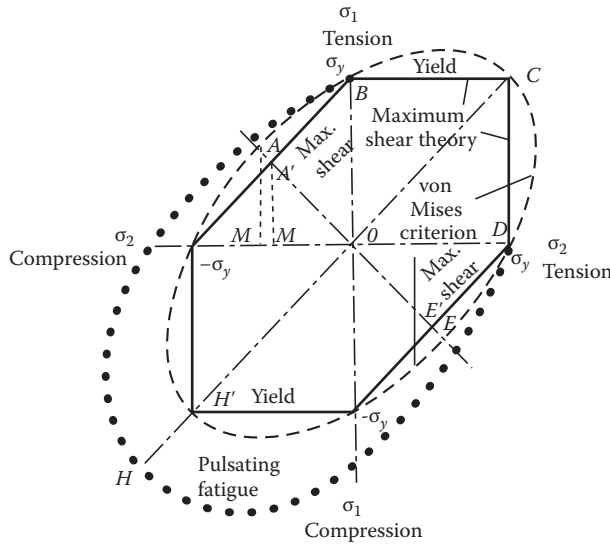
In the present-day design for ocean structures, besides the strength and deformation properties considered earlier, it is necessary to determine the possibility of failure through crack growth in them. A structural component is said to have failed when it can no longer carry the load acting on it in a satisfactory manner. The failure can occur through either excessive deformation (yielding) or fracture or excessive fatigue cracking of the component under consideration. A number of strength theories have been developed to describe the failure of materials [36] under one-, two-, and three-dimensional stress states, once the failure state under uniaxial tension or compression can be estimated from simple tests.

The theories commonly used for brittle materials are the maximum stress theory (due to Rankine) and Mohr’s (or Coulomb–Mohr) theory, and for the ductile materials, they are the maximum shear stress theory (due to Tresca and Guest) and von Mises theory (due to von Mises). The failure conditions for brittle materials are given in Figure 5.26 [37], and for ductile materials in Figure 5.27 [38]. According to the maximum stress theory, failure in brittle materials occurs in a multiaxial state of stress when either a principal tensile or compressive stress reaches the uniaxial tensile ( $\sigma_{ut}$ ) or compressive ( $\sigma_{uc}$ ) strength of the material. In Figure 5.26, the maximum failure stress criterion is represented by the square CFHJ. For torsional failure, only shear stresses are present in the cross-section ( $\sigma_x = \sigma_y = 0$ , and  $\tau_{xy} = \tau$ ). Hence, the maximum failure stress criterion for torsion is given by

$$\tau_u = \sigma_{ut} \tag{5.1}$$



**FIGURE 5.26** Biaxial conditions for strength theories of brittle materials. (W.D. Pilkey: *Formulas for Stress, Strain and Structural Matrices*, 2nd edition, 2005. Copyright Wiley-VCH Verlag GmbH & Co. KGaA. Reproduced with permission.)



**FIGURE 5.27** Biaxial conditions for strength theories of ductile materials. (W.D. Pilkey: *Formulas for Stress, Strain and Structural Matrices*, 2nd edition, 2005. Copyright Wiley-VCH Verlag GmbH & Co. KGaA. Reproduced with permission.)

and is given by the line MA (or DE) in Figure 5.26. According to Mohr’s theory, the failure criterion for brittle materials is also given in Figure 5.26. The conditions of failure are as follows:

For  $\sigma_1 \geq 0$ , and  $\sigma_2 \geq 0$  (first quadrant), with  $\sigma_1 \geq \sigma_2$

$$\sigma_1 = \sigma_{ut} \tag{5.2a}$$

For  $\sigma_1 \geq 0$ , and  $\sigma_2 \leq 0$  (second quadrant),

$$(\sigma_1/\sigma_{ut}) - (\sigma_2/\sigma_{uc}) = 1.0 \tag{5.2b}$$

For  $\sigma_1 \leq 0$ , and  $\sigma_2 \leq 0$  (third quadrant),

$$\sigma_2 = -\sigma_{uc} \tag{5.2c}$$

⋮

For  $\sigma_1 \leq 0$ , and  $\sigma_2 \geq 0$  (first quadrant), with  $\sigma_1 \geq \sigma_2$

$$-(\sigma_1/\sigma_{ut}) + (\sigma_2/\sigma_{uc}) = 1.0 \tag{5.2d}$$

It has been observed from experiments that certain tests on brittle materials seem to substantiate the maximum stress theory, and some others seem to substantiate Mohr’s theory [39].

The maximum shear stress theory, which was initially developed as a failure criterion for static yield (or failure) in ductile materials, has also been extended to fatigue failure; this is due to the fact that fatigue failure is thought to be initiated in ductile materials by maximum shear stress theory. According to this theory, failure occurs when the value of the shear stress in the material, subjected to multiaxial state of stresses, reaches the value of the failure shear stress in a uniaxial bar. When the principal stresses are used, the maximum shear stresses are given as

$$[(\sigma_1 - \sigma_2)/2], [(\sigma_2 - \sigma_3)/2], [(\sigma_3 - \sigma_1)/2] \tag{5.3}$$



The value of the shear at failure in a simple tensile test is  $(\sigma_y/2)$ . This will lead to the condition  $\sigma_1 = \sigma_y$  in the first quadrant. In the second and fourth quadrants, failure will occur when  $\sigma_1 = \sigma_y/2$ .

The von Mises failure theory is given by

$$\sigma_{eq} = \sqrt{\left[ (\sigma_1 - \sigma_2)^2 + (\sigma_2 - \sigma_3)^2 + (\sigma_3 - \sigma_1)^2 \right] / 2} \quad (5.4)$$

and failure in the material occurs when  $\sigma_{eq} = \sigma_y$ , where  $\sigma_y$  is the yield stress in the material. If  $\sigma_3 = 0$ , the Equation 5.4 reduces to

$$\sigma_{eq} = \sqrt{\sigma_1^2 - \sigma_1\sigma_2 + \sigma_2^2} \quad (5.5)$$

This relationship is shown by the dashed ellipses of Figure 5.27. For the case of torsion with  $\sigma_2 = -\sigma_1 = \tau_y$ , the von Mises criterion becomes

$$\tau_y = \sigma_y / \sqrt{3} = 0.577\sigma_y \quad (5.6)$$

or  $MA = (0.577)OB$ . Yield tests of ductile materials have shown that von Mises failure criterion represents well the failure in a variety of materials, under biaxially loaded conditions.

### 5.2.3.2 Fracture Mechanics

Before utilizing the concepts of fracture, due to either brittle failure or fatigue, it will be useful to have some understanding of the development and growth of cracks when the structures are subjected to increasing and varying static/dynamic loads. The field of fracture mechanics provides a proper approach to the understanding of failure of materials under an applied load-deformation (or stress-strain) condition. The failure theories described earlier conceive failure in terms of applied stresses and their exceedance of the tensile or compressive strength of the material. In fracture mechanics, one deals with the concept of the applied stress and the development and growth of cracks in the material. Usually, the concept is applicable only to brittle materials, in a rigorous theoretical sense, but the method has also been applied to other ductile materials, limited by certain conditions. It can also be used for scenarios where a varying rate of loading condition exists. Fracture mechanics can be approached from the development of Griffith's criterion [39] to describe the load deformation behavior of glass, considering the energy balance in the material.

As per theoretical characterization, the interparticulate bonding (or cohesive) strength (which becomes the fracture strength, when a crack develops at the particle, extending on either side) developed in a material can be expressed as follows [40]:

$$\sigma_{ft} = (E\gamma_s/r_0)^{1/2}, \quad (5.7)$$

where

$\sigma_{ft}$  = tensile fracture strength of the material,

$E$  = Young's modulus of elasticity,

$\gamma_s$  = unit area surface energy of a free surface of the fracturing solid, and

$r_0$  = interparticulate distance. Also it can be shown that  $\gamma_s = G/2$ , where  $G$  is the strain energy release rate of a brittle material.

Using typical values of  $(\gamma_s$  and  $r_0)$ , a reasonable estimate of the cohesive strength of solids will be of the order of  $E/10$ . Griffith used the energy balance, minimization, and limiting condition of a stable crack (of half-crack length  $c$ ) to derive the theoretical fracture strength of the material as

$$\sigma_{ft} = [(2E\gamma_s/\pi c)]^{1/2} = [(EG/\pi c)]^{1/2} = [(ER/\pi c)]^{1/2}, \quad (5.8)$$

where  $c = \text{half-crack length} = r_0$ , and  $G = \text{strain energy release rate} = 2\gamma_s + G_p$ , with  $G$  and  $G_p$  as the total and plastic energies dissipation per unit area of crack growth, respectively, and  $R$  is the fracture toughness of the material (per unit area).

For brittle materials such as glass, the surface energy term dominates, and  $G = 2\gamma_s = 2.0 \text{ J/m}^2$ . For ductile materials such as steel, the plastic dissipation term dominates, and  $G = G_p = 1000.0 \text{ J/m}^2$ . For polymeric materials, close to the glass transition temperature, we have intermediate values of  $G \approx 2.0$  to  $1000 \text{ J/m}^2$ .

As the half-crack length ‘ $c$ ’ of Equation 5.8 reduces to  $r_0$  (the interparticulate distance), the strength  $\sigma_{ft}$  becomes the cohesive strength [or the fracture strength =  $E/(2\pi)$ ] of the material. When this fracture strength was measured in real materials, this was found to be much less ( $\approx E/10,000$ ) than the fracture (or cohesive) strength of materials. As per Griffith, this reduction of real strength was due to the presence of flaws in the material in the form of micro- and nanocracks, reducing the effective fracture strength of materials. He showed that in a plate subjected to uniform tensile stress  $\sigma_{\text{far-field}} = [\sigma]$ , as shown in Figure 5.28 [41], the maximum stress at the crack tip can be written as

$$\sigma_{\text{max}} = \sigma_{\text{far-field}} [1 + 2(c/\rho)^{1/2}] \tag{5.9}$$

The stress concentration factor can then be defined as

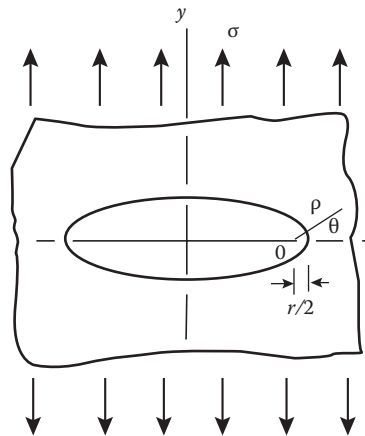
$$K_t = (\sigma_{\text{max}}/\sigma_{\text{far-field}}) = 1.0 + 2(c/\rho)^{1/2} \tag{5.10}$$

Very sharp cracks can be defined as discontinuities having zero radii of curvatures. When the radius of curvature  $\rho$  reaches a value of zero, the stress at the crack tip (or root of the notch) can become infinite, as shown in Figure 5.29 [42]; hence, a different approach is required to determine the influence of cracks on structures.

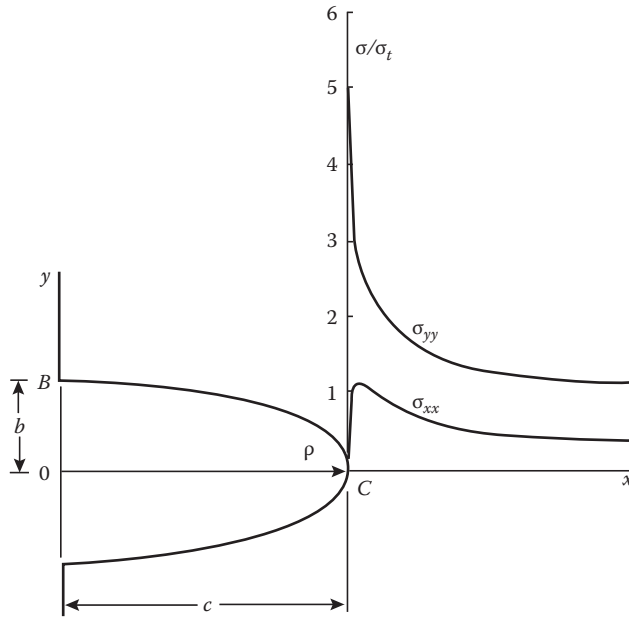
As per Westergaard [43], the stress field near a sharp crack, shown in Figure 5.30 [44], can be represented by the equation

$$\begin{Bmatrix} \sigma_x \\ \sigma_y \\ \tau_{xy} \end{Bmatrix} = \frac{K_I}{\sqrt{(2\pi r)}} \begin{Bmatrix} \cos(\theta/2)[1 - \sin(\theta/2)\sin(3\theta/2)] \\ \cos(\theta/2)[1 + \sin(\theta/2)\sin(3\theta/2)] \\ \sin(\theta/2)[\cos(\theta/2)\cos(3\theta/2)] \end{Bmatrix} \tag{5.11}$$

and  $\sigma_z = \nu(\sigma_x + \sigma_y), \quad \tau_{xz} = \tau_{yz} = 0.0$



**FIGURE 5.28** Idealized elliptical hole in an infinite plate under a far-field tensile stress  $\sigma$ . (W.D. Pilkey: *Formulas for Stress, Strain and Structural Matrices*, 2nd edition, 2005. Copyright Wiley-VCH Verlag GmbH & Co. KGaA. Reproduced with permission.)



**FIGURE 5.29** Stress concentration at an elliptical hole with  $c = 3b$ ; note the very high stress concentration at the crack tip. (From J.F. Young et al., 1998, *The Science and Technology of Civil Engineering Materials*, Prentice Hall, Upper Saddle River, NJ.)

where  $\nu$  is Poisson’s ratio,  $r$  is the distance of the point from the crack tip,  $K_I$  is the mode I stress intensity factor and has the form for an infinite solid,  $K_I = \sigma(\pi c)^{1/2}$ , see Equation 5.8.

For specimens with finite dimensions, this becomes,

$$K_I = F(c) \sigma(\pi c)^{1/2}, \tag{5.12}$$

where  $F(c)$  is a dimensionless factor dependent on the shape of the specimen, loading mode (viz., I or II or III), and crack depth  $c$ .

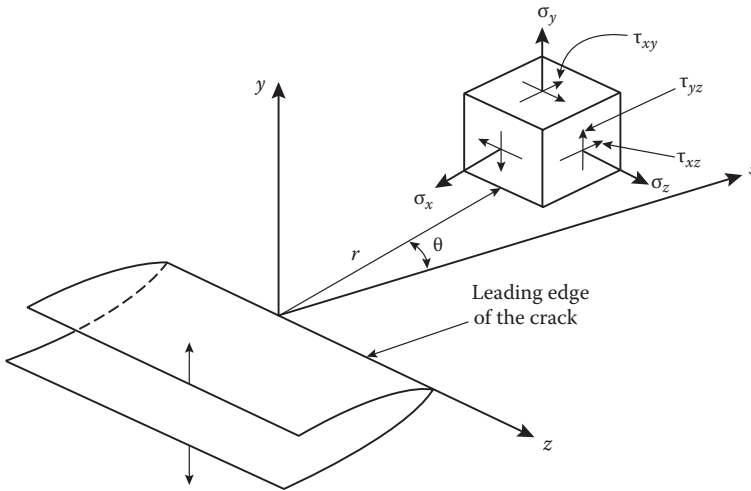
The coordinate axes used in Equation 5.11 can be seen in Figure 5.30. Moreover, it can also be seen from Equation 5.8, where the specimen undergoes fracture under plane stress conditions, that

$$(\sigma_{II})^2(\pi c)/E = K_{Ic}^2/E = 2\gamma_s = G_{Ic}, \tag{5.13}$$

where  $G_I = -[\partial U/\partial c]_P = -[\partial U/\partial c]_u$ , is the critical strain energy release rate for cracking under a fixed load  $P$  (or fixed displacement  $u$ ),  $U$  is the elastic strain energy of the cracking body,  $K_{Ic}$  is the mode I critical stress intensity factor (plane state conditions), viz., cracking under a pure tensile stress state. For cracking under plane strain conditions,  $(\sigma_{II})^2(\pi c)/E = (1 - \nu^2)K_{Ic}^2/E = 2\gamma_s = G_I$ .

Since mode I stress intensity factor  $K_I$  has been mentioned in Equations 5.12 and 5.13, it becomes necessary to introduce the other crack opening modes. Figure 5.31 [42] indicates the three basic modes of crack surface displacements that can exist in a cracking structure. While mode I shows the crack opening mode under tensile stresses, mode II, given in Figure 5.31, shows the crack sliding mode (under in-plane shear stresses), and mode III shows the tearing mode of crack growth (under transverse shear stresses).

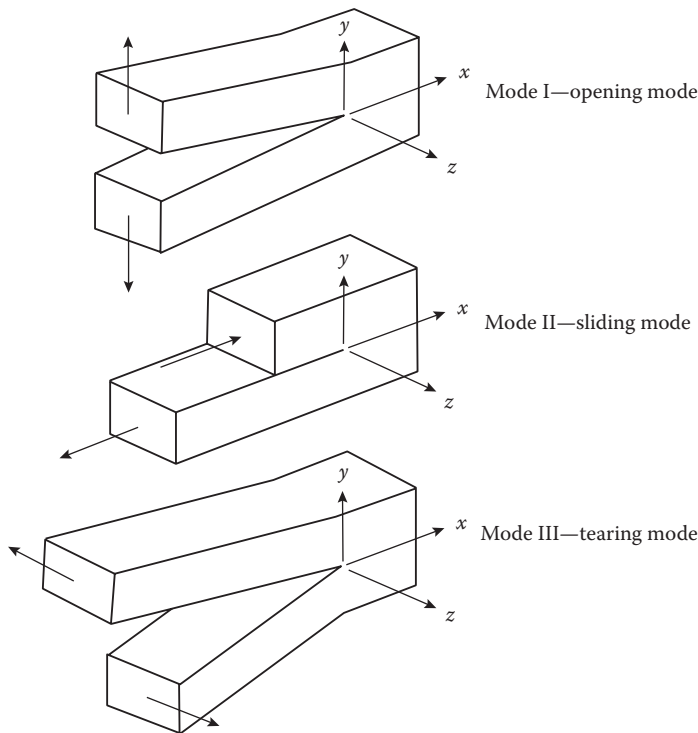
Another concept that needs to be considered is the notch sensitivity of a material. In a notch-sensitive material, the presence of a sharp notch (or crack) considerably reduces the tensile or flexural strength of the material. This occurs in elastic–brittle materials, where the temperature



**FIGURE 5.30** Coordinate system and stress displacement ahead of the crack tip (Mode I displacement). (From J.F. Young et al., 1998, *The Science and Technology of Civil Engineering Materials*, Prentice Hall, Upper Saddle River, NJ.)

conditions (or increasing strain rates) play a part in reducing the ductility of the material in the presence of a notch. The stress concentration at the notch tip becomes very high, causing the material to fail in brittle fracture. The far-field stress causing such brittle failures in materials is given by

$$\sigma_{ft} = K_{IC}/[F(c)(\pi c)^{1/2}] \tag{5.14}$$



**FIGURE 5.31** Three basic modes of crack displacements. (From J.F. Young et al., 1998, *The Science and Technology of Civil Engineering Materials*, Prentice Hall, Upper Saddle River, NJ.)

where  $K_{IC}$  is the critical stress intensity factor for the crack depth  $c$ . This ductile–brittle transition can be expressed in another manner by considering the state of stress and the shear and tensile strengths of the material. If the ratio of the actual tensile stress ( $\sigma$ ) to shear stress ( $\tau$ ), exerted in the crack tip of the material, exceeds the ratio of tensile strength ( $\sigma_{ft}$ ) to the shear strength ( $\tau_{ft}$ ) of the material, then the material will fail in a brittle manner. Otherwise, if the ratio of the tensile stress to that of the shear stress at the crack tip of the material is lower than the ratio of the tensile strength to that of the shear strength of the material, failure will occur by yielding, causing slip in the crack tip. This is represented by

$$\begin{aligned} \text{If } \sigma/\tau > \sigma_{ft}/\tau_{ft}, \text{ then brittle fracture occurs;} \\ \text{if } \sigma/\tau < \sigma_{ft}'/\tau_{ft}, \text{ then yielding and shear slip occur.} \end{aligned} \quad (5.15)$$

For many materials, service conditions such as temperature, rate of loading, and degree of triaxiality at the crack tip will also influence the ductile-to-brittle transition [40].

### Example 5.1

A point on the free surface of an offshore structural component, made of aluminum alloy 2024-T4, is subjected to the state of stress given as follows:  $\sigma_x = 60.0$  MPa,  $\sigma_y = 120.0$  MPa, and  $\tau_{xy} = 72.0$  MPa. What is the safety factor against yielding at the specified point? Yield strength of 2024-T4 aluminum is 303.0 MPa.

$$\begin{aligned} \text{Principal normal stress} = \sigma_1, \sigma_2 &= (\sigma_x + \sigma_y)/2 \pm \left[ \left\{ (\sigma_x - \sigma_y)/2 \right\}^2 + (\tau_{xy})^2 \right]^{1/2} \\ &= (60 + 120)/2 \pm \left[ \left\{ (60 - 120)/2 \right\}^2 + (72.0)^2 \right]^{1/2} = 90.0 \pm 78.0 \\ &= 168.0 \text{ and } 12.0 \text{ MPa.} \end{aligned}$$

$$\text{Third normal stress} = \sigma_3 = \sigma_z = 0.0.$$

Following Equation 5.2 [Mohr's maximum shear stress yield criterion], since both the principal stresses are positive, the failure is in first quadrant; hence,  $\sigma_{eff} = 168.0$  MPa; also,  $\sigma_{ut} = 303.0$  MPa.

$$\text{Factor of safety} = 303.0/168.0 = 1.804$$

Using von Mises theory (or Octahedral shear stress theory),

$$\sigma_{eff} = [(\sigma_1)^2 - \sigma_1\sigma_2 + (\sigma_2)^2]^{1/2} = [168^2 - (168)(12) + 12^2]^{1/2} = 162.33 \text{ MPa.}$$

$$\text{Factor of safety} = 303.0/162.33 = 1.867.$$

### Example 5.2

Grey cast iron, used for the pedestal of an offshore structural component, has a tensile strength of 220.0 MPa and a compressive strength of 780.0 MPa; these values are averages from three tests carried out on a single batch of material. (i) Assuming that the modified Mohr criterion applies, calculate the factors of safety for tensile and compressive failure in the pedestal when the stresses

at a point in the pedestal are given as  $\sigma_x = 80.0$  MPa,  $\sigma_y = -220.0$  MPa, and  $\tau_{xy} = 80.0$  MPa. (ii) A 40-mm-diameter shaft of this material is subjected to a torque of 1200 N.m.; determine the safety factor against fracture. (iii) What is the safety factor against fracture if a 130.0 kN compressive load is applied to the shaft in addition to the above?

- (i) The principal stresses are given by  $\sigma_1, \sigma_2 = (\sigma_x + \sigma_y)/2 \pm [((\sigma_x - \sigma_y)/2)^2 + (\tau_{xy})^2]^{1/2}$ .  
Therefore,

$$\begin{aligned}\sigma_1, \sigma_2 &= (80 - 220)/2 \pm \left[ \left\{ (80 + 220)/2 \right\}^2 + (80)^2 \right]^{1/2} = -70.0 \pm 170.0 \\ &= 100.00 \text{ MPa, and } -240.0 \text{ MPa.}\end{aligned}$$

The stresses are in the second quadrant; hence, Equation 5.2b applies.  
Hence,  $m[(\sigma_1/\sigma_{ut}) - (\sigma_2/\sigma_{uc})] = 1.0$ , i.e.,  $m[(100/220) - (-240/780)] = 1.0$ .

$$\text{Safety factor} = m = 1.0/(0.4345 \pm 0.3077) = 1.347$$

- (ii) Under pure torsion, Equation 5.1 governs failure, viz.,  $\tau_u = \sigma_{ut}$ .

$$\begin{aligned}\text{Torsional stresses set up in the shaft} &= \tau_{xy} = Tr/J = (1200)(20/1000)/[\pi(20/1000)^4/2] \\ &= (1200)(20)(2)(1000)^4/[1000\pi(20)^4] = 95.49 \text{ MPa.}\end{aligned}$$

Hence,  $m(\tau_{xy}) = \sigma_{ut}$ ;  $m = 220.0/95.49 = 2.304$ .

- (iii) Additional compressive stress =  $-(130)(1000)/[\pi(20/1000)^2] = -103.45$  MPa.  
Principal stresses are given by

$$\begin{aligned}\sigma_1, \sigma_2 &= (\sigma_x + \sigma_y)/2 \pm \left[ \left\{ (\sigma_x - \sigma_y)/2 \right\}^2 + (\tau_{xy})^2 \right]^{1/2} \\ \sigma_1, \sigma_2 &= (-103.45 - 0.0)/2 \pm \left[ \left\{ (-103.45 + 0.0)/2 \right\}^2 + (95.49)^2 \right]^{1/2} = -51.73 \pm 108.60 \\ &= +56.87 \text{ MPa, } -160.33 \text{ MPa.}\end{aligned}$$

The stresses are in the second quadrant; hence, Equation 5.2b applies.  
Hence,  $m[(\sigma_1/\sigma_{ut}) - (\sigma_2/\sigma_{uc})] = 1.0$ , i.e.,  $m[(56.87/220) - (-160.33/780)] = 1.0$ .

$$\text{Safety factor} = m = 1.0/(0.2585 \pm 0.2056) = 2.155.$$

### Example 5.3

Use Griffith's derived Equation 5.7 (for the cracking strength of material when a very small flaw is developed) and determine the cracking stress of a steel specimen, at very low temperatures, having a crack length of 0.2 nm,  $\gamma_s = 1.0$  J/m<sup>2</sup> and  $E = 200$  GPa.

As per Equation 5.7,  $\sigma_{ft} = [E\gamma_s/r_0]^{1/2}$ .

Also,  $r_0 = c_0$  (see Equation 5.7) =  $(2.0)(10^{-9})$  m.

Hence,

$$\begin{aligned}\sigma_{ft} &= [E\gamma_s/r_0]^{1/2} = \left[ (200)(10^9)(1.0) / \left\{ (0.2)(10^{-9}) \right\} \right]^{1/2} = (31.62)(10^{-9}) \text{ GPa} \\ &= E/6.32 \text{ GPa} \approx E/10.0 \text{ GPa.}\end{aligned}$$

**Example 5.4**

The strength of glass (used in the manufacture of beer bottles) is given as 160.0 MPa. Determine the Griffith flaw size for this material. Take  $E = 60.0$  GPa and fracture toughness of glass to be  $21.0$  J/m<sup>2</sup>.

Using Equation 5.8, viz.,  $\sigma_{ft} = [ER/\pi c]^{1/2}$ ,

$$(160)(10^6) = \{[(60)(10^9)(21.0)]/[\pi c]\}^{1/2}.$$

$$c = \{(60)(10^9)(21)/[(160)(10^6)]^2/(\pi)\} = (15.7)(10^{-6}) \text{ m} = 15.7 \text{ } \mu\text{m}.$$

$$\text{Griffith's flaw size} = (2)(15.7) = 31.4 \text{ } \mu\text{m}.$$

**Example 5.5**

The cracked plate of a certain material was stressed, until it began to crack at a constant (or fixed) load of 120.0 lb. wt. Just before the crack started to run, the deflection of the plate was 0.0985 in., and when the crack stopped, the deflection was 0.119 in. Calculate the following: (i) work done in propagating the crack and (ii) the fracture toughness of the material, if the crack area increased by 1.86 in.<sup>2</sup> during the sudden crack growth.

$$\begin{aligned} \text{(i) Work done during the sudden crack growth} &= (1/2)(120)(0.119 - 0.0985)/12 \\ &= 0.103 \text{ ft. lb.} \end{aligned}$$

$$\begin{aligned} \text{(ii) Fracture toughness} &= R = (\text{Work done})/(\text{increased in cracked area}) \\ &= 0.103/\{(1.86)/(144)\} = 7.97 \text{ J/ft.}^2 \end{aligned}$$

**Example 5.6**

Two metal strips (each of 1.0 mm thickness and 10 mm width) are glued together as shown in Figure E5.1. A small area of glue was omitted over the central section, as shown in the figure. The joint is pulled apart by two equal and opposite central forces, as shown in the figure. At what load will the glued joint start to fail? Assume the plate bending theory to hold good for the glued metal strips. Take  $E$  for the metal = 200 GPa. Assume the fracture toughness of the glue to be 330 J/m<sup>2</sup>.

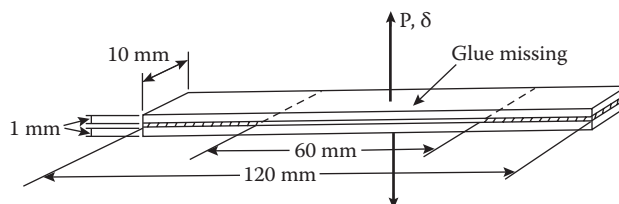
Assume the plate over the unglued portion to be a fixed plate, deforming under a central load.

$$\text{Deflection of one unglued portion of the plate} = \delta = PL^3/(192 EI).$$

$$\text{Total deflection at the location of the load} = (2)\{PL^3/(192 EI)\} = PL^3/(96 EI).$$

Hence,

$$\delta/P = L^3/(96 EI) \tag{E5.1a}$$



**FIGURE E5.1** Partially glued metal strip.



It can also be shown that the relationship between the load  $P$ , deflection  $\delta$ , and the area  $A$  of sudden cracking ( $dA \equiv bdL$ ) is given by

$$P_{\text{crack}}^2 = (2R)/[d(\delta/P)/dA], \quad (\text{E5.1b})$$

where  $\delta$  is the deflection under the applied loads,  $R$  is the fracture toughness of the material under test,  $A = \text{cracking area} = bdL$ ,  $L$  = the span of the beam under test and  $P$  is the load applied.

From Equation E5.1b,

$$\begin{aligned} P_{\text{crack}}^2 &= (2R)/d \left\{ L^3 / (96 EI) \right\} / d(bdL) \\ &= (2R)(96 EIb) / \{ d(L^3) / dL \} = 192 REIb / (3L^2) = 64 REIb / L^2 \\ &= (64)(330)(200)(10^9) \left\{ (1/12)(10)(10^{-3})(1/1000)^3 \right\} (10)(10^{-3}) / \left\{ (60)(10^{-3}) \right\}^2 \\ &= 9777.78 \text{ N}^2 \end{aligned}$$

$$P_{\text{crack}} = 98.88 \text{ N.}$$

### 5.2.3.3 Fatigue Failure and Crack Initiation

Fatigue failure results from a repeated cyclic loading acting on a particular structural component or the whole structure. The cyclic loading may be due to the cyclic repetition of a deterministic loading scenario or due to a pure random loading scenario. Fatigue failures imply that under repeated cyclic loads materials undergo progressive, internal, and permanent damage to their material fabric, which would lead to sudden and catastrophic failures in structures, unless some remedial measures are taken. There are two stages in the process of crack growth and failure under a fatigue load condition, viz., (i) initiation (nucleation), growth, and coalescence of a large number of surface-breaking, ellipse-shaped microcracks into a single flat-fronted crack at the welded joints or other hot spot regions and (ii) propagation of the flat-fronted crack through the thickness of the material to a critical depth (or thickness) that will cause fracture in the material [45–47]. The fatigue life of the specimen under consideration is given by

$$N_T = N_i + N_p, \quad (5.16)$$

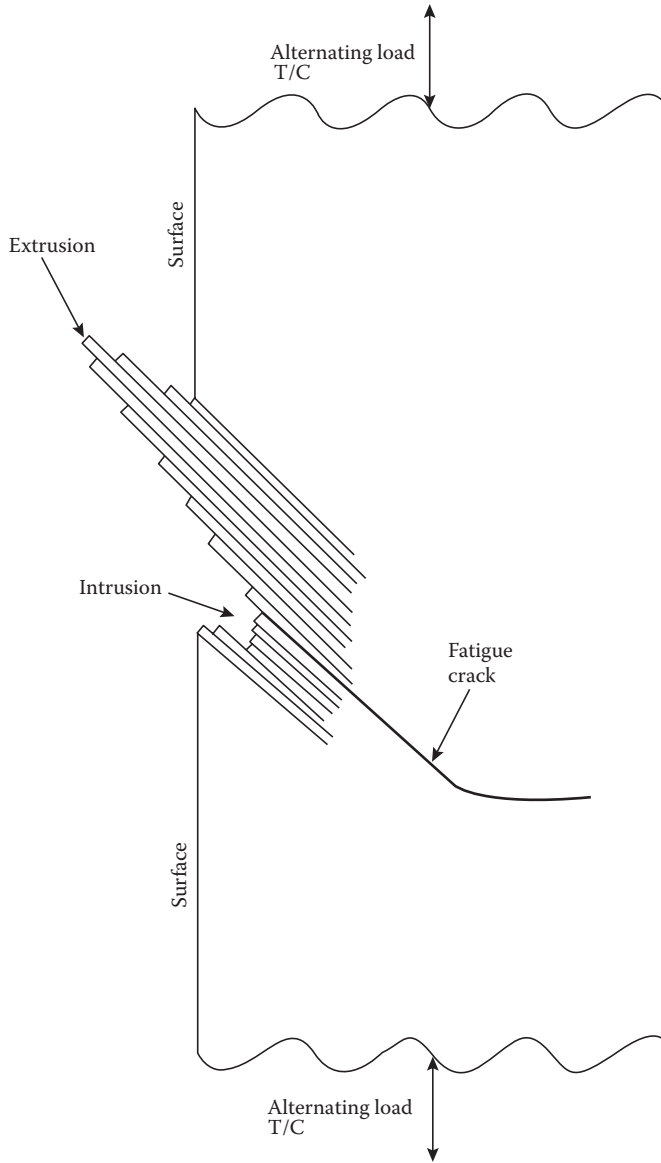
where  $N_T$  is the total fatigue life of the specimen,  $N_i$  is its crack initiation life, and  $N_p$  is its crack propagation life.

Fatigue cracks originate at a free surface where high stress concentration (called a hot spot region) occurs. This stress concentration may be caused by a preexisting flaw in the material surface, or a human-made discontinuity such as the root of a thread, rivet, or hole, or the discontinuity at which there is an abrupt change in thickness or shape (perhaps a welded region or change in thickness). The initiation of these cracks, in metal surfaces, is caused by the mechanism of slip, which causes slip bands to occur around the hot spot region (high stress concentration region) due to dislocation movements; this is illustrated in Figure 5.32 [48].

Due to these slip movements at the surface, relatively small displacements of atoms at the free surface occur (of the order of a nanometer, or  $10^{-9}$  m). Under the repeated cyclic loads, additional slips continue to occur at these regions, which will grow into a well-defined crack. In the beginning, these incipient cracks will grow along the slip planes, but subsequently, it will change direction and grow in a plane perpendicular to the principal tensile stress, as shown in Figure 5.32.

The crack initiation life,  $N_i$ , is determined using the Coffin–Manson equation with Morrow's mean stress correction [46]:

$$\Delta \epsilon / 2 \left( (\sigma'_f - \sigma_m) / E \right) (2N_i)^b + \epsilon'_f (2N_i)^c, \quad (5.17)$$



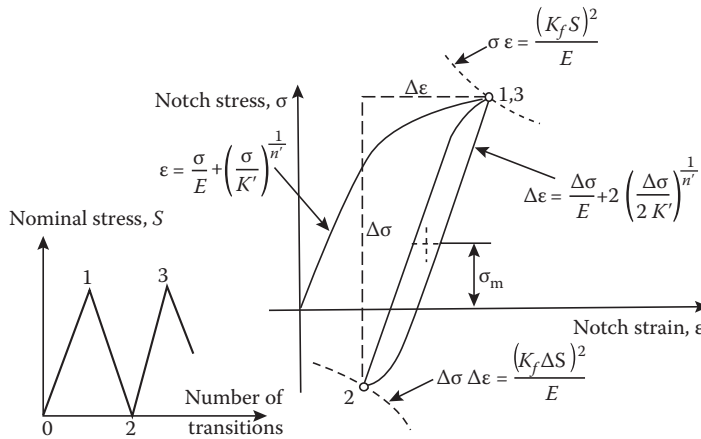
**FIGURE 5.32** Schematic diagram of crack initiation and subsequent crack growth. (From J.F. Young et al., 1998, *The Science and Technology of Civil Engineering Materials*, Prentice Hall, Upper Saddle River, NJ.)

where  $\sigma'_f$  and  $\epsilon'_f$  are the fatigue strength and ductility coefficients,  $b$  and  $c$  are the fatigue strength and ductility exponents,  $\Delta\epsilon$  is the local strain range,  $\sigma_m$  is the mean stress at the weld toe, and  $N_i$  is the crack initiation life.

The local stress and strain behavior is represented by the Ramberg–Osgood cyclic strain curve, giving the elastic and inelastic strain components as

$$\Delta\epsilon = \Delta\sigma/E + 2(\Delta\sigma/K')^{(1/n')}, \tag{5.18}$$

where  $K'$  and  $n'$  are the cyclic strength coefficient and strain hardening exponent, respectively, and  $\Delta\sigma$  is the local stress range.



**FIGURE 5.33** Schematic illustration of the local stress–strain hysteresic loop analysis. (From T. Lassen, Ph. Darcis and N. Recho. AWS Welding Journal, in *Fatigue behavior of welded joints – Part I: Statistical methods for fatigue life prediction and Part II: Physical modeling of the fatigue process*, Dec. 2005, pp. 183-s to 187-s and January 2006, pp. 19-s to 26-s.)

The definition of terms in the local stress–strain variation is shown in Figure 5.33 [46]. The stress–strain variation is governed by Neuber’s rule as

$$\Delta \epsilon \Delta \sigma = (K_t \Delta S)^2 / E, \tag{5.19}$$

where  $\Delta S$  is the nominal stress range and  $K_t$  is the elastic stress concentration factor at the weld toe.

Equation 5.19 is modified by introducing the fatigue notch factor  $K_f$  instead of  $K_t$ . Using Peterson’s equation, fatigue notch factor  $K_f$  can be represented by

$$K_f = 1.0 + (K_t - 1) / (1 + a_p / \rho), \tag{5.20}$$

where  $a_p$  is the Peterson’s material parameter, equal to  $(1.087 \times 10^5 S_u^{-2})$ ,  $S_u$  is the tensile strength of steel (in  $N/mm^2$ ), and  $\rho$  is weld toe root radius (in mm).

Following Niu and Glinka’s formulation [49],  $K_t$  can be expressed in terms of  $K_f$  as

$$K_t = 1.0 + (0.5121(\theta)^{0.572} (T/\rho)^{0.469}), \tag{5.21}$$

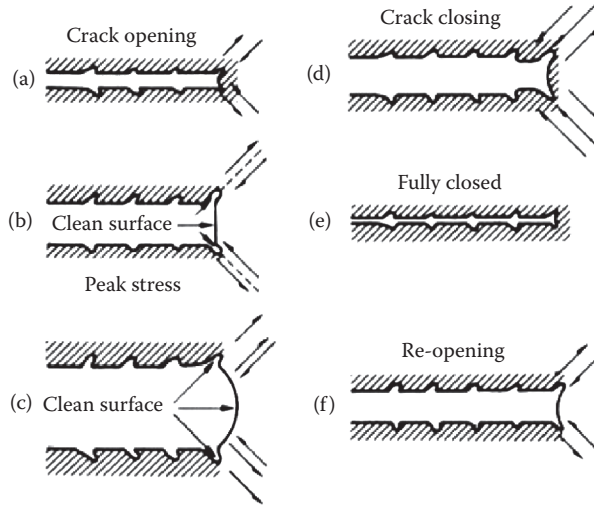
where  $T$  is thickness of plate.

Finally, combining Equations 5.17 through 5.21, the crack initiation life can be expressed as

$$\begin{aligned} N_i &= (1/2) \left\{ (K_f \Delta S) / [2(\sigma'_f - \sigma_m)] \right\}^{(1/b)} \\ &= (1/2) \left\{ (K_f \Delta S) [2(\sigma'_f - \sigma_m)] \right\}^{-(1/b)} \end{aligned} \tag{5.22}$$

### 5.2.3.4 Fatigue Failure and Crack Propagation

Beyond the crack initiation period, the crack in the specimen will propagate in a steady manner depending on the nature of the load. It is also observed that this growth of crack will always occur under shear or tensile stresses and will not occur under compressive stresses, since compression will close the cracks rather than open them. Also this crack extension under tensile loading will always occur at the crack tip. Under each loading cycle, the crack will propagate by a finite distance, and this can sometimes be as high as  $25.0 \mu m/cycle$ . The process of crack growth is shown in Figure 5.34



**FIGURE 5.34** Fatigue crack advance by crack tip sharpening (during closing) and plastic blunting (during opening) process. (From R. Reuben, 1990, Corrosion and defect evaluation, Chapter 10, in *Marine Technology Reference Book*, ed. N. Morgan, Butterworths, London.)

[50]. The crack is initially sharp, and as it opens under the tensile loading and propagates, the crack tip becomes blunted as the plastic zone develops at the crack tip. Thereafter, during the compressive unloading cycle, the material at the crack tip gets compressed and sharpens the crack tip. Moreover, during this sequential process of blunting and sharpening of the crack tip, the material experiences deformation markings called striations (or bench marks) in the fracture surface. This process of crack growth is repeated until a critical crack length is reached, beyond which the specimen fails in a brittle or ductile manner, depending on the property of the material.

Analyzing the crack growth data obtained from experimental measurements, Paris and Erdogan [51] proposed the relationship that governs the fatigue life (crack propagation) and crack growth; he stated that the range of stress intensity factor ( $\Delta K$ ) would characterize the subcritical crack growth rate in structural materials. From an examination of the fatigue crack growth rate vs. life curves obtained for a number of metal alloys, he observed that the plots of crack growth rate ( $dc/dN$ ) against the range of stress intensity factor ( $\Delta K$ ) gave straight lines on log–log scales, viz.,

$$\log (dc/dN) = m \log (\Delta K) + \log (C) \tag{5.23}$$

Rearranging Equation 5.23, one obtains

$$dc/dN = C(\Delta K)^m, \tag{5.24}$$

where  $C$  and  $m$  are known as material constants.

Since  $C$  and  $m$  are material constants, they are computed from the analysis of data from compact tension crack growth tests on the specified material. By integration of the Paris crack growth rate equation, represented by Equation 5.24, the number of cycles to failure can be presented in an S–N format by

$$N_P = (1/C) \int_{c_0}^{c_c} dc / (\Delta K)^m = (1/C) \int_{c_0}^{c_c} dc / \left( [\Delta S \sqrt{(\pi c)} F(c)] \right)^m, \tag{5.25}$$

where  $N_p$  is the crack propagation life,  $C$  and  $m$  are the material constants dependent on mean stress and environmental conditions,  $c_0$  and  $c_c$  are the initial crack depth and the crack depth at which the crack propagation life is required, and  $F(c)$  is a dimensionless fraction accounting for loading mode, crack shape, and joint geometry. Also  $\Delta K = \Delta S \sqrt{(\pi c)}$   $F(c) \geq \Delta K_{th}$ , since no crack growth is assumed to occur below  $\Delta K_{th}$ .

The dimensionless factor  $F(c)$  may be conveniently expressed as [51]

$$F(c) = F_E F_S F_T F_W F_G, \quad (5.26)$$

where

- $F_E$  = basic crack shape factor,
- $F_S$  = front face factor,
- $F_T$  = back face of finite thickness factor,
- $F_W$  = finite width factor, and
- $F_G$  = stress gradient factor.

The values of  $F_E$ ,  $F_S$ ,  $F_T$ ,  $F_W$ , and  $F_G$  are defined in Table 5.2 [52] for some welded profiles; for others, the following publications could be consulted: references [53–55].

As observed earlier, the physical and mechanical properties of materials are subject to a certain amount of variability; it is also seen that this variation in test data are relatively small for most of the structural materials. If the fatigue life vs. the nominal (far-field) stress of the specimen failing under fatigue is plotted (semi-log), it will give a curve similar to Figure 5.35 [56].

As one can see from Figure 5.35, there is considerable scatter in the fatigue stress range vs. fatigue life data. Hence, a better way to establish the fatigue life of the material will be to determine the distribution of the fatigue data and use it in design. If the fatigue data is plotted (semi-log) as fatigue cycles to failure vs. the number of specimens that failed at a particular load cycle, then the plot will look like Figure 5.36 [57]. The data give a very close approximation to a normal or Gaussian distribution (in a semi-logarithmic plot). Also it must be stated that when the range of nominal stress is near the higher end of fatigue life, the nature of the distribution is uncertain.

In order to give context to the fatigue stress range vs. life data given in earlier figures, Figure 5.37 [58] shows the plot of fatigue stress range vs. life data obtained for tubular joints tested under simulated ocean corrosion conditions; it also shows the fatigue stress range vs. life plot when the corrosion of tubular joints was minimized (or prevented) with cathodic protection of tubular joints. It is seen from Figure 5.37 that corrosion of ocean structures reduces the fatigue stress range of the tubular joints; hence, there is a required need for protecting the offshore structures with cathodic protection so that the life of offshore structures can be maintained at an optimum level.

Since fatigue stress range vs. life data is scattered, statistical considerations must be taken into account in specifying the fatigue stress range vs. life data in actual design. This is done through specifying the scatter band in terms of the standard deviation of the fatigue stress range vs. life data. Figure 5.38 [58] gives the stress range vs. life data obtained for laboratory fatigue tests with a number of lines showing the standard deviations of the mean from the median fatigue strength (or stress range) vs. life range. Since the distribution is normal (on a semi-log plot), it shows that (i) 68.3% of the data will fall within  $\pm 1.0s$  of the median curve values, (ii) 95.4% of the data will fall within  $\pm 2s$  of the median curve values, and (iii) 99.7% of the data will fall within  $\pm 3s$  of the median curve values ( $s$  is the standard deviation of the data).

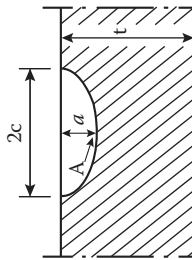
### Example 5.7

The critical stress intensity factor range for a material, being considered for use in an offshore structure, is given as 50.0 ksi $\sqrt{\text{in}}$ . Determine the critical flaw size (through-the-thickness) for

**TABLE 5.2**  
**Factors Influencing the Dimensionless Functions Accounting for Loading Mode, Crack Shape, and Joint Geometry**

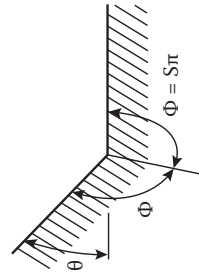
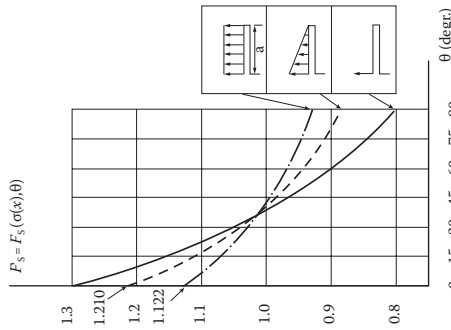
**Basic Crack Shape**

$F_E = [1 + 4.594(a/2c)^{0.65}]^{-0.5}$  where the magnitude of  $F_E$  pertains to point A in the figure shown below.

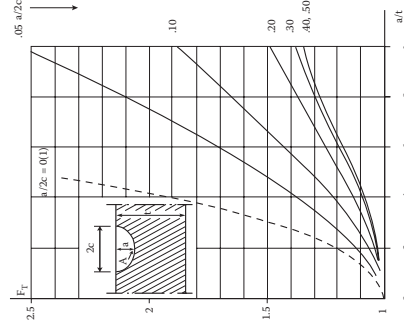


**Front Face Factor,  $F_S$**

$F_S = (F_S^*) (f_S)$ , with  $f_S = 1 - 0.16(a/2c)$ , and  $F_S^* = F_S^*(\alpha(x), \theta)$  is obtained from the curves given in figure below.

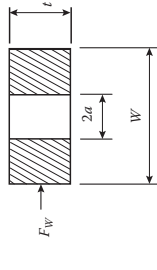


**Back Face or Finite Thickness Factor,  $F_T$**



**Finite Width Factor,  $F_W$**

For a through crack shown below,  $F_W = [1 - (0.1)(a/W)^2 + 0.96(a/W)^4] \sqrt{\sec(\pi a/W)}$  (see below for details).



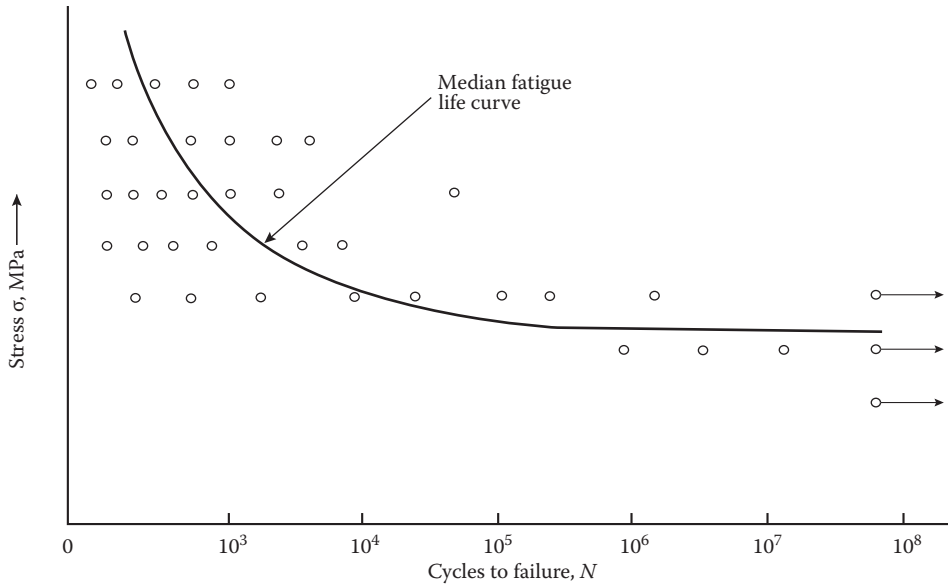
\*Through crack

**Stress Gradient Factor,  $F_G$**

This factor accounts for nonuniform crack opening stresses, due to nonuniform applied stress or stress concentration caused by geometry details. An approximate relationship is given as  $F_G/SCF = 1/[1 + (1/d)\alpha^q]$ , where SCF = stress concentration at the weld toe,  $\alpha$  = nondimensionalized crack length ( $a/t$  or  $a/W$ ), and  $d$  and  $q$  are related to decay of stress gradients.

For transverse butt welds,  $F_G = (5a/t)^{-q}$ , where  $q = \log(11.584 - 0.0588\phi)/\log(200)$ , and  $135^\circ \leq \phi \leq 180^\circ$  with  $\phi$  being the obtuse toe angle.

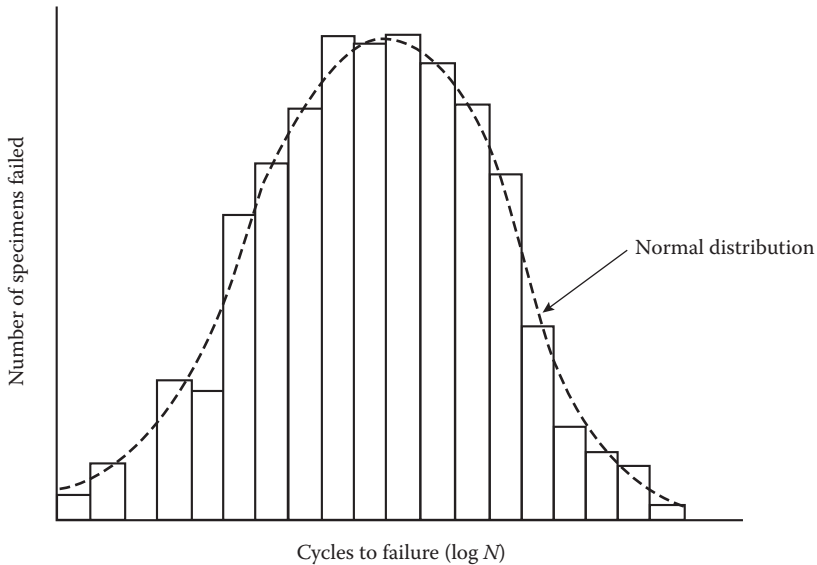
For other types of weld toes, Reference [52] should be consulted.



**FIGURE 5.35** Plot of (nominal) stress vs. life cycle (S–N) data, showing the scatter in the data. (From J.F. Young et al., 1998, *The Science and Technology of Civil Engineering Materials*, Prentice Hall, Upper Saddle River, NJ.)

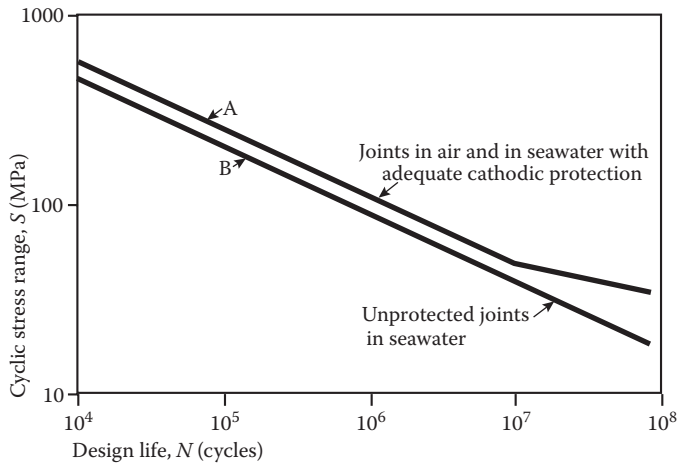
various allowable stress levels in the material, up to a value of 1000.0 ksi. [Hint: For a center-cracked through-the-thickness flaw (or crack), the stress intensity factor is given by  $\Delta K_{Ic} = \Delta S\sqrt{\pi c}$ , where  $\Delta K_{Ic}$  is the critical stress intensity range for a stress range of  $\Delta S$ .]

From Equation 5.25,  $\Delta K = \Delta S\sqrt{\pi c} F(c)$ ; when  $F(c) = 1.0$ , the equation reduces to  $\Delta K = \Delta S\sqrt{\pi c}$ . For critical flaw size, the equation becomes  $\Delta K_{Ic} = \Delta S\sqrt{\pi c}$ .

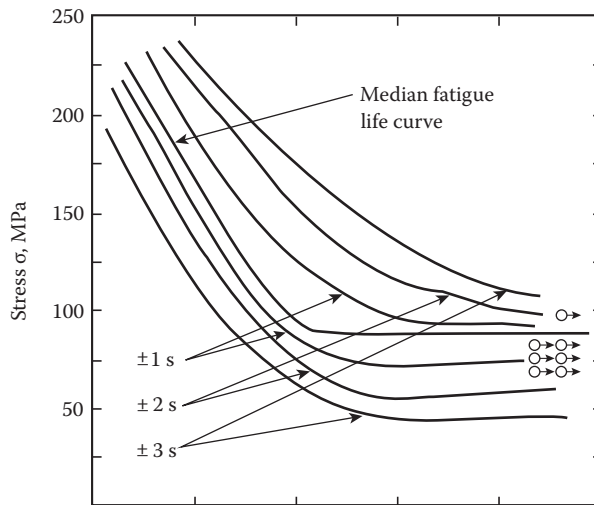


**FIGURE 5.36** Distribution of fatigue S–N data obtained at constant stress level. (From: Design and Operational Guidance on Cathodic Protection of Offshore Structures, Sub-sea Installations and Pipelines, in *Principles of corrosion and cathodic protection offshore*, The Marine Technology Directorate Ltd., p. 137, 1990. With permission.)





**FIGURE 5.37** Basic S–N curve for protected and unprotected tubular steel joints in seawater. (From J.F. Young et al., 1998, *The Science and Technology of Civil Engineering Materials*, Prentice Hall, Upper Saddle River, NJ.)



**FIGURE 5.38** Plot of S–N data collected in laboratory showing standard deviations of data. (From J.F. Young et al., 1998, *The Science and Technology of Civil Engineering Materials*, Prentice Hall, Upper Saddle River, NJ.)

Therefore,  $50.0 \text{ ksi}\sqrt{\text{in.}} = \Delta S\sqrt{(\pi c)}$ ; hence,  $c = [(50/\Delta S)^2]/\pi$ .

$\Delta S$ (ksi)	$c$ (inch)	$\Delta S$ (ksi)	$c$ (inch)
5	31.83	55	0.26
15	3.54	65	0.19
25	1.27	75	0.14
35	0.65	85	0.11
45	0.39	95	0.09

The results can be plotted as shown in Figure E5.2.

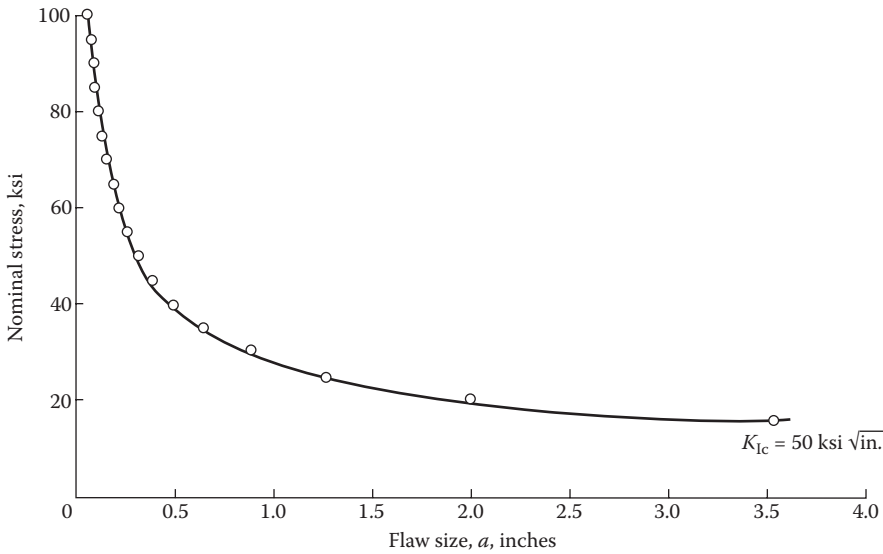


FIGURE E5.2 Critical flaw size vs. nominal stress in the specimen (in the given figure,  $c \equiv a$ , and  $a \equiv c$ ).

**Example 5.8**

A 30.0-in.-diameter, high-strength steel offshore cylindrical pressure vessel is to be designed to withstand an internal pressure of 6000 psi, with an internal parabolic flaw of maximum depth 0.5 in. ( $= c$ ). The flaw has an aspect ratio  $[c/(2a)]$  of 0.25, with  $(2a)$  as the surface length of crack. The critical stress intensity of the material is  $220.0 \text{ ksi}\sqrt{\text{in.}}$ , and the yield strength of the steel is 180 ksi. Determine the required wall thickness of the pressure vessel to resist the pressure of 6000 psi internal gas pressure. [Hint: The critical stress intensity factor range, for a surface flaw, is given by  $\Delta K_{Ic} = 1.10(M_k)(\Delta S)\sqrt{\{(\pi c)/Q\}}$ , where  $M_k$  is the magnification factor assumed to be varying linearly between 1.0 and 1.6, as  $c/t$  increases from 0.5 to 1.0 ( $t =$  thickness of the cylindrical pressure vessel). Also for  $c/t$  values less than 0.5, take  $M_k = 1.0$ . The value of the flaw shape parameter  $Q$  is given in Figure E5.3 [59].]

Since  $\Delta K_{Ic} = 1.10(M_k)(\Delta S)\sqrt{\{(\pi c)/Q\}}$ ,  $\Delta S = \{[\sqrt{Q}](\Delta K_{Ic})/[1.10(M_k)\sqrt{\pi c}]\}$ .

Trial I: For the given steel,  $\Delta K_{Ic} = 220 \text{ ksi}\sqrt{\text{in.}}$ ;  $c = 0.5 \text{ in.}$ ; in Figure E5.3, assume  $\sigma_c/\sigma_{ys} = \Delta S/\sigma_{ys} = 0.55$ , and for the given  $c/(2a) = 0.25$ ,  $Q = 1.4$ .

Take  $M_k = 1.0$  for the first trial, since  $c/t$  is unknown.

$\Delta S = \{[\sqrt{1.4}](220)/[(1.10)(1.0)\sqrt{\{(\pi)(0.5)\}}]\} = 188.81 \text{ ksi} > 180.0$  (yield stress); hence, take  $\Delta S = 180.0 \text{ ksi}$ .

For a thin cylindrical vessel,  $\Delta S = (p_{int})(\text{Dia.})/(2t)$ ; i.e.,  $(180.0)(1000) = [(6000.0)(30.0)]/(2t)$ . Hence,  $t = 0.5 \text{ in.}$

Trial II: Since  $c = t$ , we need to check for the value of  $M_k$ .  $c/t = 1.0$ ; hence,  $M_k = 1.6$ .

Assume  $\sigma_c/\sigma_{ys} = 0.8$ ; for this value of  $\sigma_c/\sigma_{ys}$ , and for the given  $(c/2a) = 0.25$ ,  $Q = 1.33$  (see Figure E5.3).

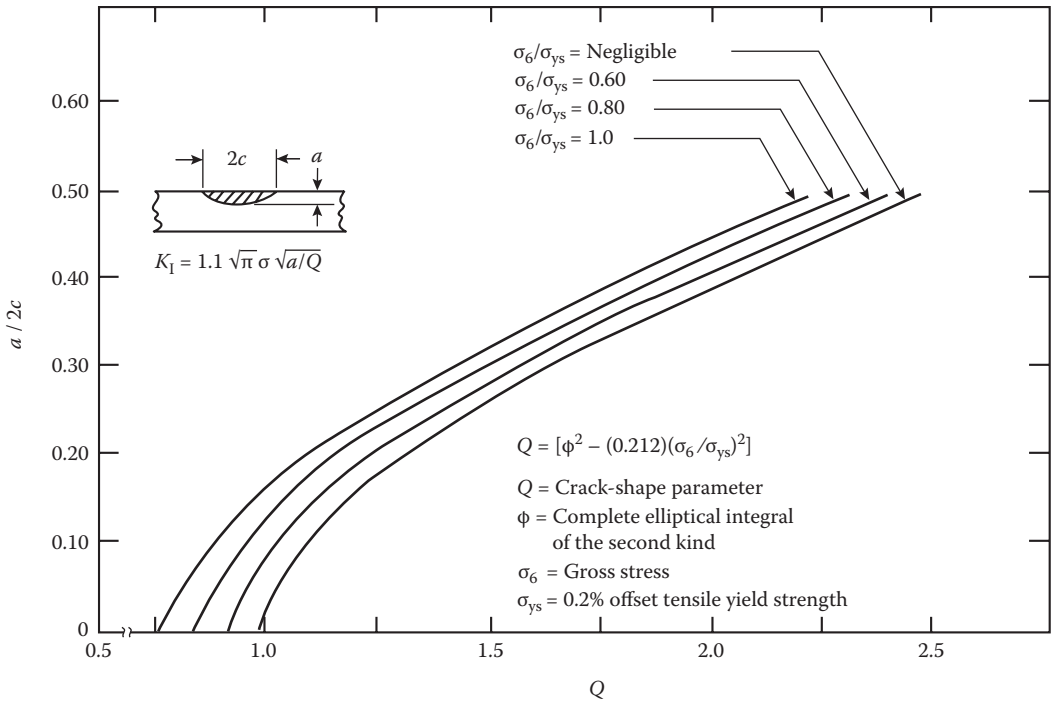
$\Delta S = \{[\sqrt{1.33}](220)/[(1.10)(1.6)\sqrt{\{(\pi)(0.5)\}}]\} = 115.02 \text{ ksi}$ . For this value of the design stress,  $(115.02)(1000.0) = (6000.0)(30.0)/\{(2.0)(t)\}$ . Therefore,  $t = 0.78 \text{ in.}$

Trial III:  $c/t = 0.5/(0.78) = 0.64$ ; hence,  $M_k = 1.0 + \{(0.14/0.5)\}(0.6) = 1.168$ .

Assume  $\sigma_c/\sigma_{ys} = 0.90$ ; for this value of  $\sigma_c/\sigma_{ys}$ , and for the given  $(c/2a) = 0.25$ ,  $Q = 1.30$  (from Figure E5.3).

For this,  $\Delta S = \{[\sqrt{1.30}](220.0)/[(1.10)(1.168)\sqrt{\{(\pi)(0.5)\}}]\} = 155.77 \text{ ksi}$ . For this value of the design stress,  $(155.77)(1000) = (6000.0)(30.0)/\{(2.0)(t)\}$ . Therefore,  $t = 0.58$ .

After a few more trials (with  $\sigma_c/\sigma_{ys} = 0.95$ ), the converged value of  $t = 0.66 \text{ in.}$



**FIGURE E5.3** Crack shape parameter  $Q$  as a function of crack ratio  $c/(2a)$ . (From S.T. Rolfe and J.M. Barsoum, 1977, *Fracture and Fatigue Control in Structures: Applications of Fracture Mechanics*, Prentice Hall Inc., Upper Saddle River, NJ, p. 159.)

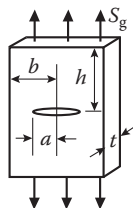
**Example 5.9**

A center-cracked plate shown in Figure E5.4a [60] has dimensions  $b = 60$  mm,  $t = 8.0$  mm, and large  $h$ , and a load  $P = 100.0$  kN is applied as shown in the figure. (i) What is the stress intensity factor  $K$  if the crack length is  $c = 15.0$  mm? (ii) If the crack length is  $c = 40$  mm? (iii) What is the critical crack length  $c_c$  for fracture, if the material is 2014-T651 aluminum? [Hint: The values of  $F(c)$  are shown in Figure E5.4b [60], for various ranges of  $\alpha = (a/b)$ .]

$$\begin{aligned} \text{Remote stress} = S_g \text{ in Figure E5.4a } [= \Delta S \text{ in Equation 5.25}] &= \{(100)/(1000)\} / \{(2)(60)(8)\} \\ &= 104.17 \text{ N/mm}^2 = 104.17 \text{ MPa.} \end{aligned}$$

(i) For  $c$  [=  $a$  in Figure E5.4a] = 15.0 mm,  $\alpha = (15.0)/60 = 0.25$ . Since it is less than 0.25,

$$F(c) = F = 1.0.$$



**FIGURE E5.4** Stress intensity factors for a center-cracked plate under remote tensile force; use only case (a) in panel (b). (From N.E. Dowling, 1999, *Mechanical Behavior of Materials*, Prentice Hall, Upper Saddle River, NJ.)

Hence,

$$\begin{aligned}\text{stress intensity factor} &= \Delta K_I \text{ [in Equation 5.25]} = (\Delta S)\sqrt{\pi c} \\ &= (104.17)\sqrt{\{(\pi)(15.0/1000)\}} = 22.61 \text{ MPa}\sqrt{\text{m}}.\end{aligned}$$

(ii) When  $c = 40.0$  mm,  $\alpha = 40.0/60.0 = 0.66$ .

$$F(c) = F = (1.0 - 0.5\alpha + 0.326\alpha^2)/\sqrt{(1.0 - \alpha)} = \{1.0 - (0.5)(0.66) + (0.326)(0.66)^2\}/\sqrt{(1.0 - 0.66)} = 0.812/(0.5740) = 1.414.$$

Hence,

$$\begin{aligned}\text{stress intensity factor} &= \{F(c)\}(\Delta S)\sqrt{\pi c} = (1.414)(104.17)\sqrt{\{(\pi)(40.0/1000)\}} \\ &= 52.22 \text{ MPa}\sqrt{\text{m}}.\end{aligned}$$

(a) Values for small  $a/b$  and limits for 10% accuracy:

$$(a) \quad K = S_g \sqrt{\pi a}$$

$$(a/b \leq 0.4)$$

$$(b) \quad K = 1.12 S_g \sqrt{\pi a}$$

$$(a/b \leq 0.6)$$

$$(c) \quad K = 1.12 S_g \sqrt{\pi a}$$

$$(a/b \leq 0.13)$$

(b) Expressions for any  $\alpha = a/b$

$$(a) \quad F = \frac{1 - 0.5\alpha + 0.326\alpha^2}{\sqrt{1 - \alpha}} \quad (h/b \geq 1.5)$$

$$(b) \quad F = \left(1 + 0.122 \cos^4 \frac{\pi\alpha}{2}\right) \sqrt{\frac{2}{\pi\alpha} \tan \frac{\pi\alpha}{2}} \quad (h/b \geq 2)$$

$$(c) \quad F = 0.265(1 - \alpha)^4 + \frac{0.857 + 0.265\alpha}{(1 - \alpha)^{3/2}} \quad (h/b \geq 1)$$

(iii) For 2014-T651 aluminum, the critical stress intensity factor  $= \Delta K_{Ic} = 24.0$  MPa $\sqrt{\text{m}}$ .

Since critical crack length is not known, the value has to be determined by a process of trial and error. For  $\alpha \leq 0.4$ ,  $F(c) = F = 1.0$ . Hence,

$$\begin{aligned}\Delta K_{Ic} &= (1.0)(\Delta S)\sqrt{\pi c_c} \\ &= (1.0)(104.17)\sqrt{\pi c_c} = 24.0 \text{ MPa}\sqrt{\text{m}}\end{aligned}$$

Solving for  $c_c = 16.9$  mm.

This leads to,  $\alpha = 16.9/60.0 = 0.282 \leq 0.4$ ; hence,  $F(c) = 1.0$  only.

The critical crack length is 16.9 mm; it must be remembered that this has an error of 10%. If this error is to be removed, then the other equation given for  $\alpha$  equal to any value in Figure E5.4b should be solved, and the critical depth  $c_c$  should be obtained.

### Example 5.10

Determine the crack propagation life of an A514 steel plate with an initial edge crack of 0.3 in. and subjected to axial tensile load. The fatigue stress is varying between 50.0 ksi ( $S_{max}$ ) and

30.0 ksi ( $S_{\min}$ ), giving a stress range of  $\Delta S = 20.0$  ksi. The yield strength of A514 steel is given as  $\sigma_{ys} = 100.0$  ksi, and a critical stress intensity factor of  $\Delta K_{Ic} = 150$  ksi $\sqrt{\text{in}}$ . [Hint: It is given that  $\Delta K_I = 1.12(\Delta S)\sqrt{(\pi c)}$  for an edge crack in tension, and for the material,  $(dc/dN) = (0.66)(10^{-8})(\Delta K_I)^{2.25}$ .]

- (i) Calculate the critical crack for the material at 50.0 ksi =  $c_{cr} = [(\Delta K_{Ic})/[(1.12)(\sqrt{\pi})(S_{\max})]]^2 = [(150.0)/\{(1.12)(\sqrt{\pi})(50)\}]^2 = 2.28$  in.
- (ii) The crack growth equation is to be integrated in an incremental manner; hence, a coarse increment of 0.2 in. is assumed to expedite the computations. Hence, the incremental form of the crack growth becomes,  $(dc/dN) = (0.66)(10^{-8})(\Delta K_I)^{2.25}$ .

As a result,

$$\begin{aligned} dN &= (dc)/\{(0.66)(10^{-8})(\Delta K_I)2.25\} = (dc)/\{(0.66)(10^{-8})\{1.12(\Delta S)\sqrt{(\pi c)}\}^{2.25}\} \\ &= (dc)/\{(0.66)(10^{-8})(1.2904)(20.0)^{2.25}(3.625)(c)^{1.125}\} \\ &= (dc)c^{-1.125}\{1.0/(2612)(10^{-5})\} = (38,291.84)(c)^{-1.125}(dc) \end{aligned}$$

Integrating between  $c_0 = 0.3$  in. and  $c_{\text{final}} = 2.28$  in., one obtains

$$\int_0^{N_p} dN \int_{c_0}^{c_{\text{final}}} dc \{(38,291.84)(c)^{-1.125}\};$$

i.e.,

$$\begin{aligned} N_p &= 38,291.84 \left[ \left( c^{-0.125}/(-1.125+1.0) \right) \right]_{0.3}^{2.28} \\ &= -(38,291.84)(8)[2.28^{-0.125} - (0.3)^{-0.125}] \\ &= -(38,291.84)(0.902 - 1.1624) = 79,769.56 \text{ cycles} \end{aligned}$$

Hence, the crack propagating life of the steel plate = 79,769.56 cycles.

#### 5.2.4 INTRODUCTION TO PROPERTIES OF A RANGE OF MATERIALS USED IN THE OCEAN

The effects of the ocean environment on materials used in the ocean are quite different from that used onshore, in a number of areas. One area is the constancy of thermal variation in the ocean, viz., the temperature ranges within relatively narrow limits of  $-2^\circ\text{C}$  to  $38^\circ\text{C}$ . Another area is the salt content of the ocean water, which ranges between 34.0 and 41.0 ppt (by weight), depending on the location of sampling (see Table 5.1). Moreover, seawater is relatively corrosive, in comparison with the onshore air. Since water is relatively incompressible and its density is 800.0 times that of air (at  $10^\circ\text{C}$ ), the shock and other effects are transmitted through the ocean over large distances. Also the oceans impose very large static and dynamic loads on structures operating in the ocean. Hence, materials used in the ocean environment must be able to handle large environmental loads and have reduced corrosion influence, high fatigue life and strength, and ease of fabrication; in addition, it should also be economical compared to other alternate materials such as aluminum, titanium, concrete, etc. This section discusses the various categories of materials used in the ocean, such as low-strength (mild) steels, medium-strength steels, high-strength steels, aluminum alloys, titanium alloys, fiberglass, composites, and reinforced concrete, giving some details on their physical and mechanical properties.

#### 5.2.4.1 Alloys of Iron and Steel

Plain carbon structural steel is the most widely used construction material in the ocean, since it is cheap, readily available, and easy to fabricate. In aerated ocean water, unprotected steel and cast iron corrode quite fast, at a rate of 3.0 to 5.0 mpy (milli-inches per year); initial rates during the first few months can be as high as three to five times the above value. As time goes on, the corrosion rate decreases. Since the corrosion film produced on the surface is loosely adherent, the film gets continuously disrupted and removed by the mechanical action of waves in the splash zone; in this case, the corrosion rate can be much higher. The corrosion rate of steel in the ocean is affected by temperature, salinity, and dissolved oxygen concentration. If anaerobic bacteria are present in the ocean bottom sediments, then corrosion rate is accelerated. Hence, the steel structures need to be protected with some form of corrosion protection, such as coatings and/or cathodic protection, using magnesium sacrificial anodes or impressed current method. Also high-strength steels are susceptible to hydrogen embrittlement, especially at the crack tips, which may lead to increased crack growth rates and perhaps to catastrophic failures.

#### 5.2.4.2 Low-Carbon Steels

Table 5.3 [61–65] describes a few of the salient characteristics of low-strength steels used in the ocean environment. These types of steels are used for hull/tower structures, tanks, pressure vessels, and others. In Table 5.3, # 1, # 6, and # 7 steels will be utilized in most of merchant and a few naval vessels. Steels given as # 2, # 4, and # 5 will be used for pressure vessels and tanks; # 3 and # 8 will be used for general ocean engineering structures. As a group, they have better notch toughness characteristics over regular low-carbon steels and, at the same time, have better weldable characteristics. They also have better fatigue strengths.

#### 5.2.4.3 Medium-Strength Steels

For ships transiting the circumpolar regions and structures located in the sub-Arctic/Arctic regions, higher notch toughness and higher strength are required; also cranes and booms used in ships and offshore structures need to have high energy absorption capacity. Under these situations, medium-strength, quenched, and tempered steels are used, shown in Table 5.4 [61, 62, 64, 65]. Quenching and tempering of steels result in better values for nil ductility temperatures and improved impact strength, as indicated in Table 5.4. Increased ductility and toughness result from tempering, while quenching prevents the transformation of austenitic phase to crystallographic constituents with lower strength. The quenching and tempering result in finer grain size, which leads to improvements in NDT and Charpy impact strengths. Also the quenched and tempered steels are sensitive to plate thickness, which affects their physical and mechanical characteristics. This can be seen from Figure 5.15, shown earlier, where the plate ultimate strength and the impact strength are observed to be a function of plate thickness. HY-130 steel has the highest cost, while ASTM A 517-67 T-1 has the lowest cost.

#### 5.2.4.4 High-Strength Steels

Higher strengths in steel, to the value of 150–300 ksi, are achieved by reducing impurities (such as P, S, O, N, and Sb) present in steel. These steels have improved fatigue and energy absorption characteristics. Maraging steels, which have high yield strengths of 150,000 to 300,000 psi, also have relatively higher ductility. These steels can also be heat-treated to have higher notch toughness and impact strength. Table 5.5 [61–64, 66] gives some of the important properties of high-strength steels used in the ocean. In addition to its strength and elongation characteristics, it also lists the weldability, NDT temperatures, toughness, and annual corrosion rates. Compared to medium-strength steels, these maraging and other high-strength steels have improved toughness strengths over extended temperature ranges. They are used for modern naval vessels and for pressure vessels carrying liquefied natural gas, as well as underwater structures.

**TABLE 5.3**  
**Physical and Mechanical Properties of Low-Strength Steel Alloys**

#	Material and Specification	Minimum Yield Strength (2% offset) $\sigma_y$ (psi*10 <sup>3</sup> )	Ultimate Strength $\sigma_u$ (psi*10 <sup>3</sup> )	Elongation (%)	Heat Treatment	Nil Ductility Temperature (°C)	Toughness (ft. lb.)	Weldability	Cost <sup>a</sup> (Cents/lb.)	Corrosion Rate (Range) (mpy)
1	ABS-Class B	32.0–34.0	56.0–70.0	21.0–22.0	None	-20 to +40	20.0 (M) (Ch)	Good	13	3 to 5 (G) 15 to 20 (F)
2	AISI 1020	43.0	75.0	36.5	Annealed	-20.0 to 40.0	89.0–93.0 (Iz)	Good	15.0	3 to 5 (G) 15 to 20 (S)
3	AISI 1040	62.0	89.0	33.0	Annealed	-20.0 to 40.0	36.0–72.0 (Iz)	Special	15.0	3 to 5 (G) 15 to 20 (S)
4	ASTM A-242	40.0–60.0	60.0–80.0	22.0–24.0	☼	-20 to +40	25.0 (M) (Ch)	Good	15	3 to 5 (G) 10 to 15 (F)
5	ASTM A-441	40.0–60.0	60.0–80.0	22.0–24.0	☼	0 to +70	25.0 (M) (Ch)	Good	15	3 to 5 (G) 10 to 15 (F)
6	ABS-Class BH	47.0	71.0	19.0	☼	-40 to +40	25.0 (M)(Ch)	Good	15	3 to 5 (G) 15 to 20 (F)
7	MIL-S-16113C HTS	47.0	80.0	20.0	Normalized	-60 to +20	20.0 (M) (Ch)	Good	20	3 to 5 (G) 15 (F)
8	ASTM A-302	50.0	80.0	15.0	None	-20 to +50	20.0 (M) (Ch)	Special	22	3 to 5 (G) 15 to 20 (F)
9	CB-C-Mn	60.0	80.0	19.0	Quenched and tempered	-75 to -40	20.0 (M) (Ch)	Good	18	3 to 5 (G) 15 to 20 (F)

Note: ☼—Plates above 3/4 in. shall be normalized. M—Minimum; G—Generally; S—In splash zone; F—First year; Ch—Charpy; Iz—Izod.  
<sup>a</sup> Data as of August 1970; present worth is approximately 5.58 times the given value [64].



**TABLE 5.4**  
**Physical and Mechanical Properties of Medium-Strength Steel Alloys**

No.	Material and Specification	Yield Strength (2%) $S_y$ , psi * $10^3$	Ultimate Strength $S_u$ , psi * $10^3$	Elongation (%)	Heat Treatment	Nil Ductility Temperature (°F)	Toughness (ft. lb.)	Weldability	Cost <sup>a</sup> (Cents/lb.)	Corrosion Rate (Range) (mpy)
1	MIL-S-16216 HY-80	80 (M)	90.0–100.0	20	Quenched and tempered	–130 or lower	20.0 at –60°F (Ch)	Preheat required	50	2 to 4 (G)
2	ASTM A 543	85	105	16	Quenched and tempered	–120	25.0 at –4°F (Ch)	Preheat required	38	Higher (S)
3	MIL-S-16216 HY-100	100	120	18	Quenched and tempered	–100	25.0 at –4°F (Ch)	Preheat required	50	2 to 4 (G)
4	ASTM A 517-T-1	100	120	18	Quenched and tempered	–50	25.0 at –4°F (Ch)	Preheat required	30	Higher (S)
5	HY-130	140	148	16	Quenched and tempered	–100	10 to 12 (Iz)	Preheat required	100	2 to 4 (G)
6	AISI 410 tempered	35–85	65–110	25–35	Annealed, tempered, and hardened	–320	25 at –80°F (Ch)	Fair	40	3 to 5 (G) 15 to 20 (S)

Note: M—Minimum; G—Generally; S—In splash zone; F—First year; Ch—Charpy; Iz—Izod.

<sup>a</sup> Data as of August 1970; present worth is approximately 5.58 times the 1970 value [64].

**TABLE 5.5**  
**Physical and Mechanical Properties of High-Strength Steel Alloys**

No.	Material and Specification	Yield Strength (2%) $S_y$ , psi * $10^3$	Ultimate Strength $S_t$ , psi * $10^3$	Elongation (%)	Heat Treatment	Toughness Charpy V-notch (ft. lb.)	Weldability	Cost <sup>a</sup> (Cents/lb.)	Corrosion Rate (Range) (mpy)
1	AISI 4340	270	287	11	Quenched and tempered	11 <sup>b</sup>	Preheat required	70	1 to 4 (G) 7 to 12 (R)
2	300-M	242	289	10	Quenched and tempered	23 at +70°F; 11 at -200°F	Fair	100	1 to 4 (G) 7 to 12 (R)
3	Maraging, 18 Ni-200	200	210	15	✱	85 at 70°F 45 at -320°F	Good	220	1 to 4 (G) 7 to 12 (R)
4	Maraging, 18 Ni	268	275	11	Annealed and air-cooled	23 at 70°F 20 at -200°F	Good	230	1 to 4 (G) 7 to 12 (R)
5	Maraging, 18 Ni-300	300	305	12	✱	....	Good	240	1 to 4 (G) 7 to 12 (R)
6	9Ni-4Co-0.20 C	220	250	12-19	Austenitized, water/oil cooled; twice-tempered	40 at 70°F; 40-60 at -200°F	Good	....	1 to 4 (G) 7 to 12 (R)

Note: ✱—Annealed and age-hardened. M—Minimum; G—Generally; S—In splash zone; F—First year; Ch—Charpy; Iz—Izod; R—Running water.

<sup>a</sup> Data are as of August 1970; present worth is approximately 5.58 times the given value [64].

<sup>b</sup> Izod test impact strength in ft./lb.

#### 5.2.4.5 Aluminum Alloys

Recently, aluminum alloys have found increased usages in the deck portions of naval vessels (in superstructures, deck houses and interior structural components), as well as in high-speed boats. Use of aluminum leads to lighter-weight structures since the specific weight ratio of aluminum-to-steel is 0.4. Also the cost of aluminum alloys is 1.90 times less than that of steel, on an equal strength basis. Aluminum has an added advantage in that it can perform without much corrosion protection in terms of coatings or cathodic protection. Aluminum is tough and resilient and has sufficient impact resistance, in comparison with low-strength carbon steels. As can be observed from Table 5.6, the mechanical properties of strength and deformation can be improved greatly by the special heat treatment procedures mentioned therein, such as H-112/113, H-24, H-321/343, or T-6; this would involve heat treatment followed by strain hardening with thermal stabilization. Many aluminum alloys can be welded together by gas metal arc welding (GMAW) process. In addition, the endurance strengths of various aluminum alloys [i.e., the stress range which the structure can sustain to a fatigue life of  $(5.0)(10^8)$  cycles] are also given in Table 5.6 [61, 63, 66].

#### 5.2.4.6 Titanium Alloys

Titanium alloys are extensively used in aircraft structures and engines due to its lightweight and very high strength, resulting in a high strength-to-weight ratio. It also has very good corrosion resistance and a relatively high modulus of elasticity; it is also nonmagnetic. It has very good cavitation resistance in both freshwater and seawater and, as such, are used in propellers. Similar to steel, titanium alloys properties are also influenced by the thickness of the material; the mechanical properties of thicker specimens are lower than thinner specimens. Titanium is as strong as steel but 45% lighter; it is 60% heavier than aluminum but is more than twice as strong. Owing to its almost noncorrosive nature, it is an excellent material for ocean use; it is virtually inert in ambient temperature seawater. The very good corrosion resistance of titanium alloys is due to the formation of a dense and tightly adherent oxide film that forms on the surface of the components; these films are resistant to breakdown of chloride ions in seawater. The only disadvantage is that the cost of production is very high and the availability of titanium is not very large; hence, these are not widely used in ocean structures. Table 5.7 [61, 63, 66] gives some of the essential properties of important titanium alloys that can be used for ocean structures. The table also gives the fatigue resistance of some of the titanium alloys, which seem to be fairly good.

#### 5.2.4.7 Nonmetallic Materials

The most prominent nonmetallic material used in ocean application is reinforced concrete, used in the construction of gravity, underwater, and other offshore structures. Other materials used often in ocean structures include fiber-reinforced plastic (FRP), composite materials, and polymers such as rubber, PVC, polyethylene, Bakelite, and others. Some of these properties are listed in Table 5.8 [61, 63, 65, 66]. It can be seen from the table that the FRP, composites, and polymers outperform the other nonmetallic materials in the strength (tensile) vs. unit weight ratios; it is seen that the carbon fiber composites and Kevlar composites are the best of the number of materials considered in the study.

Since concrete materials are rarely used in tension, only the concrete compression strength properties are used in the computation of strength-to-weight (or modulus/weight) ratios. Comparing steel and concrete, it can be seen that the ratios of modulus to weight and tensile (or compressive for concrete) strength to weight may not differ very much.

#### Example 5.11

Determine the materials for the following use: (i) steel for application in the Arctic region, needing a Charpy V-notch impact energy higher than 70 lb. ft., at a temperature of  $-4^{\circ}\text{F}$ ;

**TABLE 5.6**  
**Physical and Mechanical Properties of Aluminum Alloys**

No.	Material	Yield Strength S <sub>y</sub> <sup>a</sup> ksi	Tensile Strength S <sub>t</sub> ksi	Elongation (%)	Charpy V-notch Impact (ft. lb.)	Endurance Strength S <sub>f</sub> (ksi) 5*10 <sup>8</sup> cycles	Welding	Metal Treatment	Corrosion Rate (Range) (mpy)
1	5083	21	42	22	20	19	Yes	Annealed	1 to 3 (M)
2	5083	33	46	16	15	23	Yes	H-113	1 to 3 (M)
3	5086	17	38	14	19	21-23	Yes	H-112	1 to 3 (M) 6 to 8(A)
4	5086	37	47	10	14	21-23	Yes	H-34	1 to 3 (M) 6-8 (A)
5	5456	37	51	10	16	22-24	Yes	H-321	≤5 (M) 25-30 (H)
6	5456	43	56	16	8	22-24	Yes	H-343	≤5 (M) 25-30 (H)
7	6061	40	45	12	6	9-14	Yes	T-6	5-10 (A) 25-30 (H)
8	7079	68	78	14	3	23	No	T-6	11-20 (M) 50-75 (H)

Note: CA—Cast aluminum; M—Minimum; A—Average; H—High.  
<sup>a</sup> Minimum value at 0.2% permanent set.

**TABLE 5.7**  
**Major Characteristics of Titanium Alloys**

#	Designation	Yield Strength at 2% Offset, $S_y$ (ksi)	Tensile Strength, $S_t$ (ksi)	Elongation (%)	Modulus of Elasticity, $(E) \times (10^6)$ (ksi)	Toughness, Charpy V-notch (ft. lb.)	Fatigue Strength at $10^7$ Cycles (ksi)	Welding	Heat Treatment	Corrosion Rate (mpy)
1	Ti-35A to Ti-100A	25	35	17-30	15.0	11-40	—	Yes	Annealed	Virt. inert; susceptible to SCC
2	Ti-35A to Ti-100A	$\leq 90$	$\leq 100$	—	15.0	11-40	63	Yes	Cold worked	Virt. inert; susc. SCC
3	Ti 6-2-1-0.8Mo	95-100	110-119	10-12	17.0	30.0	—	Yes	Annealed	Virt. inert; susc. SCC
4	Ti 6Al-4V	120-128	130-138	10-12	16.5	10-20	75	Yes	Annealed	Virt. inert; susc. SCC
5	Ti 6Al-4V	155	165-170	8	16.5	10-20	92	Yes	Aged	Virt. inert; susc. SCC
6	ASTM B 265-58T-5, Ti-6 Al-4V	160	170	13	16.4	10	—	Yes	Water-quenched and aged	Virt. inert; susc. SCC
7	ASTM B 265-58T-7	170	189	18	—	—	—	Yes	Water-quenched and aged	Virt. inert; susc. SCC
8	Ti-4 Al-4Mn	140	150	18	—	—	—	Yes	Sheet	Virt. inert; susc. SCC

*Note:* SCC—Stress corrosion cracking.

**TABLE 5.8**  
**Physical and Mechanical Properties of Nonmetallic Materials**

No.	Material	Density (lb./in. <sup>3</sup> )	Specific Gravity	Tensile Strength (S <sub>t</sub> ) ksi	Compressive Strength (S <sub>c</sub> ) ksi	Modulus of Elasticity (E*10 <sup>6</sup> ) psi	Modulus-to-Density Ratio (10 <sup>6</sup> ft.)	Tensile-Strength- to-Density Ratio (10 <sup>3</sup> ft.)	Elongation (%)
1	Glass (tempered)	0.120	2.13–2.15	0.5–40	>200	7.4–10.0	5.14–6.94	0.35–27.78	—
2	Fiberglass polyester mat	0.054	1.49	16.9	27	1.45	2.24	—	—
3	High-modulus carbon fiber/epoxy (unidirect.)	0.059	1.63	180.0	80.0	31.17	44.09	254.27	0.6
4	High-strength carbon fiber/epoxy (unidirect.)	0.056	1.55	225	94.3	20.05	29.75	334.32	1.1
5	Kevlar-49/epoxy (unidirect.)	0.050	1.38	320.0	275.0	18.0–20.0	16.19–18.12	333.38	1.8
6	Glass fiber/E-epoxy	0.091	1.85	140.0	....	5.70	5.22	128.21	2.5
7	Polyester resin	0.044	1.22	9.0	20.0	0.51	0.97	17.05	—
8	Polyurethane foam—Rigid	0.0046	0.56–0.64	2.5–3.0	—	0.0145	0.26	45.29–54.35	—
9	Concrete: cast in place	0.086	2.35–2.40	0.22–0.62	3.5–7.5	3.0–6.0	2.91 <sup>a</sup> –5.81 <sup>a</sup>	3.39 <sup>a</sup> –7.27 <sup>a</sup>	—
10	Concrete: lightweight	0.061	1.68	....	4.5	2.0	2.73 <sup>a</sup>	Very low	—
11	Concrete: high-strength	0.083– 0.090	2.30–2.50	0.6–1.2	10.0–14.0	2.9–8.00	2.69 <sup>a</sup> –8.03 <sup>a</sup>	9.26 <sup>a</sup> –14.05 <sup>a</sup>	—
12	Ferrocement	0.090	2.49	1.0	6.5	4.0	3.70 <sup>a</sup>	6.02 <sup>a</sup>	—

<sup>a</sup> The compressive strength is used for concrete materials.

(ii) steel for use in a liquefied natural gas (LNG) tanker, that are in contact with LNG (at a temperature of  $-240^{\circ}\text{F}$ ); and (iii) steel for use in the equatorial belt, where temperatures can rise to a maximum of  $+122^{\circ}\text{F}$ .

- (i) From the values given in Tables 5.3, 5.4 and 5.5, the suitable materials are obtained as
- (a) For application in the Arctic region, with a Charpy value of 75.0 lb. ft. and a temperature of  $-4^{\circ}\text{F}$ , only the following steels are found suitable, viz.,
- AISI 1020 with an Izod toughness value of 89.0 to 93.0 lb. ft. (only Izod value is available) at  $-4.0^{\circ}$  to  $+104.0^{\circ}$ , and the tensile strength is 75,000 psi.
  - Maraging steel, 18 Ni-200, with a Charpy toughness value of 85.0 lb. ft. at  $70^{\circ}\text{F}$  to 45.0 lb. ft. at  $-320^{\circ}\text{F}$ ; the tensile strength is 200,000 psi. Cost of this steel is nearly 15 times more than the AISI 1200. Linearly interpolating, toughness at  $-4^{\circ}\text{F} = 45.0 + (85.0 - 45.0)[70.0 - (-4.0)]/[70.0 - (-320.0)] = 52.6$  lb. ft., which is less than the 70.0 required.

If cost is not a parameter to be considered, then the maraging steel 18 Ni-200 will be used in the fabrication since it is a high-strength steel; otherwise AISI 1200, which is much cheaper and which has a better toughness value at  $-4^{\circ}$  will be used.

- (ii) For an LNG tanker, carrying LNG at a temperature of  $-200^{\circ}\text{F}$ , the following steels can be considered, viz.,
- AISI 410 tempered steel with a NDT of  $-320^{\circ}\text{F}$  can be used. Toughness is 25.0 lb. ft. at  $-80^{\circ}\text{F}$ ; tensile strength is 65–110 ksi; cost is \$2.23/lb.
  - Maraging 18 Ni-200 steel, with a NDT of  $-320^{\circ}\text{F}$  can also be used; toughness is 45.0 at  $-320^{\circ}\text{F}$ ; tensile strength is 275.0 ksi; cost is \$12.28/lb. (nearly 5.50 times more than the AISI 410 tempered steel).

If cost was not a determining factor, then Maraging 18 Ni-200 steel will be used for the fabrication of the LNG tanker.

- (iii) Steel in equatorial belt, where temperature can rise up to  $122^{\circ}\text{F}$ .
- Any of the steels mentioned in Tables 5.3 through 5.5 can be used.

### Example 5.12

Determine the underwater weight of a steel tubular member, 0.80 m in diameter (outer), 15.0 m in length and having a thickness of 0.025 m that is to be used in the underwater portion of a drilling rig. In order to reduce its underwater weight, a syntactic foam cylinder is added to the outside of this tubular member. Compute the thickness of this foam cylinder if the underwater weight of the tubular member is to be reduced by 30%.

Density of steel =  $0.286 \text{ lb./in.}^3$  ( $7920 \text{ kgf/m}^3$ ) and density of syntactic foam =  $0.0046 \text{ lb./in.}^3$  ( $127 \text{ kgf/m}^3$ ).

Density of ocean water =  $1030 \text{ kgf/m}^3$ .

Buoyant weight of submerged steel =  $(\pi Dt)/\rho_{\text{sub}} = (22/7)(0.80)(0.025)(15.0)(7920 - 1030) = 6496.30 \text{ kgf}$ .

This weight is to be reduced by  $= (0.30)(6496.30) = 1948.9 \text{ kgf}$ .

Let  $T$  be the thickness of the syntactic foam wrapped around the steel tubular member.

Buoyant weight of syntactic foam =  $(22/7)[\{(0.80+2T)^2 - (0.80)^2\}/4](15)(127.0 - 1030) = -42,570(0.80T + T^2) = -1948.90 \text{ kgf}$

Solving  $T = 0.0536 \text{ m}$ .

### Example 5.13

Differentiate between the use of lightweight concrete and cast-in-situ normal strength concrete for constructing a habitat 12.0 ft. in diameter, 50.0 ft. long, and 1.0 ft. thick. List their significant differences in physical characteristics and determine how much ballast is required to sink the habitat in the ocean.



**NORMAL STRENGTH CONCRETE**

Unit weight of normal strength concrete =  $0.086 \text{ lb./in.}^3 = 148.61 \text{ lb./cu. ft.}$

Volume of the habitat material =  $\pi Dtl = (\pi)(12.0)(1.0)(50) = 1885.7 \text{ cu. ft.}$

Volume of the habitat =  $\pi(D^2/4)l = (\pi)(122/4)(50) = 5654.9 \text{ cu. ft.}$

If the habitat is to sink, then its weight must be more than the weight of the volume of water displaced by the habitat =  $(5654.9)(64.0) = 361,913.6 \text{ lb.}$

Weight of the habitat =  $(1885.7)(148.61) = 280,233.9 \text{ lb.}$

Ballast required to sink the normal strength concrete must be greater than =  $361,913.6 - 280,233.9 = 81,679.7 \text{ lb.}$

**LIGHTWEIGHT CONCRETE**

Unit weight of lightweight concrete =  $0.061 \text{ lb./in.}^3 = 105.41 \text{ lb./cu. ft.}$

Weight of lightweight concrete habitat =  $(1885.7)(105.41) = 198,771.6 \text{ lb.}$

Ballast required to sink the lightweight concrete habitat must be greater than =  $361,913.6 - 198,771.6 = 163,142.0 \text{ lb.}$

**Example 5.14**

The hoop compressive stress  $S$  of a submerged sphere with “thin” walls is given by  $S = \left(\frac{R}{2t}\right)p$ , where  $R$  is the radius,  $t$  is the sphere wall thickness, and  $p$  is the external pressure. Using the materials given in Table 5.8, design the smallest sphere that will support 1000 lb. (concentrated load) at a water depth of 600.0 ft. in seawater (density of 64.0 lb./ft. 3). Do not use wood or glass. The sphere has inside air at 1.0 atmospheric pressure. [Hint: Assume the concentrated load to be a distributed pressure load, over the exposed area of the hemisphere, multiplied by a factor of 3.0 to get the equivalent pressure load.]

Pressure of water at a depth of 600.0 ft. =  $(600)(64.0) = 38,400 \text{ psf} = 266.7 \text{ psi.}$

Replaced concentrated load =  $(3.0)(1000)/[(\pi)(R^2)] = (954.93/R^2) \text{ psi} = p_1 \text{ psi.}$

Internal pressure = 1.0 atmosphere = 14.7 psi.

Net external pressure acting on the shell =  $(266.7 + p_1 - 14.7) = q \text{ psi.}$

Stress on the wall of the shell due to this pressure =  $qR/2t \leq \sigma_{\text{allowable}} = \sigma_{\text{max}}/F.S.$

Let  $R/t$  ratio for the submerged shell be taken as 100.

Hence, stress on the shell wall =  $(q)(100)/2 = 50 q.$

Choosing four materials from Table 5.8, viz., high-strength carbon fiber–epoxy, Kevlar 49 epoxy, high-strength concrete and ferrocement, the minimum diameters for the spherical vessel are determined.

- (i) Compressive strength of high-strength carbon fiber–epoxy composite = 80.0 ksi.  
Use a factor of safety of 5.0.

$$(50)(266.7 + p_1 - 14.7) = 80,000/5 = 16,000.$$

$p_1 = 68.0 = 954.93/R^2$ ; hence,  $R = 3.75 \text{ in.}$  and  $t = 0.0375 \text{ in.}$

Buckling pressure on a spherical shell =  $0.84(E)(t/R)^2 = (0.84)(31.17)(10^6)(1/100)^2 = 2618.3 \text{ psi} > 266.7 - 14.7 + 68 = 320.0 \text{ psi.}$  Hence, OK.

- (ii) For Kevlar 49 epoxy,  $p_1 = (275,000)/5/50 + 14.7 - 266.7 = 848 = 954.93/R^2$ ; hence,  $R = 1.06 \text{ in.}$ , and  $t = 0.0106 \text{ in.}$

Buckling pressure on the shell =  $(0.84)(19)(1,000,000)(1/100)^2 = 1596 \text{ psi} > 1100.00.$  Hence, OK.

- (iii) For high-strength concrete,  $p_1 = (12,000)/5/50 + 14.7 - 266.7 = -204.0$ ; hence, this is not feasible.

We need to have a higher  $R/t$  ratio; take an  $R/t$  ratio of 15.0. Hence, stress on shell wall =  $qR/(2t) = (q)(15)/2 = 7.5 q$ .

$p_1 = 12,000/5/7.5 + 14.7 - 266.7 = 320 + 14.7 - 266.7 = 68.0 = 954.93/R^2$ ; hence,  $R = 3.75$  in., and  $t = 0.25$  in.

Buckling pressure on the shell =  $(0.84)(5.5)(10^6)(1/15)^2 = 20,704.0$  psi > 320.0 psi. Hence, OK.

- (iv) For ferrocement,  $p_1 = 6500/5/7.5 + 14.7 - 266.7 = 173.3 + 14.7 - 266.7 = -78.7$  psi; this is not feasible.

The  $R/t$  ratio has to be reduced. Let  $R/t = 8.0$

Hence, stress on the shell wall =  $q(R/t)/2 = 4q$ .

$p_1 = 6500/5/4 + 14.7 - 266.7 = 325 + 14.7 - 266.7 = 73.0 = 954.93/R^2$ ; hence,  $R = 3.62$  in., with  $t = (3.62/8) = 0.45$  in.

## 5.3 RANGE OF MATERIAL PROPERTIES AND MATERIAL SELECTION

### 5.3.1 INTRODUCTION

The selection and use of materials for ocean structures, by designers, is generally based on their prior experience and expertise with different structural designs for ocean applications; it is not based a rigorous analytical procedure since there is a large range of materials available for consideration, each one fulfilling only a certain range of requirements needed for ocean use. Moreover, the availability of different materials are restricted by the inventory maintenance at the local and global levels, depending on the costs and gains made by the distributors; besides, many new materials are constantly being developed for the market place by various industries, having equivalent or some improved versions of the material properties available earlier. Hence, some sort of subjective priority has to be imposed on their selection.

The purpose of this section is to examine in a broad manner the range of available engineering materials and their capabilities for use in the structures considered in this study. The broad classification of materials available for ocean use has been already made in Section 5.2.4, viz.,

- (i) Metals such as (a) ferrous alloys having low, medium, and high strengths; (b) aluminum alloys with high strengths; and (c) titanium alloys; and
- (ii) Nonmetallic materials such as polymers, polymer composites.

These properties are given in Tables 5.3 through 5.8. Only a limited number of available materials are listed in these tables; for a larger range of materials, other books such as those of Schenck [61], Taggart [62], Dexter [63], Murray [65], Lynch [66], Sheno and Wellicombe [67], Masubuchi [68] and Reuben [69] should be consulted in selecting a material for use in the ocean. In this section, only a methodology for the preliminary choice is given; hence, the material selection will only be a coarse selection, and fine-tuning of the choice has to be made after a very detailed consultation, data gathering, and analysis.

Materials are required for ocean use in the fabrication of structures such as ship/naval vessel hulls and superstructures, ocean structures used for oil and gas exploration/storage, oil and gas pipelines, seawater/other fluid-carrying pipes, structures monitoring ocean environmental parameters (such as buoys, sub-marine floats, etc.), and OTEC power plants. Since most of these structures have been designed, fabricated, and put to use earlier, the selection for future use relies on how these choices were made in the past and how those materials performed in the ocean environment during its on-site location. Many times the codes of practice assist in the proper selection of materials for design. In addition to material properties, an effective designer would also consider the compatibility of the constituent material during the fabrication and operation stages. The interrelationship between material properties, fabricability, design, costs, and operational environment should be properly estimated by asking questions such as “How will the material perform in the ocean environment?”, “How will the various components of the structure be fabricated?”, “What materials will be used in the fabrication of the overall structure and how will they

**TABLE 5.9**  
**Fabricability of Various Classes of Materials**

Mat. Type	Cast.	Mould.	Cut.	Forg.	Sheet Form.	Weld.	Braz./ Solder.	Adh. Bond.	Appl. Coat.
C-Mn steels	b	c	a	a	a	a	a	c	c
Low-alloy steels	b	c	b	a	b	b	b	c	c
Stainless steels	b	c	a	a	a	a	a	b	a
Aluminum alloys	b	c	a	a	b	b	b	a	b
Copper alloys	a	c	a	a	a	a	c	a	a
Thermoplastics	c	a	b	c	a	a	c	b	a
Thermosets	c	a	b	c	b	c	c	a	a

*Source:* With kind permission from Springer Science+Business Media: *Marine Materials in Marine Technology*, The marine environment, marine structures and the role of materials technology (Chapter 1), 1994, p. 13, R. Reuben.

*Note:* a—A process commonly used for the material class; b—One which may be used, with some precautions or modifications; c—A process which either cannot or is rarely used for the material.

be joined together?”, “Are the materials choices within the budgeted costs?” and “How will the materials behave on a long term in the ocean environment?”.

Since fabricability or constructability of the ocean structure is an important facet of the material choice for ocean use, some general considerations required for the purpose are listed in Table 5.9 [70]. In addition to fabricability, the material should also be cheap if the material is to be used in a generic type of structure, which is to be fabricated in large quantities. Recent considerations which should be accounted for are (i) recyclability or disposability of the structure after its useful life has ended and (ii) fire hazard and its prevention or minimization.

### 5.3.2 RANGE OF MATERIAL PROPERTIES FOR OCEAN STRUCTURES

For general mechanical use, a coarse selection of material can be easily carried out using a smaller of number of important material properties; also as a case for illustration, only a few of the generic materials, shown in Tables 5.3 through 5.8, are chosen in this study. Moreover, for preliminary analyses of most of the important ocean structures, an initial and viable material choice (or screening) can be made based on their strength, stiffness, and density (or weight) characteristics. Additional considerations for ocean use, during the preliminary stage, would also include the corrosion resistance and toughness of the materials under consideration; besides the above, the cost and fabricability constraints should also be included in a preliminary choice of material for use in structural fabrication. The ranges of material properties from which a sample material can be identified for the use at hand are obtained from Tables 5.3 through 5.8. It can be observed from the values given in Tables 5.3 through 5.8 that the ranges of material properties, shown in Table 5.10 [61–64, 66], can be obtained; from these ranges, a few materials can be identified as target materials during the preliminary stage of analysis.

### 5.3.3 SELECTION OF MATERIALS FOR OCEAN STRUCTURES

In order to illustrate the material selection procedure, an illustrative problem is worked out in the section below.

#### Example 5.15

In this section, an illustrative study is carried out to examine the process that would be carried out during the preliminary choice of candidate materials for ship hulls, based on some of the

**TABLE 5.10**  
**Ranges of Properties of Material for Choice during Preliminary Analysis**

Materials	Density	Yield Strength	Tensile Strength	Elongation	Modulus of	Tough. Charp./	Fatigue	Weldability/	Corrosion	
	Range (lb./in. <sup>3</sup> )	Range, S <sub>y</sub> (ksi) (2% Offset)	Range, S <sub>t</sub> (ksi)	Range (%)	Elasticity Range, (E)×(10 <sup>6</sup> ) (ksi)	Iz. V-notch Range (ft. lb.)	Strength at 10 <sup>7</sup> cycles, Range (ksi)	Brazing/ Soldering/ Adhes. Bond. Range	Cost (\$/lb.)	Rate (mpy)
Low-strength steel alloys	0.282–0.286	32.0–62.0	56.0–89.0	15.0–36.5	30.0	20.0–93.0	50–55% of S <sub>t</sub> (MH)	Good	0.15–0.22 <sup>b</sup>	3–5 (G) 15–20 (S)
Medium-strength steel alloys	0.286–0.289	80.0–140.0	90.0–148.0	16.0–35.0	30.0	10.0–25.0	40–50% of S <sub>t</sub> (MH)	Good to fair (preheat required)	0.30–1.00 <sup>b</sup>	2–5 (G) 15–20 (S)
High-strength steel alloys	0.288–0.293	200.0–300.0	210.0–305.0	11.0–19.0	29.0	11.0–60.0	40% of S <sub>t</sub> (MH)	Good to fair (preheat required)	0.70–2.40 <sup>b</sup>	1–4 (G) 7–12 (R)
Aluminum alloys	0.096–0.102	17.0–68.0	38.0–78.0	10.0–22.0	10.3–10.4	3.0–20.0	9.0–24.0	Good to fair	0.85–1.05 <sup>c</sup>	1–20 (G) 25–75 (H)
Titanium alloys	0.159–0.163	25.0–170.0	35.0–189.0	8.0–30.0	15.0–17.0	10.0–40.0	63.0–92.0	Good to fair	11.0–17.0 <sup>c</sup>	Inert (G) Susc. to SCC
Fiber-reinforced polymers	0.047–0.058	—	2.0–9.0	—	1.45–31.17	8–15	12.5–21.0	Good	5.00–12.00 <sup>e</sup>	—
Polymers	0.033–0.079	—	16.0–200.0	0.60–2.50	0.015–0.51	—	—	Good	2.0–12.0 <sup>c</sup>	—
Concrete products	0.058–0.090	—	3.5–14.0 <sup>a</sup>	—	2.0–8.00	—	—	Good	0.06–0.15 <sup>d</sup>	—

*Note:* MH—Fatigue life is much higher at 10<sup>8</sup> cycles; G—General; S—Splash zone; R—In running water; H—Highest value; SCC—Stress corrosion cracking.  
<sup>a</sup> Compressive strength.  
<sup>b</sup> Data are as of August 1970; present worth is approximately 5.58 times the given value [64].  
<sup>c</sup> Data are as of June 1977; present worth is approximately 3.55 times the given value [64].  
<sup>d</sup> Data are as of 2004; present value is 1.14 times the given value [64].

important properties considered in Table 5.10. First some of the relevant materials that could be used in the fabrication of ship hulls are chosen and listed in Table 5.11, based on their acceptable material properties. These properties are separated into primary, secondary and some other requisite ones; of the ten properties listed in Table 5.10, strength (2% offset yield strength), toughness and Young’s modulus (representing stiffness) are taken as primary (or important) properties necessary for the design of ship hulls transiting the cold oceans. Corrosion, weldability (or fabricability) and weight (or represented by its density) are taken as important secondary properties. Cost is taken as another separate important factor that should be considered separately as an important property. These materials with their classified properties are given in Table 5.11.

If the properties are around the acceptable range, they are listed as acceptable in Table 5.11; if the magnitude of properties are much higher than the required design values, then they are classified as overprovision, and if they are under the required design values, then they are classified as underprovision. Relative weights are assigned to each of these identified primary and secondary properties, based upon their importance to the design and fabrication of the ship hull, as shown in Table 5.12. From these assigned weights, the normalized weights for all the selected materials are computed, and then the rating for each material is obtained by dividing each of the weights by the largest weight obtained in the table. The material that has the highest rating (viz., 1.0) is taken as the optimum material for the purpose.

From the weights assigned for each property of the materials, under consideration, the most optimum material to be used in the fabrication of a ship hull is the low-strength steel CB-C-MN, as

**TABLE 5.11**  
**Preliminary Material Selection Procedure**

Material	Property Requirements						A Parallel Important Property
	Primary Property			Secondary Property			
	Yield Strength (ksi)	Toughness (ft. lb.)	Young’s Modulus (E)×(10 <sup>6</sup> ) (ksi)	Corrosion Rate (mpy)	Weldability (or Fabricability)	Density (lb./in. <sup>3</sup> )	
CB-C-Mn	60.0 (A)	20.0 to 40.0 (−20°F) (A)	30.0 (A)	3 to 5 (G) 15 to 20 (F) (A)	Good (A)	0.283 (A)	1.00 (A)
ASTM A 543	85 (A)	20.0 (−60°F) (A)	30.0 (A)	2 to 4 (G) High (S) (A)	Fair (preheat required) (A)	0.287 (A)	2.12 (A)
HY-130	140 (A)	10–12 (−4°F) (u)	30.0 (A)	2 to 4 (G) Higher (S) (A)	Fair (preheat required) (A)	0.289 (A)	5.58 (o)
Maraging, 18 Ni-200	200 (o)	45 (−320°F) (A)	29.0 (A)	1 to 4 (G) 7 to 12 (R) (A)	Fair (heat treatment required) (A)	0.291 (A)	12.83 (o)
Aluminum A 5456	43 (u)	8 (u)	10.3 (A)	≤5 (M) 25–30 (H) (o)	Good (A)	0.099 (A)	3.48 (A)
Ti 6-2-1-0.8 Mo	95–100 (A)	30 (−40°F) (A)	16.0 (A)	Virtually inert (A)	Fair (heat treatment required) (A)	0.161 (A)	39.05–60.35 (o)
High-strength carbon fiber/epoxy (unidirect.)	225 (o)	8–15 (20°F) (u)	31.17 (A)	Inert (A)	Good (A)	0.056 (u)	17.75–42.60 (o)

Note: A—Acceptable; o—Overprovision; e—Excessive; u—Underprovision.

**TABLE 5.12**  
**Final Material Selection Data**

Material	Property Requirements						A Parallel Important Property
	Primary Property			Secondary Property			
	Yield Strength (ksi) (25)	Toughness (ft. lb.) (25)	Young's Modulus (E)×(10 <sup>6</sup> ) (ksi) (15)	Corrosion Rate (mpy) (8)	Weldability (or Fabricability) (8)	Density (lb./in. <sup>3</sup> ) (4)	
CB-C-Mn	60.0	15.0 (−60°F)	30.0	4 (G) 18 (F)	Good	0.283	1.00
ASTM A 543	85	20.0 (−60°F)	30.0	3 (G) High (S)	Fair (preheat required)	0.287	2.12
HY-130	140	8.0 (−60°F)	30.0	3 (G) Higher (S)	Fair (preheat required)	0.289	5.58
Ti 6-2-1-0.8 Mo	98	25 (−60°F)	16.0	Virtually inert (say 1)	Fair (heat treatment required)	0.161	50.00

*Note:* Weight assigned for each material is given in brackets on the top, along with the material properties. The toughness values given in the table are only approximate values, reduced to −60°F. G—General; F—Fast running water; S—Splash zone.

shown in Table 5.13. In spite of its low strength compared to HY-130, the low-strength steel seems to have uniformly better weights for toughness, modulus of elasticity, weldability and present-day costs. If the present-day costs were removed out of Table 5.13, then ASTM A543 will become the most optimum material followed by Ti 6-2-1-0.8Mo. Consequently it will be seen that the overall rating is heavily dependent upon the weights given for each material property, which is dependent upon the task for which the material is being used and the importance of each property to the task. For more detailed considerations the additional material given by Dexter [63], Murray [65], Lynch [66], Reuben [69], and Crane et al. [71] should be taken into account.

**TABLE 5.13**  
**Weighted and Normalized Data for All the Materials, and Their Overall Rating, Shown in Table 5.12**

Material	Yield Strength	Toughness	Young's Modulus	Corrosion Rate	Weldability (Fabricability)	Density	Present Costs	Overall Weight	Overall Rating
CB-C-Mn	10.71	15.0	25.0	2.00	8.00	2.24	15.0	77.95	1.00
ASTM A 543	15.18	20.0	25.0	2.66	4.00	2.24	7.08	76.16	0.98
HY-130	25.0	8.0	25.0	2.66	4.00	2.23	2.69	69.68	0.89
Ti 6-2-1-0.8 Mo	17.5	25.0	13.33	8.0	4.00	4.00	0.30	68.13	0.87

*Note:* Weights for corrosion rate, density, and cost are obtained from the reciprocal values given in the table.

## 5.4 MARINE CORROSION AND BIODEGRADATION

### 5.4.1 INTRODUCTION

Corrosion is probably the best known deterioration mechanism in any ocean structure, which operates in the ocean environment; the deterioration occurs due to an electrochemical reaction that occurs between the material of the structure and the moist environment in which the structure is situated. In structures located in the ocean, corrosion can be defined as “any electrochemical process that leads to the formation of dissolved metallic ions in aqueous solution, which may go to form inorganic compounds that may get deposited on the structural surface”. Figure 5.1, given earlier, shows the various ranges of corrosion that can take place in an ocean structure as a function of its depth of submergence; it is seen that the corrosion is the highest at the splash zone near the ocean surface and also near the ocean bottom, where SRB action can occur, due to the oil sludge deposited at the bottom during some accidental spillage. In addition corrosion in metals can also occur due to the bio-fouling of the ocean structure. The presence of corrosion in metallic structures reduces the effective depth of material available to carry the design load of the structure; instead of the commonly used load factor of 1.5, it necessitates the use of a higher load factor or the merging up into the initial design the effective reduction caused by the presence of corrosion in the material. Also it may require preventive measures that minimize the loss of material due to the presence of corrosion.

### 5.4.2 BASIC MECHANISMS IN CORROSION

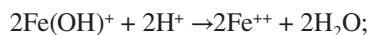
When an electrochemical reaction occurs during corrosion, four factors must be present simultaneously, viz., (i) the anode area, represented by the metal area, where corrosion occurs by oxidation resulting in the loss of electron ions; (ii) the cathode area, once again represented by the metal or semi-conducting area, where a reduction equation occurs, by the utilization of the electron ions lost from the anodic area; (iii) the electrolyte, represented by ocean water (or even moist air), is in contact with the anodic and cathodic areas and transfers the electron ions (from anode to cathode); and (iv) an electron flow path between the anode and cathode, represented metal surface. The process is represented by Figure 5.39 [72].

In a galvanic cell, two dissimilar metals (viz., iron and copper electrodes, in Figure 5.39) are placed in electrical contact in the presence of oxygen and water (or even moisture); it is not always necessary to have two dissimilar metals to activate the process of galvanic corrosion. Anode–cathode pairs can be set up on the steel surface itself (as shown in Figure 5.39b) where different locations have difference electrochemical potentials or tendencies for oxidation. Even a minor difference in material composition, residual strain, or oxygen/electrolyte concentration can set an electrical potential difference between possible anodic and cathodic sites in the material surface, as shown in Figure 5.39b.

As indicated in step (i) given above, at the anodic surface, oxidation of iron takes place (resulting in iron dissolution), resulting in the loss of four electrons, as shown in Equation 5.27.

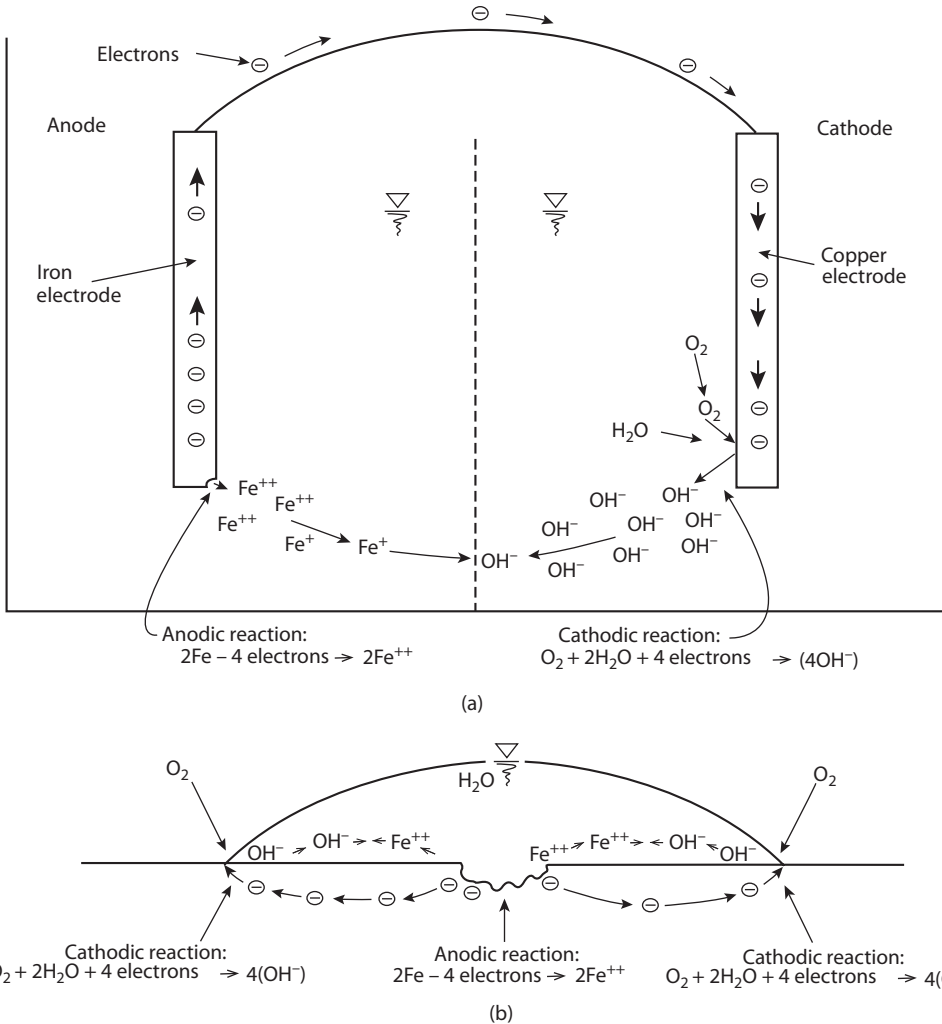


Also the above equation is arrived at [73] through a number of sub-reactions, viz.,



the rate of loss of iron is determined by the second of the above three equations.



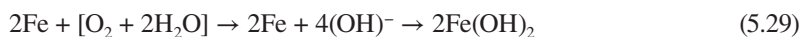


**FIGURE 5.39** Schematic representation of the general corrosion process, where the cathodic and anodic areas are evenly distributed over the metallic surface: (a) representation of a galvanic cell, in the presence of ocean water, and (b) corrosion on metal surface exposed to water (or even humid air). (From J.F. Young et al., 1998, *The Science and Technology of Civil Engineering Materials*, Prentice Hall, Upper Saddle River, NJ.)

At the copper (or cathodic) surface [given as step (ii)] shown in Figure 5.39a, oxygen reduction occurs according to the reaction given in Equation 5.28, viz.,



The actual metallic loss occurs at the anodic (metal) surface as shown by Equation 5.27. In losing the electrons, the iron atoms are changed to ferrous ions ( $Fe^{++}$ ), which dissolves in the electrolyte solution around the anodic region, as indicated in Figure 5.39a. The dissolved ferrous ion diffuses to the cathodic region and combines with the hydroxyl ions  $[(OH)^-]$  to form a precipitate of ferrous hydroxide  $[Fe(OH)_2]$  as per the Equation 5.29, which gets deposited on the cathodic region, as a loosely adherent nonprotective layer.



The hydrous ferrous oxide  $[\text{Fe}(\text{OH})_2 = \text{FeO} \cdot \text{H}_2\text{O}]$  is further oxidized to form the red colored hydrous ferric oxide  $(\text{Fe}_2\text{O}_3 \cdot n\text{H}_2\text{O})$ , which is known as rust.

### Example 5.16

Determine the potentials for the following reactions:

- (i)  $\text{Fe} + \text{H}_2\text{SO}_4 = \text{Fe}^{++} + \text{SO}_4^{--} + \text{H}_2$ ; (ii)  $2\text{Ag} + \text{H}_2\text{SO}_4 \rightarrow 2\text{Ag}^+ + \text{SO}_4^{--} + \text{H}_2$ ; and (iii)  $2\text{Ag} + \text{O}_2 + \text{H}_2\text{SO}_4 \rightarrow 2\text{Ag}^{++} + \text{SO}_4^{--} + \text{H}_2\text{O}$ .

### Answer to Example 5.16

- (i) The  $\text{SO}_4^{--}$  does not enter into the corrosion equation. Using Table 5.14 [73], the potential needed is that between the hydrogen ion and ferrous ion, viz.,  $E(\text{H}/\text{H}^+) - E(\text{Fe}/\text{Fe}^{++}) = 0.0 - (-0.44) = 0.44 \text{ V}$ .
- (ii)  $E(\text{H}/\text{H}^+) - E(\text{Ag}/\text{Ag}^+) = 0.0 - 0.80 = -0.80 \text{ V}$ .
- (iii) Here water is produced by the oxygen reduction in acid; hence,  $E(\text{O}/\text{O}^{--}) - E(\text{Ag}/\text{Ag}^+) = 1.229 - 0.800 = 0.429 \text{ V}$ .

**TABLE 5.14**  
**Standard Electrochemical Potentials of Relevance to Marine Corrosion at 25°C**

#	Electrode	Half-Cell Reaction (When the Electrode Is Cathode)	Potential (mV)
1	(Li) $\text{Li}^+$	$\text{Li}^+ + \text{e}^- = \text{Li}$	-3045
2	(K) $\text{K}^+$	$\text{K}^+ + \text{e}^- = \text{K}$	-2922
3	(Ca) $\text{Ca}^{++}$	$\text{Ca}^{++} + 2\text{e}^- = \text{Ca}$	-2870
4	(Na) $\text{Na}^+$	$\text{Na}^+ + \text{e}^- = \text{Na}$	-2712
5	(Mg) $\text{Mg}^{++}$	$\text{Mg}^{++} + 2\text{e}^- = \text{Mg}$	-2340
6	(Al) $\text{Al}^{+++}$	$\text{Al}^{+++} + 3\text{e}^- = \text{Al}$	-1660
7	(Ti) $\text{Ti}^{++}$	$\text{Ti}^{++} + 2\text{e}^- = \text{Ti}$	-1630
8	(Mn) $\text{Mn}^{++}$	$\text{Mn}^{++} + 2\text{e}^- = \text{Mn}$	-1050
9	(Zn) $\text{Zn}^{++}$	$\text{Zn}^{++} + 2\text{e}^- = \text{Zn}$	-763
10	(Fe) $\text{Fe}^{++}$	$\text{Fe}^{++} + 2\text{e}^- = \text{Fe}$ (ferrous)	-440
11	(Ni) $\text{Ni}^{++}$	$\text{Ni}^{++} + 2\text{e}^- = \text{Ni}$	-250
12	(H) $\text{H}^+$	$2\text{H}^+ + 2\text{e}^- = \text{H}_2$	0.0
13	(AgCl) $(\text{AgCl})^+$	$(\text{AgCl})^+ + \text{e}^- = \text{AgCl}$	+222
14	(Normal calomel electrode— $\text{Hg}_2\text{Cl}_2$ ) $(\text{Hg}_2\text{Cl}_2)^{++}$	$(\text{Hg}_2\text{Cl}_2)^{++} + 2\text{e}^- = \text{Hg}_2\text{Cl}_2$	+280
15	(Cu) $\text{Cu}^{++}$	$\text{Cu}^{++} + 2\text{e}^- = \text{Cu}$	+337
16	( $\text{O}_2$ in water)	$\text{O}^{++} + 2[\text{H}^+ + (\text{OH})^-] + 4\text{e}^- = 4(\text{OH})^-$	+401 (pH = 14)
17	(Fe) $\text{Fe}^{+++}$	$\text{Fe}^{+++} + 3\text{e}^- = \text{Fe}$ (ferric)	+771
18	(Ag) $\text{Ag}^+$	$\text{Ag}^+ + \text{e}^- = \text{Ag}$	+800
19	(Pt) $\text{Pt}^{++}$	$\text{Pt}^{++} + 2\text{e}^- = \text{Pt}$	+1200
20	(Oxygen reduction in acid)	$\text{O}_2 + 2\text{H}^+ + 2\text{e}^- = \text{H}_2\text{O}$	+1229

All metals can be classified according to their ability to set up the electrical potential between the anode and the cathodic metal surfaces. Table 5.14 [61, 65, 69, 76] shows some selected materials used in the ocean and the potential differences that can be set up between them. Metals which oxidize readily (viz., that give up electrons) are called as “base metals” and those which oxidize less readily are referred to as “noble metals”. The basic electrochemical process that occurs during corrosion and results in metal wastage can be represented by the reaction,



where,  $M$  represents the metal,  $z$  its valency and  $e^{-}$  the electron.

The electrochemical reaction shown in Equation 5.30 is called an electrochemical half-cell in that it is only half the complete set of reactions that would occur during the process of corrosion. An electrochemical cell consists of two half-cells, viz., the anode and the electrolyte (which forms one half-cell) and the cathode and electrolyte (the other half-cell), as shown in Figure 5.39b. The two half-cells may use the same electrolyte, or they may use different electrolytes. In a full electrochemical cell, ions, atoms, or molecules from one half-cell lose electrons (oxidation) to their electrode while ions, atoms, or molecules from the other half-cell gain electrons (reduction) from their electrode, as shown in Figure 5.39a and b.

The above electrochemical reaction, shown in Equation 5.30, leads to the Nernst equation [74], and can be summarized by its electrochemical potential as

$$E = E^0 + (RT/zF)\ln\{M^{z+}/[M]\}, \quad (5.31)$$

where  $E$  is the electrochemical potential in volts,  $E^0$  is the standard electrochemical potential (in volts at 25°C) of the reaction (at unit concentration of metal in the solution),  $z$  is the number of electrons transferred in the reaction,  $R$  is the universal gas constant = (8.3143 J/mol),  $T$  is the temperature (in K),  $M^{z+}$  is the activity of metal in solution,  $M$  is the activity of metal (considered to be unity) and  $F$  is the Faraday constant (96,500 A/s).

Its more common representation is given by

$$E = E^0 + (RT/zF)\ln(M^{z+}) \quad (5.32)$$

where  $M$  the concentration of the metal (before its dissolution in the electrolyte) is taken as unity. All metals can therefore be classified in terms of their ability to undergo such a reaction, and the standard electrochemical potential relationship, given in Equation 5.32, is used for this purpose. Table 5.14 shows the electrochemical potentials that can be set up during these reactions.

### Example 5.17

Determine the electric potential, of a platinum electrode, in a  $10^{-5}$  g-ion/L solution of platinum at 25°C.

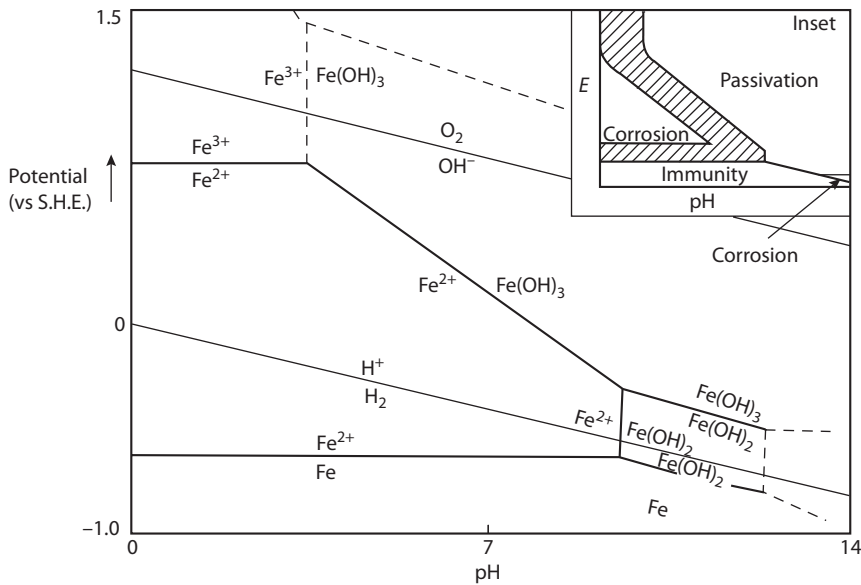
Using the Nernst Equation 5.31,  $E = E^0 + (RT/zF)\ln\{M^{z+}/[M]\}$ , one can calculate the new electric potential generated, viz.,  $E = E_0 - (2.3)(RT/zF)\ln(M^{z+}/M)$ .

From Table 5.14, for platinum  $E_0 = 1.200$  V;  $z = 2$ ;  $M^{z+}$  is the concentration of platinum in the solution =  $10^{-5}$ ; and  $M = 1.0$ .

So,

$$\begin{aligned} E &= E^0 + (RT/zF)\ln\{M^{z+}/[M]\} \\ &= 1.20 + (2.3)\left[\frac{(8.3143)(273 + 25)}{(2)(96,500)}\right]\ln\left\{\frac{(10^{-5})}{1}\right\} \\ &= 1.20 + (-0.1476) = \pm 1.052 \text{ V.} \end{aligned}$$

The formation of a thin corrosive layer on the cathodic region can be demonstrated by the thermodynamic and kinetic theories given in Equations 5.27 through 5.33. The thermodynamic theory



**FIGURE 5.40** Potential vs. pH (Pourbaix) diagram for the iron–water system at 25°C. (From M. Pourbaix, 1974, *Atlas of Electrochemical Equilibria in Aqueous Solutions*, 2nd English Edition, National Association of Corrosion Engineers, Houston, TX.)

given by Equation 5.32 was established largely by Pourbaix [75] and is represented by the electric potential vs. pH diagrams for different materials. A simple illustration of this diagram development is shown in Figure 5.40, which shows the behavior of iron in waters of variable pH value. It was assumed in this study that the water contained only hydrogen and hydroxyl ions; the presence of other ions such as chlorides would have substantial effect on the shape of the Pourbaix diagram.

For instance, the first stage of corrosion of iron in water starts with the dissolution of ferrous ions, which can be represented by the following equilibrium equations, viz.,



Using Equation 5.4 and Table 5.14,  $E = -0.44 + 0.0295 \lg (C_{\text{Fe}^{2+}})$ , where  $E^0$  is the standard electrochemical potential =  $-0.44$  V (from Table 5.14), and the term  $(RT/zF) \{\ln (M^{z+})\}$  at a temperature of 25°C =  $[(8.3143)(273 + 25)/\{(2)(965000)\}] \{(2.303)\} \lg (C_{\text{Fe}^{2+}}) = (0.0295) \{\lg (C_{\text{Fe}^{2+}})\}$ , with  $C_{\text{Fe}^{2+}}$  being the concentration of ferrous ions in the solution.

For further details of this electrochemical corrosion process, other books that give more detailed treatment of marine corrosion process should be consulted [69, 76, 77].

### 5.4.3 CORROSION AND MICROBIAL EFFECTS OF OCEAN ENVIRONMENT

Even though some of the general principles involved in the degradation of materials, including corrosion, have been discussed briefly earlier in Sections 5.1.2 through 5.1.3, the purpose of the present section discuss in greater detail the corrosive effects of the ocean environment on the structural materials used.

#### 5.4.3.1 Ocean Atmosphere

The corrosive nature of the ocean atmosphere is enhanced by a number of parameters such as moisture, chemical conditions, temperature, weather factors such as wind and rain, location of the point under consideration above the ocean, orientation of the corroding surface, pollutants and biological

organisms. Moisture influences the corrosive aspects of the ocean materials through humidity and rainfall; in addition the period of wetness and the chemical or electrochemical nature of the sprayed water and dew also affect the corrosion of materials exposed to ocean atmosphere. The principal chemical conditions that affect the materials in ocean atmosphere are the airborne levels of salt and contaminants such as sulfur and carbon dioxide. Solids such as sand, dust and ice also have an influence on the corrosion of the materials, dependent on the wind speed. The airborne salt is dependent on the height above the ocean surface, and can make substantial differences in corrosion rates, even for few tens of meters. Presence of sulfur dioxide is found to increase the corrosion rates of steel and zinc in ocean structures. Orientation of the corroding surface to wind and spray directions affects the corrosion of the material surface by increasing or decreasing the exposure to spray, runoff, solar-cum-wind drying of the surfaces, washing of surfaces by rain, and any abrasive erosion of material surfaces.

Plastic materials are degraded by the solar radiation through the presence of ultraviolet rays, especially in the ranges between 290 and 400 nm, with a peak sensitivity depending on the nature of the plastic material under consideration. Temperature has an effect on the brittleness and strength of plastics; at very low temperatures, it becomes brittle and at higher temperatures, the plastic material loses its strength. Moreover embrittlement of crack tip occurs in ferritic steels when the temperature decreases.

#### 5.4.3.2 Seawater

Some aspects of the seawater chemistry have been discussed in Section 5.1.2.1; in this section the factors that influence corrosion of seawater is discussed. The most important factor that affects the corrosion of materials is its oxygen content in seawater. For carbon steels the increase of oxygen content in seawater increases the corrosion rates substantially. Other dissolved gases such as carbon dioxide, ammonia and hydrogen sulfide also affect specific materials based on their alloy contents.

The salinity of seawater does not vary very much in the open ocean, but can be reduced at deltaic regions where fresh water flows into the ocean, and increased in relatively enclosed seas (see Table 5.1). The major effect of salinity is to increase the conductivity of ocean water, which will allow large surfaces of ocean structures to be brought into electrolytic contact; incidentally conductivity also contributes to the cathodic protection of structural surfaces. Also the presence of chloride ions in ocean water reduces the passivation of surfaces and makes them open to corrosion. In addition, the presence of calcium/magnesium/strontium carbonates in ocean water produces “chalking” (or precipitation) of these solids on cathodic surfaces, which result in the reduction of the cathodic protection effects.

The intermittent wetting and drying of well-aerated seawater on the structural surfaces existing at the water surface level, viz., the splash zone, leads to a very high free corrosion rate. Also it is difficult structural materials at this zone since it cannot be cathodically protected. As stated earlier in Section 5.1.1 water depth also has a great influence on the corrosivity of surfaces, depending on oxygen content, temperature, hydrostatic pressure and variations in the above quantities, depending on the global and local location of the structure. Generally speaking increase of temperature increases the corrosion rate, but it must be borne in mind that the increasing temperature also reduces the solubility of oxygen content in ocean water. Hydrostatic pressure also influences the anaerobic bacterial action occurring near the seabed and contributes to the pitting corrosion of materials. At low ocean water velocities, lead to reduced metal ion concentration and increased oxygen content at the corroding surface; reduced metal ion always leads to an increased corrosion rate while increased oxygen content can lead to either increased corrosion rate or decreased corrosion rate, depending on the passivation of the corroded surface. Higher ocean water velocities will also lead to increased susceptibility to corrosion. Oldfield and Todd [78] gave the following equation for computing the corrosion rate of carbon steels in ocean water, viz.,

$$\text{Corrosion rate (mm/year)} = R_{\text{mppy}} = \{0.0565 C_0 U_0\} / \{\text{Re}^{0.125} \text{Pr}^{0.75}\}, \quad (5.34)$$

where  $R_{\text{mmpy}}$  is the corrosion rate in mils (or mm) per year,  $Re$  = Reynold's number of water flow,  $Pr = (c_p \mu / k)$  the Prandtl's number describes one portion of the temperature effect which results in increased diffusion of oxygen,  $C_0$  the oxygen concentrations in ppb (parts), and  $U_0$ , the flow speed (cm/sec). Also  $c_p$  is the specific heat,  $\mu$  is the dynamic viscosity and  $k$  is the thermal conductivity; normal value of  $Pr$  in water is around 7 at 20°C.

In addition, the use of biocides (particularly chlorine) for preventing bio-fouling, has its own influence on the corrosion rate in metals. As per Hartt [79] the corrosion rate  $R_{\text{mmpy}}$  (in mm per year) can also be taken as

$$R_{\text{mmpy}} = (3.15)(10^7) \left[ \frac{(MW)(I)}{(z\rho F)} \right], \quad (5.35)$$

where  $R_{\text{mmpy}}$  = corrosion rate in mm per year,  $(MW)$  is the atomic weight (in gram/mole) of the metal in question,  $I$  is the current density (in A/mm<sup>2</sup>),  $\rho$  is the density of metal (gram/mm<sup>3</sup>),  $z$  is the valency of the metal and  $F$  is the Faraday's constant.

### 5.4.3.3 Mineral, Mud, and Hydrocarbon Products

Since offshore resources are initially transported to the shore or the associated offshore structure, through pipelines, one needs to consider the effects produced as a consequence of this transport. When a solid-laden fluid is piped to the nearby platform or to shore through pipelines, it has the potential to damage the piping by corrosion–erosion, and will be heavily dependent on the particle velocity in the fluid. During hydrocarbon production (as well as during dredging of offshore mineral sediments), the pumped hydrocarbon fluid contains sand and other mineral matter; also the drilling of oil and gas wells involves the use of drill mud, which is a slurry of heavy oxides in a fluid carrier.

The factors that influence the corrosivity of ocean sediments may be positive or negative, being greater or smaller than the ocean water. For metal pipelines buried in ocean sediments, the nonbiological factors that influence corrosion are the oxygen content and its accessibility (depending on the particle size of sediments), pH, temperature, salt, contaminant and resistivity [80]. Resistivity in ocean sediments is important in the design of cathodic protection (CP) systems. It should be noted that hydrocarbons themselves are not corrosive to metals, and any corrosivity of the ocean sediments is mainly due to their water content, oxygen, hydrogen sulfide and carbon dioxide.

Soil resistivity is a function of soil moisture and the concentrations of ionic soluble salts and is considered to be most comprehensive indicator of a soil's corrosivity. Typically, the lower the resistivity, the higher will be the corrosivity as indicated in Table 5.15 [81, 82].

---

**TABLE 5.15**  
**Corrosivity Ratings Based on Soil Resistivity**

Soil Resistivity	Corrosive Rating
>20,000	Essentially noncorrosive
10,000 to 20,000	Mildly corrosive
5000 to 10,000	Moderately corrosive
3000 to 5000	Corrosive
1000 to 3000	Highly corrosive
<1000	Extremely corrosive

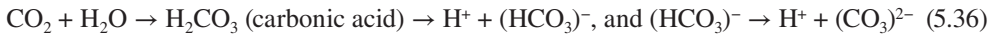
*Source:* From Distance Learning Corrosion course. Soil resistivity measurement, Royal Military College of Canada, Kingston, Ontario, Canada, 2008. <http://www.corrosion-doctors.org/Corrosion-Kinetics/Ohmic-drop-soil.htm>.

---

Plastic pipes are susceptible to damage by organic chemicals; the effects may be either physical or chemical. This damage is often enhanced by stress in the pipelines producing cracking, crazing (finely interconnected cracks) or brittle cracking.

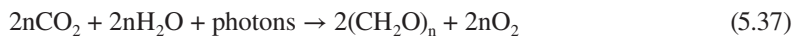
#### 5.4.3.4 Carbon Dioxide

When carbon dioxide dissolves in ocean water, it produces the weak carbonic acid, which ionizes to, viz.,



The relative concentrations of  $\text{CO}_2$ ,  $\text{H}_2\text{CO}_3$ , and the deprotonated forms  $(\text{HCO}_3)^-$  (bicarbonate) and  $(\text{CO}_3)^{2-}$  (carbonate) depend on the pH of ocean water. In neutral or slightly alkaline water (pH > 6.5), the bicarbonate form predominates (>50%) becoming the most prevalent (>95%) at the pH of seawater, while in very alkaline water (pH > 10.4) the predominant (>50%) form is carbonate. The presence of large quantities of bicarbonates accelerates corrosion by supplying hydrogen ions to the corrosion process.

In ocean water, photosynthesis of organic matter takes place in the presence of sunlight to produce chlorophyll, viz.,



This chlorophyll production occurs to a depth of about 150.0 m in the ocean. During air–sea exchange and respiration in plants (and algae) the chlorophyll is broken down to form carbon dioxide and water, viz.,



Once again a process similar to that given by Equation 5.35 occurs, increasing corrosion process. The pH of seawater ranges from 7.5 to 8.3 (influenced by the inorganic carbon content), and the presence of high levels of magnesium, calcium and carbonate ions in ocean water would also lead sometimes to the precipitation of scales of magnesium hydroxide and calcium carbonate on the cathodic surface [64], in the presence of hydroxyl ions  $[(\text{OH})^-]$  which are present during the oxygen reduction process (see Figure 5.39).

Under conditions of elevated pressure (during natural gas production or drilling process), the dissolved carbon dioxide can lead to increased corrosion rates. As per DeWaard and Williams [83], the corrosion rate  $\nu$ , in mm/year, is given by

$$\log(\nu) = 7.96 - [(2.32)(10^3)] / [t + 273] - (5.55)(10^{-3}) t + (0.671) \lg (P_{\text{CO}_2}), \quad (5.39)$$

where  $\nu$  = the corrosion rate, in mm/year,  $t$  the temperature in °C, and  $(P_{\text{CO}_2})$ , the partial pressure of  $\text{CO}_2$  is given by  $(P_{\text{CO}_2})$  [in bars =  $(355)(10^{-6})$ ].

This equation is widely used in the prediction of carbonic corrosion rates in oil and gas transportation systems.

#### 5.4.3.5 Biological and Microbiological Environments

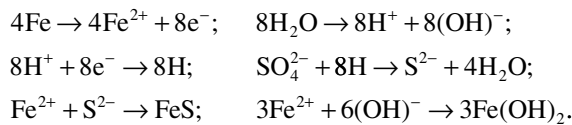
Macrobiological and microbiological processes are of great importance in deciding on the susceptibility of materials to corrosion degradation in the ocean environment. These two processes affect all materials in the ocean environment to a greater or lesser extent, and can be physical or chemical in nature. Besides the above, bio-fouling also contributes to the degradation process in ocean materials.

When a material is immersed in ocean water, a film of nonliving organic material is formed (20–80 nm thick) on the surface within a few hours; this initial film alters the electrostatic characteristics and wettability of the metal surface, facilitating its colonization by bacteria. Thereafter



a film of microbial matter—which may include bacteria, fungi, archaea, algae, plankton, and others—begins to colonize this nonliving organic layer and produces a layer of slime [84]. This changes the biochemistry of the surface and makes it receptive to macro-fouling organisms. These microbes play a significant role in affecting the corrosion half-cell reactions. As far as the metallic corrosion is concerned the most important microorganisms are the classes of bacteria called anaerobic (oxygen-deficient) bacteria (otherwise called sulfate-reducing bacteria, or SRB); especially the classes *Desulfovibrio* and *Desulfotomaculum*, are common. *Desulfovibrio salixigens* requires at least 2.5% concentration of sodium chloride, but *D. vulgaris* and *D. desulfuricans* can grow in both fresh and salt water. *D. africanus* is another common corrosion-causing microorganism. Besides the above a number of other microbes mentioned earlier also play some part in the corrosion process.

The SRB, acting on steel surfaces, carry out the reduction of sulfate ions by taking up the molecular hydrogen and forming sulfides and producing iron oxides. The mechanism proposed by Kuhr and Flugt and given in [85] is shown below in Equation 5.40.



This produces the final reaction,



As one could see from Equation 5.35, the corrosion rate is independent of any enzyme activity from the microbes present in the bio-fouling organisms; but the microbes control the corrosion rate through the metabolic action given in Equation 5.40. In addition to the effects given in Equation 5.40, the SRBs can also metabolize the sulfate ions present in ocean water (2500 mg/L) to produce hydrogen sulfide solutions (1000 mg/L) to its almost saturation solubility.

Bacterial/microbial corrosion can affect the corrosion rate of many other materials, used in the ocean environment. Concrete is susceptible to corrosion degradation due to the acidic conditions brought about by the action of anaerobic bacteria. Freshly placed concrete has a pH of approximately 11 or 12, depending upon the mix design. This high pH is the result of the formation of calcium hydroxide [ $\text{Ca}(\text{OH})_2$ ] as a by-product of the hydration of cement. A surface pH of 11 or 12 will not allow the growth of any bacteria; however, the pH of the concrete is slowly lowered over time by the effect of carbon dioxide ( $\text{CO}_2$ ), present in ocean water, and hydrogen sulfide gas ( $\text{H}_2\text{S}$ ), produced by the anaerobic bacteria (acting on the accidental spill of sour crude in the vicinity of the tower).  $\text{CO}_2$  produces carbonic acid and  $\text{H}_2\text{S}$  produces thiosulfuric and polythionic acid. These gases dissolve into the water on the moist surfaces and react with the calcium hydroxide to reduce the pH of the surface. Eventually the surface pH is reduced to a level, which can support the growth of bacteria (pH = 9 to 9.5). Once the pH of the concrete is reduced to around pH = 9, biological colonization can occur. Most species of bacteria in the genus *Thiobacillus* (especially, of the type concretivorous) have the unique ability to convert hydrogen sulfide gas to sulfuric acid in the presence of oxygen. The thiosulfuric acid produced in the pores of concrete in ocean water attacks the matrix of the concrete, which is commonly composed of calcium silicate hydrate gel (CSHG), calcium carbonate from aggregates (when present) and unreacted calcium hydroxide. Although the reaction products are complex and result in the formation of many different compounds, the process can be generally described. The primary product of concrete due to the action of the weak thiosulfuric acid is calcium sulfate ( $\text{CaSO}_4$ ), which is a pasty white mass deposited on concrete surfaces. In areas where high flows intermittently scour the structural walls above the water line (or at the bottom of the sea, where subset currents exist), concrete structural deterioration can be particularly fast. As a

consequence of the washing off of the “protective” coating of gypsum with high seawater or current flows, fresh surfaces are therefore exposed to acid attack, which accelerates the process [86, 87].

The bio-deterioration of plastics occurs mainly due to the presence of macroorganisms such as marine borers (principally *Pholodidae*) and the deterioration is due to physical damage. Also it is observed that the damage is very slight, even for very long exposures. Moreover it is observed that concrete structures do not appear to be susceptible to damage by marine fouling organisms; physical surveys of structures existing in ocean environment for more than fifty years have not been damaged in spite of the extensive marine bio-fouling.

#### 5.4.4 FORMS OF CORROSION

The various forms of corrosion that can occur in the ocean environment have been shown earlier, in Figures 5.11 and 5.12. They are classified into groups based on the dominant corrosion mechanisms, viz., (i) electrochemical corrosion mechanism and (ii) combined electrochemical-cum-mechanical mechanism. The following subgroups belong to each of them. The dominant electrochemical corrosion categories are (i) general corrosion, (ii) galvanic corrosion, (iii) crevice corrosion, (iv) pitting corrosion, (v) intergranular corrosion, and (vi) differential environmental-influenced corrosion. The following four categories belong to the combined electrochemical-cum-mechanical corrosion, namely, (i) fretting corrosion, (ii) corrosion–erosion based corrosion, (iii) stress–corrosion cracking, and (iv) corrosion fatigue.

##### 5.4.4.1 General Corrosion

The general corrosion occurs almost uniformly over the whole surface area, since anodic sites are distributed all over the metal surface. The rate of metal loss (by weight), per unit area, is given by [88]:

$$C = 10^{-3} (i)[(MW)/F], \quad (5.41)$$

where

- $C$  = rate of metal lost expressed in kg.s/m,
- $MW$  = molecular weight (g),
- $F$  = Faraday’s constant, expressed as (C/g mole), and
- $i$  = corrosion current density (in A/m<sup>2</sup>).

If corrosion rate is to be expressed in terms of metal thickness loss in one year then [89],

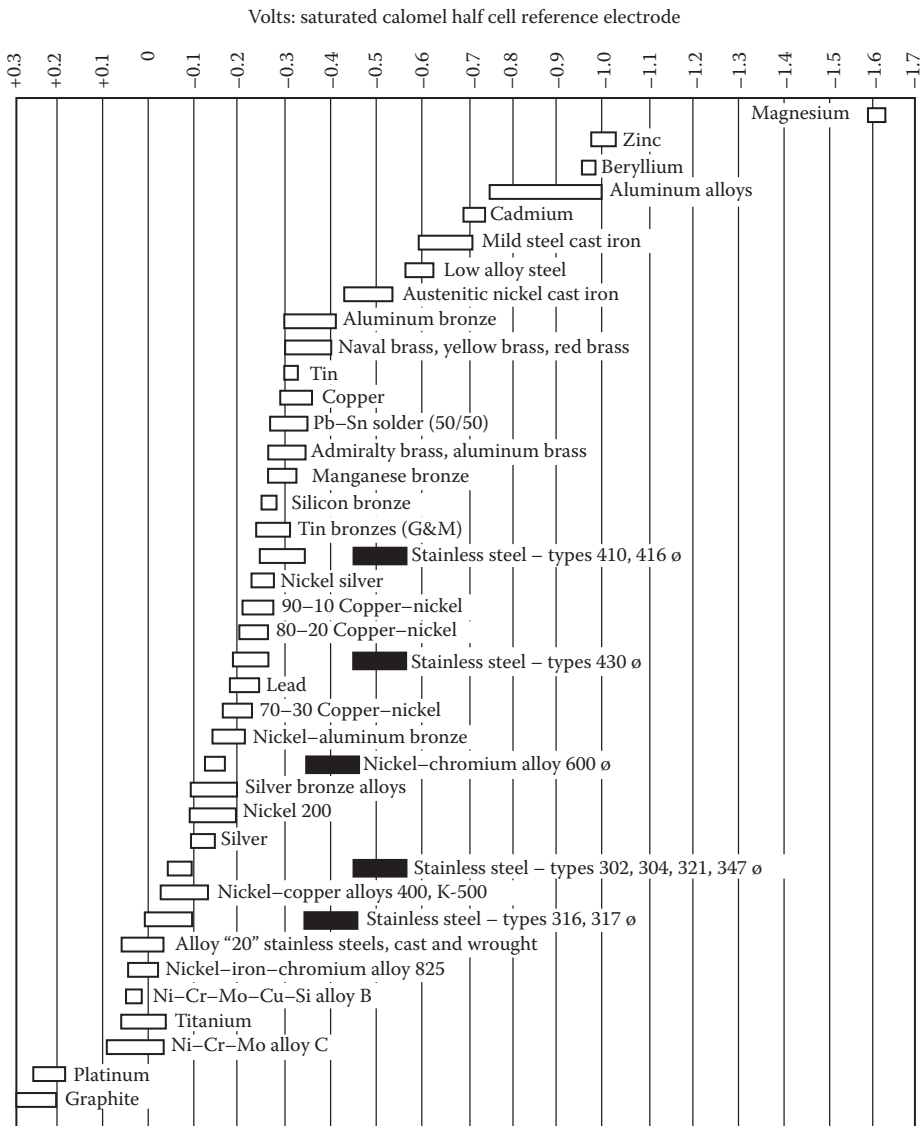
$$r = (3.15)(10^{13})(C/D), \quad (5.42)$$

where  $r$  = metal thickness loss (in  $\mu\text{m}/\text{year}$ ) and  $D$  = metal density in  $\text{kg}/\text{m}^3$ .

Generally in design, a penetration rate of 25  $\mu\text{m}/\text{year}$  would be considered acceptable, and rates above 200  $\mu\text{m}/\text{year}$  would require some sort of corrosion protection. In the noncritical areas of a thick-walled structural component, corrosion rates of a few thousand  $\mu\text{m}/\text{year}$  may be permitted. The main uncertainty in corrosion allowance would be the nature of the corroded profile since it may not be flat; hence, knowledge of the maximum possible corrosion pit depth is required by the designer.

##### 5.4.4.2 Galvanic Corrosion

Galvanic (or bimetallic corrosion) takes place when a second more noble metal is connected to the corroding metal. The corrosion rate may increase substantially depending on the ratio of noble metal surface area to that of the base metal and the polarization characteristics of the two metals. In case of alloys, the galvanic series shown in Table 5.14 has only a limited usage. In this case, a better galvanic series for engineering alloys, shown in Figure 5.41 [90] should be used.



**FIGURE 5.41** A practical galvanic series for engineering alloys in seawater. Certain alloys marked with the symbol Ø may become more active in poorly aerated or shielded areas and exhibit a potential near -0.5 v. (From R. Reuben, 1990, Corrosion and defect evaluation, Chapter 10, in *Marine Technology Reference Book*, ed. N. Morgan, Butterworths, London.)

### 5.4.4.3 Crevice Corrosion

Crevice corrosion is caused by the material composition difference at the local level produced in the electrolyte. When local mixing in the electrolyte is prevented by some stagnant condition, the corrosion of stainless steel is aggravated. Normally crevice corrosion is associated with the passivating metals, such as stainless steels in electrolytes, that contain aggressive anions such as chlorides.

### 5.4.4.4 Pitting Corrosion

Pitting is the name given to the highly localized corrosion, shown in Figure 5.11d that takes place when sheltering of water, poorly oxygenated conditions or stagnation occurs around a corroding

surface. Even though crevice corrosion will be something similar to the pitting corrosion, crevice corrosion requires a macroscopic change of environment, whereas pitting corrosion would require highly localized microscopic heterogeneities

#### **5.4.4.5 Intergranular Corrosion**

When certain portions of a metal surface are more susceptible to corrosion than others, this may sometimes turn out to be due the effect of intergranular corrosion. The best known example is the poorly heat-treated stainless steels (of the austenitic type) where they contain sufficient carbon and are heated for a long time at a temperature ranging between 500°C and 800°C; the carbon precipitates at the grain boundaries as chromium carbide. The removal of chromium leaves the metal surface less passive to the corrosive environment; this type of corrosion becomes dominant in austenitic stainless steels when welding it used to join parts together.

#### **5.4.4.6 Differential Environmental Influences**

When parts of the same metal surface are exposed to varying environmental conditions, viz., to the differential aeration cells with different amounts of oxygen (in the electrolyte), then this type of corrosion occurs.

#### **5.4.4.7 Fretting Corrosion**

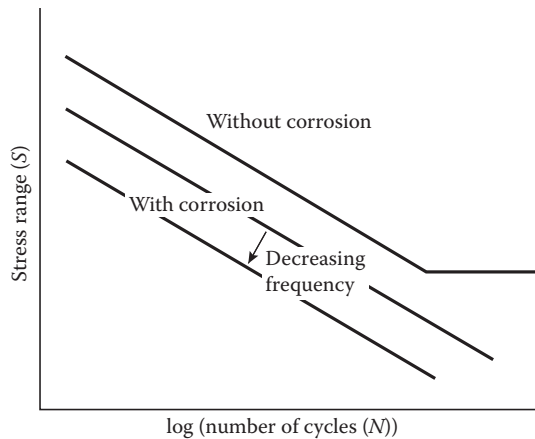
Fretting corrosion takes place when corrosion occurs due to wear between two moving surfaces (wear–corrosion) or when wear occurs due to the presence of corrosion (corrosion–wear) between the two moving surfaces; generally wear–corrosion is referred to as fretting corrosion. This is clearly illustrated in Figure 5.12, which shows the different stages of wear–corrosion. In addition, if the applied loads between the moving parts are also oscillatory, then there is a possibility of corrosion fatigue also being present in fretting corrosion.

#### **5.4.4.8 Corrosion–Erosion**

When wear of parts are associated with fluid flow, the corrosion is called corrosion–erosion. Usually such corrosion takes place when extremes of fluid flow occur around the structural components submerged in seawater; sometimes this may occur even at lower velocities of fluid flow due the material being susceptible to flow effects. The flowing fluid removes the corrosion products formed on the surface, exposing more intact surfaces to this type of corrosion. The erosion of metals can be brought about by the impingement of water, cavitation or by turbulent flow around exposed surfaces. Cavitation can remove material from the surface even without corrosion being present at the surface. Moreover, suspended particles in the flowing water will also increase the erosion process.

#### **5.4.4.9 Stress Corrosion Cracking**

Stress corrosion cracking must be avoided at all costs as it is one of the most destructive types of corrosion. If cracks are formed on the metal surface, in a region of very high stress concentration, then there is a possibility that these cracks will develop and progress under the combined action of the crack-opening stress and the corrosion embrittlement action at the crack tip; this is illustrated in Figure 5.12. The stress corrosion reaction thus occurs only over a very small area of the exposed surface of the structure; but it grows very fast and reduces the load-bearing capacity of the structural component. The presence of residual stresses, in conjunction with applied stresses, could also increase the stress corrosion cracking rates. At a given stress level, stress corrosion cracking is dependent upon the temperature of the environment, composition of the steel or metal alloy, chloride content of the fluid around the structure, electric potential developed due to the corrosion process, and oxygen content of the seawater.



**FIGURE 5.42** Influence of corrosion in the fatigue strength curves. (From R. Reuben, 1990, Corrosion and defect evaluation, Chapter 10, in *Marine Technology Reference Book*, ed. N. Morgan, Butterworths, London.)

#### 5.4.4.10 Corrosion Fatigue

Corrosion fatigue occurs when corrosion takes place in a material undergoing fatigue degradation. As explained earlier (see Section 5.2.3.4) the fatigue strength of the structure or structural component is reduced further by the occurrence of corrosion in seawater; also it is further reduced when the structural component or the structure is set in motion by the dynamic wave (or even wind), as shown in Figure 5.42 [91]. Due to the presence of the corrosive environment, the anodic areas of the crack tip are preferentially dissolved to increase the rate at which cracks propagate in the material of the structure.

#### Example 5.18

You have been asked to design cylindrical condenser tubes, for a ship condenser. Using strength of materials theory, compute the wall thickness necessary to contain the steam at 15.0 psi differential in 2.0 in. inner diameter 70/30 Cu-Ni tubes and then calculate how thick your corrosion allowances have to be if you wanted them to last 20 years with a flow rate of 7.0 ft./s. Let the temperature of seawater be 70°F.

Yield strength of 70/30 Cu-Ni tube = 125.0 MPa ( $\approx$  18.0 ksi); use a factor of safety = 2.25. Hence, allowable stress =  $18/2.5 = 7.2$  ksi.

Using thin cylinder theory,  $t = [pD/(2\sigma_{hoop})] = (15)(2)/\{(2)(7.2)(1000)\} \approx 0.0021$  in.; it is a thin tube.

Minimum permissible thickness = 1.0 mm; required thickness for strength requirements = 0.05 mm.

(i) Using Equation 5.34,

$$R_{mmpy} = \{0.0565 C_0 U_0\} / \{Re^{0.125} Pr^{0.75}\}.$$

$$U_0 = (7.0)(30.48) = 213.36 \text{ cm/s.}$$

$$C_0 = \text{Oxygen concentration in ppb in seawater} = 4.0 \text{ to } 8.0 \text{ ppb} \approx 8.0.$$

$$Re = \text{Reynolds' number of flow} > 4000.0.$$

$$Pr = \text{Prandtl's number} = 7.0 \text{ for water.}$$

$$R_{mmpy} = (0.0565)(8.0)(213.36) / [(4000)^{0.125}(7.0)^{0.75}] = 7.9 \text{ mmpy} \approx 8.0 \text{ mmpy.}$$

$$\text{Corrosion allowance} = (20)(8.0) = 160 \text{ mm.}$$

(ii) Using Equation 5.35,

$$R_{\text{mmpy}} = (3.15)(10)^7 \left[ \frac{(MW)(l)}{(z\rho F)} \right].$$

$MW$  of 70/30 Cu/Ni alloy  $\approx 60.15$ ;  $l \approx 10^{-5}$ ;  $z \approx 2.0$ ;  $\rho = 8.95 \text{ kg/dm}^3$

{ $= (8.95)(10^{-3}) \text{ g/mm}^3$ };  $F = \text{Faraday constant} = 96,500 \text{ A/s}$ .

$$R_{\text{mmpy}} = (3.15)(10)^7 \left[ \frac{(60.15)(10^{-5})}{(2.0)(8.95)(10^{-3})(96,500)} \right] = 10.97 \text{ mmpy}.$$

Hence, corrosion allowance  $= (10.97)(20) = 219.4 \text{ mm}$ .

(iii) Using Equation 5.41, corrosion rate in  $\mu\text{m/year}$  is given by  $r = (3.15) (10^{13}) (CD)$ , with  $C = 10^{-3} (i)/(MW)/(F)$ .

With  $i = \text{corrosion current density (in A/m}^2\text{)}$ ; current voltage for 70/30 Cu–Ni alloy =  $-0.20 \text{ V}$ ; and  $D = 8950 \text{ kg/m}^3$ . For this voltage,  $I = (4 \text{ to } 5)(10^{-6}) \text{ A/m}^2$ .

Take  $i = (4.0)(10^{-6}) \text{ A/m}^2$ .

$$C = \left\{ \frac{(10^{-3})(4.0)(10^{-6})(60.15)}{(96500)} \right\} = (24.932)(10^{-13}).$$

$$R = (3.15)(10^{13})(24.932)(10^{-13})/(8950) = (8.77)(10^{-3}) \mu\text{m/year} = 8.77 \text{ mmpy}.$$

Hence, corrosion allowance  $= (8.77)(20) = 175.4 \text{ mm}$ .

All the three formulations give answers close to one another.

## 5.4.5 CORROSION PROTECTION

The methodologies that can be used in the protection of materials in the ocean environment depend on the mechanism involved in the corrosion process. For instance, the procedures used against corrosion of metals in ocean water will be different from the degradation of polymers against ultraviolet radiation. Five basic methods are used for preventing or minimizing corrosion of metallic structures, viz., (i) use of protective coatings, (ii) cathodic protection, (iii) anodic protection, (iv) alter the environment and make it noncorrosive (called inhibition), and (v) use of corrosion-resistant steels. Protection against microbes or bio-fouling agents is carried by using biocides or antifouling agents. Protection of polymers (or plastics) is carried out mainly by using agents in polymers that will minimize the UV radiation damage. Protection of concrete is made by making it suitably resistant against water penetration, salt intrusion (chlorides, carbonates, sulfates and sulfides), abrasion, frost damage, and reinforcement corrosion.

### 5.4.5.1 Protective Coatings

Coatings act as barriers that prevent the access of the corrosive environment to the surface of the protected material. Since most of the coatings are rarely impermeable, it should be realized they should be used in conjunction with some amount of cathodic protection or inhibition. Also since coatings are likely to be damaged by chemical or mechanical action, the possible existence of a local damage in the coating should also be reckoned with in the selection of the coating material. Various possible types of coatings that can be used in an offshore context are given in Table 5.16 [92], given below. When using coating, it is essential to ensure that adequate bonding is achieved at the metal-primer surface, and some type of cleaning or other preparatory surface treatment is usually required to do this.

Coatings are used in the ocean environment for the corrosion protection of structures, where it becomes a back-up to the cathodic protection. The two types of coating procedures available are the metallic/inorganic coatings and organic coatings; these are shown in Table 5.16. Metallic (or inorganic) coatings can be applied by a variety of means including plating, hot-dipping, spraying and cladding. The metal applied may be either anodic or cathodic to the substrate and the behavior will be different depending on whether it is anodic or cathodic to the substrate. Cupro-nickels and monels have been used as cathodic metallic coatings on substrate steels in the splash zones; cupro-nickels are also resistant to bio-fouling mechanisms.

The most familiar application of anodic metallic coatings is in galvanizing, where a layer of zinc is applied to the substrate, usually by hot dipping. The advantage of an anodic coating is that the

**TABLE 5.16**  
**Coating Procedures and the Mode of Application**

#	Metallic/Inorganic	Organic (Paints, Varnishes, and Lacquers)
1	Chemical conversion	Inhibition
2	Electrodeposition	Cathodic protection against "holidays or uncoated patches"
3	Hot-dipped (galvanizing)	Anodic metal addition
4	Flame sprayed	—
5	Diffusion	—
6	Cladded	—
7	Vapor deposition	—

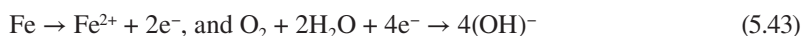
*Source:* With kind permission from Springer Science+Business Media: *Materials Marine in Marine Technology*, From marine corrosion and biodeterioration (Chapter 3), 1994, p. 66 (modified), R. Reuben.

substrate will form the cathodic member of any galvanic couple produced by local disruption of the coating. If the self-corrosion rate of the coating metal is reasonably low this type of coating forms a very good stable coating system. Another type of anodic metallic coating is the flame-sprayed aluminum. Inorganic coatings can be applied by a variety of procedures including fusion, surface conversion and casting. Some of these coatings are (i) artificially thickened oxide on anodized aluminum, (ii) concrete, and (iii) fused glass.

Organic coatings form the greatest part of the coatings used in the ocean environment. Along with surface preparation of the metal surface, appropriate selection of the type and thickness of coating material are also very important. Organic coatings are polymer based and permeable to oxygen and moisture. These coatings should possess the following characteristics: (i) Coating should be resistant to alternate wetting and drying. (ii) The coating should be resistant to the passage of ions (such as chlorides, sulfates and carbonates), which will make the ocean water electrolytic. Osmotic pressure should not be allowed to be developed in between the paint coating and the substrate since it will lead to blistering. (iii) The coating should be dielectric in nature so that it will resist the flow of electrons from the cathodic surface and the anodic sites of the substrate. In addition, it should not permit electro-osmosis across the coating. (iv) The external surface of the coating must be resistant to various corrosive influences present in ocean water. (v) The adhesion of the coating to the substrate is very important, and this must be uniform over the whole coated area. As an example of the range of high-build coatings available for use as coating systems for offshore structures, the paper by Coke [93] should be consulted since he discusses a number of coating systems used in the Gulf of Mexico context.

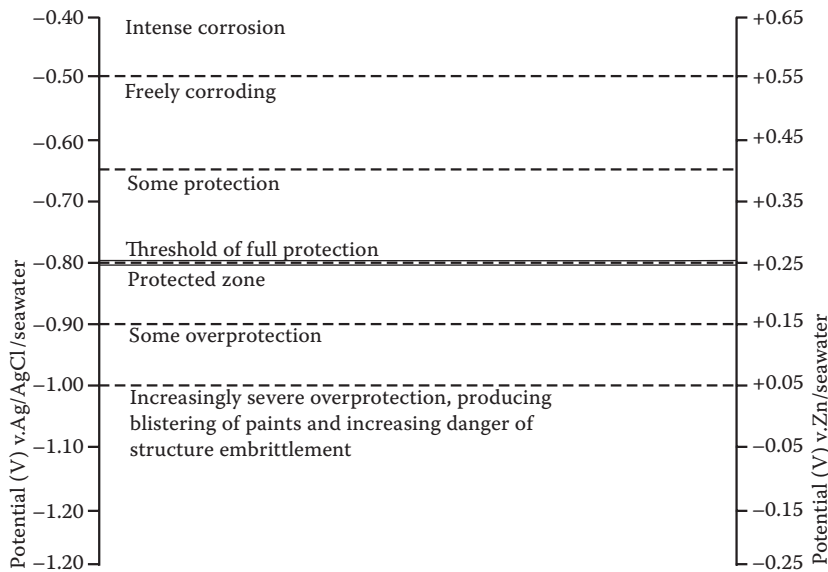
#### 5.4.5.2 Cathodic Protection

Cathodic protection consists of depressing the p-potential of a corroding surface to inhibit the anodic dissolution. In simple electrochemical terms, this can be explained as supplying an excess of electrons to the corrosion cell. For instance when steel corrodes in ocean water, the following actions take place,



This losing of electrons and the subsequent corrosion of the metal surface can be minimized or completely prevented when an adequate supply of electrons is provided to the metal surface by the cathodic protection system; the supply of electrons to the metallic surface opposes the dissolution of





**FIGURE 5.43** Corrosion cathodic protection and overprotection regimes expressed as a function of electrode potential. (From The Marine Technology Directorate Ltd., 1990. In *Design and operational guidance on cathodic protection of offshore structures, subsea installations and pipelines*, Chapter 2 on Principles of corrosion and cathodic protection offshore, p. 35, 1990. With permission.)

iron and assists in the reduction of oxygen. Care must be taken to see that the electric potential of the surface is not reduced too much since this may enable the evolution of hydrogen ions from the electrolyte, which may lead to embrittlement of the steel surface. The sacrificial anode and impressed current cathodic protection systems have already been given earlier in Figure 5.13.

These principles of over- and under- protection are illustrated in Figure 5.43 [94], which shows the cathodic protection of steel in ocean water. The accepted criterion for full protection of steel in aerated seawater is a polarized potential of  $-800$  mV, with respect to a silver/silver chloride/seawater reference electrode (see Table 5.14) [95, 96], which shows presence of microbial-assisted corrosion, a value of  $-900$  mV is recommended. In the case of high-strength steels (with yield strength  $\geq 700$  MPa) it is essential to avoid overpolarization, and for this reason the potential should fall between  $-800$  mV and  $-950$  mV. If the potential is allowed to fall below  $-950$  mV, then there is a possibility of blistering of paint coatings and the material becoming embrittled. Also if the potential falls below  $-500$  mV, there is a possibility of intense corrosion occurring in the metal surface.

### 5.4.5.3 Anodic Protection

Anodic protection is based upon the phenomenon of passivation, where the elevation of the potential of a metallic surface can result in a sudden drop of corrosion rate; anodized aluminum is an example of passive anodic protection. This route is not encouraged since the presence of chloride ions in ocean water destabilizes the passive films present on metal surfaces.

### 5.4.5.4 Corrosion Inhibition and Electrolyte Modification

Corrosion inhibitors are those chemicals that directly or indirectly result in the formation of adherent films on metal surfaces, which render them resistant to corrosion. The inhibitor can be added to the electrolyte or applied to the surface to be protected. These inhibitors can be either organic or inorganic. Inorganic inhibitors are chromate or silicate or phosphate salts which dissolve in water; organic inhibitors possess amine groups as a part of their structure.

**EXERCISE PROBLEMS**

- (i) List five for each of the following: (a) metallic materials, (b) polymeric materials, and (c) composite materials used in the offshore environment. (ii) Selecting one from each category in (i), list the various chemical, physical, and mechanical properties possessed by each of the selected materials. (iii) Give the difference between the physical and mechanical properties of materials.
- (i) Compute the ratio of yield strength to tensile strength for (a) low-, medium-, or high-strength steel and (b) high-strength aluminum alloy. (ii) Determine the ratio of fatigue strengths at 10<sup>6</sup> cycles to tensile strengths of the above materials.
- (i) A material made of steel has a tensile strength of 120,000 psi. Give a reasonable estimate of its fatigue strength. (ii) State when you would use the creep strength of a material as a basis for structural design. (iii) Explain in detail what you understand by elastic and plastic deformations in (a) steel and (b) copper alloy (yellow brass).
- Determine the materials for the following use: (i) steel for application in the Arctic region, needing a Charpy V-notch impact energy higher than 80 lb. ft., at a temperature of  $-18^{\circ}\text{C}$ ; (ii) steel for use in a liquefied natural gas (LNG) tanker that is in contact with LNG (at a temperature of  $-150^{\circ}\text{C}$ ); and (iii) steel for use in the equatorial belt, where temperatures can rise to a maximum of  $+50^{\circ}\text{C}$ .
- (i) Name three materials that have good cavitation resistance in water. (ii) State how you would cathodically protect an underground cast iron pipe. (iii) How would you make a piping system to carry seawater at  $95^{\circ}\text{C}$ ?
- (i) Name five materials that would have long lead times for procurement. (ii) Explain the meaning of minimum-order requirements. (iii) Cite a case where product liability would be a concern and state how you would deal with it. (iv) Compare the costs of making a base plate 15.0 mm  $\times$  100.0 mm  $\times$  100.0 mm of (a) carbon steel and (b) PVC.
- (i) Differentiate between thermoplastic and thermosetting polymers. (ii) Name five types of thermoplastic and thermosetting polymers used in offshore application. (iii) Explain the difference between soft vinyl used in seat covers and polyvinyl chloride plastic used in hard plumbing piping.
- Explain the following: (i) The modulus of rupture of a polymer depends on (a) temperature, (b) loading time, (c) fraction of covalent cross-links, (d) molecular orientation, (e) crystallinity, and (f) degree of polymerization. (ii) The tensile strength of a polymer depends on (a) temperature, (b) strain rate, (c) molecular orientation, and (d) degree of polymerization. (iii) The toughness of a polymer is affected by (a) temperature, (b) strain rate, and (c) molecular orientation.
- Classify the following plastics (thermosetting or thermoplastic): (i) phenol-formaldehyde, (ii) silicon rubber, (iii) PVC, (iv) polyethylene, (v) paper, (vi) Mylar drafting paper, (vii) foamed polystyrene, (viii) foamed polyurethane (rigid), (ix) most paints and varnishes, (x) most rubbers, and (xi) asphalt.
- Briefly describe the following: (i) corrosion occurrence in a steel offshore structure, (ii) concrete for underwater use, and (iii) welded and prefabricated tubular connections used in offshore structures.
- (i) Name (a) a reducing environment and a material that can resist attack of such an environment and (b) an oxidizing environment and a material that can resist attack of such an environment. (ii) What is the significance of an aqueous environment, with a pH of 4, on carbon steel? (iii) What is the galvanic effect of fastening aluminum sheeting to the deck of an offshore structure using steel rivets? (iv) How does soil resistivity affect corrosion of buried pipelines? (v) Steel corrodes in salt water at the rate of 10.0 mpy. What should be the corrosion allowance to get 10 years of service from a steel vessel in a marine environment? (vi) Give the best anode materials to provide cathodic protection to buried pipes.

12. (i) Explain why corrosion of metals is called electrochemical in nature. (ii) Name the four elements that must be present simultaneously, at a location, for corrosion to occur, and explain how the flow of current and electrons occur. (iii) Give the significance of the standard hydrogen electrode (SHE) and explain how the electrode potentials of different metals are obtained. (iv) Differentiate between the standard electrode potential series and the galvanic series. (v) Explain the terms (a) “passivity” and its application to metals and (b) “cathodic and anodic protection.”
13. (i) Concrete can be made with cement and sand. What is the need for using coarse aggregates in concrete? (ii) Explain hydraulic cement and outline the methods that are used to assist the hardening of concrete under water. (iii) A concrete is to be made with a mix of 1.0 part cement, 1.50 part sand and 3.25 part coarse aggregate by volume, with a water–cement ratio of 0.50 by weight. The sand weighs 100 lb./ft.<sup>3</sup>, coarse aggregate weighs 90 lb./ft.<sup>3</sup>, and the specific gravity of cement is 3.15. Determine the absolute volume of each component in ft.<sup>3</sup> per bag of cement.
14. Differentiate between the use of lightweight concrete and cast-in-situ normal strength concrete for constructing a habitat 15.0 ft. in diameter, 60.0 ft. long, and 1.0 ft. thick. List their significant differences in physical characteristics and determine how much ballast is required to sink the habitat.
15. (i) A concrete consists of 60% by volume of limestone aggregate (fine and coarse) plus 40% by volume of cement paste. Estimate the Young’s modulus of the concrete if  $E$  for limestone is 63.0 MPa and  $E$  for cement paste is 25.0 MPa. (ii) Why is the tensile strength of conventional concrete only about 4.0 MPa? How can the tensile strength of cement be increased by improvements in processing? What is the maximum value of tensile strength of concrete that can be obtained by processing improvements?
16. A barge of 120.0 ft. length, 20.0 ft. width, and 15.0 ft. height is to be built. Discuss the use of fiberglass versus ferrocement as the building material and comment on the differences of physical characteristics.
17. Determine the underwater weight of a steel tubular member, 0.60 m in diameter (outer) and 10.0 m in length and having a thickness of 0.02 m, that is to be used in the underwater portion of a drilling rig. In order to reduce its underwater weight, a syntactic foam cylinder is added to the outside of this tubular member. Compute the thickness of this foam cylinder if the underwater weight of the tubular member is to be reduced by 25%.
18. The beam at the base of an offshore drilling rig is loaded by the static load of the rig to a stress of 15,000 psi. During an extreme wind event, the beam is hit by a large wave that produces an additional stress of 12,000 psi in the same direction as the static stress, at a rate of 15.0 in./in. s. As shown in Figure 5.17, the steel (of the beam) has static yield strength of 27,000 psi and ultimate static tensile yield strength of 57,000 psi. (i) Assuming that the material behaves as shown in Figure 5.17 and that the load is such that the stresses can be added, compute the yield and ultimate tensile strengths of the steel, when it is loaded at this strain rate. (ii) Determine the ratio of static stress to low-strain-rate yield and tensile strengths. (iii) Determine the same ratios at the specified rates for the combined stresses.
19. The hoop compressive stress  $S$  of a submerged sphere with “thin” walls is given by  $S = \left(\frac{R}{2t}\right)p$ , where  $R$  is the radius,  $t$  is the sphere wall thickness, and  $p$  is the external pressure. Use the materials given in Table 5.8 and design the smallest sphere that will support 1000 lb. (concentrated load) at a water depth of 600.0 ft. in seawater (density of 64.0 lb./ft.<sup>3</sup>). Do not use wood or glass. The sphere has inside air at 1.0 atmospheric pressure.
20. A search process was initiated to select the best material to be used for the fabrication of the hull required for a petrel frigate. The following materials, given in Table P5.1, were found to be suitable from an initial selection. The vessel is to operate in the sub-Arctic

**TABLE P5.1**  
**Materials Data**

Material	Tensile Strength (MPa) (20)	Toughness (MPa.m) (20)	Cost—Relative to Mild Steel (10)	Corrosion Pit Depth (mm) (5)	Weldability (5)	Charpy Impact Strength (J) (5)	Transition Temperature (°C) (5)
Mild steel	470	51.7	1.0	1.78	E	5	0
Notch mild steel	485	53.4	1.1	1.55	G	27	-20
Crack arresting steel	520	52.0	1.15	1.12	P	40	-30
HY-80	840	84.0	6.0	0.90	G	85	-84
HY-100	810	90.0	7.0	0.95	G	90	-84

*Note:* Weights for each operation are given within brackets; average density of steel is 77,000 N/m<sup>3</sup>.

and temperate regions of the Atlantic Ocean, wherein the temperatures, to which the vessel will be subjected, are likely to vary between 30°C and -40°C. Using the data given in Table P5.1 (along with the weights), determine the best available material for the job.

21. Toughness of a material can be defined by determining the area under the stress-strain curve of a tensile test on the material. Assume that the various low-strength steels given in Table 5.2 have a stress-strain curve represented by two straight lines, with the initial line having a slope of  $E$  (Young's modulus of the material) and the other line connecting the yield strength to the ultimate strength (at final elongation) of the chosen steel. (i) Determine an equation for the toughness of the low-strength steel based on  $E$ ,  $\sigma_y$ ,  $\sigma_u$ , and percentage elongation. (ii) Find the toughest and the least tough of the low-strength steels given in Table 5.3, using the above equation; also, compute the energy absorption per unit volume of the material. (iii) Determine the cheapest steel based on unit energy absorption per dollar. (iv) Compare in a similar manner the data given on medium-strength and high-strength steels, using the values given in Table 5.4 and Table 5.5. (v) Making use of the derivations given in (i), obtain the toughness of the aluminum alloy given in Table 5.6, and compare these values against the Charpy V-notch impact values and their ratios of fatigue to tensile strengths. Comment on any correlations you observe, and explain these correlations.
22. A pressure hull of a deep-sea submersible is to be designed to descend to a depth of 35,000 ft. The external pressure at this depth is approximately 100.0 MPa, and the design pressure is to be taken as 200.0 MPa. The pressure hull is in the form of a thin-walled sphere with a specific radius ( $r$ ) of 1.0 m and of a uniform thickness ( $t$ ). The sphere can fail in any one of the two ways given below: (i) external pressure buckling at a pressure of  $p_b$  given by  $p_b = 0.3E\left(\frac{t}{r}\right)^2$  or (ii) yield or compressive failure at a pressure of  $p_b = 2\sigma_f\left(\frac{t}{r}\right)$ , where  $E$  is the Young's modulus and  $\sigma_f$  is the appropriate yield or compressive failure stress. The basic design requirement is that the pressure hull should have the minimum possible mass to resist the design pressure. (i) Compute the minimum mass for the two design scenarios presented above. (ii) Using the two scenarios given above, calculate the minimum mass and wall thickness of the pressure if the materials given in Table P5.2 are used for the design; also, determine the limiting failure mechanism for each of the two materials. What is the optimum material for the pressure hull? Determine the mass, wall thickness, and limiting failure mechanism for that hull.

**TABLE P5.2**  
**Material Properties**

Material	$E$ (GPa)	$\sigma_f$	Density— $\rho$ (kg/m <sup>3</sup> )
Alumina	390.0	5000.0	3900.0
Glass	70.0	2000.0	2600.0
Alloy steel	210.0	2000.0	7800.0
Titanium alloy	120.0	1200.0	4700.0
Aluminum alloy	70.0	500.0	2700.0

23. The hull of a deep-sea submersible is to be designed to operate at a depth of 6000.0 m below the sea level. The performance of the vessel is to be rated based on the high yield strength, high compressive strength, weight-to-displacement ratio, and the compressibility (change in volume of the pressure hull per unit change of pressure). In addition, high specific strength, high specific modulus, excellent resistance to seawater corrosion, ease of maintainability, excellent resistance to fatigue loading, and resistance to attack by biological organisms should also be considered. From the given properties in Table P5.3 and Table P5.4 [97], select the best materials to be considered.
24. Structures made of conventional ceramics have a fracture toughness of about 5.5 MPa√m, while advanced ceramics may have a value of 20.7 MPa√m. (i) For the same applied load, how big a surface edge crack can the advanced ceramics tolerate relative to the conventional ceramics? (ii) For the same surface crack size, determine how much stress can the advanced ceramics tolerate before fracture? (iii) What is Weibull statistics and what does the Weibull modulus signify? (iv) Seven samples of a rare metal, each of 164.0 cm<sup>3</sup> volume, show flexural strength of 605, 595, 650, 630, 640, 615, and 620 MPa. Determine

**TABLE P5.3**  
**Properties and Performance Indices of Some Candidate Materials for the Pressure Capsule of a Deep-Sea-Operating Vehicle**

Material	Yield Strength,		Comprehensive Strength, $\sigma_c$ (MPa)	$E$ (GPa)	$\sigma_f/\rho$ (10 <sup>3</sup> m)	$\sigma_c/\rho$ (10 <sup>3</sup> m)
	$\sigma_f$ (MPa)	$\rho$ (kg/m <sup>3</sup> )				
Pressure vessel steel <sup>a</sup>	965	7800	1034	215	12.61	13.51
Fiberglass <sup>b</sup>	200	1993	780	41	10.22	39.90
Glass-ceramic <sup>c</sup>	69	2500	345	86	2.81	14.07
Al alloy <sup>d</sup>	400	2796	280	70	14.58	10.21
Ti alloy <sup>e</sup>	830	4540	827	116	18.64	19.16

Source: G. Lewis, 1990, *Selection of Engineering Materials*, Prentice Hall, Upper Saddle River, NJ, p. 99.

<sup>a</sup> HY-140, a quenched and tempered Ni–Cr–Mo–V steel.

<sup>b</sup> Unidirectional E glass fiber reinforced epoxy resin (fiber volume fraction = 0.60); all property values are in the fiber direction.

<sup>c</sup> Pyroceram 9608.

<sup>d</sup> 1100-0.

<sup>e</sup> Ti-6Al-4V.

**TABLE P5.4**  
**Properties and Performance Indices of Some Candidate Materials for the Outer Hull of a Deep-Sea-Operating Vehicle**

Property	Unidirectional E Glass Fiber Reinforced Epoxy Resin <sup>a</sup>	Unidirectional Boron Fiber Reinforced Epoxy Resin <sup>a</sup>	Unidirectional Kevlar Fiber Reinforced Epoxy Resin <sup>a</sup>	Aluminum Alloy 1100-0
Tensile strength <sup>b</sup> (MPa)	1103	1300	1670	380
Comprehensive strength <sup>b</sup> (MPa)	780	2500	276	280
Shear strength (MPa)	70	69	69	160
Yield strength, $\sigma_y$ (MPa)	200	1100	1240	400
Endurance strength at $10^6$ cycles (MPa)	260	1070	1000	275
Tensile modulus <sup>b</sup> , $E$ (GPa)	41	207	86	70
Comprehensive modulus <sup>b</sup> (GPa)	35	207	86	70
Shear modulus (GPa)	2	7	2	28
Density, $\rho$ (kg m <sup>-3</sup> )	1993	1990	1366	2796
Poisson's ratio, $\nu$	0.25	0.30	0.30	0.35
$E/(1 - \nu^2)^{0.5}$ (GPa)	42	217	90	75
$10^3 \sigma_y (1 - \nu)/E$	3.66	3.72	10.09	3.71

Source: G. Lewis, 1990, *Selection of Engineering Materials*, Prentice Hall, Upper Saddle River, NJ, p. 99.

<sup>a</sup> Fiber volume fraction = 0.60.

<sup>b</sup> In the fiber direction, except for the Al alloy, which has isotropic properties.

(a) the characteristic strength and Weibull modulus and (b) the maximum tensile design stress for a 1 out of 1 million probability of failure.

25. A welder works in a dry welding capsule that fits tightly over an underwater tubular structure at depths of 650.0 ft. The capsule must remain pressurized at sea bottom pressure when brought to the surface in order to decompress the welder. Lifetime will not be in excess of 1000 dives, and the average time in the ocean will not go beyond one day per trip. The capsule will be raised or lowered very slowly by a crane, mounted on a barge. Select an appropriate material for the hull of the capsule.
26. A cable is to hold a taut-moored buoy at a location, where the water depth is 300.0 m. The buoy will be subjected to waves having an average wave period of 3.5 s, and the buoy has to be at the location for a period of two years. During storms, the cable will be subjected to large high-speed wave shocks. A composite cable is also a possibility, since the maximum shock loading is expected to occur at the surface of the ocean, and the lower part of the cable is behaving similar to a spring. Select a suitable material.
27. A vehicle assisting an underwater swimmer needs 450.0 N of buoyancy at depths of up to 100.0 m. The vehicle must be as compact as possible and may remain under "fully wet" conditions for weeks outside a saturated habitat used for underwater operations. Select a buoyancy material to suit the purpose.
28. Cheap and very long fencing material, which will remain under water for years and require minimum amount of maintenance, is required for the fencing of a subsea, sea fish-farming operation. The wave forces exerted on the fencing material will be very low since the bay in which the fish farming is carried out is a sheltered one. Antifouling operation is carried out on the fence by periodically lifting the material above the seawater and allowing the growth to dry; then, the residue still remaining on the fencing material will be burned using the flamethrowers. Choose a material for the purpose.



29. A manned research remotely operated vehicle (ROV) will dive to the deepest ocean depths. The vehicle must be as light as possible to minimize the buoyancy systems required. It will be required to perform not more than 200 dives during its lifetime. The vessel will be in water for no more than one day during each dive. The highest emergency rate of descent or ascent is supposed to be 5.0 m/s. Select a material for the outer hull of the ROV.

## REFERENCES

1. R. Reuben, 1990. Corrosion and defect evaluation (Chapter 10), in: *Marine Technology Reference Book*, edited by N. Morgan, Butterworths, London, p. 10/13.
2. R. Reuben, 1994. Marine corrosion and bio-deterioration (Chapter 3), in: *Materials in Marine Technology*, Springer-Verlag, London, p. 60.
3. M.B. Leeming, 1998. Durability of concrete in and near the sea (Chapter 3), in: *Concrete in Coastal Structures*, edited by R.T.L. Allen, Thomas Telford, London, p. 79.
4. J.F. Wilson, 1984. *Dynamics of Offshore Structures*, John Wiley & Sons, New York, p. 450.
5. P.M. Palermo, 1976. Structural integrity criteria for navy hull materials, *Naval Engineers Journal*, October 1976, pp. 73–86.
6. E.J. Czyryca, D.P. Kiel and R. DeNale, 2003. Meeting the challenge of higher and lighter warships, *Advanced Materials and Processes Technology Information Analysis Center (AMPTIAC) Quarterly*, Volume 7, # 3, pp. 63–70.
7. R. Reuben, 1994. The marine environment, marine structures and the role of materials technology (Chapter 1), in: *Materials in Marine Technology*, Springer-Verlag, London, p. 2.
8. Major ion composition of seawater, *Water Conditioning and Purification Magazine*, Volume 47, # 1, January 2005. LennTech Water Treatment and Air Purification Holding BV, Delft, The Netherlands. <http://www.lennotech.com/composition-seawater.htm>
9. G. Anderson, 2008. Course notes on Marine Science, Section 2.1.1 (Seawater Composition) for Sea Crew volunteers, Santa Barbara City College, Santa Barbara, California, USA [notes revised on October 2008]. <http://www.marinebio.net/marinescience/02ocean/swcomposition.htm>.
10. J.F. Anthoni, 2006. *The Chemical Composition of Seawater*. [www.seafriends.org.nz/oceano/seawater.htm](http://www.seafriends.org.nz/oceano/seawater.htm).
11. J. Gaythwaite, 1981. *The Marine Environment and Structural Design*, Van Nostrand Reinhold Company, New York, pp. 275–280.
12. A. Pipe, 1981. Marine corrosion on offshore structures, Proceedings of a Conference held on September 13–14, 1979, at the University of Aberdeen, Scotland, pp. 13–21.
13. R. Reuben, 1994. On marine environment, marine structures and the role of materials technology (Chapter 1), in: *Materials in Marine Technology*, Springer-Verlag, London, pp. 4–5.
14. H. Sheets, 1975. Selection of materials for ocean application (Chapter 6), in: *Introduction to Ocean Engineering*, edited by H. Schenck, Jr., McGraw-Hill Book Company, New York, p. 165.
15. K. Masubuchi, 1979. *Materials for Ocean Engineering*, MIT Press, Cambridge, MA, p. 70.
16. W.G. Babcock and E.J. Czyryca, 2003. Role of materials in ship design and operation, *Advanced Materials and Processes Technology Information Analysis Center (AMPTIAC) Quarterly*, Volume 7, # 3, pp. 31–36.
17. H. Sheets, 1975. Selection of materials for ocean application (Chapter 6), in: *Introduction to Ocean Engineering*, edited by H. Schenck, Jr., McGraw-Hill Book Company, New York, p. 163.
18. K. Masubuchi, 1979. *Materials for Ocean Engineering*, MIT Press, Cambridge, MA, p. 57.
19. R. Reuben, 1990. Corrosion and defect evaluation (Chapter 10), in: *Marine Technology Reference Book*, edited by N. Morgan, Butterworths, London, p. 10/8.
20. R. Reuben, 1990. Corrosion and defect evaluation (Chapter 10), in: *Marine Technology Reference Book*, edited by N. Morgan, Butterworths, London, p. 10/11.
21. R. Reuben, 1990. Corrosion and defect evaluation (Chapter 10), in: *Marine Technology Reference Book*, edited by N. Morgan, Butterworths, London, p. 10/26.
22. P.C. Kreiger, 1984. The skin of concrete, composition and properties, *Materiaux et Constructions*, Volume 17, # 100, pp. 275–283.
23. M.B. Leeming, 1998. Durability of concrete in and near the sea (Chapter 3), in: *Concrete in Coastal Structures*, edited by R.T.L. Allen, Thomas Telford, London, pp. 71–81.
24. J.F. Young, S. Mindess, R.J. Gray and A. Bentur, 1998. *The Science and Technology of Civil Engineering Materials*, Prentice Hall, Englewood Cliffs, NJ, p. 295.



25. H. Sheets, 1975. Selection of materials for ocean application (Chapter 6), in: *Introduction to Ocean Engineering*, edited by H. Schenck, Jr., McGraw-Hill Book Company, New York, p. 154.
26. H. Sheets, 1975. Selection of materials for ocean application (Chapter 6), in: *Introduction to Ocean Engineering*, edited by H. Schenck, Jr., McGraw-Hill Book Company, New York, p. 164.
27. H. Sheets, 1975. Selection of materials for ocean application (Chapter 6), in: *Introduction to Ocean Engineering*, edited by H. Schenck, Jr., McGraw-Hill Book Company, New York, p. 165.
28. Material data sheet, 2006. Air hardening steels, in hot and cold rolled state, Salzgitter Flachstahl, Ein Unternehmen der Salzgitter Gruppe, Germany, 10 pages. <http://www.salzgitter-flachstahl.de/en/>
29. K. Masubuchi, 1979. *Materials for Ocean Engineering*, MIT Press, Cambridge, MA, p. 101.
30. K. Masubuchi, 1979. *Materials for Ocean Engineering*, MIT Press, Cambridge, MA, p. 100.
31. K. Masubuchi, 1979. *Materials for Ocean Engineering*, MIT Press, Cambridge, MA, p. 110.
32. K. Masubuchi, 1979. *Materials for Ocean Engineering*, MIT Press, Cambridge, MA, p. 134.
33. K. Masubuchi, 1979. *Materials for Ocean Engineering*, MIT Press, Cambridge, MA, p. 135.
34. R. Reuben, 1994. Mechanical properties and design for marine use (Chapter 2), in: *Materials in Marine Technology*, Springer-Verlag, London, p. 23.
35. J.F. Young, S. Mindess, R.J. Gray and A. Bentur, 1998. Portland cement concrete (Chapter 11), *The Science and Technology of Civil Engineering Materials*, Prentice Hall, Englewood Cliffs, NJ, p. 234.
36. W.D. Pilkey, 2005. *Formulas for Stress, Strain and Structural Matrices*, Second Edition, John Wiley & Sons, Hoboken, NJ, p. 26.
37. W.D. Pilkey, 2005. *Formulas for Stress, Strain and Structural Matrices*, Second Edition, John Wiley & Sons, Hoboken, NJ, p. 27.
38. W.D. Pilkey, 2005. *Formulas for Stress, Strain and Structural Matrices*, Second Edition, John Wiley & Sons, Hoboken, NJ, pp. 24–29.
39. A.A. Griffith, 1921. The phenomena of rupture and flow in solids, *Philosophical Transactions of Royal Society, Series A*, Volume 221, pp. 163–198.
40. J.F. Young, S. Mindess, R.J. Gray and A. Bentur, 1998. Atomic bonding (Chapter 1) and Yielding and fracture (Chapter 6), in: *The Science and Technology of Civil Engineering Materials*, Prentice Hall, Englewood Cliffs, NJ, pp. 8–14, 123–127.
41. W.D. Pilkey, 2005. *Formulas for Stress, Strain and Structural Matrices*, Second Edition, John Wiley & Sons, Hoboken, Englewood Cliffs, NJ, p. 50.
42. J.F. Young, S. Mindess, R.J. Gray and A. Bentur, 1998. *The Science and Technology of Civil Engineering Materials*, Prentice Hall, Englewood Cliffs, NJ, p. 124.
43. Westergaard, H.M., 1939. Bearing pressures and cracks, *Journal of Applied Mechanics*, Volume 6, pp. 49–53.
44. J.F. Young, S. Mindess, R.J. Gray and A. Bentur, 1998. *The Science and Technology of Civil Engineering Materials*, Prentice Hall, Englewood Cliffs, NJ, p. 125.
45. J.F. Young, S. Mindess, R.J. Gray and A. Bentur, 1998. *The Science and Technology of Civil Engineering Materials*, Prentice Hall, Englewood Cliffs, NJ, p. 152–170.
46. T. Lassen, Ph. Darcis and N. Recho, 2005–2006. Fatigue behavior of welded joints—Part I: Statistical methods for fatigue life prediction and Part II: Physical modeling of the fatigue process, *AWS Welding Journal*, Dec. 2005, pp. 183s–187s and January 2006, pp. 19s–26s.
47. H. Remes, 2005. A theoretical model to predict fatigue life of laser welded joints, Ship Structural Design Seminar, Maritime Institute, Espoo, Finland, March 2005, 6 pp.
48. J.F. Young, S. Mindess, R.J. Gray and A. Bentur, 1998. *The Science and Technology of Civil Engineering Materials*, Prentice Hall, Englewood Cliffs, NJ, p. 154.
49. X. Niu and G. Glinka, 1987. The weld profile effect on the stress intensity factors in weldments. *International Journal of Fracture*, Volume 35, pp. 3–20.
50. R. Reuben, 1990. Corrosion and defect evaluation (Chapter 10), in: *Marine Technology Reference Book*, edited by N. Morgan, Butterworths, London, p. 10/33.
51. P Paris and F Erdogan, 1963. A critical analysis of crack propagation laws, *Journal of Basic Engineering, Transactions of the American Society of Mechanical Engineers*, December 1963, pp. 528–534.
52. A. Almar-Naess, 1985. *Fatigue Handbook: Offshore Steel Structures*, Tapir, Norges Tekniske hogskole, Trondheim, Norway, pp. 103–113.
53. N.E. Dowling, 1999. *Mechanical Behavior of Materials*, Prentice Hall, Upper Saddle River, NJ, p. 301.
54. H. Tada, P.C. Paris and G. Irwin, 2000. *The Stress Analysis of Cracks Handbook*, 3rd edition, American Society of Mechanical Engineers, New York.
55. Y. Murakami (Editor), 1987. *Stress Intensity Factors Handbook*, Volumes I and II, Pergamon Press, New York.

56. J.F. Young, S. Mindess, R.J. Gray and A. Bentur, 1998. *The Science and Technology of Civil Engineering Materials*, Prentice Hall, Englewood Cliffs, NJ, p. 161.
57. The Marine Technology Directorate Ltd., 1990. Principles of corrosion and cathodic protection offshore (Chapter 2), in: *Design and Operational Guidance on Cathodic Protection of Offshore Structures, Subsea Installations and Pipelines*, The Marine Technology Directorate Ltd., London, p. 137.
58. J.F. Young, S. Mindess, R.J. Gray and A. Bentur, 1998. *The Science and Technology of Civil Engineering Materials*, Prentice Hall, Upper Saddle River, NJ, p. 162.
59. S.T. Rolfe and J.M. Barsoum, 1977. *Fracture and Fatigue Control in Structures: Applications of Fracture Mechanics*, Prentice Hall, Englewood Cliffs, NJ, p. 159.
60. N.E. Dowling, 1999. *Mechanical Behavior of Materials*, Prentice Hall, Englewood Cliffs, NJ, p. 301.
61. H. Sheets, 1975. Selection of materials for ocean application (Chapter 6), in: *Introduction to Ocean Engineering*, edited by H. Schenck, Jr., McGraw-Hill Book Company, New York, pp. 167–191.
62. I.L. Stern, 1980. Materials and welding (Chapter 8), in: *Ship Design and Construction*, edited by R. Taggart, The Society of Naval Architects and Marine Engineers, New York, pp. 339–372.
63. S.C. Dexter, 1979. *Handbook of Oceanographic Engineering Materials*, John Wiley & Sons, New York, pp. 47–282.
64. S.H. Williamson, 2008. Six ways to compute the relative value of a U.S. dollar amount, 1774 to present, *Measuring Worth*. <http://www.measuringworth.com/uscompare/index.php>
65. G.T. Murray (Editor), 1997. *Handbook of Materials Selection for Engineering Applications*, Marcel Dekker, Inc., New York, pp. 79–162, 209–244, 293–354.
66. C.T. Lynch, 1989. *Practical Handbook of Material Science*, CRC Press, Inc., Boca Raton, FL, pp. 327–348, 421–518.
67. R.A. Shenoi and J.F. Wellicome (Editors), 1993. *Composite Materials in Maritime Structures*, Volume I: Fundamental Aspects and Volume II: Practical Considerations, Cambridge University Press, Cambridge, London, UK.
68. M. Masubuchi, 1970. *Materials for Ocean Engineering*, MIT Press, Boston, MA, pp. 38–241.
69. R. Reuben, 1994. *Materials in Marine Technology*, Springer-Verlag, New York, pp. 19–160.
70. R. Reuben, 1994. *Materials in Marine Technology*, Chapter 1, Springer-Verlag, London, p. 13.
71. F.A.A. Crane, J.A. Charles and J. Furness, 1997. *Selection and Use of Engineering Materials*, Butterworth Heinemann Ltd., UK, 352 pp.
72. J.F. Young, S. Mindess, R.J. Gray and A. Bentur, 1998. *The Science and Technology of Civil Engineering Materials*, Prentice Hall, Englewood Cliffs, NJ, p. 301.
73. R. Reuben, 1994. *Materials in Marine Technology*, Springer-Verlag, New York, p. 48.
74. R. Reuben, 1990. Corrosion and defect evaluation (Chapter 10), in: *Marine Technology Reference Book*, edited by N. Morgan, Butterworths, London, p. 10/6.
75. M. Pourbaix, 1974. *Atlas of Electrochemical Equilibria in Aqueous Solutions*, 2nd English Edition, National Association of Corrosion Engineers, Houston, TX.
76. R. Reuben, 1990. Corrosion and defect evaluation (Chapter 10), in: *Marine Technology Reference Book*, edited by N. Morgan, Butterworths, London, pp. 10/1–10/42.
77. C. Petersen and G. Soltz, 1975. Ocean corrosion (Chapter 5), in: *Introduction to Ocean Engineering*, edited by H. Schenck, Jr., McGraw-Hill Book Company, New York, pp. 120–149.
78. J.W. Oldfield and B. Todd, 1979. Corrosion of metals in de-aerated seawater, *Desalination*, Volume 31, pp. 365–383.
79. W.H. Hartt, 1991. Corrosion prevention of offshore structures (Chapter 17), in: *Offshore Structures*, Volume 2, edited by D.V. Reddy and M. Arockiasamy, R.E. Krieger Publishing Company, Malabar, FL, pp. 235–248.
80. K.P. Fisher and B. Bue, 1981. Corrosion and corrosivity of steel in Norwegian marine sediments, *Underground Corrosion*, edited by E. Escalante, ASTM STP 741, ASTM, Philadelphia, PA, pp. 24–31.
81. P.R. Roberge, 2006. Corrosion in soils (Chapter 5), in: *Corrosion Basics: An Introduction*, Second Edition, NACE Press Book, Houston, TX.
82. Distance Learning Corrosion Course, 2008. *Soil Resistivity Measurement*, Royal Military College of Canada, Kingston, Ontario, Canada. <http://www.corrosion-doctors.org/Corrosion-Kinetics/Ohmic-drop-soil.htm>
83. C. deWaard and D.E. Milliams, 1975. Prediction of carbonic corrosion in natural gas pipelines, Proceedings, First International Conference on Internal and External Protection of Pipes, British Hydraulic Research Association Report F1-1-F1-7, Cranfield, UK.
84. H.A. Videla and L.K. Herrera, 2005. Microbiologically influenced corrosion—looking to the future, *International Microbiology*, Volume 8, pp. 169–180. [www.im.microbios.org](http://www.im.microbios.org)

85. A.K. Tiller, 1983. Electrochemical aspects of microbial corrosion—an overview, Proceedings, Conference on Microbial Corrosion, Metals Society, London, pp. 54–65.
86. W.E. Shook and L.W. Bell, 1998. Corrosion control in concrete pipe and manholes, Adapted from: Technical Presentation at Water Environmental Federation October, '98 Orlando, Florida, [www.conshield.com/images/CSTI001\\_Corrosion\\_Control\\_in\\_Concrete\\_Pipe\\_and\\_Manholes.pdf](http://www.conshield.com/images/CSTI001_Corrosion_Control_in_Concrete_Pipe_and_Manholes.pdf).
87. G.R. Hall, 1989. Control of micro-biologically induced corrosion of concrete in wastewater collection and treatment systems, *Materials Performance*, Volume 28, # 10, pp. 45–50.
88. R. Reuben, 1990. Corrosion and defect evaluation (Chapter 10), in: *Marine Technology Reference Book*, edited by N. Morgan, Butterworths, London, p. 10/4.
89. R. Reuben, 1990. Corrosion and defect evaluation (Chapter 10), in: *Marine Technology Reference Book*, edited by N. Morgan, Butterworths, London, p. 10/8.
90. R. Reuben, 1990. Corrosion and defect evaluation (Chapter 10), in: *Marine Technology Reference Book*, edited by N. Morgan, Butterworths, London, p. 10/9.
91. R. Reuben, 1990. Corrosion and defect evaluation (Chapter 10), in: *Marine Technology Reference Book*, edited by N. Morgan, Butterworths, London, p. 10/12.
92. R. Reuben, 1994. Marine Corrosion and Biodeterioration (Chapter 3) in *Materials in Marine Technology*, Springer-Verlag, New York, p. 66.
93. J.R. Coke, 1990. Protective coatings for offshore equipment and structures, *Materials Performance*, Volume 29, # 5, pp. 35–38.
94. The Marine Technology Directorate Ltd., 1990. Principles of corrosion and cathodic protection offshore (Chapter 2), in: *Design and Operational Guidance on Cathodic Protection of Offshore Structures, Subsea Installations and Pipelines*, The Marine Technology Directorate Ltd., London, p. 35.
95. DET Norske Veritas, 1986. *Cathodic Protection Design*, Veritas recommended practice RPB 401.
96. National Association of Corrosion Engineers, 1983. Corrosion control of steel fixed offshore platform associated with petroleum production, *NACE Publication RP-01-76*, NACE, Houston, TX.
97. G. Lewis, 1990. *Selection of Engineering Materials*, Prentice Hall, Englewood Cliffs, NJ, p. 99.



---

# 6 Environmental Forces on Offshore Structures

## 6.1 INTRODUCTION

The designs of offshore structures have been governed by many factors such as the required deck space, deck facilities to be provided and the associated loads, number of wells to be drilled, etc., along with the meteorological and oceanographic loads imposed by the environment, in which these structures have to operate. One should know well enough the environmental conditions the structure will face so that the design loads the structure has to resist can be specified within a certain probability of exceedance. The loads for which an offshore structure must be designed can be classified into the following categories: (i) permanent (dead) loads; (ii) operating (live) loads; (iii) environmental loads including earthquakes; (iv) construction and installation loads; and (v) accidental loads.

### 6.1.1 PERMANENT (OR DEAD) LOADS

The dead load consists of (i) the self-weight of the whole structure; (ii) the weight of the permanent ballast, grout, and equipment, located within and on the structure; (iii) external and internal hydrostatic pressure of a permanent nature (including the buoyancy forces); and (iv) reaction to the above, for example, cable forces that act on the structure to keep it in position or reaction forces at the base of an articulated tower. Typical dead loads for a fixed steel offshore platform are given in Chapter 2.2 (refer to Tables 2.1 and 2.2, along with Figures 2.6 and 2.7).

### 6.1.2 OPERATING (OR LIVE) LOADS

Live loads are loads that could vary in magnitude, position, and direction during the period under consideration and that are related to operations and normal use of the offshore structure. The live loads are made up of (i) self-weight of personnel, occupying the structure at any time; (ii) the weight of all nonpermanent equipment (used in drilling, production, etc.), facilities (for example, living quarters, furniture, life support systems, life boats, heliport, etc.), consumable supplies, liquids, gas, ballast, etc.; (iii) forces generated during operations, for example, drilling, vessel mooring, helicopter landing, evacuation systems, crane operations, etc.; and (iv) static/impact loads due to anchoring cables and protective fenders. The necessary data for computation of all operating loads are provided by the operator and the equipment manufacturers. The data need to be critically evaluated by the designer. An example of a detailed live load specification is given in Table 6.1 [1] where the values in the second and third columns are for design of the portions of the structure directly affected by the loads; the reduced values in the fourth column are for the structure as a whole. As per the recent DNV code DNV-OS-C101 [2] for offshore steel structures, the above live loads have been updated to that given in Table 6.2 [2]. The actual loads for preliminary design are to be chosen as the maximum of the loads obtained from Tables 6.1 and 6.2.

When specific load data are not available, the following values recommended by as the British Standard BS6235 [1] can be used for the preliminary design process, viz., (i) crew quarters and passageways at a load intensity of 3.2 kN/m; (ii) working areas at a load intensity of 8.5 kN/m<sup>2</sup>;

**TABLE 6.1**  
**Minimum Design Live Load Specification**

Types of Loading Areas to Be Taken into Account	Load Intensity for Portions of the Structure (kN/m <sup>2</sup> )		Load Intensity for the Structure as a Whole (kN/m <sup>2</sup> )
	Flooring and Joists	Other Components	<sup>a</sup>
Typical Components Considered →			
Process zone (around wells and large-scale machines)	5.0 <sup>b</sup>	5.0 <sup>b</sup>	2.5
Drilling zone	5.0 <sup>b</sup>	5.0 <sup>b</sup>	2.5
Catwalks and walking platforms (except emergency exits)	3.0	2.5	1.0
Stairways (except emergency exits)	4.0	3.0	0.0
Module roofing	2.0	1.5	1.0
Emergency exits	5.0	5.0	0.0
	<b>Storage Areas</b>		
Storage floors: heavy	18.0	12.0	8.0 <sup>c</sup>
Storage floors: light	9.0	6.0	4.0 <sup>c</sup>
Delivery zone	10.0	10.0	5.0
Nonattributed area	6.0	4.0	3.0

Source: BS6235. *Code of Practice for Fixed Offshore Structures*, British Standards Institution, London, 1982. Used with permission.

- <sup>a</sup> This column gives the loads to be taken into account for the structure's overall calculation. These values are the input for the computer runs.
- <sup>b</sup> Additional point load, equal to the weight of the heaviest part likely to be moved around, with the provision of a minimum load of 5 kN. Point loads are assumed as applied over a (0.3 × 0.3-m) surface area.
- <sup>c</sup> Applied on the whole flooring surface (including traffic).

and (iii) storage areas at a load intensity of ( $\rho gH$ ) kN/m<sup>2</sup>. In the above, ( $\rho g$ ) is the specific weight of stored materials, which should not be less than 6.87 kN/m<sup>3</sup>, and  $H$  is the storage height (m).

### 6.1.3 ENVIRONMENTAL LOADS (FORCES)

As mentioned in Chapter 3, the basic design parameters that are relevant to structural design are based on winds, waves, currents, tides (and governing water levels), marine growth, site seismicity, superstructure icing, and stationary and mobile ice on the ocean surface. More will be said on these loads in the subsequent sections of this chapter.

### 6.1.4 CONSTRUCTION AND INSTALLATION LOADS (FORCES)

The loads considered herein are temporary in nature and occur only during the fabrication and installation of the offshore structure or its structural components. Lifting of various structural components, during process of fabrication, generates lifting forces, which need to be taken into consideration in design. Moreover, installation forces are generated during load-out, transportation to the site, launching, and upending of the offshore structure; in addition, lift forces are also generated during this installation procedure. In estimating the actual design conditions during this construction and installation phase, the return period should be based on conditions specified by the various codes. The return periods are (i) three times the fabrication and installation period, as per DNV code [3]; (ii) specified by the owner, as per the API code provisions [4], and (iii) 10 years as per the BS code provisions [1].

**TABLE 6.2**  
**Live or Variable Functional Loads on Deck Areas**

	Local Design		Primary Design	Global Design
	Distributed Load, $p$ (kN/m <sup>2</sup> )	Point Load, $P$ (kN)	Apply Factor to Distributed Load	Apply Factor to Primary Design Load
Storage areas	$q$	$1.5 q$	1.0	1.0
Lay down areas	$q$	$1.5 q$	$f$	$f$
Lifeboat platforms	9.0	9.0	1.0	May be ignored
Area between equipment	5.0	5.0	$f$	May be ignored
Walkways, staircases and platforms, crew spaces	4.0	4.0	$f$	May be ignored
Walkways and staircases for inspection only	3.0	3.0	$f$	May be ignored
Areas not exposed to other functional loads	2.5	2.5	1.0	–

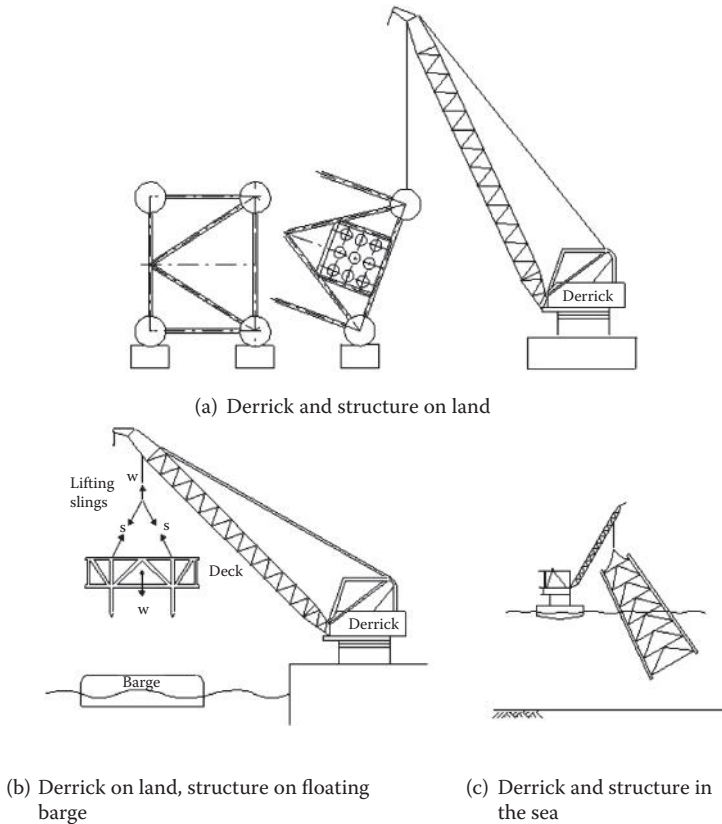
*Source:* Offshore Standard. DNV-OS-C101, *Design of Offshore Steel Structures, General (LRFD Method)*, Det Norske Veritas, Hovik, Norway, pp. 12–20, 2008. Used with permission.

*Note:* Wheel loads to be added to distributed loads, wherever relevant. The loads may be considered to be acting over an area of 300 by 300 mm. Point loads,  $p$ , to be applied over an area of 100 by 100 mm at the most severe position; it is not to be added as distributed or wheel loads.  $q$  is to be evaluated for each case. Lay down areas is not to be designed for less than 15.0 kN/m<sup>2</sup>.  $f$  is the minimum of [1.0, (0.5 + 3/√A)], where A is the loaded area in m<sup>2</sup>. Global load cases shall be established based on “worst-case” characteristic combinations, complying with the limiting global criteria to the structure. For buoyant structures, this criteria are established by the requirements for the floating position in still water and intact and damaged stability requirements, as documented in the operational manual, considering variable load on the deck and in tanks.

### 6.1.4.1 Lifting Forces

As indicated by Figure 6.1 [5], the lifting forces are dependent on a number of factors: (i) weight of the structural component being lifted; (ii) number and location of lifting eyes used for the lift; (iii) angle between each sling and the vertical axis; and (iv) conditions under which the lift is performed. All members and connections of a lifted component are to be designed for the computed forces, resulting from static equilibrium of the lifted component weight and the sling tensions. API-RP2A [4] also recommends that lifting eyes and the connections to the supporting structural members should be designed for the combined action of the static sling load and a horizontal force equal to 5% this load (to compensate for the lateral motion of the lifted component), applied perpendicular to the pad-eye at the center of the pin hole. All these design forces are applied as static loads if the lifts are performed in the fabrication yard. However, when this lifting operation is carried out on a floating vessel, then dynamic load factors should be applied to the computed static lifting forces. API-RP2A recommends two values of dynamic load factors, viz., 2.0 and 1.35 (minimum); the first value is for designing the pad-eyes, as well as all members and their end connections framing the joint where the pad-eye is attached. The second value is used for all other members transmitting lifting forces. During the load-out of offshore structures, at sheltered locations, the corresponding load factors are to be reduced to 1.5 and 1.15, respectively.





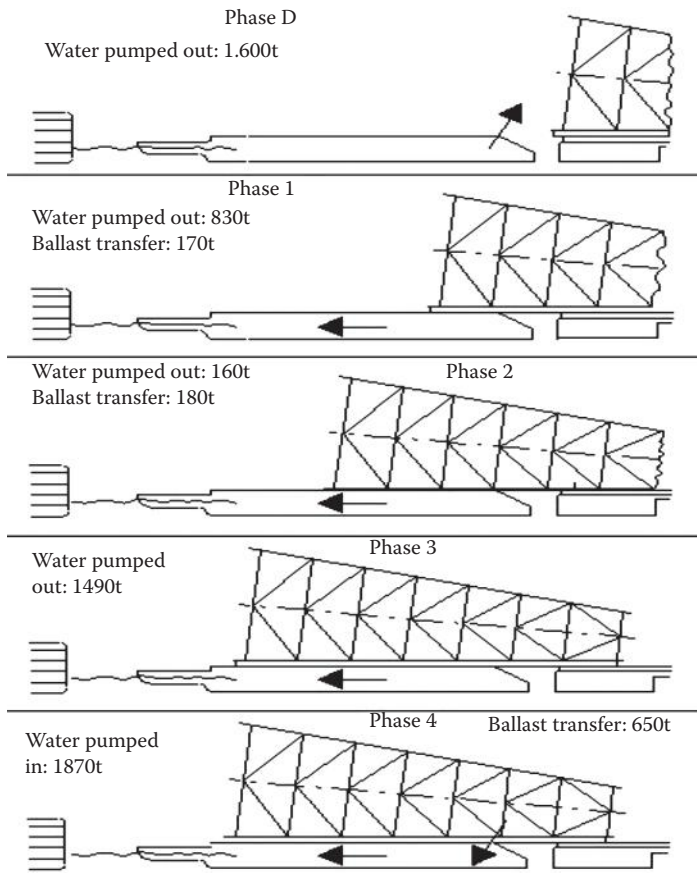
**FIGURE 6.1** Lifting operations under various site conditions. (From ESDEP [The European Steel Design Education Programme] Course Notes [Pre-Standard Version of the Euro Codes]. *European Steel Design Course, WG15A Structural Systems: Offshore*. Available at <http://www.esdep.org/members/master/toc.htm>, 1993. With permission.)

#### 6.1.4.2 Load-Out Forces

The load-out forces are generated when the structure, from the fabrication yard, is loaded onto the barge. Load-out can be carried out by direct lift or by skidding the structure onto the barge. If the direct lift load-out during this process is similar to the one at sea, the lifting forces need not be computed, because lifting up in the open sea creates a more severe loading condition requiring higher dynamic load factors. If load-out is done by skidding the structure onto the barge, a number of static loading conditions must be considered, with the jacket supported on its side. Such loading conditions arise from the different positions of the jacket during the load-out phase (as shown in Figure 6.2 [5]), from movement of the barge due to tidal fluctuations, marine traffic, or change of draft, and from possible support settlements. Since movement of the jacket is slow, all loading conditions can be taken as static. Typical values of friction coefficients for calculation of skidding forces are given in Table 6.3 [5].

#### 6.1.4.3 Transportation Forces

When offshore structural components, such as a jacket and a deck, are transported offshore on barges or under self-floating (under tow) conditions, forces are generated due to their motion on the ocean surface. The generated transportation forces are dependent on the self-weight, geometry, and support conditions for the structure (placed on the barge or floating buoyantly) and also on the environmental conditions (waves, winds, and currents) that are encountered during transportation.



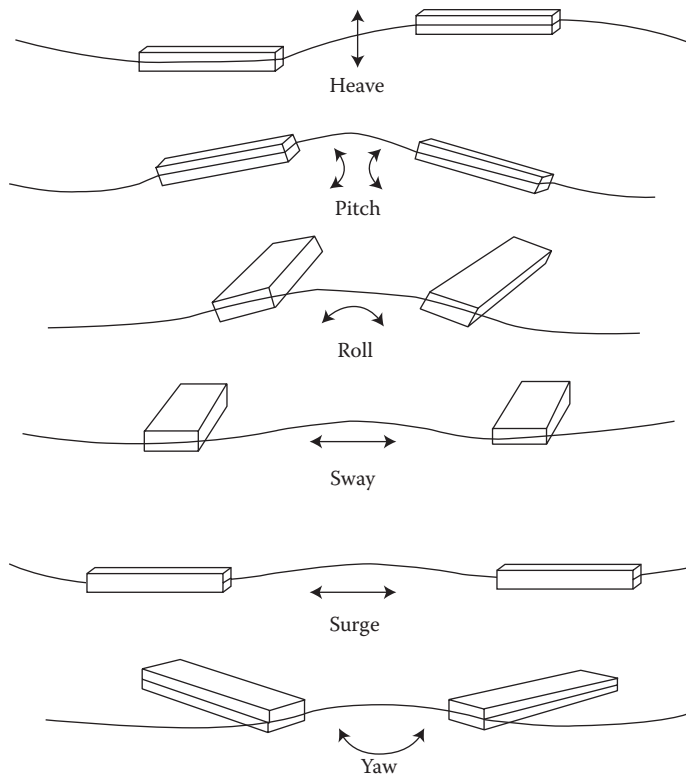
**FIGURE 6.2** Various stages of sliding of the structure, during load-out on to the barge. (From ESDEP [The European Steel Design Education Programme] Course Notes [Pre-Standard Version of the Euro Codes]. *European Steel Design Course, WG15A Structural Systems: Offshore*. Available at <http://www.esdep.org/members/master/toc.htm>, 1993. With permission.)

The types of motion that a floating structure may experience are shown schematically in Figure 6.3 [5]. To minimize the associated risks and to provide a safe transport of the structural components from the fabrication yard to the platform site, the following conditions should be followed, viz., (i) prior experience along the tow route; (ii) exposure time and reliability of predicted “weather windows”; (iii) accessibility of nearby safe havens, under an unexpected extreme weather state; (iv) suitability and

**TABLE 6.3**  
**Frictional Coefficients during the Skidding of the Structure onto the Barge**

#	Conditions of Friction between Surfaces	Frictional Coefficient
1	Steel on steel, without lubrication	0.25
2	Steel on steel, with lubrication	0.15
3	Steel on Teflon	0.10
4	Teflon on Teflon	0.08

Source: ESDEP (The European Steel Design Education Programme) Course Notes (*Pre-Standard Version of the Euro Codes*). *European Steel Design Course, WG15A Structural Systems: Offshore*. Available at <http://www.esdep.org/members/master/toc.htm>, 1993. Used with permission.



**FIGURE 6.3** Types of possible motions encountered for a rigid floating body. (From ESDEP [The European Steel Design Education Programme] Course Notes [Pre-Standard Version of the Euro Codes]. *European Steel Design Course, WG15A Structural Systems: Offshore*. Available at <http://www.esdep.org/members/master/toc.htm>, 1993. With permission.)

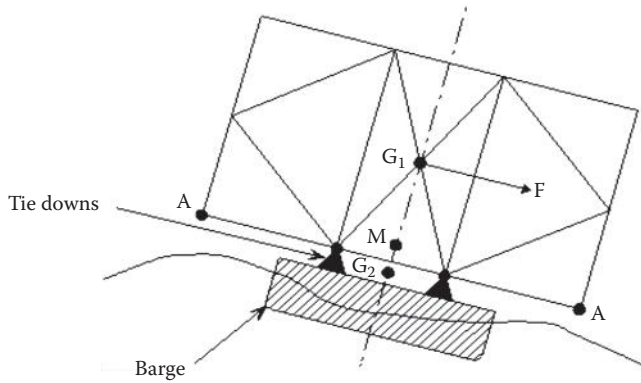
appropriateness of the seasonal weather system; and (v) appropriate return periods for determining design wind, wave, and current conditions [5]. For open sea conditions, the following may be considered as typical control design values, as per API-RP2A [4], viz., (i) roll amplitude roll of  $20^\circ$ ; (ii) pitch amplitude of  $10^\circ$ ; (iii) roll or pitch period of 10.0 s; and (iv) heave acceleration of 0.2 g.

When transporting a large jacket structure by a tow barge, stability considerations against capsizing of the barge-jacket combine, will become a primary design condition due to the high center of gravity of the jacket; in addition the relative stiffness of jacket and barge may also need to be taken into account. Moreover, wave slamming forces that could result during a heavy roll motion of the tow (Figure 6.4 [5]) should also be considered when structural analyses are carried out for designing the tie-down braces and the jacket members affected by the induced loads.

#### 6.1.4.4 Launching and Upending Forces

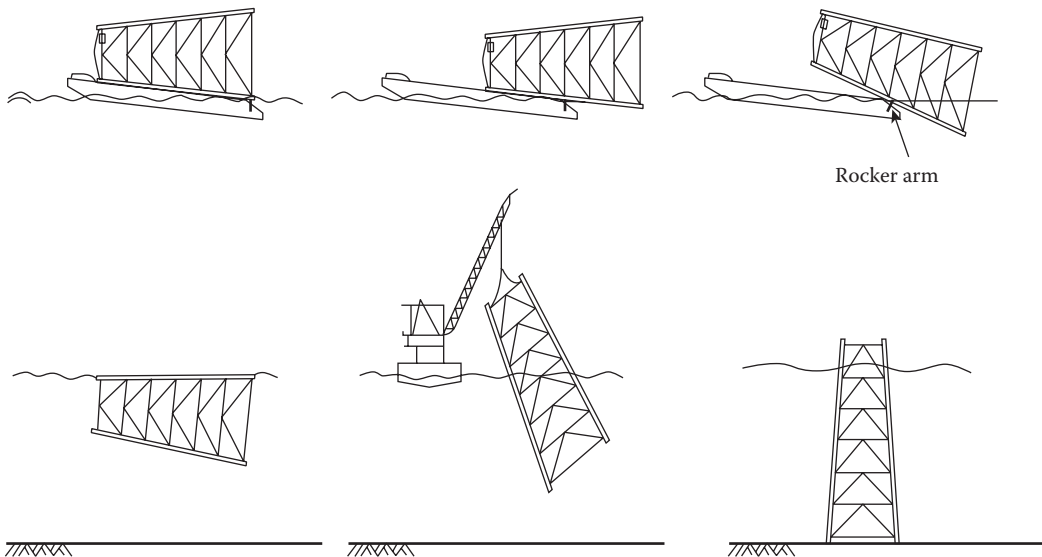
These forces are generated during the launch of a jacket, from the barge into the sea, and during the subsequent upending of the jacket structure into its proper vertical position so as to rest on the seabed. A schematic view of these operations can be seen in Figure 6.5 [5].

To start the launching operation, the barge is ballasted to an appropriate draft and trim angle and thereafter the jacket is pulled toward the stern of the barge, by a winch. During the launching and upending operations of the jacket structure, at the offshore location, operations and numerical calculations are carried out considering five different stages, viz., (i) sliding phase of the jacket structure along the skid beams on the top of the barge; (ii) balanced rotation of the jacket on the rocker arm, located at the stern of the barge; (iii) simultaneous sliding and rotating motion of the



- F = Component of gravity plus inertia
- $G_1$  = Center of gravity of jacket
- $G_2$  = Center of gravity of the tow
- M = Metacenter of the tow
- A = Areas of potential impact

**FIGURE 6.4** Schematic view of the tow barge and the jacket undergoing motion. (From ESDEP [The European Steel Design Education Programme] Course Notes [Pre-Standard Version of the Euro Codes]. *European Steel Design Course, WG15A Structural Systems: Offshore*. Available at <http://www.esdep.org/members/master/toc.htm>, 1993. With permission.)



**FIGURE 6.5** Launching and upending operations carried out on the jacket, at the installation site. (From ESDEP [The European Steel Design Education Programme] Course Notes [Pre-Standard Version of the Euro Codes]. *European Steel Design Course, WG15A Structural Systems: Offshore*. Available at <http://www.esdep.org/members/master/toc.htm>, 1993. With permission.)

jacket structure; (iv) detachment and free flotation of the jacket, about its equilibrium position; and (v) upending of the jacket by a proper combination of controlled flooding and lifting by a derrick barge. During stages (iv) and (v), variable hydrostatic forces will be acting on the jacket structure, which have to be considered for all wetted members. Buoyancy computations are made for every stage of the operation to ensure a fully controlled and stable motion of the barge-jacket combine as well as the detached jacket structure.

### 6.1.5 ACCIDENTAL LOADS (FORCES)

According to the DNV rules [2], accidental loads are loads generated during abnormal operation conditions or during technical failure of the structure; these conditions may occur as a result of accident or some exceptional circumstances. Accidental loads are generated on an offshore structure by (i) impact of dropped objects; (ii) collision impact of two bodies, of which one may be stationary or moving; (iii) unexpected explosions that may occur within or outside the mobile/stationary structure; (iv) sudden fire(s) caused from an explosive or nonexplosive source; (v) unintended change in the distribution of ballast or flooding of a ballast/hull compartment; (vi) sudden failure of the mooring lines; and (vii) the sudden loss of dynamic positioning system, resulting in the loss of position and heading. These accidental loads are specified as a separate category in the Norwegian Petroleum Directorate (NPD) regulations [6], but not in API-RP2A [4], BS6235 [1] or the DOE-OG rules [7]. Special measures should be undertaken to reduce the risk from accidental loads. For instance, the protection of wellheads or other critical equipment from a dropped object can be provided by specially designed, impact resistant covers. As per the NPD regulations [6], an accidental load can be disregarded if its annual probability of occurrence is less than  $10^{-4}$ . This number is meant as an order of magnitude estimate and is extremely difficult to compute.

#### Example 6.1

A  $10.0 \times 10.0$ -m two-way interior bay composite steel/concrete floor of an offshore platform, continuous over several supports, supports dead and live loads given by Tables 6.1 and 6.2. Compute the design moments for the floor.

#### Solution for Example 6.1

The interior panel of a two-way continuous floor panel is designed in this section. The moments in the panel are taken from available design textbook values. The floor is supported at 10.0-m interval (both ways) by interior columns. The top floor is assumed to be composed of 0.08-m-thick concrete-steel composite floor supported over steel beams placed at every 1.0-m intervals. These continuous joists transmit loads to main girders, which are assumed to be fixed-supported to the columns.

*Dead loads:* Dead weight of floor panel per m length of steel joist (spaced at 1.0-m interval transversely) =  $(2500)(0.08)(9.81)(1) = 1962.0$  N. Assuming the joist to be continuous, the interior bending moments are  $(wl^2/12)$ , over the main girder and  $(wl^2/24)$ , at the center of beam. Use a  $W 250 \times 45$  beam as the transverse beam.

$$\text{Self-weight of the transverse beam} = 45 \times 9.81 = 442 \text{ N/m.}$$

$$\text{Total weight per unit length of beam} = 1962 + 442 = 2404 \text{ N/m.}$$

*Live loads:* From Table 6.2, the loads for areas between equipment are given as a live distributed load of  $5.0 \text{ kN/m}^2$  and a central concentrated load of  $5.0 \text{ kN}$ .

Considering the load factors given in Table 6.5 are the following; for dead load = 1.3 and for live load = 1.3.

Hence, the design loads are distributed load =  $1.3(2404 + 5000) = 10,366$  N/m. Concentrated load =  $1.3(5000) = 6500$  N.

*The design moment for the transverse beam:* Over the main girder due to distributed loads =  $(10,366)(10^2)/12 = 86,383$  N m; over the main girder, due to concentrated load =  $WL/8 = (6500)(10)/8 = 8125$  N m. Total design moment =  $82,383 + 8125 = 90,508$  N m.

### Example 6.2

In the above Example 6.1, assume that the floor system is made up of truss-type connection in both directions (instead of a composite floor), having a depth of 1.0 m and spaced at 1.0 m between parallel trusses. What is the approximate force present in a typical upper/lower chord bar member at midspan?

Assuming the use of open-web joists for the floors (instead of the transverse beam), for a span of 10.0 m, the heaviest K-series of open-web joist should have a depth of 28 in. (0.71 m).

$$\text{Weight of the truss member} = (12.5 \times 3.28 \times 0.4536 \times 9.81) = 182.0 \text{ N/m.}$$

$$\text{Total dead load per unit length of the beam} = 1962 + 182.0 = 2144.0 \text{ N.}$$

Hence, the design loads are the following: distributed loads =  $1.3(5000 + 2144.0) = 9287.0$  N/m; concentrated loads =  $(1.3) \times (5000) = 6500.0$  N.

Design bending moments for the earlier transverse beam (which the open web steel joist (OWSJ) truss girder is replacing): total design bending moment =  $(9287)(10^2)/12 + 6500 \times 10/8 = 77,391.7 + 8125 = 85,516.7$  N m.

Moreover, assuming that the bending moment is resisted only by the top and bottom member of the truss (and the shear is resisted by the diagonal member of the truss), the load carried by each member of the truss =  $(85,516.7)/(0.71) = 120,446.0$  N. Assuming a 20-mm diameter for the truss member, the stress in the member =  $(120,446.0)/[(\pi)(20^2)/4] = 383.0$  MPa; needs to use a high strength steel or a stronger series of OWSJ.

## 6.2 DESIGN CONDITIONS FOR LOADS (FORCES) ACTING ON THE STRUCTURE

### 6.2.1 LIMIT STATE, PROBABILITY, AND SAFETY

The structural design process involves a number of computational procedures, based on certain assumptions, viz., (i) the loads to which a structure will be subjected must be estimated; (ii) the design criteria for which the structure is to be designed identified; and (iii) member sizes chosen in a preliminary manner and validated by detailed computations. All engineering design criteria have a common goal, viz., (i) ensuring structural safety under the on-site applied environmental and other structural loads; and (ii) the functional conditions specified for the structure are not exceeded in the on-site response of the structure. In order to achieve the above-stated criteria, designers have nowadays accepted design procedures based on limit state design scenarios. The limit state design scenarios, which the structure must satisfy under the applied loads, are the following, viz., (i) ultimate (or ULS); (ii) serviceability (or SLS); (iii) fatigue (FLS); and (iv) accidental limit states (ALS) [2]. A limit is set for a number of performance (or functional) parameters the design must satisfy, under the operating (or extremal) environmental and other load conditions; the usual limit parameters considered are the structure's (or the individual member's) deflection, strength, crack size/extent, vibration stress levels, repeated stress cycle levels and corrosion/fire durability. The overall structural safety will then be determined on the basis of design principles implemented in the design, fabrication, and inspection of the structure, against structural failure; the structure's residual strength against total collapse in the case of structural failure of vital elements should also be assessed.

The various factors considered in the analysis and design of structures, such as loads, structural geometry, and material properties (such as strength, deformation, etc.) are subjected to varying degrees of uncertainty and randomness. In addition, many idealizations and simplifying assumptions are made use of in the theories used for structural analysis and design. Other factors such as construction methods, workmanship, quality control in the formation and fabrication of the structure and its components, variable nature of the loading, and the probable design life of the structure also influence the characterization of the strength properties and performance of the structure. Hence, any realistic and rational representation of safety must be based on statistical and probabilistic analyses [8].

Taking into account all the randomness and uncertainties present in the design, they can be categorized into load effects,  $S$ , on the structure, and the structural resistance (or strength),  $R$ , which can be represented by two probability distribution curves shown schematically in Figure 6.6 [8]. It is also assumed that the parameters of loads and strength are independent of one another. The level of safety of a structural element or the structure is considered to be satisfactory if the design load effect ( $S_d$ ) does not exceed the design resistance ( $R_d$ ), that is,  $R_d \geq S_d$ ; if  $R_d \leq S_d$ , the structure is unsafe (or will fail). The equation  $S_d = R_d$  defines a limit state.

Considering Figure 6.6, for the load effect of  $S_1$ , the probability that the structural resistance  $R < S_1$  is given by

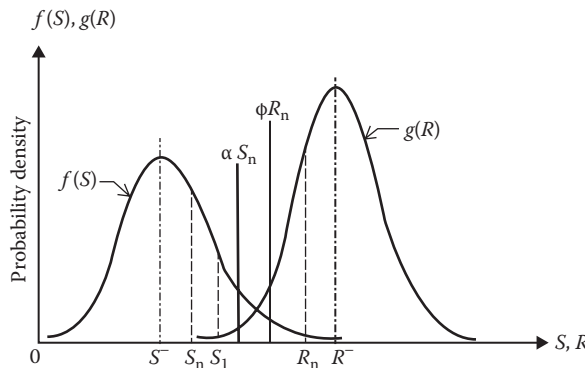
$$\int_0^{S_1} g(R) dR \tag{6.1}$$

The probability that the load effect is  $S_1$  is given by  $f(S_1)$  and, taking into account all the possible values from 0 to  $S_1$ , the probability of failure (represented by  $R < S$ ) is obtained from Figure 6.6 as

$$P_F = \int_0^\infty f(S) \left[ \int_0^S g(R) dR \right] dS \tag{6.2}$$

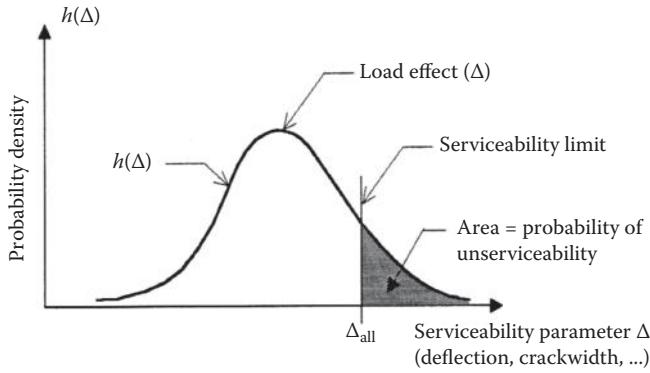
Similarly, the probability of unserviceability, such as exceeding a deflection limit may be obtained from Figure 6.7 [8] as

$$P_F = \int_{\Delta_{all}}^\infty h(\Delta) d\Delta \tag{6.3}$$



**FIGURE 6.6** Frequency distribution of load effects  $S$  and resistance  $R$ . (From S.U. Pillai, D.W. Kirk, and M.A. Erki, *Reinforced Concrete Design*, 3rd Edition, McGraw-Hill Ryerson Ltd., Toronto, Canada, pp. 47–58, 1999. With permission.)





**FIGURE 6.7** Probability of serviceability for deflection  $\Delta$ . (From S.U. Pillai, D.W. Kirk, and M.A. Erki, *Reinforced Concrete Design*, 3rd Edition, McGraw-Hill Ryerson Ltd., Toronto, Canada, pp. 47–58, 1999. With permission.)

where  $h(\Delta)$  is the frequency distribution of the serviceability parameter (such as deflection, crack width, etc.) and  $\Delta_{all}$  is the limiting allowable value. A rational methodology in the design will be to limit its probability of failure to an “acceptable” low level.

**6.2.2 LIMIT STATE DESIGN**

Limit state design is also called the load and resistance factor design (LRFD); in this design procedure, the probability of failure of a structure is reduced (or underestimated) by underestimating its resistance  $R$  and/or overestimating its load effects  $S$ , thus ensuring that

$$R \geq S \tag{6.4}$$

Equation 6.4 can be restated in a probabilistic format by

$$\phi R_n \geq \alpha S_n \tag{6.5}$$

where  $R_n$  is the nominal structural (or member) resistance determined on the basis of nominal material and geometric properties,  $\phi$  is the resistance factor (also called capacity reduction or performance factor), always less than unity, which reflects the uncertainties present in determining  $R_n$ ,  $S_n$  is the total nominal load effect based on the specified (or computed) loads on the structure (or specimen), and  $\alpha$  is the load factor (usually  $>1$ ) that reflects the potential overloads and uncertainties associated with the determination of  $S_n$ .

The prime requirement of a structure is that it be serviceable and also be safe from collapse during its lifetime. Limit states define the limit of structural conditions representing the serviceability or collapse of the structure (or member) that must be limited or prevented by proper design. The limit states corresponding to safety are called the ultimate limit states (ULS) (viz., those of overturning, sliding, strength, buckling, fracture, fatigue, etc.) and those that restrict the intended use and occupancy of the structure are called as serviceability limit states (SLS) (viz., of deflection, cracking, spalling, vibration, etc.).  $R_n$  will represent the generalized (external) forces (such as moment, axial force, shear force, etc.) that act on the structure for the ultimate limit states; whereas for the serviceability states  $R_n$  will represent the allowable limit states of structural response (such as deflection, crack width, stress, vibration level, etc.). In actual practice, Equation 6.5 is written as

$$\alpha S = \alpha_{Dn} F_{Dn} + \alpha_{Ln} F_{Ln} + \alpha_{En} F_{En} + \alpha_{\Delta n} F_{\Delta n} \tag{6.6}$$

where  $F_{Dn}$ ,  $F_{Ln}$ ,  $F_{En}$ , and  $F_{\Delta n}$  represent the nominal dead (or permanent) load, live load, environmental load and displacement effects, respectively, and  $\alpha_{Dn}$ ,  $\alpha_{Ln}$ ,  $\alpha_{En}$ , and  $\alpha_{\Delta n}$  the corresponding load/deformation factors. Acceptable values for all these factors are given in different codes. In the DNV code [2], the design load for an  $i$ th parameter (such as dead, live,...etc.) is obtained by multiplying the characteristic (or nominal) load by a given load factor:

$$F_{di} = \alpha_{di} F_{di} \quad (6.7)$$

where  $F_{di}$  is the design load,  $\alpha_{di}$  is the load factor, and  $F_{di}$  is the characteristic (or nominal) computed load, for the  $i$ th parameter (such as dead, live, environmental, seismic, and displacement-based loads).

The design load effect is the most unfavorable combined load effect derived from the design loads, and may, if represented by one single quantity, be expressed by

$$S_d = q(F_{d1}, \dots, F_{dn})$$

where  $S_d$  is the design load effect and  $q$  is the load effect function. If the relationship between the load and the load effect is linear, the design load effect may be determined by multiplying the characteristic load effects by the corresponding load factors:

$$S_d = \sum_{i=1}^n \alpha_{di} F_{di} \quad (6.8)$$

where  $F_{di}$  is the characteristic load effect for the  $i$ th parameter.

*Characteristic load:* As per the DNV code [2], the characteristic values for the different groups of limit states in the operating design conditions shall be based on conditions specified below: (i) for the uls load combination, the characteristic value corresponds to a load effect with an annual probability of exceedance equal to, or less than,  $10^{-2}$  (100 years) (see the values given in Table 6.4 [2] for greater details); (ii) for the ALS (accidental limit state) load combination for a damaged structure, the characteristic load effect is determined as the most probable annual maximum value; (iii) for the FLS, the characteristic value is defined as the expected load history; and (iv) for the SLS, the characteristic value is a specified value, dependent on operational requirements.

*Load factors for ULS:* For analysis of ULS, two sets of load combinations shall be used when combining design loads as defined in Table 6.5 [2]. The combinations denoted by (a) and (b) shall

**TABLE 6.4**  
**Proposed Combinations of Different Environmental Loads to Obtain ULS Combinations with  $10^{-2}$  Annual Probability of Exceedance and ALS Loads with Return Periods Not Less than One Year**

Limit State	Wind	Wave	Current	Ice	Sea Level
ULS	$10^{-2}$	$10^{-2}$	$10^{-1}$	–	$10^{-2}$
	$10^{-1}$	$10^{-1}$	$10^{-2}$	–	$10^{-2}$
	$10^{-1}$	$10^{-1}$	$10^{-1}$	$10^{-2}$	Mean water level
ALS	Return period not less than 1 year	Return period not less than 1 year	Return period not less than 1 year	–	Return period not less than 1 year

Source: Offshore Standard. DNV-OS-C101, *Design of Offshore Steel Structures, General (LRFD Method)*, Det Norske Veritas, Hovik, Norway, pp. 12–20, 2008. With permission.

**TABLE 6.5**  
**Load Factors  $\alpha_d$  for Ultimate Limit State**

Combinations of Design Loads	Load Categories			
	<i>D</i>	<i>L</i>	<i>E</i>	$\Delta$
(a)	1.3	1.3	0.7	1.0
(b)	1.0	1.0	1.3	1.0

*Source:* Offshore Standard. DNV-OS-C101, *Design of Offshore Steel Structures, General (LRFD Method)*, Det Norske Veritas, Hovik, Norway, pp. 12–20, 2008. With permission.

*Note:* The load categories are *D* = permanent or dead loads; *L* = variable functional or live loads; *E* = environmental loads (include those due to wind, wave, current, tide, marine growth, seismic, snow, and ice); and  $\Delta$  = deformation loads.

be considered in both the operating and temporary conditions. The load factors are generally applicable for all types of structures, but other values may be specified in the respective object standards.

*Load factor for FLS:* The structure shall be able to resist expected fatigue loads, which may occur during temporary and operation design conditions. When there is a possibility of significant cyclic loads occurring in other phases, for example, wind excitation during fabrication, such cyclic loads shall be included in the fatigue load estimates. The load factor  $\alpha_d$  in the FLS is 1.0 for all load categories.

*Load factor for SLS:* For analyses of SLS the load factor  $\alpha_d$  is 1.0 for all loads categories, both for temporary and operating design conditions.

*Load factor for ALS:* The load factors  $\alpha_d$  in the ALS is 1.0.

As per the National Building Code of Canada [9], the following equation is prescribed for computing the overall design loads.

$$\phi R > \alpha_D D + \psi \gamma \{ \alpha_L L + \alpha_Q Q + \alpha_T T \} \quad (6.9)$$

where  $\phi$  = resistance factor;  $\psi$  = load combination factor;  $\gamma$  = importance factor;  $\alpha_D$  = dead load factor;  $\alpha_L$  = live load factor;  $\alpha_Q$  = earthquake load factor; and  $\alpha_T$  = thermal effect (temperature) load factor.

Generally, in civil engineering design, earthquake loads are normally regarded as accidental loads [10], but in offshore engineering, they are treated as environmental loads; this practice has been followed in Chapter 3 and will be followed herein.

### Example 6.3

The offshore structure is designed with a maximum “freeboard” height  $h$  of 55.0 ft. above the mean sea level (with a deck height of 15.0 ft.), as shown in Figure E6.1. The height corresponds to a 10% probability of being exceeded by the existing sea waves in a year. (i) What is the probability that the structure will be subjected to waves exceeding the available 55.0 ft. “freeboard,” within the return period of the design “freeboard” height? (ii) If it is assumed that, when subjected to waves exceeding the design “freeboard” height, there is a probability of 20% for the structure to be damaged, what is the probability of damage to the structure within three years?

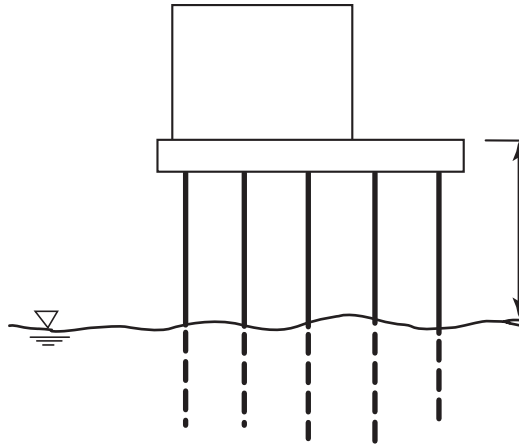


FIGURE E6.1 The given offshore structure.

- (i) Return period of the design wave is  $= 1/(0.10) = 10$  years.  
Hence,  $P(h > 55.0 \text{ ft. in } 10 \text{ years}) = 1.0 - (0.90)^{10} = 1.0 - 0.349 = 0.651$ .
- (ii) The probability of damage should take into account the possibility of exceeding the given 55.0 ft. “freeboard” 0, 1, 2, or 3 times in three years, assuming that the likelihood of more than one exceedance during one year is negligible. Also assume the statistical independence of the structural damage for more than one exceedance.  
 $P(\text{no damage in three years}) = (1.00)(0.90)^3 + (0.80)[(3)(0.10)(0.90)^2] + (0.80)^2[(3)(0.10)^2(0.90)] + (0.80)^3(0.10)^3 = 0.729 + 0.1944 + 0.0173 + 0.0005 = 0.9412$ .  
Hence,  $P(\text{damage in 3 years}) = 1.0 - 0.9412 = 0.0588$ .

**Example 6.4**

The maximum impact pressure of ocean waves on coastal structures may be computed by the equation

$$p_{\max} = 2.7\rho(K/D)u^2 \text{ (in psf)} \tag{E6.1}$$

where  $\rho$  is the mass density of water,  $K$  is the length of the hypothetical piston,  $D$  is the thickness of air cushion, and  $u$  is the horizontal velocity of the advancing wave. Assume that the wave crest has a forward velocity,  $u$ , of 5.0 ft./s, with a coefficient of variation of 20%. The mass density of sea water is 1.98 slugs/ft.<sup>3</sup>, and the ratio of  $(K/D) = 30.0$ . Determine the mean and standard deviation of the peak impact pressure.

- (i) Take  $u = 5.0 \text{ ft./s}$  as the mean value of the wave velocity; hence, according to Equation E6.1,  
 $E(p_{\max}) \approx (2.7)(1.98)(30)(5.0)^2 = 4010 \text{ psf} = 27.84 \text{ psi}$ .  
Also,  $\text{Var}(p_{\max}) \approx \text{Var}(dp_{\max}/du)\text{Var}(u) = [(2.7)(1.98)(30)\{2(5.0)\}]^2[(0.20)(5.0)]^2 = 2,572,174.4$ .  
Standard deviation of the peak pressures  $= \sqrt{2,572,174.4} = 1603.8 \text{ psf} = 11.14 \text{ psi}$ .

**6.3 ENVIRONMENTAL FORCES**

**6.3.1 INTRODUCTION**

Environmental influences such as wind, waves, current, tides, subsea earthquakes, mobile ocean ice, movement/slumping of seabed, marine growth and temperature, generate the environmental loads

acting on offshore structures. The dominant characteristic parameters of these environmental influences, which govern the design loads exerted on these structures, are identified from site-specific studies carried out to acquire or generate the relevant data. The mean return periods, required in the design of such structures, for these environmental events vary from one specification code to another. In American and Norwegian design practices, the return period of the event is taken as 100 years, whereas in the British codes, it is specified as 50 years or greater. More recently, these design periods are determined from the probability of exceedance, specified in the different codes, as shown earlier in Table 6.4 [2]. For example, the design parameters used for the White Rose platform, located in the Jeanne d'Arc Basin in 120.0 m deep waters, 350 km east of St. John's, NL, Canada are given in Table 6.6 [10, 11]. Details of design criteria, simplifying assumptions, required data, etc., can be obtained from the regulations and codes of practice listed in References [1–9, 12, 13].

### 6.3.2 WIND FORCES

Wind loads act on all the exposed portions of the offshore structure (both exterior and transparent interior portions), as well as on the equipment, movable loads, housing, helipad, derrick, etc. located on the deck. An important parameter pertaining to wind data is the time interval over which wind speeds are averaged. For averaging intervals less than 1 min, wind speeds are classified as gusts; these gust factors have been given earlier in Table 3.5. For averaging intervals of 1 min or longer they are classified as sustained wind speeds. The wind speeds vary over the height as shown in Figure 6.8 [14], as well as over the transverse surface area, depending on the terrain roughness the wind encounters as it traverses various terrains.

Three different equations have been given in Chapter 3, viz., Equations 3.6, 3.11, and 3.12, to compute the wind velocity profile in the vertical direction; these equations are shown in Table 6.7. An additional API code-suggested form is given below as [15, 16]

$$U_z = U_{z_0} (z/z_0)^{(1/n)} \quad (6.10)$$

where  $U_z$  is the mean wind velocity at height  $z$  above the mean sea level,  $U_{z_0}$  is the wind velocity at a reference height  $z_0$  (typically 10 m above mean sea level), and  $n$  is an index dependent on the sea state, distance from the land, and the averaging period for the wind.  $(1/n)$  is taken as approximately equal to 1/13 for gusts and 1/8 for sustained winds in the open ocean. Using the computed design wind speed of  $U_z$  (m/s), the static horizontal wind force  $F_w$  (N), acting on a projected area  $A$  (m<sup>2</sup>) in the direction of the wind velocity, can be determined as follows:

$$F_{wz} = (1/2) C_D \rho_w U_z^2 A \quad (6.11)$$

where  $\rho_w$  is the wind density ( $\rho \approx 1.225$  kg/m<sup>3</sup>), and  $C_D$  is the shape coefficient ( $C_s = 1.5$  for beams and rectangular areas of buildings,  $C_s = 0.5$  for cylindrical sections, and  $C_s = 1.0$  for total projected area of structure under consideration) [15, 16]; additional values for the drag coefficients are given in Table 6.8 [17].

If gust factors are to be explicitly accounted for, then the values given in Table 3.5 must be used to multiply the 1-h average wind speed computed by Equation 6.10 with a value of (1/8) for the coefficient  $(1/n)$ . The shielding and solidity effects also can be accounted for, as per the judgment and experience of the designer using appropriate design coefficients. When waves and winds act simultaneously on the structure, for the combined action of wind and wave loads on the structure, the highest of the loads obtained from the calculations using (i) a 1-min sustained wind speed combined with the extreme waves and (ii) 3-s gusts, should be used in Equation 6.11 or any other relevant equation (refer to DNV [3] and DOE-OG [13] code rules).

**TABLE 6.6**  
**Environmental Parameters for the Design of White Rose Platform**

Return Period (years)	Wave Data				
	Significant Wave Height (m)	Maximum Wave Height (m)	Associated Spectral Peak Period (s)		
1	10.5	19.7	13.5		
10	12.7	23.8	14.9		
25	13.5	25.2	15.4		
50	14.1	26.3	15.8		
100	14.7	27.4	16.1		
Wind Speed Data (m/s)					
	1.0 h mean	10 min mean	1.0 min mean	15.0 s mean	3.0 s mean
1	23.6	25.0	28.8	31.2	33.7
10	27.7	29.4	33.8	36.6	39.6
25	28.8	30.5	35.1	38.0	41.2
50	29.7	31.5	36.2	39.2	42.5
100	30.5	32.3	37.2	40.3	43.6
Current Data (cm/s)					
	Period	Maximum Speed	Mean Velocity	Direction	
Near surface	July–October 1984	82.0	19.0	Southwest	
Mid-depth	July–November 1984	31.0	1.8	Southeast	
Near bottom	August–November 1985	50.6	2.0	Southeast	
Tidal Levels, Storm Surges and Tsunami Level Increase					
	Unit	1.0 year	10 years	100 years	
Maximum astronomical tide	Unit (m) range	1.04	1.04	1.04	
Storm surge	Unit (m) range	1.04	1.27	~ 1.51	
Tsunami level	(m) above msl	~ 0.0	0.11	1.20	
Ambient Design Environmental Conditions					
	Maximum	Minimum			
Air temperature (°C)	26.5	17.3			
Water temperature (surface) (°C)	15.4	1.7			
Water temperature (20 m depth) (°C)	14.3	1.7			
Water temperature (50 m depth) (°C)	5.6	1.7			
Iceberg Data					
Mass (t)	220,000 t	–			
Speed (kmph)	9.8	0.77			
Sea Ice Occurrence	Mean Cover	Average Number of Weeks			
Within 25 km	54 to 57 %	2.3 to 2.6			

(continued)

**TABLE 6.6 (Continued)**  
**Environmental Parameters for the Design of White Rose Platform**

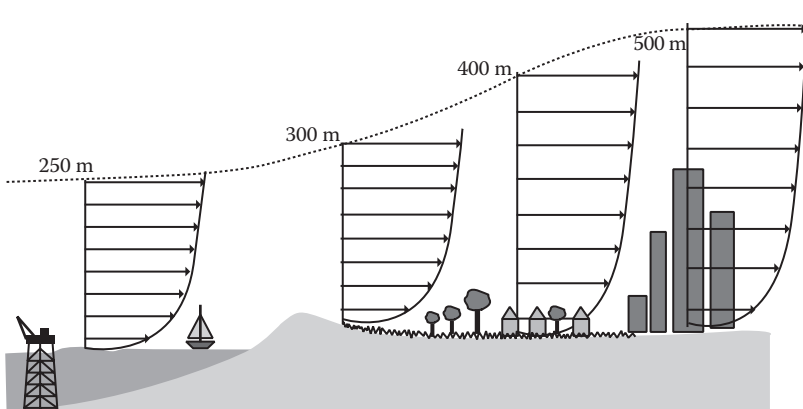
Marine Growth Thickness (mm)	
Elevation above Mean Sea Level	Marine Growth Thickness (mm)
Above +2.5 m	To be determined
+2.5 to -1.5 m	50
-1.5 to -7.5 m	150
-7.5 to -14.5 m	100
Below -14.5 m	50

Source: White Rose Development Authority, Design philosophy and criteria. *Development Plan*, Volume 2, Section 8, pp. 260–276, 2001. Husky Oil. *White Rose Oilfield Project Description*, 42 pp. Available at <http://www.cnlopb.nl.ca/pdfs/wrproj.pdf>, March 2000. Reproduced with permission.

The drag coefficients are also velocity dependent, as shown in Figure 6.9 [18], which shows that the coefficient of drag for any shape reduces as the flow becomes turbulent, depending on its Reynolds flow number ( $Re = \rho_a U_z L / \mu_a = U_z L / \nu_a$ ), where  $\rho_a$  is the mass density of air,  $L$  is a characteristic linear dimension,  $\mu_a$  is the dynamic viscosity of air, and  $\nu_a$  is the kinematic viscosity of air. The figure also shows that at a constant Reynolds flow number, the coefficient of drag is independent of the size (or diameter) of the structure. Figure 6.10 [19] shows the variation of the drag force coefficient as a function of Reynolds number for a long circular cylinder and a long thin rectangular beam section. It seems to support the values given in Figure 6.9.

When the wind direction is not normal to the resisting surface of the structure (or a member), as shown in Figure 6.11 [20], the wind forces are computed using the area of the structure projected normal to the wind direction. In this case, Equation 6.11 has to be modified to compute the actual forces acting on the structure, as given below:

$$\begin{aligned}
 F_{w_z} &= (1/2) C_D \rho_a U_z^2 (A_{\text{projected}}) \\
 &= (1/2) C_D \rho_a U_z^2 [\text{Acos}(\alpha)] = (1/2) C_D \rho_a U_z^2 \text{Acos}(\alpha)
 \end{aligned}
 \tag{6.12}$$



**FIGURE 6.8** Wind speed (mean) and gradient height variation with respect to height, over various terrains. (From N. Haritos, *Electronic Journal of Structural Engineering [EJSE] Special Issue: Loading on Structures*, p. 58, 2007. With permission.)



**TABLE 6.7**  
**Governing Wind Force Equations, Given in Chapter 3**

#	Designation	Wind Velocity Equation
1	Equation 3.6	$\bar{U}_z = 2.5u_w \{ \ln(z/z_0) + 5.75(z/h) - 1.875(z/h)^2 - 1.333(z/h)^3 + 0.25(z/h)^4 \}$ $= 2.5u_w \{ \ln(z/z_0) + 5.75(z/h) \}$ (see Section 3.3.3 for definition of notations).
2	Equation 3.11	$\bar{U}_z = \bar{U}_{10} \ln\{(z + z_0)/z_0\} / \ln\{(z_R + z_0)/z_0\} \text{ (ft.)}$ with $z_0 = 2.91 \times 10^{-5} (\bar{U}_{10}^2/g)$ (see Section 3.3.3 for definition of notations).
3	Equation 3.12	$\bar{U}_z = \bar{U}_{10} (z/10)^{1/7}$ (see Section 3.3.3 for definition of notations).

where  $\alpha$  is the angle of inclination of the member axis to the direction of wind flow. When a structure is composed of many members as in an offshore steel structure, then the wind forces have to be computed for each member and then summed up over the whole height and transverse dimensions of the structure. In a similar manner, the overturning moment acting on the offshore structure about its bottom or a given reference height can also be computed.

**Example 6.5**

Consider the small lighthouse tower shown in Figure E6.2 and determine the total wind force  $F$  acting on the deck and the lantern, assuming a basic sustained wind speed (with gust effect included) of 170.0 mph. Also locate the resultant distance  $b$  above the base of the deck.

The problem is worked out using three different formulations (for the sake of comparison).

(i) The sustained wind speed is assumed to be a constant over the height; (ii) Equation 6.10; and (iii) Equation 3.6.

(i) Wind speed is assumed to be constant over the height of the structure: Wind speed (gust factor correction included) =  $U_z = 170.0 \text{ mph} = (170)(5280)/(3600) = 249.33 \text{ ft./s}$ .

The total wind speed on the deck (as per Equation 6.11) =  $F_{wz} = (1/2) C_D \rho_w U_z^2 A$ , where  $C_D = 1.5$  (maximum from Table 6.8 for a rectangle, and 0.75 for a cylinder);  $\rho_w = (2.38)(10^{-3}) \text{ slug/ft.}^3$ ;  $A = (40)(15) = 600.0 \text{ ft.}^2$ ; and  $U_z = 249.33 \text{ ft./s}$ .

Hence, the wind force on the rectangular-faced deck =  $(1/2)(1.5)(2.38)(10^{-3})(249.33)^2(600) = 66,563.20 \text{ lbf}$ .

Wind force on the cylindrical lantern =  $(1/2)(0.75)(2.38)(10^{-3})(249.33)^2(20 \times 10) = 11,093.86 \text{ lbf}$ .

Total wind force = 77,657.06 lbf.

Wind moment about the base =  $(66,563.20)(7.5) + (11,093.86)(15 + 10) = 499,224.00 + 277,346.56 = 776,570.86 \text{ lb ft}$ .

Distance of wind force resultant above the base of deck =  $(776,570.86)/(77,657.06) = b = 10.0 \text{ ft}$ .

(ii) Wind speed is assumed to vary according to Equation 6.10.

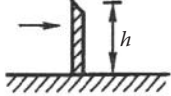
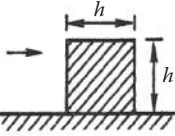
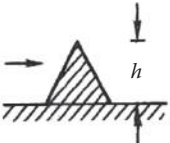
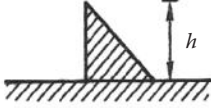
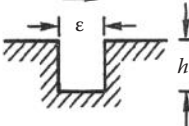
Equation 6.10 is given as  $U_z = U_{z_0} (z/z_0)^{(1/n)}$ , with  $(1/n) = (1/13)$ , when the wind gusts are included. Take  $z_0 = 30.0 \text{ ft}$ , and assume that it designates the bottom height of the deck, above mean sea level (since no other data are given).

Hence,  $U_z$  at the center of the deck =  $(249.33)(z/30.0)^{(1/13)}$ .

For the deck,  $U_z = (249.33)(37.5/30.0)^{(1/13)} = 253.65 \text{ ft./s}$ .

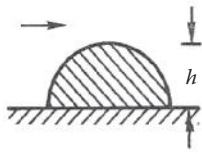
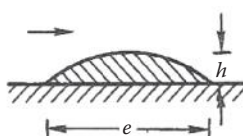

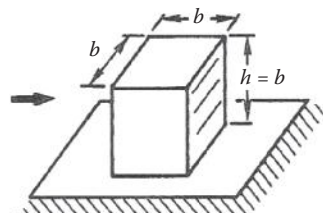
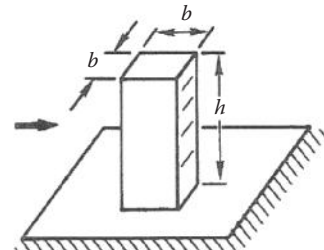
$U_z$  at a height of 5.0 ft. above the base of the cylinder =  $(249.33)(50/30)^{(1/13)} = 259.32 \text{ ft./s}$ .

**TABLE 6.8**  
**Drag Coefficients  $C_D$  for Different Shapes in a Fluid Environment**

Protuberance	Drag Coefficient, $C_D$ and Remarks
1. Fence section 	1.4
2. Square section 	1.2
3. Equilateral triangle section 	1.0
4. Right triangle 	+ 1.3 + 1.0
5. Gap section 	$0.01 h > e > 0.1 h$ $0.258 h > e > 20 h$

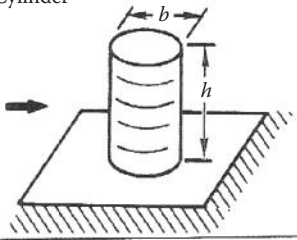
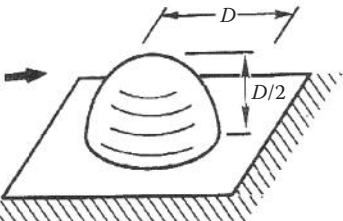
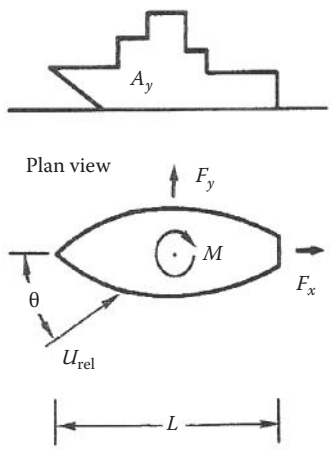
(continued)

**TABLE 6.8 (Continued)**  
**Drag Coefficients  $C_D$  for Different Shapes in a Fluid Environment**

Protuberance	Drag Coefficient, $C_D$ and Remarks
<p>6. Semicircle section</p> 	<p>0.8</p>
<p>7. Bump section</p> 	<p><math>15(h/e)^2</math>,  for <math>0 &lt; h/e &lt; 0.16</math></p>
<p>8. Sheet metal joint section</p> 	<p>→ 0.4  ← 0.2</p>
<p>9. Cube</p> 	<p>Flow normal to face (shown)</p> $C_D = \begin{cases} 1.05 \\ 1.65 \\ 1.18 \end{cases}$ <p>Flow diagonal to face</p> $C_D = \begin{cases} 0.80 \\ 1.65 \end{cases}$ <p><math>A = b^2</math></p>
<p>10. Rectangular solid</p> 	<p>Flow normal to face (shown)</p> $C_D = \begin{cases} 1.3 \\ 1.5 \end{cases}$ <p>Flow diagonal to face</p> $C_D = \begin{cases} 1.25 \\ 1.05 \end{cases}$ <p><math>A = b^2, 1 &lt; h/b &lt; 4</math></p>

(continued)

**TABLE 6.8 (Continued)**  
**Drag Coefficients  $C_D$  for Different Shapes in a Fluid Environment**

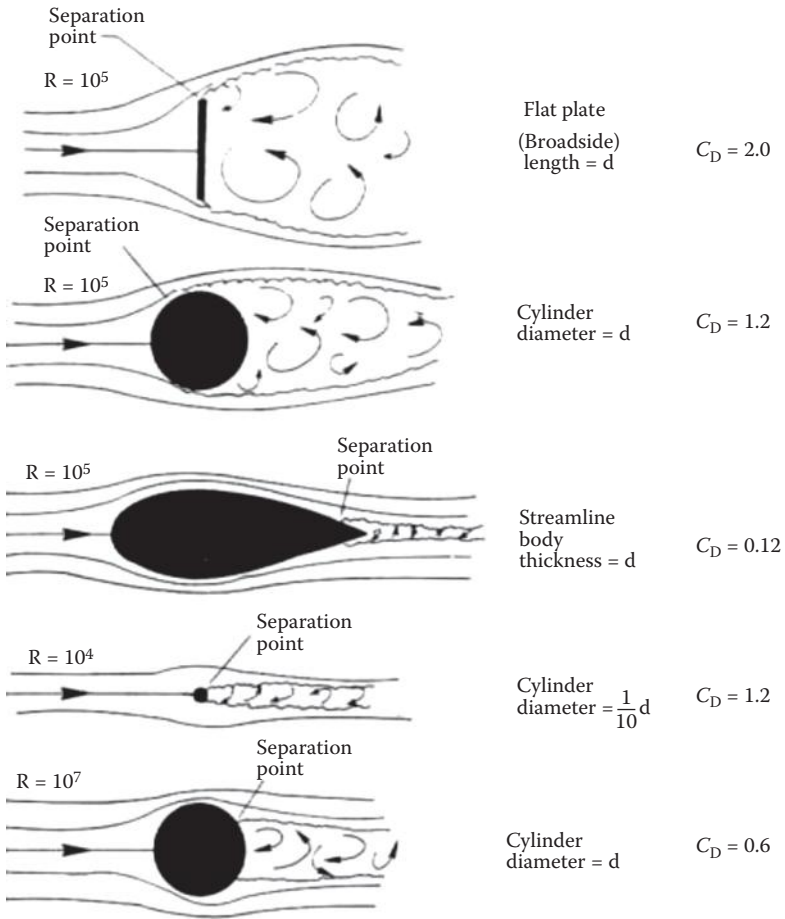
Protuberance	Drag Coefficient, $C_D$ and Remarks
<p>11. Cylinder</p> 	<p><math>C_D = 0.75</math></p> <p><math>0.5 &lt; h/b &lt; 5</math></p>
<p>12. Hemisphere</p> 	<p><math>0.4 &lt; C_D &lt; 0.6,</math></p> <p><math>10^3 &lt; Re &lt; 2 \times 10^4.</math></p> <p><math>C_D = 0.1, Re &gt; 2 \times 10^5.</math></p> <p><math>Re = UD/\nu.</math> <math>\nu</math> is kinematic viscosity</p> <p><math>A = \pi D^2/8</math></p>
<p>13. Ship hull above waterline</p> 	<p><math>F_x = \frac{1}{2} \rho U_{rel}^2 A_x C_x</math></p> <p><math>F_y = \frac{1}{2} \rho U_{rel}^2 A_y C_y</math></p> <p><math>M = \frac{1}{2} \rho U_{rel}^2 A_y L C_M</math></p> <p> <math>C_y = 0.9 \sin \theta</math>  <math>C_x = 0.6 \sin \theta</math>  <math>C_M = 0.1 \sin \theta</math> </p> <p style="text-align: right;">} Typical values</p> <p><math>A_x</math> = Frontal projected area</p> <p><math>A_y</math> = Lateral projected area (show</p> <p><math>U_{rel}</math> = Relative wind</p>

Source: R.D. Blevins, *Applied Fluid Dynamics Handbook*, Van Nostrand Reinhold Company, pp. 310–312, 1984. Reproduced with permission.

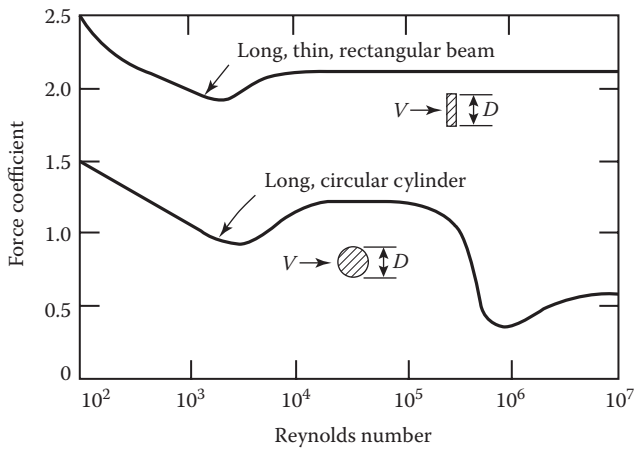
$U_z$  at a height of 15.0 ft. above the base of the cylinder =  $249.33(60.0/30.0)^{(1/13)} = 262.985$  ft./s.

Wind force on the rectangular-shaped deck =  $(1/2)(1.50)(2.38)(10^{-3})(253.65)^2(600) = 68,906.34$  lbf.

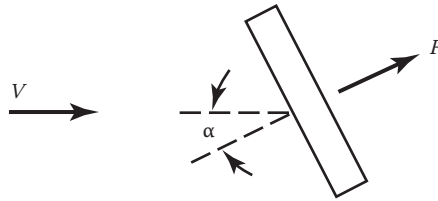
Wind force on the cylindrical lantern at a height of 5.0 ft. above the base of the cylinder =  $(1/2)(0.75)(2.38)(10^{-3})(259.32)^2(10 \times 10) = 6001.78$  lbf.



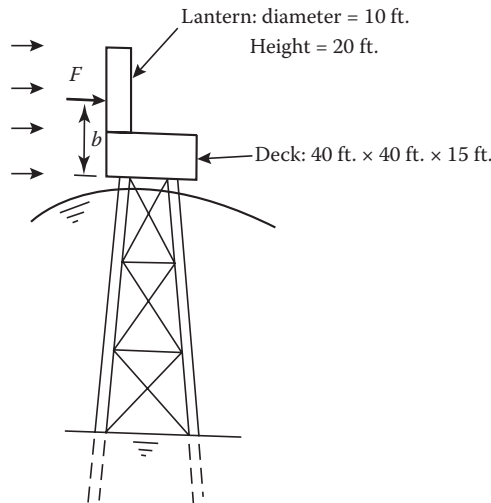
**FIGURE 6.9** Dependence of  $C_D$  on Reynold's numbers for various shapes. (From D. Darling, *Internet Encyclopedia of Science*. Available at [http://www.daviddarling.info/encyclopedia/D/drag\\_coefficient.html](http://www.daviddarling.info/encyclopedia/D/drag_coefficient.html), 2010. With permission.)



**FIGURE 6.10** Dependence of drag coefficient on Reynolds number. (From T.H. Dawson, *Offshore Structural Engineering*, Prentice Hall Inc., Englewood Cliffs, NJ, p. 94; p. 70, 1983. With permission.)



**FIGURE 6.11** Wind force acting on an inclined member. (From T.H. Dawson, *Offshore Structural Engineering*, Prentice Hall Inc., Englewood Cliffs, NJ, p. 95, 1983. With permission.)



**FIGURE E6.2** Small lighthouse tower.

Wind force on the cylindrical lantern at a height of 15.0 ft. above the base of the cylinder =  $(1/2)(0.75)(2.38)(10^{-3})(262.985)^2(10 \times 10) = 6172.63$  lbf.

Total wind force on the structure =  $68,906.34 + 6001.78 + 6172.63 = 81,080.75$  lbf.

Wind moment above the base =  $(68,906.34)(7.5) + (6001.78)(20.0) + (6172.63)(30.0) = 792,003.15$  lb. ft.

Distance of wind force resultant above the base of deck =  $(792,003.15)/(81,080.75) = 9.768$  ft.

(iii) Wind speed is assumed to vary according to shortened form of Equation 3.6.

Equation 3.6 is given as  $U_z \approx 2.5u_* \{ \ln(z/z_0) + 5.75(z/h) \}$ .

As per Charnock's law,  $[(U_{z_0^*})^2/(z_0g)] = 60.0$  (in metric units) (see Equation 3.8).

Taking  $U_{z_0^*} = 249.33$  ft./s, the value of  $z_0$  is computed as 0.08 m (~0.20 ft.) (in FPS units), by trial and error.

Also  $u_* = \bar{U}_{z_0^*} / \{ 2.5 \ln(10/z_0) \}$  (in metric units) (see Equation 3.7).

Hence,  $u_* = (249.33/3.281) / \{ (2.5) \{ \log(10/(0.20/3.281)) \} \} = 5.96$  m/s (= 19.555 ft./s).

By Equation 3.9, the boundary layer height  $h$  is given by  $h = u_* / (6f_c)$ .

Also by Equation 3.10,  $f_c = 2\Omega \sin(\theta)$ .

Taking a latitude of St. John's, NL,  $\theta = 48^\circ$ ,  $f_c = (2.0)(72.9)(10^{-6}) \sin(48^\circ) = (1.079)(10^{-4})$ .

Hence,  $h = (5.96) / \{ (6.0)(1.079)(10^{-4}) \} = 9206.05$  m.

$U_z$  at 37.5 ft. =  $(2.5)(5.96) [ \ln\{ (37.5/3.281) / (0.06) \} + 5.75 \{ (37.5/3.281) / 9206.06 \} ] = (14.9) [ 5.25 + 0.0071 ] = 78.331$  m/s (= 257.003 ft./s).

$U_z$  at 50.0 ft. =  $(2.5)(5.96) [ \ln\{ (50.0/3.281) / (0.06) \} + 5.75 \{ (50.0/3.281) / 9206.06 \} ] = (14.9) [ 5.537 + 0.0095 ] = 82,643$  m/s (= 271.15 ft./s).

$$U_z \text{ at } 60.0 \text{ ft.} = (2.5)(5.96)[\ln\{(60.0/3.281)/0.06\} + 5.75\{(60.0/3281)/9206.06\}] = (14.9)[5.72 + 0.0114] = 85.4 \text{ m/s} (= 280.191 \text{ ft./s}).$$

$$\text{Wind force on the rectangular-shaped deck} = (1/2)(1.50)(2.38)(10^{-3})(257.003)^2(600) = 70,755.0 \text{ lbf.}$$

$$\text{Wind force at the cylindrical lantern at a height of 5.0 ft. above the base of the cylinder} = (1/2)(0.75)(2.38)(10^{-3})(271.15)^2(10 \times 10) = 6561.87 \text{ lbf.}$$

$$\text{Wind force on the cylindrical lantern at a height of 15.0 ft. above the base of the cylinder} = (1/2)(0.75)(2.38)(10^{-3})(280.191)^2(10 \times 10) = 7006.75 \text{ lbf.}$$

$$\text{Total wind force on the structure} = 70,755.0 + 6561.87 + 7006.75 = 84,323.62 \text{ lbf.}$$

$$\text{Wind moment above the base} = (70,755.0)(7.5) + (6561.87)(20) + (7006.75)(30) = 530,662.50 + 131,237.4 + 210,202.5 = 872,102.4 \text{ lb. ft.}$$

$$\text{Distance of wind force resultant above the base of deck} = (872,102.4/84,323.62) = 10.34 \text{ ft.}$$

All the three formulations give almost similar results, the maximum difference being + 8.59%.

### Example 6.6

Consider the small lighthouse tower, shown in Figure E6.3a and b, and determine the maximum wind force exerted on the cylindrical legs, deck, and lantern, assuming a mean wind velocity of 120 mph. The maximum gust factor at the location is 1.60; also, locate the distance of its resultant force above the base of the deck. Take the drag coefficients from the tables given in Table 6.8.

### Solution for Example 6.6

The maximum wind force can occur in two different directions, viz., (i) Perpendicular to the beam direction, or (ii) along the diagonal direction. The wind force is obtained by using the shortened form of Equation 3.6 given in Table 6.7. Forces have to be calculated over four portions of the structure, viz., (i) four columns; (ii) on the deck; (iii) on the residential quarters; and (iv) lantern. The center of gravities of the respective portions are, viz., (i) 35.0 ft. from msl; (ii) 51.0 ft. from msl; (iii) 60.0 ft. from msl; and (iv) 65.0 ft. from msl. Also the distance of 25.0 ft. is taken to be equal to the distance from msl to the bottom of the deck; in addition, the areas of column over which wind would act are considered to be zero (since wave forces will be acting over the column areas).

*Beam wind:* The areas exposed to the wind in the perpendicular to the beam direction are (i) for the deck [= (20.0)(60.0)] = 1200 ft.<sup>2</sup>; (ii) for the residential quarters [= (15.0)(12.0)] = 180.0 ft.<sup>2</sup>; and (iii) for the lantern [= (30)(12)] = 360.0 ft.<sup>2</sup>

*Diagonal wind:* The areas exposed to wind action are

$$(i) \text{ For the deck } [(60 + 40)\{\sin(33.7^\circ)\}(20)] = 1109.7 \text{ ft.}^2$$

$$(ii) \text{ For the quarters } [(15 + 25)\{\sin(33.7^\circ)\}(12)] = 266.32 \text{ ft.}^2$$

$$(iii) \text{ For the lantern } [(30)(12)] = 360.0 \text{ ft.}^2$$

Design wind speed (at a height of 10.0 m, above the sea level) is given as = (120.0)(1.6) = 192.0 mi./h = 281.6 ft./s; it is considered to be the same for all the three components.

As shown earlier in Example 6.5, the values of  $u_*$ ,  $z_0$ , and  $h$  have to be computed in an iterative manner; they are obtained as  $u_* = 11.33 \text{ ft./s}$ ,  $z_0 = 0.066 \text{ ft.}$ , and  $h = 25,901.0 \text{ ft.}$

$$\text{At } z = 35 \text{ ft., } U_z = (2.5)(11.33)[\ln(35/0.066) + (5.75)(35)/(25,901)] = 178.05 \text{ ft./s (deck).}$$

$$\text{At } z = 51 \text{ ft., } U_z = (2.5)(11.33)[\ln(51/0.066) + (5.75)(51)/(25,901)] = 188.84 \text{ ft./s (quarters).}$$

$$\text{At } z = 60 \text{ ft., } U_z = (2.5)(11.33)[\ln(60/0.066) + (5.75)(60)/(25,901)] = 193.50 \text{ ft./s (lantern).}$$



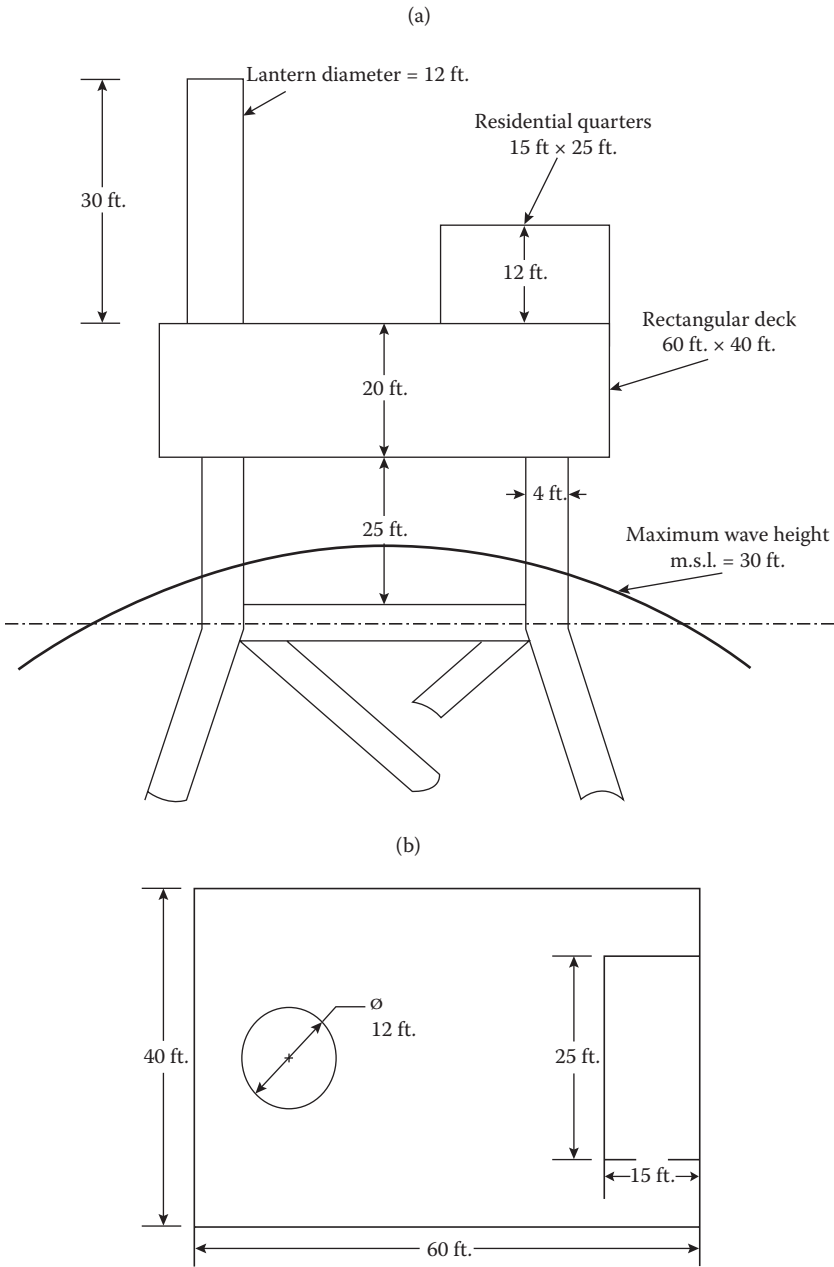


FIGURE E6.3 (a) Elevation and (b) plan of lighthouse tower.

$$\text{For beam wind, using Table 6.8, } C_D = \begin{bmatrix} \text{for the deck} \\ \text{for the quarters} \\ \text{for the lantern} \end{bmatrix} = \begin{bmatrix} 1.65 \\ 0.75 \\ 1.65 \end{bmatrix}.$$

$$\text{For the diagonal wind, using Table 6.8, } C_D = \begin{bmatrix} \text{for the deck} \\ \text{for the quarters} \\ \text{for the lantern} \end{bmatrix} = \begin{bmatrix} 1.65 \\ 0.75 \\ 1.65 \end{bmatrix}.$$

The wind load for the perpendicular to the beam case =  $(0.5)(2.4 \times 10^{-3})(1.65)(1200)(178.05 \times 1.6)^2 + (0.5)(2.4 \times 10^{-3})(1.65)(180)(188.84 \times 1.6)^2 + (0.5)(2.4 \times 10^{-3})(0.75)(360)(193.50 \times 1.6)^2 = 192,828.10 + 32,536.10 + 31,056.10 = 256,420.3 \text{ lb.}$

The wind load for the diagonal case =  $(0.5)(2.4 \times 10^{-3})(1.65)(1109.7)(178.05 \times 1.6)^2 + (0.5)(2.4 \times 10^{-3})(1.65)(266.32)(188.84 \times 1.6)^2 + (0.5)(2.4 \times 10^{-3})(0.75)(360)(193.50 \times 1.6)^2 = 178,317.80 + 48,138.0 + 31,056.10 = 257,511.9 \text{ lb.}$

Hence, the diagonal-to-the-deck structure wind imposes a slightly larger force on the structure. For the wind moments acting at the level of the bottom of the deck structure:

- (i) Wind moment at the bottom of the deck for perpendicular-to-the-beam case =  $(192,828.10)(10) + (32,536.10)(26) + (31,056.10)(35) = 1.9283 \times 10^6 + 0.8459 \times 10^6 + 1.0870 \times 10^6 = 3.8612 \times 10^6 \text{ lb ft.}$
- (ii) Wind moment at the bottom of the deck for the diagonal case =  $(178,317.8)(10) + (48,138.0)(26) + (31,056.10)(35) = 1.7832 \times 10^6 + 1.2516 \times 10^6 + 1.0870 \times 10^6 = 4.1218 \times 10^6 \text{ lb ft.}$

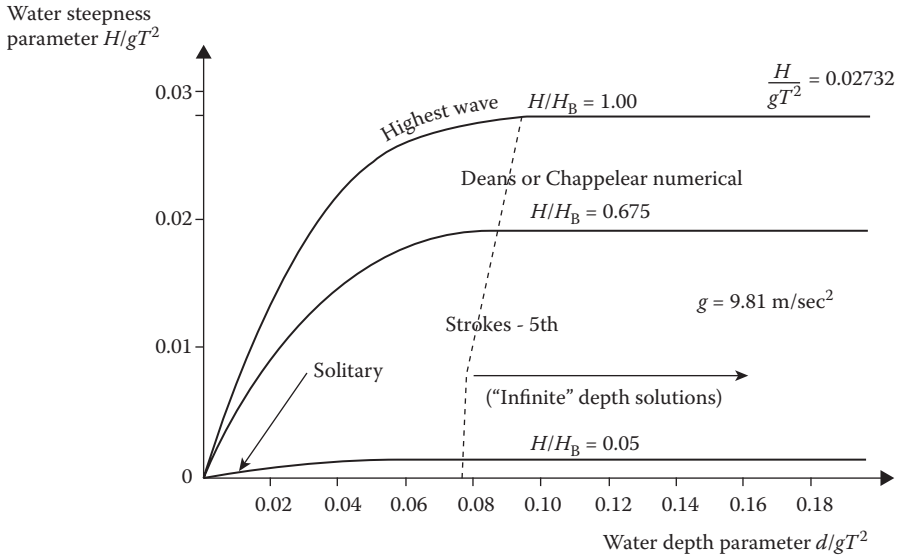
The wind moment for the diagonal to the deck structure gives the highest moment at the base of the deck.

### 6.3.3 WAVE FORCES

The wave loading of an offshore structure is usually the most important of all environmental loadings for which the structure must be designed. The forces on the structure are caused by the motion of the water due to the waves that are generated by the action of the wind on the surface of the sea. Determination of these forces requires the solution of two separate, although interrelated problems. The first is the sea state computed using an idealization of the wave surface profile and the wave kinematics given by an appropriate wave theory. The second is the computation of the wave forces on individual members and on the total structure, from the wave kinematics obtained in the first computation.

Wave forces on offshore structures are computed in two different formats. (i) In Method I, the design wave is computed, based on a “100-year return period” wave, and then the design wave loads acting on the structures are computed by an appropriate method. The computations do not consider any dynamic behavior of the structure, but apply the computed wave loads on the respective structural nodes (or joints) as static loads, and compute the structural response. (ii) Method II is the wave spectral formulation, wherein an appropriate wave spectra is selected based on the statistical analysis of the wave scatter diagram, measured (or identified) for the site of installation of the structure. Structural analysis is carried out in the frequency domain, if dynamic analyses for extreme wave loadings are required in the case of deepwater structures. Since the analyses are based on the statistical nature of the computed wave data, one can also obtain the most probable maximum force and response during the lifetime of the structure.

As indicated earlier in Section 3.4.3, the ranges of applicability of different wave theories (see Figure 6.12 [21]), developed over the years, is given below for a wide range of the parameters  $(H/gT^2)$  and  $(d/gT^2)$  [ $0.0 < (H/gT^2) < 0.03$ ;  $0.0 < (d/gT^2) < 0.20$ ]. It is always not possible to exactly specify the precise ranges in which the different wave theories mentioned earlier are valid. It can be generally stated that the small amplitude linear wave theories are valid for deepwater [ $(d/gT^2) > 0.08$ ]. From



**FIGURE 6.12** Selection of proper wave theory for wave force computation. (From ESDEP [The European Steel Design Education Programme] Course Notes, *Lecture 15A.2: Loads (I), Section 2.2, Introduction and Environmental Loads*. Available at <http://www.esdep.org/members/master/toc.htm>, 1993. With permission.)

Figure 6.12, it can be observed that when the value of  $(H/gT^2)$  is larger than 0.001, the Stokes waves should be employed; in particular, when  $(H/gT^2)$  is greater than 0.04, Stokes fifth-order wave theory should be employed as shown in Figure 6.12. The higher order Stokes waves are good for very steep waves in deepwater, and for transitional waves, when the wave is not very steep. For steep waves in any water depth, numerical wave theory, due to either Dean or Chappellear, always gives very good results.

**6.3.3.1 Wave Statistics**

In the ocean, actual waves do not occur as regular waves, but as irregular sea states composed of waves of different frequencies, having different headings. The unidirectional irregular waves can be obtained by the linear superposition of an infinite number of regular waves with varying frequencies (refer to Figure 3.36). The random sea state can be described using the wave energy density spectrum  $S(f)$ , as described earlier in Section 3.4.4. Wave directionality can also be introduced by means of a directional spreading function  $D(f,\varphi)$ , where  $\varphi$  is the angle of the wave approach direction and the directional wave spectrum  $S(f,\varphi)$  can be written as

$$S(f,\varphi) = S(f) \cdot D(f,\varphi) \tag{6.13a}$$

The directional wave spreading function  $D(f,\varphi)$  satisfies the equality given below [3.59], viz.

$$\int_0^\infty S(f) \int_{-\pi}^{+\pi} D(f,\varphi) d\varphi df = \int_0^\infty S(f) df \tag{6.13b}$$

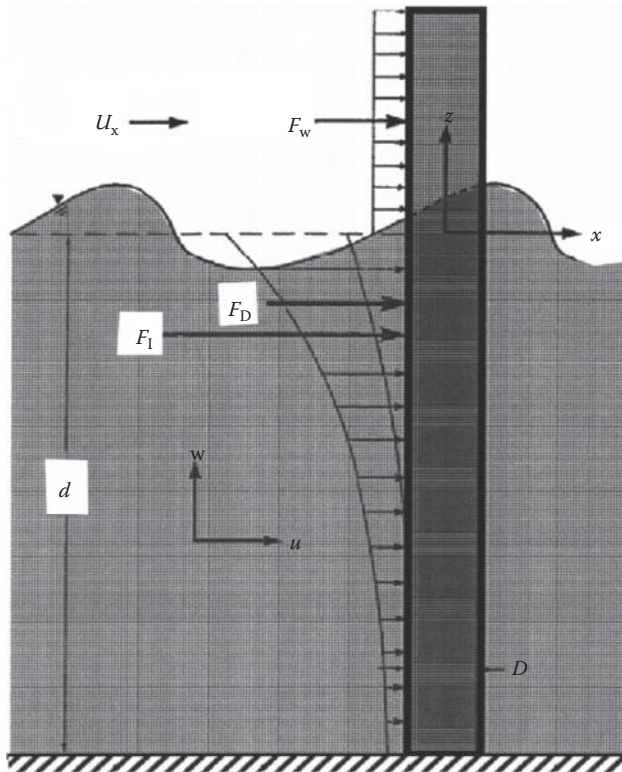
**6.3.4 WAVE FORCES ON OFFSHORE STRUCTURES**

Structures subjected to the wave environment experience forces that are much larger than that generated by wind forces. These forces result from the dynamic water pressures caused by the fluid

particle flowing past the stationary or moving structure; it can also be conceived as that due to the fluid field deformations occurring around the structure, causing fluid particle acceleration/decelerations and directional changes. Two distinct types of wave actions can be distinguished for understanding the forces exerted on the structures. (i) Slender and transparent (to fluid flow) structures that produce no significant influence on the wave field around the structures. The forces exerted on the structures can be empirically visualized as that due to the fluid acceleration and velocity dependent actions, in the direction of fluid flow. The total forces acting on the structure can be calculated by summing up the contributions from the acceleration- and velocity-dependent effects of the fluid, using Morison–O’Brien’s equation [22]; it has been observed from detailed experimental studies that the Morison–O’Brien’s equation could be applied only when  $D/L \leq 0.2$ , where  $D$  is the member diameter (or transverse dimension) and  $L$  is the wavelength. (ii) Large volume structures that exert significant influence on the wave field around the structures; these structures generate wave diffraction and reflection that considerably influence the forces exerted on them. The exact forces exerted on these structures can be determined only by numerical computations using wave diffraction and reflection concepts.

#### 6.3.4.1 Wave Forces on Slender Vertical Cylindrical Members

The steel substructures (or jackets) of bottom-fixed offshore structures can usually be regarded as hydrodynamically transparent. Figure 6.13 [23] shows a vertical cylinder, embedded in the sea bottom, subjected to wave forces due to a moving surface wave. It also shows the wind forces,  $F_w$ , exerted on the wind-exposed portion of the cylinder, due to a wind velocity of  $U_x (= V)$ . The wave forces on the submerged members, per unit length of the can therefore be calculated by Morison–O’Brien’s



**FIGURE 6.13** Wave and wind loads on a bottom-fixed vertical cylinder.  $V \equiv U_x$ ; submerged cylinder height  $h \equiv d$  = the depth of water at the site. (From N. Haritos, *Electronic Journal of Structural Engineering [EJSE] Special Issue: Loading on Structure*, pp. 59, 2007. With permission.)

equation, which expresses the wave force as the sum of an inertia force proportional to the wave particle acceleration and a nonlinear drag force proportional to the square of the particle velocity, viz.

$$f_x = f_I + f_D \quad (6.14)$$

where  $f_I$  is the inertial forces acting on the cylinder (per unit height) due to the acceleration of the wave particles around the cylinder, and  $f_D$  is the drag forces acting on the vertical cylinder due to the velocity of the fluid particles around the cylinder. The linear inertial force acting on the sea bottom piercing cylinder, per unit height, is given by

$$f_I = [\rho_w C_M (\pi D^2/4)](\dot{u}) \quad (6.15)$$

where  $[\rho_w C_M (\pi D^2/4)]$  is the mass of the volume of fluid undergoing acceleration,  $\rho_w$  is the mass density of seawater,  $C_M$  is the coefficient for the mass of water accelerating with the cylindrical structural member ( $= 1.0 + C_a$ , where  $C_a$  is the added mass of water),  $D$  is the diameter of the cylindrical member, and  $\dot{u}$  is the fluid particle acceleration at the center of the unit height cylinder. The nonlinear fluid drag force  $f_D$  per unit height is given by

$$f_D = [(1/2)\rho_w C_D(D)(1)](u)|u| \quad (6.16)$$

where  $C_D$  is the drag coefficient of the fluid flowing past the cylindrical structural member, with a particle velocity of  $u$ . Hence, the total fluid force acting on the cylinder, per unit height, is given by

$$f_x = f_I + f_D = [\rho_w C_M (\pi D^2/4)](\dot{u}) + [(1/2)\rho_w C_D(D)(1)](u)|u| \quad (6.17)$$

In the above format, Equation 6.17 is valid for fixed tubular cylinders of unit height; when wave forces acting over the whole cylinder is to be taken into account, the above equation has to be integrated over the whole immersed height of cylinder ( $h = d$ ). While considering the motion response of the whole cylindrical structure, under wave loads, the procedure for wave force computation should take into account the relative motion between the cylinder and the fluid particle around it [24]. Values of  $C_D$  and  $C_M$  depend on the wave theory used (since Reynolds number will depend upon wave velocity), surface roughness, and the flow parameters. According to API-RP2A [25], the drag and inertia coefficients are given as,  $C_D \sim 0.6$  to  $1.2$  and  $C_M \sim 1.3$  to  $2.0$ .

The drag and inertia coefficients,  $C_D$  and  $C_M$ , vary with respect to the maximum wave velocity,  $u_{max}$ , and the wave period,  $T$ , and are related through dimensionless variables known as Reynolds and Keulegan–Carpenter numbers. The two numbers are given by

$$Re = (\rho_w u_{max} D)/\mu_w; K_C = (u_{max} T)/D \quad (6.18)$$

where  $\rho_w$  and  $\mu_w$  represent the mass density and dynamic viscosity of water,  $u_{max}$  is the maximum wave particle velocity at the surface of the sea,  $T$  is the wave period, and  $D$  is the diameter or transverse (to wave propagation direction) dimension of the structure. It has been observed that when  $K_C < 10.0$ , inertia forces dominate; for  $10.0 < K_C < 20.0$ , both the inertia and drag forces are significant. When  $K_C > 20.0$ , then drag forces become progressively dominant. Figures 6.14 [23] and 6.15 [23] show the dependence of the mass (or inertia) and drag coefficients on the Keulegan–Carpenter number,  $K_C$ .

The total horizontal force exerted on the structure by the propagating wave is obtained as

$$F_{Total} = \int_{-d}^0 f_x dz \quad (6.19)$$

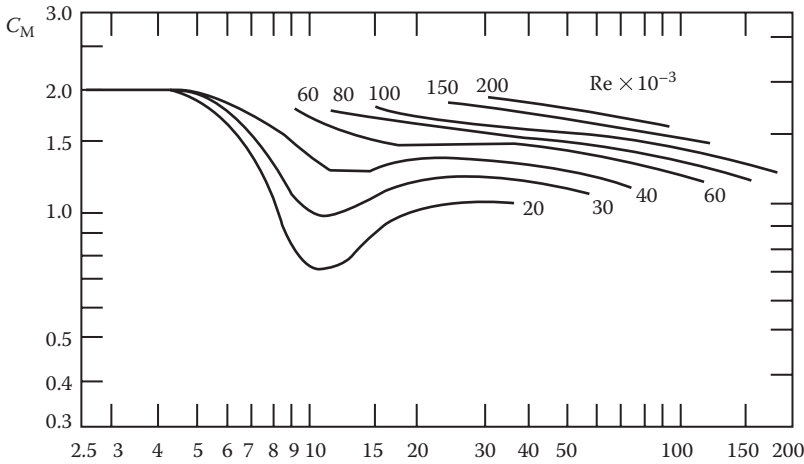


FIGURE 6.14 Dependence of mass coefficient  $C_M$  on  $Re$  and  $K_C$ . (From N. Haritos, *Electronic Journal of Structural Engineering [EJSE] Special Issue: Loading on Structure*, pp. 59, 2007. With permission.)

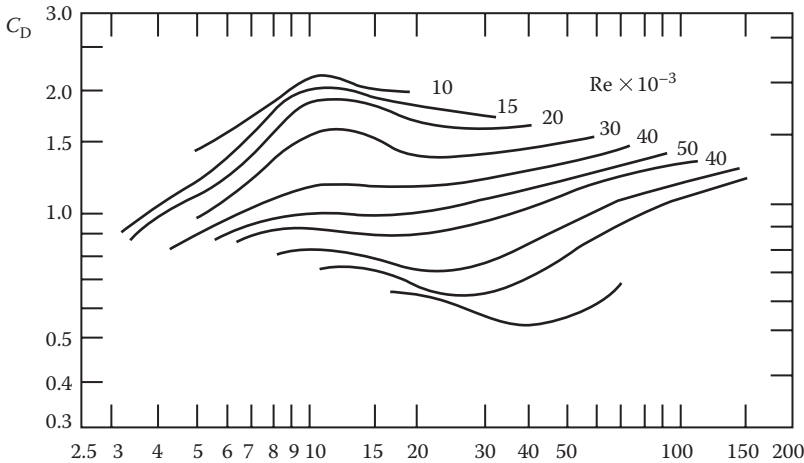


FIGURE 6.15 Dependence of drag coefficient  $C_D$  on  $Re$  and  $K_C$ . (From N. Haritos, *Electronic Journal of Structural Engineering [EJSE] Special Issue: Loading on Structure*, pp. 59, 2007. With permission.)

It should be noted from Equation 6.20 that the integration limits are from the sea bottom to the sea surface. In a similar manner, the total moment about the base is given by

$$M_{\text{Total}} = \int_{-d}^0 f_x(d+z) dz \tag{6.20}$$

### 6.3.4.2 Linearization of Nonlinear Wave Drag Force

According to Morison–O’Brien’s equation, given in Equation 6.17, the drag force is nonlinear. This nonlinear formulation is used in the design wave concept. However, for the determination of a transfer function needed for frequency domain calculations, the drag force has to be linearized in a suitable manner [26, 27]. A common approach is to calculate the linearized drag term from equating the energy dissipation from the linear and nonlinear drag contribution (equivalent linearization)

or by minimizing the error between the linear and nonlinear force (stochastic linearization). The equivalent linearization procedure is as follows, viz., Equation 6.17 is written in a generic form as

$$f_x(t) = f_{1x}(t) + f_{D_{xlin}}(t) = (C_M)[\rho_w(\pi/4)D^2/4]\dot{u} + (1/2)(\rho_w D)(\bar{C}_D)u \quad (6.21)$$

where

$$f_{D_{xlin}}(t) = (1/2)(\rho_w D)(\bar{C}_D)u \quad (6.22)$$

where  $\bar{C}_D$  linearized equivalent drag coefficient.

The linearization factor between the drag components of Equation 6.17 and 6.21 is obtained by equating the energy in a quarter of the oscillation period, viz.

$$\int_0^{(T/4)} C_D |u| u dt = \int_0^{(T/4)} (\bar{C}_D u) u dt \quad (6.23)$$

In regular waves, the above linearization leads to

$$f_{D_{xlin}}(t) = (1/2)(\rho_w D)(\bar{C}_D)u = (1/2)(\rho_w D)\{C_D(1.2004\rho_u)\}u \quad (6.24)$$

Hence, equivalent drag coefficient ( $\bar{C}_D$ ) in Equation 6.19 is given as  $\{C_D(1.2004\sigma_u)\}$ . For regular waves, the value of standard deviation of the wave particle velocity is  $\sigma_u$ , given by  $(u_a/\sqrt{2})$ , where  $u_a$  is the amplitude of the wave particle velocity. In irregular (or random) waves, the above linearization leads to

$$\begin{aligned} f_{D_{xlin}}(t) &= (1/2)(\rho_w D)(\bar{C}_D)u = (1/2)\rho_w D \{C_D \sqrt{(8\pi/3)}\sigma_u\}u \\ &= (1/2)(\rho_w D)\{C_D(1.596\sigma_u)\}u \end{aligned} \quad (6.25)$$

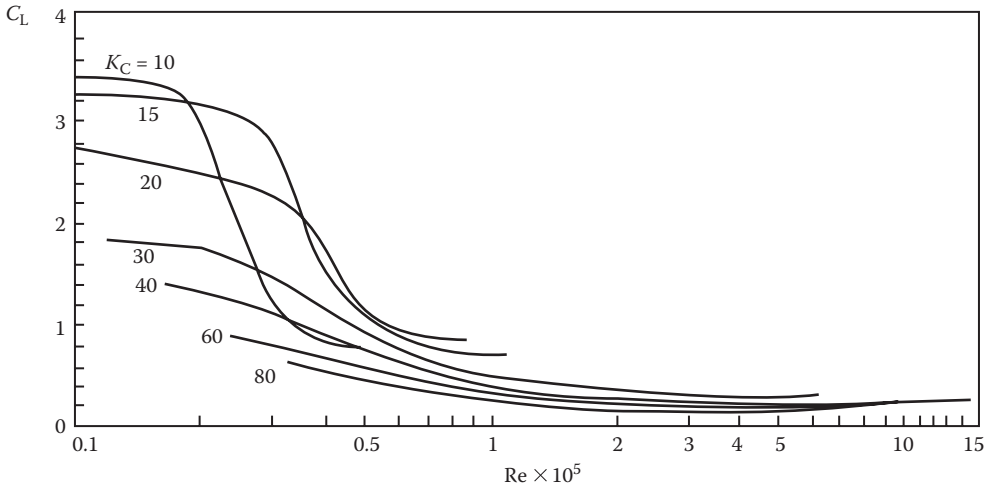
where  $\sigma_u$  is the standard deviation of the velocity spectrum and  $u(t)$  is the random velocity time trace. Hence, for a random wave  $\bar{C}_D$  is given as equal to  $C_D[1.596\sigma_u]$ .

In addition to the in-line wave forces given by Morison–O'Brien's equation, the lift forces  $F_L$  and the slamming forces  $F_S$  are usually neglected in computing the global responses, but they could become important for designing the local members. For a member section of unit length, these forces are expressed as

$$\begin{aligned} f_{y_{lift}} &= (1/2)\rho_w C_L D(w|w|); \text{ and} \\ f_{z_{slamming}} &= (1/2)\rho_w C_S D(w|w|) \end{aligned} \quad (6.26)$$

where  $C_L$  and  $C_S$  are the lift and slamming coefficients, respectively, and  $w$  is the fluid velocity in the vertical direction. Lift forces are perpendicular to the local member axis; the fluid velocity  $w$  and the lift forces are related to the vortex shedding frequency. The vortex shedding frequency  $n$  is dependent on the Strouhal number,  $N_s$ , which is dependent on structural member shape and Reynolds number,  $Re$ . Typically  $N_s$  will be 0.2, when  $[(2.5) \times (10^2) < Re < (2.5) \times (10^5)]$ . Wave





**FIGURE 6.16** Dependence of lift force coefficient on flow parameters  $Re$  and  $K_C$ . (From N. Haritos, *Electronic Journal of Structural Engineering [EJSE] Special Issue: Loading on Structure*, pp. 60, 2007. With permission.)

slamming forces acting on the underside of horizontal members near the mean water level are impulsive and nearly vertical. Lift forces can be estimated by taking  $C_L \sim 1.3C_D$ . The dependence of the lift coefficient on the Reynolds and Keulegan–Carpenter numbers is shown in Figure 6.16 [28]. For tubular members, the wave slamming coefficient  $C_S$  is given by  $C_S \sim \pi$  [21]. To compute the total forces acting on the member, the length of the member has to be taken into consideration.

### 6.3.4.3 Wave Forces Obtained from Airy's Linear Wave Theory

Using small amplitude waves and linear waves obtained using Airy's wave theory (given in Section 3.4.2), the total wave forces acting on the vertical cylinder can be taken as [29]

$$F_{\text{Total}_x}(t) = F_{I_x}(t) + F_{D_x}(t) \quad (6.27)$$

where  $F_{I_x}$  is the inertial force in the  $x$ -direction and  $F_{D_x}$  is the drag force in the  $x$ -direction. The total force acting on the vertical cylindrical member is obtained by using Equation 6.17 in Equation 6.19. The drag force is given by

$$F_{D_x}(t) = [(\pi\rho_w DH^2 LC_D)/(16T^2)][\{2k(\eta + d) + \sinh 2k(\eta + d)\}/\sinh^2(kd)] \\ * |\cos(kx - \omega t)| \cos(kx - \omega t) \quad (6.28)$$

where  $a = (H/2) =$  wave amplitude,  $\eta =$  wave amplitude at time  $t$ ,  $(H/2) \cos(kx - \omega t)$ ,  $H =$  wave height,  $\kappa = (2\pi/L)$ ,  $\omega = (2\pi/T)$ ,  $L$  the wavelength, and  $T$  the wave period. In a similar manner, the inertial force is given by

$$F_{I_x}(t) = [(\pi^2\rho_w D^2 HLC_M)/(4T^2)][\sinh k(\eta + d)/\sinh(kd)]\{\sin(kx - \omega t)\} \quad (6.29)$$

The total moment acting on the vertical cylinder, about its base, is given as [29]

$$M_{\text{Total}_y} = M_{D_y} + M_{I_y}$$

The wave drag moments about the base are given by

$$M_{D_y}(t) = -[(\rho_w DH^2 L^2 C_D)/(64T^2)] * [2k^2(\eta + d)^2 + 2k(\eta + d)\sinh 2k(\eta + d) - \cosh 2k(\eta + d) + 1] / \sinh^2(kd) * |\cos(kx - \omega t)| \cos(kx - \omega t) \quad (6.30a)$$

and the inertial wave forces acting on the vertical cylinder are (about the base) given as

$$M_{I_y}(t) = -[(\pi\rho_w D^2 HL^2 C_M)/(8T^2)] [k(\eta + d)\sinh k(\eta + d) - \cosh k(\eta + d) + 1] / \sinh kd \sin(kx - \omega t) \quad (6.30b)$$

To determine the maximum of the wave force acting on the vertical cylinder, one has to determine the maximum drag and inertial forces acting on the cylinder at time =  $t_1$ , and then add them together. It can also be written as

$$F_{\max} = \sqrt{[(F_{D_{\max}})^2 + (F_{I_{\max}})^2]} \quad (6.31)$$

The maximum drag force is obtained as

$$F_{D_{\max}} = [(\pi\rho_w DH^2 LC_D)/(16T^2)] [2k(H/2 + d) + \sinh 2k(H/2 + d)] / \sinh^2(kd) \quad (6.32)$$

The maximum inertia force is obtained as

$$F_{I_{\max}} = [(\pi^2\rho_w D^2 HLC_M)/(4T^2)] [\sinh k(H/2 + d) / \sinh(kd)] \quad (6.33)$$

The relative significance of the drag and inertia forces on the column can be obtained by determining the ratio between the maximum drag and inertial forces as

$$(F_{D_{\max}})/(F_{I_{\max}}) = A_1(H/D), \text{ with} \\ A_1 = \{1/(4\pi)\}(C_D/C_M)[(2k)(H/2 + d) + \sinh\{(2k)(H/2 + d)\}] / [\sinh(kd)\{\sinh k(H/2 + d)\}] \quad (6.34)$$

The approximate values of  $A_1$ , for various values of  $d/L$ , taking  $C_D/C_1 = 0.5$ , are given in Table 6.9; the ratios of  $H/L$  are varied from 0.03 to 0.15. It can be seen that when  $d/L$  is greater than 0.30 and  $0.03 > H/L > 0.07$ , the ratio of the drag force by inertial force becomes less than 0.10 ( $H/D$ ). Thus, for this restricted water depth ( $d/L < 0.30$ ) and possible wave heights (since wave breaks at  $H/L$  ratio  $> 0.08$ ), the drag forces will be much less than 10% of the inertia forces even when the  $H/D$  ratio is equal to unity (which means that the diameter of the structure is equal to the wave height). For such cases, the effect of the drag forces can be neglected in an approximate analysis. When  $H/D$  ratio becomes larger than 1.0, the ratio of drag forces to inertial forces will become larger than 10%.

As indicated in Figure 6.12, when  $d/L$  ratio is greater than 0.50 [or  $L/(gT^2) > 0.08$ ] and  $H/L$  ratio is smaller than 0.05 [or  $L/(gT^2) < 0.008$ ], the linear (Airy's) wave theory can be used to compute the wave forces. When  $d/L$  ratio is smaller than 0.5 or  $H/L$  ratio is greater than 0.05, other wave theories must be used to compute the wave forces. For nonlinear waves, second-order Stokes waves, given

**TABLE 6.9**  
**Value of  $A_1$  in Equation 6.34**

(d/L) Ratio	(H/L) = 0.03		(H/L) = 0.07	
	(2k)(d + H/2)	$A_1(H/D)$	(2k)(d + H/2)	$A_1(H/D)$
0.03	0.565	0.847	0.817	0.866
0.07	1.068	0.367	1.320	0.378
0.15	2.074	0.178	2.325	0.187
0.30	3.958	0.105	4.210	0.115
0.50	6.472	0.090	6.723	0.101
1.00	12.755	0.0875	13.066	0.102
$\infty$	$\infty$	0.0875	$\infty$	0.098

Note: It is assumed that  $(H/D) = 1.0$ .

in Equations 3.48 through 3.52 (or higher-order Stokes waves),  $Re$  can be used along with the values given in Table 3.8 for wave particle velocities and accelerations for wave force computation.

#### 6.3.4.4 Effects of Relative Motion of the Structure

In Equations 6.15 through 6.18, the vertical cylindrical structural motions are assumed to be zero, when the drag and inertia wave forces exerted on the cylindrical structure are computed. In any offshore environment, the structure will experience small motions under the action of wind/wave/current forces exerted on it. This relative motion of the structure to its initial position in space will influence the forces exerted on the structure. When the motion of the structure is considered, then the wave forces exerted on the structure will be modified as follows, viz., Equations 6.15 and 6.16 will become

$$f_I = [\rho_w C_M (\pi D^2 / 4)] (\dot{u}) - \rho_w (C_M - 1.0) (\pi D^2 / 4) \ddot{x} \quad (6.35)$$

and

$$f_D = [(1/2)(\rho_w D) C_D] (u - \dot{x}) |u - \dot{x}| \quad (6.36)$$

The last term in Equation 6.35 represents the force associated with the water acceleration, due to the pile motion; since the relative acceleration of the fluid with respect to a moving structure is given by  $(\dot{u} - \ddot{x})$ , and the fluid associated with the structural motion is given by  $\{\rho_w (C_M - 1.0) (\pi D^2 / 4)\}$ . If  $F$  represents the additional forces associated with the motion of the unit length of the vertical cylindrical structure (such as those associated with the structural damping, wind, and current forces, etc.) and  $f_x$ , the forces associated with the wave motion over the structure, then using Newton's first law of motion, the equation for the motion of the unit segment of the vertical cylindrical structure can be written as

$$m\ddot{x} = F + f \quad (6.37)$$

Using Equations 6.35 and 6.36, Equation 6.37 can be written as

$$\begin{aligned} m\ddot{x} = & [\rho_w C_M (\pi D^2 / 4)] (\dot{u}) - \rho_w (C_M - 1.0) (\pi D^2 / 4) \ddot{x} \\ & + [(1/2)(\rho_w D) C_D] (u - \dot{x}) |u - \dot{x}| \end{aligned} \quad (6.38)$$

Equation 6.38 can be rearranged to give the final equation of motion for the unit length of the vertical cylindrical structure as

$$(m + m')\ddot{x} = [\rho_w C_M (\pi D^2 / 4)](\dot{u}) + [(1/2)(\rho_w D)C_D](u - \dot{x})|u - \dot{x}| \quad (6.39)$$

$$\text{where } m' = \rho_w (C_M - 1.0)(\pi D^2 / 4)$$

$m'$  is defined as the mass (of water) that will be added to the structural mass of the unit length of the structure to give the equivalent effect produced due to its submergence in water; in technical terms,  $m'$  is called as the added mass of water.

Added mass of structure is the inertial mass of fluid added to an accelerating/decelerating structure that is set in motion by the surrounding fluid as the fluid moves past the structure. For simplicity in calculation, it can be represented by the product of a dimensionless coefficient and the mass of a volume of fluid, displaced by the moving structure. The dimensionless coefficient is called the added mass coefficient of the structure. The structural damping and stiffness terms associated with Equation 6.39 can be added to the left-hand side to fully represent the complete equation of motion.

### Example 6.7

A 9-in. diameter vertical pile is fixed to the seabed, in 30.0 ft. depth of water. It is subjected to 2.0 ft. high waves of 20.0 ft. wavelength. Determine the maximum force and the maximum moment about the base. Take  $\rho_f = 2.00$  slugs/ft.<sup>3</sup>, and  $\nu$ , the kinematic viscosity of fluid =  $1.05 \times 10^{-5}$  ft.<sup>2</sup>/s. Also  $C_D = 1.0$  and  $C_M = 2.0$ .

Since  $d/L = 30/20 = 1.5 > 0.5$ , the pile is located in deep water; use deepwater formulations.

Using  $L = (gT^2)/(2\pi)$ ,  $T^2 = (2\pi)(20.0)/(32.2) = 3.903$ . Hence,  $T = 1.976$  s.

From Table 3.7,  $u_{\max} = (\pi H/T)e^{kz} = [(\pi) \times (2.0)/(1.976)]e^{(2\pi)(1.0)} = 4.3534$  ft./s.

To find Re, find the maximum  $u$  at  $z = 0.0$  ft.; hence,  $\max(u) = (2\pi)(2.0)/(1.976) = 3.178$  ft./s.

$Re = [\max(u)](D/\nu) = (3.178)(0.75)/(1.05 \times 10^{-5}) = (2.27)(10^5)$ ; hence, flow is subcritical; see Figure 6.10.

$K_C = [\max(u)](T/D) = (3.178)(1.976)/(0.75) = 8.373 < 10.0$ ; hence, inertia force dominates.

Hence, the total force is given by Equation 6.27 as  $F_{\text{Total}_x}(t) = F_x(t) + F_{D_x}(t)$ .

$$F_{D_x}(t) = [(\pi\rho_w DH^2 LC_D)/(16T^2)]\{[2k(\eta + d) + \sinh 2k(\eta + d)]/\sinh^2(kd)\}^* |\cos(kx - \omega t)| \cos(kx - \omega t) = 11.315 |\cos(2\pi/1.976)t| \cos\{(2\pi/1.976)t\} = 11.315 |\cos(3.18t)| \cos(3.18t)$$

$$F_{I_x}(t) = [(\pi^2 \rho_w D^2 H LC_M)/(4T^2)] [\sinh k(\eta + d)/\sinh(kd)] \{\sin(kx - \omega t)\} = -77.87 \sin(3.18t).$$

$$F_{\text{Total}_x}(t) = -77.87 \sin(3.18t) + 11.315 |\cos(3.18t)| \cos(3.18t) \text{ lbf.}$$

Maximum force occurs when  $(3.18t) \approx (3\pi)$ .

Hence,  $F_{\text{tot max}} = 77.871$  lbf.

Also the maximum moment is given by  $M_{\text{Total}_y} = M_{D_y} + M_{I_y}$ , where

$$M_{D_y}(t) = -[(\rho_w DH^2 L^2 C_D)/(64T^2)]^* \{[2k^2(\eta + d)^2 + 2k(\eta + d)\sinh 2k(\eta + d) - \cosh 2k(\eta + d) + 1]/\sinh^2(kd)\}^* |\cos(kx - \omega t)| \cos(kx - \omega t)$$

and

$$M_{ly}(t) = -[(\pi \rho_w D^2 H L^2 C_M) / (8 T^2)] \\ \{ [k(\eta + d) \sinh k(\eta + d) - \cosh k(\eta + d) + 1] / \sinh kd \} \sin(kx - \omega t)$$

Substituting the values of different variables, one gets

$$M_{\max} = 2166.08 \sin(3.18t) - 665.29 |\cos(3.18t)| \cos(3.18t).$$

The maximum of the above occurs when  $(3.18t) = (\pi/2)$ .  
Hence,  $M_{\text{tot max}} = 2166.08 \text{ lb ft}$ .

### Example 6.8

A pressure gauge, placed on top of a 1.0-m-diameter pipeline (which is located on the seabed, which is 10.0 m below the mean sea level), measures an average maximum wave pressure of 10.0 N/cm<sup>2</sup>. The average wave period is 10.0 s. Compute the wavelength, wave height, and wave pressure (exerted on top of the pipeline). Also compute the wave forces acting on the pipeline (per unit length), in the vertical direction, assuming the pipe to be rough. Use Airy wave theory. Unit mass of seawater = 1026 kg/m<sup>3</sup>.

As per Equation 3.41,

$$p = -\rho g z - \rho \frac{\partial \phi}{\partial t} = -\rho g z + (\rho g H / 2) [\cosh k(d + z) / \cosh(kd)] \cos(kx - \sigma t) = -p = -\rho g z + (\rho g H / 2) \\ [\cosh k(d + z) / \cosh(kd)] = -(1026)(9.81)(-9) + (1026)(9.81)(H/2)$$

$$\times [\cosh \{ (2\pi/L)(10.0 - 9.0) \} / \cosh \{ (2\pi/L)(10) \}] = 90,585.54 + 5032.53H [\cosh(2\pi/L) / \cosh(20\pi/L)].$$

The wavelength  $L$  is computed iteratively by using the equation  $L = (gT^2/2\pi) \tanh(2kd)$ ;  $L$  is obtained as = 92.42 m.

From the pressure gauge readings, measured  $p_{\text{average}} = 10.0 \text{ N/cm}^2 = (10)(100)^2 = 100,000 \text{ N/m}^2$ .

Hence,  $p = 100,000 = 90,585.54 + 5032.53 (H) [\cosh (2\pi/92.42) / \cosh(20\pi/92.42)] = 90,585.59 + 4070.86H$ .

Wave height is obtained as  $H = (100,000 - 90,585.54) / (4070.86) = 2.32 \text{ m}$ .

The wave force in the vertical direction, acting on the pipeline, is given as [30]

$$F_z = C_M \rho V dw/dt + (1/2) C_D \rho A w |w| + (1/2) C_L \rho A u |u| + (1/2) C'_L \rho A.$$

In the above equation,  $V = (\pi D^2/4) = 0.7854 \text{ m}^2$ ;  $A = D = 1.0 \text{ m}$ ;  $C_M = 1.0$ ;  $C_D = 0.55$ ;  $C_L = 0.45$ ; and  $C'_L = 0.45$ .

$$d(w)/dt = -[(2\pi^2 H) / T^2] [\sinh k(d + z) / \sinh(kd)] \sin(kx - \omega t) = -0.3331 \sin(kx - \omega t).$$

$$u = (\pi H / T) [\cosh(k(d + z) / \sinh(kd)) \cos(kx - \omega t) = 1.0025 \cos(kx - \omega t).$$

$$w = (\pi H / T) [\sinh(k(d + z) / \sinh(kd)) \sin(kx - \omega t) = 0.03382 \sin(kx - \omega t).$$

The uplift force acting on the pipeline =  $(1.0)(1026)(0.7854) \{ -0.3331 \sin(kx - \omega t) \} + (1/2)(0.55) (1026)(1.0) \{ (0.0382) \sin(kx - \omega t) \} \{ (0.0382) \sin(kx - \omega t) \} + (1/2)(0.45)(1026)(0.45) \{ 1.0025 \cos(kx - \omega t) \} \{ 1.0025 \cos(kx - \omega t) \} + (1/2)(0.45)(1026.0)(1.0) = -268.42 \sin(kx - \omega t) + 0.647 \{ \sin(kx - \omega t) \} \{ \sin(kx - \omega t) \} + 232.006 \{ \cos(kx - \omega t) \} \{ \cos(kx - \omega t) \} + 230.85$ .

When  $\sin(kx - \omega t) = 1.0$ ,  $\cos(kx - \omega t) = 1.0$ , and uplift force on the pipeline =  $-268.42 + 0.647 + 0.0 + 230.85 = -36.93 \text{ N}$ .

When  $\sin(kx - \omega t) = 0.0$ ,  $\cos(kx - \omega t) = 1.0$ , and uplift force on the pipeline =  $0.0 + 0.0 + 232.01 + 230.85 = 462.86 \text{ N}$ .

**Example 6.9**

Determine the maximum wave force exerted by Airy waves of height 20.0 ft. and length 300.0 ft. on a 4.0-ft. diameter pile, extending from the seafloor to above the maximum water surface elevation. Assume the water depth at the site to be 80.0 ft. Take  $C_D = 1.0$  and  $C_M = 2.0$ .

$$L = 300.0 \text{ ft.} = [gT^2/(2\pi)] \tan(2\pi d/L) = [(32.2)(T^2)/(2\pi)] \tan [(2\pi)(80)/300] = 4.778T^2.$$

$$T^2 = 62.788.$$

Hence,  $T = 7.924 \text{ s}$ .

According to Equation 6.28, the drag force exerted on the pile is given as (with  $x = 0.0$ )

$$F_{D_x}(t) = [(\pi \rho_w D H^2 L C_D)/(16T^2)] \{ [2k(\eta + d) + \sinh 2k(\eta + d)] / \sinh^2(kd) \}^* |\cos(kx - \omega t)| \cos(kx - \omega t) = \\ [(\pi)(1.99)(4.0)(20.0)^2(300)(1.0)/\{(16)(7.924)^2\}] \{ [(2)(2\pi/300)(10 + 80) + \sinh \{(2)(2\pi/300)(10 + 80)\}] / \{\sinh^2 \\ (2\pi \times 80.0/300)\} \} |\cos(\omega t)| \cos(\omega t) = [2987.0 (3.7699 + 21.6766)/(6.6418)] |\cos(\omega t)| \cos(\omega t) = 11,444.09 \\ |\cos(\omega t)| \cos(\omega t) \text{ lb.}$$

According to Equation 6.29, the inertial force exerted on the pile is given as (at  $x = 0$ ,  $\omega t = \pi/2$  and  $z = 80.0 \text{ ft.}$ )

$$F_i(t) = [(\pi^2 \rho_w D^2 H L C_M)/(4T^2)] [\sinh k(\eta + d) / \sinh(kd)] \{\sin(kx - \omega t)\} \\ = -[(\pi^2)(1.99)(4)^2(20)(300)(2.0)/\{(4)(7.924)^2\}] \times [\sinh\{(2\pi \times 80)/300\} / \sinh(2\pi \times 80/300)] \sin(\omega t) \\ = -15,104.23 \sin(\omega t)$$

$$\text{Hence, } F_{\max} = [(11,444.04)^2 + (15,104.23)^2]^{(1/2)} = 18,881.44 \text{ lb.}$$

**6.3.4.5 Wave Forces on Arbitrarily Oriented Cylindrical Members**

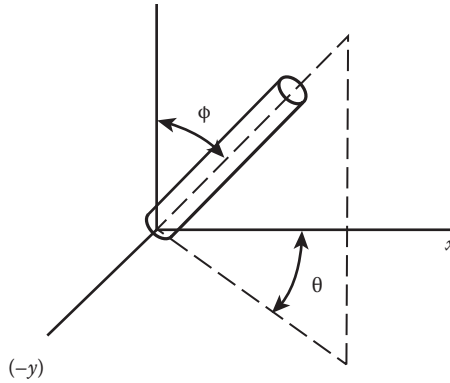
When forces acting on a fixed offshore platform are to be computed, the procedure presented above will not be sufficient. Since the platform contains a number of arbitrarily oriented tubular members, subjected to regular/irregular wave action in the seaway, the formulation developed by Chakrabarti et al. [31] has to be used to compute the wave forces. This will involve the resolving of water particle velocity and acceleration components into components normal (to the member) and tangential to the (longitudinal) axis of the cylindrical member, shown in Figure 6.17 [31]. For the sake of convenience let us assume that the wave is propagating in the positive  $x$ -direction, and the arbitrary inclinations of the cylinder be  $\phi$  (to the  $+z$ -axis) and  $\theta$  (from the projection of the member on the horizontal  $xy$ -plane, as shown in Figure 6.17). The resulting water particle motion will have (i) horizontal ( $u$ ) and vertical ( $w$ ) velocities and (ii) horizontal ( $a_x$ ) and vertical ( $a_z$ ) accelerations. Since the tangential drag coefficient (to be used in the force computations) is usually smaller than 0.05, the effect of the tangential component of the water particle velocities and accelerations can be safely neglected in the computation of wave forces.

The magnitude  $v$  of the water velocity normal to the cylinder axis is given by

$$v = [u^2 + w^2 - (c_x u + c_z w)^2]^{(1/2)}, \quad (6.40)$$

and the components of the above normal velocity, in the  $x$ ,  $y$ , and  $z$  directions are given, respectively, by

$$\begin{aligned} u_n &= u - c_x(c_x u + c_z w), \\ v_n &= c_y(c_x u + c_z w), \\ w_n &= w - c_z(c_x u + c_z w) \end{aligned} \quad (6.41)$$



**FIGURE 6.17** Arbitrarily oriented cylindrical member submerged in the ocean and subjected to wave forces; only the negative portion of the  $y$ -axis is shown. (From S.K. Chakrabarti et al., *Wave Forces on a Randomly Oriented Tube*, Proceedings of the Seventh Offshore Technology Conference, Houston, TX, pp. 433–441, 1975. With permission.)

where

$$\begin{aligned} c_x &= \sin(\phi) \cos(\theta), \\ c_y &= -\sin(\phi) \sin(\theta) \\ c_z &= \cos(\phi) \end{aligned} \quad (6.42)$$

The components of the water particle accelerations in the  $x$ ,  $y$ , and  $z$  directions are given, respectively, by

$$\begin{aligned} a_{nx} &= a_x - c_x(c_x a_x + c_z a_z), \\ a_{ny} &= -c_y(c_x a_x + c_z a_z) \\ a_{nz} &= a_z - c_z(c_x a_x + c_z a_z) \end{aligned} \quad (6.43)$$

Using the above values of the various velocity and acceleration components, the components of the respective wave forces, per unit length of cylindrical member, are obtained by using the generalized form of Morison–O’Brien’s equation as

$$\begin{aligned} f_x &= (1/2)\rho_w C_D(D)v u_n + \rho_w C_I(\pi D^2/4)a_{nx}, \\ f_y &= (1/2)\rho_w C_D(D)v v_n + \rho_w C_I(\pi D^2/4)a_{ny}, \\ f_z &= (1/2)\rho_w C_D(D)v w_n + \rho_w C_I(\pi D^2/4)a_{nz} \end{aligned} \quad (6.44)$$

The total forces, in the respective directions, are obtained by the numerical integration of the respective wave forces per unit length, over the whole length of the member, viz.

$$F_x = \int_s f_x ds, F_y = \int_s f_y ds, \text{ and } F_z = \int_s f_z ds \quad (6.45)$$



In case the variation of the particle velocities and accelerations, over the length of the submerged and inclined members, are not appreciable, then the total forces on the individual members can be obtained as

$$F_x = f_x L, F_y = f_y L, \text{ and } F_z = f_z L. \tag{6.46}$$

**Example 6.10**

Determine the horizontal and vertical components of the wave force per unit length acting at the midlength of member 1–2 of the side face shown in Figure E6.4, assuming wave-induced water motion described by  $u = 13.7$  ft./s,  $v = 4.21$  ft./s,  $a_x = 4.01$  ft./s<sup>2</sup>, and  $a_y = -6.76$  ft./s<sup>2</sup>.

As per Equation 6.40, water velocity normal to the member 1–2 is given by

$$v = [u^2 + w^2 - (c_x u + c_z w)^2]^{(1/2)}.$$

As per Equation 6.41, the velocity components are given by

$$u_n = u - c_x(c_x u + c_z w)$$

$$v_n = c_y(c_x u + c_z w)$$

$$w_n = w - c_z(c_x u + c_z w)$$

As per Equation 6.42, the directional cosine components are

$$c_x = \sin(\phi)\cos(\theta)$$

$$c_y = -\sin(\phi)\sin(\theta)$$

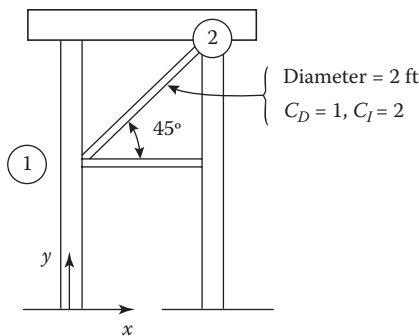
$$c_z = \cos(\phi)$$

As per Equation 6.43, the acceleration components are

$$a_{nx} = a_x - c_x(c_x a_x + c_z a_z)$$

$$a_{ny} = -c_y(c_x a_x + c_z a_z)$$

$$a_{nz} = a_z - c_z(c_x a_x + c_z a_z)$$



**FIGURE E6.4** Offshore tower. ( $C_I = C_M$ ).

As per Equation 6.44, the force components are

$$f_x = (1/2)\rho_w C_D(D)v u_n + \rho_w C_l(\pi D^2/4)a_{nx}$$

$$f_y = (1/2)\rho_w C_D(D)v v_n + \rho_w C_l(\pi D^2/4)a_{ny}$$

$$f_z = (1/2)\rho_w C_D(D)v w_n + \rho_w C_l(\pi D^2/4)a_{nz}$$

Also, axes have been changed from Figure 6.17 to Figure E6.4.  $x \equiv x$ ,  $y \equiv z$ , and  $z \equiv -y$ ; hence,  $u \equiv u$ ;  $v \equiv w$ ;  $w = -v$ ;  $a_x \equiv a_x$ ;  $a_y = a_z$ ; and  $a_z = -a_y$ .

In this problem,  $\theta = 0^\circ$  and  $\phi = 45^\circ$ .

Hence,  $c_x = 1/\sqrt{2}$ ,  $c_y = 0.0$ ,  $c_z = 1/\sqrt{2}$ . Hence,  $v = [u^2 + v^2 - (1/\sqrt{2}u + 1/\sqrt{2}v)^2]^{(1/2)} = [(1/2)(u - v)^2]^{(1/2)} = [(1/2)(13.7 - 4.21)^2]^{(1/2)} = 6.71$  m/s.

$$\text{Also, } u_n = u - (1/\sqrt{2})(1/\sqrt{2}u + 1/\sqrt{2}v) = (1/2)(u - v) = (1/2)(13.7 - 4.21) = 4.745 \text{ ft./s.}$$

$$v_n = v - (1/\sqrt{2})(1/\sqrt{2}u + 1/\sqrt{2}v) = (1/2)(u - v) = (1/2)(4.21 - 13.7) = -4.745 \text{ ft./s.}$$

$$a_{nx} = a_x - (1/\sqrt{2})(1/\sqrt{2}a_x + 1/\sqrt{2}a_y) = (1/2)(a_x - a_y) = (1/2)[4.01 - (-6.76)] = 5.385 \text{ m/s}^2.$$

$$a_{ny} = a_y - (1/\sqrt{2})(1/\sqrt{2}a_x + 1/\sqrt{2}a_y) = (1/2)(a_y - a_x) = (1/2)[-6.76 - (4.01)] = -5.385 \text{ m/s}^2.$$

The forces per unit length, in the respective directions, are given as

$$f_x = (0.5)(64.0/32.2)(1.0)(2.0)(6.71)(4.745) + (64.0/32.2)(2.0)(\pi)(2.0^2/4)(5.385) = 63.28 + 67.28 = 130.56 \text{ lbf/ft.}$$

$$f_y = (0.5)(64.0/32.2)(1.0)(2.0)(6.71)(-4.745) + (64.0/32.2)(2.0)(\pi)(2^2/4)(-5.385) = -63.28 - 67.28 = -130.56 \text{ lbf/ft.}$$

### 6.3.4.6 Wave Forces on Large Diameter Structures

When (diameter/wave length) ratio of a structure, shown in Figure 6.13, is greater than 0.2, the effect of incident and diffracted wave potentials should be considered to compute the wave forces exerted on a large diameter cylindrical structure [28, 32]. The forces are obtained by integrating the incident and diffraction wave pressure distribution over the whole submerged height of the cylindrical structure; the wave moments are obtained by taking moments of the pressure distribution about the base of the structure. The wave diffraction force and wave diffraction moment (about the base) are obtained as

$$F(t) = (2\rho_w g H/k^2)[A(ka)\tanh(kd)]\cos(\omega t - \alpha) \quad (6.47)$$

and

$$M(t) = (2\rho_w g H/k^2)A(ka)[(kd)\tanh(kd) + \text{sech}(kd) - 1]\cos(\omega t - \alpha) \quad (6.48)$$

where

$$A(ka) = [\{J_1'(ka)\}^2 + \{Y_1'(ka)\}^2]^{(1/2)} \text{ and} \quad (6.49)$$

$$\alpha = (\{J_1'(ka)\}/\{Y_1'(ka)\})$$

with  $a$  = radius of the cylindrical structure =  $(D/2)$ ,  $k = (2\pi/L)$ ,  $D$  the diameter of the cylindrical structure,  $(\cdot)$  denotes differentiation of the function with respect to radius  $r$ ,  $J_1'(ka)$  and  $Y_1'(ka)$

represent Bessel functions of the first and second kinds of the first order, respectively. For other shapes of structures (nonylindrical) special purpose software such as WAMIT [33] should be used.

**Example 6.11**

A proposed navigational aid tower (to mark the shallow region), shown in Figure E6.5, is supported by a single steel column 22.5 ft. high, having an outside diameter of 20.0 ft. The wall thickness is 1 in. The deck on top of the column supports the navigational aid. Assume that the column is supported on top of a concrete footing of diameter 30.0 ft. (which is embedded below the seabed level) and 5.0 ft. deep, as shown in Figure E6.5 [19]. Compute the wave forces acting on the cylinder due to an Airy wave of height 4.0 ft. and period 4.0 s, using (i) airy wave theory for small cylinders and (ii) diffraction wave theory for large diameter structures. Also, compute the wave moments acting at the base of the cylindrical structure. Take  $C_D = 1.0$  and  $C_M = 2.0$ .

To compare the results, the force is integrated from the msl to the seabed; hence,  $\eta$  is taken as zero.

- (i) Using Morison–O’Brien’s equation for a cylinder

$$F_{D_x}(t) = [(\pi \rho_w D H^2 L C_D) / (16 T^2)] \{ [2k(\eta + d) + \sinh 2k(\eta + d)] / \{ \sinh^2(kd) \} \} \cos(kx - \omega t) \cos(kx - \omega t) = [(\pi)(1.99)(20.0)^2(68.28)(1.0) / \{(16)(4.0)^2\}] \{ [(4\pi)(13) / (68.28) + \sinh(4\pi)(13) / (68.28)] / \{ \sinh^2 \{ (2)(\pi)(13) / (68.28) \} \} \} \cos(kx - \omega t) \cos(kx - \omega t) = (666.99) \{ [2.391 + 5.425] / (2.258) \} \cos(kx - \omega t) \cos(kx - \omega t) = 2308.8 |\cos(kx - \omega t)| \cos(kx - \omega t) \text{ lb.}$$

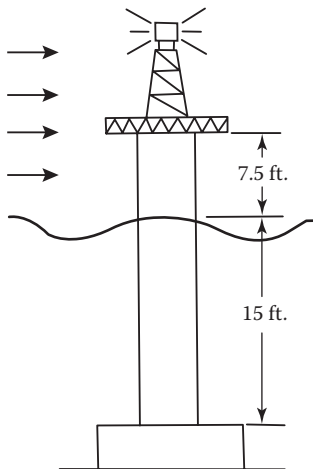
$$F_{I_x}(t) = [(\pi^2 \rho_w D^2 H L C_M) / (4 T^2)] [\sinh k(\eta + d) / \sinh(kd)] \{ \sin(kx - \omega t) \} = [(\pi^2)(1.99)(20)^2(4.0)(68.28)(2.0) / (4 \times 4^2)] \times [\sinh(2\pi \times 13 / 68.28) / \sinh(2\pi \times 13 / 68.28)] \{ \sin(kx - \omega t) \} = 67,052.7 (1.503 / 1.503) \{ \sin(kx - \omega t) \} = 67,052.7 \{ \sin(kx - \omega t) \} \text{ lb.}$$

$$F_{\max} = \sqrt{\{ (67,053)^2 + (2309)^2 \}} = 67,093 \text{ lb.}$$

The force acting on the cylinder is inertial force dominated.

- (ii) The wave force on the cylinder, according to diffraction wave theory is given by Equation 6.47 by

$$F(t) = (2\rho_w g H / k^2) [A(ka) \tanh(kd)] \cos(\omega t - \alpha),$$



**FIGURE E6.5** Navigational aid tower. (From T.H. Dawson, *Offshore Structural Engineering*, Courtesy of Prentice Hall Inc., Upper Saddle River, NJ, p. 70 and 94, 1983. With permission.)

where

$$A(ka) = [J_1'(ka)]^2 + \{Y_1'(ka)\}^2]^{(1/2)}$$

$$\alpha = (J_1'(ka))/\{Y_1'(ka)\}$$

From the given data,  $a = D/2 = 20.0/2 = 10.0$  ft.;  $T = 4.0$  s;  $d = 13.0$  ft.;  $L = [(gT^2)/(2\pi)]\tanh(2\pi d/L)$ ; solving this equation iteratively, one obtains  $L = 68.28$  ft.

As per the recurrence relations between Bessel functions and their derivatives  $J_n'(ka) = (1/ka)[(ka)J_{n-1}(ka) - nJ_n(ka)]$ ; hence,  $J_1'(ka) = J_0(ka) - (1/ka)J_1(ka)$ ; similarly,  $Y_1'(ka) = Y_0(ka) - (1/ka)Y_1(ka)$ .

$$ka = (2\pi/L)(D/2) = (\pi D/L) = (\pi)(20.0)/(68.28) = 0.9202.$$

$$J_0(0.9202) \sim 0.82; J_1(0.9202) \sim 0.39$$

$$Y_0(0.9202) \sim 0.02; Y_1(0.9202) \sim -0.8$$

$$J_1'(ka) = J_0(ka) - (1/ka)J_1(ka) \sim 0.82 - (1/0.9202)(0.39) = 0.3961.$$

$$Y_1'(ka) = Y_0(ka) - (1/ka)Y_1(ka) \sim 0.02 - (1/0.9202)(-0.8) = 0.8894.$$

$$A(ka) = A(0.9202) = [J_1'(ka)]^2 + \{Y_1'(ka)\}^2]^{(1/2)} = [(0.3961)^2 + (0.8894)^2]^{(0.5)} = 0.9736$$

$$\tanh(kd) = \tanh[(2\pi)(13)/(68.28)] = 0.8325$$

$$\alpha = (J_1'(ka))/\{Y_1'(ka)\} = (0.3961/0.8894) = 0.4454.$$

$$F_{\max} = (2)(1.99)(32.2)(4.0)(0.9736)(0.8325)/[(2\pi)/(68.28)]^2 = 49,067.17 \text{ N}.$$

The diffraction force is nearly 73% of the inertial force computed by Morison–O'Brien's equation.

### 6.3.5 CURRENT FORCES

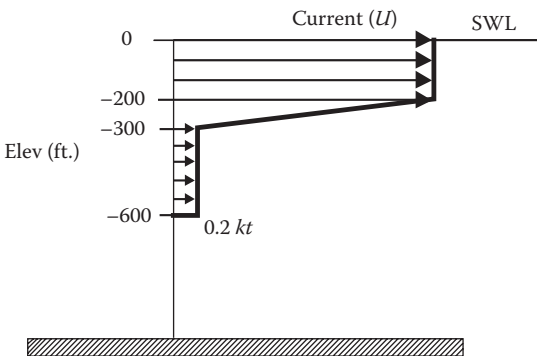
As explained in Section 3.5.1, the dominant sources of currents are tides, wind drag forces on top of the ocean surface, global circulation caused by temperature differences between various ocean thermal regimes and Coriolis effects (for instance, Gulf Stream), and river discharge. Currents impose drag forces on fixed or moored or floating ocean structures and modify their motions. Current velocity profiles vary vertically with the highest values near the surface, although this need not be true always, as shown earlier in Figure 3.41. In some stratified estuaries (or even deepwater oceans) where different types of density waters (fresh water from the river and sea water from the ocean) mix, a current shear may exist resulting in the bottom current being opposite to the surface current, as shown in Figure 3.41. Figure 3.41 shows some typical current profiles, those due to tide, wind, tide  $\pm$  wind, and river flow.

#### 6.3.5.1 Current Velocity Profiles

For engineering calculations, it is usually assumed that the depth variation of tidal currents follows the one-eighth power law (see Equation 6.10) and that for the wind generated currents, speed variation follows a linear form, being a maximum at the water surface and zero at the sea bottom; for design purposes the wind-generated current speed may be approximated to vary linearly from a maximum of 1.0% to 3.0% of the sustained wind speed, at the surface, to zero at the sea bottom. Wind-generated currents may exceed one knot (0.5144 m/s) under certain conditions and should be added in a vectorial manner, to the prevailing tidal currents.

During extreme wind or storm conditions, wind-generated currents will also exist simultaneously with the motion of surface water waves; in addition, the direction of wind-current velocities and wave particle velocities will not be along the same or opposite directions, but inclined at an angle. However, for the sake of conservative design practice, the wind-generated current may always be assumed to act in the same direction as that of wave particle velocities (holds true for deepwater depths); the wind-generated current profile, for the Gulf of Mexico, given in Figure 3.42, can be used as a typical current velocity profile for deep water depths; According to API codes, for shallow and intermediate water depths, the current velocities must be added vectorially to the wave particle velocities (based on wave–current joint probability) before using these velocities for force computation [34]. For instance, the design of offshore structures in the Gulf of Mexico are generally governed by the hurricane-related wind and wave conditions; the wave–current interactions must be taken into account by accounting for the interaction angle between the design wave direction, modification factor and the direction of wind-generated current. Details are to be obtained by consulting the code provisions. The various current profiles discussed in Section 3.5.1 are shown in a tabular format in Table 6.10.

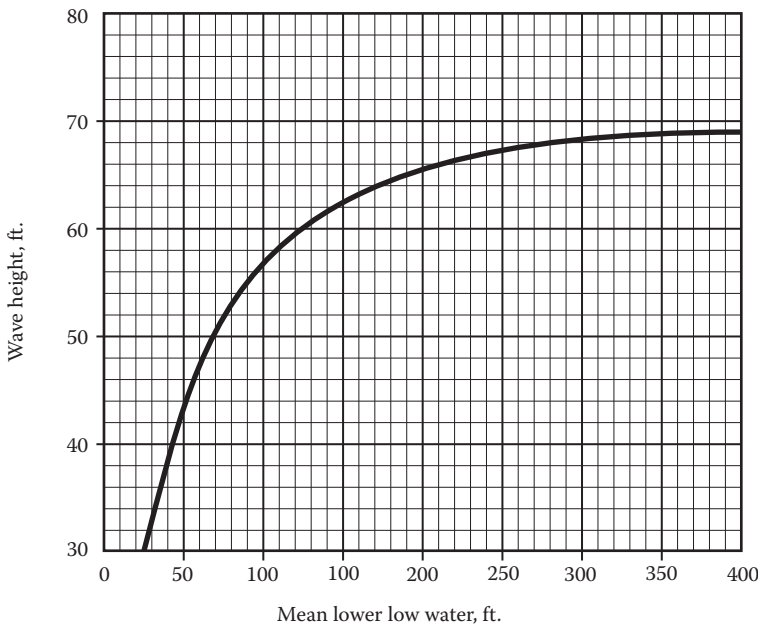
**TABLE 6.10**  
**Wind-Generated Current Velocity Equations Given Earlier in Section 3.5.1**

#	Type of Current	Governing Equation	Variables Used in the Equation
1	Tidal current	$U_z = U_{z_0} (z/z_0)^{(1/n)}$ in the direction of the tide.	$U_{z_0}$ = Wind speed at reference height $z_0$ . Also $n = 8$ for offshore context.
2	Wind-generated current	Varies linearly from a maximum of 1.0% to 3.0% of sustained wind velocity (at the ocean surface) to 0.0 at sea bottom.	–
3	Wind-generated current	$u_c = \left( u_{*_{\text{current}}} / \kappa (1 + z_{0_{\text{bottom}}} / h + z_{0_{\text{surface}}} / h) \right) \cdot$ $\left[ \ln \left\{ (z_{0_{\text{bottom}}} + z) / z_{0_{\text{bottom}}} \right\} - \ln \left\{ (h + z_{0_{\text{surface}}} - z) / (h + z_{0_{\text{surface}}}) \right\} \right]$ <p>with <math>u_{*_{\text{current}}}</math> the shear speed of current expressed as a function of reference wind speed <math>U_R</math> (<math>= (1.82) \times (10^{-3}) U_R</math>) and <math>\kappa</math> von Karman’s constant (<math>= 0.4</math>); Also <math>z_{0_{\text{bottom}}} = 0.2</math> and <math>z_{0_{\text{surface}}} = (3.3) \times (10^{-4})</math>. Also <math>U_R</math> is the reference wind speed at a height of 10.0 m above msl.</p>	$z_{0_{\text{surface}}} = (3.3) \times (10^{-4}) h$ ; $z_{0_{\text{bottom}}} (\approx 0.2)$ ; $h$ the depth of water at the site; and $z$ the depth of the point under consideration.
4	Wind/wave generated currents	The two current velocities are to be added as vectors; for the sake of conservative design, the velocities can be simply added assuming that there is no phase difference.	–
5	Wind- and wave-generated current—as per API code		–

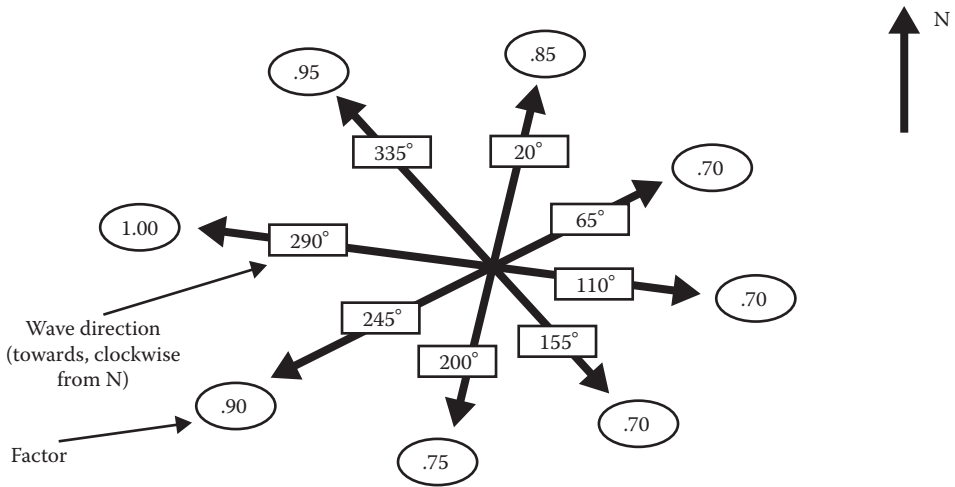
The use of last equation in Table 6.10 (#4) gives a current velocity profile similar to the tidal current velocity profile given in Figure 3.41 for tidal current velocity; this may be applicable to the Gulf of Mexico region where the water circulation is caused by temperature differences among various ocean thermal regimes, boundary currents, and Coriolis effects on wind, producing the Gulf Stream. For a general wind-shear situation on the ocean surface, the linear current velocity profile given in the second equation in Table 6.10 (#2) would be more relevant than that given in the last equation (#4).

When a structure is to be located at an ocean site, subjected to hurricane wave conditions (such as that encountered for an offshore structure, located in the Gulf of Mexico, at north of 27°N and west of 86°W) specific details are required; these details can be obtained from the code recommended specific to the site. The API code recommends the following for the hurricane-prone site in the Gulf of Mexico. The wave heights are to be based on the mean lower low water (MLLW) level of the ocean, and are to be modified for various water depths as shown in Figure 6.18 [35]. Figure 3.46 could be used to understand the various tidal level or datum referred to in this section.

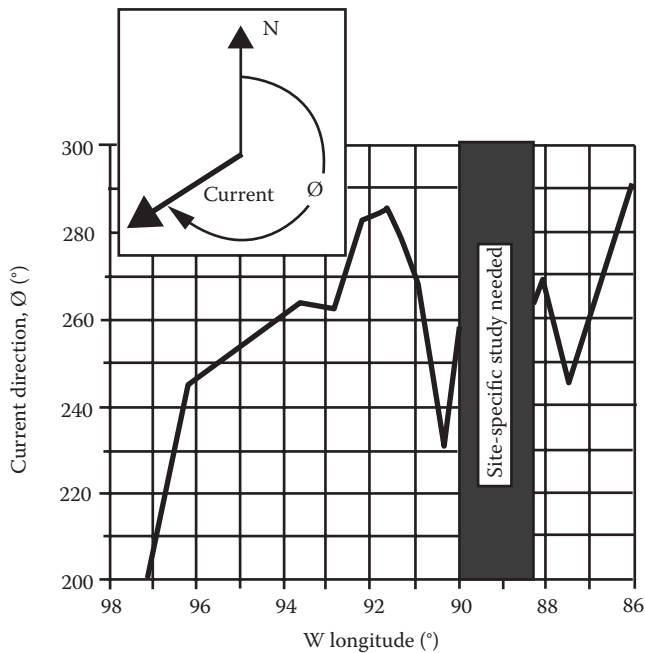
The wave heights are also to be modified according to the wave direction by the factors given in Figure 6.19 [36]; as shown in Figure 6.19, the modification factors for wave heights vary from 0.70 to 1.00 depending on the dominant wave direction. Moreover, the design wind-wave current direction, which is dependent on the site longitude, is to be taken into consideration as shown in Figure 6.20 [36].



**FIGURE 6.18** Omnidirectional design wave height vs. MLLW for the Gulf of Mexico (for north of 27°N and west of 86°W). For sea water depth >400.0 ft., the wave height increases linearly from 69.0 ft. at 400.0 ft. to 70.5 ft. at 1000.0 ft. (From API-RP2A-LRFD, *Recommended Practice for Planning, Designing and Constructing Fixed Offshore Platforms—Load and Resistance Factor Design*, American Petroleum Institute, Washington, DC, p. 38, 1993. With permission.)



**FIGURE 6.19** Design wave directions and factors to be applied for omnidirectional wave heights for the Gulf of Mexico (for north of 27°N and west of 86°W). (From API-RP2A-LRFD, *Recommended Practice for Planning, Designing and Constructing Fixed Offshore Platforms—Load and Resistance Factor Design*, American Petroleum Institute, Washington, DC, p. 39, 1993. With permission.)



**FIGURE 6.20** Design current directions (toward) with respect to North, in shallow water depth < 400.0 ft., Gulf of Mexico (for north of 27°N and west of 86°W). (From API-RP2A-LRFD, *Recommended Practice for Planning, Designing and Constructing Fixed Offshore Platforms—Load and Resistance Factor Design*, American Petroleum Institute, Washington, DC, p. 39, 1993. With permission.)



**6.3.5.2 Current Forces Exerted on the Structure**

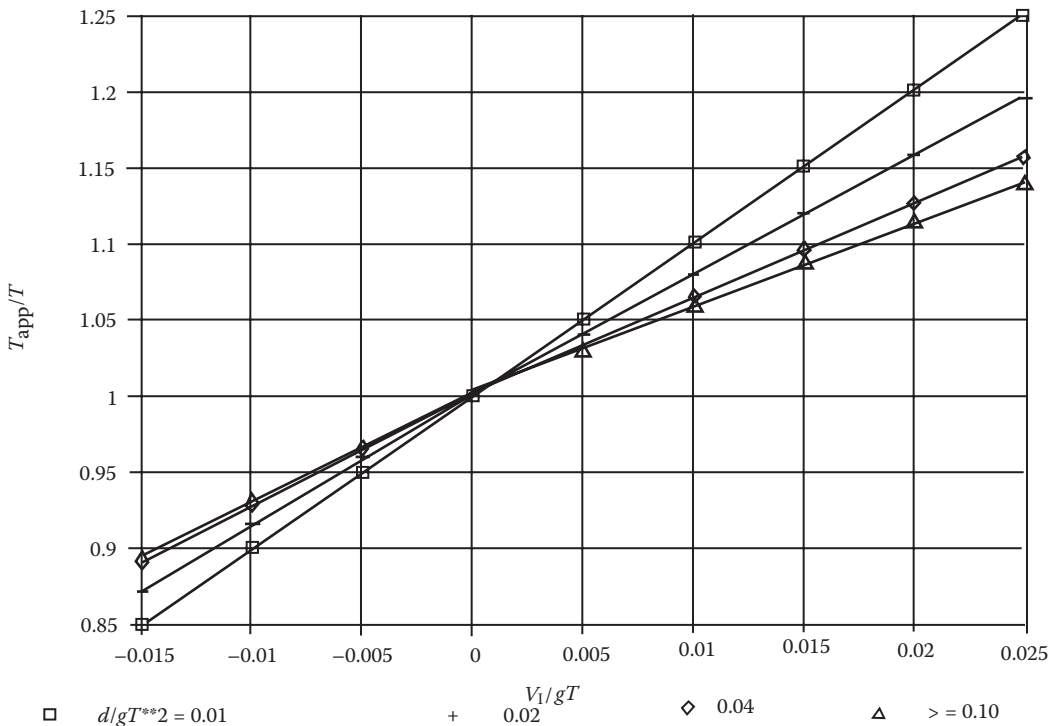
When current is acting alone on the structure, the current forces are to be computed using the following equation, viz.

$$f_{cd} = [(1/2)\rho_w C_D (D)(1)](U_c) |U_c| \tag{6.50}$$

where  $f_{cd}$  is the drag force exerted by the current velocity on unit length of the structural member, in the direction of current flow, and  $U_c$  is the current speed in the flow direction. In order to determine the forces exerted on the total structure, a procedure similar to that given in Equation 6.45 or 6.46 should be followed. The current can be due to tide, or wind or wave; care must be taken to add the current vector components properly. Also it must be seen that as per API guidelines, the in-line component of the current velocity cannot be smaller than 0.10 m/s [34].

**6.3.5.3 Forces Exerted on the Structure due to Current–Wave Interaction**

A current acting in the direction of wave tends to stretch (or shorten, if the current is acting opposite to the wave) the wavelength, as shown in Figure 6.21 [37]. To account for wave directional spreading, the wave particle velocities and accelerations must be multiplied by the wave kinematics factor, which varies from 0.85 to 0.95, for tropical storms; for extra-tropical storms, the wave kinematics factor varies from 0.95 to 1.00. The respective codes must be referred to for additional information. Moreover, the current speed near the offshore structure is reduced from the free stream values due to the blockage by the structure, as shown in Table 6.11 [38]. Consequently, wave kinematics must be adjusted for wave spreading and irregularity, combined vectorially with the current kinematics,



**FIGURE 6.21** Doppler shift in wave period due to steady current. (From API-RP2A-LRFD, *Recommended Practice for Planning, Designing and Constructing Fixed Offshore Platforms—Load and Resistance Factor Design*, American Petroleum Institute, Washington, DC, p. 28, 1993. With permission.)

**TABLE 6.11**  
**Current Blockage Factors for Gulf of Mexico Jacket-Type Structures**

# of Legs	Heading	Current Blockage Factor
3	All	0.90
4	End-on	0.80
	Diagonal	0.85
	Broadside	0.80
6	End-on	0.75
	Diagonal	0.85
	Broadside	0.80
8	End-on	0.70
	Diagonal	0.85
	Broadside	0.80

Source: API-RP2A-LRFD, *Recommended Practice for Planning, Designing and Constructing Fixed Offshore Platforms—Load and Resistance Factor Design*, 1st Edition, American Petroleum Institute, Washington, DC, p. 29; 36, 1993. Reproduced with permission.

and then adjusted for blockage. The current profile (is specified only for storm mean level) also must be stretched linearly (approximate method) to the local wave surface, using Equation 6.51, given below:

$$(z' + d) = (z + d)\{(d)/(d + \eta)\} \quad (6.51)$$

where  $d$  is the storm water depth,  $\eta$  is the water surface elevation above storm mean water, and the current speed at elevation  $z$  is known and stretched to  $z'$ , due to the vectorial adding of wave and current kinematics. In Figure 6.21,  $T$  is the wave period,  $V_1$  is the current component in the wave direction,  $d$  is the storm water depth (including storm surge and tide), and  $T_{app}$  is the apparent wave period.

### Example 6.12

A 5.0-m-diameter cylindrical structure is located in the Gulf of Mexico (29°N and 92°W), at a water depth of 30.0 m. It is assumed to be fixed to the seabed. The bottom of the top deck of the structure is located at 16.0 m above the MLLW level. Using the current value given in Table 6.12 [38], compute the maximum current forces exerted on the cylindrical structure. Use the procedure given in (v) Table 6.10 for current speed idealization.

To check for the appropriateness of the height of the bottom of the top deck, from Figure 6.18, the maximum observed wave height ~58.0 ft. = 17.68 m. Hence, the available freeboard below the deck = 16.0 – (17.68/2) = 7.16 m.

From Table 6.12, the maximum current present at the site = 3.0 knots = (3.0)(6080)(0.3048)/(3600) = 1.544 m/s.

From Figure 6.20, the dominant current direction is 280° from the north direction.

From Figure 6.19, the predominant wave direction seems to be 290° (clockwise) from north, which is almost the same as the current direction. Hence, the current speed component can be directly added to the wave particle velocity components, in estimating the maximum wave particle velocities. Moreover, the current can assumed to be a constant over the whole height of

**TABLE 6.12**  
**Guidelines for Wave, Current, and Storm Tide Values for Locations around United States**

Site Location	Inline (Open Shelf) Current Speed, $U_i$ , (and Its Range) (knot)	100-Year Maximum Wave Height, $H_m$ (and Its Range) (ft.)	Range of Wave Steepness, $S = (2\pi H_m)/(gT_m^2)$	Storm Tide $X$ (and Its Range) (ft.)	Quality of Data (1-Preliminary; 2-Hindcast; and 3-Comprehensive Measurements)
Gulf of Mexico (E of 86°W)	2 (1–3)	70 (60–80)	1/11–1/15	3 (2–5)	2
South. Calif. (Santa Barb.)	2 (1–3)	45 (35–55)	1/11–1/30	6 (5–7)	1
Gulf of Alaska (Icy Bay)	3 (2–4)	100 (90–120)	1/13–1/17	11 (10–13)	2
Lower Cook Inlet	4 (3–6)	60 (45–70)	1/10–1/11	16 (13–20)	2
Chugchi Sea ( $d > 60.0$ ft.)	2 (1–3)	50 (40–60)	1/11–1/15	6 (4–8)	3
Beaufort Sea ( $d > 50.0$ ft.)	2 (1–3)	40 (35–50)	1/13–1/17	4 (2–7)	2
Georges Bank	2 (1–13)	85 (75–95)	1/10–1/16	5 (4–6)	2
Baltimore Canyon	3 (2–4)	90 (80–100)	1/10–1/14	5 (4–6)	2
Georgia Embayment	5 (2–8)	75 (65–85)	1/11–1/15	5 (3–7)	2

Source: API-RP2A-LRFD, *Recommended Practice for Planning, Designing and Constructing Fixed Offshore Platforms—Load and Resistance Factor Design*, 1st Edition, American Petroleum Institute, Washington, DC, p. 29; 36, 1993. Reproduced with permission.

the structure, since the API procedure (Table 6.12) seems to indicate an almost a constant current value over the whole height of the structure.

Using Equation 6.50, the current force acting on the structure is given as  $F_C = \{(1/2)\rho_w C_D(D)(1)\}(U_c)|U_c|(\text{height}) = (1/2)(1030)(1.0)(5.0)(1.544)^2(30) = 184,159.06$  N.

### Example 6.13

The diameter (outside) of a cylindrical concrete structure is 15.0 ft. It is standing in 100.0 ft. depth of seawater. The wall thickness of the cylinder is 18.0 in. The maximum wave period at the site is known to be 14.0 s; also assume the maximum wave height given in Table 6.12. The structure is located in the Gulf of Mexico, at 27°N and 90.3°W. Compute the maximum force exerted on the structure. Assume the current to be represented by Equation 4 given in Table 6.10 for current speed idealization. Also consider the effect of current–wave interaction, as represented by Figure 6.21. Take  $C_M = 2.0$ ;  $C_D = 1.0$ .

For the given site, the predominant wave direction is shown in Figure 6.19 as 290° (clockwise) from north direction. Also as per Figure 6.20, the current direction is 240° (clockwise) from the north; in this direction the omnidirectional wave height has to be reduced by a factor of 0.9, when computing the (wave) + (current) forces. Also as per Table 6.12 (limited by Figure 6.18), the maximum omnidirectional wave height for the site is 57.0 ft. Hence, the wave height to be used for force computation (limited by Figure 6.19) =  $(0.9)(57.0) = 51.3$  ft.

The period will undergo an apparent shift due to wave current interaction. The maximum current at the site is given in Table 6.12 as 3.0 knots (1.544 m/s = 5.066 ft./s).

$(U_c/gT) = (5.066)/(32.2)(14.0) = 0.011$ ; also  $(d/gT^2) = (100)/\{(32.2)(14.0)^2\} = 0.0158$ . So take the apparent shift values represented by the  $\Delta$  symbols in Figure 6.21. From Figure 6.21,  $T_{app}/T = 1.065$ . As a consequence of wave-current interaction, the wave period becomes  $(1.065)(14) = 14.91$  s.

$$L_0 = (gT^2/2\pi) = (32.2)(14.91)^2/(2\pi) = 1139.3 \text{ ft.}$$

$$d/L_0 = (100.0)/1139.3 = 0.0878; \text{ for this ratio, } d/L = 0.1302.$$

$$L = 100/(0.1302) = 768.1 \text{ ft.}$$

$d/L = 15/768.01 = 0.0195 (<0.2)$ ; hence, Morison-O'Brien's theory is valid.

The horizontal wave particle velocity is given as

$$u = (\pi H/T)(\cosh k(d+z)/\sinh kd)\cos(kx - \omega t) = [(\pi)(51.3)/14.91][\{\cosh k(d+z)/\sinh kd\}]x \cos(kx - \omega t) = (10.82)(\cosh k(d+z)/\sinh kd)\cos(kx - \omega t) \text{ ft./s}$$

The horizontal wave particle acceleration is given as

$$a_x = (2\pi^2 H/T^2)\{\cosh k(d+z)/\sinh kd\}\sin(kx - \omega t) = \{(2)(\pi)^2(51.3)/14.91^2\}\{\cosh k(d+z)/\sinh kd\}[\cos(kx - \omega t)] = (4.555)\{\cosh k(d+z)/\sinh kd\}[\cos(kx - \omega t)] \text{ ft./s}^2.$$

Assuming current speed over the height also to vary as a function of  $\{\cosh k(d+z)/\sinh kd\}\sin(kx - \omega t)$  (otherwise, numerical integration has to be done over the height in steps of height intervals).

The drag force over the cylindrical structure can be obtained (from Equation 6.28) as

$$F_{D_x}(t) = (1/2)(\rho_w C_D D)[\{\pi H/T + U_c\}^2][\{2k(\eta+d) + \sinh 2k(\eta+d)\}/\{4k \sinh^2(kd)\}] * |\cos(kx - \omega t)| \cos(kx - \omega t)$$

Hence, the drag force is obtained as  $= (0.5)(1.99)(1.0)(15.0)(10.82 + 5.066)^2\{768/(8\pi)x\}[(2)(2\pi)(100 + 51.3/2)/(768) + \sinh(2)(2\pi)(100 + 51.3/2)/768]/\sinh^2(2)(\pi)(100/768)]x|\cos(kx - \omega t)|\cos(kx - \omega t) = (115,098.720)[(2.056 + 3.843)/(0.833)]|\cos(kx - \omega t)|\cos(kx - \omega t) = 815,087.0 |\cos(kx - \omega t)|\cos(kx - \omega t) \text{ lb.}$

The inertial force on the cylindrical structure is obtained as  $= C_{M\rho_w}(\pi D^2/4)(2\pi^2 H/T^2)[(1/k) \sinh k(d+\eta)/\sinh kd] \sin(kx - \omega t) = (2.0)(1.99)(\pi)(15^2/4)\{(2)(\pi)^2(51.3)/(14.91)^2\}\{768/(2\pi)\} \times [\sinh \{(2)(\pi)(100 + 51.6/2)/768\}/\sinh\{(2\pi)(100/768)\}] \sin(kx - \omega t) = (391,587.4)(1.2188/0.912) \sin(kx - \omega t) = 523,036.8 \sin(kx - \omega t) \text{ lb.}$

Hence, the maximum wave-current force  $= \sqrt{[(815,087)^2 + (523,039)^2]} = 968,471.28 \text{ lb.}$

If the current was not added to the wave particle velocity, then

$$L = (32.2)(14)^2/(2\pi) = 1004.5 \text{ ft.}$$

$$d/L_0 = 100/1004.5 = 0.0996; \text{ from tabulated values } d/L = 0.1407.$$

Hence,  $L = 100/0.1407 = 710.7 \text{ ft.}$

Then the drag force will be obtained as (Equation 6.28)  $= F_{D_x}(t) = [(\pi\rho_w D H^2 L C_D)/(16T^2)] [2k(\eta+d) + \sinh\{2k(\eta+d)\}/\sinh^2(kd)] * |\cos(kx - \omega t)| \cos(kx - \omega t) = [(\pi)(1.99)(15)(51.3)^2(711)(1)]/[(16)$

$$(14.0)^2 \{ [(2)(\pi)(100 + 51.3/2)/711] + \sinh(2)(2)(\pi)(100 + 51.3/2)/711 / \sinh^2(2)(\pi)(100/711) \} |\cos(kx - \omega t)| \cos(kx - \omega t) = (55,952.9) \{ (2.221 + 4.553)/(1.007) \} |\cos(kx - \omega t)| \cos(kx - \omega t) = 376,390.2 |\cos(kx - \omega t)| \cos(kx - \omega t) \text{ lb.}$$

The inertial force on the cylindrical structure is given as  $= F_i(t) = [(\pi^2 \rho_w D^2 H L C_m) / (4T^2)] [\sinh k(\eta + d) / \sinh kd] \sin(kx - \omega t) = [(\pi^2 (1.99)(15)^2 (51.3)(711)(2) / (4)(14^2))] [\sinh(2)(\pi)(100 + 51.3/2)/711 / \sinh(2)(\pi)(100)/711] \sin(kx - \omega t) = (411,184.0)(1.353/1.003) \sin(kx - \omega t) = 554,668.0 \sin(kx - \omega t) \text{ lb.}$

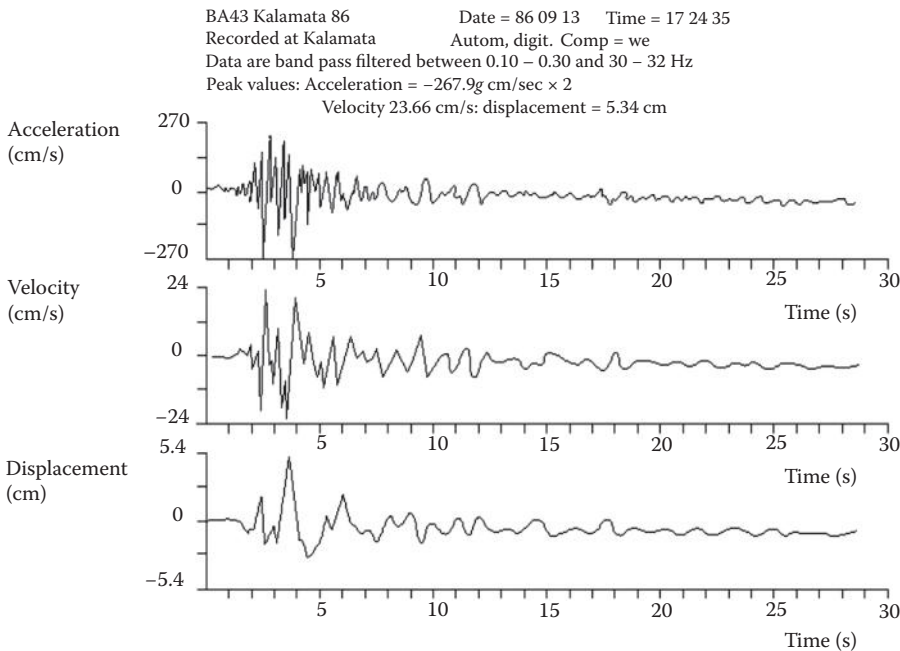
Hence, the maximum total force due to wave alone  $= \sqrt{[(373,390.2)^2 + (554,668)^2]} = 668,638.0 \text{ lb.}$

Thus it is observed that when the wave velocity and current velocity are combined, the forces acting on the structure are amplified greatly.

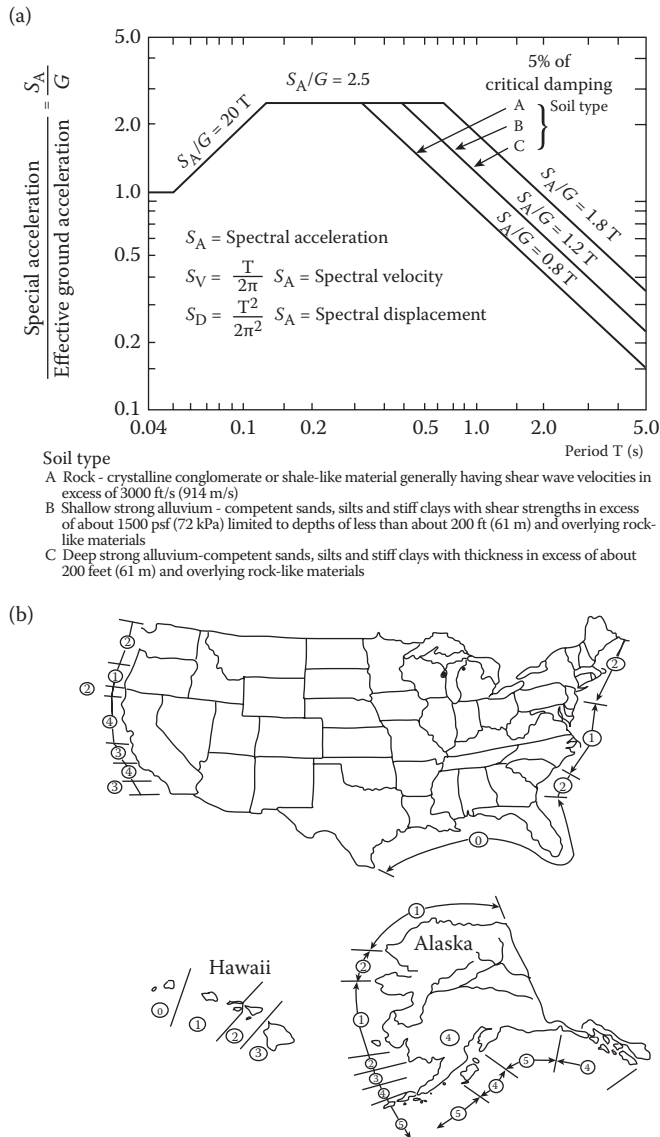
### 6.3.6 EARTHQUAKE FORCES

Structures located in a seismic offshore region are generally analyzed and designed for two levels of earthquake intensities, viz., (i) strength level earthquake intensity and (ii) ductility level earthquake intensity. For the strength-level earthquake, which is defined as having a “reasonable likelihood of not being exceeded during the platform’s life” (having a mean recurrence interval equal to 200 to 500 years), the structure will be designed to respond in an elastic manner. For the ductility level earthquake, defined as the earthquake intensity close to the “maximum possible earthquake intensity” at the site, the structure will be designed for inelastic response; the structure should also have adequate reserve strength to prevent its total collapse.

For the strength level design, the seismic loading may be specified either by sets of accelerograms, as shown in Figure 6.22 [39] or by means of design response spectra, as shown in Figure 6.23a [40]. Using the design spectra for analysis and design has a number of advantages over the time history solutions, obtained by using the seismic acceleration time history as base acceleration



**FIGURE 6.22** Time history of ground acceleration, and the corresponding (integrated) ground velocity and displacement time histories (site of earthquake is Kalamata, Greece). (From API-RP2A-LRFD, *Recommended Practice for Planning, Designing and Constructing Fixed Offshore Platforms—Load and Resistance Factor Design*, 1st Edition, American Petroleum Institute, Washington, DC, p. 147, 1993. With permission.)



**FIGURE 6.23** (a) Design response spectra, recommended by API-RP2A. (b) Seismic risk map of coastal waters of the United States. (From API-RP2A-LRFD, *Recommended Practice for Planning, Designing and Constructing Fixed Offshore Platforms—Load and Resistance Factor Design*, 1st Edition, American Petroleum Institute, Washington, DC, pp. 148–149, 1993. With permission.)

input time history. Consequently, the design response spectra are generally used for strength level designs of offshore structures. If the design spectral intensity, characteristic of the seismic hazard at the site, is denoted by  $a_{max}$ , then API-RP2A recommends using  $a_{max}$  for the two principal horizontal directions and  $0.5a_{max}$  for the vertical direction. The DNV rules, on the other hand, recommend  $a_{max}$  and  $0.7a_{max}$  for the two horizontal directions (two different combinations) and  $0.5a_{max}$  for the vertical. The value of  $a_{max}$  and often the spectral shapes are determined by site-specific seismological studies.

To use Figure 6.23a to determine the spectral acceleration, one should know the value of  $G$  the effective ground acceleration of the offshore site under consideration. The value of  $G$  is determined

**TABLE 6.13**  
**Effective Ground Acceleration  $G$  as a Function of Seismic Strength Level  $Z$  of the Site**

$Z = 0$	1	2	3	4	5
$G = 0$	0.05	0.10	0.20	0.25	0.40

Source: API-RP2A-LRFD, *Recommended Practice for Planning, Designing and Constructing Fixed Offshore Platforms—Load and Resistance Factor Design*, 1st Edition, American Petroleum Institute, Washington, DC, p. 147, 1993. With permission.

by the assigned strength level  $Z$  of the offshore site, as shown in Table 6.13 [39]; also, the value  $Z$  is shown in Figure 6.23b [40] for the offshore locations of United States.

Designs for ductility level earthquakes will generally require inelastic response analyses for which the seismic input history must be specified by sets of component accelerograms in three orthogonal directions; the time history could have been obtained from real site-specific earthquakes or simulated representative of the extreme ground motions that could occur at the platform site.

### Example 6.14

The offshore cylindrical aid-to-navigation structure, shown in Figure E6.5, is located in the coastal regions around San Francisco, CA. The region is also seismic prone. Taking seismic strength of the site to be 4, compute the pseudo-acceleration level the structure has to resist, when (i) the fundamental period of vibration of the structure is equal to 0.5 s; (ii) the fundamental period of vibration of the structure is 1.0 s. Assume that the soil at site has shear strength greater than 1500 psf, and that the layer of competent soil depth is greater than 200 ft. Also differentiate the acceleration levels that would be used according to the (a) API code and (b) DNV code.

- (a) As per the API code, for a site with  $Z = 4$ , the effective ground acceleration  $Z = 0.25$ .  
 Using Figure 6.23a,  $S_A/G$  for the soil type B in Figure 6.23a is 1.27.
  - (i) For a structure with fundamental period equal to 0.5 s,  $S_A/G = (1.2)(0.5) = 0.6$ .  
 Effective ground acceleration to be considered in analysis =  $S_A = (0.6)(0.25) = 0.15g$ .  
 Use an effective ground acceleration level of (0.15g) for both the horizontal directions and 0.075g for the vertical direction.
  - (ii) For a structure with a fundamental period equal to 1.0 s,  $S_A/G = (1.2)(1.0) = 1.2$ .  
 Effective ground acceleration to be considered in analysis =  $S_A = (1.2)(0.25) = 0.30g$ .  
 Use an effective ground acceleration level of (0.30g) for both the horizontal directions and 0.15g for the vertical direction.
- (b) As per DNV code, when the fundamental frequency of vibration is 0.5 s, use an effective ground acceleration level of 0.15g for  $x$ -direction, 0.105g for the  $y$ -direction, and 0.075g for the vertical direction.  
 When the fundamental frequency of vibration is 1.0 s, use an effective ground acceleration level of 0.30g for  $x$ -direction, 0.21g for the  $y$ -direction, and 0.15g for the vertical direction.

### 6.3.7 ICE FORCES ON OCEAN STRUCTURES

Previously in Sections 3.2.6 and 3.8, a brief description has been given regarding the various features that occur in an ice-infested ocean environment, the characteristics of ice, its properties and the various modes of ice–structure interaction that generate ice forces on ocean structures. The ice forces, transmitted to the structure, are generated due to the action of various natural environmental effects such as wind, wave, current, and thermal expansion. Due to these actions, the large ice feature (or floe) that impinge on any ocean structure may continuously fail at the ice–structure interface, when the



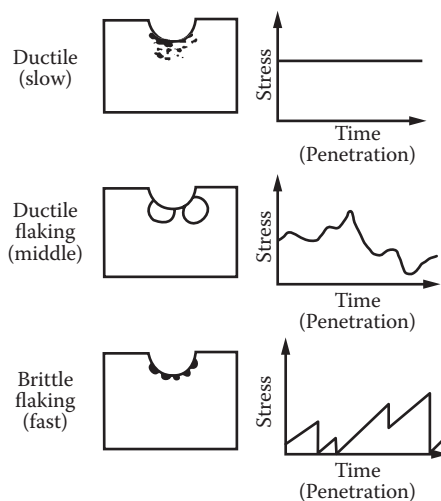
failure load resisted by the ice feature is less than the environmental forces exerted on the overall ice feature. This failure is termed as the “limit stress” failure, as shown in Figure 3.59. This failure may be generated by the crushing of the ice on the ice–structure interface or the buckling of ice feature in the near zone; other actions such as bending, splitting and ride-up may also occur during this “limit stress” interaction. Instead, if the ice resistance is such that no failure occurs on the ice–structure interface (in the near face), then the failure tends to occur in the ice field (surrounding the structure) in the far zone, away from the ice–structure interface. The structure restrains the ice field from moving ahead and this causes the environmental forces acting on the structure to increase. When these forces increase beyond a certain value, failure may occur in the resisting ice field resulting in the formation of ice ridges in the pack-ice. This failure is termed the “limit force” failure since the force exerted on the offshore structure is limited by the failure that has occurred in the ice field. The ridge building may continue to occur around the stationary ice field. Thereafter, the failure will occur around the built ice ridge and the stationary ice field; the multiyear ice may continue to move around this blocked region, as shown in subfigure 3 of Figure 3.60. The possible ice force exerted on the structure, during this ice–structure interaction scenario, is shown in Figure 3.60, where the maximum force is stated to occur during the initial impact of the ice field with the structure. The ice forces continue to decrease as ridge building occurs and may decrease further when ice flows around the blocked ice field, as shown in the figure.

A variety of structures have been used in the offshore context, and the shape of ice–structure can be generically classified as (i) cylindrical vertical structures (with single or multiple cylinders) and inclined conical structures, causing limit stress failures in ice, and (ii) structures causing limit force failure in ice. The procedures, used in computing ice forces on offshore structures, are outlined below.

### 6.3.7.1 Ice Loads on Vertical Cylindrical Structures

When various ice features interact with a cylindrical ocean structure, a number of failure mode such as crushing, buckling, fracture, and shear failure (in the vertical plane) may result due to the interaction [41]. On narrow and vertical-sided cylindrical structures, ice–structure interaction will result in ductile-creep deformation at low strain rates and in a brittle-crushing mode at high strain rates as shown in Figure 6.24 [42] (also see Figure 3.57).

The characteristic deformation map proposed by Ponter et al. [43], during this cylindrical structure-ice interaction, showing creep, crushing, spalling, radial cracking, and radial and



**FIGURE 6.24** Indentation failure modes observed in cold room tests. (From P.R. Kry, *Scale Effects on Continuous Crushing of Ice*, Proceedings of IAHR Ice Symposium, University of Laval, Quebec, Canada, 1981. With permission.)

circumferential cracking, is given in Figure 6.25 [43]. The figure shows that the failure deformation is governed by the loading strain rate (given by ice speed/transverse resisting width or diameter) and aspect ratio of interaction (given by resisting transverse width or diameter/thickness of ice feature).

According to Croasdale [41] the empirical solution available for crushing failure of ice against a vertical cylindrical structure under laboratory conditions is given by

$$F = (If_c\sigma_x)Dh = pDh \tag{6.52}$$

where  $I$  is the indentation factor,  $f_c$  is the contact factor,  $\sigma_x$  is the unconfined (or uniaxial) compressive strength of ice,  $D$  is the diameter (or transverse width) of the structure, and  $h$  is the thickness of the interacting ice sheet. The term  $p (= pDh)$  is the effective ice pressure exerted on the structure by the moving ice. The value of the indentation factor  $I$  is dependent on a number of factors such as crystallographic structure of ice, multiaxial strength of ice, strain rate in ice, and geometry of the interaction between ice and the structure. Under theoretical laboratory conditions, the normalized indentation pressure has been developed from plasticity analysis by Ralston [44], and given as

$$\text{Normalized indentation pressure} = (p/\sigma_x) \tag{6.53}$$

Using the definition of  $p$  used in Equation 6.52, the normalized indentation pressure is obtained as

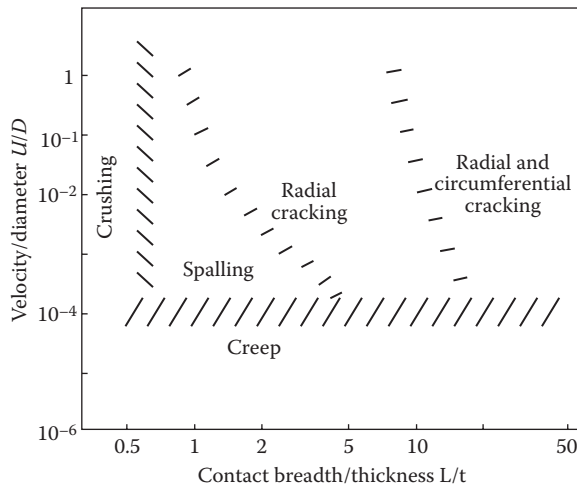
$$(p/\sigma_x) = If_c \tag{6.53a}$$

The normalized indentation pressure given from theoretical plasticity analysis by Ralston, and compared with some experimental results, is shown in Figure 6.26.

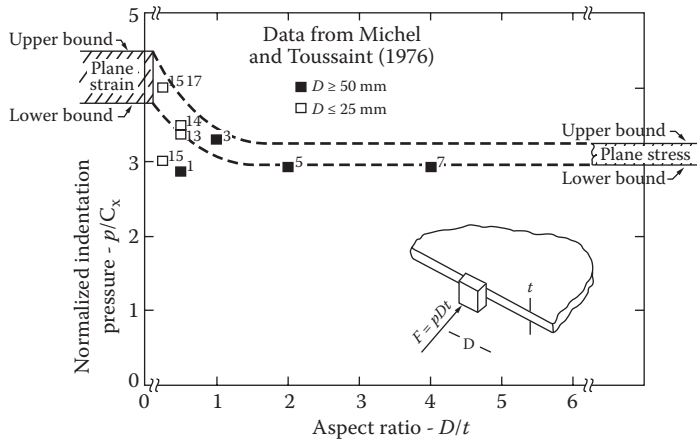
According to the derivations given by Ponter et al. [43], the ice force  $F$  acting on a platform deforming under pane strain or plane stress mode of failure can be expressed as

$$F = \phi Dh[\sigma_x(\text{strain rate}, \phi, \psi)] \tag{6.54}$$

where  $\phi$  is the normalized indentation pressure (given in Figure 6.26 [44]),  $\sigma_x$  (strain rate,  $\phi$ ,  $\psi$ ) is the uniaxial stress corresponding to the strain rate [= velocity/(diameter or transverse width)], and



**FIGURE 6.25** Deformation map in ice. (From A.R.S. Ponter et al., *Cold Regions Science and Technology*, Volume 8, Issue 2, pp. 109–118, 1983. With permission.)



**FIGURE 6.26** Comparison of computed bounds for normalized indentation pressure from test data.  $t \equiv h$  = thickness of ice sheet; also  $C_x = \sigma_x$ . (From T.D. Ralston, *An Analysis of Ice Sheet Indentation*, Proceedings of IAHR Ice Symposium, Volume I, Luleå, Sweden, pp. 13–32, 1978. With permission.)

$\psi$  is a constant dependent on plane strain/stress loading with or without slip. The values of  $\phi$  and  $\psi$  are given in Table 6.14 [45].

According to some test results reported by Exxon [41], the value of  $\phi$  given in Equation 6.54 need to be multiplied by a factor of 1.2 to make it compatible with the lower bound solution given by Equation 6.53 and Figure 6.26, when  $D/h < 1.0$ ; otherwise the values given in Table 6.14 can be used to compute the normalized indentation pressure. Moreover, under field conditions reported by Peyton [46], the effective ice pressure is given as

$$p = \sigma_x(I_f) = 0.45\sigma_x \tag{6.55}$$

As a comparative analogue, Dawson [47] gives a value of 2.5 MPa for the ice pressure; according to him, the ice load can be computed as

$$F = C\sigma_x A = pDh \tag{6.56}$$

with  $0.3 < C < 0.7$ ; in the absence of definite experimental observation use  $C = 0.7$ . The minimum field value is specified as  $p = 350.0$  lbf/in.<sup>2</sup>. Also, according to Eicken [48], the uniaxial compressive

**TABLE 6.14**  
**Ice Indentation Parameters Used in Equation 6.54**

#	Condition of Loading	$\phi$	$\psi$
1	Plane strain ( $D \ll h$ )	2.986	0.331
2	Plane stress, and free slip between ice and structure	2.986 or $(2/\sqrt{3})\{1 + (0.25)\sqrt{2(h/D)}\}$	0.441
		Take minimum of the above two values.	
3	Plane stress, but no free slip between ice and structure	2.986 or $(2/\sqrt{3})\{1.5 + (0.25)\sqrt{2(h/D)}\}$ or $(2/\sqrt{3})\{1 + (0.5)\sqrt{2(h/D)^{0.25}} + 0.25(h/D)\}$	0.331
		Take the minimum of the above three values.	

Source: A.R.S. Ponter et al., *Cold Regions Science and Technology*, Volume 8, Issue 2, pp. 109–118, 1983. Reproduced with permission.

strength of ice can be varying from 8.2 to 11.2 MPa for different types of ice, such as Nilas, pancake, first year, second year, and multiyear. Another formulation for ice forces given by Korzhavin [49] is

$$F = [If_c m (U/U_0)^{-0.333} \sigma_x] Dh = p Dh \quad (6.57)$$

where  $I$  is the indentation coefficient to account for confining effects (if ice width is greater than  $15D$ , then  $I = 2.5$ ),  $f_c$  the contact factor to account for different types of contact at ice–structure interface ( $0.4 < f_c < 0.7$ ),  $m$  the shaper factor to account for the shape of the indenter used [1.0 for rectangular, 0.9 for semicircular, and  $\{0.85(\sin \alpha)^{0.5}\}$  for wedge shape with wedge angle equal to  $(2\alpha)$ ],  $U$  the velocity of ice sheet, and  $U_0$  the nondimensionalizing reference velocity equal to 1.0 m/s. In the above equation, if  $U$  is taken as 1.0 m/s, then the ice force  $F$  becomes for a semicircular indenter (with  $f_c = 0.5$  and  $m = 0.9$ )

$$F = (1.125 \sigma_x) Dh \quad (6.58)$$

Remembering that Equations 6.54 and 6.58 are for laboratory-based ideal ice, the results given by them seem to be close together. Also if the irregular contact conditions at the ice–structure interface in the field are taken into account for the low value of  $(If_c)$  equal to 0.45 used in Equation 6.55 (and also implemented in Equations 6.54 and 6.58), then all three equations (6.54, 6.55, and 6.58) seem to be consistent.

The compressive failure strength of ice is dependent on the scale in which interaction with the structure takes place. In the laboratory, it is in the microscale level, whereas in the large-scale limit load situation the scale is in the macroscale. According to the compiled results of an “Ice Mechanics and Arctic Modeling Workshop” [50], the compressive strength of ice can be represented over a large range of scale (in terms of the area of ice involved in the interaction) by the results shown in Figure 6.27 [50]. The average strength of ice seems to vary between a values of 20.0 to 1.0 MPa, when the area of interaction varies between 0.1 and 8.0 m<sup>2</sup>, respectively (for 1.0-m<sup>2</sup> interaction ice area, the ice strength seems to be 3.0 MPa). The approximate compressive failure strength can be obtained from the values given in Figure 6.27.

### 6.3.7.2 Ice Loads on Sloping Structures

When an ice sheet approaches a sloping structure, initially, the ice begins to crush at the ice contact surface. As the ice is pushed against the structure by the driving environmental force, the ice sheet is pushed up along the inclined surface; if the surface is assumed to be two-dimensional, then the interaction can be shown by Figure 6.28 [51].

Considering the equilibrium of an interacting ice sheet, generating a normal reaction of  $N$  at the interacting interface, a tangential frictional force  $\mu N$ , a horizontal component  $H$ , and a vertical component  $V$ , the following equations can be obtained, viz.,

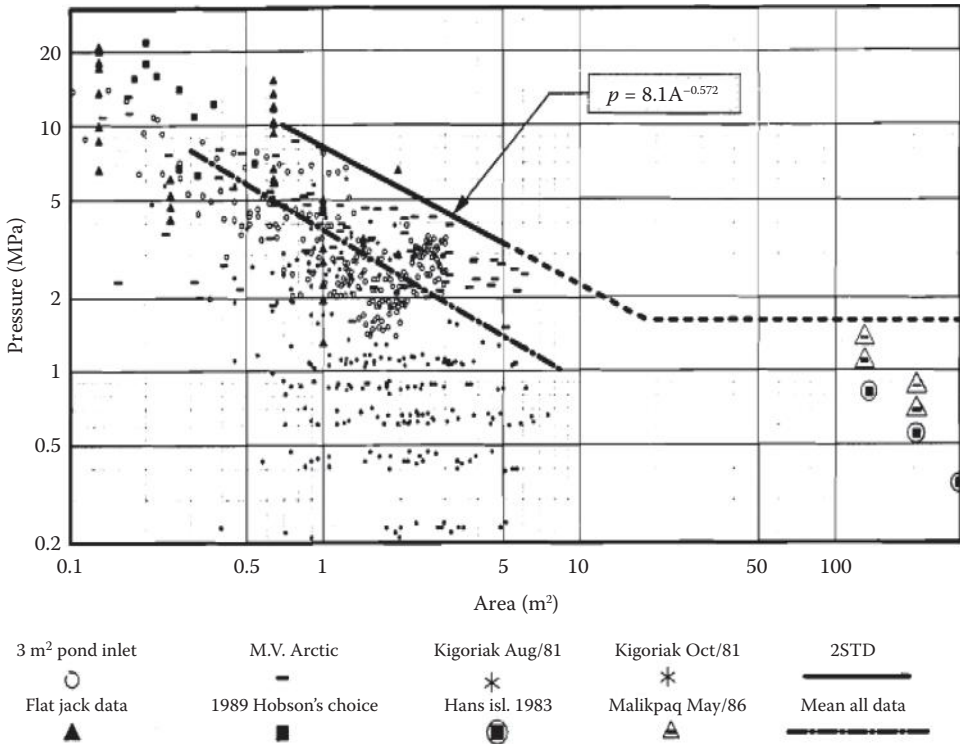
$$\begin{pmatrix} H = N \sin \alpha + \mu N \cos \alpha \\ V = N \cos \alpha - \mu N \sin \alpha \end{pmatrix}$$

Solving the above two equations one obtains (6.59)

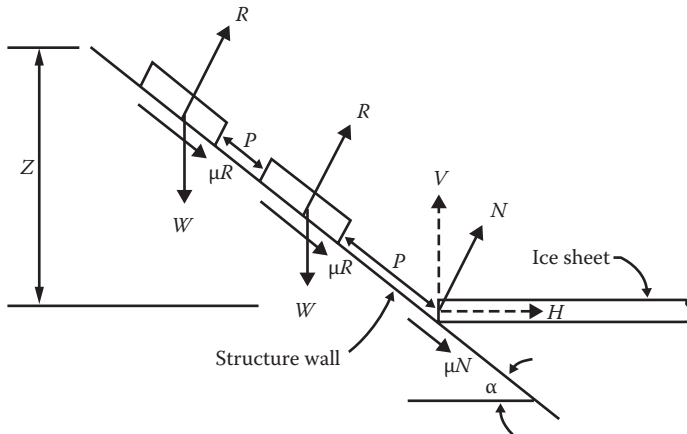
$$H = \left( \frac{\sin \alpha + \mu \cos \alpha}{\cos \alpha - \mu \sin \alpha} \right) V = C_1 V, \text{ where } C_1 = \left( \frac{\sin \alpha + \mu \cos \alpha}{\cos \alpha - \mu \sin \alpha} \right)$$

Considering the bending failure of ice occurring due to a vertical load acting at a distance of the characteristic length  $l_c$  of a floating ice sheet,  $l_c$  is given as [52]

$$l_c = \sqrt[4]{(E_i h^3) / \{12(1 - \nu_i^2)(\rho_w g)\}} \quad (6.60)$$



**FIGURE 6.27** Ice crushing pressure as a function of ice crushing area, due to interaction. (From Canadian Standards Association, General Requirements, Design Criteria, The Environment and Loads [CAN/CSA-471-92], CSA, Rexdale, Ontario, Canada. Also in [paper by K.R. Croasdale, P. Truskov, A.T. Bekker and T. Murrell], Proceedings of the Sea Ice Mechanics and Arctic Modeling Workshop, April 25-28, 1995, Anchorage, Alaska, Volume 2, p. 68, 1992. With permission.)



**FIGURE 6.28** Ice-structure with a two-dimensional sloping structure. (From A.B. Cammaert and D.B. Muggerridge, *Ice Interaction with Offshore Structures*, Van Nostrand Reinhold, New York, p. 248, 1988. With permission.)

The bending stress of failure  $\sigma_{bf}$  is given by

$$\begin{aligned} M_f &= [(\sigma_{bf} I) / \{(1 - \nu^2)(h/2)\}] = (\sigma_{bf} b h^3) / [12(1 - \nu^2)(h/2)] \\ &= \sigma_{bf} b h^2 / \{6(1 - \nu^2)\} \end{aligned} \quad (6.61)$$

Taking the moment  $M_f$  to be equal to

$$M_f = V l_c \quad (6.62)$$

and combining Equations 6.59 through 6.62, one obtains the horizontal ice force exerted on an inclined structure to be

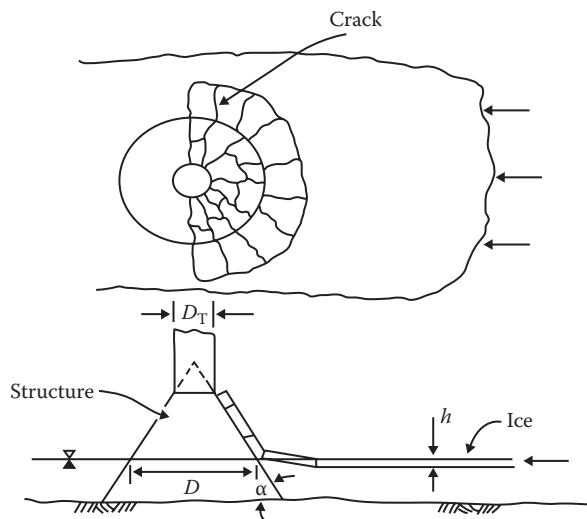
$$H = b \sigma_{bf} C_1 [(\rho_w g h^5)(1 - \nu_i^2) / E_i]^{(1/4)} \quad (6.63)$$

where  $b$  is the transverse width of the sloping surface,  $\rho_w$  is the mass density of water,  $g$  is the acceleration due to gravity,  $\nu_i$  is the Poisson's ratio of ice, and  $E_i$  is the Young's modulus of ice. If the contribution from the ice ride-up on the sloping structure is also considered, then the horizontal ice load exerted on the sloping structure is given by

$$\begin{aligned} H &= b[(0.68)\sigma_{bf} C_1 \{(\rho_w g h^5)(1 - \nu_i^2) / E_i\}^{(1/4)} + z h \rho_i g C_2], \\ \text{with } C_2 &= C_1(\sin \alpha + \mu \cos \alpha) + \{(\sin \alpha + \mu \cos \alpha) / \tan \alpha\} \end{aligned} \quad (6.64)$$

with  $z_i$  = maximum ride-up height (up to the neck). When the three-dimensional failure of a floating ice sheet against a conical structure shown in Figure 6.29 [52] is considered, the horizontal ice force exerted on the conical structure is given by [41]

$$\begin{aligned} H &= A_4[A_1 \alpha_{bf} h^2 + A_2 \rho_w g h D^2 + A_3 \rho_w g h (D^2 - D_T^2)] \\ V &= B_1 H + B_2 \rho_w g h (D^2 - D_T^2) \end{aligned} \quad (6.65)$$



**FIGURE 6.29** Ice–structure with a conical structure. (From A.B. Cammaert and D.B. Mugeridge, *Ice Interaction with Offshore Structures*, Van Nostrand Reinhold, New York, p. 249, 1988. With permission.)

The horizontal and vertical forces exerted on the conical structures can be computed by using Equation 6.65 and the values given in Figures 6.29 and 6.30 [53]. If the height of the cone above the water surface, and below the neck, does not provide enough length to dissipate the energy available in the moving ice field through bending failure and ride up of ice, then Equation 6.65 may not be exactly applicable. The component of the force due to ride-up and clearing around the conical structure may be underestimated.

Moreover, when the cone angle of the structure is  $\geq 75^\circ$ , then the ice may fail on the conical surface by crushing. For this case, Danys and Bercha [54] have given the following equation, viz.,

$$H = mn_1Dh\sigma_c \text{ and } V = mn_2Dh\sigma_c \tag{6.66}$$

where  $n_1 = \cos^2\alpha$ ,  $n_2 = \cos\alpha$ ,  $m$  = shape and contact coefficient;  $\alpha$  is inclination of the cone to the vertical,  $D$  is the diameter of the structure at water level,  $h$  is the ice floe thickness, and  $\sigma_c$  is the effective compressive strength of ice.

**6.3.7.3 Limit Loads due to Environmental Interaction**

When a moving ice feature is brought to a rest by an intervening structure (maybe a large gravity structure or an offshore island with vertical sides), the forces exerted on the structure are called as limit-momentum loads, since the momentum generated by the moving ice field (with a velocity of  $V_i$ ), as it impinges on the structure, is not sufficient for the ice feature to break through. The failure of the near face of the moving ice field is shown in Figure 6.31. Assuming that all the kinetic energy of motion associated with the ice field is dissipated during the ice–structure interaction, as given below, by the Equation 6.67, viz.,

$$\text{kinetic energy} = (1/2)(1 + C_m)(W_i/g)V_i^2 = \int_0^{x_m} F_x \, dx \tag{6.67}$$

The maximum penetration of the ice feature into the structure,  $x_m$ , and the maximum impact force,  $F_{im}$ , are given by

$$\begin{aligned} x_m &= (0.413)(LV_i)^{1.33} \{ (1 + C_m)(\rho_i/p_e) \}^{0.67} (1/R_s)^{0.33} \\ F_{im} &= 1.82h(p_eLV_i)^{0.67} \{ 1 + C_m \} R_s \rho_i \}^{0.33} \end{aligned} \tag{6.68}$$

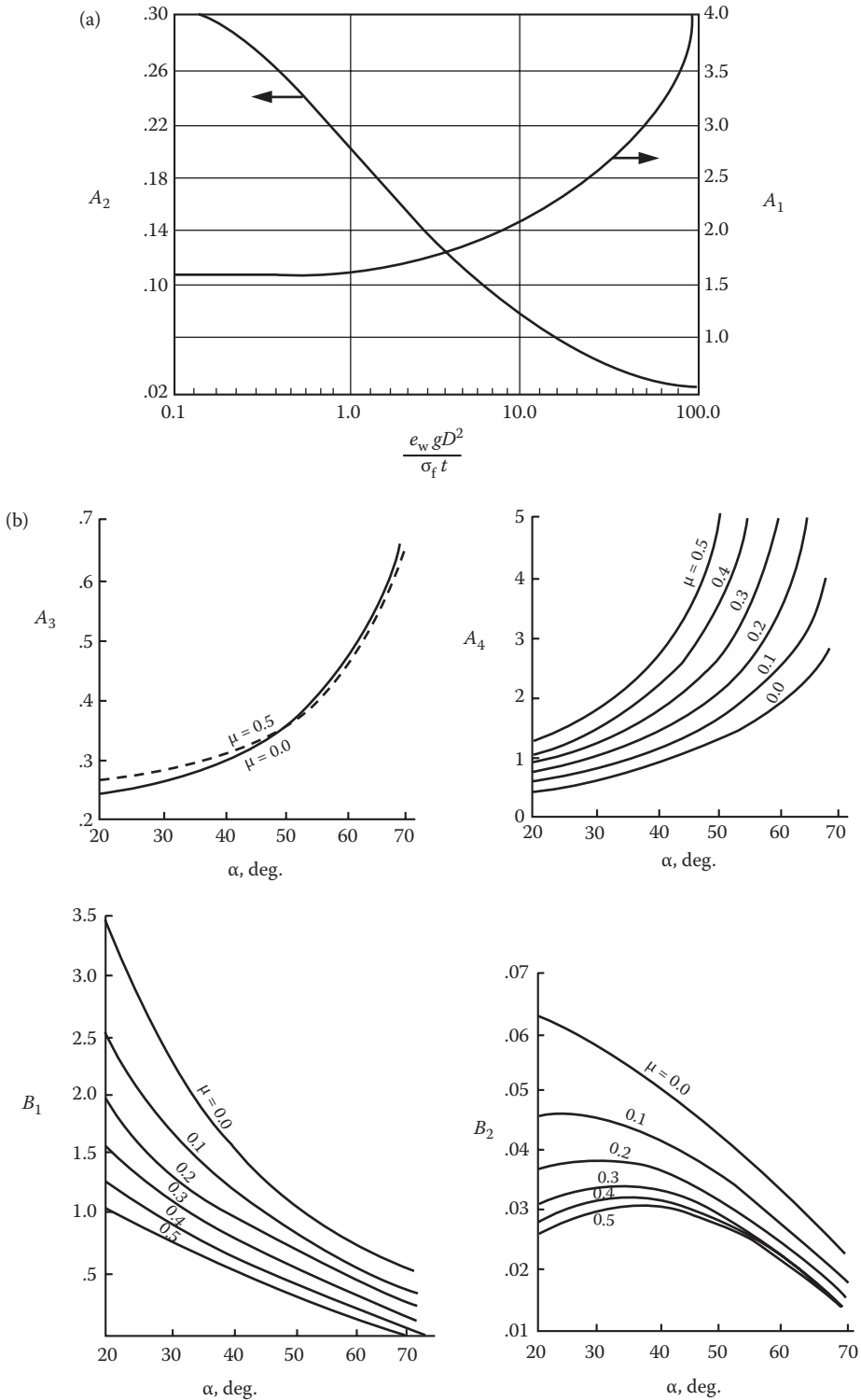
where  $C_m$  is the added mass of water,  $L$  is the width (or length) of the ice field, as shown in Figure 6.31 [55],  $p_e$  is the effective ice crushing pressure at the interface,  $\rho_i$  is the mass density of ice, and  $R_s$  is the radius of the structure.

Instead of a limit momentum situation, wherein the moving (due to wind and current forces) ice feature is stopped by the stationary structure, the force exerted on the structure by the moving ice field may be limited by the formation of ridges within the ice field. Under this circumstance, the limit-force ice load exerted on the structure is given as [56]

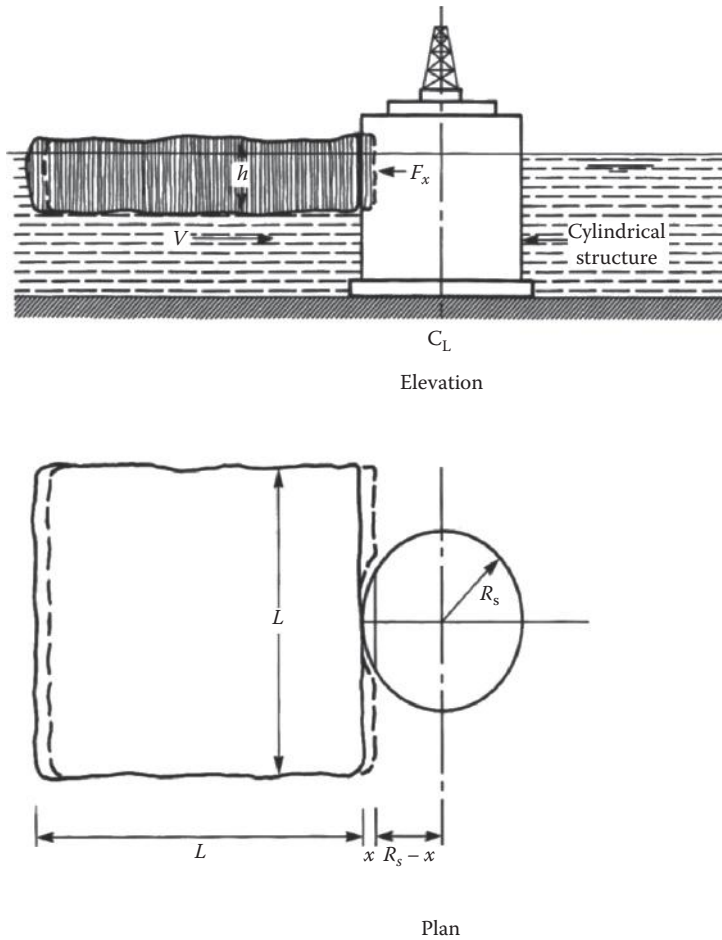
$$F_{z_{max}} = (C_a\rho_aV_a^2A) + (1/2)(C_c\rho_cV_c^2A) + (wL) \tag{6.69}$$

where  $C_a$  is the drag coefficient for air,  $V_a$  is the velocity of the wind (or air) dragging on the surface of ice,  $A = L^2$  (assumed to be a square),  $C_c$  is the coefficient of drag for the current at the site,  $V_a$  is the velocity of wind (or air),  $\rho_a$  is the mass density of air (or wind),  $\rho_c$ , is the mass density of water (in current),  $V_c$  is the current velocity at the site, and  $w$  is the ridge-building force, averaged over the width  $L$ , shown in Figure 6.32 [57].





**FIGURE 6.30** (a) Constants  $A_1$  and  $A_2$  in Equation 6.65 with  $t \equiv h$ . (b) Constants  $A_3$ ,  $A_4$ ,  $B_1$ , and  $B_2$  in Equation 6.65 with  $t \equiv h$ . (From Croasdale, K.R., *Ice Forces on Offshore Structures*, Symposium on Offshore Mechanics and Cold Ocean Engineering, Calgary, Canada, February, p. 20, 1983. With permission.)



**FIGURE 6.31** Impact of an ice feature with a cylindrical offshore structure. (From A.B. Cammaert and D.B. Muggeridge, *Ice Interaction with Offshore Structures*, Van Nostrand Reinhold, New York, p. 209, 1988. With permission.)

Other typical cases of ice force developments in offshore areas would include ridge loads on conical structures in the Arctic and sub-Arctic regions, mixed mode of failure around wide structures (such as vertical walled offshore islands and sloped artificial islands used for exploratory drilling in the cold northern regions of Canada and Russia). Other references such as those of Croasdale [41], Cammaert and Muggeridge [51], and Sanderson [58] could be consulted for the purpose.

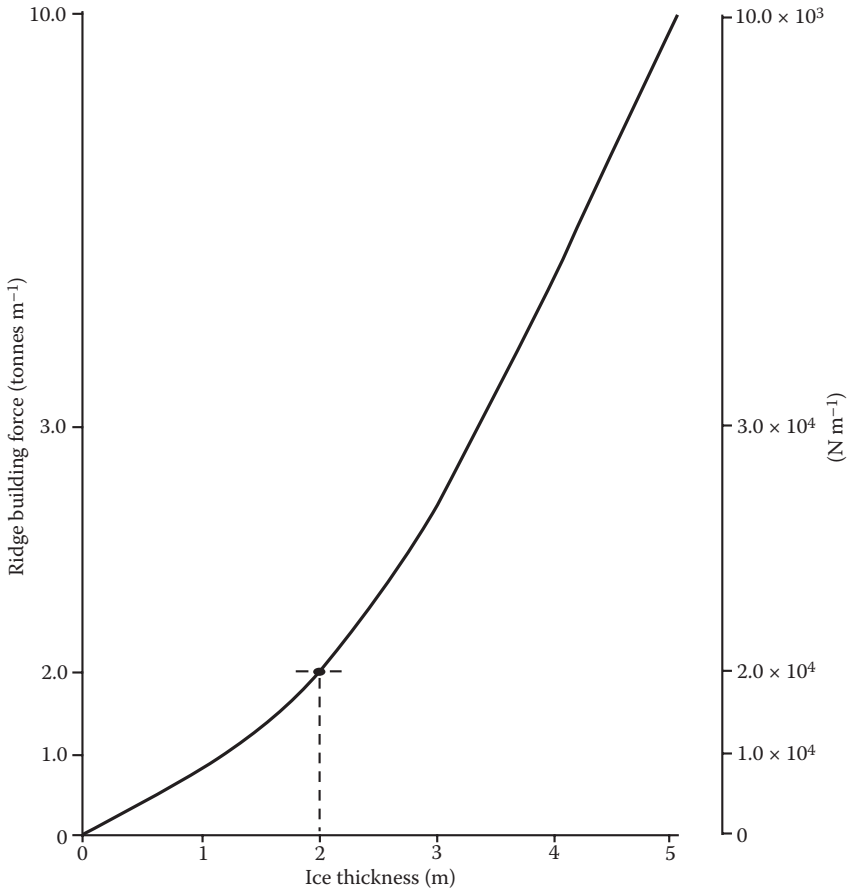
**Example 6.15**

An ice-resistant structure is supported on the top of piles, having an outside diameter of 15.0 ft. For ice sheets of thickness 3.5 ft., determine the maximum force exerted on each pile, when it is struck by the ice sheet. Crushing strength of ice is 300 lbf/in.<sup>2</sup>. Use Equations 6.52, 6.54, 6.56, and 6.58.

- (i) Ice force computation using Equation 6.52.

The relevant equation is given by  $F = (I f_c \sigma_x) Dh = p Dh$ , with  $p = I f_c \sigma_x$ .

The above equation was obtained for a flat indenter, with perfect contact ( $f_c = 1.0$ ) under laboratory conditions. Under field conditions,  $0.4 < f_c < 0.7$ , with a correction factor 0.9 for



**FIGURE 6.32** Average ridge building force vs. ice thickness. (From K.R. Croasdale, *Ice Forces on Offshore Structures*, Symposium on Offshore Mechanics and Cold Ocean Engineering, Calgary, Canada, February, p. 42, 1983. With permission.)

a circular indenter; take  $f_c = 0.4$ . From Figure 6.26,  $I$  (with  $f_c = 1.0$ ) and  $I = 3.00$  (for  $D/t = D/h = 15/3.5 = 4.29$ ).

$$p \approx (3.00)(0.4)(0.9)(300) = 324.0 \text{ lbf/in.}^2.$$

$$\text{Ice force} = F = (324.0 \times 144)(15.0)(3.5) = 2,449,440.0 \text{ lbf.}$$

(ii) Ice force computation using Equation 6.54:

The relevant equation is given by  $F = \Phi Dh[\sigma_x(\text{strain rate}, \phi, \psi)]$ .

$$\Phi = \text{minimum of } [2.986 \text{ or } (2/\sqrt{3})\{1.0 + (0.25)(\sqrt{2})(3.5/15)\}] = 1.25.$$

$$\text{Ice force} = (1.25)(15.0)(3.5)(300.0 \times 144) = 2,835,000.0 \text{ lbf.}$$

(iii) Ice force computation using Equation 6.56:

The relevant equation is given by  $F = pA = pDh$ .

$$p = (0.7)(300.0) = 210.0 \text{ lbf/in.}^2 \geq 350.0 \text{ lbf/in.}^2.$$

$$\text{Ice force} = (350.0 \times 144)(15.0)(3.5) = 2,646,000.0 \text{ lbf.}$$

(iv) Ice force computation using Equation 6.58:

The relevant equation is given by  $F = [f_c m (U/U_0)^{(-0.333)} \sigma_x] D h = p D h$ .

In the above equation, take  $U/U_0 = 1.0$ ,  $l = 2.5$ ,  $m = 0.9$ , and  $f_c = 0.55$  ( $0.4 < f_c < 0.7$ ).

$$\text{Ice force} = (2.5)(0.55)(0.9)(1.0)(300.0 \times 144)(15.0)(3.5) = 2,806,650.0 \text{ lbf.}$$

All the four formulations give results that are reasonable, the maximum difference being +15.74%.

**Example 6.16**

Compute the horizontal and vertical loads exerted on a sloping conical tower, with a slope of 45°, by an ice sheet of 1.0-m thickness. The coefficient of friction,  $\mu$ , is given as 0.30. The free board, up to the neck of the conical tower, is given as 5.0 m (from the mean sea level). Take  $\rho_w = 1040 \text{ kgf/m}^3$  and  $\rho_i = 900.0 \text{ kgf/m}^3$ . The bending strength of sea ice is given as 500.0 kPa. The diameter of the conical tower is given as 20.0 m at the mean sea level. Take the elastic modulus of ice as 7.0 GPa. Consider both the two- and three-dimensional formulations for computing the ice forces on the conical tower. Take  $\nu_i = 0.33$ .

(i) Two-dimensional formulation of the ice-sheet failure on the conical tower:

The relevant equation is given in Equation 6.64 by

$$H = b[(0.68)\sigma_{br}C_1\{(\rho_wgh^5)(1-\nu_i^2)/E_i\}^{(1/4)} + zh\rho_wgC_2],$$

$$\text{with } C_2 = C_1(\sin\alpha + \mu\cos\alpha) + \{(\sin\alpha + \mu\cos\alpha)/\tan\alpha\}$$

$$\text{Also, } C_1 = \left( \frac{\sin\alpha + \mu\cos\alpha}{\cos\alpha - \mu\sin\alpha} \right) = \{[\sin(45^\circ) + (0.3)\cos(45^\circ)]/[\cos(45^\circ) - \sin(45^\circ)]\} = \{0.7071 + (0.3)(0.7071)\}/\{0.7071 - (0.3)(0.7071)\} = (0.91923/0.49497) = 1.857.$$

$$C_2 = (1.857)(0.91923) + (0.91923)/\tan(45^\circ) = 2.626.$$

$$\text{Horizontal force on the conical structure} = H = [(0.68)(20.0)(500,000)(1.857)] \times$$

$$[(1040 \times 9.81)(1.0)^5(1.0 - 0.33^2)/(7.0 \times 1,000,000,000)]^{(0.25)} + (20.0)(5.0)(1.0)(900 \times 9.81) (2.626) = (12,627,600.0)[0.03374] + 2,378,495.40 = 472,272.24 + 2,378,495.40 = 2,850,767.64 \text{ N} = 2850.8 \text{ kN.}$$

As per Equation 6.59, vertical force on the conical structure =  $V = (H/C_1) = 2850.8/1.857 = 1535.15 \text{ kN}$ .

(ii) Three-dimensional formulation of the ice-sheet failure on the conical structure:

As per Equation 6.65, the force is given by

$$H = A_4[A_1\sigma_{br}h^2 + A_2\rho_wghD^2 + A_3\rho_wgh(D^2 - D_f^2)]$$

$$V = B_1H + B_2\rho_wgh(D^2 - D_f^2)$$

From Figure 6.30a and b, the values of the constants  $A_1, A_2, A_3, A_4, B_1$ , and  $B_2$  can be obtained.

$$(\rho_wgD^2)/(\sigma_{br}t) = [(1040)(9.81)(20^2)]/[(500)(1000.0)(1.0)] = 8.16; \text{ also } \alpha = 45^\circ.$$

$$A_1 \approx 2.0; A_2 \approx 0.095; A_3 \approx 0.31; A_4 \approx 1.9; B_1 \approx 0.75; \text{ and } B_2 \approx 0.032.$$

Horizontal force =  $(1.9)[(2.0)(500 \times 1000)(1.0)^2 + (0.095)(1040)(9.81)(1.0)(20.0)^2 + (0.31)(1040)(9.81)(1.0)(20^2 - 10^2)] = (1.9)[(1.0)(10^6) + (0.3877)(10^6) + (0.9488)(10^6)] = (4.438)(10^6) \text{ N} = 4438.0 \text{ kN}$ .

Vertical force =  $(0.75)(4438.0) + (0.032)(1040)(9.81)(1.0)(20^2 - 10^2)/(1000) = 3328.5 + 97.94 = 3425.44 \text{ kN}$ .

The three-dimensional formulation gives a horizontal force 55.68% higher than the two-dimensional formulation.

### Example 6.17

Compute the maximum ice forces exerted on an artificial gravity island by a large ice feature  $30 \times 30 \text{ km}$  due to limit force exerted on it by a driving wind of  $30 \text{ m/s}$ . The surface current speed at the bottom of ice is  $0.30 \text{ m/s}$ . The drag coefficients for wind-on-ice and water-on-ice are  $3 \times 10^{-3}$  and  $0.50$ , respectively.  $\rho_w = 1030 \text{ kg/m}^3$  and  $\rho_a = 1.26 \text{ kg/m}^3$ . The thickness of the ice feature is  $3.5 \text{ m}$ .

As per Equation 6.69, the relevant equation for force computation is given as

$$F_{z_{\max}} = (C_a \rho_a V_a^2 A) + (1/2)(C_c \rho_c V_c^2 A) + (wL)$$

From Figure 6.32,  $w = (3.0)(10^4) \text{ N/m}$ .

$$\text{Limit force exerted on the ice feature} = (3.0)(10^{-3})(1.26)(30)^2(30,000)^2$$

$$+ (0.5)(1030)(0.30)^2(30,000)^2 + (30,000)(30,000) = (3.06)(10^9)$$

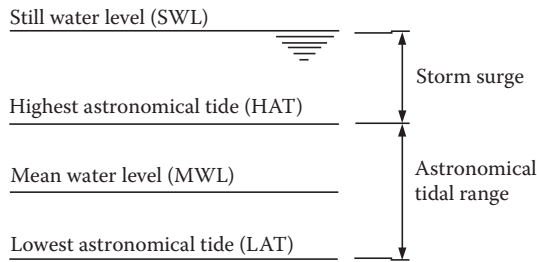
$$+ (41.72)(10^9) + (0.9)(10^9) = 45.68 \text{ GN}$$

### 6.3.8 TIDES

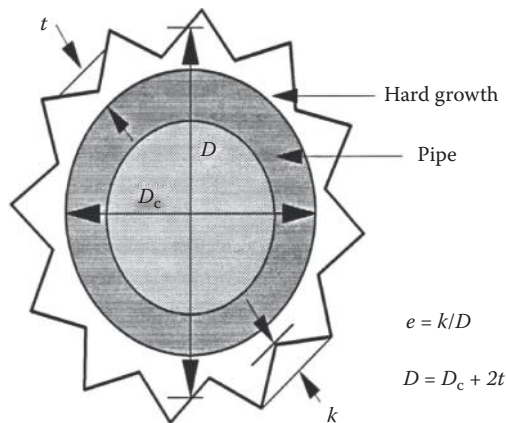
Tides have an indirect influence on wave and current loads applied on the offshore platforms, viz., through the change in the sea surface elevation. The tides that have a bearing on the wave forces are (i) astronomical tides caused by the gravitational pull exerted on the earth by the moon and the sun, and (ii) storm surges generated by the combined action of ocean wind and barometric pressure differentials caused during a storm. The combined effect of the above two types of tide is termed as the storm tide. The tide-dependent sea surface levels are shown in Figure 6.33. The astronomical tide range depends on the geographic location of the offshore structure and the phase of the moon. The maximum astronomical tide, called the spring tide, occurs at new moon, and the range varies from a few centimeters to several meters and may be obtained from special tidal maps, published for the purpose [59, 60]. Storm surges depend upon the return period of the particular storm and their ranges are between  $1.0$  and  $3.0 \text{ m}$ . While designing an offshore platform, the design mean sea level is obtained by adding the extreme storm surges to the still water level (see Figure 6.33 [21]), while for the design of boat landing places, barge fenders, upper limits of marine growth, etc., the daily variations of the astronomical tide are used.

### 6.3.9 MARINE GROWTH

Marine growth gets accumulated on submerged members of offshore structures such as columns and braces, conductors, risers, appurtenances, etc. The member size gets increased as shown in Figure 6.34 [61]. Its main effect is to increase the wave and current forces on the members by increasing the exposed areas and volumes and the drag coefficients to be used for the member, due



**FIGURE 6.33** Tidal levels associated with an offshore structure. (From the ESDEP (The European Steel Design Education Programme) Course Notes, *Lecture 15A.2: Loads (I), Section 2.2, Introduction and Environmental Loads*. Available at <http://www.esdep.org/members/master/toc.htm>, 1993. With permission.)



**FIGURE 6.34** Effective marine growth diameter and surface roughness. (From API-RP2A-LRFD, Recommended Practice for Planning, Designing and Constructing Fixed Offshore Platforms—Load and Resistance Factor Design, 1st Edition, American Petroleum Institute, Washington, DC, Commentary, p. 132, 1993. With permission.)

to its higher surface roughness. Moreover, it also increases the member mass, resulting in higher self-weight of the member. Depending upon the geographic location of the platform, the marine growth thickness ( $t$ ) can sometimes reach a thickness of 0.3 m or more. It gets accounted for in the design of the member or the overall structure through relevant increases in the diameters and masses of the various submerged members, used in the force computation for the structure.

## EXERCISE PROBLEMS

1. The transmission towers shown in Figure P6.1 support four 2-cm-diameter transmission lines over spans of 120.0 m between the towers. The towers (located at Saint John, NB) are constructed of angle iron 5 cm on a side for the main members and 3.2 cm on a side for the bracings, forming approximately equilateral triangles with the main column members. The cross section of the towers is square. Determine the maximum overturning moment on a tower due to a wind with a return period of 100 years. The height coefficient ( $n$ ) on the power line for the site is given as 0.16. The wind averaging time for gusts is 3 s. The drag coefficient for the cables is 1.2 and the density of wind is  $1.167 \text{ kg/m}^3$  (see Figure P6.2 [62], Table P6.1 [17] for additional details); use the wind variation above the reference to be as per (i) DEN provisions and (ii) the shortened equation given in the text.

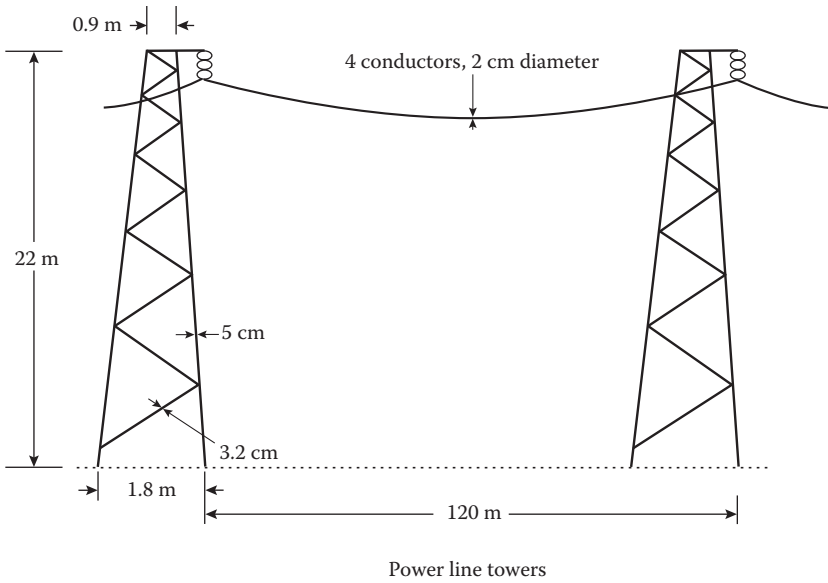


FIGURE P6.1 Electrical power transmission tower.

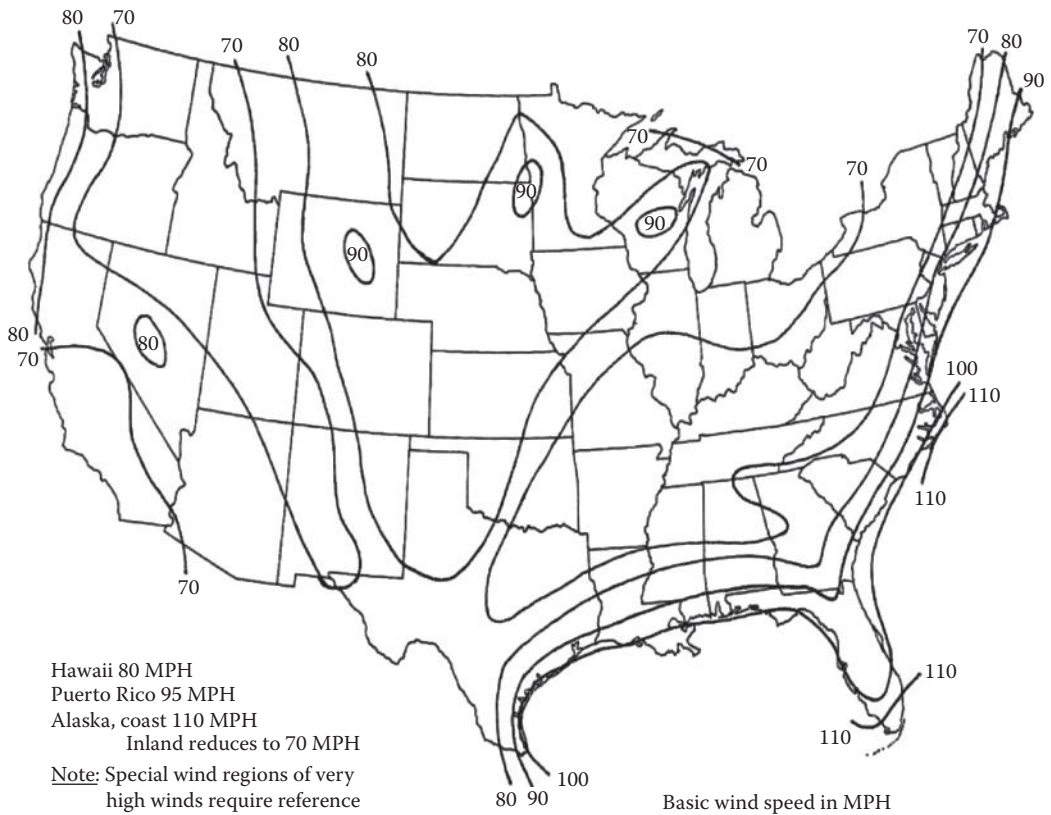
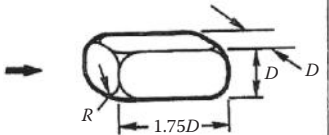
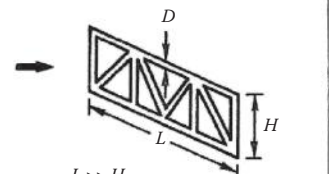
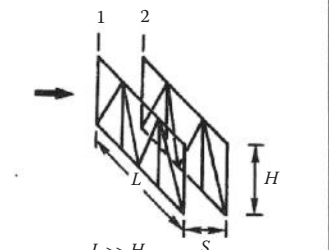


FIGURE P6.2 Fastest mile (approx.) in the United States, 30.0 ft. above ground, with a recurrence interval of 100.0 years (From B.S. Benjamin, *Structures for Architects*, Van Nostrand Reinhold Company, New York, p. 17, 1984. With permission.)

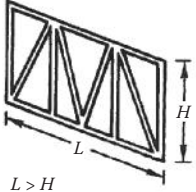

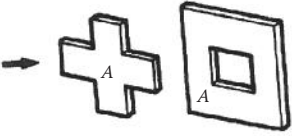
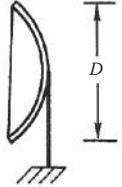


**TABLE P6.1**  
**Drag Coefficients for Bluff Bodies (at a Height of 30.0 ft. above the Ground Level)**

Geometry	Reference Area, $A$	Drag Coefficient, $C_D$ , and Remarks																																																														
<p>20. Square rod with rounded corners</p>  <p>All corners are rounded</p>	$D^2$	<table border="1"> <thead> <tr> <th rowspan="3"><math>R/D</math></th> <th colspan="2"><math>C_D</math></th> </tr> <tr> <th colspan="2">Re</th> </tr> <tr> <th><math>5.5 \times 10^5</math></th> <th><math>8.2 \times 10^6</math></th> </tr> </thead> <tbody> <tr> <td>0.0</td> <td>0.75</td> <td>0.75</td> </tr> <tr> <td>0.025</td> <td>0.60</td> <td>0.35</td> </tr> <tr> <td>0.50</td> <td>0.55</td> <td>0.25</td> </tr> <tr> <td>0.10</td> <td>0.32</td> <td>0.15</td> </tr> <tr> <td>0.20</td> <td>0.17</td> <td>0.15</td> </tr> <tr> <td>0.25</td> <td>0.17</td> <td>0.15</td> </tr> </tbody> </table> <p><math>R</math> = edge radius</p>	$R/D$	$C_D$		Re		$5.5 \times 10^5$	$8.2 \times 10^6$	0.0	0.75	0.75	0.025	0.60	0.35	0.50	0.55	0.25	0.10	0.32	0.15	0.20	0.17	0.15	0.25	0.17	0.15																																					
$R/D$	$C_D$																																																															
	Re																																																															
	$5.5 \times 10^5$	$8.2 \times 10^6$																																																														
0.0	0.75	0.75																																																														
0.025	0.60	0.35																																																														
0.50	0.55	0.25																																																														
0.10	0.32	0.15																																																														
0.20	0.17	0.15																																																														
0.25	0.17	0.15																																																														
<p>21. Open frame</p>  <p><math>L \gg H</math></p> <p>Frame details for example only.</p>	Projected solid area, $A_s$	<table border="1"> <thead> <tr> <th rowspan="2">Truss type</th> <th colspan="9">Solidarity ratio, <math>A_s/A</math></th> </tr> <tr> <th>0</th> <th>0.1</th> <th>0.2</th> <th>0.3</th> <th>0.4</th> <th>0.6</th> <th>0.8</th> <th>0.9</th> <th>1.0</th> </tr> </thead> <tbody> <tr> <td>Square edges</td> <td>2.0</td> <td>1.8</td> <td>1.7</td> <td>1.6</td> <td>1.6</td> <td>1.6</td> <td>1.6</td> <td>1.6</td> <td>2.0</td> </tr> <tr> <td>Round edge, <math>Re &lt; 2 \times 10^5</math></td> <td>1.5</td> <td>1.3</td> <td>1.3</td> <td>1.2</td> <td>1.2</td> <td>1.2</td> <td>--</td> <td>--</td> <td>--</td> </tr> <tr> <td>Round edge, <math>Re &gt; 5 \times 10^5</math></td> <td>1.1</td> <td>0.9</td> <td>0.9</td> <td>0.8</td> <td>0.8</td> <td>0.8</td> <td>--</td> <td>--</td> <td>--</td> </tr> </tbody> </table> <p><math>A</math> = total area = <math>HL</math>  <math>Re = UD/\nu</math></p>	Truss type	Solidarity ratio, $A_s/A$									0	0.1	0.2	0.3	0.4	0.6	0.8	0.9	1.0	Square edges	2.0	1.8	1.7	1.6	1.6	1.6	1.6	1.6	2.0	Round edge, $Re < 2 \times 10^5$	1.5	1.3	1.3	1.2	1.2	1.2	--	--	--	Round edge, $Re > 5 \times 10^5$	1.1	0.9	0.9	0.8	0.8	0.8	--	--	--													
Truss type	Solidarity ratio, $A_s/A$																																																															
	0	0.1	0.2	0.3	0.4	0.6	0.8	0.9	1.0																																																							
Square edges	2.0	1.8	1.7	1.6	1.6	1.6	1.6	1.6	2.0																																																							
Round edge, $Re < 2 \times 10^5$	1.5	1.3	1.3	1.2	1.2	1.2	--	--	--																																																							
Round edge, $Re > 5 \times 10^5$	1.1	0.9	0.9	0.8	0.8	0.8	--	--	--																																																							
<p>22. Multiple frames</p>  <p><math>L \gg H</math></p>	Projected solid area, $A_s$	<p>Drag coefficient of 1st truss given by frame 21.                      Drag coefficient of second or more trusses given by</p> $\alpha C_D \Big _{\text{frame 21}}$ <p>where <math>\alpha = f(A_s/A, S/L)</math></p> <table border="1"> <thead> <tr> <th rowspan="2"><math>S/H</math></th> <th colspan="6"><math>\alpha</math></th> </tr> <tr> <th colspan="6"><math>A_s/A</math></th> </tr> <tr> <th></th> <th>0.1</th> <th>0.2</th> <th>0.3</th> <th>0.4</th> <th>0.5</th> <th>0.6 to 1.0</th> </tr> </thead> <tbody> <tr> <td>0.5</td> <td>0.95</td> <td>0.75</td> <td>0.55</td> <td>0.38</td> <td>0.18</td> <td>0.0</td> </tr> <tr> <td>1.0</td> <td>1.0</td> <td>0.82</td> <td>0.63</td> <td>0.50</td> <td>0.32</td> <td>0.15</td> </tr> <tr> <td>2.0</td> <td>1.0</td> <td>0.87</td> <td>0.72</td> <td>0.55</td> <td>0.43</td> <td>0.30</td> </tr> <tr> <td>3.0</td> <td>1.0</td> <td>0.90</td> <td>0.75</td> <td>0.61</td> <td>0.48</td> <td>0.35</td> </tr> <tr> <td>4.0</td> <td>1.0</td> <td>0.92</td> <td>0.77</td> <td>0.65</td> <td>0.50</td> <td>0.40</td> </tr> <tr> <td>6.0</td> <td>1.0</td> <td>0.94</td> <td>0.83</td> <td>0.70</td> <td>0.60</td> <td>0.50</td> </tr> </tbody> </table> <p><math>A</math> = total area = <math>HL</math></p>	$S/H$	$\alpha$						$A_s/A$							0.1	0.2	0.3	0.4	0.5	0.6 to 1.0	0.5	0.95	0.75	0.55	0.38	0.18	0.0	1.0	1.0	0.82	0.63	0.50	0.32	0.15	2.0	1.0	0.87	0.72	0.55	0.43	0.30	3.0	1.0	0.90	0.75	0.61	0.48	0.35	4.0	1.0	0.92	0.77	0.65	0.50	0.40	6.0	1.0	0.94	0.83	0.70	0.60	0.50
$S/H$	$\alpha$																																																															
	$A_s/A$																																																															
	0.1	0.2	0.3	0.4	0.5	0.6 to 1.0																																																										
0.5	0.95	0.75	0.55	0.38	0.18	0.0																																																										
1.0	1.0	0.82	0.63	0.50	0.32	0.15																																																										
2.0	1.0	0.87	0.72	0.55	0.43	0.30																																																										
3.0	1.0	0.90	0.75	0.61	0.48	0.35																																																										
4.0	1.0	0.92	0.77	0.65	0.50	0.40																																																										
6.0	1.0	0.94	0.83	0.70	0.60	0.50																																																										

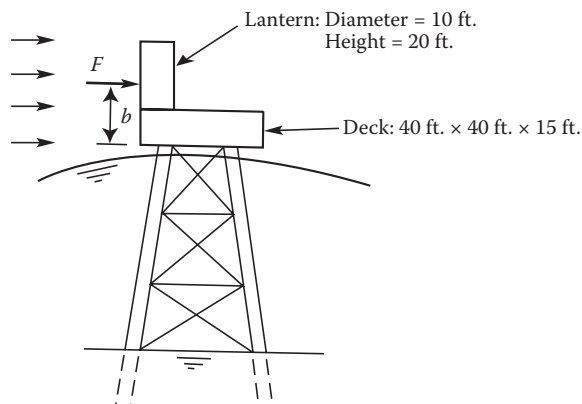
(continued)

**TABLE P6.1 (Continued)**  
**Drag Coefficients for Bluff Bodies (at a Height of 30.0 ft. above the Ground Level)**

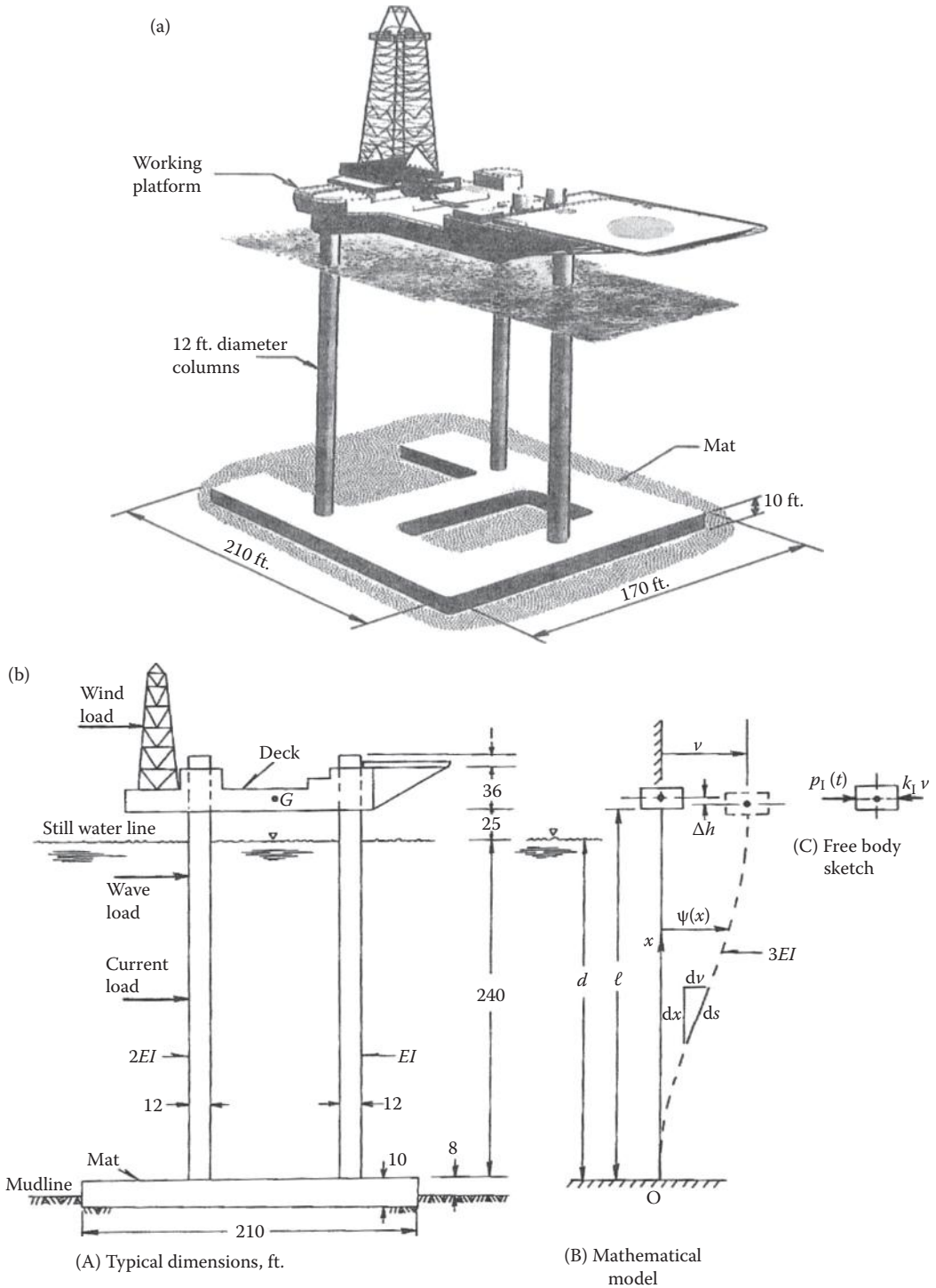
Geometry	Reference Area, $A$	Drag Coefficient, $C_D$ , and Remarks																																									
<p>23. Effect of aspect ratio on open frame</p>  <p><math>L &gt; H</math></p>	<p>Projected solid area, <math>A_s</math></p>	<p><math>\beta C_D</math> frame 20, frame 21</p> <p>where <math>\beta = F(H/L, A_s/A)</math></p> <table border="1" data-bbox="628 484 1032 672"> <thead> <tr> <th rowspan="2"><math>H/L</math></th> <th colspan="5"><math>\beta</math></th> </tr> <tr> <th colspan="5"><math>A_s/A</math></th> </tr> <tr> <th></th> <th>0.25</th> <th>0.50</th> <th>0.90</th> <th>0.95</th> <th>1.0</th> </tr> </thead> <tbody> <tr> <td>0</td> <td>1.0</td> <td>1.0</td> <td>1.0</td> <td>1.0</td> <td>1.0</td> </tr> <tr> <td>0.02</td> <td>0.99</td> <td>0.98</td> <td>0.97</td> <td>0.95</td> <td>0.89</td> </tr> <tr> <td>0.05</td> <td>0.98</td> <td>0.97</td> <td>0.95</td> <td>0.89</td> <td>0.75</td> </tr> <tr> <td>0.2</td> <td>0.95</td> <td>0.92</td> <td>0.88</td> <td>0.78</td> <td>0.59</td> </tr> </tbody> </table> <p><math>A = \text{total area} = HL</math></p>	$H/L$	$\beta$					$A_s/A$						0.25	0.50	0.90	0.95	1.0	0	1.0	1.0	1.0	1.0	1.0	0.02	0.99	0.98	0.97	0.95	0.89	0.05	0.98	0.97	0.95	0.89	0.75	0.2	0.95	0.92	0.88	0.78	0.59
$H/L$	$\beta$																																										
	$A_s/A$																																										
	0.25	0.50	0.90	0.95	1.0																																						
0	1.0	1.0	1.0	1.0	1.0																																						
0.02	0.99	0.98	0.97	0.95	0.89																																						
0.05	0.98	0.97	0.95	0.89	0.75																																						
0.2	0.95	0.92	0.88	0.78	0.59																																						
<p>24. Average Man</p> 	<p>See data at right</p>	<p>→ <math>C_D A = 9 \text{ ft}^2 (0.84 \text{ m}^2)</math></p> <p>† <math>C_D A = 1.2 \text{ ft}^2 (0.11 \text{ m}^2)</math></p> <p>• <math>C_D A = 5 \text{ ft}^2 (0.46 \text{ m}^2)</math></p> <p>Sitting → <math>C_D A = 6 \text{ ft}^2 (0.56 \text{ m}^2)</math></p> <p>Crouching → <math>C_D A = 2 \text{ to } 3 \text{ ft}^2 (0.19 \text{ m}^2 \text{ to } 0.28 \text{ m}^2)</math></p>																																									
<p>25. Various plate sections</p> 	<p>Solid area</p>	<p><math>C_D = 1.2</math></p> <p>Solidity is 40% to 70% of square plate of same overall dimensions</p>																																									
<p>26. Porous parabolic dish</p> 	<p><math>\frac{\pi D^2}{4}</math></p>	<table border="1" data-bbox="619 1267 1130 1373"> <thead> <tr> <th>Porosity</th> <th>0</th> <th>0.1</th> <th>0.2</th> <th>0.3</th> <th>0.4</th> <th>0.5</th> </tr> </thead> <tbody> <tr> <td>→ <math>C_D</math></td> <td>1.42</td> <td>1.33</td> <td>1.20</td> <td>1.05</td> <td>0.95</td> <td>0.82</td> </tr> <tr> <td>← <math>C_D</math></td> <td>0.95</td> <td>0.92</td> <td>0.90</td> <td>0.86</td> <td>0.83</td> <td>0.80</td> </tr> </tbody> </table> <p>Porosity = open area/total area.</p> <p><math>Re = 2 \times 10^6</math></p>	Porosity	0	0.1	0.2	0.3	0.4	0.5	→ $C_D$	1.42	1.33	1.20	1.05	0.95	0.82	← $C_D$	0.95	0.92	0.90	0.86	0.83	0.80																				
Porosity	0	0.1	0.2	0.3	0.4	0.5																																					
→ $C_D$	1.42	1.33	1.20	1.05	0.95	0.82																																					
← $C_D$	0.95	0.92	0.90	0.86	0.83	0.80																																					

Source: R.D. Blevins, *Applied Fluid Dynamics Handbook*, Van Nostrand Reinhold Company, pp. 336–337, 1984. Reproduced with permission.

2. Consider the small light tower shown in Figure P6.3 [63] and determine the total wind force  $F$  on the deck and lantern, assuming a wind speed (with gust factor) of 170 mph. Also locate its resultant distance  $b$  above the base of the deck. Take the given wind speed to be at a height of 33 ft. above msl. The wind speed variation above the surface (msl) is governed by (i) DEn guidelines and (ii) The actual equation given in the text for wind [ $\rho_{\text{air}} = 1.293 \text{ kg/m}^3$ ,  $z_0 = 0.01$ ,  $C_d = 0.7$ ,  $\phi = 50^\circ$  (latitude of site)].
3. The jack-up platform, shown in Figure P6.4a [64] and Figure P6.4b [65], extends 190 ft. above the still water line. (a) Assuming the deck height to be 25 ft. and platform size to be 210 ft.  $\times$  170 ft. (plan form), compute the wind forces exerted on the structure in terms of forces and turning moments about the base of the columns of the jack-up platform. (b) Assuming each story level of the rig (seven story) to be 20 ft. high and braced in a simple manner, as shown in Figure P6.4b, and the structural members to be 12  $\times$  12-in. equal angles for inclined columnar members and 8  $\times$  8 in. for horizontal/inclined bracings, determine the wind forces on the drilling derrick considering the transparency of the structure. Consider the wind to be blowing along the longitudinal direction of the jack-up drilling rig, and the dimensions of the drilling derrick to be 40  $\times$  40 ft. at its base and 19  $\times$  19 ft. at its top (assume all stories to be of similar shape). Assume that the jack-up rig is operating in the Gulf of Mexico and the operating wind speed is 30 m/s. Use the NBCC (Canada) provisions to compare the wind forces obtained by Morison–O'Brien's equation (along with the 1-min wind speed, given in Table P6.2 [66]).
4. Consider the small light tower, shown in Figure P6.5a and b, and determine the maximum wind force exerted on the cylindrical legs, deck, and lantern, assuming a mean wind velocity of 120 mph. The maximum gust factor at the location is 1.60; also, locate the distance of its resultant force above the base of the deck. Take the drag coefficients from the tables given in Table P6.1.
5. The coefficients  $C_D$  and  $C_M$  of a cylinder are dependent on a number of parameters such as (i) Reynolds number; (ii) Keulegan–Carpenter number; and (iii) the cylinder roughness. Explain, clearly, the meaning of surface roughness of a cylinder, and how this would affect the value of the coefficients  $C_D$  and  $C_M$  under steady-state and periodic flow conditions.
6. A cylindrical pipe with diameter 1.00 m, extends 25.0 m above the water surface, and is supporting a small wind-speed measuring device (anemometer) at its top. The average 1 min sustained wind speed measured by the anemometer, at the site, is computed to be 128.0 kmph. Compute the maximum wind force acting on the tower, using the average



**FIGURE P6.3** Light tower located on top of an offshore platform. (From T.H. Dawson, *Offshore Structural Engineering*, Prentice Hall Inc., Englewood Cliffs, NJ, p. 147, 1983. With permission.)



**FIGURE P6.4** (a) Jack-up platform. (J.F. Wilson, *Dynamics of Offshore Structures*, p. 5, 1984. Copyright Wiley-VCH Verlag GmbH & Co. KGaA. Reproduced with permission.) (b) Vertical cross-sectional details of the jack-up platform. (J.F. Wilson, *Dynamics of Offshore Structures*, p. 42, 1984. Copyright Wiley-VCH Verlag GmbH & Co. KGaA. Reproduced with permission.)

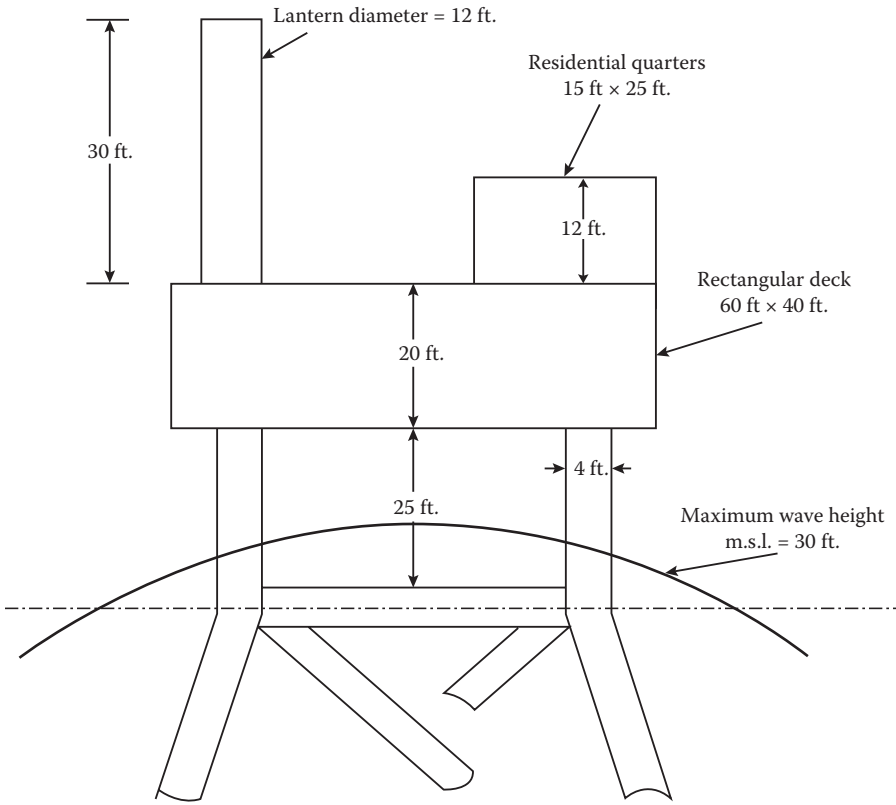
**TABLE P6.2**  
**Wind Averaging Duration for Offshore Drilling Rigs**

Fastest Mile (mph)	Duration (s)					
	60	30	20	10	5	0.5
60	1.0	1.08	1.12	1.18	1.24	1.37
120	–	1.0	1.04	1.10	1.12	1.29

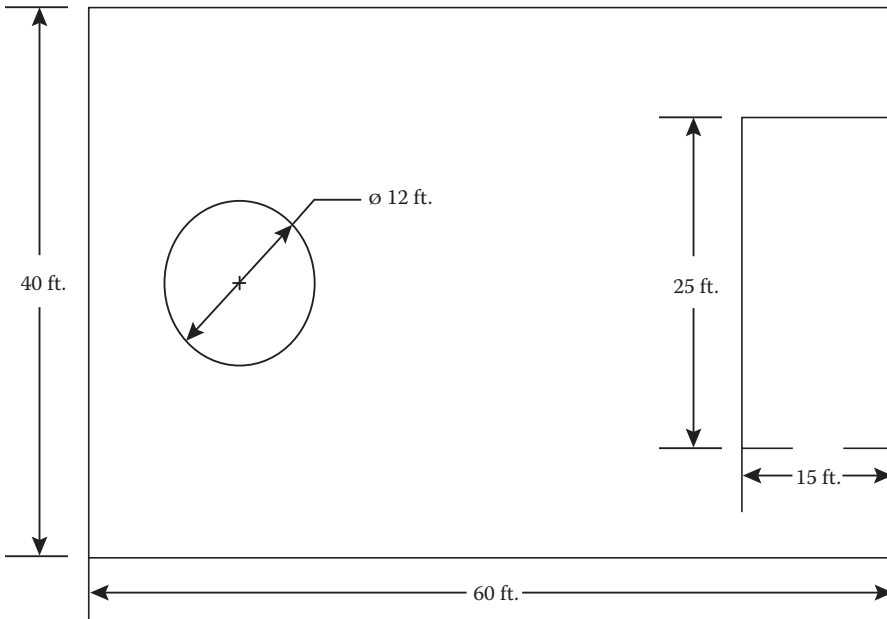
Source: T.H. Dawson, *Offshore Structural Engineering*, Prentice Hall Inc., Englewood Cliffs, NJ, p. 148, 1983. With permission.

wind speed (per minute) at a height of 12.5 m above the water surface as the uniform wind speed acting over the whole pipe.

7. Briefly discuss the following: (i) Wind averaging period and its effect on wind energy spectrum; (ii) extreme response analysis for the wind loads on structures; and (iii) Reynold's and Keulegan–Carpenter's numbers.
8. A vertical cylindrical pipe, of height 60.0 ft. above the seabed, is standing at a water depth of 50.0 ft. The pipe is considered to be fixed rigidly to the sea floor, and the pipe diameter is 3.0 ft. The pipe is acted on by a uniform current of speed 4.0 ft./s, and its surface is assumed to be smooth. Compute the total force and moment acting at the base of the tower. Mass density of seawater is taken as 2.00 slugs/ft.<sup>3</sup>, and its kinematic viscosity is taken as  $1.26 \times 10^{-6}$  ft.<sup>2</sup>/s.
9. A harbor jetty extends a distance of 2000.0 ft. into the ocean, and is supported by a 12.0-in.-diameter cylindrical wood piles, spaced at 10.0 ft. c/c; the width of the jetty is 30.0 ft., and the piles are also spaced at 10.0 c/c in the transverse (to the length) direction. The depth of the deck of the jetty is 3.5 ft. and its bottom is located at a height of 18.0 ft. above the mean high tide level. The depth of sea water level varies from a mere 15.0 ft. near the shore to a depth of 60.0 ft. at its end. The maximum vertically averaged long-shore current is given as 4.0 ft./s, and the average (over 1.0 min) wind speed is 120 mph (at a height of 30.0 ft., above mean sea level). Compute the maximum force and moment acting at the sea floor for a single pile at the seaward end of the jetty.
10. To collect site-specific oceanographic data, a tower is installed in a water depth of 30.0 m. A dynamic pressure gage, located 16.0 m above the bottom, senses an average maximum dynamic pressure of 7.0 kN/m<sup>2</sup> at a period of 9.0 s. (a) Find (i) the wave height; (ii) the wavelength; and (iii) the wave celerity. Is this the maximum wave height that is present at the site? Why? (b) Assuming the tower to be a cylinder of 3.0 m diameter, find the dynamic wave forces and moments acting on the structure ( $C_D = 1.2$ ,  $C_I = 2.05$ ).
11. Compute the maximum wave force exerted by Airy wave of height 15.0 ft. and length 250.0 ft. on a 4.5-ft.-diameter pile, extending from the sea floor to above the maximum water elevation. Assume that the depth of immersion of the pile (during still water conditions) is 90.0 ft. Let  $C_D = 1.0$  and  $C_I = 2.0$ .
12. A framed platform (with four main columns) is to be installed in St. George's Bank, at a water depth of 30.0 m, having a maximum wave height of 15.0 m, and wave period 15.0 s. Assuming that the platform is composed of vertical piles of 1.0-m diameter only (neglecting the braces) spaced at 20.0 m c/c, find the maximum environmental loads that will act on the structure. Use only Airy's wave equation.
13. A vertical, circular pile with a diameter of 1.0 m, standing in water 30 m deep is subjected to a 4-m-high, 11-s wave. Calculate and plot the drag, inertia, and total force distributions along the pile at the instant the wave crest is 20 m seaward of the pile.
14. For a vertical pile of diameter 8 ft. extending from the sea-floor to above the maximum water elevation, determine the maximum horizontal force, and associated base moment caused by a



(a) Elevation

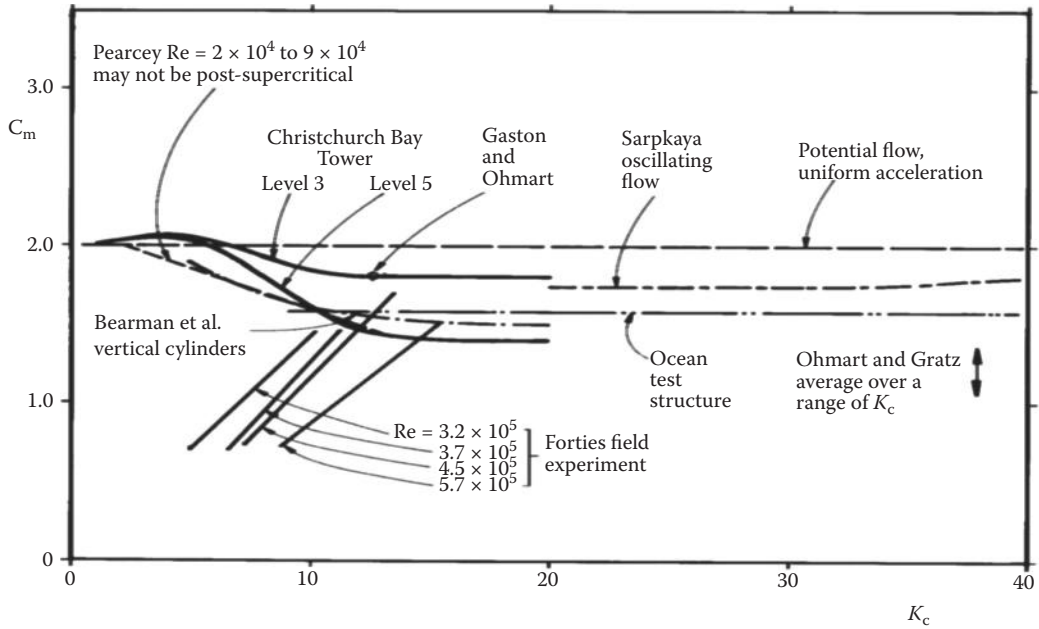


(b) Plan

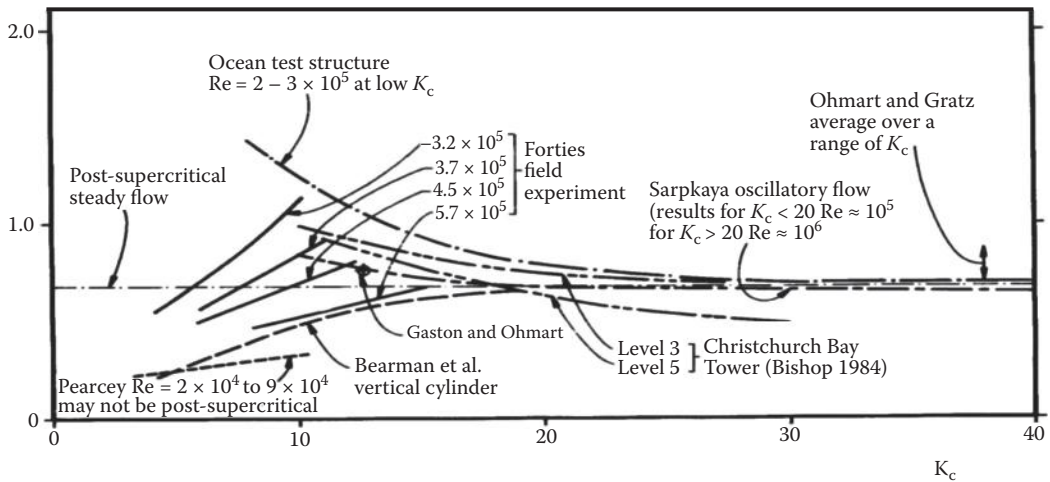
FIGURE P6.5 Elevation and plan of a light tower located on top of an offshore platform.

Stokes wave of height 70 ft. and length 750 ft. moving over sea water 150.0 ft. deep. Assume that  $C_D = 1.0$ ,  $C_I = 2.0$ . Compare the forces obtained with those obtained using Airy's wave theory.

- A vertical pile with a diameter of 9 in. is located in 30 ft. of water and is subjected to 2-ft.-high waves of 20-ft. length. Determine the maximum wave force exerted on the pile and the maximum moment about the base.  $\rho_f = 2.00$  slugs/ft.<sup>3</sup> and  $\nu$  the kinematic viscosity of fluid =  $1.05 \times 10^{-5}$  ft.<sup>2</sup>/s (slug is the unit of mass in FPS system). Choose the hydrodynamic coefficients from Figure P6.6a and b [67].



(a)

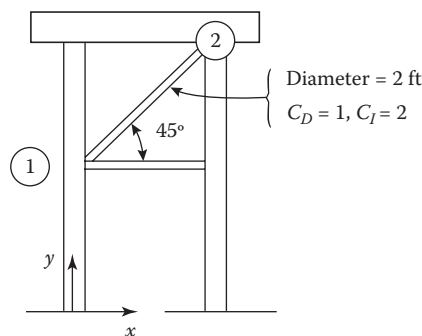


(b)

**FIGURE P6.6** (a)  $C_M$  (top) and (b)  $C_D$  (bottom) for clean vertical cylinders in post-supercritical flow. (From N.D.P. Baltrop and A.J. Adams, *Dynamics of Fixed Marine Structures*, Butterworth-Heinemann, London, p. 316, 1991. With permission.)

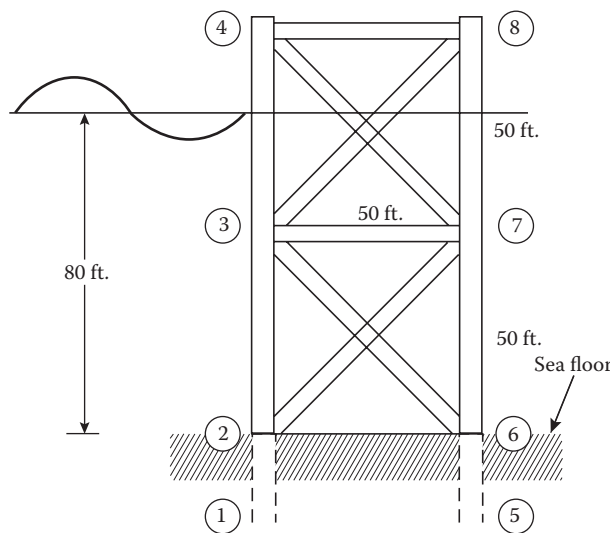


16. A spherical buoy of diameter 3.0 ft. is moored in deep seawater, at a depth of 4.5 ft. below the mean sea level. Regular wave trains, of length 200.0 ft. and height 8.0 ft., pass over the site. What will be the maximum force on the buoy, considering the drag and inertia forces on it?
17. (a) A spherical buoy is fully immersed in a tidal flow. Calculate the drag force exerted on the buoy, knowing that the buoy diameter is 8.0 ft., and the current acting on the buoy is 2.5 knots. The buoy is moored at a depth of 100.0 ft. Take density of sea water to be 64.0 lb./ft.<sup>3</sup> and the kinematic viscosity of sea water to be  $1.26 \times 10^{-5}$  ft.<sup>2</sup>/s. (b) Assuming that the buoy weighs 3000 lb. and that the diameter of the mooring line is 1.5 in. in diameter (average) steel cable, compute the forces acting at the cable ends. Assume that the cable makes a parabolic profile, and the angles at the top and at the bottom are 60° and 25°, respectively.
18. A surface buoy is located at a water depth of 70.0 m and is anchored at a location with a cable rope, weighing 5.0 kgf/m (buoyant weight). The water drag force acting on the buoy is 5.00 kN. Determine the length of the cable rope required for the purpose if the cable is to maintain an angle of 20° at the anchor location. Assume that the cable is inextensible and that the cable assumes a catenary shape under its self-weight. Compute the distance of the buoy from the anchor location.
19. A submerged horizontal cylinder, anchored to the sea floor in deep water (just beneath the still water level surface), is 15.0 ft. long and 3.25 ft. in diameter, and regular wave trains of length 450.0 ft., period 10.00 s, and height 12.0 ft. are passing over it. Considering the maximum wave force only: (a) Compute the ratio of maximum inertia force to the maximum drag force. (b) If this shape was anchored at a depth of 60.0 ft. (below still water level), compute the maximum inertia force from the same waves (now in shallow water) and say whether it is greater or smaller than the inertial force of the deep water case. (c) By how much would the drag force on the cylinder be reduced if it was anchored at 30.0 ft. below the water surface?
20. A horizontal cylindrical brace of an offshore tower, having a diameter of 2.5 m and a length of 25.0 m, is located 6.0 m below the still water level. The water depth is 55.0 m for a wave with a period of 12.5 s and height of 6.0 m. Compute and plot the wave force vs. time of the force history acting on the tower for one wave cycle. Kinematic viscosity of sea water is  $9.75 \times 10^{-7}$  m<sup>2</sup>/s and the mass density of sea water is 1,030 kg/m<sup>3</sup>. Use Reynold's number and Keulegan–Carpenter number to compute the flow coefficients  $C_D$  and  $C_M$ .
21. Determine the horizontal and vertical components of the wave force per unit length acting at the mid-length of member 1–2 of the side face shown in Figure P6.7 [68], assuming a wave-induced water motion described by  $u = 15.0$  ft./s,  $v = 5.20$  ft./s,  $a_x = 4.20$  ft./s<sup>2</sup>, and  $a_y = -6.50$  ft./s<sup>2</sup>. Take suitable coefficients for drag and inertia forces.



**FIGURE P6.7** Typical offshore structure. (From T.H. Dawson, *Offshore Structural Engineering*, Prentice Hall Inc., Englewood Cliffs, NJ, p. 148, 1983. With permission.)

22. Calculate the peak load imposed upon the light tower shown in Figure P6.3 by a 1.5-m-high wave with a period of 7.0 s. The water depth at the tower location is 30.0 m. Assume that the wave is sinusoidal. Use Morison's equation and assume negligible dynamic response. Total load on the tower is  $F = F_D + F_I$ , viz., drag and inertia load (due to wind and wave). Using the results of problem 6.2, find the ratio of wind force to total force exerted on the tower.
23. A dynamic pressure gauge, placed on top of a 1.0-m-diameter pipeline (located on the seabed) in a water depth of 10.0 m, measures an average maximum pressure of 5.0 N/cm<sup>2</sup>, having an average period of 10.0 s. Find the wavelength, wave height, and the wave pressure (exerted at the base of the pipeline). Also compute the wave forces acting on the pipeline (per unit length), in the vertical direction, assuming the pipe to be rough. Take the average values of the relevant coefficients, assuming  $C_L = C_L$ .
24. A dynamic pressure gauge located 1.0 m off the bottom in 10.0-m depth of water measures a maximum pressure of 7.0 N/cm<sup>2</sup> and has a wave period of 12.0 s. Find the wavelength, celerity, and height. Mass density of sea water is 1026.0 kg/m<sup>3</sup>.
25. The steel structure, shown in two dimensions in Figure P6.8 [69], is acted upon by Airy waves of height 20.0 ft. and length 450.0 ft. (a) Determine the maximum total horizontal force and the associated time  $\omega t$ . All four faces of the structure are similar. Vertical members have outside diameter of 3.5 ft. and wall thickness of 1.25 in. The horizontal and inclined members have outside diameter of 2.25 ft. and wall thickness of 0.75 in. Assume that  $C_D = 1$  and  $C_I = 2$ . (b) Determine equivalent joint loads for the instant  $\omega t$ , when the horizontal wave force is maximum.
26. A vertical cylindrical member of height 150.0 ft. (shown as 1-2-3 in Figure P6.9 [70]) is located in the ocean at a depth of 120.0 ft. and is subjected to forces due to Airy's waves. The wave height is 30.0 ft., and the associated wavelength is 600.0 ft. The diameter of the cylinder is 6.0 ft. and the wall thickness is 2.0 in. Compute the equivalent nodal loads at nodes 1, 2, and 3. Assume that  $x = 0.0$  and  $t = 6.0$  s.
27. The unbraced platform shown in Figure P6.10 [71] has four legs, each of diameter  $D$  and length  $l_0$ , separated by distance  $l$ . The legs are subjected to a single, simple plane wave where wavelength  $l > D$ . Ignore the fluid drag forces and also ignore the motion ( $x$ ) of the



**FIGURE P6.8** Offshore jacket structure. (From T.H. Dawson, *Offshore Structural Engineering*, Prentice Hall Inc., Englewood Cliffs, NJ, p. 151, 1983. With permission.)



31. A (seismic) array (modeled as a smooth cylinder) is towed horizontally at a speed of 25 fps, fully submerged in deep water. The array, which is 4.0 in. in diameter and 120.0 ft. in length, is enveloped by a turbulent boundary layer. Determine the viscous drag force on the smooth cylinder, assuming  $\rho = 2.00 \text{ slugs/ft.}^3$  and  $\nu = 1.05 \times 10^{-5} \text{ ft.}^2/\text{s}$ . Also let  $C_D = 2.5 \times 10^{-3}$  for  $R_L = 10^6$ .
32. A framed platform is to be installed in Cook Inlet, Gulf of Alaska, at a water depth of 40.0 m. Besides the wave, current, and wind loads, the platform will also be subjected to ice loads exerted by 0.50-m-thick ice floes moving with the current. Assuming the platform to be composed of vertical piles of 1.0-m diameter only (neglecting the effect of braces), find the maximum environmental loads to which the structure will be subjected. Also compute the various load combinations used in design. Assume the environmental data given in the API code. Use only Airy's wave equation and the shortened form of wind equation; include the effect of current on wave, marine growth, and other relevant factors.
33. (a) A vertical circular cylindrical tower is located in a sea with a mean water depth  $d$ . The height of waves at the site is  $H$ . Using Morison–O'Brien's equation, state how you would compute the forces and moments (about the base) acting on the structure [force/unit height =  $C_I \rho \left( \pi \frac{D^2}{4} \right) \dot{u} + \left( \frac{1}{2} \right) \rho C_D D |u| u$  where  $u$  = wave particle velocity,  $\dot{u}$  = wave particle acceleration,  $C_I$  = inertial coefficient,  $C_D$  = drag coefficient, and  $D$  is the diameter of the cylinder]. (b) If the above cylinder is inclined at an angle of  $45^\circ$  to the wave (in the direction of wave propagation; see Figure P6.11) explain how you would compute the wave forces acting on the cylindrical tower. (Assume that the tower still projects above the surface of the wave.)
34. Compute the horizontal and vertical loads exerted on a sloping conical tower, with a slope of  $45^\circ$ , by an ice sheet of 1.0-m thickness. The coefficient of friction  $\mu$  is given as 0.30. The free-board, up to the narrow neck, is given as 5.0 m from the water level.  $\rho_w = 1.040 \text{ kg/m}^3$  and  $\rho_i = 900.0 \text{ kg/m}^3$ . The bending strength of sea ice is taken as 500.0 kPa. The diameter of the conical tower is taken as 20.0 m at the mean sea level. Take the elastic modulus of ice as 7.0 GPa. Consider both (i) two- and (ii) three-dimensional formulation in computing the ice loads on the conical tower.
35. From laboratory tests, the curves given in Figure P6.12 [72] and Table 6.14, where the indentation strength  $p = \frac{F}{(Dt)}$ , are obtained. From theoretical analysis, the equation

$$F = (\Phi Dt) F_\sigma \left[ \left( \frac{u}{D} \right) / \Phi \Psi \right]$$

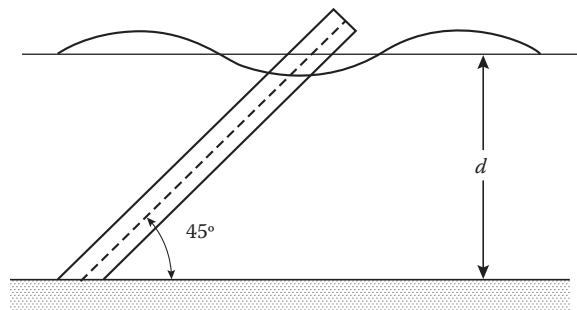
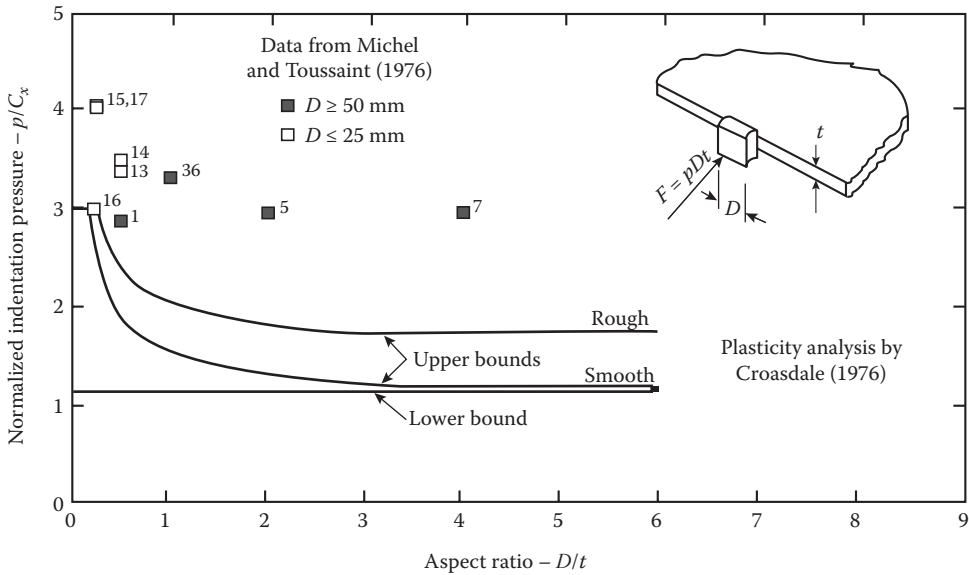
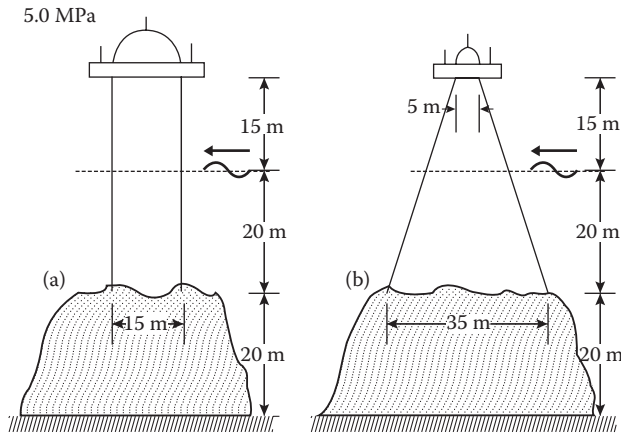


FIGURE P6.11 Inclined cylindrical tower.



**FIGURE P6.12** Normalized indentation pressure at constant effective strain rate. (From T.D. Ralston, *Ice Force Design Considerations for Conical Offshore Tower*, Section 3.2, Figure 6, Fourth OAC Conference, St. John's, NL, Canada, 1978. With permission.)

- is obtained, where  $\Phi$  and  $\Psi$  are given in Table 6.14 and the term  $(u/D)/\Phi\Psi$  is designated as the strain rate  $\dot{\epsilon}$ . Determine the failure strength (force) of a 2.0 ft. thick ice as it is indented by a 3.0-ft.-diameter column from (i) laboratory tests and (ii) field tests. For field tests, take  $p = If_c\sigma_0$ , where  $I$  is the indentation factor,  $f_c$  is the contact factor, and  $\sigma_0$  is the uniaxial compression strength of ice at  $\dot{\epsilon} = 10^{-3}$ .
36. Compute the ice forces exerted on an artificial gravity (due to soil weight) island by a large ice feature  $25 \times 25$  km due to limit force exerted on it by a driving wind of 40 m/s. The surface current speed at the bottom of ice is 0.25 m/s. The drag coefficients of wind-on-ice and water-on-ice are  $3 \times 10^{-3}$  and 0.50, respectively.  $\rho_w = 1030$  kg/m<sup>3</sup> and  $\rho_a = 1.26$  kg/m<sup>3</sup>. The thickness of the ice feature is 4.0 m.
  37. An ice-resistant structure is supported on piles of 15-ft. outside diameter. For ice sheets 3.5 ft. thick, having a crushing strength of 300 lb./in.<sup>2</sup>, determine the maximum force exerted on each pile when struck by the ice. Use the ice force equations given in the textbook and compute the ice forces exerted on the structure.
  38. An ice ridge, 20 m wide and 15 m deep, impinges on a conical structure that is 25-m diameter at the water level. The ridge is pushed against the conical structure, having a side slope of 45°, by a wind of 120 kmph. Determine the maximum horizontal and vertical forces experienced by the conical structure as the ridge fails and clears around the structure. Take  $\mu = 0.3$ ,  $E = 7.0$  GPa, and  $\sigma_{\text{bending}} = 0.5$  MPa.
  39. Determine the limit force experienced by an Arctic sand island, protected by concrete slabs, as an arctic ice pack of areal extent  $40.0 \times 40.0$  km is pushed by a cold wind of 120 kmph. A current of 0.6 m/s is acting on the bottom side of the ice pack. The ice pack is estimated to have an average thickness of 4.0 m over the nonridged portion. Air density = 1.293 kg/m<sup>3</sup>; water density = 1.030 kg/m<sup>3</sup>;  $C_c = 0.06$ ;  $C_{10} = 3 \times 10^{-3}$ . How would you determine whether the sand island would resist this ice force?
  40. Two concepts, shown in Figure P6.13a and b, were proposed for an offshore light house to be located in an ice-infested area, off the coast of the Avalon Peninsula, Newfoundland,



**FIGURE P6.13** Two concepts proposed for a lighthouse, located in an ice-infested offshore region.

Canada. The depth of water at the site of the lighthouse was 40.0 m, and the lighthouse was being located on a steep hilly rise of the sea-bottom, to identify the area that was dangerous to ships transporting crude from Hibernia. The ice sheet in the area grew to a maximum thickness of 0.60 m and often moved with a maximum velocity of 2.0 m/s. Small icebergs weighing up to a maximum of 100,000 t and moving with a maximum speed of 1.5 m/s were also observed in the vicinity of the proposed light house. Determine the maximum forces these ice features are likely to exert on the proposed lighthouse concepts. The average unconfined compressive strength of sea ice was observed to be 3.0 MPa while the average unconfined impact strength of glacial ice was measured as 5.0 MPa.

41. An artificial island is to be installed in the Canadian sector of the Beaufort sea. The island is to be conical with sloping sides; the top diameter of the platform is 100 m with a free-board of 5.0 m, and the first year ice thickness is expected to reach a maximum of 1.5 m. The sides of the island slopes at an angle of 1:4, and the sides are protected with armor units. Assume the angle of friction between the ice and the sides of the platform to be 0.6. Compute the maximum ice force that is likely to be exerted on the island.

## REFERENCES

1. BS6235, 1982. *Code of Practice for Fixed Offshore Structures*, British Standards Institution, London.
2. Offshore Standard, 2008. DNV-OS-C101, *Design of Offshore Steel Structures, General (LRFD Method)*, Det Norske Veritas, Hovik, Norway, pp. 12–20.
3. DNV, 1977. *Rules for the Design, Construction and Inspection of Offshore Structures*, Det Norske Veritas (DNV), Oslo, 1977 (with corrections 1982).
4. API-RP2A-LRFD, 1993. *Recommended Practice for Planning, Designing and Constructing Fixed Offshore Platforms—Load and Resistance Factor Design*, 1st edition, American Petroleum Institute, Washington, DC.
5. ESDEP (The European Steel Design Education Programme), 1993. Course Notes, (*Pre-Standard Version of the Euro Codes*). *European Steel Design Course, WG15A Structural Systems: Offshore*. Available at <http://www.esdep.org/members/master/toc.htm>.
6. Norwegian Petroleum Directorate (NPD), 1985. Regulation for Structural Design of Load-bearing Structures Intended for Exploitation of Petroleum Resources.
7. Health and Safety Executive, 2005. *Status of Technical Guidance and Information on Design, Construction and Operation of Offshore Installations*, Issued September 2003, Revised November 2005, London, UK.
8. S.U. Pillai, D.W. Kirk and M.A. Erki, 1999. *Reinforced Concrete Design*, 3rd Edition, McGraw-Hill Ryerson Ltd., Toronto, Canada, pp. 47–58.
9. National Building Code of Canada, 1995. Published by NRC Institute for Research in Construction, National Research Council Canada, Ottawa, Ontario, Canada.



10. White Rose Development Authority, 2001. Design philosophy and criteria. *Development Plan*, Volume 2 Section 8, pp. 260–276.
11. Husky Oil, March 2000. *White Rose Oilfield Project Description*, 42 pp. Available at <http://www.cnlopb.nl.ca/pdfs/wrproj.pdf>.
12. BS EN. 1998. Parts 1 to 6, 1998. *Design of Structures for Earthquake Regions*, British Standards Institute, London, UK.
13. DOE-OG, 1985. *Offshore Installation: Guidance on Design and Construction*, Dept. of Energy, Offshore Technology Division, HMSO Books Publication Centre, London, UK.
14. N. Haritos, 2007. Introduction to the analysis and design of offshore structures—An overview, electronic *Journal of Structural Engineering (EJSE) Special Issue: Loading on Structures*, p. 58.
15. ESDEP (The European Steel Design Education Programme), 1993. Course Notes, *Lecture 15A.2: Loads (I), Section 2.1, Introduction and Environmental Loads*. Available at <http://www.esdep.org/members/master/toc.htm>.
16. API-RP2A-LRFD, 1993. *Recommended Practice for Planning, Designing and Constructing Fixed Offshore Platforms—Load and Resistance Factor Design*, 1st Edition, American Petroleum Institute, Washington, DC, p. 34.
17. R.D. Blevins, 1984. *Applied Fluid Dynamics Handbook*, Van Nostrand Reinhold Company, pp. 310–312.
18. D. Darling, 2010. *Internet Encyclopedia of Science*. Available at [http://www.daviddarling.info/encyclopedia/D/drag\\_coefficient.html](http://www.daviddarling.info/encyclopedia/D/drag_coefficient.html).
19. T.H. Dawson, 1983. *Offshore Structural Engineering*, Prentice Hall Inc., Englewood Cliffs, NJ, p. 94; 70.
20. T.H. Dawson, 1983. *Offshore Structural Engineering*, Prentice Hall Inc., Englewood Cliffs, NJ, p. 95.
21. ESDEP (The European Steel Design Education Programme), 1993. Course Notes, *Lecture 15A.2: Loads (I), Section 2.2, Introduction and Environmental Loads*. Available at <http://www.esdep.org/members/master/toc.htm>.
22. J.R. Morison, M.P. O'Brien, J.W. Johnson and S.A. Schaaf, 1950. Forces exerted by surface waves on piles, *Petroleum Transactions, American Institute of Mining Engineering*, Volume 189, pp. 149–154.
23. N. Haritos, 2007. Introduction to the analysis and design of offshore structures — An overview, *Electronic Journal of Structural Engineering (EJSE) Special Issue: Loading on Structure*, pp. 59.
24. G. Clauss, E. Lehmann and C. Ostergaard, 1992. *Offshore Structures, Volume I: Conceptual Design and Hydromechanics*, Springer-Verlag, London, pp. 330–340.
25. API-RP2A-LRFD, 1993. *Recommended Practice for Planning, Designing and Constructing Fixed Offshore Platforms—Load and Resistance Factor Design*, 1st Edition, American Petroleum Institute, Washington, DC, pp. 29–31.
26. R. van 't Veer, 2008. *Application of Linearized Morison load in Pipe Lay Stinger Design*, Proceedings of the ASME 27th International OMAE conference, Estoril, Portugal, June 15–20, 10 pp.
27. J. Wolfram, 1998. On alternative approaches to linearization and Morison's equation for wave forces, *Proc. R. Soc. London*, Volume 455, pp. 2957–2974.
28. N. Haritos, 2007. Introduction to the analysis and design of offshore structures—An overview, *Electronic Journal of Structural Engineering (EJSE) Special Issue: Loading on Structure*, pp. 60.
29. A.S.J. Swamidas, 1997. *Engineering 8751: Coastal and Ocean Engineering Manual*, Memorial University, St. John's, NL, Canada, pp. 328–334.
30. D.V. Reddy, 1991. *Offshore Pipelines*, Chapter 9, in *Offshore Structures* by D.V. Reddy and M. Arockiasamy, Krieger Publishing Company, Malabar, FL, p. 9.
31. S.K. Chakrabarti, W.A. Tam and A.L. Wolbert, 1975. *Wave forces on a Randomly Oriented Tube*, Proceedings of the Seventh Offshore Technology Conference, Houston, TX, pp. 433–441.
32. R.C. MacCamy and R.A. Fuchs, 1954. *Wave Forces on Piles: a Diffraction Theory*, U.S. Army coastal Engineering Center, Technical memorandum # 69.
33. WAMIT, 1999–2008. *The State of the Art in Wave Structure Interaction*, WAMIT Inc., Boston, MA, available at [info@wamit.com](mailto:info@wamit.com).
34. API-RP2A-LRFD, 1993. *Recommended Practice for Planning, Designing and Constructing Fixed Offshore Platforms—Load and Resistance Factor Design*, American Petroleum Institute, Washington, DC, pp. 34–42.
35. API-RP2A-LRFD, 1993. *Recommended Practice for Planning, Designing and Constructing Fixed Offshore Platforms—Load and Resistance Factor Design*, American Petroleum Institute, Washington, DC, p. 38.
36. API-RP2A-LRFD, 1993. *Recommended Practice for Planning, Designing and Constructing Fixed Offshore Platforms—Load and Resistance Factor Design*, American Petroleum Institute, Washington, DC, p. 39.



37. API-RP2A-LRFD, 1993. *Recommended Practice for Planning, Designing and Constructing Fixed Offshore Platforms—Load and Resistance Factor Design*, American Petroleum Institute, Washington, DC, p. 28.
38. API-RP2A-LRFD, 1993. *Recommended Practice for Planning, Designing and Constructing Fixed Offshore Platforms—Load and Resistance Factor Design*, 1st Edition, American Petroleum Institute, Washington, DC, p. 29; 36.
39. API-RP2A-LRFD, 1993. *Recommended Practice for Planning, Designing and Constructing Fixed Offshore Platforms—Load and Resistance Factor Design*, 1st Edition, American Petroleum Institute, Washington, DC, p. 147.
40. API-RP2A-LRFD, 1993. *Recommended Practice for Planning, Designing and Constructing Fixed Offshore Platforms—Load and Resistance Factor Design*, 1st Edition, American Petroleum Institute, Washington, DC, pp. 148–149.
41. K.R. Croasdale, 1983. *Ice Forces on Offshore Structures*, Symposium on Offshore Mechanics and Cold Ocean Engineering, Calgary, Canada, February, 49 pp.
42. P.R. Kry, 1981. *Scale Effects on Continuous Crushing of Ice*, Proceedings of IAHR Ice Symposium, University of Laval, Quebec, Canada.
43. A.R.S. Ponter, A.C. Palmer, D.J. Goodman, M.F. Ashby, A.G. Evans, and J.W. Hutchinson, 1983. The force exerted by a moving ice sheet on an offshore structure: I: The creep mode, *Cold Regions Science and Technology*, Volume 8, Issue 2, pp. 109–118.
44. T.D. Ralston, 1978. *An Analysis of Ice Sheet Indentation*, Proceedings of IAHR Ice Symposium, Volume I, Luleå, Sweden, pp. 13–32.
45. A.R.S. Ponter, A.C. Palmer, D.J. Goodman, M.F. Ashby, A.G. Evans and J.W. Hutchinson, 1983. The force exerted by a moving ice sheet on an offshore structure: I: the creep mode, *Cold Regions Science and Technology*, Volume 8, Issue 2, pp. 109–118.
46. H.R. Peyton, 1968. *Ice and Marine Structures*, *Ocean Industry*.
47. T.H. Dawson, 1983. *Offshore Structural Engineering*, Prentice Hall, Inc., Englewood Cliffs, NJ, p. 144.
48. H. Eicken, 2006. *Sea Ice Microstructure and Ice Nomenclature*, Hajo Eicken's Homepage. Available at <http://www.gi.alaska.edu/snowice/sea-lake-ice/eicken.html>.
49. K.N. Korzhavin, 1962. *Action of Ice on Engineering Structures*, USSR Academy of Science, Siberian Branch, Translation published by CRREL Draft Translation # 260, Hannover (1971).
50. Canadian Standards Association, 1992. General Requirements, Design Criteria, The Environment and Loads (CAN/CSA-471-92), CSA, Rexdale, Ontario, Canada. Also in (paper by K.R. Croasdale, P. Truskov, A.T. Bekker and T. Murrell), Proceedings of the Sea Ice Mechanics and Arctic Modeling Workshop, April 25–28, 1995, Anchorage, Alaska, Volume 2, p. 68.
51. A.B. Cammaert, and D.B. Muggeridge, 1988. *Ice Interaction with Offshore Structures*, Van Nostrand Reinhold, New York, p. 248.
52. Cammaert, A.B. and D.B. Muggeridge, 1988. *Ice Interaction with Offshore Structures*, Van Nostrand Reinhold, New York, p. 249.
53. Croasdale, K.R., 1983. *Ice Forces on Offshore Structures*, Symposium on Offshore Mechanics and Cold Ocean Engineering, Calgary, Canada, February, p. 20.
54. J.V. Danys and F.G. Bercha, 1976. *Investigations of Ice Forces on a Conical Structure*, *Ocean Engineering*, Elsevier, Volume 3, Issue 5, pp. 299–310.
55. A.B. Cammaert and D.B. Muggeridge, 1988. *Ice Interaction with Offshore Structures*, Van Nostrand Reinhold, New York, p. 209.
56. K.R. Croasdale, 1983. *Ice Forces on Offshore Structures*, Symposium on Offshore Mechanics and Cold Ocean Engineering, Calgary, Canada, February, p. 39.
57. K.R. Croasdale, 1983. *Ice Forces on Offshore Structures*, Symposium on Offshore Mechanics and Cold Ocean Engineering, Calgary, Canada, February, p. 42.
58. T.J.O. Sanderson, 1988. *Ice Mechanics—Risks to Offshore Structures*, Graham and Trotman Ltd, London.
59. Canadian Hydrographic Services, Department of Fisheries and Ocean, 2010. *Tides, Currents and Water Levels*, Canadian Hydrographic Services. Available at [chsinfo@dfo-mpo.gc.ca](mailto:chsinfo@dfo-mpo.gc.ca).
60. D. Pentcheff, 2009. *WWW Tide/Current Predictor*, Department of biological Sciences, University of South Carolina, Columbia, SC, available at <http://tbone.biol.sc.edu/tide>.
61. API-RP2A-LRFD, 1993. *Recommended Practice for Planning, Designing and Constructing Fixed Offshore Platforms—Load and Resistance Factor Design*, 1st Edition, American Petroleum Institute, Washington, DC, Commentary, p. 132.
62. B.S. Benjamin, 1984. *Structures for Architects*, Van Nostrand Reinhold Company, p. 17.
63. T.H. Dawson, 1983. *Offshore Structural Engineering*, Prentice Hall Inc., Englewood Cliffs, NJ, p. 147.

64. J.F. Wilson, 1984. *Dynamics of Offshore Structures*, John Wiley & Sons, New York, p. 5.
65. J.F. Wilson, 1984. *Dynamics of Offshore Structures*, John Wiley & Sons, New York, p. 42.
66. T.H. Dawson, 1983. *Offshore Structural Engineering* Prentice Hall, Englewood Cliffs, NJ, p. 148.
67. N.D.P. Baltrop and A.J. Adams, 1991. *Dynamics of Fixed Marine Structures*, Butterworth-Heinemann, p. 316.
68. T.H. Dawson, 1983. *Offshore Structural Engineering*, Prentice Hall, Englewood Cliffs, NJ, p. 151.
69. T.H. Dawson, 1983. *Offshore Structural Engineering*, Prentice Hall, Englewood Cliffs, NJ, p. 149.
70. J.F. Wilson, 1984. *Dynamics of Offshore Structures*, John Wiley & Sons, New York, p. 120.
71. T.D. Ralston, 1978. *Ice Force Design Considerations for Conical Offshore Tower*, Fourth OAC Conference, St. John's, NL, Canada [figure from section 3.2, Figure 6 in the given reference].

---

# 7 Fundamental Considerations for Framed Offshore Structural Analysis

## 7.1 INTRODUCTION

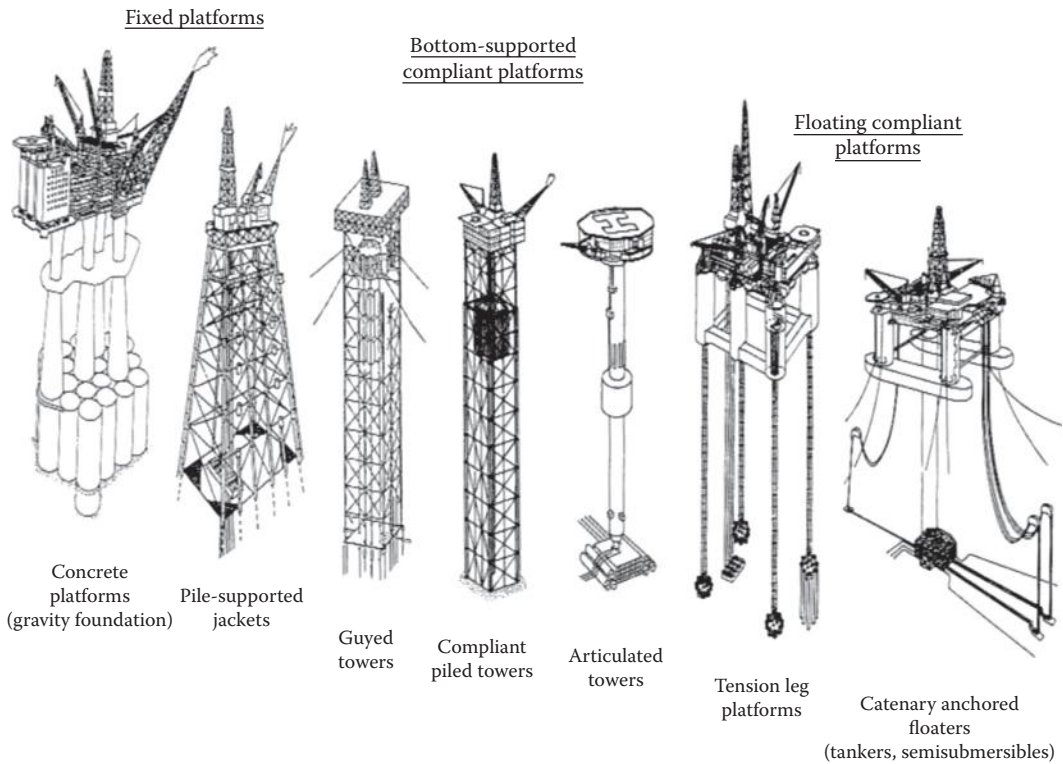
Some of the alternative designs of offshore structures that are possible in the ocean environment are given in Figure 7.1 [1]. These offshore structures can be broadly classified as (i) bottom-fixed/founded structures, (ii) bottom-supported compliant structures, and (iii) compliant floating structures. Bottom-fixed structures consist of fixed steel jacket platforms, concrete gravity platforms, and the hybrid (concrete base with steel jacket supporting the top steel deck structures). They are comparatively stiff structures embedded into/supported on relatively soft ocean sediments. The framed steel jacket structure is supported on a number of deep-driven main/skirt pile clusters, with mud mats, as shown in Figure 7.2 [2]. The gravity structure is supported on a large concrete gravity base, with skirts (located below the concrete base) penetrating deep into the soft top soil. Under the wave excitation, the structures exhibit high elastic restoring forces, and as such, the structural displacements are considered to be small. In the case of bottom-supported compliant structures, the relative vertical motion between the well heads (at bottom) and the deck should be minimized. Moreover, if subsea (seabed) completions are used as in the case of the floating compliant platform shown in Figure 7.1, the connection to the seabed can be made with the less-costly flexible risers and control lines; in this case, the structural motions (rather than displacements) will be much higher.

## 7.2 SITE CHARACTERISTICS AND MODELING PROCEDURES FOR ANALYSES

The determination of the functional and environmental loads acting on offshore structures is described in the earlier chapters. This chapter primarily deals with the task of modeling and analyzing bottom-fixed/embedded offshore structures subjected to loadings that are time-independent (or static). The essential purpose of the analysis of an offshore structure is to verify that the designed structure will withstand the operational and environmental loads imposed on it during its design life.

### 7.2.1 STRUCTURAL SKELETON FOR FORCE APPLICATION AND ANALYSIS

Since actual offshore structures are quite complex, the first consideration in analysis is to establish an idealized model for the overall geometry of the structure, dependent on the analytical procedure to be utilized. In the present-day context of availability of many computational procedures, the finite element method will be the most obvious method to be utilized to model the whole structure as it stands in the ocean environment. Since this type of modeling will involve the utilization of enormous computational and financial resources, approximated or minimized models will generally be used in the preliminary or other earlier analyses to establish initial sizing of the structural

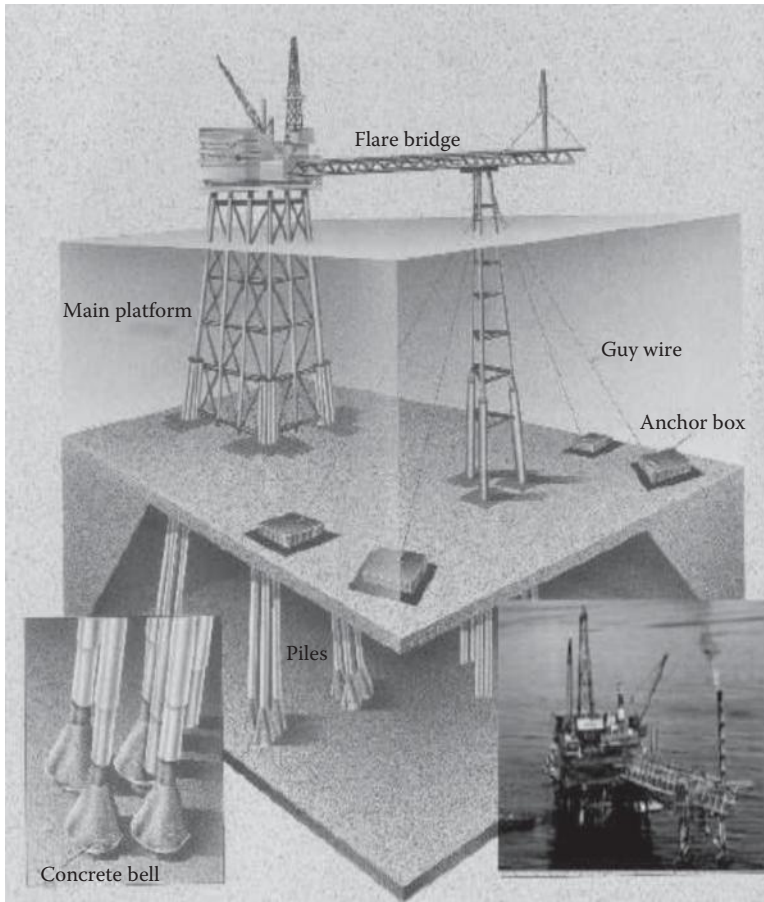


**FIGURE 7.1** Different types of offshore structures installed in an offshore environment. (With kind permission from Springer Science+Business Media: *Offshore Structures, Volume I: Conceptual Design and Hydromechanics*, 1992, p. 32, C. Clauss, E. Lehmann, and C. Ostergaard.)

components and elements. The major difficulty in establishing this model is that member sizes and other details are usually not known at the beginning of analysis; therefore, certain assumptions have to be made concerning the configuration and the size of its component members. Assumed configurations and dimensions will usually change depending on the number of cycles of analyses carried out. Also most of the operational and environmental loads exerted on the structure due to superstructure loads, waves, winds, and gravity (self-weight), acting on an offshore structure, will be dependent on the size and geometrical dimensioning of the members and component substructures.

For instance, let it be assumed that one has to visualize the steps that would be taken to mathematically model the offshore steel jacket platform shown Figure 7.3 [3], consisting of (i) top deck, (ii) intermediate template (jacket), and (iii) bottom pile foundations. Deck structure consists of subcomponents such as drilling derrick, helideck, crew quarter, cranes, skid beams, deck plating/beams/columns, longitudinal trusses, wind girders (or trusses), etc. The template (jacket) components consist of legs, horizontal and vertical bracing, conductor bracing, launch runners, launch trusses, and appendages such as boat landings, barge bumpers, and walkways. Foundation components consist of mud mat, skirt pile sleeves, skirt pile bracing, and piles.

The preliminary model for analysis of the jacket structure will consider only the static analysis of the jacket alone (shown in Figure 7.4 [4]) with the jacket fixed at the bottom or with the embedded

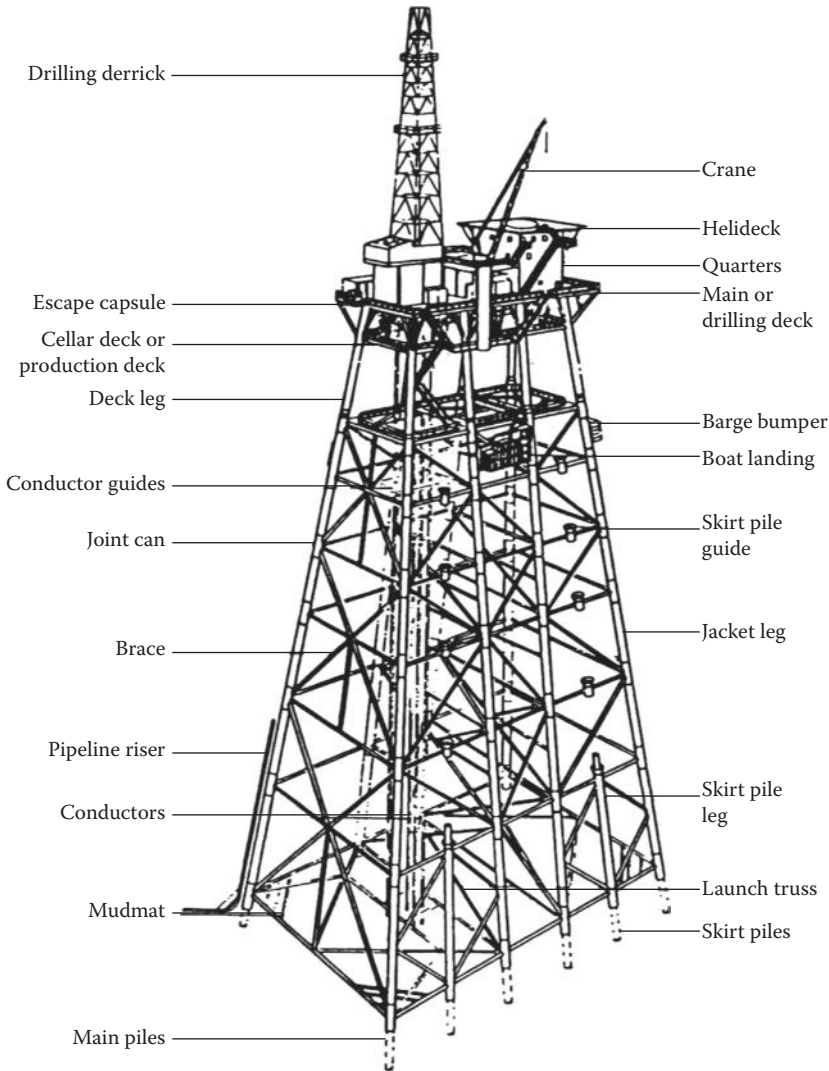


**FIGURE 7.2** Partially exposed view of an offshore steel jacket platform embedded in the ocean bed by deep penetration piles. (From Surya3303, 2003, Slideshow presentation by Surya3303 on Offshore Platform Design. Available at <http://www.slideshare.net/surya3303/offshore-structures-presentation>, Accessed on July 2011. With permission.)

pile effect considered through a short length of equivalent pile of length equal to  $3.5D$  to  $8.5D$  ( $3.5D$  to  $4.0D$  for stiff clays,  $4.5D$  to  $7.0D$  for intermediate strength clays, and  $7.0D$  to  $8.5D$  for very soft clays), with  $D$  as the external diameter of the pile, as shown in Figure 7.5a [5]. An alternate modeling procedure is indicated in Figure 7.5b [5]; in this model, the equivalent pile length is taken as  $6.0D$  for general soils [5]. The top deck weights will be distributed to the top nodes of the structural model according to the portion of the load to be carried by the individual nodes. In addition, the environmental loads will be also applied to the proper nodes while carrying out the static response to the applied environmental loads.

An alternate model for reducing the size of the matrix to be solved in the finite element analysis of the platform is to consider the effect of the soil to be replaced by linear/nonlinear soil springs, spaced at a maximum spacing of  $L_b/7$ , where  $L_b$  represents the bending wavelength of the embedded pile, given as

$$L_b = (2\pi)[(4EI)/(kD)]^{(1/4)} \quad (7.1)$$

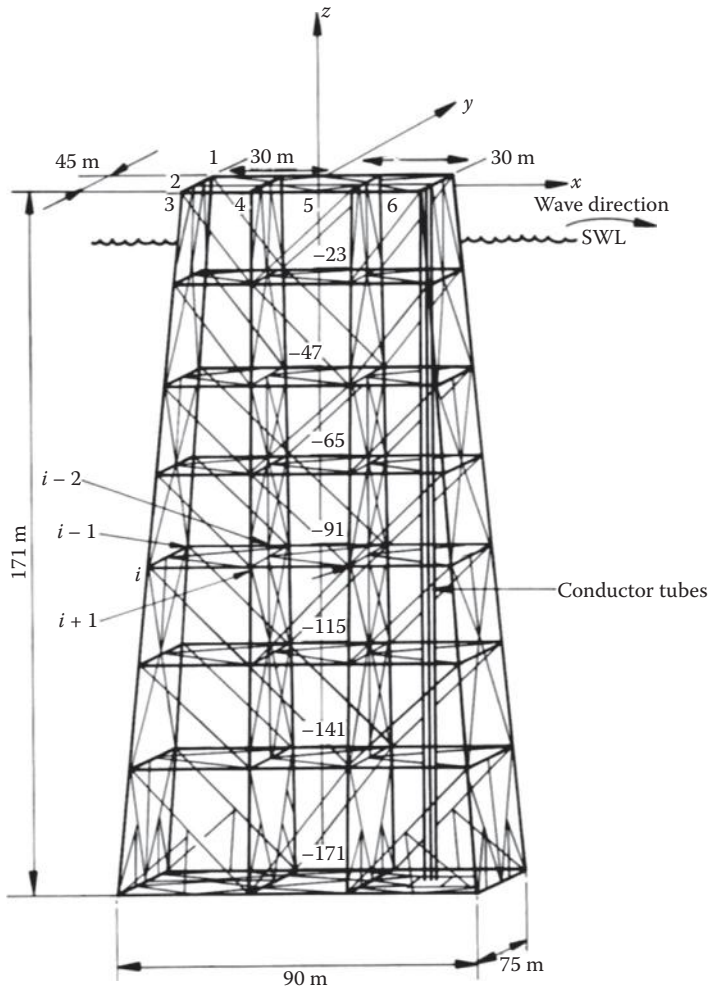


**FIGURE 7.3** Steel jacket offshore structure fixed to the seabed with deep-driven piles. (From B. McClelland and M.D. Reifel, *Planning and Design of Fixed Offshore Platforms*, Van Nostrand Reinhold Company, New York, p. 519, 1986. With permission.)

where  $E$  is the Young's modulus of the pile,  $I$  is the moment of inertia of the pile section along the axis of bending,  $D$  is the diameter of the pile, and  $k$  is the soil pressure exerted per unit length of the pile [5]. When the dynamic properties of the structures are to be estimated, then a lumped mass modeling approach shown in Figure 7.6 [6] is used in reducing the size of the model to be used in dynamic analysis.

Similar models for a guyed tower platform and a gravity offshore structure are shown in Figures 7.7 through 7.12. Figures 7.7 through 7.9 show the types of modeling used for an offshore guyed tower, located at a water depth of 1600 ft. (~ 487.0 m). Figure 7.7 [7] gives a perspective view of the guyed tower, while Figure 7.8 [8] gives the structural model that will be used for the static finite



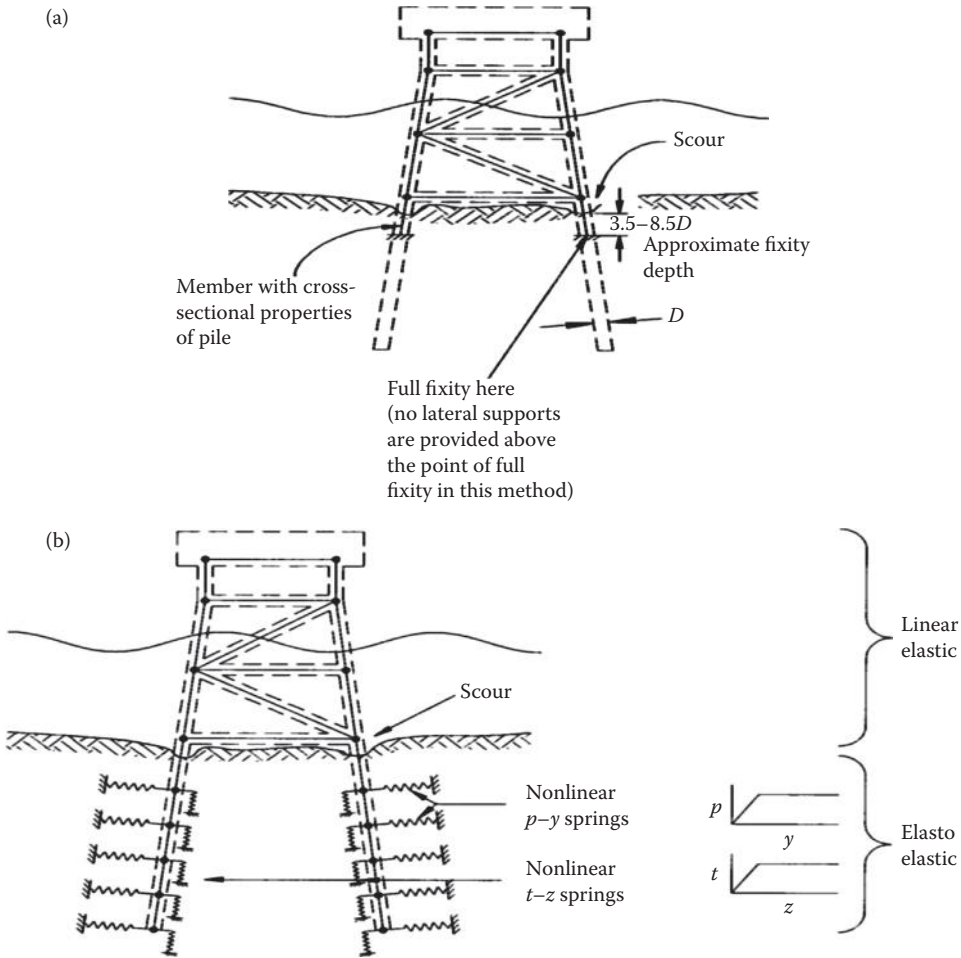


**FIGURE 7.4** Finite element model of the jacket structure of a fixed offshore jacket platform. (From M.H. Patel, *Offshore Structures*, in: *Marine Technology Reference Book*, Butterworths, London, UK, pp. 2/50 (Figure 2.47), 1990. With permission.)

element analysis of the tower structure. Figure 7.9 [9] shows the lumped mass model of the guyed tower with line and rotational springs representing the guy resistance and the soil resistances. As per reference [7], the following values are used for the linear and rotational spring constants representing the guy and soil resistances:  $k_{x\text{-hor-guy}} = 275.0$  kips/ft.;  $k_{x\text{-soil}} = (5.845)(10^3)$  kips/ft.,  $k_{\theta\text{-soil}} = (2.726)(10^7)$  kips ft., and  $k_{x\theta\text{-soil}} = k_{\theta x\text{-soil}} = - (1.705)(10^4)$  kips.

Figures 7.10 through 7.12 represent the analytical numerical modeling used for an offshore gravity structure. Figure 7.10 [10] gives a pictorial view of the gravity platform as it stands in an offshore environment. Figure 7.11 [2] gives a detailed finite element representation of the gravity platform used for determining the static response of the platform structure. Figure 7.12 [11] represents the

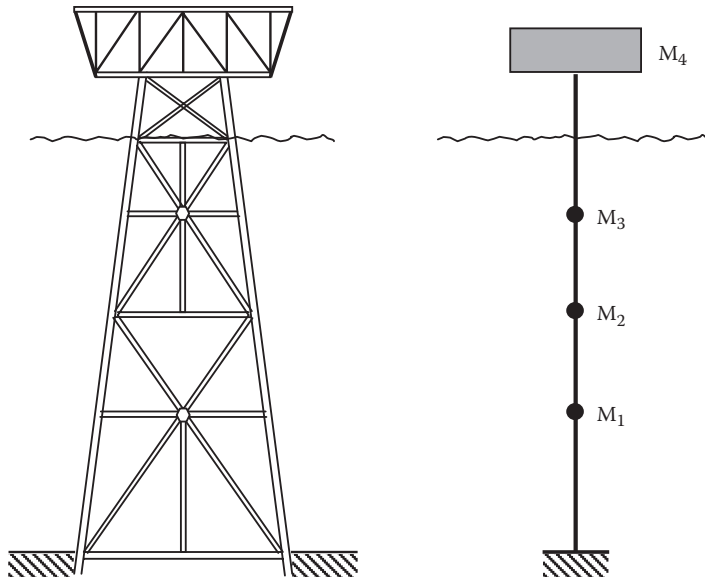




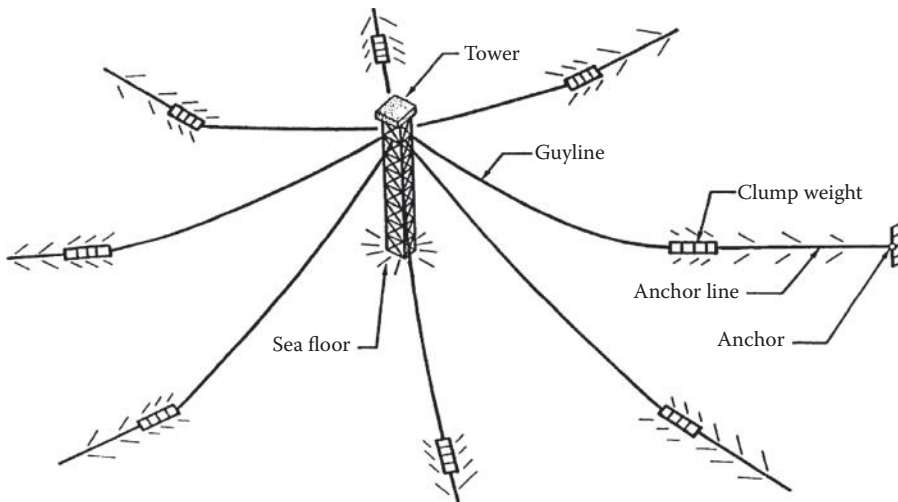
**FIGURE 7.5** (a) One type of approximate modeling of pile effect by considering the piles to be fixed below a certain depth ( $= 3.5$  to  $8.0$  diameter of piles). (b) Alternate model for pile foundation model, with the soil modeled as linear or nonlinear springs. (From N.D.P. Barltrop and A.J. Adams, *Dynamics of Fixed Marine Structures*, Butterworth Heinemann Ltd., Oxford, UK, p. 210, 1991. With permission.)

lumped mass modeling of the gravity platform structure, used for computing the dynamic response of the platform. It can be seen that the top deck structure and the vertical hollow shaft structure are represented by interconnected stick-type modeling; the bottom storage tank (caisson) structure is represented by rigid interconnected links supported on linear springs in three directions ( $x$ ,  $y$ , and  $z$ ) and a rotational spring in the  $\theta_y$  (and/or  $\theta_x$ ) direction. The spring constants for the different linear and rotational directions can be obtained from Table 7.1 (see also Table 7.2) [12]; other properties required for subsequent computations are also given in Table 7.1 (see also Figure 7.13).

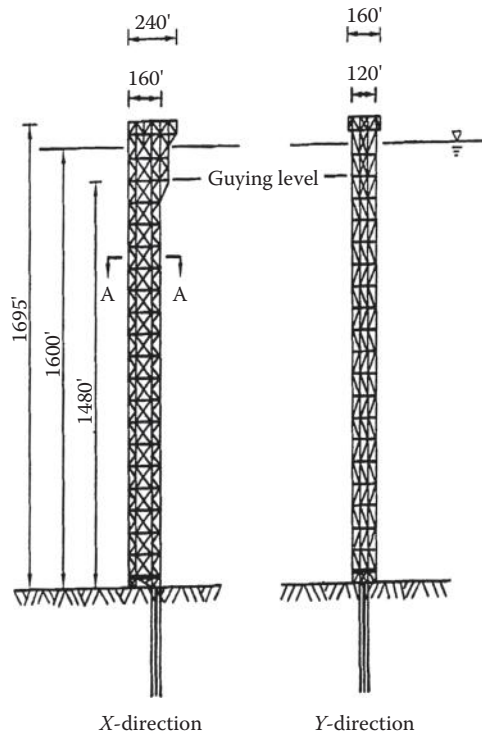
In the subsequent pages, the details of the above modeling procedures will be outlined in simple and straightforward manner using stiffness, finite element, and lumped-mass-modeling procedures. Relevant equations and matrices will be taken from existing formulations, and the procedure for solving the different problems will be neatly outlined.



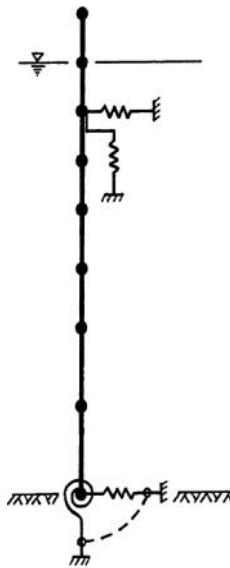
**FIGURE 7.6** Lumped mass idealization of an offshore jacket structure. (With kind permission from Springer Science+Business Media: *Meccanica*, Stochastic seismic analysis of offshore towers, 19, 1984, p. 236, A. Cerami.)



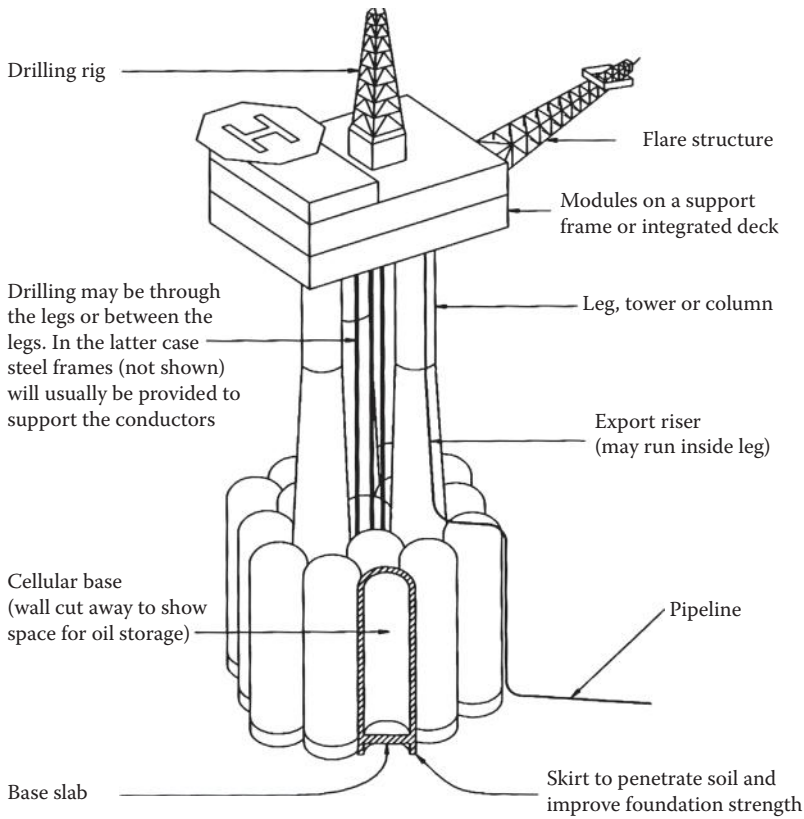
**FIGURE 7.7** Offshore guyed tower system. (From G.D.J. Hahn, *Dynamic Response of Offshore Guyed Towers*, Ph.D. thesis submitted to Rice University, Houston, TX, p. 128, 1985. With permission.)



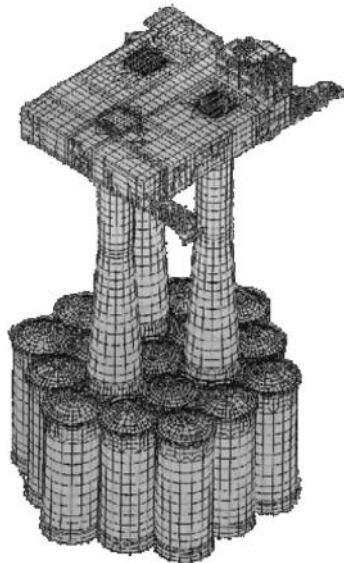
**FIGURE 7.8** Structural details of the guyed tower. (From G.D.J. Hahn, *Dynamic Response of Offshore Guyed Towers*, Ph.D. thesis submitted to Rice University, Houston, TX, p. 134, 1985. With permission.)



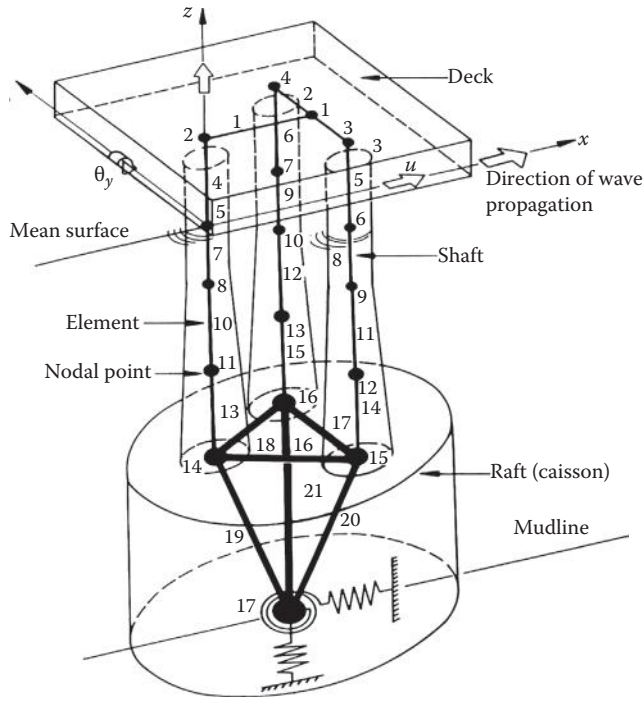
**FIGURE 7.9** Stick-like model of a guyed tower. (From G.D.J. Hahn, *Dynamic Response of Offshore Guyed Towers*, Ph.D. thesis submitted to Rice University, Houston, TX, p. 130, 1985. With permission.)



**FIGURE 7.10** Concrete platform structure. (From N.D.P. Barltrop and A.J. Adams, *Dynamics of Fixed Marine Structures*, Butterworth Heinemann Ltd., Oxford, UK, p. 4, 1991. With permission.)



**FIGURE 7.11** Detailed finite element modeling of an offshore gravity platform. (From Surya3303, 2003, Slideshow presentation by Surya3303 on Offshore Platform Design. Available at <http://www.slideshare.net/surya3303/offshore-structures-presentation>, July 30, 2003. With permission.)



**FIGURE 7.12** Lumped mass model of a ground-supported offshore gravity structure. (From M.H. Patel, *Offshore Structures*, in: *Marine Technology Reference Book*, Butterworths, London, UK, pp. 2/50, Figure 2.52, 1990. With permission.)

**TABLE 7.1**  
**Foundation Properties for Rigid Circular/Rectangular Shape on Elastic Half-Space**

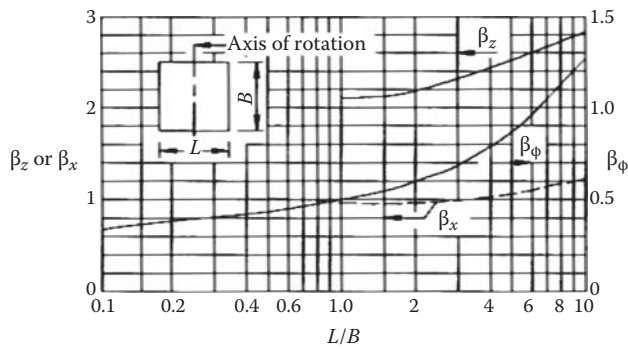
Foundation Shape:	Circular	Rectangular
	<b>Spring Stiffness <math>K</math></b>	<b>Effective Mass <math>M, I, J</math></b>
Vertical ( $z$ )	$\frac{4GR}{1-\nu}$	$\frac{1.08\rho R^3}{1-\nu}$
Horizontal ( $x$ )	$\frac{8GR}{2-\nu}$	$\frac{0.76\rho R^3}{2-\nu}$
Rocking ( $\psi$ )	$\frac{8GR^3}{3(1-\nu)}$	$\frac{0.64\rho R^5}{1-\nu}$
Torsion ( $\theta$ )	$\frac{16GR^3}{3}$	$0.24\rho R^5$
	<b>Damping Coefficient <math>C</math></b>	<b>Spring Stiffness <math>K</math></b>
Vertical ( $z$ )	$\frac{3.4R^2}{1-\nu}\sqrt{\rho G}$	$\frac{G}{(1-\nu)}\beta_z\sqrt{BL}$
Horizontal ( $x$ )	$\frac{4.6R^2}{2-\nu}\sqrt{\rho G}$	$2(1+\nu)G\beta_x\sqrt{BL}$
Rocking ( $\psi$ )	$\frac{0.65R^4}{(1-\nu)}\sqrt{\rho G}$	$\frac{G\beta\phi BL^2}{1-\nu}$
Torsion ( $\theta$ )	$1.32R^4\sqrt{\rho G}$	$\frac{3GJk_T}{(1-\nu)\sqrt{BL}}$

Source: N.D.P. Barltrop and A.J. Adams, *Dynamics of Fixed Marine Structures*, Butterworth Heinemann Ltd., Oxford, UK, p. 202, 1991.

Note:  $R$  = radius of the foundation;  $\rho$  = soil mass density;  $B, L$  = width and length of rectangular foundation;  $G$  = shear modulus;  $\nu$  = Poisson's ratio;  $\beta_n, \beta_z$ , and  $\beta_\phi$  = coefficients given in Figure 7.13 [13];  $M$  = mass of foundation;  $I$  = rocking inertia of foundation;  $J$  = torsional inertial of foundation;  $k_T$  = coefficient given in Figure 7.13 [12];  $C$  = radiation damping coefficient.

**TABLE 7.2**  
**Values of  $k_T$  Required for Properties Given in Table 7.1**

Aspect Ratio, $L/B$	$k_T$				
	$\nu = 0.1$	0.2	0.3	0.4	0.5
1	1.00	0.938	0.868	0.972	0.704
1.5	1.01	0.942	0.864	0.770	0.692
2.0	1.02	0.945	0.870	0.784	0.686
3.0	1.05	0.975	0.906	0.806	0.700
5.0	1.15	1.050	0.950	0.850	0.732
10.0	1.25	1.160	1.040	0.940	0.940



**FIGURE 7.13** Coefficients  $\beta_n$ ,  $\beta_z$ , and  $\beta_\phi$  for rectangular foundations. (From N.D.P. Barltrop and A.J. Adams, *Dynamics of Fixed Marine Structures*, Butterworth Heinemann Ltd., Oxford, UK, p. 203, 1991. With permission.)

### 7.3 HYDROSTATIC PRESSURE AND BUOYANCY

Hydrostatic pressure loads on a partially or fully submerged structure or its component members occur due to the weight of the water column above the structure/member and due to the movement of the water around the structure or its component member due to the passage of waves over its location. The hydrostatic pressure acting on the submerged members generates additional horizontal/vertical loads and stresses, which are not taken into account in the load computation given earlier in Chapter 6. These stresses have to be considered in the design of the members, along with the loads and stresses generated by other loads mentioned in Chapter 6.

As per API code, the equivalent hydrostatic head ( $H_{eq.st}$ ) due to the passage of waves over a location is given by [14]

$$H_{eq.st} = -z + (H/2) \left[ \frac{\cosh \{k(d+z)\}}{\cosh(kd)} \right] \tag{7.2}$$

where  $z$  is the depth ( $z$  is  $-ve$  when measured downward from the mean sea level) of the point of reference in the structure/member (including the tidal variation), and  $d$  is the seawater depth at the location. The water pressure generated by the equivalent hydrostatic head is given by

$$p_{eq. st.} = \gamma_w H_{eq. st.} \tag{7.3}$$

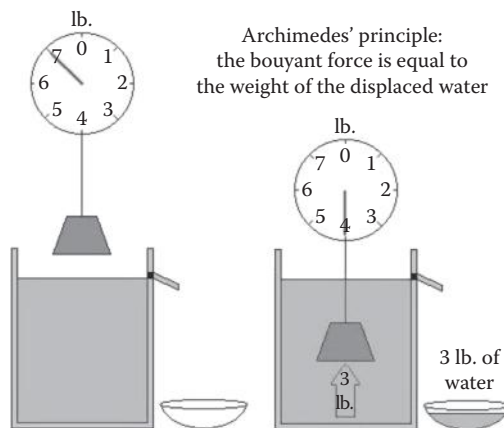
In addition to the equivalent hydrostatic pressure acting on the structure, an additional buoyant force also is generated due to this submergence of the body in water; this buoyant force is generated by the hydrostatic pressure acting on the structure/element. The hydrostatic pressure at a point, located at a distance of  $z$ , is given as

$$p = \gamma_w z \tag{7.4}$$

This buoyant force is present on the submerged element/structure even in the absence of wave action on the body. As per the Archimedes principle, illustrated in Figure 7.14 [15], the buoyancy force of any submerged body is vectorially equal and opposite to the weight of the fluid displaced by the body and has the same line of action.

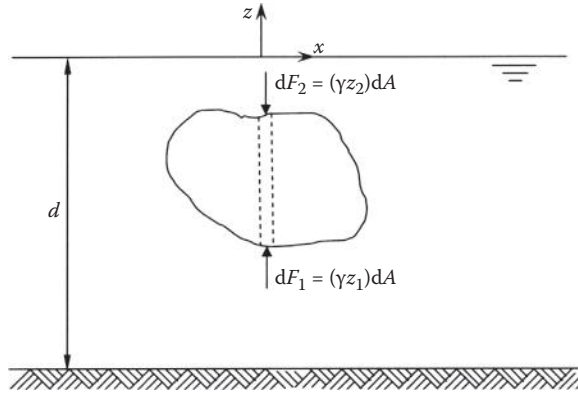
In order to estimate the buoyant force on the submerged body, consider the submerged irregular body shown in Figure 7.15 [16], and assume that an incremental vertical volume of the body has an end area of  $dA$  and height  $(z_1 - z_2)$ . The net vertical upward force is given by

$$\begin{aligned} dF &= dF_1 - dF_2 = \gamma_w \{d - (z_1 + d)\}dA - \gamma_w \{d - (z_2 + d)\}dA \\ &= \gamma_w (z_2 - z_1)dA \end{aligned} \tag{7.5}$$



**FIGURE 7.14** Illustration of the buoyancy principle. (From Rle 7.1, Fluids at Rest BSN-UST batch 2011. Available at <http://fluidsatrest.ash.com/archimedes.html>, September 21, 2010 at 5:45 p.m.)





**FIGURE 7.15** Buoyant forces on floating and submerged bodies. In the figure, the vertical axis is assumed to be the  $z$ -axis, located at the mean sea level. Hence,  $h \equiv d; y = z + h; y_1 = z_1 + h; y_2 = z_2 + h$ . (From T.H. Dawson, *Offshore Structural Engineering*, Prentice Hall Inc., Englewood Cliffs, NJ, p. 138, 1983. With permission.)

The total upward force on the body is obtained as

$$\text{upward force} = \gamma_w \int (z_2 - z_1) dA = \gamma_w B = F_B \tag{7.6}$$

where  $F_B$  is the buoyant force acting on the body, and  $B$  is the total volume of water displaced by the submerged body. It can also be shown by taking a horizontal incremental element of the body, and integrating the hydrostatic pressure forces over the whole body, that the net horizontal force acting on the submerged volume of the body is equal to zero. Thus, it is seen that the hydrostatic pressure force acting on the body causes the buoying up by a force equal to the weight of the volume of water displaced by the submerged body. This conclusion is also found to be true when the body is partially submerged.

When computing the weight of an offshore structure/element submerged in water, it must be remembered that the structure/element is buoyed up by the fluid column above it. Hence, the submerged weight of the structure/element in water is given by

$$W_{\text{submerged}} = W - F_B = W - \gamma_w B \tag{7.7}$$

### 7.4 PRELIMINARY CONSIDERATIONS FOR STATIC ANALYSIS AND DESIGN

The design of offshore structures is dominantly influenced by the type of environmental load combinations that act on them. Generally, these loads are governed by the wind–wave–current loading exerted on the structures; sometimes these conditions may be greatly modified by the ice loads exerted on structures located in the Arctic and sub-Arctic regions or by the seismic loads in

seismic-prone offshore regions of the world. According to the API code [17], the following design conditions must be considered in the analysis of offshore structures:

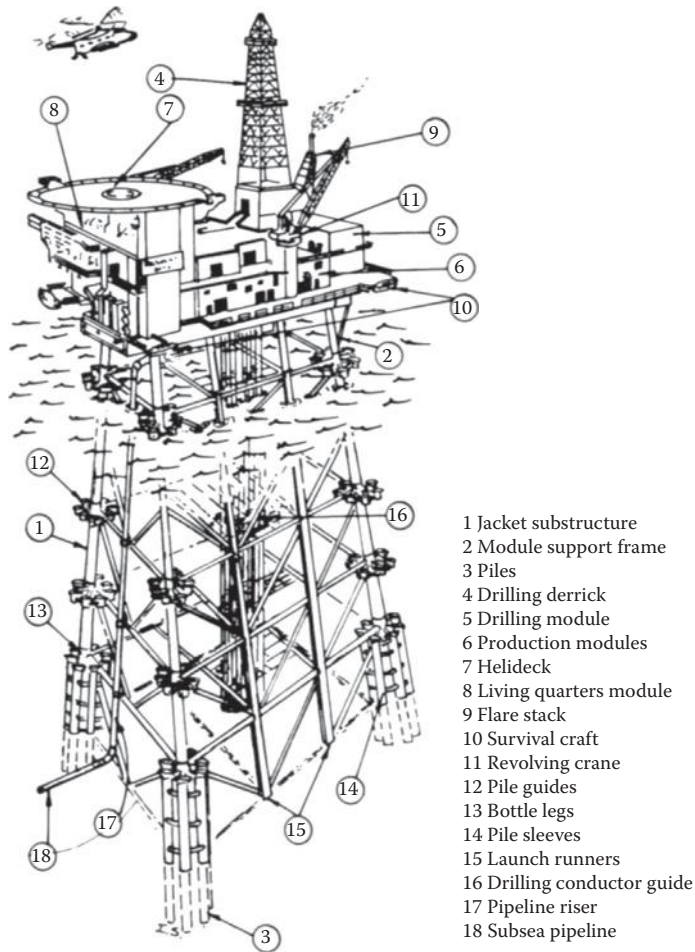
- (i) Design for in-place conditions, which will include resistance of the structure to gravity loads, wind–wave–current loads, ice loads, earthquake loads, and accidental (including impact) loads. The loads computed for the structure must consider the maximum loads likely to be exerted during the drilling, production, and work-over operations, singly or in combination. In addition, the fatigue resistance requirements of the structure also must be considered.
- (ii) The structural analysis must also consider the loads that will be applied on the structure during its fabrication, transportation, and installation operations. If offshore structures are to be relocated to new sites, then loads resulting from the removal, site-loading onto barge, transportation, and installation should be considered.
- (iii) The strength of stability check to be applied to the design of individual member must take into consideration the load factor to be applied according to Table 6.5; in addition, the resistance factor must also be applied to the nominal strength of each member.
- (iv) Usually, a three-dimensional elastic structural analysis is found to be sufficient; but in the case of the jacket structure and the lateral pile–soil system, it may be necessary to carry out nonlinear pile–soil analysis to ensure load-displacement compatibility between the two components of the offshore structure.
- (v) Careful consideration should be given to provide sufficient redundancy in the structure against failure based on the system reliability analysis.
- (vi) Corrosion protection should be provided according to the governing specifications such as NACE RP-01-76 [17].
- (vii) Finally, the analysis should also take into account the stresses and deformations induced by temperature variation, creep, relaxation, and uneven settlement.

Steel offshore structures are usually template or jacket structures, similar to the ones shown in Figures 7.3 through 7.6 and 7.16. As shown in Figure 7.16 [18], the structure consists of a prefabricated steel framed substructure that is towed to the site of installation, made upright, and fixed to the seabed by driving steel tubular piles through the hollow legs of the template structure. Thereafter a prefabricated deck is added on the top of the template structure; in addition to the above three components, the provision of drilling slots (for marine risers or conductors) must also be taken into account since nearly 40% of the wave load exerted on the offshore structure may result from the wave loads acting on these drilling risers. In some cases, these drilling slots may be around 60 to 80 [19].

The jacket structure is normally constructed using cylindrical steel tubular members (of moderate diameters of 48 in. or less) for all its component members. The designer developing the jacket configuration must bear in mind some of the constraints that may pop up as he or she designs the structure. Some of these constraints are as follows: (i) installation constraints based on availability of lift vessels and lift cranes; depending on the capacity of these cranes and vessels, the jacket structure may have to be fabricated in different lengths and joined together on-site; (ii) length constraints of piles depending on the availability of pile-driving equipment; and (iii) fabrication constraints depending on the availability of fabrication yards, lifting yard cranes, and water depth limitations of the available port facilities [20].

The piles for the platform are installed through each of its main leg. In addition, skirt piles may be driven with underwater hammers or with above-water hammer and a pile chaser (or follower) that connects the above-water hammer to the skirt piles near the bottom of the sea. Typical shear and axial load capacities of common types of offshore piles are given in Table 7.3 [21].

While selecting the configuration of an offshore template platform, for heavier equipment-carrying platforms in shallow water, it is better to start with the deck section of the platform. For



**FIGURE 7.16** Offshore steel template structure. (From J.G. Timar, *Lectures on Offshore Engineering, Institute of Building Technology and Structural Engineering, Aalborg University, Aalborg, Denmark, Spring, 1978.* With permission.)

other types of platforms, it is better to start with the analysis and design of jacket and pile structures. The configuration of the jacket platform is dependent on the number of main piles required for accommodating the platform loads and equipment and to resist the environmental loads applied on the structure; in addition, the strength of foundation soils will also play a great part in selecting the configuration.

The capacities of piles have been given in Table 7.3; the load ranges are only approximate and are heavily dependent on the soil type encountered at the site of installation. The spacing between platform main legs is dependent on the arrangement of legs (or columns) of the deck. From an optimum standpoint, the leg spacing ranges from  $30 \times 30$  to  $45 \times 45$  ft., which once again depends on the span lengths used for the loads on deck beams, girders, and trusses. When the template structures are located in very deep waters, much greater leg spacing may be appropriate. In addition, the platform drilling/production rig requirements, well spacing/location, launch runner spacing, etc., also control the leg spacing. Maximum range for leg batter is 1:8 (horizontal to vertical); a corner leg, inclined at a batter of 1:7 in each direction, will result in a true batter of 1:5.05 (some operators use a 1:5 batter

**TABLE 7.3**  
**Ultimate Shear and Axial Load Capacities of Offshore Piles**

Pile Diameter (in.)	Lateral (tons)	Axial (tons)
30	50–75	250–750
36	70–90	500–1000
39	80–110	1000–1750
42	110–125	1500–2250
48	120–150	2000–2500
54	150–200	2250–2750
60	200–250	up to 3000
72	225–275	up to 4000
84	250–350	up to 5000

Source: B. McClelland and M.D. Reifel, *Planning and Design of Fixed Offshore Platforms*, Van Nostrand Reinhold Company, New York, p. 536, 1986.

for the corner leg). For deepwater structures, the batter has been reduced to as little as 1:16 (to 20) so that the base size is compatible with the reach of the mobile cranes in the fabrication yard.

Horizontal bracing members are required to stabilize the jacket space frame and to support the well conductors, sumps, etc. Jacket bay height is somewhat dependent on the allowable span of well conductors. However, it has been found to be an optimum if the primary diagonal braces in the vertical jacket templates are at an approximately 45° angle intersection with the legs. The top level of the horizontal bracing of the jacket structures is located at 10 to 15 ft. above the mean sea level; higher elevation should be considered for the top level of horizontal bracings when fatigue damage becomes important because of the presence of larger storm waves generated due to the presence of frequent storms. The bottom level of the horizontal bracings is located near the mud line.

Typical jacket framing styles are given earlier in Figure 2.9; typically, they consist of single-diagonal or K-braced panels; engineers have also used x-braced panels in many recent structures so as to reduce the effective length of the constituent bracing members of the jacket. When the x-braced panel is used, one leg of the x-brace is in compression, and the other leg tends to be in tension; as such, the tensile member restrains the compression leg from its out-of-plane deformation. Moreover, in the case of x-bracing, the joint at the center will require careful modeling and analysis to maintain its integrity and fatigue tolerance.

Most structural elements in a jacket platform will be subjected to a combined loading of compressive and bending forces. As a result, the effective slenderness of these members would become a limiting factor in its selection. For initial sizing of primary jacket braces, the brace size is to be limited by its  $kl/r$  ratio, which is kept between 80 and 90. From experience, it has been found that the diameter of the tubular element (in inches) is approximated as one-third of the span length (in feet); thus, for a 60.0-ft. span, the diameter is approximately 20.0 in. A slightly higher  $kl/r$  ratio may be used for secondary braces. In addition, the cross-sectional stability of the tubular member also should be maintained; this is found to be dependent on the diameter-to-thickness ratio ( $d/t$ ) of the tubular member. A rough guideline for the initial selection of the wall thickness of tubular members is given in Table 7.4 [22].

These factors, along with the guidelines given for  $kl/r$  ratios and pile capacities, will provide some conservative estimate for starting the preliminary analysis of jackets located in moderate

**TABLE 7.4**  
**Guidelines for Selecting Wall Thickness of Tubular Members**

Structural Element	$d/t$
Jacket leg (ungrouted)	45
Jacket leg joint	30–45
Jacket brace	40–60
Jacket brace joint section	35–40
Deck leg	35–40
Deck truss brace	35–45

Source: B. McClelland and M.D. Reifel, *Planning and Design of Fixed Offshore Platforms*, Van Nostrand Reinhold Company, New York, p. 539, 1986.

water depths. For deeper waters, an alternate approach is suggested. Here the emphasis is placed in reducing the wave forces acting on the jacket structures. Since fatigue considerations may become the dominant criteria in the design of members located in deeper waters, it is recommended that the  $D/t$  ratio be reduced and the  $kl/r$  ratio be increased as much as possible.

### Example 7.1

The offshore platform tower in Figure E7.1 [23] has been provided with the following particulars for a preliminary sizing of the jacket members. Using the particulars provided for the tower and the guidelines given in Tables 7.3 and 7.4, determine suitable member sizes for jacket columns, horizontal and diagonal braces, and pile hollow tubular members.

*Due to vertical loads alone:* From subsequent readings given in the section from which the above problem was formulated, it was found that the platform load of 10,000 kips given above was made up of the sum of a deck load of 7000 kips and a jacket (structure and pile) load of 3000 kips. Consequently, the maximum vertical load carried by eight main columns (neglecting the load shared with the secondary column members) =  $(7000 + 1000 + 3000)$  kips = 11,000 kips. The contributions from the secondary piles  $R_{S3}$  and  $R_{S4}$  are neglected.

$$\text{Vertical load taken by each column member} = (11,000/8) \text{ kips} = 1375 \text{ kips.}$$

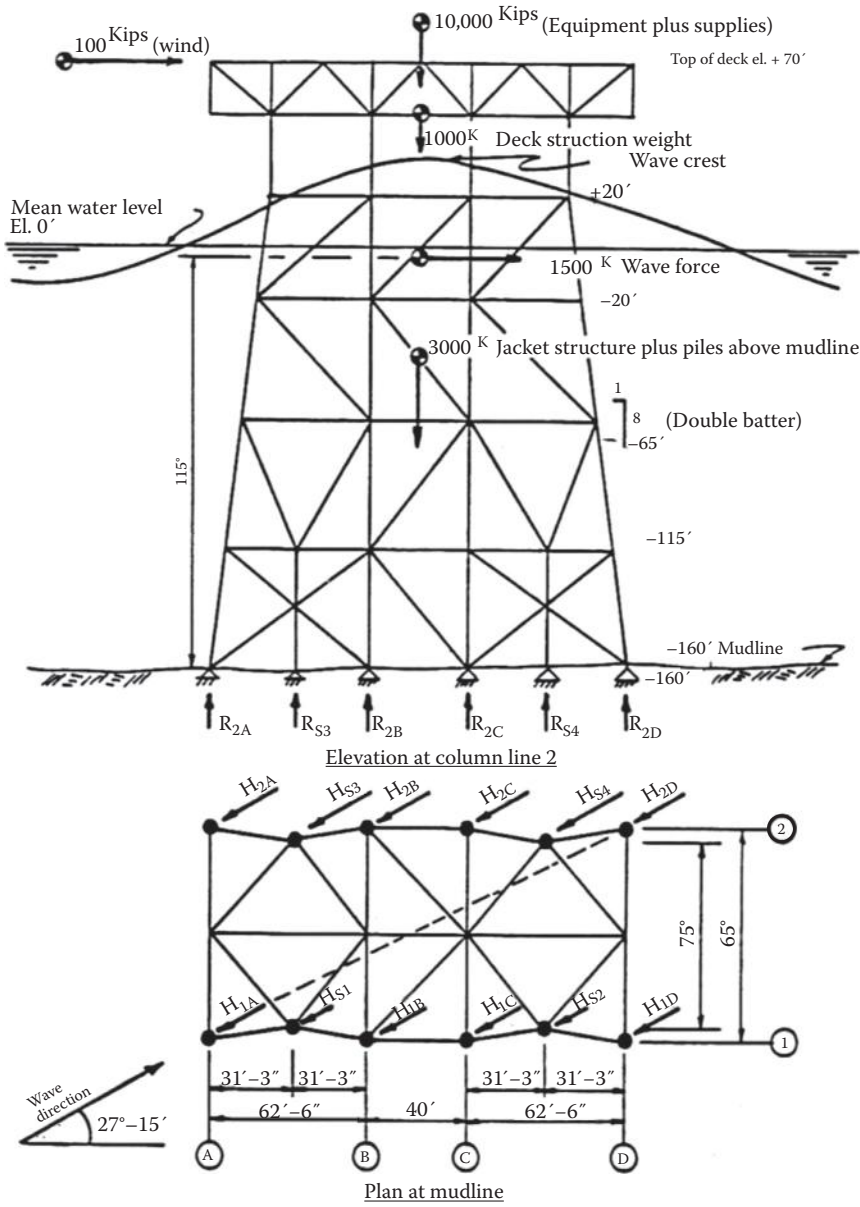
*Due to external wave and wind loads (horizontal):* Assuming the wind and wave loads to be acting in the same direction, and resolving the forces to be acting through the platform center, the vertical reaction due to the wind and wave loads are obtained as follows:

$$\text{Wave force component along the length of platform (x-direction)} = 1500 \cos(27.25^\circ) \text{ kips} = 1333.53 \text{ kips.}$$

$$\text{Wave force component along the width of platform (y-direction)} = 1500 \sin(27.25^\circ) \text{ kips} = 686.81 \text{ kips.}$$

$$\text{Wind force component along the length of platform (x-direction)} = 100 \cos(27.25^\circ) \text{ kips} = 88.90 \text{ kips.}$$

$$\text{Wind force component along the width of platform (y-direction)} = 100 \sin(27.25^\circ) \text{ kips} = 45.79 \text{ kips.}$$



**FIGURE E7.1** Platform details for computing preliminary tubular member sizes. (From Course Notes on General Design of Fixed Offshore Structures, University of Texas, Austin, TX, 1979.)

If  $R'_{2A}$ ,  $R'_{2B}$ ,  $R'_{2C}$ , and  $R'_{2D}$  are the contributions from the forces acting along the  $x$ - $z$  plane, then

$$R'_{2B} = (-R'_{2C}) = (R'_{2A})(20.0/82.5) = (0.2424)R'_{2A} \text{ or } (-0.2424)(R'_{2D})$$

Taking the moment about the center of the plan form, about the  $y$ - $z$  plane,

$$-(2 \times 2)(R'_{2A})(82.5) - (2 \times 2)(0.2424R'_{2A})(20) = (1333.53)(115) + (88.90)(230)$$

Hence,  $R'_{2A} = -(173,802.95)/(349.39) = -497.45$  kips.

$$R'_{2D} = +497.45 \text{ kips (compression)}$$

Similarly,  $R''_{2A}$ ,  $R''_{2B}$ ,  $R''_{2C}$ , and  $R''_{2D}$  are the contributions from the forces acting along the  $y$ - $z$  plane; then

$$R''_{2A\text{-left}} = (-R''_{2A\text{-right}}) = R''_{2B\text{-left}} = (-R''_{2B\text{-right}}) = R''_{2D\text{-left}} = (-R''_{2D\text{-right}}) = R''_{2C\text{-left}} = (R''_{2C\text{-right}}).$$

Taking the moment of the forces about the  $x$ - $z$  plane,

$$R''_{2A\text{-left}}(4 \times 2)(42.5) = (686.81)(115) + (45.79)(230)$$

$$(R''_{2A\text{-left}}) = (89,514.9/340) = 263.28 \text{ kips (compression)}$$

$$R_{2D\text{-left}} = R'_{2D\text{-left}} + R''_{2D\text{-left}} = 497.45 + 263.28 = 760.73 \text{ kips.}$$

*Total loads:* Total maximum vertical reaction at  $D = (1375.0 + 760.73) = 2135.73$  kips

Assume a double batter of 1 to 8 for the corner columns.

Neglecting the effect of the horizontal shear component along the pile, the maximum reaction along the pile length =  $(2135.73)/(8/\sqrt{66}) = 2168.84$  kips.

From Table 7.3, for a load of 2168.84 kips, the member diameter for the pile is equal to 48 in.

Also for the column, the diameter of the bottom column = 48 in.

(Note: If the interior secondary columns were assumed to contribute to the vertical reactions, then the pile/column diameter may reduce to 42 in.)

For the brace, the force taken by the brace member needs to be known; this can be done by a preliminary truss analysis or a frame analysis with the given loads. Assuming the diagonal braces to resist the horizontal forces only, the force components in the six diagonal braces =  $(6)(F_{\text{diagonal brace}} \cos(45^\circ)) = (4.243)(F_{\text{diagonal brace}}) = (1500.0 + 100.0)\{\cos(27.25^\circ)\}$  kips = 1422.43 kips.

$$(F_{\text{diagonal brace}}) \text{ in each member} = (1422.43/4.243) = 335.24 \text{ kips.}$$

From Table 7.3, the member diameter is 30.0 in. for this load.

Using Table 7.4, for the jacket pile foundation,  $D/t = 45.0$ ; hence, the thickness of pile =  $(48/45) \sim 1.067 = 1.125$  in.

For the vertical column member at the bottom, the  $D/t$  ratio is 30 to 35. Taking a ratio of 35, the thickness of the bottom column member =  $(48/35) \sim 1.37 = 1.375$  in.

For the horizontal brace, the  $D/t$  ratio is = 40 to 60. Taking a ratio of 50, thickness of the brace member is =  $(30/50) \sim 0.625$  in. The same is used for diagonal brace also.



## 7.5 FINITE ELEMENT APPLICATIONS FOR FRAMED OFFSHORE STRUCTURAL ANALYSES

### 7.5.1 INTRODUCTION

This section deals with the prefinal state of the design process of an offshore structure where the computed static and dynamic environmental/other loads are applied on the structure, and the resulting stresses, strains, and deformations are computed by a chosen computational procedure. These values are then used in the design process to ensure the availability of sufficient structural and fatigue strengths to satisfy the governing code provisions. As outlined earlier, the static and dynamic structural analyses of offshore structures are more involved due to the possible nonlinear behavior dependent on soil–structure interaction and wave/wind drag force effects.

Shallow-water steel template (or jacket) structures can be analyzed with acceptable accuracy by using a quasi-static environmental loading and linear elastic analysis, modified suitably for the presence of nonlinear soil behavior (by using nonlinear  $p$ – $y$  curve soil springs). In this approach, wind and current loads are assumed to apply static loads on the structure along with the maximum of the applied dynamic wave loads and the resultant loads, stresses/strains, and deformations in the component members computed. This procedure assumes that the resonant frequencies of the offshore structure are sufficiently separated from the wave/wind frequencies, and the resultant dynamic magnifications of stresses/deformations are very small. This quasi-static analysis may not be suitable for deepwater structures, which are slender due to the combined effects of water depth and cost economization. In such cases, a judicious mixture of many quasi-static analyses and a few dynamic analyses (to provide proper stress cycles for fatigue analysis) are used to provide values for design of the offshore structure. Only the procedure for the quasi-static analysis of offshore structures will be highlighted herein.

The developments in computer technology and numerical analysis procedures, such as finite element methods, have facilitated the quicker and efficient analysis of offshore structures. The basic theory underlying the finite element procedure used in the analysis of fixed steel template structures is the direct stiffness method, which will be described in detail in the subsequent sections. The basis of the method is that the structures to be analyzed are discretized into a number of small elements, considering the framed jacket or the top deck to be made up of an assembly of truss and/or beam elements; in the case of the bottom-supported concrete gravity structures, the structure is considered to be made up of an assembly of beam and/or plate/shell elements. In this method, the displacements of various nodal points (in the respective  $x$ ,  $y$ , and/or  $z$  directions) are taken as the unknowns, and the resultant deformations are determined by the use of the finite element procedure. The necessary steps are given below [24]:

- (i) As a first step, the physical data for the structural configuration, member properties, and support constraints are assumed based on guidelines given and prior experience of the analyst. The structure is then discretized into its component elements (truss, beam, or plate/shell elements) based on the number of unknown nodal displacements considered for the structure. The nodes are identified and systematically numbered using the available optimum indexing procedure.
- (ii) The local stiffness matrix of the element is then computed, transformed into its global stiffness matrix, and assembled into the global stiffness matrix for the structure.
- (iii) The loads acting on the component members and their corresponding nodes are then assembled into a global load vector; in this process, the member loads are transformed into their equivalent nodal loads.
- (iv) The boundary degrees of freedom are rearranged and eliminated before solving the assembled global stiffness matrix and load vector for the unknown nodal displacements.

- (v) The displacements are used in the corresponding local member stiffness matrix and equivalent nodal loads to compute the member forces and the corresponding member stresses and strains.

In the subsequent sections, the details of this formulation are presented for steel jacket platforms, starting from a two-dimensional representation of structures composed of truss and beam elements; thereafter, the procedure for a three-dimensional formulation of the problem is given.

### 7.5.2 USE OF TRUSS ELEMENTS IN OFFSHORE STRUCTURAL MODELING

Component structures of an offshore platform, such as deck structures, are modeled with one-dimensional elements having only axial (or along member) deformations; these elements are otherwise known as *truss elements* since the component elements in a truss structure have only deformations along their length directions. The truss elements can be located in a two-dimensional  $x$ - $z$  plane or in a three-dimensional  $x$ - $y$ - $z$  space. Plane structures having axially loaded members, in the  $x$ - $z$  plane, are generally referred to as plane trusses, and space structures that have members carrying only axial forces, in the  $x$ - $y$ - $z$  space, are called space trusses.

Plane trusses consist of straight members, which are inclined to one another in a single plane and which carry only tension or compression forces in them. From statics, it can easily be seen that the conditions for this last requirement to be met are that applied forces exist only at the joints connecting the members, that no applied moments exist, and that the members are free to rotate at the joints so as to prevent the need for the presence of bending/torsion moments.

### 7.5.3 PLANE TRUSSES

To analyze such structures, we consider now the case of an axially loaded member (or element) inclined at an angle  $\alpha$  to the horizontal as shown in Figure 7.17 [25]. We choose horizontal and vertical coordinate axes  $x$  and  $z$  and inclined axes  $\bar{x}$  and  $\bar{z}$ , as shown. The first are referred to as system axes and the second as the member axes.

Let  $f_{1x}, f_{1z}$  and  $f_{2x}, f_{2z}$  denote  $x$ - and  $z$ -force components at positions 1 and 2 of the bar, respectively, and let  $\bar{f}_{1x}, \bar{f}_{1z}$  and  $\bar{f}_{2x}, \bar{f}_{2z}$  denote corresponding  $\bar{x}$ - and  $\bar{z}$ -force components at these positions. Also assume  $l$  to be the length of the bar,  $A$  the cross-sectional area, and  $E$  the Young's modulus of elasticity of the bar material. From geometry, we may easily establish the following transformation equations between the force components at position 1:

$$\begin{aligned}\bar{f}_{1x} &= f_{1x} \cos \alpha + f_{1z} \sin \alpha, \\ \bar{f}_{1z} &= -f_{1x} \sin \alpha + f_{1z} \cos \alpha\end{aligned}\tag{7.8}$$

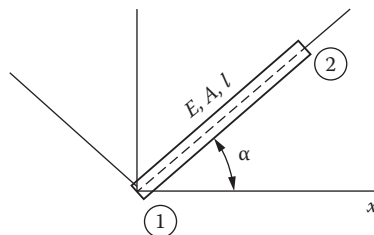


FIGURE 7.17 Inclined plane-truss member. (From T.H. Dawson, *Offshore Structural Engineering*, Prentice Hall Inc., Englewood Cliffs, NJ, p. 37, 1983. With permission.)

and

$$\begin{aligned} f_{1x} &= \bar{f}_{1x} \cos \alpha - \bar{f}_{1z} \sin \alpha, \\ f_{1z} &= \bar{f}_{1x} \sin \alpha + \bar{f}_{1z} \cos \alpha \end{aligned} \quad (7.9)$$

with similar equations applying at position 2.

In matrix notation, these become

$$\begin{Bmatrix} \bar{f}_{1x} \\ \bar{f}_{1z} \\ \bar{f}_{2x} \\ \bar{f}_{2z} \end{Bmatrix} = \begin{bmatrix} \cos \alpha & \sin \alpha & 0 & 0 \\ -\sin \alpha & \cos \alpha & 0 & 0 \\ 0 & 0 & \cos \alpha & \sin \alpha \\ 0 & 0 & -\sin \alpha & \cos \alpha \end{bmatrix} \begin{Bmatrix} f_{1x} \\ f_{1z} \\ f_{2x} \\ f_{2z} \end{Bmatrix} \quad (7.10)$$

$$\begin{Bmatrix} f_{1x} \\ f_{1z} \\ f_{2x} \\ f_{2z} \end{Bmatrix} = \begin{bmatrix} \cos \alpha & -\sin \alpha & 0 & 0 \\ \sin \alpha & \cos \alpha & 0 & 0 \\ 0 & 0 & \cos \alpha & -\sin \alpha \\ 0 & 0 & \sin \alpha & \cos \alpha \end{bmatrix} \begin{Bmatrix} \bar{f}_{1x} \\ \bar{f}_{1z} \\ \bar{f}_{2x} \\ \bar{f}_{2z} \end{Bmatrix} \quad (7.11)$$

Notice that the square matrix of the second set of these equations is just the matrix of the first set with rows and columns interchanged; that is, the second set is just the transpose of the first set. Thus, if  $[T]$  denotes the first matrix, called the transformation matrix between  $\bar{x}$  and  $x$  coordinates, then  $[T]^T$  may be used to denote the second matrix. Hence,

$$\begin{aligned} \{\bar{f}\} &= [T]\{f\}, \\ \{f\} &= [T]^T\{\bar{f}\} \end{aligned} \quad (7.12)$$

The discussion above has been concerned with force components at positions 1 and 2 of the member. Obviously, however, similar results also apply to the respective  $x$ - and  $y$ -displacement components  $u_1, w_1$  and  $u_2, w_2$  at positions 1 and 2 and corresponding  $\bar{x}$ - and  $\bar{y}$ -displacement components  $\bar{u}_1, \bar{w}_1$  and  $\bar{u}_2, \bar{w}_2$ . Thus we can also write,

$$\begin{aligned} \{\bar{u}\} &= [T]\{u\}, \\ \{u\} &= [T]^T\{\bar{u}\} \end{aligned} \quad (7.13)$$

where the displacement vectors  $\{u\}$  and  $\{\bar{u}\}$  are given by

$$\{\bar{u}\} = \begin{Bmatrix} \bar{u}_1 \\ \bar{w}_1 \\ \bar{u}_2 \\ \bar{w}_2 \end{Bmatrix}, \quad \{u\} = \begin{Bmatrix} u_1 \\ w_1 \\ u_2 \\ w_2 \end{Bmatrix}, \quad (7.14)$$

Since member 1–2 is subjected to a uniaxial loading along its axis  $\bar{x}$  only,

$$\bar{f}_{1z} = \bar{f}_{2z} = 0 \quad (7.15)$$

Also, the force  $\bar{f}_{1\bar{x}}$  and  $\bar{f}_{2\bar{x}}$  can be expressed as

$$\begin{aligned} \bar{f}_{1x} &= -(EA/l)(\bar{u}_2 - \bar{u}_1) = -k(\bar{u}_2 - \bar{u}_1) \\ \bar{f}_{2x} &= (EA/l)(\bar{u}_2 - \bar{u}_1) = k(\bar{u}_2 - \bar{u}_1) \end{aligned} \quad (7.16)$$

where  $k = (EA/l)$ .

Using the earlier formulations given for Equation 7.13, the vector matrix equations can be expressed as

$$\{\bar{f}\} = [\bar{K}]\{\bar{u}\} \quad (7.17)$$

where  $[\bar{K}]$  denotes the stiffness matrix of the member, relative, of course, to member axes. The member stiffness matrix is given as

$$\bar{K} = (EA/l) \begin{vmatrix} 1 & 0 & -1 & 0 \\ 0 & 0 & 0 & 0 \\ -1 & 0 & 1 & 0 \\ 0 & 0 & 0 & 0 \end{vmatrix} \quad (7.18)$$

Using Equations 7.12 and 7.13, the relation given in Equation 7.17 may be written alternatively as

$$[T]\{f\} = [\bar{K}][T]\{u\} \quad (7.19)$$

Premultiplying both sides of Equation 7.19 by  $[R]^T$  and noticing that

$$[T]^T[T] = \begin{bmatrix} 1 & 0 & 0 & 0 \\ 0 & 1 & 0 & 0 \\ 0 & 0 & 1 & 0 \\ 0 & 0 & 0 & 1 \end{bmatrix} = [I] \quad (7.20)$$

we have

$$\{f\} = [T]^T [\bar{K}][T]\{u\} \quad (7.21)$$

so that by comparison with  $\{f\} = [K]\{u\}$ , the stiffness matrix  $[K]$  of the member associated with the system axes is given by

$$\{K\} = [T]^T [\bar{K}][T] \quad (7.22)$$

Equation 7.22 provides the general transformation relation for the stiffness matrix between member and system axes. We may now expand Equation 7.21 to find  $[K]$  expressible explicitly as

$$[K] = \frac{EA}{l} \begin{bmatrix} \lambda^2 & \lambda\mu & -\lambda^2 & -\lambda\mu \\ \lambda\mu & \mu^2 & -\lambda\mu & -\mu^2 \\ -\lambda^2 & -\lambda\mu & \lambda^2 & \lambda\mu \\ -\lambda\mu & -\mu^2 & \lambda\mu & \mu^2 \end{bmatrix} = k \begin{bmatrix} \lambda^2 & \lambda\mu & -\lambda^2 & -\lambda\mu \\ \lambda\mu & \mu^2 & -\lambda\mu & -\mu^2 \\ -\lambda^2 & -\lambda\mu & \lambda^2 & \lambda\mu \\ -\lambda\mu & -\mu^2 & \lambda\mu & \mu^2 \end{bmatrix} \quad (7.23)$$

where  $\lambda = \cos \alpha$  and  $\mu = \sin \alpha$ .

Equation 7.23 gives the stiffness matrix of a member with respect to the given set of system axes  $x$  and  $z$ . When the structure under consideration has several nonaligned members making up the structural system, then the stiffness matrix of each corresponding member can be computed using the directional cosines ( $\lambda$ ,  $\mu$ ) of the particular member and its joint (nodal) displacements with respect to common system axes. Then the individual matrix of each element can be properly added (by assembly) using the direct stiffness method to obtain the stiffness matrix of the entire structure. Thereafter, appropriate boundary conditions involving force or displacement components, pertaining to specific joints (or nodes) of members, can be applied, and the size of the stiffness matrix equation of the structure can be reduced. The matrix force-displacement equation of the system is solved to determine the unknown displacements of the given system. Thereafter, the remaining unknown force components of the structural system can be determined using the computed known displacements. Care must be taken to see that the boundary conditions specified would give a unique set of values to the unknown displacements of the structural system; in other words, sufficient and proper displacement constraints must be provided to eliminate the possibility of rigid-body movement of the structure.

Once the joint displacements are known, we may also calculate the internal forces acting at the ends of each member. For a given member, we have, in particular, from Equation 7.21 the force-deflection equation relative to system axes given by

$$\begin{Bmatrix} f_{1x} \\ f_{1z} \\ f_{2x} \\ f_{2z} \end{Bmatrix} = \left( \frac{EA}{l} \right) \begin{bmatrix} \lambda^2 & \lambda\mu & -\lambda^2 & -\lambda\mu \\ \lambda\mu & \mu^2 & -\lambda\mu & -\mu^2 \\ -\lambda^2 & -\lambda\mu & \lambda^2 & \lambda\mu \\ -\lambda\mu & -\mu^2 & \lambda\mu & \mu^2 \end{bmatrix} \begin{Bmatrix} u_1 \\ w_1 \\ u_2 \\ w_2 \end{Bmatrix} \quad (7.24)$$

Considering, for example, the components  $f_{2x}$  and  $f_{2z}$ , we find from this equation that

$$f_{2x} = \left( \frac{EA}{l} \right) [\lambda^2(u_2 - u_1) + \lambda\mu(w_2 - w_1)]$$

$$f_{2z} = \left( \frac{EA}{l} \right) [\lambda\mu(u_2 - u_1) + \mu^2(w_2 - w_1)] \quad (7.25)$$

From Equation 7.10, we also have the axial member force  $S_{1-2} = \bar{f}_{2x}$  given by

$$S_{1-2} = \lambda f_{2x} + \mu f_{2z} \quad (7.26)$$

So that, on using Equation 7.25 and the identity  $\lambda^2 + \mu^2 = 1$ , we find

$$S_{1-2} = \frac{EA}{l} [\lambda(u_2 - u_1) + \mu(w_2 - w_1)] \tag{7.27}$$

which expresses the axial internal force of the member 1–2 in terms of system displacements. More generally, we may write the equation giving the axial internal force in member  $m-n$  as

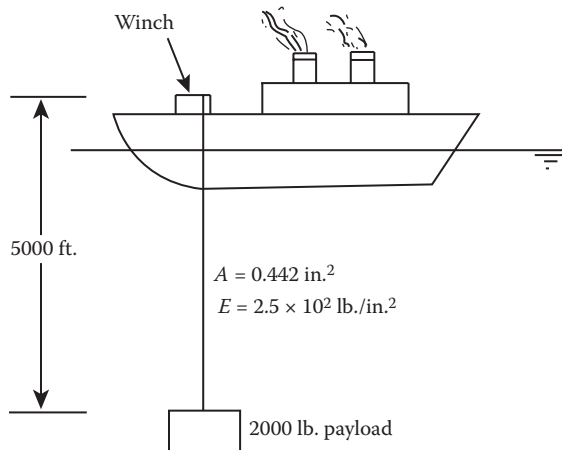
$$S_{m-n} = \frac{EA}{l} [\lambda(u_n - u_m) + \mu(w_n - w_m)] \tag{7.28}$$

We note that if  $S_{m-n}$  is positive, the member will be in tension; if negative, the member will then be in compression. The corresponding tensile or compressive stress is obtained by dividing  $S_{m-n}$  by the sectional area  $A$  of the member. The sign convention to be used with Equation 7.21 follows from our original consideration of the bar in Figure 7.17 and takes the following form. Let  $\alpha$  denote the angle between the horizontal system axis  $x$  and the member axis  $\bar{x}$ , with  $\bar{x}$  positive in the direction from end coordinate  $m$  to end coordinate  $n$  of a bar  $m-n$ . Then Equation 7.21 will give the stiffness matrix  $[K]_{mn}$  such that

$$\begin{Bmatrix} f_{mx} \\ f_{mz} \\ f_{nx} \\ f_{nz} \end{Bmatrix} = [K_{mn}] \begin{Bmatrix} u_m \\ w_m \\ u_n \\ w_n \end{Bmatrix} \tag{7.29}$$

**Example 7.2**

A winch and cable system shown in Figure E7.2 carries a payload at the end of the cable. The payload has an effective weight of 2000 lb. The cable weighs 0.66 lb./ft. Determine the displacements and internal forces along the cable using the direct stiffness method discussed above.



**FIGURE E7.2** Winch and cable system, located in a ship.

Let the 5000-ft.-long cable be divided into four segments, each of length 1250 ft.; each segment of the cable weighs  $(1250)(0.66) = 825.0$  lb. Hence, the load at each end of the cable will be equal to  $412.5 (= 825/2)$  lb.

Also the axial stiffness of the cable segment  $= (AE/\ell) = (0.442/144)(2.5)(10^6)(144)/(1250) = 884$  lb./ft.

As shown in Figure E7.3, the joint loads for the members 1–2, 2–3, 3–4, and 4–5 are indicated as  $F_1, F_2, F_3, F_4,$  and  $F_5$ . The forces are equal to

$$F_1 = 412.5 \text{ lb.}; F_2 = F_3 = F_4 = (412.5 + 412.5) = 825.0 \text{ lb.}; \text{ and } F_5 = 412.5 \text{ lb.}$$

Also  $(F_5)_{\text{Total}} = 412.5 + 2000 = 2412.5$  lb.

$(F_1)_{\text{Total}} = \text{unknown.}$

From Equation 7.18, the stiffness matrix is given as

$$\bar{K} = (EA/l) \begin{vmatrix} 1 & 0 & -1 & 0 \\ 0 & 0 & 0 & 0 \\ -1 & 0 & 1 & 0 \\ 0 & 0 & 0 & 0 \end{vmatrix}$$

If the vertical degree of freedom of the bar element is removed from the above matrix system of equations, we obtain the reduced stiffness matrix of the system as

$$(AE/\ell) \begin{bmatrix} 1 & -1 \\ -1 & 1 \end{bmatrix} = \begin{bmatrix} k & -k \\ -k & k \end{bmatrix}, \text{ where } k = (AE/\ell) = 884 \text{ lb./ft.}$$

Hence for elemental segment 1–2, the stiffness matrix is given by

$$\begin{bmatrix} k & -k \\ -k & k \end{bmatrix} \begin{Bmatrix} u_1 \\ u_2 \end{Bmatrix}$$

Similarly for the elemental segments 2–3, 3–4, and 4–5, the stiffness matrices will be, respectively,

$$\begin{bmatrix} k & -k \\ -k & k \end{bmatrix} \begin{Bmatrix} u_2 \\ u_3 \end{Bmatrix}$$

$$\begin{bmatrix} k & -k \\ -k & k \end{bmatrix} \begin{Bmatrix} u_3 \\ u_4 \end{Bmatrix}$$

and

$$\begin{bmatrix} k & -k \\ -k & k \end{bmatrix} \begin{Bmatrix} u_4 \\ u_5 \end{Bmatrix}$$

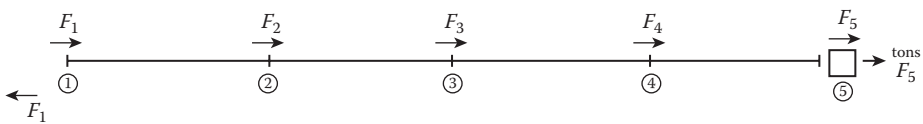


FIGURE E7.3 Discretized winch and cable system.



Assembling all the four stiffness matrices, one can obtain the cable-winch system stiffness matrix as

$$\begin{bmatrix} k & -k & 0 & 0 & 0 \\ -k & 2k & -k & 0 & 0 \\ 0 & -k & 2k & -k & 0 \\ 0 & 0 & -k & 2k & -k \\ 0 & 0 & 0 & -k & k \end{bmatrix} \begin{Bmatrix} u_1 \\ u_2 \\ u_3 \\ u_4 \\ u_5 \end{Bmatrix} = \begin{bmatrix} 884 & -884 & 0 & 0 & 0 \\ -884 & 1768 & -884 & 0 & 0 \\ 0 & -884 & 1768 & -884 & 0 \\ 0 & 0 & -884 & 1768 & -884 \\ 0 & 0 & 0 & -884 & 884 \end{bmatrix} \begin{Bmatrix} u_1 \\ u_2 \\ u_3 \\ u_4 \\ u_5 \end{Bmatrix}$$

The assembled force vector is given by

$$\begin{Bmatrix} (F_1)_{\text{Total}} \\ 825.0 \\ 825.0 \\ 825.0 \\ 2412.5 \end{Bmatrix}$$

Since  $(F_1)_{\text{Total}}$  is unknown and  $u_1$  is equal to zero (at the fixed end), the system matrices given in the above two expressions can be written as

$$\begin{bmatrix} 1768 & -884 & 0 & 0 \\ -884 & 1768 & -884 & 0 \\ 0 & -884 & 1768 & -884 \\ 0 & 0 & -884 & 884 \end{bmatrix} \begin{Bmatrix} u_2 \\ u_3 \\ u_4 \\ u_5 \end{Bmatrix} = \begin{Bmatrix} 825.0 \\ 825.0 \\ 825.0 \\ 2412.5 \end{Bmatrix}$$

Solving the above system matrix, one can obtain the displacements as

$$\begin{Bmatrix} u_2 \\ u_3 \\ u_4 \\ u_5 \end{Bmatrix} = \begin{Bmatrix} 5.53 \text{ ft.} \\ 10.13 \text{ ft.} \\ 13.79 \text{ ft.} \\ 16.52 \text{ ft.} \end{Bmatrix}$$

Using the 5x5 system matrix given above, the first row of the matrix will give the following equation for obtaining the cable end force:

$$(F_1)_{\text{Total}} = (884)(u_1) - (884)(u_2) = 0.0 - (884)(5.53) = -4888.0 \text{ lb.}$$

Since  $F_{\text{Total}} = F_1 + 412.5 = -4888.0 \text{ lb.}$ , the member end force  $F_1 = -4888.0 - 412.5 = -5300.5 \text{ lb.}$  (upward force at the end of the member, which is a tensile force).

Solving for the individual member forces, for member 1-2 (or member 1), the member end forces are

$$\begin{bmatrix} k & -k \\ -k & k \end{bmatrix} \begin{Bmatrix} u_1 \\ u_2 \end{Bmatrix} = \begin{Bmatrix} f_1^{(1)} \\ f_2^{(1)} \end{Bmatrix} \text{ and is given as } \begin{bmatrix} 884 & -884 \\ -884 & 884 \end{bmatrix} \begin{Bmatrix} 0.0 \\ 5.53 \end{Bmatrix} = \begin{Bmatrix} f_1^{(1)} \\ f_2^{(1)} \end{Bmatrix}$$

$$= \begin{Bmatrix} -4888.0 \text{ lb.} \\ +4888.0 \text{ lb.} \end{Bmatrix}$$

Similarly, for member 2–3 (or member 2), the member end forces are given by

$$\begin{bmatrix} k & -k \\ -k & k \end{bmatrix} \begin{Bmatrix} u_2 \\ u_3 \end{Bmatrix} = \begin{Bmatrix} f_2^{(2)} \\ f_3^{(2)} \end{Bmatrix} \text{ and is given as } \begin{bmatrix} 884 & -884 \\ -884 & 884 \end{bmatrix} \begin{Bmatrix} 5.53 \\ 10.13 \end{Bmatrix} = \begin{Bmatrix} f_2^{(2)} \\ f_3^{(2)} \end{Bmatrix} \\ = \begin{Bmatrix} -4066.4 \text{ lb.} \\ +4066.4 \text{ lb.} \end{Bmatrix}$$

Similarly for member 3–4 (or member 3), the member end forces are given by

$$\begin{bmatrix} k & -k \\ -k & k \end{bmatrix} \begin{Bmatrix} u_3 \\ u_4 \end{Bmatrix} = \begin{Bmatrix} f_3^{(3)} \\ f_4^{(3)} \end{Bmatrix} \text{ and is given as } \begin{bmatrix} 884 & -884 \\ -884 & 884 \end{bmatrix} \begin{Bmatrix} 10.13 \\ 13.79 \end{Bmatrix} = \begin{Bmatrix} f_3^{(3)} \\ f_4^{(3)} \end{Bmatrix} \\ = \begin{Bmatrix} -3235.44 \text{ lb.} \\ +3235.44 \text{ lb.} \end{Bmatrix}$$

Similarly for member 4–5 (or member 4), the member end forces are given by

$$\begin{bmatrix} k & -k \\ -k & k \end{bmatrix} \begin{Bmatrix} u_4 \\ u_5 \end{Bmatrix} = \begin{Bmatrix} f_4^{(4)} \\ f_5^{(4)} \end{Bmatrix} \text{ and is given as } \begin{bmatrix} 884 & -884 \\ -884 & 884 \end{bmatrix} \begin{Bmatrix} 13.79 \\ 16.52 \end{Bmatrix} = \begin{Bmatrix} f_4^{(4)} \\ f_5^{(4)} \end{Bmatrix} \\ = \begin{Bmatrix} -2413.0 \text{ lb.} \\ +2413.0 \text{ lb.} \end{Bmatrix}$$

Finally, the member stresses are computed as follows:

$$\text{for member 1, } \sigma_1 = (-4888.0/0.442) = -11,060.0 \text{ lb./in.}^2$$

$$\text{for member 2, } \sigma_2 = (-4066.4/0.442) = -9200.0 \text{ lb./in.}^2$$

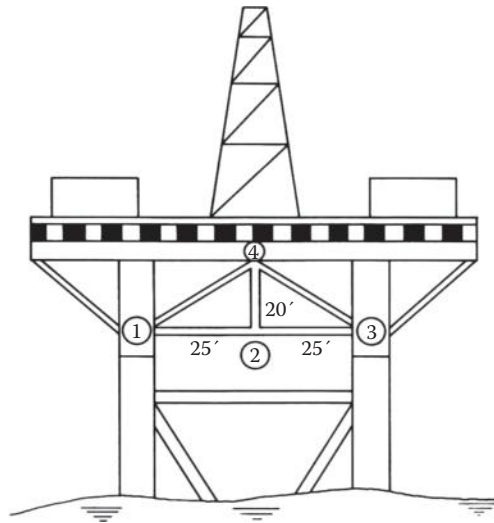
$$\text{for member 3, } \sigma_3 = (-3235.4/0.442) = -7320.0 \text{ lb./in.}^2$$

$$\text{for member 4, } \sigma_4 = (-2413.0/0.442) = -5459.3 \text{ lb./in.}^2$$

The minus (–) sign indicates that the stress is acting opposite to the positive direction assumed for the problem; in this case, the force is a tensile force acting along the corresponding member.

### Example 7.3

The deck of an offshore platform together with equipment weighs 500 kips (500,000 lb.). It is supported by four corner piles and two side trusses, as indicated in the two-dimensional sketch of Figure E7.4 [26]. The truss members are steel ( $E = 30 \times 10^6 \text{ lb./in.}^2$ ) with sectional areas  $A = 2.25 \text{ in.}^2$ . As an approximation, each support point (five on each side face) may be assumed to take  $W/10 = 50.0$  kips of the load. Under this condition, we wish to determine the deflections, reactions, and internal-member forces of the truss 1-2-3-4 assuming zero displacements at coordinates 1 and 3.



**FIGURE E7.4** Deck of the offshore platform. This matrix connects the forces and displacements at the indicated coordinates according to the equation.

To solve this problem, one should first construct the matrix stiffness equation for the structure using the direct stiffness method. Choosing  $x$ - and  $z$ -axes with  $x$  horizontal and positive to the right and  $z$  vertical and positive upward, one obtains

$$[K] = \left( \frac{EA}{l_1} \right) \begin{bmatrix} 1.476 & 0.381 & -1 & 0 & 0 & 0 & -0.476 & -0.381 \\ 0.381 & 0.305 & 0 & 0 & 0 & 0 & -0.381 & -0.305 \\ -1 & 0 & 2 & 0 & -1 & 0 & 0 & 0 \\ 0 & 0 & 0 & 1.250 & 0 & 0 & 0 & -1.250 \\ 0 & 0 & -1 & 0 & 1.476 & -0.381 & -0.476 & 0.381 \\ 0 & 0 & 0 & 0 & -0.381 & -0.305 & 0.381 & -0.305 \\ -0.476 & -0.381 & 0 & 0 & -0.476 & 0.381 & 0.952 & 0 \\ -0.381 & -0.305 & 0 & -1.250 & 0.381 & -0.305 & 0 & 1.860 \end{bmatrix}$$

where  $l_1 = 25$  ft.

This matrix connects the forces and displacements at the indicated coordinates according to the equation.

$$\{F\} = [K]\{u\}$$

where

$$\{F\} = \begin{Bmatrix} F_{1x} \\ F_{1z} \\ F_{2x} \\ \cdot \\ \cdot \\ F_{4z} \end{Bmatrix}, \quad \{u\} = \begin{Bmatrix} u_1 \\ w_1 \\ u_2 \\ \cdot \\ \cdot \\ w_4 \end{Bmatrix}$$

The boundary conditions are expressible as

$$\begin{aligned}u_1 = w_1 = u_3 = w_3 = 0 \\ F_{2x} = F_{2z} = F_{4x} = 0 \\ F_{4z} = -50.0 \text{ kips}\end{aligned}$$

Using these, we obtain the following reduced equations:

$$\begin{Bmatrix} F_{1x} \\ F_{1z} \\ F_{3x} \\ F_{3z} \end{Bmatrix} = \frac{EA}{l_1} \begin{bmatrix} -1 & 0 & -0.476 & -0.381 \\ 0 & 0 & -0.381 & -0.305 \\ -1 & 0 & -0.476 & 0.381 \\ 0 & 0 & 0.381 & -0.305 \end{bmatrix} \begin{Bmatrix} u_2 \\ w_2 \\ u_4 \\ w_4 \end{Bmatrix}$$

and

$$\begin{Bmatrix} F_{2x} \\ F_{2y} \\ F_{4x} \\ F_{4y} \end{Bmatrix} = \frac{EA}{l_1} \begin{bmatrix} 2 & 0 & 0 & 0 \\ 0 & 1.250 & 0 & -1.250 \\ 0 & 0 & 0.952 & 0 \\ 0 & -1.250 & 0 & 1.860 \end{bmatrix} \begin{Bmatrix} u_2 \\ w_2 \\ u_4 \\ w_4 \end{Bmatrix}$$

Inverting this last equation and substituting for the applied forces, we find

$$\begin{aligned}u_2 = u_4 = 0; \\ w_2 = w_4 = -0.0304 \text{ ft.}\end{aligned}$$

The reaction forces may next be determined from the first of the reduced equations above as

$$\begin{aligned}F_{1x} = -F_{3x} = 31.30 \text{ kips} \\ F_{1z} = F_{3z} = 25.03 \text{ kips}\end{aligned}$$

Finally, the internal forces in each member may be determined from Equation 7.28 as

$$\begin{aligned}S_{1-2} = S_{2-3} = S_{2-4} = 0 \\ S_{1-4} = S_{3-4} = -40.06 \text{ kips}\end{aligned}$$

The stress  $\sigma_{m-n}$  in member  $m-n$  is obtained from the corresponding internal force by dividing by the load-carrying sectional area of the member. We have

$$\begin{aligned}\sigma_{1-2} = \sigma_{2-3} = \sigma_{2-4} = 0 \\ \sigma_{1-4} = \sigma_{3-4} = -17,804 \text{ lb./in.}^2\end{aligned}$$

If the material is ordinary construction steel having a yield stress of, say, 36,000 lb./in.<sup>2</sup>, we thus see that the truss as designed has a factor of safety of  $36,000/17,804 = 2.02$  with respect to failure by yield.

In this example, the weights of the individual members were neglected. If one wishes to include them in the analysis, one may calculate the weight of each member and place half this weight at each end joint as an applied downward force. This will allow inclusion of the weight at each end joint as an applied downward force, thus allowing the inclusion of the weight of the structure in the axial loads carried by the members. It will not, however, account for the small bending stresses induced by the actual distributed weights of the various members.

#### 7.5.4 SPACE TRUSSES

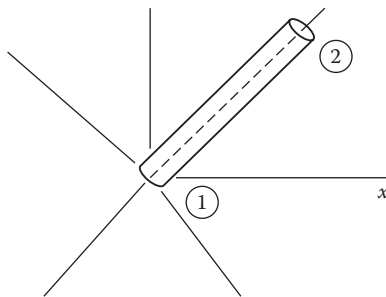
The procedure given above applies only to two-dimensional alignments of structural members subjected to tension or compression loading (in the plane of the truss) obtained for the case of plane-truss problems. In order to extend the work to three dimensions for space-truss problems, we should consider member 1–2, as shown in Figure 7.18 [27].

The local or member axes are denoted by  $\bar{x}$ ,  $\bar{y}$ ,  $\bar{z}$  and the reference or system axes by  $x$ ,  $y$ ,  $z$ . In addition, the following notations are assumed for the angles between the two sets of axes:

$$\begin{aligned}\alpha_{x\bar{x}} &= \text{angle between } (x, \bar{x}), \alpha_{y\bar{x}} = \text{angle between } (y, \bar{x}) \\ \alpha_{z\bar{x}} &= \text{angle between } (z, \bar{x}), \alpha_{x\bar{y}} = \text{angle between } (x, \bar{y}) \\ \alpha_{y\bar{y}} &= \text{angle between } (y, \bar{y}) \\ \alpha_{z\bar{z}} &= \text{angle between } (z, \bar{z})\end{aligned}\tag{7.30}$$

From geometry, the equations expressing the force components at positions 1 and 2 of the member relative to system and member axes are easily seen to be similar to the earlier two-dimensional equations, given by Equation 7.12, and expressible in matrix notation as

$$\begin{aligned}\{\bar{f}\} &= [T]\{f\} \\ \{f\} &= [T]^T\{\bar{f}\}\end{aligned}\tag{7.31}$$



**FIGURE 7.18** Truss member inclined in a three-dimensional space. (From T.H. Dawson, *Offshore Structural Engineering*, Prentice Hall Inc., Englewood Cliffs, NJ, p. 54, 1983. With permission.)

where the column matrices  $\{\bar{f}\}$  and  $\{f\}$  are given by

$$\{\bar{f}\} = \begin{Bmatrix} \bar{f}_{1x} \\ \bar{f}_{1y} \\ \bar{f}_{1z} \\ \bar{f}_{2x} \\ \bar{f}_{2y} \\ \bar{f}_{2z} \end{Bmatrix}, \quad \{f\} = \begin{Bmatrix} f_{1x} \\ f_{1y} \\ f_{1z} \\ f_{2x} \\ f_{2y} \\ f_{2z} \end{Bmatrix}, \quad (7.32)$$

and where the matrix  $[T]$  is given by

$$\{\bar{f}\} = \begin{Bmatrix} \bar{f}_{1x} \\ \bar{f}_{1y} \\ \bar{f}_{1z} \\ \bar{f}_{2x} \\ \bar{f}_{2y} \\ \bar{f}_{2z} \end{Bmatrix}, \quad \{f\} = \begin{Bmatrix} f_{1x} \\ f_{1y} \\ f_{1z} \\ f_{2x} \\ f_{2y} \\ f_{2z} \end{Bmatrix} \quad (7.33)$$

with

$$\begin{aligned} \lambda_{\bar{x}} &= \cos(\alpha_{x\bar{x}}), \\ \mu_{\bar{x}} &= \cos(\alpha_{y\bar{x}}), \\ \nu_{\bar{x}} &= \cos(\alpha_{z\bar{x}}), \\ &\cdot \\ &\cdot \\ &\cdot \\ &\cdot \\ \nu_{\bar{x}} &= \cos(\alpha_{z\bar{x}}) \end{aligned} \quad (7.34)$$

Similarly, for the displacements, we have

$$\begin{aligned} \{\bar{u}\} &= [T]\{u\}, \\ \{u\} &= [T]^T\{\bar{u}\} \end{aligned} \quad (7.35)$$

where

$$\{\bar{u}\} = \begin{Bmatrix} \bar{u}_1 \\ \bar{v}_1 \\ \bar{w}_1 \\ \bar{u}_2 \\ \bar{v}_2 \\ \bar{w}_2 \end{Bmatrix}, \quad \{u\} = \begin{Bmatrix} u_1 \\ v_1 \\ w_1 \\ u_2 \\ v_2 \\ w_2 \end{Bmatrix} \tag{7.36}$$

As in the earlier two-dimensional treatment, we have the force-deflection equation for the member expressible as

$$\{\bar{f}\} = [\bar{K}]\{\bar{u}\} \tag{7.37}$$

Using Equations 7.31 and 7.35, this may be written as

$$[T]\{f\} = [\bar{K}][T]\{u\} \tag{7.38}$$

On premultiplying both sides of the expression by  $[T]^T$  and noticing that

$$[T]^T[T] = \begin{bmatrix} 1 & 0 & 0 & 0 & 0 & 0 \\ 0 & 1 & 0 & 0 & 0 & 0 \\ 0 & 0 & 1 & 0 & 0 & 0 \\ 0 & 0 & 0 & 1 & 0 & 0 \\ 0 & 0 & 0 & 0 & 1 & 0 \\ 0 & 0 & 0 & 0 & 0 & 1 \end{bmatrix} = [I] \tag{7.39}$$

this equation becomes

$$\{f\} = [T]^T[\bar{K}][T]\{u\} \tag{7.40}$$

so that by comparison with  $\{f\} = [K]\{u\}$ , we have the stiffness of the member given in terms of system axes by

$$[K] = [T]^T[\bar{K}][T] \tag{7.41}$$

Taking  $[\bar{K}]$  as

$$[\bar{K}] = \left( \frac{EA}{1} \right) \begin{bmatrix} 1 & 0 & 0 & 0 & 0 & 0 \\ 0 & 1 & 0 & 0 & 0 & 0 \\ 0 & 0 & 1 & 0 & 0 & 0 \\ 0 & 0 & 0 & 1 & 0 & 0 \\ 0 & 0 & 0 & 0 & 1 & 0 \\ 0 & 0 & 0 & 0 & 0 & 1 \end{bmatrix} \tag{7.42}$$



and using Equations 7.33 and 7.41, we find

$$[K] = \left( \frac{EA}{l} \right) \begin{bmatrix} \lambda^2 & & & & & & \\ \lambda\mu & \mu^2 & & & & & \\ \lambda\nu & \mu\nu & \nu^2 & & & & \\ -\lambda^2 & -\lambda\mu & -\lambda\nu & \lambda^2 & & & \\ -\lambda\mu & -\mu^2 & -\mu\nu & \lambda\mu & \mu^2 & & \\ -\lambda\nu & -\mu\nu & -\nu^2 & \lambda\nu & \mu\nu & \nu^2 & \end{bmatrix} \quad \text{symmetric} \quad (7.43)$$

where  $\lambda$ ,  $\mu$ , and  $\nu$  are written for  $\lambda_{\bar{x}}$ ,  $\mu_{\bar{x}}$ ,  $\nu_{\bar{x}}$ ; also “symmetric” means that elements  $k_{ij}$  are equal to elements  $k_{ji}$ .

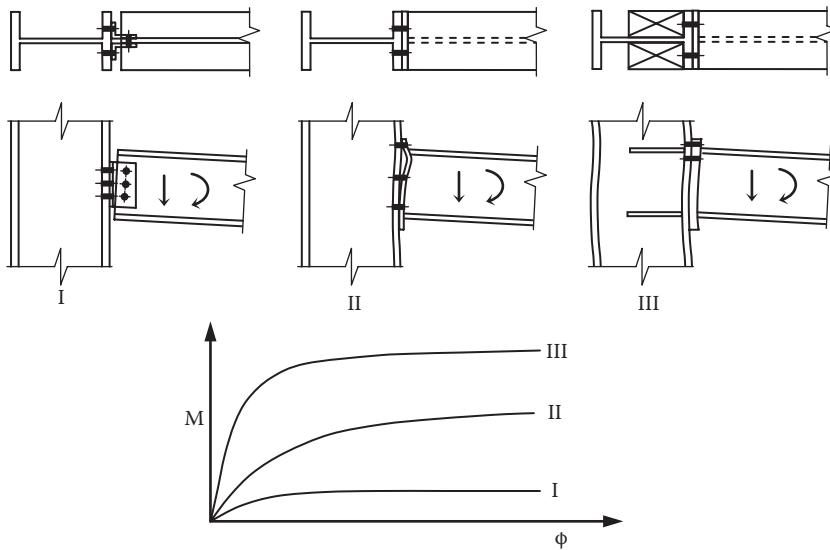
In solving space-truss problems with the help of this expression, we proceed exactly as in the two-dimensional case and write the stiffness matrix for each member, relative to system axes, adding zero rows and columns to indicate nondependence on system coordinates not involved. We then add these matrices using the direct stiffness method and employ appropriate boundary conditions to solve for displacements and unknown reaction forces. Finally, internal forces may be established using equations of the form

$$S_{m-n} = \bar{f}_{nx} = \lambda f_{2x} + \mu f_{2y} + \nu f_{2z} \quad (7.44)$$

where  $f_{2x}$ ,  $f_{2y}$ , and  $f_{2z}$  are determined from Equation 7.40 when applied to member  $m-n$ . The corresponding tensile or compressive stress is then determined by dividing  $S_{m-n}$  by the sectional area of the member as in the case of plane-truss members.

### 7.5.5 USE OF BEAM ELEMENTS IN OFFSHORE STRUCTURAL MODELING

In Section 7.5.2, only component members subjected to axial loads were considered; even though the actual structural loads were transverse, they produced only axial loads in the component members of the truss structures since the loads were only applied at the structural joints (or nodes) that were hinged. In other situations, the component members are likely to be subjected to transverse loads and moments, which will generate bending moments and shear/axial forces in them. These structures are denoted as framed structures, which can be located in a two-dimensional (plane frame) or three-dimensional space (space frame). In order to analyze these structures, the above basic matrix formulation for trusses needs to be extended to members and structures that can resist bending moments, shear forces, and torsional moments. Whereas the joints of truss structures are considered to be free to rotate at the connecting joints, framed structures are generally assumed to have rigid joints that preserve the relative angles between the attached members at the joints, before and after loading the structure. An example is the right-angled joint illustrated in Figure 7.19 [28]. Depending on the type of connections employed in connecting the beam member to the column member, the joint can be classified as (i) hinged, as shown in Figure 7.19I; (ii) partially fixed, as in Figure 7.19II; and (iii) fully fixed as in Figure 7.19III, providing a rigid connection. In a rigid jointed structure, the 90° angular spacing of the members at the joint is maintained even though the joint rotates; hence, with rigid joints in a structure, all members connected at the joint will undergo the same rotation as the joint itself.



**FIGURE 7.19** Illustration of possible joint connections and the consequent moment-rotation diagrams in a structure: I—hinged; II—partially fixed; and III—fully fixed. (From AISC LRFD, Design of Fully Restrained Moment Connections, PDH Course S154 at www.PDHcenter.com and www.PDHonline.org AISC LRFD 3rd Edition. Available at <http://www.inti.gov.ar/cirsoc/pdf/acero/s154content.pdf>. Accessed October 9, 2010.)

**7.5.5.1 Plane Frames**

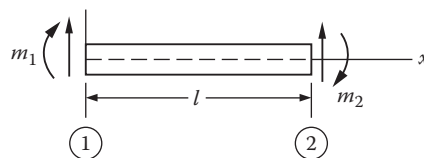
In the present section, we consider the matrix formulation for the analysis of plane frames, that is, frames having all their members lying in a single plane. Joints connecting members will be assumed rigid in the sense described above.

**7.5.5.2 Member Stiffness Matrix for Horizontal Beam Member**

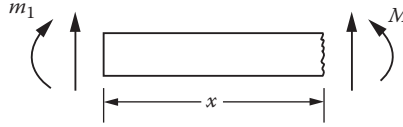
Consider the member 1–2, shown in Figure 7.20 [29], having moments and vertical forces  $m_1$  and  $f_{1z}$  at position 1 and  $m_2$  and  $f_{2z}$  at position 2. The vertical forces are assumed positive when acting in the positive  $z$ -direction, and the moments are assumed positive when acting clockwise. Restricting attention to the case where the cross section of the member is symmetric about a vertical axis through its centroid, the vertical deflection  $w(x)$  of the centroidal  $x$ -axis of the member is known from solid mechanics to be governed by the equation

$$EI_{yy} \frac{d^2w}{dx^2} = M(x) \tag{7.45}$$

where  $E$  denotes Young’s modulus,  $I_{yy}$  denotes the moment of inertia of the cross section of the member about its centroidal  $y$ – $y$  axis, and  $M(x)$  denotes the internal moment, assumed positive counterclockwise when acting on a right-hand face, as illustrated in Figure 7.21 [27].



**FIGURE 7.20** Structural member 1–2, subjected to joint bending moments and vertical forces. (From T.H. Dawson, *Offshore Structural Engineering*, Prentice Hall Inc., Englewood Cliffs, NJ, p. 52, 1983. With permission.)



**FIGURE 7.21**  $Q$  is the internal shear force and  $M$  is the internal moment in the member. (From T.H. Dawson, *Offshore Structural Engineering*, Prentice Hall Inc., Englewood Cliffs, NJ, p. 54, 1983. With permission.)

Considering Figure 7.21, and using statics, one arrives at the relationship

$$M = m_1 + xf_{1z} \quad (7.46)$$

Combining Equations 7.45 and 7.46 and integrating, one obtains (for constant  $EI_{yy}$ )

$$EI_{yy} \frac{dw}{dx} = m_1 x + f_{1z} \frac{x^2}{2} - EI_{yy} \theta_{1y} \quad (7.47)$$

and

$$EI_{yy} w = \frac{m_1 x^2}{2} + f_{1z} \frac{x^3}{6} - EI \theta_{1y} x + EI w_1 \quad (7.48)$$

where the boundary conditions

$$w = w_1, \quad \frac{dw}{dx} = -\theta_{1y} \quad (7.49)$$

have been used at  $x = 0$ , that is, at position 1.  $\theta_{1y}$  is considered to be positive in the same sense as that of  $m_1$ .

When the boundary conditions at position 2 are substituted, viz.,

$$\text{at } x = l, w = w_2 \text{ and } \frac{dw}{dx} = -\theta_{2y} \quad (7.50)$$

one obtains the following set of equations from Equations 7.47 and 7.48:

$$\begin{aligned} EI \theta_2 &= -m_1 l - f_{1y} \frac{l^2}{2} + EI_{yy} \theta_{1y} \\ EI w_2 &= \frac{m_1 l^2}{2} + f_{1z} \frac{l^3}{6} - EI_{yy} \theta_{1y} l + EI w_1 \end{aligned} \quad (7.51)$$

Solving the set of Equation 7.51 for  $m_1$  and  $f_{1z}$ , one obtains

$$\begin{aligned} m_1 &= \frac{6EI_{yy}}{l^2} (w_2 - w_1) + \frac{2EI}{l} (2\theta_{1y} + \theta_{2y}) \\ f_{1z} &= -\frac{12EI_{yy}}{l^3} (w_2 - w_1) - \frac{6EI}{l^2} (\theta_{1y} + \theta_{2y}) \end{aligned} \quad (7.52)$$

In addition, from equilibrium of the entire member (Figure 7.21), one obtains

$$\begin{aligned} m_2 &= -m_1 - lf_{1z} \\ f_{2z} &= -f_{1z} \end{aligned} \tag{7.53}$$

Hence,

$$\begin{aligned} m_2 &= \frac{6EI_{yy}}{l^2}(w_2 - w_1) + \frac{2E}{l}I_{yy}(\theta_{1y} + 2\theta_{2y}) \\ f_{2z} &= \frac{12EI_{yy}}{l^3}(w_2 - w_1) + \frac{6EI_{yy}}{l^2}(\theta_{1y} + \theta_{2y}) \end{aligned} \tag{7.54}$$

Consequently, the matrix stiffness equation for the member can be expressed as

$$\begin{Bmatrix} f_{1z} \\ m_1 \\ f_{2z} \\ m_2 \end{Bmatrix} = \left( \frac{EI_{yy}}{l^4} \right) \begin{bmatrix} 12l & -6l^2 & -12l & -6l^2 \\ -6l^2 & 4l^3 & 6l^2 & 2l^3 \\ -12l & 6l^2 & 12l & 6l^2 \\ -6l^2 & 2l^3 & 6l^2 & 4l^3 \end{bmatrix} \begin{Bmatrix} w_1 \\ \theta_{1y} \\ w_2 \\ \theta_{2y} \end{Bmatrix} \tag{7.55}$$

In addition to the transverse forces and moments acting at each end of the member, we may also consider the presence of axial forces in the member 1–2. Using Equation 7.24 for an axially loaded member, we can get the form of the stiffness equation for these axial forces as

$$\begin{Bmatrix} f_{1x} \\ f_{1z} \\ f_{2x} \\ f_{2z} \end{Bmatrix} = \frac{EA}{l} \begin{bmatrix} \lambda^2 & \lambda\mu & -\lambda^2 & -\lambda\mu \\ \lambda\mu & \mu^2 & -\lambda\mu & -\mu^2 \\ -\lambda^2 & -\lambda\mu & \lambda^2 & \lambda\mu \\ -\lambda\mu & -\mu^2 & \lambda\mu & \mu^2 \end{bmatrix} \begin{Bmatrix} u_1 \\ w_1 \\ u_2 \\ w_2 \end{Bmatrix} \tag{7.56}$$

For a horizontal member  $\theta = 0.0^\circ$ ; hence,  $\lambda = \cos(0.0) = 1.0$  and  $\sin(0.0) = 0.0$ . As a result, Equation 7.56 reduces to

$$\begin{Bmatrix} f_{1x} \\ f_{1z} \\ f_{2x} \\ f_{2z} \end{Bmatrix} = \frac{EA}{l} \begin{bmatrix} 1.0 & 0.0 & -1.0 & 0.0 \\ 0.0 & 0.0 & 0.0 & 0.0 \\ -1.0 & 0.0 & 1.0 & 0.0 \\ 0.0 & 0.0 & 1.0 & 0.0 \end{bmatrix} \begin{Bmatrix} u_1 \\ w_1 \\ u_2 \\ w_2 \end{Bmatrix} \tag{7.57}$$

Consequently, one can combine Equations 7.56 and 7.57 immediately to give

$$\begin{Bmatrix} f_{1x} \\ f_{1z} \\ m_1 \\ f_{2x} \\ f_{2z} \\ m_2 \end{Bmatrix} = \begin{bmatrix} \frac{EA}{l} & 0 & 0 & -\frac{EA}{l} & 0 & 0 \\ 0 & \frac{12EI_{yy}}{l^3} & -\frac{6E}{l^2}I_{yy} & 0 & -\frac{12E}{l^3}I_{yy} & -\frac{6E}{l^2}I_{yy} \\ 0 & -\frac{6EI_{yy}}{l^2} & \frac{4EI_{yy}}{l} & 0 & \frac{6EI_{yy}}{l^2} & \frac{2EI_{yy}}{l} \\ -\frac{EA}{l} & 0 & 0 & \frac{EA}{l} & 0 & 0 \\ 0 & -\frac{12EI_{yy}}{l^3} & \frac{6EI_{yy}}{l^2} & 0 & \frac{12EI_{yy}}{l^3} & \frac{6EI_{yy}}{l^2} \\ 0 & -\frac{6EI_{yy}}{l^2} & \frac{2EI_{yy}}{l} & 0 & \frac{6EI_{yy}}{l^2} & \frac{4EI_{yy}}{l} \end{bmatrix} \begin{Bmatrix} u_1 \\ w_1 \\ \theta_{1y} \\ u_2 \\ w_2 \\ \theta_{2y} \end{Bmatrix} \tag{7.58}$$

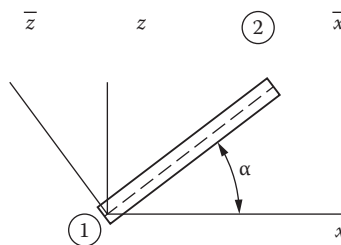
Equation 7.58 gives the stiffness matrix of the horizontal member 1–2 in the global coordinate system.

**7.5.5.3 Member Stiffness Matrix for Arbitrarily Oriented Member**

As in the case of uniaxially loaded members, we may consider the stiffness matrix of a member 1–2 inclined with respect to system axes. We take  $(\bar{x}, \bar{z})$  to denote member axes and  $(x, z)$  to denote system axes, as shown in Figure 7.22 [27]. The transformation between member and system components for this problem can be established from our previous considerations for axially loaded members. Remembering that the moments  $m_1$  and  $m_2$  can be regarded as vectors normal to the  $x$ – $y$  plane, we see that these, as well as the corresponding angles  $\theta_{\text{node1}}$  and  $\theta_{\text{node2}}$ , will be unaffected by the transformation.

Hence, the transformation equations relating member-force components with system-force components may be written as

$$\begin{aligned} \{\bar{f}\} &= [T]\{f\} \\ \{f\} &= [T]^T\{\bar{f}\} \end{aligned} \tag{7.59}$$



**FIGURE 7.22** Member 1–2 of an inclined plane frame. (From T.H. Dawson, *Offshore Structural Engineering*, Prentice Hall Inc., Englewood Cliffs, NJ, p. 54, 1983. With permission.)

where  $\{\bar{f}\}$  and  $\{f\}$  are given by

$$\{\bar{f}\} = \begin{Bmatrix} \bar{f}_{1\bar{x}} \\ \bar{f}_{1\bar{z}} \\ \bar{m}_1 \\ \bar{f}_{2\bar{x}} \\ \bar{f}_{2\bar{z}} \\ \bar{m}_2 \end{Bmatrix}, \quad \{f\} = \begin{Bmatrix} f_{1x} \\ f_{1z} \\ m_1 \\ f_{2x} \\ f_{2z} \\ m_2 \end{Bmatrix}, \quad (7.60)$$

and the transformation matrix  $[T]$  is given from Equation 7.8 and the equivalent vectorial nature of the moments  $m_1$  and  $m_2$  as

$$[T] = \begin{bmatrix} \lambda & \mu & 0 & 0 & 0 & 0 \\ -\mu & \lambda & 0 & 0 & 0 & 0 \\ 0 & 0 & 1 & 0 & 0 & 0 \\ 0 & 0 & 0 & \lambda & \mu & 0 \\ 0 & 0 & 0 & -\mu & \lambda & 0 \\ 0 & 0 & 0 & 0 & 0 & 1 \end{bmatrix} \quad (7.61)$$

with  $\lambda = \cos \alpha$ ,  $\mu = \sin \alpha$ .

Similarly, for the displacement components,

$$\begin{aligned} \{\bar{u}\} &= [T]\{u\} \\ \{u\} &= [T]^T\{\bar{u}\} \end{aligned} \quad (7.62)$$

where  $\{\bar{u}\}$  and  $\{u\}$  are given by

$$\{\bar{u}\} = \begin{Bmatrix} \bar{u}_1 \\ \bar{w}_1 \\ \bar{\theta}_{1y} \\ \bar{u}_2 \\ \bar{w}_2 \\ \bar{\theta}_{2y} \end{Bmatrix}, \quad \{u\} = \begin{Bmatrix} u_1 \\ w_1 \\ \theta_{1y} \\ u_2 \\ w_2 \\ \theta_{2y} \end{Bmatrix} \quad (7.63)$$

Using the above relations with the member stiffness equation

$$\{\bar{f}\} = [\bar{K}]\{\bar{u}\} \quad (7.64)$$

one can easily obtain the relationship

$$[K] = [T]^T[\bar{K}][T] \quad (7.65)$$





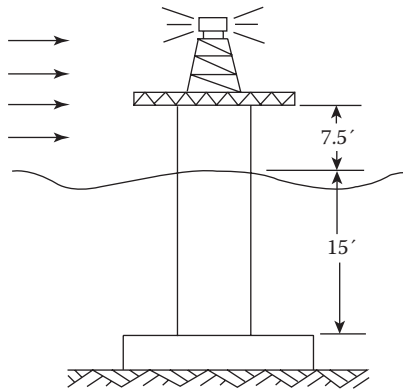
where  $A$  and  $I_{yy}$  denote, respectively, the cross-sectional area and moment of inertia of the cross section about its centroidal axis  $y - y$ , and  $\bar{z}$  denotes the vertical distance from the centroid of the section to the edge of the member. Similarly, the shear stress is expressed in terms of the shear force  $Q$  by the equation

$$\tau = \frac{QS}{I_{yy}b} \tag{7.69}$$

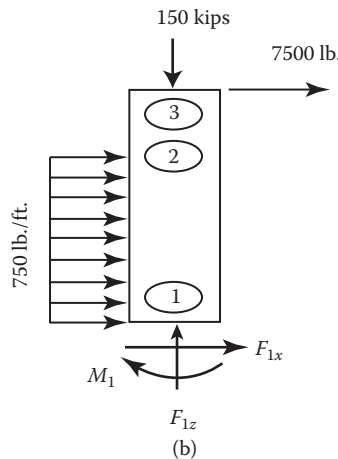
where  $S$  is the first moment of the area  $A$  above the plane on which the shear stress is calculated,  $I_{yy}$  is as defined above, and  $b$  denotes the width of the material on the plane on which shear stress is computed.

**Example 7.4**

The aid to navigational (ATN) tower, shown in Figure E7.5, is supported by a single steel column 22.5 ft. high, having an outside diameter of 4.5 ft. and a wall thickness of 1.5 in. The steel column



(a)



(b)

**FIGURE E7.5** (a) Aid to navigation tower and (b) wind and wave forces acting on the tower. (From T.H. Dawson, *Offshore Structural Engineering*, Prentice Hall Inc., Englewood Cliffs, NJ, p. 70, 1983. With permission.)

is embedded in a concrete footing as shown in Figure E7.5a [30]. Consider the horizontal wind and wave forces acting on the tower to be represented by the concentrated load (7500 lb.) and distributed horizontal forces (750 lb./ft.) acting on the tower as shown in Figure E7.5b. Moreover, the self-weight of the column and the deck weight are considered to be concentrated at its upper end and equal to a downward force of 150 kips. Determine the top deck deflection and the maximum stresses within the column members.

In order to solve this problem, the support column is divided into two members of unequal lengths (to facilitate the finite element formulation by separating at the region of wave force discontinuity) 1–2 and 2–3, as shown in Figure E7.4b. The stiffness matrices for these two members can be obtained from Equation 7.65. Using units of pounds and feet, we have  $E = 4.32 \times 10^9$  lb./ft.<sup>2</sup>,  $I = 4.114$  ft.<sup>4</sup>,  $A = 1.718$  ft.<sup>2</sup>. For member 1–2 ( $\lambda = 0$ ,  $\mu = 1$ ,  $l = l_1 = 15$  ft.), the stiffness matrix is found to be

$$[K]_{1-2}\{u\}_{1-2} = (E) \begin{bmatrix} 0.0146 \sim 0.015 & 0 & 0.110 & 0.0146 \sim 0.015 & 0 & 0.110 \\ 0 & 0.115 & 0 & 0 & -0.115 & 0 \\ 0.110 & 0 & 1.097 & -0.110 & 0 & 0.549 \\ -0.016 & 0 & -0.110 & 0.016 & 0 & -0.110 \\ 0 & -0.115 & 0 & 0 & 0.115 & 0 \\ 0.110 & 0 & 0.549 & -0.110 & 0 & 1.097 \end{bmatrix} \begin{Bmatrix} u_1 \\ w_1 \\ \theta_{1y} \\ u_2 \\ w_2 \\ \theta_{2y} \end{Bmatrix}$$

And for member 2–3 ( $\lambda = 0$ ,  $\mu = 1$ ,  $l = l_1 = 7.5$  ft.), one finds

$$[K]_{2-3}\{u\}_{2-3} = (E) \begin{bmatrix} 0.117 & 0 & 0.439 & -0.117 & 0 & 0.439 \\ 0 & 0.229 & 0 & 0 & -0.229 & 0 \\ 0.439 & 0 & 2.194 & -0.439 & 0 & 1.097 \\ -0.117 & 0 & -0.439 & 0.117 & 0 & -0.439 \\ 0 & -0.229 & 0 & 0 & 0.229 & 0 \\ 0.439 & 0 & 1.097 & -0.439 & 0 & 2.194 \end{bmatrix} \begin{Bmatrix} u_2 \\ w_2 \\ \theta_{2y} \\ u_3 \\ w_3 \\ \theta_{3y} \end{Bmatrix}$$

The joint loadings equivalent to the  $w_0 = 0.750$  kip/ft. = 750 lb./ft. distributed wave loading are, from the discussion above,

$$F_{1x} = F_{2x} = \frac{w_0 l_1}{2} = \frac{(750)(15)}{2} = 5625 \text{ lb.}$$

$$M_1 (= M_{1 \text{ eq.it.load}}) = -M_2 (= -M_{2 \text{ eq.it.load}}) = \frac{w_0 l_1^2}{12} = \frac{(750)(15)^2}{12} = 14,062.5 \text{ ft.lb.}$$

Combining these with the actual loadings on the structure, given by,

$$F_{3x} = 7500 \text{ lb.}, \quad F_{3z} = -150,000 \text{ lb.}$$

We have the force boundary conditions at joints 2 and 3 given as

$$\begin{aligned} F_{2x}^T &= 5625 \text{ lb.}, & F_{2z}^T &= 0.0, & M_2^T &= -14,062.5 \text{ ft.lb.}, \\ F_{3x}^T &= 7500 \text{ lb.}, & F_{3z}^T &= -150,000 \text{ lb.}, & M_3^T &= 0.0 \end{aligned}$$

The displacement boundary conditions at joint 1 are

$$u_1 = w_1 = \theta_{1y} = 0$$

The force matrices for elements 1–2 and 2–3 are

$$\{f\}_{1-2} = \begin{Bmatrix} f_{1x} \\ f_{1z} \\ m_1 \\ f_{2x} \\ f_{2z} \\ m_2 \end{Bmatrix}, \{f\}_{2-3} = \begin{Bmatrix} f_{2x} \\ f_{2z} \\ m_2 \\ f_{3x} \\ f_{3z} \\ m_3 \end{Bmatrix}$$

Implementing the boundary displacement and force conditions, one obtains the following reduced matrix equations for member 1–2:

$$\begin{Bmatrix} F_{1x}^T \\ F_{1z}^T \\ M_1^T \end{Bmatrix} = (E) \begin{bmatrix} -0.015 & 0 & 0.110 \\ 0 & -0.115 & 0 \\ -0.110 & 0 & 0.549 \end{bmatrix} \begin{Bmatrix} u_2 \\ w_2 \\ \theta_{2y} \end{Bmatrix} \quad (\text{E7.1})$$

And the assembled force-displacement matrix for the whole structure is given by

$$\begin{Bmatrix} F_{2x}^T \\ F_{2z}^T \\ M_2^T \\ F_{3x}^T \\ F_{3z}^T \\ M_3^T \end{Bmatrix} = (E) \begin{bmatrix} 0.133 & 0 & 0.329 & -0.117 & 0 & 0.439 \\ 0 & 0.344 & 0 & 0 & -0.229 & 0 \\ 0.329 & 0 & 3.291 & -0.439 & 0 & 1.097 \\ -0.117 & 0 & -0.439 & 0.117 & 0 & -0.439 \\ 0 & -0.229 & 0 & 0 & 0.229 & 0 \\ 0.439 & 0 & 1.097 & -0.439 & 0 & 2.194 \end{bmatrix} \begin{Bmatrix} u_2 \\ w_2 \\ \theta_{2y} \\ u_3 \\ w_3 \\ \theta_{3y} \end{Bmatrix}$$

$$= \begin{Bmatrix} 5625 \\ 0.0 \\ -14,062.5 \\ 7500 \\ -150,000 \\ 0.0 \end{Bmatrix}$$

Using the known values of the total loads in this second equation and solving for the displacements, one obtains

$$u_2 = (1.107)(10^{-3}) \text{ ft.}; w_2 = -(3.035)(10^{-4}) \text{ ft.}; \theta_{2y} = (1.197)(10^{-4}) \text{ rad.},$$

$$u_3 = (2.064)(10^{-3}) \text{ ft.}; w_3 = -(4.551)(10^{-4}) \text{ ft.}; \theta_{3y} = (1.316)(10^{-4}) \text{ rad.}$$

The total forces and total moment at the foundation are then determined from the first reduced equation (A) as

$$F_{1x}^T = -13,118.7 \text{ lb.}; \quad F_{1z}^T = 150,182.6 \text{ lb.} \approx 150,143.0 \text{ lb.}; \quad M_1^T = 241,146.1 \text{ ft.lb.}$$

The actual reaction forces and moment at joint 1 are determined for  $F_x$ ,  $F_y$ , and  $M$  as follows. We have

$$F_{1x} = F_{1x}^T - f_{1 \text{ eq.jt.load}} = -13,118.7 - 5625.0; \text{ hence, } F_{1x}^T = -18,743.7 \text{ (should be } -18,750.0)$$

$$F_{1z} = F_{1z}^T = 150,143.0 \text{ lb.}$$

$$\text{Also, } M_1^T = M_1 + M_{\text{eq.joint.load}}$$

Hence,

$$M_1 = M_1^T - m_{1 \text{ eq.jt.moment}} = -241,146.1 - 14,062.5 = -255,208.6 \text{ ft.lb.}$$

In order to compute the member stresses, one needs to know the internal forces acting at the ends of the members.

Considering now the internal forces and moments acting on the ends of member 1–2 (due to deformation of the member), the forces and moments are determined by multiplying the stiffness matrix for this member by the displacements and rotations at joints 1 and 2. We find

$$f_{1x}^T = -13,118.7 \text{ lb.}; \quad f_{1z}^T = 150,143.0 \text{ lb.}; \quad m_1^T = -241,146.1 \text{ ft.lb.}$$

$$f_{2x}^T = 13,118.7 \text{ lb.}; \quad f_{2z}^T = -150,143.0 \text{ lb.}; \quad m_2^T = 41,012.6 \text{ ft.lb.}$$

The actual forces and moments are determined by obtaining the internal member forces in members 1–2 and 2–3. The internal member forces in member 1–2 are computed as,

$$f_{1x} = f_{1x}^T - (15)(750)/2 = -13,118.7 - 5625.0 = -18,743.7 \text{ lb.}; \quad f_{1z} = 150,143.0 \text{ lb.};$$

$$m_1 = m_1^T - (750)(15)^2/12 = -241,146.1 - 14,062.5 = -255,208.6 \text{ ft.lb.};$$

$$f_{2x} = f_{2x}^T - (15)(750)/2 = 13,118.7 - 5625.0 = 7493.7 \text{ lb.};$$

$$m_2 = m_2^T + (750)(15)^2/2 = 41,012.6 + 14,062.5 = 59,075.1 \text{ ft.lb.}$$

The maximum moment is seen to occur at joint 1 and to equal  $-186,600 \text{ ft. lb.}$  The extreme bending stresses existing there are thus,

$$\sigma_b = \pm \frac{m_1 z_{\max}}{I_{yy}} = \pm \frac{(-255,208.6)(2.25)}{4.114} = \pm 139,576.9 \text{ lb./ft.}^2 \quad (= -969.3 \text{ lb./in.}^2)$$

The axial force along the member is seen to be constant and equal to  $-150,143.0 \text{ lb.}$  The axial stress is thus

$$\sigma_a = \frac{F}{A} = \frac{-150,143.0}{1.718} = -87,394.1 \text{ lb./ft.}^2$$

The maximum normal stress of  $\sigma = \sigma_b + \sigma_a$  occurs on the compressive side of the bending member at joint 1 and is obtained as

$$\sigma = -139,576.9 - 87,394.1 = -226,971.0 \text{ lb./ft.}^2 \text{ } (-1576.2 \text{ lb./in.}^2)$$

Consider the internal forces and moments acting on member 2–3. The forces and moments are determined by multiplying the stiffness matrix for this member by the displacements and rotations at joints 2 and 3. As shown earlier, we can compute the member end forces as

$$f_{2x} = f_{2x}^T = -7255.3 \text{ lb. (instead of } -7493.7); f_{2z} = 149,915.5 \text{ lb. (instead of } 150,000.0 \text{ lb.);}$$

$$m_2 = m_2^T = -57,245.22 \text{ (instead of } -55,075.1 \text{ ft.lb.);}$$

$$f_{3x} = f_{3x}^T = -7,255.3 \text{ lb. (instead of } -7500.0 \text{ lb.); } f_{3z} = -149,915.5 \text{ lb. (instead of } 150,000.0 \text{ lb.);}$$

$$m_3 = m_3^T = -864.9 \text{ ft.lb. (instead of } 0.0)$$

Since no other loads are acting on this member, these total internal end forces and moments are the actual internal forces/moments acting on the member. Thus, one can compute the internal stresses as shown below.

Maximum bending stress occurs at joint 2 and is given as

$$\sigma_b = \pm \frac{m_2 z_{\max}}{I_{yy}} = \pm \frac{(-57,245.22)(2.25)}{4.114} = \pm 31,313.1 \text{ lb./ft.}^2$$

The maximum axial stress in member 2–3 is

$$\sigma_a = \frac{(-149,915.5)}{(1.718)} = -87,261.4 \text{ lb./ft.}^2$$

The maximum normal stress  $\sigma = \sigma_b + \sigma_a$  in this member is thus seen to occur on the compressive side of the bending member at joint 2 and is obtained as

$$\sigma = -31,313.1 - 87,261.4 = -118,574.5 \text{ lb./ft.}^2 \text{ } (-823.4 \text{ lb./in.}^2)$$

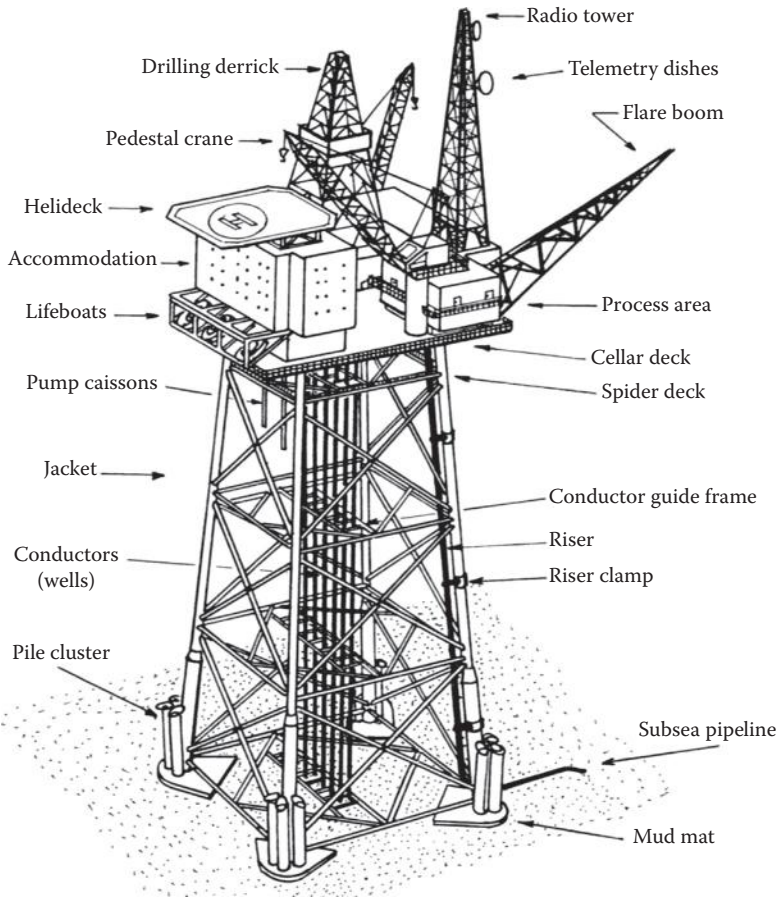
From the solution given above, the horizontal deck deflection (at joint 3) and the maximum longitudinal stress in the column (at joint 1) are obtained as

$$u_3 = (2.064)(10^{-3}) \text{ ft.} = 0.0248 \text{ in.};$$

$$\sigma = -1576.2 \text{ lb./in.}^2 \text{ (at joint 1)}$$

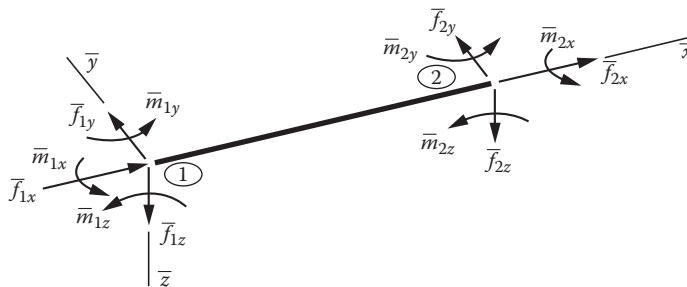
### 7.5.5.5 Space Frames

The most general representation, for a framed structure, located in a three-dimensional space consists of a three-dimensional assemblage of members, as shown in Figure 7.23 [31]; the tower is composed of many structural members interconnected at different orientations to form a framed structure. Each member of the framed tower is inclined at different angles to the global  $x, y, z$ -axes and is subjected to axial and transverse loadings and twisting and bending moments, as shown in



**FIGURE 7.23** Framed offshore structure. (From A. Mather, *Offshore Engineering, Part 3*, Witherby and Company Limited, London, p. 19, 1995.)

Figure 7.24 [32]. The forces and moments acting on the member are referred to member axes  $\bar{x}$ ,  $\bar{y}$ ,  $\bar{z}$ , with  $\bar{y}$  and  $\bar{z}$  in the plane of the cross section and  $\bar{x}$  along the member axis. The forces are assumed positive when they act in the direction of the member axes, and the moments are assumed positive according to the right-hand rule. Associated with these forces and moments are corresponding displacements and angular rotations, assumed positive in the same sense as the forces and moments.



**FIGURE 7.24** General loading on a structural member. (From T.H. Dawson, *Offshore Structural Engineering*, Prentice Hall Inc., Englewood Cliffs, NJ, p. 77, 1983.)



Having the member stiffness  $[\bar{K}]$  for each member, the stiffness  $[K]$  of the structure can, of course, be determined by transforming each to system axes and adding using the direct stiffness method. The transformation from member to system axes is given, as earlier, by

$$[K] = [T]^T [\bar{K}] [T] \quad (7.73)$$

where  $[T]$  denotes the transformation matrix. This can be expressed in terms of submatrices  $[T_s]$  and  $[0]$  as

$$[R] = \begin{bmatrix} [T_s] & [0] & [0] & [0] \\ [0] & [T_s] & [0] & [0] \\ [0] & [0] & [T_s] & [0] \\ [0] & [0] & [0] & [T_s] \end{bmatrix} \quad (7.74)$$

with  $[T_s]$  and  $[0]$  defined by

$$[T_s] = \begin{bmatrix} \lambda_{\bar{x}} & \mu_{\bar{x}} & \nu_{\bar{x}} \\ \lambda_{\bar{y}} & \mu_{\bar{y}} & \nu_{\bar{y}} \\ \lambda_{\bar{z}} & \mu_{\bar{z}} & \nu_{\bar{z}} \end{bmatrix}, \quad [0] = \begin{bmatrix} 0 & 0 & 0 \\ 0 & 0 & 0 \\ 0 & 0 & 0 \end{bmatrix} \quad (7.75)$$

where  $\lambda_{\bar{x}}$  denotes the cosine of the angle between the  $x$  and  $\bar{x}$  axes,  $\mu_{\bar{x}}$  denotes the cosine of the angle between the  $y$  and  $\bar{x}$  axes,  $\nu_{\bar{x}}$  denotes the cosine of the angle between the  $z$  and  $\bar{x}$  axes, etc.

The stiffness matrix of the structure is generated by assembling all the local matrices into a global stiffness matrix; similarly, the global force vector for the whole structure is also generated from the individual global force vectors of all the elements. Once the global force vector and stiffness matrices are assembled, boundary conditions can be applied and displacements and stresses determined as indicated in the solution of earlier problems. The level of computational difficulty is, however, increased enormously for large three-dimensional structures, and the most feasible methodology for solving such problems is through the use of a fully automated structural analysis computer program. A number of these programs, such as ABAQUS, ANSYS, NASTRAN, ADINA, StruCAD\*3D, SAFI 3D, and others are available commercially. Their use involves mainly the specification of the geometrical and mechanical properties of the individual members constituting the structure. The structural coordinates ( $x, y, z$ ) of the member ends, relative to system axes, and the appropriate boundary conditions of the structure also should be specified. From these given conditions, the global stiffness matrix of the structure can be assembled by the selected software and joint displacements, and internal end forces and moments can be computed automatically.

### Example 7.5

A steel monopod tower, shown in Figure E7.6, is subjected to wave loads. The caisson is driven deeply into the underlying stiff soil and as such can be assumed to be fixed at the seabed level. The diameter of the monopod caisson is 8.0 ft. and has wall thickness of 2.0 in. The weight of the top deck and the drill rig is 1000 kips. The depth of water at the site is 60.0 ft., and the maximum wave height is expected to be 20.0 ft. with a period of 10.0 s. (i) Find the wave loads exerted on the monopod tower; (ii) find the maximum stresses set up in the tower; and (iii) making relevant simplifying assumptions, compute the maximum displacement of the tower at the deck level. The allowable stress steel is  $(0.6\sigma_y)$ , and the yield strength of steel is 36,000 psi. Take  $E$  of steel to be  $(30.0)(10^6)$  psi. Assume  $C_M = 2.0$  and  $C_D = 1.0$ .



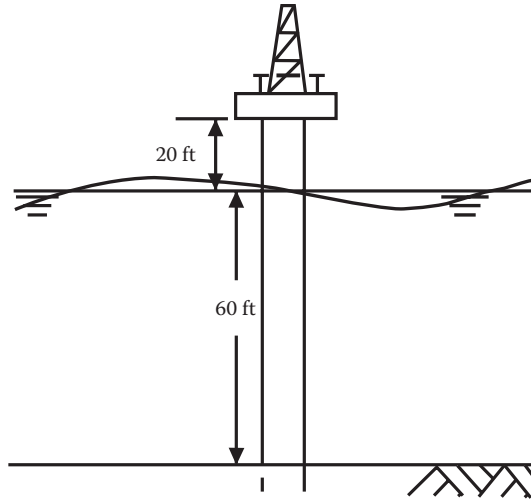


FIGURE E7.6 Steel monopod tower, in 60.0 ft. depth of water.

Wave loads: Using Morison–O’Brien’s equation, the inertial and drag forces are given as

$$F_I = -\{(\rho_w C_M)/(2k)\}(\pi D^2/4)(\omega^2 H)[\sinh(ky)/\sinh(kh)]\sin(\omega t)$$

$$F_D = \{(\rho_w C_D D)/(32k)\}[\{\sinh(2ky)/\sinh^2(kh)\} + \{2ky/\sinh^2(kh)\}]\cos(\omega t)\cos(\omega t) \quad (E7.2)$$

In this problem,  $\rho_w = 1.99$  slug (lb. s<sup>2</sup>/ft.);  $C_M = 2.0$ ;  $k = (2\pi/L)$ ;  $D = 8.0$  ft.;  $y_{\max} = 60 + 10 = 70.0$  ft.;  $h = 60.0$  ft.;  $C_D = 1.0$ ;  $H = 20.0$  ft.;  $T = 10.0$  s.

Wavelength for the wave is computed iteratively or by referring to given tables:

$$L_0 = (gT^2/2\pi) = (32.2)(10^2)/(2\pi) = 512.5 \text{ ft.}$$

For  $h/L_0 = (60/512.5) = 0.1171$ , from the given tables,  $h/L = 0.1557$ . Hence,  $L = 60.0/0.1557 = 385.37$  ft.

(i) Using these values in Equation E7.2, one obtains

$$F_{I_{\max}} = -48,445.24 \sin(\omega t) = 48,445.20 \text{ lb., when } (\omega t) = 270^\circ$$

$$F_{D_{\max}} = 26,468.23 \cos(\omega t)\cos(\omega t) \text{ lb.} = 26,468.23 \text{ lb., when } (\omega t) = 0.0^\circ$$

$$F_{\max} = [(48,445.24)^2 + (26,468.23)^2]^{(0.5)} = 55,204.24 \text{ lb.}$$

Similarly, the wave moment about the base can be computed from the given equations as

$$M_I = -\{(\rho_w C_I)/(2k^2)\}(\pi D^2/4)(\omega^2 H)Q_1 \sin(\omega t)$$

$$M_D = \{(\rho_w C_D D)/(64k^2)\}(\omega H)^2 Q_2 \cos(\omega t)\cos(\omega t) \quad (E7.3)$$

$$Q_1 = [\{(ky)\sinh(ky) - \cosh(ky) + 1.0\}/\sinh(kh)]$$

$$Q_2 = [\{(2ky)(\sinh ky) - \cosh(2ky) + 2(ky)^2 + 1.0\}/\sinh^2(kh)]$$

Substituting the above values, the maximum values of  $Q_1 = 0.7331$  and  $Q_2 = 5.8373$  are obtained when  $(\omega t) = 330^\circ$ .

$$M_{I_{\max}} = 1,088,671.3 \text{ lb.ft.}$$

$$M_{D_{\max}} = 646,747.3 \text{ lb.ft.}$$

$$M_{\max} = 1,088,671.3 + 646,747.3 = 1,735,418.6 \text{ lb.ft.}$$

(ii) Assuming the force resultant and moment resultant to occur at the same instant:

Distance of the force resultant from the base =  $(1,735,418.60/55,204.24) = 31.44 \text{ ft.}$

$$I = [(\pi/64)(96^4 - 92^4)] = (6.526)(10^5) \text{ in.}^4$$

$$EI \text{ for the monopod tower} = (30)(10^6)[(\pi/64)(96^4 - 92^4)] = (1.9579)(10^{13}) \text{ lb. in.}^2 \\ = (1.36)(10^{11}) \text{ lb. ft.}^2$$

Maximum bending stress at the bottom of the tower =  $[(BM)_{\max}(D/2)]/I$

$$= [(1.7354)(10^6)(12)(4.0)(12)]/[(6.526)(10^5)] \\ = 153.18 \text{ psi (stress level is much below the failure stress)}$$

(iii) Using the wave load as an equivalent concentrated load, the deflection at the deck level is given by

$$= (PL_{\text{resultant}}^3/3EI) + (PL_{\text{resultant}}^2)/(2EI)(80.0 - 31.44) = (1/EI)[55,204.24\{(1/3)31.44^3 + (31.44^2)(48.56)(1/2)\}] \\ = (1/EI)[(5.719)(10^8) + (1.325)(10^9)] \text{ ft.} = \{(18.969)(10^8)\}/\{(1.958)(10^{11})\} = (9.688)(10^{-3}) \text{ ft} = 0.1162 \text{ in.}$$

### Example 7.6

The outside diameter of a concrete cylindrical structure, shown in Figure E7.7, standing in a 100.0-ft. depth of water, is 8.0 ft. in diameter, with a wall thickness of 18.0 in. The maximum wave height at the location is expected to be 25.0 ft. with a period of 14.0 s. The structure has a freeboard of 30.0 ft., as shown in the figure. Considering two elements for the cylindrical structure, and assuming linear variations of wave loads between the nodal points, calculate the equivalent joint loads at nodes 1, 2, and 3 for the structure. Also assemble the total stiffness matrix for the structure and determine the displacements of the structure at nodes 2 and 3. Assume  $E_{\text{concrete}} = 20.0 \text{ GPa}$ .

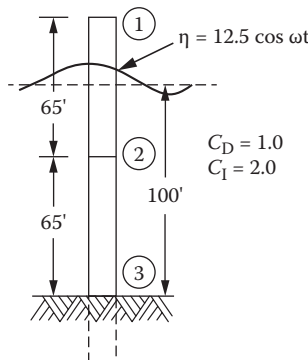


FIGURE E7.7 Concrete cylindrical tower in water.

$$(\Delta F)_{\text{per unit height}} = (\rho_w C_M)(\pi D^2/4)(\dot{U}) + (\rho_w C_D/2)(D)|U|U \quad (\text{E7.4})$$

Wave particle velocities and accelerations are given as (with  $y$  measured from the sea-bottom)

$$\begin{aligned} U &= (\omega H/2)[\cosh(ky)/\sinh(kd)] \cos(kx - \omega t) \\ &= (\omega H/2)[\cosh(ky)/\sinh(kd)] \cos(\omega t) \text{ at } x = 0.0 \\ \dot{U} &= (\omega^2 H/2)[\cosh(ky)/\sinh(kd)] \sin(kx - \omega t) \\ &= -(\omega^2 H/2)[\cosh(ky)/\sinh(kd)] \sin(\omega t) \text{ at } x = 0.0 \end{aligned} \quad (\text{E7.5})$$

The given data are  $d = 100.0$  ft.;  $H/2 = 12.5$  ft.;  $T = 14.0$  s.

Hence,  $L_0 = (gT^2/2\pi) = (32.2)(14^2)/(2\pi) = 1004.5$  ft.

$$(d/L_0) = 100/1004.5 = 0.995.$$

Using the given tables,  $d/L = 0.1406$ .

$$L = 100/0.1406 = 711.24 \text{ ft.}$$

$$\Omega = (2\pi)/T = (2\pi)/14 = 0.4488 \text{ rad/s}$$

$$U = (\omega H/2)[\cosh(ky)/\sinh(kd)]\cos(\omega t) \quad (\text{E7.6})$$

$$\begin{aligned} U &= (0.4488)(25.0/2)(1/\sinh\{(2\pi)(100)/711.24\}) \cosh(ky) \cos(\omega t) \\ &= (5.61)(0.9971) \cosh(ky) \cos(\omega t) = 5.594 \cosh(ky) \cos(\omega t) \end{aligned}$$

Also,

$$\begin{aligned} \dot{U} &= -(\omega^2 H/2)[\cosh(ky)/\sinh(kd)] \sin(\omega t) = -(0.4488)^2(25/2)(0.9971)\cosh(ky)\sin(\omega t) \\ &= -2.5104 \cosh(ky) \sin(\omega t) \end{aligned}$$

Using Equation E7.4,  $\Delta F_1 = (\rho_w C_M)(\pi D^2/4)(\dot{U}) = (1.99)(2.0)(\pi \times 8^2/4)[-2.5104 \cosh(ky) \sin(\omega t)] = -502.22 \cosh(ky) \sin(\omega t)$

$\Delta F_D = (\rho_w C_D/2)(D)|U|U = (1.99)(1.0/2)(8.0) [5.594 \cosh(ky) \cos(\omega t)][5.594 \cosh(ky) \cos(\omega t)] = 249.07 [\cosh(ky) \cos(\omega t)][\cosh(ky) \cos(\omega t)]$

Assuming that  $\Delta F_{\text{max}}$  occurs at  $(\omega t) = 135^\circ$  or  $315^\circ$

amplitude at  $[(\omega t) = 315^\circ] = 12.5 \cos(315^\circ) = 8.84$  ft.

$$\Delta F_{\text{max}} = -(502.22)[\cosh\{(2\pi/711.24)(100.0 + 8.84)\}]\{\sin(315^\circ)\} = 532.41 \text{ lb./ft.}$$

$$\begin{aligned} \Delta F_{D_{\text{max}}} &= 249.07[\cosh\{(2\pi)(108.84)/711.24\}]\{\sin(315^\circ)\} | \cosh\{(2\pi/711.24)(108.84)\} \cos(315^\circ) | \\ &= 279.91 \text{ lb./ft.} \end{aligned}$$

$$\Delta F_{\text{max}} = 532.41 + 279.91 = 812.32 \text{ lb./ft. at } (y = 108.84 \text{ ft.})$$

Similarly,  $\Delta F_{\max} = 415.32 + 170.33 = 585.65$  lb./ft. at  $y = 65$  ft.

At  $y = 0.0$  ft.,  $\Delta F_{\max} = 335.12 + 124.54 = 479.66$  lb./ft.

Assuming the (load)/(per unit length) acting on the elements 1–2 and 2–3 to be the average of the load distribution at the top and bottom of the elements:

Average load per unit length acting on the portion of top element 1–2 =  $(812.32 + 585.65)/2 = 699.0$  lb./ft.

Average load per unit length acting on the bottom element =  $(585.65 + 479.66)/2 = 532.66$  lb./ft.

The assembled stiffness matrix is obtained as

$$[K] = (10^7) \begin{bmatrix} 9.92 & 322.48 & -9.92 & 322.48 & 0.0 & 0.0 \\ 322.48 & 13975.8 & -322.48 & 6987.90 & 0.0 & 0.0 \\ -9.92 & -322.48 & 19.84 & 0.0 & -9.92 & 322.48 \\ 322.48 & 6987.90 & 0.0 & 27951.6 & -322.48 & 6987.90 \\ 0.0 & 0.0 & -9.92 & -322.48 & 9.92 & -322.48 \\ 0.0 & 0.0 & 322.48 & 6987.90 & -322.48 & 13975.8 \end{bmatrix} \begin{Bmatrix} u_1 \\ \theta_1 \\ u_2 \\ \theta_2 \\ u_3 \\ \theta_3 \end{Bmatrix} \quad (E7.7)$$

The assembled load vector is given as

$$\{F\} = \begin{Bmatrix} F_{1x}^{(1)} + 17,311.45 \\ M_{1z}^{(1)} + 187,540.71 \\ 31,352.96 \\ -19,561.22 \\ 0.0 \\ 0.0 \end{Bmatrix} \quad (E7.8)$$

Since  $(u_1, \theta_1)$  are equal to zero, the reduced stiffness matrix is given by

$$[K]\{u\} = (10^7) \begin{bmatrix} 19.84 & 0.0 & -9.92 & 322.48 \\ 0.00 & 27951.6 & -322.48 & 6987.90 \\ -9.92 & -322.48 & 9.92 & -322.48 \\ 322.48 & 6987.90 & -322.48 & 13975.8 \end{bmatrix} \begin{Bmatrix} u_2 \\ \theta_2 \\ u_3 \\ \theta_3 \end{Bmatrix} \quad (E7.9)$$

and the reduced force vector is obtained as

$$\{F\} = \begin{Bmatrix} 31,352.96 \\ -19,561.22 \\ 0.0 \\ 0.0 \end{Bmatrix} \quad (E7.10)$$

Solving for the deformations of the tower

$$\{u\} = \begin{Bmatrix} u_2 \\ \theta_2 \\ u_3 \\ \theta_3 \end{Bmatrix} = \begin{Bmatrix} -(5.22)(10^{-4}) \text{ ft.} \\ -(1.192)(10^{-5}) \text{ rad} \\ (-9.16)(10^{-4}) \text{ ft.} \\ -(6.140)(10^{-5}) \text{ rad} \end{Bmatrix}$$

## 7.6 FORMULATION OF SOLID–FLUID INTERACTION PROBLEMS

A large amount of literature is available on the aspects of fluid–structure interaction and on the theory/measurement of forces exerted on rigid and deformable bodies moving or at rest in dynamic wave environments. Excellent state-of-the-art reviews and assessment of the merits and relevance of these publications have been given by Clauss et al. [33], Chakrabarti [34], Sumer and Fredsoe [35], and Sarpkaya [36]. In this brief presentation, necessary physical ideas and the governing nondimensional parameters, used presently to characterize these wave forces, are explained briefly before one proceeds to the formulation of the basic equations that govern the motion of these structures in a wave field.

A large variety of offshore structures have been used in the offshore environment; they are primarily composed of small tubular members (jacket-type platforms, spar platforms, etc.), large volume cylindrical/rectangular caissons (gravity or hybrid gravity-jacket platforms), or large-sized vertical, horizontal, and inclined circular/square cylindrical structures [tension-leg and floating production storage and off-loading (FPSO) platforms]. Hence, a variety of formulations have been developed for determining these wave forces and using them in computing the offshore structural responses. Wave forces on offshore structures have been computed by procedures incorporating three different methodologies, viz., (i) Morison–O’Brien’s equation; (ii) Froude–Krylov theory; and (iii) diffraction theory [34].

When a component structural member is much smaller than the wavelength, Morison–O’Brien’s equation is used to compute the wave forces on an offshore structure; the force is assumed to be obtained by the linear superposition of the drag and inertia forces exerted on the structure. When the drag forces acting on the structure are small, and the structure is relatively small with respect to the wavelength, the Froude–Krylov theory is applied to compute the wave forces; it utilizes the (wave) pressure–area concept to compute the wave forces acting on the structure. When the size of the structure is almost the same as the wavelength of the component waves, then the diffraction wave theory is used to compute the wave forces acting on the structure; in this, the presence of the structure is considered to modify the wave field around the structure, and this modified (or diffracted) wave field must be considered in the wave force computation. In all the above three procedures, the deformations of the structure also should be considered if this additional consideration leads to a significant increase in the magnitude of force acting on the structure.

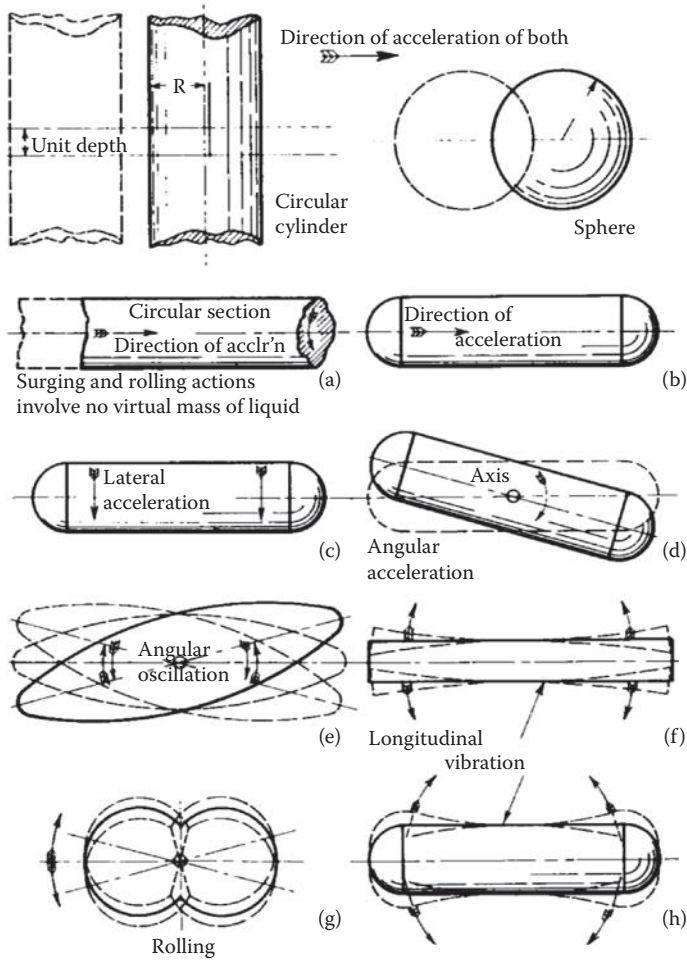
Using dimensional analysis, through the Buckingham Pi theorem, the nondimensional wave force acting on an offshore structure can be represented by the nondimensional equation [34]

$$f_x / (\rho_w u_0^2 D) = \Phi[(t/T), (u_0 T/D), (u_0 D/\nu), (\pi D/L)] \quad (7.76)$$

where  $(t/T)$  = nondimensional time,  $(u_0 T/D)$  = Keulegan–Carpenter number (KC),  $(u_0 D/\nu)$  = Reynolds number (Re), and  $(\pi D/L)$  = diffraction parameter.

In Equation 7.76,  $f_x$  is the force per unit height of the structural component under consideration,  $t$  is the time,  $T$  is the wave period,  $L$  is the wavelength,  $u_0$  is the maximum horizontal wave particle velocity,  $\rho_w$  is the mass density of water,  $\nu$  is the kinematic viscosity of water, and  $D$  is the characteristic dimension (for instance, the diameter of a vertical cylinder or the transverse width of a rectangular or square section). The Keulegan–Carpenter number is a *dimensionless quantity* that gives the relative importance of the *drag forces* over *inertia* forces; when the KC number is small, the inertia force dominates, and when the KC number is large, drag forces are important. Similarly, when the diffraction parameter is small, the drag forces are dominant, and when the diffraction parameter is large, the drag effects are small. The dependence of these numbers on the force coefficients such as  $C_M$  and  $C_D$  are given earlier in Sections 6.3.2 (in Figures 6.9 and 6.10) and 6.3.4.1 (in Figures 6.14 through 6.16).

The various motions associated with an offshore structure can be seen from Figure 7.25 [37], which shows the motions of cylindrical, spherical, or other types of structures executing rigid body or vibrational motions in the ocean. Figure 7.25a shows the motion of an isolated, circular cylindrical (or spherical) solid for which the incident fluid velocity is perpendicular to its longitudinal axis; Figure 7.25b shows the rolling, surging, swaying, yawing, and vibrational motions of different structures in the open seaway.



**FIGURE 7.25** Types of accelerated motion of different bodies in an open seaway: Horizontal (or surge), lateral (sway), vertical (heave), pitch, roll and yaw (From H.E. Saunders, *Hydrodynamics in Ship Design*, The Society of Naval Architects and Marine Engineers, New York, p. 57, 59, 1957. With permission.)

Consider the motion of a rigid, horizontal, fully submerged, circular cylindrical solid in seawater, for which the incident water velocity and acceleration are perpendicular to its longitudinal axis, as shown in Figure 7.25. Assuming the body to have displacement, velocity, and acceleration of  $(u, \dot{u}, \ddot{u})$ , the force per unit length required to hold the rigid cylinder stationary in the wave will be made up of an accelerative force dependent on the acceleration  $\dot{U}$  of the water particles and a damping force dependent on the velocity  $U_x$  of the water particles, moving around the body. The net force acting on the unit transverse length of the body can be written as  $f_x$  given by

$$\begin{aligned}
 f_x &= C_M[(\text{volume of fluid mass})_{\text{perpendicular to flow}}]\dot{U}_x \\
 &+ \left(\frac{1}{2}\right)C_D[(\text{area of fluid mass})_{\text{perpendicular to flow}}]U_x|U_x| \\
 &= C_M[(\rho_w)(\pi D^2/4)(1)]\dot{U}_x + (1/2)C_D[(\rho_w)(D)(1)]U_x|U_x|
 \end{aligned}
 \tag{7.77}$$

The coefficient of mass,  $C_M$ , and the coefficient of drag,  $C_D$ , have been given earlier in Sections 6.3.2 and 6.3.4.1. The coefficient of mass  $C_M$  is defined as made up of that due to the acceleration of the fluid mass displaced by the structural volume  $\left[ (\rho_w) \left( \frac{\pi D^2}{4} \right) (1) \right]$  per unit length and an associated mass of water accelerating with the structure; this mass is called the added mass of the fluid. Hence, the coefficient of mass,  $C_M$ , is given as

$$C_M = 1 + C_A \quad (7.78)$$

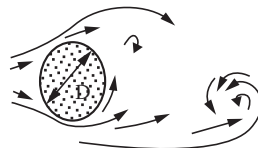
where  $C_A$  is the added mass coefficient. Added mass is the inertial mass added to a system due to the fact that the body is either accelerating or decelerating in the fluid; the moving body influences or carries along some volume of surrounding fluid as it moves through it. While modeling this aspect in fluid–structure interaction, it can be modeled as a specified volume of fluid moving along with the body with the same acceleration or deceleration; it should be kept in mind that, in actuality, a much larger volume of fluid will be accelerated or decelerated to various degrees. The added mass can be incorporated into the more common Morison–O’Brien’s equation by considering the effective mass of the moving body as the sum of the body mass and the added mass.

Using Newton’s second law and the above considerations for the added mass, the force equation for a spherical body of moving in a fluid, with an acceleration  $a$ , can be written as

$$\begin{aligned} f_{I_x} = ma \text{ becomes } f_{I_x} &= (m_{\text{fluid mass}} + m_{\text{added}})(a) = (1 + C_A)m_{\text{fluid mass}}(a) \\ &= C_M \left[ \left( \frac{\pi D^2}{4} \right) \rho_w \right] (a) \end{aligned} \quad (7.79)$$

where  $C_M = (1 + C_A)$ ;  $a$  is the acceleration of the fluid mass displaced by the spherical body,  $f_{I_x}$  gives the inertial force acting on the body,  $m_{\text{fluid mass}}$  is the mass of the fluid displaced by the volume of the spherical body, and  $C_A$  is the coefficient used for the additional mass of water accelerating with the spherical body.

Using conventional derivations, it can be shown that the added mass for a submerged spherical body of radius  $r$  is equal  $\left\{ \left( \frac{4}{3} \pi r^3 \right) (\rho_w) \right\}$  to [38]. In real fluids, such as seawater, flow separation occurs behind the moving body (such as a cylinder) as shown in Figure 7.26 [39]. This flow separation is often accompanied by differential time-dependent pressure forces that oppose the cylinder motion. When such details of flow are not available, then  $C_A$  can be taken as one leading to a value of  $C_M$  being equal to 2.0.



**FIGURE 7.26** Flow separation effects occurring behind a cylindrical body. (From C.E. Brennen, *A Review of Added Mass and Fluid Inertial Forces*, Report CR 62.10 (N62583-81-MR-554), Naval Civil Engineering Laboratory, Port Hueneme, CA, 50 p., 1982. With permission.)

In addition to added mass, another parameter that contributes to force generation as a body moves through seawater is the viscous friction drag coefficient,  $C_D$ , which relates the velocity-dependent force,  $f_{D_x}$ , to the fluid velocity as

$$f_{D_x} = (1/2)C_D\rho_w\{(D)(1)\}|U_x|U_x \quad (7.80)$$

The use of the absolute value sign on one of the velocity terms enables the drag force to be acting always in the direction of the seawater velocity. The linear addition of the inertia and velocity effects given by Equations 7.74 and 7.75 would lead to Equation 7.73. As given earlier in Chapter 6, the mass coefficient  $C_M$  and drag coefficient  $C_D$  are dependent upon the Reynolds number  $Re$  and Keulegan–Carpenter number  $KC$  given in Sections 6.3.2 and 6.3.4.1.

Linear superposition of Equations 7.79 and 7.80 gives the wave force equation given as Morison–O’Brien’s equation 7.77. It should be borne in mind that the force coefficients  $C_M$  and  $C_D$  are not mere constants but dependent on flow parameters such as Reynolds number, Keulegan–Carpenter number, cylinder roughness, and maximum water wave velocity at the ocean surface [34]:

$$\begin{aligned} C_M &= C_M(\text{Re}, \text{KC}, \text{cylinder roughness}) \\ C_D &= C_D(\text{Re}, \text{KC}, \text{cylinder roughness}) \end{aligned} \quad (7.81)$$

Equation 7.81 will be modified if the phenomena of (i) proximity effects of structures or free/boundary surface; (ii) three-dimensional flow conditions; (iii) fluid compressibility; (iv) relative movement of structure with respect to fluid flow; (v) cavitation; and (vi) influence of currents on water wave are considered [39].

If the structural motions were also considered in the above study, then Equation 7.77 will be correspondingly modified. Assuming that the structure is moving in the same direction as the fluid with the motions  $(u, \dot{u}, \ddot{u})$ , the wave force acting on the moving structure is given by

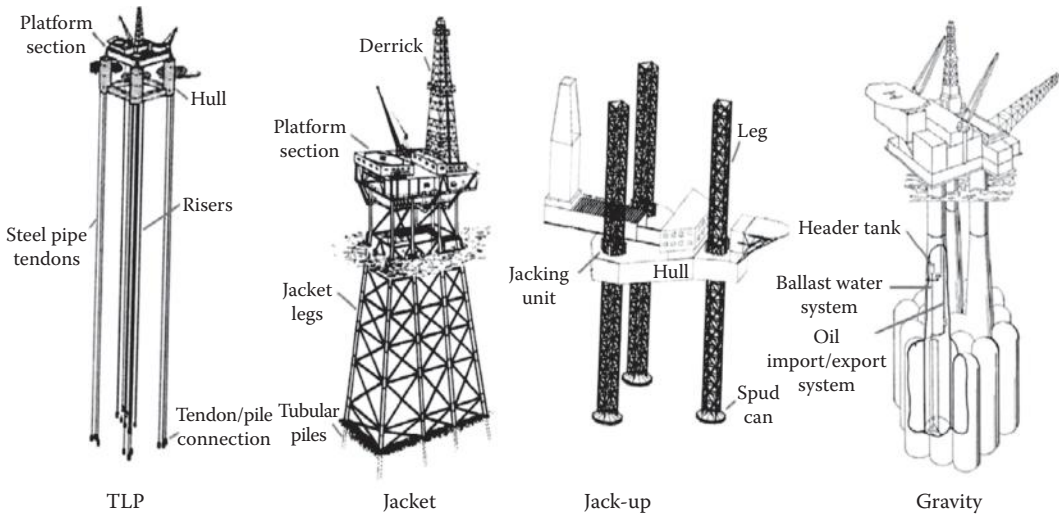
$$\begin{aligned} f_x &= C_M[(\text{volume of fluid mass})_{\text{perpendicular to flow}}](\dot{U}_x - \ddot{u}) \\ &+ \left(\frac{1}{2}\right)C_D[(\text{area of fluid mass})_{\text{perpendicular to flow}}](U_x - \dot{u})|U_x - \dot{u}| \\ &= C_M[(\rho_w)(\pi D^2/4)(1)](\dot{U}_x - \ddot{u}) + (1/2)C_D[(\rho_w)(D)(1)](U_x - \dot{u})|U_x - \dot{u}| \end{aligned} \quad (7.82)$$

## 7.7 SIMPLIFIED LUMPED MASS/STIFFNESS CONSIDERATIONS FOR DYNAMIC ANALYSES

### 7.7.1 INTRODUCTION

The dynamic analysis of offshore structures is generally one of the most demanding tasks faced by the engineering analyst. In addition to the usual complexities encountered in the land-based structures, offshore structures have the added complications that arise due to their placement in the dynamic ocean environment leading to water–structure interaction effects and dynamic response considerations. Figure 7.27 [40] gives some of the typical structures that are encountered in the ocean environment, consisting of fixed and rather rigid structures (jacket, gravity, etc.), flexible structures (such as tall and slender jacket, jack-up, etc.), and compliant structures (compliant piled



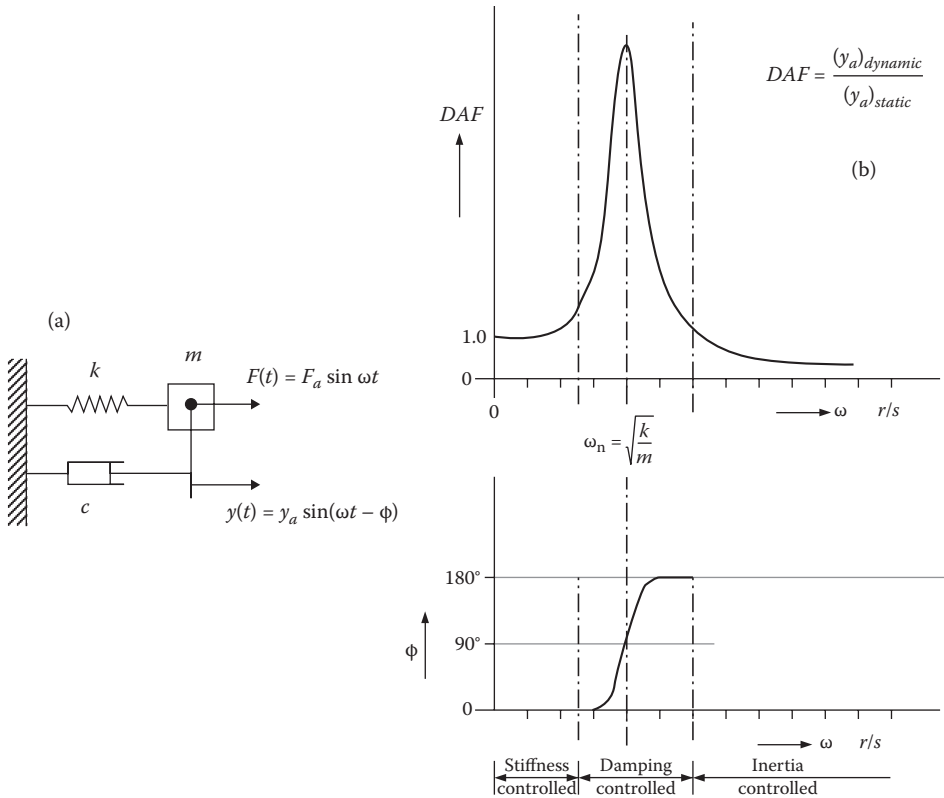


**FIGURE 7.27** Typical offshore structures encountered in the offshore environment. (From N. Haritos, *Electronic Journal of Structural Engineering (EJSE) Special Issue: Loading on Structures*, p. 59, 2007. With permission.)

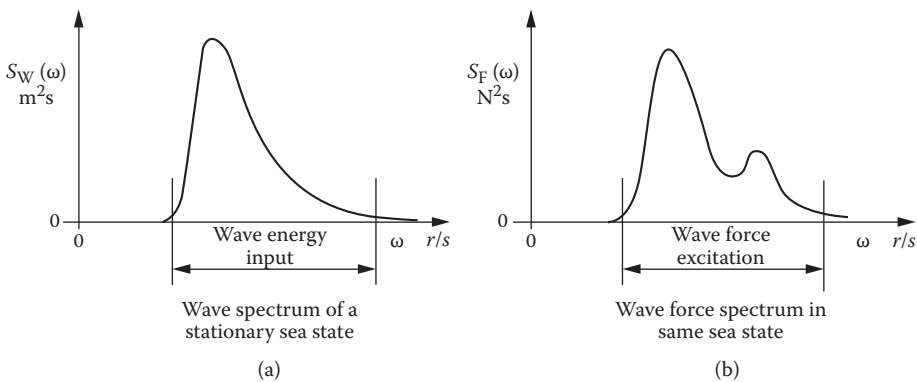
tower or CPT, TLP, semi-submersibles, etc.). In addition to considering peculiar demands in terms of hydrodynamic loading effects, additional considerations need to be given to properly model the foundation support conditions and character of the riser systems used for oil extraction. Invariably nonlinearities are present during the water–structure and soil–structure interaction, and the resultant modeling needs to be carefully made so as to include their effects. Hence, a proper discussion of the requisite dynamic modeling procedures is beyond the scope of the book; but sufficient details are given in this section to enable one to understand the procedure so that anyone can (on his or her own) develop dynamic models for a general situation.

Figure 7.28 [41] shows the response of a single-degree-of-freedom (SDOF) system subjected to a dynamic excitation. As shown in Figure 7.28, the system responds in a linear quasi-statistical manner since it is controlled by the stiffness property of the system. When the frequency of excitation increases, the system begins to exhibit the dynamic nature of the system response. When the excitation frequency approaches the natural frequency of the system, the response increases drastically exhibiting resonant behavior of the system. When the frequency of excitation increases beyond the natural frequency of the system, the response begins to decrease due to the change in phase difference between the load and the response. Finally, the displacements become smaller than the quasi-static displacements, and the response is inertia force controlled. These three states of response are clearly shown in Figure 7.28.

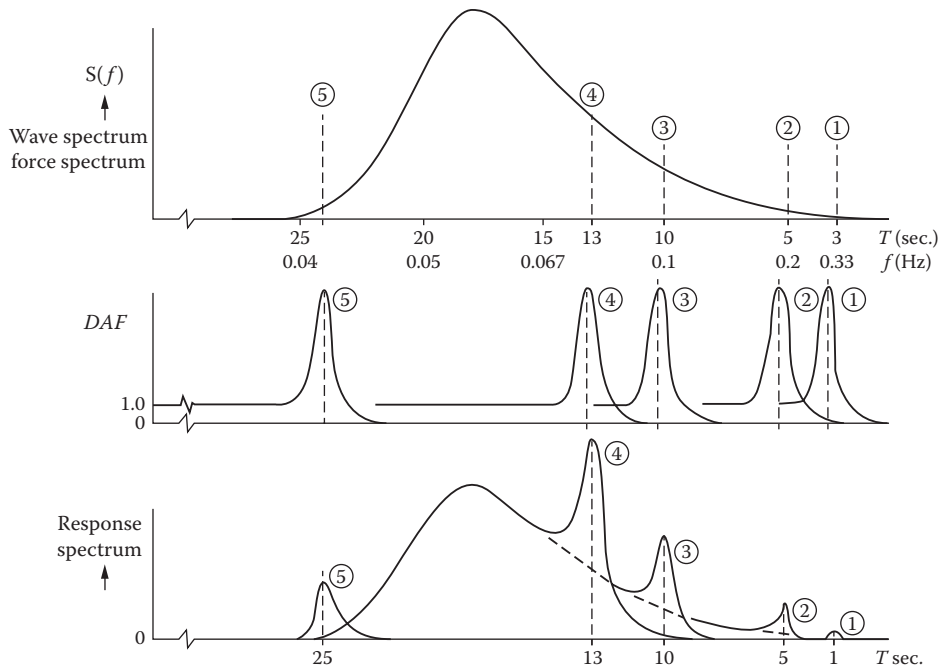
Since offshore structures are quite complex and the structure has infinite degrees of freedom, the motion cannot be fully described by an SDOF system equation. If some of these frequencies are within the range of wave excitation, then these frequency effects also need to be considered in estimating the system response. Figure 7.28 shows the system response for a structure subjected to a harmonic excitation only. However, the waves in the ocean environment are not harmonic; they are irregular. The sea state can be described by the superposition of many waves of different amplitudes, directions, phase differences, and frequencies (or periods). If the waves can be assumed to be coming from one direction only, then the sea state can be described by a single wave spectrum that shows the relationship between the wave amplitudes and wave frequencies (or periods), as shown in Figure 7.29a [41]. When the waves are multidirectional, then the spectrum will be represented by a three-dimensional spectral surface having wave amplitudes, wave frequencies, and wave directions as the three coordinates.



**FIGURE 7.28** (a) Model of a damped SDOF system; and (b) Dynamic magnitude and phase of the response of the damped SDOF system. (From W. de Vries, *Compliant Bottom Mounted Support Structure Types*, Upwind deliverable WP4.2.4 Report on compliant bottom mounted support structure types, Project funded by the European Commission under the Sixth [EC] RTD, Project UpWind, Contract # 019945 [SES6], p. 15, 2009. With permission.)



**FIGURE 7.29** Schematic for dynamic wave force model in the ocean. (From W. de Vries, *Compliant Bottom Mounted Support Structure Types*, Upwind deliverable WP4.2.4 Report on compliant bottom mounted support structure types, Project funded by the European Commission under the Sixth [EC] RTD, Project UpWind, Contract # 019945 [SES6], p. 15, 2009. With permission.)

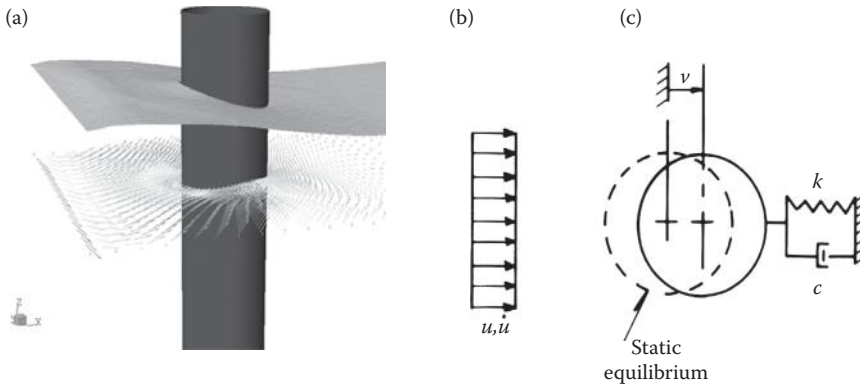


**FIGURE 7.30** Dynamic response of an MDOF system. Note: The horizontal scale is linear in period for the sake of clarity. (From W. de Vries, *Compliant Bottom Mounted Support Structure Types*, Upwind deliverable WP4.2.4 Report on compliant bottom mounted support structure types, Project funded by the European Commission under the Sixth (EC) RTD, Project UpWind, Contract # 019945 [SES6], pp. 16 and 17, 2009. With permission.)

Using Morison–O’Brien’s approach, the force can be considered to be composed of the summation of inertial and drag forces acting on the offshore structural system. Since drag effects are nonlinear, the wave force spectrum will be irregular as shown in Figure 7.29b [41]. When the response spectrum for the offshore structure is constructed, then this spectrum will show a peak at the wave spectrum, as well as at the natural frequency of the structure. When a multi-degree-of-freedom (MDOF) structural system is considered, the response spectrum peaks will be governed by both the dynamic response of the structure, as given by the dynamic amplitude factor (or dynamic magnitude factor) for the respective frequencies, and by the magnitude of the energy present in the wave; in addition, it will also depend on the wave energy present around the natural frequencies of the structural system. This characterization of the response spectrum of an MDOF system is illustrated in Figure 7.30. The six lowest frequencies of the structure are given as 0.04, 0.05, 0.067, 0.10, 0.20, and 0.33 Hz; the wave spectrum is assumed to have its maximum amplitude at 0.055 Hz. Then the response spectrum of the structure can be obtained as shown in Figure 7.30c [42]. It is also observed that the quasi-static response of the structure is almost zero.

## 7.7.2 CHARACTERIZATION OF OFFSHORE STRUCTURE AS AN SDOF SYSTEM

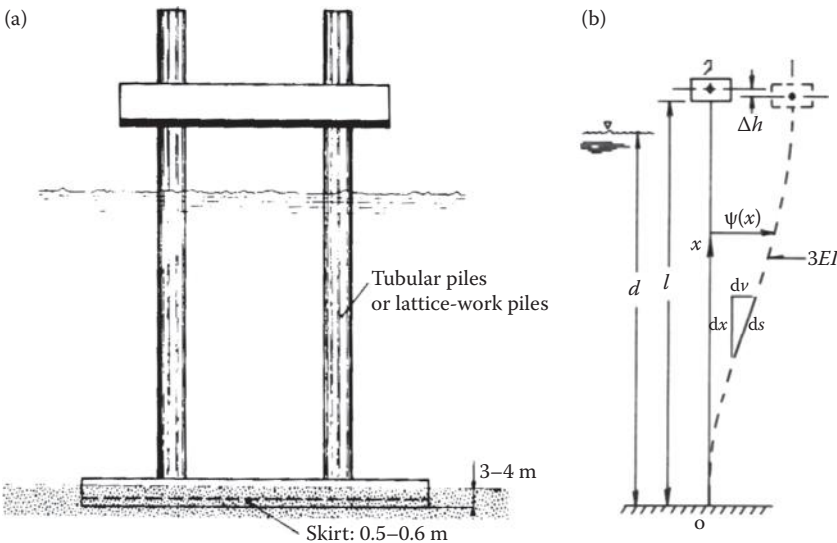
A simple representation of the motion of an offshore structure would assume that the body is moving in a plane and the associated equations of motion are written down in a straightforward manner using either Newton’s second law or Lagrange’s energy methods. The simplest representation will have only an SDOF of motion for the structure, which will uniquely define the structure’s position with respect to the axis of motion. In order to illustrate, consider the motion of a single vertical test cylinder (fixed to the bed of a wave basin, shown in Figure 7.31a) [43]; the associated wave motion is shown in Figure 7.31b and an SDOF system for the vibrating cylinder is shown in Figure 7.31c.



**FIGURE 7.31** (a) Test cylinder in a wave basin. (b) Wave loads acting on a portion of a test cylinder. (c) Approximate schematic modeling of the motion of the test cylinder. (From P. Woodburn and P. Gallagher, *EXPRO-CFD: Progress in Fluid Structure Interaction*, MARNET-CFD Final Meeting, 20–21 March 2003, p. 3, 2003. With permission.)

The sketch in Figure 7.31c will represent the lumped mass model of the cylinder fixed to the seabed, having a bending stiffness  $k$  of  $[3EI/l^3]$ , with  $EI$  being the product of Young’s modulus  $E$  and the moment of inertia  $I$  of the cylinder, and  $l$  being the height of the cylinder up to the point of the centroid of the wave load acting on the cylinder. The mass  $m$  of the SDOF model is the lumped mass of the model from energy considerations being equal to  $0.229 mL$ , with  $m$  as the distributed mass of the cylinder per unit length and  $L$  being the height of the cylinder. The horizontal motion of the cylinder along the horizontal  $x$ -axis is given by the displacement coordinate  $u = u(t)$ .

The rocking gravity base jack-up platform, shown in Figure 7.32 [44], is another structure that can be easily modeled as an SDOF system. The structure can be visualized as a rigid body on an elastic foundation, and if its motion can be restricted to plane rotation about the fixed axis through  $O$  at the midpoint of its base, then its position can be described by the single rotational coordinate



**FIGURE 7.32** (a) Gravity rectangular base jack-up platform; and (b) SDOF (translational mode) model for the platform. (From P. Le Tirant, *Seabed Reconnaissance and Offshore Soil Mechanics*, Editions Technip 27, Paris, France, p. 401, 1979. With permission.)

$\theta = \theta(t)$ . The above model will come in handy when the overall dynamic equilibrium is to be described for the system, as well for its stability considerations.

Using either Newton's second law or Lagrange's energy methods, the equation of motion for the above systems can be, respectively, obtained for the translational motion as

$$m\ddot{u} = \sum F_x \quad (7.83)$$

or, for the rotational motion (assuming that the platform executes a rocking motion in which the bottom foundation primarily rocks while the vertical legs do not deform elastically), as

$$J_o\ddot{\theta} = \sum M_o \quad (7.84)$$

where  $m$  is the lumped mass of the SDOF system,  $\sum F_x$  is the sum of all the forces acting on the system (including all the restoring and dissipative forces in the system) along the coordinate of motion  $u$ ,  $J_o$  is the mass moment of inertia about an axis through  $O$ , and  $\sum M_o$  is the sum of all the moments acting on the system for the rotational motion  $\theta$ .

The type of forces that constitute the sums on the left-hand sides of Equations 7.83 and 7.84 can be categorized into three main groups. The first group will consist of (i) the applied forces "mg" and (ii) the equivalent forces generated at the motion coordinate  $u$  (or  $\theta$ ) due to the environmental forces such as those due to winds, waves, and currents; these are calculated using Morison–O'Brien's equation. Other types of environmental forces such as those due to earthquakes, impact, and ice also could be included under this category. The net time-dependent force, due to all externally applied force components in the direction of  $u(t)$ , is denoted by  $f_{\text{ext}}(t)$ , and the net time-dependent moment about the fixed point  $O$ , due to all externally applied forces in the system described by the rotational coordinate  $\theta$ , is denoted by  $M_{\text{ext}}(t)$ .

The second group will consist of the reaction forces, generated mainly due to restoration effects produced by the deformations (such as those due to displacements and rotations produced in the system) to govern the force equilibrium of the system. The "springing-back" type of reaction (or restoring forces) occurs when the flexible structure deforms at the location. If the motion of the SDOF system is represented by the motion coordinate  $u$ , then the total restoring forces exerted by all flexible supports in the  $u$  direction is denoted by  $f_{\text{restoring}}(t)$ . The simplest reaction forces occur at immovable supports such as at the fixed point on a rigid body in pure rotation in a plane. If the motion of the SDOF system is represented by the coordinate  $\theta$ , then the restoring moment is denoted by the function  $M_{\text{restoring}}(t)$ .

The third group of forces consists of the dissipative forces, which can be due to friction or viscous damping forces that depend only on the velocity coordinate such as  $\dot{u}$  or  $\dot{\theta}$ . Similar to the restoring force/moment functions  $f_{\text{ext}}(t)$  [or  $M_{\text{restoring}}(t)$ ] in the respective coordinate  $u$  (or  $\theta$ ), the corresponding dissipative force/moment terms are denoted by  $f_{\text{dissipative}}(\dot{u})$  [or  $M_{\text{dissipative}}(\dot{\theta})$ ]. Hence, Equations 7.83 and 7.84 can be explicitly written as

$$\begin{aligned} m_{\text{buoyant}}\ddot{u} &= \sum F_x = F_{x_{\text{ext}}} + F_{x_{\text{restoring}}} + F_{x_{\text{dissipative}}} \\ J_o\ddot{\theta} &= \sum M_o = M_{\theta_{\text{ext}}} + M_{\theta_{\text{restoring}}} + M_{\theta_{\text{dissipative}}} \end{aligned} \quad (7.85)$$

### 7.7.3 SDOF MODELS IN OFFSHORE STRUCTURES

Using Equations 7.82 and 7.85, the dynamic equation of motion for an SDOF system can be expressed as

$$\begin{aligned}
 m_{\text{buoyant}}\ddot{u} &= \sum F_x = F_{x_{\text{ext}}} + F_{x_{\text{restoring}}} + F_{x_{\text{dissipative}}} \\
 f_{x_{\text{external}}} &= C_M[(\rho_w)(\pi D^2/4)(1)](\dot{U}_x - \dot{u}) + (1/2)C_D[(\rho_w)(D)(1)](U_x - \dot{u})|U_x - \dot{u}| \\
 F_{x_{\text{restoring}}} &= -ku = -k u \\
 F_{x_{\text{dissipative}}} &= -c\dot{u}
 \end{aligned} \tag{7.86}$$

where  $k$  is the restoring spring stiffness and  $c$  is the damping coefficient for the SDOF system. Finally, Equation 7.86 can be rearranged to give the final equation of motion as

$$\begin{aligned}
 [m_{\text{buoyant}} + C_M\{(\rho_w)(\pi D^2/4)(1)\}](\ddot{u}) + c(\dot{u}) + k(u) \\
 = C_M[(\rho_w)(\pi D^2/4)(1)](\dot{U}) + (1/2)C_D[(\rho_w)(D)(1)](U_x - \dot{u})|U_x - \dot{u}|
 \end{aligned} \tag{7.87}$$

The buoyant mass of the structure is equal to the actual mass of the structure minus the weight of an equivalent volume of water  $[(\rho_w)(\pi D^2/4)(1)]$ . Hence, Equation 7.87 can be rewritten as

$$\begin{aligned}
 [m_{\text{structure}} + C_A\{(\rho_w)(\pi D^2/4)(1)\}](\ddot{u}) + c(\dot{u}) + k(u) \\
 = C_M[(\rho_w)(\pi D^2/4)(1)](\dot{U}) + (1/2)C_D[(\rho_w)(D)(1)](U_x - \dot{u})|U_x - \dot{u}|
 \end{aligned} \tag{7.88}$$

Equation 7.88 leads to the final standard form used in standard textbooks on ocean structures as

$$\begin{aligned}
 [m_{\text{structure}} + m_{\text{added}}](\ddot{u}) + c(\dot{u}) + k(u) \\
 = C_M[(\rho_w)(\pi D^2/4)(1)](\dot{U}) + (1/2)C_D[(\rho_w)(D)(1)](U_x - \dot{u})|U_x - \dot{u}|
 \end{aligned} \tag{7.89}$$

It is seen from Equation 7.88 that the drag term depends on the product of the relative velocity term  $(U_x - \dot{u})|U_x - \dot{u}|$  between the fluid and the cylinder, whereas the term involving  $C_M$  depends on the fluid motion only; hence, Equation 7.85 becomes nonlinear due to the drag term. It can be seen from Section 6.3.4.2, where the linearization of the drag term has been discussed, that the equivalent linearized drag coefficient can be written as a constant value of  $\bar{C}_D$  where it is given as  $= \{C_D(1.2004\sigma_u)\}$  for regular waves, with  $\sigma_u$  as the standard deviation for the wave particle velocity over a quarter wave period. For irregular waves, it is given as equal to  $\{C_D[1.596\sigma_u]\}$ . As a consequence of the above discussions, Equation 7.89 can be linearized and rewritten as

$$\begin{aligned}
 [m_{\text{structure}} + m_{\text{added}}](\ddot{u}) + c(\dot{u}) + k(u) \\
 = C_M[(\rho_w)(\pi D^2/4)(1)](\dot{U}) + (1/2)(\bar{C}_D)[(\rho_w)(D)(1)](U_x - \dot{u})
 \end{aligned} \tag{7.90}$$

In Equation 7.90, the coefficient  $\bar{C}_D$  is equal to the values given in the above section for regular and irregular waves, depending on the standard deviation of wave particle velocities of the wave conditions considered.

### Example 7.7

A tubular cross brace is welded to the relatively rigid and stationary legs of a jacket platform and is moving horizontally under the action of the wave forces acting on the brace. Assume full fixity conditions for the horizontal brace and determine the SDOF equation for the brace subjected to the wave action.

The horizontal load  $q(t)$  acting on the brace of length  $\ell$  can be written down as

$$q(t) = \bar{C}_D \rho_w \left( \ell \frac{D}{2} \right) (U) + C_M \rho_w \left( \ell \frac{D^2}{4} \right) (\dot{U}) \quad (\text{E7.11})$$

where  $U$  and  $\dot{U}$  are the wave particle velocity and acceleration, respectively. Assume the beam to be located along the  $x$ -axis and deflection to be along the  $y$ -axis. Since the model is an SDOF system, the mass is assumed to be located at the center of the beam. Using Equation 7.87 as the governing equation, the modeled mass for the SDOF system, considering the wave forces acting on the structure, can be expressed as

$$m_{\text{modeled}} = \left[ \bar{m}_0 + C_A \rho_w \left( \frac{\pi}{4} D^2 \right) \right] (c_1 \ell) \quad (\text{E7.12})$$

in which  $C_A$  is the added mass from the wave–structure interaction, and the modeled mass factor  $c_1$  can be obtained from energy considerations, assuming a deformation function. From classical mechanics considerations, the factor  $c_1$  is obtained as 0.37.

Considering the deformation of a fixed brace, acted upon by a central load  $P$ , the deformation equation for the beam is obtained as (using Macaulay's method) follows.

For a fixed-fixed beam subjected to a central load  $P$ , the displacement  $u$

along the length of the beam is given by (using Macaulay's method)

$u = [(P/2)\{(x^3/6) - (1/3)\{(x - L/2)^3 - L(x^2/8)\}\}]/(EI)$ . Hence, displacement at the center  $x = (L/2)$  is given by

$$(u)_{x=(L/2)} = (P/2)[\{(L^3/48) - (0.0) - L^3/32\}]/EI = -[PL^3/(192EI)]. \quad (\text{E7.13})$$

The stiffness,  $k_{\text{modelled}}$ , of a single-degree-of-freedom system of the beam (of length  $L$ ), can be obtained by considering two elements of length  $(L/2)$ , for the centrally-loaded end-fixed beam of length  $L$  (with the appropriate force, displacement and rotation conditions at the three nodes of the beam), and assembling together the matrix equations given by Equation 7.57 as

$$k_{\text{modeled}} = [\text{Load}/(\text{deformation under the load, at the load-point})] = [(192EI)/L^3]$$

The minus sign indicates that the deformation is in the negative direction. Considering the damping terms in the system, it can be expressed as (using Equation 7.86)

$$c_{\text{modeled}} = c + (1/2)(\bar{C}_D)[(\rho_w)(D)(1)] = c + (1/2)(\bar{C}_D)[(\rho_w)(D)] \quad (\text{E7.14})$$

Hence, the SDOF system can be written as

$$m_{\text{modeled}}\ddot{V} + C_{\text{modeled}}\dot{V} + k_{\text{modeled}}V = C_M[(\rho_w)(\pi D^2/4)(1)](\dot{U}) + (1/2)(\bar{C}_D)[(\rho_w)(D)(1)](U) \quad (\text{E7.15})$$

The wave particle velocities  $U$  and wave particle accelerations  $\dot{U}$  can be determined from the wave theory used, and then the equation can be solved numerically.

### Example 7.8

Consider the horizontal motion of the jack-up drilling rig in Figure 7.32a. Assume that each of the four tubular legs has full end fixity, viz., that they are clamped at the mat or mud-line and also at the deck level. Figure 7.32b shows the simplified schematic diagram and defines the deformation geometry. Of the three types of loads that are likely to act on the structure (wind, wave, and current), assume that the wave load dominates and the effects of the other two loads can be neglected. For simplifying the problem, assume that this total horizontal load acts at the deck level, and assume the deck to be rigid (Figure 7.32b). Since cross braces are absent, the structural stiffness can be taken as four times that for a single leg, or  $4(k_{\text{vertical leg}})$ . Consistent with this loading and the structural restraints, the dominant mode shape is assumed to be as that shown in Figure 7.32b. Neglect rotational motion of the deck; assume the mass of the deck to be lumped at the bottom of the deck. Let  $u = u(t)$  define the horizontal deformation of the deck (mass =  $m_{\text{deck level}}$ ) at the deck level. Considering the distributed mass of the vertical legs, the equivalent lumped mass of the leg using kinetic energy considerations is given as

$$m_{\text{(vert. leg equivalent)}} = 4(\bar{m}_0\ell)f_{\text{lumped mass}} = 4(\bar{m}_0\ell)(0.375) \quad (\text{E7.16})$$

where  $\ell$  is the height of the vertical leg,  $(\bar{m}_0)$  is the unit mass of the vertical leg, and  $f_{\text{lumped mass}}$  is the factor obtained from equivalent energy considerations.

Similarly, for the added mass along the immersed portion of the leg,

$$m_{\text{added mass equivalent}} = [C_A\rho_w(\pi D^2/4)(d)]f_{\text{lumped mass}} = [C_A\rho_w(\pi D^2/4)(d)](0.375) \quad (\text{E7.17})$$

where  $C_A$  is the added mass coefficient,  $\rho_w$  is the mass density of seawater,  $D$  is the diameter of vertical leg,  $d$  is the depth of water at the site, and  $f_{\text{lumped mass}}$  is the lumped mass factor obtained using kinetic energy considerations.

Consequently, the total lumped mass at the deck level is given as

$$m_{\text{total}} = 4(\bar{m}_0\ell)(0.375) + [C_A\rho_w(\pi D^2/4)(d)](0.375) + m_{\text{deck}} \quad (\text{E7.18})$$

Assuming that most of the system damping is produced by the submerged portions of the legs and also assuming that the hydrodynamic damping can be a linearized form, one obtains the system damping as

$$C_{\text{equivalent}} = 4[\bar{c}d + C'_D(\rho_w D/2)d] \quad (\text{E7.19})$$

The beam stiffness coefficient is obtained from the use of beam theory as

$$k_{\text{equivalent}} = 4(12EI/L^3) = 48EI/L^3 \quad (\text{E7.20})$$



The stiffness of  $(12EI/L^3)$  assumes that the two ends are rigidly fixed; this may not be a feasible option at the deck end. Hence,  $k_{equivalent}$  is usually an upper limit, and the actual stiffness may be less. The equation of motion of the jack-up platform with four legs and a gravity base can be written down as

$$m_{Total}\ddot{u} + c_{equivalent}\dot{u} + k_{equivalent}u = F(t) \tag{E7.21}$$

The force  $F(t)$  is the equivalent force acting on the SDOF system of the platform model.

**Example 7.9**

Using the modified Pierson–Moskowitz wave height spectrum, shown in Figure E7.8 for a significant wave height of  $H_s = 49.21$  ft., determine the variance for the surge displacement of a four-column tension leg platform (TLP). The given data are as follows: total cable pretension = 15,000 tons; weight = 63,000 tons; added mass for the whole structure is equal to 15%; the transfer function for displacement is given by  $H(j\omega) = (j)[(4\pi)/8](\rho_w g D^2 C_M) e^{j(\omega t)}$ . The diameter of the columns and pontoons are equal to 50.0 ft.;  $H_s = 49.21$  ft.; water depth = 450.0 ft. (= cable length).

Total mass of the (four) columns of the TLP = (TLP mass + added mass)

$$= (\text{TLP weight}/g)(1.0 + 0.15) = (63,000)(2000)/(32.2)(1.15) = (4.500)(10^6) \text{ slugs}$$

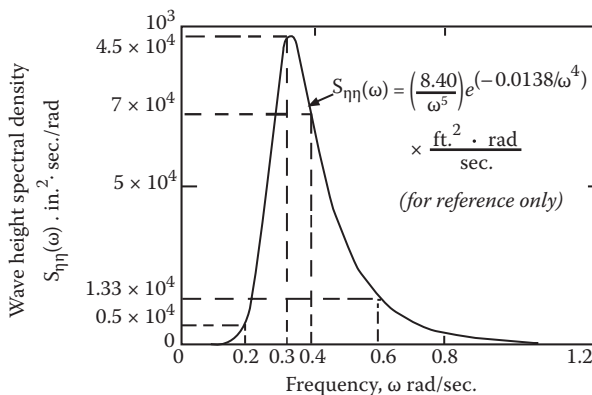
The variance of the structural response spectrum is given by

$$= [ \{ [(4\pi)/8](\rho_w g D^2 C_M) \}^2 \int_{0.0}^{1.2} \frac{S_{\eta\eta}(\omega) d\omega}{[(K_1 - m_1 \omega^2)^2 + (c_1 \omega)^2]} = \sum_{0.0}^{1.2} \frac{S_{\eta\eta}(\omega)(\Delta\omega)}{[(K_1 - m_1 \omega^2)^2 + (c_1 \omega)^2]} ] \tag{E7.22}$$

$$\{ [(4\pi)/8](\rho_w g D^2 C_M) \}^2 = [ (4\pi/8)(1.99)(32.2)(50.0)^2(2.0) ]^2 = [ (5.033)(10^5) ]^2$$

The integral summation is computed in the following tabular format:

Mid-freq. (rad/s)	(A) = $S_{\eta}(\omega)$	(B) = $(K_1 - m_1 \omega^2)^2$	(C) = $(c_1 \omega)^2$	(D) = (B) + (C)	(E) = (A)/(D)	(F) = (E)x [(5.033)(10 <sup>5</sup> )] <sup>2</sup>
0.2	$0.5 \times 10^4$	$1.25 \times 10^{10}$	$1.00 \times 10^6$	$1.25 \times 10^{10}$	$4.0 \times 10^{-7}$	102,010
0.3	$9.5 \times 10^4$	$1.13 \times 10^{11}$	$2.26 \times 10^6$	$1.13 \times 10^{11}$	$8.4 \times 10^{-7}$	214,221
0.4	$7.0 \times 10^4$	$4.25 \times 10^{11}$	$4.02 \times 10^6$	$4.25 \times 10^{11}$	$1.65 \times 10^{-7}$	42,079
0.6	$1.33 \times 10^4$	$2.41 \times 10^{12}$	$9.04 \times 10^6$	$2.41 \times 10^{12}$	$5.52 \times 10^{-9}$	1408
0.8	$0.5 \times 10^4$	$7.91 \times 10^{12}$	$1.60 \times 10^7$	$7.91 \times 10^{12}$	$6.32 \times 10^{-9}$	1612



**FIGURE E7.8** Wave height power spectral density –  $S_{\eta\eta}(\omega)$ .

$$\begin{aligned}
 (\sigma_u)^2 &= (102,010)(0.1) + (214,221)(0.1) + (42,079)(0.1) + (1408)(0.2) + (1612)(0.2) \\
 &= 36,435 \text{ in.}^2 = 253 \text{ ft.}^2
 \end{aligned}$$

Hence,  $\sigma_u = \sqrt{(253.0)} = 15.91 \text{ ft.}$

Once the standard deviation of the horizontal motion is known, then the displacement of the TLP from the mean position can be determined.

### Example 7.10

Calculate the natural surge and heave periods of the CONOCO's TLP shown in Figure E7.9. The given data are as follows: water depth = 482.0 ft.; draft = 98.0 ft.; column diameter (each column) = 49.0 ft.; displacement = 56,960.0 tons (short);  $E$  of tethers =  $(14.0)(10^6)$  lb./in.<sup>2</sup>; total area of the mooring cables = 800.0 in.<sup>2</sup>; total pre-tension of tethers = 12,670.0 tons (short);  $\rho_w = 1.99$ ; added mass coefficient for surge = 1.0; and added mass coefficient for heave = 0.20.

$$\begin{aligned}
 \text{Total mass of the platform for sway motion} &= (1.0 + 1.0)(\text{displacement of the TLP}) \\
 &= (2.0)(56,960.0)(2000)/(32.2) \\
 &= (7.076)(10^6) \text{ slugs.}
 \end{aligned}$$

$$\begin{aligned}
 \text{Stiffness of the TLP for sway motion} &= (\text{total pre-tension in the vertical legs})/(\text{length of cables}) \\
 &= (12,670.0)(2000)/(384.0) = (6.599)(10^4) \text{ lb./ft.}
 \end{aligned}$$

$$\text{Surge frequency} = [\text{stiffness/mass}]^{(0.5)} = [(6.599)(10^4)/(7.076)(10^6)]^{(0.5)} = 0.0966 \text{ rad/s} = 65.06 \text{ s}$$

$$\begin{aligned}
 \text{Total mass of the platform for heave motion} &= (1.0 + 0.2)(\text{displacement of the TLP}) \\
 &= (1.20)(56,960)(2000)/(32.2) = (4.2455)(10^6) \text{ slug}
 \end{aligned}$$

$$\begin{aligned}
 \text{Stiffness of the TLP for heave motion} &= [\text{vertical stiffness of the cables} \\
 &+ (\text{fluid forces/unit height}) \text{ due to the} \\
 &\text{column submergence}] = [(AE/L_{\text{cable}}) + (\rho_w g) \\
 &(\text{column area})(4)]
 \end{aligned}$$

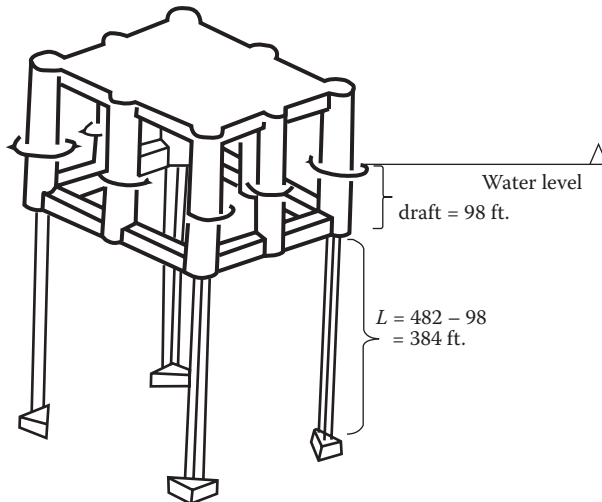


FIGURE E7.9 Schematic of CONOCO's TLP.

$$= [(800.0)(14.0)(10^6)/(384) + (1.99)(32.2)(\pi/4)(49)^2(4)] = [(29.167)(10^6) + (0.483)(10^6)]$$

$$= (29.65)(10^6) \text{ lb./ft.}$$

$$\text{Heave frequency} = \{[(29.65)(10^6)] / \{ (4.2455)(10^6) \} \}^{0.5} = 2.643 \text{ rad/s} = 2.378 \text{ s}$$

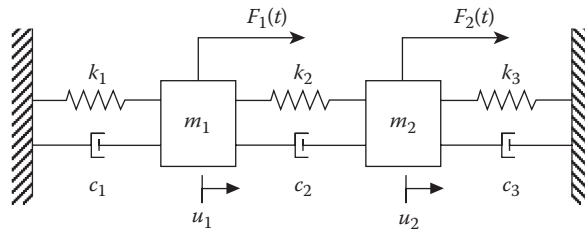
### 7.7.4 MDOF SYSTEMS

In discussing the MDOF systems, it must be remembered that an offshore structure has a large amount of degrees of freedom, and developing a model to include all these degrees-of-freedom is not necessary to have an insight into the relevant issues involved in the dynamic modeling. Since each degree-of-freedom (DOF) requires one governing equation, only a few of the DOFs will be used in modeling the offshore structure. The equations are written in the matrix format, considering the mass, damping, and stiffness components of the structure. A number of methods have been used in the formulation of dynamic equations for an MDOF system, viz., Lagrange’s equation, Hamilton’s principle, stiffness/flexibility approaches, or the direct use of Newton’s second theorem on motion. In this study, only the direct approach using Newton’s second theorem on motion will be used, making use of lumped mass/stiffness models; only linear and elastic structural behavior will be considered.

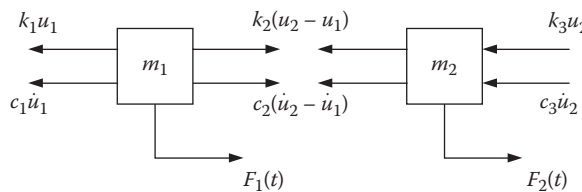
#### 7.7.4.1 Two-Degrees-of-Freedom System

Consider the motion of the two-degrees-of-freedom system shown in Figure 7.33 [45]; the system includes mass, stiffness, and damping elements for the formulation of the equation of motion.

The free-body diagrams of each degree of freedom of motion, viz.,  $u_1(t)$  and  $u_2(t)$ , are shown in Figure 7.34 [45].



**FIGURE 7.33** Two-degree-of-freedom model of a structure. (Imported from Internet Resources, *Multi-Degree-of-Freedom Vibration: Introductory Topics*, pp. 516–517, 2011. Accessed on August 3, 2011.)



**FIGURE 7.34** Free-body diagram of the forces acting on each mass. (*Multi-Degree-of-Freedom Vibration: Introductory Topics*, pp. 516–517, 2011, imported from Internet resources. Accessed on August 3, 2011.)

$$\begin{aligned}
 F_1(t) - c_1\dot{u}_1 - k_1u_1 + c_2(\dot{u}_2 - \dot{u}_1) + k_2(u_2 - u_1) &= m_1\ddot{u}_1 \\
 F_2(t) - c_3\dot{u}_2 - k_3u_2 - c_2(\dot{u}_2 - \dot{u}_1) - k_2(u_2 - u_1) &= m_2\ddot{u}_2
 \end{aligned}
 \tag{7.91}$$

The above can be reorganized to give the generic form

$$\begin{aligned}
 m_1\ddot{u}_1 + (c_1 + c_2)\dot{u}_1 - c_2\dot{u}_2 + (k_1 + k_2)u_1 - k_2u_2 &= F_1(t) \\
 m_2\ddot{u}_2 + (c_2 + c_3)\dot{u}_2 - c_3\dot{u}_1 + (k_2 + k_3)u_2 - k_2u_1 &= F_2(t)
 \end{aligned}
 \tag{7.92}$$

Equation 7.92 can be easily expressed in the usual matrix-vector form as

$$\begin{bmatrix} m_1 & 0 \\ 0 & m_2 \end{bmatrix} \begin{Bmatrix} \ddot{u}_1 \\ \ddot{u}_2 \end{Bmatrix} + \begin{bmatrix} c_1 + c_2 & -c_2 \\ -c_2 & c_2 + c_3 \end{bmatrix} \begin{Bmatrix} \dot{u}_1 \\ \dot{u}_2 \end{Bmatrix} + \begin{bmatrix} k_1 + k_2 & -k_2 \\ -k_2 & k_2 + k_3 \end{bmatrix} \begin{Bmatrix} u_1 \\ u_2 \end{Bmatrix} = \begin{Bmatrix} F_1(t) \\ F_2(t) \end{Bmatrix}
 \tag{7.93}$$

Equation 7.93 can also be expressed in the standard matrix-vector form as

$$[m]\{\ddot{u}\} + [c]\{\dot{u}\} + [k]\{u\} = \{F(t)\}
 \tag{7.94}$$

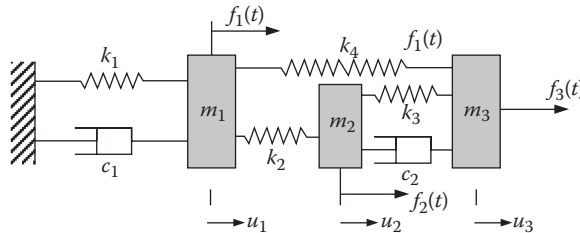
It can be seen by comparing Equations 7.93 and 7.94 that the matrices  $[m]$ ,  $[c]$ , and  $[k]$  are symmetric.

**7.7.4.2 Three-Degrees-of-Freedom System**

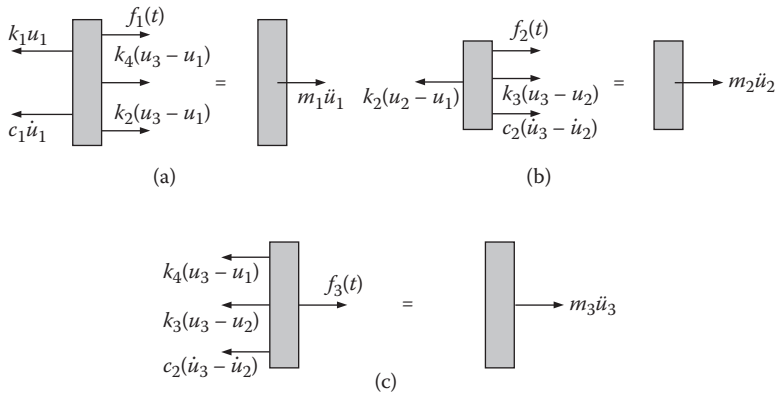
The lumped mass model of the three-degrees-of-freedom damped system is shown in Figure 7.35 [46].

The necessary free body diagram for each of the moving mass is given in Figure 7.36 [46]. From the three free body diagrams, the relevant equations of motion can be obtained. Using Newton’s second equation of motion, the three equations of motion can be expressed as

$$\begin{aligned}
 m_1\ddot{u}_1 + c_1\dot{u}_1 + (k_1 + k_2 + k_4)u_1 - k_2u_2 - k_4u_3 &= f_1(t) \\
 m_2\ddot{u}_2 + c_2(\dot{u}_2 - \dot{u}_3) + (k_2 + k_3)u_2 - k_2u_1 - k_3u_3 &= f_2(t) \\
 m_3\ddot{u}_3 + c_2(\dot{u}_3 - \dot{u}_2) + (k_3 + k_4)u_3 - k_3u_2 - k_4u_1 &= f_3(t)
 \end{aligned}
 \tag{7.95}$$



**FIGURE 7.35** Lumped mass model of a three-degrees-of-freedom structure. (From Single Degree-of-Freedom Systems. Available at [www.efunda.com/formulae/vibrations/sdof\\_intro.cfm](http://www.efunda.com/formulae/vibrations/sdof_intro.cfm). Accessed on April 3, 2011.)



**FIGURE 7.36** Free body diagram for (a) mass 1; (b) mass 2; and (c) mass 3. (From Single Degree-of-Freedom Systems. Available at [www.efunda.com/formulae/vibrations/sdof\\_intro.cfm](http://www.efunda.com/formulae/vibrations/sdof_intro.cfm). Accessed on April 3, 2011.)

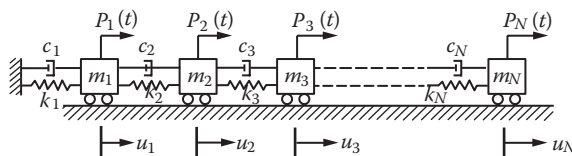
The above equations can be expressed in a matrix form as,

$$\begin{bmatrix} m_1 & 0 & 0 \\ 0 & m_2 & 0 \\ 0 & 0 & m_3 \end{bmatrix} \begin{Bmatrix} \ddot{u}_1 \\ \ddot{u}_2 \\ \ddot{u}_3 \end{Bmatrix} + \begin{bmatrix} c_1 & 0 & 0 \\ 0 & c_2 & -c_2 \\ 0 & -c_2 & c_2 \end{bmatrix} \begin{Bmatrix} \dot{u}_1 \\ \dot{u}_2 \\ \dot{u}_3 \end{Bmatrix} + \begin{bmatrix} k_1 + k_2 + k_4 & -k_2 & -k_4 \\ -k_2 & k_2 + k_3 & -k_3 \\ -k_4 & -k_3 & k_3 + k_4 \end{bmatrix} \begin{Bmatrix} u_1 \\ u_2 \\ u_3 \end{Bmatrix} = \begin{Bmatrix} f_1(t) \\ f_2(t) \\ f_3(t) \end{Bmatrix} \tag{7.96}$$

Equation 7.96 can be expressed in an abbreviated matrix equation form similar to Equation 7.93.

### 7.7.4.3 Many-Degrees-of-Freedom System

Consider the system of masses, springs, and dashpots connected together as shown in Figure 7.37 [47].



**FIGURE 7.37** MDOF systems. (From J.W. Smith, *Vibration of Structures: Applications in Civil Engineering Design*, Chapman and Hall, New York, p. 71, 1988. With permission.)

By making use of Newton’s second equation of motion, the following equations of motion can be written for each degree of freedom:

$$\begin{aligned}
 m_1\ddot{u}_1 + c_1\dot{u}_1 + k_1u_1 + c_2(\dot{u}_1 - \dot{u}_2) + k_2(u_1 - u_2) &= P_1(t) \\
 m_2\ddot{u}_2 + c_2(\dot{u}_2 - \dot{u}_1) + k_2(u_2 - u_1) + c_3(\dot{u}_2 - \dot{u}_3) + k_3(u_2 - u_3) &= P_2(t) \\
 m_3\ddot{u}_3 + c_3(\dot{u}_3 - \dot{u}_2) + k_3(u_3 - u_2) + c_4(\dot{u}_3 - \dot{u}_4) + k_4(u_3 - u_4) &= P_3(t) \\
 \dots\dots\dots & \\
 \dots\dots\dots & \\
 m_N\ddot{u}_N + c_N(\dot{u}_N - \dot{u}_{N-1}) + k_N(u_N - u_{N-1}) &= P_N(t)
 \end{aligned}
 \tag{7.97}$$

Equation 7.97 can be expressed in a matrix form as indicated below.

**7.7.4.4 Solution Procedures**

The solutions for Equations 7.93, 7.95, and 7.97 can be generalized as a mathematical procedure as

$$u(t) = u_{\text{homogeneous}}(t) + u_{\text{particular}}(t)
 \tag{7.98}$$

The homogeneous part deals with the free vibration of the system, and the particular part of the above solution deals with the solution specific to the load acting on the system. In solving the homogeneous part of the above equations, the homogeneous part will lead to the eigen-solution, wherein the free or damped (real or complex) vibration frequencies and real or complex eigen-vectors of the modal response will be obtained. In order to find the platform response under the given loads, a number of procedures have been developed, depending upon the forcing function being harmonic or of a general nature. Classical solutions are available in standard textbooks available on structural dynamics. Some of these are (i) modal decoupling and synthesizing using the Duhamel’s integral approach and (ii) complex frequency response (or transfer function) approach for a general random load function. Detailed solutions to specific problems are beyond the scope of the present book. Only a brief indication for the direction of solution will be discussed herein.

$$\begin{aligned}
 &\left[ \begin{array}{cccccc} m_1 & 0 & 0 & 0 & 0 & 0 \\ 0 & m_2 & 0 & 0 & 0 & 0 \\ 0 & 0 & m_3 & 0 & 0 & 0 \\ \cdot & \cdot & \cdot & \cdot & \cdot & \cdot \\ \cdot & \cdot & \cdot & \cdot & \cdot & \cdot \\ 0 & 0 & 0 & 0 & 0 & m_N \end{array} \right] \left\{ \begin{array}{c} \ddot{u}_1 \\ \ddot{u}_2 \\ \ddot{u}_3 \\ \cdot \\ \cdot \\ \ddot{u}_N \end{array} \right\} + \left[ \begin{array}{cccccc} c_1 + c_2 & -c_2 & 0 & \cdot & \cdot & 0 \\ -c_2 & c_2 + c_3 & -c_3 & \cdot & \cdot & 0 \\ 0 & -c_3 & c_3 + c_4 & \cdot & \cdot & 0 \\ \cdot & \cdot & \cdot & \cdot & \cdot & \cdot \\ \cdot & \cdot & \cdot & \cdot & \cdot & \cdot \\ 0 & 0 & 0 & 0 & -c_N & c_N \end{array} \right] \left\{ \begin{array}{c} \dot{u}_1 \\ \dot{u}_2 \\ \dot{u}_3 \\ \cdot \\ \cdot \\ \dot{u}_N \end{array} \right\} \\
 &+ \left[ \begin{array}{cccccc} k_1 + k_2 & -k_2 & 0 & \cdot & \cdot & 0 \\ -k_2 & k_2 + k_3 & -k_3 & \cdot & \cdot & 0 \\ 0 & -k_3 & k_3 + k_4 & \cdot & \cdot & 0 \\ \cdot & \cdot & \cdot & \cdot & \cdot & \cdot \\ \cdot & \cdot & \cdot & \cdot & \cdot & \cdot \\ 0 & 0 & 0 & 0 & -k_N & k_N \end{array} \right] \left\{ \begin{array}{c} u_1 \\ u_2 \\ u_3 \\ \cdot \\ \cdot \\ u_N \end{array} \right\} = \left\{ \begin{array}{c} P_1(t) \\ P_2(t) \\ P_3(t) \\ \cdot \\ \cdot \\ P_N(t) \end{array} \right\}
 \end{aligned}
 \tag{7.99}$$

The modal superposition procedure, along with the Duhamel integral approach, will lead to the time domain solution as

$$u(t) = \sum [\Phi]_N \{Y(t)\} \tag{7.100}$$

where  $[\Phi]_N$  indicates the  $N$  columns of eigenvectors for  $N$  frequencies of the problem, and

$$\{Y_i(t)\}, i = 1 \text{ to } N \tag{7.101}$$

gives the solution for the  $N$  normal coordinates for the specific loads specified in the problem, and  $N$  is the number of modes considered in the solution.

Once again, the details of the procedure are to be taken from standard textbooks available for solving such equations [48, 49].

The complex frequency response function (or the transfer function) approach will lead to the power spectral density  $S_{u_m}(\omega)$ , in frequency domain, as

$$S_{u_m}(\omega) = \sum \Phi_i^2 |H_i(j\omega)|^2 S_{F_i}(\omega), i = 1, \dots, N \tag{7.102}$$

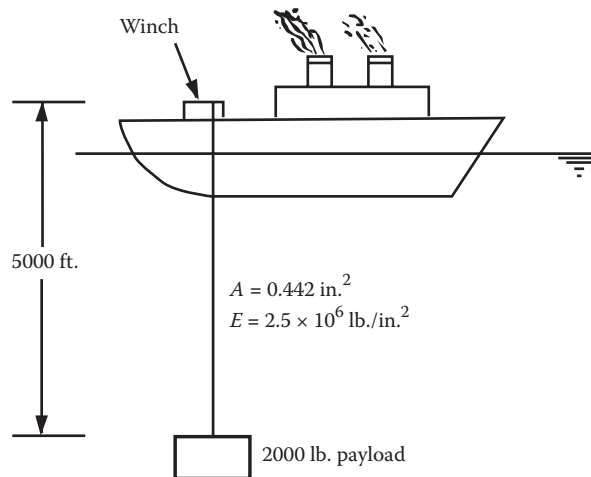
where  $\Phi_i$  is the  $i$ th modal vector, and  $S_{F_i}(\omega)$  is the power spectral density function of the forcing function.

$$|H_i(j\omega)|^2 = (1.0)[K_i^2 \{1.0 - (4\xi_i^2 - 2.0)(\omega/\omega_i)^2 + (\omega/\omega_i)^4\}] \tag{7.103}$$

where  $\omega_i$  is the  $i$ th modal frequency,  $\xi_i$  is the  $i$ th modal damping ration, and  $K_i$  is the modal stiffness for the  $i$ th frequency.  $S_{F_i}(\omega)$  is the spectral density of the excitation force for the  $i$ th mode.

**Example 7.11**

The winch and cable system, shown in Figure E7.10, carries a payload of 2000 lb., at the end of the cable. Take the ship to be a stiff and massive system with no motion. The cable weighs



**FIGURE E7.10** Winch cable system.

0.66 lb./ft. Compute the natural frequencies of the system considering it as (i) a one-degree-of-freedom system with mass and stiffness, with the cable providing stiffness and the total mass of the cable and payload taken to contribute to its dynamic behavior; (ii) a one-degree-of-freedom system with mass and stiffness, with the cable providing an equivalent mass (considering the varying inertial effects over the length of the cable) to the payload mass along with stiffness; and (iii) a three-degree-of-freedom system, considering the cable mass (along with the payload) to contribute to the inertial motion of the system, as well as to its stiffness motion (vertical displacement).

Given data:

Weight of the payload = 2000 lb.

Total length of cable = 5000 ft.

Cable weight/unit length = 0.66 lb./ft.

Cable cross-sectional area = 0.442 in.<sup>2</sup>

Modulus of elasticity of cable = (2.5)(10<sup>6</sup>) lb./in.<sup>2</sup>

- (i) *SDOF system*: Assuming the total mass of the cable to be lumped along with the payload mass.

Use an added mass coefficient of 1.0:

$$\begin{aligned} \text{Mass of the SDOF system} &= [2000 + (1.0 + 1.0)(5000)(0.66)]/(32.2) \\ &= 8600/32.2 = 267.08 \text{ slug.} \end{aligned}$$

$$\text{Stiffness of the cable system} = (AE/L)_{\text{cable}} = (0.442)(2.5)(10^6)/(5000) = 221 \text{ lb./ft.}$$

$$\begin{aligned} \text{Fundamental frequency of vibration} &= \sqrt{[(\text{Stiffness})/(\text{Mass})]} = \sqrt{[(221.0)/(267.08)]} \\ &= 0.910 \text{ rad/s} = 0.1448 \text{ Hz (or the period of motion is equal to 6.91 s)} \end{aligned}$$

- (ii) *SDOF system with proper inertial force correction to the cable mass.*

Use the same added mass for the cable. Equivalent mass of the cable per unit length

$$= (0.66)(1.0 + 1.0)/32.2 = 0.04099 \text{ slug/ft.}$$

Assuming the cable to swing as a pendulum, with a tip velocity as  $u_0$  (ft./s), the velocity along the cable length will vary as  $(y/5000)u_0$ .

$$\begin{aligned} \text{The kinetic energy of the total system} &= (1/2)(2000/32.2)(u_0)^2 + (1/2) \int_0^{5000} (0.04099)[(y/5000)u_0]^2 (dy) \\ &= 31.06(u_0)^2 + (1/2)(0.04099)(1/5000)^2(u_0)^2[y^3/3]_0^{5000} = [31.06 + 34.16](u_0)^2 = 65.22(u_0)^2 \end{aligned}$$

Hence, lumped mass = (2)(65.22) = 130.44 slug.

Stiffness of the cable remains the same, being equal to 221 lb./ft.

Hence, the corrected fundamental frequency of vibration =  $\sqrt{[(221.0)/(130.44)]}$

$$= 1.3016 \text{ rad/s} = 0.2071 \text{ Hz (or the period of motion is 4.827 s).}$$

- (iii) *Three-degrees-of-freedom system.*

Considering the lumping points to be at each of the 1/3 cable length point, the mass lumping points will be at (i) for the first mass, [(1/3)(5000) ft.] = 1666.7 ft.; (ii) for the second



mass,  $[(2/3)(5000) \text{ ft.}] = 3333.3 \text{ ft.}$ ; and (iii) for the third mass, 5000 ft. The lumped mass model is shown in Figure E7.11.

The masses are

$$\begin{aligned} m_1 &= 68.32 \text{ slugs} \\ m_2 &= 68.32 \text{ slugs} \\ m_3 &= (2000/32.2 + 68.32) = 130.43 \text{ slugs} \end{aligned} \tag{E7.23}$$

Similarly, the three stiffnesses of the system are given by

$$\begin{aligned} k_1 &= k = (0.442)(2.5)(10^6)/(5000/3) \text{ lb./ft.} = 663.0 \text{ lb./ft.} \\ k_2 &= k = 663.0 \text{ lb./ft.} \\ k_3 &= k = 663.0 \text{ lb./ft.} \end{aligned} \tag{E7.24}$$

Hence, following Equation 7.91 and making  $k_4 = 0.0$  and  $c_1 = c_2 = 0.0$ , the equations of motion can be written as

$$\begin{aligned} m_1 \ddot{u}_1 + (k_1 + k_2)u_1 - k_2 u_2 &= 0.0 \\ m_2 \ddot{u}_2 + (k_2 + k_3)u_2 - k_2 u_1 - k_3 u_3 &= 0.0 \\ m_3 \ddot{u}_3 + (k_3)u_3 - k_3 u_2 &= 0.0 \end{aligned} \tag{E7.25}$$

Following Equation 7.92, the equation of motion can be written as

$$\begin{bmatrix} m_1 & 0 & 0 \\ 0 & m_2 & 0 \\ 0 & 0 & m_3 \end{bmatrix} \begin{Bmatrix} \ddot{u}_1 \\ \ddot{u}_2 \\ \ddot{u}_3 \end{Bmatrix} + \begin{bmatrix} 2k & -k & 0.0 \\ -k & 2k & -k \\ 0.0 & -k & k \end{bmatrix} \begin{Bmatrix} u_1 \\ u_2 \\ u_3 \end{Bmatrix} = \begin{Bmatrix} 0.0 \\ 0.0 \\ 0.0 \end{Bmatrix} \tag{E7.26}$$

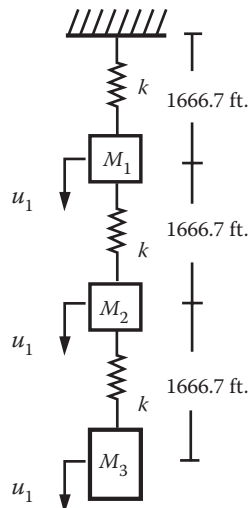


FIGURE E7.11 Three-degrees-of-freedom lumped mass model of the cable.

Assuming a harmonic displacement of  $u_i = A_i e^{j\omega t}$ , with  $i = 1$  to 3, Equation E7.26 reduces to

$$\begin{bmatrix} (2k - m_1\omega^2) & -k & 0.0 \\ -k & (2k - m_2\omega^2) & -k \\ 0.0 & -k & (k - m_3\omega^2) \end{bmatrix} \begin{Bmatrix} A_1 \\ A_2 \\ A_3 \end{Bmatrix} (e^{j\omega t}) = \begin{Bmatrix} 0.0 \\ 0.0 \\ 0.0 \end{Bmatrix} \quad (\text{E7.27})$$

Substituting the values of  $m_1$ ,  $m_2$ ,  $m_3$  and  $k$ , Equation E7.27 becomes

$$\begin{bmatrix} \{(2)(663) - 68.32\omega^2\} & -(663) & 0.0 \\ -(663) & \{(2)(663) - 68.32\omega^2\} & -(663) \\ 0.0 & -(663) & \{(2)(663) - 68.32\omega^2\} \end{bmatrix} \begin{Bmatrix} A_1 \\ A_2 \\ A_3 \end{Bmatrix} (e^{j\omega t}) = \begin{Bmatrix} 0.0 \\ 0.0 \\ 0.0 \end{Bmatrix} \quad (\text{E7.28})$$

Hence, the determinantal equation is given as

$$\begin{bmatrix} \{(2)(663) - 68.32\omega^2\} & -(663) & 0.0 \\ -(663) & \{(2)(663) - 68.32\omega^2\} & -(663) \\ 0.0 & -(663) & \{(2)(663) - 68.32\omega^2\} \end{bmatrix} = 0.0 \quad (\text{E7.29})$$

The characteristic equation of Equation E7.29 becomes

$$\omega^6 - 48.52\omega^4 + 565.12\omega^2 - 915.5 = 0.0 \quad (\text{E7.30})$$

The solution to Equation E7.30 is obtained as  $\omega_1 = 1.388$  rad/s (= 0.221 Hz or 4.53 s);  $\omega_2 = 3.884$  rad/s (= 0.618 Hz or 1.618 s); and  $\omega_3 = 5.613$  rad/s (= 0.893 Hz or 1.119 s).

It is seen from the last result that the present fundamental frequency did not change very much from its earlier value of 1.3016 rad/s (difference ~ 6.67%).

## EXERCISE PROBLEMS

- Describe clearly what type of loads you would consider in designing a fixed platform for loads experienced during (i) fabrication of the platform and (ii) installation of the structure at the proposed site.
- A steel column of diameter 6.0 in. and wall thickness 0.50 in. is loaded in the downward direction by two forces  $P_1 = 25.0$  kips and  $P_2 = 40.0$  kips, as shown in Figure P7.1. (a) Assemble the stiffness matrix for the whole structure (1-2-3-4). (b) Compute the displacements at nodes 2 and 3. (c) Determine the stresses in the three members constituting the structure. Let  $E = 30.0$  ksi.
- The simple truss shown in Figure P7.2 is subjected to a horizontal load at node 1. (a) Compute the general stiffness matrix for the truss structure. (b) Determine the horizontal and vertical components of displacement at node 1. (c) Determine the stresses in members 1 and 2. Assume that all the areas of the bars are equal to 1.0 in.<sup>2</sup>,  $L = 100.0$  in., and  $E = 10.0 \times 10^6$  psi.
- Consider the simplified steel support truss of an offshore tower, shown in Figure P7.3, and determine the reduced stiffness matrix (eliminating the fixed boundary degrees-of-freedom). Assume that the drilling rig weighs 30.0 tons and that 1/4 of the rig load is acting at each of nodes 4 and 5. Consider joints 1 and 3 to be fixed against displacements (both in  $x$  and  $y$  directions), joints 4 and 5 to be free for only vertical ( $y$ ) displacements, and joint 2

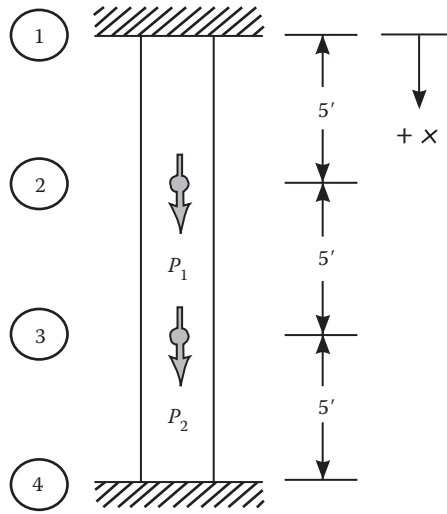


FIGURE P7.1 Steel column.

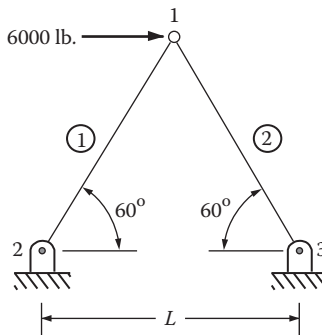


FIGURE P7.2 Simple triangular truss.

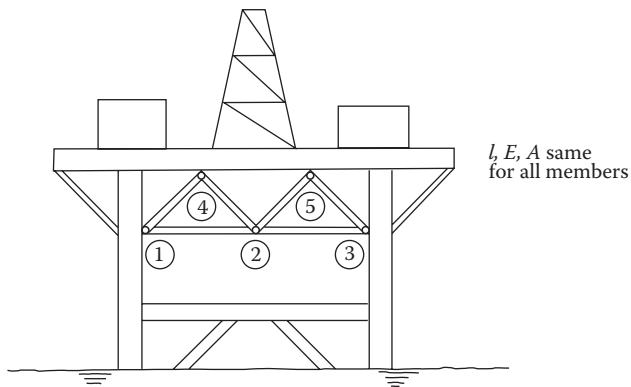
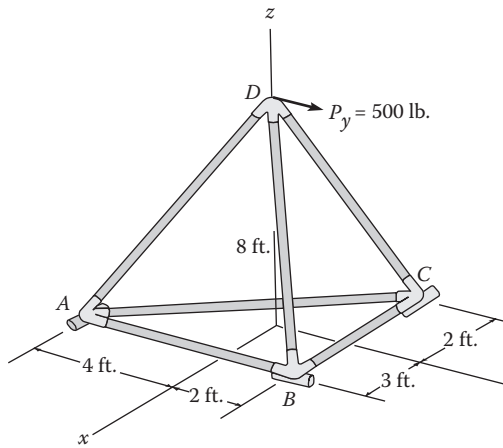


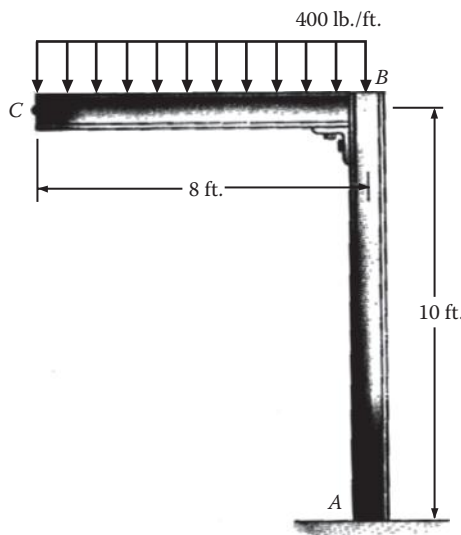
FIGURE P7.3 Simplified steel support of an offshore tower. (From T.H. Dawson, *Offshore Structural Engineering*, Prentice Hall Inc., Englewood Cliffs, NJ, 1983. With permission.)

to be free for  $x$  and  $y$  displacements. Assume the interior spacing between the vertical columns to be 30.0 ft. and the depth of the deck truss to be 10 ft. Compute the displacements at nodes 2, 4, and 5.  $A = 2.0 \text{ in.}^2$  and  $E = 30.0 \times 10^6 \text{ psi}$ .

5. A triangular truss structure, shown in Figure P7.4, is to be used for mounting an ATN buoy at the top. Assuming the wave and current load acting at the top node D to be equal to 2500 lb. and that the points A, B, and C are fixed against displacements, determine the displacements at D. Let  $A = 3.0 \text{ in.}^2$  and  $E = 30 \times 10^6 \text{ psi}$ .
6. The frame shown in Figure P7.5 is subjected to a distributed load acting on the top. It is also subjected to a horizontal load of 600 lb., as shown in the figure. Compute (i) displacements at B and C, treating AB and BC as two beam elements; (ii) internal forces and moments acting in the tow members; and (iii) the maximum stresses in the beam AB. Use a 16 in.  $\times$  57 lb. wide flange section for the beams.  $E = 30 \times 10^6 \text{ psi}$ .



**FIGURE P7.4** Triangular space truss. (From R.C. Hibbeler, 2006. *Structural Analysis*, Pearson Prentice Hall, Upper Saddle River, NJ, p. 130. With permission.)



**FIGURE P7.5** Plane frame. (From R.C. Hibbeler, 2009. *Structural Analysis*, Pearson Prentice Hall, Upper Saddle River, NJ, p. 397. With permission.)

7. A simplified offshore structure, consisting of four steel cylindrical legs of diameter (outside) 3.5 ft. and of wall thickness 1.5 in., is shown in Figure P7.6a and b. The horizontal braces connecting the four columns at their upper ends rigidly are 2.5 ft. thick (0.50-in. wall thickness). At the deck level, the platform is supporting a rig and some additional equipment weighing 160.0 kips; the four sides of the structure are identical to the diagram given in Figure P7.6a. During a winter storm condition, the whole structure is subjected to a wind loading of 10.0 kips and a wave load of 50.0 kips and is considered to act in a simplified manner as shown in Figure P7.6b. In addition to the weights on the deck, the self-weight of the deck is determined to be 60.0 kips. The foundation support is assumed to provide a hinged support as shown in Figure P7.6b. Determine the displacements at the deck bracings level and the maximum stresses in the members of the structure;  $E = 30 \times 10^6$  psi.
8. The concrete cylindrical structure of wall thickness 1.5 ft., shown in Figure P7.7, is installed in shallow waters of depth 15 ft. It is acted upon by an Airy's wave of height 8.0 ft. and period 10 s. The outside diameter of the concrete member is 5.0 ft., and the wall thickness is 1.00 ft. Assume that  $x = 0.0$  and  $\omega t = 8.0$  for the maximum force on the tower, considering both the drag and inertia forces. Assume  $C_D = 1.0$  and  $C_I = 2.0$ . (a) Considering one beam element (25.0 ft. long) for the representation of the tower for stiffness analysis, determine the maximum forces experienced by the tower at its base. Also find its response at the top of the tower. (b) For the purpose of analysis, assume that the part of the tower,

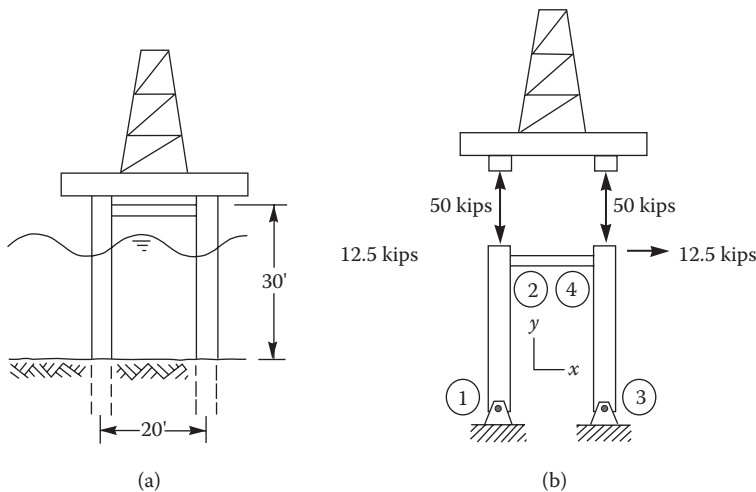


FIGURE P7.6 (a) Simplified elevation of an offshore tower. (b) Simplified force transmission in the tower.

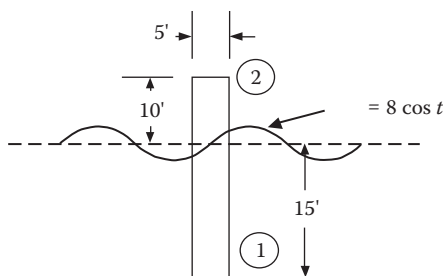


FIGURE P7.7 Offshore structure.

below the sea bed, is to be replaced by an equivalent free-standing cylindrical tower of the same diameter and 3.0 ft. long, which is fully fixed at its base and elastically connected to the tower above; assume that the wave force acts only on the portion exposed to wave action. Using two beam elements (each 12.5 ft. long) for modeling the tower, compute the wave forces, moments, and responses of the tower at the respective nodal points 1 and 2, located at the bottom.  $E_{\text{concrete}} = 20 \text{ GPa}$ .

9. Determine equivalent joint loads, for the concrete cylindrical vertical offshore structure shown as 1-2-3 in Figure P7.8, assuming an Airy's wave of height 35 ft. and length 500 ft. in a water depth of 120 ft. The outside diameter of the member is 10.0 ft. Assume that  $x = 0$ ,  $t = 5.8$ ,  $C_D = 1$ , and  $C_I = 2.96$ .
10. For the four-legged steel structure shown in two dimensions in Figure P7.9, determine the maximum horizontal force and associated time  $\omega t$ , arising from Airy's wave of height 12 ft. and length 300 ft. The water depth is 60 ft. Assume that  $C_D = 1$  and  $C_I = 2$ . All four faces of the structure are identical. The outside diameter of each leg is 2.75 ft.
11. A cylindrical buoy, shown in Figure P7.10, is ballasted with weights such that the buoy has a low center of gravity. Assuming  $v$  to be the vertical displacement of the buoy and  $m$  to be the mass of the buoy, as it undergoes vertical motion, determine the dynamic equation of motion of the buoy. Use the added mass of the buoy. If the height  $T$  of the buoy is 1.0 m and it weighs 1.5 t, determine the natural period of the vertically oscillating buoy. The density of seawater is 1030.0 kg/m.

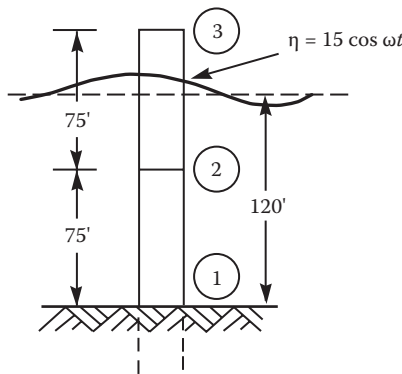


FIGURE P7.8 Cylindrical offshore structure.

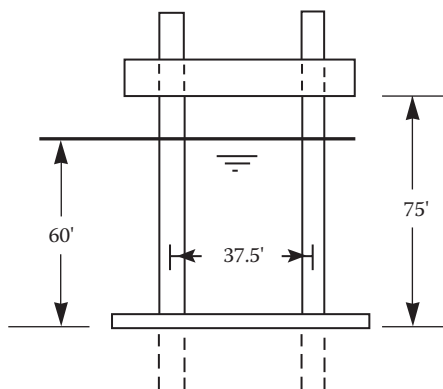


FIGURE P7.9 Four-legged offshore steel structure.

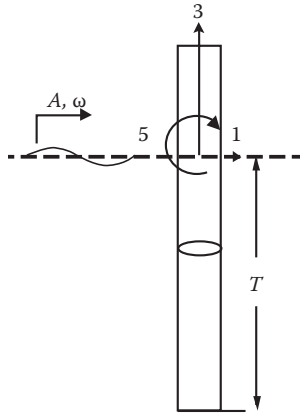


FIGURE P7.10 Cylindrical buoy.

12. Derive the heave (vertical) equation of motion for a spherical buoy that is in stable equilibrium on the surface of ocean water, when it is submerged to half its depth. Taking the mass of the sphere to be  $M$  and the radius of the sphere to be  $R$ , determine the natural frequency of vertical oscillation in water with, and without, considering the added mass of water. If the radius  $R = 0.75$  m and the seawater density is  $1030 \text{ kg/m}^3$ , what is the natural frequency of the oscillating buoy in hertz?
13. Write the equation of motion of the system shown in Figure P7.11 in terms of its mass, damping, and stiffness matrices.
14. Briefly explain the concept of (i) Duhamel’s integral and (ii) pseudo-velocity.
15. (a) Clearly explain the following terms: (i) geometric similitude; (ii) kinematic similitude; and (iii) dynamic similitude. (b) Explain the following flow parameters: (i) Reynolds number; (ii) Strouhal number, (iii) Keulegan–Carpenter; (iv) Ursell number; (v) Weber number; and (vi) roughness ratio.
16. A cantilever beam 10 m high and made of tubular steel cross section, 0.60-m diameter and 20-mm wall thickness, is installed in a water depth of 7.0 m and subjected to regular waves of period 9.5 s and wave height of 2.0 m. Find the maximum dynamic response of the platform. Mass density of the seawater =  $1030 \text{ kg/m}^3$  and that of steel =  $7680 \text{ kg/m}^3$ . Young’s modulus of steel = 206.0 GPa. Assume modal damping ratio of the platform to be 0.05. Model the cantilever to bend in its fundamental mode. Take  $C_d = 1.0$  and  $C_m = 1.8$ .
17. Compute the natural frequency of a light tower consisting of a single steel pile supporting a small rectangular structure containing batteries and control gear for the navigation

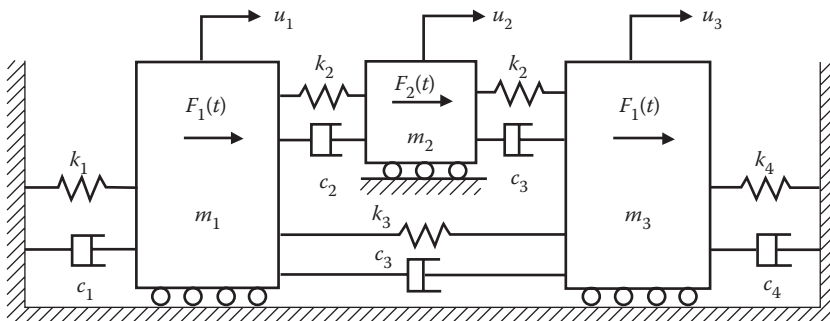
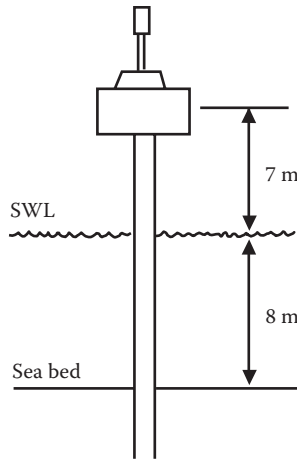


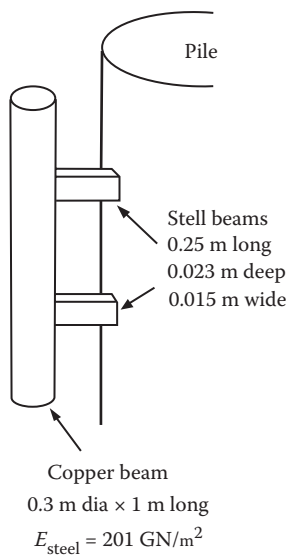
FIGURE P7.11 Lumped mass MDOF system.



**FIGURE P7.12** Light tower for an aid-to-navigation beacon.

beacon above, as shown in Figure P7.12. The data given are as follows: external diameter of pile,  $D = 324$  mm; wall thickness,  $t = 9.5$  mm; water depth,  $d = 8$  m; height of tip mass above SWL = 7 m; pile mass,  $m = 73.8$  kg/m; tip mass,  $M = 300$  kg; second moment of area of pile,  $I = 0.116 \times 10^{-3}$  m<sup>4</sup>; Young's modulus of pile,  $E = 205 \times 10^9$  N/m<sup>2</sup>; effective mass in water,  $m_w$ /unit dimension:  $m_w = 73.8$  (pile mass) + 74.8 (internal water) + 84.5 = 233.1 kg/m. In the absence of other data, the apparent pile fixity is taken as  $6D$  below the sea bed ( $\sim 2.0$  m), and the effective pile length = 17 m; neglect the soil mass contributing to the motion. Assume the light tower to behave as a cantilever beam, bending its fundamental mode of vibration.

18. Consider possible forms of motion for the anode, shown in Figure P7.13, fixed to the leg of an offshore tower. In this case, the movement normal to the line of the anode (and transverse to the plane joining the center lines of the anode and leg) is the most likely to be a problem and is considered. Other motions (i.e., in line with the anode) are possible but, for



**FIGURE P7.13** Anode fixed to the column of an offshore tower.



simplicity, are not considered here. Determine the fundamental frequency of the anode. The given data are as follows: (i) beams are fixed at junction with pile; (ii) added mass of water equal to the mass of the water = 71 kg; and (iii) mass of steel beams is neglected.

19. Compute the horizontal response of the light tower shown in Figure P7.14 (using the data given for Figure P7.21), subjected to a horizontal sinusoidal load of amplitude 330 N at a frequency of 0.33 Hz applied at the top (this load is approximately equivalent to a wave train of height 1.5 m and period 3 s). Compare the response of the tower if the above force is applied as a static load at the top of the tower.
20. Using the lumped mass method, calculate the natural frequencies of the light tower shown in Figure P7.15a and b, and find the mode shapes (use the data given for Figure P7.21). Lump the mass at the midpoint of the tower and at the top of the tower.

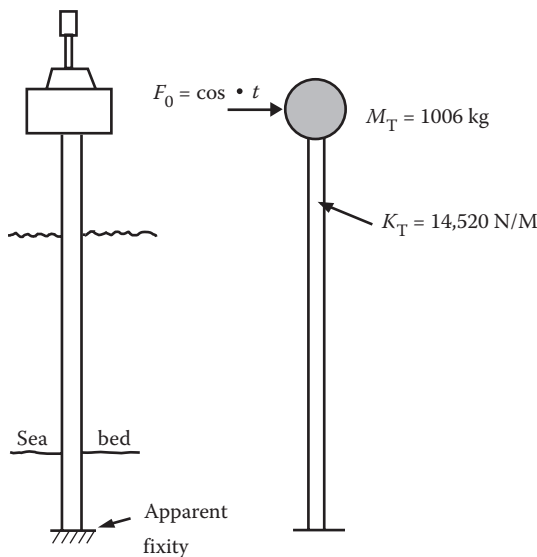


FIGURE P7.14 SDOF lumped mass model for the light tower shown on the right.

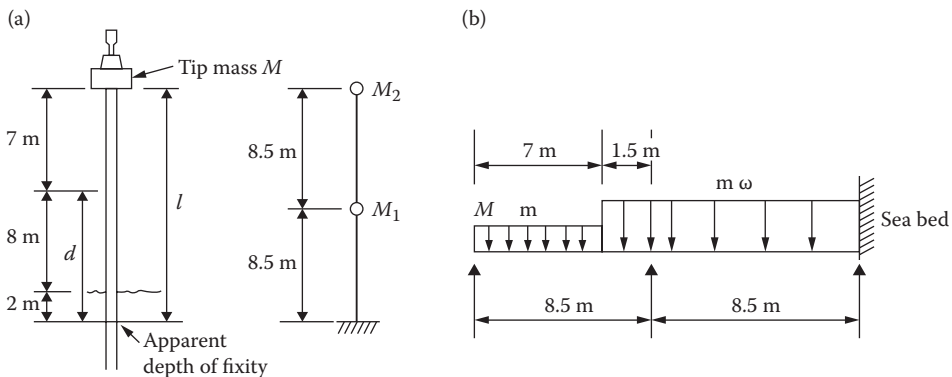


FIGURE P7.15 (a) Two-degrees-of-freedom lumped mass model for the light tower shown on the right. (b) Modeled forces acting on the modeled light tower.

21. (a) Using Rayleigh–Ritz energy methods, and approximate deflection functions, determine the natural frequencies of the light tower shown in Figure P7.14. The approximate functions are as follows: (i)  $y = [1 - \cos \{(\pi x/2L) - 1\}y_0]$ ; and (ii)  $y = ax^2(x - 4L)^2$ . (b) Using two-degree-of-freedom lumped mass methods, and a cantilever deflection function,  $y = a(x^4 - 4Lx^3 - 6L^2x^2)$ , determine the natural frequencies of the light tower.
22. A schematic of Exxon’s guyed tower is shown in Figure P7.16. Determine the fundamental frequency considering the tower and deck as rigid, and the guys represented by a linear spring. The tower is made up of four corner tubular members 2 m (OD) and 0.07 m thick (area = 0.4244 m<sup>2</sup>, mass density = 7850 kg/m<sup>3</sup>). The weight of the cross members is equal to that of the four corner members. Assume added mass equal to the displaced volume and volume of cross members equal to that of the four corner members [seawater density 10,065 kN/m<sup>3</sup>].
23. (a) For the TLP shown in Figure P7.17, assume the added mass = displaced water mass and show that the surge natural frequency is given by

$$\omega_n = \sqrt{\frac{g}{d} \left[ \frac{1 - \frac{W}{\Delta}}{1 + \frac{W}{\Delta}} \right]}$$

- where  $W$  = platform weight,  $\Delta$  = water displaced by the platform,  $d$  = water depth, and  $g = \frac{T}{l}$ .
- (b) Calculate the natural frequency using the equation in part (a).
  - (c) Check the stability of the TLP shown below.
  - (d) Determine the surge and heave frequencies.
  - (e) Determine the surge response amplitude value for a wave period of 15 s.
  - (f) Determine the spectral response value from the Pierson–Moskowitz wave spectrum.
24. For constructing a tanker terminal in a river estuary, a number of concrete cylindrical piles were sunk into the riverbed and left free standing. Each pile was 1 m in diameter and protruded 20 m out of the riverbed. The density of the concrete was 23.54 kN/m<sup>3</sup>, modulus of elasticity 14.11 GPa, and  $g = 9.81$  m/s<sup>2</sup>. Determine the fundamental frequency of vibration of a cylindrical pile.
  25. (a) Derive the differential equation for small motion of the mass  $m$  shown in Figure P7.18a. Consider the bar to be weightless. (b) A partially filled oil drum floats in the sea, as shown

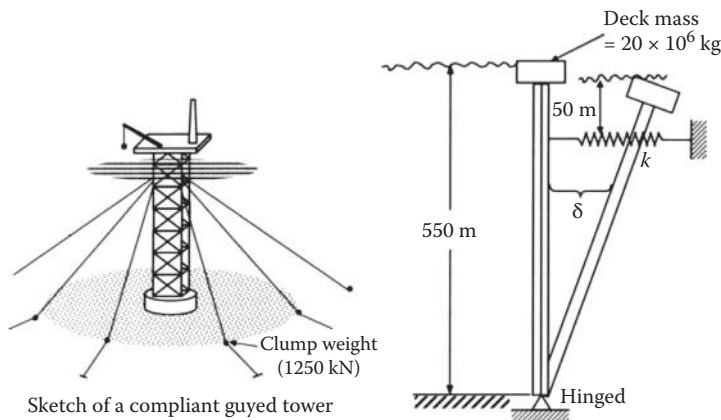


FIGURE P7.16 Exxon’s guyed tower and its lumped mass model.

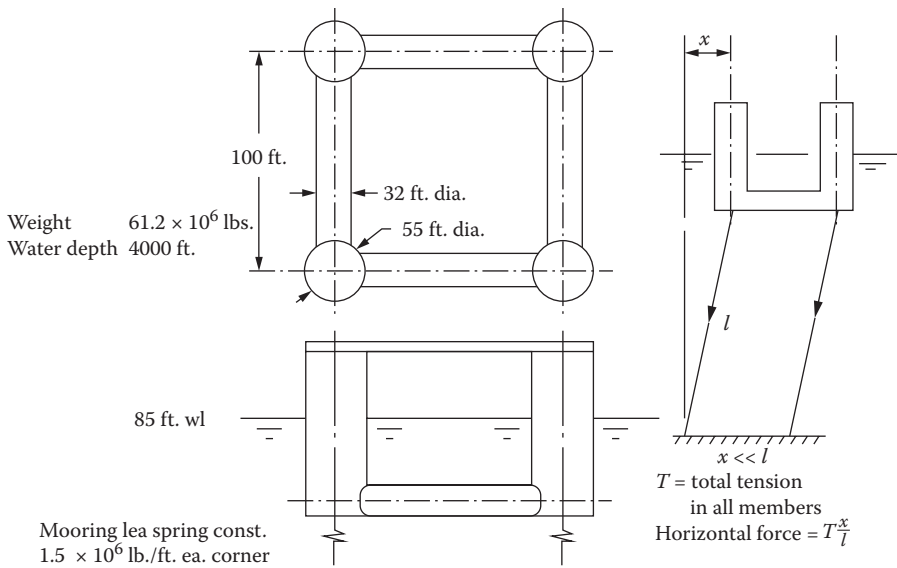


FIGURE P7.17 Tension leg platform.

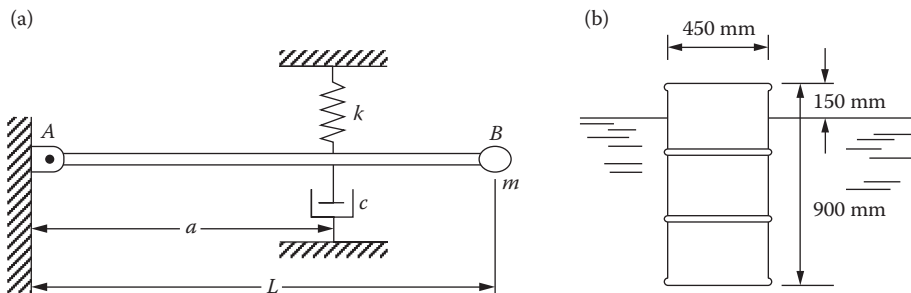


FIGURE P7.18 (a) Rigid beam with end mass; and (b) floating drum in the open seaway.

in Figure P7.18b. Determine the frequency of vertical motion as it bobs up and down. Seawater mass density = 1.025.

26. A square steel plate (2 ft.  $\times$  2 ft.  $\times$  0.4 in. thick), shown in Figure P7.19, is built-in at the bottom of a ship located at 21.0 ft. of water. The plate is subjected to a blast (concentrated) loading history at its center. Compute the approximate maximum displacement for the impulse loading shown using an SDOF model. Neglect damping.  $\nu = 0.3$ ,  $E = 30 \times 10^6$  psi.
27. (a) What are diffraction forces? When do they become significant? (b) Determine the transfer function, expressed in complex form, for the wave loading given by

$$\bar{q} = -\frac{\pi}{4} C_M \rho D^2 \frac{H}{2} \omega^2 \frac{\cosh k(z+d)}{\sinh kd} \sin \omega t$$

28. (a) Explain the need for using the Nyquist frequency for the optimum sampling interval. (b) What is spectral density? (c) Explain the concept of stationarity and ergodicity. (d) The variance for the deflection of an offshore structure was found to be 23.1 ft.<sup>2</sup>. Determine the maximum displacement based on a Gaussian process. (e) Explain the concept of a normalized eigenvector.

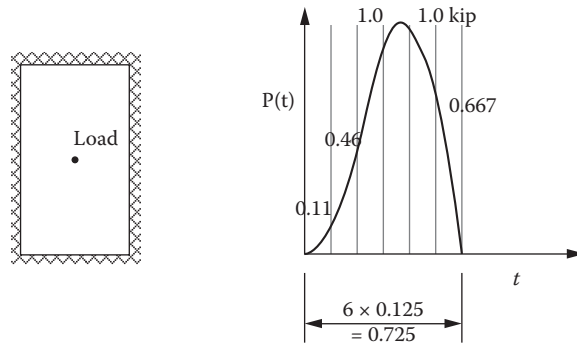


FIGURE P7.19 Steel plate at the bottom of a ship hull.

29. Determine the natural frequency and mode shapes of the two-degrees-of-freedom system of an offshore pile structure, shown in Figure P7.20.  $I = 0.116 \times 10^{-3} \text{ m}^4$ ;  $E = 205 \times 10^9 \text{ N/m}^2$ . (Hint:  $\text{Det}\{[k] - \omega^2[m]\} = 0$ .)
30. In order to cut down the natural frequency of an offshore platform [idealized as an undamped SDOF system ( $k_1, M$ )], a liquid sloshing tank [which may be treated as another spring-mass system ( $k_2, M$ )] is mounted on the deck. The schematic is shown in Figure P7.21. Determine the spring constant ( $k_2$ ) of the added system required to cut down the amplitude of the platform mass ( $M$ ) to zero.

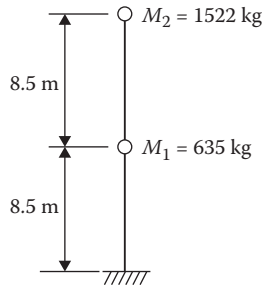


FIGURE P7.20 Lumped mass model of the two-degrees-of-freedom system.

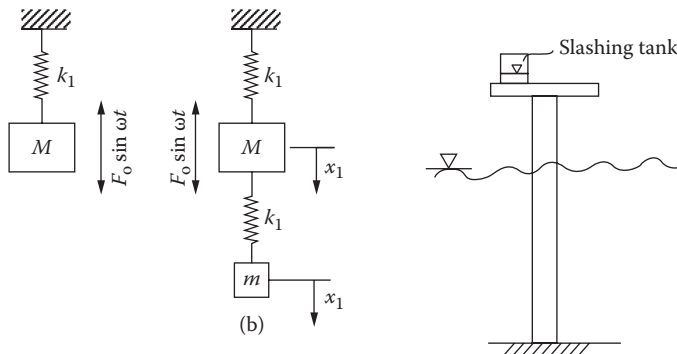


FIGURE P7.21 Offshore platform with a liquid sloshing tank.

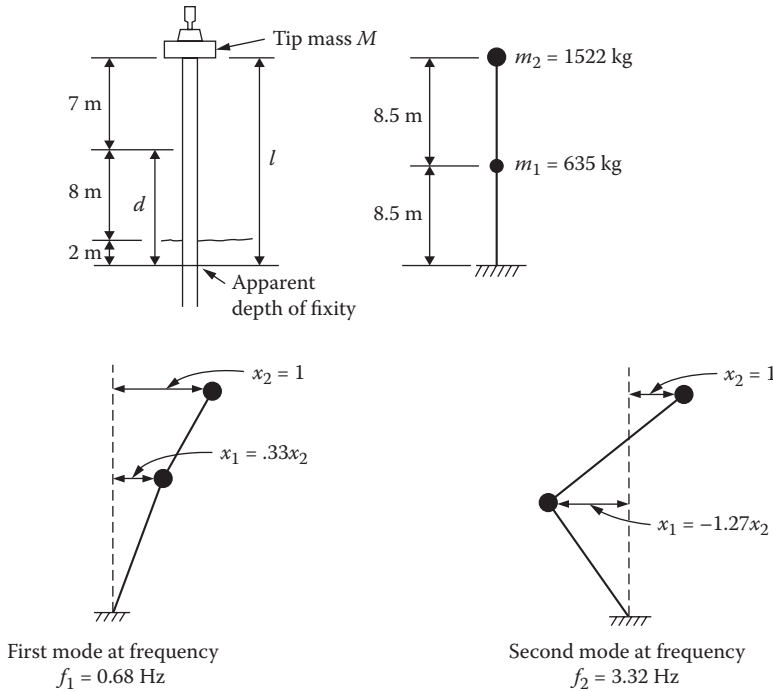


FIGURE P7.22 Idealized two-degrees-of-freedom model of an offshore platform.

31. The idealized two-degrees-of-freedom model of an offshore tower is shown in Figure P7.22. The loading is a JONSWAP spectrum given by

$$S_n(f) = \left[ \frac{ag^2}{16\pi^4 f^5} \right] \left\{ e^{-1.25 \left( \frac{f_m}{f} \right)^4} \right\} \gamma^\alpha,$$

where  $\alpha = 0.076 \left( \frac{\bar{f}_m}{2.84} \right)^{0.733}$ ,  $g = 9.81 \text{ m/s}^2$ ,  $f_m = \frac{1}{T} =$  wave frequency = peak frequency,  $\gamma$

$= 3.3$  (usually),  $a = e^{\left[ \frac{-(f-f_m)}{2(\sigma f_m)^2} \right]}$ ,  $\bar{f}_m = \frac{\left( \frac{H_s^2}{8} \right) (f_m^4)}{g^2 (5.2 \times 10^{-6})}$ , and  $\sigma = 0.07$  for  $\omega < 0.07$  and  $\omega > 0.09$ .

For a significant wave height of  $H_s = 1.5 \text{ m}$ ,  $T = 6 \text{ s}$ , determine the spectral displacement response at the top mass for a frequency of  $0.68 \text{ Hz}$ . ( $= f$ ), with  $E = 205 \times 10^9 \text{ N/m}^2$ .

$$[K] = \begin{bmatrix} 531 \times 10^3 & -166 \times 10^3 \\ -166 \times 10^3 & 66 \times 10^3 \end{bmatrix} \text{ N/m}$$

REFERENCES

1. C. Claus, E. Lehmann and C. Ostergaard, 1992. *Offshore Structures, Volume I: Conceptual Design and Hydromechanics*, Springer-Verlag, London, p. 32.
2. Surya3303. 2003. *Slideshow presentation by Surya3303 on Offshore Platform Design*. Available at <http://www.slideshare.net/surya3303/offshore-structures-presentation>, accessed on January 20, 2011.

3. B. McClelland and M.D. Reifel, 1986. *Planning and Design of Fixed Offshore Platforms*, Van Nostrand Reinhold Company, New York, p. 519.
4. M.H. Patel, 1990. Offshore Structures, in: *Marine Technology Reference Book*, Butterworths, London, pp. 2/50 (Figure 2.47).
5. N.D.P. Barltrop and A.J. Adams, 1991. *Dynamics of Fixed Marine Structures*, Butterworth Heinemann Ltd., Oxford, UK, p. 210.
6. A. Cerami, 1984. Stochastic seismic analysis of offshore towers, *Meccanica*, Volume 19, p. 236.
7. G.D.J. Hahn, 1985. *Dynamic Response of Offshore Guyed Towers*, Ph.D. thesis submitted to Rice University, Houston, TX, p. 128.
8. G.D.J. Hahn, 1985. *Dynamic Response of Offshore Guyed Towers*, Ph.D. thesis submitted to Rice University, Houston, TX, p. 134.
9. G.D.J. Hahn, 1985. *Dynamic Response of Offshore Guyed Towers*, Ph.D. thesis submitted to Rice University, Houston, TX, p. 130.
10. N.D.P. Barltrop and A.J. Adams, 1991. *Dynamics of Fixed Marine Structures*, Butterworth Heinemann Ltd., Oxford, UK, p. 4.
11. M.H. Patel, 1990. Offshore Structures, in: *Marine Technology Reference Book*, Butterworths, London, UK, pp. 2/50 (Figure 2.52).
12. N.D.P. Barltrop and A.J. Adams, 1991. *Dynamics of Fixed Marine Structures*, Butterworth Heinemann Ltd., Oxford, UK, p. 202.
13. N.D.P. Barltrop and A.J. Adams, 1991. *Dynamics of Fixed Marine Structures*, Butterworth Heinemann Ltd., Oxford, UK, p. 203.
14. American Petroleum Institute, 1993. *Recommended Practice for Planning, Designing and Constructing Fixed Offshore Platforms – Load and Resistance Factor Method (RP 2A – LRFD)*, 1st Edition, Washington DC, p. 50.
15. Rle 7.1, Fluids at Rest BSN-UST batch 2011. Available at <http://fluidsatarest.ash.com/archimedes.html>, accessed on September 21, 2010.
16. T.H. Dawson, 1983. *Offshore Structural Engineering*, Prentice Hall Inc., Englewood Cliffs, NJ, p. 138.
17. American Petroleum Institute, 1993. *Recommended Practice for Planning, Designing and Constructing Fixed Offshore Platforms – Load and Resistance Factor Method (RP 2A – LRFD)*, 1st Edition, Washington DC, p. 25.
18. J.G. Timar, 1978. *Lectures on Offshore Engineering, Institute of Building Technology and Structural Engineering*, Aalborg University, Aalborg, Denmark, Spring.
19. B. McClelland and M.D. Reifel, 1986. *Planning and Design of Fixed Offshore Platforms*, Van Nostrand Reinhold Company, New York, pp. 522; 526.
20. B. McClelland and M.D. Reifel, 1986. *Planning and Design of Fixed offshore Platforms*, Van Nostrand Reinhold Company, New York, pp. 532–535.
21. B. McClelland and M.D. Reifel, 1986. *Planning and Design of Fixed Offshore Platforms*, Van Nostrand Reinhold Company, New York, p. 536.
22. B. McClelland and M.D. Reifel, 1986. *Planning and Design of Fixed Offshore Platforms*, Van Nostrand Reinhold Company, New York, p. 539.
23. Course Notes EOC 6431, 2001. Offshore structures: Framed platforms, in: *Dr. D.V. Reddy's Course Material* Florida Atlantic University, Boca Raton, FL, 100 pp.
24. M.H. Patel, 1990. Offshore structures, in: *Marine Technology Reference Book*, edited by N. Morgan, Butterworths, London, pp. 2/48–2/49.
25. T.H. Dawson, 1983. *Offshore Structural Engineering*, Prentice Hall Inc., Englewood Cliffs, NJ, p. 37.
26. T.H. Dawson, 1983. *Offshore Structural Engineering*, Prentice-Hall Inc., Englewood Cliffs, NJ, p. 82.
27. T.H. Dawson, 1983. *Offshore Structural Engineering*, Prentice Hall Inc., Englewood Cliffs, NJ, p. 54.
28. AISC LRFD 2001. Design of Fully Restrained Moment Connections, PDH Course S154 at [www.PDHcenter.com](http://www.PDHcenter.com) and [www.PDHonline.org](http://www.PDHonline.org) AISC LRFD 3rd Edition. Available at <http://www.inti.gov.ar/cirsoc/pdf/acero/s154content.pdf>, accessed on October 9, 2010.
29. T.H. Dawson, 1983. *Offshore Structural Engineering*, Prentice Hall Inc., Englewood Cliffs, NJ, p. 52.
30. T.H. Dawson, 1983. *Offshore Structural Engineering*, Prentice Hall Inc., Englewood Cliffs, NJ, p. 70.
31. A. Mather, 1995. *Offshore Engineering, Part 3*, Witherby and Company Limited, London, p. 19.
32. T.H. Dawson, 1983. *Offshore Structural Engineering*, Prentice Hall Inc., Englewood Cliffs, NJ, p. 77.
33. G. Clauss, E. Lehmann and C. Ostergaard, 1992. *Offshore Structures, Volume 1, Conceptual Design and Hydromechanics*, Springer-Verlag, London, pp. 1–144.
34. Chakrabarti, 2008. *Hydrodynamics of Offshore Structures*, WIT Press, Southampton, UK, pp. 168–211.

35. B.M. Sumer and J. Fredsoe, 2007. *Hydromechanics of Vibrating Cylinders*, World Scientific Publishing Company (pvt.), Covent Garden, London, pp. 37–120.
36. T. Sarpkaya, 2010. *Wave Forces on Offshore Structures*, Cambridge University Press, New York, pp. 109–171.
37. H.E. Saunders, 1957. *Hydrodynamics in Ship Design*, The Society of Naval Architects and Marine Engineers, New York, p. 57; 59.
38. MIT Open Course Ware, 2011. Naval Civil Engineering Laboratory in Drag (Physics). CBS Interactive Inc. Available at [http://www.search.com/reference/Added\\_Mass](http://www.search.com/reference/Added_Mass).
39. C.E. Brennen, 1982. *A Review of Added Mass and Fluid Inertial Forces*, Report CR 62.10 (N62583-81-MR-554), Naval Civil Engineering Laboratory, Port Hueneme, CA, 50 p.
40. N. Haritos, 2007. Introduction to the analysis and design of offshore structures – An overview, *Electronic Journal of Structural Engineering (EJSE) Special Issue: Loading on Structures*, p. 59.
41. Wybren de Vries, 2009. *Compliant Bottom Mounted Support Structure Types*, Upwind deliverable WP4.2.4 Report on compliant bottom mounted support structure types, Project funded by the European Commission under the sixth (EC) RTD, Project UpWind, Contract # 019945 (SES6), p. 15.
42. Wybren de Vries, 2009. *Compliant Bottom Mounted Support Structure Types*, Upwind deliverable WP4.2.4 Report on compliant bottom mounted support structure types, Project funded by the European Commission under the sixth (EC) RTD, Project UpWind, Contract # 019945 (SES6), pp. 16 and 17.
43. P. Woodburn and P. Gallagher, 2003. *EXPRO-CFD: Progress in Fluid Structure Interaction*, MARNET-CFD Final Meeting, 20th–21st March 2003, p. 3.
44. P. Le Tirant, 1979. *Seabed Reconnaissance and Offshore Soil Mechanics*, Editions Technip 27, Paris, France, p. 401.
45. Imported from Internet Resources, 2011. *Multi-Degree-of-Freedom Vibration: Introductory Topics*, pp. 516–517.
46. Single Degree-of-Freedom Systems. Available at [www.efunda.com/formulae/vibrations/sdof\\_intro.cfm](http://www.efunda.com/formulae/vibrations/sdof_intro.cfm).
47. J.W. Smith, 1988. *Vibration of Structures: Applications in Civil Engineering Design*, Chapman and Hall, New York, p. 71.
48. R.W. Clough and J. Penzien, 2003. *Dynamics of Structures (Chapters 3–7, 12, 13, 24 and 25)*, Third Edition, McGraw-Hill Book Company, New York, pp. 176–207; 482–517.
49. R.R. Craig, Jr., 1981. *Structural Dynamics: An Introduction to Computer Methods (Chapters 3–8, 13–15)*, John Wiley & Sons, New York, pp. 49–186, 295–380.
50. T.H. Dawson, 1982. *Offshore Structural Engineering*, Prentice Hall Inc., Englewood Cliffs, NJ, p. 82.
51. R.C. Hibbeler, 2006. *Structural Analysis*, Pearson Prentice Hall, Upper Saddle River, NJ, p. 130.
52. R.C. Hibbeler, 2009. *Structural Analysis*, Pearson Prentice Hall, Upper Saddle River, NJ, p. 397.





---

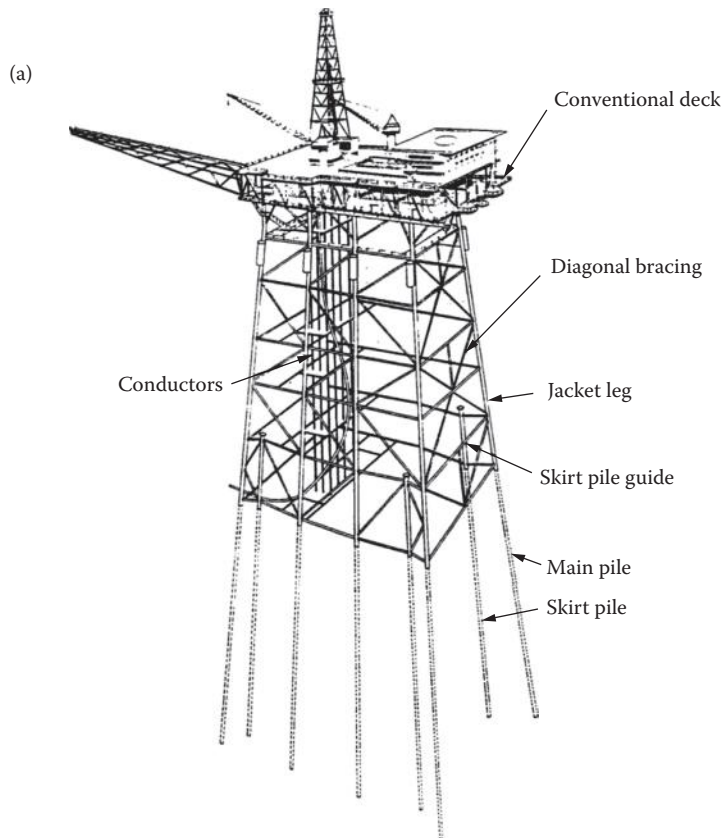
# 8 Analysis and Design Considerations for Framed Steel Offshore Platforms

## 8.1 INTRODUCTION

Steel offshore structures are most usually fabricated in the form of jacket (or template) structures, as discussed in Chapter 2. Typical jacket offshore structures, with the associated structural components, are shown in Figure 8.1, viz., steel framed offshore structures with (a) an integrated deck [1] and (b) a modular deck assembly [2]. Hence, the structural analyst and designer must take into consideration the various conditions that need to be considered in the analyses and designs of the platform components. The jacket is normally fabricated using hollow cylindrical steel members both for main legs and the cross/horizontal bracings. The interior jacket legs are usually vertical, whereas the exterior legs and the supporting piles are often inclined so as to provide a broader and more efficient base for resisting horizontal loadings; as given earlier in Chapter 7.4, the maximum inclination of these legs is limited to 1:7 (in each direction, leading to a batter of 1:5 for the corner legs) because of on-site installation difficulties; it is much smaller for deepwater steel structures. The vertical and inclined support piles provide vertical support for the deck loading and minimize the pullout forces generated by the horizontal and vertical wind and wave loads. The penetration depth of these piles, into the ocean floor, is generally more than 200 ft. to provide the required horizontal and vertical resistance against the applied wind/wave loads. The analysis and design of a modular structure should also reckon with the presence of a deck support frame, as well as the launch girders for the modular deck.

In carrying out a preliminary stress analysis on an offshore structure, it is often found to be sufficient to consider only two cases where the direction of wave motion is along each of the principal horizontal axes of the structure and limit attention to a two-dimensional frame analysis, as indicated in Figure 8.2 [3]. Of course, when the geometry of the structure is complex as not to be amenable for two-dimensional modeling and subsequent analysis, or when more accurate results are desired, a complete three-dimensional structural analysis should be employed with the assumed wave directions. Such analyses (both preliminary and detailed) are readily carried out with fully automated general-purpose digital computer software packages such as ANSYS, ASAS, ABAQUS, ADINA, NASTRAN, SESAM, SACS, MAESTRO, GeniE, MARCS, and/or other specialized software packages (WAMIT with WAFRONT, AQWA, WINPOST, WINDOS, DYNFLOAT, VISUAL ORCAFLEX, VERSAT P3D, etc.) to determine the applied loadings, member sizes, and corresponding structural responses/stresses [4, 5].

The stress analysis described above generally requires that requisite considerations be given to the interaction of the structure with the support piles. This is especially important for soft-soil conditions, where large deflections and rotations of the piles and the connected structural elements may occur at the seabed. As explained in an earlier chapter (see Section 7.1), this effect may be treated by assuming equivalent free-standing short piles fixed at their base and having stiffness properties approximating those of the actual embedded piles. Inclusion of these additional structural elements into the overall structure then allows direct analysis of the structure by the



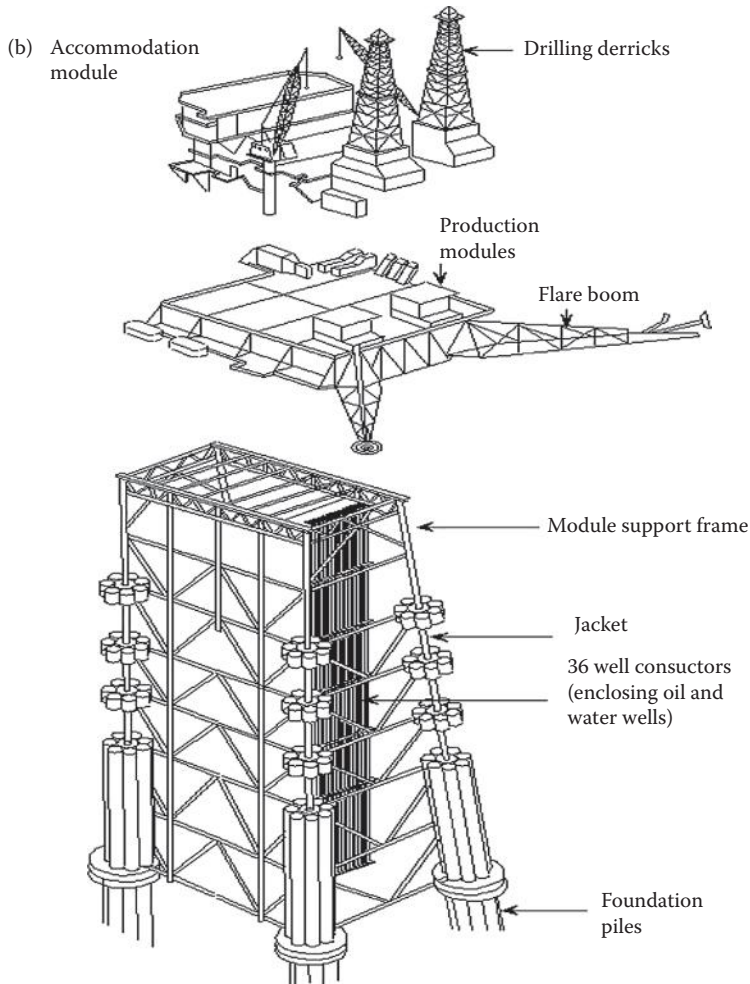
**FIGURE 8.1** Steel framed offshore structure. (a) With an integrated deck. (From C.A. Swanland, *Steel Piled Platforms*, Chapter 5 in *Overview of Offshore Engineering*, Course Notes, Held in Houston, TX, 72 pp., 1992.) (b) With a modular deck. (From Lecture 15 A—Offshore Structures—General Introduction, p. 12. Available at <http://www.scribd.com/doc/24246962/Offshore-Structure>.)

methods described in Chapter 7. The pile behavior may also be considered as a whole (instead of free-standing short piles), considering linear or nonlinear ( $p$ - $y$  curves) soil behavior and a detailed three-dimensional analysis carried out, utilizing the most relevant software identified from the list given earlier.

### 8.1.1 DESIGN CONSIDERATIONS

All the structural components of the platform should be investigated for all the possible loading scenarios listed below and then analyzed and designed for the most critical loadings imposed on them. The allowable load and resistance factor must be used for the various load combinations mentioned earlier in Section 6.2. The various design scenarios to be examined in this detailed investigation would include the following.

*Design for in-place conditions:* The platform structure should be designed to resist (i) all the gravity loads; (ii) wind, wave, and current loads; (iii) earthquake loads; and (iv) possible accidental loads occurring during its service life. Each mode of operation of the platform such as drilling, production, work-over, or combinations thereof must be considered. Moreover, the platform components must also be able to meet the fatigue requirements imposed on them by the dynamic ocean environment.

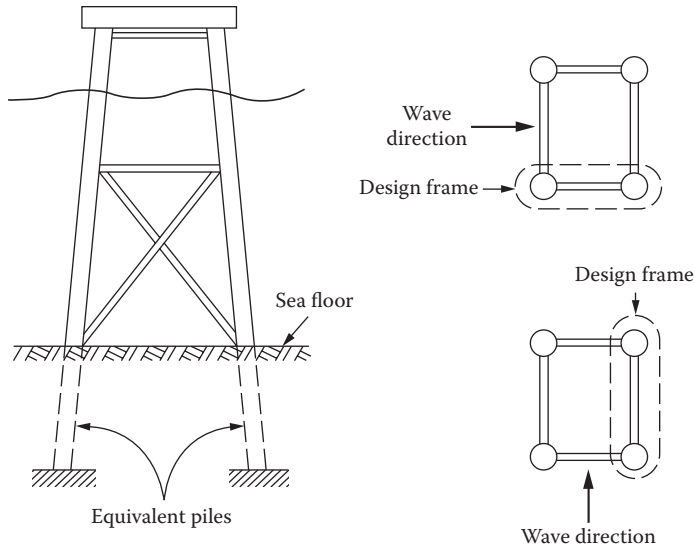


Note the launch girders in the jacket and the conventional pile guides

**FIGURE 8.1** (Continued) Steel framed offshore structure. (a) With an integrated deck. (From C.A. Swanland, *Steel Piled Platforms*, Chapter 5 in *Overview of Offshore Engineering*, Course Notes, Held in Houston, TX, 72 pp., 1992.) (b) With a modular deck. (From Lecture 15 A—Offshore Structures—General Introduction, p. 12. Available at <http://www.scribd.com/doc/24246962/Offshore-Structure>.)

The gravity loads should include (i) the total weight of platform including decks, jacket, piling, boat landings, barge bumpers, and all the other deck/jacket structural appurtenances; (ii) drilling package loads such as chemical package [mud pumps, active and reserve mud tanks, bulk bins, cementing units, drilling supplies (such as barite cement and casing), drilling water tanks, mixing hoppers, cranes and crane pedestals, pipe racks, etc.]; (iii) engine package loads such as generators, motor control panels and associated units, air compressor, distillation unit, diesel oil storage tank, etc.; (iv) personnel quarters and heliport; (v) production equipment loads; and (vi) miscellaneous loads such as hook loads, potable water loads, skid base loads, etc.

The wind, wave, and current loads to be considered in analysis have been given in Sections 6.3.2 through 6.3.5. The design premises should be assumed in such a way as to produce the maximum design forces exerted on the structure. The earthquake loads should be computed for the design earthquake specified for the site.



**FIGURE 8.2** Preliminary design considerations for structural analysis. (From T.H. Dawson, *Offshore Structural Engineering*, Prentice Hall, Englewood Cliffs, NJ, p. 156, 1983.)

*Design for construction conditions:* The platform should also be designed to resist the loads exerted on the platform structure during its fabrication, transportation, and installation. If the platform is to be relocated to a new site, then the loads resulting from removal from the present site, loading onto the tow barge, transportation, upgrading, and reinstallation should also be taken into account, in addition to the construction loads.

*Redundancy:* While designing any offshore structure, the presence of redundancy should be considered, and framing patterns that provide alternate load paths should be preferred over the one with only one path.

*Corrosion protection:* The corrosion protection of the structure should be considered according to the provisions of NACE RP-01-76 [6].

*Deformation loads:* While designing the structures, consideration should be given for the stresses induced by deformation loads such as temperature change, creep, relaxation, pre-stressing, uneven settlement, etc.

### 8.1.2 DESIGN CODES AND PROVISIONS

General guidance for the design of steel offshore structures can be found in the publications such as AISC/ANSI Code of Standard Practice for Steel Buildings and Bridges [7], CAN/CSA Offshore Structures Code S471 [8], CAN/CSA-S16.1—Limit States Design of Steel Structures [9], Structural Use of Steelwork in Building, Code of Practice for Fire Resistant Design—Parts 1 to 9 (BS 5950) [10], and Euro Code 3: Design of Steel Structures (EC) [11]. Specific recommendations for the design of steel offshore structures can be found in the publication Recommended Practice for Planning, Designing and Constructing Fixed Offshore Platforms—RP 2A-LRFD [12]; the procedures listed herein for analysis and design follow the detailed instructions given in the above API code. In order to illustrate the various platform components that need to be considered in the analysis and design of the steel jacket platform, the preliminary analysis and design of the platform components are given in the following sections.

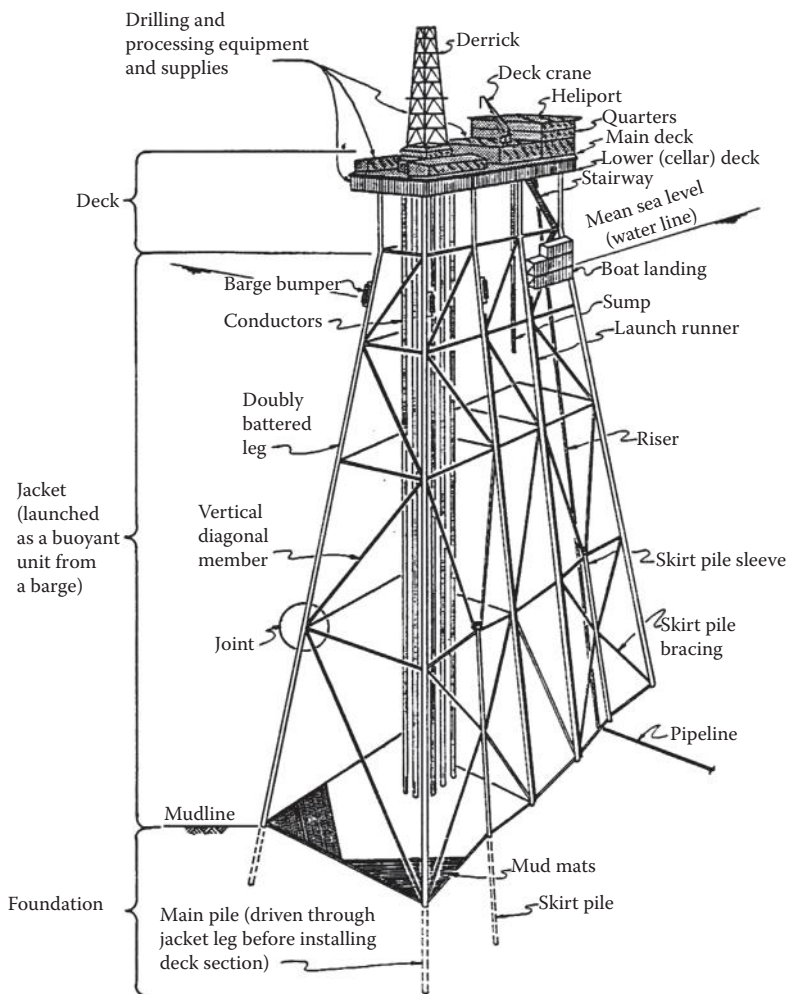
## 8.2 PRELIMINARY DESIGN CONSIDERATIONS FOR STEEL JACKET OFFSHORE STRUCTURES

### 8.2.1 TYPICAL PRELIMINARY DESIGN

The design process is illustrated through a solved problem, given below.

#### Example 8.1

Consider the steel template platform shown in Figure E8.1 [13] and determine the forces and stresses acting in (i) a typical equivalent pile member; (ii) a typical frame member; and (iii) a typical deck member. The preliminary dimensions are given in Table E8.1 [14]. The design wave has a height of 48.0 ft. and a period of 12.0 s. It is assumed to be propagating along the diagonal to the bottom of the deck of the template structure. The mean water depth under the storm conditions is 160 ft. The deck (with equipment) weighs 1000 kips, and wind force on the upper exposed part of the structure is equal to 100 kips (acting in the same direction as the wave). The computed loads on the deck from dead, live, wind, and wave loads are also given in Table E8.1. Take the loads



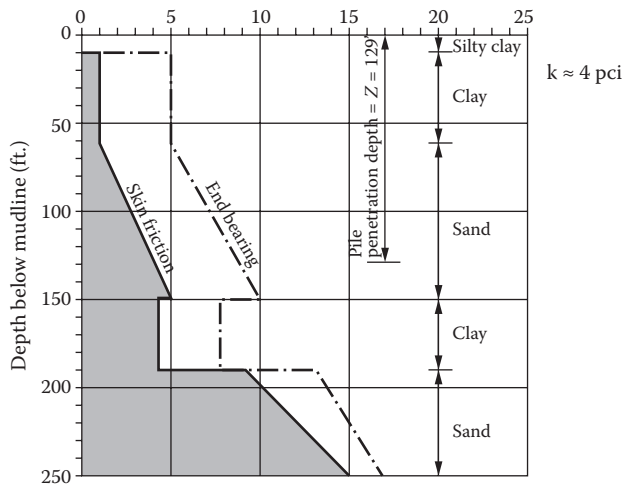
**FIGURE E8.1** Preliminary configuration of a steel template platform. (From Course Notes on General Design of Fixed Offshore Structures, University of Texas, Austin, TX, p. 3.1, 1979.)

**TABLE E8.1**  
**Member Properties and Loads**

	Diameter, $D$ (in.)	Wall Thickness (in.)
1. Column piles	48.0	1.125
2. Diagonal and horizontal braces	30.0	0.625
3. Vert. col. members.	48.0	1.375
Equivalent Loads and Moments Acting on the Platform Structure		Overturning Moments Acting on the Platform (ft. kip.)
1. Deck equipment and weight	-1000 kips, vertical (downward)	0.0
2. Live loads on the deck	-7000 kips, vertical (downward)	0.0
3. Generated buoyant loads and moments	+2086.1 kips, vertical (upward)	-1396.0 ( $M_x$ ), -2018.0 ( $M_y$ )
		At an angle (- 124.7°)
4. Wind loads along the platform diagonal (18.4°)	+94.9 kips ( $F_x$ ) +31.6 kips ( $F_y$ ) at an angle of 18.4°	-7.620.0 ( $M_x$ ) +21,824.0 ( $M_y$ ) at an angle of 108.4°
5. Wave loads along the platform diagonal; current load exerted by 3.0 ft./s speed current	+1,413.8 kips ( $F_x$ ) +469.9 kips ( $F_y$ ) at an angle of 18.4°	-54,940.0 ( $M_x$ ) +165,757.0 ( $M_y$ ) at an angle of 108.3°
6. Dead load of the other structural members	-3222.0 kips, vertical (downward)	+2110.0 ( $M_x$ ) +3051.0 ( $M_y$ ) at an angle of +55.3°

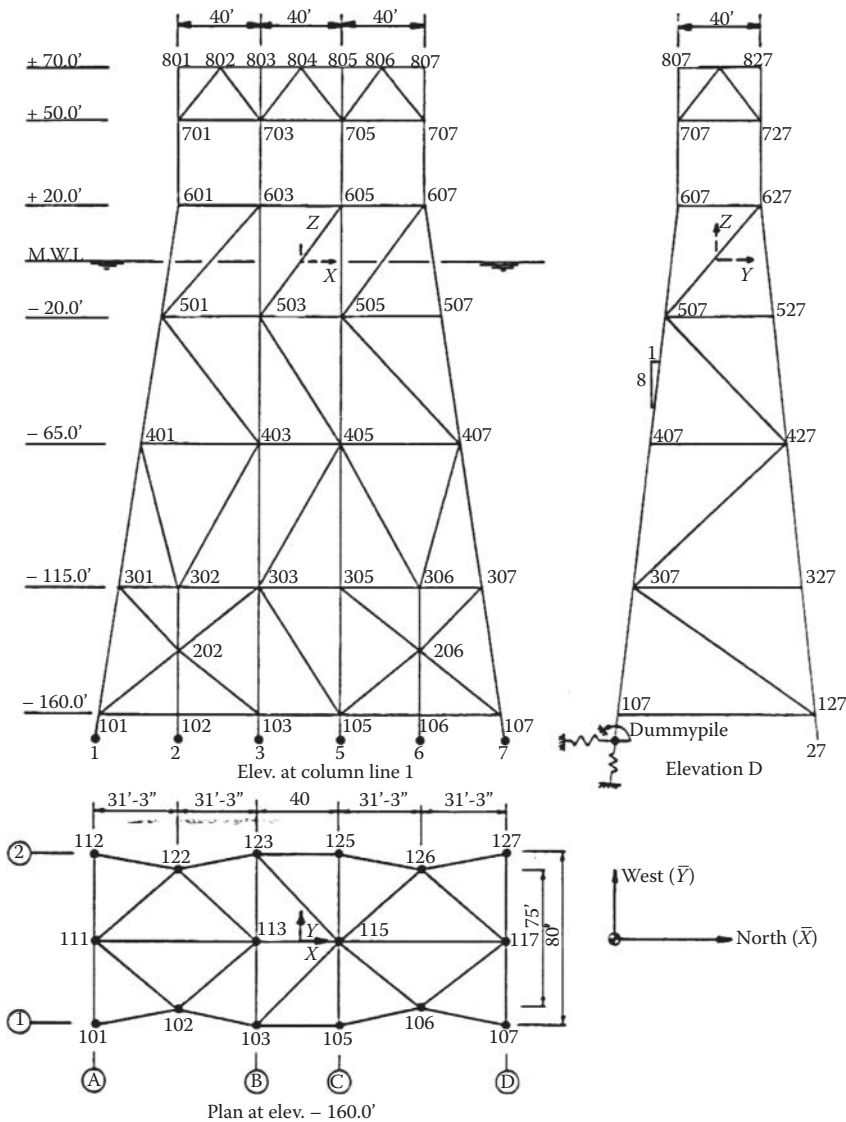
Source: Course Notes on General Design of Fixed Offshore Structures, University of Texas, Austin, TX, pp. 4.24-4.25, 1979.

Note: The diagonal angle between the top deck diagonal (bottom of the top deck) and the  $x$ -axis =  $\tan^{-1}(40/120) = 18.43^\circ$  to the  $x$ -axis.



**FIGURE E8.2** Ultimate unit skin frictional strength and end bearing strength of the soil, below the mudline (values in ksf units). (From Course Notes on General Design of Fixed Offshore Structures, University of Texas, Austin, TX, p. 3.5, 1979.)





**FIGURE E8.3** Finite element model of the steel jacket template. (From Course Notes on General Design of Fixed Offshore Structures, University of Texas, Austin, TX, p. 4.4, 1979.)

acting on the top of the pile to be that on the equivalent pile, carry out a pile analysis on the pile, and determine the embedment depth of the pile. Compare the embedment length obtained in this procedure with that given in API code provisions. Use the soil data for the embedded pile to be represented by the soil friction and end bearing strength data given in Figure E8.2 [15]. Take the equivalent pile length to be given by the guidelines in Sections 4.4.2 and/or 7.2.1. The details of the finite element model, used in the analysis, are shown in Figure E8.3 [16].

## 8.2.2 MINIMUM EMBEDMENT LENGTH OF PILES (OF COLUMNS)

### 8.2.2.1 Embedment Length

Assuming that all the 12 piles of the steel template structure share in carrying the loads exerted on the platform, the loads exerted on the piles can be obtained by computing the vertical pile reactions

(at the bottom of the column members) due to the vertical and horizontal loads (given in Table E8.1) acting on the structure. This can be achieved by taking moment equilibrium of the forces acting on the platform, about its centroid, in the  $x$ - $z$  or  $y$ - $z$  planes.

Refer to the earlier calculations shown in Figure E7.1 (Section 7.4).

Vertical loads applied on the top of piles (see Table E8.1; assumed to be distributed equally all over the surface area of the platform, and shared equally by all the column-pile members interacting with the seabed)  $= (-1000.0 - 7000 + 2086.1 - 3222.0)/12 = (-9135.9)/12 = -761.33$  kips (– sign indicates that the force is compression)

Assume reactions  $R'_{2A}$ ,  $R'_{2B}$ ,  $R'_{2C}$ , and  $R'_{2D}$  to be the reactions produced due to forces acting along the  $x$ -direction. Also the reactions  $R'_{S3}$  and  $R'_{S4}$  are the reactions produced in the secondary piles due to forces acting along the  $x$ -direction. From basic considerations of Figure E7.9, and taking moments on the  $y$ - $z$  plane,

$$R'_{2B} = (-R'_{2C}) = (R'_{2A})(20.0/82.5) = (0.2424)R'_{2A} \text{ or } (-0.2424)(R'_{2D})$$

Also,

$$R'_{S3} = (-R'_{S4}) = (R'_{2A})(51.25/82.5) = (0.6212)R'_{2A} \text{ or } (-0.6212)(R'_{2D}).$$

Moreover, let the reactions  $R''_{2A-left}$ ,  $R''_{2A-right}$ ,  $R''_{2B-left}$ ,  $R''_{2B-right}$ ,  $R''_{2C-left}$ ,  $R''_{2C-right}$ ,  $R''_{2D-left}$ , and  $R''_{2D-right}$  be the reactions produced by the forces acting along the  $y$ -direction; similarly,  $R''_{S3-left}$ ,  $R''_{S3-right}$ ,  $R''_{S4-left}$ , and  $R''_{S4-right}$  are the reactions produced in the secondary piles due to forces acting in the  $y$ -direction. Hence,

$$\begin{aligned} (-R''_{2A-left}) &= R''_{2A-right} = (-R''_{2B-left}) = R''_{2B-right} = (-R''_{2C-left}) = R''_{2C-right} \\ &= (-R''_{2D-left}) = R''_{2D-right} \end{aligned}$$

Also,

$$\begin{aligned} (-R''_{S3-left}) &= R''_{S3-right} = (-R''_{S4-left}) = R''_{S4-right} = (-R''_{2A-left})(37.5/40) \\ &= (-0.938)R''_{2A-left} = (0.938)(R''_{2A-right}) \end{aligned}$$

Taking the moment of the horizontal forces about the  $y$ - $z$  plane (at the sea bottom; for the values of horizontal components of wind and wave forces acting on the platform, see Table E8.1),

$$(2 \times 2)R'_{2A}(82.5) + (2 \times 2)(0.2424R'_{2A})(20) + (2 \times 2)(0.6212R'_{2A})(51.25) = (1413.8)(115) + (94.9)(230).$$

Hence,

$$R'_{2A} = (184,380.0)/(476.74) = 386.75 \text{ kips (tension)}$$

$$R'_{2D} = -386.75 \text{ kips (compression)}$$

Similarly, for the forces acting on the  $x$ - $z$  plane, taking the moment of the forces gives

$$-(4 \times 2)R''_{2A-left}(40) - (2 \times 2)(0.938)R''_{2A-left}(37.5) = (469.9)(115) + (31.6)(230)$$



$$R''_{2A\text{-left}} = -(61,306.5)/(460.7) = -133.07 \text{ kips (compression)}$$

Hence, the *maximum vertical compressive load* acting on the corner pile is

$$= R_{2D\text{-left}} = \text{Vert. load} + R'_{2D} + R''_{2D\text{-left}} = -761.33 - 386.75 - 133.07 = -1,281.15 \text{ kips}$$

Considering the horizontal shear loads at the base of the tower (assuming it to be distributed equally at all the column base locations),

$$H_{\text{shear at A}} = (1500.0 + 100.0)/12 = 133.33 \text{ kips}$$

$$H_{\text{shear at A}} \text{ perpendicular to the pile} = 133.33\{\sin(18.4)\} = 42.09 \text{ kips}$$

$$H_{\text{shear at A}} \text{ along the pile} = (133.33)\{\cos(18.4^\circ)\} = 126.51 \text{ kips}$$

The pile has a double batter of 1:8 in both directions. Resolving the vertical reactions and the horizontal shears, acting on the corner pile, the maximum normal compressive load and shear load acting on the column can be computed:

$$R_{D\text{-max}} = (1281.15)[8/\sqrt{(66)}] + (126.51)[2/\sqrt{(66)}] = 1261.59 + 31.14 = 1292.73 \text{ kips}$$

$$\text{Maximum shear force on the pile (perpendicular to the pile)} = [ \{(1281.15)(2/\sqrt{(66)}) - (126.51)$$

$$\{8/\sqrt{(66)}\}^2 + (42.09)^2\}^{(1/2)} = 195.41 \text{ kips}$$

$$\text{Maximum axial compressive load on the pile} = 1292.73 \text{ kips}$$

$$\text{Factored ultimate bearing capacity load for pile design} = (1.5)(1292.73) = 1939.10 \text{ kips}$$

According to Section 4.5.2.2, Equation 4.30, the bearing capacity of a pile is given as

$$Q = Q_s + Q_p = \sum_{i=1}^n f_i A_{si} + q A_p \quad (\text{E8.1})$$

with  $n$  = the number of diametral variations present in the pile.

Let  $h$  be the depth of embedment. Use the actual on-site measured soil strength data given in Figure E8.2 for the pile of diameter 48 in.

Assuming  $h$  to lie at the bottom of the second clay layer (at 190.0 ft. below the seabed),  $1939.10 \geq (\pi)(48/12)[(1.0)(60.0 - 10.0) + \{(1/2)(5.0 + 1.0)\}(150.0 - 60.0) + (190.0 - 150.0)(4.0)] + (\pi/4)(4)^2(8) = (12.57)(50.0 + 270.0 + 160.0) + (100.53) = 6,134.1$  kips. Hence, the depth of penetration needed is much less than this.

Assume the pile to be embedded to a depth of  $h$ , reaching the bottom of the first sand layer (at 150.0 ft., from the top):

$$1939.10 = (\pi)(4.0)[(1.0)(60.0 - 10.0) + (1.0)(h - 60.0) + (1/2)(4.0)\{(h - 60.0)/(90.0)\}(h - 60.0)] + (\pi/4)(4)^2(10) = (4\pi)[50.0 + (h - 10.0) + (2/90)(h - 60)^2] + 125.66.$$

Solving one obtains an embedment depth of 77.5 ft. for the pile. Take  $h = 78.0$  ft.

In order to check whether the short equivalent pile height is smaller than this embedment depth of piles, the available equations are used for the purpose.

### 8.2.2.2 Equivalent Short Pile Length

- (i) Using the short equivalent pile relationship given by Equation 4.32, the equivalent short pile height  $h_1$  is given by

$$h_1 = 1.4 \sqrt[4]{(EI/k_s)} \quad (\text{E8.2})$$

for piles in preloaded clays, where  $k_s$  is the subgrade modulus for clay  $\approx 67.0c_u$ , and  $c_u$  is the undrained shear strength of clayey soil. Also  $(3D) < h_1 < (8.5D)$ , where  $D$  is the outer diameter of the pile.

$$D = 48.0 \text{ in.}; \text{ wall thickness} = 1.125 \text{ in. (see Table E8.1)}$$

$$I = (\pi/64)(48^4 - 45.75^2) = 45,528.81 \text{ in.}^4$$

Also, let  $k_s = (67)(4.0) \text{ lb./in.}^3$  (in Figure E8.2)

$$h_1 = 1.4 \sqrt[4]{(EI/k_s)} = (1.4)[\{(30)(10^6)(45,528.81)\}/268]^{(0.25)} = 374.06 \text{ in.} = 31.17 \text{ ft.} \sim 32.0 \text{ ft.}$$

- (ii) As per Figure 7.5, the given condition for short pile length is  $3.5D < h_1 < 8.5D$ , where  $D$  is the diameter of the structure. Assuming the soil to be very soft,  $7.0D < h_1 < 8.5D$ . The given diameter of the pile is 4.0 ft.; hence, 28.0 ft.  $< h_1 < 34.0$  ft.

Therefore, the computed length  $h_1$  of the short pile ( $h_1 = 31.17$  ft.) is within the approximately specified bounds of 28.0 ft.  $< h_1 < 34.0$  ft., and this seems to be ok.

### 8.2.2.3 Sufficiency of Selected Column Pile Section for Short Pile

Since the pile height, assumed in Section 8.2.2.2, considers the pile to be fixed at its bottom,

$$I = 45,528.81 \text{ in.}^4; A = (\pi/4)(48^2 - 45.75^2) = 165.67 \text{ in.}^2; \text{ and } E = (30.0)(10^6) \text{ lb./in.}^2$$

$$\text{Computed } h_1 = 32.0 \text{ ft.} = 384.0 \text{ in.}$$

$$\text{Maximum shear load on top of pile} = 195.41 \text{ kips}$$

$$\text{Bending moment at the fixed end of the pile} = (195.41)(384) = 75,037.44 \text{ kips in.}$$

$$\text{Computed maximum axial load in the pile} = 1292.73 \text{ kips}$$

$$\text{Maximum bending stress in the pile section} = (P/A) + (M)(D/2)/(I) = (1292.73/165.67) + (75,254.35)(48/2)/(45,528.81) = (7.80 + 39.67) \text{ ksi} = 47.47 \text{ ksi}$$

As per API code, section D.2.2, the resistance compression factor is 0.85. Hence, the required minimum yield strength of the offshore steel =  $(47.47/0.85) = 55.85 \text{ ksi} < 60.0 \text{ ksi}$  (the nominal yield strength of offshore steel).

The chosen section is OK.

### 8.2.3 TOP DECK ANALYSIS FOR IMPOSED LOADS

Considering the top deck shown in Figure E8.4 [17], the loads applied on the top deck members, as well as on its vertical support legs, will be dependent on the weights of drilling deck, production deck equipment, deck supplies, and others. Generally, a larger deck load will be used in the preliminary design for member sizing. From established conventions, it is known that the size of the vertical column below the deck is equal to the size of the main column of the steel jacket template; hence, the diameter of the vertical column members below the deck is also taken to be equal to 48.0 in. with a wall thickness 1.375 in.

A number of scenarios can be identified for the top deck analysis and design. The most commonly accepted scenarios consist of (i) the sufficiency of the vertical column to the top deck to resist the applied wind, wave, and gravity loads; (ii) a truss-type deck supporting the main deck of the steel jacket structure; (iii) flooring of the cellar deck consisting of beam and plate type construction; (iv) the flooring of the top deck, above the cellar deck, to be made up of beam and plate type construction; and (v) suitable jacket structure members. An alternate design to the beam and plate type floor construction is to consider the floor design to be made up of corrugated steel/composite panel floor.

### 8.2.3.1 Sufficiency of Vertical Column below Top Deck

The sufficiency of the vertical column members (below the deck) to resist the compressive, bending, shear, and hydrostatic pressure loads acting on the column members must be considered. The effects of buckling behavior and a possible load combination that will generate a critical load scenario must also be considered.

#### 8.2.3.1.1 Loads Acting on Column Member from Applied Deck Loads and Wave/Wind Loads

The applied loads on the platform are shown in Figure E8.4. The wave pressure profiles exerted on the jacket structure members are shown in Figure E8.5 [18].

The wave pressure exerted on the tower will be due to a nonlinear wave since (see Figure 3.31)  $(H/1gT^2) = [48.0/\{(32.3)(12)^2\}] = 0.0104$  and  $(d/1gT^2) = [160/(32.2)(12)^2] = 0.0345$ ; consequently, from Figure 3.31, the wave theory must be based on either stream function theory or Stokes' fifth-order wave theory. Using the stream function wave theory, the wave pressures (along with the current forces) have been numerically computed (with the wave crest profile located at the center of the platform—for the maximum wave load scenario). It can be seen that the wave–current pressure on the bottom portion of member (601–701) (see Figure E8.3) is given in Figure E8.5 as 250.0 psf; also the wave–current pressure load is acting up to a height of 15.0 ft. above the bottom of the member (say up to a height of 195.0 ft. above the seabed).

Using Figures E8.4 and E8.5, the horizontal load and moment acting on each column member (say 601–701) are calculated (wave–current pressure is assumed to be constant over the height).

Assume the total wind load to be acting at the center of the cellar deck (see Table E8.1 and Figure E8.3). Hence, bending moment at the base of the member (601–701) = bending moment (due to wind + due to wave–current interaction) =  $(100/8)(30.0 + 20.0/2) + (15)(1.0)(15/2) = 500.0 + 112.5 = 612.5$  kips ft.

$$\text{Factored moment} = (1.35)(612.5) = 796.25 \text{ kips ft.}$$

Vertical support reaction at the bottom of the member (601–701) = due to gravity loads acting on the portion above the mean sea level + reaction produced on the column due to wind and wave loads. One-third of the self-weight of structural members is assumed to act above the mean sea level.

$$\begin{aligned} \text{Vertical reaction due to gravity weights} &= (1/8)[7000.0 + 1000.0 + (1/3)(3222.0)] = 1134.3 \text{ kips} \\ \text{Factored load} &= (1.3)(1134.3) = 1474.9 \text{ kips} \end{aligned}$$

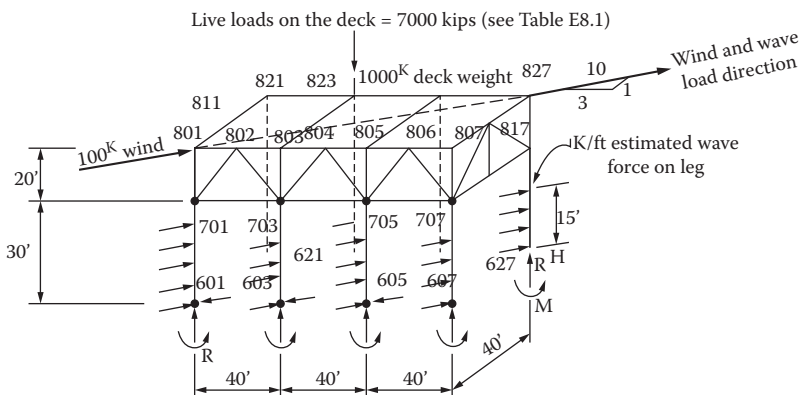
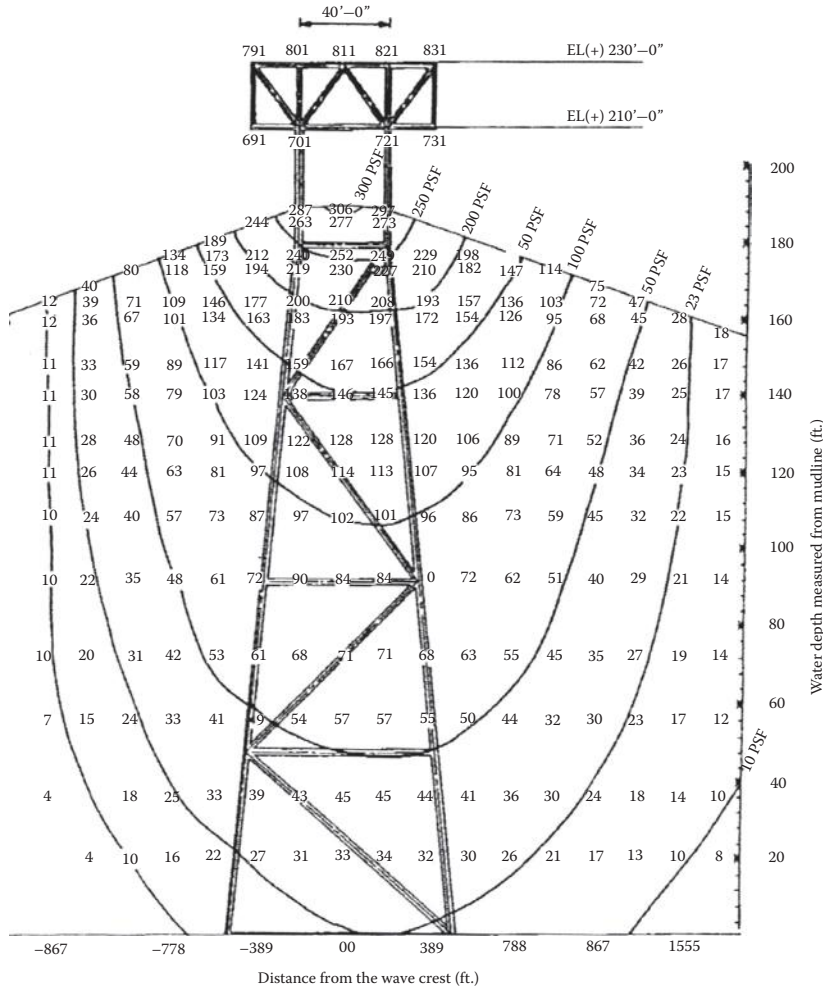


FIGURE E8.4 Applied loads on top deck. (From Course Notes on General Design of Fixed Offshore Structures. University of Texas, Austin, TX, p. 3.11, 1979.)



**FIGURE E8.5** Horizontal wave pressures due to the given wave and current profiles. (From Course Notes on General Design of Fixed Offshore Structures, University of Texas, Austin, TX, p. 4.20, 1979.)

Vertical compressive reaction produced on the leeward side of wave and wind forces = [(94.9)(30.0 + 20.0)/{(60.0)(4) + (20.0)(4)} + (31.6)(30.0 + 20.0)/{(40/2)(4 × 2)}] + [(15.0)(1)(8)(0.949)(15/2)/{(60.0)(4) + (20.0)(4)} + (15.0)(1)(8)(0.316)(15/2)/{(40/2)(4 × 2)}] = 14.83 + 9.88 + 2.67 + 1.78 = 29.16 kips

Maximum upward (compressive) factored reaction on the leeward column = 1474.9 + (1.35)(29.16) = 1512.81 kips

8.2.3.1.2 Global and Local Buckling Strength of Column Member

Outer diameter of column = 48.0 in.; radius of gyration = [(1/4)√(D<sub>o</sub><sup>2</sup> + D<sub>i</sub><sup>2</sup>)] = 0.35D = (0.35)(48) = 16.8 in.; length of the member = 30.0 ft. (see Figure E8.3). As per Table D.3.1 of the API code [19], effective length of factor = K = 1.5.

$$\lambda = (KL/r)(F_y/E)^{(0.5)} = [(1.5)(30.0)(12)/(16.8)][(60.0)/(30.0)(1000)]^{(0.5)} = 1.438 > \sqrt{(2.0)} [= 1.414]$$

$$F_{cn} = \text{permitted axial compressive strength of the column} = (F_y/\lambda^2) = 60.0/(1.438)^2 = 29.02 \text{ ksi}$$

$f_c$  = actual stress in the column member = [(maximum compressive reaction in the column)/(cross-sectional area)] = (1512.81)/(201.41) = 7.51 ksi (stress is much lower than the permitted value); hence, member size seems to be OK for global buckling.

Considering inelastic local buckling of the thin tube, the nominal inelastic buckling strength of the thin stressed skin of the tube =  $F_{xc} = F_y$ , since  $(D/t) = 34.91 \leq 60.0$ .

Hence, the column member seems to be safe against local buckling, since the actual stress in the tube is 7.30 ksi.

#### 8.2.3.1.3 Bending Strength of Tubular Members

Moment of inertia (of area) =  $(\pi/64)(48^4 - 45.25^4) = 54,776.80 \text{ in.}^4$

Actual bending stress due to factored loads,  $f_b = (M)(c)/I = (796.25)(12)(24)/(54,776.80) = 4.19 \text{ ksi}$

$D/t = 34.91$ ; it lies between  $1500/F_y (= 25.0)$  and  $3000/F_y (= 50.0)$ .

Nominal bending stress permissible =  $[1.13 - 2.58 (F_y D)/(Et)](Z/S)F_y$

Elastic section modulus =  $S = I/c = (54,776.80)/24 = 2282.37 \text{ in.}^3$

Plastic section modulus of a cylindrical section =  $Z = [(D_o^3 - D_i^3)/6] = 2989.97 \text{ in.}^3$

Nominal bending stress permissible =  $F_{bn} = [1.13 - (2.58)(60.0)(48)/\{(30)(1000)(1.375)\}](2989.37/2282.37)(60.0) = 74.65 \text{ ksi}$

As per the API code provisions,  $f_b < \Phi_b F_{bn} = (0.95)(74.65) = 70.91 \text{ ksi}$ ; hence, the section seems to be sufficient to safely resist the bending loads imposed on the column below the deck.

#### 8.2.3.1.4 Beam Shear

Horizontal shear in the column = 27.5 kips

Shear stress in the cross section =  $(2V/A) = (2)(27.5)/(207.35) = 0.265 \text{ ksi}$

Permissible shear stress in the column member =  $\Phi_v F_{vn} = (0.95)(F_y/\sqrt{3}) = 32.91 \text{ ksi}$

Actual stress is very low; hence, it is OK.

#### 8.2.3.1.5 Hydrostatic Pressure and Hoop Buckling

Hydrostatic pressure at the base of member 601–701 = (load factor)(weight density of seawater)(wave height above the bottom of the member) =  $(1.3)(64.0)(15.0) = 1248.0 \text{ psf} = 8.67 \text{ psi}$

Hoop stress =  $f_h = (p)(D)/(2t) = (8.67)(48.0)/(2 \times 1.375) = 151.33 \text{ psi}$  (very low)

As per API section D.2.5.2, permissible hoop stress =  $\Phi_h F_{hc}$ , where  $F_{hc}$  is the nominal critical buckling strength.

Elastic buckling stress of the tubular column member =  $(2C_h Et/D)$ , where  $C_h$  is dependent on the geometric parameter  $M = (L/D)\sqrt{\{(2D)/t\}}$ .

$M = \{(30)(12)/(48)\}[(2) \times (48)/1.375]^{(0.5)} = 62.67$ , which is greater than 55.86 [= 1.6( $d/t$ )]

Hence,  $C_h = (0.44)(t/D) = (0.44)(1.375)/(48) = 0.0126$ .

$F_{hc} = (2C_h Et/D) = (2)(0.0126)(30 \times 1000)(1.375)/(48.0) = 21.66 \text{ ksi} \leq (0.55)F_y (= 33.0 \text{ ksi})$

Permissible hoop stress =  $\Phi_h F_{hc} = (0.80)(21.66) = 17.33 \text{ ksi} > 151.55 \text{ psi}$ . Hence, the buckling strength is OK; no stiffening rings are needed.

#### 8.2.3.1.6 Combined Axial Compression and Bending Loads on the Column

The column member should satisfy the following three interaction conditions:

$$(f_c/\Phi_c F_{cn}) + (1/\Phi_b F_{bn}) \sqrt{\left[1.0 - \{(C_{my} f_{by})/f_c\}(\Phi_c F_{ey})\right]^2 + \left[1.0 - \{(C_{mz} f_{bz})/f_c\}(\Phi_c F_{ez})\right]^2} \leq 1.0 \quad (\text{E8.3})$$

$$1.0 - \cos[(\pi f_c)/(2\Phi_c F_{xc})] + [(f_{by}^2 + f_{bz}^2)]^{(0.5)} / (\Phi_b F_{bn}) \leq 1.0 \quad (\text{E8.4})$$

$$F_c < \Phi_c F_{xc} \quad (\text{E8.5})$$

As computed earlier,  $F_{xc} = F_y$ .

Since the member is a cylindrical member, the slenderness ratios  $\lambda_y$  and  $\lambda_z$  are the same.

$\lambda = (KL/r)(F_y/E)^{(0.5)} = 1.438$ . Hence,  $\lambda_y = \lambda_z = 1.438$  (computed earlier)

$F_{cn} = 29.02$  ksi; also  $\Phi_c = 0.85$

$f_c = 7.51$  ksi (computed earlier)

$(f_c/(\Phi_c F_{cn})) = \{7.51/(0.85 \times 29.02)\} = 0.3044$

$F_{bn}$  = nominal bending strength = 74.65 ksi (computed earlier); also  $\Phi_b F_{bn} = 70.91$  (computed earlier in Section 8.2.3.1.3)

$[1.0/(\Phi_b F_{bn})] = 1.0/70.91 = 0.014$ ; hence, the contribution from bending to this interaction effect is assumed to be negligible (since the actual bending stress in the column has been computed earlier to be = 4.19 ksi). Only axial compression effect predominates.

Hence, the above three equations are assumed to be satisfied.

The selected column member seems to be OK for the section analyzed in this part of the study.

### 8.2.3.2 Analysis and Design of Deck Framing Members

The deck of the offshore structure provides a suitable and sufficient workspace above the water surface, where drilling, production, residential, and other necessary operations can be safely carried out. In the process of achieving this, the various components of the deck such as deck floor, deck framing, and deck columns must transfer their loads safely to the steel jacket structure. The jacket substructure in its turn safely transfers the loads coming onto it to the foundation below. In order to achieve this safe load transfer, a number of deck system designs are available. In the present case, shown in Figure E8.6 [20], the load transfer from the deck to the jacket substructure is achieved by (i) using a beam and plate type construction for the top steel deck; (ii) longitudinal and transverse trusses that take the load from the top floor and transfer to the bottom floor of the deck through the tubular diagonal truss members; (iii) bottom flooring that provides a protected space to carry out some storage or other essential operations; and (iv) the supporting columns of the top deck, designed earlier in Section 8.2.3.1.

#### 8.2.3.2.1 Plate Floor for the Main Deck

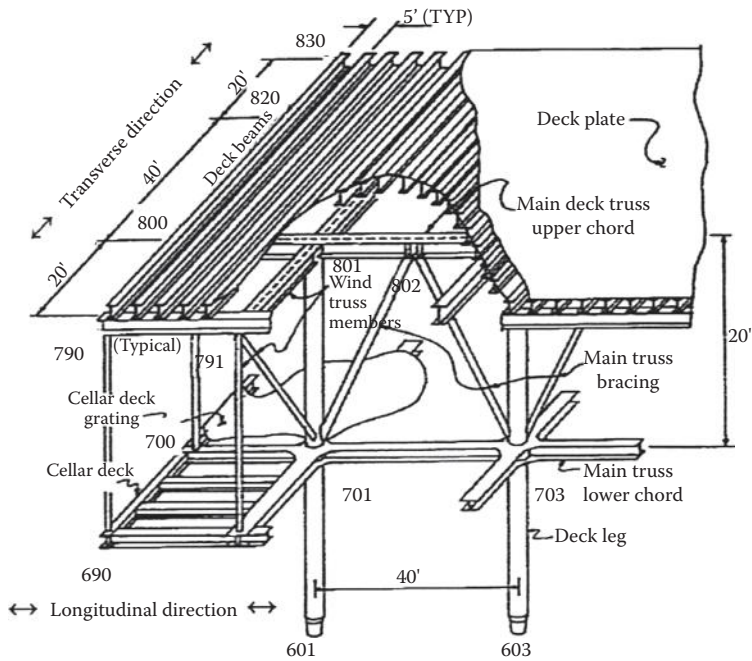
The loading details are provided in Sections 6.1.1 and 6.1.2, as well as in Tables 6.1 and 6.2. The dead loads acting on the floor are to be taken from the design dead loads given in Section 6.1.1; live loads are to be taken from Tables 6.1 and 6.2. The live load for the floor seems to be around 0.188 kips/ft.<sup>2</sup> (9.0 kN/m<sup>2</sup>). In addition, a concentrated live load of 1.1 kips is to be considered in design, distributed over an area of (1.0)(1.0) ft.<sup>2</sup>, at the center of the plate.

Considering a width of 1.0 ft. for the floor; the effective span for the floor (see Figure E8.7 [21]) is  $is = \ell = 5.0 - (8/12) = 4.333$  ft.

Considering a 0.625-in.-thick plate for the floor; the self-weight of plate =  $(0.625/12)(486)(1.0)(1.0) = 25.31$  lb./ft.<sup>2</sup>

Live load on the floor = 188.0 lb./ft.<sup>2</sup>

Factored distributed load per unit width of floor (see Section C.2 of the API code) = 1.3(dead load) + 1.5(live load) =  $q_f = (1.3)(25.31) + (1.5)(188.0) = 315.0$  lb./ft.<sup>2</sup>



**FIGURE E8.6** Deck structure with the cellar deck. (From Course Notes on General Design of Fixed Offshore Structures, University of Texas, Austin, TX, p. 3.11, 1979.)

Factored concentrated load =  $P_f = (1.5)(1.1) = 1.65$  kips; this load is assumed to be acting at the center of the plate.

Maximum bending moment acting at the center of the plate =  $(q_f \ell^2)/(12) + (P_f \ell/8)$  [approximate value] =  $[(315.0)(4.333)^2/12] + (1.65)(1000.0)(4.333)/(8) = 492.84 + 893.06 = 1385.90$  lb. ft./ft. = 1385.90 lb. in./in.

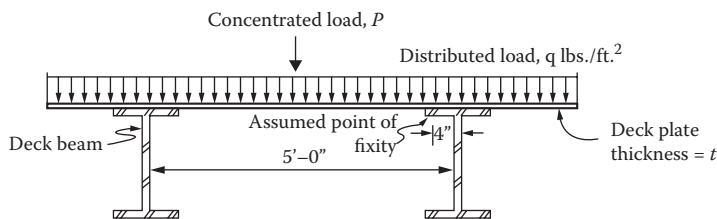
Using A36 steel, the resistance factor for bending (Section H.2 in the API Code) is = 0.85.

Permissible maximum bending stress =  $(0.85)(36.0) = 30.6$  ksi

$I = (1/12)(1)(t)^3 = t^3/(12)$ .

$M = (f_b)(I/c) = (30.6)[(t^3)/12]/(t/2) = 5.1 t^2$  kips in./in.

$t = [1.3859/5.1]^{(0.5)} = 0.520$  in. ~ 0.625 in.



**FIGURE E8.7** Plate and beam construction of main deck floor. (From Course Notes on General Design of Fixed Offshore Structures, University of Texas, Austin, TX, p. 3.14, 1979.)



8.2.3.2.2 Floor Beam for Top Deck Floor

The loading details are provided in Sections 6.1.1 and 6.1.2. The main deck loading details are shown in Figure E8.8 [21]. The transverse width of the floor plate that contributes to the beam loading is equal to 5.0 ft.

Using a W24 × 76 wide-flange I beam for the beam section, as per the calculations above,  $q_1 = (5)(0.315) + [(1.65/5)\{(1/2)(20/4 + 40/4)\}] + \text{self-weight} = (1.575 + 2.475) + 0.076 = 4.126 \text{ kips/ft}$ .

Maximum bending moment (over the interior support) =  $(q_1)(\ell^2)/10 = (4.126)(40)^2/10 = 660.16 \text{ kips ft}$ .

Required sectional modulus =  $(660.16)(12)/(30.6) = 258.88 \text{ in.}^3$

A wide-flange I-section of size W24 × 104 lb. gives the sectional modulus of 258 in.<sup>3</sup>

Hence, the section is OK.

8.2.3.2.3 Longitudinal Beam Supporting the Top Deck Floor Beams

The loading details are as shown in Figure E8.9. The top chord of the main longitudinal truss of the deck is assumed to perform two functions, viz., (i) being the compression upper chord of the truss, carrying only normal stresses, and (ii) acting as a bending member of the top deck to carry the load transmitted from the respective floor beams spaced at 5.0 ft. c/c intervals. The beam is assumed to be made up of two channel sections, placed back to back, and connected to the cylindrical diagonal chord members of the main truss; the channels are also properly stiffened at intervals to prevent the lateral buckling of the top chord member. In addition, due to the fact that the load transfer is mainly through truss action, the back-to-back channel beams are assumed to be hinged at every nodal point of the longitudinal truss of the deck.

Self-weight of the transverse beam is assumed to be the same as that of the floor beam, viz., W24 × 104 lb. = 104.0 lb./ft.

Load on each concentrated load acting on the top chord member =  $\{10.0 + (1/2)(40.0)\}(q_1) + \text{self-weight} = (30)(4.126) + (30.0)(0.104) = 126.9 \text{ kips}$

Since the joints are assumed to be hinge connected, the bending moment at the center of the span =  $(126.9)(20/4) + (2)(126.9)(5)(15)/20 = 507.6 + 951.75 = 1459.35 \text{ kips ft}$ .

Keeping the depth of the channel to be equal to 24.0 in. deep, flange width as 12.5 in., flange thickness of 1.0 in., and the web thickness as 0.75 in.,

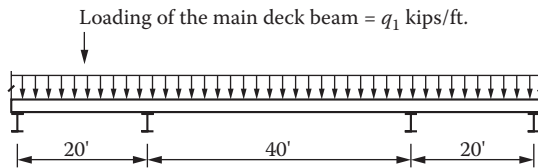


FIGURE E8.8 Loads on the main deck beam. (From Course Notes on General Design of Fixed Offshore Structures, University of Texas, Austin, TX, p. 3.14, 1979.)

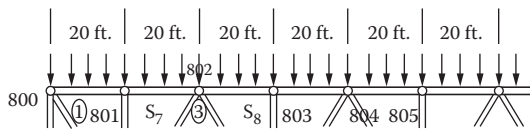


FIGURE E8.9 Loads acting on the top chord of the main transverse deck truss supporting the top and cellar decks.



Moment of inertia of the channel beam =  $(1/12)[(25 \times 24^3) - (23.5)(22^3)] = 7947.7 \text{ in.}^4$

Actual stress at the top of the flange of channel =  $(1459.35)(12)(12)/(7947.7) = 26.08 \text{ ksi} < 30.6 \text{ ksi (permitted)}$

Hence, the section seems to be OK.

A nominal plate, 3/8 in. thick and 31.0 in. wide, is used at the top to cover the channels at the top and bottom. The end connections visualized in this design can be carried out in a number of different ways, as shown in Figures E8.10 [22] and E8.11 [23]. Figure E8.10 shows one mode of connecting tubular diagonal members of the longitudinal trusses to the hinged joints on the top and bottom chord members; Figure E8.11d shows the mode of connection assumed in the truss to deck connections.

#### 8.2.3.2.4 Floor Plate in Cellar Deck

The configuration is taken to be similar to the details shown in Figure E8.7. The cellar deck is more of a storage deck than an operation deck; hence, the live loading given in Table 6.1 is much higher. The live load for the floor is around  $0.40 \text{ kips/ft.}^2$  ( $18.0 \text{ kN/m}^2$ ).

Let the plate thickness be 0.625 in.; self-weight of floor plate =  $25.31 \text{ lb./ft.}^2$ .

Considering a width of 1.0 ft. for the floor, the effective span for the floor (see Figure E8.7) is  $\ell = 5.0 - (8/12) = 4.333 \text{ ft}$ .

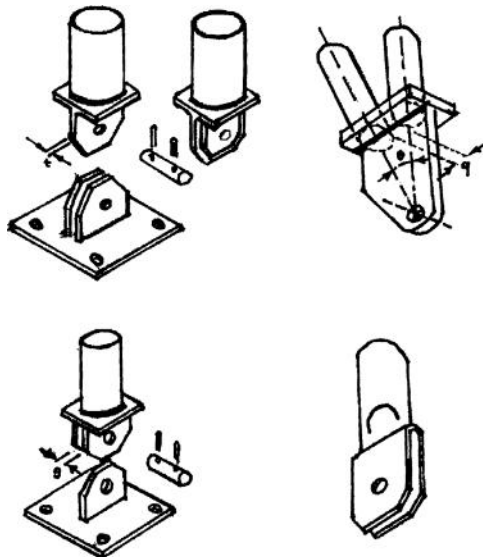
Factored distributed load per unit width of floor (see Section C.2 of the API code) =  $1.3(\text{dead load}) + 1.5(\text{live load}) = q_f = (1.3)(25.31) + (1.5)(400.0) = 637.97 \text{ kips/ft.}^2$

Factored concentrated load =  $P_f = (1.5)(1.1) = 1.65 \text{ kips}$ ; this load is assumed to be acting at the center of the plate.

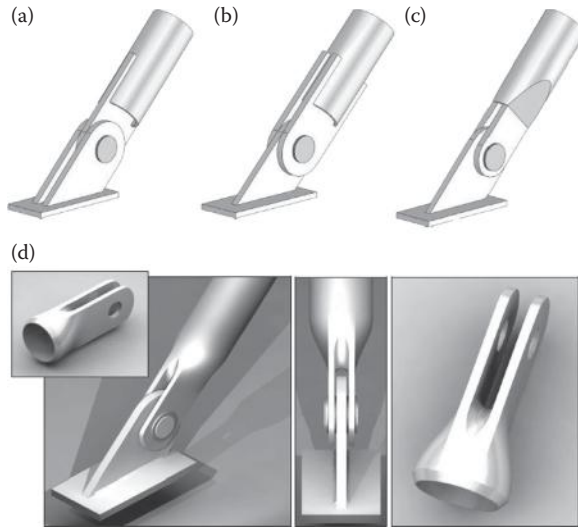
Maximum bending moment acting at the center of the plate =  $(q_f \ell^2)/(12) + (P_f \ell/8)$  [approximate value] =  $[(637.97)(4.333)^2/12] + (1.65)(1000.0)(4.333)/8 = 998.14 + 893.68 = 1891.82 \text{ lb. ft./ft.} = 1891.82 \text{ lb. in./in.}$

Using A36 steel, the resistance factor for bending is 0.85.

Permissible maximum bending stress =  $(0.85)(36.0) = 30.6 \text{ ksi}$



**FIGURE E8.10** Tubular end connections with details of end connections to provide hinged joints at the back-to-back channel chord. (From J. Wardenier, *Hollow Sections in Structural Applications*, Comite International pour le Developpement et l'Etude de la Construction Tubulaire [CIDECT] Publication, p. 8.11. Available at <http://www.cidect.org/en/>, 2009.)



**FIGURE E8.11** Another type of tubular end connection details to provide true pin connections to the back-to-back channel chord: (a)–(c) Insert into the split cylinder end; (d) cast steel “true pin” type connector. (From J.C. de Oliveira et al., *Standardized Cast Steel Connectors for Tubular Hollow Structural Sections*, CSCE 2008 Annual Conference, Quebec, Canada, pp. 6, 7, 2008.)

$$I = (1/12)(1)(t)^3 = t^3/(12)$$

$$M = (f_b)(I/c) = (30.6)[(t^3)/12]/(t/2) = 5.10 t^2 \text{ kips in./in.}$$

$$t = [1.892/5.1]^{(0.5)} = 0.606 \text{ in.} \sim 0.625 \text{ in.}$$

The thickness provided is sufficient.

8.2.3.2.5 Floor Beam below Cellar Floor Plate

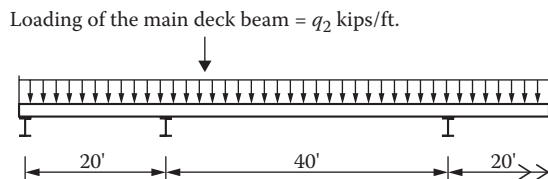
The configuration below the floor plate (Figure E8.12) will be similar to that shown in Figure E8.8, but changed in direction as shown in Figure E8.6; this becomes necessary to provide sufficient wind stiffening and torsional resistance to the whole deck. Also, the loading on the floor is a little higher.

Using a W24 × 104 wide-flange I beam for the beam section, as per the calculations above,  $q_2 = (5)(637.97) + [(1.65/5)(1000.0)\{(1/2)(20/4 + 40/4)\}] + \text{self-weight} = (3189.85 + 2475.0) + 104.0 = 5768.85 \text{ lb./ft.}$

Maximum bending moment (over the interior support)  $\sim (q_1)(\ell^2)/10 = (5.769)(40)^2/10 = 923.04 \text{ kips ft.}$

Required sectional modulus  $= (923.04)(12)/(30.6) = 361.98 \text{ in.}^3$

A wide-flange I-section of size W24 × 104 lb. (flange width is 12.50 in., flange depth is 0.75 in., and web thickness is 0.50 in.) gives the sectional modulus of 258 in.<sup>3</sup> ( $I = 3100 \text{ in.}^4$ ); hence, the



**FIGURE E8.12** Loads on the main beam in the cellar deck.

sectional modulus has to be increased. Assuming that the provision of a 0.5-in.-thick and 12.5-in.-wide plate to the flanges of the wide-flange beam would make the section sufficiently strong and stiff,

$$\text{Additional moment of inertia provided} = (1/12)(12.5)(0.5)^3 + (2)(12.5)(0.5)(12.25)^2 = 0.130 + 1800.75 = 1875.78 \text{ in.}^4$$

$$\text{Total moment of inertia} = 3100.0 + 1875.78 = 4975.78 \text{ in.}^4$$

$$\text{Hence, the sectional modulus provided now} = I/(d/2) = 4975.78/(25.0/2) = 398.06 \text{ in.}^3 > 361.98 \text{ in.}^3$$

Hence, the section is OK.

#### 8.2.3.2.6 Longitudinal Beam at the Bottom Chord of Longitudinal Truss

The loads coming onto the bottom chord of the longitudinal truss will be much less than those at the top chord (due to the changed direction of floor beams); moreover, loads will be coming as distributed loads over the beam. Load will be similar to that coming on the floor beam of the cellar deck, plus the self-weight of the longitudinal beam, supported over a 40.0-ft. span. Assume the same section as the top beam for proper connection of tubular sections. Assuming back-to-back channel sections considered earlier,

$$\text{Self-weight of longitudinal beam} = [(4)(12.5)(1.0)(12.0) + (2)(22.0)(0.75)(12.0) + (4)(1/2)(12.5)(12)](486.0)/\{(12)(12)(12)\} = 364.5 \text{ lb./ft.}$$

$$\text{Loading on this beam} = [5768.85 + (4)(1/2)(12.5)(12)(486.0)/(1728)] + 364.50 = 6217.73 \text{ lb./ft.}$$

$$\text{Maximum bending moment (over the interior support)} = (q_1)(\ell^2)/10 = (6.218)(40)^2/10 = 994.84 \text{ kips ft.}$$

$$\text{Maximum bending stress} = (994.84)(12)(12)/(7947.7) = 18.02 \text{ ksi}$$

$$\text{Required sectional modulus} = (994.84)(12)/(30.6) = 390.13 \text{ in.}^3$$

Keeping the same channel section considered earlier in Section 8.2.3.2.3, viz., the back-to-back channel section, 24.0 in. deep, 12.5 in. flange width, 1.0 flange thickness, and 0.75 in. thick web, the moment of inertia = 7947.7 in.<sup>4</sup> (computed earlier).

$$\text{Sectional modulus provided} = \{(7947.7)/(12)\} = 662.31 \text{ in.}^3 > 384.84 \text{ in.}^3$$

Hence, the section provided is quite sufficient.

Once again, the provision of nominal flange plates, 0.375 in. thick and 31.0 in. wide, at the top and bottom of the bottom chord (made up of back-to-back channels) will provide a pleasing appearance for the deck.

#### 8.2.3.2.7 Transverse Beam Supporting Cellar Deck Floor Beams

The loads of the cellar deck floor beams will be coming as concentrated loads on this beam (due to the change in direction of placing the floor beams in the floor of the cellar deck), as shown in Figure E8.13.

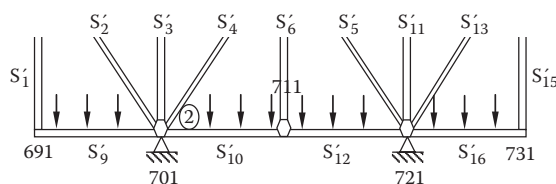


FIGURE E8.13 Transverse beam at the bottom of the cellar deck.

Self-weight of the transverse beam is assumed to be the same as that of the top truss member, viz., back-to-back channel section, 24 in. deep, 12.5 in. flange width, 1.0 in. flange thickness, and 0.75 in. web thickness =  $\frac{[(4)(12.5)(1.0)(12.0) + (2)(22.0)(0.75)(12)]}{(12 \times 12 \times 12)}(486.0) = 280.0 \text{ lb./ft.}$

Magnitude of each concentrated load acting on the bottom transverse chord member =  $\{10.0 + (1/2)(40.0)\}(q_2) + \text{self-weight} = (30)(5.7689) + (30.0)(0.280) = 181.47 \text{ kips}$

Since the joints are assumed to be hinge connected, the bending moment at the center of the 20.0 ft. span =  $(181.47)(20/4) + (2)(181.47)(5)(15)/(20) = 907.34 + 1361.03 = 2268.37 \text{ kips ft.}$

Keep the above back-to-back channel with a flange plate of 1.00-in. thickness,

Additional moment of inertia of the channel beam =  $(2)(1/12)(31.0)(1^3) + (31.0)(1.0)(12.5)^2 = 4848.92 \text{ in.}^4$

Moment of inertia of the channel beam = 7947.7 in.<sup>4</sup> (previously computed)

Total moment of inertia = 7947.7 + 4848.92 = 12,796.62 in.<sup>4</sup>

Actual stress at the top of the flange of channel =  $(2268.75)(12)(13.0)/(12,796.62) = 27.62 \text{ ksi} > 30.6 \text{ ksi (permitted)}$

Hence, the section seems to be OK.

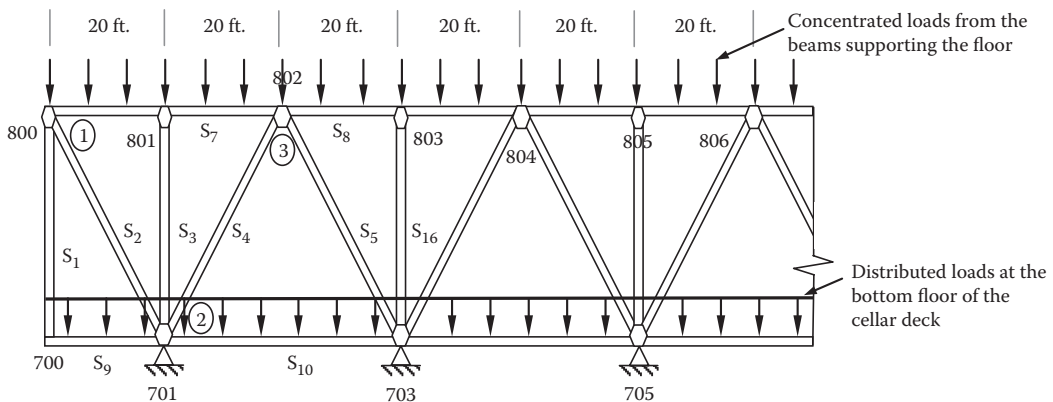
The buckling strength of this section must be checked later after determining the axial compressive/tensile load coming on this section, as a result of transverse truss action of the deck.

### 8.2.3.3 Truss Structures in the Top Deck

#### 8.2.3.3.1 Main Longitudinal Truss Members

The cross diagonals are assumed to be cylindrical members, and the main chord members (at the top and bottom) are assumed to be made up of back-to-back channels, stiffened with flange plates. While the loading on the top chord of the truss will remain the same as that computed in Section 8.2.3.2.3, the loading on the bottom floor will be higher. Considering Figures E8.3 and E8.6, the top nodes are 800, 801, 802, 803, 804, 805, 806, 807, and 808 (in the longitudinal plane of deck columns), while the bottom nodes are 700, 701, 703, 705, 707, and 708, as shown in Figure E8.14 [24]; similarly, on the other side of the deck, the corresponding nodes will be 820 to 828 on the top and 720, 721, 723, 725, 727, and 728 at the bottom. Moreover, all the truss panels (longitudinal and transverse) are stiffened with diagonal bracing to stiffen them against the wind twisting and integral deck behavior.

The load coming on the node 800 is given by  $= (126.9) + (3/2)(126.9) = 317.25 \text{ kips.}$



**FIGURE E8.14** Loads acting on the longitudinal truss of the deck. (From Course Notes on General Design of Fixed Offshore Structures, University of Texas, Austin, TX, p. 3.15, 1979.)

At each of the nodes from 801 to 807, the load acting =  $(126.9) + (3/2)(126.9) + (3/2)(126.9) = 507.6$  kips.

At node 808, the load acting = 317.25 kips.

At the bottom of the longitudinal truss, the load coming on the truss members will be much less, since the floor stiffening is assumed to be placed in the other perpendicular direction. Assuming the floor beam of the cellar deck to be spaced at the same 5.0-ft. intervals, the loads will be coming as (i) distributed loads acting on the bottom truss members and (ii) concentrated nodal loads at deck column points, transmitted through shear in the transverse chord beam supporting the cellar deck. It is assumed to act on the bottom node of the truss, located at nodes 701, 703, 705, and 707 (see Figure E8.13).

Concentrated load magnitude acting on each transverse girder of the cellar deck = (181.47 kips) (Calculated in Section 8.2.3.2.7).

Load on each of the nodes 701, 703, 705, and 707 =  $(1/2)(20.0 + 40.0)[6.218 + (2)(0.375)(12)(31.0)(486)/(1728)] + 181.47 + (2)(1/3)(181.47) + (2)(2/3)(181.47) + (2)(1/2)(181.47) = 188.89 + 181.47 + 120.98 + 241.96 + 181.47 = 914.77$  kips.

Load on node 700 (as well as node 708) is given as =  $(1/2)(20.0)(6.049 + 0.079) + (1/2)(181.47 + 120.98 + 241.96 + 181.47) = 60.49 + 362.94 = 424.22$  kips.

Load acting on the node 708 = 424.22 kips

Reaction at node 701 = (load at node 800 + load at node 700 + load at 801 + load at 701 +  $(1/2)$  (load at 802)) =  $317.25 + 424.22 + 507.6 + 914.77 + (1/2)(507.6) = 2,417.64$  kips

Reaction at node 707 = 2417.64 kips

Reactions at nodes 703 and 705 =  $(1/2)(507.6) + 507.6 + 914.77 + (1/2)(507.6) = 1929.97$  kips

Force in member  $S_3$  (node 801),  $S_6$  (node 803), and others (vertical members at nodes 805 and 807) = 507.6 kips (compression)

Force in member  $S_1$  (node 701) and node 708 = 423.43 kips (tension)

Force in member  $S_2$  (member between nodes 800 and 701) =  $(317.25 + 424.22)/\{\sin(45^\circ)\} = 1048.60$  kips (comp.)

Force in member  $S_9 = 0.0$  kip

Force in member  $S_7$  (and the member between nodes 800 and 801) =  $S_2 \{\cos(45^\circ)\} = 741.47$  kips (tension)

Force in member  $S_4 = [\text{reaction at node 701} - \{S_3 + S_2 \cos(45^\circ) - \text{nodal load at 701}\}]/\{\sin(45^\circ)\} = (2417.64 - 507.6 - 741.47 - 914.77)/\{\sin(45^\circ)\} = 358.93$  kips (compression)

Force in member  $S_{10} = \{S_2 \cos(45^\circ) - S_4 \cos(45^\circ)\} = (1048.60 - 358.93)\{1/\sqrt{2}\} = 487.67$  kips (compression)

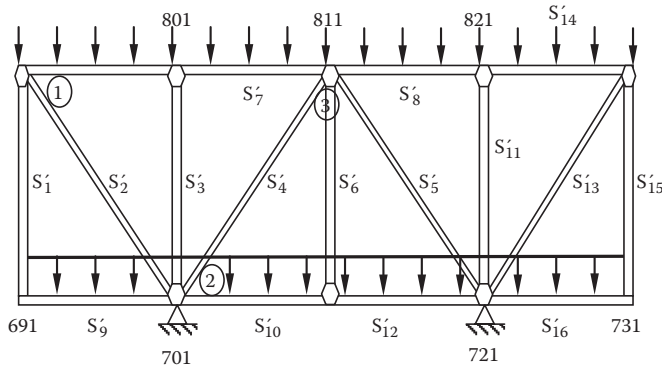
Resolving vertically, force in member  $S_5 = 507.6 - S_4 \sin(45^\circ) = [507.6 - 253.80]/(1/\sqrt{2}) = 358.93$  kips (compression)

Force in  $S_8 = \{S_4 \cos(45^\circ) - S_7 - S_5 \cos(45^\circ)\} = (358.93/\sqrt{2} - 741.47 - 358.93/\sqrt{2}) = -741.47$  kips (tension)

Hence, the cylindrical member  $S_2$  can be designed for its compressive and buckling resistance to make it suitable as a truss member. Also the tensile strength of the connections of member  $S_1$  should be checked. The top chord member  $S_7$  (or  $S_8$ ) must be checked for its interactive strength.

#### 8.2.3.3.2 Transverse Truss Members

In addition to the longitudinal truss action of the deck, the transverse truss action of the deck also must be considered for trusses along planes represented by 700–800–820–720, 701–801–821–721, 703–803–823–723, 705–805–825–725, 707–807–827–727, and 708–808–828–728. Only one truss along the plane 701–801–821–721, shown in Figure E8.15, is considered in this study; other trusses are assumed to be similar.



**FIGURE E8.15** Details of loads acting on the transverse truss of the deck.

Loading on the top members of the truss will be a distributed downward-acting load, whereas loading on the bottom members will be concentrated loads due to the loads transmitted from the floor beams of the cellar deck (see Figure E8.15).

Distributed loads acting on the top portion of the truss =  $q_1$  (see Section 8.2.3.2.2) + self-weight  
 $= 4.126 - 0.076 + 0.104 + [0.280 + (2)(0.375)(31)(12)(486)]/(1728) = (4.154) + (0.280 + 0.079) = 4.513$  kips/ft.

Magnitude of each concentrated load acting on the bottom transverse chord member =  $\{10.0 + (1/2)(40.0)\}(q_2) + \text{self-weight} = (30)(5.7689) + (30.0)[364.5 + (2)(1.0)(31.0)(12.0)(486.0)/(1728)]/(1000) = 173.06 + 17.21 = 190.27$  kips

Magnitude of concentrated load acting on the end of bottom transverse chord member =  $(10)(5.7689) + (1/3)(15.21) = 62.759$  lb.

Load acting on top node 791 to 797 =  $(1/2)(20.0)(4.513) = 45.13$  kips.

Load acting on nodes 801 to 807 (similarly on nodes 811 to 817 or nodes 821 to 827) =  $(1/2)(40.0)(4.513) = 90.26$  kips.

Load acting on nodes 831 to 837 = 45.13 kips

Load acting on node 691 (or 693, 695, or 697) =  $(10.0)(5.7689 + 0.5738) + (1/3)(190.27) + (1/2)(190.27) + (2/3)(190.27) = 63.43 + 63.42 + 95.14 + 126.85 = 348.83$  kips

Load acting on node 701 (or 703, 705, or 707) =  $(20)(5.7689 + 0.5738) + 190.27 + (2)(1/3)(190.27) + (2)(1/2)(190.27) + (2)(2/3)(190.27) = 126.85 + 190.27 + 126.85 + 190.27 + 253.69 = 887.93$  kips

Load acting on node 711 (similarly at the nodes 713, 715, 717) = 887.93 kips

Loads acting on node 721 (similarly at the nodes 723, 725, 727) = 887.93 kips

Load acting on node 731 = 348.83 kips

Reaction coming onto the column support at node 701 (or 721) =  $(45.13) + 90.26 + (1/2)(90.26) + (348.83) + (887.93) + (1/2)(887.93) = 1861.25$  kips

[Similarly, the forces coming onto the column supports at 703 (or 723), 705 (or 725), or 707 (or 727) from the transverse load distribution assumption can be computed.]

Force in member  $S'_9 = 0.0$  kip

Force in member  $S'_1 = 348.83$  kips (tension)

Force in member  $S'_2 = (45.13 + 348.83)/\cos(45^\circ) = 557.15$  kips (compression)

Force in member  $S'_7$  (or in the member between the nodes 791 to 801) =  $(557.15)\{\cos(45^\circ)\} = 393.96$  kips (tension)

Force in member  $S'_3$  (or  $S'_{11}$ ) = 90.26 kips (compression)

Force in member  $S'_4 = (\sqrt{2})[1861.25 - 887.93 - 90.26 - (557.15)(1/\sqrt{2})] = 691.68$  kips (compression)

Force in member  $S'_6 = 887.93$  kips (tension)

Force in member  $S'_{10} = S'_4(1/\sqrt{2}) - S'_2(1/\sqrt{2}) = (1/\sqrt{2})(691.68 - 557.15) = 95.13$  kips (tension)

Force in member  $S'_{12} = 95.13$  (tension)

Force in member  $S'_5 = (\sqrt{2})[887.93 + 90.26 - 691.68/(\sqrt{2})] = 691.69$  kips (compression)

Forces in other members are symmetrical, with respect to member nodes 711 to 811.

Hence, member  $S'_4$  can be designed for its compressive and buckling resistance, and member  $S'_6$  can be designed for its tensile strength.

#### 8.2.3.3.3 Design of Longitudinal and Transverse Truss Chord and Diagonal Members:

##### Design of Diagonal Member $S_2$ for Its Compressive and Buckling Strengths

Following API RP 2A-LRFD, Section D [19], permitted axial compressive stress is  $= \Phi_c F_{cn} = (0.85)(36.0) = 30.6$  ksi.

For the worked out example Problem S.7.1, the diagonal brace was 30.0 in. in outer diameter and 0.626 in. thick.

$F_c = P/A = (1048.60)/[(\pi/4)(D_o^2 - D_i^2)] = (1048.6)/(57.68) = 18.18$  ksi  $< 30.6$  ksi; hence, the section is OK.

Length between the c/c distance of the diagonal brace  $= [20^2 + 20^2]^{(0.5)} = 28.28$  ft. Subtracting a distance of 18 in. from the center of the brace end to the end face of the diagonal brace, face-to-face length of diagonal  $= 28.28 - 3.0 = 25.28$  ft.

Checking for column buckling,  $\lambda = [(KL)/(\pi r)]\sqrt{(F_y/E)}$

$$K = \text{smaller of } [0.85 \text{ or } \{1.0 - (0.4)(f_c)/(\Phi_c F_c)\}] \\ = \text{smaller of } [0.85 \text{ or } \{1.0 - (0.4)(18.18)/(30.6)\}]$$

$= \text{smaller of } (0.85 \text{ or } 0.762) = 0.762$ . Here the value of  $F_c$  was taken as  $F_{cn}$  as a first trial value.

$F_c = F_y/\lambda^2$ ; hence, the earlier assumed value for  $\lambda = \sqrt{(0.85)} = 0.922$ .

Computing the value of  $\lambda$  from the above equation

$$\lambda = [ \{ (0.762)(25.28)(12.0) \} / \{ (\pi)(0.35)(30) \} ] [ (36.0/30,000) ]^{(0.5)} = (7.008)(0.035) = 0.243$$

$$F_c = 36.0/(0.243)^2 = 519.22 \text{ ksi (too high)}$$

$K = \text{lesser value of } [0.85 \text{ or } \{1.0 - (0.4 \times 18.18)/(0.85 \times 519.22)\}] = \text{lesser of } (0.85 \text{ or } 0.984) = 0.85$

Recomputing the value of  $\lambda$ ,  $\lambda = (7.792)(0.035) = 0.273 < \sqrt{(2)}$ ; hence,

$$F_{cn} = [1.0 - (0.25)(0.273)^2](36.0) = 35.33 \text{ ksi}$$

Therefore, the brace member size seems to be OK.

Also  $(D/t) = (30.0/0.625) = 48.0 < 60.0$ .

Nominal elastic local buckling strength  $= (2.0)(0.30)(30,000)(1/48) = 375.0$  ksi (too high). Consequently, no local buckling will occur in the diagonal brace.

#### 8.2.3.3.4 Design of Member $S_1$ for Its Tensile Strength

Actual tensile stress  $= (741.47)/(57.68) = 12.85 < (0.95)(36.0) < 34.2$  ksi; hence, the section is OK.

#### 8.2.3.3.5 Design of Member $S_7$ for Its Combined Load Effect

Member  $S_7$  is subjected to loads that generate axial tension and transverse bending stresses; also there is an orthogonal truss (top) chord member that connects at one end of member  $S_7$ . Hence, the effect of the combined stresses on the strength of the member should be considered.



Force in member  $S_7$  (and the member between nodes 800 and 801) =  $S_2 \{\cos(45^\circ)\} = 741.47$  kips (tension)  
 Axial tensile stress =  $(747.47)/(105.0) = 6.92$  ksi  
 Maximum bending stress =  $(994.84)(12)(12)/(7947.7) = 18.02$  ksi  
 Maximum tensile stress in the member =  $18.02 + 6.92 = 24.94$  ksi < 34.2 ksi; hence, the section is OK.

Also, the transverse top chord member mates with this truss only at the left end of member  $S_7$ , where there is no main bending stress. Hence, that effect will be marginal.

#### 8.2.3.3.6 Design of Member $S_{10}$ for Its Combined Load Effect

The member is subjected to axial compression and transverse bending stresses; hence, the interactive effect of the joint must be considered.

Force in member  $S_{10} = 487.67$  kips (compression)  
 Cross-sectional area of member  $S_{10} = [105.0 + (2)(31.0)(1.0)] = 167.0$  in.<sup>2</sup>  
 Axial compressive stress in the section =  $(487.67)/(167.0) = 2.92$  ksi  
 Maximum bending stress = 18.02 ksi (computed earlier in Section 8.2.3.2.6)

As per AISC design procedure [26],  $(P_u/P_n) + [(M_u)/(M_n)](C_m)/(1.0 - \alpha) \leq 1.0$ ; this equation can be replaced by its equivalent, viz.,  $(f_c/F_{cn}) + (f_b/f_{bn})C_m\{1.0/(1 - \alpha)\} \leq 1.0$ .

$$\begin{aligned} f_c &= 2.92 \text{ ksi} \\ F_{cn} &= \Phi_c F_y = (0.85)(36.0) = 30.6 \text{ ksi} \\ (f_c/F_{cn}) &= (2.92/30.6) = 0.096 \\ f_b &= 18.02 \text{ ksi} \\ F_{bn} &= \Phi_b F_y = (0.95)(36.0) = 34.2 \text{ ksi} \end{aligned}$$

Also,  $C_m = 0.6 + 0.4(M_1/M_2) = 0.6$ , since no joint moment exists as per our calculations.

$$\begin{aligned} \alpha &= (P_u L^2)/(\pi^2 EI) = [(487.67)(25.28 \times 12)^2]/[(\pi^2)(30,000)(7947.7)] = 0.02 \\ (f_b/f_{bn})C_m\{1.0/(1 - \alpha)\} &= (18.02/34.2)(0.6)(1.0/0.98) = 0.323 \end{aligned}$$

Hence,  $(P_u/P_n) + [(M_u)/(M_n)](C_m)/(1.0 - \alpha) = 0.096 + 0.323 = 0.419 < 1.0$ . Consequently, the section is safe against interactive failure.

#### 8.2.3.3.7 Design of Transverse Truss Diagonal Member $S'_4$ for Its Compressive and Buckling Strengths

Axial compressive load in the member = 691.68 kips  
 Cross-sectional area = 57.68 in.<sup>2</sup> (computed earlier)  
 Permitted axial compressive stress is =  $\Phi_c F_{cn} = (0.85)(36.0) = 30.6$  ksi.  
 $F_c = 691.68/57.68 = 11.99$  ksi < 30.6 ksi; hence, the stress is OK.  
 Length between the c/c distance of the diagonal brace = 25.28 ft. (computed earlier)

Checking for column buckling,  $\lambda = [(KL)/(\pi r)]\sqrt{(F_y/E)}$

$$\begin{aligned} K &= \text{smaller of } [0.85 \text{ or } \{1.0 - (0.4)(f_c)/(\Phi_c F_c)\}] \\ &= \text{smaller of } [0.85 \text{ or } \{1.0 - (0.4)(11.99)/(30.6)\}] \\ &= \text{smaller of } (0.85 \text{ or } 0.843) = 0.843. \text{ Here the value of } F_c \text{ is taken as } F_{cn} \text{ as a first trial value.} \\ F_c &= F_y/\lambda^2; \text{ hence, the assumed value for } \lambda = 1.0/[\sqrt{(0.85)}] = 1.085. \\ &\text{Computing the value of } \lambda \text{ from the above equation} \end{aligned}$$



$$\lambda = \left[ \frac{(0.842)(25.28)(12.0)}{(\pi)(0.35)(30)} \right] \left[ \frac{36.0}{30,000} \right]^{(0.5)} = (7.744)(0.035) = 0.271$$

$$F_c = 36.0 / (0.271)^2 = 490.19 \text{ ksi (too high)}$$

$$K = \text{lesser value of } [0.85 \text{ or } \{1.0 - (0.4 \times 11.99) / (0.85 \times 490.19)\}] = \text{lesser of } (0.85 \text{ or } 0.988) = 0.85$$

Recomputing the value of  $\lambda$ :  $\lambda = (7816)(0.035) = 0.274 < \sqrt{(2)}$ ; hence,

$$F_{cn} = [1.0 - (0.25)(0.274)^2](36.0) = 35.32 \text{ ksi}$$

Hence, the brace member size seems to be OK.

$$\text{Also } (D/t) = (30.0/0.625) = 48.0 < 60.0.$$

$$\text{Nominal elastic local buckling strength} = (2.0)(0.30)(30,000)(1/48) = 375.0 \text{ ksi (too high).}$$

Consequently, no local buckling will occur in the diagonal brace.

#### 8.2.3.3.8 Design of Transverse Truss Vertical Member $S'_6$ for Its Tensile Strength

$$\text{Permitted tensile stress} = (\Phi_t)(F_y) = (0.95)(36.0) = 34.2 \text{ ksi}$$

$$\text{Actual tensile stress} = 887.93 / (57.68) = 15.39 \text{ ksi} < 34.2 \text{ ksi}$$

Hence, the member size is OK.

#### 8.2.3.4 Reassessing Sufficiency of Vertical Column below the Top Deck

According to Section 8.2.3.1.1, the moment and compressive load acting on the deck columns are computed as follows:

$$\text{Maximum factored moment due to wind and wave-current forces acting on the platform} = (1.35)(612.5) = 796.25 \text{ kips ft.}$$

$$\text{Maximum upward (compressive) factored reaction on the leeward column due to gravity, wind, and wave-current loads} = 1474.9 + (1.35)(29.16) = 1512.81 \text{ kips}$$

$$\text{Factored gravity load alone} = (1.3)(1134.3) = 1474.9 \text{ kips}$$

$$\text{Total factored vertical loads on the eight columns} = (8)(1479.9) = 11,839.2 \text{ kips}$$

$$\text{According to Section 8.2.3.3.1, the total factored vertical static loads are} = (4)(2417.64) + (4)(1929.97) = 17,390.0 \text{ kips}$$

Consequently, the present loads are much higher than the initially assumed loads on the columns; hence, we need to check the previous preliminary column design for its sufficiency. The diameter was taken equal to 48.0 in., and the wall thickness was 1.375 in.

#### 8.2.3.4.1 Global and Local Buckling Strength of Column Member

Outer diameter of column = 48.0 in.; radius of gyration =  $[(1/4)\sqrt{(D_o^2 + D_i^2)}] = 0.35D = (0.35)(48) = 16.8 \text{ in.}$  As per Table D.3.1 of the API Code [19], effective length of factor  $K = 1.5$ .

$$\lambda = (KL/r)(F_y/E)^{(0.5)} = [(1.5)(30.0)(12)/(16.8)][(60.0)/\{(30.0)(1000)\}]^{(0.5)} = 1.438 > \sqrt{(2.0)} (= 1.414).$$

$$F_{cn} = \text{permitted axial compressive strength of the column} = (F_y/\lambda^2) = 60.0 / (1.438)^2 = 29.02 \text{ ksi.}$$

$$F_c = \text{Actual stress in the column member} = [(\text{Maximum compressive reaction in the column}) / (\text{cross-sectional area})] = (2417.64) / (201.41) = 12.0 \text{ ksi} < 29.02 \text{ ksi (stress is lower than the permitted value); hence, member size seems to be OK for global buckling.}$$

Consider inelastic local buckling of the thin tube. The nominal inelastic buckling strength of the thin stressed skin of the tube  $F_{xc} = F_y$ , since  $(D/t) = 34.91 \leq 60.0$ .

$$\text{Also, nominal elastic local buckling strength} = (2.0)(C_x)(E)(t/D) = (2.0)(0.30)(30,000)(1/34.91) = 515.6 \text{ ksi (too high).}$$

Hence, the column member seems to be safe against local buckling, since the actual stress in the tube is only 12.0 ksi.

8.2.3.4.2 Bending, Shear, and Hoop Buckling Strengths of Column Tubular Members

The section considered earlier seems to be OK as per previous calculations.

8.2.3.4.3 Combined Axial Compression and Bending Loads on the Column

The column member should satisfy the three interaction conditions given in Equations E8.3, E8.4, and E8.5.

As computed earlier,  $F_{xc} = F_{y,c}$ .

Since the member is a cylindrical one, the slenderness ratios  $\lambda_y$  and  $\lambda_z$  are the same.

$\lambda = (KL/r)(F_y/E)^{0.5} = 1.438$ . Hence,  $\lambda_y = \lambda_z = 1.438$  (computed earlier).

$F_{cn} = 29.02$  ksi; also  $\Phi_c = 0.85$ .

$f_c = 12.0$  ksi (computed earlier)

$(f_c/\Phi_c F_{cn}) = \{12.0/(0.85 \times 29.02)\} = 0.4865$

$F_{bn}$  = Nominal bending strength = 74.65 ksi (computed earlier); also,  $\Phi_b F_{bn} = 70.91$  (computed earlier in Section 8.2.3.1.3).

$[1.0/(\Phi_b F_{bn})] = 1.0/70.91 = 0.014$ ; hence, the contribution from bending to this interaction effect is assumed to be negligible (since the actual bending stress in the column has been computed earlier to be = 4.19 ksi). Only axial compression effect predominates.

Hence, the above three equations are assumed to be satisfied.

The selected column member seems to be OK.

8.2.3.5 Tubular Members in Jacket Structure

Considering the wave pressures given in Figure E8.5, the horizontal wave pressure load acting on the diagonal member 405–503, shown in Figure E8.16, can be considered to be made up of a hori-

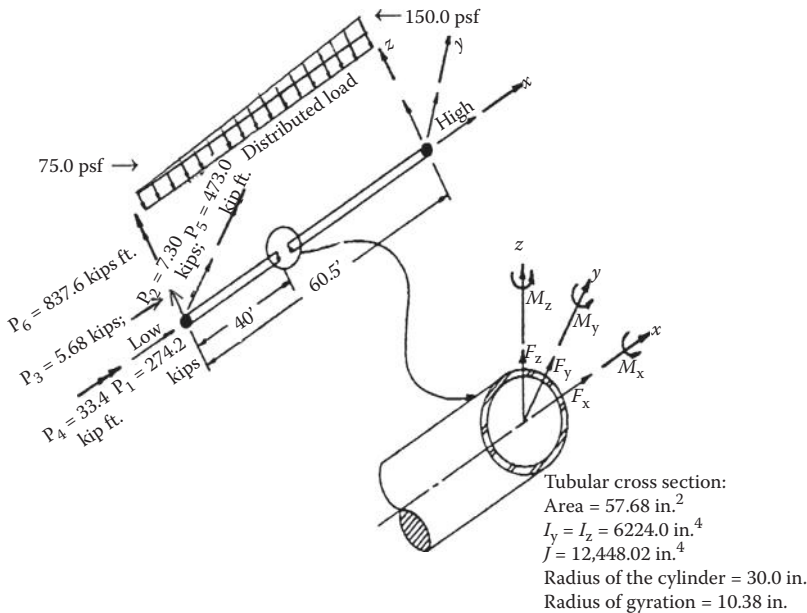


FIGURE E8.16 Design check of member 405–503 against the applied member loads.

zontal pressure load varying from 75.0 psf, at the low end, to 150.0 psf, at the high end; the vertical pressure load is assumed to be varying from 20.0 to 50.0 psf.

The chosen diameter of the member is 30.0 in., and the thickness of the tube is 0.625 in. The computed length of the member is 60.5 ft. Nominal axial compressive strength is taken as 60.0 ksi; radius of gyration =  $(1/4)[30^2 + 28.75^2]^{(0.5)} = 10.38$  in.

### 8.2.3.5.1 Design of Jacket Diagonal Member 405–503 against Imposed Loads

#### 8.2.3.5.1.1 Axial Compression in Member 405–503

Permissible compressive stress =  $\Phi_c f_{cn} = (0.85)(60.0) = 51.0$  ksi

Axial compressive stress in the member due to the factored loads =  $(274.22)/(57.68) = 4.75$  ksi  
< 51.0 ksi.

#### 8.2.3.5.1.2 Axial Buckling

$L =$  Face-to-face length =  $60.5 - (1/12)(2) [(24.0)^2 + (15)^2]^{(0.5)} = 60.5 - 4.72 = 55.78$  ft.

$\lambda = (KL/\pi r)[F_y/E]^{(1/2)} = [(0.8)(55.78)(12)/\{(\pi)(10.38)\}][60.0/30,000]^{(0.5)} = 0.73$ .

$F_{cn} = [1.0 - (0.25)(0.73)^2] (60.0) = 52.0$  ksi > 4.75 ksi.

Hence, the section is OK against buckling.

#### 8.2.3.5.1.3 Local Buckling

For inelastic buckling:  $D/t = 30.0/(0.625) = 48.0$ ; hence,  $F_{xc} = 60.0$  ksi.

For elastic local buckling,  $F_{xc} = (2)(0.3)((30,000)(0.625)/(30.0) = 375.0$  ksi (very high). The section will not buckle elastically or plastically.

#### 8.2.3.5.1.4 Bending in Local x–y and x–z Planes

For horizontal bending in the local y-axis,

$M_y = + 738.1$  kips ft. at high end (at node 503)

$S = 414.93$  in.<sup>3</sup>

$f_{by} = M/S = (738.1)(12)/(414.93) = 21.35$  ksi

$D/t = 48.0$ ; also,  $3000/F_y = 3000/60 = 50.0$

$Z = [(D_o^3 - D_i^3)/6] = [(30^3 - 28.75^3)/6] = 539.39$  in.<sup>3</sup>

Hence,  $F_{bny} = [1.13 - \{(2.58)(F_y D)\}/(Et)](Z/S)(F_y) = (1.13 - 0.25)(77.997) = 68.64$  ksi.

$\Phi_{by} F_{bny} = (0.95)(68.64) = 65.21$  ksi > 21.35 ksi; hence OK.

For vertical bending in the local z-axis,

$M_z = 1276.6$  kips ft. at high end (node 503)

$f_{bz} = (1276.6)(12)/(414.93) = 36.92$  ksi

$\Phi_{bz} F_{bnz} = 65.21$  (computed earlier) > 36.92 ksi; hence OK.

Since torsional moment and transverse shear loads are quite low, no computations have been carried out to check on the exceedance of limits for torsional and shear stresses.

#### 8.2.3.5.1.5 Hoop Buckling under Hydrostatic Pressure

Considering Figure E8.5, the maximum depth of submergence of point 405 is

$H_z \approx 91.0$  ft.

Factored pressure due to equivalent hydrostatic head =  $(1.1)(91.0)(64.0) = 6406.4$  psf

$f_h = (p)(D)/(2t) = (6406.4)(2.5)/\{(2)(0.625)\} = 12,812.8$  psi = 12.81 ksi

$M = (L/D)\sqrt{(2Dt)} = (55.85/2.5)\sqrt{\{(2)(30/0.625)\}} = 218.89 > (1.6)(D/t) > 76.8$

Hence,  $F_{he} = (2)(C_h)(E)(t)/(D) = (2)\{(0.44)(0.625/30)\}(30,000.0)(0.625)/(30) = 11.46 \text{ ksi} < [(0.55)(60.0) = 33.0 \text{ ksi}]$ .

As a result,  $F_{hc} = F_{he} = 11.46$ .

$$\Phi_h F_{hc} = (0.80)(11.46) = 9.17 \text{ ksi} < f_h (= 12.81 \text{ ksi})$$

Consequently, the diagonal member needs to be stiffened against hoop buckling.

Spacing of stiffening rings  $< [(1.13)(\sqrt{D/t}) = 7.83]$ ; hence, stiffening rings are provided such that  $L$  (the distance between the stiffening rings)  $\leq [(7.83)(2.5) \text{ ft.} = 19.57 \text{ ft.}]$ . Hence, in the diagonal member 405–503, the stiffening rings are placed along one-third the length of the diagonal member.

$$L = (55.78/3) = 18.57 \text{ ft.}$$

$$M = (18.57/2.5)\sqrt{\{(2)(30)/(0.625)\}} = 72.78 < [(1.6)(30/0.625) = 76.8]$$

$$C_h = (0.44)(0.625/30) + [(0.21)(30/0.625)^3]/(72.78)^4 = 0.0092 + 0.00083 = 0.01003$$

$$F_{he} = (2)(C_h)(Et/D) = (2)(0.01003)(30,000)(0.625)/(30.0) = 12.54 \text{ ksi}$$

$$\text{Required moment of inertia of the ring section} = (F_{he})(tLD^2)/(8E) = (12.54)(0.625)(18.57)(12)(30)^2/(8)(30,000) = 6.55 \text{ in.}^4$$

The moment of inertia required is very small; hence, use a nominal stiffener of minimum size. Let us use a circular ring stiffener of thickness 0.375 in. and 3.0-in. internal radial width. Hence, the radial ring stiffener will have an outer radius of 28.75 in. and an internal radius of 22.75 in.

#### 8.2.3.5.1.6 Interaction Effects due to Axial Compression and Bending in Two Different Directions

The jacket diagonal member should satisfy the three interaction conditions given in Equation E8.3, E8.4 and E8.5.

$$(f_c/\Phi_c F_{cn}) + (1/\Phi_b F_{bn})\sqrt{\left[1.0 - \{(C_{my}f_{by})/f_e\}/(\Phi_c F_{ey})\}^2 + \left[1.0 - \{(C_{mz}f_{bz})/f_e\}/(\Phi_c F_{ez})\}^2\right]} \leq 1.0 \quad (\text{E8.3})$$

$$1.0 - \cos[(\pi f_c)/(2\Phi_c F_{xc})] + \left[(f_{by}^2 + f_{bz}^2)\right]^{(0.5)}/(\Phi_b F_{bn}) \leq 1.0 \quad (\text{E8.4})$$

$$F_c < \Phi_c F_{xc} \quad (\text{E8.5})$$

Consider Equation E8.3. From previous calculations,

$$(f_c/\Phi_c F_{cn}) = (4.75)/(0.85)(52.0) = 0.1075$$

$$(1/\Phi_b F_{bn}) = 1.0/\{0.95(65.21)\} = 0.0161$$

$$C_{my} = \text{smaller of } [\{0.6 - (0.4)(473.0/738.1)\} \text{ not less than } 0.4 \text{ or } \{1.0 - (0.4)(4.75)/((0.85)(60.0)) \text{ or } 0.85, \text{ whichever is less}]$$

$$= \text{smaller of } [\{0.344 \text{ not less than } 0.4\} \text{ or } \{0.96 \text{ or } 0.85, \text{ whichever is less}\}] = 0.4$$

$$f_e = 65.21 \text{ psi}$$

$$(C_{my}f_{by})/f_e = (0.4)(21.35)/65.21 = 0.131$$

$$F_{ey} = 60.0/\lambda_y^2 = 60.0/(0.73) = 112.59 \text{ ksi}$$

$$\{(C_{my}f_{by})/(\Phi_c F_{ey})\} = 0.131/\{(0.85)(112.59)\} \sim 0.0$$

$$C_{mz} = \text{smaller of } [\{0.6 - (0.4)(837.6/1272.6)\} \text{ not less than } 0.4 \text{ or } \{1.0 - (0.4)(4.75)/((0.85)(60.0)) \text{ or } 0.85, \text{ whichever is less}]$$

= smaller of [ $\{0.337 \text{ not less than } 0.4\}$  or  $\{0.96 \text{ or } 0.85, \text{ whichever is less}\}] = 0.4$

$$(C_{mz}f_{bz})/f_c = (0.4)(36.92)/65.21 = 0.2265$$

$$F_{ez} = 60.0/(0.73)^2 = 112.59 \text{ ksi}$$

$$\{(C_{mz}f_{bz})/f_c\}/(\Phi_c F_{ez}) = (0.2265)/\{(0.85)(112.39)\} \sim 0.0.$$

$$(0.1075) + (0.0161)(\sqrt{2}) = 0.1075 + 0.0228 = 0.1303 < 1.0; \text{ hence OK.}$$

Consider Equation E8.4:

$$1.0 - \cos [\{(\pi)(4.75)\}/(2.0)(0.85)(52.0)] + \{(21.35)^2 + (36.92)^2\}^{0.5}/(0.95)(68.64) = 1.0 - 0.986 + (42.65)/(65.21) = 0.014 + 0.654 = 0.668 < 1.0; \text{ hence OK.}$$

Consider Equation E8.5:

$$F_c < \Phi_c F_{xc}$$

$$F_c = 52.0 \text{ ksi; also } \Phi_c F_{xc} = (0.85)(375.0) = 318.75 \text{ ksi}$$

Therefore,  $52.0 < 318.75$ ; hence, the condition is satisfied.

All the three equations are fully satisfied.

#### 8.2.3.5.1.7 Interaction Effects due to Axial Compression, Bending, and Hydrostatic Pressure

$$f_x = f_c + f_b + (0.5)f_h = 4.75 + 21.35 + (0.5)(12.81) = 32.51 \text{ ksi}$$

Also,  $(0.5)\Phi_h F_{hc} = (0.5)(0.80)(12.54) = 5.02 \text{ ksi}$ .

Hence,  $f_x > 5.02$ ; hence, no additional condition needs to be satisfied for including the effects of hydrostatic pressure.

#### 8.2.3.6 Miscellaneous Considerations for Jacket Platform

Some factors that need to be reckoned in the analysis and design of other structural members are given herein. Structural members that are not part of the main load-carrying platform structure, located around the splash zone (such as walkways, grating, handrails, and stairways), need special considerations such as the following: (i) wave effects due to vertical wave forces and slamming effects at certain wave heights; (ii) stability of these components under vertical wave loads; and (iii) corrosion and marine growth; it has been noted from past experiences that components of offshore structures located in the splash-zone area may fail due to corrosion-related fatigue failure; and (iv) vessel impact loading on the above offshore structural components is not well defined, and the exerted forces are dependent on their stiffness and energy-absorbing characteristics. Hence, proper consideration must be given for the estimation of these impact forces. Also, since the costs associated with these secondary structural component members will be more than three to four times the costs of platform jacket components, care should be exercised in the analysis and design of these structures.

Pad eyes, launching trusses, barge bumpers, boat landings, walkways, anodes, mud mats, closure plates, and other such structural components must be properly designed, and much higher load factors should be used in the design of these structural components due to uncertainty in the estimation of forces acting on them. The breakdown of weights of various structural components, in an offshore platform structure, is given in Table 8.1 [26]. It can be seen from this table that the vertical legs and transverse braces of the platform structure form the major portion of the weight. Hence, the material choice must be optimized so as to minimize the cost invested in the design and fabrication of the platform structure.

**TABLE 8.1**  
**Percentage Weights of Various Platform Components**

	Percentage of Total Jacket Weight
<b>Leg</b>	<b>39.9%</b>
Cans	14.5%
Other	25.4%
<b>Braces</b>	<b>40.8%</b>
Vertical diagonals	19.1%
Horizontals (including cans)	13.4%
Horizontal diagonals (including cans)	8.3%
<b>Other Framing</b>	<b>9.8%</b>
Conductor framing	2.9%
Launch trusses and runners	6.7%
Miscellaneous framing	0.2%
<b>Appurtenances</b>	<b>9.5%</b>
Boat landings	2.3%
Barge bumpers	2.4%
Anodes	1.8%
Walkways	1.3%
Mud mats	0.4%
Pad eyes	0.2%
Closure plates	0.2%
Flooding system	0.6%

*Source:* B. Weidler and D.I. Karsan, Analytical models, three-dimensional analysis, in: *Planning and Design of Fixed Offshore Platforms*, edited by B. McClelland and M.D. Reifel, Van Nostrand Reinhold Co., New York, p. 763, 1986. With permission.

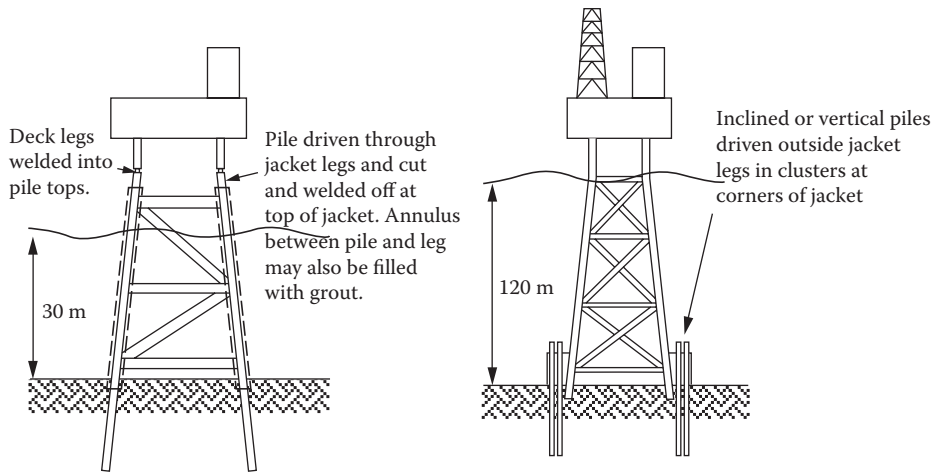
## 8.3 ANALYSIS OF PILE FOUNDATIONS FOR OFFSHORE STRUCTURES

### 8.3.1 INTRODUCTION

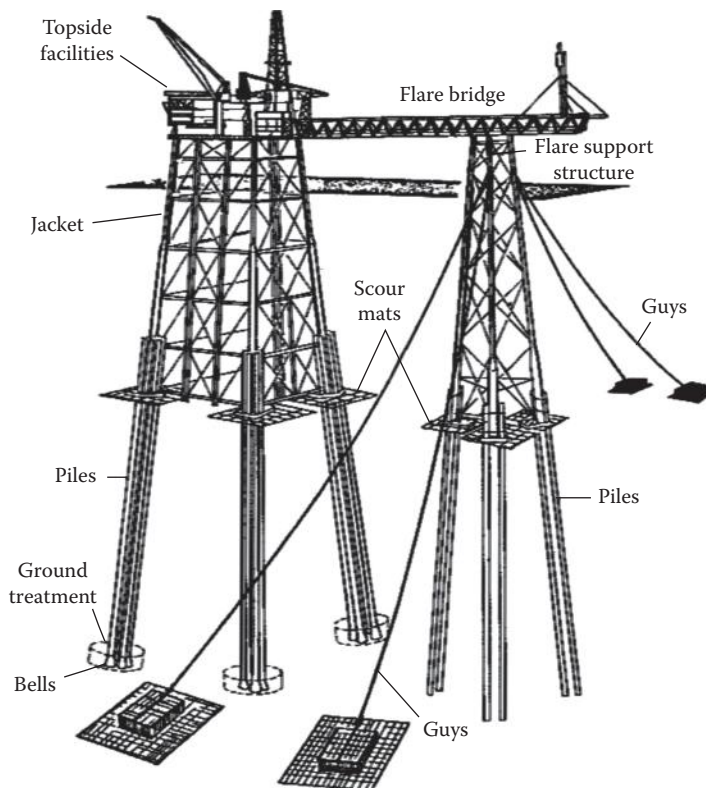
As shown in Figure 8.3 [27], pile-supported steel template offshore structures depend on piles or pile groups, driven vertically or in an inclined manner into the seabed through the columns or on their outsides, to support the structure for resisting the vertical and horizontal loads applied on them. The piles on the outside may be driven in groups in an inclined direction, as shown in Figures 8.4 [28] and 8.5 [29], or vertically down through pile caps located at the seabed, as shown in Figure 8.3, 8.6 [30], and 8.7 [31]. The pile-driving may be carried out from the ocean surface through pile guides using support vessels, as shown in Figure 8.5, or underwater using pile guides, extenders, and under water hammers, as shown in Figures 8.6 and 8.7.

### 8.3.2 SOIL–STRUCTURE INTERACTION

The development of analytical methods for soil–pile interaction has mainly been driven by the demands of offshore oil production activities. For offshore applications, where cyclic wave loading applies lateral loads on pile-supported offshore structures, a number of field and model tests have established the validity of empirically based and widely accepted “*p–y*” curve method for analysis of laterally loaded pile. This static loading analysis method has been modified and extended to cyclic loading conditions and is also usually applied to dynamic or earthquake loading cases.

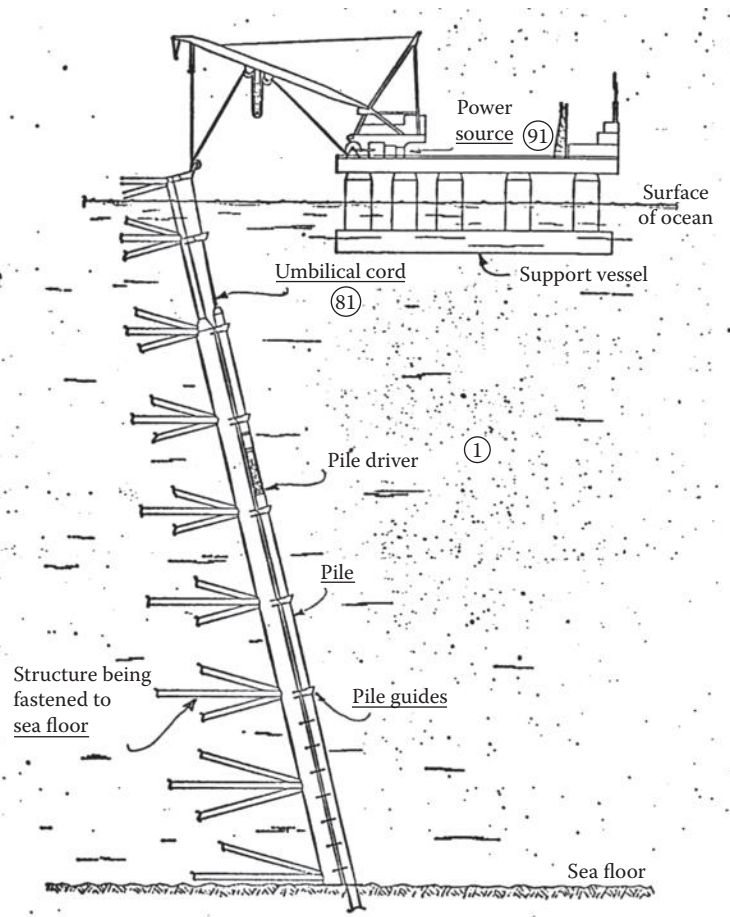


**FIGURE 8.3** Pile-supported offshore structures. (From N.D.P. Bartrop and A.J. Adams, *Dynamics of Fixed Marine Structures*, Butterworth Heinemann Ltd., Oxford, UK, p. 172, 1991.)



**FIGURE 8.4** Typical pile-supported jacket structure with inclined piles—the North Rankin A Platform. (From M. Randolph et al., *Challenges of Offshore Geotechnical Engineering*, p. 9/54. Available at [www.iransaze.com/files-for-downloading/ebglishbook/khak/Challenges\\_of\\_OffShore\\_Geotechnical\\_Engineering.pdf](http://www.iransaze.com/files-for-downloading/ebglishbook/khak/Challenges_of_OffShore_Geotechnical_Engineering.pdf), 2005. With permission.)





**FIGURE 8.5** Driving of an inclined pile through an ocean surface-based support vessel. (From Vulcanhammer. info at <http://www.vulcanhammer.org/on>, *Method and Apparatus for Pile Driving*, p. 8/14, 1979. With permission.)

Soil–structure interaction problems have been modeled along four different lines of mathematical modeling, viz., (i) beam-on-elastic (due to Hetenyi) foundation, leading to development of discrete springs applicable to the pile–soil deformation on the seabed surface only; (ii) beam-on-Winkler foundation approach leading to a pile supported on discrete springs along its length; (iii) elastic continuum approach; and (iv) finite element approach.

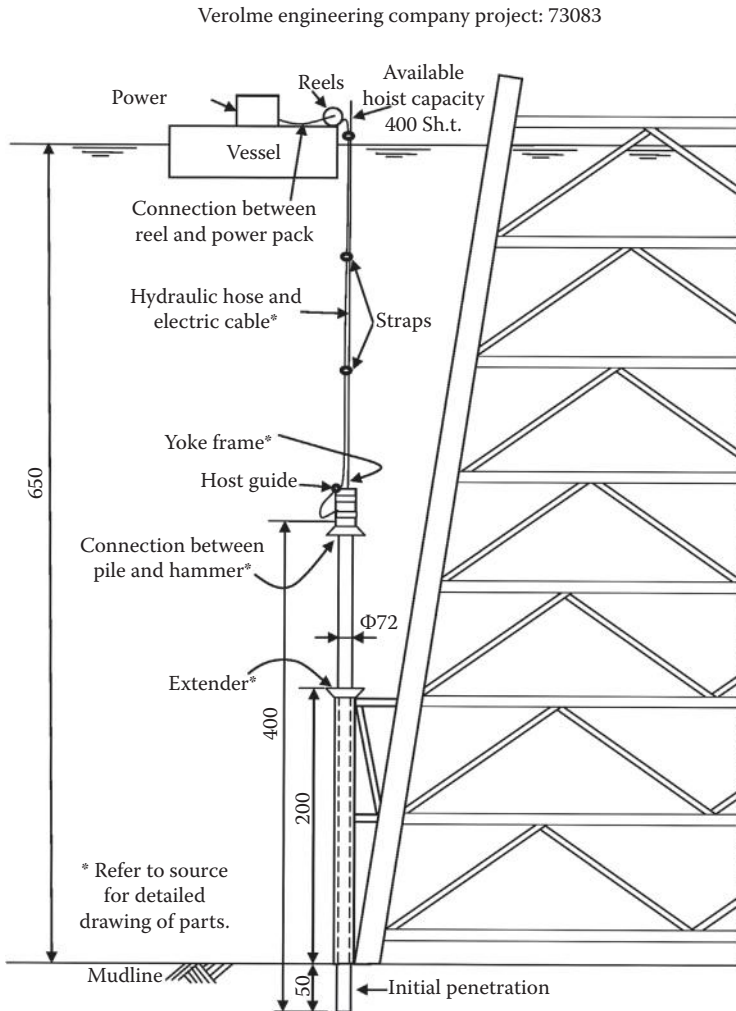
### 8.3.2.1 Beam-on-Elastic (due to Hetenyi) Foundation

In the first approach proposed by Hetényi [32, 33], the soil–structure interaction was modeled by assuming that the soil at every point in contact with the beam behaved in a linear manner. Consequently, the beam–soil interaction can be represented by the solution obtained for a beam supported on elastic foundations represented by the expression

$$EI \frac{d^4 v}{d^4 x} = p = -E_s y \quad (8.1)$$

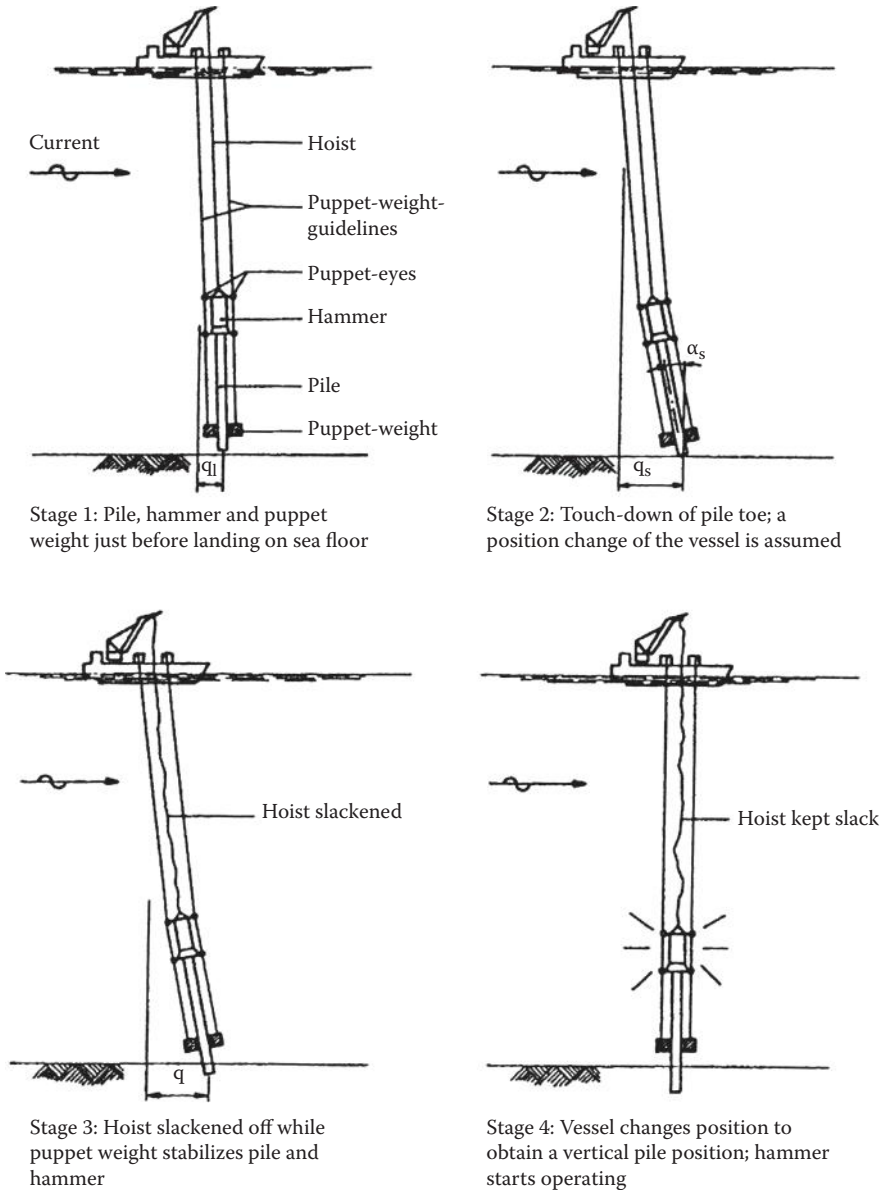
where  $EI$  is the beam (or pile) pile stiffness,  $v$  is the deformation of soil at any point in the beam,  $p$  is the soil reaction at the point where deformation is  $v$ , and  $E_s$  is the modulus of subgrade reaction. This solution, wherein the soil stiffness is treated as a constant, is only valid near the top regions





**FIGURE 8.6** Procedure for the driving of a group of vertical piles around the base of an offshore platform using an ocean surface-based support vessel. (From Vulcanhammer.info at <http://www.vulcanhammer.org/on>. Guide to pile driving equipments, Vols. I and II, *Section on Underwater Pile Driving Found in the Literature on Extensive Information on Pile Hammers*, p. 55/101, 2001. With permission.)

of the seabed soil. Many researchers have used this type of constant subgrade modulus for determining the soil pressure at the pile–soil interface (along the whole embedded length) since they have observed that the near surface modulus was the controlling factor for the pile response, and as such, the soil investigations and characterization should be focused more in this zone [34, 35]. This method has mainly been applied to static lateral pile loading problems and is therefore used for the determination of pile head stiffness terms during soil–structure problems. Broms [36, 37] has described a method for analyzing lateral pile response in cohesive and cohesion-less soils. When the soil is under undrained loading condition, he suggested using a constant subgrade modulus of  $9c_u$  ( $c_u$  = cohesive undrained strength) for the ultimate lateral soil resistance. For drained loading cases, a subgrade modulus, linearly increasing with depth, was specified and assumed equal to  $3K_p D_p \sigma'_v$ , with  $K_p$  ( $= E_p/mD$ ),  $E_p$  = elastic modulus of pile,  $D$  = diameter of the pile,  $m$  = rate of soil modulus increase with depth,  $D_p$  = critical pile depth  $\{= 4.44(E_p I_p/E_s)^{0.25}\}$ , and  $\sigma'_v$  = vertical stress at the location. Randolph and Houlsby [38] used classical plasticity theory to obtain the limiting soil pressure for undrained soil to vary from  $9c_u$  to  $12c_u$ , depending on the pile roughness.



**FIGURE 8.7** Driving of a single or group of piles on a delineated seabed using underwater hammer and ocean surface-based support vessel. (From Vulcanhammer.info at <http://www.vulcanhammer.org/on>. Guide to pile driving equipments, Vols. I and II, Section on Underwater Pile Driving Found in the Literature on Extensive Information on Pile Hammers, p. 47/101, 2001.)

**8.3.2.2 Beam-on-Winkler Foundation:  $p$ - $y$  Curve Approach**

The second approach is based on the earlier Winkler’s assumption that each layer of soil would respond independent of the behavior of the adjacent soil layers; this led to the second “beam and spring” model used to model the lateral soil loading exerted on the pile under lateral deformation into soil. In spite of neglecting the shear transfer that should occur between the layers due to the bending moment variation, this type of assumption in the modeling has given a good and useful method for determining the pile responses during both static and dynamic motions.

In this procedure, the soil medium in contact with the pile, along its depth, is discretized into a finite number of elements; each element is represented by a combination of springs and dashpots (located at its center) to represent the soil stiffness and damping at each particular soil layer. This model is called the conventional  $p$ - $y$  curve model for soil. The springs representing each layer of soil may be linear or nonlinear. Effects such as soil disturbance during installation, possible gaps between soil and the pile, cyclic strength degradation, and rate effects could also be included in this model [39–42].

In the dynamic modeling using the  $p$ - $y$  curve approach, a separate free-field site analysis is carried out to obtain the acceleration response at the site; the acceleration time history is integrated twice to obtain the time-history response at the location of the pile. Then this response of the soil is back-applied to the soil–pile springs to obtain the corrected values. This is iterated back and forth between the free-field values and  $p$ - $y$  values until convergence is obtained. The main disadvantage of this procedure is that it will introduce numerical errors due to the numerical integration procedure utilized in the computations. A fully coupled analysis has also been developed to evaluate the pile and soil responses simultaneously [43]. The details of this  $p$ - $y$  curve approach will be discussed in greater detail in Section 8.4.

### 8.3.2.3 Elastic Continuum Approach

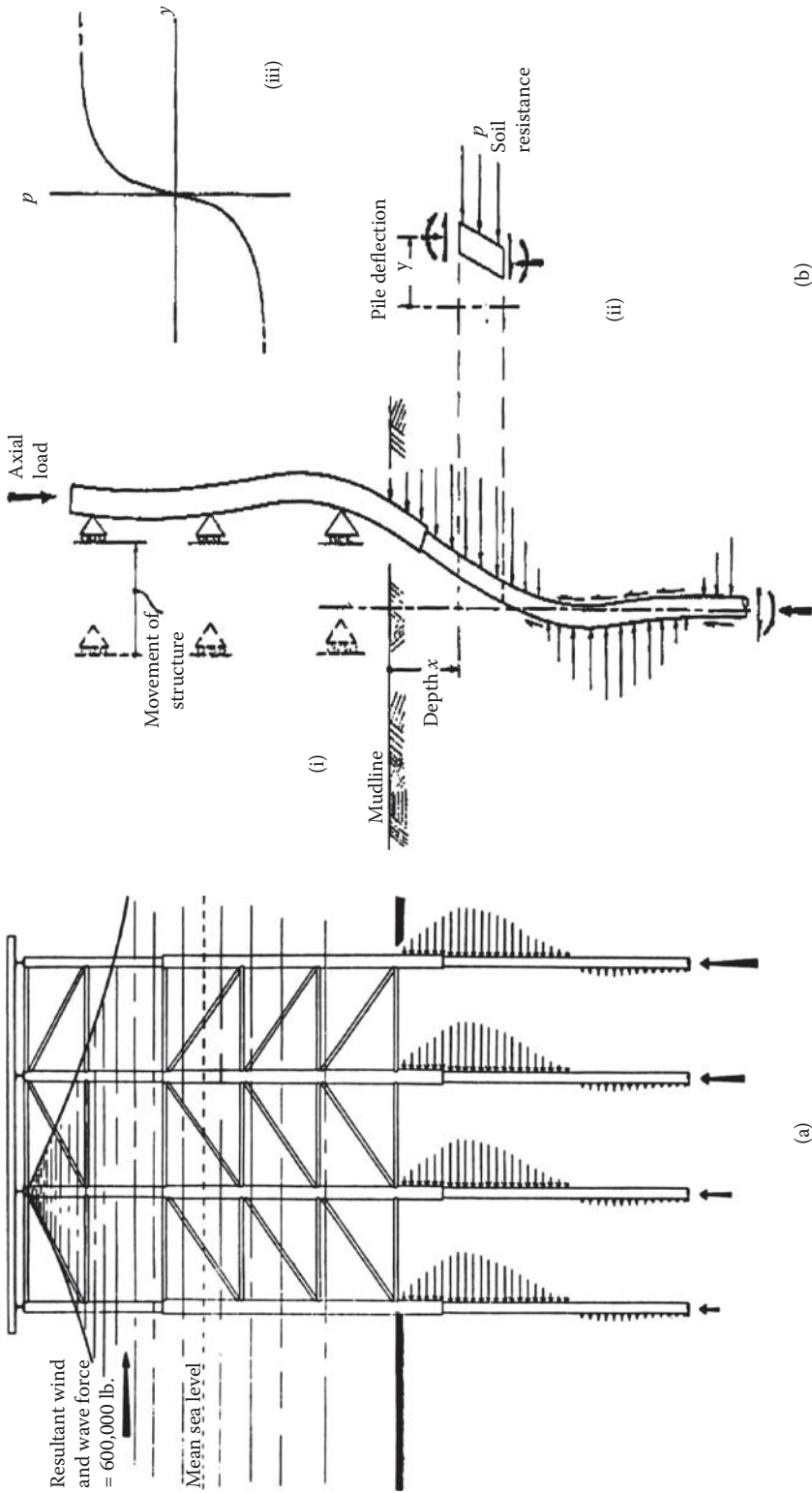
The third approach uses the closed-form solutions derived from Mindlin's equations [44] for point loads applied on the boundary or interior points in a semi-infinite soil mass. It can model the properties of a soil medium whose soil properties are constant or linearly varying or varying in a parabolic manner; moreover, the problem is applicable only for small strain steady-state vibration problems. When the soil profiles are layered, this approach cannot be used properly. Mindlin's approach was applied to soil–pile interaction problems by Poulos and his associates [45–47] for both axial and transverse loadings. He has given solutions for both single and group of piles under static loads. He has also dealt with a number of pile–soil interaction issues such as degradation of soil resistance under cyclic loads, gaps during pile–soil motion, bilinear elastoplastic springs, and friction–slider mechanism. Another researcher who has extended the continuum solution of pile–soil interaction is Novak (and his associates) [48–50] considering axial and lateral motions of single and group of piles. He has also considered the layered soils, degradation of soil strengths, and improper fixity of tower to the pile caps. Gazetas and Dobry [51] used a substructure procedure to consider the inertial and stiffness force of the tower–pile–soil interaction using a complex-valued impedance function for the pile-head stiffness. They used constant, linearly varying and parabolic soil modulus variations for representing the soil modulus; in addition, they also investigated the effect of layering in soils. Poulos [52], Gazetas [53], and Novak [54] have given extensive reviews on soil–pile interaction problems, which can be consulted for extensions in the area of pile–soil interaction.

### 8.3.2.4 Finite Element Approaches

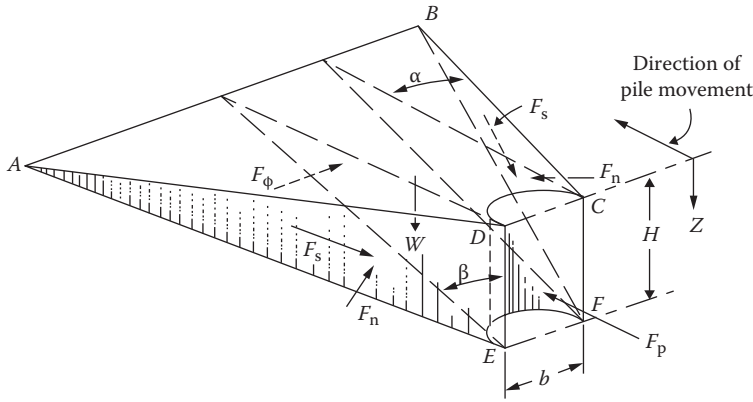
Finite element models provide the most comprehensive approaches available for investigating the soil–structure interaction problems. The advantages of the procedure include the ability to carry out the three-dimensional soil–structure analysis of the structure having single and group of piles as foundation, in a single step fully coupled manner. The major requisites in such a methodology will be (i) provision of the proper soil constitutive models that can incorporate the small-to-large-strain motions; (ii) soil degradation due to load cycling; (iii) ability to incorporate the initial soil disturbances that occur during installation; and (iv) other relevant issues such as soil scour and soil–pile gaps. Some relevant papers that need to be referred to in this area are given in references [55–61].

## 8.4 $P$ - $Y$ CURVE APPROACH

The earlier studies on the deformation behavior of laterally loaded piles were started by Skempton [62], Terzaghi [63], McClelland and Focht [39], and Matlock and Ripperger [64]. The type of pile–soil–structure interaction that will be encountered in an offshore structure due to wave loads is shown in Figure 8.8a and b [65].

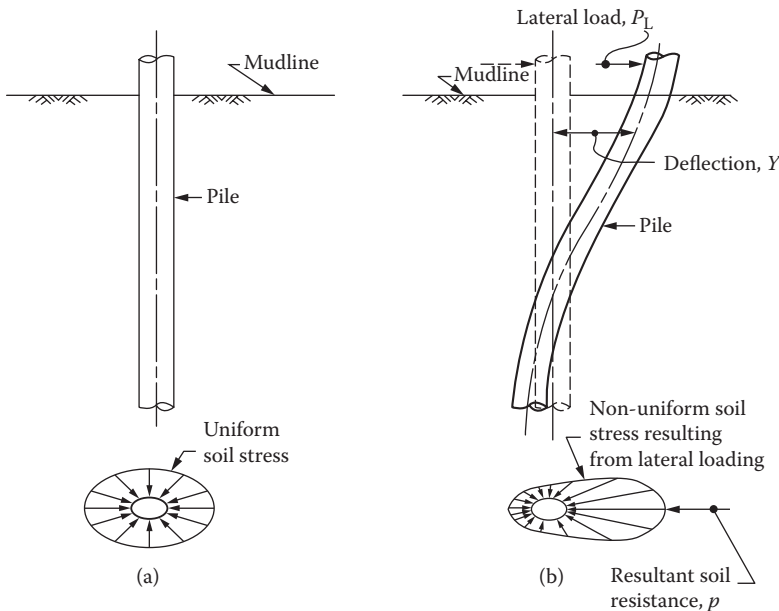


**FIGURE 8.8** (a) Lateral wave loads applied on the offshore structure and the soil resistance forces generated consequently. (From H. Matlock and L. C. Reese, Fifth International Conference on Soil Mechanics and Foundation Engineering, Paris, 1961.) (b) Schematics of the pile-soil deformation, stress-strain, and soil resistance development. (From H. Matlock, Offshore Technology Conference, Houston, TX, 1970.)

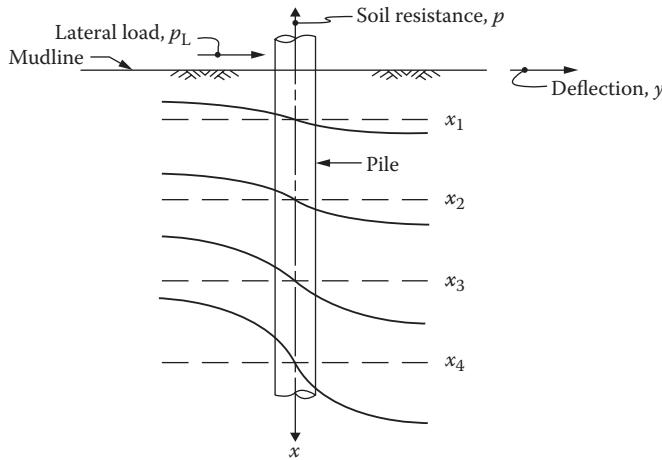


**FIGURE 8.9** Transverse passive soil pressure loads due to soil wedge. (From L.C. Reese, Discussion of soil modulus for laterally loaded piles, *Transactions, ASCE*, edited by B. McClelland and J.A. Focht, Jr., Volume 123, p. 1071, 1958. With permission.)

Reese [66] was the first to present the concept of a near surface wedge for the soil pressure on the pile (see Figure 8.9 [66]) using deep plasticity flow failure models and stated that the ultimate undrained soil resistance in clay is  $12.0c_u$ . Matlock extended the above wedge model to the nonuniform soil pressure field shown in Figure 8.10 [67]. Following Reese’s presentation on the soil failure model, Matlock and his associates conducted field and laboratory static and cyclic tests of loaded piles in soft clay and described the  $p$ – $y$  concept, in which the soil resistance  $p$  mobilized from the transverse nonuniform field surrounding the pile can be described in terms of the transverse displacement  $y$ .



**FIGURE 8.10** Definition of the  $p$ – $y$  concept for (a) pile at rest and (b) pile deforming laterally into soil. (From H. Matlock and L.C. Reese, *Transactions, Journal of the Soil Mechanics and Foundations Division, ASCE*, 86, SM5, pp. 673–694, 1961. With permission.)



**FIGURE 8.11** Family of  $p$ - $y$  curves, shown as a function of depth. (From B.J. Meyer and L.C. Reese, *Analysis of Single Piles Under Lateral Loading*, Research Report 244-1, Center for Transportation Research, Bureau of Engineering Research, University of Texas at Austin, Austin, TX, 1979. With permission.)

As shown in Figure 8.11 [68], a family of  $p$ - $y$  curves can be described showing the variation of transverse soil resistance as a function of depth; normally, the soil tends to become stiffer with depth. The model proposed for the  $p$ - $y$  curve by Matlock [40] is given by

$$p = (0.5)p_u(y/y_c)^{0.5} \tag{8.2}$$

where  $p_u$  is the ultimate soil resistance ( $= N_p c_u D$ ),  $N_p$  is the ultimate lateral soil resistance coefficient,  $D$  is the diameter of the pile,  $y_c$  is the critical pile deflection ( $= 2.5\epsilon_c D$ ), and  $\epsilon_c$  is the strain at one-half the maximum deviatoric stress in a UU triaxial compression test ( $= \epsilon_{50}$ ); these  $\epsilon_{50}$  values are given in Tables 8.2 [69] and 8.3 [40, 70, 71] for different types of soils. The ultimate soil resistance was determined from the lesser of two expressions obtained for shallow wedge failure and deep flow failure geometries (shown in Figures 8.9 through 8.11) and modified for pile diameter, depth, and loading regime. Specific charts for determining the modulus of subgrade reaction were provided.

The nondimensionalized curve representing the  $p$ - $y$  relationship shown in Equation 8.2 has been represented by the two curves shown in Figure 8.12 [40] for static and cyclic loading. This method is adopted by the API Recommended Practice RP2A [12] and is the established criterion for laterally loaded pile analysis in soft clays. Matlock has further extended this model to

**TABLE 8.2**  
**Representative Values for  $\epsilon_{50}$  for Stiff Clays**

	Average Undrained Shear Strength		
	Ksf		
	1-2	2-4	4-8
$\epsilon_{50}$ (in./in.)	0.007	0.005	0.004

Source: US Army Corps of Engineers, UFC 3-220-01A, 2004. *Deep Foundations*, United Facilities Criteria, USA Department of Defense, pp. 4-8; also USACE TI 818-02, 1998. With permission.

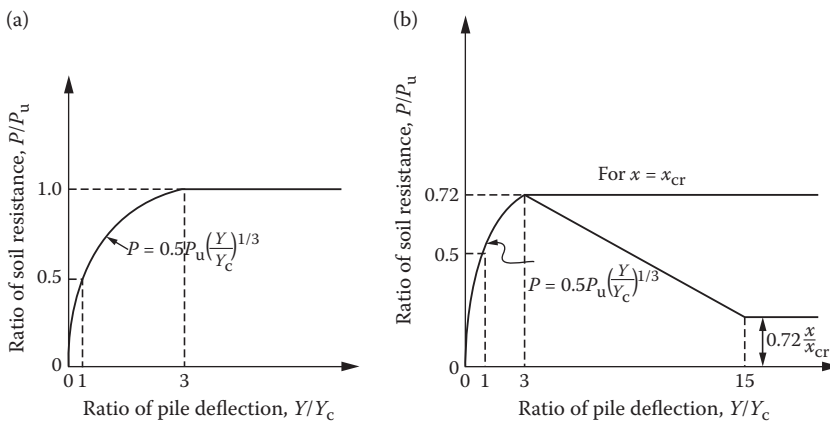
**TABLE 8.3**  
**Pertinent Soil Strength (c) and Strain (E50) Data for**  
**Generating  $p$ - $y$  Curves for Soft and Stiff Clays**

Soil Strain Parameter E50		
Soft clay	1.74 to 3.47 psi $c = 250$ to $500$ psf 12 to 24 kPa	E50 = 0.02
Medium clay	3.47 to 6.94psi $c = 500$ to $1000$ psf 24 to 48 kPa	E50 = 0.01
Stiff clay	6.94 to 13.9 psi $c = 1000$ to $2000$ psf 48 to 96 kPa	E50 = 0.007
Very stiff clay	13.9 to 27.8 psi $c = 2000$ to $4000$ psf 96 to 192 kPa	E50 = 0.005
Hard clay	27.8 to 55.6 psi $c = 4000$ to $8000$ psf	E50 = 0.004
Limestone	192 to 383 kPa	E50 = 0.001

*Note:* E50 =  $\epsilon_{50}$ .

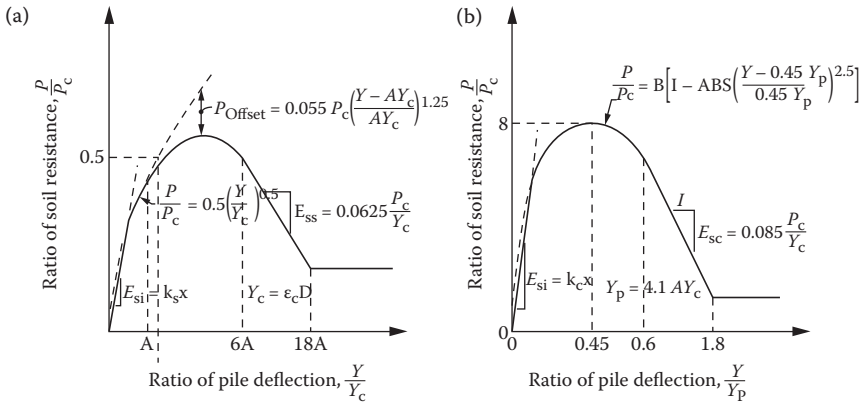
include (i) dynamic soil–structure interaction; (ii) soil model to represent the nonlinear, hysteretic, degrading soil support at the pile–soil interface; and (iii) possibility of existence of gap between the pile and soil [72].

Reese et al. [71] also conducted lateral pile load tests in an overconsolidated strain-softening stiff clay deposit and presented the characteristic  $p$ - $y$  curves shown in Figure 8.13a and b [72] for static and cyclic loading; these too are incorporated into the currently recommended API design curves.

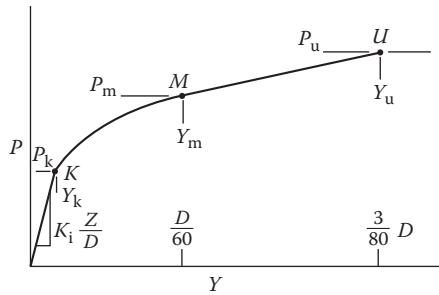


**FIGURE 8.12** Characteristic  $p$ - $y$  curve in soft clays for (a) static loading and (b) cyclic loading. (From H. Matlock, *Correlations for Design of laterally Loaded Piles in Sand*, Proceedings of Offshore Technology Conference, Paper # 1204, 18 pp., 1970.)





**FIGURE 8.13** Characteristic shape of  $p$ - $y$  curve in stiff clay for (a) static loading and (b) cyclic loading. (From H. Matlock and S. Foo, *Axial Analysis of Piles Using a Hysteretic and Degrading Soil Model*, Proc. 1st Intl. Conf. on Numerical Methods in Offshore Piling, London, pp. 127–133, 1980. With permission.)



**FIGURE 8.14** Characteristic shape of  $p$ - $y$  curve in sand. (From L.C. Reese et al., *Field Testing and Analysis of Laterally Loaded Piles in Sand*, Proceedings of Sixth Annual Offshore Technology Conference, Austin, TX, Volume II, Paper # OTC2080, pp. 473–485, 1974.)

The API recommended method for constructing  $p$ - $y$  curves in sand was the result of the work by Reese et al. [41] from the results of static and cyclic lateral load tests. The curve consisted of two straight line segments joined by a parabolic segment, as shown in Figure 8.14 [41]. Specific numerically computed charts for determining the modulus of subgrade reaction were provided earlier based on Hudson and Reese’s published studies (given in Appendices 8A and 8B, given in this chapter) [65, 73, 74]; these charts have been used in solving the problems of pile–soil interaction studies in this chapter. Reese’s most influential contribution was the introduction of the computer programs COM624P [75] and LPILE [76]; these programs provided highly efficient tools for  $p$ - $y$  analysis of static and cyclic laterally loaded piles in layered soils. Others who have also done significant work on  $p$ - $y$  curve development in piles are Stevens and Audibert [77], O’Neill and Murchison [78], and Kagawa and Kraft [79].

### 8.5 CLASSICAL DERIVATIONS FOR PILE–SOIL INTERACTION

In this approach, the standard differential equation for the bending of a beam, loaded transversely, is applied to the case of pile–soil interaction. If the soil resistance on the pile (which is acting transversely) is represented as a linear or a nonlinear function of depth, as well as transverse deformation of the pile into soil, then the differential equation for the bending of the beam can be represented by



$$EI \, d^4v/dx^4 = p(x, v) \quad (8.3)$$

where  $p$  is the transverse load experienced by the pile during pile-soil interaction,  $EI$  is the bending stiffness of the pile,  $v$  is the deformation of the pile into soil, and  $x$  is the distance along the length of the pile at which  $v$  is specified.

If Equation 8.3 is progressively integrated in terms of transverse shear, bending moment, slope, and deflection, then these can be expressed as follows:

$$\begin{aligned} \text{soil reaction: } p(x, v) &= EI \, d^4v/dx^4 \\ \text{shear: } V &= EI \, d^3v/dx^3 \\ \text{bending moment: } M &= EI \, d^2v/dx^2 \\ \text{slope of the deflected pile: } s &= dv/dx \\ \text{deflection of the pile} &= v \end{aligned} \quad (8.4)$$

The soil reaction is assumed to be a function of depth and is represented by the following:

$$\text{soil reaction } p(x, v) = -E_s(x)v \quad (8.5)$$

where  $E_s(x)$  is the depth-dependent soil modulus, and  $v$  is the displacement at any point  $x$  along the length of the pile. Hence,  $E_s(x) = -p(x, v)/v$ .

Therefore, Equation 8.3 can be rewritten as

$$EI \, d^4v/dx^4 = -E_s(x)v \quad (8.6)$$

where  $E_s(x)$  is the depth-dependent soil modulus, which is a function of depth  $x$ .

The soil reaction  $p(x, v)$ , experienced by the pile at the seabed, and, the soil modulus  $E_s(x)$ , can be represented by the plots shown in Figure 8.15 (b) and (c), respectively [80].

When the transverse load  $P_t$  at the top (or the pile head moment) increases, then the deflection  $v$  and the corresponding  $p(x, v)$  and the soil modulus  $E_s(x)$  also increase. The relationships that exist between (i)  $p(x, v)$  and  $v$  and (ii)  $E_s(x)$  and  $x$  are presented in Figures 8.16a and b [74], respectively. Factors such as pile width (or diameter), depth  $x$ ,  $EI$  (the flexural stiffness of the pile), and the nature of soil in the seabed will influence the values of  $p(x, v)$  and  $E_s(x)$ . The variation of  $E_s(x)$  with respect to depth can be expressed as

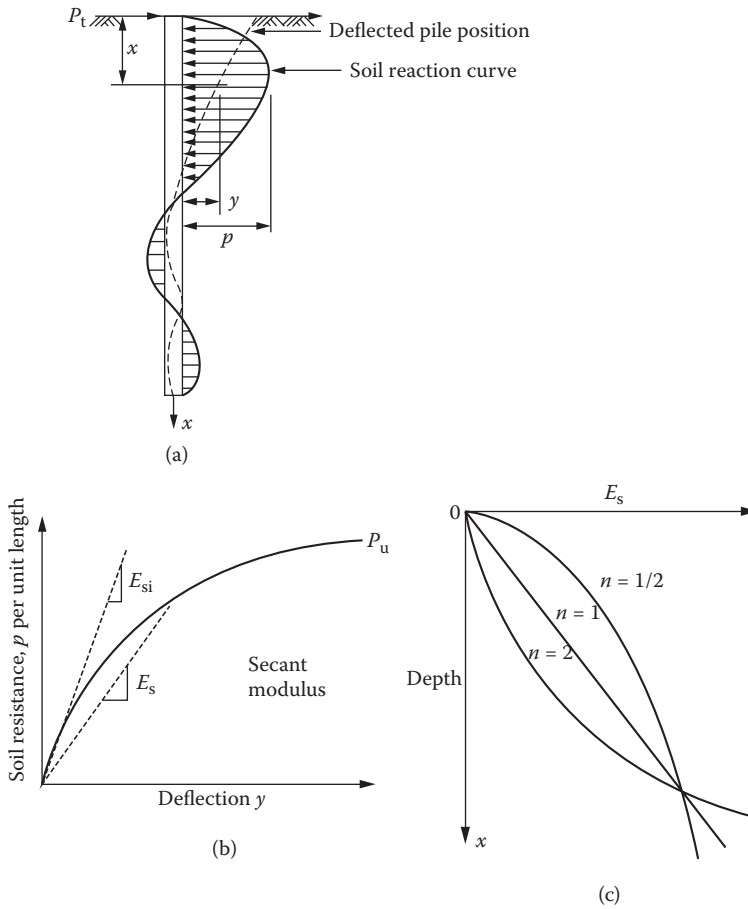
$$E_s = kx^n \quad (8.7)$$

where  $k$  = initial modulus of subgrade reaction. The value of index  $n$  depends on the type of soil and the batter of the pile. Typical values considered for  $n$  are 1/2, 1, or 2, as shown in Figure 8.15c. The most common value of  $n$  considered for seabed soil is  $n = 1.0$ , which gives the linear variation for  $E_s = kx$ .

Typical values used for various soils for the  $p$ - $y$  curve development is given in Table 8.4 [71].

Equation 8.4 can be rewritten for a linear variation of depth-dependent soil modulus as

$$EI \, d^4v/dx^4 + (kx)v = 0 \quad (8.8)$$

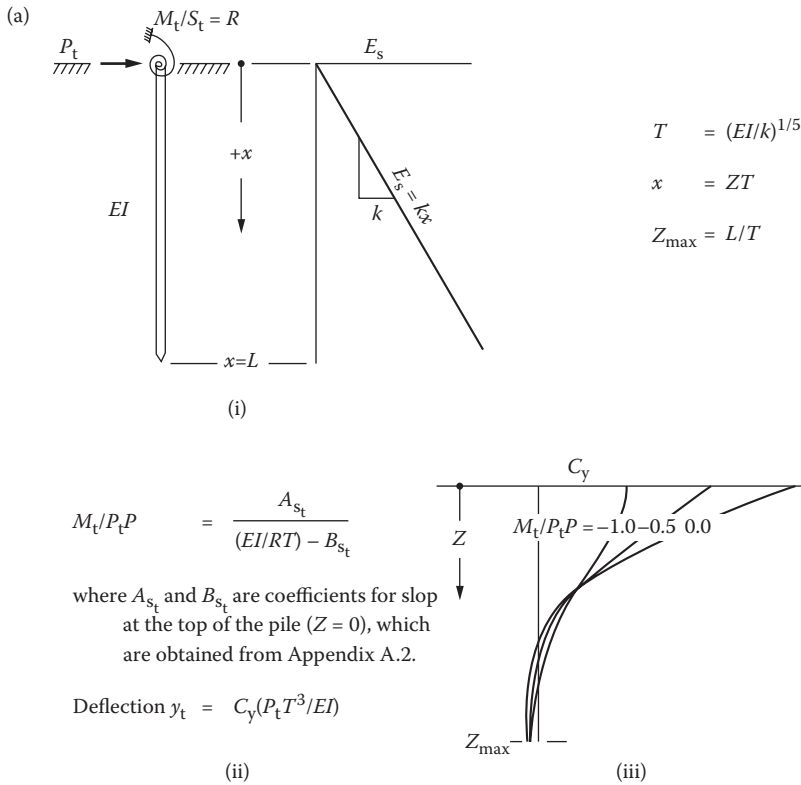


**FIGURE 8.15** Development of  $p$ - $y$  curve concept: (a) soil resistance development along the depth of the deformed pile; (b) characteristic form of a  $p$ - $y$  curve; and (c) form of variation of  $E_s$  with depth. (From V.N.S. Murthy, *Deep Foundations II: Behavior of Laterally Loaded Vertical and Battered Piles*, Marcel Dekker, New York, pp. 703, 2003. With permission.)

This equation is differentiated with respect to  $x$  once to obtain the fifth-order differential equation given by

$$d^5v/dx^5 + (1/T^5)[xdv/dx + v] = 0, \text{ where } T = [EI/k]^{(1/5)}$$

Equation 8.8 is solved subject to the conditions where at  $x = L$  (where  $L$  is very large),  $v = 0$  and  $dv/dx = 0$ . Also at the top of the pile, shear  $V = EI d^3v/dx^3 = P_t$  (or  $P_T$ ),  $M_T =$  the moment applied at the top of the pile ( $= EI d^2v/dx^2$ ) (or  $\theta =$  the pile-head rotation at the top of the pile  $= dv/dx$ ), and  $p(x,v) = EI d^4v/dx^4 = 0$ . From these five conditions, the five unknowns in the problem can be solved to obtain the pertinent parameters of the pile-soil interaction such as deformation or moment or shear or soil resistance  $[p(x,v)]$  variation along the length of the pile. These have been obtained for various soil and structural parameters and given as tabulated charts in Tables 8A.1 through 8A.6 and 8B.1 through 8B.6. In the two appendixes given at the end, the notations given in Figure 8.16a and b have been used [74].

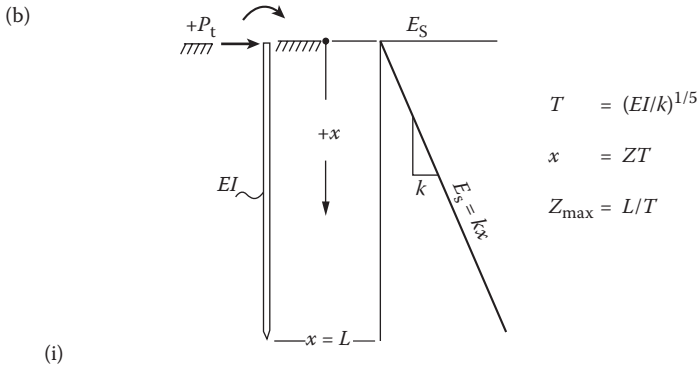


**FIGURE 8.16** (a) Notations used in Appendix 8A Tables 8A.1 to 8A.6 for determining deflection coefficients for various ratios of  $(M_t/P_tT)$ ,  $(x/T)$  and  $(L/T)_{max}$  are indicated in figures (i), (ii), and (iii). (b) Notations used in Appendix 8A Tables 8A.1 to 8A.6 for determining deflection, slope, moment, shear and reaction coefficients for various ratios of  $(M_t/P_tT)$ ,  $(x/T)$  and  $(L/T)_{max}$  are indicated in figures (i), (ii), and (iii). (From H. Matlock, and L.C. Reese, *Transactions, American Society of Civil Engineers*, 127, 3370, Part I, pp. 1220–1269, 1962.)

### 8.6 CODE-BASED FOUNDATION DESIGN FOR PILE-SUPPORTED OFFSHORE STRUCTURES

The design of piles and pile groups for transverse loading is one of the most important components in the design process for an offshore platform. Most of the environmental agents such as wind, waves, currents, earthquakes, and ice impose transverse forces on the offshore structure. These forces, along with the structure weights and operational loads, are ultimately transmitted to the soil foundation below as axial/transverse loads and moments on the pile heads of the platform, located at the seabed level. Designing and selecting the pile sections to have adequate strength and stiffness to efficiently carry these extreme loads and to transfer them safely into the soil foundation, around and below, is the objective of the pile design process, illustrated herein. The vertical and horizontal loads and moments coming at the base of the offshore structure are transferred to the seabed through side shear, end bearing, and lateral soil resistance developed through soil pressures, as shown in Figure 8.17 [81].

The axial pile resistance has two distinct components, viz., the frictional shear resistance along the pile shaft length and the end bearing resistance at the pile bottom. The axial resistance development of the pile is figuratively described in Figure 8.18 [82] in normally consolidated clays. The soil



$$T = (EI/k)^{1/5}$$

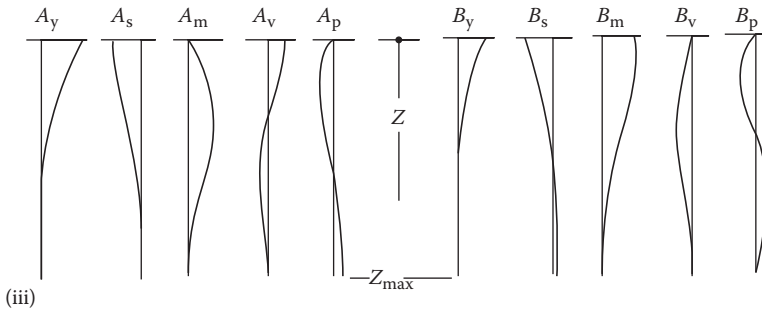
$$x = ZT$$

$$Z_{\max} = L/T$$

(i)

Deflection	$y = (P_t T^3/EI)A_y + (M_t T^2/EI)B_y$
Slope	$S = (P_t T^2/EI)A_s + (M_t T/EI)B_s$
Moment	$M = (P_t T)A_m + (M_t)B_m$
Shear	$V = (P_t)A_v + (M_t/T)B_v$
Soil reaction	$p = (P_t)A_p + (M_t/T^2)B_p$

(ii)



(iii)

**FIGURE 8.16** (Continued) (a) Notations used in Appendix 8A Tables 8A.1 to 8A.6 for determining deflection coefficients for various ratios of  $(M_T/P_T T)$ ,  $(x/T)$  and  $(L/T)_{\max}$  are indicated in figures (i), (ii), and (iii). (b) Notations used in Appendix 8A Tables 8A.1 to 8A.6 for determining deflection, slope, moment, shear and reaction coefficients for various ratios of  $(M_T/P_T T)$ ,  $(x/T)$  and  $(L/T)_{\max}$  are indicated in figures (i), (ii), and (iii). (From H. Matlock, and L.C. Reese, *Transactions, American Society of Civil Engineers*, 127, 3370, Part I, pp. 1220–1269, 1962.)

near the top plays relatively a minor role in the overall soil strength development in the pile; in this case, less than 10% of the soil strength is developed in the top 30% of pile depth.

### 8.6.1 AXIAL RESISTANCE OF PILES

For vertical compressive loading, the necessary equation has been given earlier by Equation 4.30:

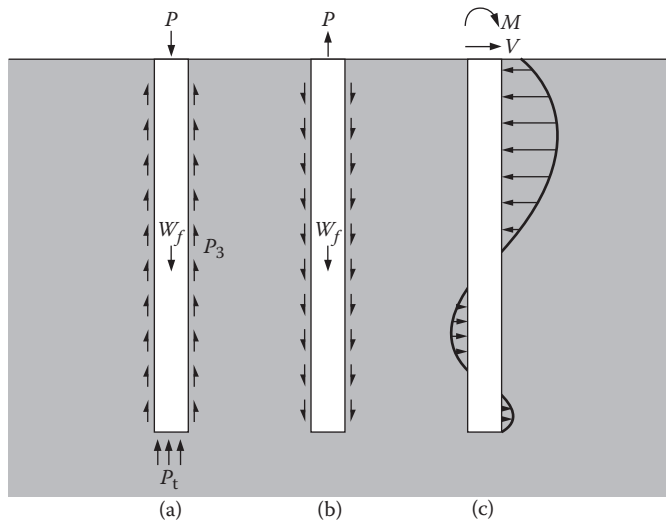
$$Q_{\text{ultimate}} = Q_{\text{side shear}} + Q_{\text{end bearing}} = \sum_i^n f_i A_i + q A_{\text{pile end}} \tag{4.30}$$

**TABLE 8.4**  
**Values of Soil Modulus Parameter  $k$  for Clays**

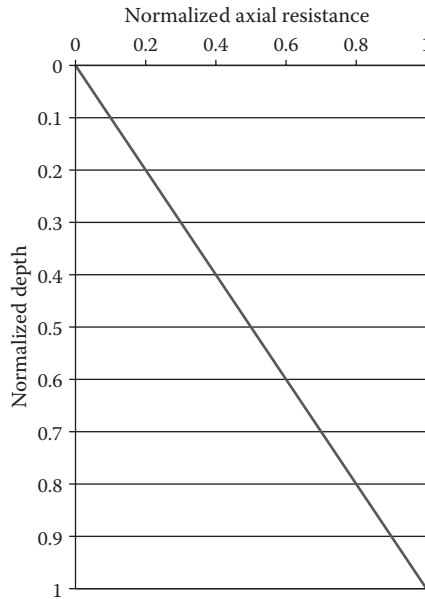
Soil Modulus Parameter $k$ for Clays			
Average Undrained Shear Strength		Static	Cyclic
Soft clay	$c = 1.74$ to $3.47$ psi	30 pci	–
	250 to 500 psf		
	12 to 24 kPa	8140 kPa/m	–
Medium clay	$c = 3.47$ to $6.94$ psi	100 pci	–
	500 to 1000 psf		
	24 to 48 kPa	27,150 kPa/m	–
Stiff clay	$c = 6.94$ to $13.9$ psi	500 pci	200 pci
	1000 to 2000 psf		
	48 to 96 kPa	136,000 kPa/m	54,300 kPa/m
Very stiff clay	$c = 13.9$ to $27.8$ psi	1000 pci	400 pci
	2000 to 4000 psf		
	96 to 192 kPa	271,000 kPa/m	108,500 kPa/m
Hard clay	$c = 27.8$ to $55.6$ psi	2000 pci	800 pci
	4000 to 8000 psf		
	192 to 383 kPa	543,000 kPa/m	217,000 kPa/m

Source: L.C. Reese et al., *Field Testing and Analysis of Laterally Loaded Piles in Stiff Clay*, Paper # 2312, Proceedings of Offshore Technology Conference, Richardson, TX, pp. 671–690, 1975. With permission.

Note: These criteria are used by LPILE1 to calculate  $p$ - $y$  curves internally: Option 1 - Soft Clay (Matlock 1970); Option 2 - Stiff Clay below the watertable (Reese et al. 1975); Option 3 - Stiff Clay above the watertable (Reese and Welch 1975); and Option 4 - Sand (Reese et al. 1974).



**FIGURE 8.17** Possible modes of load transfer through a driven pile: (a) compressive loads through surface shear and bottom-end bearing; (b) tensile pullout by surface shear forces; and (c) transverse and bending loads by lateral soil pressures. (From D.P. Coduto, *Foundation Design: Principles and Practice*, 2nd Edition, Prentice Hall, Englewood Cliffs, NJ, p. 377, 2001. With permission.)



**FIGURE 8.18** Total axial and pile end soil resistance. (From D. Murff, *Design of Laterally Loaded Piles for Offshore Platforms*, Lecture Presented at Texas A&M University, College Station, TX, p. 3, 2003.)

where the summation sign becomes necessary when there are  $n$  number of pile diameter variations in the driven pile. A similar equation is given in Section G.4 of the API code [83]. The values for the side frictional shear and end bearing in cohesive soil is given as

$$f_i = \alpha_i c_{ui} \quad (8.9)$$

where  $\alpha_{ui}$  = a dimensionless factor and  $c_{ui}$  = undrained shear strength of the soil at the point under consideration, for the  $i$ th variation in pile cross section;  $\alpha_i = (0.5) \psi_i^{(-0.5)}$  for  $\psi_i \leq 1.0$ ;  $\alpha_i = (0.5) \psi_i^{(-0.25)}$  for  $\psi_i > 1.0$ , with a constraint that  $\alpha_i \leq 1.0$ , where  $\psi_i = c_{ui}/p'_0$  and  $p'_0$  effective overburden pressure at the point under consideration. The end bearing strength  $q$  of cohesive soil is given as  $q = (9.0) c_{u_{\text{pile bottom}}}$ .

The frictional shear is assumed to act both on the inside and outside of the pile, unless the pile end is blocked by a plug.

The values for the side frictional shear and end bearing in cohesion-less (or sandy) soil is given by

$$f = K p'_0 \tan(\delta) \quad (8.10)$$

where  $K$  = dimensionless coefficient of lateral earth pressure and  $\delta$  is the friction angle between the soil and pile wall, given in Table 8.5 [84]. Also,  $q = p'_0 N_q$  where  $N_q$  is a dimensionless bearing capacity factor, given in Table 8.5.

The design parameters for various types of cohesion-less soils are given in Table 8.5.

**TABLE 8.5**  
**Design Parameters for Cohesion-Less Siliceous Soil**

Density	Soil Description	Soil-Pile Friction Angle, $\delta$ Degrees	Limiting Skin Friction Values kPa (kips/ft. <sup>2</sup> )	$N_q$	Limiting Unit End Bearing Values MPa (kips/ft. <sup>2</sup> )
Very loose	Sand	15	47.8 (1.0)	8	1.9 (40)
Loose	Sand-silt**				
Medium	Silt				
Loose	Sand	20	67.0 (1.4)	12	2.9 (60)
Medium	Sand-silt**				
Dense	Silt				
Medium	Sand	25	81.3 (1.7)	20	4.8 (100)
Dense	Sand-silt**				
Dense	Sand	30	95.7 (2.0)	40	9.6 (200)
Very dense	Sand-silt**				
Dense	Gravel	35	114.8 (2.4)	50	12.0 (250)
Very dense	Sand				

Source: American Petroleum Institute, Recommended Practice for Planning, Designing and Constructing Fixed Offshore Platforms (RP 2A-LRFD), Washington, DC, 1993.

\* The parameters listed in this table are intended as guidelines only. Where detailed information such as in situ cone tests, strength tests on high quality samples, model tests, or pile driving performance is available, other values may be justified.

\*\* Sand-silt includes those soils with significant fractions of both sand and silt. Strength values generally increase with increasing sand fractions and decrease with increasing silt fractions.

*Group of piles:* For a group of piles, when the pile spacing is less than eight diameters, group effects must be considered [85]. For piles embedded in clays, the group capacity may be less than the sum of all the individual pile capacities, making up the group. For piles embedded in sands, the pile group capacity may be higher than the sum of the capacities of the piles in the group. The group settlement in clay or sand will be relatively higher than that of a single pile subjected to the average load of the pile group.

According to Coduto [86], the group efficiency of pile effects is represented by the ratio  $\eta$  and the load  $P_g$  carried by a group of  $n$  piles and is given as

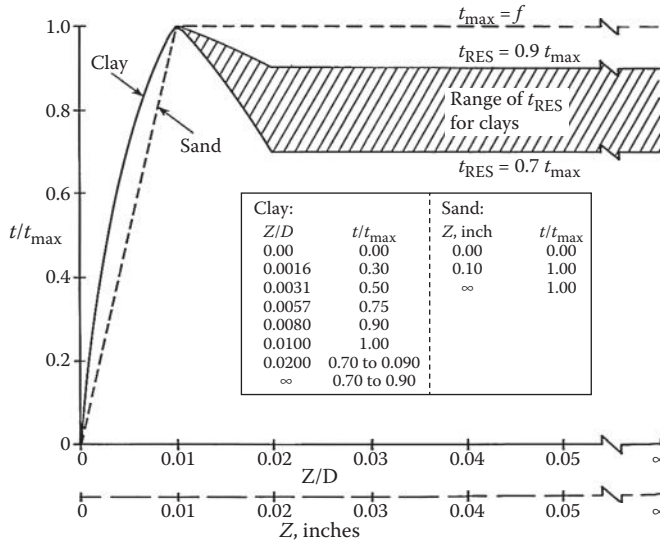
$$P_g = \eta n P_{\text{single pile}} \quad (8.11)$$

where  $\eta$  is the group efficiency factor,  $n$  = number of piles in the group, and  $\eta$  is given as  $\eta = 1.0 - \theta\{[n-1]m + (m-1)n\}/\{90.0(mn)\}$ , where  $m$  = number of rows of piles (in a rectangular group of piles),  $n$  = number of piles in a row, and  $\theta = \tan^{-1}(B/s)$  in degrees, with  $B$  = diameter of a single pile and  $s$  the spacing between piles.

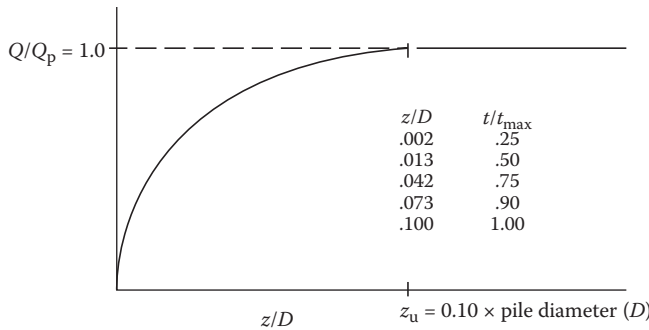
Probably for a circular pile groups, the values of  $m = n$  in Equation 8.11, and the equivalent lateral dimensions are to be determined from the square having the same area as the circle; the spacing is to be determined from the number of piles (in the circular area) to be accommodated in the equivalent square area.

*Development of soil reaction for axially loaded piles:* The axial resistance of the pile is provided by a combination of soil-pile adhesion (providing shear resistance to penetration) and end bearing resistance generated (due to end compressive stresses). The mobilization of transverse shear resistance is dependent on the pile deformation ( $z$ ) into soil versus the mobilized pile adhesion ( $t$ ) given by  $t-z$  curves (shown in Figure 8.19 [87]). The mobilization of end bearing resistance is dependent on the local pile deformation versus mobilized end bearing capacity, given by  $Q-z$  curves (shown in Figure 8.20 [88]).

The shape of the  $t-z$  curves at soil displacements greater than  $z_{\text{max}}$  shown in Figure 8.19 should be carefully considered. It is often observed that the values of the residual adhesion ratio ( $t_{\text{res}}/t_{\text{max}}$ ) at the



**FIGURE 8.19** Relationship between soil shear resistance development ( $t/t_{max}$ ) versus pile deformation into soil. (From American Petroleum Institute, *Section G on Foundation Design in the Recommended Practice for Planning, Designing and Constructing Fixed Offshore Platforms—Load and Resistance Factor Design (RP 2A-LRFD)*, American Petroleum Institute, Washington, DC, p. 70, 1993. With permission.)

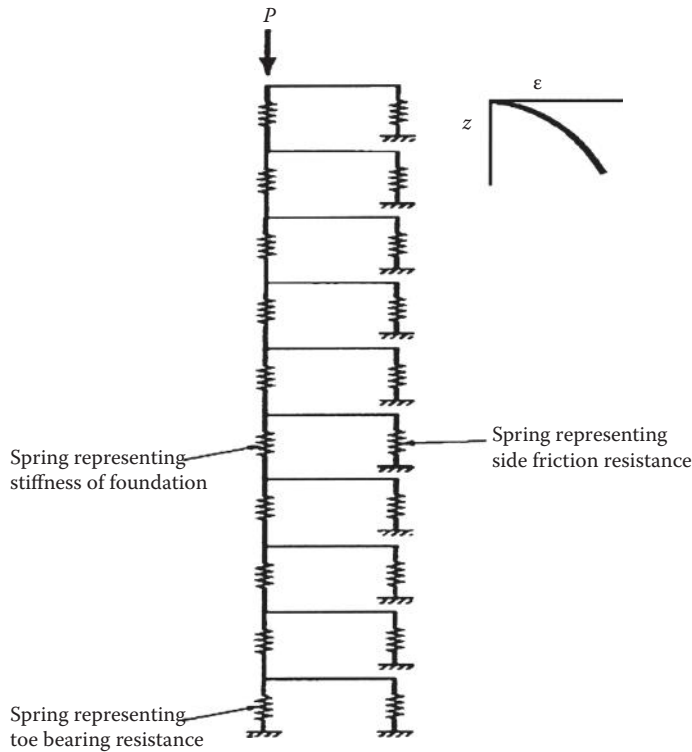


**FIGURE 8.20** Relationship between soil bearing resistance development at the bottom versus pile tip deformation into soil. (From American Petroleum Institute, *Section G on Foundation Design in the Recommended Practice for Planning, Designing and Constructing Fixed Offshore Platforms—Load and Resistance Factor Design (RP 2A-LRFD)*, American Petroleum Institute, Washington, DC, p. 71, 1993. With permission.)

axial pile deformation (into soil), at which it occurs, are dependent on the soil stress–strain behavior, stress–strain history, pile load sequence, and other factors. Additional information is available in references [89, 90]. The development of the  $t-z$  curve is dependent on deformations obtained from the numerical model shown in Figure 8.21 [91] to compute the deformation of the pile foundation at the point under consideration.

The model divides the foundation into a number of components and represents each component to have a certain soil modulus (of elasticity). The side-friction (or shear) resistance acting on each component is modeled as a nonlinear spring as shown in the  $t-z$  curve in Figure 8.21 [91]; in this plot,  $t$  is the load acting on the component element, and  $z$  is the settlement of the component. Similarly, the bearing capacity load acting at the base of the pile end is also represented by a corresponding nonlinear spring, as shown in the figure. The required load is applied on top of this model, and the





**FIGURE 8.21** Numerical model used in  $t$ - $z$  method. (From D.P. Coduto, *Foundation Design: Principles and Practice*, 2nd Edition, Prentice Hall, Englewood Cliffs, NJ, p. 551, 2001. With permission.)

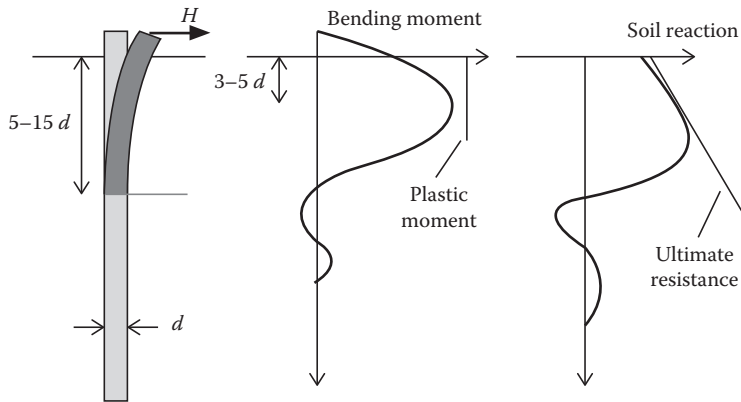
subsequent deformation is taken as the foundation deformation. This model explicitly considers the axial compression of the foundation soil, and its variation along the pile length; hence, the model is more precise, depending on the accuracy with which the  $t$ - $z$  curves are defined. In order to be more accurate, the experimental  $t$ - $z$  curves have been obtained by back-calculating the  $t$ - $z$  curves from measurements obtained from instrumented load tests on piles.

## 8.6.2 SOIL REACTION FOR LATERALLY LOADED PILES

Pile foundation should be designed for resisting the factored lateral loads coming upon the offshore steel template structure; the loads can be either static or dynamic. The major effect due to lateral movement of the platform structure will be felt by the soil near its surface, approximately to a depth of 15 times the pile diameter, as shown in Figure 8.22 [92]. The effects of soil scour around the platform base, as well as the influence of soil disturbance during the installation of piles, will affect the soil resistance experienced by the embedded pile.

### 8.6.2.1 Lateral Bearing Capacity for Piles in Soft Clay

For static lateral loads (as in the case of piles), the ultimate unit lateral bearing strength of soft clay  $p_u$  is found to vary between  $8c_u$  and  $12c_u$ , except at very shallow depths; it has been observed that cyclic loads cause deterioration of lateral bearing capacities of soils below that of static values. When no definite values are available for the soil at site, the following values of the bearing capacities of soil are recommended by the API RP2 code.  $p_u$  is found to increase from  $3c_u$  to  $9c_u$  as the value of  $Z$  (the depth below the seabed) increases from 0.0 to  $Z_R$ , the reference depth below which the lateral bearing capacity of soil remains constant at  $9c_u$ .



**FIGURE 8.22** Schematic of laterally loaded pile response. (From M. Randolph et al., *Challenges of Offshore Geotechnical Engineering*, p. 17/54. Available at [www.iransaze.com/files-for-downloading/ebglishbook/khak/Challenges\\_of\\_Offshore\\_Geotechnical\\_Engineering.pdf](http://www.iransaze.com/files-for-downloading/ebglishbook/khak/Challenges_of_Offshore_Geotechnical_Engineering.pdf), 2005. With permission.)

Hence, the lateral pressure  $p_u$  can be expressed as

$$p_u = (3.0)c_u + \gamma Z + (Jc_u/D)Z \quad (8.12)$$

where  $p_u = (9.0)c_u$ , for  $Z \geq Z_R$ ;  $p_u$  = ultimate lateral soil resistance (in stress units);  $c_u$  = undrained shear strength of undisturbed clay soil samples;  $D$  = pile diameter;  $\gamma$  = effective unit weight of soil;  $J$  = dimensionless empirical constant, ranging from 0.25 to 0.50;  $Z$  = depth below seabed, with  $Z = (6D)/[\gamma D/c_u + J]$ , with a provision that  $Z \geq (2.5D)$ .

### 8.6.2.2 Load–Deflection Relationships for Piles in Soft Clay

The relationship between the lateral deflection and lateral soil resistance is generally nonlinear for soft clays. The  $p$ – $y$  curve for the short-term static load is generated from the values given in Table 8.6 [93].

**TABLE 8.6**  
Values for  $(p/p_u)$  versus  $(y/y_c)$  for Static Loads

#	$p/p_u$	$y/y_c$
1	0.00	0.00
2	0.50	1.00
3	0.72	3.00
4	1.00	8.00
5	1.00	$\infty$

Source: American Petroleum Institute, *Section G on Foundation Design in the Recommended Practice for Planning, Designing and Constructing Fixed Offshore Platforms—Load and Resistance Factor Design (RP 2A-LRFD)*, American Petroleum Institute, Washington, DC, p. 71, 1993. With permission.

In Table 8.6,  $p$  is the actual lateral pressure (or resistance),  $y$  is the actual lateral deformation of the pile,  $y_c = (2.5)(\epsilon_c D)$ , and  $\epsilon_c$  is the strain that occurs at one-half the maximum stress on undrained compression tests carried out on undisturbed soil samples in the laboratory. For the case of cyclic loading, the values given in Table 8.7 [94] could be used to generate the  $p$ - $y$  curves.

### 8.6.2.3 Lateral Bearing Resistance for Piles in Stiff Clay

The static ultimate bearing pressure (or resistance) for stiff clays,  $p_u$ , has been observed to vary between  $(8.0)(c_u)$  and  $(12.0)(c_u)$ . Since the cyclic strength reduces rapidly, the ultimate static strength should be reduced when designing structures for cyclic resistance.

### 8.6.2.4 Load–Deflection Relationship for Piles in Stiff Clay

The load–deflection relationship is nonlinear for stiff clays. Since stiff clays are more brittle than soft clays, it should be taken into account that the lateral resistance decreases very rapidly at large deformation of piles in stiff clays.

### 8.6.2.5 Lateral Bearing Capacity for Piles in Sand

The ultimate bearing pressure (or resistance or capacity) for piles in sand varies from a value given by Equation 8.13 at shallow depths to that given by Equation 8.14 for deeper depths. At any given depth, the smaller of the two values given by Equation 8.13 or 8.14 is taken as the ultimate bearing capacity (or resistance or pressure):

$$p_{\text{ult\_shallow}} = (C_1 Z + C_2 D) \gamma' Z \quad (8.13)$$

where  $\gamma'$  is the effective weight of soil, and the constants  $C_1$  and  $C_2$  are obtained from Figure 8.23 [95].

For deeper depths,

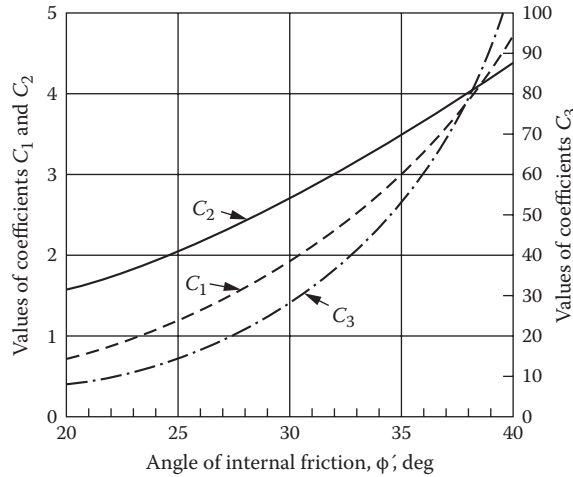
$$p_{\text{ult\_deep}} = (C_3 D) \gamma' Z \quad (8.14)$$

where the constant  $C_3$  is obtained from Figure 8.23.

**TABLE 8.7**  
**Values for  $(p/p_u)$  versus  $(y/y_c)$  for Cyclic Loads**

#	$Z > Z_R$		$Z < Z_R$	
	$p/p_u$	$y/y_c$	$p/p_u$	$y/y_c$
1	0.00	0.0	0.0	0.0
2	0.50	1.0	0.50	1.0
3	0.72	3.0	0.72	3.0
4	0.72	$\infty$	$0.72 (Z/Z_R)$	15.0
5	—		$0.72 (Z/Z_R)$	$\infty$

Source: American Petroleum Institute, *Section G on Foundation Design in the Recommended Practice for Planning, Designing and Constructing Fixed Offshore Platforms—Load and Resistance Factor Design (RP 2A-LRFD)*, American Petroleum Institute, Washington, DC, p. 72, 1993. With permission.



**FIGURE 8.23** Plot of the values of coefficients  $C_1$ ,  $C_2$ , and  $C_3$  as a function of  $\phi'$ . (From American Petroleum Institute, *Section G on Foundation Design in the Recommended Practice for Planning, Designing and Constructing Fixed Offshore Platforms—Load and Resistance Factor Design [RP 2A-LRFD]*, American Petroleum Institute, Washington, DC, p. 73, 1993. With permission.)

**8.6.2.6 Load Deflection ( $p$ - $y$ ) Curves for Piles in Sand**

The lateral soil pressure (or resistance or capacity) versus the lateral deformation of the pile in a sandy seabed is nonlinear in nature and can be approximated to that given in Equation 8.15:

$$p = Ap_u \tanh \left[ \frac{(kZ)}{(Ap_u)} y \right] \tag{8.15}$$

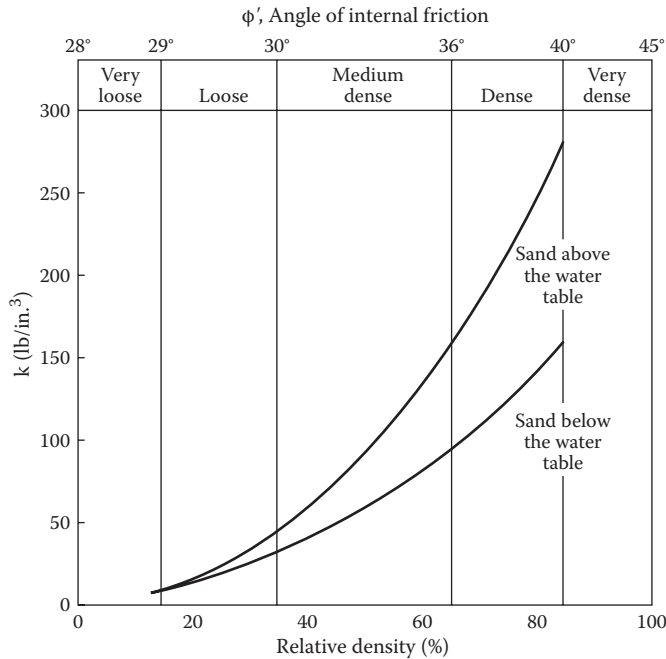
where  $p$  is the lateral soil resistance,

$$A = \left\{ \begin{array}{l} = 0.9, \text{ for cyclic loading} \\ = \{3.0 - (0.8Z)/D\}, \text{ for static loading} \end{array} \right\}$$

$p_u$  = ultimate bearing capacity (or strength) at depth  $Z$  below seabed, in force per unit length; and  $k$  = initial lateral soil modulus (or reaction), in force per unit area, per unit deformation into soil, is given in Figure 8.24 [95].

**8.6.3 INFLUENCE OF GROUP OF PILES**

As per API provisions, when piles are spaced closer than eight times the diameter of the pile, which represents the general situation, pile group effects should be considered in the analysis. For the case of a group of  $n$  axially loaded piles, driven into clayey soils, the load bearing effect of the group of piles would be less than  $n$  times the load bearing capacity of a single pile; whereas the load bearing capacity of a group of  $n$  axially loaded piles, driven into a sandy stratum in the seabed, will be more than  $n$  times the capacity of a single pile. The settlement of a group of piles, whether in clay or sand, will be always greater than a single pile subjected to the average pile load of the pile group.



**FIGURE 8.24** Plot of the initial modulus of lateral soil reaction in force per area per unit (lateral) deformation as a function of  $\phi'$ . (From American Petroleum Institute, *Section G on Foundation Design in the Recommended Practice for Planning, Designing and Constructing Fixed Offshore Platforms—Load and Resistance Factor Design (RP 2A-LRFD)*, American Petroleum Institute, Washington, DC, p. 73, 1993. With permission.)

While considering the lateral behavior, for piles and pile groups having the same fixity conditions, and embedded in clays or sands, the lateral deformation of a pile group will always be greater than that of a single pile carrying the average load of the pile group. The factors that influence the lateral load carrying capacity of a pile group are (i) spacing of piles; (ii) pile flexibility relative to the soil; (iii) ratio of pile penetration into soil to the pile diameter; and (iv) variation of soil shear strength and modulus of soil stiffness, with respect to the depth of soil.

### 8.6.4 THICKNESS OF PILE WALL

The pile load capacity must be checked as given in Section 8.2.2. The pile loads should be checked using the beam-column equation 8.8 given below:

$$\left[ \frac{f_c}{\phi_c F_{cn}} \right] + f_b / \{ \phi_b F_{bn} (1.0 - \sum P\Delta / M) \} \leq 1.0 \tag{8.16}$$

where  $\sum P\Delta$  is the first-order  $P$ - $\Delta$  moments due to factored gravity loads; and  $f_c$ ,  $F_{cn}$ ,  $\phi_c$ ,  $f_b$ ,  $F_{bn}$ ,  $\phi_b$ , and  $M$  have been defined earlier in Sections 8.2.3.1 through 8.2.3.5.

The  $D/t$  ratio of the entire length of the pile should be such as to prevent the local buckling under the stresses set up in the pile walls. For piles that are to be driven by hammers having a capacity of 800 blows per meter penetration (or 250 blows per foot), the minimum pile wall thickness  $t$  should not be less than

**TABLE 8.8**  
**Minimum Pile Wall Thickness**

Pile Diameter, $D$		Nominal Wall Thickness, $t$	
mm	in.	mm	in.
610	24	13	1/2
762	30	14	9/16
914	36	16	5/8
1067	42	17	11/16
1219	48	19	3/4
1524	60	22	7/8
1829	72	25	1
2134	84	23	1 1/8
2438	96	31	1 1/4
2743	108	34	1 3/8
3048	120	37	1 1/2

*Source:* American Petroleum Institute, *Section G on Foundation Design in the Recommended Practice for Planning, Designing and Constructing Fixed Offshore Platforms—Load and Resistance Factor Design (RP 2A-LRFD)*, American Petroleum Institute, Washington, DC, p. 74, 1993. With permission.

$$t = \begin{cases} = 6.35 + D/100 & (\text{with } t, D \text{ in mm units}) \\ = 0.25 + D/100 & (\text{with } t, D \text{ in in. units}) \end{cases} \quad (8.17)$$

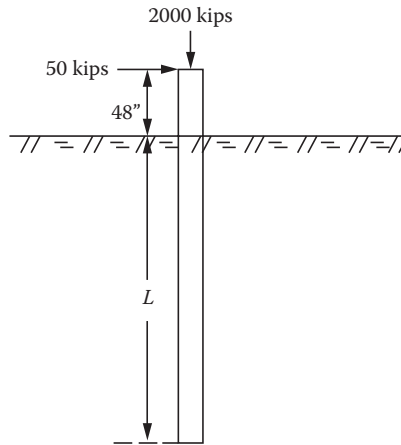
The minimum pile wall thickness specified in the API RP2A code is given in Table 8.8 [96].

### 8.6.5 LENGTH OF PILE SECTIONS

A number of factors have to be considered in selecting the pile lengths to be used in increasing the pile length required for supporting the applied loads, including (i) capability of the lift equipment to raise, lower, and stab the pile lengths as well as the pile driving hammer on the pile section to be driven into the seabed; (ii) the possibility of a sudden large downward movement of the pile due to the penetration of the jacket leg closure; (iii) driving and lifting stresses in piles and the changed wall thickness and material properties around the field weld regions; (iv) modification of soil properties around the pile tip during the stoppage of pile driving during welding of pile sections together; and (v) dynamic (pile driving) stresses due to hammer weight and hammer action. In addition to the above, each pile section is also required to contain a cutoff allowance of 0.5 to 15 m (at each end) to permit the removal of the damaged pile end sections.

#### Example 8.2

A 33-in. (outer) diameter and 1.5-in. wall thickness steel pile is subjected to maximum axial and bending loads, as shown in Figure E8.17. Determine the pile embedment length,  $L$ , and deflection

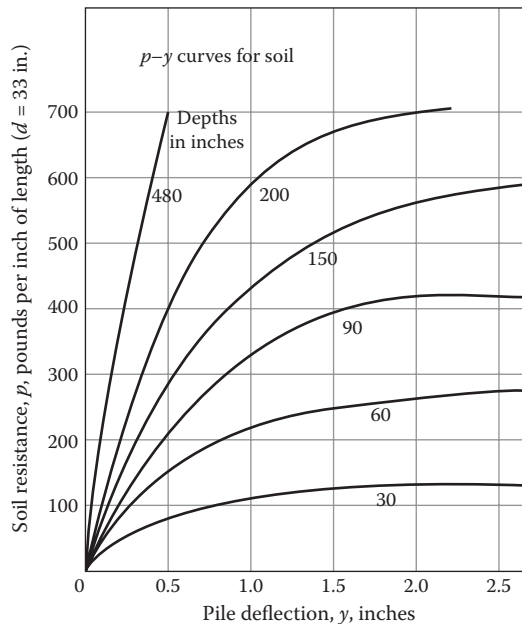


**FIGURE E8.17** Steel pile subjected to axial and horizontal loads.

and moment curves. From the computed curves, also check whether the maximum stress in the pile exceeds the permissible value of stress in the material of the pile. The soil strength condition below the seabed level is to be taken from the values shown in Figure E8.2. The  $p$ - $y$  curve for soil is given in Figure E8.18.  $E_s = (30.0)(10^6)$  psi;  $\sigma_{yield} = 50.0$  ksi; and  $\sigma_{permissible} = (0.67)\sigma_{yield}$ .

Assuming the depth of embedment of the pile to be  $z$  feet below the seabed:

$$P_{ultimate} = P_{shear} + P_{end bearing} = \{(\pi)(33)/12\}[(1.0)(z - 10.0) + (1/2)(4.0)(150.0 - 60.0) + (3.0)(190.0 - 150.0) + (8.0)(z - 190.0) + (1/2)\{(6.0)(z - 190.0)/60\}(z - 190.0)] + (\pi/4)(33/12)^2[13.0 + \{(4.0)(z - 190.0)/(60.0)\}] = 2000.0 \text{ kips}$$



**FIGURE E8.18**  $p$ - $y$  curve for the soil in which the pile is driven. (From H. Matlock and L.C. Reese, Generalized Solutions for Laterally Loaded Piles, *Transactions, American Society of Civil Engineers*, Volume 127, Issue 3370, Part I, pp. 1220–1269, 1962. With permission.)

This equation has to be solved by a trial-and-error method.  
 Assuming  $z = 200.0$  ft.,  $P_{ultimate} = 5463.6$  kips.

For  $z = 150.0$  ft.,  $P_{ultimate} = 2524.0$  kips.

For  $z = 130.0$  ft.,  $P_{ultimate} = 2078.4$  kips.

Consequently, a minimum embedment depth of 130.0 ft. seems to be sufficient to carry the maximum load of 2000.0 kips on each pile.

Diameter of pile = 33.0 in.;  $I_{pile} = (\pi/64)[33^4 - 30^4] = 18,453.0$  in.<sup>4</sup>;  $L = (130.0)(12) = 1560.0$  in.;  $P_T = 50,000.0$  lb.;  $M_T = (50,000.0)(48) = 2,400,000$  lb. in.;  $E = (30.0)(10^6)$  psi

The bending moment generated by the bending of the pile by axial load is neglected.

(i) Trial I:

Taking  $E_{soil} = Kx$  and  $T = 100.0$  in.,

$$K_{trial I} = (EI/T^5) = 55.36 \text{ lb./in.}^3$$

$Z_{max} = (L)/(T) = 1560/100 = 15.6 > 10.0$  (available maximum value); hence, take  $Z_{max} = 10.0$ .

From the given equation for transverse deflection  $y$  of the pile (see Figure 8.16b),

$$y = [(P_T T^3)/EI](A_y) + [(M_T T^2)/EI]B_y = 0.090325 A_y + 0.04336 B_y$$

Table E8.2 is prepared using the values given in Table 8B.1 (see Appendix 8B).

$T$  obtained from first trial =  $[(EI)/(k_{average})]^{(1/5)} = 156.04$  in.

(ii) Trial II:

Taking  $T = 150.0$  in. and  $E_s = kx$ ,

$$K_{trial II} = (EI/T^5) = 7.29 \text{ lb./in.}^3$$

$Z_{max} = (L)/(T) = 1560/150.0 = 10.4 > 10.0$  (available maximum value); hence, take  $Z_{max} = 10.0$ .

From the given equation for transverse deflection  $y$  of the pile,

$$y = [(P_T T^3)/EI](A_y) + [(M_T T^2)/EI]B_y = 0.3048 A_y + 0.09756 B_y$$

Table E8.3 is prepared using the values given in Table 8B.1 (see Appendix 8B).

$T$  obtained from the second trial =  $[(30.0)(10^6)(18,452.98)]/4.84]^{(1/5)} = 162.81$  in.

(iii) Trial III:

Taking  $T = 158.0$  in. and  $E_s = kx$ ,

$$K_{trial III} = (EI/T^5) = 5.622 \text{ lb./in.}^3$$

**TABLE E8.2**  
**Computed Values of  $y$ ,  $p/y$ ,  $E_s$  and  $E_s/x$  in Trial I**

Depth (in.)	Nondimen. Depth	Deflection Coeff.		Deflection (in.)	Value of $p$ from Figure E8.18	$E_s$ (psi)	$k$ (lb./in. <sup>3</sup> )
		Obtained from Table 8B.1					
$x$	$x/T$	$A_y$	$B_y$	$y$	$P$	$-p/y$	$E_s/x$
0.0	0.0	2.435	1.623	0.2903	- 0.0	0.0	—
30.0	0.30	1.952	1.143	0.2259	- 48.0	212.5	7.083
60.0	0.60	1.495	0.752	0.1676	- 60.0	358.0	5.967
90.0	0.90	1.086	0.448	0.1178	- 60.0	510.6	5.667
150.0	1.50	0.817	0.065	0.0766	- 60.0	783.2	5.221
240.0	2.40	0.013	- 0.098	0.00542	- 60.0	—	—
<b>Average value of <math>k</math></b>							5.985



**TABLE E8.3**  
**Computed Values of  $y$ ,  $p/y$ ,  $E_s$  and  $E_s/x$  in Trial II**

Depth (in.)	Nondimen. Depth	Deflection Coeff. Obtained from Table 8B.1		Deflection (in.)	Value of $p$ from Figure E8.18	$E_s$ (psi)	$k$ (lb./in. <sup>3</sup> )
		$A_y$	$B_y$				
$x$	$x/T$			$y$	$P$	$-p/y$	$E_s/x$
0.0	0.0	2.435	1.623	0.9005	0.0	—	—
30.0	0.30	2.112	1.453	0.7562	- 105.0	138.85	4.628
60.0	0.60	1.796	1.003	0.6453	- 180.0	278.94	4.649
90.0	0.90	1.499	0.752	0.5290	- 210.0	396.98	4.411
150.0	1.00	0.962	0.364	0.3287	- 215.0	684.09	4.561
240.0	1.60	0.381	0.029	0.1189	- 170.0	1429.77	5.957
<b>Average value of <math>k</math></b>							<b>4.840</b>

$Z_{max} = (L)/(T) = 1560/158.0 = 9.87 \sim 10.0$  (available maximum value); hence, take  $Z_{max} = 10.0$ .  
From the given equation for transverse deflection  $y$  of the pile,

$$y = [(P_T T^3)/EI](A_y) + [(M_T T^2)/EI]B_y = 0.3562 A_y + 0.1082 B_y$$

Table E8.4 is prepared using the values given in Table 8B.1 (see Appendix 8B).  
 $T$  obtained from the third trial =  $[(30.0)(10^6)(18,452.98)/4.041]^{(1/5)} = 168.78$  in.; take  $T \sim 170.0$  in.

(iv) Subsequent trials:

This could be continued until convergence occurs; in this case, for the sake of illustration, this value is assumed to have converged and the subsequent calculations are shown in the following section. The final deflection of the pile is given by (obtained from Table 8B.1)

$$y = [(P_T T^3)/EI](A_y) + [(M_T T^2)/EI]B_y = 0.4437 A_y + 0.1253 B_y$$

The bending moment variation in the pile is given by the equation (obtained from Table 8B.1)

$$M = (P_T T)A_m + (M_T)B_m = (8.5)(10^6) A_m + (2.4)(10^6) B_m$$

These values are given in Table E8.5.

From the computed bending moments in the pile and the applied axial loads,

$$\text{Area of the pile section} = (\pi/4)[(D_o^2 - D_i^2)] = 148.44 \text{ in.}^2$$

$$\text{Maximum stress in the pile} = (P_T)/A + (M_{max})(c/I) = (2,000,000.0)/(148.44) + (8.380)(10^6)(16.5)/(18,452.98) = 13,473.43 + 7493.09 = 20,966.52 \text{ psi} < [(0.67)(50,000.0) = 34,500.0 \text{ psi}]$$

Hence, the pile section is OK for withstanding the stresses imposed on it.

**TABLE E8.4**  
**Computed Values of  $y$ ,  $p/y$ ,  $E_s$  and  $E_s/x$  in Trial III**

Depth (in.)	Nondimen. Depth	Deflection Coeff. Obtained from Table 8B.1		Deflection (in.)	Value of $p$ from Figure E8.18	$E_s$ (psi)	$k$ (lb./in. <sup>3</sup> )
		$A_y$	$B_y$				
$x$	$x/T$			$y$	$P$	$-p/y$	$E_s/x$
0.0	0.0	2.435	1.623	1.0430	—	—	—
30.0	0.1899	2.130	1.309	0.9003	- 105.0	116.63	3.888
60.0	0.3797	1.828	1.031	0.7627	- 190.0	249.11	4.152
90.0	0.5696	1.540	0.788	0.6338	- 240.0	378.67	4.207
150.0	0.9494	1.026	0.406	0.4092	- 240.0	586.51	3.910
240.0	1.5190	0.447	0.096	0.1696	- 165.0	972.88	4.050
<b>Average value of <math>k</math></b>							<b>4.041</b>

**TABLE E8.5**  
**Converged Values of  $y$ ,  $p/y$ ,  $E_s$  and  $E_s/x$  in Final Trial**

Nondimen. Depth	Depth (in.)	Deflection Coefficients		Moment Coefficients		Deflection (in.)	Moment (lb. in.)
		$A_y$	$B_y$	$A_m$	$B_m$		
$z$	$x = zT$						
0.0	0.0	2.435	1.623	0.000	1.000	1.284	(2.400)(10 <sup>6</sup> )
0.2	34.0	2.112	1.293	0.198	0.999	1.0991	(4.081)(10 <sup>6</sup> )
0.4	68.0	1.793	1.003	0.379	0.987	0.9213	(5.590)(10 <sup>6</sup> )
0.6	102.0	1.495	0.752	0.531	0.960	0.7580	(6.818)(10 <sup>6</sup> )
0.8	136.0	1.216	0.540	0.649	0.914	0.6072	(7.710)(10 <sup>6</sup> )
1.0	170.0	0.962	0.364	0.727	0.852	0.4724	(8.224)(10 <sup>6</sup> )
1.2	204.0	0.738	0.223	0.767	0.775	0.3550	(8.380)(10 <sup>6</sup> )
1.4	238.0	0.544	0.112	0.772	0.681	0.2653	(8.213)(10 <sup>6</sup> )
1.6	272.0	0.381	0.029	0.746	0.594	0.1727	(7.766)(10 <sup>6</sup> )
1.8	306.0	0.247	-0.030	0.696	0.498	0.1058	(7.111)(10 <sup>6</sup> )
2.0	340.0	0.141	-0.070	0.621	0.404	0.0538	(6.308)(10 <sup>6</sup> )
2.5	425.0	-0.020	-0.105	0.422	0.200	-0.0220	(4.067)(10 <sup>6</sup> )
3.0	510.0	-0.075	-0.089	0.224	0.059	-0.0444	(2.054)(10 <sup>6</sup> )

(v) Comparison with API RP2A provisions:

Also the above deformation profiles can be compared with the provisions given in the API RP2A code [83]. Using Figures 8.23 and 8.24, the  $p$ - $y$  relationship given in the code can be compared. Assume medium dense sand with an internal angle of friction of 25° and a buoyant weight of 10.0 kN/m<sup>3</sup> (64.0 lb./ft.<sup>3</sup>). Using Equations 8.13 and 8.14, the coefficients  $C_1$ ,  $C_2$ , and  $C_3$  can be determined.

Using Equation 8.13,

$$p_{\text{ultimate shallow}} = (C_1X + C_2D)\gamma'X = [1.22X + 2.05(33)](64.0/1728)X = 0.045 X^2 + 2.506 X \quad (\text{E8.6})$$

Using Equation 8.14,

$$p_{\text{ultimate deep}} = C_3D \gamma'X = (15.0)(33)(64.0/1728)X = 18.33 X \quad (\text{E8.7})$$

Using Equation 8.15, the soil resistance ( $p$ ) versus displacement ( $y$ ) relationship is given by

$$p = Ap_u \tanh [(kX)/(Ap_u)y] \quad (\text{E8.8})$$

$$A = 3.0 - (0.8)X/D = 3.0 - (0.8/33)X = 3.0 - 0.02424 X \geq 0.9$$

When  $X > 86.63$  in.,  $A < 0.90$ ; hence, for  $X > 86.63$  in.,  $A = 0.90$  (code given values).

Also from Figure 8.24, initial  $k$  for subgrade modulus  $\sim 5.0$ .

Table E8.6 compares the code-based values with the computed values obtained above.

The values based on code computations seem to agree well (the maximum difference between the test-based computation and code-based computation is 19.15%) with the results from the curves generated from experiments; perhaps the sandy soil used for experiments may be less dense than the medium dense soil used in the numerical computations.

### Example 8.3

A 48-in. (outer) diameter and 1.5-in. wall thickness steel pile, shown in Figure E8.19, is subjected to the maximum axial and bending loads shown in the figure. In addition, the pile top is restrained from rotation by the pile head, and the rotational restraint  $R_t$  provided at the top of the pile is given

**TABLE E8.6**  
**Comparison of Experimentally Generated Values with Code-Based Computations**

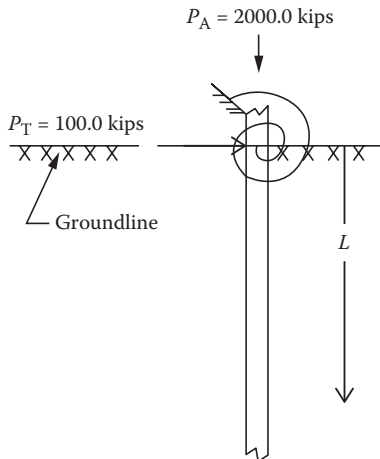
Nondimen. Depth	Depth (in.)	Value of $p$ Ultimate from Equation A (psi)	Value of $p$ Ultimate from Equation B (psi)	Deflection from Computed Values (in.)	Value of $p$ from Figure E8.18 (psi)	Value of $p$ from Equation C (psi)
$Z$	$x = zT$	$p_{ult. shallow}$	$p_{ult. deep}$	$Y$	$p_{from tests}$	$-p_{computed}$
0.0	0.0	0.0	0.0	1.284	0.0	0.0
0.2	34.0	137.24	623.22	1.0991	- 135.0	- 166.17
0.4	68.0	378.49	1246.44	0.9213	- 230.0	- 279.20
0.6	102.0	723.79	1866.6	0.7580	- 325.0	- 346.79
0.8	136.0	1173.14	2492.88	0.6072	- 320.0	- 393.06
1.0	170.0	1726.52	3116.1	0.4724	- 320.0	- 392.83
1.2	204.0	2383.94	3739.32	0.3550	- 290.0	- 358.70
1.4	238.0	3145.41	4362.54	0.2653	- 275.0	- 314.40
1.6	272.0	4010.91	4985.76	0.1727	- 210.0	- 234.54
1.8	306.0	4980.46	5608.98	0.1058	- 140.0	- 161.80
2.0	340.0	6054.04	6232.20	0.0538	- 60.0	- 91.45
2.5	425.0	9193.18	7790.25	-0.0220	+ 20.0	+ 46.75
3.0	510.0	12,982.6	9348.30	-0.0444	+ 90.0	+ 113.21

Note: As per the code provisions, lower values between the computed values from Equations A and B must be taken.

as  $(5.7)(10^9)$  lb. in./rad. Determine the pile embedment length,  $L$ , and deflection and moment curves. From the computed curves also check whether the maximum stress in the pile exceeds the permissible value of stress in the material of the pile. The soil strength condition below the seabed level is to be taken from the values shown in Figure E8.2. The  $p$ - $y$  curve for soil is given in Figure E8.18; in using this  $p$ - $y$  curve, there is an inherent limitation that the curve generated for a 33-in.-diameter pile is assumed to be valid for the 48.0-in.-diameter pile also.  $E_s = (30.0)(10^6)$  psi;  $\sigma_{yield} = 50.0$  ksi; and  $\sigma_{permissible} = (0.67)\sigma_{yield}$ .

Since the pile diameter is larger ( $D = 48$  in.), the embedment length of the pile will be shorter. Assume that the depth of embedment of the pile is  $z$  feet below the seabed.

For  $z > 190.0$  ft.,



**FIGURE E8.19** Loads acting on the restrained pile.

$$P_{\text{ultimate}} = P_{\text{shear}} + P_{\text{end bearing}} = \{(\pi)(48)/12\}[(1.0)(z - 10.0) + (1/2)(4.0)(150.0 - 60.0) + (3.0)(190.0 - 150.0) + (8.0)(z - 190.0) + (1/2)\{(6.0)(z - 190.0)/60\}(z - 190.0)] + (\pi/4)(48/12)^2[13.0 + \{(4.0)(z - 190.0)\}/(60.0)] = 2000.0 \text{ kips}$$

This equation has to be solved by a trial-and-error method.

Assuming  $z = 150.0$  ft.,  $P_{\text{ultimate}} = 4146.9$  kips.

For  $z = 120.0$  ft.,  $P_{\text{ultimate}} = 2492.3$  kips.

For  $z = 110.0$  ft.,  $P_{\text{ultimate}} = 2052.5$  kips.

For  $z = 109.0$  ft.,  $P_{\text{ultimate}} = 2011.6$  kips; anyhow round it up to  $L = 110.00$  ft.

Take pile embedment depth to be 109.0 ft.

Diameter of pile = 48.0 in.;  $I_{\text{pile}} = (\pi/64)[48^4 - 45^4] = 59,287.3 \text{ in.}^4$ ;  $L = (109.0)(12) = 1308.0 \text{ in.}$ ;  
 $P_T = 100,000.0 \text{ lb.}$ ;  $E = (30.0)(10^6) \text{ psi}$

The bending moment generated by the bending of the pile by axial load is neglected.

(i) Trial I:

Taking  $E_{\text{soil}} = Kx$  and  $T = 150.0$  in.,

$$K_{\text{trial I}} = (EI/T^5) = 23.42 \text{ lb./in.}^3$$

$Z_{\text{max}} = (L)/(T) = (110)(12)/150 = 8.80$ ; hence, take  $Z_{\text{max}}$  (the nearest one) = 10.0.  
 Therefore, Tables 8A.1 through 8A.6 have to be used.

$$y = [(P_T T^3)/EI](C_y) = 0.1897 C_y$$

$$M_T/(P_T T) = A_{S_T}/[ET/(R_T T) - B_{S_T}] = \frac{-1.623}{\left[ \frac{(30.0)(10^6)(5.93)(10^4)}{(5.7)(10^9)(150.0)} \right] - (-1.750)} = -0.4337$$

From the above values, Table E8.7 is prepared using the values given in Table 8A.1 (see Appendix 8A).

$T$  obtained from first trial =  $[(EI)/(k_{\text{average}})]^{(1/5)} = 169.95 \text{ in.} = 198.0 \text{ in.}$

**TABLE E8.7**  
**Computed Values of  $y$ ,  $p/y$ ,  $E_s$  and  $E_s/x$  in Trial I**

Depth (in.)	Nondimen. Depth	Deflection Coeff. $C_y$		Value of $p$ from Figure E8.18		$E_s$ (psi)	$k$ (lb./in. <sup>3</sup> )	
		Obtained from Table 8A.1	Deflection $y = 0.1897A_y$ (in.)	(lb./in.)	$P$			
$X$	$x/T$	$C_y$	$y$	$P$	$-p/y$	$E_s/x$		
0.0	0.0	1.732	0.329	0.0	0.0	—		
30.0	0.20	1.551	0.294	-60.0	204.82	6.83		
60.0	0.40	1.361	0.258	-100.0	387.60	6.46		
90.0	0.60	1.169	0.222	-120.0	540.54	6.01		
120.0	0.80	0.982	0.186	-130.0	698.92	5.82		
150.0	1.00	0.805	0.153	-135.0	882.35	5.88		
180.0	1.20	0.656	0.124	-120.0	967.74	5.38		
210.0	1.40	0.495	0.094	-110.0	1170.2	5.57		
270.0	1.80	0.258	0.049	-70.0	1428.6	5.29		
375.0	2.50	0.018	0.013	-40.0	3076.9	—		
<b>Average value of <math>k</math> across the depth of pile</b>							<b>5.905</b>	

(ii) Trial II:

$$K_{\text{trial II}} = 12.54 \text{ lb./in.}^2$$

$$Z_{\text{max}} = L/T = (110)(12)/(198.0) = 7.77; \text{ hence, take } Z_{\text{max}} = 6.67.$$

$$y = [(P_T T^3)/EI](C_y) = (100,000)(198)^3/[(30)(10^6)(5.93)(10^4)] C_y = 0.4363 C_y$$

$$M_T/(P_T T) = A_{ST}/[ET/(R_T T) - B_{ST}] = \frac{-1.623}{\left[ \frac{(30.0)(10^6)(5.93)(10^4)}{(5.7)(10^9)(198.0)} \right] - (-1.749)} = -0.488$$

From the above values, Table E8.8 is prepared using the values given in Table 8A.1 (see Appendix 8A).

$$T_{\text{obtained}} = [EI/k_{\text{obtained}}]^{(1/5)} = [(30)(10^6)(5.93)(10^4)/(4.245)]^{(1/5)} = 211.1 \text{ in}$$

(iii) Trial III:

$$K_{\text{trial II}} = 12.54 \text{ lb./in.}^2$$

$$Z_{\text{max}} = L/T = (110)(12)/(211.1) = 6.253; \text{ hence, take } Z_{\text{max}} = 10.0.$$

$$y = [(P_T T^3)/EI](C_y) = (100,000)(211.10)^3/[(30)(10^6)(5.93)(10^4)] C_y = 0.5288 C_y$$

$$M_T/(P_T T) = A_{ST}/[ET/(R_T T) - B_{ST}] = \frac{-1.623}{\left[ \frac{(30.0)(10^6)(5.93)(10^4)}{(5.7)(10^9)(211.10)} \right] - (-1.749)} = -0.5029$$

The relevant values are computed and given in Table E8.9; from the average value of  $k$  obtained from Table E8.9, the value of  $T$  is computed.

$$T_{\text{obtained}} = [EI/k_{\text{obtained}}]^{(1/5)} = [(30)(10^6)(5.93)(10^4)/(3.725)]^{(1/5)} = 216.70 \text{ in.} \sim 217.0 \text{ in.}$$

The difference between the earlier (trial II) and the present one is that the  $T_{\text{obtained}}$  in the present trial exceeds the earlier one by 5.60 in.; hence, the value of  $T$  is assumed to have converged.

**TABLE E8.8**  
**Computed Values of  $y$ ,  $p/y$ ,  $E_s$  and  $E_s/x$  in Trial II**

Depth (in.)	Nondimen. Depth	Deflection Coeff. $C_y$		Deflection $y =$ 0.4363 $C_y$ (in.)	Value of $p$ from Figure E8.18 (lb./in.)	$E_s$ (psi)	$k$ (lb./in. <sup>3</sup> )
		Obtained from Table 8A.1	$C_y$				
$x$	$x/T$		$C_y$	$Y$	$P$	$-p/y$	$E_s/x$
0.0	0.0	1.687		0.736	0.0	0.0	—
39.6	0.20	1.515		0.661	-120.0	181.54	4.584
79.2	0.40	1.333		0.582	-220.0	378.01	4.773
118.8	0.60	1.115		0.487	-250.0	513.35	4.321
158.4	0.80	0.967		0.422	-290.0	687.20	4.338
198.0	1.00	0.794		0.346	-270.0	780.35	3.941
237.6	1.20	0.635		0.277	-260.0	938.63	3.950
277.2	1.40	0.492		0.215	-240.0	1116.3	4.027
356.4	1.80	0.367		0.160	-230.0	1437.5	4.033
495.0	2.50	0.029		0.127	-200.0	1574.8	—
<b>Average value of <math>k</math> across the depth of pile</b>							<b>4.245</b>

**TABLE E8.9**  
**Computed Values of  $y$ ,  $p/y$ ,  $E_s$  and  $E_s/x$  in Trial III**

Depth (in.)	Nondimen. Depth	Deflection Coeff.		Value of $p$ from Figure E8.18 (lb./in.)	$E_s$ (psi)	$k$ (lb./in. <sup>3</sup> )
		$C_y$ Obtained from Table 8A.1	Deflection $y =$ 0.5288 $C_y$ (in.)			
$x$	$x/T$	$C_y$	$y$	$P$	$-p/y$	$E_s/x$
0.0	0.0	1.681	0.8890	0.0	0.0	—
42.22	0.20	1.510	0.7985	- 120.0	150.28	3.560
84.44	0.40	1.329	0.7028	- 240.0	341.49	4.044
126.66	0.60	1.145	0.6055	- 280.0	462.43	3.651
168.88	0.80	0.965	0.5193	- 320.0	616.21	3.649
211.10	1.00	0.793	0.4193	- 320.0	763.18	3.615
253.32	1.20	0.634	0.3353	- 300.0	894.72	3.532
295.54	1.40	0.492	0.2602	- 285.0	1095.31	3.706
337.76	1.60	0.367	0.1941	- 270.0	1391.04	4.118
379.98	1.80	0.260	0.1375	- 200.0	1454.55	3.828
527.75	2.50	0.182	0.0962	- 180.0	1871.10	3.545
<b>Average value of <math>k</math> across the depth of pile</b>						<b>3.725</b>

(iv) Final converged values:

$Z = L/T_{converged} = (110.0)(12)/(217.0) = 6.083$ ; hence, use  $Z_{max} = 10.0$  and find the values of deflection and bending moments.

For finding the final deformed shape, use Table 8A.1 to find the coefficient  $C_y$ .

$$y = [P_T T^3 / (EI)] C_y = \{[(100,000)(217.0)^3] / \{(30)(10^6)(5.93)(10^4)\}\} C_y = 0.5743 C_y$$

$$M_T / (P_T T) = A_{ST} / [ET / (R_i T) - B_{ST}] = \frac{-1.623}{\left[ \frac{(30.0)(10^6)(5.93)(10^4)}{(5.7)(10^9)(217.0)} \right] - (-1.749)} = -0.5092$$

hence,  $M_T = -0.5092(P_T T)$ .

Moment distribution in the pile is given by

$$M = (P_T T) A_M + M_T B_M = (100,000.0)(217.0) A_M + [(-0.5092)(100,000.0)(217.0)] B_M$$

$$= (2.17)(10^7) A_M - (1.105)(10^7) B_M$$

The values of  $A_M$  and  $B_M$  are obtained from Table 8B.1. Once these values are obtained from the table, the deflection and bending moment profiles can be obtained as shown in Table E8.10.

(v) Comparison with API RP2A provisions:

Also the above deformation profiles can be compared with the provisions given in the API RP2A code [83]. Using Figures 8.23 and 8.24, the  $p-y$  relationship given in the code can be compared. Assume medium dense sand with an internal angle of friction of 25° and a buoyant weight of 10.0 kN/m<sup>3</sup> (64.0 lb./ft.<sup>3</sup>).

Using Equations 8.13 and 8.14, the coefficients  $C_1$ ,  $C_2$ , and  $C_3$  can be determined.

Using Equation 8.13

$$p_{ultimate\ shallow} = (C_1 X + C_2 D) \gamma' X = [1.22X + 2.05(48)](64.0/1728)X = 0.045 X^2 + 3.644 X \quad (E8.6)$$

Using Equation 8.14

$$p_{ultimate\ deep} = C_3 D \gamma' X = (15.0)(48)(64.0/1728)X = 26.67 X \quad (E8.7)$$

**TABLE E8.10**  
**Converged Values of  $y$ ,  $p/y$ ,  $E_s$  and  $E_s/x$  in Final Trial**

Nondimensional Depth Coefficient Z	Depth $X=ZT$ (in.)	Deflection Coeff. from Table A.1 ( $C_y$ )	Moment Coefficients from Table 8B.1		Deflection Profile = $(0.5743)C_y$ (in.)	Moment Profile $M = (2.17)(10^7)A_M - (1.105)(10^7)B_M$ (lb. in.)
			$A_M$	$B_M$		
0.0	0.0	1.673	0.000	1.000	0.961	$-(1.105)(10^7)$
0.2	36.6	1.504	0.198	0.999	0.864	$-(0.674)(10^7)$
0.4	73.2	1.334	0.379	0.987	0.766	$-(0.268)(10^7)$
0.6	109.8	1.142	0.531	0.960	0.656	$+(0.092)(10^7)$
0.8	146.4	0.963	0.649	0.914	0.553	$+(0.398)(10^7)$
1.0	183.0	0.791	0.727	0.852	0.454	$+(0.636)(10^7)$
1.6	292.8	0.364	0.746	0.594	0.209	$+(0.963)(10^7)$
2.0	366.0	0.174	0.628	0.404	0.100	$+(0.916)(10^7)$
2.5	457.5	0.030	0.422	0.200	0.017	$+(0.695)(10^7)$
3.0	549.0	-0.0337	0.225	0.059	-0.019	$+(0.423)(10^7)$
3.5	640.5	-0.0468	0.081	-0.016	-0.027	$+(0.205)(10^7)$
4.0	732.0	-0.0339	0.000	-0.042	-0.019	$+(0.021)(10^7)$

Using Equation 8.15, the soil resistance ( $p$ ) versus displacement ( $y$ ) relationship is given by

$$p = Ap_u \tanh [(kX)/(Ap_u)y] \tag{E8.8}$$

$$A = 3.0 - (0.8)X/D = 3.0 - (0.8/48X) = 3.0 - 0.01667 X \geq 0.9$$

When  $X > 86.63$  in.,  $A < 0.90$ ; hence, for  $X > 125.98$  in.,  $A = 0.90$ .

Also, initial  $k$  for subgrade modulus  $\sim 5.0$  (from Figure 8.24).

Table E8.11 compares the code-based values with the computed values obtained above.

**TABLE E8.11**  
**Comparison of Experimentally Generated Values with Code-Based Computation**

Nondimensional Depth Z	Depth (in.)	Value of $p$ Ultimate from Equation A	Value of $p$ Ultimate from Equation B	Deflection from Computed Values (in.)	Value of $p$ from Figure E8.18 (psi)	Value of $p$ from Equation C (psi)
		$p_{ult. shallow}$ (psi)	$p_{ult. deep}$ (psi)	$y$	$p_{from tests}$	$-p_{computed}$
0.0	0.0	0.0	0.0	0.961	0.0	0.0
0.2	36.6	193.65	976.12	0.864	-120.0	-152.23
0.4	73.2	507.86	1952.24	0.766	-230.0	-271.70
0.6	109.8	942.63	2928.37	0.656	-270.0	-347.86
0.8	146.4	1497.97	3904.49	0.553	-300.0	-393.06
1.0	183.0	2173.86	4880.61	0.454	-320.0	-409.28
1.6	292.8	4924.90	7808.98	0.209	-240.0	-305.49
2.0	366.0	7361.72	9761.22	0.100	-180.0	-182.95
2.5	457.5	11,085.91	12,201.53	0.017	-30.0	-38.88
3.0	549.0	15,563.60	14,641.83	-0.019	+50.0	+52.16
3.5	640.5	20,794.79	17,082.14	-0.027	+90.0	+86.47
4.0	732.0	26,779.49	19,522.44	-0.019	+80.0	+69.54

Note: As per the code provisions, lower values between the computed values from Equations A and B must be taken.

The values based on code computations seem to agree fairly well (the maximum difference between the test-based computation and code-based computation is around 23.68%) with the results obtained from the curves generated from experiments on 33-in.-diameter piles; this difference is to be expected since the  $p$ - $y$  curve used in this study was more flexible (since a 48-in. pipe used in this problem will be flatter and thus give a stiffer  $p$ - $y$  curve than that used for this study).

### Example 8.4

A 33-in. (outer) diameter and 1.5-in. wall thickness steel pile (shown in Figure E8.17) is driven into the soil at the site; it is subjected to the maximum axial and bending loads as shown in the figure. Determine the pile embedment length,  $L$ , if (i) the pile is embedded in a normally consolidated medium clay [with an undrained shear strength of 40.0 kPa (835.0 psf) and a buoyant density of 8.0 kN/m<sup>3</sup> (51.0 lb./ft.<sup>3</sup>)]; (ii) the pile is embedded in a normally consolidated stiff clay [with an undrained shear strength of 80.0 kPa (1.670 ksf) and a unit buoyant weight of 8.2 kN/m<sup>3</sup> (52.0 lb./ft.<sup>3</sup>)]; and (iii) the pile is embedded in medium dense sand with a wet soil–pile friction angle of 25° and a buoyant wet weight of 10.0 kN/m<sup>3</sup> (64.0 lb./ft.<sup>3</sup>). Using the API code relationships given in API RP2A [83], determine the axial and lateral strength of the pile cross section (also refer to Tables 4.7 and 4.11).

- (i) Normally consolidated medium clay:

Taking the value of  $\psi_i = c_{ui}/p'_0 = 1.0$  for normally consolidated soil,  $\alpha = 0.5$ .

Hence, the side frictional shear strength is  $f = (0.5)c_{ui} = 0.5c_u = (0.5)(p'_0) = (0.5)(\gamma'z)$ , where  $p'_0$  is the effective overburden pressure at the point under consideration.

Pile end bearing stress is equal to overburden soil pressure, which is equal to  $\gamma'z$ , where  $z$  is the depth of pile required to resist the applied vertical load.

Applied vertical load is a maximum of 2000.0 kN.

$$2,000,000 = \pi(33/12)(1/2)(0.5 \gamma'z)(z) + [(\pi/4)(33/12)^2](\gamma'z) = \gamma'(2.16z^2 + 5.94z) = 110.16z^2 + 302.92z.$$

Solving the equation, one obtains a pile embedment length of  $z = 133.5$  ft.

This depth is the same as that given during earlier calculations in Example 8.2.

Verifying this with the limitations provided in the code, the pile end bearing strength is given by

$$9c_u = (9)(835.12) = 7516.0 \text{ lb./ft.}^2$$

For a depth of 133.0 ft., the buoyant soil stress = (133.0)(51.0) = 6783.0 lb./ft.<sup>2</sup> (<7516.0 lb./ft.<sup>2</sup>)

Hence, the computed soil depth is OK since it does not violate any code provisions.

- (ii) Normally consolidated stiff clay:

As in problem (i),  $f = (0.5)(\gamma'z) = (0.5)(52.0) = 26.0z$  (psf).

Hence,  $2,000,000 = \pi(33/12)(1/2)(26z)(z) + (\pi/4)(33/12)^2(52.0)(z) = 112.31z^2 + 308.85z$

Solving the equation, one obtains a pile embedment depth of  $z = 132.0$  ft.

Verifying this with the limitations provided in the API code, the pile end bearing strength is given by

$$9c_u = (9.0)(1.670 \text{ ksf}) = 15.03 \text{ ksf}$$

For a depth of 132.0 ft., the buoyant soil stress = (132.0)(52.0) = 6864.0 psf (< 15,030 psf).

Hence, the computed soil depth is OK, since it does not violate any code provisions.

- (iii) Medium dense sand:

For noncohesive soils such as sands, the pile friction is given as

$f = Kp'_0 \tan(\delta)$ ; in this case,  $K = 1.0$  (assuming a closed ended pile). Also  $\delta = 25^\circ$ .

Also  $p'_0 = \gamma'z$ . Hence,  $f = (1.0)(64.0)\{\tan(25^\circ)\} = 29.84 \text{ lb./ft.}^3$

Therefore,  $2,000,000 = \pi(33/12)(1/2)(29.84z)(z) + (\pi/4)(33/12)^2(64.0z) = 128.90z^2 + 380.13z$ .

Solving the above equation, one obtains a value of  $z = 123.0$  ft.

Checking the code restrictions,  $q \leq N_q p'_0 \leq (20.0)(123)(64.0) = 157,440 \text{ psf}$  or 100.0 ksf.

For a depth of 123.0 ft., the buoyant soil stress = (123.0)(64.0) = 7872.0 psf ( $\leq 100,000$  psf).

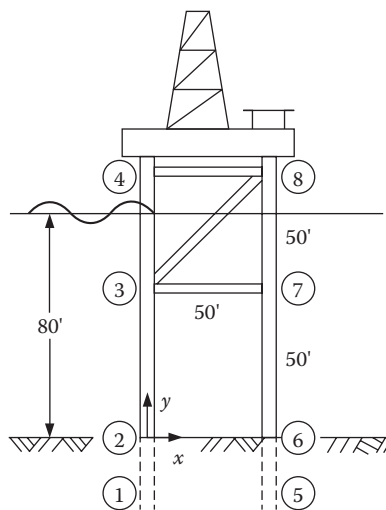
Hence, the computed soil depth is OK.



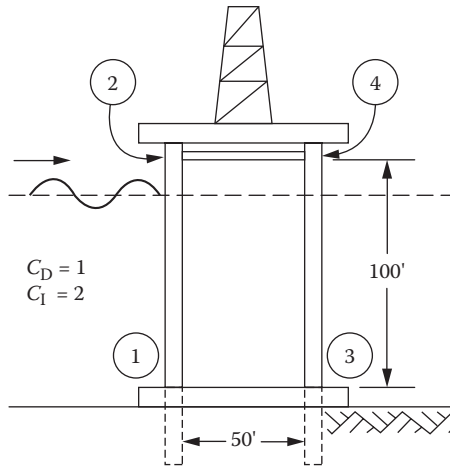
**EXERCISE PROBLEMS**

1. When installing a fixed offshore platform, what are the various design conditions and loads that should be considered while designing the platform?
2. An offshore steel jacket platform is to be designed for a water depth of 80.0 ft. The wave particulars are wave height = 18.0 ft., wavelength = 350.0 ft., and the wave travels perpendicular to member 2-3-4 of the structure shown in Figure P8.1 [97]. All the four faces of the structure are similar. The outside diameters of all the vertical (main) column members are given as 3.5 ft., having a wall thickness of 1.625 in. The diameters of all the cross and horizontal stiffening members are given as 2.25 ft. with a wall thickness of 0.625 in. The deck weighs 650.0 kips, and the maximum wind load on the upper part of the structure (exposed to wind) is 125.0 kips. Using stiffness analysis for plane frames, determine (i) the joint forces and the member loads acting on members 3-7 and 3-8; (ii) the joint displacements and rotations at the respective joints; and (iii) the member stresses occurring in members 3-4, 3-7, and 3-8. (iv) Considering transverse bending for member 2-3, determine the corrected stress values due to the applied loads.
3. A simplified concept of an offshore steel jacket platform, shown in Figure P8.2 [98], is made up of four main columns of diameter 4.0 ft. and of wall thickness 1.0 in. It is connected together at its top by four horizontal cylindrical stiffeners of diameter 2.0 ft. and of wall thickness 0.50 in. Assume that the columns are fixed against displacement and rotation, at its bottom nodes 1-3, through the provision of rigid structural members. The stiffness matrix for the structure is given by

$$\begin{bmatrix} u_2 \\ v_2 \\ \theta_2 \\ u_4 \\ v_4 \\ \theta_4 \end{bmatrix} = 10^{-7} \begin{bmatrix} 13,320.0 & 96.64 & 1684.0 & 133,080.0 & -96.64 & 1681.0 \\ 96.64 & 225.6 & 1.933 & 96.64 & 0.1483 & 1.933 \\ 684.0 & 1.933 & 47.52 & 1681.0 & -1.933 & 19.79 \\ 133,080.0 & 96.64 & 1681.0 & 1,330,800.0 & -96.62 & 1684.4 \\ -96.64 & 0.1483 & -1.933 & -96.62 & 225.6 & -1.933 \\ 1681.0 & 1.933 & 19.79 & 1684.4 & -1.933 & 47.53 \end{bmatrix} \begin{bmatrix} F_{2,x} \\ F_{2,y} \\ M_{2,z} \\ F_{4,x} \\ F_{4,y} \\ M_{4,z} \end{bmatrix}$$



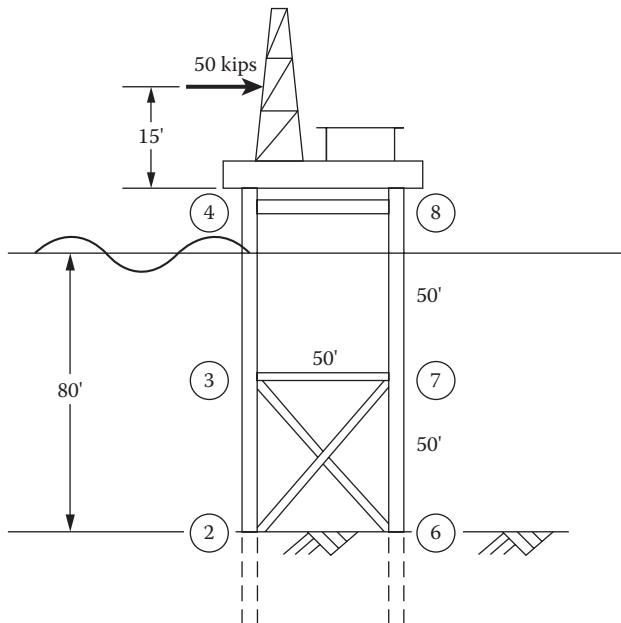
**FIGURE P8.1** Offshore steel jacket platform. (From T.H. Dawson, 1983, *Offshore Structural Engineering*, Prentice Hall, Englewood Cliffs, NJ. With permission.)



**FIGURE P8.2** Simplified model of an offshore jacket platform. (From T.H. Dawson, 1983, *Offshore Structural Engineering*, Prentice Hall, Englewood Cliffs, NJ. With Permission.)

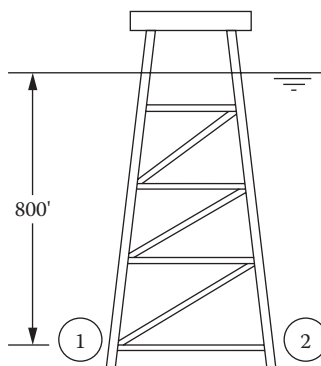
where  $u$  and  $v$  are expressed in feet,  $\theta$  is in radians,  $F_x$  and  $F_y$  are in kips, and  $M_z$  is in feet kips. (a) The platform, located at a water depth of 80.0 ft., is subjected to wave forces due to linear Airy's waves of height 22.0 ft. and length 400.0 ft. Compute the maximum horizontal force and the associated time  $\omega t$ ; consider a 3-D structure. (b) Compute the joint loads as per the method indicated in the textbook. (c) If in addition to the wave loading, the side face also carries load of 300.0 kips due to self-weight, acting midway between the two legs of the side, and also 60.0 kips of wind loading acting 12.0 ft. above level 2-4, determine the maximum (axial plus bending) stress induced in members 1-2, 3-4, and 2-4 (due to all the loads).

4. The structure shown in Figure P8.3 [99] is subjected to a horizontal wind load of 80.0 ft. kips acting 15.0 ft. above the level of member 1-2, on the drill rig shown at the top of the

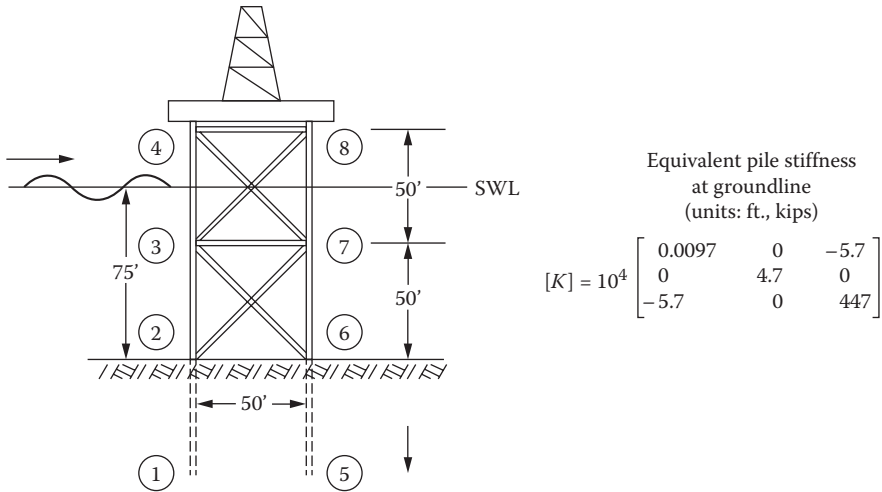


**FIGURE P8.3** Offshore steel jacket tower. (From T.H. Dawson, 1983, *Offshore Structural Engineering*, Prentice Hall, Englewood Cliffs, NJ. With permission.)

- fixed jacket structure; in addition, it is also subjected to wave forces due to a linear wave of height 23.0 ft. and of length 400.0 ft. The deck weight carried by the side frame is equal to 350.0 kips. The vertical column diameter is 4.5 ft., with a wall thickness of 1.5 in. The horizontal and inclined stiffeners are of diameter 2.25 m and of wall thickness 0.75 in. assuming an equivalent pile length of 12.0 ft. (with an area of 0.170 m<sup>2</sup> and a moment of inertia of 2.50 ft.<sup>4</sup>. Assume that the horizontal and inclined stiffener members are not flooded. (a) Determine the maximum stresses (bending + axial) generated in members 1-2 and 6-7. (b) Also determine the maximum dynamic amplification factor under the given loads, considering the wave loads to be dynamic.
5. The jacket structure shown in Figure P8.4 [100] is standing at a water depth of 850.0 ft., and unflooded member 1-2 is located at a depth of 800.0 ft. below the still water level. The outside diameter of the bracing member 1-2 is 4.0 ft. with a wall thickness of 0.75 in. (a) Compute the maximum hoop stress  $\sigma_\theta$  and the longitudinal stress  $\sigma_z$  in the given member due to hydrostatic loading. (b) Compute the associated compressive and hoop stresses at the end of the bracing member (end restraint) due to the same hydrostatic loading. (c) Check the acceptability of the above computed stresses if the yield stress of the above steel is 36,000 psi. (d) Assuming that ring stiffeners are spaced at every 10.0-ft. interval, along the member 1-2, and that the thickness of the ring stiffener is 3.00 in., determine the width of the ring stiffener.
6. The front elevation of a steel offshore platform is shown in Figure P8.5 [101]; the other three sides of the structure are identical, and it is also cross-stiffened, in the horizontal direction, at each joint (vertical) level. Consider only a plane frame action for the applied forces. The structure is immersed at a water depth of 75.0 ft., as shown in the figure. The vertical columnar members have a diameter of 4.5 ft. and wall thickness of 1.625 in.; all other braces (inclined and horizontal) have an outside diameter of 2.25 in. and wall thickness of 0.625 in. The deck weight is given as 600.0 kips. Model the structure as a single-degree-of-freedom structure [by applying a horizontal load at node 4 (and 8) level and determining the static deflection for unit load]. Assume that the tubular members, below the mean sea level, are fully flooded, and that the inertial coefficient  $C_I = 2.0$  (while computing the added mass of the structural components immersed in water). Also consider the equivalent pile height to be 20.0 ft. Assume the horizontal wave load to be sinusoidal having a magnitude of 120.0 kips (due to a wave of height 35.0 ft. and period 10.0 s). Determine the dynamic magnification factor for the structural motion.



**FIGURE P8.4** Simplified deepwater jacket structure. (From T.H. Dawson, 1983, *Offshore Structural Engineering*, Prentice Hall, Englewood Cliffs, NJ. With permission.)



**FIGURE P8.5** Steel jacket offshore platform. (From T.H. Dawson, 1983, *Offshore Structural Engineering*, Prentice Hall, Englewood Cliffs, NJ. With permission.)

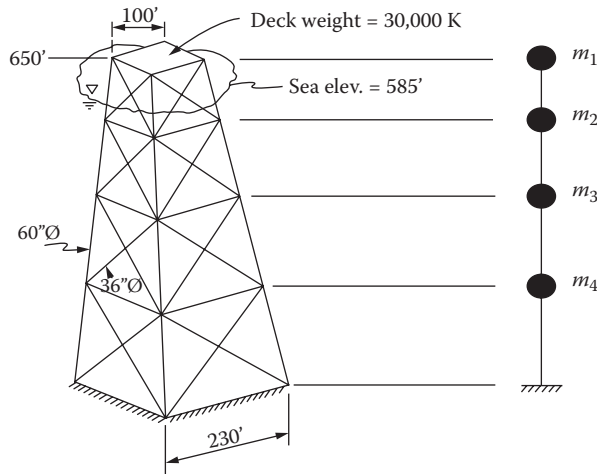
7. An offshore steel jacket structure of height 650.0 ft. is shown in Figure P8.6 [102], with its lumped mass model; the structure is located at a water depth of 585.0 ft. The stiffness and the lumped mass matrices are given as

$$[K] = \begin{bmatrix} 1.961 & -2.742 & 0.5046 & 0.2503 \\ -2.742 & 5.597 & -3.042 & 0.1698 \\ 0.5046 & -3.042 & 5.063 & -2.568 \\ 0.2503 & 0.1698 & -2.568 & 4.691 \end{bmatrix} \times 10^7 \text{ lb./ft.}$$

$$[M] = \begin{bmatrix} 960.0 & 0.0 & 0.0 & 0.0 \\ 0.0 & 116.0 & 0.0 & 0.0 \\ 0.0 & 0.0 & 150.0 & 0.0 \\ 0.0 & 0.0 & 0.0 & 176.0 \end{bmatrix} \times 10^3 \text{ slugs}$$

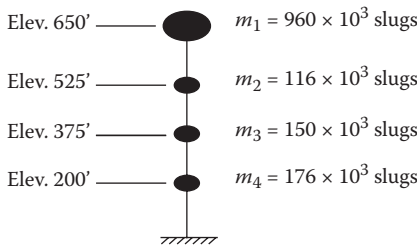
Assume Rayleigh damping  $[C] = \alpha[M] + \beta[K]$  for the system, with 2% equivalent critical modal damping for the first two modes. The tower is subjected to wave excitation due to a Pierson–Moskowitz spectrum with a significant wave height of 12.5 ft. and a peak wave period of 8.0 s. Compute the RMS value of the deck structural response at the top of the tower. [Hint:  $S_{rr}(f) = S_{ii}(f) * H_{ri}(f)$ , where  $S_{rr}(f)$  is the response spectral value, at frequency  $f$  (Hz), due to the action of wave input spectrum  $S_{ii}(f)$  on the transfer function of the system for unit input  $H_{ri}(f)$ .]

8. The helideck configuration of an offshore platform, for a Sikorsky S-58T helicopter, is 70.0 ft.  $\times$  70.0 ft. in plan form. Assuming the deck to be stiffened (with I-beams) in one direction only, and that the stiffened deck (at 4.0 ft.  $c/c$ ) is supported by a three-bay (at 20.0 ft.  $c/c$ , either way), two-story (each story height is 10.0 ft.) frame structure, design the helideck platform. The gross weight of the helicopter is 13.0 kips; wheel base is 29.9 ft.; tire pressure is 75.0 psi in main wheels and 60.0 psi on tail wheel. The impact factor for loading is taken as 1.5. Consider 1/9 of the helicopter weight to be taken by the tail wheel and 4/8 of the helicopter weight to be taken by each of the main wheels, spaced at 14.0 ft.  $c/c$ . Along with the self-weight, an additional live load of 40.0 lb./ft.<sup>2</sup> or the computed impact load has



Weight summary for tower model (kips)

	DOF	Deck equipment	Steel	Enclosed water	Virtual	Total
Top	1	30,000	637	133	131	30,901
	2		1268	1289	1182	3739
	3		1524	1724	1578	4826
	4		1798	2032	1837	5667



**FIGURE P8.6** Offshore steel jacket structure. (From T. R. Gaul, 1981, Structural Dynamics: Basic Concepts and Application, Short Course on Design of Fixed Offshore Structure held at University of Houston, TX, Figures 45 and 46. With permission.)

to be considered in the design computations. The impact area is to be determined from the given tire pressure and the footprint to be computed according to provisions.

9. A clay soil has negligible ( $\sim 0.0$ ) undrained shear strength at the seabed, and the strength varies linearly, increasing at a rate of  $0.01 \text{ kip/ft.}^2$  per linear foot; the clay stratum extends up to a depth of  $450.0 \text{ ft}$ . Determine the depth to which a  $4.5\text{-ft}$ -diameter pile must be driven in this clay stratum to support a maximum load of  $2500.0 \text{ kips}$ . The density of steel (in air) is  $0.484 \text{ kip/ft.}^3$  and that of soil is  $0.105 \text{ kip/ft.}^3$ . Use Table P8.1 [103] to compute the frictional resistance of soils to penetration. Use a factor of safety of  $1.5$ .
10. A clay stratum located at the seabed has a varying undrained shear strength of  $C = C_0 + by$ , with  $C_0 = 0.50 \text{ kip/ft.}^2$ ,  $b = 0.010 \text{ kip/ft.}^3$ , and  $y$  being the depth below the seabed. Determine the depth to which a steel pile of outside diameter  $7.0 \text{ ft}$ . (with a wall thickness of  $2.5 \text{ in.}$ ) needs to be driven such that it can carry a compressive load of  $3500.0 \text{ kips}$ . Consider a factor of safety of  $1.5$ . Take the submerged weight of soil to be  $0.038 \text{ kip/ft.}^3$  and that of steel to be  $0.420 \text{ kip/ft.}^3$ .
11. A sandy soil deposit has a submerged unit weight of  $48.0 \text{ lb./ft.}^3$ . A steel pile of outside diameter  $4.5 \text{ ft}$ . (having a wall thickness of  $0.75 \text{ in.}$ ) is to be used to support a compressive load of  $2500 \text{ kips}$ .

**TABLE P8.1**  
**Typical Design Parameters for Computing Axial Pile Capacity in Different Soils**

Clay <sup>a</sup>	Sand <sup>b</sup>
$\alpha = 1.0, 0.0 \leq C \leq 0.5 \text{ kip/ft.}^2$	$\delta = 30^\circ, \gamma_s = 40.0 \text{ to } 70.0 \text{ lb./ft.}^3$
$\alpha = 1.25 - 0.50C, 0.50 \leq C \leq 1.5 \text{ kips/ft.}^2$	$K = 0.7, f(\text{max}) = 2.0 \text{ kips/ft.}^2$
$\alpha = 0.5, C \geq 1.5 \text{ kips/ft.}^2$	$N_q = 40.0, q(\text{max}) = 200.0 \text{ kips/ft.}^2$
For all clays, $N_c = 9.0$	

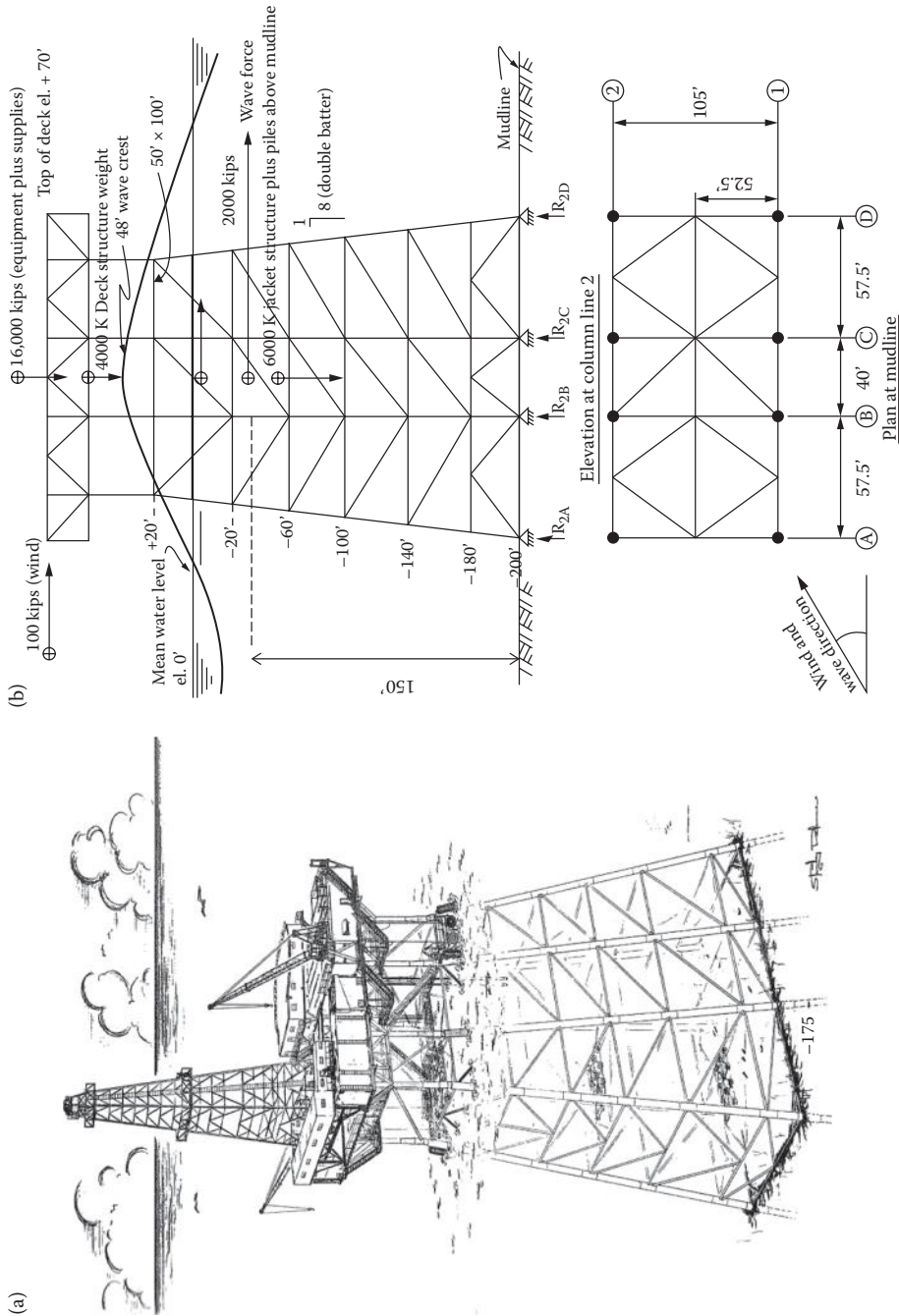
Source: T.H. Dawson, 1983, *Offshore Structural Engineering*, Prentice Hall, Englewood Cliffs, NJ. With permission.

<sup>a</sup> For clays,  $f = \alpha C$ ,  $q = N_c C$ , where  $C$  = undrained shear strength,  $f$  = side frictional resistance per unit area,  $q$  = end bearing resistance, and  $\alpha$  and  $N_c$  being dimensionless coefficients.

<sup>b</sup> For sands,  $f = K\gamma_s y \tan \delta$ ,  $q = N_q \gamma_s L$ , where  $\gamma_s$  = submerged density of soil,  $\delta$  = effective friction angle of sand,  $y$  = depth below the seabed,  $L$  = length of pile, and  $K$  and  $N_q$  being dimensionless coefficients.

Determine the depth to which the pile must be driven to support the applied load. Assume that the submerged weight of steel is 420.0 lb./ft.<sup>3</sup>, submerged weight of sand is 48.0 lb./ft.<sup>3</sup>, and the factor of safety to be used in the computation is 1.5. Use the values given in Table P8.1.

12. A group of four piles, placed on a square plan form, of size 100.0 × 100.0 ft., supports an offshore structure. The piles are expected to carry a horizontal load (due to wave and wind actions) of 2200 kips and a vertical load of 3000.0 kips. The outside diameters of the piles are 6.5 ft., with a wall thickness of 1.25 in. Determine the depth to which the piles should be driven to provide sufficient vertical and horizontal loads exerted on the structure. The horizontal load is considered to act at a height of 160.0 ft. from the bottom of the piles. Assume the worst case loading scenario to be that where the transverse wind and wave loads act at an angle of 45° to the faces of the structure. Take the soil properties to be the same as those given in Problem 8.10. The vertical pile loads are the same on all the four columns, and horizontal loads generate the same but symmetrically opposed vertical forces on the two extreme columns.
13. The framed structure in Figure P8.7a is subjected to a wave load of 2000.0 kips and a wind load of 200.0 kips, as shown in Figure P8.7a and b [104, 105]. The structure is installed at a water depth of 200.00 ft. The equipment and the supplies on the deck weigh 16,000 kips, while the self-weight of the top deck is 4000 kips. The jacket of the framed structure weighs 6000 kips. The unit skin friction, the end bearing strength, and the lateral resistance of soil (to bending of pile) are to be taken from the figures given in Figure E8.2 and Figure P8.8. Find (i) maximum pile axial load and shear and (ii) preliminary pile size (diameter and thickness) and penetration depth. Assume an approximate soil subgrade modulus of 6.0 lb./in.<sup>3</sup>.  $E = 30 \times 10^6 \text{ psi}$ .
14. A proposed offshore steel platform consists of four legs, 4.0 ft. in diameter, and each having 1.0-in. wall thickness, braced at the top and bottom with eight horizontal members of large axial stiffness and negligible bending stiffness. A side face of the structure is shown in Figure P8.2. The piles for each of the four legs of the platform are the same size as the vertical legs of the platform and are driven 300.0 ft. into the seafloor. The soil deposit of the foundation is of sand having an ultimate lateral soil resistance of  $p = NDK_p \gamma_s y$  and an elastic soil resistance of  $p = ku$ ,  $N = 1.8$ ,  $K_p = \frac{(1 + \sin \theta)}{(1 - \sin \theta)}$ ,  $\theta = 35^\circ$ ,  $\gamma_s = 50 \text{ lb./ft.}^3$ ,  $k = 1.20 \text{ kips/in.}^2$ ,  $K = 0.7$ ,  $N_q = 40$ ,  $\delta = 30^\circ$ ,  $f_{\text{max}} = 2 \text{ kips/ft.}^2$ ,  $q_{\text{max}} = 200 \text{ kips/ft.}^2$ ,  $E_{\text{steel}} = 30 \times 10^6 \text{ psi}$ , and  $k_a = 190 \text{ kips/ft.}^3$ . For the horizontal and vertical loadings shown (acting on one side alone), check (i) the adequacy of the preliminary design considering API provision for main column member design; (ii) the pile design considering axial pile capacity, and pile response to lateral loading; and (iii) the equivalent length of the pile. Take the factor of safety of 2.5 for the pile and 1.5 for the main column members. Assume any missing data and justify its choice.



**FIGURE P8.7** (a) Fixed framed platform structure for deepwater. (From J.H. Evans and J.C. Adamchak, 1969, *Ocean Engineering Structures, Volume I* (Course Notes), MIT Press, Cambridge, MA, p. 175.) (b) Plan and elevation of the fixed framed platform structure. (From J.B. Weidler and D.I. Karsan, 1986, *Analytical models and three-dimensional analysis*, Chapter 17, in *Planning and Design of Fixed Offshore Platforms*, eds. B. McClelland and M.D. Reifel, Van Nostrand Reinhold Company, New York, p. 549. With permission.)

15. A steel pile with 33-in. (outer) diameter and 1.5-in. wall thickness is subjected to axial and bending loads, as shown in Figure P8.9. Determine the pile embedment length  $L$  and the pile deflection and moment curves.  $E_s = 30 \times 10^6 \text{ lb./in.}^2$ . From the computed curves, also check whether the maximum stress in the pile is within the allowable permission value.  $\sigma_{\text{yield}} = 50.0 \text{ ksi}$ ;  $\sigma_{\text{permissible}} = 0.67\sigma_y$ . Soil data for axial and bending loads are in the Appendixes 8A and 8B.
16. An offshore platform is fixed to the seabed by pile foundations. The pile diameter is 36.0 in. (OD) and has a length of 150.0 ft.; it is subjected to a horizontal load of 75,000.0 lb. and a moment of  $3.5 \times 10^5 \text{ lb. ft.}$  on the top of its pile head. Assuming the soil modulus curve given in Figure P8.9 and Figure E8.18, and a freestanding pile in soil, determine the deflection of the pile and the moment of resistance developed along the length of the embedded pile.  $E_{\text{steel}} = 30 \times 10^6 \text{ psi}$ ;  $I = 18,000.0 \text{ in.}^4$ .

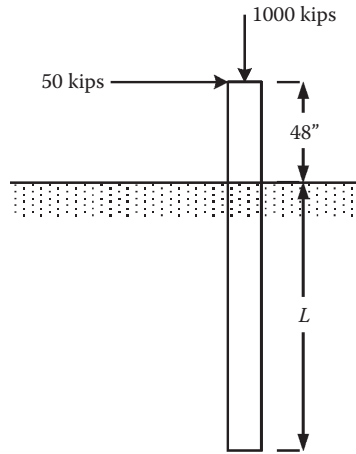


FIGURE P8.8 Pile embedded in soil.

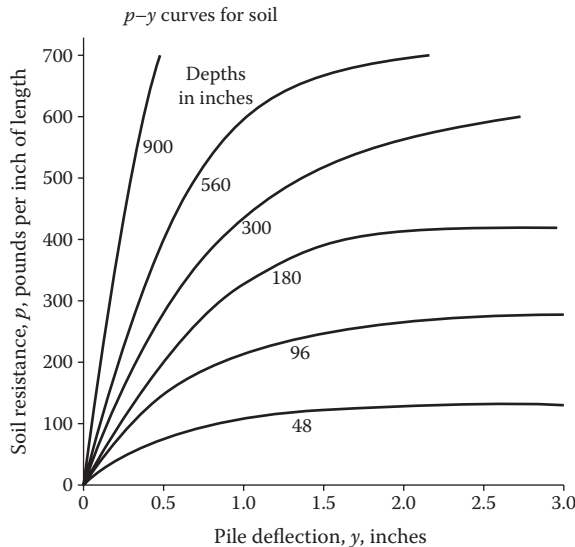


FIGURE P8.9 Transverse load versus deflection of an embedded pile in soil (modified). (From H. Matlock and L.C. Reese, Generalized Solutions for Laterally Loaded Piles, *Transactions, American Society of Civil Engineers*, Volume 127, Issue 3370, Part I, pp. 1220–1269, 1962. With permission.)



APPENDIX 8A

TABLE 8A.1

Deflection Coefficients  $C_y$  for Elastic Piles for Values of  $Z_{max} = 10.0$  and Linear Variation of  $E_s$  with Respect to Depth  $x$

Z	$M_t/P_tT$										
	-1.0	-0.9	-0.8	-0.7	-0.6	-0.5	-0.4	-0.3	-0.2	-0.1	0.0
.0	0.812	0.975	1.137	1.299	1.461	1.624	1.786	1.948	2.111	2.273	2.435
.1	0.820	0.965	1.111	1.256	1.401	1.546	1.692	1.837	1.982	2.128	2.273
.2	0.819	0.948	1.077	1.207	1.336	1.465	1.594	1.724	1.853	1.982	2.112
.3	0.809	0.924	1.038	1.152	1.267	1.381	1.495	1.609	1.724	1.838	1.952
.4	0.793	0.893	0.994	1.094	1.194	1.294	1.395	1.495	1.595	1.696	1.796
.5	0.771	0.858	0.945	1.032	1.120	1.207	1.294	1.381	1.469	1.556	1.643
.6	0.743	0.818	0.893	0.969	1.044	1.119	1.194	1.270	1.345	1.420	1.495
.7	0.711	0.775	0.839	0.904	0.968	1.032	1.096	1.160	1.224	1.288	1.353
.8	0.676	0.730	0.784	0.838	0.892	0.946	1.000	1.054	1.108	1.162	1.216
.9	0.638	0.683	0.727	0.772	0.817	0.862	0.907	0.951	0.996	1.041	1.086
1.0	0.598	0.634	0.671	0.707	0.744	0.780	0.814	0.853	0.889	0.926	0.962
1.2	0.515	0.537	0.559	0.582	0.604	0.626	0.649	0.671	0.788	0.817	0.738
1.4	0.432	0.443	0.454	0.465	0.476	0.488	0.499	0.510	0.521	0.533	0.544
1.6	0.351	0.354	0.357	0.360	0.363	0.366	0.369	0.372	0.375	0.378	0.381
1.8	0.277	0.274	0.271	0.268	0.265	0.262	0.259	0.256	0.253	0.250	0.247
2.0	0.211	0.204	0.197	0.190	0.183	0.176	0.169	0.162	0.155	0.148	0.141
2.5	0.085	0.075	0.064	0.054	0.043	0.033	0.022	0.012	0.001	0.009-	0.020-
3.0	0.014	0.005	0.004-	0.013-	0.022-	0.031-	0.040-	0.048-	0.057-	0.066-	0.075-
3.5	0.016-	0.022-	0.028-	0.034-	0.039-	0.045-	0.051-	0.056-	0.062-	0.068-	0.074-
4.0	0.022-	0.025-	0.028-	0.031-	0.033-	0.036-	0.039-	0.042-	0.045-	0.047-	0.050-
4.5	0.017-	0.018	0.019-	0.020-	0.021-	0.022-	0.022-	0.023-	0.024-	0.025-	0.026-
5.0	0.010-	0.010-	0.010-	0.010-	0.009-	0.009-	0.009-	0.009-	0.009-	0.009-	0.009-
10.0	0.000	0.000	0.000	0.000	0.000	0.000	0.000	0.000	0.000	0.000	0.000

Source: M. Novak, *Piles under Dynamic Loads: State of the Art*, Proceedings, 2nd International Conference on Recent Advances in Geotechnical Earthquake Engineering and Soil Dynamics, St. Louis, MO, 1991.

Note:  $E_s = kx$ ;  $Z_{max} = 10.0$ .

**TABLE 8A.2**  
**Deflection Coefficients  $C_y$  for Elastic Piles for Values of  $Z_{max} = 4.0$  and Linear Variation of  $E_s$  with Respect to Depth  $x$**

$Z$	$M_t/P_tT$										
	-1.0	-0.9	-0.8	-0.7	-0.6	-0.5	-0.4	-0.3	-0.2	-0.1	0.0
.0	0.821	0.984	1.146	1.308	1.471	1.633	1.796	1.958	2.121	2.283	2.445
.1	0.829	0.974	1.120	1.265	1.411	1.556	1.702	1.847	1.992	2.138	2.283
.2	0.828	0.957	1.087	1.216	1.346	1.475	1.604	1.734	1.863	1.992	2.122
.3	0.819	0.933	1.048	1.162	1.276	1.391	1.505	1.619	1.734	1.848	1.962
.4	0.803	0.903	1.004	1.104	1.204	1.305	1.405	1.505	1.605	1.706	1.806
.5	0.781	0.868	0.955	1.043	1.130	1.217	1.304	1.392	1.479	1.566	1.653
.6	0.754	0.829	0.904	0.979	1.054	1.129	1.205	1.280	1.355	1.430	1.505
.7	0.722	0.786	0.850	0.914	0.978	1.042	1.106	1.170	1.234	1.299	1.363
.8	0.687	0.741	0.795	0.849	0.902	0.956	1.010	1.064	1.118	1.172	1.226
.9	0.649	0.694	0.738	0.783	0.828	0.872	0.917	0.961	1.006	1.051	1.095
1.0	0.609	0.646	0.682	0.718	0.754	0.791	0.827	0.863	0.899	0.936	0.972
1.2	0.527	0.549	0.571	0.593	0.615	0.637	0.659	0.681	0.703	0.725	0.747
1.4	0.444	0.455	0.466	0.476	0.487	0.498	0.509	0.520	0.531	0.542	0.552
1.6	0.364	0.366	0.369	0.371	0.374	0.376	0.379	0.381	0.384	0.386	0.388
1.8	0.289	0.286	0.282	0.279	0.275	0.272	0.268	0.265	0.261	0.258	0.254
2.0	0.222	0.215	0.207	0.200	0.192	0.185	0.177	0.170	0.162	0.154	0.147
2.5	0.091	0.080	0.069	0.058	0.047	0.035	0.024	0.013	0.002	0.009-	0.020-
3.0	0.007	0.002-	0.012-	0.021-	0.031-	0.040-	0.050-	0.059-	0.069-	0.078-	0.088-
3.5	0.048-	0.054-	0.059-	0.065-	0.071-	0.076-	0.082-	0.088-	0.094-	0.099-	0.105-
4.0	0.093-	0.094-	0.096-	0.097-	0.099-	0.100-	0.102-	0.103-	0.105-	0.106-	0.108-

Source: M. Novak, *Piles under Dynamic Loads: State of the Art*, Proceedings, 2nd International Conference on Recent Advances in Geotechnical Earthquake Engineering and Soil Dynamics, St. Louis, MO, 1991.

Note:  $E_s = kx$ ;  $Z_{max} = 4.0$ .

**TABLE 8A.3**  
**Deflection Coefficients  $C_y$  for Elastic Piles for Values of  $Z_{max} = 3.5$  and Linear Variation of  $E_s$  with Respect to Depth  $x$**

$Z$	$M_t/P_tT$										
	-1.0	-0.9	-0.8	-0.7	-0.6	-0.5	-0.4	-0.3	-0.2	-0.1	0.0
.0	0.857	1.020	1.184	1.348	1.511	1.675	1.839	2.002	2.166	2.330	2.493
.1	0.864	1.010	1.157	1.304	1.450	1.597	1.743	1.890	2.037	2.183	2.330
.2	0.862	0.992	1.123	1.253	1.384	1.515	1.645	1.776	1.906	2.037	2.167
.3	0.852	0.967	1.083	1.198	1.314	1.429	1.545	1.660	1.776	1.891	2.007
.4	0.835	0.936	1.038	1.139	1.240	1.342	1.443	1.545	1.646	1.748	1.849
.5	0.812	0.900	0.988	1.077	1.165	1.253	1.342	1.430	1.518	1.607	1.695
.6	0.783	0.859	0.936	1.012	1.088	1.164	1.241	1.317	1.393	1.470	1.546
.7	0.751	0.816	0.881	0.946	1.011	1.076	1.141	1.206	1.271	1.337	1.402
.8	0.714	0.769	0.824	0.879	0.934	0.989	1.044	1.099	1.154	1.209	1.263
.9	0.676	0.721	0.767	0.812	0.858	0.904	0.949	0.995	1.040	1.086	1.132
1.0	0.635	0.672	0.709	0.746	0.784	0.821	0.858	0.895	0.932	0.970	1.007
1.2	0.550	0.573	0.595	0.618	0.641	0.664	0.687	0.710	0.733	0.756	0.778
1.4	0.464	0.475	0.487	0.498	0.510	0.522	0.533	0.545	0.557	0.568	0.580
1.6	0.380	0.383	0.386	0.389	0.392	0.395	0.398	0.401	0.405	0.408	0.411
1.8	0.301	0.298	0.295	0.292	0.289	0.285	0.282	0.279	0.276	0.273	0.270
2.0	0.228	0.221	0.214	0.206	0.199	0.192	0.184	0.177	0.169	0.162	0.155
2.5	0.076	0.064	0.052	0.040	0.028	0.016	0.004	0.008	0.020-	0.032-	0.044-
3.0	0.044-	0.056-	0.068-	0.080-	0.092-	0.104-	0.116-	0.128-	0.140-	0.152-	0.164-
3.5	0.152-	0.162-	0.173-	0.183-	0.194-	0.205-	0.215-	0.226-	0.236-	0.247-	0.257-

Source: M. Novak, *Piles under Dynamic Loads: State of the Art*, Proceedings, 2nd International Conference on Recent Advances in Geotechnical Earthquake Engineering and Soil Dynamics, St. Louis, MO, 1991.

Note:  $E_s = kx$ ;  $Z_{max} = 3.5$ .

**TABLE 8A.4**  
**Deflection Coefficients  $C_y$  for Elastic Piles for Values of  $Z_{max} = 3.0$  and Linear Variation of  $E_s$  with Respect to Depth  $x$**

$Z$	$M_t/P_tT$										
	-1.0	-0.9	-0.8	-0.7	-0.6	-0.5	-0.4	-0.3	-0.2	-0.1	0.0
.0	0.967	1.143	1.318	1.494	1.670	1.845	2.021	2.197	2.372	2.548	2.723
.1	0.968	1.126	1.284	1.442	1.600	1.758	1.916	2.074	2.232	2.390	2.548
.2	0.961	1.102	1.243	1.385	1.526	1.667	1.808	1.950	2.091	2.232	2.373
.3	0.945	1.071	1.196	1.322	1.447	1.573	1.699	1.824	1.950	2.075	2.201
.4	0.922	1.033	1.144	1.255	1.366	1.477	1.588	1.699	1.809	1.920	2.031
.5	0.893	0.991	1.088	1.185	1.282	1.379	1.477	1.574	1.671	1.768	1.865
.6	0.859	0.944	1.028	1.113	1.197	1.282	1.366	1.451	1.535	1.619	1.704
.7	0.821	0.894	0.966	1.039	1.112	1.184	1.257	1.330	1.402	1.475	1.548
.8	0.779	0.841	0.903	0.965	1.026	1.088	1.150	1.212	1.274	1.335	1.397
.9	0.734	0.786	0.838	0.890	0.942	0.994	1.046	1.098	1.149	1.201	1.253
1.0	0.688	0.730	0.773	0.816	0.859	0.902	0.944	0.987	1.030	1.073	1.116
1.2	0.590	0.617	0.644	0.671	0.699	0.726	0.753	0.780	0.807	0.834	0.861
1.4	0.491	0.505	0.520	0.534	0.548	0.563	0.577	0.592	0.606	0.621	0.635
1.6	0.393	0.397	0.401	0.406	0.410	0.414	0.419	0.423	0.427	0.431	0.436
1.8	0.298	0.294	0.290	0.287	0.283	0.279	0.276	0.272	0.268	0.265	0.261
2.0	0.207	0.197	0.187	0.177	0.167	0.157	0.147	0.137	0.127	0.118	0.108
2.5	0.004-	0.025-	0.045-	0.066-	0.087-	0.108-	0.129-	0.150-	0.170-	0.191-	0.212-
3.0	0.202-	0.231-	0.260-	0.289-	0.319-	0.348-	0.377-	0.406-	0.435-	0.464-	0.493-

Source: M. Novak, *Piles under Dynamic Loads: State of the Art*, Proceedings, 2nd International Conference on Recent Advances in Geotechnical Earthquake Engineering and Soil Dynamics, St. Louis, MO, 1991.

Note:  $E_s = kx$ ;  $Z_{max} = 3.0$ .

**TABLE 8A.5**  
**Deflection Coefficients  $C_y$  for Elastic Piles for Values of  $Z_{max} = 2.6$  and Linear Variation of  $E_s$  with Respect to Depth  $x$**

$Z$	$M_t/P_tT$										
	-1.0	-0.9	-0.8	-0.7	-0.6	-0.5	-0.4	-0.3	-0.2	-0.1	0.0
.0	1.115	1.320	1.526	1.731	1.936	2.141	2.346	2.551	2.757	2.962	3.167
.1	1.107	1.292	1.478	1.663	1.849	2.034	2.220	2.405	2.591	2.776	2.962
.2	1.089	1.256	1.423	1.590	1.757	1.924	2.090	2.257	2.424	2.591	2.758
.3	1.064	1.213	1.362	1.511	1.661	1.810	1.959	2.108	2.257	2.407	2.556
.4	1.031	1.164	1.296	1.429	1.561	1.694	1.826	1.959	2.091	2.224	2.357
.5	0.992	1.109	1.226	1.343	1.460	1.577	1.694	1.810	1.927	2.044	2.161
.6	0.949	1.051	1.153	1.255	1.357	1.459	1.561	1.664	1.766	1.868	1.970
.7	0.900	0.989	1.077	1.165	1.254	1.342	1.431	1.519	1.607	1.696	1.784
.8	0.848	0.924	1.000	1.075	1.151	1.226	1.302	1.377	1.453	1.528	1.604
.9	0.794	0.857	0.921	0.984	1.048	1.112	1.175	1.239	1.302	1.366	1.429
1.0	0.737	0.789	0.842	0.894	0.947	0.999	1.051	1.104	1.156	1.209	1.261
1.2	0.619	0.651	0.684	0.716	0.749	0.781	0.814	0.847	0.879	0.912	0.944
1.4	0.498	0.513	0.529	0.544	0.559	0.575	0.590	0.606	0.621	0.637	0.652
1.6	0.376	0.377	0.378	0.378	0.379	0.380	0.381	0.381	0.382	0.383	0.383
1.8	0.256	0.244	0.232	0.220	0.207	0.195	0.183	0.170	0.158	0.146	0.134
2.0	0.138	0.114	0.090	0.066	0.042	0.018	0.006-	0.030-	0.054-	0.078-	0.102-
2.5	0.151-	0.201-	0.252-	0.303-	0.353-	0.404-	0.455-	0.505-	0.556-	0.606-	0.657-
2.6	0.208-	0.264-	0.320-	0.376-	0.431-	0.487-	0.543-	0.599-	0.655-	0.711-	0.766-

Source: M. Novak, *Piles under Dynamic Loads: State of the Art*, Proceedings, 2nd International Conference on Recent Advances in Geotechnical Earthquake Engineering and Soil Dynamics, St. Louis, MO, 1991.

Note:  $E_s = kx$ ;  $Z_{max} = 2.6$ .

TABLE 8A.6

Deflection Coefficients  $C_y$  for Elastic Piles for Values of  $Z_{\max} = 2.2$  and Linear Variation of  $E_s$  with Respect to Depth  $x$

$Z$	$M_t/P_t T$										
	-1.0	-0.9	-0.8	-0.7	-0.6	-0.5	-0.4	-0.3	-0.2	-0.1	0.0
.0	1.268	1.543	1.817	2.091	2.365	2.640	2.914	3.188	3.462	3.737	4.011
.1	1.247	1.496	1.745	1.994	2.243	2.492	2.741	2.990	3.239	3.488	3.737
.2	1.218	1.442	1.667	1.891	2.116	2.341	2.565	2.790	3.014	3.239	3.464
.3	1.180	1.381	1.582	1.783	1.985	2.186	2.387	2.589	2.790	2.991	3.193
.4	1.135	1.314	1.493	1.672	1.850	2.029	2.208	2.387	2.566	2.745	2.924
.5	1.084	1.241	1.399	1.556	1.714	1.871	2.029	2.187	2.344	2.502	2.659
.6	1.027	1.164	1.302	1.439	1.576	1.713	1.850	1.987	2.125	2.262	2.399
.7	0.966	1.084	1.202	1.320	1.437	1.555	1.673	1.790	1.908	2.026	2.143
.8	0.902	1.001	1.100	1.199	1.298	1.397	1.497	1.596	1.695	1.794	1.893
.9	0.835	0.916	0.997	1.079	1.160	1.241	1.323	1.404	1.485	1.567	1.648
1.0	0.765	0.829	0.894	0.958	1.022	1.087	1.151	1.215	1.280	1.344	1.409
1.2	0.620	0.653	0.686	0.718	0.751	0.783	0.816	0.848	0.881	0.914	0.946
1.4	0.472	0.475	0.478	0.482	0.485	0.488	0.491	0.494	0.497	0.500	0.504
1.6	0.322	0.298	0.273	0.249	0.224	0.200	0.175	0.151	0.126	0.102	0.077
1.8	0.172	0.121	0.070	0.019	0.032-	0.083-	0.134-	0.185-	0.236-	0.287-	0.338-
2.0	0.022	0.055-	0.132-	0.209-	0.286-	0.363-	0.440-	0.517-	0.594-	0.671-	0.748-
2.2	0.127-	0.230-	0.333-	0.436-	0.539-	0.641-	0.744-	0.847-	0.950-	1.053-	1.155-

Source: M. Novak, *Piles under Dynamic Loads: State of the Art*, Proceedings, 2nd International Conference on Recent Advances in Geotechnical Earthquake Engineering and Soil Dynamics, St. Louis, MO, 1991.

Note:  $E_s = kx$ ;  $Z_{\max} = 2.2$ .

## APPENDIX 8B

TABLE 8B.1

**Coefficients for Deflection, Slope, Moment, Shear Force, and Soil Reaction for Elastic Piles for Values of  $Z_{\max} = 10.0$  and Linear Variation of  $E_s$  with Respect to Depth  $x$**

$Z$	$A_Y$	$A_S$	$A_M$	$A_V$	$A_P$	$B_Y$	$B_S$	$B_M$	$B_V$	$B_P$	$Z$
0.0	2.435	1.623-	0.000	1.000	0.000	1.623	1.749-	1.000	0.000	0.000	0.0
0.1	2.273	1.618-	0.100	0.988	0.227-	1.453	1.649-	1.000	0.007-	0.145-	0.1
0.2	2.112	1.603-	0.198	0.956	0.422-	1.293	1.549-	0.999	0.028-	0.259-	0.2
0.3	1.952	1.578-	0.291	0.906	0.586-	1.143	1.450-	0.994	0.058-	0.343-	0.3
0.4	1.796	1.545-	0.379	0.840	0.718-	1.003	1.351-	0.987	0.095-	0.401-	0.4
0.5	1.643	1.503-	0.459	0.763	0.822-	0.873	1.253-	0.976	0.137-	0.436-	0.5
0.6	1.495	1.453-	0.531	0.677	0.897-	0.752	1.156-	0.960	0.181-	0.451-	0.6
0.7	1.353	1.397-	0.595	0.585	0.947-	0.641	1.061-	0.939	0.226-	0.449-	0.7
0.8	1.216	1.335-	0.649	0.489	0.973-	0.540	0.968-	0.914	0.270-	0.432-	0.8
0.9	1.086	1.268-	0.693	0.392	0.977-	0.448	0.878-	0.885	0.312-	0.403-	0.9
1.0	0.962	1.197-	0.727	0.295	0.962-	0.364	0.791-	0.852	0.350-	0.364-	1.0
1.2	0.738	1.047-	0.767	0.109	0.885-	0.223	0.628-	0.775	0.414-	0.267-	1.2
1.4	0.544	0.893-	0.772	0.056-	0.761-	0.112	0.482-	0.688	0.456-	0.157-	1.4
1.6	0.381	0.741-	0.746	0.193-	0.609-	0.029	0.354-	0.594	0.477-	0.046-	1.6
1.8	0.247	0.596-	0.696	0.299-	0.445-	0.030-	0.245-	0.498	0.476-	0.055	1.8
2.0	0.141	0.464-	0.628	0.371-	0.283-	0.070-	0.155-	0.404	0.456-	0.140	2.0
2.5	0.020-	0.200-	0.422	0.424-	0.049	0.105-	0.006-	0.200	0.350-	0.263	2.5
3.0	0.075-	0.040-	0.225	0.349-	0.226	0.089-	0.057	0.059	0.213-	0.268	3.0
3.5	0.074-	0.034	0.081	0.223-	0.257	0.057-	0.065	0.016-	0.095-	0.200	3.5
4.0	0.050-	0.052	0.000	0.106-	0.201	0.028-	0.049	0.042-	0.017-	0.113	4.0
4.5	0.026-	0.042	0.032-	0.027-	0.117	0.009-	0.028	0.039-	0.021	0.041	4.5
5.0	0.009-	0.025	0.033-	0.013	0.046	0.000	0.011	0.026-	0.029	0.002	5.0
10.0	0.000	0.000	0.000	0.000	0.000	0.000	0.000	0.000	0.000	0.000	10.0

Source: M. Yegian and S.K. Wright, *Lateral Soil Resistance-Displacement Relationships for Pile Foundations in Soft Clay*, Proceedings of the Fifth Offshore Technology Conference, held at Houston, TX, Paper # OTC 1893, pp. 663-676, 1973.

Note:  $E_s = kx$ ;  $Z_{\max} = 10.0$ .

TABLE 8B.2

Coefficients for Deflection, Slope, Moment, Shear Force, and Soil Reaction for Elastic Piles for Values of  $Z_{\max} = 4.0$  and Linear Variation of  $E_s$  with Respect to Depth  $x$

$Z$	$A_Y$	$A_S$	$A_M$	$A_V$	$A_P$	$B_Y$	$B_S$	$B_M$	$B_V$	$B_P$
0.0	2.445	1.624-	0.000	1.000	0.000	1.624	1.753-	1.000	0.000	0.000
0.1	2.283	1.619-	0.100	0.991	0.228-	1.454	1.653-	1.000	0.006-	0.145-
0.2	2.122	1.604-	0.198	0.959	0.424-	1.294	1.553-	0.998	0.026-	0.259-
0.3	1.962	1.580-	0.291	0.906	0.589-	1.143	1.453-	0.994	0.057-	0.343-
0.4	1.806	1.546-	0.378	0.841	0.722-	1.003	1.354-	0.987	0.094-	0.401-
0.5	1.653	1.505-	0.459	0.762	0.827-	0.873	1.256-	0.975	0.137-	0.436-
0.6	1.505	1.455-	0.531	0.676	0.903-	0.752	1.159-	0.960	0.180-	0.451-
0.7	1.363	1.399-	0.594	0.583	0.954-	0.641	1.064-	0.939	0.226-	0.448-
0.8	1.226	1.337-	0.647	0.486	0.981-	0.539	0.972-	0.914	0.270-	0.431-
0.9	1.095	1.270-	0.691	0.387	0.986-	0.446	0.882-	0.885	0.312-	0.402-
1.0	0.972	1.199-	0.725	0.290	0.972-	0.362	0.795-	0.852	0.350-	0.362-
1.2	0.747	1.049-	0.764	0.102	0.896-	0.220	0.632-	0.775	0.413-	0.264-
1.4	0.552	0.896-	0.767	0.066-	0.773-	0.109	0.485-	0.688	0.455-	0.152-
1.6	0.388	0.745-	0.739	0.206-	0.622-	0.025	0.357-	0.595	0.474-	0.040-
1.8	0.254	0.602-	0.686	0.314-	0.457-	0.035-	0.248-	0.500	0.471-	0.064
2.0	0.147	0.471-	0.616	0.389-	0.294-	0.075-	0.157-	0.407	0.450-	0.151
2.5	0.020-	0.217-	0.400	0.445-	0.051	0.112-	0.005-	0.208	0.336-	0.280
3.0	0.088-	0.070-	0.194	0.361-	0.263	0.095-	0.063	0.076	0.191-	0.284
3.5	0.105-	0.012-	0.051	0.200-	0.368	0.057-	0.083	0.014	0.067-	0.200
4.0	0.108-	0.003-	0.000	0.000	0.431	0.015-	0.085	0.000	0.000	0.060

Source: M. Yegian and S.K. Wright, *Lateral Soil Resistance-Displacement Relationships for Pile Foundations in Soft Clay*, Proceedings of the Fifth Offshore Technology Conference, held at Houston, TX, Paper # OTC 1893, pp. 663-676, 1973.

Note:  $E_s = kx$ ;  $Z_{\max} = 4.0$ .

TABLE 8B.3

Coefficients for Deflection, Slope, Moment, Shear Force, and Soil Reaction for Elastic Piles for Values of  $Z_{\max} = 3.5$  and Linear Variation of  $E_s$  with Respect to Depth  $x$

$Z$	$A_Y$	$A_S$	$A_M$	$A_V$	$A_P$	$B_Y$	$B_S$	$B_M$	$B_V$	$B_P$
0.0	2.493	1.636-	0.000	1.000	0.000	1.636	1.755-	1.000	0.000	0.000
0.1	2.330	1.632-	0.100	0.988	0.233-	1.466	1.655-	1.000	0.008-	0.147-
0.2	2.167	1.617-	0.197	0.956	0.433-	1.305	1.555-	0.998	0.027-	0.261-
0.3	2.007	1.592-	0.290	0.900	0.602-	1.155	1.456-	0.994	0.061-	0.346-
0.4	1.849	1.559-	0.377	0.832	0.740-	1.014	1.357-	0.986	0.098-	0.406-
0.5	1.695	1.517-	0.456	0.754	0.848-	0.884	1.259-	0.974	0.140-	0.442-
0.6	1.546	1.468-	0.527	0.664	0.927-	0.763	1.162-	0.958	0.186-	0.458-
0.7	1.402	1.412-	0.589	0.567	0.981-	0.651	1.067-	0.937	0.232-	0.456-
0.8	1.263	1.351-	0.641	0.467	1.011-	0.549	0.975-	0.911	0.277-	0.439-
0.9	1.132	1.284-	0.682	0.365	1.019-	0.456	0.885-	0.882	0.320-	0.410-
1.0	1.007	1.214-	0.714	0.264	1.007-	0.372	0.799-	0.848	0.359-	0.372-
1.2	0.778	1.068-	0.747	0.068	0.934-	0.229	0.637-	0.769	0.424-	0.274-
1.4	0.580	0.918-	0.742	0.108-	0.812-	0.116	0.492-	0.679	0.468-	0.163-
1.6	0.411	0.773-	0.705	0.256-	0.657-	0.031	0.365-	0.583	0.489-	0.049-
1.8	0.270	0.638-	0.642	0.370-	0.486-	0.031-	0.259-	0.485	0.488-	0.056
2.0	0.155	0.518-	0.559	0.449-	0.309-	0.074-	0.171-	0.389	0.468-	0.148
2.5	0.044-	0.298-	0.314	0.497-	0.110	0.120-	0.131-	0.181	0.351-	0.300
3.0	0.164-	0.199-	0.095	0.346-	0.492	0.120-	0.022	0.046	0.184-	0.359
3.5	0.257	0.183-	0.000	0.000	0.901	0.106-	0.030	0.000	0.000	0.370

Source: M. Yegian and S.K. Wright, *Lateral Soil Resistance-Displacement Relationships for Pile Foundations in Soft Clay*, Proceedings of the Fifth Offshore Technology Conference, held at Houston, TX, Paper # OTC 1893, pp. 663-676, 1973.

Note:  $E_s = kx$ ;  $Z_{\max} = 3.5$ .

**TABLE 8B.4**  
**Coefficients for Deflection, Slope, Moment, Shear Force, and Soil Reaction for Elastic Piles for Values of  $Z_{max} = 3.0$  and Linear Variation of  $E_s$  with Respect to Depth  $x$**

$Z$	$A_Y$	$A_S$	$A_M$	$A_V$	$A_P$	$B_Y$	$B_S$	$B_M$	$B_V$	$B_P$
0.0	2.723	1.756-	0.000	1.000	0.000	1.756	1.818-	1.000	0.000	0.000
0.1	2.548	1.751-	0.100	0.987	0.255-	1.579	1.718-	1.000	0.008-	0.158-
0.2	2.373	1.736-	0.197	0.950	0.475-	1.413	1.618-	0.998	0.030-	0.283-
0.3	2.201	1.712-	0.289	0.893	0.660-	1.256	1.519-	0.993	0.064-	0.377-
0.4	2.031	1.679-	0.375	0.818	0.812-	1.109	1.420-	0.985	0.105-	0.444-
0.5	1.865	1.637-	0.453	0.731	0.933-	0.972	1.322-	0.972	0.152-	0.486-
0.6	1.704	1.589-	0.521	0.635	1.022-	0.845	1.225-	0.955	0.201-	0.507-
0.7	1.548	1.534-	0.579	0.527	1.083-	0.727	1.131-	0.932	0.253-	0.509-
0.8	1.397	1.473-	0.626	0.417	1.118-	0.618	1.039-	0.904	0.302-	0.495-
0.9	1.253	1.409-	0.662	0.304	1.128-	0.519	0.950-	0.871	0.352-	0.467-
1.0	1.116	1.341-	0.687	0.192	1.116-	0.428	0.865-	0.834	0.396-	0.428-
1.2	0.861	1.201-	0.704	0.025-	1.034-	0.271	0.707-	0.747	0.472-	0.325-
1.4	0.635	1.063-	0.679	0.218-	0.889-	0.144	0.567-	0.647	0.525-	0.202-
1.6	0.436	0.932-	0.618	0.378-	0.697-	0.043	0.449-	0.538	0.552-	0.069-
1.8	0.261	0.817-	0.530	0.495-	0.470-	0.037-	0.352-	0.427	0.553-	0.066
2.0	0.108	0.722-	0.423	0.564-	0.215-	0.099-	0.278-	0.319	0.526-	0.198
2.5	0.212-	0.581-	0.143	0.492-	0.530	0.208-	0.178-	0.094	0.346-	0.521
3.0	0.493	0.556-	0.000	0.000	1.480	0.291-	0.162-	0.000	0.000	0.874

Source: M. Yegian and S.K. Wright, *Lateral Soil Resistance-Displacement Relationships for Pile Foundations in Soft Clay*, Proceedings of the Fifth Offshore Technology Conference, held at Houston, TX, Paper # OTC 1893, pp. 663-676, 1973.

Note:  $E_s = kx$ ;  $Z_{max} = 3.0$ .

**TABLE 8B.5**  
**Coefficients for Deflection, Slope, Moment, Shear Force, and Soil Reaction for Elastic Piles for Values of  $Z_{max} = 2.6$  and Linear Variation of  $E_s$  with Respect to Depth  $x$**

$Z$	$A_Y$	$A_S$	$A_M$	$A_V$	$A_P$	$B_Y$	$B_S$	$B_M$	$B_V$	$B_P$
0.0	3.167	2.052-	0.000	1.000	0.000	2.052	2.016-	1.000	0.000	0.000
0.1	2.962	2.047-	0.100	0.987	0.296-	1.855	1.916-	1.000	0.008-	0.186-
0.2	2.758	2.032-	0.197	0.944	0.552-	1.669	1.816-	0.998	0.035-	0.334-
0.3	2.556	2.008-	0.288	0.879	0.767-	1.492	1.716-	0.993	0.073-	0.448-
0.4	2.357	1.975-	0.372	0.793	0.943-	1.325	1.617-	0.983	0.122-	0.530-
0.5	2.161	1.934-	0.446	0.691	1.081-	1.169	1.520-	0.968	0.179-	0.584-
0.6	1.970	1.886-	0.510	0.578	1.182-	1.021	1.424-	0.947	0.238-	0.613-
0.7	1.784	1.832-	0.561	0.455	1.249-	0.884	1.331-	0.920	0.301-	0.619-
0.8	1.604	1.774-	0.601	0.329	1.283-	0.755	1.240-	0.887	0.362-	0.604-
0.9	1.429	1.712-	0.627	0.200	1.286-	0.636	1.153-	0.848	0.421-	0.572-
1.0	1.261	1.649-	0.641	0.072	1.261-	0.524	0.071-	0.803	0.476-	0.524-
1.2	0.944	1.521-	0.630	0.170-	1.133-	0.326	0.921-	0.698	0.569-	0.391-
1.4	0.652	1.400-	0.575	0.376-	0.913-	0.155	0.793-	0.577	0.630-	0.217-
1.6	0.383	1.294-	0.483	0.531-	0.613-	0.007	0.690-	0.448	0.653-	0.011-
1.8	0.134	1.208-	0.367	0.618-	0.240-	0.123-	0.613-	0.319	0.633-	0.221
2.0	0.102-	1.148-	0.241	0.622-	0.203	0.240-	0.562-	0.198	0.563-	0.480
2.5	0.657-	1.094-	0.010	0.182-	1.642	0.506-	0.519-	0.007	0.136-	1.266
2.6	0.766-	1.094-	0.000	0.000	1.993	0.558-	0.519-	0.000	0.000	1.451

Source: M. Yegian and S.K. Wright, *Lateral Soil Resistance-Displacement Relationships for Pile Foundations in Soft Clay*, Proceedings of the Fifth Offshore Technology Conference, held at Houston, TX, Paper # OTC 1893, pp. 663-676, 1973.

Note:  $E_s = kx$ ;  $Z_{max} = 2.6$ .

TABLE 8B.6

**Coefficients for Deflection, Slope, Moment, Shear Force, and Soil Reaction for Elastic Piles for Values of  $Z_{\max} = 2.2$  and Linear Variation of  $E_s$  with Respect to Depth  $x$**

$Z$	$A_Y$	$A_S$	$A_M$	$A_V$	$A_P$	$B_Y$	$B_S$	$B_M$	$B_V$	$B_P$
0.0	4.011	2.743–	0.000	1.000	0.000	2.743	2.583–	1.000	0.000	0.000
0.1	3.737	2.738–	0.099	0.980	0.374–	2.489	2.483–	1.000	0.014–	0.249–
0.2	3.464	2.723–	0.195	0.926	0.693–	2.246	2.383–	0.997	0.048–	0.449–
0.3	3.193	2.699–	0.284	0.840	0.958–	2.013	2.283–	0.989	0.104–	0.604–
0.4	2.924	2.667–	0.363	0.733	1.170–	1.789	2.185–	0.976	0.170–	0.716–
0.5	2.659	2.627–	0.430	0.609	1.330–	1.576	2.089–	0.955	0.246–	0.788–
0.6	2.399	2.581–	0.484	0.468	1.439–	1.372	1.994–	0.927	0.326–	0.823–
0.7	2.143	2.531–	0.523	0.318	1.500–	1.177	1.904–	0.890	0.411–	0.824–
0.8	1.893	2.477–	0.548	0.168	1.514–	0.991	1.817–	0.845	0.491–	0.793–
0.9	1.648	2.422–	0.557	0.019	1.483–	0.813	1.735–	0.792	0.568–	0.732–
1.0	1.409	2.366–	0.552	0.126–	1.409–	0.644	1.659–	0.731	0.636–	0.644–
1.2	0.946	2.260–	0.500	0.384–	1.135–	0.326	1.526–	0.593	0.742–	0.391–
1.4	0.504	2.169–	0.403	0.570–	0.705–	0.031	1.423–	0.438	0.787–	0.044–
1.6	0.077	2.101–	0.278	0.656–	0.123–	0.245–	1.351–	0.283	0.753–	0.392
1.8	0.338–	2.059–	0.148	0.610–	0.609	0.511–	1.309–	0.143	0.624–	0.919
2.0	0.748–	2.040–	0.044	0.401–	1.496	0.770–	1.291–	0.041	0.378–	1.541
2.2	1.155–	2.037–	0.000	0.000	2.542	1.028–	1.288–	0.000	0.000	2.262

Source: M. Yegian and S.K. Wright, *Lateral Soil Resistance-Displacement Relationships for Pile Foundations in Soft Clay*, Proceedings of the Fifth Offshore Technology Conference, held at Houston, TX, Paper # OTC 1893, pp. 663–676, 1973.

Note:  $E_s = kx$ ;  $Z_{\max} = 2.2$ .

## REFERENCES

1. C.A. Swanland, 1992. Steel Piled Platforms, Chapter 5 in *Overview of Offshore Engineering*, Course Notes, Held in Houston, TX, 72 pages.
2. Lecture 15 A – Offshore Structures – General Introduction, p. 12. Available at <http://www.scribd.com/doc/24246962/Offshore-Structure>. Accessed on September 10, 2011.
3. T.H. Dawson, 1983. *Offshore Structural Engineering*, Prentice Hall, Englewood Cliffs, NJ, p. 156.
4. INTECSEA Group Engineering Software, 2011. From the website of Worley Parsons Available at [http://www.intec.com/expertise/floating\\_systems/naval\\_architecture/engineering\\_software/default.asp](http://www.intec.com/expertise/floating_systems/naval_architecture/engineering_software/default.asp). Accessed April 5, 2011 at 1-50 p.m.
5. Structural Analysis Software Packages, pp. 31–42. Available at [http://uqu.edu.sa/files2/tiny\\_mce/plugins/filemanager/files/4041296/MHI-Waleed-Project-SoftwareCompared.pdf](http://uqu.edu.sa/files2/tiny_mce/plugins/filemanager/files/4041296/MHI-Waleed-Project-SoftwareCompared.pdf). Accessed April 6, 2011.
6. NACE RP 0176-94, 1994. *Corrosion Control of Steel Fixed Offshore Platforms Associated with Petroleum Production*, NACE International, Houston, TX.
7. AISC 303-05, 2005. *AISC/ANSI Code of Standard Practice for Steel Buildings and Bridges*, American Institute of Steel Construction, Chicago, TX.
8. D.M. Masterson and R. Frederking, 2006. *Experience with the Canadian Standards Association Offshore Structures Code*, Proceedings of the Sixteenth ISOPE Conference, San Francisco, CA, pp. 14–19.
9. Canadian Standards Association, 2009. *CAN/CSA-S16.09—Design of Steel Structures*, 7th Edition, Mississauga, Ontario, Canada, CSA, 198 pages.
10. British Standards (BS) and Codes Related to Steel Construction, 2003. Available at <http://mdmetric.com/tech/bssteelcode.pdf>. Accessed April 9, 2011.
11. F. Bijlaard, 2008. *Euro Code 3: Design of Steel Structures Ready for Practice, Euro Codes Background and Application, Lecture Presented at Faculty of Civil Engineering and Geosciences*, Technical University of Delft, Holland. Available at [http://eurocodes.jrc.ec.europa.eu/doc/WS2008/EN1993\\_1\\_Bijlaard.pdf](http://eurocodes.jrc.ec.europa.eu/doc/WS2008/EN1993_1_Bijlaard.pdf). Accessed April 10, 2011.
12. American Petroleum Institute, 1993. *Recommended Practice for Planning, Designing and Constructing Fixed Offshore Platforms – Load and Resistance Factor Design (RP 2A-LRFD)*, American Petroleum Institute, Washington, DC, 224 pp.



13. Course Notes on General Design of Fixed Offshore Structures, 1979. University of Texas, Austin, TX, p. 3.1.
14. Course Notes on General Design of Fixed Offshore Structures, 1979. University of Texas, Austin, TX, pp. 4.24–4.25.
15. Course Notes on General Design of Fixed Offshore Structures, 1979. University of Texas, Austin, TX, p. 3.5.
16. Course Notes on General Design of Fixed Offshore Structures, 1979. University of Texas, Austin, TX, p. 4.4.
17. Course Notes on General Design of Fixed Offshore Structures, 1979. University of Texas, Austin, TX, p. 3.11.
18. Course Notes on General Design of Fixed Offshore Structures, 1979. University of Texas, Austin, TX, p. 4.20.
19. American Petroleum Institute, 1993. *Section D on Cylindrical Member Design, Recommended Practice for Planning, Designing and Constructing Fixed Offshore Platforms – Load and Resistance Factor Design (RP 2A-LRFD)*, American Petroleum Institute, Washington, DC, pp. 49–54.
20. Course Notes on General Design of Fixed Offshore Structures, 1979. University of Texas, Austin, TX, p. 3.11.
21. Course Notes on General Design of Fixed Offshore Structures, 1979. University of Texas, Austin, TX, p. 3.14.
22. J. Wardenier, 2009. *Hollow Sections in Structural Applications, Comite International pour le Development et l'Etude de la Construction Tubulaire (CIDECT) Publication*, p. 8.11. Available at <http://www.cidect.org/en/>.
23. J.C. de Oliveira, M.G. Gray, J.A. Packer and N. Christopoulos, 2008. *Standardized Cast Steel Connectors for Tubular Hollow Structural Sections*, CSCE 2008 Annual Conference, Quebec, Canada, pp. 6,7.
24. Course Notes on General Design of Fixed Offshore Structures, 1979. University of Texas, Austin, TX, p. 3.15.
25. C.G. Salmon, and J.E. Johnson, 1990. *Steel Structures: Design Behavior – Emphasizing Load and Resistance Factor Design*, HarperCollins Publishers, New York, pp. 761–767.
26. B. Weidler and D.I. Karsan, 1986. Analytical Models, Three-dimensional analysis, in: *Planning and Design of Fixed Offshore Platforms*, edited by B. McClelland and M.D. Reifel, Van Nostrand Reinhold Co., New York, p. 763.
27. N.D.P. Barltrop, and A.J. Adams, 1991. *Dynamics of Fixed Marine Structures*, Butterworth Heinemann Ltd., Oxford, UK, p. 172.
28. M. Randolph, M. Cassidy, S. Gourvenec, and C. Erbrich, 2005. *Challenges of Offshore Geotechnical Engineering*, p. 9/54. Available at [www.iransaze.com/files-for-downloading/ebglishbook/khak/Challenges\\_of\\_OffShore\\_Geotechnical\\_Engineering.pdf](http://www.iransaze.com/files-for-downloading/ebglishbook/khak/Challenges_of_OffShore_Geotechnical_Engineering.pdf).
29. Vulcanhammer.info, 1979. Available at <http://www.vulcanhammer.org/on>. *Method and Apparatus for Pile Driving*, p. 8/14.
30. Vulcanhammer.info, 2001. Available at <http://www.vulcanhammer.org/on>. Guide to pile driving equipments, Vols. I and II, *Section on Underwater Pile Driving Found in the Literature on Extensive Information on Pile Hammers*, p. 55/101.
31. Vulcanhammer.info, 2001. Available at <http://www.vulcanhammer.org/on>. Guide to pile driving equipments, Vols. I and II, *Section on Underwater Pile Driving Found in the Literature on Extensive Information on Pile Hammers*, p. 47/101.
32. M. Hetényi, 1946. *Beams on Elastic Foundation: Theory With Applications in the Fields of Civil and Mechanical Engineering*. University of Michigan Press, Ann Arbor, MI.
33. Chapter 3 SSPSI Analytical Methods: Theory, Code and Practice. Available at <http://nisee.berkeley.edu/meymand/files/chap3.pdf>. Accessed June 15, 2011.
34. H. Matlock, and L.C. Reese, 1960. Generalized solutions for laterally loaded piles, *Journal of Soil Mechanics and Foundations Division, ASCE*, Volume 86, Issue SM5, Part I, October, pp. 63–91.
35. M.T. Davisson, and H.L. Gill, 1963. Laterally loaded piles in a layered soil system, *Journal of the Soil Mechanics and Foundations Engineering, ASCE*, Volume 89, Issue SM3, pp. 63–94.
36. B. Broms, 1964. The lateral resistance of piles in cohesive soils, *J. Soil Mech. Found. Div. ASCE*, Volume 90, Issue SM2, pp. 27–63.
37. B. Broms, 1964. Lateral resistance of piles in cohesion-less soils. *ASCE Journal of the Soil Mechanics and Foundation Division Proceedings (JSMFD)*, Volume 90, Issue SM3, pp. 123–156.
38. M.F. Randolph, and G.T. Houlsby, 1984. The limiting pressure on a circular pile loaded laterally in cohesive soil, *Géotechnique*, Volume 34, Issue 4, pp. 613–623.

39. B. McClelland, and J.A. Focht Jr., 1958. Soil modulus for laterally loaded piles, *Transactions, American society of Civil Engineers*, Volume 123, Issue 2954, pp. 1049–1063.
40. H. Matlock, 1970. *Correlations for Design of Laterally Loaded Piles in Sand*, Proceedings of Offshore Technology Conference, Paper # 1204, 18 pp.
41. L.C. Reese, W.R. Cox, and F.D. Koop, 1974. *Field Testing and Analysis of Laterally Loaded Piles in Sand*, Proceedings of Sixth Annual Offshore Technology Conference, Austin, Texas, Volume II, Paper # OTC2080, pp. 473–485.
42. L.C. Reese, 1977. Laterally loaded piles: program documentation, *ASCE Journal of Geotechnical Engineering*, Volume 103, Issue GT4, pp. 287–305.
43. T.M.H. Lok, 1999. *Numerical Modeling of Seismic Soil-Pile-Superstructure Interaction in Soft Clay*, PhD. Thesis, Department of Civil and Envir. Eng., University of California, Berkeley, CA.
44. R.D. Mindlin, 1936. Force at a point in the interior of a semi-infinite solid, *Journal of Applied Physics*, Volume 7, Issue 5, pp. 195–202.
45. H.G. Poulos, 1971. Behavior of laterally loaded piles: Parts I and II – Single piles and pile groups, *Journal of Soil Mechanics and Foundations Division*, Volume 97, Issue SM5, pp. 711–731; 733–751.
46. H.G. Poulos, 1979. *An Approach for the Analysis of Offshore Pile Groups*, Proceedings of the Conference on Numerical Methods in Offshore Piling, Institute of Civil Engineers, London, pp. 119–126.
47. H.G. Poulos, and T.S. Hull, 1989. The role of analytical mechanics in foundation engineering, *Foundation Engineering, Current Principles and Practices*, ASCE, Volume 2, pp. 1578–1606.
48. M. Novak, and T. Nogami, 1977. Soil–pile interaction in horizontal vibration, *International Journal of Earthquake Engineering and Structural Dynamics*, Volume 5, pp. 263–281.
49. M. Novak, and B.E.I. Sharnouby, 1984. Evaluation of dynamic experiments on pile group, *ASCE Journal of Geotechnical Engineering*, Volume 110, Issue 6, pp. 738–756.
50. Novak, M., and M. Sheta, 1980. *Approximate Approach to Contact Effects of Piles*, Proceedings of a Session, Sponsored by Engineering Division at the ASCE National Convention, October 30, 1980.
51. G. Gazetas, and R. Dobry, 1984. Simple radiation damping model for piles and footings, *Journal of Engineering Mechanics ASCE*, Volume 110, Issue 6, pp. 937–956.
52. H.G. Poulos, 1989. Pile behavior–theory and application, *Geotechnique*, Volume 39, Issue 3, pp. 365–415.
53. G. Gazetas, 1991. Foundation vibrations, in: *Foundation Engineering Handbook*, edited by H.Y. Fang, 2nd Edition, Van Nostrand Reinhold Company, New York, pp. 553–593.
54. M. Novak, 1991. *Piles Under Dynamic Loads: State of the Art*, Proceedings, 2nd International Conference on Recent Advances in Geotechnical Earthquake Engineering and Soil Dynamics, St. Louis, MO, Volume 3, pp. 2433–2456.
55. M. Yegian, and S.K. Wright, 1973. *Lateral Soil Resistance-Displacement Relationships for Pile Foundations in Soft Clay*, Proceedings of the fifth Offshore Technology Conference, held at Houston, TX, Paper # OTC 1893, pp. 663–676.
56. R.L. Kuhlemeyer, 1979. Static and dynamic laterally loaded piles, *Journal of Geotechnical Engineering Division, ASCE*, Volume 105, Issue GT2, pp. 289–304.
57. D. Angelides, and J.M. Roesset, 1981. Nonlinear lateral dynamic stiffness of piles, *Journal of Geotechnical Engineering Division, ASCE*, Volume 107, Issue GT11, pp. 1443–1460.
58. A. Trochianis, J. Bielak, and P. Christiano, 1988. *A Three-Dimensional Nonlinear Study of Piles Leading to the Development of a Simplified Model*, Report. R-88-176, Dept. of Civil Eng., Carnegie Inst. of Technology, December.
59. D. Brown, C. Shie, and M. Kumar, 1989. *P-Y Curves for Laterally Loaded Piles Derived from Three Dimensional Finite Element Model*, Proc. 3rd Intl. Symposium on Numerical Models in Geomechanics, Niagara Falls, pp. 683–690.
60. G. Wu, and W. Finn, 1997. Dynamic elastic analysis of pile foundations using finite element method in the frequency domain, *Canadian Geotechnical Engineering Journal*, Volume 34, Issue 1, pp. 34–43.
61. G. Wu, and W. Finn, 1997. Dynamic nonlinear analysis of pile foundations using finite element method in the time domain, *Canadian Geotechnical Engineering Journal*, Volume 34, Issue 1, pp. 44–52.
62. A.W. Skempton, 1953. *The Bearing Capacity of Clays*, Building Research Congress, Division I, Part III, pp. 180–189.
63. K. Terzaghi, 1955. Evaluation of coefficients of sub-grade reaction, *Geotechnique*, Volume 5, pp. 297–326.
64. H. Matlock, and E.A. Ripperger, 1958. *Procedures and Instrumentation for Tests on a Laterally Loaded Pile*, Proceedings, Eighth Texas Conference on Soil Mechanics and Foundation Engineering, Special Publication # 29, Bureau of Engineering Research, The University of Texas, Austin, TX.

65. H. Matlock, and L.C. Reese, 1961. *Foundation Analysis of Offshore Pile Supported Structures*, Proceedings of the Fifth International Conference on Soil Mechanics and Foundation Engineering, Paris, July, Paper # 3B/14, pp. C-91 to C-97.
66. L.C. Reese, 1958. Discussion of soil modulus for laterally loaded piles, *Transactions, ASCE*, edited by B. McClelland and J.A. Focht, Jr., Volume 123, p. 1071.
67. H. Matlock, and L.C. Reese, 1961. Generalized solutions for laterally loaded piles, *Transactions, Journal of the Soil Mechanics and Foundations Division, ASCE*, Volume 86, Issue SM5, pp. 673–694.
68. B.J. Meyer, and L.C. Reese, 1979. *Analysis of Single Piles Under Lateral Loading*, Research Report 244-1, Center for Transportation Research, Bureau of Engineering Research, University of Texas at Austin, Austin, TX.
69. US Army Corps of Engineers, UFC 3-220-01A. *Deep Foundations*, United Facilities Criteria, USA Department of Defense, pp. 4–8; also USACE TI 818-02, 1998, 2004.
70. *Soil Properties (LPILE and COM624P) – p-y Curve*. Available at [epg.modot.mo.gov/documents/321\\_p\\_y\\_Curve\\_Criteria.pdf](http://epg.modot.mo.gov/documents/321_p_y_Curve_Criteria.pdf). Accessed September 7, 2011.
71. L.C. Reese, W.R. Cox, and F.D. Koop, 1975. *Field Testing and Analysis of Laterally Loaded Piles in Stiff Clay*, Paper # 2312, Proceedings of Offshore Technology Conference, Richardson, TX, pp. 671–690.
72. H. Matlock, and S. Foo, 1980. *Axial Analysis of Piles Using a Hysteretic and Degrading Soil Model*, Proc. 1st Intl. Conf. on Numerical Methods in Offshore Piling, London, pp. 127–133.
73. H. Matlock, and L.C. Reese, 1956. *Non-Dimensional Solutions for Laterally Loaded Piles, with Soil Modulus Assumed Proportional to Depth*, Proceedings of the Eighth Texas Conference on Soil Mechanics and Foundation Engineering, Special Bulletin # 29, Bureau of Engineering Research, The University of Texas, Austin, TX.
74. H. Matlock, and L.C. Reese, 1962. Generalized solutions for laterally loaded piles, *Transactions, American Society of Civil Engineers*, Volume 127, Issue 3370, Part I, pp. 1220–1269.
75. S.T. Wang, and L.C. Reese, 1993. *COM624P—Laterally Loaded Pile Analysis Program for the Microcomputer*, Version 2.0, Final Report, Report # FHWA-SA-91-048, USA Federal Highway Administration, 504 pp.
76. L.C. Reese, and S.T. Wang, 1997. *LPILE Plus 3.0 Technical Manual of Documentation of Computer Program*, Ensoft, Inc., Austin, TX.
77. J.B. Stevens, and J.M.E. Audibert, 1979. *Re-examination of p-y Curve Formulations*, Paper # 3402, Proceedings of Offshore Technology Conference, Houston, TX, Volume 2, pp. 397–403.
78. M.W. O'Neill, and J.M. Murchison, 1983. *An Evaluation of p-y Relationships in Sands*, A report to the American Petroleum Institute, PRAC 82-41-1, University of Texas, Houston, TX. Also in Research Report # GT-DF02-83, University of Houston, Department of Civil Engineering, May 1983.
79. T. Kagawa, and L.M. Kraft, 1980. Lateral load deflection relationships of piles subject to dynamic loading, *Soils and Foundations*, Volume 20, Issue 4, pp. 19–36.
80. V.N.S. Murthy, 2003. *Deep Foundations II: Behavior of Laterally Loaded Vertical and Battered Piles*, Marcel Dekker, New York, pp. 703.
81. D.P. Coduto, 2001. *Foundation Design: Principles and Practice*, 2nd Edition, Prentice Hall, Englewood Cliffs, NJ, p. 377.
82. D. Murff, 2003. *Design of Laterally Loaded Piles for Offshore Platforms*, Lecture Presented at Texas A&M University, College Station, TX, p. 3.
83. American Petroleum Institute, 1993. *Section G on Foundation Design in the Recommended Practice for Planning, Designing and Constructing Fixed Offshore Platforms—Load and Resistance Factor Design (RP 2A-LRFD)*, American Petroleum Institute, Washington, DC, pp. 64–77.
84. American Petroleum Institute, 1993. *Section G on Foundation Design in the Recommended Practice for Planning, Designing and Constructing Fixed Offshore Platforms—Load and Resistance Factor Design (RP 2A-LRFD)*, American Petroleum Institute, Washington, DC, p. 67.
85. American Petroleum Institute, 1993. *Section G on Foundation Design in the Recommended Practice for Planning, Designing and Constructing Fixed Offshore Platforms—Load and Resistance Factor Design (RP 2A-LRFD)*, American Petroleum Institute, Washington, DC, p. 73.
86. D.P. Coduto, 2001. *Foundation Design: Principles and Practice*, 2nd Edition, Prentice Hall, Englewood Cliffs, NJ, p. 539.
87. American Petroleum Institute, 1993. *Section G on Foundation Design in the Recommended Practice for Planning, Designing and Constructing Fixed Offshore Platforms—Load and Resistance Factor Design (RP 2A-LRFD)*, American Petroleum Institute, Washington, DC, p. 70.

88. American Petroleum Institute, 1993. *Section G on Foundation Design in the Recommended Practice for Planning, Designing and Constructing Fixed Offshore Platforms—Load and Resistance Factor Design (RP 2A-LRFD)*, American Petroleum Institute, Washington, DC, p. 71.
89. L.M. Kraft, J.A. Focht, and S.P. Amarasinghe, 1981. Friction capacity of piles driven into clay, *ASCE Journal of the Geotechnical Engineering Division*, Volume 107, pp. 1521–1541.
90. H.M. Coyle and I.H. Sulaiman, 1967. Skin friction for steel piles in sand, *Journal of the Soil Mechanics and Foundation Division*, Volume 93, Issue SM6, pp. 261–278.
91. D.P. Coduto, 2001. *Foundation Design: Principles and Practice*, 2nd Edition, Prentice Hall, Englewood Cliffs, NJ, p. 551.
92. M. Randolph, M. Cassidy, S. Gourvenec, and C. Erbrich, 2005. *Challenges of Offshore Geotechnical Engineering*, p. 17/54. Available at [www.iransaze.com/files-for-downloading/ebglishbook/khak/Challenges\\_of\\_Offshore\\_Geotechnical\\_Engineering.pdf](http://www.iransaze.com/files-for-downloading/ebglishbook/khak/Challenges_of_Offshore_Geotechnical_Engineering.pdf).
93. American Petroleum Institute, 1993. *Section G on Foundation Design in the Recommended Practice for Planning, Designing and Constructing Fixed Offshore Platforms—Load and Resistance Factor Design (RP 2A-LRFD)*, American Petroleum Institute, Washington, DC, p. 71.
94. American Petroleum Institute, 1993. *Section G on Foundation Design in the Recommended Practice for Planning, Designing and Constructing Fixed Offshore Platforms—Load and Resistance Factor Design (RP 2A-LRFD)*, American Petroleum Institute, Washington, DC, p. 72.
95. American Petroleum Institute, 1993. *Section G on Foundation Design in the Recommended Practice for Planning, Designing and Constructing Fixed Offshore Platforms—Load and Resistance Factor Design (RP 2A-LRFD)*, American Petroleum Institute, Washington, DC, p. 73.
96. American Petroleum Institute, 1993. *Section G on Foundation Design in the Recommended Practice for Planning, Designing and Constructing Fixed Offshore Platforms—Load and Resistance Factor Design (RP 2A-LRFD)*, American Petroleum Institute, Washington, DC, p. 74.
97. T.H. Dawson, 1983. *Offshore Structural Engineering*, Prentice Hall, Inc., Englewood Cliffs, NJ, p. 158.
98. T.H. Dawson, 1983. *Offshore Structural Engineering*, Prentice Hall, Inc., Englewood Cliffs, NJ, p. 223.
99. T.H. Dawson, 1983. *Offshore Structural Engineering*, Prentice Hall, Inc., Englewood Cliffs, NJ, p. 224.
100. T.H. Dawson, 1983. *Offshore Structural Engineering*, Prentice Hall, Inc., Englewood Cliffs, NJ, p. 225.
101. T.H. Dawson, 1983. *Offshore Structural Engineering*, Prentice Hall, Inc., Englewood Cliffs, NJ, p. 219.
102. T.R. Gaul, 1981. *Structural Dynamics: Basic Concepts and Application*, Short Course on Design of Fixed Offshore Structure held at University of Houston, Fig. 45 and 46.
103. T.H. Dawson, 1983. *Offshore Structural Engineering*, Prentice Hall, Inc., Englewood Cliffs, NJ, p. 236.
104. J.H. Evans, and J.C. Adamchak, 1969. *Ocean Engineering Structures*, Volume I (Course Notes), MIT Press, Cambridge, MA, p. 175.
105. J.B. Weidler, and D.I. Karsan, 1986. Analytical models and three-dimensional analysis, in: *Planning and Design of Fixed Offshore Platforms*, edited by B. McClelland and M.D. Reifel, Van Nostrand Reinhold Company, New York, p. 549 (modified).

---

# 9 Analysis and Design of Concrete Gravity Platforms

## 9.1 INTRODUCTION AND DESIGN ENVIRONMENTAL CONDITIONS

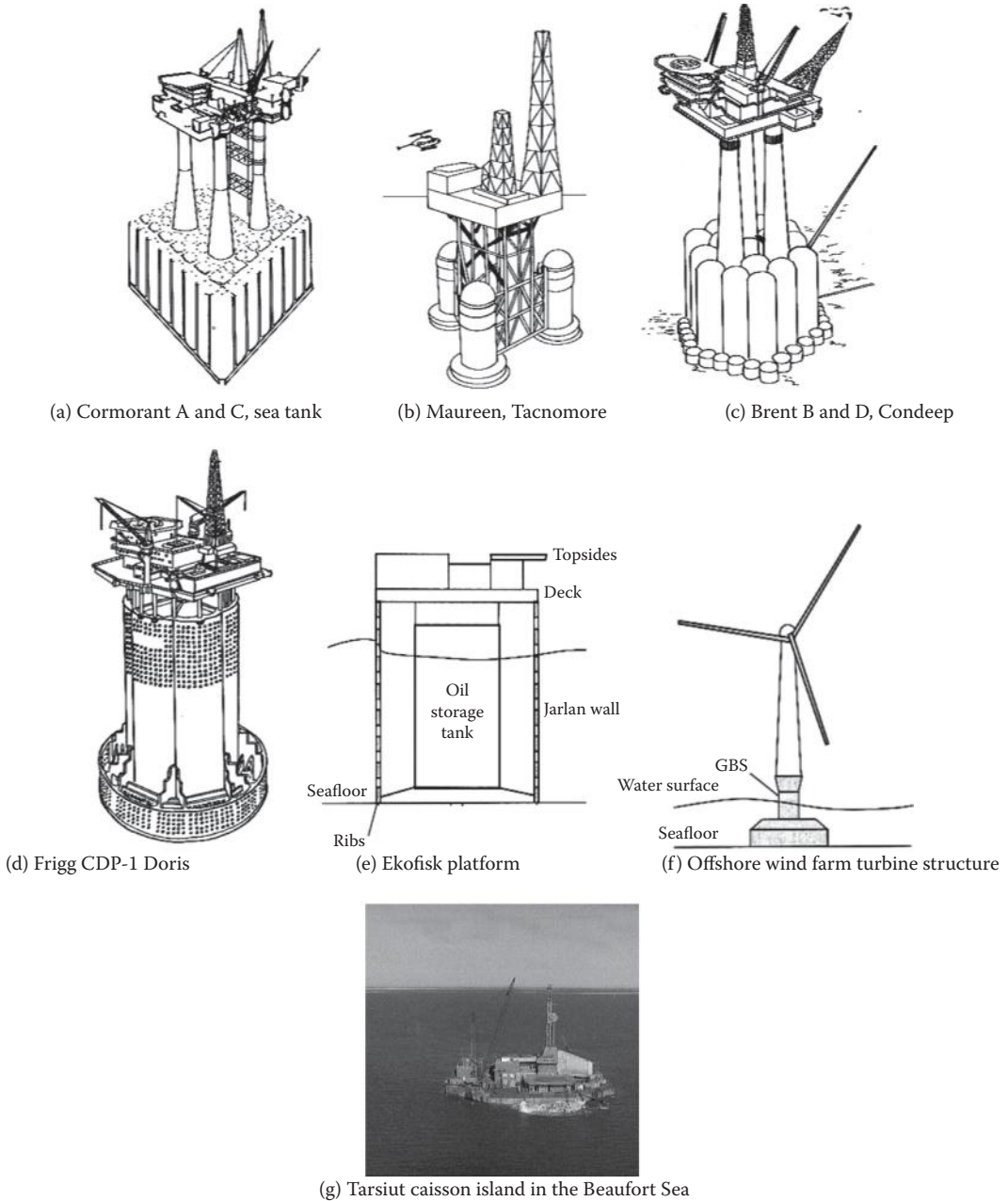
### 9.1.1 INTRODUCTION

Gravity platforms have been used during the past in the harsh/ice-infested Arctic ocean environmental contexts for drilling/production/storage of offshore oil; recently, they have also been used for generating energy from strong offshore winds. A variety of configurations have been in use, as shown in Figure 9.1a through g [1–4], ranging from the North Sea gravity platforms (shown in Figure 9.1a through e), offshore wind farms (shown in Figure 9.1f), to the Arctic gravity structures (shown in Figure 9.1g). These structures have proved to be competitive alternatives to the commonly used steel jacket structures due to their large deck capacity, rapid construction/installation times, and the availability of stronger soils (in comparison with the soft Gulf of Mexico soils). In spite of these obvious advantages for gravity base structures (GBS), it must be remembered that both concrete gravity base and steel jacket structures have been used side by side in the northern North Sea as shown in Figure 9.2 [5]. The preference for a certain structure is based on the abundance and connectedness of oil in the field, preference of the owner, and the economy involved in the development of the field. While the North Sea gravity structures have been installed in water depths ranging from 70.0 to 320.0 m, the Arctic gravity structures have been installed in much shallower water depths ranging from 9.0 to 18.0 m [6].

### 9.1.2 STRUCTURAL COMPONENTS OF GRAVITY PLATFORM

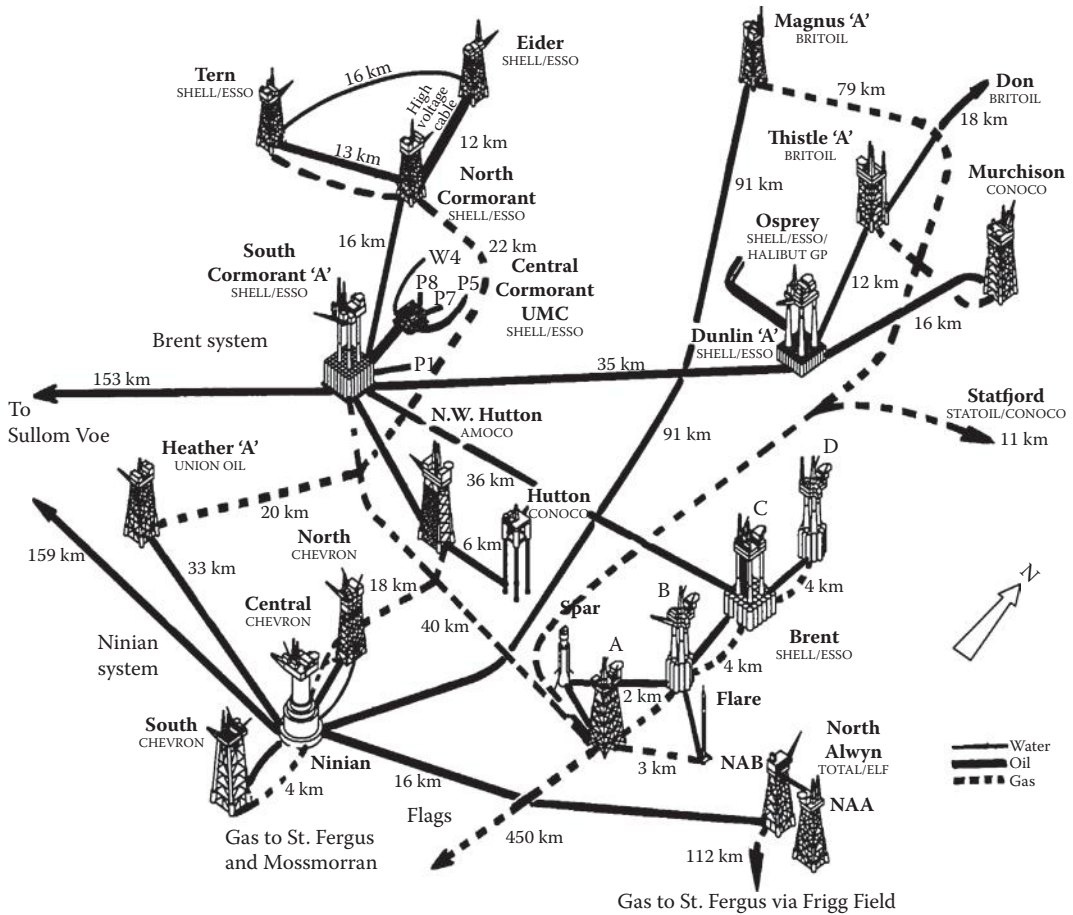
The typical components of a gravity base offshore structure consist of (i) caissons; (ii) base slab; (iii) foundation skirts; (iv) vertical towers; (v) deck superstructure; (vi) integrated or modular deck facilities; (vii) conductors and risers; and (viii) mechanical equipment. Caissons fulfill different functions during different phases of construction, installation, and in situ behavior. During the construction and tow-out phase, the caissons provide requisite buoyancy needed for such operations; both solid (sand) and liquid ballasts are stored in the caisson to control the floating structural stability of the GBS. After the installation, the caissons will contain either seawater or crude oil at all times. The base slab of the GBS functions to resist (i) the upward hydrostatic pressures exerted on the bottom during its tow-out and deck-mating operations and (ii) local pressures exerted on the base slab after its installation due to the unevenness of the surface of contact with the bottom soils and due to the local bearing pressures exerted on the base itself or that transmitted through the skirts. Usually, the base slab is pre-stressed to prevent the development of tensile stresses during the passage of extreme design waves after the installation of the GBS. The massive weight of the gravity base slab also assists in providing additional stability during its tow-out and installation phases. Concrete and/or steel skirts provided below the foundation slab of the GBS penetrate the near-surface marine sediments and enable the efficient transfer of the structural weights and forces to the underlying seabed soils; they also enhance the platform shear resistance. Typical skirt depths range from 1.0 to 5.0 m; but when the subbase soils are weaker (as in the case of Gullfaks C and Snorre platforms), they can extend to much larger depths, say, 20.0 m or more.





**FIGURE 9.1** (a–e) Typical gravity platforms installed in North Sea; (f) offshore wind farm; and (g) Tarsiut caisson island in the Beaufort Sea.

Towers are essentially vertical extensions of some preselected caissons of the GBS and constitute the upper structural elements of the platform substructure (similar to the steel jacket structure). The primary task of the towers is to support the vertical and horizontal loads acting on the deck structure and provide the minimum obstruction (or maximum transparency) to the waves passing through the GBS. The towers also enclose the well conductors, riser pipes, and mechanical



**FIGURE 9.2** Pipeline systems connecting the various fields in the North Sea, consisting of steel jacket structure, GBS, TLP, and other types of structures. (From G.S. Epperson, Gravity Platforms, Lecture 6, *Overview of Offshore Engineering*, Course Notes, Houston, TX, 50 pp. 1992.)

equipment necessary for the operation of the GBS. The deck structure provides the requisite stiff and rigid subbase required for supporting the drilling/production facilities of the platform along with the crew quarters.

The conductors are large diameter pipes (say, around 0.75 m or more) through which the wells are drilled; they are usually placed inside the towers of the GBS. Marine risers are pipes through which the crude oil or gas, produced in the platform, flows to and fro from the platform. Once again, due to safety considerations, the risers are usually placed within the towers of the GBS. The facilities located on the GBS are dictated by the requirements of the particular field. Generally, they consist of a helideck, one or two cranes, workshops, oil/gas separation equipment, electrical-control modules, export gas compressors, power-generation gas turbines, major pumps, heavy-wall vessels for liquid mud, and others.

### 9.1.3 TYPICAL DESIGN ENVIRONMENTAL CONDITIONS

Typical field and environmental data available for a North Sea GBS are given in Table 9.1 [5–9] and is shown in Figure 9.3 [10].

**TABLE 9.1**  
**Typical GBS Field and Environmental Data for North Sea**

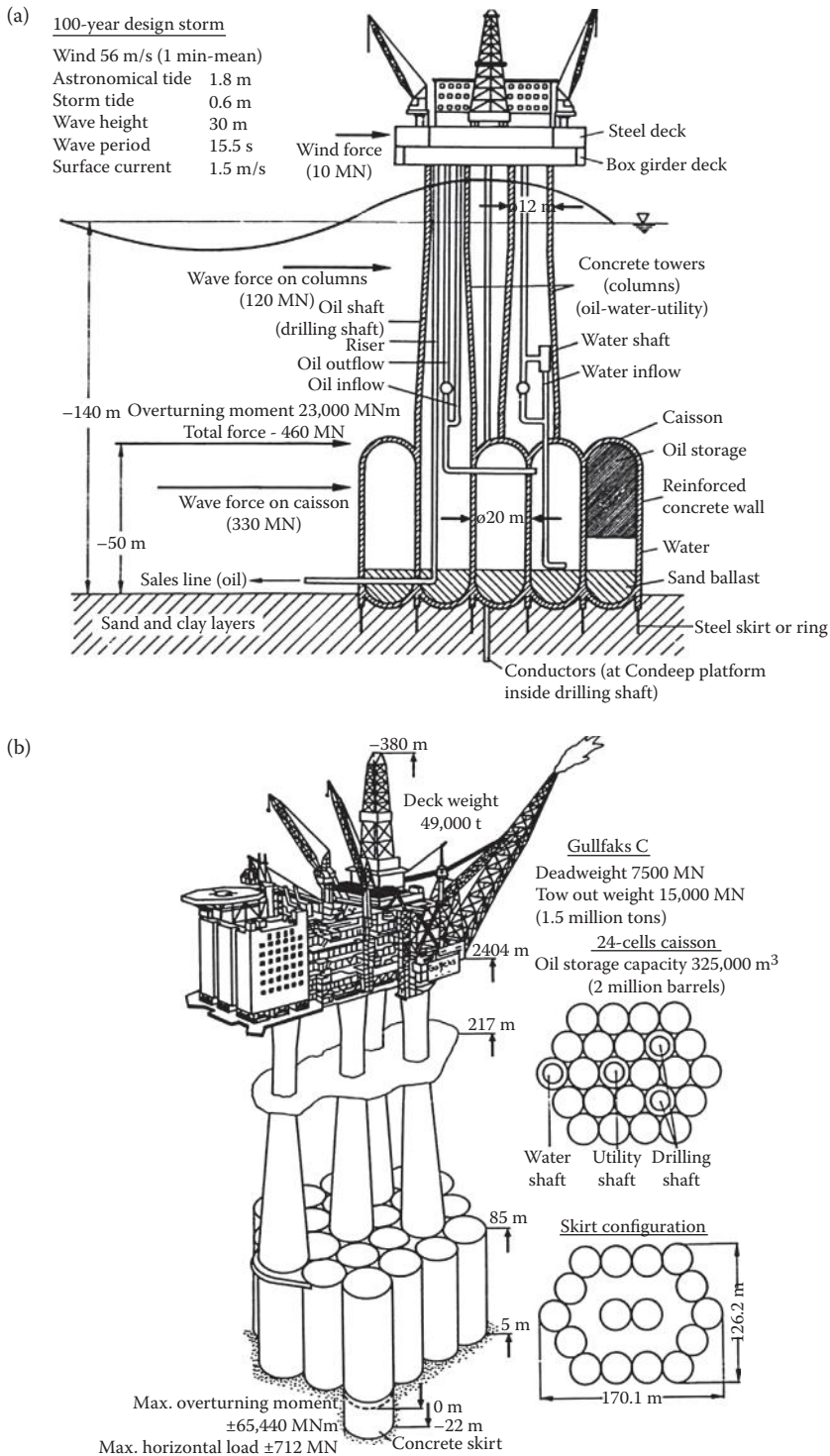
#	Particulars	Capacity
1	Crude oil storage capacity	1,000,000 barrels
2	Oil production rate	200,000 BPD
3	Gas production rate	28.0 million m <sup>3</sup>
4	Submerged weight of concrete structure	180,000 tons
5	Weight of deck with facilities	50,000 tons
6	Volume of concrete	65,000 m <sup>3</sup>
7	Volume of ballast	70,000 m <sup>3</sup>
8	Undrained soil strength	4.8–48.0 kN/m <sup>2</sup> for soft soils 48.0–192.0 kN/m <sup>2</sup> for medium soils >192.0 kN/m <sup>2</sup> for stiff soils
9	100-year storm wave height	30.0 m
	100-year storm wave period	15.5 s
	Diffraction effects become dominant when the structural transverse dimension becomes greater than (1/5) (wave length) as shown in Figure 9.2.	
10	Extreme wind for the North Sea	45.0 m/s for 10.0-min time averaged wind. Gust factors with 10.0-min averaging period for wind gusts of 3.0, 60.0, 120.0, and 180.0 s are 1.23, 1.05, 1.02, and 1.00, respectively
11	Extreme current speeds	1.0 to 2.0 m/s
12	Sheet ice loads Floating ice ridge loads	Thickness can be up to 1.2 m. Ridge height can vary from 6.0 to 12.0 m
13	Magnitude (typical) of horizontal wave force	50,000 tons
14	Magnitude (typical) of wave overturning moment	2,000,000 ton m

#### 9.1.4 ANALYSIS AND DESIGN ASPECTS OF GRAVITY PLATFORM

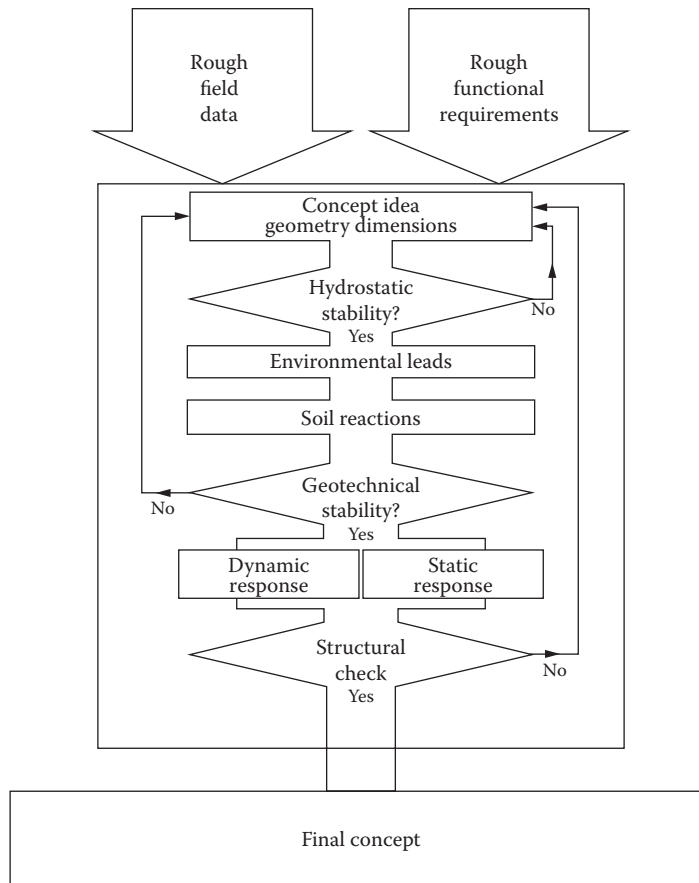
The initial platform concept is identified in consultation with the clients and the offshore contractors; then the detailed analysis and design have to consider a number of different aspects as outlined in Figure 9.4 [11] consisting of the following: (i) identification of the design environmental parameters and the initial geometry of the gravity platform; (ii) assessment of hydrostatic stability of the identified geometry of the structure; (iii) computing the environmental loads exerted on the platform structure and assessing the soil characteristics below the platform foundations; from these data, the geotechnical stability of the structure is determined, subject to the given design provisions given in the governing code (provided by the American Petroleum Institute, American Concrete Institute, American Bureau of Shipping, Det Norske Veritas, British Standards Institute, Lloyds Register, Bureau Veritas, Canadian Standards Association, or any other agency) [12–20]; (iv) the sufficiency of the platform components' strength to the applied loads is determined; and (v) if the platform strength is not sufficient to meet the design specifications given by the relevant code, then the above procedure is repeated until all the design specifications for the structure are satisfied.

If the analysis and design are carried out as per the API RP2A provisions for a gravity platform structure, the following aspects must be considered in its analysis and design: (i) stability of the





**FIGURE 9.3** Typical platform and environmental data on gravity platforms in the North Sea: (a) Condeep platform at Brent field and (b) Gullfaks C platform. (With kind permission from Springer Science + Business Media: *Offshore Structures, Volume I: Conceptual Design and Hydromechanics*, 1992, pp. 66–67, C. Clauss, E. Lehmann, and C. Ostergaard.)



**FIGURE 9.4** Various aspects involved in the analysis and design of a gravity platform. (From I. Holland et al., *Design of Offshore Concrete Structures*, Spon Press, New York, p. 35, 2000. With permission.)

gravity platform against overturning, bearing, sliding failures, or combinations thereof; (ii) static deformation of the platform foundations, including possible damage to platform or components attached to it; (iii) dynamic foundation characteristics and its behavior under the applied dynamic loads; (iv) hydraulic instability such as scour or piping under water wave action, and the potential for structural and foundation failure (such as that due to liquefaction and others); and (v) installation of the gravity platform, including penetration and pull-out of shear skirts or the foundation base itself (which may happen during extreme overturning conditions) and the effects of pressure buildup (during the passage of the crest of extreme wave passing over the structure) or drawdown of trapped water underneath the base (during the passage of the valley of the extreme wave over the structure). Other codes also consider effects of cumulative cyclic loading and long-term settlement of the platform and subsidence of soils below the platform foundations, besides the above.

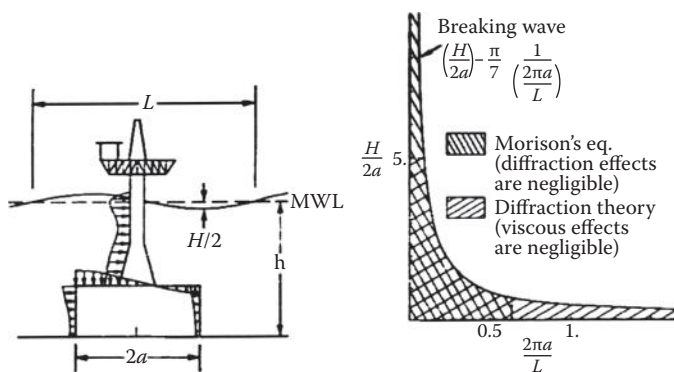
Generally, four types of structural analyses are carried out for a gravity platform as stated in Section 6.2.1, viz., (i) survivability of the platform (called ULS), under the action of wave/current/wind loads having a recurrence period of 50 or 100 years; (ii) platform response under operating (or serviceability limit state) environmental conditions; usually, the wave/current/wind loads are estimated with a recurrence period of 1 or 5 years (or with a probability of occurrence as shown in Table 6.4); (iii) fatigue assessment using fatigue limit state (FLS) conditions specified by the code; and (iv) accidental limit state.

**9.1.5 SALIENT FEATURES TO BE CONSIDERED IN ANALYSIS AND DESIGN**

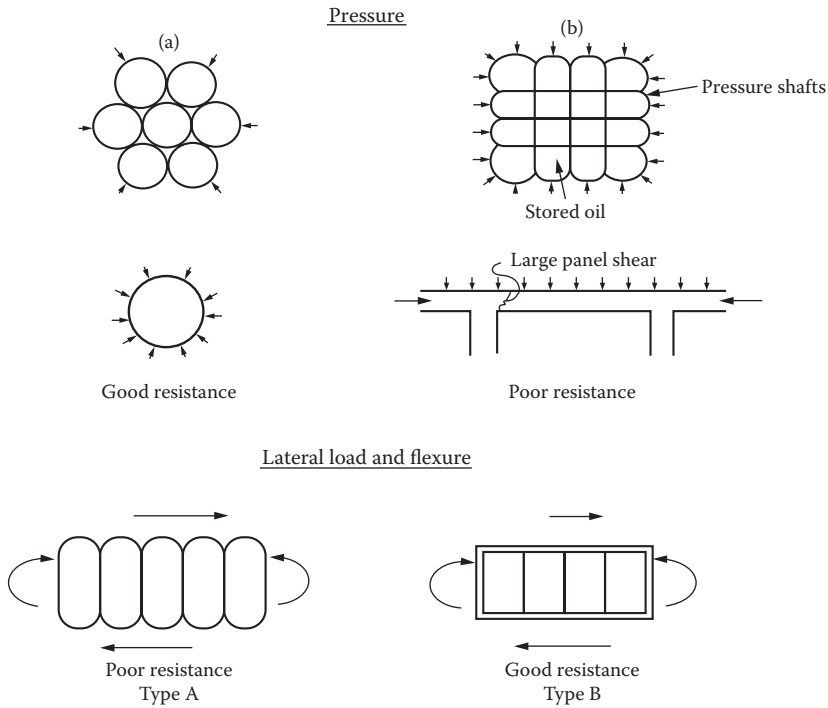
The wave load computation on a gravity platform needs to consider the importance of considering the wave drag and inertial forces. It has been observed that the ratio of water particle orbit dimension to the characteristic (along-wave) gravity platform dimension controls the need to consider the drag effects in the computation for wave forces exerted on the various components of the gravity platform; this is shown in Figure 9.5 [5], where the maximum value of the ratio (wave particle orbit dimension/maximum along-wave dimension of the platform) is shown as  $H/(2a)$ , with  $H$  as the wave height (which is equal to the maximum dimension of the wave particle orbit) and  $2a$  as the maximum along-wave dimension of the structure. When  $H/(2a)$  is very small, the drag forces become very negligible, and one needs to consider the wave inertial forces only; this is contrary to the wave effects on steel jacket platforms where the drag forces dominate. Generally, when the above-mentioned ratio is smaller than 0.2, the analysis should consider the effects of wave diffraction as shown in Figure 9.5.

It has been observed that during the deck-mating procedures or the installation-at-site operations of a gravity platform structure, the differential pressures between the caisson interior and exterior have been computed to be in the range of 1.25 to 1.50 MPa; this external pressure could lead to an implosive failure of the caisson, if the structure is not properly designed to resist this effect. Two types of caisson designs have been used by the industry, as shown in Figure 9.6 [5], viz., (i) an interconnected assembly of vertical cylindrical cells (as shown in Figure 9.6a) and (ii) an assembly of rectangular cellular box-type structures constituting an interconnected vertical-wall-plate system, with outer walls of cylindrical-cellular profiles (as shown in Figure 9.6b). In both cases, the ambient hydrostatic pressure is resisted by the cylindrical shell-type structures generating in-plane compressive stresses. When bending effects are also taken into consideration, the behavior seems to be different for both.

When both bending and axial compressive effects are taken into account, a number of other factors also have to be taken into account. For a tall cylindrical caisson construction shown in Figure 9.6a, the stresses near the top and bottom, where the end cap joins the cylindrical caisson large bending stresses, are developed due to deformation incompatibility; hence, care should be taken in designing such structures for bending. While compressive stability of cylinders is well ensured due to their small  $\{(Diameter (D))/(wall\ thickness, t)\}$  ratios, the bending stresses may generate tensile or shear failure (in concrete) at the end-cap-cylinder junction. Moreover, the overall stability of the structure to bending loads (in the vertical plane) may be much less than that provided by an interconnected rectangular cell wall system shown in Figure 9.6b. In the case of the structural configuration shown in Figure 9.6b, the rectangular walls must be designed to ensure the lateral



**FIGURE 9.5** Region of applicability of diffraction wave effects to GBS. (From G.S. Epperson, Gravity Platforms, Lecture 6, *Overview of Offshore Engineering*, Course Notes, Houston, TX, 50 pp. 1992.)



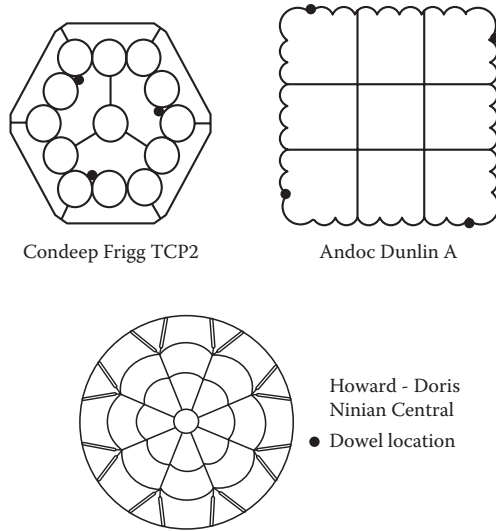
**FIGURE 9.6** Advantages and disadvantages of possible structural systems for offshore gravity platforms. (a) Tall cylindrical shell-type of construction, and (b) inter-connected shell wall system. (From G.S. Epperson, Gravity Platforms, Lecture 6, *Overview of Offshore Engineering*, Course Notes, Houston, TX, 50 pp. 1992.)

stability under in-plane compressive stresses. This configuration fares better for bending loads acting in the vertical plane of the structure since the complex box configuration resists the bending loads much better than the cylindrical caisson-cum-end-cap configuration. The design of both the configurations should ensure that the overall structural stability is assured under both compressive (horizontal and vertical) and bending loads acting on the system, which depends on  $D/t$  and  $L/D$  ratios ( $L$  being the height of the caisson) and the amount of reinforcing steel used in the section.

Steel or concrete skirts and steel dowels (of pipe section) that protrude below the bottom of the caisson structure are provided below the vertical caissons. These components penetrate the seabed, before the other components, and help to keep the gravity structure in position. In addition to keeping the gravity structure in position, the skirts also (i) confine the soft soil layer on the top of seabed and help to transfer the platform loads to competent soils below; (ii) provide stable seabed soil conditions and thus minimize the scour around the gravity platform foundations; and (iii) enable the proper grouting of the bottom of the gravity platform, with weak cement grout, to provide proper distribution of the bearing stresses at the bottom.

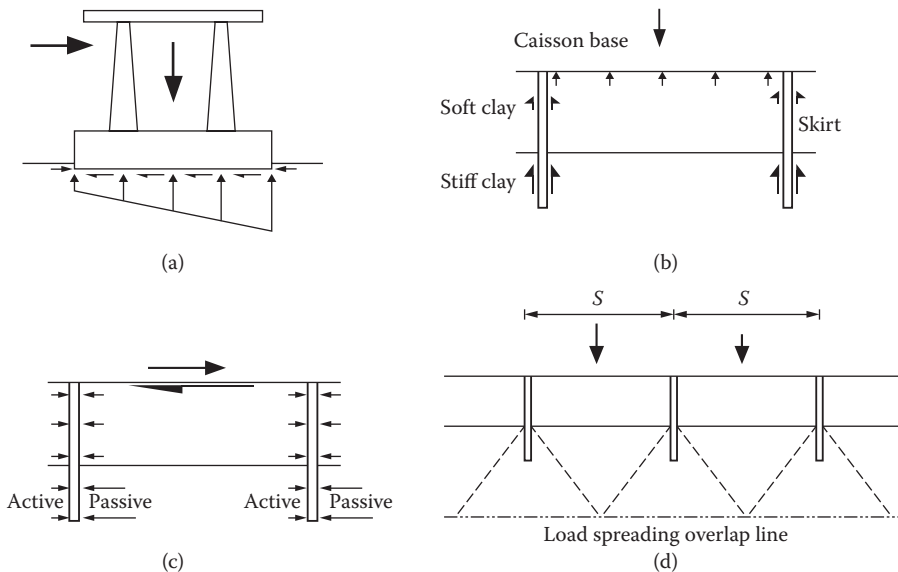
Dowels are typically vertical steel (hollow) piles of 2.0-m diameter, and they protrude below the bottom of the steel or concrete skirts by a few meters. They contact the seabed first and keep the structure on location as the fluidized soft soil layer on top of the seabed and the water below the foundation are expelled out from the bottom of the gravity foundation by the slowly settling gravity platform. Typical arrangement of steel skirts below various gravity platforms of the North Sea is shown in Figure 9.7 [21].

The skirts transfer part of the vertical loads acting on the platform to competent soils below by providing skin friction and end bearing; in addition, they also have to resist the active and passive lateral loads acting on them during their penetration into the soil, as shown in Figure 9.8 [22]. The



**FIGURE 9.7** Typical geometry of steel skirts of the gravity platforms, at the base of the storage tanks. (From H.G. Poulos, *Marine Geotechnics*, Unwin Hyman, London, p. 207, 1988. With permission.)

steel skirts are steel plates of 20.0 to 30.0 mm thick, whereas the concrete skirts are 1.0 m or more in thickness. The height of the skirt is determined by the height required to transfer the total platform loads (required only during the initial stages of installation) to the seabed soil through skin friction and end bearing provided by the skirts; in addition to transferring the vertical loads, they also provide a shear key against horizontal sliding loads. The structural design computation of skirts will require (i) computation of skirt length and spacing and (ii) computation of soil reaction forces and



**FIGURE 9.8** Factors considered in the design of skirts: (a) soil resistance stresses for the overall platform behavior; (b) vertical load transfer; (c) lateral load transfer; and (d) spreading of load into foundation soil. (From E.T.R. Dean, *Offshore Geotechnical Engineering: Principles and Practice*, Thomas Telford Limited, London, p. 326, 2010. With permission.)

stresses that are required for the design of the skirts and their connections to the bottom of caisson [23–25]. Skirt lengths and spacing are required to (i) induce the critical failure mechanisms in the gravity platform soil to be deep enough so that there is a requisite margin of safety against global failure under the design loads; and (ii) minimize the platform settlements, soil scour around the platform base, and the fluidization of soil inside the skirt compartments during installation.

The main concern during the penetration of skirts into seabed is to keep the platform vertical and to avoid piping of seabed fluid below the skirts. This is achieved by (i) providing large pipes on the seabed to expel the water trapped within the skirt compartments into the sea; (ii) providing holes in skirts at various levels; and (iii) sluicing seabed fluid (water + soil) trapped within the skirt compartments into the cylindrical caisson cells through valves [21]. Also, in certain situations, the tilting of the gravity platform is minimized by regulating the fluid pressure in the various skirt compartments separately so that differential overpressures or suction pressures are applied to the bases of the caisson cells. A number of design scenarios have been presented by Dean [26] that need to be considered in keeping the gravity platforms in their vertical position during their installation on site. Also subskirt grouting of the space between the seabed and the spherical end cap of the caissons is carried out (i) to prevent further penetration of the gravity platform caissons into the seabed; (ii) to keep the soil bearing pressures acting at the bottom of the caissons more or less uniform and to prevent the overstressing of the caisson cell walls during subsequent ballasting or subsequent environmental loading; and (iii) to prevent piping through water pockets that may be present below the foundation.

In order to illustrate the various facets that need to be considered during the analysis and design of a gravity platform, a number of simplified models of a monopod gravity platform are solved in Section 9.2.

## 9.2 BEARING CAPACITIES OF GRAVITY PLATFORM FOUNDATION

### 9.2.1 REQUIREMENTS IN DESIGN

Enormous forces are exerted on the gravity platform foundations due to their size, self-weight, weight of installed machinery and equipment, and the forces exerted on them by the wave, wind, and other forces. For instance, the tow-out weight of the 380.0-m-tall Ekofisk platform (shown in Figure 9.3b), placed in 217.0-m water depth, was found to be 15.0 million tonnes. The 24 cellular caisson of the gravity base stored 2,000,000 million barrels ( $325,000 \text{ m}^3$ ) of crude oil. The horizontal force exerted on the base of the gravity platform structure was computed to be 712.0 MN, and the overturning moment exerted on the platform about its base was obtained as 65,440.0 MN m. The platform foundation had to resist these large forces safely. The overall stability of foundation had to be checked for the forces acting on the structure due to a “100-year wave.” The degradation of the foundation strength due to the previous stress cycling of the soil had to be taken into account while verifying its sufficiency against the imposed forces. If the foundation soil was sandy, then the significant pore pressures developed during the passage of a storm might be dissipated quickly; but if the foundation soil was of clay, then very little dissipation of pore pressures would occur during the passage of a single or a number of subsequent storms. Under such situations, the stability would improve with time for platforms supported on sands and normally consolidated clays; if the soil in the foundation was of overconsolidated dilating clays, then the possibility that the increasing cyclic displacements might decrease the overall stability of the foundations had to be taken into account [27]. As such, the design of a gravity platform foundation against the applied environmental loads becomes quite complex.

The hydrostatic pressures and loads to which the gravity platform foundation base slab is subjected are extremely important for structural design. When the gravity platform is ballasted down during its installation phase, the caissons of the gravity platform are only partially full and the slab must withstand a hydrostatic pressure of  $1.41 \text{ MN/m}^2$ , if the depth of submergence of the platform is 140.0 m as shown in Figure 9.3a, or a hydrostatic pressure of  $2.18 \text{ MN/m}^2$ , if the depth is around



220.0 m as shown in Figure 9.3b. In addition to this, uneven soil reaction forces on the skirt system that arise due to site slope and surface undulations will impose additional stresses on the bottom surface. Hence, it becomes essential to anticipate uncertainties in the range of stresses and loads for which the base is to be designed and to examine a range of possible scenarios for the installation location, so that a proper design can be carried out. This will also help in the design of a ballast system that would control the installation of the platform safely [28].

According to the API Code provisions [29], the stability conditions are defined as follows:

*For bearing resistance.* The ultimate bearing resistance should satisfy the following conditions:

$$P_{DB} \leq \phi_{SB} Q_{DB} \quad (9.1)$$

where  $Q_{DB}$  = ultimate bearing capacity of the foundation as determined by the equations given below;  $P_{DB}$  = ultimate bearing load (under extreme or operating conditions using factored loads); and  $\phi_{SB}$  is the shallow foundation resistance factor on bearing capacity = (0.67).

*For sliding resistance.* The ultimate sliding resistance of the foundation should satisfy the following condition:

$$P_{DS} \leq \phi_{SS} H_{DS} \quad (9.2)$$

where  $H_{DS}$  is the ultimate sliding resistance of the foundation as determined by the equations given below;  $P_{DS}$  = sliding load (under extreme or operating conditions using factored loads); and  $\phi_{SS}$  is the shallow foundation resistance factor on sliding capacity (=0.80).

Soil strength can be expressed as the maximum stress under the given limiting conditions; specifically, strength is expressed in terms of the shear stress, which is equal to half the deviator stress in an undrained triaxial test. The undrained shear strength  $s_u$  is the shear strength measured in a test without drainage of pore water; it is now represented by the symbol  $s_u$  rather than the earlier symbol  $c_u$ . The drained strength is measured in a test with drainage of pore water. Drained strength is usually expressed in terms of the mobilized friction angle  $\phi'$  and the effective cohesion intercept  $c'$  of Mohr's envelope. Many design calculations for sands involve drained conditions and, as such, are expressed in terms of the drained (or effective) friction angle. For general soil, both the effective cohesion intercept  $c'$  and the effective friction angle  $\phi'$  must be specified.

### 9.2.2 UNDRAINED BEARING CAPACITY OF FOUNDATION SOIL

The undrained bearing capacity of foundation soil (with the friction angle  $\phi = 0.0$ ) is specified by the API RP2A [29] code as

$$Q = (s_u N_c K_c + \gamma X) A' \quad (9.3)$$

where  $Q$  = maximum vertical load at failure (in force units);  $s_u$  = undrained shear strength of soil (in stress units);  $N_c$  = a dimensionless constant for cohesion, equal to 5.14 for  $\phi = 0$ ,  $\phi$  = undrained friction angle = 0.0;  $\gamma$  = total unit weight of undrained soil;  $X$  = depth of embedment of foundation;  $A'$  = effective area of the foundation depending on the load eccentricity; and  $K_c$  is the correction factor that accounts for load inclination, footing shape, depth of embedment, inclination of base, and inclination of ground surface.

The correction factor  $K_c = i_c s_c d_c b_c g_c$  is used for cohesive strength, where the (load) inclination factor  $i_c$  is given by  $i_c = i_q - (1.0 - i_q)/(N_c \tan \phi)$  for  $\phi > 0.0$ ; or  $i_c = 1.0 - (mH)/(B'L s_u N_c)$  for  $\phi = 0.0$ ;  $i_q = [1.0 - H/(Q + B'L s_u \cot \phi)]^m$  for  $\phi > 0.0$ ;  $B'$  and  $L'$  are the breadth and length of the equivalent

rectangular foundation area  $A'$ , respectively; foundation shape factor  $s_c$  is given by  $s_c = 1.0 + (B'/L')(N_q/N_c)$  for the equivalent rectangular shape of foundation; and  $s_c = 1.0 + (N_q/N_c)$  for centric load; otherwise,  $s_c$  is the same as that for an equivalent rectangular shape of foundation.

The (embedment) depth factor  $d_c = d_q - (1.0 - d_q)/(N_c \tan \phi)$ , with  $d_q = 1.0 + (2.0)(\tan \phi)(1.0 - \sin \phi)^2(D/B')$ . The gravity foundation base inclination factor  $b_c = b_q - (1.0 - b_q)/(N_c \tan \phi)$ , for  $\phi > 0.0$ ; it is equal to  $b_c = 1.0 - (2\nu/N_c)$ , with  $\nu$  as the slope of foundation base in radians. The ground slope inclination factor  $g_c = 1.0 - (2\beta)/N_c$ .

It is also observed that the dimensionless constant for cohesion  $N_c$  is related to the dimensionless constant  $N_q$  for soil surcharge depth  $X$  (depth of embedment) by  $N_c = (N_q - 1.0)\cot(\phi)$ . The factor  $m$  is dependent on the angle  $\theta$ , which is the angle between the maximum horizontal load (at sliding failure of the foundation) and the long axis of the foundation; it is given by

$$m = m_L \cos^2 \theta + m_B \sin^2 \theta, \text{ with } m_L = (2.0 + L'/B')/(1.0 + L'/B') \text{ and } m_B = 2.0 + (2.0 + B'/L')/(1.0 + B'/L'). \quad (9.4)$$

The effective dimensions of the equivalent footing are given by  $A' = 2s = B'L' =$  reduced area, where  $L' = [(2s)\{(R + e)/(R - e)\}^{(1/2)}]^{(1/2)}$ ; and  $B' = (L')\{(R - e)(R + e)\}^{(1/2)}$ , with  $s = (\pi R^2)/2 - [e(R^2 - e^2)^{(1/2)} - R^2 \sin^{-1}(e/R)]$ .

$e$  is the eccentricity of the applied load maximum vertical load at failure (given by  $Q') = M/Q'$ . For a rectangular footing, there will be two eccentricities  $e_1$  and  $e_2$  given by  $e_1 = M_1/Q'$  and  $e_2 = M_2/Q'$ ; also  $L' = L - 2e_1$  and  $B' = B - 2e_2$ . When the load is vertical and centric, then Equation 9.3 is reduced for a rectangular foundation to  $Q$  (maximum vertical load per unit length of foundation at failure) =  $5.14s_u A_0$ , where  $A_0 =$  actual foundation area per unit length in the load direction. For a centrally loaded circular foundation

$$Q = 6.17s_u A \quad (9.5)$$

where  $A =$  actual foundation area.

### 9.2.3 DRAINED BEARING CAPACITY OF FOUNDATION SOIL

The drained bearing capacity of a foundation soil (with the friction angle  $\phi' = 0.0$ ) is specified by the API RP2A code as follows.

The maximum net vertical downward load that a gravity foundation can support under drained condition is given by

$$Q' = [c'N_c K_c + qN_q K_q + (1/2)\gamma'BN_\gamma K_\gamma]A' \quad (9.6)$$

with  $Q' =$  maximum vertical load at failure,  $c' =$  effective cohesion intercept of Mohr envelope, and  $N_q = \{e^{(\pi \tan \phi')}\tan^2(45^\circ + \phi'/2)\}$ , which is a dimensionless function of  $\phi'$  for surcharge due to embedment depth  $X$ . Also,  $N_c = (N_q - 1.0)\cot(\phi')$ , a dimensionless function of  $\phi'$  for cohesion, and  $N_\gamma =$  an empirical dimensionless function of  $\gamma'$  and  $\phi'$  that can be  $\approx (2.0)(N_q + 1.0)\tan(\phi')$  for soil weight in the failure wedge.

The term  $\phi'$  is the effective friction angle,  $\gamma'$  is the effective unit weight of drained soil,  $B$  is the minimum lateral foundation dimension,  $A'$  is the effective area of the foundation depending on the load eccentricity, and  $K_c$ ,  $K_q$ , and  $K_\gamma$  are the correction factors accounting for cohesion, surcharge soil above the base of the foundation, and the soil weight in the failure wedge, respectively.

The terms  $K_q$  and  $K_\gamma$  are defined as

$$K_q = i_q s_q d_q b_q g_q \text{ and } K_\gamma = i_\gamma s_\gamma d_\gamma b_\gamma g_\gamma \quad (9.7)$$



where  $i_q = [1.0 - \{H/\{Q + B'L's_q \cot(\phi)\}\}]^m$ ;  $s_q = 1.0 + (B'/L')\tan(\phi)$ , for rectangular and equivalent rectangular-shaped foundations; for centric loads on a circular foundation,  $i_q = 1.0 + \tan(\phi)$ ;  $d_q = 1.0 + \{2\tan(\phi)\}\{1.0 - \sin(\phi)\}^2(D/B')$ ;  $b_q = b_\gamma = \{1.0 - \nu\tan(\phi)\}$  for  $\phi > 0.0$ ; and  $g_q = g_\gamma = \{1.0 - \tan(\phi)\}^2$ .

For the correction factors for the soil wedge in the failure zone,  $i_\gamma = [1.0 - H/\{Q + B'L's_q \cot(\phi)\}]^{(m+1)}$ ;  $s_\gamma = 1.0 - (0.4)(B'/L')$  for rectangular and equivalent rectangular-shaped foundations;  $s_\gamma = 0.6$  for centric load on circular foundations  $d_\gamma = 1.0$ ;  $b_\gamma = b_q$ ;  $g_\gamma = g_q$ .

When  $c' = 0.0$  (usually sand), two special cases are encountered. When a vertical centric load is applied on a rectangular foundation, with the ground and the foundation bottom truly horizontal, then for a rectangular footing,

$$Q = (1/2)\gamma'BN_\gamma A_0 \quad (9.8)$$

For a circular or square footing,

$$Q = (0.3)\gamma'BN_\gamma A_0 \quad (9.9)$$

### 9.2.4 SLIDING RESISTANCE OF FOUNDATION SOIL

The sliding resistance of the foundation soil at failure is given by

for undrained analysis:

$$H = s_u A \quad (9.10)$$

where  $H$  = maximum horizontal load at failure,

for drained analysis:

$$H = c'A + Q'\tan(\phi') \quad (9.11)$$

### 9.2.5 ULTIMATE CAPACITIES OF SHALLOW FOUNDATIONS

It should be noted that if data were available on cyclic loading of foundations, then the ultimate capacities should be determined after cyclic loading effects have been taken into account. If loading occurs very quickly so that no drainage occurs with nil dissipation of excess pore pressures, then an “undrained analysis” is to be carried out. The soil may be treated with  $\phi = 0.0$ , and the stability of the foundation is governed by the appropriate undrained shear strength [29].

If the loading is very slow such that no excess pore pressures are developed (viz., complete drainage occurs under the applied loads), and sufficient time has passed after a previous application of loads on the soil medium, then a “drained analysis” can be carried out. The stability of the foundation is governed by the drained shear strength of the soil; the drained shear strength is to be determined from the Mohr–Coulomb effective stress failure envelope, viz., the cohesion intercept,  $c'$ , and the effective friction angle,  $\phi$ , are to be used in the computation of the drained strength of the foundation soil.

For the sliding analysis, given by Equations 9.10 and 9.11, a horizontal plane of failure must be ensured by the provision of structural constraints such as shear skirts at close spacing. If required, consideration must also be given to the side shear forces developed and passive soil forces on the form of the sliding body. When shear skirts or other similar devices are not provided or for certain combinations of structure weight versus soil strength, failure may occur along the soil–structure interface of the foundation. For this situation, reduced soil strength parameters should be used in Equations 9.10 and 9.11 and should be coupled with specialized experimental tests that will determine the effective coefficient of friction along the soil–structure interface.

When (i) the foundation conditions are highly nonhomogeneous or anisotropic, (ii) loading conditions deviate considerably from the simple conditions assumed above, or (iii) loading rates are such that the soil conditions at the foundations cannot be clearly specified as drained or undrained, the determination of the stability conditions is not straightforward as given by Equations 9.3 through 9.11. Under such conditions, other relevant procedures must be used to estimate the strength of the foundation strengths.

### Example 9.1

The foundation of a gravity platform is a circle of diameter 80.0 m and is embedded in soil to a depth of 2.0 m. The platform is subjected to the following factored loads and moments:  $F_{\text{vert(max)}} = 2,000,000$  kN;  $F_{\text{horizontal}} = \pm 510,000$  kN;  $M_{\text{max}} = 20.0 \times 10^6$  kN m, and  $\Delta P_{\text{vertical}} = \pm 100,000.0$  kN. The angle of internal friction in soil  $\phi' = 25^\circ$ . The angle of friction between the gravity foundation and soil is  $30^\circ$ . The unit weight of wet soil is  $17.5$  kN/m<sup>3</sup>. The undrained shear strength of soil  $s_u$  (or  $c$  or  $c_u$  as per API RP2A notation) in the foundation is  $60$  kN/m<sup>2</sup>. The initial void ratio of soil  $e_0 = 0.63$ , and the compression index of soil is given as  $C = 0.30$ . The Poisson's ratio of soil is given as  $0.45$ , and the shear modulus of soil is taken as  $G = 1000s_u$ . The effective cohesion of the soil  $c'_v$  is given as  $20.0$  kN/m<sup>2</sup>. Check the stability of the foundation for (i) undrained bearing capacity, (ii) drained capacity, and (iii) sliding stability. Use API provision for design. Assume any other missing data. Also, if the structure is unstable in the undrained or drained state, how will you make the structure stable?

- (i) Undrained bearing capacity of soil:

$$\text{Maximum load eccentricity} = e = M/P_{V-\text{min}} = (20.0)(10^6)/(1,900,000) = 10.53 \text{ m}$$

As per API provisions [30], the undrained bearing capacity of foundation is given by Equation 9.3. Also the drained bearing capacity of the foundation soil is given by Equation 9.6.

When the load is eccentric, the effective area of the base is obtained by using Equation 9.4. The effective area of the foundation contact is given by

$$A' = L'B'$$

$$s = \pi(40)^2/2 - [(10.53)\{40^2 - 10.53^2\}^{(1/2)} + (40)^2\sin^{-1}(10.53/40.0)] = 1680.71 \text{ m}^2$$

$$L' = [(2.0)((1680.71)\{40.0 + 10.53\}/(40.0 - 10.53))^{(1/2)}]^{(1/2)} = 66.34 \text{ m}$$

$$B' = (66.34)(29.47/50.53)^{(1/2)} = 50.66 \text{ m}$$

$$A' = L'B' = 3360.78 \text{ m}^2$$

As per Equation 9.3, the undrained bearing capacity  $Q'$  of the foundation is dependent on the values of  $N_c$ ,  $K_c$ ,  $s_u$ , and  $X$ . The values of  $N_c$ ,  $N_q$ , and  $N_\gamma$  are given in Figure 4.53. According to the figure, the values of  $N_c$ ,  $N_q$ , and  $N_\gamma$  for a value of  $\phi' = 25^\circ$ , are given as  $N_c = 20.71$ ,  $N_q = 10.86$ , and  $N_\gamma = 10.87$ .

Hence, the undrained bearing capacity of the platform foundation is given by

$$Q = (s_u N_c K_c + \gamma X) A'$$

where  $K_c = i_c s_c d_c b_c g_c$  and the factors  $i_c$ ,  $s_c$ ,  $d_c$ ,  $b_c$ , and  $g_c$  are, respectively, the correction factors for load inclination, foundation shape, depth of embedment, foundation inclination, and seabed slope below the platform foundation. In the present case,

$$Q = [(60.0)(20.71)K_c + (17.5)(2.0)](3360.78)$$

When  $\varphi > 0^\circ$ , then  $i_c = i_q - (1.0 - i_q)/\{N_c \tan(\varphi)\}$ ;  $i_q = [1.0 - H/\{Q + (B'L_c)\cot(\varphi)\}]^m$

$$m = m_L \cos^2(\theta) + M_B \sin^2(\theta), \text{ with } m_L = (2.0 + L'/B')/(1.0 + L'/B')$$

$$m_B = (2.0 + B'/L')/(1.0 + B'/L')$$

Hence,  $m_L = [2.0 + (66.34/50.66)]/[1.0 + (66.34/50.66)] = 1.433$

$$m_B = [2.0 + (50.66/66.34)]/[1.0 + (50.66/66.34)] = 1.567$$

$$m = 1.433 \cos^2(90^\circ) + 1.567 \sin^2(90^\circ) = 1.567$$

$$i_q = [1.0 - (510,000)/\{Q + (50.66)(66.34)(60.0)\cot(25^\circ)\}]^{1.567}$$

In the above equation,  $Q$  is an unknown value; hence, the proper value has to be determined by a process of trial and error.

*Trial I:* Assume the value of  $K_c = 1.0$ ; hence  $Q = [(60.0)(20.71)(1.0) + (17.5)(2.0)](3360.78) = 4,293,732.5$  kN.

Therefore,  $i_q = [1.00 - 0.1079]^{1.567} = 0.8361$ .

$$i_c = 0.8361 - (1.0 - 0.8361)/\{(20.71)\tan(25^\circ)\} = 0.8361 - 0.0170 = 0.8191$$

For eccentric loads on circular foundations, one should use the shape factors used for an eccentrically loaded rectangular footing.

$$s_c = 1.0 + (B'/L')(N_q/N_c) = 1.0 + (50.66/66.34)(10.86/20.71) = 1.4004$$

$$\begin{aligned} d_q &= 1.0 + (2.0)\tan(\varphi)[1.0 - \sin(\varphi)]^2(D/B') \\ &= 1.0 + (2.0)\tan(25^\circ)[1.0 - \sin(25^\circ)]^2(80.0/50.66) = 1.491 \end{aligned}$$

$$d_c = d_q - (1.0 - d_q)/\{N_c \tan(\varphi)\} = 1.491 - (1.0 - 1.491)/\{(20.71)\tan(25^\circ)\} = 1.491 + 0.051 = 1.542$$

$$b_q = [1.0 - (\nu)\tan(\varphi)]^2 = 1.0$$

$$b_c = 1.0 - (1.0 - b_q)/\{N_c \tan(\varphi)\} = 1.00$$

$$g_q = [1.0 - \tan(\beta)]^2 = 1.0$$

$$g_c = 1.0 - (1.0 - g_q)/\{N_c \tan(\varphi)\} = 1.00$$

**(Note:** that in the last two calculations,  $\nu$  and  $\beta$  are the base and ground inclinations of the gravity platform foundations; here they are equal to 0.0.)

Hence,  $K_c = i_c s_c d_c b_{cg} g_c = (0.8191)(1.4001)(1.542)(1.00)(1.00) = 1.7684$ .

Applying this value of  $K_c$  in Equation 9.3,

$$Q = [(60.0)(20.71)(1.7684) + (17.5)(2.0)](3360.78) = 7,249,471.3$$
 kN

Since the difference between the earlier and the present value of  $Q$  is nearly 40.77%, a second trial is made to find the correct value.

*Trial II:* Take the previous value of  $K_c = 1.7684$ .

$$i_q = [1.0 - (510,000)/\{7,249,471.3 + (50.66)(66.34)(60.0)\cot(25^\circ)\}]^{1.567} = 0.8979$$

$$i_c = 0.8979 - (1.0 - 0.8979)/\{(20.71)\tan(25^\circ)\} = 0.8873$$

Since all the other coefficients needed for the computation of the correction term  $K_c$  do not change,

$$K_c = (0.8873)(1.4001)(1.542)(1.00)(1.00) = 1.9156$$

Corrected  $Q = [(60.0)(20.71)(1.9156) + (17.5)(2.0)](3360.78) = 8,125,726.7$  kN. The difference between the earlier and present one is 10.78%.

*Trial III:* Take the previous value of  $K_c = 1.9156$ .

$$i_q = [1.0 - 510,000 / \{8,125,726.7 + (50.66)(66.34)(60.0)\cot(25^\circ)\}]^{1.567} = 0.9082$$

$$i_c = 0.9082 - (1.0 - 0.9082) / \{(20.71)\tan(25^\circ)\} = 0.8987$$

Correction factor  $K_c = (0.8987)(1.4001)(1.542)(1.0)(1.0) = 1.9403$

Corrected  $Q = [(60.0)(20.71)(1.9403) + (17.5)(2.0)](3,360.78) = 8,220,524.3$  kN

Percentage error = 1.15%. If needed for accuracy's sake, a few more trial runs could be made until the difference becomes less than 1.0%. In this case, the value is assumed to have converged.

Hence, the undrained bearing capacity of the foundation is 8,220,524.3 kN.

Maximum factored vertical load on the foundation = 2,000,000.0 + 100,000 = 2,100,000.0 kN

Buoyant factored load of the gravity platform = 2,100,000 -  $(\pi/4)(80^2)(10.05) = 2,049,483.2$  kN (=  $P_{DB}$ )

As per API code provisions,  $P_{DB} \leq \Phi_{SB}Q_{DB}$ . Hence,  $\Phi_{SB}Q_{DB} = (0.67)(8,220,524.3) = 5,507,751.3$  kN > 2,049,483.2 kN.

Therefore, the undrained soil foundation is quite safe against the vertical load coming on the soil.

(ii) Drained bearing capacity of the foundation soil:

It is given by Equation 9.6 as

$$Q' = [c'N_cK_c + qN_qK_q + (1/2)\gamma'BN_\gamma K_\gamma]A'$$

The respective correction factors are  $K_c = i_c s_c d_c b_c g_c$ ,  $K_q = i_q s_q d_q b_q g_q$ ,  $K_\gamma = i_\gamma s_\gamma d_\gamma b_\gamma g_\gamma$ .

The computed value (after three trials) of  $i_q = (0.9082)$  has already been calculated.

$$s_q = 1.0 + (B'/L')\tan(\varphi') = 1.0 + (50.66)/(66.34)\tan(25^\circ) = 1.0 + (0.764)(0.466) = 1.356$$

$$d_q = 1.491; b_q = 1.0; g_q = 1.0 \text{ (calculated earlier)}$$

$$K_q = (0.9082)(1.356)(1.491)(1.0)(1.0) = 1.8362$$

Hence,  $Q = (c_u N_c K_c + \gamma X)A' = [(60.0)(20.71)(1.9403) + (17.5)(2.0)](3360.78) = 8,220,524.3$  kN.

$$i_\gamma = [1.0 - H / \{Q + (B'L')\cot(\varphi')\}]^{(m+1)} = [1.0 - (510,000) / \{(8,220,524.3) + (50.66)(66.34)(60.0)\cot(25^\circ)\}]^{2.567} = [0.9411]^{2.567} = 0.8557$$

$$s_\gamma = 1.0 - (0.4)(B'/L') = 0.6945$$

$$d_\gamma = 1.0; b_\gamma = 1.0; g_\gamma = 1.0$$

$$K_\gamma = (0.8557)(0.6945)(1.0)(1.0)(1.0) = 0.5942$$

Drained bearing capacity of the foundation soil =  $Q' = [(20.0)(20.71)(1.9403) + (17.5)(2.0)(10.86)(1.8362) + (0.5)(17.5)(70.898)(10.87)(0.5942)](3360.78) = 18,512,764.0 \text{ kN} (= Q_{DB})$

The drained cohesive intercept (in Mohr's circle) is taken as equal to  $c'$ , the effective cohesive strength of soil; also the minimum lateral dimension is taken as the square root of the area of the circular foundation).

For bearing strength failure (as per API RP-2A provisions),  $P_{DB} \leq \Phi_{SB}Q_{DB}$ .

$$P_{DB} = 2,049,483.2 \text{ kN}$$

$$\Phi_{SB}Q_{DB} = (0.67)(18,512,764.0) = 12,403,551.9 \text{ kN} > P_{DB} (= 2,049,483.2 \text{ kN})$$

Hence, the drained bearing strength is quite sufficient to resist the maximum vertical load coming on the drained foundation.

(iii) Sliding Resistance of the Foundation

- (a) For undrained soil, sliding resistance of the foundation =  $H = cA = (60.0)(\pi/4)(80)^2 = 301,592.9 \text{ kN}$ , where  $c$  is the undrained shear strength of soil.

For a stable foundation, the sliding resistance should be greater than the factored applied horizontal load (= 510,000.0 kN).

As per API RP-2A provisions,  $P_{DS} \leq \Phi_{SS}Q_{DS}$ .

$$\Phi_{SS}Q_{DS} = (0.80)(301,592.9) = 241,274.32 \text{ kN} < 510,000.00 \text{ kN}$$

Hence, the foundation is unsafe against sliding failure under undrained condition.

The horizontal sliding resistance of the gravity platform foundation can be increased by (i) providing a larger base area; (ii) increasing the depth of embedment; (iii) providing skirts in the embedded portion of the soil to increase the passive wedge failure area [31], as shown in Figure E9.1; and (iv) decreasing the pore pressure inside the skirt section of the embedded portion by slowly draining the soil volume in between the skirts by pumping out the pore water using suction pumps provided around the foundation outside the skirt volume [32].

- (b) For drained soil, the sliding resistance of the foundation =  $H = c'A + Q'\tan(\varphi')$ .

$$H = (20.0)(\pi/4)(80.0)^2 + (18,512,764.00)\tan(25^\circ) = 8,733,174.6 \text{ kN}$$

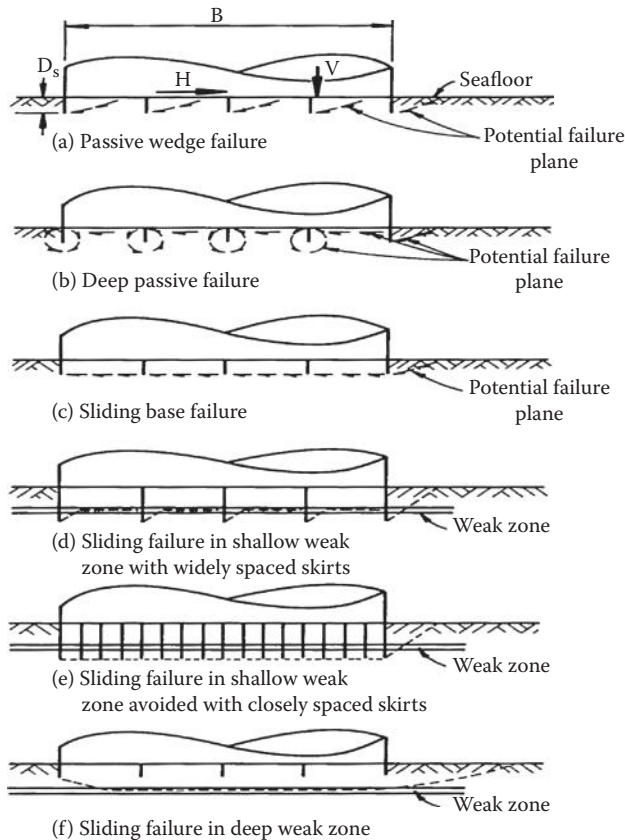
As per API RP-2A provisions,  $P_{DB} \leq \Phi_{SB}Q_{DB}$

$$510,000 (P_{DB}) \leq (0.80)(8,733,174.6) (< 6,986,539.7) \text{ kN}$$

Hence, the drained sliding resistance is quite sufficient to resist the horizontal load coming on the platform.

Assuming that the bearing strength of the foundation was sufficient to resist the applied vertical loads, and that the skirts provided were sufficient to resist suitably the vertical and horizontal loads applied to each of them, six possible types of failure modes were identified by Young et al. [31] as shown in Figure E9.1. In the failure shown in Figure E9.1a, the passive wedge failure shows that each skirt tends to push a passive wedge of soil transversely and upward, as the skirt resists the tendency to move due to the applied loads. As shown in the figure, a sudden crack or active failure zone may develop behind the last skirt. In the failure model shown in Figure E9.1b, shear deformation is developed around the base of the gravity platform, whereas around the base of the skirts, the soil tends to flow backward while the platform tends to move forward under the applied loads.

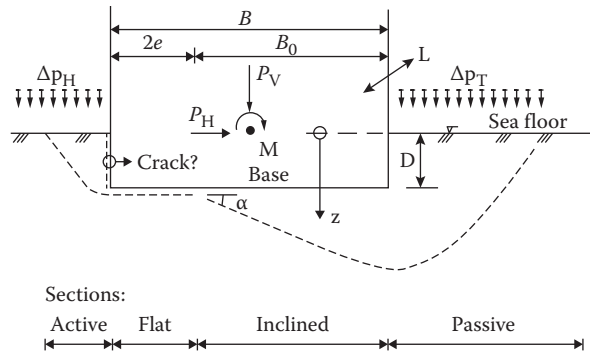
In the failure model shown in Figure E9.1c, the shear failure plane tends to develop at the bottom level of the skirts. In addition, a potential passive wedge type failure develops around the skirt in front, and an active failure zone tends to develop around the skirt at the back. Figure E9.1d and e depicts the type of failure that is likely to occur



**FIGURE E9.1** Possible sliding failure modes of gravity platforms. (From A.G. Young et al., *Geotechnical Considerations in Foundation Design of Offshore Gravity Structures*, Proceedings of 7th Annual Offshore Technology Conference, Houston, TX, Paper # OTC 2371, pp. 367–386, 1975. With permission.)

when a thin weak layer of soil is interspersed in between two strong layers of soil. If this weak layer exists much below the depth of the skirts, a deep-seated failure zone may develop as shown in Figure E9.1f.

In addition to the above, deep-seated failures may also result due to a combination of vertical loads, horizontal loads, and resulting moments about the base of the gravity platform foundation. In Figure E9.2 [33], a deep-seated slip surface bearing failure occurs over the reduced area of the foundation. According to Chaney and Demars [34], a number of different soil failure models have been presented by different researchers, viz., (i) deep-seated slip surface failure presented by Lauritzen and Schjetne [33, 35]; (ii) CARL and CARV failure models presented by Andersen [36] in which the gravity platform foundation experiences a combination of translation and forward rotation in the direction of the applied equivalent horizontal load; and the soil moves in the forward direction, with a passive failure zone in the forward part of the soil and an active failure of soil combined with a reverse bearing capacity failure at the trailing skirt and beneath the caisson foundation; (iii) distorted CARL-type failure presented earlier by Young et al. [31]; and (iv) sliding block mode failure presented by Georgiadis and Michalopoulos [37], in which the platform foundation moves forward, as well as downward, generating blocks of soil moving in an inclined manner downward, horizontally and moving in an inclined manner upward, along the failure zone in the front. As per Puzrin and Randolph [38] and Randolph and Gourvenec [39], two- and three-dimensional finite element results have been presented using soils with elastoplastic behavior having realistic failure criteria to verify and improve the conclusions obtained from the above models.



**FIGURE E9.2** Limit equilibrium stability analysis of gravity platform foundation. (From R.C. Chaney and K.R. Demars, *Offshore structure foundations*, in: *Foundation Engineering Handbook*, 2nd Edition, edited by H.Y. Fang, Van Nostrand Reinhold, New York, p. 705, 1991. With permission.)

## 9.3 STATIC DEFORMATION OF GRAVITY PLATFORM FOUNDATION

### 9.3.1 INTRODUCTION

The deformation of the gravity platform due to self-weight of the platform and the applied environmental/other loadings acting on the platform tends to affect the integral behavior and serviceability of the structure and its components. Deformations have to be limited to make the platform and its components serviceable since (i) the overall settling down of the platform with respect to sea level will affect the usability of the provided boat landing system and reduce the air gap such that an unduly large wave will generate large impact forces that will damage the bottom members of the platform deck; (ii) the overall tilt of platform, resulting from differential settlements of the gravity platform, will affect the various mechanical and process components/machinery located on the deck and impair the ability of persons to work on the platform safely; and (iii) excessive deformations will result in failure of conductors and their connections to subsea pipelines and cables.

According to Eide and Andersen [32], the gravity platforms experience (i) immediate or short-term deformation due to elastic or elastoplastic soil deformations (for clays, it is based on undrained characteristics, whereas for sands, it is based on drained characteristics), resulting primarily from shear deformation (or shear straining) of the soil; (ii) gradual deformation due to the effects of cyclic loading and changes of load conditions over time (this occurs due to factors such as yielding and stress redistribution in clayey-type soils under undrained conditions) and creep settlements under constant volume; and (iii) long-term deformations due to primary and secondary consolidation of foundation soil and regional subsidence of soil; these changes are associated with the gradual dissipation of pore pressures, redistribution of stresses in soil, and the attendant volume changes in soil.

### 9.3.2 IMMEDIATE OR SHORT-TIME DEFORMATIONS

Immediate or short-time deformations occur almost immediately after the application of the platform load or the environmental loads (due to waves, winds, or other effects). The major part of the short-term deformations of a gravity platform occurs during its installation stage. The deformations are either elastic or elastoplastic. They can be estimated using a finite element program incorporating an appropriate elastoplastic constitutive model or by the methods of settlement calculation for shallow foundations described in standard textbooks [40–42]. Any of the methods such as (i) load spreading method, based on the earlier Boussinesq's and Mindlin's solutions for stresses in elastic media [40–44]; (ii) empirical correlation [40, 45]; and (iii) strain influence factor [40, 46] can be used in the computation of the vertical short-term deformation of the soil.

9.3.2.1 API Code Provisions

According to the API RP2A code, the *short-term deformations* of the foundation soil are given by the following:

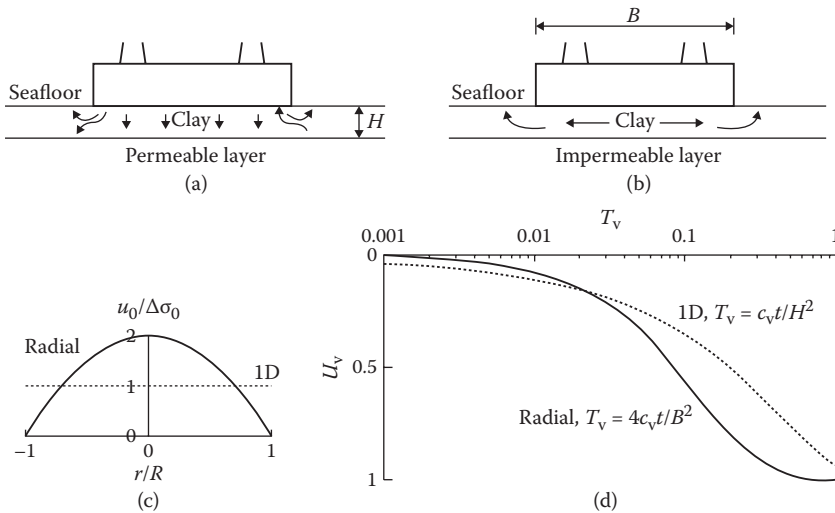
$$\begin{aligned}
 & \text{(i) vertical deformation: } u_v = [(1.0 - \nu)/(4GR)]P_v \\
 & \text{(ii) horizontal deformation: } u_h = [(7.0 - 8\nu)/(32(1.0 - \nu)GR)]H \\
 & \text{(iii) rocking deformation: } \theta_r = [(3.0)(1.0 - \nu)/(8GR^3)]M \\
 & \text{(iv) torsional deformation: } \psi_t = [(3.0)/(16GR^3)]T
 \end{aligned}
 \tag{9.12}$$

where  $u_v, u_h$  = vertical and horizontal deformations of the gravity platform;  $\theta_r, \psi_t$  = overturning and torsional rotations;  $P_v, H$  = vertical and horizontal loads acting on the gravity platform;  $M, T$  = overturning and torsional moments;  $\nu$  = Poisson’s ration for soil; and  $R$  = radius of the gravity platform foundation.

If the foundation soil is soft (or flexible) or the loading on the soil is sufficiently heavy so as to generate very high stresses throughout a large portion of soil, then Equation 9.12 will be quite inappropriate; numerical approaches using finite element or other approaches should be used to compute the appropriate deformations in the soil; in addition, the softening of soil due to cyclic loading should be considered.

9.3.3 PRIMARY CONSOLIDATION

Terzaghi’s theory of consolidation was briefly reviewed in Section 4.4.8. The one-dimensional theory is often used as a first approximation for the consolidation settlements of type (iii) deformation, mentioned in Section 9.3.1. Figure 9.9a [47, 48] shows a situation in which this approximation is



**FIGURE 9.9** Simplified model for consolidation beneath a gravity platform resting on a thin layer of compressible clay: (a) one-dimensional consolidation in a thin clay layer underlain by a relatively permeable soil layer; (b) radial consolidation underlain by a relatively impermeable layer; (c) initial vertical stress beneath the caisson base; and (d) degree of consolidation  $U_v$  versus the time factor  $T_v$ . (From R.E. Olson and J. Lai, Application of Terzaghi’s theory of consolidation to problems involving radial flow, unit 4, in: *Advanced Soil Mechanics*, Department of Construction Engineering, Chaoyang University of Technology, Taiwan, pp. 50–67, 2002. With permission.)



reasonably accurate. The gravity base rests on a relatively thin layer of clay of height  $H$ , overlying a sand layer that can serve as an effective drain. Because  $H$  is much smaller than the caisson breadth, the principal flow of water will be vertical into the sand layer. Figure 9.9b [48] shows an alternative situation where the radial consolidation equation (rather than the one-dimensional vertical consolidation) is more appropriate. The gravity base rests on a thin compressible layer overlying a relatively impermeable soil or rock. The flow of water is primarily radial.

The initial increase in the pore water pressure for the one-dimensional case equals the average vertical stress ( $P_{\text{vert\_buoyant}}/A$ ), where  $P_{\text{vert\_buoyant}}$  is the buoyant weight of the platform, and  $A$  is the area of the platform base. This average stress is fairly uniform across the base, but there will be a rapid change in the values (due to fluid drainage) at the extremities of the base of the platform. When radial consolidation is considered, the equal-strain analysis gives an initial parabolic pore pressure distribution (see Figure 9.9c), with the largest pore pressure being twice the computed average vertical stress at the base of the caisson [47, 48]. Since the effective soil stresses do not change immediately (undrained conditions), the foundation tends to bend upward at the center due to the larger stresses (and hence the loads) acting there. Figure 9.9d shows the degree of consolidation  $U$  (or  $U_v$ ) plotted against time factor  $T$  (or  $T_v$ ) for the two analyses. For the one-dimensional case,  $T = c_v t/H^2$  (see Equation 4.27), where  $c_v$  is the coefficient of consolidation of the clay layer, and  $t$  is time from loading. For instance, when a gravity platform is supported on a 10-m-deep clay layer with a coefficient of consolidation of 1.0 m<sup>2</sup>/year, nearly all the long-term settlement will have occurred when  $T = 1.0$ , corresponding to a consolidation duration  $t$  of 100.0 years. For the radial case, using the equal strain theory for a rigid base,  $T = (4.0)(c_v t/B^2)$ , where  $B$  is the transverse dimension (for a rectangular foundation) or the diameter of the foundation (for a circular foundation). It has been found that all the consolidation is completed when  $T = 0.4$ . Hence, for a gravity platform with a 100.0-m-diameter foundation supported by a clay layer with a coefficient of consolidation of 1.0 m<sup>2</sup>/year, we have a consolidation duration  $t$  of 1600.0 years.

Excess pore pressures would also develop as a consequence of cyclic loading during the lifetime of the gravity platform structure. These are considered in type (ii) gradual settlements in Section 9.3.1. Since different portions of the foundation soil experience different cyclic stresses, the excess pore pressures will be different, and a more complex pattern of fluid flow and volumetric compression would develop in the three-dimensional soil body; moreover, the coefficient of consolidation of the soil will vary across the three-dimensional continuum, which will also affect the above analyses. Consequently, a targeted finite element program and proper engineering intuition and judgment should be able to solve these complex issues.

### 9.3.3.1 Secondary Consolidation

Secondary consolidation (also called as secondary compression) occurs during and after the primary consolidation, outlined in Section 9.3.3; it occurs due to the stress redistribution taking place during primary consolidation. The process appears to be one in which fluid flow is driven by a gradient that is not associated with excess pore pressures [49, 50]. It produces significant deformations for silts and silty clays.

### 9.3.3.2 API Code Provisions

According to API RP2A provisions, the vertical *long-term deformation* of the gravity platform foundation soil is given by [30, 51]

$$u_v = \{(hC)/(1 + e_0)\} \log_{10}\{(q_0 + \Delta q)/q_0\} \quad (9.13)$$

where  $u_v$  = vertical deformation;  $h$  = layer thickness;  $e_0$  = initial void ration of the soil;  $C$  = compression index of the soil over the load range considered;  $q_0$  = initial effective vertical stress; and  $\Delta q$  = added effective vertical stress.

In using Equation 9.13, if the layer beneath is very thick and homogeneous, then the layer should be subdivided into suitable number of thinner layers and the deformation computed. The total deformation

of the gravity foundation is obtained by the sum of settlement of the individual layers. The compression characteristics needed for using Equation 9.13 are to be obtained from one-dimensional consolidation tests conducted on the soil under consideration, as mentioned in Section 4.4.8.

Equation 9.13 can be used only for a simplified estimate of the long-term deformation of the foundation. In order to calculate it more realistically, complex three-dimensional numerical schemes having coupled formulations for soil stresses and pore pressures are required. Since creep, load redistribution, and differential settlements are to be accounted for in computing the long-term settlements of the soil media having complex layering and nonlinear and variable soil profiles, care should be exercised in the choice of the numerical procedure utilized for the purpose.

Bowles [41] stated that for onshore structures not subjected to extensive cyclic loading, immediate settlement and long-term primary consolidation settlement could be estimated quite accurately with the use of simple calculations stated above. He also observed that the computed rate of consolidation settlement was often inaccurate. Hence, in using the API RP2A given relationships, it would be wise to ensure that the case under consideration is not very sensitive to the rate of settlement.

### 9.3.4 REGIONAL SUBSIDENCE

Regional subsidence is due to the removal of hydrocarbons from a deep reservoir, without replacing the drawn-out volume by water injection. This removal reduces the pore oil pressure in the reservoir; consequently, the effective stress on the solids in the reservoir increases. This ultimately leads to a large settling down of the sand or rock skeleton, leading to regional settlement of the ground surface. For instance, a soil subsidence about 4.0 m occurred in the Ekofisk platform during the first 20 years of operation [52]. The principal oil-bearing stratum under the Ekofisk platform was of chalk. It has been computed that the soil subsidence by 2011 would be between 6 and 11 m. In addition to the large-scale regional subsidence given above, much smaller amounts of subsidence would also be caused by changes in the pore water pressure in soil layers that are confined between impermeable layers of soil, before the development of the field under consideration. These changes occur as a result of various holes and cracks made in the confining soil layers of the oil field due to site investigation boreholes and hydrocarbon wells.

### 9.3.5 OTHER CONSIDERATIONS

The tendency for the occurrence of soil scour around the outer edges of a gravity platform foundation is increased due to the increase in speed of the water flowing out of the skirt compartments as the platform settles down during the final stage of gravity platform installation. This increases the possibility of fluidization (or otherwise called as liquefaction) of soils near the edges of the gravity platform foundation, thus eroding the soil around the platform base and exposing the foundation skirts. Liquefaction also occurs when excess pore pressures are generated in sandy soils beneath the platform foundation due to the passage of storm waves over the platform or when an earthquake occurs near the platform region. Depending on the magnitudes of the excess pore pressures, the pore pressure gradients may become sufficiently high that the effective stresses in the soil at the edge of the caisson reduce to near zero, causing the soil to almost lose its strength completely.

## 9.4 ANALYSIS AND DESIGN OF GRAVITY PLATFORM SUBJECTED TO WIND AND WAVE LOADS

### 9.4.1 INTRODUCTION

The analysis and design of a concrete gravity platform is similar to that given in Chapter 8 for steel template structures. Design site characteristics (such as depth and soil properties) will be given along with the environmental parameters such as wind velocities, wave heights, and periods. The

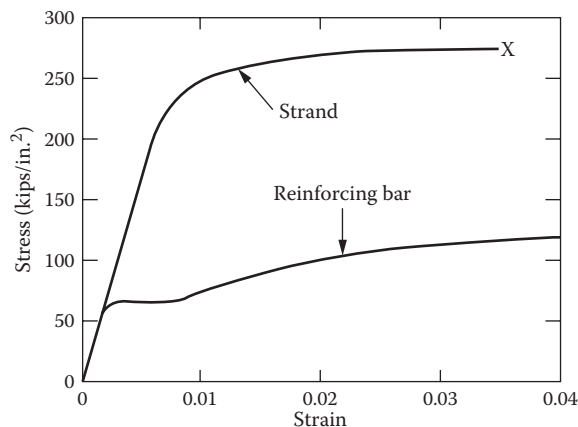
use of concrete as the construction material for the gravity platform gives a very good compressive strength for the platform structure (being around 30.0 to 40.0 MPa for normal strength concretes and 80.0 to 100.0 MPa for high strength concretes), but the tensile strength is very low, being around 10% to 15% for normal strength concretes and around 8.0% to 10.0% for high strength concretes. This necessitates that some additional load-carrying capacity should be given in the tensile direction. This is usually provided by the use of pre-stressed reinforced concrete wherein the strength and deformation characteristics of the usual reinforced concrete are enhanced by the provision of high strength steel wires or strands, provided in small protective ducts that keep them free from being encapsulated in concrete. The behavior of normal strength steel bars and high strength pre-stressing strands is given in Figure 9.10 [53]. When the member is pre-stressed, the net effect on the member is to unload the tensile stress in the concrete (by making it compressive); hence, the concrete does not crack under any bending load since it experiences only compressive stresses. The inclusion of normal (or medium) strength reinforcing steel bars increases the ultimate strength and deformation capacities of the pre-stressed members.

In this section, the simplified analysis of the concrete gravity platform is based on the understanding that the forces and deformations of the structure are governed predominantly by the stiffness forces generated in the structure. This would mean that the behavior of the structure can be described by the matrix equation given below:

$$[K]\{u\} = \{F_{\max}\} \quad (9.14)$$

where  $[K]$  is the stiffness matrix of the structure of representing the resistance of the platform structure to deformation  $\{u\}$  in the direction of the applied load  $\{F_{\max}\}$ .

This would in essence limit the analysis to gravity platform structures whose fundamental frequency of vibration would be in the range of 0.3 Hz or more (normal operational and dominant wave frequencies will be much less than 0.3 Hz); this seems to be a reasonable approximation since the mass of most of the concrete gravity structures will be very high, and the stiffness of soil continuum on which the structure is resting or in which it is embedded will be rather low. Anyhow, it must be remembered that the ocean environment in which the structure is embedded is subjected to extreme wind, wave, and cyclonic forces, and the structure must be designed to resist any of the effects produced by these forces. Hence, any meaningful design of offshore structures should consider the dynamic effects produced by these environmental forces and design the structures to resist these forces.



**FIGURE 9.10** Typical stress–strain curves of pre-stress steel strands and medium strength reinforcing steel bars. (From T.H. Dawson, *Offshore Structural Engineering*, Prentice Hall Inc., Englewood Cliffs, NJ, p. 194, 1983. With permission.)

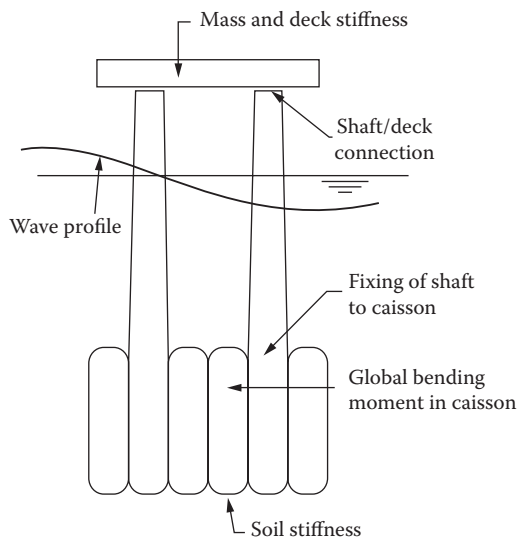
### 9.4.2 ASSUMPTIONS MADE IN SIMPLIFIED ANALYSIS

In the material presented below using a simplified analysis and design of a concrete gravity platform, the following assumptions are made to make the material presented below to be solved with simple hand calculations using a digital calculator:

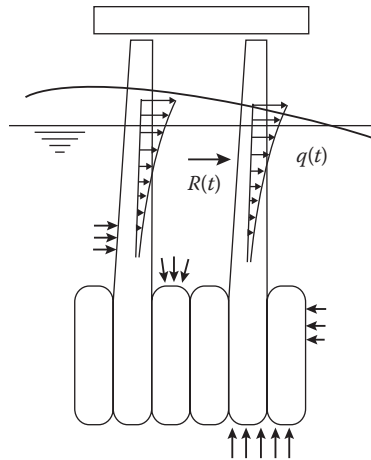
(i) The platform deck is connected through a hinge connection to the cylindrical vertical columns of the gravity platform, as shown in Figure 9.11 [54]. Hence, the load transfer, from the deck to the vertical columns, occurs only through shear; the deck bending moments are not transferred to the structures below. The design forces for the columns are computed with the design wave placed at the mean sea level of one of the vertical columns; the corresponding forces on the other ocean-surface piercing columns are computed with the above placement of the wave profile. The wave passage is assumed to exert forces only on the outer surfaces of the exposed gravity platform. The bottom surface of the gravity platform is subjected to soil stiffness forces that tend to act as soil pressures on the bottom surfaces of the caisson foundations of the platform.

The forces acting on the gravity platform are shown in Figure 9.12 [55]. The hydrodynamic wave forces are assumed to act along the center line of the vertical columns, as well as along the center line of the bottom caissons, in the direction of the wave motion. The wind forces also act in a similar manner along the surfaces exposed normally to its direction of motion. The hydrostatic forces due to the depth of the structural components below the sea surface act normal to the exposed exterior surfaces of the platform. The uplift fluid forces, expressed in terms of undrained pore pressures caused by the buoyant weight of the gravity platform, act normal to the bottom surfaces of the gravity platform foundation, as shown in the figure.

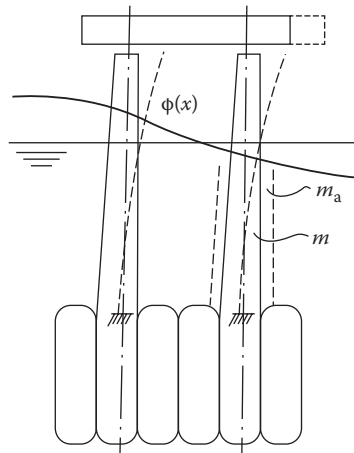
The resultant deformations of the gravity platform are indicated in Figure 9.13 [56]. The deformations occur in the direction of the fluid motions. Since the top deck is assumed to be hinge-connected to the top of the vertical cylindrical towers of the structure, it moves as a rigid body as shown in Figure 9.13. The vertical cylindrical towers approximately deform, in a cantilever beam manner, as if they are fixed rigidly at the base of the spherical roof of the bottom caissons; even though the bottom caissons deform locally, and rotate globally due to the overall deformations of the soil medium below the base of the gravity structure, they are neglected since they are very small.



**FIGURE 9.11** Simplifying assumptions made for the platform connections and foundation support. (From I. Holland et al., *Design of Offshore Concrete Structures*, Spon Press, New York, p. 52, 2000. With permission.)



**FIGURE 9.12** Equivalent forces acting normal to the exposed surfaces of the gravity platform. (From I. Holland et al., *Design of Offshore Concrete Structures*, Spon Press, New York, p. 53, 2000. With permission.)

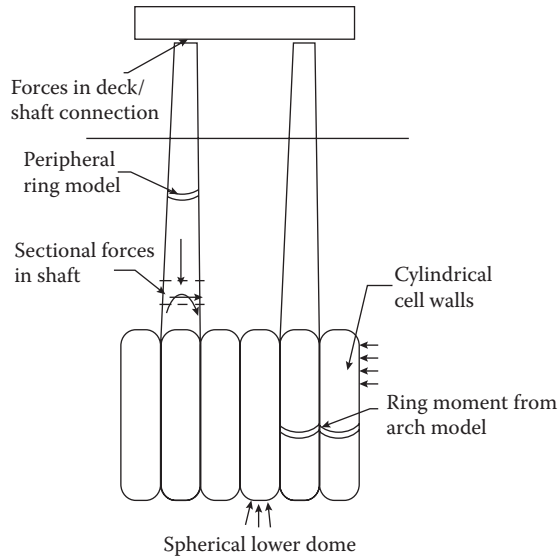


**FIGURE 9.13** Simplified deformation shape of the gravity platform structure. (From I. Holland et al., *Design of Offshore Concrete Structures*, Spon Press, New York, p. 54, 2000. With permission.)

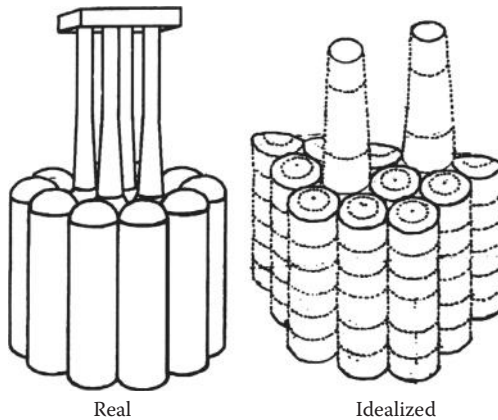
The skirt members, located in the gravity platform base, deform due to the forces acting on them as shown in Figure 9.8b and c.

In designing the various components of a gravity platform, the procedure shown in Figure 9.14 [57] is utilized in calculating the forces acting on each subcomponent of the platform and the requisite cross section of the component. The forces transferred from the top deck to the bottom cylindrical towers are through shear actions at the deck–column interfaces. The forces are computed at the center of various subsections of the component under consideration, as shown in Figure 9.15 [58]. Depending on the importance of the component, each subsection may be of height varying between 10.0 and 15.0 m, as shown in Figure 9.15. The forces acting on each subsection of the component is computed at its center.

For both the vertical cylindrical columns and the bottom caissons forming the foundations of the gravity platform, the design must consider the behavior as (i) a cylindrical segment of a ring (or a fixed arch) subjected to fluid pressures due to both hydrostatic and hydrodynamic actions and (ii) a cantilever beam subjected to axial and bending loads in a global manner. The caisson top is designed as a spherical shell subjected to hydrostatic and hydrodynamic fluid pressures in a radial direction. Since the caisson junctions are quite complex, their design is based on detailed finite



**FIGURE 9.14** Salient design considerations for the gravity platform components. (From I. Holland et al., *Design of Offshore Concrete Structures*, Spon Press, New York, p. 60, 2000. With permission.)



**FIGURE 9.15** Conceptual model of the gravity platform for structural analysis and design. (From G.S. Epperson, Gravity Platforms, Lecture 6, in: *Overview of Offshore Engineering*, Course Notes, Houston, TX, p. 48, 1992. With permission.)

element computations carried out for that part of the structure. The caisson bottom is designed for the pore pressures acting on the bottom spherical shell section. In addition, both the vertical cylindrical tower as well as the cylindrical caisson with its spherical top and bottom must be designed to resist the forces acting on them as shells; the components must also be designed to resist their implosive failures. The skirts need to be designed to resist the outward bending action of the undrained pore pressures (or drained active soil pressures) due to accidental exposure of the complete skirt by erosion of the surrounding soil on the outside.

### 9.4.3 ADDITIONAL CONSIDERATIONS FOR DYNAMIC BEHAVIOR OF PLATFORM COMPONENTS

Even though it is mentioned in Section 9.4.1 that the member forces are governed primarily by the stiffness forces generated by the statical bending of the component members of the gravity

platforms, the dynamic deformations caused by the consequent inertial motions of the platform members also impose additional forces on the component members. The significance of these forces depends on the ratio of inertial forces to stiffness forces produced in the individual member. In order to illustrate the dynamic modeling and analysis of a gravity platform, a simplified model used for carrying out the dynamic analysis is shown in Figure 9.16 [59].

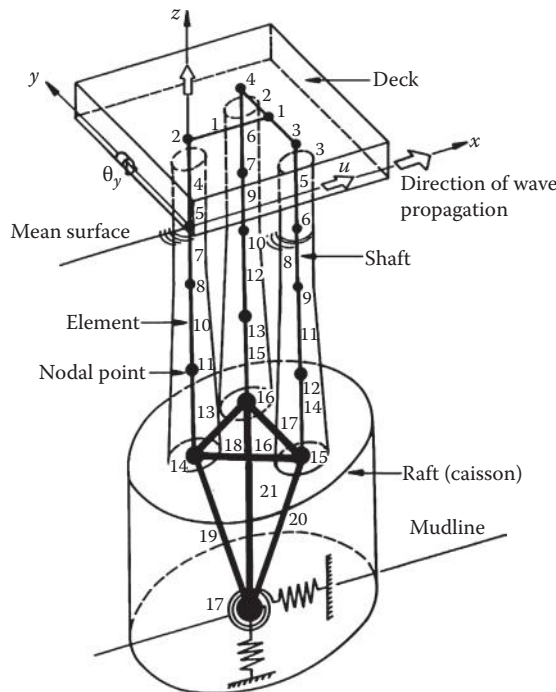
In the dynamic model of the gravity platform given in Figure 9.16, the platform caisson foundation is considered to be made up of three stiff beams, supported at the bottom by three springs, representing the lateral, vertical, and rotational stiffnesses of the soil foundation supporting the gravity platform; at the top of the caissons, once again, the above-mentioned three stiff beams are joined together to form a stiff framework. Each of the vertical cylindrical columns of the gravity platform is modeled as a lumped mass beam model with four degrees of freedom; at the top, representing the bottom of the top deck, the three lumped mass models are joined together by three stiff beams, representing the stiffnesses of the deck, at this location. Equivalent dynamic wave forces are applied at the corresponding lumped mass points of the vertical cylindrical lumped mass beam model.

According to API RP2A-LRFD code provisions [60], the three springs given in Figure 9.16 representing the vertical, lateral, and rotational (rocking motion) stiffnesses of the soil foundation are given by

$$\begin{aligned}
 \text{Vertical stiffness } k_v &= (4.0)(GR)/(1.0 - \nu), \\
 \text{Horizontal stiffness } k_h &= (32.0)(GR)(1.0 - \nu)/(7.0 - 8\nu), \\
 \text{Rotational (rocking) stiffness } k_\theta &= (8.0)(GR^3)/(3.0(1.0 - \nu)),
 \end{aligned}
 \tag{9.15}$$

where  $G$  = elastic shear modulus of soil;  $R$  is the radius of the base, and  $\nu$  is the Poisson's ratio of the soil below the platform base.

The dynamic analysis can be carried out as indicated in Sections 7.7.4.3 and 7.7.4.4.



**FIGURE 9.16** Gravity platform model for dynamic analysis. (From R. Nataraja and C.L. Kirk, *Dynamic Response of a Gravity Platform under Random Wave Forces*, Proceedings of Offshore Technology Conference, Houston, TX, Paper # 2904, pp. 199–209, 1977. With permission.)



### Example 9.2

The idealized concrete monotower, shown in Figure E9.3, is located in a water depth of 160.0 m. The cylindrical caisson (at bottom) of 90.0-m diameter is filled with crude oil, and the vertical column is filled with seawater up to the still waterline. The cylindrical tower supporting the top deck is 20.0 m in diameter, and the wall thickness is 0.60 m. The bottom caisson is made up of a central caisson of 30.0-m diameter (stepped to 20.0 m, just above the hemispherical dome), 60.0-m height, and of wall thickness 0.60 m; it is surrounded by six concentric cylindrical caissons of the same diameter, height, and wall thickness, giving the bottom caisson of 90.0-m diameter. The top of the six bottom caissons (except the central one) is made hemispherical so that it is able to resist the hydrostatic and hydrodynamic pressures applied on top in an effective manner. The bottom slab is of thickness 1.0 m. Pertinent data are given as follows: deck mass =  $5.0 \times 10^7$  kg; caisson is filled with crude oil of specific gravity 0.98; column/caisson concrete density =  $2500.0 \text{ kg/m}^3$ ; seawater density =  $1025.0 \text{ kg/m}^3$ ; effective cohesion =  $60.0 \text{ kN/m}^2$ ;  $\phi_c = 25^\circ$ ; unit weight of soil =  $17.5 \text{ kN/m}^3$ ; Poisson's ratio of soil = 0.45;  $G = 1000s_u$ ;  $s_u$  = (undrained) shear strength of soil =  $120.0 \text{ kN/m}^2$ ; initial void ratio = 0.63; and compression index of soil = 0.30. Assume that the platform is underlain by a silty-clay layer of thickness 15.0 m, and a very thick sandy stratum exists below the clay layer. The structure is subjected to forces due to (i) a maximum wave of 25.0-m height and a period of 14.5 s and (ii) a maximum 1-h-average wind speed of 200 kmph; the wind averaging periods have been given as 10.0 min (for the top deck and the exposed part of the cylindrical tower) and 10.0 s (for the drill rig). Determine (I) whether this structure floats in its unballasted or ballasted position. Take  $C_D = 1.0$  and  $C_M = 1.0 + C_a = 1.0 + 1.0 = 2.0$ , with the coefficient of added mass given by  $C_a$ . (II) Locate the center of mass  $G$  and the center of buoyancy  $B$  for the unballasted structure when it is in its vertical position. (III) Check the ballasted structure against overturning, sliding, and bearing failures. (IV) Determine the short- and long-term settlements of the foundation. (V) Determine the plane rocking frequency and transverse response (maximum) of the tower (at the top of deck level) as it responds to wave excitation. Use 30% added inertia and 10% hydrodynamic damping. Assume that it rocks about the center  $O$  of its base.

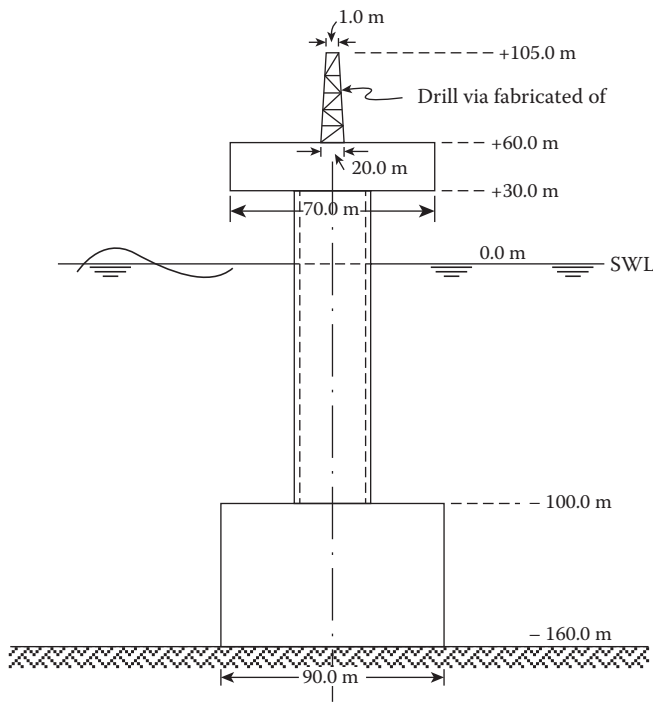


FIGURE E9.3 Idealized monotower gravity platform structure.



## (I)–(II) Stability of the ballasted and unballasted gravity platform

## (a) Weight of various components of the platform

The platform is considered to be made up of stepped sections consisting of (i) the bottom caisson of 60.0-m height and 90.0-m diameter; (ii) an equivalent cylindrical section of diameter 87.2 m and height 6.37 m [=  $4R/(3\pi)$ ], which represents the effect of the hemispherical domes of the bottom caisson; and (iii) cylindrical tower of outside diameter 20.0 m and depth of submergence 93.63 m.

$$(1) \text{ Weight of the top deck is given as } = 5.0 \times 10^7 \text{ kg} = (4.91)(10^2) \text{ MN}$$

$$\text{Center of gravity above the seabed (approximated)} = 205.0 \text{ m}$$

$$(2) \text{ Weight of the cylindrical tower supporting the deck (above the caisson)} = (\pi/4)(20.0^2 - 18.8^2)(123.63)(2500)(9.81) = (1.109)(10^2) \text{ MN}$$

$$\text{Center of gravity above the seabed} = 128.19 \text{ m.}$$

$$(3) \text{ Weight of the unballasted bottom cylindrical caisson (including the top spherical domes)} = [(7)(\pi/4)(30.0^2 - 28.8^2)(59.0) + (6)\{(1/2)(4/3)(\pi)(15.0^3 - 14.4^3)\}](2500.0)(9.81) + \text{Weight of concrete in the spaces between the vertical cylinders in the bottom caisson} = (22,887.51 + 4888.52)(2500.0)(9.81) + (1.0)(10^8) = (7.812)(10^2) \text{ MN}$$

$$\text{Center of gravity above seabed} = 35.5 \text{ m.}$$

$$(4) \text{ Weight of the base slab} = (\pi/4)(90^2)(1.0)(2500.0)(9.81) = (1.56)(10^2) \text{ MN}$$

$$\text{Center of gravity above seabed} = 0.5 \text{ m.}$$

$$(5) \text{ Weight of water contained in cylindrical tower} = (\pi/4)(18.8^2)(123.63)(1025.0)(9.81) + (\pi/4)(28.8^2)(65.37)(1025.0)(9.81) = (3.45 + 4.282)(10^8) \text{ N} = (7.733)(10^2) \text{ MN}$$

$$\text{Center of gravity above the seabed} = 73.27 \text{ m.}$$

$$(6) \text{ Weight of ballast crude oil} = (6)[(\pi/4)(28.8^2)(59.0) + (1/2)(4/3)(14.4^3)](0.98)(1000.0)(9.81) = (23.319)(10^2) \text{ MN}$$

$$\text{Center of gravity above seabed} = 32.11 \text{ m.}$$

$$\text{Total weight of the ballasted platform} = (4.91 + 1.109 + 7.812 + 1.56 + 7.733 + 23.319)(10^2) \text{ MN} = (46.443)(10^2) \text{ MN}$$

$$\text{Total weight of the unballasted platform} = (46.443)(10^2) - (23.319)(10^2) = (23.124)(10^2) \text{ MN}$$

## (b) Buoyant weight of the platform:

$$\text{Buoyant weight of the ballasted caisson} = [(7.812)(10^2) + (1.56)(10^2) + (23.319)(10^2) + (\pi/4)(28.8^2)(59.0)(1025.0)(9.81)] - [(\pi/4)(90^2)(60.0)(1025.0)(9.81) + (6)(1/2)(4/3)(15.0^3)(1025.0)(9.81) + (6.37)(\pi/4)(30)^2(1025.0)(9.81)] = (7.812 + 1.560 + 23.319 + 3.865)(10^2) - (38.381 + 1.358 + 0.453)(10^2) = - (3.636)(10^2) \text{ MN}$$

$$\text{Buoyancy of the ballasted caisson} = - (38.381 + 1.358 + 0.453)(10^2) \text{ MN} = - (40.192)(10^2) \text{ MN}$$

$$\text{Center of buoyancy of the ballasted caisson above seabed (approximate)} = 30.0 \text{ m}$$

$$\text{Buoyant weight of the cylindrical tower supporting the deck (above the bottom caisson)} = [(1.109)(10^2) + (3.451)(10^2)] - [(\pi/4)(20.0^2)(93.63)(1025.0)(9.81) + [1.109 + 3.451 - 2.958](10^2) = (1.601)(10^2) \text{ MN}$$

Buoyancy of the cylindrical tower supporting the deck =  $-(2.958)(10^2)$  MN

Center of buoyancy of the cylindrical tower above the seabed =  $(66.37) + (93.63/2) = 113.19$  m

Weight of the top deck =  $(0.5)(9.81)(10^2) = (4.91)(10^2)$  MN

Center of gravity of the top deck above the seabed = 220.0 m

Consequently, the buoyant weight of the ballasted platform =  $-(3.636)(10^2) + (1.601)(10^2) + (4.91)(10^2) = (2.875)(10^2)$  MN.

Rotational inertia of the buoyant platform  $\sim \{[(4.91)(10^8)/(9.81)](205.0)^2\} + \{(1.109)(10^8)/(9.81)](128.19)^2 + \{(3.451)(10^8)/9.81\}(113.19)^2 - \{(2.958)(10^8)/(9.81)](113.19)^2 - \{(3.636)(10^8)/(9.81)](30.0)^2 = [(21.013) + (1.858) + 4.507 - 3.863 - 0.334](10^{11})$  kg m<sup>2</sup> =  $(23.181)(10^{11})$  kg m<sup>2</sup>

Since the net weight is downward, the ballasted platform will be stable in position and will not float.

When the platform is not ballasted, the buoyant weight of the platform =  $(23.124)(10^2) - (38.381)(10^2) - (1.358)(10^2) - (0.453)(10^2) - (2.958)(10^2) = -(19.618)(10^2)$  MN.

Since the net weight of the unballasted platform is negative, the platform will float.

(c) Stability of the unballasted gravity platform:

Total mass of the unballasted platform =  $[4.91/9.81 + 1.109/9.81 + 7.812/9.81 + 1.56/9.81 + 7.733/9.81](10^8)$  kg =  $(2.374)(10^8)$  kg

First moment of the mass of the unballasted platform above its base slab =  $[(4.91/9.81)(205.0) + (1.109/9.81)(128.19) + (7.812/9.81)(35.5) + (1.56/9.81)(0.5) + (7.733/9.81)(73.27)](10^8)$  kg m =  $[102.604 + 14.492 + 28.270 + 0.080 + 57.757](10^8)$  kg m =  $(203.203)(10^8)$  kg m

Center of mass of the unballasted structure above the base slab =  $[(203.203)(10^8)]/[(2.374)(10^8)] = 85.60$  m

Equivalent (seawater) volume of the unballasted gravity platform =  $[(2.374)(10^8)]/(1025.0) = (2.316)(10^5)$  m<sup>3</sup>

Volume of the caisson alone (without the hemispherical portion of the six cylindrical portions) =  $(\pi/4)(90^2)(60.0) = (3.817)(10^5)$  m<sup>3</sup>

Hence,

the depth of submergence of the bottom caisson =  $\{[(2.316)(10^5)]/[(3.817)(10^5)]\}(60.0) = 46.406$  m

Moment of inertia of the cross section at the water plane =  $(\pi/64)(90)^4 = (3.221)(10^6)$  m<sup>4</sup>

Distance between the metacenter and the center buoyancy =  $[(3.221)(10^6)]/[(2.316)(10^5)] = 13.91$  m

Center of buoyancy of the unballasted caisson above the base slab =  $(46.406/2) = 23.203$  m

Distance between the center of mass and the center of buoyancy =  $85.60 - (46.406/2) = 62.397$  m

Since the distance between the center of buoyancy and the center of mass of the unballasted gravity platform exceeds the distance between the metacenter and the center of buoyancy, the platform is unstable in its unballasted position [i.e., metacenter is below the center of mass (or gravity)].

(III) Overturning, sliding, and bearing resistances of the gravity platform:

(a) Wave forces acting on the gravity platform:

As per Figure 3.31, the wave theory to be chosen is dependent on the ratios of  $(H/gT^2)$  and  $(d/gT^2)$ . According to the data given,

$$H/gT^2 = (25.0)/[(9.81)(14.5^2)] = 0.0121$$

$$d/gT^2 = (160.0)/[(9.81)(14.5^2)] = 0.0776$$

This would lead to the use of Stoke’s fifth-order wave theory for wave force computation; since this would involve an extensive numerical computation, this is not attempted in this study. Using Table 3.7, the deepwater wave is defined by the  $d/L$  ratios; for deepwater wave,  $L_0 = (g/2\pi)T^2$ .

$(d/L_0) = (160.0)/\{[(9.81)(14.5)^2]/(2\pi)\} = 0.487$ ; since the value is very close to 0.5, which is the starting point for the deepwater wave (according to Table 3.7), a linear Airy’s wave theory formulation is used in computing the wave forces on the gravity platform. This is justified since the iterated (water depth)/(wave length) ratio  $(d/L)$  will be a little higher ( $\approx 0.4891$ ) from the tables given in Shore Protection Manual [60].

Moreover, one also needs to check whether diffraction effects need to be considered for the structure. As per Section 6.3.4.7, diffraction effects become dominant when (diameter/wavelength)  $\geq 0.2$ . Hence, in this case, for the cylindrical tower supporting the top deck,  $(D/L) = (20.0/328.70) = 0.0609 < 0.2$ ; therefore, linear wave is sufficient for the wave force on the cylindrical tower structure. For the short cylindrical structure representing the hemispherical domes on top of the bottom (individual) cylindrical caissons,  $(D/L)$  ratio =  $(87.2/328.70) = 0.2653$ ; hence, diffraction effects should be considered for this short portion of the bottom caisson. Also for the bottom caisson,  $(D/L)$  ratio =  $(90.0/328.70) = 0.2738$ ; consequently, diffraction effects should also be considered for the caisson.

(1) Cylindrical tower supporting the top deck:

Using Airy’s wave theory and Morison–O’Brien’s equation (see Sections 3.4.2.1 and 6.3.4.1),

Wave force acting on the structure is given as  $F_{\text{Total}} = (F_{\text{Drag}}) + (F_{\text{Inertial}})$

$$\begin{aligned}
 F_{\text{Drag}} &= \int_{-d}^0 (f_{\text{Drag}}) dz = \int_{-d_1}^0 [(1/2)\rho w C_D (D)] (u)|u| dz \\
 &= \int_{-d_1}^0 [(1/2)\rho w C_D (D)] (u)|u| dz = [(1/2)\rho w C_D (D)] \cdot [(\pi H/T)^2 (1/\sinh kd)^2] \\
 &\quad \cdot \left[ \int_{-d_1}^0 \{ \cosh k(d+z) \} \{ \cos(kx - \sigma t) \} \{ \cosh k(d+z) \} \{ \cos(kx - \sigma t) \} dz \right] \quad \text{(E9.1)} \\
 &= [(1/2)\rho_w C_D (D)] \cdot [(\pi H/T)^2 (1/\sinh kd)^2] [ | \cos(kx - \sigma t) | \cos(kx - \sigma t) ] \\
 &\quad \cdot \int_{-d_1}^0 \{ \cosh k(d+z) \}^2 dz
 \end{aligned}$$

The term within the brackets in Equation E9.1 on integration becomes

$$\begin{aligned}
 \int_{-d_1}^0 \{ \cosh k(d+z) \}^2 dz &= \int_{-d_1}^0 (1/2) [ 1.0 + \cosh \{ 2(kd + kz) \} ] dz \\
 &= (1/2) [ z + (1/2k) \sinh(2kd + 2kz) ]_{-d_1}^0 \\
 &= (1/2) [ (d_1) + (1/2k) \{ \sinh 2k(d) - \sinh 2k(d - d_1) \} ] \quad \text{(E9.2)}
 \end{aligned}$$

Hence,

$$F_{\text{Drag}} = \left[ \left\{ (1/2) \rho_w C_D(D) \right\} \cdot \left\{ (\pi H/T)^2 (1/\sinh kd)^2 \right\} \right] \\ \cdot (1/2) \left[ (d_1) + (1/2k) \{ \sinh 2k(d) - \sinh 2k(d - d_1) \} \right] \\ \cdot \left[ |\cos(kx - \sigma t)| \cos(kx - \sigma t) \right] \quad (\text{E9.3})$$

When  $x = 0$ ,

$$F_{\text{Drag}} = \left[ \left\{ (1/2) \rho_w C_D(D) \right\} \cdot \left\{ (\pi H/T)^2 (1/\sinh kd)^2 \right\} \right] \\ \cdot (1/2) \left[ (d_1) + (1/2k) \{ \sinh 2k(d) - \sinh 2k(d - d_1) \} \right] \\ \cdot \left[ |\cos(\sigma t)| \cos(\sigma t) \right] \quad (\text{E9.4})$$

Substituting the values for  $\rho_w = 1025.0 \text{ kg/m}^3$ ,  $C_D = 1.0$ ,  $D = 20.0 \text{ m}$ ,  $H = 25.0 \text{ m}$ ,  $T = 14.5 \text{ s}$ ,  $k = (2\pi/L) = [2\pi/(160.0/0.4891)] = 0.01921$ ,  $d = 160.0 \text{ m}$ , and  $d_1 = 93.63 \text{ m}$ , one obtains

$$F_{\text{Drag}} = (10,250.0)(8354.20) |\cos(\sigma t)| \cos(\sigma t) = (0.8563)(10^8) |\cos(\sigma t)| \cos(\sigma t) \text{ N}$$

Similarly,

$$F_{\text{Inertial}} = \int_{-d}^0 (f_{\text{inertial}}) dz = \int_{-100.0}^{0.0} \left[ \rho_w C_M (\pi D^2 / 4) \right] (\dot{u}) dz \\ = \left[ \rho_w C_M (\pi D^2 / 4) \right] (2\pi^2 H / T^2) \int_{-100.0}^0 \left\{ \cosh k(d+z) / \sinh kd \right\} \sin(kx - \sigma t) dz \quad (\text{E9.5})$$

Substituting the values,

$$F_{\text{Inertial}} = (644,026.49)(2.347) \left[ (1/k) \sinh k(d+z) \right]_{-100.0}^{0.0} \sin(kx - \sigma t) \\ = (1.512)(10^6) \left\{ (1.0)/(0.01921) \right\} (10.787 - 1.425) \sin(kx - \sigma t) \\ = (7.3665)(10^8) \sin(kx - \sigma t) \text{ N} = -(7.3665)(10^8) \sin(\sigma t) \text{ (when } x = 0.0)$$

Total horizontal wave force on the cylindrical portion of the gravity platform  
 $= (0.8563)(10^8) |\cos(\sigma t)| \cos(\sigma t) - (7.3665)(10^8) \sin(\sigma t) \text{ N}$

Maximum wave force on the cylindrical portion of the platform  $= \pm(0.737)(10^8) \text{ N}$

Assuming the forces to vary approximately in a (truncated) exponential manner, the center of action (from the seabed) of the wave forces on the cylindrical structure  $\simeq 66.37 + (2/3)(93.63) = 128.82 \text{ m}$ .

(2) Wave forces on the section of caisson, representing the hemispherical domes:

We have to compute the diffraction forces acting on the cylindrical section representing the hemispherical domes. As per Section 6.3.4.7, the diffraction wave forces are computed by following the formulations given in references [61, 62] as

$$F(t) = (2\rho_w g H / k^2) [A(ka) \{ \sinh k(d - d_1) - \sinh k(d - d_2) \} / \cosh kd] \cos(\omega t - \alpha) \quad (\text{E9.6})$$

where the parameters of Equation E9.5 are given below as

$$A(ka) = \left[ \{J_1'(ka)\}^2 + \{Y_1'(ka)\}^2 \right]^{1/2}$$

$$\alpha = \left( \{J_1'(ka)\} / \{Y_1'(ka)\} \right) \tag{E9.7}$$

with  $d_1$  and  $d_2$  being the depths of the equivalent dome-cylinder section from the sea level.

$$a = (87.2/2) = 43.6 \text{ m}$$

$$J_1'(ka) = (1/2) \left[ J_0 \{ (0.01921)(43.6) \} - J_2 \{ (0.01921)(43.6) \} \right] = (1/2)(0.82 - 0.08) = 0.37$$

$$Y_1'(ka) = (1/2) \left[ Y_0(0.8375) - Y_2(0.8375) \right] = (0.5) \left[ (0.05) - (-2.0) \right] = 1.025$$

In the above computations,  $J_0(ka)$ ,  $J_2(ka)$ ,  $Y_0(ka)$  and  $Y_2(ka)$  are the Bessel functions of first and second kinds (of order  $n = 0, 2$ ) for the argument  $(ka)$ .

$$\alpha = (0.37)/(1.025) = 0.361 \text{ rad} = 20.68^\circ$$

$$A(0.8375) = \left[ (0.37)^2 + (1.025)^2 \right]^{1/2} = 1.089$$

$$F(t) = \left[ (2.0)(1025.0)(9.81)(25.0)(1.0/0.01921)^2(1.089) \right] \left[ \sinh(0.01921)(160.0 - 93.63) \sinh(0.01921)(160.0 - 100.0) \right] \left[ 1.0 / \{ \cosh(0.01921)(160.0) \} \right] \left[ \cos(\omega t - 0.361) \right] = \left[ (1.4837)(10^9) \right] \left[ (0.2206) / (10.833) \right] \left[ \cos(\omega t - 0.361) \right] = (3.021)(10^7) \cos(\omega t - 0.361) \text{ N}$$

Maximum wave force from this part of the platform that will be in phase with the maximum of the cylindrical tower above =  $(3.021)(10^7) \cos(-0.361) = \pm(2.826)(10^7) \text{ N}$ . Approximate center of action (from the seabed) of the wave forces on this section of the gravity platform  $\sim 60.0 + (1/2)(6.37) = 63.185 \text{ m}$ .

(3) Wave forces on the bottom caisson section:

The diffraction forces on the bottom caisson section is computed using Equations E9.6 and E9.7, with  $d_1 = 100.0 \text{ m}$  and  $d_2 = 160.0 \text{ m}$  as

$$A = 90.0/2 = 45.0 \text{ m}; ka = (0.01921)(45.0) = 0.8645$$

$$J_1'(ka) = (1/2)(0.80 - 0.085) = 0.3575$$

$$Y_1'(ka) = (1/2) \left[ 0.03 - (-1.90) \right] = 0.965$$

$$\alpha = (0.3575)/(0.965) = 0.3704 \text{ rad} = 21.23^\circ$$

$$A(0.8645) = \left[ (0.3575)^2 + (0.965)^2 \right]^{1/2} = 1.029$$

$$F(t) = \left[ (2.0)(1025.0)(9.81)(25.0)(1.0/0.01921)^2(1.029) \right] \left[ \sinh(0.01921)(160.0 - 100.0) - \sinh(0.01921)(160.0 - 160.0) \right] \left[ 1.0 / \{ \cosh(0.01921)(160.0) \} \right] \left[ \cos(\omega t - 0.3704) \right]$$

$$= \left[ (1.4019)(10^9) \right] \left[ \left\{ (1.4253) - (0.0) \right\} / 10.833 \right] \left[ \cos(\omega t - 0.3704) \right]$$

$$= (1.844)(10^8) \cos(\omega t - 0.3704) \text{ N}$$

Maximum wave force in this section that is in phase with that on the cylindrical tower above =  $(1.844)(10^8)\cos(-0.3704) = \pm(1.719)(10^8)$  N. Since the wave force varies close to an exparabolic curve, the approximate center of action (from the seabed) of this wave force on the gravity platform  $\sim(3/4)(60.0) \sim 45.0$  m.

- (4) Total wave forces and moments about the base of the platform:

$$\begin{aligned} \text{Total maximum horizontal wave force} &= \pm(0.737)(10^8) \pm (2.826)(10^7) \pm (1.719)(10^8) \\ &= (5.282)(10^8) \text{ N} \end{aligned}$$

$$\begin{aligned} \text{Total maximum wave moment about the base} &= [(0.737)(10^8)](128.82) + \\ &+ [(2.826)(10^7)](63.185) + [(1.719)(10^8)](45.0) = (190.89)(10^8) \text{ N m} \end{aligned}$$

- (b) Wind forces acting on the gravity platform:

According to Equation 6.11, the wind forces acting on any structure is given by

$$F_{wz} = (1/2)C_D\rho_w U_z^2 A \quad (\text{E9.8})$$

where  $C_D$  is the drag coefficient for the surface,  $\rho_w$  is the mass density of air,  $U_z$  is the mean wind velocity (over the averaging wind duration) used for the surface, and  $A$  is the exposed area. According to Table 6.7, the simplest wind velocity equation for wind at a height of  $z$  above the mean sea level is given by

$$\bar{U}_z = \bar{U}_{10}(z/10)^{1/7} \quad (\text{E9.9})$$

where  $U_{10}$  is the mean wind velocity at a height of 10.0 m above the mean sea surface level.

- (1) Exposed part of the cylindrical tower:

From Table 3.5, for a wind averaging period of 10.0 min, gust factor = 1.0.

$$\begin{aligned} \text{Wind velocity on the cylindrical tower at 10.0 m above mean sea level} \\ = (200.0)(1000.0)/\{(60)(60)\} = 55.56 \text{ m/s} \end{aligned}$$

$$\text{Wind velocity at 30.0 m above mean sea level} = (55.56)(30/10)^{(1/7)} = 65.01 \text{ m/s}$$

$$\begin{aligned} \text{Taking the average wind velocity as the wind velocity over the cylindrical tower} \\ = (55.56 + 65.01)/2 = 60.28 \text{ m/s} \end{aligned}$$

$$\begin{aligned} \text{Reynold's number for the wind flow [63]} &= (\nu)(D)/\nu = (60.28)(20.0)/\{(14.20)(10^{-6})\} \\ &= (8.49)(10^{-7}) \text{ m}^2/\text{s} \end{aligned}$$

As per Table 6.9,  $C_D = 0.60$ .

$$\text{Density of air [64]} = 1.293 \text{ kg/m}^3$$

$$\begin{aligned} \text{Wind forces over the exposed part of the cylindrical tower} \\ = (1/2)(0.60)(1.293)\{(1.0)(60.28)\}^2\{(20.0)(30.0)\} = (0.846)(10^6) \text{ N} \end{aligned}$$

$$\text{Center of the force acting on cylindrical tower from seabed} = 160.0 + 15.0 = 175.0 \text{ m}$$

$$\text{Wind moment about the seabed} = \{(0.846)(10^6)\}(175.0) = (1.481)(10^8) \text{ N m}$$

- (2) Over the top deck (deck height varies from 30.0 to 60.0 m):

From Table 3.5, for a wind averaging period of 10.0 min, gust factor = 1.0.

Wind velocity at 30.0 m above mean sea level = 65.01 m/s (computed earlier)

Wind velocity at 60.0 m above mean sea level =  $(55.56)(60/10)^{(1/7)} = (55.56)(1.292) = 71.784$  m/s

Average wind speed over the top deck =  $(65.01 + 71.784)/2 = 68.397$  m/s

From Table 6.8, for a cubic structure and short cylindrical structure,  $C_D$  varies between 1.05 and 1.15; hence,  $C_D$  is taken as 1.10.

Wind forces over the top deck =  $(1/2)(1.10)(1.293)\{(1.0)(68.397)\}^2\{(30.0)(70.0)\} + (1/2)\{(0.95)(1.10)\}(1.293)\{(1.0)(68.397)\}^2\{(30.0)(70.0)\} = (6.986)(10^6)$  N

Center of force acting on the top deck from the seabed =  $160.0 + 30.0 + 15.0 = 205.0$  m

Wind moment about the seabed =  $\{(6.986)(10^6)\}(205.0) = (1.432)(10^9)$  N m

(3) Over the drilling rig:

The rig is assumed to be composed of  $0.15 \times 0.15$  equal angular cross sections.

From Table 3.5, for a wind averaging period of 10.0 s and a basic wind speed of 120.0 mph (~192.0 kmph), the gust factor = 1.10.

The drill rig is divided into two sections, viz., (i) between 60.0 and 80.0 m above the mean sea level and (ii) between 80.0 and 105.0 m above the mean sea level.

Wind velocity at 60.0 m above mean sea level = 71.784 m/s (computed earlier)

Wind velocity at a height of 80.0 m above the mean sea level =  $(55.56)(80.0/10.0)^{(1/7)} = (1.3459)(55.56) = 74.78$  m/s

Average wind velocity between 60.0 and 80.0 m above the mean sea level =  $(71.784 + 74.78)/2 = 73.28$  m/s

Average width of the equivalent rectangular section =  $\{[(1.0) + (9.0)(20.0/45.0)] + 10.0\}/2 = 7.5$  m

As per Table P6.1, #22, solidity ratio is given as =  $[(20.0)(0.15)(2) + (7.5)(0.15) + (21.36)(0.15)]/\{(20.0)(7.5)\} = (10.329)/(150.0) = 0.069$ .

Consequently, the coefficient of drag for the windward truss frame = 1.94.

Wind force over this truss section =  $(1/2)(1.94)(1.293)\{(1.10)(73.28)\}^2\{10.329\} + (1/2)\{(0.95)(1.94)(1.293)\}\{(1.10)(73.28)\}^2\{10.329\} = (8.42 + 8.0)(10^4) = (16.42)(10^4)$  N

Center of force acting on this section of drill rig, above the seabed =  $220.0 + 10.0 = 230.0$  m

Wind velocity at a height of 105.0 m above the mean sea level =  $(55.56)(105.0/10.0)^{(1/7)} = (55.56)(1.3992) = 77.66$  m/s

Average wind velocity between 80.0 and 105.0 m =  $(74.78 + 77.66)/2 = 76.22$  m/s

Average width of the equivalent rectangular section =  $(5.0 + 1.0)/2 = 3.0$  m

As per Table P6.1, #22, solidity ratio is given as =  $[(25.0)(0.15)(2) + (3.0)(0.15) + (25.2)(0.15)]/\{(25.0)(3.0)\} = (11.73)/(75.0) = 0.1564$ .

Consequently, the coefficient of drag for the windward truss frame = 1.94.

$$\text{Wind force over this truss section} = (1/2)(1.94)(1.293)\{(1.10)(73.28)\}^2\{11.73\} + (1/2)(0.91)(1.94)(1.293)\{(1.10)(73.28)\}^2\{11.73\} = (9.56 + 8.70)(10^4) = (18.26)(10^4) \text{ N}$$

$$\text{Center of force acting on this section of drill rig, above the seabed} = 220.0 + 20.0 + 12.5 = 252.5 \text{ m}$$

$$\text{Wind moment about the seabed} = \{(16.42)(10^4)\}(230.00) + \{(18.26)(10^4)\}(252.5) = (8.39)(10^7) \text{ N m}$$

(4) Total wind forces and moments acting on the gravity platform:

$$\text{Horizontal wind forces acting on the gravity platform} = (0.846)(10^6) + (6.986)(10^6) + (0.1826)(10^6) = (8.015)(10^6) \text{ N}$$

$$\text{Wind moments about the seabed} = (1.481)(10^8) + (14.32)(10^9) + (0.839)(10^7) = (16.64)(10^8) \text{ N m}$$

(c) Overturning resistance of the in situ gravity platform about the seabed:

$$\text{Total vertical loads acting on the gravity platform} = (4.6443)(10^9) \text{ N}$$

$$\text{Total horizontal load acting on the platform} = (5.282)(10^8) + (8.015)(10^6) = (5.362)(10^8) \text{ N}$$

$$\text{Total moments about the seabed} = (190.89)(10^8) + (16.64)(10^8) = (207.53)(10^8) \text{ N m}$$

$$\text{Eccentricity of the vertical load about the base of the gravity platform} = (M)/(P_v) = 4.468 \text{ m}$$

Since the eccentricity of the load is less than one-sixth of the platform diameter (= 15.0 m), the platform is safe against the overturning forces.

(d) Bearing capacities of the foundation soil:

(1) Undrained bearing capacity of soil:

Using calculations similar to the one given in Example 9.1, the following values are obtained:

$$S = \pi(45)^2/2 - [(4.468)\{45^2 - 4.468^2\}^{(1/2)} + (45)^2\sin^{-1}(4.468/45.0)] = 2779.40 \text{ m}^2$$

$$L' = [(2.0)(2779.40)\{(45.0 + 4.468)/(45.0 - 4.468)\}^{(1/2)}]^{(1/2)} = 78.365 \text{ m}$$

$$B' = (78.365)(40.532/49.468)^{(1/2)} = 70.934 \text{ m}$$

$$A' = L'B' = 5558.74 \text{ m}^2$$

As per Equation 4.37, the undrained bearing capacity of the foundation is given by Equation A.1. The value of  $N_{c'}$ ,  $N_{q'}$ , and  $N_{\gamma'}$  are given in Figure 4.53. According to the figure, the values of  $N_{c'}$ ,  $N_{q'}$ , and  $N_{\gamma'}$  for a value of  $\phi' = 25^\circ$ , are given as  $N_{c'} = 20.71$ ,  $N_{q'} = 10.86$ , and  $N_{\gamma'} = 10.87$ .

Hence, the undrained bearing capacity of the platform foundation is given by

$$Q = (c_u N_c K_c + \gamma X)A'$$

$K_c = i_c s_c d_c b_c g_c$ , the factors  $i_c$ ,  $s_c$ ,  $d_c$ ,  $b_c$ , and  $g_c$  are, respectively, the correction factors for load inclination, foundation shape, depth of embedment, foundation



inclination, and seabed slope below the platform foundation. In the present case,  $X = 0.0$ ; hence,

$$Q = [(120.0)(20.71)K_c](5558.74)$$

When  $\varphi > 0^\circ$ , then  $i_c = i_q - (1.0 - i_q)/\{N_c \tan(\varphi)\}$ ;  $i_q = [1.0 - H/(Q + (B'L')\cot(\varphi))]$

$$m = m_L \cos^2(\theta) + M_B \sin^2(\theta), \text{ with } m_L = (2.0 + L'/B')/(1.0 + L'/B')$$

$$m_B = (2.0 + B'/L')/(1.0 + B'/L')$$

Hence,  $m_L = [2.0 + (78.365/70.934)]/[1.0 + (78.365/70.934)] = 1.475$

$$m_B = [2.0 + (70.934/78.365)]/[1.0 + (70.934/78.365)] = 1.525$$

$$m = 1.475 \cos^2(90^\circ) + 1.525 \sin^2(90^\circ) = 1.525$$

$$i_q = [1.0 - (536,200)/\{Q + (70.934)(78.365)(120.0)\cot(25^\circ)\}]^{1.525}$$

In the above equation,  $Q$  is an unknown value; hence, the proper value has to be determined by a process of trial and error.

*Trial 1:* Assume the value of  $K_c = 1.0$ ; hence,  $Q = [(120.0)(20.71)(1.0)](5558.74) = 13,814,580.7$  kN.

$$\text{Hence, } i_q = [1.00 - 0.0352]^{1.525} = 0.9468.$$

$$i_c = 0.9468 - (1.0 - 0.9468)/\{(20.71)\tan(25^\circ)\} = 0.9468 - 0.0055 = 0.9413$$

For eccentric loads on circular foundations, one should use the shape factors used for an eccentrically loaded rectangular footing.

$$s_c = 1.0 + (B'/L')(N_q/N_c) = 1.0 + (70.934/78.365)(10.86/20.71) = 1.4747$$

$$d_q = 1.0 + (2.0)\tan(\varphi)[1.0 - \sin(\varphi)]^2(D/B') = 1.0 + (2.0)\tan(25^\circ)[1.0 - \sin(25^\circ)]^2(90.0/70.934) = 1.395$$

$$d_c = d_q - (1.0 - d_q)/\{N_c \tan(\varphi)\} = 1.395 - (1.0 - 1.395)/\{(20.71)\tan(25^\circ)\} = 1.395 + 0.041 = 1.436$$

$$b_q = [1.0 - (v)\tan(\varphi)]^2 = 1.0$$

$$b_c = 1.0 - (1.0 - b_q)/\{N_c \tan(\varphi)\} = 1.00$$

$$g_q = [1.0 - \tan(\beta)]^2 = 1.0$$

$$g_c = 1.0 - (1.0 - g_q)/\{N_c \tan(\varphi)\} = 1.00$$

Note that in the last two calculations,  $v$  and  $\beta$  are the base and ground inclinations of the gravity platform foundations; here, they are equal to 0.0.

Hence,  $K_c = i_c s_c d_c b_c g_c = (0.9413)(1.4747)(1.436)(1.00)(1.00) = 1.9934$ .

Applying this value of  $K_c$  in Equation A.1,

$Q = [(120.0)(20.71)(1.9934)](5558.74) = 27,537,985.1$  kN. Since the difference between the earlier and the present value of  $Q$  is nearly 49.83%, a second trial is made to find the correct value.

*Trial II:* Take the previous value of  $K_c = 1.9934$ .

$$i_q = [1.0 - (536,200)/(27,537,985.1 + (70.934)(78.365)(120.0)\cot(25^\circ))]^{1.525} = 0.9719$$

$$i_c = 0.9719 - (1.0 - 0.9719)/[(20.71)\tan(25^\circ)] = 0.9690$$

Since all the other coefficients needed for the computation of the correction term  $K_c$  do not change,

$$K_c = (0.9690)(1.4747)(1.436)(1.00)(1.00) = 2.052$$

$$\text{Corrected } Q = [(120.0)(20.71)(2.052)](5558.74) = 28,347,519.49 \text{ kN}$$

The difference between the earlier and present one is 2.86%.

*Trial III:* Take the previous value of  $K_c = 2.052$ .

$$i_q = [1.0 - 510,000/(28,347,519.49 + (0.9727)(78.365)(120.0)\cot(25^\circ))]^{1.525} = 0.9727$$

$$i_c = 0.9727 - (1.0 - 0.9727)/[(20.71)\tan(25^\circ)] = 0.9699$$

$$\text{Correction factor } K_c = (0.9699)(1.4747)(1.436)(1.0)(1.0) = 2.054$$

$$\text{Corrected } Q = [(120.0)(20.71)(2.054)](5558.74) = 28,375,148.7 \text{ kN}$$

Percentage error = 0.01%. In this case, the value is assumed to have converged. Hence, the undrained bearing capacity of the foundation is = 28,375,148.7 kN.

Maximum factored vertical load on the foundation (load factor = 1.0) =  $(4.6443)(10^9)$  kN.

Buoyant factored load of the gravity platform (computed earlier) =  $(1.0)(2.875)(10^5)$  (=  $P_{DB}$ )

As per API code provisions,  $P_{DB} \leq \Phi_{SB}Q_{DB}$ . Hence,  $\Phi_{SB}Q_{DB} = (0.67)(28,375,148.7) = 19,011,349.6 \text{ kN} > 287,500 \text{ kN}$ .

Therefore, the undrained soil foundation is quite safe against vertical load coming on the soil.

(2) Drained bearing capacity of the foundation soil:

It is given as

$$Q' = [c'N_cK_c + qN_qK_q + (1/2)\gamma'BN_\gamma K_\gamma]A'$$

The respective correction factors are

$$K_c = i_c s_c d_c b_c g_c | K_q = i_q s_q d_q b_q g_q | K_\gamma = i_\gamma s_\gamma d_\gamma b_\gamma g_\gamma$$

The computed value (after three trials) of  $i_q$  (= 0.9727) has already been calculated.

$$s_q = 1.0 + (B'/L')\tan(\phi') = 1.0 + (70.934)/(78.365)\tan(25^\circ) = 1.422$$

$$d_q = 1.436; b_q = 1.0; g_q = 1.0 \text{ (calculated earlier)}$$

$$K_q = (0.9727)(1.422)(1.436)(1.0)(1.0) = 1.9862$$

Hence,

$$Q = (c_c N_c K_c) A' = [(120.0)(20.71)(1.9862)](5558.74) = 27,438,520.0 \text{ kN.}$$

$$i_y = [1.0 - H/\{Q + (B'L'c)\cot(\varphi')\}]^{(m+1)} = [1.0 - (536,200)/\{(27,438,520.0) + (70.934)(78.365)(120.0)\cot(25^\circ)\}]^{2.525} = [0.9814]^{2.525} = 0.9537$$

$$s_y = 1.0 - (0.4)(B'/L') = 0.638$$

$$d_y = 1.0; b_y = 1.0; \text{ and } g_y = 1.0$$

$$K_y = (0.9537)(0.638)(1.0)(1.0)(1.0) = 0.6085$$

Equivalent  $B$  of the circular foundation = 79.760 m

$$\text{Drained bearing capacity of the foundation soil} = Q' = [(60.0)(20.71)(2.052) + 0.0 + (0.5)(17.5)(79.760)(10.87)(0.6085)](5558.74) = 39,833,939.0 \text{ kN} (= Q_{DB})$$

The drained cohesive intercept (in Mohr's circle) is taken as equal to  $c'$ , the effective cohesive strength of soil; also the minimum lateral dimension is taken as the square root of the area of the circular foundation.

For bearing strength failure (as per API RP-2A provisions),  $P_{DB} \leq \Phi_{SB} Q_{DB}$ .

$$P_{DB} = 287,500.0 \text{ kN}$$

$$\Phi_{SB} Q_{DB} = (0.67)(39,833,939.0) = 26,688,739.1 \text{ kN} > P_{DB} (= 287,500.0 \text{ kN})$$

Hence, the drained bearing strength is quite sufficient to resist the maximum vertical load coming on the drained foundation.

(e) Sliding resistance of the foundation:

(1) For undrained soil: sliding resistance of the foundation =  $H = cA = (120.0)(\pi/4)(90)^2 = 763,407.02 \text{ kN}$ , where  $c$  is the undrained shear strength of the soil.

For a stable foundation, the sliding resistance should be greater than the factored applied horizontal load (= 536,200.0 kN).

As per API RP-2A provisions,

$$P_{DS} \leq \Phi_{SS} Q_{DS}$$

$$\Phi_{SS} Q_{DS} = (0.80)(763,407.02) = 610,725.6 \text{ kN} > 536,200.00 \text{ kN}$$

Hence, the foundation is safe against sliding failure under undrained condition.

Provisionally, additional bottom soil resistance against sliding can be provided as mentioned for increasing the sliding resistance in Example 9.1.

(2) For drained soil: the sliding resistance of the foundation =  $H = c'A + Q'\tan(\varphi')$ .

$$H = (60.0)(\pi/4)(90.0)^2 + (39,833,939.0)(\tan(25^\circ)) = 18,956,574.60 \text{ kN}$$

per API RP-2A provisions,

$$P_{DB} \leq \Phi_{SB} Q_{DB}$$

$$536,200 \text{ kN} \leq (0.80)(18,956,574.60) (< 15,165,259.5 \text{ kN})$$

Hence, the drained sliding resistance is quite sufficient to resist the horizontal load coming on the platform.

(IV) Short- and long-term settlements of the gravity platform:

According to Equation 9.12, the *short-term deformations* are given by

$$\text{Buoyant weight of the platform} = (2.875)(10^2) \text{ MN} = (2.875)(10^5) \text{ kN}$$

$$\text{Total horizontal loads acting on the platform} = (5.362)(10^8) \text{ N} = (5.362)(10^5) \text{ kN}$$

$$\text{Total overturning moment about the base} = (207.53)(10^8) \text{ N m} = (207.53)(10^5) \text{ kN m}$$

$$\text{Shear modulus of the foundation soil} = 1000s_u = (1000.0)(120.0) \text{ kN}$$

$$\begin{aligned} \text{Short-term vertical deformation} &= (1.0 - \nu)P_v / \{(4.0)(GR)\} \\ &= (1.0 - 0.45)\{(2.875)(10^5)\} / \{(4.0)\{(1000.0)(120.0)\}(90.0)\} = 3.66 \text{ mm} \end{aligned}$$

$$\begin{aligned} \text{Short-term horizontal deformation} &= (7.0 - 8\nu)H / \{(32.0)(1.0 - \nu)(GR)\} \\ &= \{7.0 - (8.0)(0.45)\}\{(5.362)(10^5)\} / \{(32.0)(1.0 - 0.45)\{(1000.0)(120.0)\}(90.0)\} \\ &= 9.05 \text{ mm} \end{aligned}$$

$$\begin{aligned} \text{Short-term rocking rotation of the platform} &= (3.0)(1.0 - \nu)M / \{(8.0)GR^3\} \\ &= (3.0)(1.0 - 0.45)\{(207.53)(10^5)\} / \{(8.0)\{(1000.0)(120.0)\}(90.0)^3\} \\ &= (0.0489)(10^{-3}) \text{ rad} = 0.0028^\circ \end{aligned}$$

According to Equation 9.13, the long-term settlements are given by

$$u_v = \{(hC)/(1 + e_0)\} \log_{10}\{(q_0 + \Delta q)/q_0\}$$

Initial average soil stress due to 7.5-m thickness of silty-clay layer =  $q_0 = (7.5)\{17.5 - (1025.0)(9.81)/(1000.0)\} = 7.445 \text{ kN/m}^2$

Additional stress imposed on the soil due to buoyant weight =  $\Delta q_0 = \{(2.875)(10^5)\} / \{(\pi/4)(90)^2\} = 45.192 \text{ kN/m}^2$

Hence, the long-term vertical settlement of the platform is given as =  $\{15.0(0.30)/(1.0 + 0.63)\} \log_{10}\{(7.445 + 45.192)/(7.445)\} = 2.345 \text{ m}$ .

(V) Rotational frequency and maximum transverse response of the gravity platform at the level of top of deck:

$$\text{Rotational frequency} = [\text{rotational inertia/rotational stiffness}]^{(1/2)}$$

Rotational inertia of the buoyant platform [see items I and II (b)] =  $(23.181)(10^{11}) \text{ kg m}^2$

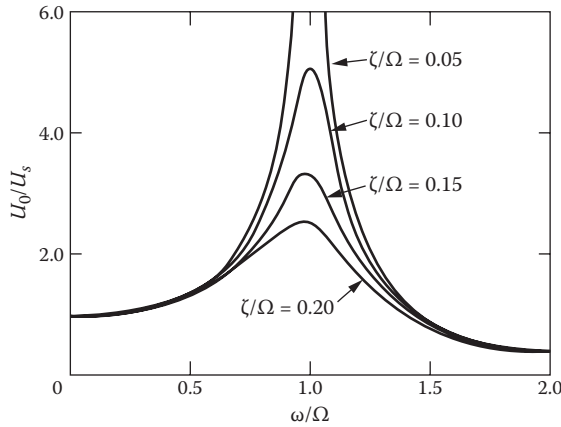
From item IV, rotational stiffness = (rotational moment)/rocking rotation =  $[(207.53)(10^8)] / [(0.0489)(10^{-3})] = (42.44)(10^{13}) \text{ N m/rad}$

$$\begin{aligned} \text{Rotational frequency} &= \{[(42.44)(10^{13})] / [(23.181)(10^{11})]\}^{(1/2)} = 13.53 \text{ rad/s} = 13.53/(2\pi) = \\ &2.153 \text{ Hz} (= 0.464 \text{ s}) \end{aligned}$$

This seems to be far-off from the dominant wave frequency of 14.5 s on the stiffness-dominant side [see Figure E9.4 [65], with  $\omega/\Omega = (1/14.5)/(1/0.464) = 0.0320$ ].

Hence, the dynamic magnification factor is  $\sim 1.0$  (shown in Figure E9.4 as  $U_0/U_s$ ).

The displacement of the top of the platform under the maximum wave excitation will be  $\{(0.0489)(10^{-3})\}(220.0) = 0.0108 \text{ m} = 10.8 \text{ mm}$ .



**FIGURE E9.4** Dynamic magnification factor diagram. (From T.H. Dawson, *Offshore Structural Engineering*, Prentice Hall, Inc., Englewood Cliffs, NJ, p. 218, 1983. With permission.)

**Example 9.3: Design of Salient Components of the Gravity Platform**

Considering the same data as those given in Example 9.2, design the platform components, viz., (i) cylindrical tower; (ii) a typical caisson; (iii) a typical spherical dome of the caisson; (iv) spherical bottom of the cylindrical caissons; and (v) bottom skirts on the periphery of the foundation. The foundation slab of 1.0 m thick is assumed to be properly integrated with the 6.37-m-high hemispherical dome section on the bottom of the caissons. Also assume that the platform has foundation skirts of reinforced concrete of thickness 0.60 m and 3.0 m deep (assuming the cylindrical tower skirts to be similar to those shown in Figure 9.3a and b).

*Assumptions:* (i) Making use of the analysis simplifications shown in Figures 9.11 through 9.14, and the simplifications illustrated in Figure 9.15, the computations are made for every 15.0-m-height sections for the caissons and every 20.0-m sections for the vertical cylindrical tower sections. (ii) The load from the top deck is dominantly transferred as shear loads at the deck–cylindrical–tower interface, with zero bending moments at this interface. (iii) The interface between the bottom of the cylindrical tower of 20.0-m diameter and the top of the interior caisson of 30.0-m diameter has to be properly designed; a convenient transformation between the two components would be to have the frustum of a conical shell to connect between the two cylindrical shell components of the gravity platform, at the levels between 85.0 and 93.63 m below the mean sea level. (iv) The bending moments due to wave forces are computed in an approximate manner by multiplying the total wave forces (obtained by integration) and the computed approximate distance to the center of computed wave force.

(I) Design forces and pressures on the gravity platform component members:

(i) Cylindrical tower sections

The computations given in Section II (i) (of Example 9.2) are selectively made use of to reduce the computations made in this section (viz., Equations E9.1 and E9.5 are made use of either before or after integration).

For the tower bending, the bending moment shear forces are computed at depths (below the mean sea level) of –20.0, –40.0, –60.0, –80.0, and –85.0 m, whereas for the cylindrical section or cylindrical arch section, forces are computed at depths of 10.0, 30.0, 50.0, 70.0, and 82.5 m.

(a) Bending moments and shear forces for tower bending

At  $z = + 30.0$  m:

$$\text{Bending moment} = 0.0$$

$$\text{Shear force} = [(6.986)(10^6) + (16.42)(10^4) + (18.26)(10^4)] \text{ N} = (7.3328) \text{ MN (computed earlier)}$$

$$\text{Axial load} = 491.0 \text{ MN (computed earlier)}$$

At  $z$  (or  $d_1$ ) = -20.0 m:

$$\text{Shear force due to wind} = [(7.3328)(10^6) + (0.846)(10^6)] \text{ N} = 8.1788 \text{ MN}$$

$$\begin{aligned} \text{Bending moment due to wind} &= (7.3328)(30.0 + 20.0) + (0.846)\{(30.0/2) + 20.0\} \\ &= 366.64 + 29.61 = 396.25 \text{ MN m} \end{aligned}$$

Shear force due to wave action (from Equations E9.1 and E9.2)

$$= \left\{ \left[ \frac{1}{2} \rho_w C_D(D) \right] \cdot \left[ \frac{\pi H/T}{2} \right]^2 \left( \frac{1}{\sinh kd} \right)^2 \right\} \left[ \frac{1}{2} \right] \left[ z + \left( \frac{1}{2} k \right) \sinh(2kd + 2kz) \right]_{-d_1}^0 +$$

$$\left[ \rho_w C_M \left( \frac{\pi D^2}{4} \right) \right] \left[ \frac{2\pi^2 H/T^2}{2} \right] \left[ \left( \frac{1}{k} \right) \sinh \pi k(d+z) \right]_{-d_1}^{0,0}$$

$$= (10,250.0)(2.629)(0.5)[606.42 + 20.0 - (26.028)(10.787)] + (644,026.5)(2.347)(173.902 - 115.425) \text{ N} = 4,657,238.8 + 88,389,751.2 \text{ N} = 93.047 \text{ MN}$$

$$\text{Bending moment due to wave action} = (93.047)(2/3)(20.0) = 1240.63 \text{ MN m}$$

$$\text{Total shear force at this section} = 8.1788 + 93.047 = 101.226 \text{ MN}$$

$$\text{Total bending moment at this section} = 396.25 + 1240.63 = 1636.88 \text{ MN m}$$

$$\text{Total axial load} = 491.0 + (\pi/4)(20.0^2 - 18.8^2)(50.0)(2500.0)/(10^6) = 491.0 + 4.571 = 495.571 \text{ MN}$$

At  $z$  (or  $d_1$ ) = -40.0 m:

$$\text{Shear force due to wind} = 8.1788 \text{ MN (computed earlier)}$$

$$\begin{aligned} \text{Bending moment due to wind} &= (7.3328)(50.0 + 20.0) + (0.846)\{(30.0/2) + 40.0\} \\ &= 513.30 + 46.53 = 559.83 \text{ MN m} \end{aligned}$$

Shear force due to wave action =

$$\left\{ \left[ \frac{1}{2} \rho_w C_D(D) \right] \cdot \left[ \frac{\pi H/T}{2} \right]^2 \left( \frac{1}{\sinh kd} \right)^2 \right\} \left[ \frac{1}{2} \right] \left[ z + \left( \frac{1}{2} k \right) \sinh(2kd + 2kz) \right]_{-d_1}^0 +$$

$$\left[ \rho_w C_M \left( \frac{\pi D^2}{4} \right) \right] \left[ \frac{2\pi^2 H/T^2}{2} \right] \left[ \left( \frac{1}{k} \right) \sinh k(d+z) \right]_{-d_1}^{0,0}$$

$$= (10,250.0)(2.629)(0.5)[606.42 + 40.0 - 258.37] + (644,026.5)(2.347)[173.902 - 74.196] \text{ N} = 5.228 + 150.709 \text{ MN} = 155.937 \text{ MN}$$

$$\text{Bending moment due to wave action} = (155.937)(2/3)(40.0) = 4158.32 \text{ MN m}$$

$$\text{Total shear force at this section} = 8.1788 + 155.937 = 164.116 \text{ MN}$$

$$\text{Total bending moment at this section} = 559.83 + 4158.32 = 4718.15 \text{ MN m}$$

$$\text{Total axial load} = 495.571 + (\pi/4)(20.0^2 - 18.8^2)(20.0)(2500.0)/(10^6) = 495.927 + 1.828 = 497.755 \text{ MN}$$

At  $z$  (or  $d_1$ ) = -60.0 m:

$$\text{Shear force due to wind} = 8.1788 \text{ MN}$$

$$\begin{aligned} \text{Bending moment due to wind} &= (7.3328)(70.0 + 20.0) + (0.846)(30.0/2 + 60.0) \\ &= 659.952 + 63.45 = 723.40 \text{ MN m} \end{aligned}$$

Shear force due to wave action =

$$\left[ \left( \frac{1}{2} \right) \rho_w C_D (D) \cdot \left[ \left( \frac{\pi H}{T} \right)^2 \left( \frac{1}{\sinh kd} \right)^2 \right] \left( \frac{1}{2} \right) [z + (1/2k) \sinh(2kd + 2kz)] \right]_{-d_1}^0 +$$

$$\left[ \rho_w C_M (\pi D^2 / 4) \right] \left[ \left( 2\pi^2 H / T^2 \right) \right] \left[ (1/k) \sinh k(d + z) \right]_{-d_1}^0$$

$$\begin{aligned} &= (10,250.0)(2.629)(0.5)[606.42 + 60.0 - 57.712] + (644,026.5)(2.347)[173.902 - 44.054] \text{ N} \\ &= (8.202 + 196.269) \text{ MN} = 204.471 \text{ MN} \end{aligned}$$

$$\text{Bending moment due to wave action} = (204.471)(2/3)(60.0) = 8178.84 \text{ MN m}$$

$$\text{Total shear force at this section} = 8.1788 + 204.471 = 164.116 \text{ MN}$$

$$\text{Total bending moment at this section} = 723.40 + 8178.84 = 8902.24 \text{ MN m}$$

$$\begin{aligned} \text{Total axial load} &= 497.755 + (\pi/4)(20.0^2 - 18.8^2)(20.0)(2500.0)/(10^6) \\ &= 497.755 + 1.828 = 499.583 \text{ MN} \end{aligned}$$

At  $z$  (or  $d_1$ ) = -80.0 m:

$$\text{Shear force due to wind} = 8.1788 \text{ MN}$$

$$\begin{aligned} \text{Bending moment due to wind} &= (7.3328)(90.0 + 20.0) + (0.846)(30.0/2 + 80.0) = 806.61 + 80.37 \\ &= 886.98 \text{ MN m} \end{aligned}$$

Shear force due to wave action

$$= \left[ \left( \frac{1}{2} \right) \rho_w C_D (D) \cdot \left[ \left( \frac{\pi H}{T} \right)^2 \left( \frac{1}{\sinh kd} \right)^2 \right] \left( \frac{1}{2} \right) [z + (1/2k) \sinh(2kd + 2kz)] \right]_{-d_1}^0 +$$

$$\left[ \rho_w C_M (\pi D^2 / 4) \right] \left[ \left( 2\pi^2 H / T^2 \right) \right] \left[ (1/k) \sinh k(d + z) \right]_{-d_1}^0$$

$$\begin{aligned} &= (10,250.0)(2.629)(0.5)[606.42 + 80.0 - 22.027] + (644,026.5)(2.347)[173.902 - 20.496] \text{ N} \\ &= (8.952 + 231.879) \text{ MN} = 240.831 \text{ MN} \end{aligned}$$

$$\text{Bending moment due to wave action} = (240.831)(2/3)(80.0) = 12,844.32 \text{ MN m}$$

$$\text{Total shear force at this section} = 8.1788 + 240.831 = 249.01 \text{ MN}$$

$$\text{Total bending moment at this section} = 886.98 + 12,844.32 = 13,731.3 \text{ MN m}$$

$$\begin{aligned} \text{Total axial load} &= 499.583 + (\pi/4)(20.0^2 - 18.8^2)(20.0)(2500.0)/(10^6) \\ &= 499.583 + 1.828 = 501.411 \text{ MN} \end{aligned}$$

At  $z$  (or  $d_1$ ) = -85.0 m:

$$\text{Shear force due to wind} = 8.1788 \text{ MN}$$

$$\begin{aligned} \text{Bending moment due to wind} &= (7.3328)(110.0 + 5.0) + (0.846)(30.0/2 + 85.0) = 843.271 + 84.60 \\ &= 927.87 \text{ MN m} \end{aligned}$$

Shear force due to wave action

$$= \left[ \left\{ \left( \frac{1}{2} \right) \rho_w C_D (D) \right\} \cdot \left[ \left( \frac{\pi H}{T} \right)^2 \left( \frac{1}{\sinh kd} \right)^2 \right] \left[ \frac{1}{2} \right] \left[ z + \left( \frac{1}{2} k \right) \sinh(2kd + 2kz) \right]_{-d_1}^0 + \right. \\ \left. \left[ \rho_w C_M (\pi D^2 / 4) \right] \left[ \left( 2\pi^2 H / T^2 \right) \right] \left[ \left( \frac{1}{k} \right) \sinh k(d+z) \right]_{-d_1}^{0.0} \right.$$

$$= (10,250.0)(2.629)(0.5)[606.42 + 85.0 - 15.844] + (644,026.5)(2.347)[173.902 - 15.208] \text{ N} = \\ (9.103 + 239.871) \text{ MN} = 249.974 \text{ MN}$$

$$\text{Bending moment due to wave action} = (249.974)(2/3)(85.0) = 14,108.514 \text{ MN m}$$

$$\text{Total shear force at this section} = 8.1788 + 249.974 = 258.15 \text{ MN}$$

$$\text{Total bending moment at this section} = 927.87 + 14,108.514 = 15,036.384 \text{ MN m}$$

$$\text{Total axial load} = 501.411 + \left( \frac{\pi}{4} \right) (20.0^2 - 18.8^2) (5.0) (2500.0) / (10^6) + \\ 0.457 = 501.868 \text{ MN}$$

- (b) In plane cross-sectional forces for cylindrical shell or arch action due to wave action only

At  $z = -10.0$  m:

In plane cross-sectional hydrostatic force due to submergence at a depth of 10.0 m below the sea surface =  $(1025.0)(9.81)(10.0) = 100,552.5 \text{ N} = 100.55 \text{ kN/m}^2$

In plane cross-sectional hydrodynamic force on the cylindrical tower (of diameter 20.0 m) due to wave action at a depth of 10.0 m below the sea surface

$$= \left[ \left\{ \left( \frac{1}{2} \right) \rho_w C_D (D) \right\} \cdot \left[ \left( \frac{\pi H}{T} \right)^2 \left( \frac{1}{\sinh kd} \right)^2 \right] \cdot \left\{ \cosh k(d+z) \right\}^2 + \right.$$

$$\left. \left[ \rho_w C_M (\pi D^2 / 4) \right] \left[ \left( 2\pi^2 H / T^2 \right) \right] \left\{ \cosh k(d+z) / \sinh(kd) \right\} \right.$$

$$= (10,250.0)(2.629)(8.445) + (644,026.49)(2.347)(0.8699) \\ = (227,569.5 + 1,314,880.1) \text{ N} = 1,542,449.6 \text{ N/unit height} = 1.543 \text{ MN/m}$$

$$\text{Hydrodynamic pressure per unit area} = 1.543/20 = 77.15 \text{ kN/m}^2$$

At  $z = -30.0$  m:

In plane cross-sectional hydrostatic force due to submergence at a depth of 30.0 m below the sea surface =  $(1025.0)(9.81)(30.0) = 301,657.5 \text{ N} = 301.66 \text{ kN/m}^2$

In plane cross-sectional hydrodynamic force on the cylindrical tower (of diameter 20.0 m) due to wave action at a depth of 30.0 m below the sea surface

$$= \left[ \left\{ \left( \frac{1}{2} \right) \rho_w C_D (D) \right\} \cdot \left[ \left( \frac{\pi H}{T} \right)^2 \left( \frac{1}{\sinh kd} \right)^2 \right] \cdot \left\{ \cosh k(d+z) \right\}^2 + \right.$$

$$\left. \left[ \rho_w C_M (\pi D^2 / 4) \right] \left[ \left( 2\pi^2 H / T^2 \right) \right] \left\{ \cosh k(d+z) / \sinh(kd) \right\} \right.$$

$$= (10,250.0)(2.629)(4.198) + (644,026.49)(2.347)(0.6134) = (113,124.6 + 927,172.61) \text{ N} \\ = 1.040 \text{ MN/m}$$

$$\text{Hydrodynamic pressure per unit area} = 1.040/20 = 52.01 \text{ kN/m}^2$$



At  $z = -50.0$  m:

In plane cross-sectional hydrostatic force due to submergence at a depth of 50.0 m below the sea surface =  $(1025.0)(9.81)(50.0) = 502,762.5 \text{ N} = 502.76 \text{ kN/m}^2$

In plane cross-sectional hydrodynamic force on the cylindrical tower (of diameter 20.0 m) due to wave action at a depth of 50.0 m below the sea surface

$$\begin{aligned}
 &= \left[ \left( \frac{1}{2} \right) \rho_w C_D (D) \right] \cdot \left[ \left( \frac{\pi H}{T} \right)^2 \left( \frac{1}{\sinh kd} \right)^2 \right] \cdot \{ \cosh k(d+z) \}^2 \\
 &+ \left[ \rho_w C_M \left( \frac{\pi D^2}{4} \right) \right] \left[ \left( \frac{2\pi^2 H}{T^2} \right) \right] \{ \cosh k(d+z) / \sinh(kd) \} \\
 &= (10,250.0)(2.629)(2.2436) + (644,026.49)(2.347)(0.4484) \\
 &= (60,458.85 + 677,770.13) \text{ N} = 738.23 \text{ kN/m}
 \end{aligned}$$

Hydrodynamic pressure per unit area =  $36.91 \text{ kN/m}^2$

At  $z = -70.0$  m:

In plane cross-sectional hydrostatic force due to submergence at a depth of 70.0 m below the sea surface =  $(1025.0)(9.81)(70.0) = 703,867.5 \text{ N} = 703.87 \text{ kN/m}^2$

In plane cross-sectional hydrodynamic force on the cylindrical tower (of diameter 20.0 m) due to wave action at a depth of 70.0 m below the sea surface

$$\begin{aligned}
 &= \left[ \left( \frac{1}{2} \right) \rho_w C_D (D) \right] \cdot \left[ \left( \frac{\pi H}{T} \right)^2 \left( \frac{1}{\sinh kd} \right)^2 \right] \cdot \{ \cosh k(d+z) \}^2 \\
 &+ \left[ \rho_w C_M \left( \frac{\pi D^2}{4} \right) \right] \left[ \left( \frac{2\pi^2 H}{T^2} \right) \right] \{ \cosh k(d+z) / \sinh(kd) \} \\
 &= (10,250.0)(2.629)(1.371) + (644,026.49)(2.347)(0.3504) \\
 &= (36,944.68 + 529,640.17) \text{ N} = 566.58 \text{ kN/m}
 \end{aligned}$$

Hydrodynamic pressure per unit area =  $566.58/20.0 = 28.33 \text{ kN/m}^2$

At  $z = -82.5$  m:

In plane cross-sectional hydrostatic force due to submergence at a depth of 82.5 m below the sea surface =  $(1025.0)(9.81)(82.5) = 829,558.13 \text{ N} = 829.56 \text{ kN/m}^2$

In plane cross-sectional hydrodynamic force on the cylindrical tower (of diameter 20.0 m) due to wave action at a depth of 82.5 m below the sea surface

$$\begin{aligned}
 &= \left[ \left( \frac{1}{2} \right) \rho_w C_D (D) \right] \cdot \left[ \left( \frac{\pi H}{T} \right)^2 \left( \frac{1}{\sinh kd} \right)^2 \right] \cdot \{ \cosh k(d+z) \}^2 \\
 &+ \left[ \rho_w C_M \left( \frac{\pi D^2}{4} \right) \right] \left[ \left( \frac{2\pi^2 H}{T^2} \right) \right] \{ \cosh k(d+z) / \sinh(kd) \} \\
 &= (10,250.0)(2.629)(1.1173) + (644,026.49)(2.347)(0.3164) \\
 &= (30,108.16 + 478,248.15) \text{ N} = 508.36 \text{ kN/m}
 \end{aligned}$$

Hydrodynamic pressure per unit area =  $508.36/20.0 = 25.42 \text{ kN/m}^2$

- (ii) Hemispherical domes at the top of the caisson:  
 The maximum hydrostatic pressure on top of the hemispherical domes are calculated at a depth of  $(= 100.0 - 6.37/2)$  96.82 m below the mean sea level. Hydrostatic pressure on the top of hemispherical domes  $= (1025.0)(9.81)(96.82) = 973,549.31 \text{ N/m}^2 = 973.55 \text{ kN/m}^2$ .  
 (The hydrodynamic pressure is neglected.)
- (iii) Hemispherical domes at the bottom of the caissons:  
 The design pressures are considered to be at a depth of 160.0 m below the mean sea level; both the hydrostatic fluid pressure as well as the pore pressure at the bottom of the platform are computed and the design loads assumed as the larger of the two computed pressures.  
 Hydrostatic pressure at the bottom hemispherical section of the caissons  $= (160.0)(9.81)(1025.0) = 1,608,840.0 \text{ N} = 1640.84 \text{ kN/m}^2$ .  
 Pore pressure in the soil due to the buoyant weight of the platform (computed in item IV of Example 9.2)  $= 45.488 \text{ kN/m}^2$ .  
 Hence, the hydrostatic pressure controls the design of the bottom domes of the caissons.
- (iv) Caisson sections of the gravity platform foundation:  
 Since the hydrostatic pressures control the design of the caisson section, they are computed only for the lowermost section of the caissons, located at a depth of 152.5 m (top of the bottom hemispherical sections) below the mean sea level.  
 Design pressure for the platform caisson cross sections  $= (152.5)(1025)(9.81) = 1,533,425.63 \text{ N/m}^2 = 1533.43 \text{ kN/m}^2$ .  
 The bending moment in the caisson is computed at the bottom of the platform (in a conservative manner) in item II (c) of the Example 9.2  $= (207.53)(10^8) \text{ N m} = 20,753.0 \text{ MN m}$ .  
 Moment of inertia of the bottom-most section of the caissons (assuming the central caisson to be located at the center and the other six caissons to be allocated symmetrical with respect to a diametral line)  $= (\pi/64)(30.0^4 - 28.8^4) + (4)[(\pi/4)(30.0^2 - 28.8^2)(15.0)^2 + (\pi/64)(30.0^4 - 28.8^4)] + (2)[(\pi/4)(30.0^2 - 28.8^2)(45.0)^2 + (\pi/64)(30.0^4 - 28.8^4)]$   
 $= 5990.10 + (4)(12,468.98 + 5990.10) + (2)(112,220.83 + 5990.10)$   
 $= (5990.10 + 73,836.32 + 236,421.86) \text{ m}^4 = 316,248.28 \text{ m}^4$   
 Maximum bending stress in the caisson wall  $= My/I = (20,753.0)(10^6)(45.0)/(316,248.28) = 65,622.49 \text{ N/m}^2 = 65.623 \text{ kN/m}^2$   
 The bending stress is very small in the caisson walls.
- (v) Skirt walls of the gravity platform foundation:  
 The active pressure load on the skirt walls is assumed to be due to the pore pressure in the soils, due to the buoyant weight of the platform  $= 45.192 \text{ kN/m}^2$ .
- (II) Design of structural elements of the concrete gravity platform:
- (i) Cylindrical tower sections  
 While designing the cylindrical tower sections, two factors must be kept in mind, namely, that the tower is pre-stressed along its vertical axis, and that the tower is reinforced vertically and transversely to make it deform elastically (and to prevent sudden collapse in case of accidental extreme overloads), as well as to resist the applied loads safely. Following the procedure outlined in Holland et al. [66], the outer walls of the vertical cylinder and the caissons can be designed initially as ring beams for the following conditions:

The elastic length of the ring beam (or arch) is given by

$$l_e = (Rt)^{0.5} / \{(3.0)(1.0 - \nu^2)\}^{0.25}$$

The design edge moment (of the ring or arch) is given by

$$M_0 = (pl_e^2)/2 \quad (\text{E9.10})$$

The design shear force is given by

$$V_0 = \rho l_e$$

The compression force  $N_\phi$  (in the ring or arch) is given by

$$N_\phi = \rho R$$

In the above equation,  $R$  is the radius of the cylindrical tower (or caisson) to the center of the wall;  $t$  is the wall thickness;  $\nu$  is the Poisson's ratio of concrete;  $p$  is the hydrostatic pressure on the outer walls of the cylindrical tower (or caisson); and  $l_e$  is the elastic length of the ring (or arch) on which the load acts.

The pre-stress in the section is controlled by the maximum tensile stress that is likely to occur in the cross section under the applied vertical (compressive) and horizontal bending loads.

Considering the maximum compressive and bending stresses due to the applied loads (at a depth of  $-82.5$  m below the mean sea level),

Total maximum shear force at this section = 258.15 MN

Total bending moment at this section = 15,036.384 MN m

Total axial load = 501.868 MN

Cross-sectional area ( $A$ ) of the vertical cylindrical tower =  $(\pi/4)(20.0^2 - 18.8^2) = 36.568 \text{ m}^2$

Neglecting the effect of the vertical reinforcements provided (load factor = 1.1),

$$\sigma_{\text{axial}} = (1.1)P/A = (1.1)(501.868)/36.568 = 15.097 \text{ MPa}$$

Moment of inertia of the cross section =  $(\pi/64)(20^4 - 18.8^4) = 7836.63 \text{ m}^4$

Maximum bending stress (load factor = 1.3) =  $\sigma_{\text{bending}} = Mc/I = \{(1.3)(15,036.384)\}/(10.0)/7836.63 = \pm 24.944 \text{ MPa}$ .

If the pre-stress is not applied, then maximum tensile stress in the cross section =  $24.944 - 15.097 = 9.847 \text{ MPa}$ .

Assuming an accidental 25% overload in the applied loads, the maximum tensile stress =  $(1.25)(9.847) = 12.309 \text{ MPa}$ .

Hence, the pre-stressing load required in the columns =  $(36.568)(12.309) = 450.12 \text{ MN}$ .

Assuming a strength of 1500.0 MPa for the pre-stressing tendons [67],

Cross-sectional area of the pre-stressing tendons required =  $(450.12)/(1500.0) = 0.3001 \text{ m}^2$

Assuming a cluster of 10 19.0-mm-diameter-strand pre-stressing tendons (cross-sectional area  $\sim 220.0 \text{ mm}^2$ ),

$$\text{Number of tendons required} = (0.3001)(10^6)/\{(10)(220.0)\} \sim 137$$

Spacing of the pre-stressing tendons in the vertical cylindrical tower =  $(\pi)(19.4)(1000)/(137) = 444.9 \text{ mm}$  (seems to be OK)

Considering the hoop reinforcement in the tower, the design pressure (from item i.i.b) =  $(1.1)(829.56) + (1.3)(25.42) = 945.562 \text{ kPa}$ .

$$I_e = (Rt)^{0.5} / \{(3.0)(1.0 - \nu^2)\}^{0.25}; \text{ hence, } I_e = \{(9.4)(0.6)\}^{0.5} / \{(3.0)(1.0 - 0.12^2)\}^{0.25} = (2.374) / (1.311) = 1.811 \text{ m.}$$

$$\text{Factored bending moment} = \rho(I_e)^2 / 2 = (945.562)(1.811)^2 / (2.0) = 1.551 \text{ MN m}$$

$$\text{Moment of inertia} = (1/12)(1)(0.60 - 0.075)^3 = 0.1447 \text{ m}^4$$

Maximum bending stress =  $Mc/I = \pm 2.813$  MPa; this is a very low bending stress.

$$\text{Hoop stress} = (\rho)R = (945.562)(9.7) = 9.172 \text{ MPa}$$

Hence, the hoop ring section is not having any tensile stress.

Also, the shear stress in the section  $[68] = VS/(2t)$ .

$$S = (2/3)[(R_{\text{outer}})^3 - (R_{\text{inner}})^3] = (2/3)[(10.0)^3 - (9.4)^3] = 112.944 \text{ m}^3$$

$$\text{Maximum shear stress} = \{(258.15)(112.944)\} / \{(7836.63)(2)(0.60)\} = 3.10 \text{ MPa}$$

$$\text{Maximum axial stress} = -15.097 - 24.944 = -40.041 \text{ MPa}$$

Principal tensile stress when shear is considered =  $(-40.041/2) + [(40.041/2)^2 + (3.10)^2]^{0.5} = -20.02 + 20.25 = 0.23$  MPa.

This is much smaller than the allowable critical value of  $(4.0)(\sqrt{\sigma'_c})$  (in FPS units) =  $(4.0)(\sqrt{6500}) = 322.5$  psi = 2.225 MPa.

Hence, the maximum tensile stress generated in the vertical cylindrical tower is within the permitted values.

Considering the cracking moment  $M_c$  in the cross section,

$$2.225 = (M_c)C/I - P/A - (\sigma_{\text{pre-stress}})(A_{\text{pre-stress}})/A = (M_c)(10.0)/(7836.63) - (1.1)(501.868)/(36.568) - (1500)(0.3001)/(36.568)$$

Solving, we get  $M_c = 23,221.50$  MN m.

Cracking moment/applied maximum moment =  $(23,321.50)/(15,036.384) = 1.544$ ; hence, the section is quite strong.

(ii) Caisson section

The caisson wall is also designed in a similar manner.

Design pressure for the platform caisson cross sections (computed earlier) = 1533.43 kN/m<sup>2</sup>

Considering the hoop reinforcement in the caisson section, the design pressure (from Section I.i.b) =  $(1.1)(1533.43) = 1686.77$  kPa.

$$I_e \text{ (computed earlier)} = 1.811 \text{ m}$$

$$\text{Factored bending moment} = \rho(I_e)^2 / 2 = (1.6868)(1.811)^2 / (2.0) = 2.7661 \text{ MN m}$$

$$\text{Moment of inertia} = (1/12)(1)(0.60 - 0.075)^3 = 0.1447 \text{ m}^4$$

Maximum bending stress =  $Mc/I = \pm 5.018$  MPa; this is a very low bending stress.

$$\text{Hoop compressive stress} = (\rho)R = (1.687)(9.7) = +16.364 \text{ MPa}$$

Hence, the hoop ring section is not having any tensile stress.

Considering the implosive failure of the caisson walls under hydrostatic loads, Albertson [69] states that the implosion pressure is given by,

$$p_{\text{implosion}} = f'_c [2.05(t/D_0) - 0.028],$$

where  $f'_c$  = compressive strength of concrete,  $t$  = thickness of concrete wall and  $D_0$  is the outer diameter of the cylindrical shell wall.

$$\sigma'_c = 45.0 \text{ MPa} = 6500 \text{ psi}$$

$$\text{Implosion pressure} = (45.0)[(2.05)(0.60/30.0) - 0.028] = 0.585 \text{ MPa.}$$

Design pressure for the platform caisson cross sections (computed earlier) = 1533.43 kN/m<sup>2</sup>.

Using a thickness of 1.0 m, the implosion pressure =  $(45.0)[2.05(1.00/30.0) - 0.028]$  = 1.815 MPa

Hence, the caisson wall of 1.0 m is sufficient to resist implosive failure.

In addition to the above, a factor of safety of 3 needs to be available (on implosion strength) for long-term exposure of any underwater operating structure; this can be provided by providing a high-strength concrete of for the caisson tanks.

(iii) Hemispherical domes of the bottom caisson:

$$\text{Actual pressures exerted on the hemisphere} = (1.1)(973.55) = 1070.91 \text{ kPa}$$

The stress in the skin of the concrete spherical dome by membrane theory [70] is =  $(pR/2) = (1.070.91)(15.0/2) = 8031.79 \text{ kPa}$ .

According to Kahn [71], the implosive strength of the spherical end closure of a concrete cylindrical shell caisson is given by,  $p_{\text{im}} = 0.219 \sigma'_c$ . This would give an implosion stress =  $(0.219)(45.0) = 9.855 \text{ MPa}$ . Hence the stress in the dome at the bottom of the caisson seems to be ok. The long-term exposure will reduce the implosion stress; this is overcome by the adoption of a high strength concrete for the whole caisson, as mentioned before.

Considering the flexural failure of the dome wall due to implosion, the implosive failure pressure [72] =  $(2.0)\{(E)/(1.0 - \nu^2)\}(t/D_{\text{outer}})^3 = (2.0)\{(22,098.0)/(1.0 - 0.12^2)\}(0.60/30)^3 = 0.3587 \text{ MPa} = 358.7 \text{ kPa}$ .

This seems to be much lower than the actual pressures exerted on the hemisphere =  $(1.1)(973.55) = 1070.91 \text{ kPa}$ .

Hence, this section needs to be redesigned.

Using a hemispherical section of 1.0-m thickness for dome walls,

$$\text{Implosive failure pressure permitted} = (2.0)\{(22,098.0)/(1.0 - 0.12^2)\}(1.0/30)^3 = 1.661 \text{ MN.}$$

This is much higher than the actual pressures exerted on the hemisphere.

Hence, the 1.0 m thick hemispherical dome section seems to be ok for resistance against implosion; but long term exposure will require a higher implosion strength. This is provided by the adoption of a high-strength concrete for the caissons, the domes and the foundation slab.

(iv) Caisson sections of the gravity platform foundation:

The preceding section is used also for the bottom domes.

(v) Skirt walls of the gravity platform foundation:

Assuming that the skirt walls are subjected to the transverse active pore water pressure of the undrained foundation soil,

Maximum design bending moment =  $(1.1)(45.192)(3.0)^2/(2.0) = 223.70 \text{ kN m}$

Bending stress =  $Mc/I = (223.70)(0.30)/[(1/12)(1.0)(0.60)^3] = 3728.33 \text{ kPa}$

This seems to be a little higher than the tensile bending stress permitted in the section.

Hence, the skirt section has to be redesigned.

Considering a skirt wall thickness of 1.0 m,

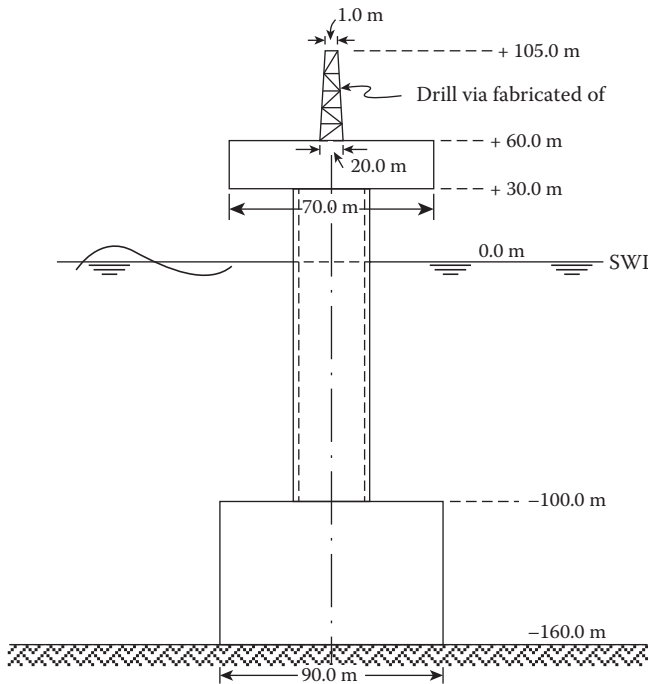
Bending stress in the section =  $(223.70)(0.50)/[(1/12)(1.0)(1.0)^3] = 1342.2 \text{ kPa}$

The bending stress is within the permissible stress allowed; in addition, the influence of the vertical soil pressure from the bottom on the active soil pressure and its effect on this bending stress need to be considered in this analysis.

Hence, the section is considered to be safe.

**EXERCISE PROBLEMS**

1. A gravity platform is to be installed at a specified offshore location far from the shore. The top deck modules are fabricated on shore, while the concrete gravity base (with columns) is fabricated at a near-shore deepwater site. Explain how the modules are assembled on the structure and then towed to the site and located in position.
2. The concrete monotower, shown in Figure P9.1, is located at a water depth of 160.0 m. The caisson is filled with oil, and the leg is filled with seawater up to the still waterline. Assume



**FIGURE P9.1** Concrete monotower.

the leg diameter to be 25.0 m and the thickness of the legs to be 0.5 m. The pertinent platform data are given as follows: deck mass =  $1.5 \times 10^7$  kg (with the assembly in deck); caisson mass (with oil) =  $2.0 \times 10^8$  kg; concrete mass density =  $2500.0 \text{ kg/m}^3$ ; and seawater density =  $1025.0 \text{ kg/m}^3$ . Calculate the ballast mass to be added to the bottom of the caisson and the location of the center of the ballast mass such that the center of mass and the center of buoyancy are coincident.

3. Explain, clearly, the various types of underwater surveys that are carried out usually on an offshore platform. Detail the procedures used and the facilities required to carry out the survey with (i) a diver and (ii) a remotely operated vehicle.
4. The concrete monotower, shown in Figure P9.1, is located in a water depth of 160.0 m. The caisson is filled with oil, and the vertical column is filled with seawater up to the still waterline. Pertinent data are given as follows: deck mass =  $3.0 \times 10^7$  kg; caisson mass (with oil) =  $4.0 \times 10^8$  kg; caisson mass (without oil) =  $1.5 \times 10^8$  kg; column concrete density =  $2500.0 \text{ kg/m}^3$ ; seawater density =  $1025.0 \text{ kg/m}^3$ ; effective cohesion =  $60.0 \text{ kN/m}^2$ ;  $\phi_c = 25^\circ$ ; unit weight of soil =  $17.5 \text{ kN/m}^3$ ; Poisson's ratio of soil = 0.45;  $G = 1000s_u$ ;  $s_u$  = shear strength of soil =  $120.0 \text{ kN/m}^2$ ; initial void ratio = 0.63; and compression index of soil = 0.30. The structure is subjected to forces due to (i) a maximum wave of 25.0-m height and a period of 14.5 s and (ii) a maximum wind of 200 kmph. (a) Does this structure float if it is raised just slightly from the bottom? Would it float in its unballasted position? (b) Locate the center of mass  $G$  and the center of buoyancy  $B$  for the unballasted structure when it is in its vertical position. (c) Check the structure against overturning, sliding, and bearing failures. Determine the short- and long-term settlements of the foundation. (d) Determine the plane rocking frequency and response (maximum) of the tower as it responds to wave excitation. Use 30% added inertia and 10% hydrodynamic damping. Assume that it rocks about the center  $O$  of its base.
5. The foundation of a gravity platform is a circle of diameter 100.0 m. The platform is subjected to the following loads and moments:  $F_{\text{vert(max)}} = 200,000 \text{ t}$ ;  $F_{\text{vert(min)}} = 150,000 \text{ t}$ ;  $F_{\text{horizontal}} = 50,000 \text{ t}$ ; and  $M_{\text{max}} = 2.0 \times 10^6 \text{ t m}$ . Undrained cohesive strength of the sandy clay foundation is  $15.0 \text{ t/m}^2$ . The buoyant density of soil is  $0.9 \text{ t/m}^3$  and its angle of internal friction  $\theta = 30^\circ$ . Check the stability of the foundation for its vertical and horizontal resistances. Assume any other missing data.
6. (a) A circular concrete footing, of depth 15.0 m and of diameter 45.0 m, is utilized to support a gravity platform at a water depth of 60.0 m. The submerged unit weight of the concrete footing is  $1450.0 \text{ kgf/m}^3$  and that of the sandy layer on the seabed is  $680.0 \text{ kgf/m}^3$ . The shear modulus of soil is given as 7.0 GPa. Find the vertical settlement of the foundation. (b) If the underlying sediment is an overconsolidated clay having compression properties  $C_r = 0.025$ ;  $C_c = 0.195$ ; and  $\sigma_m = 600 + 24y \text{ kgf/m}^2$  ( $y$  being the depth below the seabed), determine the maximum differential settlement of the foundation. Take the submerged unit weight of the soil to be  $630.0 \text{ kgf/m}^3$  and consider the buoyancy of the structure.
7. A monotower gravity platform, shown in Figure P9.2a, is to be designed for installation in George's Bank at a water depth of 150.0 m. In the load computation, consider the effect of vertical loads, the buoyancy effect, and the wave (horizontal and vertical) and wind loads on the platform. The structure is subjected to forces due to the maximum height wave and the maximum velocity wind possible at the site. The platform also has steel skirts placed in two concentric circles, as shown in Figure P9.2b, one at the outside periphery and the other at one-half the diametric location, divided into 12 sectors by radial skirts, each enclosing an angle of  $30^\circ$ ; inside the inner circle is devoid of radial skirts. (a) Design the skirts and assume the height of the skirts to be the depth of embedment. Check the structure against overturning, sliding, and bearing failures. Assume the strength to depend on drained condition. (b) Determine the short- and long-term settlements of the foundation. Given data include the following: deck mass =  $4.5 \times 10^7$  kg; caisson mass (with oil) =  $6.0 \times 10^8$  kg; caisson mass (without oil) =  $2.0 \times 10^8$  kg;

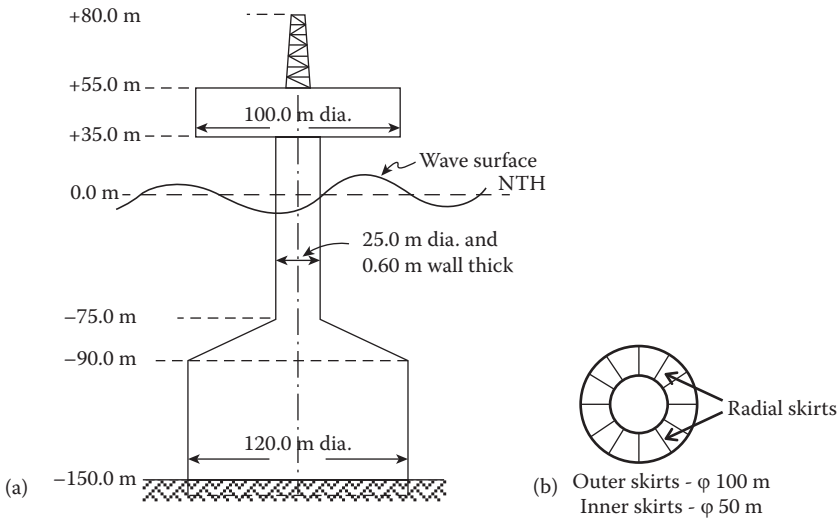


FIGURE P9.2 (a) Typical monopod gravity platform. (b) Steel skirts.

column concrete density = 2500 kg/m<sup>3</sup>; seawater density = 1030 kg/m<sup>3</sup>; effective cohesion = 50.0 kN/m<sup>2</sup>;  $f = 28^\circ$ ; unit weight of soil = 18.0 kN/m<sup>3</sup>; Poisson's ratio for soil = 0.45;  $G = 800s_u$ ;  $s_u$  = drained shear strength of soil = 120.0 kPa; initial void ratio = 0.60; compression index of soil = 0.30;  $C_d = 1.2$ ; and  $C_m = 2.0$ . Consider the drill rig to be equivalent to a tubular steel section of diameter 1.0 m. Assume any other relevant data.

8. A skirt is to be designed for a gravity platform for the following conditions: (i) 120.0-m-diameter circular base consisting of 19 vertical cylindrical cells, each 22.0 m in diameter, and equipped with a steel skirt of height  $h$  and thickness  $t$ ; (ii) maximum weight of the gravity platform, in water, is equal to 210,000 t; (iii) plate thickness available for use as skirts are 20.0 and 25.0 mm; and (iv) maximum cone penetration resistance is equal to 20.0 MPa, and lateral frictional strength of ocean bottom soil is 200.0 kPa. Design the skirt.
9. A gravity platform is to be protected from scour at its bottom generated due to the dynamic wave and current forces acting on the structure. Explain the various measures you would take to prevent the scour damage of the platform.
10. The concrete monotower, shown in Figure P9.3 [72], is in 160.0 m of water. The caisson is filled with oil, and the leg is filled with seawater up to the still waterline. Pertinent data are

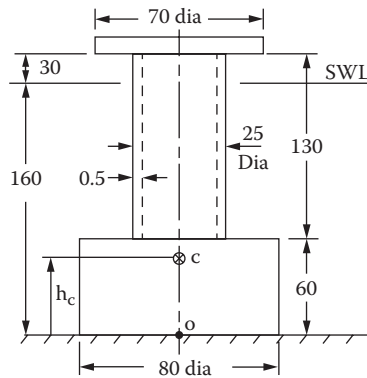
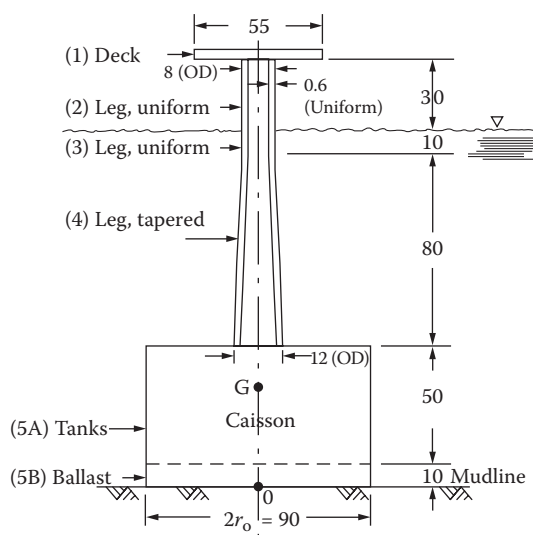


FIGURE P9.3 Concrete monotower. (J.F. Wilson: *Dynamics of Offshore Structures*, p. 30, 1984. Copyright Wiley-VCH Verlag GmbH & Co. KGaA. Reproduced with permission.)



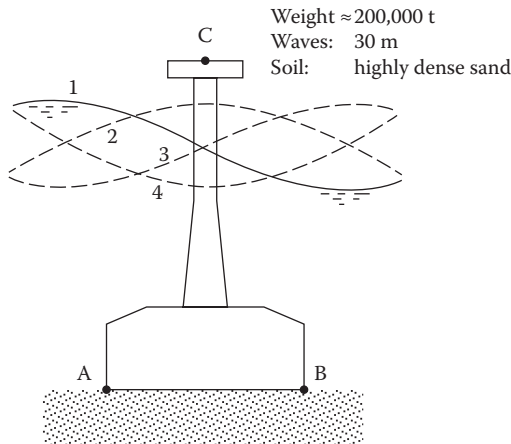
- given as follows: deck mass =  $2.0 \times 10^7$  kg; caisson mass (filled) =  $2.0 \times 10^8$  kg; concrete density =  $2450 \text{ kg/m}^3$ ; and seawater density =  $1030 \text{ kg/m}^3$ . (a) Does this structure float if it is raised just slightly from the bottom? If so, what is the minimum deck mass needed to keep it floating? (b) Locate the center of mass  $G$  and the center buoyancy  $B$  for this structure when in the upright position. If the answer to part a is positive, use your recommended deck weight to locate  $G$ . (c) Calculate the position of the center of buoyancy for a small angle of tilt,  $\theta$ . (d) Discuss the stability of this structure, or the structure as modified in part a, if a thin layer of the soil foundation behaves as a liquid under repeated oscillations,  $\theta = \theta(t)$ .
11. The foundation of a gravity platform is a circle of diameter 120.0 m. The platform is subjected to the following loads and moments:  $F_{\text{vert(max)}} = 250,000 \text{ t}$ ;  $F_{\text{vert(min)}} = 180,000 \text{ t}$ ;  $F_{\text{horizontal}} = 120,000 \text{ t}$ ; and  $M_{\text{max}} = 2.5 \times 10^6 \text{ t m}$ . The angle of internal friction  $\phi = 40^\circ$  and  $\phi' = 32^\circ$ . The angle of friction between the gravity foundation and soil is  $30^\circ$ . The buoyant weight of soil is  $0.9 \text{ t/m}^2$ . The undrained shear strength of soil in the foundation is  $20 \text{ t/m}^2$ . The effective cohesion intercept of Mohr envelope is  $8.0 \text{ t/m}^2$ . Assume that the depth of embedment is nil. Check the stability of the foundation for (i) sliding; (ii) undrained bearing capacity; and (iii) drained capacity. Use API provision for design. Assume any other missing data.
  12. An underwater repair on an offshore concrete gravity platform is to be carried out using tremie concrete. Outline the procedure you would use and the precautions to be taken in carrying out the above task efficiently.
  13. The concrete gravity platform, given in Figure P9.4 [73], is subjected to wind, wave, and ice forces (at the mean water level). The maximum design wind speed is  $40 \text{ m/s}$ , and the wind is assumed to act over the portion of the platform, exposed to wind action (above mean sea level). The wave regime is equivalent to a significant wave of  $10.0\text{-m}$  height and  $14.0\text{-s}$  wave period. The ice load is exerted by an ice field of  $1.0\text{-m}$  average thickness. Check the adequacy of the design considering API provisions for bearing capacity of the foundation, dynamic amplification of horizontal and rocking motion, and short-term and long-term foundation deformation. Take a factor of safety =  $2.5$ . The deck load is equivalent to  $50,000 \text{ kN}$ . Assume that the hollow column (vertical leg) is filled with water up to the mean sea level; the caisson at the bottom is approximately cylindrical consisting of two components, viz., (i) a cluster of vertical cylindrical



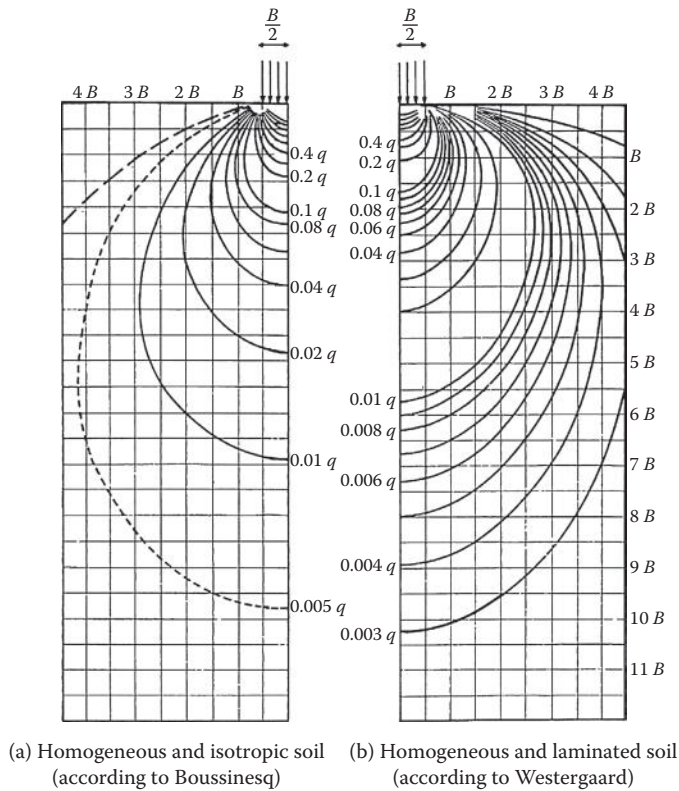
**FIGURE P9.4** Concrete gravity platform. (From P. Le Tirant, *Seabed Reconnaissance and Offshore Soil Mechanics for the Installation of Petroleum Structures*, Editions Technip, Paris, p. 352, 1979. With permission.)

tanks 50 m high, which displace 70% of the volume of seawater occupied by a cylinder of height  $l = 50$  m and radius  $r_o = 45$  m. These tanks are filled with oil and the average density of the tanks with their contents is  $900 \text{ kg/m}^3$ ; the cylinder is assumed to be a homogeneous solid of this density; and (ii) the portion of the tank, constituting the base and ballast. This part is also assumed to be a homogeneous cylindrical solid 10.0 m high and 90.0 m in diameter with a density of  $2000.0 \text{ kg/m}^3$ . Make approximate wind and wave force calculations for the drilling rig, considering the mean diameters of the tapering portion of the platform column.  $\sigma_{ice} = 1.5 \text{ MPa}$ . The rectangular platform deck is assumed to be completely impervious to wind on all four sides. The foundation soil is of clay having an undrained shear strength of  $C = \alpha\gamma$ , where  $\alpha = 2.0 \text{ kN/m}^3$ ; effective angle of friction  $= 20^\circ$ ; and submerged specific weight of  $7.9 \text{ kN/m}^3$ . Added mass coefficient  $= 1.0$ ;  $G_s = 30 \text{ MPa}$ ;  $\nu_s = 0.33$ ; and  $e_o = 0.30$ . Assume the foundation soil layer to be 100.0 m thick. Initial effective vertical stress is based on the undrained bearing capacity of soil, while the added effective stress is dependent on the drained bearing capacity. Assume any missing data and justify its choice.

14. A gravity monotower, shown in Figure P9.5 [74], is located at a North Sea site of water depth 150.0 m. The foundation diameter is 100.0 m. The platform weighs 200,000 t and is subjected to 100-year waves of height 30.0 m and period 15.0 s. Take the horizontal wave load to be a maximum of 70,000 t and the maximum overturning moment to be  $3.0 \times 10^6 \text{ t m}$ . (a) Using (i) Boussinesq's formulation (for isotropic soils) and (ii) Westergaard's formulation (for layered soils), compute the approximate stresses that will be exerted in soil at the top (due to the central rectangular strip) and at 100 m below the top for still water and 100-year wave conditions (use the two curves in Figure P9.6 [75]). Does the above value depend on the mechanical characteristics of the soil, on which the tank is founded? (b) If the foundation slab of the monotower were assumed to be flexible, using Figure P9.7 [76], discuss how the above stresses would change if the soil is assumed to be (i) sand (take  $\nu = 0.25$ ) and (ii) clay (take  $\nu = 0.49$ ).
15. The Ekofisk tank structure, located in the British Sector of the North Sea and shown in Figure P9.8, is 93.0 m in diameter and situated in waters 70.0 m deep. The vertical weight of the tank is 190,000 t and is subjected to a horizontal wave and wind load of 78,600 t, acting at a height of 31.7 m from the base of the tank. Assume that the foundation slab of the structure is not equipped with skirts. (a) Find the bearing capacity of the foundation soil if the structure is founded on (i) sand and (ii) stiff clay. (b) Find the factor of safety of the structure against overturning and



**FIGURE P9.5** Concrete gravity monotower platform. (From P. Le Tirant, *Seabed Reconnaissance and Offshore Soil Mechanics for the Installation of Petroleum Structures*, Editions Technip, Paris, p. 358, 1979. With permission.)



**FIGURE P9.6** Stress distribution beneath a square foundation. (From P. Le Tirant, *Seabed Reconnaissance and Offshore Soil Mechanics for the Installation of Petroleum Structures*, Editions Technip, Paris, p. 356, 1979. With permission.)

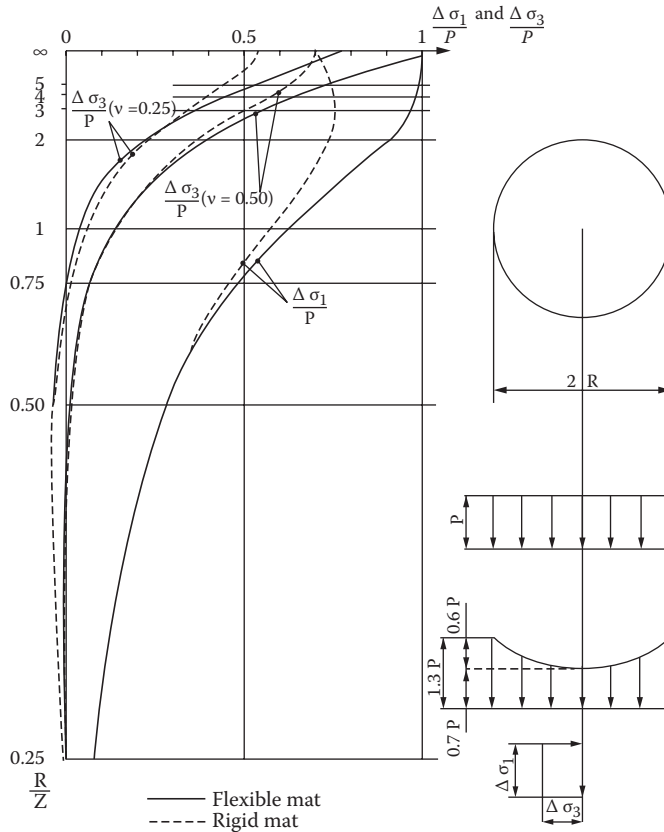
- slip for the above two types of foundation media. Assume that the density of wet sand is 1.6 t/m<sup>3</sup> and that the angle of internal friction is 37°. The cohesion of stiff clay is 6000 kPa.
16. The offshore structure shown in Figure P9.9 [77] is resting on top of an elastic soil. Determine the deflection of the deck due to a horizontal load applied at the deck level, as shown in the figure. The member properties are shown in the figure. The stiffness matrix of the structure is given below.

$$\begin{bmatrix} F_{2x} \\ M_2 \\ F_{3x} \\ M_3 \end{bmatrix} = \begin{bmatrix} (a+k_1) & b & -a & b \\ b & (2c+k_3) & -b & c \\ -a & -b & a & -b \\ b & c & -b & 2c \end{bmatrix} \begin{bmatrix} U_2 \\ \theta_2 \\ U_3 \\ \theta_3 \end{bmatrix}$$

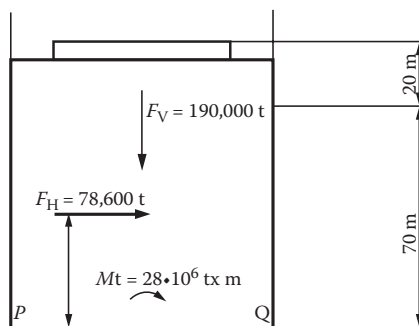
where

$$a = 12 \frac{EI}{l^3}, \quad b = 6 \frac{EI}{l^2}, \quad c = 2 \frac{EI}{l},$$

$$k_1 = 32(1-\nu) \frac{\mu}{(7-8\nu)}, \quad k_2 = 4\mu \frac{R}{(1-\nu)}, \quad \text{and} \quad k_3 = \frac{8}{3} \mu \frac{R^3}{(1-\nu)}$$



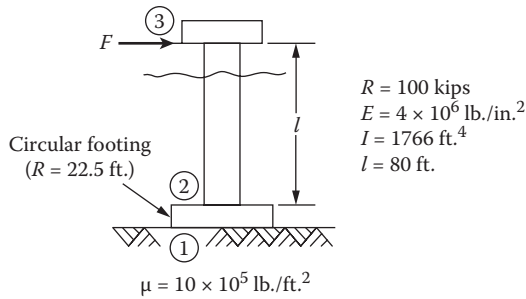
**FIGURE P9.7** Stress distribution beneath the axis of a circular foundation. (From P. Le Tirant, *Seabed Reconnaissance and Offshore Soil Mechanics for the Installation of Petroleum Structures*, Editions Technip, Paris, p. 356, 1979. With permission.)



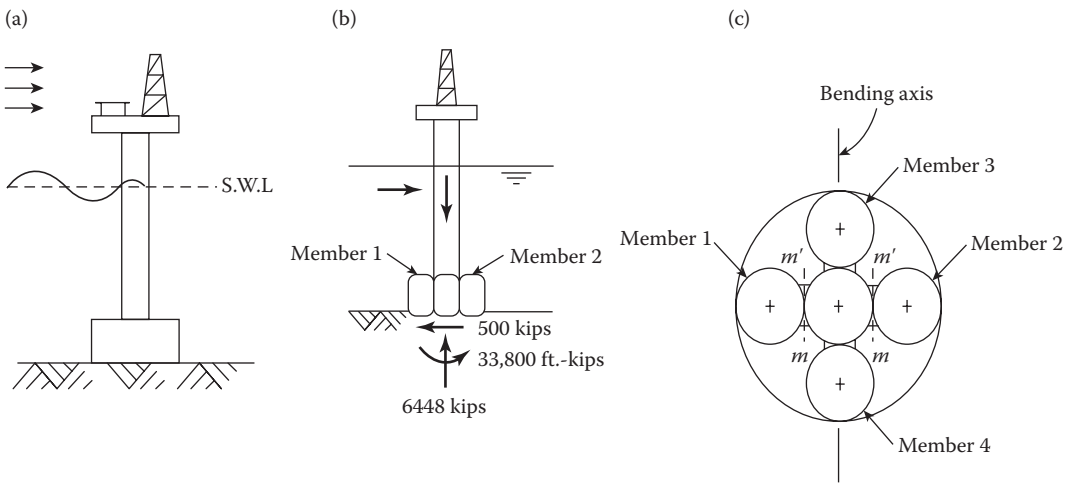
**FIGURE P9.8** Ekofisk tank structure. (From P. Le Tirant, *Seabed Reconnaissance and Offshore Soil Mechanics for the Installation of Petroleum Structures*, Editions Technip, Paris, p. 384, 1979. With permission.)

with  $R$  being the radius of the footing,  $\mu$  being the elastic shear modulus of soil, and  $\nu$  being the Poisson's ratio of soil. The soil springs are given by  $k_1$  representing the sliding stiffness,  $k_2$  representing the vertical stiffness, and  $k_3$  representing the rotational stiffness.

17. A concrete offshore platform shown in Figure P9.10a [78] consists of a heavy base of diameter 45.0 ft. and of height 15.0 ft. An operating deck and associated equipment, weighing 8000.0 kips, is supported by a single hollow cylindrical column of external diameter



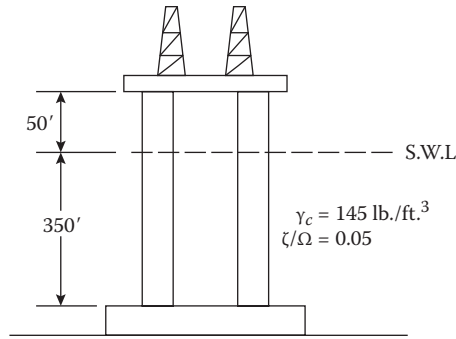
**FIGURE P9.9** Offshore gravity structure. (From T.H. Dawson, *Offshore Structural Engineering*, Prentice Hall, Inc., Englewood Cliffs, NJ, p. 267, 1983. With permission.)



**FIGURE P9.10** Elevation and cross section of a typical gravity platform. (From T.H. Dawson, *Offshore Structural Engineering*, Prentice Hall, Inc., Englewood Cliffs, NJ, p. 201, 206, 1983. With permission.)

16.0 ft. and of wall thickness 2.0 ft. The column is pre-stressed through cables and is made of high strength concrete weighing 160.0 lb./ft.<sup>3</sup>. The structure stands in a water depth of 90.0 ft. and is acted upon by a wind force of 110.0 kips (center of force at a distance of 110.0 ft.) above the sea bottom and a wave force of 700.0 kips (center of force at a distance of 64.0 ft.). (a) Determine (i) the area of pre-stressing cables required for the column if no tension force was to develop at the base of the column, under the above-mentioned loads; take the maximum allowable stress in the pre-stressing cable to be 140.0 kips/in.<sup>2</sup>; (ii) the diagonal tensile stress associated with the maximum shear stress and the cracking moment, assuming a concrete strength of 9000 psi. (b) Determine the ultimate moment capacity of the column. Assume that the pre-stressing cables are placed at the center of the 2.0 ft.-thick walls at 90° angles. (c) Suppose the base of the structure is not massive, as indicated in Figure P9.10a, but is made of an assembly of one central column (mentioned above) and four other similar concentric cylindrical cells of height 30.0 ft., outer diameter 16.0 ft., and wall thickness 1.25 ft., as shown in Figure P9.10b and c. Taking the loading to be the same, determine the pre-stressing cable requirements, along with the cracking moment and the diagonal tension in the base.

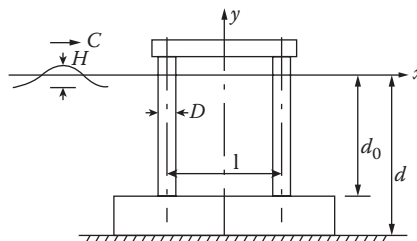
18. An offshore gravity platform of the “Sea Tank” type (shown in Figure P9.11 [79]) consists of four concrete columns, each of 50.0-ft. external diameter and wall thickness 1.5 ft. The



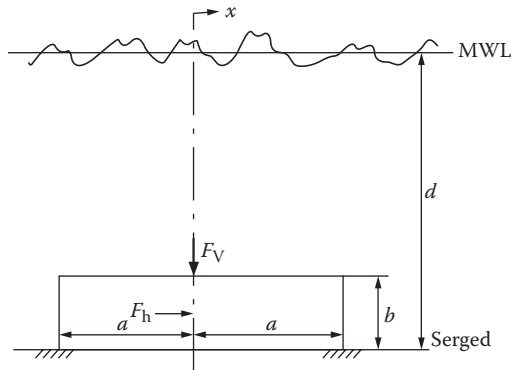
**FIGURE P9.11** Offshore gravity platform of the “Sea Tank” type. (From T.H. Dawson, *Offshore Structural Engineering*, Prentice Hall, Inc., Englewood Cliffs, NJ, p. 208, 1983. With permission.)

four columns rest on top of a thick rectangular concrete base of height 50.0 ft. The deck and associated equipment weigh 25,000.0 kips. Assuming the columns to be flooded to the mean sea level, determine the dynamic amplification factor for waves of height 20.0 ft. and period 11.0 s. Assume that the structure is standing in a water depth of 400.0 ft., and the bottom of the deck of the platform is located at a height of 50.0 ft. above the mean sea level. Prior computations show that a force of 100.0 kips acting at the deck level of the platform will deflect by 0.056 in.

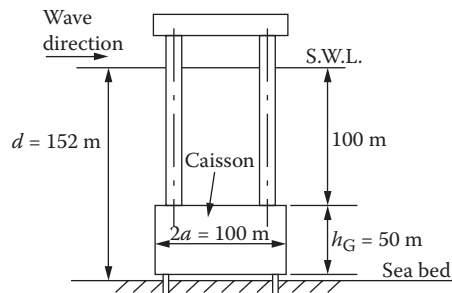
19. (a) Assume that the structure shown in Figure P9.11 is resting on top of a clay medium having a cohesive strength of 1.1 kips/ft.<sup>2</sup>, an effective angle of internal friction of 22.0°, and a buoyant weight of 45.0 lb./ft.<sup>3</sup>. Determine the initial and long-term bearing capacities of the foundation footing. Take a factor of safety of 2.5. (b) Determine the bearing capacity of the footing if the soil foundation is made up of sand with an angle of internal friction of 32° and a buoyant weight of 55.0 lb./ft.<sup>3</sup>. Use the same factor of safety. (c) Compute the maximum differential settlement of the foundation for the above structure.
20. A four-column gravity platform, shown in Figure P9.12 [80], is subjected to a wave of length 250.0 m and height 18.0 m. The platform is situated in a sea depth of 120.0 m. (a) Neglecting the drag forces exerted on the columns of diameter  $D = 5.0$  m, determine the spacing  $l$  between the legs of the platform such that the horizontal force on the base is a minimum. (b) Compute the maximum horizontal wave force (inertial) exerted on the foundations and the corresponding value of  $l$ . Take  $C_m = 2.0$  and  $\rho_{\text{seawater}} = 1030.0$  kg/m<sup>3</sup>.
21. A square gravity platform resting on the seabed, shown in Figure P9.13 [81], is subjected to dynamic wave pressures due to a random wave field represented by its wave height spectrum  $S_{\text{HH}}(\omega)$ . Compute (i) the vertical force and (ii) the horizontal force exerted on the structure by the random wave field in terms of  $S_{\text{HH}}(\omega)$ . Ignore diffraction effects.



**FIGURE P9.12** Four-column gravity platform. (From Lecture Notes on Wave Forces on Offshore Structures. Cranfield Institute of Technology, UK, Examination Paper, January 1974.)



**FIGURE P9.13** Square caisson foundation of a gravity platform. (From Lecture Notes on Wave Forces on Offshore Structures. Cranfield Institute of Technology, UK, Examination Paper, January 1981.)



**FIGURE P9.14** Square base gravity platform. (From Lecture Notes on Wave Forces on Offshore Structures. Cranfield Institute of Technology, UK, Examination paper, January 1977.)

22. The schematic of a square base gravity platform is shown in Figure P9.14 [82]. It is subjected to a regular Airy's wave of height  $H (= 2.0 \text{ m})$  and period  $T (= 8.0 \text{ s})$ . Calculate the maximum horizontal pressure force on the gravity platform. Assume that the diffraction coefficient for the wave force acting on the sides of the bottom caisson is given by  $C_D = 1.75$ .

## REFERENCES

1. H.G. Poulos, 1988. *Marine Geotechnics*, Unwin Hyman, London, p. 13.
2. C.J.F. Clausen, E. DiMaggio, J.M. Duncan and K.H. Andersen, 1975. *Observed Behavior of the Ekofisk Oil Storage Tank Foundation*, Proceedings of Offshore Technology Conference, Houston, TX, Paper # OTC 2373, pp. 406.
3. E.T.R. Dean, 2010. *Offshore Geotechnical Engineering: Principles and Practice*, Thomas Telford Limited, London, pp. 298.
4. Available at [www.harrypalmgalleries.ab.ca/galarctdrill/tarsuit.html](http://www.harrypalmgalleries.ab.ca/galarctdrill/tarsuit.html). Accessed October 4, 2011.
5. G.S. Epperson, 1992. Gravity platforms, lecture 6, *Overview of Offshore Engineering*, Course Notes, Houston, TX, 50 pp.
6. A. Mather, 1995. *Offshore Engineering: An Introduction*, Witherby and Company Limited, London, p. 33.
7. K. Harstveit, 2005. *Extreme Value Analysis of Hind Cast Wind Data From the Maritime Areas Surrounding Norway*, Norwegian Meteorological Institute Report # no. 17/2005 Climate, Oslo, Norway, 45 pp.
8. O.M. Faltinsen, 1990. Wave Loads on Offshore Structures, *Annual Review of Fluid Mechanics*, Volume 22, pp. 35–56.



9. B.A. Harper, J.D. Kepertz and J.D. Ginger, 2010. *Guidelines for Converting between Various Wind Averaging Periods in Tropical Cyclone Conditions*, World Meteorological Organization, Geneva, Switzerland, Report WMO/TD # 1555, p. 5.
10. C. Clauss, E. Lehmann and C. Ostergaard, 1992. *Offshore Structures, Volume I: Conceptual Design and Hydromechanics*, Springer-Verlag, London, pp. 66–67.
11. I. Holland, O.T. Gudmestad and E. Jersin, 2000. *Design of Offshore Concrete Structures*, Spon Press, New York, p. 35.
12. American Petroleum Institute First Edition, 1993. *Recommended Practice for Planning, Designing and Constructing Fixed Offshore Platforms – Load Resistance Factor Design—API-RP 2A-LRFD*, 226 pp. Also American Petroleum Institute (2002), API RP 2A – WSD: Recommended Practice for Planning, Designing and Constructing Fixed Offshore Platforms, 21st Edition.
13. American Concrete Institute, Farmington Hills, Michigan, 1997. *Guide for the Design and Construction of Fixed Offshore Concrete Structures*, ACI 357R-84 (reaffirmed 1997).
14. American Bureau of Shipping (ABS), 1997. *Rules for Building and Classing Offshore Installations*, Special Committee on Offshore Installations, New York.
15. British Standards Institution, 1982. *BS 6235: Code of Practice for Fixed Offshore Structures*, London, England. Also BS ISO 19903, Petroleum and Natural Gas Industries, 2006. Fixed Concrete Offshore Structures.
16. UK Department of Energy, 1990. *DoE Offshore Installations: Guidance on Design and Construction*.
17. Lloyds Register of Shipping, 1988. *LRS Code for Offshore Platforms*, London.
18. Det Norske Veritas, 1989. DnV: Rules for the classification of fixed offshore installations, Det Norske Veritas (DnV), Hovik, Norway. Also: DnV-OS-C502. Offshore Concrete Structures, 2004-07; DnV-OS-C503. Concrete LNG Terminal Structures and Containment Systems; DnV-OSS-102. Rules for Classification of Floating Production and Storage Units; DnV-OSS-103. Rules for Classification of LNG/LPG Floating Production and Storage Units of Installations.
19. Bureau Veritas, 1975. *BV: Rules and Regulations for the Construction and Classification of Offshore Platforms*, Paris.
20. Canadian Standards Association (CSA), Code for the Design, Construction, and Installation of Fixed Offshore Structures: S471-04. General Requirements, Design Criteria, the Environment, and Loads; S474-04. Concrete Structures; S472-04: Foundations. S475-03: Sea Operations.
21. H.G. Poulos, 1988. *Marine Geotechnics*, Unwin Hyman, London, p. 207.
22. E.T.R. Dean, 2010. *Offshore Geotechnical Engineering: Principles and Practice*, Thomas Telford Limited, London, p. 326.
23. S. Lacasse and T.B. D’Orazio, 1988. Soil reaction stresses on offshore gravity platforms, *ASCE Journal of Geotechnical Engineering*, Volume 114, Issue 11, pp. 1277–1299.
24. K.J. McNanus and N.R.R. Burdon, 2001. *Lateral Resistance of Shallow Foundations*, NSSEE Conference, Paper # 6.03.1, 11 pp.
25. J.D. Murff and T.W. Miller, 1977. *Stability of Offshore Gravity Structure Foundations by the Upper Bound Method*, Proceedings of Offshore Technology Conference, Houston, TX, Paper # OTC 2896, Volume 3, pp. 147–154.
26. E.T.R. Dean, 2010. *Offshore Geotechnical Engineering: Principles and Practice*, Thomas Telford Limited, London, pp. 302–314.
27. R.C. Chaney and K.R. Demars, 1991. Offshore structure foundations, in: *Foundation Engineering Handbook*, 2nd Edition, edited by H.Y. Fang, Van Nostrand Reinhold, New York, pp. 704–711.
28. B.J. Watt, 1976. General practice for gravity structures (article 14), Gravity structures – Installation and other problems (article 15), *Offshore Soil Mechanics*, Course Lecture Notes of a course held at Cambridge University, London, pp. 271–284; 285–307.
29. American Petroleum Institute, 1993. API-RP 2A-LRFD, *Recommended Practice for Planning, Designing and Constructing Fixed Offshore Platforms – Load Resistance Factor Design—API-RP 2A-LRFD*, 1st Edition, pp. 75–77; 195–200.
30. American Petroleum Institute, 1993. API-RP 2A-LRFD, *Recommended Practice for Planning, Designing and Constructing Fixed Offshore Platforms – Load Resistance Factor Design—API-RP 2A-LRFD*, 1st Edition, pp. 75–77.
31. A.G. Young, L.M. Kraft and J.A. Focht, 1975. *Geotechnical considerations in Foundation Design of Offshore Gravity Structures*, Proceedings of 7th Annual Offshore Technology Conference, held at Houston, TX, Paper # OTC 2371, pp. 367–386.
32. O. Eide, and K.H. Andersen, 1984. *Foundation Engineering for Gravity Structures in the Northern North Sea*, Publication # 154, Norwegian Geotechnical Institute, Norway.



33. E.T.R. Dean, 2010. *Offshore Geotechnical Engineering: Principles and Practice*, Thomas Telford Limited, London, pp. 318–321.
34. R.C. Chaney and K.R. Demars, 1991. Offshore structure foundations, in: *Foundation Engineering Handbook*, 2nd Edition, edited by H.Y. Fang, Van Nostrand Reinhold, New York, p. 705.
35. R. Lauritzen and K. Schjetne, 1976. *Stability calculations for offshore gravity structures*, Proceedings of VIII Offshore Technology Conference, Houston, Texas, Paper # OTC2431B, Volume II, Paper # 2431, pp. 76–82.
36. K.H. Andersen, 1991. Foundation design of offshore gravity structures, in: *Cyclic Loading of Soils*, edited by M.P. O'Reilly and S.F. Brown, Blackie Limited, London, pp. 122–173.
37. M. Georgiadis and P. Michalopoulos, 1988. Bearing capacity of gravity base on layered soils, *ASCE Journal of Geotechnical Engineering*, Volume 111, Issue 6, pp. 712–729.
38. A.M. Puzrin and M.F. Randolph, 2003. Generalized framework for three-dimensional upper bound limit analysis in Tresca material, *Journal of Applied Mechanics*, Volume 70, Issue 1, pp. 91–100.
39. M.F. Randolph and S. Gourvenec, 2011. *Offshore Geotechnical Engineering*, Spon Press, New York.
40. B.M. Das, 1997. *Advanced Soil Mechanics*, Taylor and Francis, Washington, DC, pp. 49–96, 399–425.
41. J.E. Bowles, 1979. *Physical and Geotechnical Properties of Soils*, McGraw-Hill Book Co., New York, pp. 273–345.
42. H.G. Poulos and E.H. Davies, 1974. *Elastic Solutions for Soil and Rock Mechanics*, John Wiley & Sons Inc., New York.
43. J. Boussinesq, 1938. *The Distribution of Pressure Under a Uniformly loaded Elastic Strip Resting on Elastic-Isotropic Ground*, IInd Congress of IABSE, Berlin, Germany, Final Report, Volume 2, pp. 144–149.
44. R. Mindlin, 1936. Force at a point in the interior of a semi-infinite solid, *Physics*, Volume 7, pp. 195–202.
45. D'Appolonia, H.G. Poulos and C.C. Ladd, 1971. Initial settlement of spread footings on clay, *Journal of Soil Mechanics and Foundation Division, ASCE*, Volume 97, Issue SM10, pp. 1359–1378.
46. J.P. Schmertmann and J.P. Hartman, 1978. Improved strain influence factor diagrams, *Journal of Geotechnical Engineering Division, ASCE*, Volume 104, Issue GT 8, pp. 1131–1135.
47. R.E. Olsen, 1977. Consolidation under time dependent loading, *ASCE Journal of the Geotechnical Engineering Division*, Volume 103, Issue GT1, pp. 55–60.
48. R.E. Olson and J. Lai, 2002. Application of Terzaghi's theory of consolidation to problems involving radial flow, unit 4, in: *Advanced Soil Mechanics*, Department of Construction Engineering, Chaoyang University of Technology, Taiwan, pp. 50–67.
49. E.T.R. Dean, 2010. *Offshore Geotechnical Engineering: Principles and Practice*, Thomas Telford Limited, London, pp. 158–165.
50. G. Mesri and B. Vardhanabhuti, 2005. Secondary compression, *ASCE Journal of Geotechnical and Geoenvironmental Engineering*, Volume 131, Issue 3, pp. 398–401.
51. B.M. Das, 1997. *Advanced Soil Mechanics*, 2nd Edition, Taylor and Francis, Washington, DC, pp. 431–435.
52. J.P. Johnson, D.W. Rhett and W.T. Siemers, 1988. *Rock Mechanics in the Ekofisk Reservoir in the Evaluation of Subsidence*, Proceedings of Offshore Technology Conference, Houston, TX, Paper # 5621.
53. T.H. Dawson, 1983. *Offshore Structural Engineering*, Prentice Hall Inc., Englewood Cliffs, NJ, p. 194.
54. I. Holland, O.T. Gudmestad and E. Jersin, 2000. *Design of Offshore Concrete Structures*, Spon Press, New York, p. 52.
55. I. Holland, O.T. Gudmestad and E. Jersin, 2000. *Design of Offshore Concrete Structures*, Spon Press, New York, p. 53.
56. I. Holland, O.T. Gudmestad and E. Jersin, 2000. *Design of Offshore Concrete Structures*, Spon Press, New York, p. 54.
57. I. Holland, O.T. Gudmestad and E. Jersin, 2000. *Design of Offshore Concrete Structures*, Spon Press, New York, p. 60.
58. G.S. Epperson, 1992. Gravity platforms, lecture 6, in: *Overview of Offshore Engineering*, Course Notes, Houston, TX, pp. 48.
59. R. Nataraja and C.L. Kirk, 1977. *Dynamic Response of a Gravity Platform Under Random Wave Forces*, Proceedings of Offshore Technology Conference, Houston, TX, Paper # 2904, pp. 199–209.
60. US Army Corps of Engineers, 1984. *Shore Protection Manual Volume I*, 4th Edition, Department of the Army, Waterways Experimental Station, Corps of Engineers, Coastal Engineering Research Center, Vicksburg, MS, Tables C-1, C-2 and C-3.
61. R.C. MacCamy and R.A. Fuchs, 1954. *Wave Forces on Piles: A Diffraction Theory*, U.S. Army Coastal Engineering Center, Technical memorandum # 69.

62. M. Rahman, S.N. Bora and M.G. Satish, 1999. A note on second-order wave forces on a circular cylinder in finite water depth, *Applied Mechanics Letters*, Volume 12, pp. 63–70.
63. The Engineering ToolBox, Available at [http://www.engineeringtoolbox.com/air-absolute-kinematic-viscosity-d\\_601.html](http://www.engineeringtoolbox.com/air-absolute-kinematic-viscosity-d_601.html). Accessed November 7, 2011.
64. Society of Amateur Scientists, 2004. *Engineering Material Properties*. Available at <http://www.sas.org/engineerByMaterial.html>. Accessed November 7, 2011.
65. T.H. Dawson, 1983. *Offshore Structural Engineering*, Prentice Hall, Inc., Englewood Cliffs, NJ, p. 218.
66. I. Holland, O.T. Gudmestad and E. Jersin, 2000. *Design of Offshore Concrete Structures*, Spon Press, New York, pp. 60–62.
67. E.G. Nawy, 2003. *Reinforced Concrete: A Fundamental Approach*, Prentice Hall – Pearson Education, Inc., Upper Saddle River, NJ, pp. 615–617.
68. T.H. Dawson, 1983. *Offshore Structural Engineering*, Prentice Hall, Inc., Englewood Cliffs, NJ, pp. 200–202.
69. N.D. Albertson, 1973. In *Influence of compressive strength and wall thickness on behavior of concrete cylindrical hulls under hydrostatic loading*, Technical Report R-790, Naval Civil Engineering Laboratory, Port Hueneme, CA, p. 10.
70. J.H. Evans and J.C. Adams, 1969. *Ocean Engineering Structures, Volume I (Course Notes)*, The MIT Press, Cambridge, MA, p. 83.
71. L.F. Kahn, 1971. In *Influence of end-closure stiffness on behavior of concrete cylindrical hulls subjected to hydrostatic loading*, Technical Report R-740, Naval Civil Engineering Laboratory, Port Hueneme, CA, p. 27.
72. D.P. Billington, 1982. *Thin Shell Concrete Structures*, McGraw-Hill Book Company, New York, pp. 110–113.
73. J.F. Wilson, *Dynamics of Offshore Structures*, John Wiley, New York, 1984, p. 30.
74. P. Le Tirant, 1979. *Seabed Reconnaissance and Offshore Soil Mechanics for the Installation of Petroleum Structures*, Editions Technip, Paris, p. 352.
75. P. Le Tirant, 1979. *Seabed Reconnaissance and Offshore Soil Mechanics for the Installation of Petroleum Structures*, Editions Technip, Paris, p. 358.
76. P. Le Tirant, 1979. *Seabed Reconnaissance and Offshore Soil Mechanics for the Installation of Petroleum Structures*, Editions Technip, Paris, p. 356.
77. P. Le Tirant, 1979. *Seabed Reconnaissance and Offshore Soil Mechanics for the Installation of Petroleum Structures*, Editions Technip, Paris, p. 384.
78. T.H. Dawson, 1983. *Offshore Structural Engineering*, Prentice Hall, Inc., Englewood Cliffs, NJ, p. 267.
79. T.H. Dawson, 1983. *Offshore Structural Engineering*, Prentice Hall, Inc., Englewood Cliffs, NJ, p. 201 and 206.
80. T.H. Dawson, 1983. *Offshore Structural Engineering*, Prentice Hall, Inc., Englewood Cliffs, NJ, p. 227.
81. Cranfield Institute of Technology, 1974. Lecture Notes on Wave Forces on Offshore Structures, Examination held on January 1974.
82. T.H. Dawson, 1983. *Offshore Structural Engineering*, Prentice Hall, Inc., Englewood Cliffs, NJ, p. 208.
83. Cranfield Institute of Technology, 1977. Lecture Notes on Wave Forces on Offshore Structures, Examination held on January 1977.

# Essentials of Offshore Structures

## Framed and Gravity Platforms

“The authors are extremely well known in this subject and have produced an excellent book suitable for students and graduates working in the field of offshore structure design. The book is thoroughly recommended.”

—Professor William Dover, Emeritus Shell Professor, University College London

*Essentials of Offshore Structures: Framed and Gravity Platforms* presents a clear demonstration of both the theory and application of the relevant procedures of structural, fluid, and geotechnical mechanics to offshore structures. It provides a multitude of solved problems and sample problems to solve that offers readers a strong understanding of the analysis and design of steel-framed and base-supported concrete gravity offshore structures.

The book highlights sensible engineering applications for offshore structural design, research, and development. It includes material on preliminary costing, structural form and design, assembly of components, environmental characteristics of the construction site, factors governing the material choice, forces acting on the installed structure, and overall structural design.

Separate chapters detail the factors that influence the pile embedment and concrete gravity foundation characteristics, material choice including fatigue and corrosion, estimation of ocean environmental forces that will be exerted on the offshore structures, and other analysis fundamentals that the reader needs to possess. The final two chapters give detailed insights into the analysis and design of framed and concrete gravity platform offshore structures using API code procedures. The book includes practical problems with worked solutions at the end of each chapter, more than 200 illustrations, and an inclusive presentation of the analysis and design of steel and concrete offshore structures.

68822

